

AD-A215 024

DTIC ACCESSION NUMBER

LEVEL

PHOTOGRAPH THIS SHEET

DTIC FILE COPY

INVENTORY

AFOSR-TR-89-1508

DOCUMENT IDENTIFICATION

JUN 1979

DISTRIBUTION STATEMENT A

Approved for public release;  
Distribution Unlimited

DISTRIBUTION STATEMENT

ACCESSION FOR

NTIS GRA&I ☒

DTIC TAB ☐

UNANNOUNCED ☐

JUSTIFICATION

BY

DISTRIBUTION /

AVAILABILITY CODES

DIST

AVAIL AND/OR SPECIAL

A-1

DISTRIBUTION STAMP

QUALITY  
INSPECTED  
1

DTIC  
ELECTE  
DEC 04 1989  
S E D

DATE ACCESSIONED

DATE RETURNED

89 11 29 107

DATE RECEIVED IN DTIC

REGISTERED OR CERTIFIED NO.

PHOTOGRAPH THIS SHEET AND RETURN TO DTIC-PDAC



IEEE  
2nd International  
Pulsed Power Conference

AD-A215 024

SouthPark Inn  
Lubbock, Texas  
June 12-14, 1979

**Joint Sponsors:**

South Plains Section IEEE  
Air Force Aero Propulsion Laboratory  
Air Force Office of Scientific Research  
Electronics Technology  
and Devices Laboratory, U.S. Army  
Naval Surface Weapons Center  
Office of Naval Research  
Office of Laser Fusion  
Office of Fusion Energy



Digest of  
Technical Papers

**Editors:**

A. H. Guenther  
M. Kristiansen

## REPORT DOCUMENTATION PAGE

Form Approved  
OMB No. 0704-0188

1a. REPORT SECURITY CLASSIFICATION			1b. RESTRICTIVE MARKINGS		
2a. SECURITY CLASSIFICATION AUTHORITY			3. DISTRIBUTION/AVAILABILITY OF REPORT Approved for public release; distribution unlimited.		
2b. DECLASSIFICATION/DOWNGRADING SCHEDULE					
4. PERFORMING ORGANIZATION REPORT NUMBER(S)			5. MONITORING ORGANIZATION REPORT NUMBER(S) <b>AFOSR-TR. 89-1508</b>		
6a. NAME OF PERFORMING ORGANIZATION Department of Electrical Engineering		6b. OFFICE SYMBOL (if applicable)		7a. NAME OF MONITORING ORGANIZATION  AFOSR	
6c. ADDRESS (City, State, and ZIP Code) Texas Tech University Lubbock, TX		7b. ADDRESS (City, State, and ZIP Code) BLDG 410 BAFB DC 20332-6448			
8a. NAME OF FUNDING/SPONSORING ORGANIZATION AFOSR		8b. OFFICE SYMBOL (if applicable)		9. PROCUREMENT INSTRUMENT IDENTIFICATION NUMBER  AFOSR 79-0077	
8c. ADDRESS (City, State, and ZIP Code)  BLDG 410 BAFB DC 20332-6448		10. SOURCE OF FUNDING NUMBERS			
		PROGRAM ELEMENT NO. 61102F	PROJECT NO. 2301	TASK NO. A7	WORK UNIT ACCESSION NO.
11. TITLE (Include Security Classification)  IEE. 3 International Pulsed Power Conference					
12. PERSONAL AUTHOR(S) A.H. Guenther/ M. Kristiansen					
13a. TYPE OF REPORT Final		13b. TIME COVERED FROM _____ TO _____		14. DATE OF REPORT (Year, Month, Day) Feb 80	
15. PAGE COUNT 521					
16. SUPPLEMENTARY NOTATION					
17. COSATI CODES			18. SUBJECT TERMS (Continue on reverse if necessary and identify by block number)		
FIELD	GROUP	SUB-GROUP			
19. ABSTRACT (Continue on reverse if necessary and identify by block number)					
20. DISTRIBUTION/AVAILABILITY OF ABSTRACT <input checked="" type="checkbox"/> UNCLASSIFIED/UNLIMITED <input type="checkbox"/> SAME AS RPT <input type="checkbox"/> DTIC USERS					
21. ABSTRACT SECURITY CLASSIFICATION unclassified					
22a. NAME OF RESPONSIBLE INDIVIDUAL			22b. TELEPHONE (Include Area Code) 767-4904		22c. OFFICE SYMBOL NP

~~AFOSR-TR-89-0045~~

DIGEST OF TECHNICAL PAPERS  
2nd IEEE International Pulsed Power Conference

SouthPark Inn  
Lubbock, Texas  
June 12-14, 1979

~~AFOSR-TR-89-1508~~



Editors

A. H. Guenther  
Air Force Weapons Laboratory  
Chairman, Technical Program  
Committee

M. Kristiansen  
Dept. of Electrical Engineering  
Texas Tech University  
Conference Chairman

2nd IEEE Pulsed Power Conference Joint Sponsors: South Plains Section IEEE, Air Force Aero Propulsion Laboratory, Air Force Office of Scientific Research, Electronics Technology and Devices Laboratory, U. S. Army, Naval Surface Weapons Center, Office of Naval Research, Office of Laser Fusion, Office of Fusion Energy.



*"The views and conclusions contained in this document are those of the authors and should not be interpreted as necessarily representing the official policies or endorsements, either expressed or implied, of the South Plains Section IEEE, Air Force Aero Propulsion Laboratory, Air Force Office of Scientific Research, Electronics Technology and Devices Laboratory, U.S. Army, Naval Surface Weapons Center, Office of Naval Research, Office of Laser Fusion, Office of Fusion Energy, or the U.S. Government."*

Library of Congress Catalog Card Number 79-90330  
IEEE Catalog Number 79CHI505-7



## PREFACE

Pulsed power in all its varied meanings is showing no sign of abatement in activity. It is becoming a technology of increasing importance in numerous new and novel applications, growing from its well-established base in energy and defense related research and development. One indication of its vitality is this Digest of Technical Papers for the 2nd IEEE International Pulsed Power Conference. The organizers were counseled by many that there would not be enough material that could be covered at this meeting nor would there be a sufficient diversity of interest. However, from our first such conference during November 1976, held in Lubbock as well, we have recorded a fifty percent increase in attendance to almost 300, with well over 100 invited and contributed presentations. There were twenty-five attendees from 10 foreign countries including Belgium, Canada, Denmark, England, France, Israel, Japan, Poland, the USSR, and West Germany.

As a result of this growth and with the realization that this conference serves as the principal forum for the exchange of information in the highly specialized and unique field of pulsed power technology, several actions and events have taken place. First, the present technical program committee, which adequately insures that the interests of the principal players in the field will be served, have been designated a permanent standing committee to organize and maintain this conference series. Secondly, we have agreed to hold this meeting biennial, alternating with the well-known Modulator Symposium. It is our present intention that the 3rd IEEE International Pulsed Power Conference will be held in Albuquerque, NM during 1981 with Art Guenther of the Air Force Weapons Laboratory as Conference Chairman and Tom Martin of Sandia Laboratories,

Albuquerque, as Chairman of the Technical Program Committee.

One interesting sidelight of this years meeting was a contest to select a conference symbol which could be used with all future meetings and correspondence. We wished the symbol to be easily recognized and to uniquely depict pulse power. To our pleasant surprise almost fifty entries were received and from these the Technical Program Committee selected the symbol shown on the title page of these proceedings. The winner was Capt. Charles W. Schubert, Jr. of the U.S. Air Force Flight Dynamics Laboratory, Wright-Patterson AFB, Ohio. He received a Texas Instruments TI-59 fully programmable calculator graciously donated by the manufacturer. Congratulations to Capt. Schubert and many thanks to TI.

Our conference had the distinct honor of being able to recognize the many contributions of Mr. Peter Haas to the development of pulse power technology in the United States. Mr. Haas recently retired from his position as Deputy Director for Science and Technology, Defense Nuclear Agency, after a distinguished career in the Federal Civil Service. We all recognize that he has not really retired but just entered into another role and we can count on his continued vigorous and outspoken support for further development in pulsed power technology.

Besides the excellent technical content and Texas hospitality, the meeting could not have transpired without the sponsorships of several key organizations. Thus we would like to call your special attention to the following sponsors:

The Air Force Aero Propulsion Laboratory

The Air Force Office of Scientific Research

The Electronics Technology and Devices  
Laboratory, U.S. Army

The Naval Surface Weapons Center and

The Office of Naval Research; all of

The Department of Defense, and from the Department of Energy;

The Office of Laser Fusion and the Office of Fusion Energy.

The Conference was most effectively organized locally by the Department of Electrical Engineering, Texas Tech University under Dr. Russell H. Seacat, Chairman, and the South Plains Section of IEEE, Lewis Thomas, Section President, with Travis Simpson, Martha Smith, and Deanya Wood of the Texas Tech EE Department, as Local Chairman, Conference Secretary, and Secretarial Assistant, respectively. To all of these people go our deepest appreciation and a hardy "well-done"!

To those who worked so diligently on the organization and preparation of the 2nd IEEE-PPC, may we add our sincere appreciation and thanks. See you in Albuquerque in '81.

A. H. Guenther  
Air Force Weapons Lab.  
Chairman, Tech. Program Committee

M. Kristiansen  
Texas Tech University  
Conference Chairman

Presentation  
at  
Award Luncheon  
June 13, 1979  
SPECIAL AWARD



Peter Haas  
Defense Nuclear Agency  
Retired

"For many contributions to a strong and vigorous pulse power program through sound management, steadfast conviction and farsighted technical acumen".

## 2nd International IEEE Pulsed Power Conference

### Technical Program Committee

A. H. Guenther, Chairman  
Air Force Weapons Lab.  
Kirtland AFB  
Albuquerque, NM 87117

T. R. Burkes  
Texas Tech Univ.  
Dept. of Elect. Eng.  
Lubbock, TX 79409

J. Farber  
Defense Nuclear Agency  
Washington, DC 20305

R. Fitch  
Maxwell Labs.  
Precipco, Inc.  
9244 Balboa Ave.  
San Diego, CA 92123

W. Gagnon  
Lawrence Livermore Lab.  
P.O. Box 808  
Livermore, CA 94550

A. S. Gilmour, Jr.  
State Univ. of New York/Buffalo  
4232 Ridge Lea Rd.  
Amherst, NY 87545

R. Gullickson  
AFOSR/NP, Bolling AFB  
Washington, DC 20332

E. Kemp  
Los Alamos Scientific Lab.  
P.O. Box 1663  
Los Alamos, NM 87545

T. Martin  
Sandia Lab.  
Dept. 4250  
Albuquerque, NM 87113

M. F. Rose  
Naval Surface Weapons Center  
Code F-404  
Dahlgren, VA 22448

S. Schneider  
U.S. Army Electronics Technology  
and Devices Lab.  
Ft. Monmouth, NJ 07703

I. Smith  
Ian Smith, Inc.  
3115 Gibbons Dr.  
Alameda, CA 94501

P. Turchi  
Naval Research Lab.  
Code 6770  
Washington, DC 20375

R. L. Verga  
Air Force Aero Propulsion Lab.  
POD  
Wright-Patterson AFB, OH 45433

### Local Organization Committee

Travis L. Simpson  
Local Chairman  
Texas Tech Univ.

Martha Smith  
Conference Secretary  
Texas Tech Univ.

Deanya Wood  
Secretarial Assistant  
Texas Tech Univ.

**2nd IEEE International Pulsed Power Conference  
South Park Inn, Lubbock, Texas**

	Navajo Room	Aztec Room	Bronze Room	Mayan Room	Other
<b>MONDAY, June 11:</b> 8:00 p.m.-10:00 p.m.	Registration				
<b>TUESDAY, June 12</b> 8:00 a.m.- 5:00 p.m.	Registration				
9:00 a.m.- 9:30 a.m.		Opening Session			
9:30 a.m.-11:00 a.m.		Plenary Session I			
11:00 a.m.-11:20 a.m.					Coffee-Patio
11:20 a.m.-12:20 p.m.		I-Electron and Ion Diodes	II-Magnetic Components	III-Power Conditioning I	
12:20 p.m.- 1:45 p.m.					Lunch
1:45 p.m. - 3:15 p.m.		IV-Breakdown Mechanisms	V-Novel Applications	VI-Power Conditioning II	
3:15 p.m.- 3:35 p.m.					Coffee-Patio
3:35 p.m.- 5:05 p.m.		VII-Switching I	VIII-Accelerators I	IX-Power Conditioning III	
5:00 p.m.- 8:00 p.m.					Cocktail Party Patio (Hosted by IEEE South Plains Sect.)
<b>WEDNESDAY, June 13</b> 8:00 a.m.- 5:00 p.m.	Registration				
9:00 a.m.-10:30 a.m.		Plenary Session II			
10:30 a.m.-10:50 a.m.					Coffee-Patio
10:50 a.m.-12:05 p.m.		X-Switching II	XI-Applications I	XII-Inductive and Capacitive Energy Storage Systems I	
12:05 p.m. - 2:00 p.m.					Conference Luncheon- Patio
2:00 p.m. - 3:15 p.m.		XIII-Switching III	XIV-Electro-Mechanical Energy Storage Systems I	XV-Inductive and Capacitive Energy Storage Systems II	
3:15 p.m. - 3:35 p.m.					Coffee-Patio
3:35 p.m. - 5:05 p.m.		XVI-Switching IV	XVII-Electro-Mechanical Energy Storage Systems II	XVIII-Diagnostics and Miscellaneous	
<b>THURSDAY, June 14</b> 9:00 a.m.-10:30 a.m.		Plenary Session III			
10:30 a.m.-10:50 a.m.					Coffee-Patio
10:50 a.m.-12:05 p.m.		XIX-Switching V	XX-Applications II	XXI-Vacuum Power Flow	
12:05 p.m. - 1:30 p.m.					Lunch
1:30 p.m. - 3:00 p.m.		XXII-Post Deadline Papers (See Bulletin Board)			
3:00 p.m. - 5:30 p.m.					Tours of Pulsed Power, Plasma, and Laser Research Facilities at Texas Tech Univ

Library of Congress Catalog Card Number 79-90330

IEEE Catalog Number 79CH1505-7

## TABLE OF CONTENTS

### Plenary Session I:

Chairman: A. H. Guenther,  
Air Force Weapons Lab.

- P1.1 Overview of Inertial Confinement Fusion (Invited)  
G. Canavan . . . . . 1
- P1.2 Pulsed Power for Fusion (Invited)  
T. H. Martin . . . . . 3
- P1.3 Pulsed High-Current Electron Technology (Invited)  
G. A. Mesyats . . . . . 9

### Plenary Session II:

Chairman: A. Kolb,  
Maxwell Lab.

- P2.1 New Hydrogen Thyratrons for Advanced High Power Switching (Invited)  
D. Turnquist, R. Caristi, S. Friedman, S. Merz, R. Plante, N. Reinhardt . . . . . 17
- P2.2 Accelerator Module of "Angara-5" (Invited)  
S. V. Basenkov, O. A. Gusev, Ju. A. Istomin, Ju. V. Koba, G. M. Latmanizova, A. M. Pasechnikov, B. P. Pevchev, O. P. Pecherskii, A. S. Perlin, L. I. Rudakov, V. P. Smirnov, V. I. Chetvertkov, I. R. Jampol'skii . . . . . 25
- P2.3 Review and Status of Antares (Invited)  
J. Jansen . . . . . 31

### Plenary Session III:

Chairman: E. Abramyan, Institute of High Temperatures, USSR

- P3.1 Electromagnetic Guns, Launchers and Reaction Engines (Invited)  
H. Kohn, K. Fine, F. Williams, P. Mongeau . . . . . 42
- P3.2 The Near and Long Term Pulse Power Requirements for Laser Driven Inertial Confinement Fusion (Invited)  
W. L. Gagnon, E. K. Freytag, R. Fitch . . . . . 49

### Session I: Electron and Ion Diodes

Chairman: R. Detweiler, AF  
Office of Scientific Research

- 1.1 Repetitively Pulsed Electron Beam Diode Lifetime and Stability  
M. T. Buttram . . . . . 61
- 1.2 Voltage Distribution and Current in a Cylindrical Relativistic Diode  
N. W. Harris . . . . . 63
- 1.3 Simulations of Intense Relativistic Electron Beam Generation by Foilless Diodes  
M. E. Jones, L. E. Thode . . . . . 68
- 1.4 Ion Beam Generation Through a Moving Plasma Boundary  
M. Dembinski, P. K. John . . . . . 72

### Session II: Magnetic Components

Chairman: K. Freytag,  
Lawrence Livermore Lab.

- 2.1 Fundamental Limitations and Design Considerations for Compensated Pulsed Alternators (Invited)  
K. M. Tolik, W. F. Weldon, M. D. Driga, W. L. Bird, H. H. Woodson, H. G. Rylander . . . . . 76
- 2.2 Use of Transformers in Producing High Power Output from Homopolar Generators  
W. H. Lupton, R. D. Ford, H. B. Lindstrom, I. M. Vitkovitsky, D. Conte . . . . . 83
- 2.3 Design of Pulse Transformers for PFL Charging  
G. J. Rohwein . . . . . 87

### Session III: Power Conditioning I

Chairman: R. Fontana, Air Force  
Institute of Technology

- 3.1 Pulse Sharpening in Ferrite Transmission Lines  
M. Weiner . . . . . 91

- 3.2 High Power Pulse Modeling of Co-axial Transmission Lines  
J. P. O'Loughlin. . . . . 96
- 3.3 Light Activated 10 kV Low Jitter Pulser  
J. D. Galbraith . . . . . 100
- 3.4 Command Charge Using Saturable Inductors  
S. Black, T. R. Burkes . . . . . 102

#### Session IV: Breakdown Mechanisms

Chairman: R. Fitch,  
Maxwell Lab.

- 4.1 Investigations of Fast Insulator Surface Flashover (Invited)  
J. E. Thompson, J. Lin, K. Mikkelsen, M. Kristiansen . . . . . 106
- 4.2 Breakdown in Small, Flowing Gas Spark Gaps  
W. K. Cary, Jr., D. D. Lindberg, J. W. Rice . . . . . 114
- 4.3 Electron Densities in Laser-Trig-gered Spark Gap Discharges  
R. J. Crumley, P. F. Williams, M. A. Gundersen, A. Watson . . . . . 119
- 4.4 Electrical Breakdown in Water in the Microsecond Regime  
D. B. Fenneman, R. Gripshover . . . . . 122
- 4.5 Pulsed Electron Field Emission From Prepared Conductors  
G. B. Frazier . . . . . 127

#### Session V: Novel Applications

Chairman: J. Farber,  
Defense Nuclear Agency

- 5.1 Investigation Into Triggering Lightning with a Pulsed Laser  
C. W. Schubert, Jr., J. R. Lippert . . . . . 132
- 5.2 Long ARC Simulated Lightning Attachment Testing Using a 150 kW Tesla Coil  
R. K. Golka . . . . . 136

- 5.3 High Density Z-Pinch Pulse-Power Supply System  
W. C. Nunnally, L. A. Jones, S. Singer . . . . . 142
- 5.4 The Design of Solenoids for Generating High Magnetic Fields  
P. Byszewski . . . . . 148
- 5.5 Analysis of a Distributed Pulse Power System Using a Circuit Analysis Code  
L. O. Hoeft . . . . . 149
- 5.6 Determination of Line Voltage In Self-Magnetically Insulated Flows  
C. W. Mendel, Jr., J. P. VanDevender, G. W. Kuswa . . . . . 153

#### Session VI: Power Conditioning II

Chairman: T. R. Burkes,  
Texas Tech University

- 6.1 Versatile High Energy Capacitor Discharge System  
V. N. Martin . . . . . 157
- 6.2 A 130 kV Low Impedance Multiple Output Trigger Generator  
A. H. Bushnell and C. S. Dobbie, A. P. Krickhuhn . . . . . 161
- 6.3 Low-Impedance, Coaxial-Type Marx Generator with a Quasi-Rectangular Output Waveform (Invited)  
M. Obara, Y. Sakato, C. K. Lee, T. Hashimoto, T. Fujioka . . . . . 165
- 6.4 The Design Approach to a High-Voltage Burst Generator (Invited)  
D. B. Cummings, H. G. Hammon, III . . . . . 172

#### Session VII: Switching I

Chairman: B. Bernstein,  
Physics International



- 7.1 High Pressure Surface Spark Gaps  
W. J. Sarjeant, A. J. Alcock,  
K. E. Leopold . . . . .179
- 7.2 Parallel Combinations of Pre-Ionized, Low Jitter Spark Gaps  
W. A. Fitzsimmons and L. Rosocha.184
- 7.3 A Streamer Model for High Voltage Water Switches  
F. J. Sazama, V. L. Kenyon, III .187
- 7.4 Low Prepulse, High Power Density Water Dielectric Switching  
D. J. Johnson, J. P. VanDevender,  
T. H. Martin. . . . .191
- 7.5 Contacts for Pulsed High Current; Design and Test  
P. Wildi . . . . .195
- 7.6 The Early Counterpulse Technique Applied to Vacuum Interrupters  
R. W. Warren . . . . .198

#### Session VIII: Accelerators

Chairman: I. Smith,  
Ian Smith, Inc.

- 8.1 Development of High Current Electron Pulse Accelerators (Invited)  
E. Abramyan, G. D. Kuleshov . . .202
- 8.2 Status of the Upgraded Version of the NRL Gamble II Pulse Power Generator  
J. R. Boller, J. K. Burton, J. D. Shipman, Jr. . . . .205
- 8.4 Emittance Measurements on Field Emitter Diodes  
B. Kulke, R. Kihara . . . . .209
- 8.5 On the Development of a Repetitively Pulsed Electron Beam System  
G. A. Tripoli . . . . .214

#### Session IX: Power Conditioning III

Chairman: R. Verga, Air Force  
Aero Propulsion Lab.

- 9.1 Development of High Repetition-Rate Pulse Power Generators  
R. J. Sojka, G. K. Simcox . . .217

- 9.2 Frozen-Wave Hertzian Generators: Theory and Applications  
M. L. Forcier, M. F. Rose, L. F. Rinehart, R. J. Gripshover. . . .221
- 9.3 A 500 kV Rep-Rate Marx Generator (Invited)  
J. Shannon . . . . .226
- 9.4 A High Current Pulser for Experiment #225, "Neutrino Electron Elastic Scattering,"  
C. Dalton, G. Krausse, W. J. Sarjeant . . . . .232
- 9.5 KrF Laser-Triggered SF<sub>6</sub> Spark Gap for Low-Jitter Timing  
W. R. Rapaport, J. Goldhar,  
J. R. Murray, M. D'Addario . . .236

#### Session X: Switching: II

Chairman: R. Wasneski, Naval  
Air Systems Command

- 10.1 Effects of Surrounding Medium on the Performance of Exploding Aluminum Foil Fuses  
T. L. Berger . . . . .237
- 10.2 High Power, Very Long Pulse Testing of a 200 KV Tetrode Regulation Tube  
J. Stabley, B. Gray . . . . .242
- 10.3 Withdrawn
- 10.4 Very Fast, High Peak Power Planar Triode Amplifiers for Driving Optical Gates  
W. L. Gagnon, S. J. Davis,  
M. M. Howland . . . . .246
- 10.5 Vacuum Arc Switched Inverter Tests at 2.5 MVA  
R. N. Miller, A. S. Gilmour, Jr. .250

#### Session XI: Applications I

Chairman: J. Jansen, Los Alamos  
Scientific Labs

- 11.1 300-kJ, 200-kA Marx Module for Antares  
K. B. Riepe, J. Jansen, J. Bickford, W. Turner . . . . .254

- 11.2 A Large-Area Cold-Cathode Grid-Controlled Electron Gun for Antares  
W. R. Scarlett, K. R. Andrews,  
H. Jansen . . . . .261
- 11.3 The Antares Laser Power Amplifier  
R. D. Stine, G. F. Ross, C.  
Silvernail . . . . .265
- 11.4 A Double-Sided Electron Beam Generator for KrF Laser Excitation  
L. Schlitt . . . . .269
- 11.5 Electric Discharge Characteristics of Cable PFN Used as a Pump  
R. R. Butcher, S. H. Gurbaxani .273
- Session XII: Inductive and Capacitive Energy Storage Systems I
- Chairman: K. Whitcham,  
Lawrence Livermore Labs
- 12.1 Trident--A Megavolt Pulse Generator Using Inductive Energy Storage (Invited)  
D. Conte, R. D. Ford, W. H. Lupton, I. M. Vitkovitsky . . .276
- 12.2 Inductive Storage--Prospects for High Power Generation  
J. K. Burton, D. Conte, R. D. Ford, W. H. Lupton, V. E. Scherrer, I. M. Vitkovitsky . . . . .284
- 12.3 Considerations for Inductively Driven Plasma Implosions (Invited)  
D. L. Smith, R. P. Henderson, R. E. Reinovsky. . . . .287
- Session XIII: Switching III
- Chairman: E. Kunhardt,  
Texas Tech University
- 13.1 High Repetition Rate Miniature Triggered Spark Switch  
M. F. Rose, M. T. Glancy . . . .295
- 13.2 Surface Aging in High Repetition Rate Spark Switches with Aluminum and Brass Electrodes  
M. T. Glancy, M. F. Rose . . . .301
- 13.3 Spark Gap Erosion Results  
R. Petr, D. Barrett, T. R. Burkes. 308
- 13.4 Long-Life High-Repetition-Rate Triggered Spark Gap  
H. Watson . . . . .313
- 13.5 Testing of a 100 kV, 100 HZ, Rep-Rate Gas Switch  
A. Ramrus, J. Shannon. . . . .320
- Session XIV: Electro-Mechanical Energy Storage Systems I
- Chairman: P. Turchi, Naval Research Lab.
- 14.1 Rebuilding the Five MegaJoule Homopolar Machine at the University of Texas  
K. M. Tolh, J. H. Gully, R. C. Zowarka, M. Brennan, W. L. Bird, W. F. Weldon, H. G. Rylander, H. H. Woodson . . . . .325
- 14.2 Computer Aided Electrical Analysis of Homopolar Generator Driven, Bitter Plate Storage Inductors with Radial Current Diffusion  
D. J. T. Mayhall, H. G. Rylander, W. F. Weldon, H. H. Woodson . . . . .330
- 14.3 Testing and Analysis of a Fast Discharge Homopolar Machine (FDX) (Invited)  
T. M. Bullion, M. D. Driga, J. H. Gully, H. G. Rylander, K. M. Tolh, W. F. Weldon, H. H. Woodson, R. Zowarka . . . . .333
- 14.4 Pulsar: An Inductive Pulse Power Source  
E. C. Chare, W. P. Brooks, M. Cowan . . . . .343
- Session XV: Inductive and Capacitive Energy Storage Systems II
- Chairman: R. Ford, Naval Research Lab.

- 15.1 Preliminary Inductive Energy Transfer Experiments  
R. P. Henderson, D. L. Smith, R. E. Reinovsky . . . . . 347
- 15.2 Application of PFN Capacitors in High Power Systems  
R. D. Parker . . . . . 351
- 15.3 Withdrawn
- 15.4 Safety Grounding Switches in Large Experiments; General Considerations and the TEXT Application  
P. Wildi . . . . . 355
- 15.5 Inductance and Resistance Characteristics of Single-Site Untriggered Water Switches in Water Transfer Capacitor Circuits  
P. W. Spence, Y. G. Chen, G. Frazier, H. Calvin. . . . . 359
- Session XVI: Switching IV
- Chairman: S. Schneider, U.S. Army Electronics Technology and Devices Lab.
- 16.1 Hollow-Anode Multigap Thyratrons (Invited)  
H. Menown, C. V. Neale. . . . . 363
- 16.2 High Frequency Thyatron Evaluation  
G. Hill, T. R. Burkes . . . . . 364
- 16.3 Repetitive Electron Beam Controlled Switching  
R. F. Fernsler, D. Conte, I. M. Vitkovitsky . . . . . 368
- 16.4 Orientation Independent Ignitron  
R. J. Harvey, J. R. Bayless. . . 372
- 16.5 Stabilization of Metal-Oxide Bulk Switching Devices with Diffused Bi Contacts  
B. Lalevic, M. Shoga, M. Guishi, S. Levy . . . . . 376
- Session XVII: Electro-Mechanical Energy Storage Systems II
- Chairman: W. L. Gagnon, Lawrence Livermore Labs
- 17.1 Magnetic Optimization for Pulsed Energy Conversion  
W. K. Tucker, W. P. Brooks, R. E. Wilcox, W. D. Markiewicz, E. C. Chare . . . . . 381
- 17.2 Design of the Armature Windings of a Compensated Pulsed Alternator Engineering Prototype  
J. H. Gully, W. L. Bird, H. G. Rylander, W. F. Weldon, H. H. Woodson, T. M. Bullion . . . . . 385
- 17.3 The Mechanical Design of a Compensated Pulsed Alternator Prototype  
M. Brennan, W. L. Bird, J. H. Gully, M. L. Spann, K. M. Tolks, W. F. Weldon, H. G. Rylander, K. M. Tolks, W. F. Weldon, H. H. Woodson. 392
- 17.4 The Design, Assembly, and Testing of a Desk Model Compensated Pulsed Alternator  
M. Pichot, W. L. Bird, M. Brennan, M. D. Driga, J. H. Gully, H. G. Rylander, K. M. Tolks, W. F. Weldon, H. H. Woodson . . . . . 398
- 17.5 A Compressed Magnetic Field Generator Systems Model  
J. E. Gover . . . . . 402
- 17.6 Application of Subsystem Summary Algorithms for High Power System Studies  
F. C. Brockhurst . . . . . 406
- Session XVIII: Diagnostics and Miscellaneous
- Chairman: C. J. Jouys, Atomic Energy Commission, France
- 18.1 A Computerized Measuring System for Nanosecond Risetime Pulsed Accelerators  
D. Pellinen, S. Ashby, P. Gillis, K. Nielsen, P. Spence . . . . . 410
- 18.2 Withdrawn
- 18.3 A 33-GVA Interrupter Test Facility  
W. M. Parsons, E. M. Honig, R. W. Warren . . . . . 414

18.4 Analysis of the Multiphase Inductor-Converter Bridge M. Ehsani, R. L. Kustom, R. E. Faja . . . . .	419	20.1 Balanced, Parallel Operation of Flashlamps B. M. Carder, S. T. Merritt. . . . .	454
18.5 Distributed Parameter Model of the Trestle Pulser T. H. Lehman, R. L. Hutchins, R. Fisher . . . . .	425	20.2 Applying a Compensated Pulsed Alternator to a Flashlamp Load for Nova B. M. Carder, S. T. Merritt . . . . .	459
18.6 Compton Scattering of Photons from Electrons in Magnetically Insulated Transmission Lines K. L. Brower, J. P. VanDevender . . . . .	429	20.3 Applying a Compensated Pulsed Alternator to a Flashlamp Load for Nova--Part II W. L. Bird, D. J. T. Mayhall, W. F. Weldon, H. G. Rylander, H. H. Woodson . . . . .	463
Session XIX: Switching V		20.4 A Compact $5 \times 10^{12}$ Amp/Sec Rail-gun Pulser for a Laser Plasma Shutter L. P. Bradley, E. L. Orham, I. F. Stowers . . . . .	467
Chairman: M. F. Rose, Naval Surface Weapons Center		20.5 Fast Rising Transient Heavy Current Spark Damage to Electrodes A. Watson . . . . .	471
19.1 Simulation of Inductive and Electromagnetic Effects Associated with Single and Multi Channel Triggered Spark Gaps S. Levinson, E. E. Kunhardt, M. Kristiansen, A. H. Guenther . . . . .	433	Session XXI: Vacuum Power Flow	
19.2 An Electron-Beam Triggered Spark Gap K. McDonald, M. Newton, E. E. Kunhardt, M. Kristiansen, A. H. Guenther . . . . .	437	Chairman: T. H. Martin, Sandia Labs	
19.3 Low Jitter Laser Triggered Spark Gap Using Fiber Optic L. L. Hatfield, H. C. Harjes, M. Kristiansen, A. H. Guenther, K. H. Schönbach. . . . .	442	21.1 Influence of Nonuniform External Magnetic Fields and Anode-Cathode Shaping on Magnetic Insulation in Coaxial Transmission Lines M. A. Mostrom . . . . .	475
19.4 A 3 MV Low Jitter Triggered Gas Switch D. B. Cummings, H. G. Hammon, III . . . . .	446	21.2 MITL--A2-D Code to Investigate Electron Flow Through Non-Uniform Field Region of Magnetically Insulated Transmission Lines E. L. Neau, J. P. VanDevender . . . . .	479
19.5 Characterization of High Power Gas Switch Failure Mechanisms E. E. Nolting . . . . .	450	21.3 Magnetic Insulation in Short Coaxial Vacuum Structures M. S. DiCapua, T. S. Sullivan . . . . .	483
Session XX: Applications II		21.4 A Low Inductance 2 MV Tube Y. G. Chen, K. Mashima, J. Benford . . . . .	487
Chairman: W. Baker, Air Force Weapons Lab		21.5 Withdrawn	

Pl.1

INVITED

# OVERVIEW OF INERTIAL CONFINEMENT FUSION

Gregory H. Canavan

Office of Inertial Fusion  
U.S. Department of Energy  
Cermantown, MD 20767

## Abstract

Progress and plans for the U.S. program in inertial confinement fusion are reviewed with emphasis on the pulsed power aspects of pellet driver technology. The program has grown in five years from early experiments at the sub-terawatt level to construction of large facilities capable of peak power on target of about 100 TW. Driver technology options have broadened from glass and CO<sub>2</sub> lasers to short wavelength lasers, electron and light ion beams, and high energy heavy ion accelerators. Except for the heavy ion drivers, near term emphasis has been placed on single-shot systems to establish scientific feasibility at greatly reduced cost compared to rep-rate facilities. However, as the program develops attention must be given to components and subsystems necessary for reliable rep-rated operation.

## 71.2

## INVITED

## PULSED POWER FOR FUSION\*

T. M. MARTIN

Pulsed Power Systems Dept., Sandia Laboratories  
Albuquerque, New Mexico 87185

Abstract

Research conducted in support of the pulsed power approach to fusion has resulted in the creation of an extendable accelerator technology that could be used at levels up to 100 TW and 30 MJ. These types of accelerators are efficient (about 30 to 50 percent) and for ion outputs in the 1 to 3 MJ range they may provide an approach to economically feasible 200 MW electric power reactor. Repetitive pulsing of the pulsed power system for  $>10^9$  shot lifetimes must be solved along with ion beam concentration, bunching, and drifting.

Summary

In this paper we first describe Sandia's modular pulsed power approach and provide projections concerning future accelerators.

Second, the technology for repetitively pulsed (trap rate) accelerators is outlined. Recent encouraging results at  $10^5$  to  $10^6$  shots were obtained which could lead to reliable, long life systems.

Third, a reactor scenario is presented which uses the unique capabilities of the efficient pulsed power systems and plasma channel transport of the particles to provide a small, economically feasible system.

Introduction

Pulsed power accelerators originated at the Atomic Weapons Research Establishment (AWRE) during 1962-64 in a group directed by J. C. Martin. The first applications were flash radiography and transient radiation effects studies and the field has diversified rapidly into several areas. Some of the present applications are plasma compression,

intense  $\alpha$ -beam generation, intense light and heavy ion beam generation, electro-magnetic pulse testing, lightning simulation, and laser excitation. Potentially, the largest economic impact of pulsed power could be in electrical power generation by inertial confinement fusion where the relatively high efficiency of pulse power drivers make them the optimum of the various methods considered.

The basis of pulsed power technology is the ability to store and switch large quantities of energy and power economically. The technology encompasses Marx generators, compressed field generators, high voltage pulse transformers, triggered and untriggered switching, pulse forming lines, vacuum insulation, magnetically insulated lines and beam forming diodes. Presently, currents to 3 MA rising at  $4 \times 10^{14}$  amps/second and voltages rising at  $4 \times 10^{15}$  V/second have been achieved. The accelerator for particle beam fusion research at Sandia Laboratories utilizes many of these new techniques.

The Sandia fusion accelerator operating sequence begins with a Marx generator where energy storage capacitors are charged in parallel and discharged in series. Since voltage breakdown limits in liquids are determined partially by pulse length, short charge times are important throughout the accelerator and low inductance is desirable. The energy flows from the Marx into the intermediate store capacitor. A gas insulated triggered switch is then actuated to transfer the intermediate store capacitor energy to the water insulated pulse forming line (PFL). Untriggered switching in the PFL then provides many current carrying channels for low inductance and launches a 50 ns electrical

pulse towards the vacuum insulator. After passage through the vacuum insulator, one of the most inductive components in the accelerator, the power per unit area is increased during transport through magnetically insulated transmission lines to the diodes. The energy in the electromagnetic wave is then converted to a particle beam by a diode and guided to the target by a magnetized plasma column which prevents beam dispersion. Many beams are formed and then are overlapped on the target to provide further power concentration. Fig. 1 shows the progress and expectations in achieving power density with electrons, and Fig. 2 shows similar data for ion beams. Power densities of  $\sim 10^{12}$  W/cm<sup>2</sup> are thought to be necessary for pellet ignition.

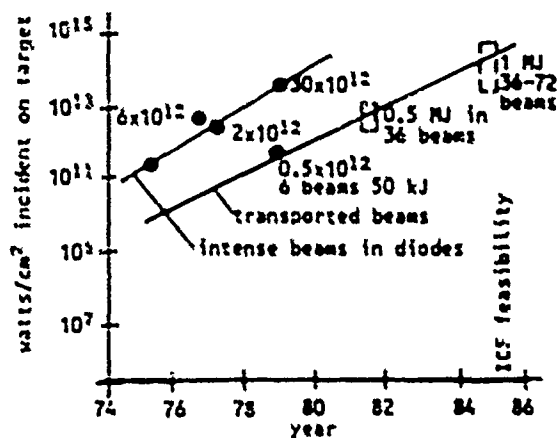


Fig. 1. Achieved and Projected Electron Power Densities.

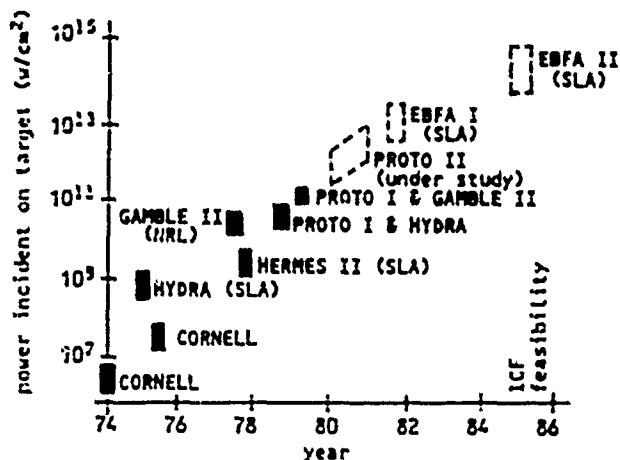


Fig. 2. Achieved and Projected Light Ion Beam Power Densities.

The two basic driver approaches to ICF are lasers and particle beam drivers. Basically the lasers are strong in the ability to maximize power density but are weak in efficiency and total energy. The particle beam drivers reverse these trends.

#### Fusion Accelerator Technology

One of the important results from the Sandia pulse power program is the demonstration of the flexibility and extendability of the modular approach to pulsed power. Fig. 3 shows the history of the Sandia ICF accelerator program and projects for the future.

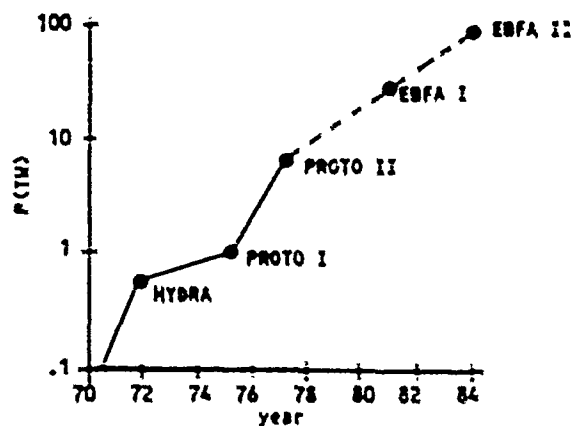


Fig. 3. Particle Beam Fusion Accelerator Output.

Hydra<sup>1</sup> is water insulated with a single output per line with a 1 MV, 500 kA, 50 kJ output. Proto I<sup>2</sup> is a two-sided, triggered oil switched, 2 MV, 500 kA, 20 kJ accelerator. Proto II<sup>3</sup> is a 1.5 MV, 6 MA, 250 kJ, self-breaking water switched accelerator, and EBFA I has 36 modules and is designed for 2 MV, 15 MA, and 1 MJ. EBFA II will be a 100 TW upgrade of EBFA I.

Fig. 4 is a cutaway conception of EBFA I which shows the modules and their components. The outside tank diameter is 30.5 m, and it is 4.8 m high. The 36 (6 μh) Marx generators<sup>4</sup> with a total energy of 4 MJ are contained in a 4.8 m by 4.5 m annular volume which is filled with 1.9 million liters of transformer oil. The Marxes transfer their energy through a 1.2 m diameter polyurethane oil-water interface insulator to the 20 nf water insulated capacitor in about .6 μsec. Three-megavolt gas

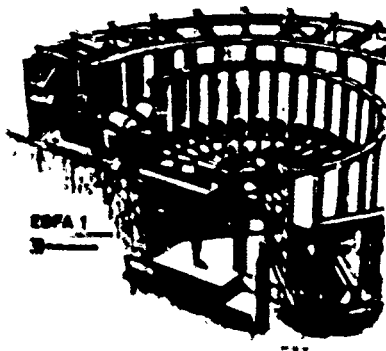


Fig. 4. EBFA I

switches are then triggered simultaneously and charge the water insulated pulse forming lines in 150 ns. Ten untriggered point-plane gaps per module then release a 45 ns long pulse from the transmission lines into the 30 ns vacuum insulator. The generator power pulse is then conducted to the target vicinity by the 6.8 m long magnetically insulated transmission lines.

EBFA I output parameters are shown in Fig. 5 for electron beam operation. In the light ion mode, as now contemplated, beam bunching due to voltage shaping and beam drifting will provide enhanced peak power at the target at a somewhat lower output energy.

#### EBFA BASELINE DESIGN PARAMETERS

PULSE LENGTH - FWHM...	35 ns
PEAK POWER.....	30 TW
CURRENT.....	15.0 MA
VOLTAGE.....	2.0 MV
ENERGY.....	1.0 MJ
ENERGY STORAGE.....	oil insulated - 4 MJ
PULSE FORMING.....	water insulated
POWER TRANSMISSION...	magnetically insulated

Fig. 5. EBFA Projected Parameters.

The modular approach to pulse power has several advantages. First, intensive studies on component reliability and lifetime can be obtained in small modules early in the program. Second, no single module limits the accelerator performance. For instance, previous designs, such as Hydra, have rise time limitations established by switch and vacuum insulator inductance because of the basic accelerator physical dimensions. Third, a single

module can be fabricated relatively quickly and inexpensively to check compatibility of components, manufacturing techniques, and engineering design prior to main accelerator procurement. A first production module is useful for physics experiments and to acquaint personnel with accelerator characteristics 1 to 2 years before the large accelerator is available. Our first production unit now being tested is shown in Fig. 6. We see the intermediate energy store, the SF-6 gas switch, the trigger isolation coil, the two pulse forming lines, the pre-pulse isolation shield, and the beginning of the transmission line. Fig. 7 shows a different view of the pulse forming lines, the transmission line transformer and the outside region of the vacuum insulator stack. The magnetically insulated transmission lines and the anode cathode arrangement are shown in Fig. 8 and 9. Typical A-K gaps are 2.5 mm for a 5 cm diameter cathode.

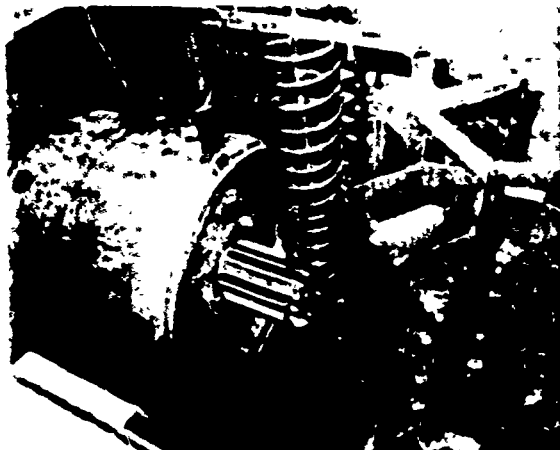


Fig. 6. Hydramite Back Section View

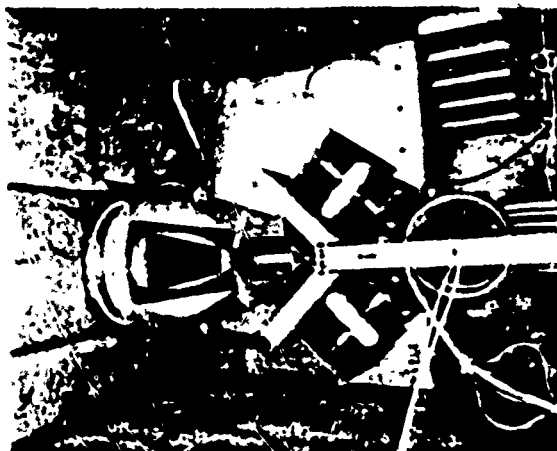


Fig. 7. Hydramite Front Section View



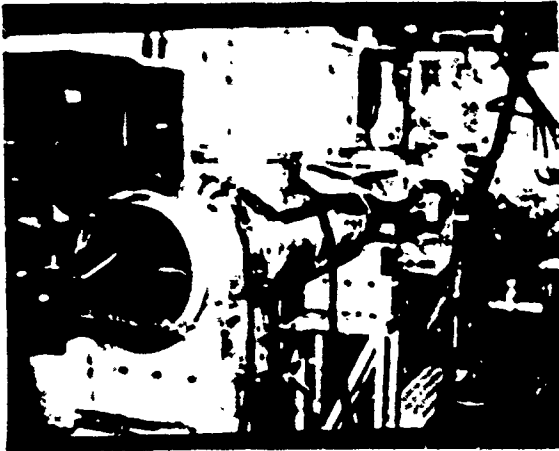


Fig. 8. Mite Magnetically Insulated Line.

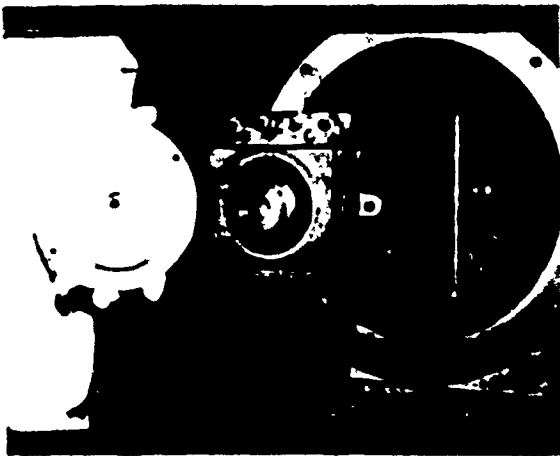


Fig. 9. Mite Anode Cathode Gap

Self-magnetically insulated lines permit extremely high levels of power concentrations<sup>5</sup>. The magnetic fields from preceding electrons trap following electrons and return them to the conductor from which they were emitted. This process inhibits the vacuum breakdown and electric fields of 2 MV/cm in the main transmission lines and 7 MV/cm in A-K gaps are obtained. These fields provide up to  $.16 \text{ MV/cm}^2$  for about 40 ns and allow for minimal particle drift distance to the target.

If the EBFA I modules are used in the full solid angle other than just a plane, then very large outputs are obtainable as shown in Fig. 10. An extrapolated level of 400 TW and 16 MJ is possible. Another method for obtaining higher output would be to upgrade the present module. This is also shown.

ACCELERATING SCHEME	INCREASING ENGINEERING CONSTANT COST/OUTPUT					
	CMA I		CMA II		FULL SPACE	
	T <sub>0</sub>	W <sub>0</sub>	T <sub>0</sub>	W <sub>0</sub>	T <sub>0</sub>	W <sub>0</sub>
PRESENT FACILE 125 kJ	75	1	65	2	400	16
PRESENT TEST 160 kJ	45	1.8	35	2.7	375	22
SUPERMITE 225 kJ PMAI	50	1.1	100	1.7	640	24
SUPERMITE UPGRADE 330 kJ PMAI	145	4.7	290	9.4	>1200	>40

Fig. 10. Present and Possible Accelerator Outputs.

#### Rep Rate Operation

A 300 kV, 100 Hz, 30 kW average power pulser<sup>6</sup> has been in operation at Sandia since September 1977. Efficient reliable pulse power systems with long lifetime ( $>10^8$  shots) will be needed for ICF reactors. Continuous operation for extended periods without major maintenance or repair are required.

The 30 kW rep rate system is shown in Fig. 11. It consists of a low voltage capacitor bank, a voltage step-up transformer, a pulse forming line (PFL), a high voltage switch, and a load resistor or a diode. The system uses a dual resonance transformer for charging the PFL to provide maximum efficiency. The pulser has provided pulses for several hours at the rate of 100 pps. Approximately  $10^8$  shots have been fired with no major component failure.

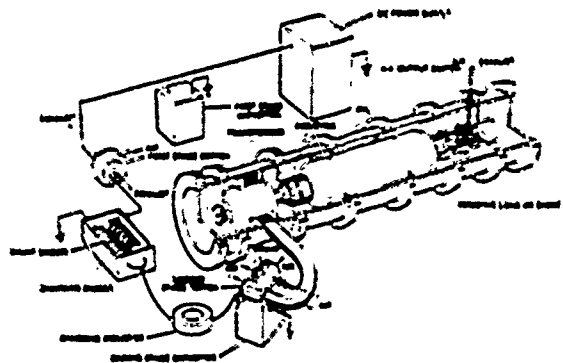


Fig. 11. 350 kV, 100 pps, 30 kW Electron Beam Accelerator

The initial problems of switch erosion and vacuum diode operation under repetitive conditions have been investigated.

First, the switch erosion was shown to have negligible effect. Fig. 12 shows the time of breakdown for  $10^6$  consecutive shots. The standard deviation is 44 ns or 1.0% of the nominal breakdown voltage. This data shows that there should be no prefires for triggered switch operation at a reasonable operating point such as 90% of the self breakdown voltage.

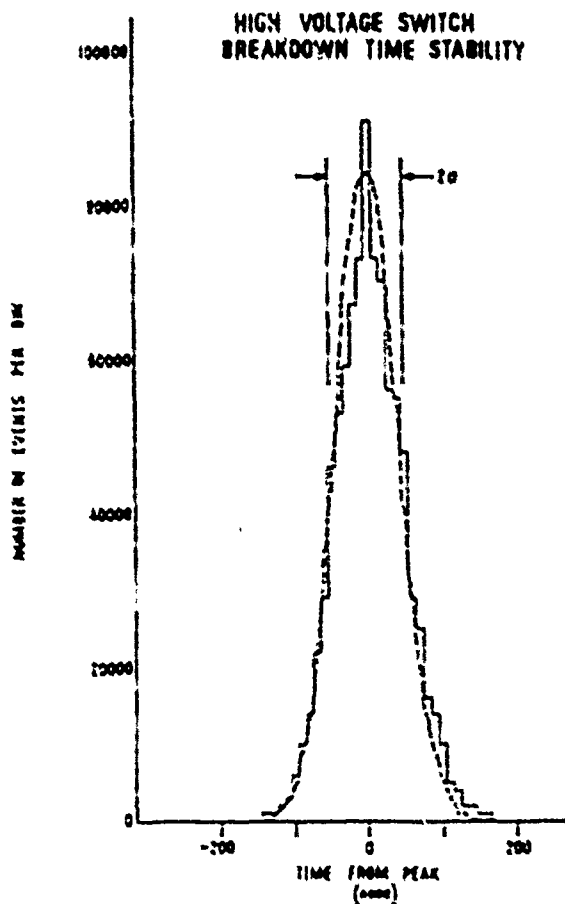


Fig. 12. High Voltage Switch Stability

The switch lifetime data showed a switch erosion rate of  $2 \times 10^{-8} \text{ cm}^3/\text{shot}$  for a density of  $18 \text{ g/cm}^3$ . It was estimated that a removal of  $12 \text{ cm}^3$  would widen the gap spacing and increase the breakdown voltage by 10%. These numbers provide an estimated lifetime of  $5 \times 10^3$  shots. Fig. 13 details the 700 kV output switch test.

Second, a 100 kV, 10 kA electron beam diode<sup>7</sup> was shown to have an operating lifetime of at least 110,000 shots with a projected lifetime in excess

#### HIGH VOLTAGE SWITCH

Mass loss, large electrode (Elkonite), gm	0.352
Mass loss, small electrode (Elkonite), gm	0.187
Charge transfer per shot, coulombs	$8.5 \times 10^{-4}$
Charge transfer total, coulombs	650
Action per shot, $\text{amp}^2\text{-sec}$	5
Action total, $\text{amp}^2\text{-sec}$	$5 \times 10^6$
Erosion, g/coulomb	
Large electrode	$5.4 \times 10^{-4}$
Small electrode	$2.9 \times 10^{-4}$
Erosion, g/ $\text{amp}^2\text{-sec}$	
Large electrode	$7 \times 10^{-8}$
Small electrode	$4 \times 10^{-8}$

Fig. 13. High Voltage Switch Parameters

of  $10^6$  shots at  $1000 \text{ A/cm}^2$  anode loading. Fig. 14 shows the anode and cathode. The cathode became a poorer emitter with increasing shots. A means to restore the cathode's emission characteristics by carbonizing the cathode was demonstrated. The diode parameters are shown in Fig. 15.

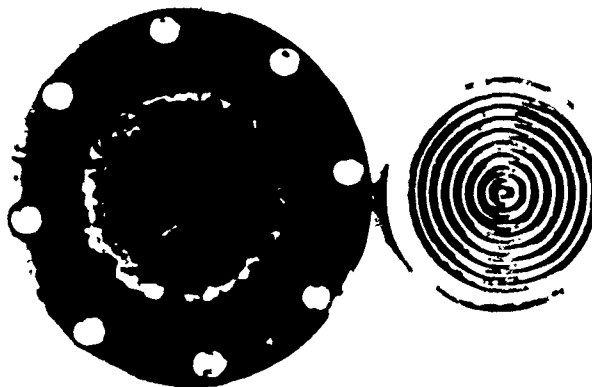


Fig. 14. Repetitively Pulsed Anode Cathode.

#### REPETITIVELY PULSED ELECTRON BEAM DIODE

10 Ω  
200 kV  
20 kA  
 $1.5 \text{ kA/cm}^2$   
30 Hz

Fig. 15. Repetitively Pulsed Electron Beam Diode.

### Power Reactor Concept

One possible 200 MWe reactor system is shown in Fig. 16<sup>8,9</sup>. The energy storage section contains the primary energy store, either capacitive or inductive. The energy is compressed and pulse shaped as previously outlined and then transmitted through the containment wall up to the reactor chamber by magnetically insulated power flow lines.

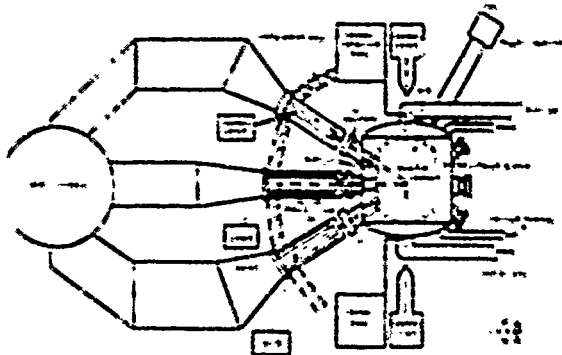


Fig. 16. Particle Beam Driven Reactor.

The reactor chamber is small (2 m radius) and will contain 60 MJ/pellets at 10 pps. Approximately 2 MJ of beam energy is supplied to the gain 30 pellet. The reactor chamber contains 50 torr of neon-helium which absorbs and moderates the pellet energy. Laser initiated channels which are heated by a capacitive discharge conduct the particle beam to the target. A larger view of the beamline geometry is shown in Fig. 17. This shows the guiding laser beam, vacuum insulator, containment wall, and dual vane window arrangement. The vanes open for an instant to allow beam passage and then close to maintain the anode cathode vacuum.

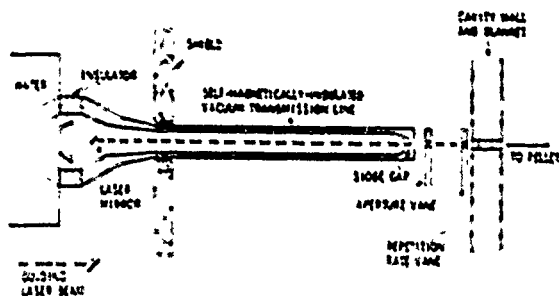


Fig. 17. Particle Beam Reactor Beamline

Fig. 18 shows efficiency effects on power reactors.  $\eta_D$  is the driver efficiency,  $C_{min}$  is the pellet gain necessary to provide a 75% useful output. This means that 25% of the energy will be recirculated to power the driver. The effect of efficiency on reactor chamber size and pellet gain are dramatic.

	10% DRIVER EFFICIENCY	50% DRIVER EFFICIENCY
$\eta_D$	10%	50%
$C_{min}$	25	5
POWER FLOW TO REACTOR	25%	100% - 25%
POWER FLOW FROM REACTOR	75%	75% - 25%
CHARGE AND DISCHARGE	100% - 25%	100% - 25%

Fig. 18. Power Reactor Comparison

### Conclusions

The modular ICF pulsed power concept has provided the possibility for systems ranging to 1000 TW and 30 MJ with modest improvements in technology and further improvements in reliability. The rep rate capability of these systems appears good, but the data base is small and expansion of this area is needed. A reactor design indicates that a small, economically feasible power plant may be possible using this pulsed power technology.

### References

1. T. N. Martin, "The Hydra Electron Beam Generator," IEEE Transactions on Nuclear Science, Vol. NS-20, No. 3-ID3, Particle Accelerator Conf., p. 289, June 1973.
2. K. R. Prestwich, "MARP, A Short Pulse, High Current Electron Beam Accelerator," IEEE Transactions on Nuclear Science, Vol. NS22, No. 3, 1975 Particle Accelerator Conf., p. 975, June 1975.

3. T. J. Marxin, J. P. VanDevender, D. L. Johnson, D. H. McDaniel, M. Aker, "PROTO IX - A Short Pulse Water Insulated Accelerator," International Topical Conf. on Electron Beam Research & Technology, Albuquerque, NM, Vol. 1, p. 450, November 3-5, 1975.
4. D. L. Johnson, "Initial PROTO IX Pulsed Power Tests," Proceedings International Pulsed Power Conf., Paper IEE-1, Texas Tech University, November 9-11, 1976.
5. J. P. VanDevender, "Self-Magnetically Insulated Power Flow," Proceedings of IEEE 2nd International Pulsed Power Conf., Lubbock, Texas, June 12-14, 1979.
6. M. T. Buttram, G. J. Rohwein, "Operation of a 300 kV, 100 Hz, 30 kW Average Power Pulsar," 13th Pulse Power Modulator Symposium, Buffalo, NY, June 20-22, 1978.
7. M. T. Buttram, "Operation of a Repetitively Pulsed 300 kV, 10 kA Electron Beam Diode," IEEE Transactions on Nuclear Science, 1979 Particle Accelerator Conf., June 1979.
8. D. L. Cook, M. A. Sweeney, "Design of a Compact Particle Beam Driven Inertial Confinement Fusion Reactor," Proceedings of ANS 3rd Topical Meeting on the Technology of Controlled Nuclear Fusion, Santa Fe, NM, May 1978.
9. D. L. Cook, M. A. Sweeney, "Critical Environmental Considerations for Particle Beam Driven ICF Reactor Materials, Journal of Nuclear Materials, to be published, 1979.

---

\*This work was supported by the U. S. Department of Energy under Contract DE-AC04-76-DP00789.

## PULSED HIGH-CURRENT ELECTRON TECHNOLOGY

G. A. Masys

High Current Electronics Institute  
of Academy of Science, USSR  
Siberian Branch, Tomsk

Abstract

The use of high-power pulse technology and explosive electron emission enables one to construct new pulsed electron devices. The present report gives the results of an intensive investigation of high-power pulse generation, electron beam geometry and the application of these beams to the production of ultra high frequency, laser and X-ray radiation. This report is based on results obtained at the Institute of High-Current Electronics.

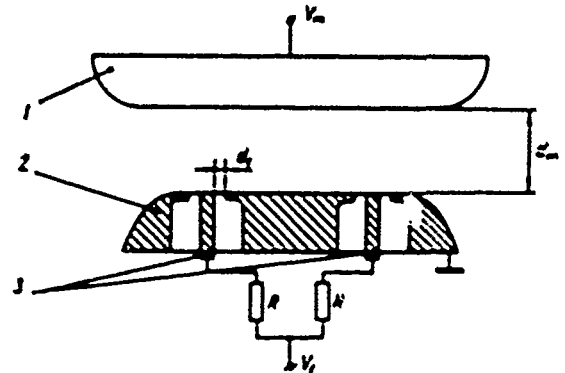
Pulse GenerationSwitches

To develop nanosecond high power pulse generators one should have switches which exhibit large  $di/dt$  characteristics as well as nanosecond trigger jitter. Previously, a method had been suggested for controlling megavolt gas spark gaps using nanosecond duration electron beams [1]. This approach is based on rapid electric-field distortion when an electron beam with optimum values of beam current and power are injected into the gap. For a discharge voltage of  $2 \times 10^6$  V, a delay time,  $\tau_d = 15 \pm 1$  ns, has been obtained using a 200 keV electron beam of 20 ns duration and a beam current of 5 A [2,3].

The characteristics of trigatron megavolt switches was also investigated [4,5] (Fig. 1). It has been determined that with such triggering, nanosecond delay times can be achieved only when the initiation is carried out with electric field distortion at the tip of the triggering electrode. It is necessary that the discharge develops simultaneously in the main gap and triggering region.

The dependence of the delay  $\tau_d$  and trigger stability  $\pm \tau_d$  were investigated for both polarities of the gap, the applied voltage  $V_m$  and triggering  $V_t$

voltages. The lowest  $\tau_d$  and  $\pm \tau_d$  were obtained for a  $+V_t$  and a  $-V_m$  (Fig. 2). This result is explained by the fact that the initial stage of the trigatron breakdown process is a point (trigger electrode) to plane (basic electrode) discharge for which there is a well known polarity effect, i.e., if the point has positive polarity the breakdown voltage is significantly lower than if it is charged negatively. With a discharge voltage of  $10^6$  V and  $V_t = 10^5$  V we obtained  $\tau_d = 5 \pm 0.5$  ns (Fig. 3). Using trigatron triggering, multichannel (up to 3 channels) switching was achieved in megavolt switches.

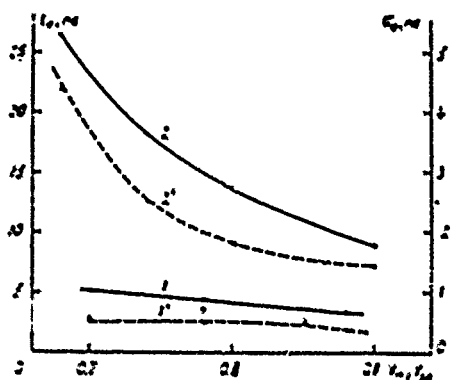


The scheme of double-channel trigatron.  
1,2 - the main electrodes; 3 - the triggering electrode.  
 $d_m$  - the main gap;  $d_t$  - the triggering gap;  
 $V_m$  - the main voltage;  $V_t$  - the triggering voltage

Fig. 1

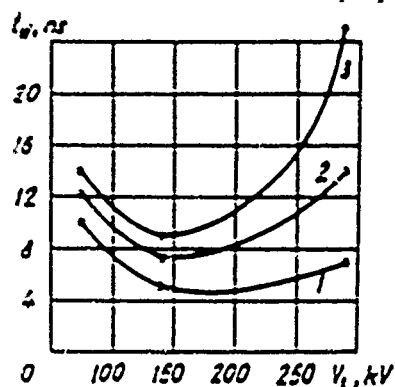
The effect of gaseous mixtures ( $\text{SF}_6$ ,  $\text{N}_2$ , Ar,  $\text{H}_2$ ) on triggering and commutation characteristics of megavolt switches were investigated. It was found that the addition of Ar to high dielectric strength gases such as  $\text{SF}_6$  decreases  $\tau_d$  and  $\tau_c$  and improves multi-channel operation. However, large concentrations of gaseous mixture increases

the switching time (Fig. 4). Therefore, to improve conditions for parallel operation of a large number of spark channels, one should use small (up to 10%) additions of Ar which do not result in significant degradation of the switching process.



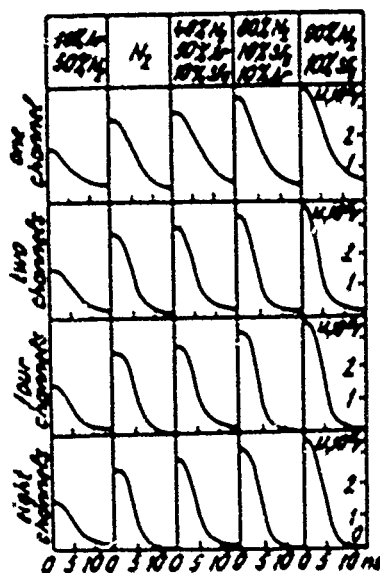
The delay time and its standard deviation  $G_d$  of the trigger vs. under-voltage rise-time characteristics in the gap  $U_m/U_0$  at various potentials of the main  $U_m$  and of the triggering  $U_i$  in the mixture of 0.25-0.75  $N_2$ , 0.75-1.0 and  $G_d$  at  $U_m$  and  $U_i$ , 0.75-1.0 and  $G_d$  at  $U_m$  and  $U_i$ .

Fig. 2



The trigger time  $t_d$  vs. triggering pulse amplitude  $U_i$  at various under-voltages in the gap  $U_m/U_0$ .  $U_m/U_0 = 0.93$ ; 2-0.75; 3-0.7.

Fig. 3



Oscillograms of the voltage drop in the gap for various gas mixtures.

Fig. 4

#### Marx Pulse Generators

In some cases, in particular for parallel operation Marx pulse generators must be triggered with a minimum variance in trigger delay. A Marx generator with operating voltage less than 3 MV has been constructed using three-electrode gaps in which the central electrode is capacitively coupled to that of the preceding stage. The generator was constructed with segmented stacked stages and immersed in a column of oil. Along the stages there is a column of gaps which, after each firing, is flushed and refilled with dry air at pressure of 1-2 atm. When operating into a 170 ohm load, the Marx generator mean delay time is 350 ns with an operating time jitter of 5 ns and output voltage rise-time of 60 ns. The charging voltage per stage is 85 kV. The generator's self-inductance is 13  $\mu H$  and contains 33 stages. Pressure control in the gap column enables one to adjust the delay time from 350 to 550 ns. The generators can operate both independently and in parallel and are principally used for switch testing. One of the above generators can act as a primary storage for an electron pulse accelerator using a water dielectric. The accelerator has the following parameters: an electron

beam voltage up to 1 MV, beam current - up to 300 kA, pulse-duration of the electron current is 70 ns. Through a controlled commutator a single storage line of 39 ohm impedance is discharged through a coaxial transformer of 2.3 ohm impedance. The electron beam is formed in the diode, containing a disk insulator. The interelectrode spacing  $d$  being of the order of 1 cm, ratio  $R/d \approx 1$  ( $R$  - radius of cathode). Using the accelerator, we have investigated the regimes of electron - beam geometry in diodes with a large value of  $v/v_0$ . To analyze the plasma generated in the diode, laser scattering off plasma electrons and interferometry are used. Due to the very low jitter in the operation of the Marx generator and gap, good coincidence of electron current pulse and laser diagnostic devices was achieved in the accelerator.

#### The "Module" Installation

At the Institute of High-Current Electronics several pulse generators have been constructed, each of which is used for various investigations [5]. One of them, the "module" installation, has the following parameters: output voltage is 2.3 MeV, current - 2.9 MA, total stored energy - 100 kJ. The installation consists of six parallel coaxial lines with water insulation discharged through gas gaps into a common transmission line (Fig. 5). This line is then discharged into the load. All six lines are incorporated into a common vessel and charged with a pulsed linear transformer during  $1.4 \times 10^{-6}$  s. The pulsed linear transformer is constructed as a set of 14 similar sections. Each section includes two transformer stages whose primaries are connected in parallel and the secondaries in series. The primary energy is stored in four capacitors. The transformer has a ferromagnetic core.

The "Module" installation is used for investigating magnetic compression of electrically vaporized thin cylindrical liners. Numerical calculations made using magneto-hydrodynamic computer programs show the efficiency of such a compression method for obtaining very high plasma velocities ( $2 \times 10^7$  cm/s), high densities and temperatures (some keV).

A calculation for the "Module" installation indicates one can achieve a compressional speed of  $10^7$  cm/s and temperatures of 1 keV.

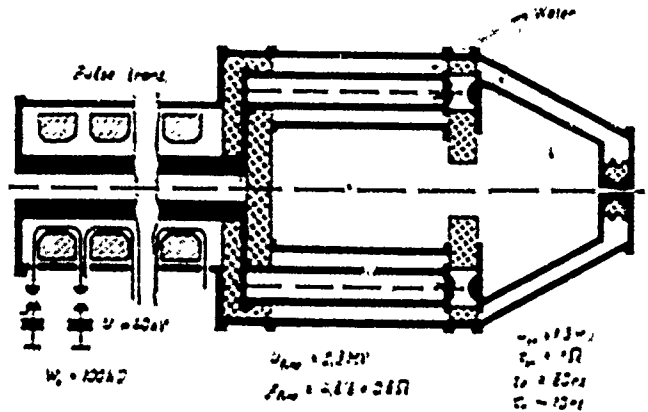


Fig. 5

#### High-Frequency Pulsed Electron Accelerator

A relativistic electron beam accelerator with pulse repetition frequency of 100 Hz was constructed at the Institute. The electron energy was  $5 \times 10^5$  eV, current -  $5 \times 10^3$  A, pulse duration - 25 ns with rise time of 3 ns. A pulsed Tesla transformer built in the pulse-forming line was used as a charging arrangement for this line (Fig. 6) [7,8].

High speed gas flow between the pulse sharpening-gap electrodes was employed to obtain low jitter in the pulse generator. It was shown that at the given pulse repetition frequency, a jitter lower than 1% could be obtained by selection of proper gas flow.

The electron beam was formed in a foilless coaxial diode whose cathode was placed in a homogeneous magnetic field of  $5 \times 10^3$  Oersts. The beam was transported in a cylindrical vacuum wave guide with the beam being deposited on a cooled collector. Studies of the vacuum diode operating stability showed that variance of the total diode current and cathode voltage pulse parameters depends on both the cathode material and the electric field strength at the emitting surface. Reproducibility < 10% could be achieved in diode current and voltage.

This accelerator was used in the construction of a

high-power  $\text{H}_2 + \text{Ar}$  laser (efficiency  $\sim 1.5\%$ ) [9], and for constructing a pulsed 100 MW microwave radiation generator (prf = 50 Hz, efficiency  $\sim 10\%$ ) [10].

### Processes in Accelerator Diodes

#### The Material and Shape of Emitters

At present, explosive emitters of various materials and shapes are used in cathodes. From the literature it is often not clear in what way the emitter material and geometry are chosen. Since explosive emission leads to emitter erosion, it is obvious that for long-lived explosive - cathodes those most preferable are emitters with constant cross sections as a function of height (foils and wires).

A controlled number of emitting centers on the cathode of a large surface can be easily created using thin-wire cylindrical emitters. However, in this case, some problems arise concerning the choice of material and optimal emitter diameter, i.e., a diameter for which the electric field strength is sufficient for exciting explosive emission during the pulsed voltage risetime while, on the other hand, leading to minimal emitter erosion. A study showed that for each specific set of operating conditions there is an optimal diameter whose value increases with pulse duration and current amplitude. The importance of the optimal diameter is illustrated in Fig. 7.

As a result of breakdown, erosion characteristics and parameters of originating whiskers were determined for several emitter materials. From this study a set of materials preferred for creation of long-lived explosion-emission cathodes was derived. Emitters made of different materials having identical geometry were tested under similar conditions. The results of these experiments presented in Figs. 8 and 9 indicate that copper emitters have the best erosion reproducibility.

Cylindrical copper emitters are preferable for constructing explosion-emissive cathodes of large surface area for operation under repetitive firings in diodes evacuated by standard oil vacuum pumps.

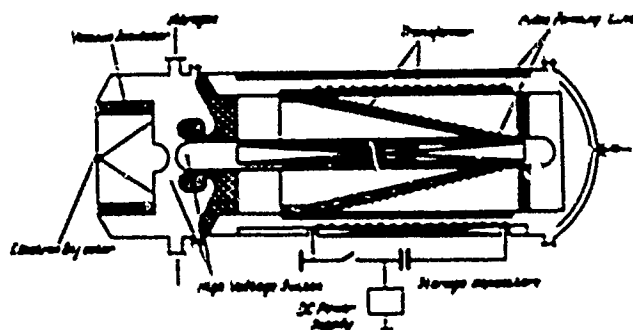
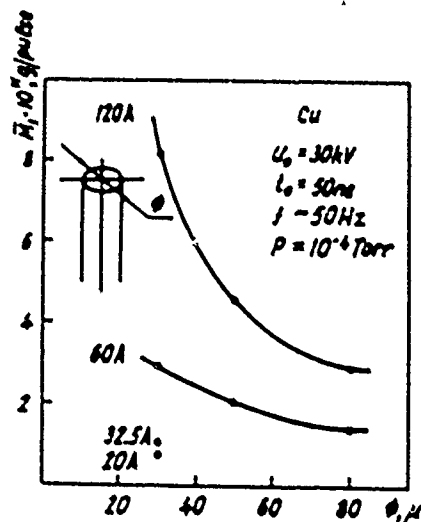


Fig. 6



Dependence of the mass removal per pulse from the cylinder cathode on the emitter diameter.

Fig. 7

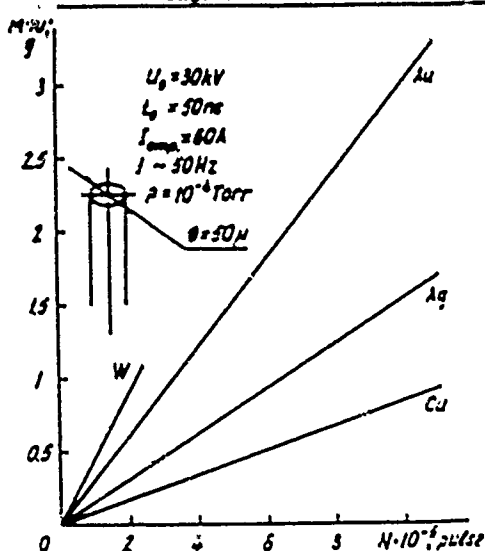



Fig. 8 Dependence of the mass removal from the cylinder emitter on the pulse number.



Cathode material	Ti	Ni	Nb	Al	Cu	C	Pb	Emitter geometry
N, pulse	3	3	10	45	$5 \cdot 10^3$	$13 \cdot 10^4$	$43 \cdot 10^4$	
$i_{amp}, A$	60	60	60	60	60	87	25	
$\bar{I}_e, 10^{-4} A$	-	-	-	-	1.8	28	13	
$\gamma, 10^5 A/cm^2$	-	-	-	-	1.2	14.2	20	
$\bar{V}_e, 10^4 V/cm$	-	-	-	-	12.5	63	12.7	
$R_N, \mu$	25	25	25	25	35	17.5	275	
$\delta, \mu$	50	50	50	50	50	80	50	

$$U_0 = 30 kV; f \sim 50 Hz; P = 10^{-4} Torr$$

Test results of the foil emitters.

Fig. 9

#### Magnetic Insulation of Diodes

At present, high-current hollow electron beams formed in foilless diodes with magnetic insulation (Fig. 10) are widely used in ultrahigh frequency applications. Recent investigations of magnetically-insulated diodes, an extension of our work published in 1970, showed that the current pulse duration is limited by a breakdown both across [15] and along a magnetic field as a result of cathode-plasma expansion. The breakdown velocity across a magnetic field of  $10^5 Oe$  is  $5 - 8 \times 10^5$  cm/s, and along the field  $2 - 3 \times 10^7$  cm/s. The breakdown speed across the magnetic field can be decreased by a factor of 2 - 3 when the cathodes are constructed of separated emission centers [16]. The study showed that in a magnetic field the plasma homogeneity at the cathode increases. It was shown that by decreasing the screening effect of the magnetically confined electron layer as well as by multiplication of emissive centers, improved performance results [17]. Figure 11 illustrates the growth of the emissive boundary with reference to the initial center of emission. The study showed that using cathodes with explosive emission in the magnetic field enable one to attain a highly stable hollow electron beam with a current uniformity of better than 1%.

Theoretical [18] and experimental [19] investigations of the perveance of cylindrical magnetically insulated diode were made. The most important conclusion of the theory (using the strong guiding mag-

netic field approximation) is that the electron energy in the drift tube can be twice (or more) as large as the initial energy of the beam, with the current being equal to the limiting generator system current. Measurements performed of beam current and potential for these hollow beams are in a good agreement with the results of the analytical and numerical calculations. This enables one to conclude that the beam current is determined by the acceleration space in the diode rather than being limited by the generator system, as has been previously suggested in a number of theoretical and experimental works.

#### High Power Gas Lasers

Investigations of pulsed gas discharge lasers sustained by an electron beam were made at the Institute [20-24]. Our array of electron-beam accelerators and pulsed power supplies allowed a parametric investigation of discharge characteristics (energy content, volt-ampere characteristics, and stage volume) to be made over a wide range of pulse durations from  $10^{-8}$  s to  $10^{-4}$  s. Cases studied included: nitrogen,  $CO_2 + N_2$ , and mixtures of noble gases with halogens  $Ar + Xe + NF_3$ ,  $Ar + Xe + CCl_4$ , etc.

Using the results of these investigations several experimental lasers have been constructed.

(a) "LAD-1" - a laser operating at atmospheric pressure with an active volume of  $10^4$  l. The laser uses a mixture of  $CO_2 : N_2 : He$  in the ratio of 1:1:3. An electron beam was injected through an aperture with a cross section of  $10 \times 100$  cm covered with a titanium foil of 50  $\mu m$  thickness. With an electron beam density of  $1 A/cm^2$  and a mean electron energy of 200 keV for a duration of  $10^{-6}$  s, the energy injected into the gaseous volume was 4500 J, and radiation energy ( $\lambda = 10.6 \mu m$ ) was 500 J. The laser efficiency was 30%.

(b) "LAD-2" - a laser with an active region volume of 270 l. The electron-beam cross section was  $30 \times 300$  cm. An electron beam of  $0.4 A/cm^2$  density and 2  $\mu s$  duration was employed to excite the medium. Laser operation was very stable at a field strength of 4.2 kV/cm using a mixture of  $CO_2, N_2$ ,

and He. The power source was a capacitor bank of 15  $\mu$ F capacitance charged to 125 kV voltage. The laser output was 7.5 kJ, an efficiency of 26%.

(c) A tunable CO<sub>2</sub> laser covering the range of 9 to 11  $\mu$ m at 6 atm pressure of CO<sub>2</sub>: N<sub>2</sub> = 1:1. A smooth tuning was obtained over the aforementioned spectral range. Individual R and P branch lines were easily identifiable over a range of 86 cm<sup>-1</sup>. Spectral frequency scanning was accomplished by use of a diffraction grating. The output energy density of this tunable radiation was 5 J/cm<sup>2</sup> at the line center with ~ 50% modulation in between lines. Pulse duration was 40 ns.

(d) Several excimer lasers are being investigated which are excited by both an electron beam and a sustained electric discharge. Using the e-beam excited mixture Ar + Xe + CCl<sub>4</sub>, XeCl molecule radiation ( $\lambda$  = 308 nm) with a radiation power of 10 J/l and an efficiency of 3% was obtained.

A discharge supported by a 50 nsec e-beam enables one to excite XeF and XeCl to output power of 10<sup>5</sup> W/cm<sup>2</sup> with pulse duration  $2 \times 10^{-8}$  s.

#### Powerful Nano- and Subnanosecond X-ray Pulses

A series of 3 pulsed X-ray machines with radiation energy from 90 to 600 keV was developed and manufactured in the USSR for flaw detection in materials. The use of nanosecond pulse generators and X-ray tubes based on explosive emission permitted the reduction in overall size. Further decreases in the nanosecond X-ray emitter sizes is limited by the non-reproducible breakdown characteristics and by the value of the anode-cathode gap in the vacuum X-ray tube.

Investigations of vacuum diodes in the subnanosecond range showed that with pulse duration shorter than 1 ns the interelectrode gap value can be depressed to 0.1 - 0.2 mm without danger of its shorting by a cathode flare plasma. The current density at the anode can be raised to 10<sup>6</sup> A/cm<sup>2</sup> without the use of special focusing devices, and the tube vacuum insulator sizes can decrease sig-

nificantly [25]. We were able to construct a miniature X-ray tube of 10 mm diameter, powered through a section of coaxial cable (7.5 mm external diameter and 30 cm in length). The power supply was a nanosecond generator from the X-ray device MIR-2d (Fig. 12) which charged a subnanosecond pulse forming line over 3 - 5 ns, providing a high over-voltage on the sharpening gap. Pulse duration was limited with a crowbar switch.

Measurements, made using a magnetic analyzer, of the electron energies in the tube, showed that when charging the pulse forming line to 150 kV for a pulse duration ~ 0.5 ns, the voltage in the tube was 80 - 100 kV. Output was limited by line and sharpening gap losses. The maximum radiation dose (30 mR per pulse at the distance of 1 cm from the anode) was achieved with an anode-cathode distance of 0.2 mm. However, in some cases, holes of 0.1 - 0.15 mm diameter were produced in the 0.1 mm thickness tungsten anode. Increasing the gap to 0.5 mm decreased the dose to 25 mR/pulse, but provided a prolonged operation of the tube and anode. Results did not depend on pressure variation in the tube over the range of 10<sup>-1</sup> to 10<sup>-3</sup> torr.

In this regime the electric-field strength at the inner conductor of the coaxial cable is 1 MV/cm; therefore, its lifetime is limited to 10<sup>5</sup> pulses, at which time the cable is replaced. It should be noted that the impedance of a cable insulation breakdown (single-channel) is so high that it does not in fact influence the dose value. A halving of the dose per pulse was observed only with the appearance of 5 to 6 breakdown channels.

The dose value and small size of the tube focus can make it very useful for flaw detection of industrial goods with both narrow and long cavities.

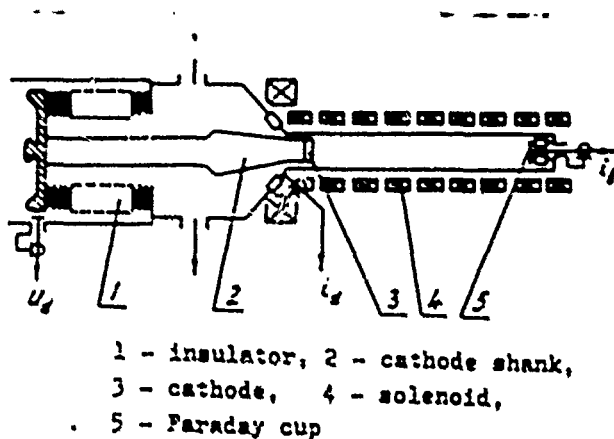


Fig. 10

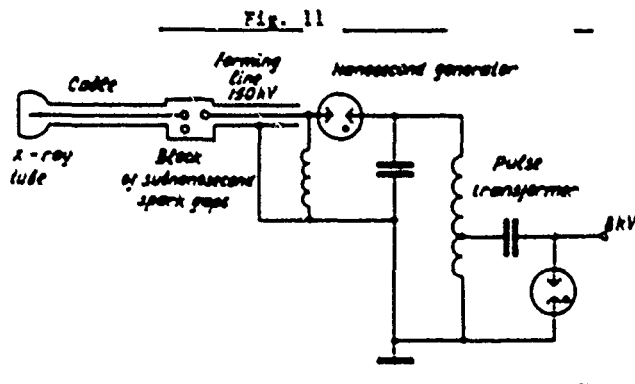
a)  $t_0 = 300 \text{ ns}$       b)  $t_0 = 1.3 \mu\text{s}$ 

Fig. 12

## References

1. G. A. Masyats, Generation of a Nanosecond, High Power Pulses, Soviet Radio, 1974.
2. B. M. Kovalchuk, V. V. Kremnev, G. A. Masyats, Yu. F. Potalitsyn, Proc. X International Conference on Phenomena in Ionized Gases, Oxford, 1971.
3. A. A. Elchaninov, V. G. Emelyanov, B. M. Kovalchuk, Yu. F. Potalitsyn, Discharge in Megavolt Spark Gap Initiated by Electron Beam, Proc. XI International Conference on Phenomena in Ionized Gases, Praha, 1973, p. 194.
4. A. A. Elchaninov, V. G. Emelyanov, B. M. Kovalchuk, G. A. Masyats, Yu. F. Potalitsyn, (Soviet Scientific Instruments), Priory i Tekhnika Eksperimenta, #2, 1974, p. 103-105.
5. V. G. Emelyanov, B. M. Kovalchuk, V. A. Lavrinovich, G. A. Masyats, Yu. F. Potalitsyn, (Soviet Scientific Instruments), Priory i Tekhnika Eksperimenta, #4, 1975, p. 89-91.
6. (News of Thermonuclear Fusion's Research in USSR), Novosti Termoladernykh Issledovaniy v SSSR, #2, p. 6-7, 1979.
7. G. A. Masyats, V. V. Mayrov, V. P. Osipov, Priory i Tekhnika Eksperimenta, #2 p. 102, 1969.
8. F. Ya Zagulov et. al., Priory i Tekhnika Eksperimenta 1976, #5.
9. Yu. I. Bichkov et. al., (Letters to Soviet Journal Technical Physics), Pisma Zhurnal Tekhnicheskoi Fiziki, #22, v.2, 1976, p. 1052.
10. V. I. Belousov, et. al., Pisma Zhurnal Tekhnicheskoi Fiziki, #23 v. 4, 1978.
11. G. P. Bashenov et. al., (Soviet Journal Technical Physics), #6, v. 43, 1973, p. 1255-1261.
12. D. I. Proskourovsky, E. B. Yankelievitch, B. A. Koval, (Soviet Radiotechnics and Electronics), Radiotekhnika i Elektronika, #2, v.21 1976, p. 342-349.
13. E. A. Litvinov, G. A. Masyats, D. I. Proskourovsky, E. B. Yankelievitch, VII International Symposium on Discharges and Electrical Insulation in Vacuum, Novosibirsk, 1976, p. 55-69.
14. R. B. Bakst, and G. A. Masyats, Proc. IV International Symposium on Discharges and Electrical Insulation in Vacuum, Waterloo, Canada, 1970. (also Izvestiya Vuz, Fizika, #7 1970, p. 144).
15. R. B. Bakst, S. P. Bougasev, V. I. Koshelev and G. A. Masyats, Proc. II International Topical Conference on High Power Electron and Ion Beam Research and Technology, Ithaca, 1977, p. 761.
16. V. I. Koshelev, (Soviet Plasma Physics), Fizika Plazmy, #3, v.5, 1979, p. 698.
17. G. A. Masyats, D. I. Proskourovsky, V. F. Puchkarev, Proc. VIII International Symposium on Discharges and Electrical Insulation in Vacuum, Albuquerque, 1978, p. C4-1.
18. A. I. Fedosov et. al., Izvestiya Vuz, Fizika, #10, 1977, p. 134.
19. S. Ya. Belomytsev, et. al., VIII International Symposium on Discharges and Electrical Insulation in Vacuum, Albuquerque, 1978, p. E3-11.

20. Yu.I. Bychkov, Yu.D. Korolev, G. A. Mesyats, (Soviet Physic's News), Uspekhi Fizicheskikh Nauk, #3, v. 126, 1978, p. 451-477.
21. S. P. Bougaer, et.al., Pisma Zhurnal Tekhnicheskoi Fiziki, #10, v. 1, 1975, p. 492-496.
22. Yu.I. Bychkov, et.al., (letters to Sov. Journal Tehn. Phys.), Pisma Zhurnal Tekhnicheskoi Fiziki, #5, v. 2, 1976, p.212-216.
23. Yu.I. Bychkov, et.al., (Soviet New Academy of Sciences USSR) #14, v. 1, 1975.
24. G. A. Mesyats, Pisma Zhurnal Tekhnicheskoi Fiziki, #14, v. 1, 1975.
25. G. A. Mesyats, V. G. Shpak, Pisma Zhurnal Tekhnicheskoi Fiziki, v. 3, 1977, p. 708.

P2.1  
INVITED

NEW HYDROGEN THYRATRONS FOR ADVANCED HIGH POWER SWITCHING

D. Turnquist, R. Caristi, S. Friedman, S. Merz, and R. Plante  
EG&G Inc., Salem, Massachusetts

N. Reinhardt  
Consultant, Lexington, Massachusetts

ABSTRACT

Recent advances in high power switching have led to the development of new hydrogen thyratrons operating at high ppr and high di/dt with low jitter and long life.

Short commutation times, dependent on internal pressure and geometry, and on the method of triggering, combine with inductance less than 1/4 nh/kv to give di/dt on the order of  $10^{12}$  amperes per second. Experimental results are in agreement with those predicted by newly derived theoretical models.

Operation at peak currents up to 75 ka has been achieved for 10 us pulses, and much higher currents can be achieved at shorter pulse widths.

Tests at 1 MW of average power have verified thyatron scaling laws at tens of amperes average and kiloamperes r.m.s. Thyatron operation at average power levels far in excess of 1 MW is possible.

INTRODUCTION

Hydrogen thyratrons satisfy the switching needs of many repetitive pulse power systems. Thyatron designs originally developed for pulse radar use have proven to be sufficiently flexible to accommodate a variety of applications quite different from radar modulators. However, new switching requirements have arisen that cannot presently be met by existing switches of any kind, and projected requirements are even more severe. In general, a ten-fold increase in thyatron capability is necessary to meet present requirements, as shown in Table 1.

Hydrogen thyratrons are desirable in many new systems for the same reasons that led to their original development. These are: 1) a repetition rate capability of some tens of kilohertz, limited by high voltage recovery times of a few microseconds; 2) life of thousands of operational hours, not limited by coulomb or pulse count; and 3) a very low time jitter (less than 1 nanosecond,

with a power gain of the order of  $10^3$  to  $10^5$ , and a stable, very low conduction impedance.

The inherent advantages of thyratrons over other types of switches mandate the extension of thyatron technology to much higher voltages, currents, and power levels.

Table 1. Present thyatron maximum ratings vs. new switching requirements

	Typical Standard Thyratrons	Immediate New Requirements
VOLTAGE HOLDOFF (kv)	<45	50 to 250
PEAK CURRENT (ka)	<5	20 to 50
di/dt (a/s)	< $10^{10}$	0.8 to $5 \times 10^{12}$
AVERAGE CURRENT (Adc)	<4	5 to 50
PEAK POWER (W)	< $2 \times 10^8$	$10^9$ to $10^{10}$
AVERAGE POWER (MW)	<0.09	0.1 to 10

HIGH di/dt

We have been studying tube operation at high di/dt up to  $10^{12}$  amperes/second, in a regime where the tube itself has a significant effect on di/dt. We have identified, analyzed, and controlled the major factors that determine the rate of current rise. These are: 1) the trigger plasma density and distribution at the onset of commutation (determined by the grid configuration and the method of triggering); 2) the plasma growth rate (determined by the fill gas pressure); and 3) the effective inductance (determined by the distribution of the internal discharge as well as by the geometry of the tube and its external current return).

### Triggering

To achieve minimum switching delay and maximum circuit  $di/dt$ , the tube must be designed for such operation and the correct method of triggering must be used.

To obtain the best initial conditions for commutation, the trigger discharge must establish a relatively high plasma density near the cathode surface. To obtain low inductance, the discharge must be spread over the cathode surface to the maximum extent. To aid this process, an auxiliary (pretrigger) grid is used. Figure 1 shows an experimental, low-inductance design. The auxiliary grid,  $a_1$ , is located between the cathode and the control grid, and its geometry is designed to confine the trigger plasma near the cathode.

To fully form the discharge before commutation, the auxiliary discharge is prepulsed with as high a current as is practicable. We have had good results with an auxiliary driver which produces an open circuit voltage of 2 kv with a source impedance of 10 ohms, and a 1- $\mu$ s pulse width. Higher drive has not produced observable improvements with 3-inch and 4.5-inch diameter tubes.

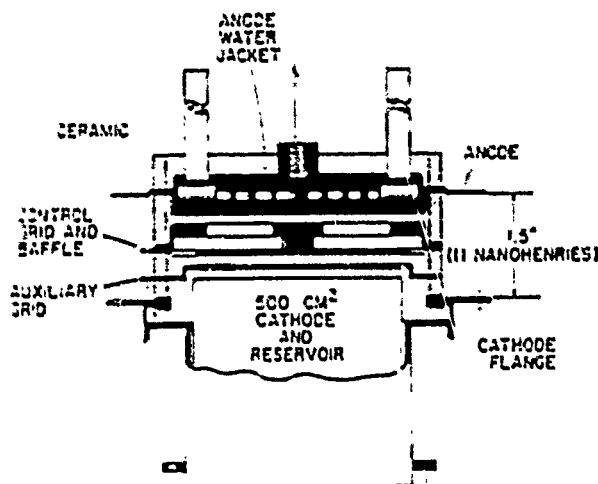


Figure 1. HY-5313 thyatron cross section.

A high current auxiliary grid prepulse is necessary but not sufficient to achieve high  $di/dt$ . When the ion density near the grid baffle apertures reaches a high enough value (apparently on

the order of  $10^{11}$  ions/cm<sup>3</sup>), the tube will commutate, regardless of the state of the discharge near the cathode. If a weak auxiliary current is used (e.g., 20 to 100 ma), triggering density will not be reached, and a separate control grid pulse must then be used to trigger the tube. This is undesirable; we have previously reported that  $di/dt$  is lower when the trigger pulse is applied to the control grid as opposed to the auxiliary grid(1).

One way to avoid these difficulties is by making the interelectrode spacings (and ambipolar diffusion times) large. However, long spacings are inimical to low inductance, and for the purpose of increasing  $di/dt$ , negative bias can serve the same end. In the example of Figure 1, the electrode spacings are reduced to 2-4 mm. To prevent premature commutation, negative control grid bias is used. Figure 2 shows the effect of bias on a similar (but slightly smaller) tube. The effect of the bias is to lengthen the time available for the auxiliary current to grow and to spread on the cathode. A small bias produces a significant increase in  $di/dt$ .

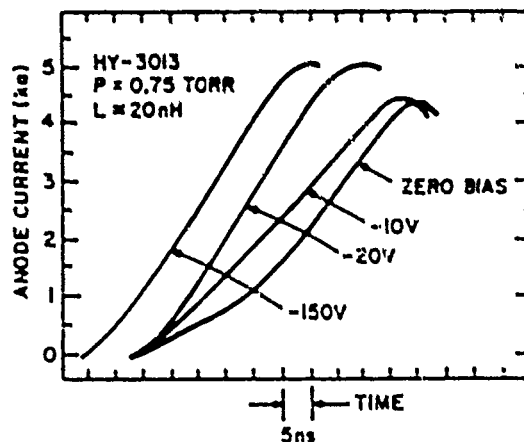


Figure 2. Effect of negative control grid bias on anode current rise.

The increase in  $di/dt$  with increased commutation delay is in accord with reasonable plasma production rates ( $10^6$  to  $10^8$  ions per second). Calculation of the effects of bias as shown in Figure 2 yields a 22% increase in  $di/dt$ ; we have observed a 25% increase.

## Comutation

### Models for the Commutating Thyatron

We have now developed models for the hydrogen thyatron that can predict the behavior of thyatron-switched pulse circuits. We assume that the thyatron can be modeled by two series elements: a constant inductance, dependent only on geometry, and an exponentially falling resistance or voltage, with a time constant,  $\tau_i$ , dependent only on gas pressure.

### Analytical Approach

This approach treats the commutating tube as a voltage source (in series with the tube's inductance) acting to oppose the rise of the circuit current. The instantaneous source voltage is shown in Figure 3.

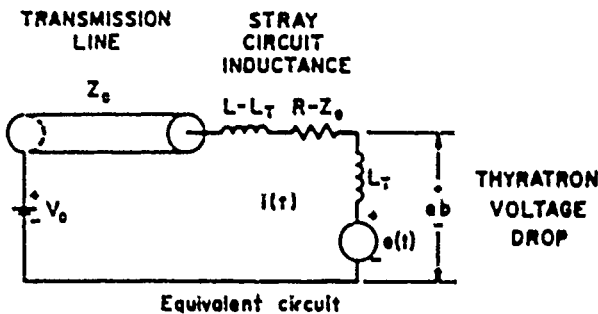
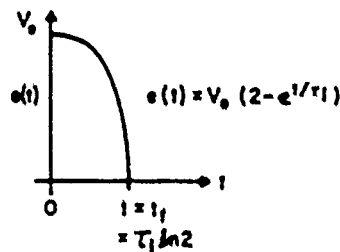


Figure 3. Circuit model of thyatron.

The time constant  $\tau_i$  depends only on the gas pressure, and it decreases as pressure increases. Typical values for  $\tau_i$  are 10-30 ns, corresponding to total anode fall times of about 5-20 ns. The "steady-state" tube drop is ignored, and  $e(t) = 0$  for  $t > \tau_i$  when the thyatron behaves as an inductor.

With standard transient analysis techniques, this model has been used to accurately predict the rising portion of the current waveform, the time and magnitude of the peak current, and the width of the current pulse for thyatron-switched pulse forming circuits. An example is shown in Figure 4.

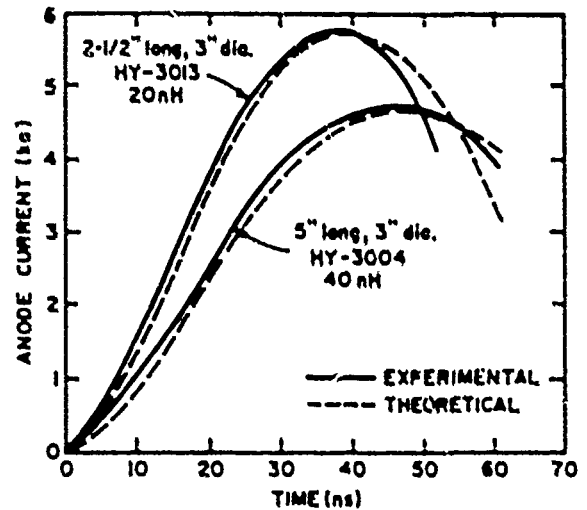


Figure 4. Comparison of experimental and theoretical anode currents.

### Numerical Approach

The numerical approach gives equally good results by treating the commutating tube as a time-dependent resistance,  $R(t)$ , in series with the tube inductance,  $L_T$ .  $R(t)$  is assumed to decrease exponentially and the differential equation of the circuit is then solved numerically. The numerical approach can be extended to more complex tube models such as those involving a time-varying discharge diameter, or to time-varying loads.

### Resistive Fall Time

That part of the anode fall due to plasma density growth in the grid-anode region (sometimes called the "resistive fall time") is a strong function of the tube's gas pressure, a trait shared with other gas discharge switches.

Figure 5 shows the total voltage fall time as a function of pressure for several types of gas discharge switches in high inductance circuits. Although the data are imprecise, and various gas species are involved, the relationship evident over 9 decades of pressure is striking.

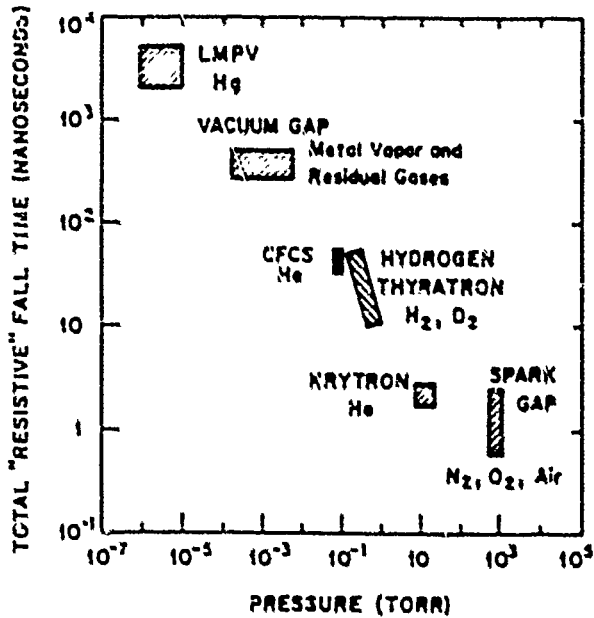


Figure 5. "Resistive" fall time (closure time) as a function of operating pressure for various gas discharge switches.

Using the analytic model, we can characterize the family of gas switches, plotting the average value of  $di/dt$  per volt switched, as a function of pressure. Figure 6 shows that for a particular pressure there is a corresponding maximum  $di/dt$

per volt, forming a boundary within which switching can occur. Within this region there are other upper bounds determined by the inductance. The region of greatest interest lies between  $di/dt/V$  values of  $10^7$  and  $10^8$  amperes/second/volt.

It is obvious that high operating pressure is required for fast switching. For hydrogen thyratrons, this means 0.6 torr or higher.

#### Inductance

Provided that the initial plasma conditions are properly established during triggering, and that the resistive fall limit is not reached, then the self-inductance of the tube and its current return will dominate the switching operation. The inductance can be calculated from the physical dimensions of the discharge and the current return, making the assumption that the discharge fills the tube to the diameter of the grid apertures.

To achieve low inductance, physically short versions of standard tubes have been built and tested. Figure 4 shows the results.

In a low impedance Blumlein system, we have achieved  $di/dt = 1 \times 10^{12}$  amperes per second at 47 kv with an H<sub>1</sub>-5313, consistent with calculated values. Testing up to 2 kHz and up to 50 kv is continuing with this system.

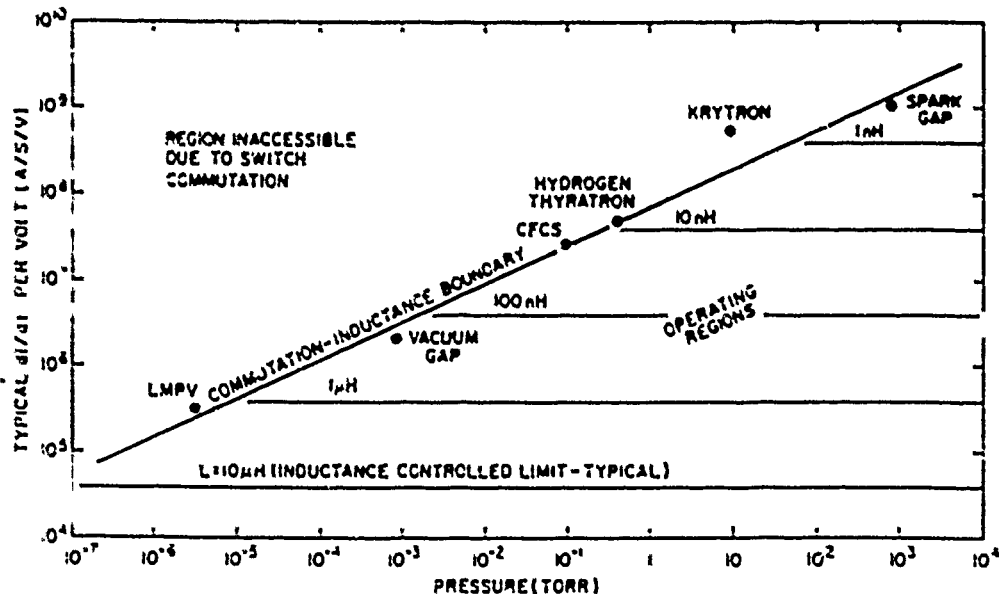


Figure 6. Limits imposed on  $di/dt$  per volt due to commutation effects and circuit inductance.



Further increases in tube diameter and improvements in geometry are projected to give inductances of only a few nanohenries, and  $di/dt$  per volt approaching  $1.5$  amperes/second/volt.

### HIGH VOLTAGE DESIGNS

High voltage implies long insulators and long, multistage tubes with low pressures. Lower inductance and short commutation times imply short tubes with the minimum number of high voltage stages, operated at high pressure. Since conventional insulators are meant to operate under adverse environmental conditions, much of the necessary reduction in insulator length is possible simply by using more highly stressed insulators in a controlled dielectric environment.

### Pulse Charging

Command pulse charging, with only a short dwell time at full voltage, gives an increase in dynamic over static breakdown voltage that can be used to advantage to reduce insulator lengths, reduce the number of high voltage sections, and increase the gas pressure. Figure 7 shows the effect at two anode-grid spacings. The pulse charging advantage is clearly seen, giving high breakdown voltages at high pressures.

In fast pulse charging, the applied voltage is distributed across the various stages in accordance with the interelectrode and stage-to-current-return capacitances. The distribution will be nonuniform, with the highest voltages appearing across the upper stages. Figure 8, shows a case with constant capacitances. Substantially uniform distribution can result only when  $C_2 \ll C_1$ . Alternatively, the capacitances can be tailored to provide a more uniform distribution. The maximum  $\text{apv}$  is thus determined by the maximum voltage tolerable by the upper stage. An optimum number of stages exists.

An important further set of compromises in the design of a high voltage, multistage, low inductance thyratron concerns the relative diameters of the tube and its coaxial current return. The demand for low inductance requires a close-fitting current return, in conflict with the need to reduce the capacitance to ground. Furthermore, the dielectric stress between the current return and the tube becomes significant at high voltages. The usable tube-to-current-return radius ratios are found to lie between 1:2 and 1:4.

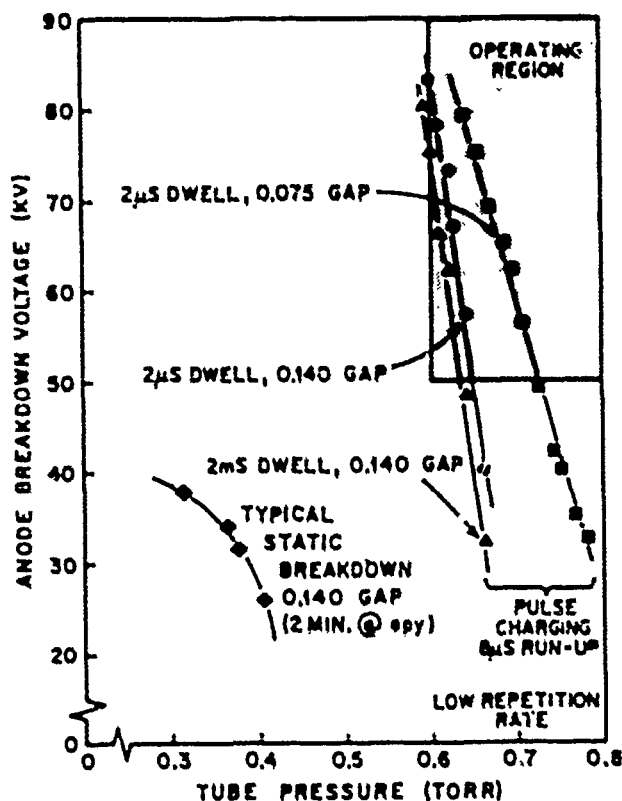


Figure 7. Anode breakdown voltage with pulse charging.

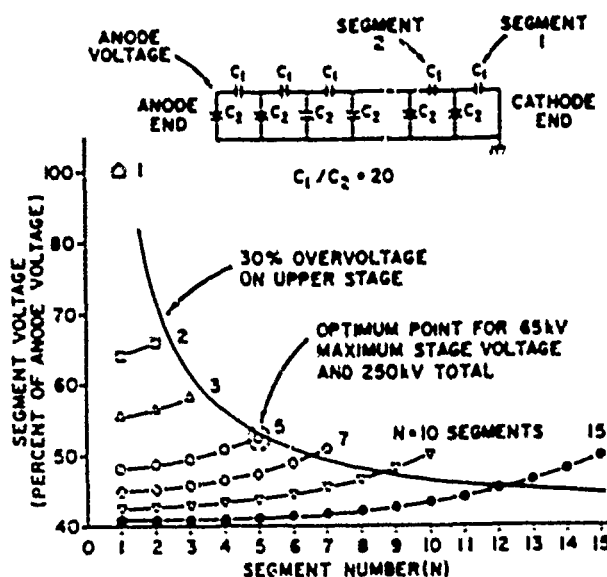


Figure 8. Voltage distribution on multistage tubes.

## Materials

The lower limit for the stage length, and thus the minimum inductance for a practical device, is partly determined by the ceramic breakdown properties. We have therefore investigated breakdown for insulators subjected to spatially nonuniform stress patterns with high voltage pulses to simulate actual operation. We conclude that for tubes operated in oil, pulse holdoff at a ceramic stress of 50 kv per inch is acceptable. During switching, the upper sections of the tube are stressed to progressively higher levels, until the upper section must hold off the entire applied voltage, perhaps for tens of nanoseconds. Under these conditions, a stress level of 150 kv/inch is being used in our experiments.

## High Voltage Thyratrons

Figure 9 shows a design for a five-stage, 250 kv tube based on the principles described above, compared with a 10-stage tube designed for 250 kv operation in air. The latter operated at over 200 kv, at high peak and average power(4,5). Tubes of the new design are expected to operate at 250 kv, with peak currents in excess of 20 ka and pulse repetition rates of at least 1 kHz. Calculated inductance is less than 60 nH.

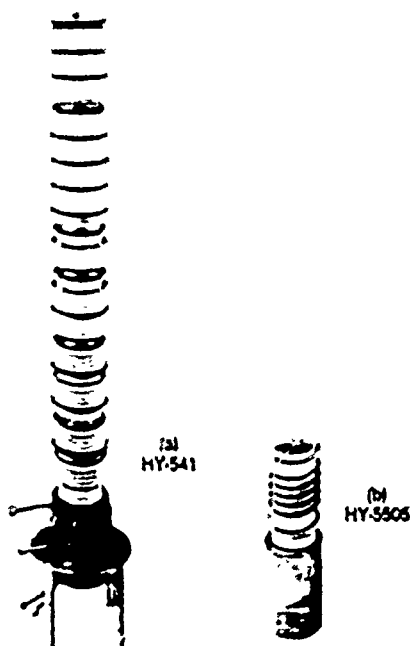


Figure 9. (a) Conventional and (b) low inductance multistage tubes designed for 250 kv.

## ANODE DISSIPATION

Thyratron specifications contain a "Plate Break-down Factor,"  $P_b$ , intended to limit anode dissipation to tolerable levels. Although it has long been recognized that this factor is inadequate to describe the problem, it has only recently been possible to quantify anode dissipation in high  $di/dt$  circuits. The result of our analysis is to replace the old  $P_b$  factor with a new factor, defined as

$$\pi_b = \text{voltage} \times \text{repetition rate} \times di/dt \\ (\text{epy prr } di/dt)$$

The model described above has been used to calculate anode heating when switching a transmission line charged to a voltage,  $V$ . Defining a circuit time constant,  $L/Z$  (with  $L$  the total switch and connecting inductance, and  $Z$  the total impedance of the line plus the load directly across the switch), we can show that the anode dissipation energy per pulse,  $W$ , is a function of  $\tau_i/\tau_L$  as shown in Figure 10, and the power dissipation is directly proportional to  $\pi_b$ . Anode dissipations consistent with the above calculation have been observed in practice for tubes operated at high  $di/dt$ .

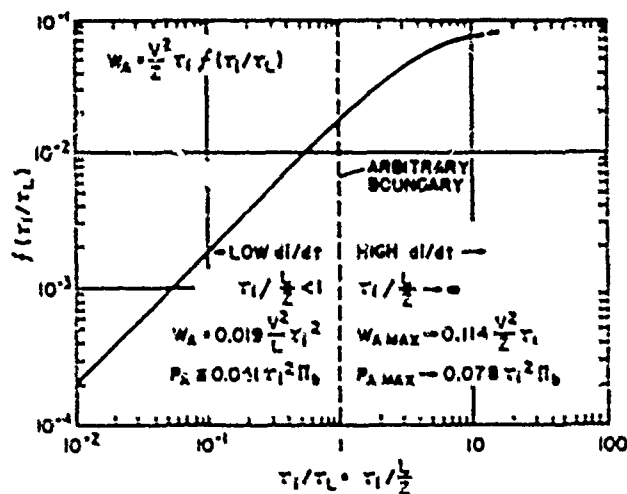


Figure 10. Anode heating in a transmission line circuit.

At a few tens of kilovolts with a fast circuit, the anode dissipation can become substantial, i.e., several hundred watts per kilohertz of repetition rate. The magnitude depends critically on  $\tau_i$ , normally for thyratrons about 30 ns

(corresponding to a 20 ns fall time). This can be reduced to at least 20 ns at higher pressures ( $>0.6$  torr). On the other hand, reduction of pressure can cause much higher  $\tau_f$ , with the resultant high dissipation causing excessive anode heating. Thyratrons for fast switching applications must therefore operate at relatively high fill pressures to minimize anode dissipation as well as to promote high  $di/dt$ .

#### HIGH AVERAGE POWER THYRATRONS

The work performed in recent high power development relied heavily on advances made in earlier programs (3,4,6,7). Designing a thyatron specifically for pulse power operation at a megawatt required that the scaling laws for peak and average currents be validated at very high average powers. This has now been done at the megawatt level(2), and the way is now clear to switching several tens of megawatts in hydrogen thyratrons of relatively modest physical size.

Forward holdoff design principles for high power are basically the same as for low power. The structures used at a megawatt are different only in their overall size, heat capacity, and fault resistance. The principles for minimizing tube inductance apply equally to high power designs, and produce less conduction loss.

#### Peak Current

Peak current limitations result from two effects: cathode arcing and grid quenching(6,8). Both are pulse-width-dependent. The cathode arc limit current density varies as  $1/\tau_p^{1/3}$ . It is also dependent on the specific resistivity of the cathode surface(8), and hence on its temperature and state of activation. With pulse widths of about 10  $\mu$ s, the current density for arcing (usually at the cathode's extremities) is usually 30-40 a/cm<sup>2</sup>, a limit now verified at the 75 ka level.

When grid quenching occurs, the tube's impedance rises abruptly, usually resulting in an arc. Quenching is pressure and time dependent, is most often seen in pulses several microseconds long, and occurs at current densities close to those calculated to produce a MHD pinch within the grid structure. We have now verified a long-standing design criterion of 10 ka/in.<sup>2</sup> of grid aperture at the 75 ka level.

At short pulse widths (100 ns or less), quenching has been difficult to produce and cathode arc limits are high. For example, with 14 ka, 50 ns pulses from a 100 cm<sup>2</sup> cathode, passing through a 0.3 in. grid aperture area, no arcing occurred. Other experiments with larger tubes, but somewhat lower peak current densities, give consistent results.

#### Average Current

In thyatron ratings, d.c. and a.c. average current limitations appear, beyond which excessive heating is likely, causing short tube life.

Most of the dissipation due to d.c. average current is absorbed in the grid structures. The greatest burden is carried by the control grid, which must absorb the losses of a 30 to 50 volt Langmuir double sheath and the discharge column drop of about 20 v/cm, and some part of the cathode heat as well. The total thermal conductivity from grid-face to external heat-sink must be high enough to prevent any part of the grid from reaching temperature ( $>400^\circ\text{C}$ ) for the grid to emit and destroy the tube. Total grid thermal conductivity thus becomes a limitation on the maximum average d.c. current.

The a.c. average (r.m.s.) current (ranging into the kiloamperes) is also an operational limit, due to resistive ( $I^2R$ ) heating in the cathode coating and its support and connecting structures. The oxide cathode typically used in thyratrons has surface resistivities of 2-10 ohm-cm<sup>2</sup> and generates heat over its utilized area (itself dependent upon the peak current, in accordance with the cathode utilization equations(3)).

At high peak currents, the r.m.s. current often becomes the major limitation. At short pulse lengths, when the discharge may not be spread well on the cathode, this limit may become especially severe, and resistive heating of small portions of the cathode may limit the total average power that can be switched.

#### Scaling Relationships

The current-carrying ability of thyratrons depends primarily on the grid aperture and cathode areas. These in turn depend on the tube diameter. Figure 11 shows peak and average currents feasible with various tube diameters, together with the r.m.s.

current limitations of earlier designs. In Figure 11, the behavior for continuous operation with pulse widths of 10  $\mu$ s is used as a base, and is shown extended for shorter pulses, or for burst-mode operation. Also shown is the predicted characteristic of a 16-inch diameter tube. Such a tube would have an arc limit greater than 350 ka peak, and an average current limit of 200 amperes, giving an average power switching capability in the tens of megawatts. We believe that the ultimate capabilities in peak and average current are limited only by the maximum practical diameter for ceramic envelopes.

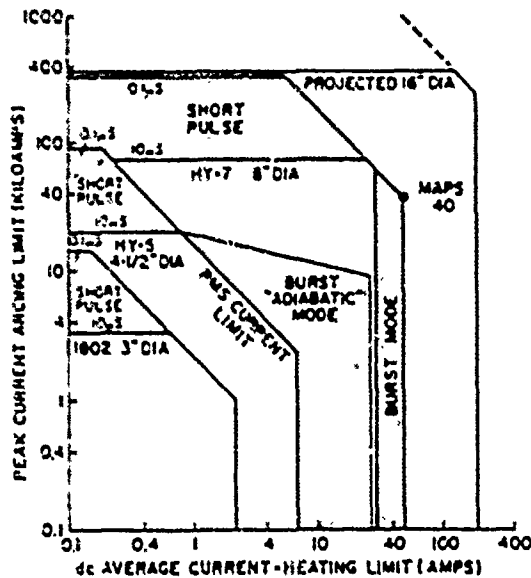


Figure 11. Performance vs. size.

### CONCLUSIONS

Hydrogen thyratrons can meet the switching requirements of advanced high power systems. Recent advances in thyatron design have significantly extended the fast switching and high power capabilities of this family of high repetition rate switches. Low inductance thyratrons have been built for high di/dt operation, the optimum triggering method has been determined, and their performance during commutation has been calculated.

Those aspects of thyatron design that are consistent with high di/dt are also consistent with high power, leading in both cases to short structures of relatively large diameter, in which holdoff is obtained by careful control of insulator loading and environment. In prospect is a new family of hydrogen thyratrons with much higher di/dt, voltage, and power capabilities.

### ACKNOWLEDGMENTS

The work presented in this paper has been supported in part by:

NSWC, Dahlgren, Virginia  
 LASL, Los Alamos, New Mexico  
 ERADCOM, Fort Monmouth, New Jersey  
 AFAPL, Dayton, Ohio  
 MIRADCOM, Redstone Arsenal, Alabama

### REFERENCES

1. S. Friedman, S. Goldberg, J. Hamilton, S. Merz, R. Plante, and D. Turnquist, *Proceedings, IEEE Thirteenth Pulse Power Modulator Symposium*, Buffalo, New York, pp. 129-134, 1978.
2. J. Hamilton, S. Merz, R. Plante, D. Turnquist, N. Reinhardt, J. Creedon, and J. McGowan, "Development of a 40 kV Megawatt Average Power Thyatron (MAPS-40)," *Proceedings, IEEE Thirteenth Pulse Power Modulator Symposium*, New York, pp. 135-143, 1978.
3. S. Goldberg and J. Rothstein, *Advances in Electronics and Electron Physics*, Academic Press, New York, Vol. 14, pp. 207-264, 1961.
4. J.E. Creedon, et al., "Adiabatic Mode Operation of Thyratrons for Megawatt Average Power Applications," *IEEE Conference Record, Twelfth Modulator Symposium*, February 1976.
5. J.E. Creedon and S. Schneider, "Megawatt Average Power Adiabatic Mode Thyratrons," *Proceedings, International Pulsed Power Conference*, Texas Tech University, Lubbock, November 1976.
6. A. Shea and D. Turnquist, "Research Studies for Cathode and Grid Elements for Super Power Switches," U.S. Army Signal Corps Contract DA 39-039 sc 85339, Final Report, September 1962.
7. A.W. Coolidge, "Research and Development of Superpower Thyratrons, Phase II-b" Final Report, U.S. Army Signal Corps Contract DA 36-039 sc 74350, 1963.
8. J.E. Creedon, S. Schneider, and F. Cannata, "Cathode-Grid Phenomena in Hydrogen Thyratrons," *Proceedings, Seventh Symposium on Hydrogen Thyratrons and Modulators*, p. 16, May 1962.

## P2.2

## INVITED

## ACCELERATOR MODULE OF "ANGARA - 5"

S.V. Basenkov, O.A. Gusev, Ju.A. Istomin, Ju.V. Koba, G.M. Latmanizova  
A.M. Pasechnikov, B.P. Pavchev, O.P. Pecherskii, A.S. Perlin  
L.I. Rudakov, V.P. Smirnov, V.I. Chetvertkov, I.R. Jazpol'skii

I.V. Kurchatov Institute of Atomic Energy  
Moscow USSR

Abstract

Features and design principles of the inertial confinement fusion multi-module "Angara-5" accelerator are considered.

The computed output parameters of an individual module are as follows:

$$U = 2 \text{ MeV}; I = 0.8 \text{ MA}; \tau_{1/2} = 90 \text{ ns}; W = 102 \text{ kJ}$$

The predicted output was compared with the pulse-shaping line mock-up measurements. According to these measurements the end-on section contributes 21 per cent of the total pulse-shaping line capacitance. The end-on section capacitance was accounted for in computations via transmission line sections with appropriate impedance values. The reasonable choice of the pulse-shaping equivalent circuit was confirmed by experimental data and were in good agreement with calculations based on system design features.

ANGARA - 5. GENERAL DESIGN

The  $10^{-8}$  -  $10^{-9}$  s pulsed Relativistic Electron Beam (REB) inertial confinement program [1] has recently received new impetus due to the development of 10-100 TW accelerators [2,3]. Target heating requirements limit the diode voltage to 2 - 4 MV such that specific accelerators should have a low output impedance and generate currents of  $10^7$  -  $10^8$  A.

The problems of developing a 100 TW, 0.1 Ohm accelerator were analyzed in 1974 [2]. The multi-module type accelerator was found to present many advantages. The total independence of modules and module groups allows the opportunity for preliminary module development and test. It ensures over-

all facility safety in case one of the modules breaks down. The facility shall consist of several tens of identical modules such that it will be possible to utilize already well developed 1-2 Ohm output accelerator technology. The omission of one or a few modules would result in an insignificant total power decrease. So, in principle, experiments should not be interrupted during repair and maintenance operations. These considerations have caused the multi-module design of "Angara - 5" developed by the I.V. Kurchatov Institute of Atomic Energy and the D.V. Efremov Institute of Electro-Physical Apparatus.

The Angara-5 accelerator is designed for target heating experiments using 48 REB generator modules. The latter are located around the explosion chamber in a two-floor structure with 24 modules on each floor. The total beam energy is 4.8 MJ. The half-width beam duration is 90 ns. The total beam current is up to 40 MA with diode voltages up to 2 MV. Fig. 1 shows the general accelerator lay-out. There is a 6 m diameter explosion chamber in the center. Two possible ways of transporting the REB energy to the central target surface inside the chamber are being considered. The first is based upon vacuum transmission lines, which may be disc-shaped. The REB energy is transported along these disc-shaped lines towards the diode in which the external target shell represents the anode. The required  $10^{13}$  W/cm<sup>2</sup> energy flux along the line can be achieved at  $E = 4 \text{ MV/cm}$  average field inside the line which is feasible due to the magnetic self-insulation [4]. An alternative transport scheme would involve the production of an inertially confined relativistic

electron sheath, the beam being injected into the sheath making use of external cusp magnetic fields [5].

The beam energy arrives at the explosion chamber along magnetic self-insulation vacuum lines having a 30 cm diameter and 3.5 m length. The line length is determined by the high-voltage diode insulator size (assuming a 60 kV/cm permissible surface electric field). The electric field in the vacuum line is 2 MV/cm. The vacuum line impedance was calculated according to the Brillouin electron flow in the gap [6,7].

The high-voltage diodes are connected to pulse-shaping Blumlein lines via water-insulated transmission lines. The transmission line diameter is 1.2 m, its length being 5 m due to the Marx generator size. The 2.5 m diameter water-filled Blumlein line has a 60 ns electric length ( $L = 1$  m) and a 2 Ohm output impedance. The Marx generator tank has a 3.2 m diameter and transformer oil is used as insulation in the Marx generator.

#### "ANGARA - 5" EXPERIMENTAL MODULE

Let us consider in more detail the "Angara-5" accelerator module. In order to lower the voltage gradients along the dielectric diaphragms and across the switch gaps as well as to improve the operation reliability, it was decided to use a Blumlein type pulse-shaping line. This choice has resulted in a larger module diameter and somewhat more sophisticated design. Fig. 2. presents a cross-section of an experimental "ANGARA-5" module. This module has been assembled at the I.V. Kurchatov IAE.

The Marx generator 1 consists of three parallel circuits. Each circuit consists of 14 stages. Each stage contains four 0.4  $\mu$ F, 100 kV condensers connected in a parallel-series configuration and are charged up to  $\pm 89$  kV. The stages are placed inside 2.4 m diameter voltage-grading rings. Marx generator switching is achieved with field distortion switch-gaps pressurized with  $\text{SF}_6$  at  $\sim 1$  kg/cm<sup>2</sup>. As the condensers are tightly packed with a resulting bad stray capacitance ratio, the gaps are ex-

ternally triggered. Transverse resistive couplings are provided to improve the switching range of the central condenser array.

The Marx generator parameters are the following: 35.7 nF capacitance, 2.67 kV peak voltage, 305 kJ stored energy. Fig. 3 shows the assembled Marx generator outside its container.

The Blumlein line 7 is charged via two conductors 3. The conductors pass through section 4, separating the Marx generator from the line. The dielectric diaphragm electric fields are computed to be up to 90 kV/cm. In order to use the volume of the line in the optimum manner the wave impedances of the outer and inner lines were chosen different, namely 0.82 and 1.36 Ohm. The intermediate electrode thickness and end-on curvature radii were chosen in accordance with computed admissible electric fields in water. The computations were based upon the following relations [9] for fields 30% below the breakdown limit

(1)

$$E_+ \leq \frac{0.21}{\epsilon^{1/3} S_{\text{eff}}^{0.06}} \text{ MV/cm}; \quad E_- \leq \frac{0.42}{\epsilon^{1/3} S_{\text{eff}}^{0.06}} \text{ MV/cm}$$

The internal electrode diameter is 149 cm and the intermediate electrode thickness is 14.5 cm. This high electrode-diameter over line-length ratio results in considerable edge contribution to the total line capacitance. Mock-up measurements indicate that the end-on sections contribute 21 per cent of the 76.5 nF total line capacitance. The inner line and outer line capacitances are 30 nF and 46 nF respectively. The inner line is charged via conductor 5 which serves to inductively decouple both lines. The line is switched with 10 gas-filled triggered switches 6 located at the inner line edge. The high-voltage triggering pulses are supplied via 10 cables passing inside the conductor 5.

Prepulse is suppressed by a multi-channel gas-filled spark gap 8 following the 30 nF capacitance line section. The capacitance across the spark gap is 63 pF. The spark gap is followed by a 4.0 m long water transmission line 9 which serves as a trans-

former. The 50 nH inductance high-voltage diode 10 is of quasi-planar shape. The diode is followed by a magnetically self-insulated vacuum line 11.

Computations of line charging and switching were performed to estimate the pulse shape, the efficiency of energy transport from the Marx generator to the load and the prepulse level, the latter being of importance for normal vacuum line and diode operation. The SF<sub>6</sub> filled switch spark channel resistance was computed according the Bragin-ski formula [9]

$$R = \frac{K P^{1/3} L}{\int_0^L \frac{1}{I^{2/3}} dt} \quad (2)$$

The vacuum line load was assumed to correspond to the minimal magnetic self-insulation current in the flux limited regime at  $U = 2$  MV. The validity of the latter assumption follows from the practically linear dependence upon voltage for  $U > 0.5$  MV.

Fig. 4 presents the charging/switching scheme taking into consideration the above-cited module parameters. The charging computation takes into account the condenser resistivity which was calculated from the attenuation decrement near the lower self-frequency of the circuit of Fig. 4.

The Marx generator-to-line energy transfer efficiency was found to be up to 73%. The charging line voltage is 2.4 MV. The voltage across the prepulse spark gap is 200 kV. The diode prepulse is plotted versus time in Fig. 5. The diode prepulse magnitude  $\sim 200$  V is low enough to allow the use of short inter-electrode gaps.

The effect of edge sections was accounted for in the calculations by introducing special line sections. Fig. 6 presents the computational sectioning of the Blumlein line. The effective line length  $l_{eff}$  was found from the relation

$$C = \frac{l_{eff} \sqrt{\epsilon}}{\rho c} \quad (3)$$

with  $\rho$  representing the wave impedance of the line. The resistance and inductance of the Blumlein line spark gaps were computed according to the Bragin-ski formula. The number of spark channels in each

spark gap was varied in the calculations. The computed pulse shape of Fig. 7 was compared with line mock-up measurements. The mock-up switching resistivity was chosen equal to that of spark gaps 100 ns after triggering. The good agreement between computation and measurement has corroborated the reasonable choice of the pulse-shaping scheme. The main result of computations are pulse lengths up to 90 ns and pulse power modification due to edge capacitance effects.

Fig. 8 presents the computed pulse shape and diode energy deposition for a 50 nH diode inductance. Calculations show that the channel number should exceed 5 - 6 to limit losses in the spark gaps. A further channel number increase does not substantially improve the pulse parameters.

So the "Angara-5" module should be able to produce a  $U = 2$  MV,  $I = 0.8$  MA,  $\tau_p = 90$  ns, total energy per pulse (for  $\tau \leq 110$  ns) is 102 kJ for a constant  $R_d = 2.5$  Ohm impedance. The Marx generator-to-beam energy transfer efficiency is 33 per cent.

#### References

1. L. I. Rudakov, S. A. Samarskii, VI European Conf. on Controlled Nuclear Fusion and Plasmas Physics. Moscow 2, 487 (1973).
2. E. P. Velikhov, V. A. Glukhikh, O. A. Gusev, G. M. Latmanizova, S. L. Nedoseev, O. B. Ovchinnikov, A. M. Passechnikov, O. P. Pecherskii, L. I. Rudakov, M. P. Svin'in, V. P. Smirnov, V. I. Chatvertkov, "Angara - 5 accelerator complex". Preprint D-0301, NIIIEFA, Leningrad, 1976, (In Russian).
3. G. Yonas et al, 7th Conf. on Plasma Physics and Controlled Thermonuclear Research. CN-37-N3, Innsbruck, Austria, 23-30 Aug., 1978.
4. E. I. Baranchikov, A. V. Gordeev, V. D. Korolev, V. P. Smirnov. Zh.E.T.F. 75, 2102, 1978 (In Russian).
5. E. I. Baranchikov, A. V. Gordeev, Ju. V. Koba, V. D. Korolev, V. S. Pankina, L. I. Rudakov, V. P. Smirnov, A. D. Sukhov, E. Z. Tarumov. Intern. Topical Conf. on Electron Beam Research and Technology. November 3-5, 1975, Albuquerque v. 1, 248, Sand. 76-5122, 1976.
6. E. I. Baranchikov et al. Reports to the All-Union Conference on Thermonuclear Reactor Engineering Problems, 2, Leningrad, NIIIEFA Edition, 1977 (In Russian).

7. J. M. Creedon. J. Appl. Phys. 48, 1070 (1977).
8. Frazier, J. Vac. Sci. and Techn. 12, 1183 (1975).
9. S. I. Savannik, S. B. Vasserman, A. I. Lukin. Preprint IJaF 16 - 71, Novosibirsk, 1973 (In Russian).

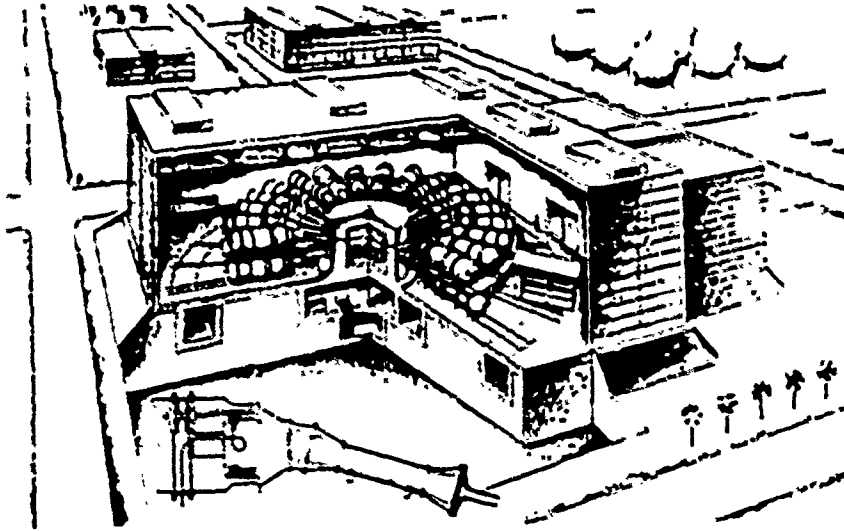


Fig. 1 General lay-out of "Angara-5" accelerator.

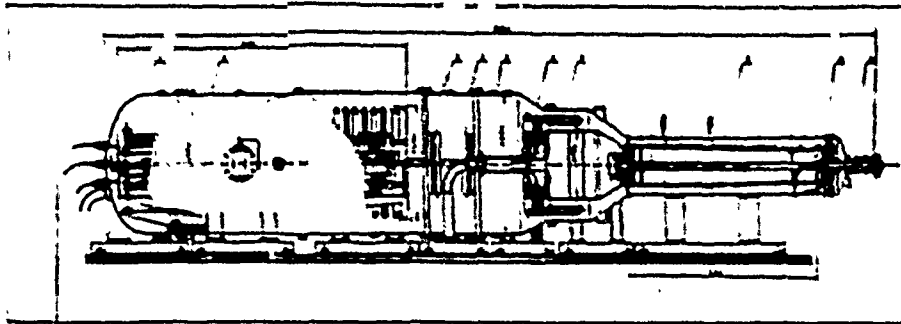


Fig. 2 Cross-section of the "Angara-5" accelerator experimental module.



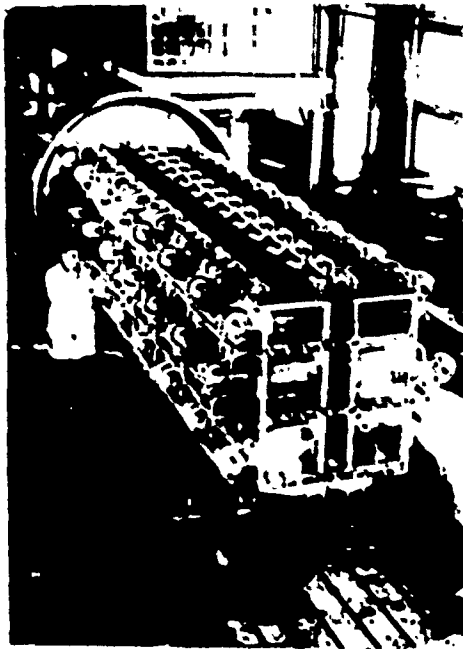


Fig. 3 Module Marx generator assembled outside the tank.

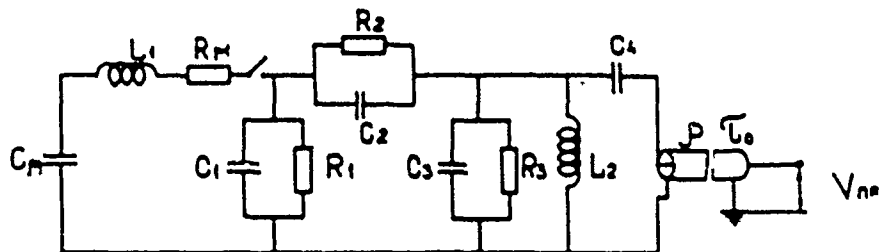


Fig. 4 Blumlein line charging equivalent circuit assumed in output pulse computations.

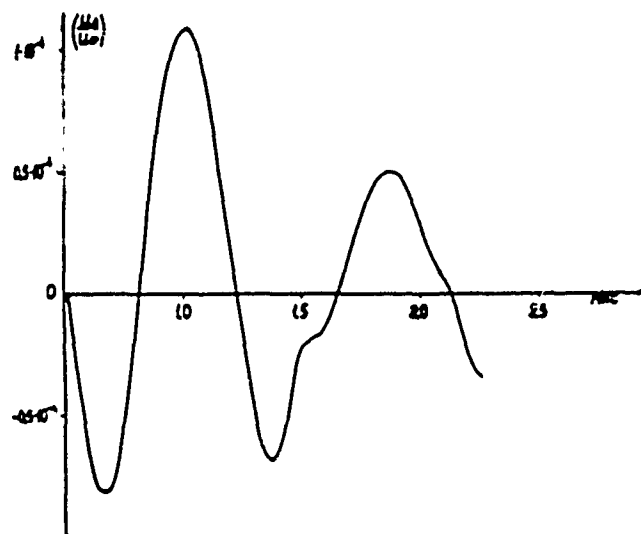


Fig. 5 Diode prepulse voltage versus time.

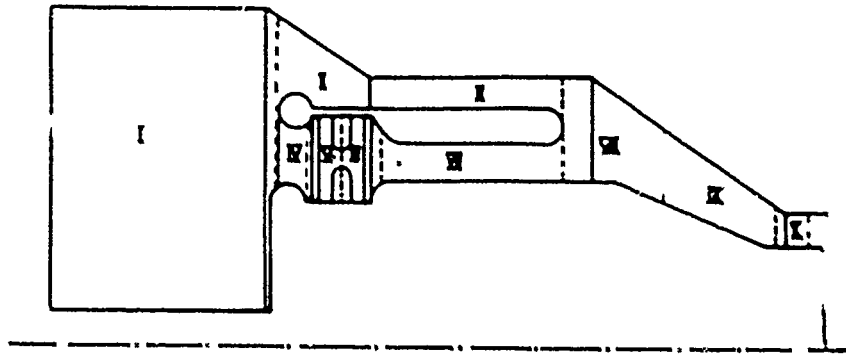


Fig. 6 Scheme of Blumlein line sectioning assumed in output pulse computations.

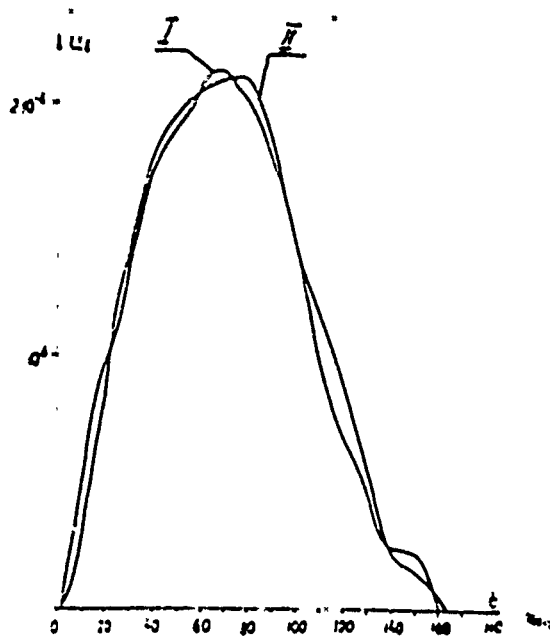


Fig. 7 Computed pulse shape compared with the pulse shape measured in mock-up conditions.

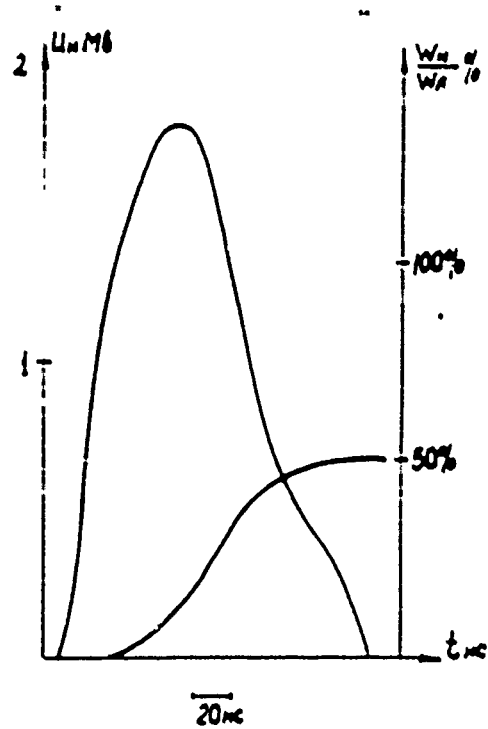


Fig. 8 Diode voltage and diode energy deposition for a 50 nH diode and 9 spark channels in each Blumlein switch.

## P2.3

## INVITED

## REVIEW AND STATUS OF ANTARES\*

Jorg Jansen

University of California, Los Alamos Scientific Laboratory  
Los Alamos, NM 87545

Abstract

The laser fusion effort at the Los Alamos Scientific Laboratory (LASL) has evolved from early experiments with an electron-beam-controlled large-aperture CO<sub>2</sub> laser to the massive engineering task of designing and building a 100-kJ laser fusion machine.

The design of Antares is based on the design of its predecessors. It builds upon technology which was developed or advanced during the design and construction of earlier machines. On one hand it is dictated by the requirements for the output, i.e., energy on target; on the other hand it is limited by existing technology or reasonable extensions thereof. Reliability and maintainability play important roles in the design considerations.

Introduction

The goal of the Laser Fusion program is to achieve inertially confined fusion for commercial and military applications. The high-power, short-pulse CO<sub>2</sub> laser developed at LASL lends itself very well to this task because of the high efficiency and capability to operate at high repetition rates. The 100-kJ Antares laser, the fourth step in the LASL development, is designed to provide this laser power for scientific breakeven experiments in 1984. This paper gives a brief overview of the evolution, design, and construction of Antares as a background for a number of detailed papers presented elsewhere at this conference.

---

\*Work performed under the auspices of the U.S. Department of Energy

Evolution

As we are gradually getting more used to the idea of very large CO<sub>2</sub> fusion lasers Antares becomes more tractable in its enormous size and complexity. Less than a decade ago the concept of such a large machine would have been unthinkable. However, development took place at a fast pace and what seemed to be an unlikely adventure then is now rapidly becoming a reality. The evolution began with the departure from the double-discharge laser.

The double-discharge laser is the kind of device upon which one would not hesitate to base the construction of a large reliable gas laser facility. It is simple, rugged, inexpensive, and easy to operate and maintain. Unfortunately, the laser energy output and the maximum aperture of a single cavity are relatively small. The size is limited by a gap-pressure product of about 20-cm-atmospheres compared to about 75-cm-atmospheres for an electron-beam sustained CO<sub>2</sub> laser.<sup>1</sup> By way of comparison, the Lumonics 620 can generate a short pulse of <100 J with an aperture of 10 x 10 cm. Translated into the energy requirement of 100 kJ for Antares, this would mean a system of 1000 beams and cavities. Such a large number of components and subsystems makes the facility reliability almost automatically questionable.

One way to overcome this problem and provide for a stable, large-aperture discharge is to feed an externally generated electron beam into the cavity. In this way, the generation of ionizing electrons and the control of their energy and density is separated from the parameters of the cavity. To build and operate such an electron-beam controlled CO<sub>2</sub> laser was successfully

attempted at AVCO and at LASL in 1970.<sup>2</sup> The success of this approach opened the door for the development of large-aperture, high-energy CO<sub>2</sub> lasers for commercial, military, and fusion applications. The number of cavities for a given requirement for total energy and beam size could be reduced considerably.

To initiate fusion experiments with a short-pulse CO<sub>2</sub> laser, a single-beam system was designed and built at LASL in 1971.<sup>3</sup> It employed for all its amplification stages, high-power electron-beam controlled discharge cavities (Fig. 1). Table I shows the characteristic features of that system.

The electron-gun energy was delivered by Marx generators which were allowed to RC decay. The pulse was terminated by diverter switches. The discharge chamber of the final amplification stage was powered by an LC generator with a diverter switch for pulse termination.

Based upon the experience with the low-energy single-beam system, a dual-beam module (Gemini) was designed and built in 1974.<sup>4</sup> The design of Gemini and, subsequently, Helios follows in principle the single-beam design. The main differences are found in the employment of one electron-beam gun for two pumping chambers, the triple passing of the gain region, and the larger aperture (14 inches vs 10 inches), Fig. 2. One of the major difficulties resulted from the use of a large-area hot cathode in the electron-beam gun. The large amount of heat deposited in the gun chamber and the thermal distortion of the cathode itself proved difficult to handle. The development and subsequent introduction of the cold cathode overcame all these problems.<sup>5</sup> The cold cathode employs an arrangement of thin tantalum foils which, upon ignition, generate plasma sites that, in turn, serve as electron emitters. Performance data of Gemini are listed in Table II.

To generate a 10-kJ laser pulse, four dual-beam modules were combined into an eight-beam

system, Helios (Fig. 3). Helios became operational in April 1978 and delivered a subnanosecond pulse of 10.7 kJ into a calorimeter in June 1978.<sup>6</sup>

The electron guns for Gemini and Helios were also driven by Marx generators with diverter switches. The discharge chambers for Gemini were powered by LC generators with diverter switches; those for Helios by Marx generators employing two-mesh type-C PFN's in each stage.

#### Antares Design

Requirements. Whereas the single-beam facility, Gemini, and Helios were designed for absorption and compression experiments, the goal for Antares is to achieve breakeven, i.e., the energy production of the target should equal or exceed the energy input to the target. Antares is designed to produce various pulse durations and output powers, ranging from a power of 100 TW with a pulse width of 1 ns to a power of 200 TW with a pulse width of 1/4 ns.<sup>7</sup> To achieve this and also leave room for considerable uncertainties in the expected performance the Antares design allows for good margins in the critical areas. Table III is a summary of the performance requirements and design margins for Antares.

The design of Antares departs from that of its predecessors. The large number of beams (72) called for "electron-beam gun economy." Thus, 12 beams were combined in an annulus around a single electron gun to form a 17-kJ power amplifier module. A more efficient Helium-free gas mix was chosen (CO<sub>2</sub>:N<sub>2</sub>/4:1). A grid was introduced in the electron gun to provide voltage independent electron-beam density control and accommodate the requirement for a considerably lower electron-beam density for the new gas mix (50 mA/cm<sup>2</sup> vs 500 mA/cm<sup>2</sup> for Helios).<sup>8</sup> To reduce the likelihood of prepulse parasitic oscillations the gain region was pumped faster and the distance between power amplifier and target was increased substantially. The major differences are listed in Table IV.

TABLE I  
CHARACTERISTIC FEATURES OF THE SINGLE-BEAM SYSTEM

Parameter	Stages 1 and 2	Stage 3	Stage 4
Electron Beam			
Energy	120 kV	155 kV	250 kV
Current	100 A	500 A	1500 A
Current Density	0.12 A/cm <sup>2</sup>	0.60 A/cm <sup>2</sup>	0.27 A/cm <sup>2</sup>
Gas			
Pressure	600 torr	1800 torr	1400 torr
Electric Field	4.3 kV/cm-atm	3.8 kV/cm-atm	3.5 kV/cm-atm
Current	5000 A	16000 A	50000 A
Current Density	6.3 A/cm <sup>2</sup>	20 A/cm <sup>2</sup>	9 A/cm <sup>2</sup>
Gain (P-20)	0.051 cm <sup>-1</sup>	0.049 cm <sup>-1</sup>	0.03 cm <sup>-1</sup>
J/liter-atm	150	150	85
Efficiency $\frac{g_o(J)E_s}{J/liter}$			3.2%(x 1/5)

TABLE II  
PERFORMANCE DATA OF A HELIOS DUAL-BEAM MODULE

Optical Design (each beam)	
Aperture	34-cm diameter
Gain Length	200 cm
Operating Pressure	1800 torr
Gas Mixture	1/4:1:3/N <sub>2</sub> :CO <sub>2</sub> :He
Gain	4%/cm (P-20, 10 $\mu$ m)
Energy Output	1250 J
Electrical Design	
Discharge Voltage	300 kV
Discharge Current	100 kA
Pulse Length	3 $\mu$ s
Energy	150 J/l-atm
Electron-Beam Voltage	250 kV
Electron-Beam Current Density	0.3 A/cm <sup>2</sup>
Pulse Length	5.0 $\mu$ s
Emitter	0.013-cm-thick Ta foil

TABLE III  
ANTARES SPECIFICATIONS

100 kJ at Target 1-ns pulse  
50 kJ at Target 0.25-ns pulse

<u>Power Amplifier Parameter</u>	<u>Design Point</u>	<u>Design Margin</u>
Mixture	CO <sub>2</sub> :N <sub>2</sub> /4:1	
Pressure	1800 torr	25% (2250 torr)
(g <sub>0</sub> - α)L	6.0	25% (7.5)
Electrical Store	5.4 MJ	25% (7.2 MJ)
Optical Aperture	60.5 cm <sup>2</sup>	13%

TABLE IV  
MAJOR DIFFERENCES BETWEEN ANTARES AND HELIOS

<u>Change</u>	<u>Antares vs Helios</u>		<u>Reason</u>
Longer distance between power amplifier and target	200 ft	20 ft	Longer buildup time of prepulse parasitics
Faster pumping to peak gain	1.5 μs	3 μs	Shorter time available for build-up of parasitic oscillation, higher efficiency
Different gas mix in power amplifier	CO <sub>2</sub> :N <sub>2</sub> 4:1	CO <sub>2</sub> :N <sub>2</sub> :He 4:1:12	Higher efficiency, no helium handling
Annular arrangement of cavities around e-gun	Number of cavities per gun 12	2	Fewer guns, large annular optics, fewer beams
Employment of current control grid in e-gun	E-beam current density 50 mA/cm <sup>2</sup>	0.5 A/cm <sup>2</sup>	Different gas mix requires lower e-beam density, better density control
Larger exit window diameter	18"	16"	Availability of larger sapphire windows
Higher discharge voltage	550 kV	330 kV	Gas mix with higher impedance
Higher e-gun voltage	500 kV	300 kV	Gas mix with higher density

Major Limitations.<sup>9</sup> The most important limitation in the design of Antares is optical in nature. A window, transparent to 10.6- $\mu$ m light, is necessary between the high-pressure (1800 torr) discharge cavity and the low-pressure ( $10^{-6}$  torr) target chamber. The best window material available is NaCl and the largest size windows made to date have a diameter of 18 inches. This, coupled with a safe limit for the energy flux of a 1-ns pulse of about  $2 \text{ J/cm}^2$ , dictates the number and aperture of the laser beams.

The mirrors are made of copper-plated aluminum by a micro-machining process. They have no influence on the selection of the beam number but limit the smallest size of the turning, folding, and focusing mirrors, and thereby the size of the space frame, target chamber, and turning towers. The inability to fabricate very large mirrors had one other effect on the final Antares design. The original plan to use annular optics was abandoned. This would have had the advantage that only 6 instead of 72 independent laser beams would have had to be managed.

Having chosen an annular arrangement of the discharge cavity, one additional limitation is imposed by the maximum permissible azimuthal magnetic field in the electron gun as well as in the cavities. Axial feed currents to the gun and cavities increase with axial length. The accompanying azimuthal magnetic field deflects electrons away from the feed end and causes non-uniform gain in the cavities. Requiring a certain degree of gain uniformity limits the length of the gun and an individual cavity. As a result, the Antares gun is fed from both ends and each cavity is subdivided into four sections.

The worst enemies of the high-energy gas laser are parasitic oscillations which can develop from spontaneous photon emission in the optical system prior to the actual shot. They can damage optical elements, cause a loss of energy and deposit prepulse energy on the target and thus destroy it.

To prevent these oscillations the gain-length-time product of each amplifier cavity has to be kept below a safe value. Computational analysis

and experimental evidence limit the single-pass gain-length in a double-pass optical design for the power amplifier cavity to  $gL \leq 6$  for a 1.5-us pumping pulse. As a consequence a high input energy of 90 J per power amplifier is required which makes a powerful electron-beam controlled amplifier necessary for the output stage of the front end.

The Antares Facility. Most of the Antares design is now completed and the major portion of the hardware is under procurement. The buildings are all under construction. A model of the entire facility is shown in Fig. 4. One recognizes clockwise from the upper left corner, the warehouse, the facilities support building, the laser and energy storage hall, the target building, the mechanical equipment building, and the office building. The front-end room is located underneath the laser hall. Figure 5 is a view of the laser hall with the 6 power amplifiers and 24 energy storage units. Figure 6 gives a clearer picture of the target chamber and the six beam turning towers.

The generation, amplification, and transport of the laser beams is schematically shown in Fig. 7.

The Antares front end (Fig. 8) generates six beams with an aperture of  $15 \times 15 \text{ cm}$  and energy of 225 J each (of this, only 90 J are utilized in an annular beam with 9-cm i.d. and 15-cm o.d.). Six oscillators are used to generate six tunable beams which are combined into one single beam. In addition to six switchout Pockels cells there are four Pockels cells in series to provide a contrast ratio (energy) of approximately  $2.4 \times 10^{12}$ . Amplification is achieved with two double-discharge amplifiers and three dual-beam modules. The dual-beam amplifiers are very similar to the Gemini and Helios amplifiers but smaller in size.

The 6 beams are directed upward into the power amplifiers which split each beam in 12 ways and provide the final two-pass amplification (Fig. 9). As indicated above, each power amplifier consists of one central electron-beam gun

surrounded by 12 discharge chambers. Because of magnetic field limitations the gun is fed tri-axially from both ends and the discharge chambers are sectioned with a resulting total of 48 chambers. Two azimuthally adjacent chambers are fed electrically through one coaxial cable with a voltage of 550 kV and a current of 40 kA. The gun is directly connected to the gun pulser which provides a gun voltage of up to 600 kV, a grid voltage of about 400-500 kV, and a cathode current of 40 kA. The output laser beams pass through 12 salt windows into the low pressure optical section where they are combined into one annular beam with the help of a periscope mirror pair.

The annular beam is then transported through an evacuated beam tube into the target building. It is turned by a set of turning mirrors into the target chamber. This is done to prevent back streaming of neutrons into the laser hall. Inside the cryogenically pumped target vacuum chamber a space frame supports a second set of flat turning mirrors and a set of focusing mirrors. A typical beam pass in the target chamber is shown in Fig. 10. The distance between the focusing mirrors and the target is approximately 1.61 m.

Pulsed electrical energy has to be delivered in different shapes and at many different places throughout Antares (Fig. 11).

The switchout cells require a very small amount of energy (approx. 10 mJ) and a relatively low voltage (12 to 25 kV). However, the risetime of the voltage pulse into 10 parallel 50-ohm loads (Pockels cell plus cable) has to be  $t_r < 1$  ns and the jitter between cells has to be  $< 50$  ps. This requirement will be met by using one fast multi-channel spark gap to energize all cells. Delays between cells will be achieved through different lengths of very low loss cables.

The preamplifiers require the following energy, voltage, current, and pulse duration:

Lumonics K-9225: 160 J, 40 kV, 2 kA, 3  $\mu$ s

Lumonics 602: 1640 J, 150 kV, 7.5 kA, 3  $\mu$ s

The Lumonics K-9225 is also operated at a repetition rate of 3 pps for alignment purposes.

The three electron guns of the driver amplifiers are fed from a common Marx generator with an energy of 25 kJ and open-circuit voltage of 630 kV. The single-mesh LC Marx is matched to the gun impedance and produces a slightly oscillatory current with a half period of 17  $\mu$ s and a peak value of 10 kA.

Each of the six driver amplifier pumping chambers is driven by a similar single-mesh Marx as above (25 kJ, 630 kV) with a peak current of 48 kA and a half period of 3.5  $\mu$ s.

Each electron gun of the power amplifier is energized by a 10-stage Marx generator (70 kJ, 600 kV, 40 kA) which is allowed to RC decay. In view of the varying requirements for electron-gun voltage and impedance, this is considered the best solution. In an earlier design stage the gun pulser was an impedance matched  $\lambda$ -type network with a peaking circuit to provide fast rising voltage for uniform gun ignition. The Marx generator feeds both ends of the electron gun where one side is connected through a tunable inductor to achieve current symmetry in the gun (Fig. 12).

Each power amplifier section (12 annular cavities) is energized by a 10-stage Marx generator with an open-circuit voltage of 1.2 MV, an energy of 300 kJ, and an LC impedance which is approximately matched to the load.<sup>10</sup> The short-pulse duration calls for a low generator inductance of about 3  $\mu$ H, which is accomplished through multiple zig-zag folding of the Marx (Fig. 13). Each Marx is connected via 6 coaxial cables to 12 anodes. The cables are dry-cured standard (145 kV) utility cables which have been tested for a pulse voltage of 1 MV.

Because of the complexity of the Antares system there exists also a very large and complex optical alignment system which is not discussed in this presentation. The electronic control system is based on a computer hierarchy (Fig. 14). A network of computers permits control of individual systems or beam lines in a stand-alone mode or the coordinated control of the entire facility. Low-level control is achieved with microcomputers (LSI-11) and intermediate-level or high-level



control with minicomputers (PDP-11/34, 60 and 70). To avoid the typical problems of transient interference in a high pulsed electro-magnetic environment all computers and computer interfaces are heavily shielded and all signal transmission takes place via fiber optic cables. A typical fiber-optic link is shown in Fig. 15. It consists of a signal generator (Pearson current transformer), an electro-optic converter, the fiber-optic cable, and an opto-electric converter.

Status of the Antares Construction. The Antares schedule (Fig. 16) as part of the overall inertial confinement fusion plan foresees that the Antares facility will become operational and ready for target experiments in the spring of 1984.

As a first step towards this goal the first beam line (of six) will be completed and checked out in the fall of 1981. The major milestones in this effort are:

- Power amplifier and energy storage system installed April '80
- Electrical and small-signal tests complete August '80
- Single-beam front-end ready November '80
- Single-sector energy extraction February '81
- 12 sector energy extraction April '81
- 17 kJ/1 ns pulse centered October '81 and focused

All Antares buildings are now fully enclosed and internal work is progressing. Figure 17 shows the target hall with its 6-ft-thick walls and 5-ft-thick ceiling. The laser hall and the front-end room will be available for joint occupancy in August 1979. It is presently anticipated that all buildings will be complete and ready for occupancy by LASL in December 1979.

Most of the components and systems development and 75% of the design are complete. All major hardware for the first beamline has been procured and will begin to arrive at LASL in June. A pumping chamber section is shown in Fig. 18. The output amplifier for the front end will be tested at LASL starting in July. The performance test of the first energy storage unit

will begin in July. Half of the control components network is on hand and is being used for software development. The electron-beam gun (Fig. 19) will be assembled and readied for test in August. Installation of the gigantic target vacuum system (beam tubes and chamber) will begin in August.

#### References

1. W. T. Leland, "Design Engineering of Large High-Pressure Gas Laser Amplifiers," SPIE, Vol. 138, Advances in Laser Technology, pp. 39-45 (1978).
2. C. Fenstermacher, et al, Bull. Am. Phys. Soc. 16, 42 (1971); Daugherty, et al, Bull. Am. Phys. Soc. 17, 399 (1972).
3. T. F. Stratton, "CO<sub>2</sub> Short Pulse Laser Technology," in High-power Gas Lasers, 1975, E. R. Pike, Ed. (The Institute of Physics, London, England, 1976), pp. 264-311.
4. S. Singer, J. S. Parker, M. J. Nutter, "Cold Cathode Electron Guns in the LASL High-Power Short-Pulse CO<sub>2</sub> Laser Program," Int. Top. Conference on Electron-Beam R&D, pp. 274-292, Nov. 3-6, 1975, Albuquerque, NM.
5. G. V. Loda, D. A. Meskar, "Repetitively Pulsed Electron-Beam Generators," Int. Top. Conference on Electron-Beam Research and Development, pp. 252-272, Nov. 3-6, 1975, Albuquerque, NM.
6. J. Ladish, "Helios, a 20-TW CO<sub>2</sub> Laser Fusion Facility," Laser '79 Opto-Electronics Conference, Munich, Germany, July 2-6, 1979.
7. T. F. Stratton, et al, "The LASL 100-kJ CO<sub>2</sub> Laser for ICF Research: Antares," in Inertial Confinement Fusion Technical Digest, Proc. Topical Meeting on Inertial Confinement Fusion, San Diego, California, February 7-9, 1978 (Optical Society of America, Washington, DC, 1977), paper TuC7.

3. W. T. Leland, et al, "Large Aperture Discharges in Electron-Beam-Sustained  $\text{CO}_2$  Amplifiers," in Proc. of the Seventh Symposium on Engineering Problems of Fusion Research, Knoxville, Tennessee, October 25-28, 1977 (IEEE, New York, NY, 1977), pp. 506-508.
9. J. Jansen and V. L. Zeigler, "Design of the Power Amplifier for the HELF at LASL," in Proc. of the Seventh Symposium on Engineering Problems of Fusion Research, Knoxville, Tennessee, October 25-28, 1977 (IEEE, New York, NY, 1977), pp. 489-493.
10. Kenneth B. Riepe and Mary Kircher, "Design of the Energy Storage System for the High Energy Gas Laser Facility at LASL," in Proc. of the Seventh Symposium on Engineering Problems of Fusion Research, Knoxville, Tennessee, October 25-28, 1977 (IEEE, New York, NY, 1977), pp. 1053-1055.

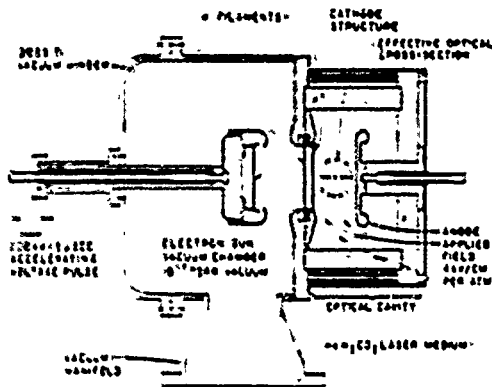


Fig. 1. Electron-beam-controlled  $\text{CO}_2$  laser amplifier.

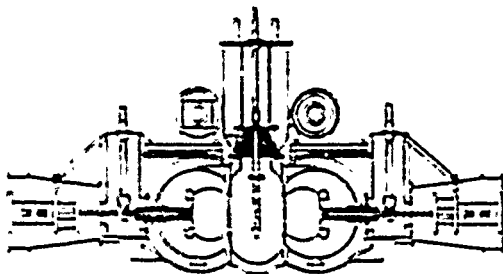
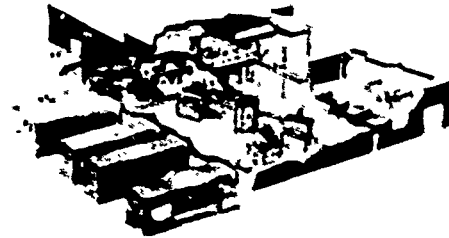


Fig. 2. Cross-sectional view of dual-beam module (Helios).



THE LASL HELIOS FACILITY

Fig. 3. The LASL Helios facility.

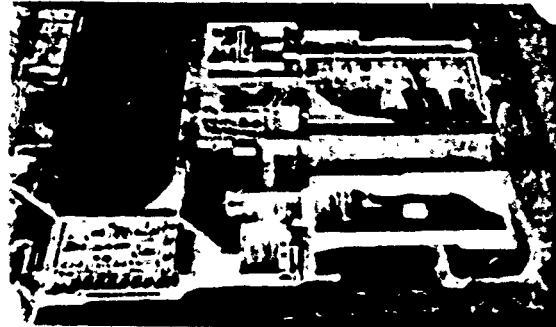


Fig. 4. Model of the Antares facility.

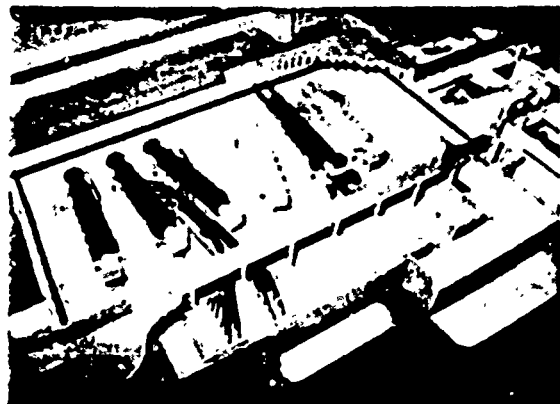
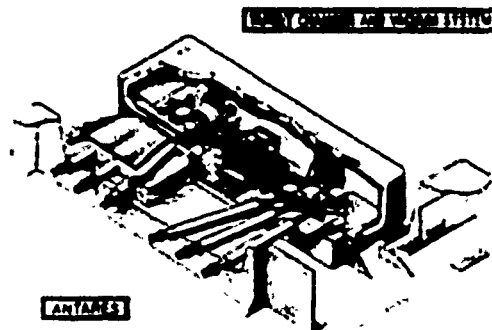


Fig. 5. Laser hall with 6 power amplifiers and 24 energy-storage units.



ANTARES

Fig. 6. Target chamber and vacuum system.

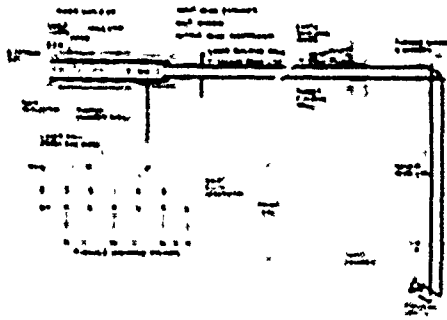


Fig. 7. Optical schematic of Antares.

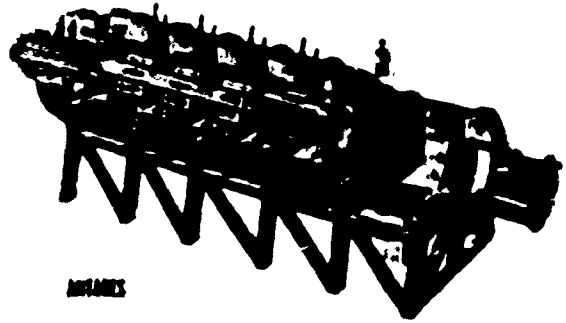


Fig. 9. Artist's conception of the power amplifier.

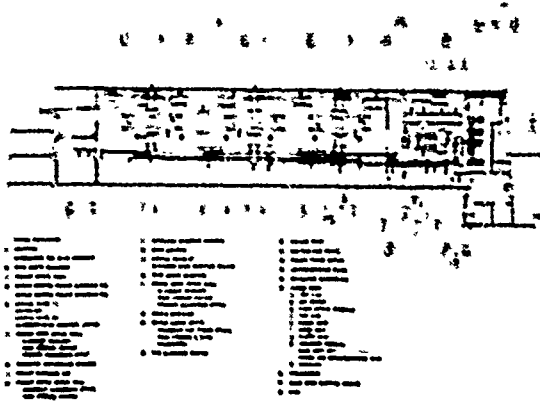
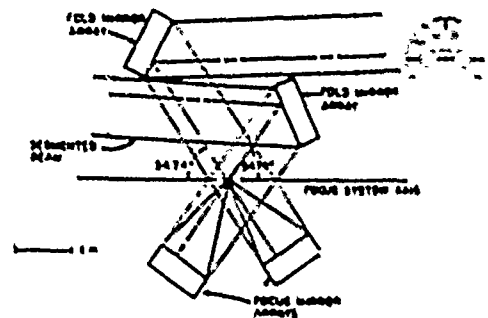


Fig. 8. Antares front end.



**Fig. 10. Antares focus system.**

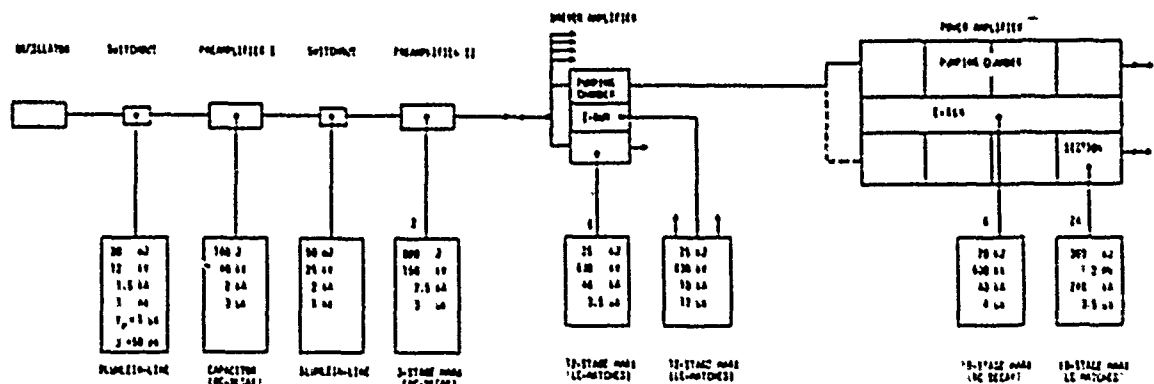


Fig. 11. Pulsed power for Antares.

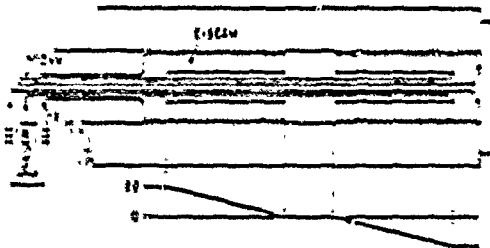


Fig. 12. Symmetric feeding of the electron-beam gun to reduce the azimuthal magnetic field.

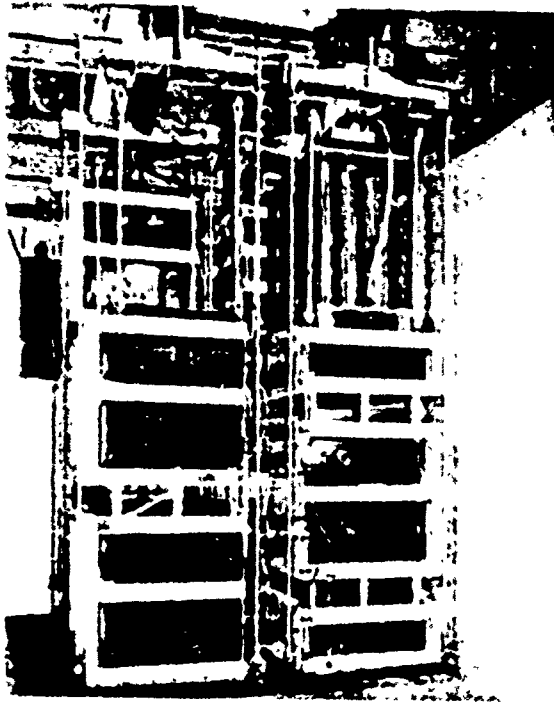


Fig. 13. Low-inductance Marx configuration.

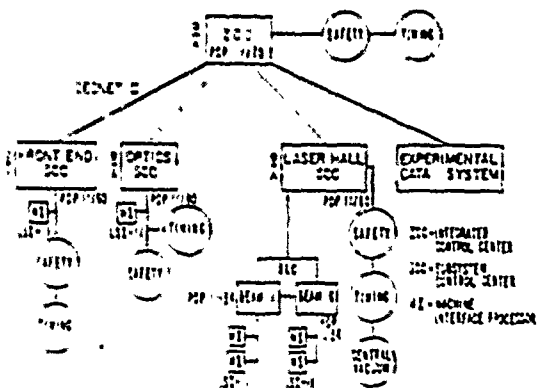


Fig. 14. Antares control system implementation.

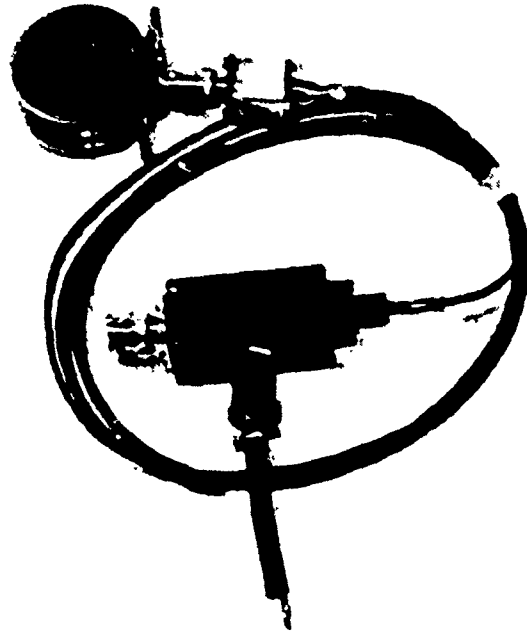


Fig. 15. Fiber-optic signal transmission link.

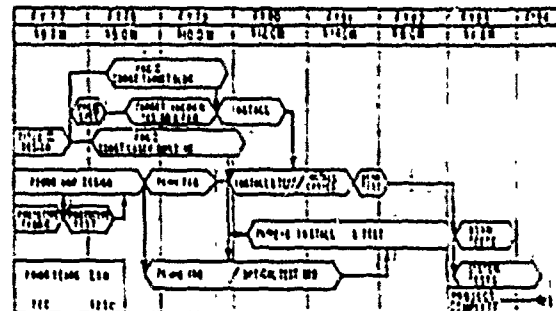


Fig. 16. Antares summary schedule.

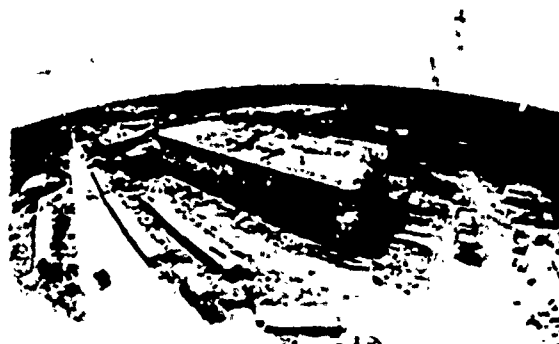


Fig. 17. Facility construction, target building in foreground.

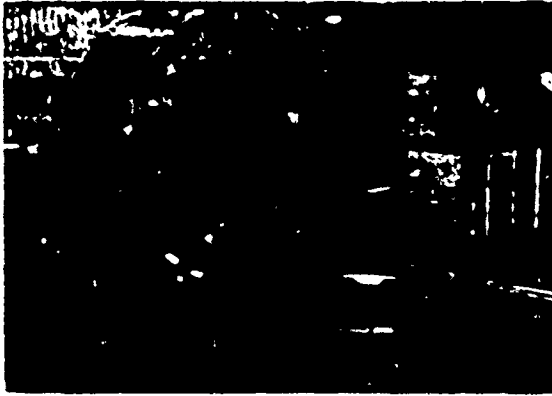


Fig. 16. Pumping chamber sections in production.

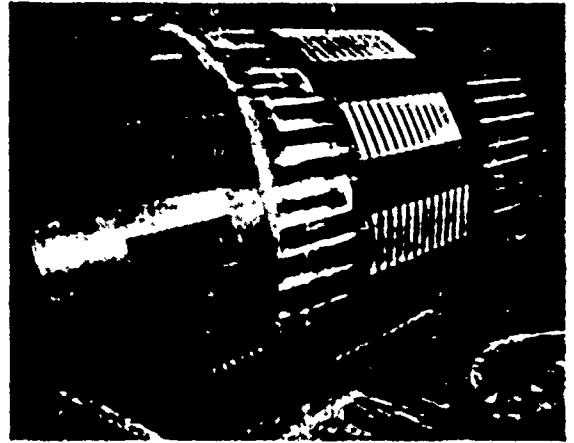


Fig. 19. One of four sections of the electron-beam-gun vacuum shell.

## P3.1

## INVITED

ELECTROMAGNETIC GUNS, LAUNCHERS AND REACTION ENGINES<sup>\*</sup>

Henry Kolm, Kevin Fine, Fred Williams and Peter Mongeau

Massachusetts Institute of Technology  
 Francis Bitter National Magnet Laboratory  
 Cambridge, Massachusetts, 02139

Abstract

Recent advances in energy storage, switching and magnet technology make electromagnetic acceleration a viable alternative to chemical propulsion for certain tasks, and a means to perform other tasks not previously feasible. Launchers of interest include the dc railgun driven by energy stored inertially in a homopolar generator and transferred through a switching inductor, and the opposite extreme, the synchronous mass driver energized by a high voltage alternator through an oscillating coil-capacitor circuit. A number of hybrid variants between these two extremes are also promising. A novel system described here is the momentum transformer which transfers momentum from a massive chemically driven armature to a much lighter, higher velocity projectile by magnetic flux compression. Potential applications include the acceleration of gram-size particles for hypervelocity research and for use as reaction engines in space transport; high velocity artillery; stretcher-size tactical supply and medical evacuation vehicles; the launching of space cargo or nuclear waste in one-ton packets using off-peak electric power.

Background

Magnetic guns and launchers have received periodic attention for many years, and several large systems have actually been built. The fact that none of these evolved into a practical device reflects largely the immaturity of required support technology and lack of coordinated follow-up programs. The most recent survey of the field was made by the Naval Weapons Laboratory in 1972, and the report contains all significant prior references<sup>1</sup>.

Since 1972 considerable attention has been devoted to linear electric motors in the context of air cushion and magnetically levitated high speed trains; an extensive review published in 1975 contains over 140 references<sup>2</sup>. Most early efforts utilized linear induction motors (LIMs) which do not lend themselves to high acceleration. There evolved one concept, however, the linear synchronous motor (LSM) first

proposed by Powell and Danby<sup>3</sup> and ultimately implemented by Kolm and Thornton<sup>4</sup> at MIT; it is synthetically synchronized and is capable of very high acceleration, efficiency and speed. G.K.O'Neill of Princeton University proposed using the LSM for launching lunar raw materials into very precise orbits to permit interception at a space manufacturing site<sup>5</sup>, thus re-inventing a concept first proposed by Arthur C. Clarke<sup>6</sup> in 1950. O'Neill and Kolm developed the "mass driver" as part of two NASA-AMES summer studies in 1976 and 1977, and a group of students constructed the first demonstration model at MIT. It was exhibited at the 1977 Princeton Symposium on Space Manufacturing<sup>8</sup> and also on the occasion of the first flight of the orbiter Enterprise in August 77. A second, more sophisticated mass driver is presently under construction at Princeton and MIT, with support from NASA-Lewis<sup>9</sup>.

Another significant effort was made recently by Marshall and Barber<sup>10</sup> who used the world's largest homopolar generator at the Australian National University in Canberra to power a series of experimental dc railguns. Their spectacular success might not have been of much practical interest, had it not been accompanied by equally spectacular progress in the design of practical pulse-rated homopolar generators by Woodson, Weldon and others at the University of Texas in Austin<sup>11</sup>. The group also invented a new inertial energy storage device, the "compensated alternator", or "compulsator"<sup>12</sup>. There has also been a great deal of other work in the area of energy storage in relation to requirements for ohmic

<sup>\*</sup> Study supported by U.S. Army Armament Research and Development Command, Dover NJ, under ARO Grant No. DAA8 29-78-G-0147.

<sup>\*\*</sup> Laboratory supported by the National Science Foundation.

heating of plasmas in toroidal fusion experiments, laser-induced fusion, particle beam weapons research and laser weapons research. Much of this work is directly applicable to accelerators. Equally applicable is work done in the development of large, high-intensity magnet coils, superconducting as well as normal, for MHD power generation and for solid state research. The MIT National Magnet Laboratory is a center of expertise in this area<sup>13</sup>. Related work which is doubly applicable is the development of large superconducting magnet systems for inductive energy storage at Los Alamos<sup>14</sup> and Sandia<sup>15</sup>.

In March 1977 Dr. Harry Fair, head of the Propulsion Technology Branch of the Army Research and Development Command in Dover, N.J., inquired whether any of the MIT Magneplane or Mass Driver work might have ordnance applications. It was immediately obvious that the potential applications and related concepts and technologies spanned such a vast range as to require a nationally coordinated effort. Peter Kemney and Ted Gora of ARADCOM were assigned to the task of coordinating the effort within DOD, and the present authors were funded to conduct a preliminary study. In addition, we have assembled an inter-agency steering committee and a technical advisory panel to ensure liaison with other centers of expertise.

#### Electromagnetic Accelerator Concepts

We are concerned here with linear motors which are capable of very high acceleration. This excludes at the outset the sizeable literature of linear motors<sup>16</sup> developed over the years for a variety of purposes, including traverse curtain rods, conveyor belts, solid waste separation, liquid metal pumps, high speed ground transportation, and even certain attempted launch devices. We shall characterize the features and limitations of our basic arsenal of accelerator concepts.

#### The Classic Railgun

The classic railgun is the simplest and also the most high perfected accelerator. It consists of two parallel rails connected to a source of dc current, the projectile consisting of a short-circuit slide propelled between the rails by the Lorentz force  $F = BLI/2$  newton, where  $B$  is the magnetic field intensity between the rails in tesla,  $L$  is the length

of the current path through the slide, or the gap between rails in meters, and  $I$  is the current in amperes. The factor of  $1/2$  accounts for the fact that the field is  $B$  behind the slide but zero in front of it, the average being  $B/2$ .

The classic railgun has been studied extensively by Brast and Sawle of HB Associates in the mid-sixties under NASA contract<sup>17</sup>, and more recently by Marshall and Barber<sup>10</sup> using the world's largest homopolar generator at the Australian National University in Canberra; it is capable of storing 500 MJ. Railguns can operate in two distinct modes. In the metallic conduction mode, current flows through the sliding projectile itself, and this mode has been demonstrated to a performance level of about 1 kg mass and 2,000 g (20,000 m/s<sup>2</sup>) acceleration by the switching gun used in the Canberra installation to feed the main gun. Marshall and Barber found that if the railgun is driven very hard, a plasma arc tends to bypass the projectile, leaving it behind. By using a non-conducting lexan projectile and confining the arc behind it they were able to achieve a performance level of 16 gram accelerated at 250,000 g along a 5 m barrel to a final velocity of 5.9 km/s. As railguns are extrapolated to large projectile sizes, the distinction brush conduction mode and plasma mode is likely to vanish: brush conduction will be supplemented by arc conduction as the limit of brush current is exceeded. The practical limit of railgun performance in regard to projectile size, acceleration, length and velocity will have to be explored by progressive refinement of material and engineering details, as in the case of any new technology. The Canberra work has provided sufficient information to justify the first attempt in this direction. Westinghouse<sup>18</sup>, with support from DARPA, will construct a practical railgun system including the first pulse-rated homopolar generator designed with attention to overall weight. The objective is to demonstrate feasibility of accelerating a 0.33 kg (.73 pound) projectile to a velocity of 3 km/s (9.8 ft/s), corresponding to a muzzle energy of 1.5 MJ.

To a great extent, the practical limit of railguns will depend on acceptable cost and service life. The problems relate to mechanical containment of the percussive expansion force which tends to blow the rails apart, the electromagnetic analog of barrel

pressure in a chemical gun, with the important difference that the railgun maintains more or less constant pressure throughout the acceleration. Instead of chemical corrosion, there is the destructive effect of high brush current density and the related metal vapor arc. The body of knowledge available from the study of brushes and circuit breakers does not extend to the current densities and velocities in question.

In addition to these limits, the classic railgun also faces certain fundamental limits which are not related to acceleration, but to maximum possible length or maximum muzzle velocity. As a railgun is lengthened, the resistance and inductance of the rails eventually absorb a dominant fraction of the energy. The effect is seen to begin at about five meters in the Canberra tests. Increasing velocity also causes an increasing back-emf. Current will continue to flow, even if this emf exceeds the output voltage of the homopolar generator, because the intermediate storage inductor acts as a current source. However, there is a practical limit to the voltage which can be stood off by the gap between rails, and this scales about linearly with size. Thus there are two fundamental effects which limit the amount of energy that can be transferred to the projectile, regardless of how much is available. Another shortcoming of the railgun is its inherent inefficiency. An appreciable amount of energy is contained in the rail inductance at the instant the projectile leaves, and this energy must be absorbed by a muzzle blast suppressor. A fraction might conceivably be returned to the homopolar generator. There are several means for circumventing the limitations of the classic railgun.

#### The Augmented Railgun

The magnetic field between the rails can be augmented by supplementary current which does not flow through the sliding brushes. This current can be carried by separate conductors flanking the rails (which must be farther from the projectile), or it can be added to the rail current itself by simply terminating the rails with a load resistor or inductor at the muzzle to carry a fraction of the current. The rails themselves will obviously contribute more field than auxiliary rails located farther away, but

the use of superconducting auxiliary rails might be expedient in some applications. It should be noted that railgun fields are much higher than the critical fields of superconductors. Augmentation has the obvious effect of reducing the amount of current flowing through the brushes and the projectile, and thereby the necessary conductor mass which must be accelerated.

It should also be noted that the augmenting field is twice as effective as the rail field itself. The augmenting field prevails in front of the projectile as well as behind it, thereby eliminating the factor of  $1/2$  in the Lorentz force expression. This fact is important inasmuch as it reduces to one half the rail bursting force which must be contained for a given acceleration.

Augmentation therefore ameliorates both the brush current density limitation and the bursting force containment limitation of classic railguns.

#### The Segmented Railgun

The length limitation imposed by rail resistance and rail inductance can be circumvented by simply subdividing a long railgun into short segments, each fed by an independent local energy source. This will of course involve certain commutation problems as the projectile transitions between segments, but will permit using part of the energy stored in each segment to energize the subsequent segment. The segmented railgun seems promising for launching large masses such as aircraft at low acceleration. In very long launchers, the use of multiple independent energy supplies will have other advantages as well.

#### Mass Drivers

As mentioned in the introduction, the mass driver is a direct adaptation of the linear synchronous motor first conceived and developed as the MIT Magneplane system in 1970-75<sup>4</sup>, a high-speed magnetically levitated train. The mass driver can be planar or axial depending on requirements. The axial configuration permits higher efficiency and is therefore preferred for high acceleration, while the planar configuration will accommodate payloads which need not be cylindrical and may have any arbitrary shape.

In both cases, the payload is carried by a reusable vehicle, called the bucket, which is provided with two superconducting coils carrying a persistent



current and guided without contact by repulsive eddy currents induced by the bucket motion in an aluminum guideway. The bucket is propelled by a series of drive coils which are pulsed in synchronism as the bucket passes by. The bucket operates like a surfboard riding the forward crest of a magnetic travelling wave, the wave being generated by the drive coils and synchronized by position sensors. Buckets can be launched at repetition rates of 10 per second. Each bucket releases its payload at a precise speed, is decelerated, and then returns to the starting point on a return track to be reloaded and relaunched.

Mass drivers can operate in the "push-only" mode as in the case of Mass Driver One, or in the pull-push mode of Mass Driver Two, now under construction, in which each drive coil undergoes a complete sinusoidal oscillation by being connected synchronously to a supply capacitor line. By tuning this cycle to the effective wavelength of the bucket it is possible to achieve energy transfer efficiencies, electric-to-mechanical, of better than 90 percent. We should add that the bucket-to-payload ratio is about unity, and that about half the bucket energy is recoverable by regenerative braking.

For all practical purposes, mass drivers have no velocity limit and no length limit. Acceleration has been limited thus far by the current and voltage capacity of the SCRs used for switching. Using shelf components, Mass Driver Two should achieve 500 to 1,000 g. If the SCR limitation is removed, by using ignitrons, spark gaps, or direct contact switching, performance will be limited by mechanical and thermal failure of the drive coils. Some preliminary calculations based on a four inch caliber mass driver using aluminum bucket coils and copper drive coils suggest an acceleration limit between 100,000 and 250,000 g. This is comparable to railgun performance. However, the failure mode of drive coils under fast pulse conditions is a very complex subject requiring experimental study.

All previous mass driver designs are based on a bucket coil current density of  $25 \text{ kA/cm}^2$  of cable, achieved in an operational model of the MIT magnetoplane. Superconductors should withstand up to four times this current density at the low field intensity and stored energy involved. It should also be point-

ed out that mass drivers do not necessarily require superconducting bucket coils. For periods of the order of 0.1 second it is actually possible to maintain higher current densities in normal conductors. Maximum performance mass drivers are therefore likely to utilize aluminum bucket coils, possibly precooled to liquid nitrogen temperature, fed by sliding brushes, and drive coils triggered by physical contact. Of course this would eliminate the non-contact advantages.

A unique feature of mass drivers bears emphasis: although they are energized by capacitors, the costliest, heaviest and bulkiest energy store known, each capacitor is used hundreds or thousands of times during each launch cycle by being connected to many drive coils through feeder lines. This permits the use of an efficient but slower intermediate energy store, such as a compulsator or MHD generator.

#### The Helical Railgun

The railgun is in essence a single-turn motor. A multi-turn railgun would reduce the rail current and the brush current by a factor equal to the number of turns. It therefore seems worthwhile to study a "helical railgun". In this hybrid device, the two rails are surrounded by a simple helical barrel, and the projectile or re-useable carrier is also helical. The projectile is energized continuously by two brushes sliding along the rails, and two or more additional brushes on the projectile serve to energize and commutate several windings of the helical barrel directly in front of and/or behind the projectile. The helical railgun is in fact a cross between the railgun and the mass driver.

#### Superconducting Slingshots

Accelerators based on mechanical energy storage have not been used since the day of the bow and medieval catapult, with the exception of naval aircraft launching. Mechanical energy storage devices are bulky, heavy, and slow to release their energy. The advent of practical superconducting magnets provides a good mechanical storage mechanism, the "magnetic slingshot".

Consider a short superconducting solenoid which is free to slide inside a long one. The travelling solenoid will be either attracted to or repelled from the center of the long solenoid, depending on the direction of relative magnetization. Either configura-

action can serve as an electromagnetic slingshot. In the attractive configuration, the travelling solenoid can serve as a payload-carrying shuttle bucket. Released at the breach end of the barrel coil, it will accelerate to the center, where it will release its payload at maximum velocity, come to rest at the muzzle, and then return empty to a position short of its release point, from where it can be returned to the release point by mechanical force, possibly by a thermal cycle. This oscillation is inherently loss-less, except for possible eddy currents induced in nearby metal.

In the repulsive configuration, the travelling solenoid will be moved by mechanical force from the breach to a point just beyond the center of the barrel. When released, it will be expelled from the muzzle as part of the projectile. Velocities up to several hundred m/s are attainable by slingshots.

#### The Superconducting Quench Gun

By successively quenching a line of adjacent coaxial superconducting coils forming a gun barrel, it is possible to generate a wave of magnetic field gradient travelling at any desired speed. A travelling superconducting coil can be made to ride this wave like a surfboard. The device in fact represents a mass driver or linear synchronous motor in which the propulsion energy is stored directly in the drive coils.

#### Impulse Accelerators

A brass washer placed on top of a vertically oriented pulsed field coil is driven upward, accelerated by eddy currents which tend to be  $180^\circ$  out of phase with the inducing field pulse. The resulting impulse has been used commercially since 1962 for metal forming operations, for instance for swaging terminal fittings around aircraft control cables. The process has certain applications for acceleration. It can be made into a synchronous induction motor whose performance is limited by the thermal inertia of the sliding member.

#### The Momentum Transformer

A novel concept described here for the first time is what we shall call the "momentum transformer". It makes use of a so-called "flux concentrator", first studied by Howland at MIT Lincoln Laboratory in 1960<sup>19</sup>. A flux concentrator is simply a conduc-

ting cylinder with a funnelled bore, and at least one radial slot extending from the inside to the outside surface. The cylinder is surrounded by a pulsed field winding, preferably imbedded in a helical groove to minimize hoop stresses. A fast pulsed current in the winding induces an opposite image current in the outer surface of the cylinder. Due to the radial slot, this induced current is forced to return along the inner perimeter of the cylinder, thereby generating a magnetic field in the funnelled bore. All of the magnetic flux which would have filled the pulsed field winding in the absence of the concentrator is thus compressed into the central bore, resulting in a field intensity which is higher than it would have been by about the outside-to-inside cross section ratio. The device was used at MIT for high field research and also for industrial metal forming. In 1965, Chapman<sup>20</sup> used a flux concentrator with a tapered bore for accelerating milligram metal spheres to hypervelocities. Using a first stage explosive flux compressor, Chapman managed to reach peak fields in excess of 7 megagauss, starting with an initial field of only 40 kilogauss.

The momentum transformer proposed here uses a flux concentrator as the armature or sabot in a chemically driven conventional gun. The bore of this sabot is occupied by a much smaller projectile, for instance a rod-shaped armor penetrator. The muzzle end of the gun is a pulsed field winding imbedded in a helical groove, which is excited with a current pulse sufficiently slow to penetrate the barrel and fill the bore with magnetic flux. When the sabot enters this flux region so rapidly that the effective penetration depth of the field is small, it compresses the flux into its inner bore, decelerates drastically, and expels the projectile contained in its bore at a much higher velocity. The device should have very little recoil because the muzzle coil acts like a muzzle brake, transferring much of the sabot momentum to the barrel. The process can be multi-staged with a series of nesting sabots.

#### Application to Hypervelocity Research

The acceleration of milligram to gram size pellets to hypervelocities, i.e., 10 to 100 km/s, already has a literature of three decades. Research areas include micrometeorite impact studies, equation-of-state re-

search, terminal ballistics, etc. A new application of current interest involves the achievement of fusion by pellet impact at several hundred km/s.

#### High Velocity Artillery

Projectiles in the range of ten grams to a kilogram accelerated to 3 to 10 or 20 km/s have foreseeable applications. The destruction of missiles in space, where mass is at a premium is one obvious use. Another is the possible interception of incoming rounds by ships and armored vehicles. This requires small projectiles travelling at speeds much greater than the incoming round, capable of detonating, deforming, or just deflecting them. Plasma-driven railguns already have the required capability on a laboratory basis. If incoming round interception can be accomplished with good reliability, it will make armored vehicles as obsolete as knights on horseback.

An armor penetrator fired at 3 km/s, twice present speed, needs only to be about one fifth the size to inflict equal damage. If in addition it can be propelled with available diesel fuel, tanks can be given five times present capability with drastically reduced vulnerability. We are dealing here with energy pulses in the 1 to 3 MJ range, supplied by the primary propulsion engine of the tank.

#### Stretcher-Size Logistic Supply and Medical Evacuation Vehicle

It is an irony of modern tactical warfare that an armored advance can be supported with many tons per minute of artillery, but not by a single gallon of fuel or pound of food. Helicopters and parachutes are too vulnerable for battlefield use, and the chemical gun does not lend itself to logistic supply applications. Electromagnetic launchers can fill this need.

A 300 pound stretcher or supply module can be launched from a 100-foot, truck-mounted ramp to 100 mph at 3.3 g acceleration, using only 0.14 MJ of energy. It could easily be guided to a soft landing by microwave or conventional ILS type guidance system located at the destination point. The vehicle would operate at high speed, low trajectory, be relatively invulnerable and weather-independent, and significantly less expensive and fuel-consumptive than a helicopter. It could be built using available technology.

#### Light Plane Launchers

It is interesting to study the generation of STOL aircraft which could be designed by eliminating the requirement of inordinate take-off thrust from on-board engines.

#### Space Vehicle Launcher

The application of mass drivers for lunar launching and for use as reaction engines in orbital transfer has already been studied extensively<sup>7</sup>. However, the possibility of electromagnetic earth-based launching, proposed by science fiction writers since the forties, has never before been considered seriously. On the basis of computer software developed by NASA in connection with the Venus lander<sup>21</sup>, it appears quite practical.

A telephone-pole shaped vehicle 8 inches in diameter and 20 feet in length, weighing 1.5 tonnes, accelerated to 20 km/s at sea level would traverse the 8 km atmosphere in half a second, emerging at 16 km/s, which is enough velocity to escape the solar system. It would lose 3 to 6 percent of its mass by ablation of a carbon shield. Initial projectile energy would be  $300 \times 10^9$  J, one third of which would be lost in traversing the atmosphere.

The launch energy may seem formidable, but it amounts to only 83 MW-hrs, which represents several minutes of output by a large metropolitan utility plant. The required launcher would be 20 km long at 1,000 g acceleration; it would be only 2 km long, less than a small airport runway, at 10,000 g, which should be easily attainable. Such a launcher could be installed on a hillside, or in a vertical hole made by an oversize rotary well drilling rig.

One potential application is the disposal of nuclear waste. 2,000 tons of waste will be generated between 1980 and 2000. This waste could be launched out of the solar system by using off-peak power from a utility plant at a cost corresponding to only 2 cents per kw-hr of generated power which produced the waste. Considering that the average cost of power during the period will be 22 cents per kw-hr, this waste disposal cost is very low.

#### Conclusions

Rotary motors have not yet approached the conceptual or practical limits of their potential, even after a century of intensive evolution. Fundamental

Innovation still occurs under the stimulation of new technology and new needs.

Linear motors have not been pursued to anywhere near a comparable degree, although an appreciable literature exists. Linear motors might be on the threshold of an evolution comparable to the evolution of rotary motors. The above survey indicates that there is no shortage of new concepts or uses. What makes this field exciting is the advent of new pulsed energy sources, and the challenging fact that a motor of zero curvature is virtually free of all fundamental limitations on size, acceleration and velocity.

#### References

1. Albert F. Riedl III, "Preliminary Investigation of an Electromagnetic Gun", NML Technical Note No. TN-E-10/72, July 1972, Naval Weapons Laboratory, Dahlgren VA, 22448.
2. R.D.Thornton, "Magnetic Levitation and Propulsion 1975", IEEE Trans. on Magnetics, Vol. MAG-11, No. 4, July 1975.
3. J.R.Powell and G.T.Danby, "The Linear Synchronous Motor and High Speed Ground Transport", 6th International Energy Conversion Engineering Conference, Boston, MA, 1971.
4. H.H.Kolm and R.D.Thornton, "The Magneplane: Guided Electromagnetic Flight", Proc. 1972 Applied Superconductivity Conf., Annapolis.
5. J.K.O'Neill, "The Colonization of Space", Physics Today, Vol 27 No. 9 Sep 1974, pp. 32-40.
6. A.C.Clark, "Electromagnetic Launching as a Major Contribution to Space Flight", JBIS, Vol. 9 No. 6 Nov. 1950.
7. The 1976 NASA-AMES OAST Summer Study on Space Manufacturing with non-terrestrial Materials, published by AIAA as Progress in Astronautics and Aeronautics, Space-Based Manufacturing from Non-Terrestrial Materials, Series Vol. 57, editor: M.Summerfield.  
W.Arnold, S.Scwen, S.Cohan, K.Fine, D.Kaplan H.Kolm, M.Kolm, J.Newman, G.K.O'Neill and W.Snow, "Mass Drivers", parts I, II and III, Proc. of the 1977 NASA-AMES Summer Study: "Space Resources and Space Settlements" NASA, SP-428, 1979, U.S.Govt. Printing Office.  
J.K.O'Neill and H.H.Kolm, "Mass Driver for Lunar Transport and as a Reaction Engine", Jour. of the Astron. Sciences, Vol. 15, No. 4, Jan-Mar 1976.  
J.K.O'Neill, "High Frontier", Astron. and Aeron. Mar. 1978, special issue on space industrialization.
8. H.H.Kolm, "Basic Mass Driver Reference Design" K.Fine "Basic M D Construction and Testing", J.K.O'Neill, "M D Reaction engine as Shuttle Upper Stage", F.Chilton, "MD Theory and History", Proc. of the Third Princeton-AIAA Symp. on Space Manufacturing, 1977, published by the AIAA.
9. H.Kolm, K.Fine, P.Mongeau, F.Williams, W.Snow, G.K.O'Neill: three papers on Mass Driver Two to appear in the Proceedings of the 4th Princeton AIAA Symposium on Space Manufacturing, 1979, to be published by the AIAA in late 1979.
10. S.C.Mashleigh and R.A.Marshall, "Electromagnetic Acceleration of Macroparticles and a Hypervelocity Accelerator", dissertation 1972, Dept. Engr. Phys. Australian Natl. Univ., Canberra.
11. W.F.Weldon et al., "The Design, Fabrication and Testing of a 5 MJ Homopolar Motor-Generator", Internatl. Conf. on Energy Storage, Compression and Switching, Torino, Italy, Nov. 1974.  
M.D.Drigo et al., "Fundamental Limitations and Topological Considerations for Fast Discharging Homopolar Machines", IEEE Trans. on Plasma Scien, Dec. 1975.
12. W.L.Gagnon et al, editors, "Compensated Pulsed Alternator", Lawrence Livermore Lab., July 1978.
13. MIT Francis Bitter Natl. Magnet Lab, Annual Rep. July 1977 - June 1978", Cambridge MA, 02139; see also various technical reports.
14. J.D.Lindsay and D.M.Weldon, "Loss Measurements in Superconducting Magnetic Energy Storage Coils", Report LA-6790-MS, Los Alamos Scien. Lab, Los Alamos NM May 1977.
15. M.Cowan et al., "Pulsar - a Flux Compression Stage for Coal-Fired Power Plants", Proc. 6th Internatl. Cryogenic Engr. Conf., Grenoble, France, May 76, Published by IPC Science and Technology Press Ltd. Guildford, Surrey, England.
16. S.A.Nasar and I.Boldea, "Linear Motion Electric Machines", Wiley, NY, 1976.
17. D.E.Brast and D.R.Sawle, "Feasibility Study for Development of a Hypervelocity Gun", Final Report NASA Contract NAS 8-11204, May 1965.
18. John Mole, Westinghouse Research Lab., Pittsburgh PA 15235, personal communication.
19. B.Howland and S.Foner, "Flux Concentrators", High Magnetic Fields, H.Kolm, editor, Wiley NY, 1962.
20. R.I.Chapman, "Field Compression Accelerators", Proc. Conf. on Mega Gauss Field Generation by Explosives, Frascati, Italy, Sep. 1965 (Euratom)
21. Dr. Chul Park, NASA-AMES Research Center, Moffett Field, CA, 94035; personal communication.

## THE NEAR AND LONG TERM PULSE POWER REQUIREMENT FOR LASER DRIVEN INERTIAL CONFINEMENT FUSION\*

W.L. Gagnon

Lawrence Livermore Laboratory  
Livermore, California 94550ABSTRACT

Inertial confinement fusion research is being vigorously pursued at the Lawrence Livermore Laboratory and at other laboratories throughout the world.

At the Lawrence Livermore Laboratory, major emphasis has been placed upon the development of large, Nd:glass laser systems in order to address the basic physics issues associated with light driven fusion targets.

A parallel program is directed toward the development of lasers which exhibit higher efficiencies and shorter wavelengths and are thus more suitable as drivers for fusion power plants. This paper discusses the pulse power technology which has been developed to meet the near and far term needs of the laser fusion program at Livermore.

Introduction

The Laser Fusion Program<sup>1,2,3,4</sup> is making rapid progress toward achieving thermonuclear fusion. One of the keys to this rapid progress is the sequence of laser facilities with increasing power (Fig. 1) developed at LLL in pursuit of the laser fusion program goals. Janus has yielded an extensive catalogue of laser fusion data and measurements of alpha particles demonstrating the TN nature of the implosion reaction, thus achieving the first milestone. Cyclops focused 0.6 TW on target from a single laser chain and has served as a prototype for the large, multi-arm Shiva and

\*Work performed under the auspices of the U.S. Dept. of Energy by the Lawrence Livermore Lab. under contract no. W-7405-Eng. 48.

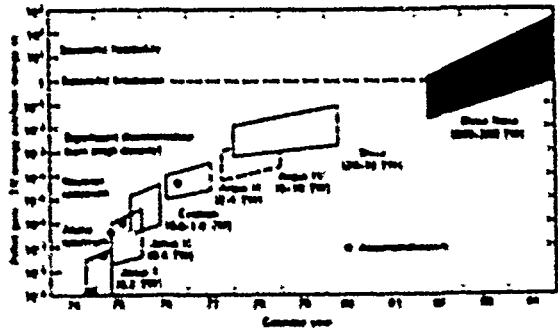


Fig. 1: LLL laser-fusion yield projections and laser systems. A series of increasingly powerful Nd:glass lasers has been built for laser fusion experiments.

and Argus systems. Argus has operated at greater than 4 TW from two laser chains and has now produced more than one billion neutrons on a single shot, with a pellet gain of  $2 \times 10^{-5}$ . Shiva, a 20 arm, 20 TW system has been operational since February 1978 and has produced a neutron yield of  $2.7 \times 10^{10}$  and compressions of 50X liquid density. Nova<sup>5</sup>, currently under construction, will produce several hundred TW of output power and demonstrate the feasibility of net energy gain with high gain microexplosions.

Each laser system in this progression has increased in both size and complexity. The pulse power hardware represents about one-quarter of the total project cost for each of these systems. For Shiva, this amounted to \$7M and for Nova we expect the pulse power system cost to exceed \$30M. We have developed reliable, cost effective, and scalable pulse power technology specifically suited to meet the needs of large Nd:glass lasers.

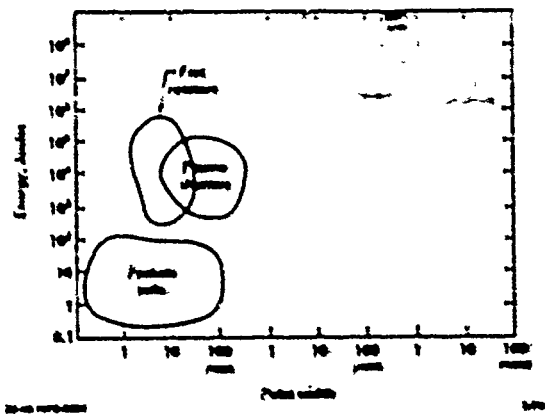


Fig. 2: Energy versus pulse width parameters for the major pulse power requirements of the laser fusion program.

Figure 2 shows the parameter space in which these pulse power requirements lie. The low energy, fast pulse circuitry addresses the needs for very fast optical switches which act to suppress amplified spontaneous emission within the laser chains, as well as to protect the laser from target reflected light. The high energy, relatively slow pulse circuitry addresses the pump requirements for these lasers, and it is in this area that most of the system cost is accounted for. This technology has been the focus of a great deal of effort<sup>6,7</sup> aimed at improving both its performance and cost effectiveness.

This paper will describe the pulse power hardware which has been developed and implemented at the Lawrence Livermore Laboratory for these large laser systems, as well as discussing some promising alternative technologies which are currently under development.

#### Laser Pumping Requirements

The laser amplifiers (see Fig. 3) are pumped with intense broadband light output from large bore xenon flashlamps. The pump energy is delivered in approximately 500 microseconds and the peak power requirements (shown in Fig. 4) far exceed the capacity of the power grid. Thus, large capacitor banks are used as intermediate storage elements. The xenon flashlamps are nonlinear resistive

loads<sup>8</sup> with two distinctly different impedance states - roughly corresponding to the time during which the lamps are in the ionization or triggering mode and the time at which the full volume of the lamp is conducting current. Typical voltage and current waveforms for a series lamp pair are shown in Fig. 5. The 35 kV voltage pulse required to initiate the ionization process is deliberately produced by the transient behavior of the bank circuitry. After full volume ionization within the lamp, the voltage and current are related by the nonlinear relationship

$$V = KI^B$$

where  $K$  is a constant determined by the geometry and gas fill pressure of the lamp. The exponent  $B$  is approximately .5 at current maximum.

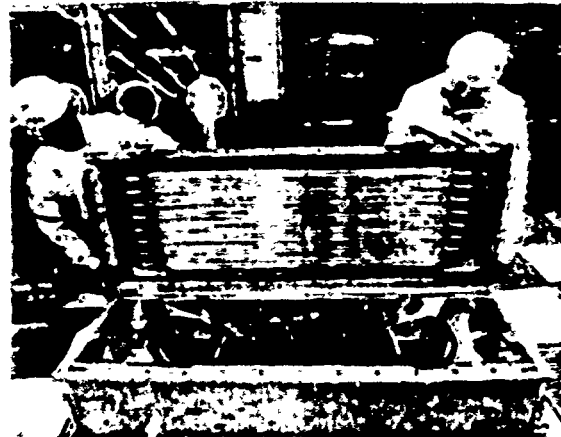


Fig. 3: A 34 cm clear aperture disk amplifier. The 16 xenon flashlamps (8 top and 8 bottom) require a total energy of 300 kJ.

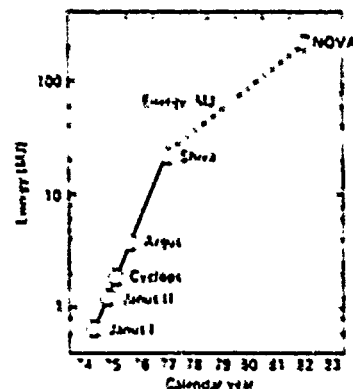


Fig. 4: The peak power requirements for lasers in the LLL Program have become increasingly large.

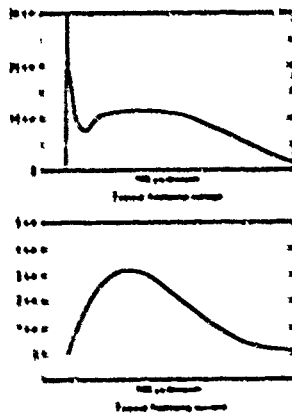


Fig. 5: Voltage and current waveforms for large bore xenon flashlamps.

The required energy per lamp depends upon the length and diameter selected. This varies from a few hundred joules for the small lamps to almost 20 kilojoules for the larger lamps. The lamps are arranged in series pairs and driven by a capacitive energy storage module which is tailored to provide the necessary energy and pulse shape. Each module contains the necessary energy storage capacitors, pulse forming inductor, dump resistors and high voltage isolating fuse. The modules are assembled as integral units and are moved with a modified fork lift. Shown in Fig. 6 is a 2.5 MJ segment of these modules as installed in the 25 MJ Shiva energy storage system.

#### Controls

The design of the controls and diagnostics for these pulse power systems is dictated by severe operational requirements.<sup>9</sup> A large number of control and diagnostic points must be addressed and these generally lie close to the pulse power circuitry where they are exposed to transients of several kilovolts. Thus a high degree of electrical isolation is essential. The early systems (Janus, Cyclops and Argus) were small enough to allow the use of hard wired relay control systems with limited diagnostic capability. Shiva and Nova are substantially larger and these control systems must be able to carry out pre-shot diagnostics, detect real time malfunctions, and implement data storage and

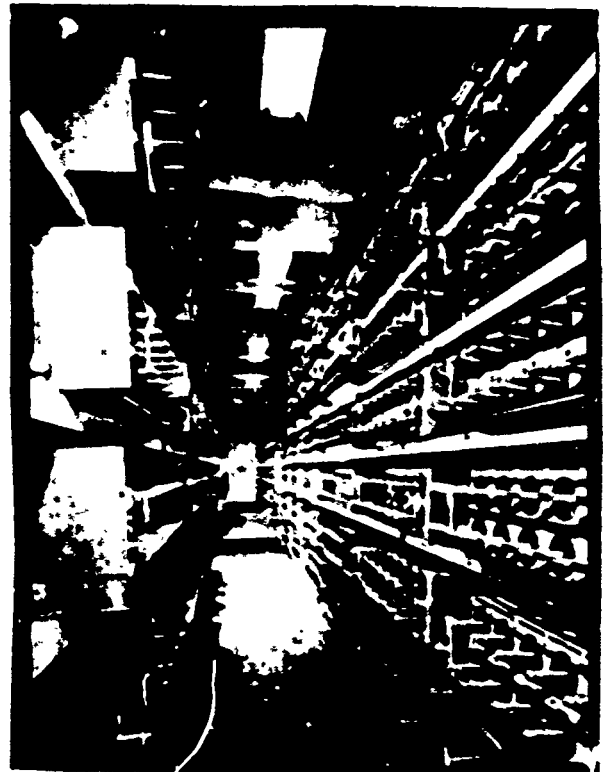


Fig. 6: A 2.5 MJ segment of the 25 MJ Shiva capacitor bank.

retrieval functions to aid in post shot troubleshooting.

With this in mind, we have developed a digital based control and diagnostic system with a high degree of electrical isolation. The control system is organized around the LSI-11 micro-computer as shown in Fig. 7. The LSI-11 internal

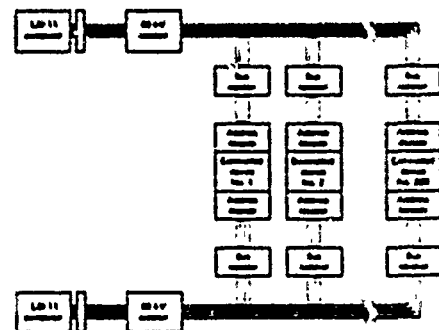


Fig. 7: Block diagram of the Shiva pulse power control system.

data bus is extended throughout the laser bay and energy storage areas to include all control and diagnostic points. As shown (Fig. 7), a 50 V, low impedance data bus extends from the LSI-11 to the interface points, 60 kilovolts of optical isolation is employed between the LSI-11 and the bus, and 3.5 kilovolts is employed between the bus and any interface point. This system has been operating successfully in the Shiva laser for the past 15 months.

For Nova, the same approach will be implemented, however, fiber-optic links will be used extensively. A prototype for the Nova control system is currently under test.

### Optical Gates

A variety of optical gates have been developed for use within the laser chains. These can be categorized as either opening gates (used to prevent amplified spontaneous emission during the pump period) or closing gates (used to protect the laser from target back reflected light).

At the small aperture points ( $\leq 10$  cm) in the laser chain, Pockels cells are used as opening gates. At apertures larger than 10 cm, Pockels cells are no longer practical because of the difficulty of growing large diameter crystals. For the large aperture applications we have developed fast rotating shutters which will be located at the focal points of the spatial filters where the beam diameter is a few millimeters.

In general, the Pockels cell circuitry supplies pulses of about 10 kV with rise times of a few nanoseconds and pulse widths of several tens of nanoseconds. The circuit<sup>10</sup> shown in Fig. 8 is currently in use in both the Shiva and Argus lasers. As shown, a single spark gap (or thyratron) switches the shields on 20 separate cables. The pulse width is set by the pulse forming cable and the load cables feed the Pockels cells. Pulse to pulse jitter is less than 10 nanoseconds.

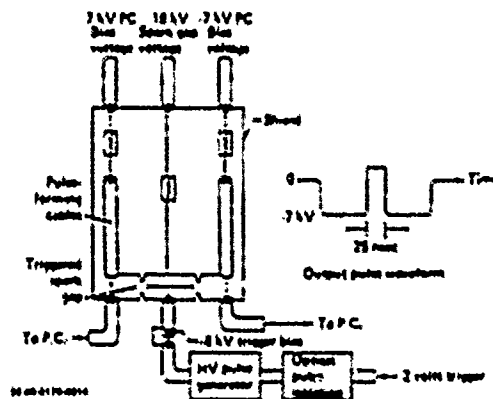


Fig. 8: Two 20-way pulsars like the one shown above are used to drive the Shiva Pockels cells. The switch can be either a triggered spark gap or a hydrogen thyratron.

The rise time and jitter requirements for the Pockels cells used in the oscillator switch-outs are considerably more severe. Here, a very narrow pulse is needed ( $\leq 10$  ns) with pulse to pulse jitters of much less than a nanosecond. For these applications we have developed planar triode pulse circuitry such as shown in Fig. 9. The use of planar triodes, constant resistance networks and high frequency circuit techniques<sup>11</sup> has made possible a family of pulse amplifiers with nanosecond rise times and jitters of less than 100 ps. Typical outputs are in the range of 5 to 15 kV.

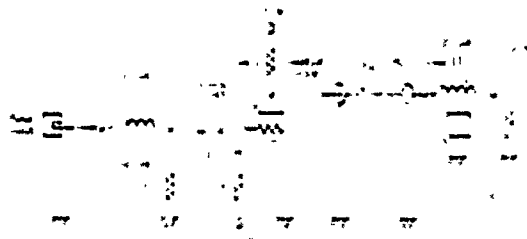


Fig. 9: Shown above is one example of a fast planar triode pulse amplifier. A number of these are currently in operation producing output voltages across Pockels cells of 3 - 5 kV with rise times of 1 - 2 ns.



Closing shutters are used to prevent target back-reflected light from reentering the laser chain and damaging optical components. Present systems employ Faraday rotator/polarizer combinations as optical gates. However, this is an expensive solution, especially at large apertures, because the energy contained in the magnetic field in the rotator glass increases directly as the volume. In addition, the rotator glass adds nonlinear path length to the beam. We have developed an alternative fast closing shutter<sup>12</sup> which is located at the final spatial filter pinhole. This shutter (shown in Fig. 10) rapidly injects a plasma of density greater than  $10^{21}/\text{cm}^3$  (the critical density for 1.06 micron light) across the spatial filter pinhole after the outgoing light pulse has passed. A plasma velocity of about 1 cm per microsecond is required to insure the pinhole is blocked before the reflected light returns. The plasma is produced by sublimating a small mass of aluminum foil with pulsed energy from the low inductance PFN shown in Fig. 11. Eight of these PFN's are Marx charged to 50 kV and discharged through multi-channel gaps into the foil. A total energy of approximately 10 kJ is required.

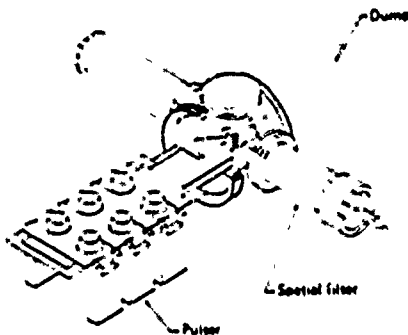


Fig. 10: A fast plasma shutter is used to inject a dense plasma across a spatial filter pinhole to block back-reflected beam from reentering the laser.

#### Long Term Requirements

In the near term, we are meeting the laser fusion pulse power requirements by implementing hardware solutions which are based upon existing technology of moderate extensions of existing technology. The longer term requirements involve developing

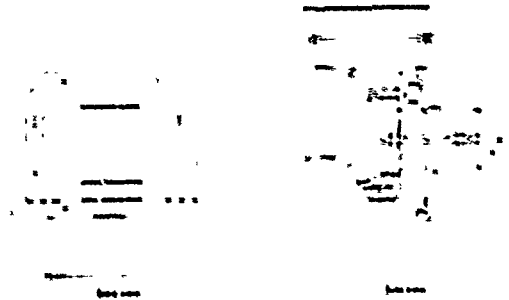


Fig. 11: Cross section of the plasma shutter pulser.

hardware which will operate reliably for  $10^7$  to  $10^8$  shots on a rep-rated basis. Further, the installed costs must approach a few dollars per joule in order for any of the inertial confinement fusion driver options to be economically feasible. This implies the development of lower cost, rep-rateable energy storage systems, reliable, high power solid state switches, and system configurations which do not involve stressing dielectrics into the corona regime. One such concept is illustrated in Fig. 12. As shown, the use of a fast discharge (50 to 100 us) primary energy source makes possible a system which eliminates the requirement for a transfer capacitor and allows for rapid charge of the output pulse forming line.

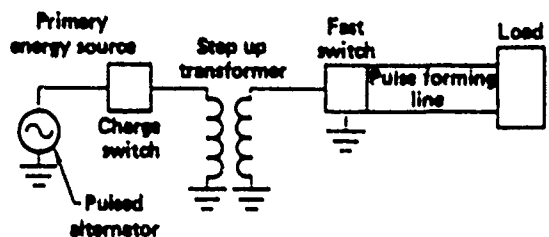


Fig. 12: The basic elements of a fast charge/discharge rep-rateable pulse power system.

A key element in this concept is the high peak power pulsed energy source and the University of Texas, Center for Electromechanics at Austin, is

currently developing such a device<sup>13,14</sup> (the compensated pulsed alternator) for the Laser Fusion Program. This machine, shown in Fig. 13, is a rotating flux compressor capable of producing megajoules of output energy over a pulse width range from several milliseconds to below 100 ns. The prototype, currently under test, is designed to drive flashlamp loads with a half millisecond pulse of about 100 kA at 6 kV. After verification of the prototype performance, a larger machine, in the several megajoule class and with an open circuit voltage of approximately 15 kV will be built. We hope to implement this technology for Phase II of the Nova project.

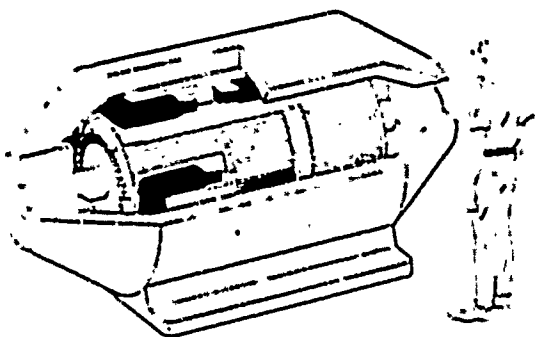


Fig. 13: Artists conception of the compensated pulsed alternator.

#### References

1. J. Nuckolls, L. Wood, A. Thiessen, G. Zimmerman, *Nature* **239**, 139, 142 (1972).
2. K.A. Brueckner and S. Jorna, "Laser-Driven Fusion" *Rev. Mod. Physics* **46** pp. 325-367, 1974.
3. J.L. Emmett, J. Nuckolls, L. Wood, "Fusion Power by Laser Implosion", *Scientific American* **230**, pp. 24-37, 1974.
4. C.M. Stickley, "Laser Fusion", *Physics Today*, pp. 50-58, May 1978.
5. "Nova" CP&D Final Report, Laser Fusion Program, LLL Misc. 111, March 1978.
6. "Glass Laser Power Conditioning" LLL Technology Transfer Seminar 1975.
7. J.R. Hutzler, W.L. Gagnon, "Development of a Reliable, Low Cost, Energy Storage Capacitor for Laser Pumping", *Proc. of the Int. Conf. on Energy Storage, Compression and Switching*, Nov. 1974.

8. J.F. Markiewicz and J.L. Emmett "Design of Flashlamp Driving Circuits", *IEEE Journal of Quantum Electronics*, Nov. 1966, pp. 707-711.
9. P.R. Rupert, L. Berkbigler, W. Gagnon, D. Critton, "A High Noise Immune, Digital Control System for the Shiva Laser", *Proc. of Seventh Symp. on Engineering Problems of Fusion Research*, Oct. 1976.
10. B.M. Carder, "Driving Pockels Cells in Multi-arm Lasers", *13th Pulse Power Modulator Symp.*, June 1978.
11. M.M. Howland, S.J. Davis, W.L. Gagnon, "Very Fast, High Peak Power Planar Triode Amplifiers for Driving Optical Gates" *Proc. of 2nd IEEE Int. Conf. on Pulsed Power*, June 1979.
12. L.F. Bradley, P. Koert "Plasma Shutter for High Power Glass Lasers", *Proc. of 8th Int. Symp. on Discharges and Electrical Insulation in Vacuum*, Sept. 1978.
13. W.F. Weldon, W.L. Bird, M.D. Driga, K.M. Tolks, H.G. Rylander, H.H. Woodson, "Fundamental Limitations and Design Considerations for Compensated Pulsed Alternators" *Proc. this Conf.*
14. W.F. Weldon, W.L. Gagnon, B.M. Carder, *Compensated Pulsed Alternator*, LLL TB007, July 1978.

Reference to a company or product name does not imply approval or recommendation of the product by the University of California or the U.S. Department of Energy to the exclusion of others that may be suitable.

#### NOTICE

"This report was prepared as an account of work sponsored by the United States Government. Neither the United States nor the United States Energy Research & Development Administration, nor any of their employees, nor any of their contractors, subcontractors, or their employees, makes any warranty, express or implied, or assumes any legal liability or responsibility for the accuracy, completeness or usefulness of any information, apparatus, product or process disclosed, or represents that its use would not infringe privately-owned rights."

## Self-Magnetically Insulated Power Flow\*

J. P. VanDevender

Sandia Laboratories, Albuquerque, New Mexico 87185

Abstract

Electromagnetic power transport through self-magnetically insulated vacuum transmission lines has been developed into a useful and reliable technology. A power density of  $160 \text{ TW/m}^2$  has been transported at  $\sim 100$  percent efficiency over six meters. The theoretical understanding of power flow through lines of constant cross section has progressed through analytical theory and 2-D electromagnetic particle simulations. However, work needs to be done on the effects of line transitions in which the cross section changes in the direction of power flow. The major features of our present understanding will be reviewed and some promising hypotheses now under investigation will be presented.

Introduction

High current particle beam accelerators for Inertial Confinement Fusion must produce approximately 30 to 100 TW of power and deliver it to the anode/cathode (A-K) gap at  $\sim 1$  meter from the target. The limiting factor<sup>1</sup> on accelerator power has been the allowable power flow through the interface between vacuum and the liquid dielectrics in the pulse forming network. Several authors<sup>2,3</sup> have proposed using many separate vacuum interfaces in parallel and transporting the power to the A-K gap through self-magnetically insulated transmission lines (MITL). In ICF accelerators, the 20-40 ns pulse width is less than or equal to the two way transit time through the vacuum line. Consequently, the power transport must be made efficient without the benefit of choosing an optimum load impedance to improve magnetic insulation. Self-magnetic insulation in these circumstances is called the long line or short pulse problem and has been the object of major research and development efforts in the EBFA<sup>4</sup> accelerator program at Sandia Laboratories and the Angara V' program at Kurchatov Laboratory.

Experiments on the long line problem at several laboratories<sup>5,8,9</sup> showed net power transport efficiencies of  $\sim 60$  percent through six to ten meter long lines with negative inner conductors. The efficiency dropped to  $\sim 40$  percent with the positive inner conductor required for light ion acceleration.

\*This work was supported by the U.S. Dept. of Energy, under Contract DE-AC04-76-DP00789.

Later experiments<sup>10</sup> on the Mite accelerator, which is one module of EBFA, revealed several loss mechanisms. When these mechanisms were avoided by redesigning the input into the MITL, the power transport improved to  $\sim 100$  percent with a negative inner conductor. The results have been interpreted as a set of criteria for efficient self-magnetic insulation.<sup>1</sup> Positive polarity operation was not attempted at that time. In a subsequent set of experiments,<sup>11</sup> which will be briefly discussed at the end of this paper, an injector convolute that operated at  $\sim 100$  percent efficiency in either polarity was developed and adopted for EBFA I.

In all of these experiments the most intrinsic loss was associated with the transition from the weakly stressed vacuum insulator to the highly stressed magnetically insulated transmission line. Much of our recent power flow research has been directed towards elucidating the physics of that loss mechanism. In this paper the basic phenomena associated with long self-magnetically insulated power transport will be reviewed, the elements of our working hypothesis on the effects of convolutes will be presented, and the implications of the hypothesis on bi-polarity input convolutes will be discussed.

Self-Magnetic Insulation in Vacuum Feed Lines of Uniform Cross Section

The self-magnetically insulated flow in a long MITL is established in the following steps as indicated in Fig. 1a-1d. When a voltage is applied to the parallel plate transmission line of impedance  $Z_0$ , a TEM wave propagates down the line as shown in Fig. 1a. When the electric field in the line reaches 25 to 40 MV/m, explosive emission<sup>12</sup> occurs on the cathode and a cathode plasma forms. A coating of carbon that is  $\sim 2 \times 10^{-5}$  m thick with a surface resistivity of  $\sim 10^3 \Omega/\text{sq}$  facilitates the formation of a spatially uniform cathode plasma. The plasma becomes a space charge limited source of electrons which are initially accelerated across the gap by the electric field, as shown in Fig. 1b. When the magnetic field from the displacement current density  $\vec{J}$  and the electron loss current density  $\vec{J}_l$  becomes sufficiently large, the electrons behind that point are prevented from reaching the anode and are magnetically insulated as shown in Fig. 1c. Since the conductance is greater than zero in the loss region, the region of loss propagates at a velocity<sup>7,10,13-16</sup> less than  $c = 3 \times 10^8 \text{ m/s}$ . Behind the lossy front, the pulse propagates at  $c$ .

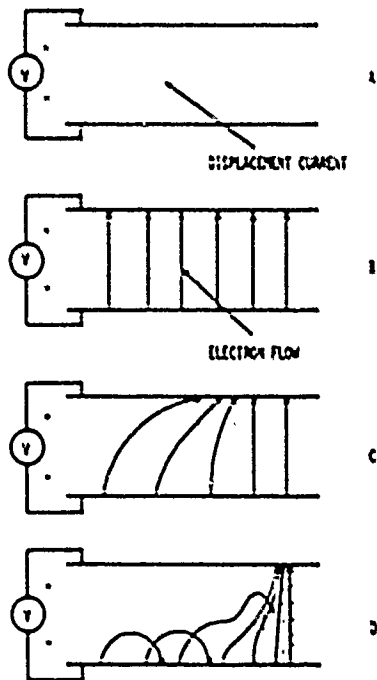


Fig. 1. The steps in which magnetic insulation is established are shown.

- $E < 25 \text{ MV/m}$ .
- $E > 25 \text{ MV/m}$ ;  $I < I_{\text{critical}}$
- $I = I_{\text{critical}}$
- The front is established;  $V/I$  = the self limited impedance.

As discussed by Kataev,<sup>13</sup> the effect is analogous to a shock wave in a gas. Since the shock velocity is less than the sound speed behind the front, the energy propagates to the shock front and steepens the pressure profile until the width of the shock front is determined solely by the nature of the dissipative process in the front. Similarly, the power flow to the lossy front in an "electromagnetic shock"<sup>13</sup> causes the voltage profile to steepen until it is limited by space-charge-limited electron flow in the front. In the Mite experiments,<sup>10</sup> the measured risetime of the front was limited by the frequency response of the Rogowski coil current monitors and the recording oscilloscope to  $< 2 \text{ ns}$  after six meters of line.

The very large  $dI/dt \geq 2 \times 10^{14} \text{ A/s}$  is advantageous for diode operation but causes rather severe diagnostic problems. When the voltage pulse has sharpened to its self-limited risetime, the structure propagates down the line as shown in Fig. 1d.

The structure of the front determines the ratio of the voltage and current behind the front and determines the sensitivity of the electron flow to perturbations in the line. The structure of the front has not been adequately investigated experimentally. However, the 2-D electromagnetic PIC simulations of Poukey and Bergeron<sup>15</sup> and the analytic theory of Gordeev<sup>17</sup> yield the following

idealized model of the front as illustrated in Fig. 2. A voltage step, which has sufficient amplitude to form the cathode plasma, propagates down the line at the velocity of  $c$ . Since the lossy front propagates at a velocity  $U_f < c$ , the duration of this precursor increases with time. In the leading edge of the lossy front, the space-charge-limited electron emission loads down the voltage. Most of the loss current is lost at a voltage of 30 to 50 percent of  $V_0$ , which is the voltage behind the front.<sup>15</sup> Both the magnetic field and the voltage increase with increasing distance into the front. Behind the loss region, the vacuum gap between the electron flow and the anode increases with increasing distance from the front. As the electron flow recedes from the anode, the effective line impedance  $\sqrt{L/C}$  increases and the voltage increases to  $V_0$ . The scale length over which the loss occurs is several times the gap width. Although the measurements of loss current density,<sup>10</sup> and precursor voltage<sup>7-10</sup> and pulse risetimes<sup>7-10</sup> are consistent with this model, the data has not been adequate to verify the details of the structure.

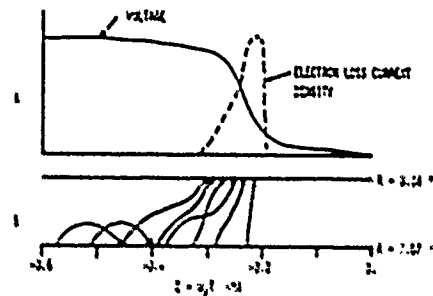


Fig. 2. From a 2-D simulation like Ref. 15 by J. W. Poukey, the voltage and loss current profiles in the front are shown in (a) and electron trajectories are shown in (b). The total loss current is 177 kA out of a total current of 450 kA for  $V_0 = 2.4 \text{ MV}$ .

The details of the front structure are important because they determine the total current  $I_T$  and boundary current  $I_B$  (i.e., the current flowing in the metal, negative electrode) through the MITL behind the front. The 1-D theories<sup>18-22</sup> have shown that a continuum of solutions exist for the total current in a MITL at a given voltage. Each solution corresponds to a different value of  $I_B/I_T$  and a different boundary to the electron flow, as illustrated in Fig. 3 for parapotential<sup>20</sup> flow in a 2 MV line of impedance  $Z_0$ . The correct solution of the 1-D flow is determined by the 2-D flow in the front.

The experiments with short, self-limited lines and long self-magnetically insulated lines have shown that the ratio of  $V_0/I_T Z_0$  is a function of the voltage.<sup>15,19,24</sup> These data are interpreted in

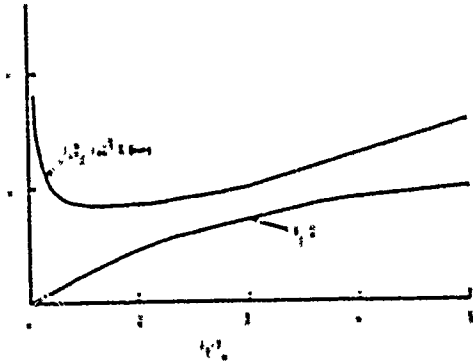


Fig. 3. The range of parapotential solutions for  $I_T$  as are function of  $I_T/I_0$  for  $V_0 = 2$  MV is shown. Each solution corresponds to a different position  $X_E$  of the electron sheath in the gap D.

Fig. 4 through the parapotential<sup>20</sup> model to yield the ratio  $I_T/I_0$  and  $X_E/d_0$  in which  $X_E$  is the thickness of the electron flow and  $d_0$  is the vacuum gap. If  $X_E/d_0 = 1$ , the electron flow entirely fills the vacuum gap and the flow is called saturated. If  $X_E/d_0 < 1$ , the flow is unsaturated and there is a vacuum gap between the flow and the anode. The ratio of  $X_E/d_0$  indicates the sensitivity of the power transport to small perturbations in the gap separation. If the flow is very close to the anode, then small perturbations in the line geometry may cause the sheath to fluctuate and part of the flow to be lost. The parapotential model may not exactly describe the flow in a MITL, for example, the 2-D simulations<sup>15</sup> show that the sheath boundary is diffuse and is not discontinuous as the parapotential model requires. However, the location of the sheath boundary agrees with the model and, both experiments<sup>7-10,23,24</sup> and simulations<sup>15</sup> have shown sufficiently good a agreement with the model to justify the utility of the model. We, therefore, conclude that the higher voltage MITL is less sensitive to gap tolerances and line perturbations, and efficient transport is more readily achieved at the higher voltages.

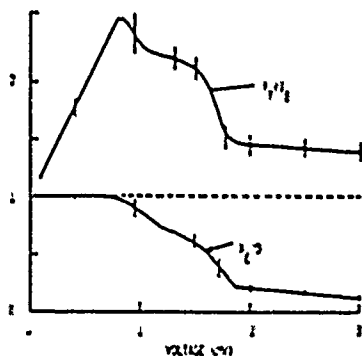


Fig. 4. The ratio of  $I_T/I_0$  and  $X_E/D$  vs.  $V$  from data in self-limited experiments.

The loss problem at low voltages is compounded by the formation of an anode plasma produced by bombardment of the anode by electrons from the saturated flow. When the anode plasma is produced, an ion loss current flows to the cathode and is not affected by magnetic insulation. This condition is followed by rapid shorting of the line as the two plasmas expand across the gap. These effects have been observed in 200 to 400 keV experiments<sup>9-11</sup> but never in 2 MeV experiments. Finally, the velocity of propagation of the front is dependent on the voltage and, hence, a larger fraction of the pulse is eroded away at low voltage. Although the velocity is pulse dependent, the experimental data in Fig. 4 and the theory in Ref. 14 can be used to estimate the front velocity  $\beta_0 c$  for a square voltage pulse as shown in Fig. 5.

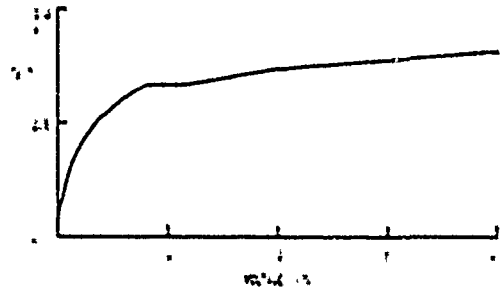


Fig. 5. The front velocity as a function of voltage.

For an input pulse of duration  $\tau_{in}$ , the duration  $\tau_{out}$  of the output pulse after  $L$  meters of line would be  $(\tau_{in} - (L/\beta_0 c)(1/\beta_0 - 1))$ . For  $\tau_{in} = 40$  ns,  $L = 6$  m,  $\tau_{out} = 10$  ns and 34 ns for  $V_0 = 0.2$  MV and 2.0 MeV respectively. Consequently, the higher voltage is extremely advantageous for efficient power and energy transport.

The power delivered to a load at the end of a self-magnetically insulated transmission line is very sensitive to the load impedance  $Z_L$ . If the vacuum wave impedance without electron flow is  $Z_0$ , then the electron space charge and current density distribution in the gap causes the line to operate at  $Z_1 = Z_0$ . For all conditions,  $\alpha$  is less than one and is a function of voltage.<sup>15,23,24</sup> At 0.5 MV and at 2 MV,  $\alpha$  equals 0.35 and 0.63 respectively. When the line is terminated in  $Z_L > Z_1$ , the difference between the load current  $I_L = V/Z_L$  and the current required for magnetic insulation,  $I_T = V/Z_1$ , is lost to the positive conductor next to the load, and there is no reflected wave. Consequently, for  $Z_L > Z_1$ , the voltage is  $V_0$ , the matched voltage.

If  $Z_L < Z_1$ , the wave is partially reflected from the load. The reflected wave increases the total current and decreases the voltage. The electron flow is compressed much closer to the cathode under such conditions and the line impedance becomes  $Z_2 \approx Z_0$ . The boundary between  $Z = Z_1$  and  $Z = Z_2 \approx Z_0$  travels back through the line. The

forward going wave with voltage  $V_0$  in the region where  $Z = Z_1$  sees a mismatch to  $Z = Z_0$  and another at  $Z = Z_L$ . Consequently, the load voltage is

$$V_L = \frac{4V_0 Z_0 Z_L}{(Z_0 - Z_1)(Z_L + Z_0)} \quad (1)$$

and the load current is  $V_L/Z_L$ . For a short circuit,  $I_L = (V_0/Z_1)(2a/(1-a))$  and is always less than twice the matched load current  $V_0/Z_1$ . The approximate load line for a MITL, based on this model is shown in Fig. 6 with data from Ref. 9 and 10.

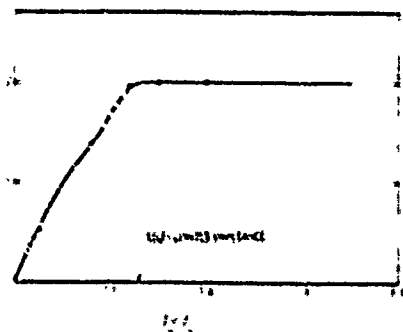


Fig. 6. The normalized load voltage as a function of  $Z_{LOAD}/Z_0$  for a line with  $V_0 = 2$  MV.

#### A Working Hypothesis for the Effects of the Convolute on Self-Magnetically Insulated Flow

The discussion in the preceding section was based on the assumption that the electron flow behind the front reaches an equilibrium and is stable. The existence of such an equilibrium in 1-D flow has been the subject of theoretical discussion<sup>18-20</sup> and has been cited to explain experimentally observed losses.<sup>9,10,19</sup> However, the Mite experiments<sup>10</sup> indicate the stability of the flow is governed by how the transition is made between the weakly stressed vacuum insulator and the highly stressed line, i.e., the injection convolute or transition section. The results of two different transition sections from the Mite experiment<sup>10</sup> are shown in Fig. 7. The 4 cm taper, in which the line separation decreased from 2 cm to 1 cm, showed severe losses in transported current and the time integrated electron energy distribution at the output as shown in Fig. 7b. The loss occurred between 0.5 and 1.5 m into the line and that region had striations on the cathode that were approximately 1 cm in axial extent and 10 cm apart. The periodic structure suggested that an instability grew with a growth length to saturation of  $\sim 0.50$  m and a wavelength of  $\sim 10$  cm. The apparent instability has not been identified.

The 13 cm taper showed excellent transport of current, and the electron energy distribution at the output agreed with that inferred from the input data as shown in Fig. 7b. There was no evidence of the striations on the cathode or of any periodic structure.

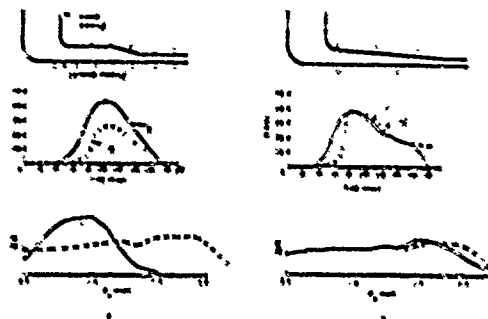


Fig. 7. Summary of the Mite data for 0.04 m transition and 0.14 m transition sections are shown in 7a and 7b respectively. The line profile, the input current  $I_0$  and output current  $I_2$ , and the electron energy distribution at the input (—) and output (---) are shown.

The interpretation of this result forms a working hypothesis that is currently being explored theoretically and experimentally at Sandia. Early 1-D theories<sup>18-21</sup> featured electrons with the canonical momentum in the direction of the electron flow  $X$  given by  $P_x = \gamma m U_x - e A_x = 0$ , in which  $\gamma$  is the usual relativistic factor for an electron with rest mass  $m$ , charge  $(-e)$ , and axial velocity  $U_x$  at a position when the vector potential in the axial direction is  $A_x$ . The 1-D flow has been generalized by C. W. Mendel<sup>22</sup> for an arbitrary distribution of  $P_x$ , and he demonstrated that electrons with  $P_{x,min} < P_x < 0$  and  $P_{x,max} > P_x > 0$  all flow in the space between electrodes. Their orbits do not intersect either the cathode or the anode. The upper and lower bounds,  $P_{x,max}$  and  $P_{x,min}$ , are determined by the self-consistent distribution of  $A_x(y)$  and the voltage  $V(y)$  across the gap.

Since  $U_x = (P_x + e A_x)/\gamma m$ , a distribution in  $P_x$  produces a distribution in  $U_x$  at any position. The electrons are either born in the uniform MITL or are born in the convolute immediately before the line. The Lagrangian of an electron in the magnetically insulated flow is given by  $L = T + eV - U_x A_x$ . From Lagrange's equation with  $P_x \equiv \partial L / \partial U_x$ ,  $dP_x/dt = \partial L / \partial X$ . In the uniform line,  $\partial L / \partial X = 0$  so  $P_x$  is a constant of the motion. If  $A_x = 0$  and  $V = 0$  at the cathode surface, then  $P_x = 0$  for the electrons originating at the cathode in the uniform line. These electrons are assumed to be the dominant electron species.

In the transition convolute leading into the uniform line,  $\partial L / \partial X \neq 0$  and  $dP_x/dt \neq 0$ . As these electrons flow through the convolute they acquire a nonzero canonical momentum and provide a second species of electrons flowing in the uniform line. The second species has a distribution  $F_1(P_x)$ , and so the total canonical momentum distribution is

$$F(P_x) = F_1(P_x) + N_0 \delta(P_x)$$

in which  $\delta(P_x) = 0$  if  $P_x \neq 0$  and  $\delta(P_x) = 1$  if  $P_x = 0$  and  $N_0$  is the number density of zero canonical momentum electrons in the flow at a position  $(x, y)$ .

The stability of the flow depends on the details of  $F(P_x)$ . Consequently, we need to estimate  $F(P_x)$  produced by a given convolute. A non-self consistent analysis of the electron flow through injector has been performed<sup>30</sup> and is based on the assumption that parapotential theory is locally applicable at each position in the convolute. The calculated distributions  $F(P_x)$  suggest that a broad distribution is correlated with efficient transport and a very narrow distribution is correlated with losses in the experiments. Further analysis is in progress and an experiment to measure  $F(P_x)$  in the uniform MITL with a laser scattering technique is being studied to determine its feasibility.<sup>31</sup>

In summary, the primary features of the working hypothesis are 1) convolutes can produce electrons with non-zero  $P_x$ , 2) these electrons flow through uniform self-magnetically insulated lines for many (50) Larmor radii, 3) these electrons interact with each other and the  $P_x = 0$  electrons of the main flow to cause the observed losses, and 4) the distribution  $F(P_x)$  is governed by the convolute geometry and determines the stability and power transport efficiency.

Bergeron and Poukey<sup>32</sup> have suggested that an instability between the beam electrons and those with  $P_x = 0$  is not necessary. Rather  $F_x(P_x)$  may have a sufficient number of electrons to account for all the losses. In their model, the beam electrons from the convolute random walk their way to the anode and are lost from the system. The hypothesis implies a very broad distribution of  $P_x$  with  $\Delta P_x \approx mc$  in the loss region in contrast to the  $\Delta P_x \approx 10^{-6} mc$  calculated from the convolute model.<sup>30</sup> The measurement of  $F(P_x)$  should test this hypothesis but it is unlikely to explain the regular striations on the cathode.<sup>10</sup>

#### Recent Experiments and Implications of the Working Hypothesis

When the polarity of the center conductor is reversed, the distribution of  $V(x, y)$  and  $A_x(x, y)$  is generally changed. For low impedance coaxial systems with a gap separation  $d \ll r$  and for parallel plate systems, the Lagrangian changes very little when the polarity changes. Two dimensional electromagnetic, PIC simulations of the two polarities in the same system with  $d/r \approx 0.7$ , showed very minor differences in the behavior of the flow.<sup>33</sup> However, if the injector convolute has inner and outer conductors of different shapes then the net power transport efficiency for the positive inner conductor is about 60 percent of that for a negative inner conductor.<sup>34</sup>

A new injector convolute<sup>11</sup> was designed and tested on Mite to reduce the asymmetry between the positive and negative polarity modes of operation. A cross section of the geometry taken through the mid-plane is shown in Fig. 8a. The vacuum impedance profile as a function of distance into the convolute was

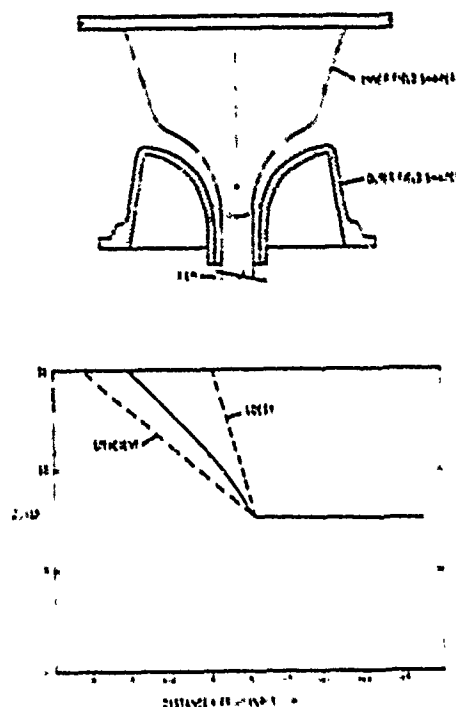


Fig. 8. The EBFA I transition section and its profile of vacuum impedance vs.  $x$  are shown.

between the lossy and the efficient profiles of Fig. 7, as shown in Fig. 8b. Since the transition is very gradual, the distribution  $F(P_x)$  is expected to be broad, although it has not been calculated, and hence is expected to cause efficient power transport. The power transport efficiency through the six meter long MITL was inferred from the total current with a self-limited load, from the voltage calculated<sup>10</sup> from the measurements of  $I_p$  and  $I_b$  in the self-limited mode, and from the short circuit current interpreted with the MITL load line in Fig. 6. These measurements indicated  $95 \pm 8$  percent power transport efficiency in either polarity. The development of an injector that works efficiently in either polarity was guided by the working hypothesis and extends the utility of EBFA I to include ion diodes that require positive polarity.

#### Conclusions

Substantial progress in developing self-magnetically insulated power flow has been made in the past three years. In regions where the cross section changes with the direction of power flow, the details of the geometry determine the behavior of the flow. The mechanism by which the geometry determines the power transport is currently under investigation. Additional research on the electron flow through convolutes of both types and all polarities may be expected to improve the power that can be delivered to an inertial confinement fusion target.

## References

1. J. P. VanDevender and D. H. McDaniel, Proc. 8th Int'l. Conf. on Discharges and Electrical Insulation in Vacuum, Albuquerque, NM, E-1 (Sept. 5-7, 1978).
2. T. H. Martin, IEEE Trans. Nucl. Sci., NS-20, 289 (1973).
3. Z. P. Velikov, V. A. Glukhiky, O. A. Gusev, G. M. Lazmanizova, S. L. Medoseev, G. B. Ovchinnikov, A. M. Pasechnikov, O. P. Percherskii, L. I. Rudakov, M. B. Swin'in, V. P. Smirnov and V. I. Chetvertkov, "ANGARA-5" Accelerator, NIIIEFA Preprint D-0301, Leningrad, USSR (1976).
4. I. D. Smith, Int'l. Topical Conf. on Electron Beam Res. and Tech., Albuquerque, NM, Vol. I, p.472 (Nov. 3-5, 1975).
5. R. G. Little, W. R. Neal and J. R. Uglum, same as Ref. 4, p. 508.
6. T. H. Martin, D. L. Johnson and D. H. McDaniel, Proc. of 2nd Topical Conf. on High Power Electron and Ion Beam Res. and Tech., Cornell Univ., Ithaca, NY, 807 (1977).
7. I. D. Smith, P. D'A. Champney and J. M. Creedon, IEEE Pulsed Power Conf., Lubbock, TX (1976).
8. E. I. Baranchikov, A. V. Gordeev, V. D. Korolev and V. P. Smirnov, Sov. Phys.-Tech. Phys. 8, 42 (1977).
9. M. DiCapua and D. G. Pellinen, J. Appl. Phys. 50, (1979).
10. J. P. VanDevender, J. Appl. Phys. 50, No. 6 (June 1979).
11. J. P. VanDevender and E. L. Neau, Sandia Labs Electron Beam Fusion Progress Report, April 1978-December 1978, Albuquerque, NM, (1979).
12. G. A. Mesyats and D. I. Proskurovskii, JETP Lett. 13, 4 (1971).
13. I. G. Kataev, Electromagnetic Shock Waves (in Russian), Sov. Radio, Moscow (1963); (in English) Iliffe Books, Ltd. London (1966).
14. K. D. Bergeron, J. Appl. Phys. 48, 3065 (1977).
15. J. W. Poukey and K. D. Bergeron, Appl. Phys. Lett. 32, 3 (1978).
16. E. I. Branchikov, A. V. Gordeev, Yu. V. Koba, V. D. Korolev, V. S. Pen'kina, L. I. Rudzkov, V. P. Smirnov, A. D. Sukhov, E. Z. Tarumov and Yu. L. Bakshaev, 6th IAEA Conf. Plasma Phys. Cont. Thermonuclear Reactions, Berchtesgaden, (1976).
17. A. V. Gordeev, Sov. Phys.-Tech. Phys. 23, 991 (1978).
18. R. V. Lovelace and E. Ott, Phys. Fluids 17, 1263 (1974).
19. A. Ron, A. A. Mondelli and N. Rostoker, IEEE Trans. Plasma Sci. PS-1, 85 (1973).
20. J. M. Creedon, J. Appl. Phys. 46, 2946 (1975) and J. M. Creedon, J. Appl. Phys. 48, 1070 (1977).
21. V. S. Varonin and A. I. Labedev, Sov. Phys.-Tech. Phys. 18, 1627 (1974).
22. C. W. Mendel, Accepted for publication in J. Appl. Phys. 50, No. 7, (July 1979).
23. S. Shope, J. W. Poukey, K. D. Bergeron, D.H.McDaniel, A.J.Toepfer and J.P.VanDevender, J. Appl. Phys. 49, 3675 (1978).
24. A. A. Kolomenskii, E. G. Krastalev and B. N. Yablokov, Sov. Phys.-Tech. Phys. 3, 247 (1977).
25. V. P. Smirnov, private communication (1978).
26. K. D. Bergeron, Phys. Fluids 20, 688 (1977).
27. A. V. Gordeev, Sov. Tech. Phys. Lett. 3, 323 (1977).
28. K. D. Bergeron, "A Slipping Stream Instability for Magnetically Insulated Electron Flow", RS4241/1005, Sandia Laboratories, Albuquerque, NM (1978).
29. M. DiCapua, D. G. Pellinen, P. D'A. Champney and D. H. McDaniel, same as Ref. 6, p.781.
30. E. L. Neau and J. P. VanDevender, IEEE 2nd Int'l. Pulsed Power Conf., Lubbock, TX (1979).
31. K. L. Brower and J. P. VanDevender, same as Ref. 30.
32. K. D. Bergeron and J. W. Poukey, Accepted for Publication J. Appl. Phys. 50 (1979).
33. J. W. Poukey, Private Communication.
34. M. DiCapua and D. G. Pellinen, Physics Int'l. Final Report, PIFR-1009, San Leandro, CA (Oct. 1978).



# Repetitively Pulsed Electron Beam Diode Lifetime and Stability\*

M. T. SUTTRAM

Sandia Laboratories, Albuquerque, New Mexico 87185

## Abstract

Repetitively pulsed vacuum beam diodes will be required for most projected inertially confined fusion systems. Yet data on the operation of diodes under repetitive pulsing is sparse. This paper discusses the operation of a 250 kV, 1.5 kA/cm<sup>2</sup> diode at repetition rates to 30 Hz for sustained runs. Short term stability is typically 3 percent (standard deviation). Longer term there is a drift toward higher impedance at the start of the pulse. Details on this drift and a comparison of this process for a rather blunt versus a sharp edged cathode are presented.

## Introduction

The development of repetitively pulsed vacuum beam diodes is crucial to most inertial confinement fusion (ICF) concepts whether the driver be electrons, light ions, or lasers. Typical pulse repetition frequencies (PRF's) being discussed are 10 Hz or less based on factors like the speed at which a reactor can be recycled between shots and the PRF needed to produce a reasonable power output (perhaps 1 GW) given a reasonable pellet yield (100 MJ). The rate limitation is not in general based on pulsed power considerations. Instead it is assumed that pulsed power systems can be developed to provide repetitively pulsed drivers of suitable PRF.

This paper addresses the operation of vacuum beam diodes in repetitive service. Problems specific to individual ICF schemes, e.g. repetitive extraction of pinched beams for particle beam applications or anode extraction foil survival in the case of laser diodes are not considered. Instead the subject is the general stability both short and long term of a diode in the absence of the transport of anode material to the cathode (blowback).

## Experimental Details

Data were taken with the RTF-I 100 Hz high voltage pulser (transformer driven, oil insulated, 9.5 Ω, 700 kV PFL<sup>2</sup>) attached to the diode shown in Fig. 1. At the left side of the figure is one side of the self-breaking gas output spark gap of RTF-I. Oil insulation ends in a diaphragm type vacuum interface designed to operate at pulse forming line

\*This work was supported by the U.S. Dept. of Energy, under Contract DE-AC04-76-DP00789.

voltages in excess of 1 MV. The cathode diameter is limited to 5 cm or less so that the beam area is at most 20 cm<sup>2</sup>. Typical operating voltages are 200 to 350 kV; thus to match the 9.5 Ω PFL the anode-to-cathode (A-K) spacing as calculated from the space charge limited flow equation

$$z = \frac{137\pi}{\sqrt{V}} \frac{d^2}{A} \quad (1)$$

is in the order of 0.5 cm. (The diode voltage  $V$  is in megavolts.  $A$  and  $d$  are the beam area and A-K spacing.) The anodes used were 0.3 cm thick aluminum plates backed by a water jacket. Calculation and experiments indicate that the anode should be able to survive beam heating rates corresponding to at least 30 Hz.

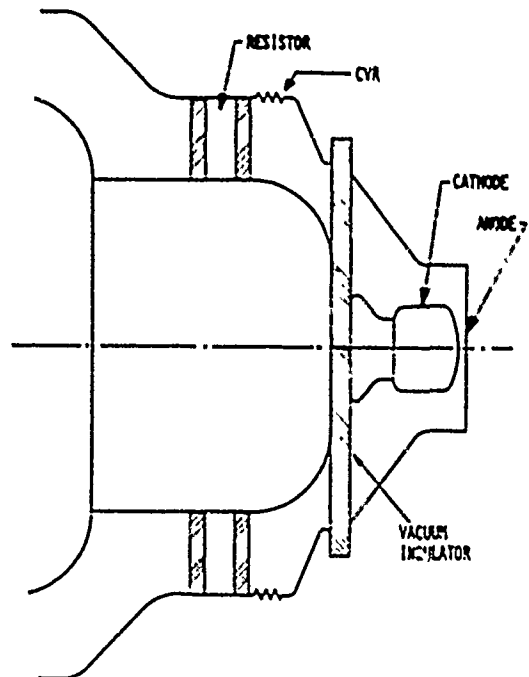


Fig. 1. Schematic of The RTF-I diode.

Diode voltage was measured with an integrated  $dV/dt$  monitor located at the output end of the high voltage gas spark gap. It reproduced the diode voltage waveform and could be consistently

calibrated. However, in common with all integrated monitors it produced a low output voltage unsuited for input to the waveform digitizer to be discussed later. In contrast a resistive voltage monitor located in the annular water resistor shown in Fig. 1 reproduced the temporal shape of the diode voltage waveform but did not appear to maintain a consistent calibration. It was originally calibrated along with the  $dV/dt$  and a capacitive monitor measuring the PFL voltage using microsecond pulses at voltages up to 90 kV. All three monitors agreed on temporal shape and amplitude. For short (<50 ns) pulses the  $dV/dt$  was later found to read 50 percent higher than the annular resistor. Measuring the leading edge of an open circuit load shot, the  $dV/dt$  gave an output voltage equal to the PFL voltage but the annular resistor was 33 percent low. This implies that the  $dV/dt$  monitor is correct. Whenever resistive monitor waveforms are used their amplitude has been rescaled to match the  $dV/dt$  monitor.

Figure 2a (upper trace) shows the annular resistor output for a typical event. It compares well with the  $dV/dt$  waveform of Fig. 2b. Diode current as measured by a 0.135  $\Omega$  low inductance resistive shunt (CVR) is shown in the lower trace of Fig. 2a. The diode has a definite "turn on" phase during which the emitting cathode plasma is forming. It is characterized by a voltage spike and a delay to significant current flow. After emission has begun the voltage drops to a plateau value which uniquely specifies the diode impedance ( $Z$ ) through the relation

$$V_{\text{PLATEAU}} = \frac{Z}{Z + Z_0} V_{\text{PFL}} \quad (2)$$

where  $Z_0$  and  $V_{\text{PFL}}$  are the PFL characteristic impedance and voltage respectively. Inductive corrections are insignificant at this point because  $dI/dt$  is small. If  $V_{\text{PFL}}$  is measured as the maximum diode voltage for an open circuit shot,  $Z$  may be computed from  $Z_0$  and the ratio  $V_{\text{PLATEAU}}/V_{\text{PFL}}$  which is independent of the probe calibration. In practice the impedance thus measured was used together with the measured diode voltage to calibrate the current measurement.

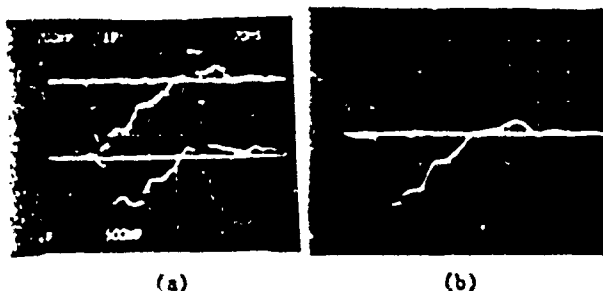


Fig. 2. Waveforms from a relatively new roll pin cathode.

- a. Voltage (upper trace, 120 kV/div)  
current (lower trace, 15 kA/div)  
20 ns/div.
- b. V voltage (20 ns/div, 120 kV/div).

A second voltage plateau (and an associated second current plateau) occurs when the voltage reflected from the diode during the turn on phase returns from re-reflection at the transformer end of the PFL. For a new cathode, as in the right photograph of Fig. 3, the two plateaus are well defined. As the cathode ages due to repetitive pulsing the turn on phase takes longer and the leading voltage spike widens and destroys the first plateau (left photo). The second plateau becomes longer with the net effect that the total energy delivered to the load remains relatively constant (to about 10 percent). This is presumed to be a consequence of the fact that there is nowhere for the energy originally stored in the PFL to go on a nanosecond time scale except into the diode. Energy reflected from the diode early in time will ultimately return and be converted into beam.

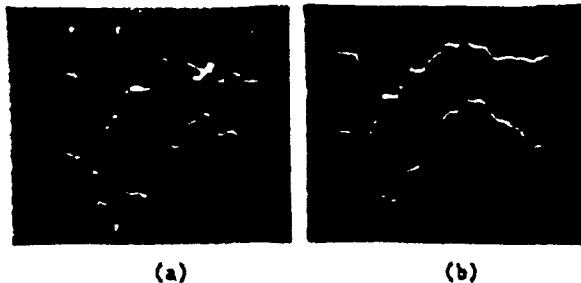


Fig. 3. Waveforms for a ring cathode.

- a. Aged cathode waveform (20 ns/cm, upper trace voltage at 120 kV/div, lower trace current at 15 kA/div).
- b. New cathode, same scales as a.

To follow the aging process and to get a good measure of shot-to-shot stability requires the analysis of many events. Processing a sufficient number of photographs to properly diagnose a repetitively pulsed diode run is time consuming and the most interesting events, e.g. those immediately preceding diode failure, may be completely lost. Therefore, a waveform digitizer capable of recording voltage and current waveforms at PRF's in excess of 100 Hz was developed. Each waveform is split into 24 separate signals using high fidelity resistive splitters. These 24 waveforms are staggered in time by 4 ns using cable delays and a small (<4 ns) time slice of each is digitized using 24 fast sampling analog-to-digital converters (ADC's). Each waveform is sampled at the same real time thus because of the staggering of the waveforms the points actually sampled are separated by 4 ns from waveform to waveform. The first sample is taken 12 ns prior to the waveform; so the first three ADC's sample baseline. Thereafter up to 80 ns of waveform may be digitized. Because the ADC's sample only negative signals any positive afterpulse is lost. The raw data from each event is stored on magnetic tape for subsequent analysis. A fraction of the data are also analysed online to monitor the progress of the experiment. The ADC's require input signals of several volts amplitude (after a 24:1 division) thus forcing the use of the resistive monitor output for the voltage waveform.

### Results

Figures 4 and 5 show digitizer outputs for a new cathode and for one aged by  $10^5$  shots. The PRF was 20 Hz. These data were taken with a cathode made of roll pins (0.16 cm diameter hollow cylinders) mounted on a brass backing (Fig. 6). The array produced a beam 5 cm in diameter. The pins have sufficient electric field enhancement at their tip to turn on quickly but also wear out rather rapidly. The pins on the outer perimeter of the cathode melted back as much as 0.2 cm during the  $10^5$  shots between the data in Figs. 4 and 5. Erosion of the inner pins was less severe. The figures show the readjustment of the voltage and current waveforms during aging as previously discussed. Notice that the impedance late in time (beyond 40 ns) is virtually unchanged during the aging process. This late in time plasma has formed on the cathode and, since the driving voltage is unchanged, the impedance should be the same.

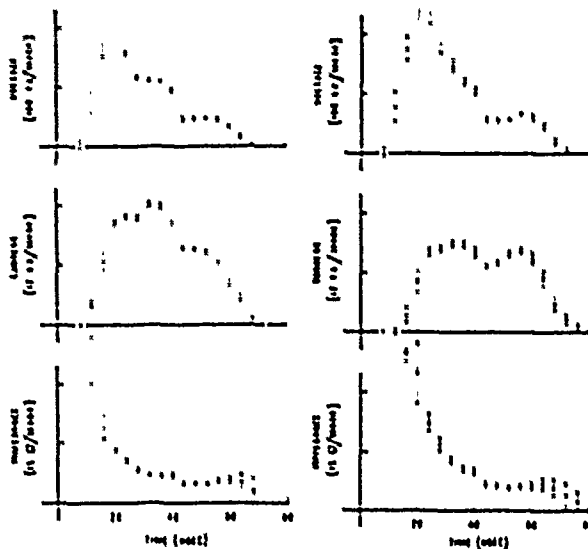


Fig. 4. Digitizer output waveforms for a new cathode (left).

Fig. 5. Digitizer output waveforms for an aged cathode (right).

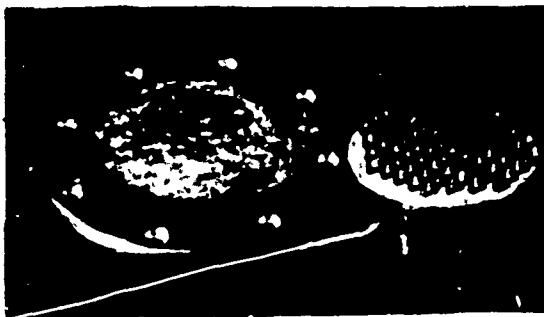


Fig. 6. Used roll pin cathode together with anode showing beam damage.

Figure 3 illustrates the aging process in another type of cathode, one without the large field enhancements present at the tips of the roll pins. This cathode exits from the edges of concentric rings cut into a brass block (Fig. 7). The waveforms are rather similar and the aging is qualitatively the same. Quantitatively the roll pin cathode ages somewhat more rapidly. If the impedance at the peak of the voltage waveform (normalized to the value at the outset) is plotted versus accumulated shots (Fig. 8), the roll pin impedance increases much more rapidly beyond 25,000 shots than the ring cathode impedance does. The roll pin impedance doubles in 50,000 shots but the ring cathode impedance requires almost twice as many.

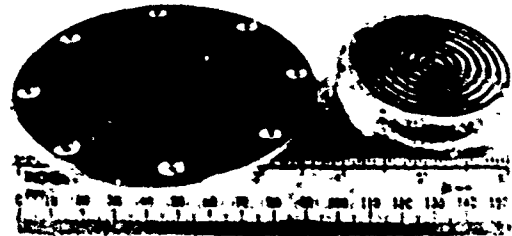


Fig. 7. Used ring cathode with anode showing beam damage.

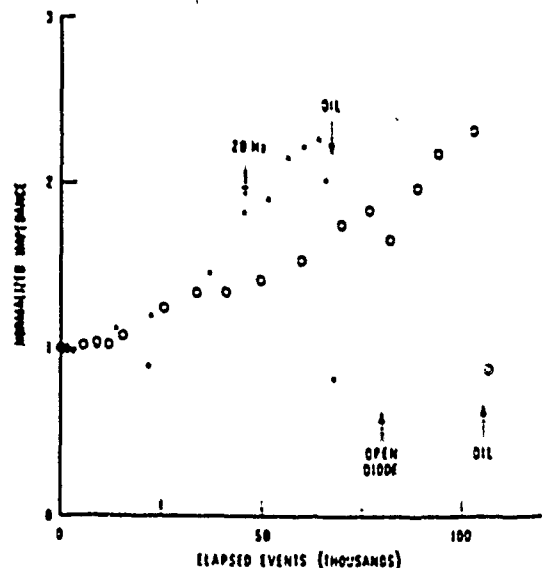


Fig. 8. Change in the diode impedance at voltage maximum vs. accumulated shots. The dots and downward pointing arrow refer to the roll pin cathode. Circles and upward arrows correspond to the ring cathode.

This plot also illustrates several other points about cathode aging. It is not strongly rate dependent. The roll pin data to 45,000 shots were taken at 10 Hz. After a change to 20 Hz the data continued along the same line. The aging process can be reversed by a light application of diffusion pump oil to the cathode surface as indicated for both cathode types. The ring cathode photographs of Fig. 3 show voltage and current for a single shot immediately after oiling an aged cathode (left) and for the second shot after oiling (right). The first shot is equivalent to an aged cathode event, the second to a fresh cathode. In fact, as illustrated in Fig. 8 after oiling the cathode becomes a better emitter than it was at the start of the run.

As regards shot-to-shot stability, Fig. 4 and 5 demonstrate that it is quite good. The "error bars" on those waveforms mark one standard deviation variances about the mean values. They are in general at the level of 3 percent, during the flat portion of the pulse and somewhat larger on the rising and falling edges. The voltage is slightly more stable than the current. Measurements of very stable calibration pulses have standard deviations below 1 percent even on the leading and trailing edges. Thus the jitter due to the digitizer is negligible (it adds quadrature with the diode jitter to produce the observed result). The data show that diode stability does not change as the cathode ages. There is apparently some variation in the rate at which cathode plasma is produced which creates the variability of the leading edge. This is reflected in a change in the overall pulse length reflected in the trailing edge jitter. This may account for the variations through the center of the pulse as well.

Runs on the roll pin and ring cathodes lasted 100,000 and 157,000 shots respectively. The roll pin data were distributed approximately equally between 10 and 20 Hz. The ring cathode data were at 20 and 30 Hz. Anode damage with the roll pins was worse at 20 Hz than was the damage from the ring cathode at 30 Hz, but in neither case was the run stopped by diode failure. The data of Fig. 8 clearly indicate the need to continue runs to the point where the aging terminates or becomes catastrophic. Such data will be taken in the near future.

### Conclusions

Vacuum beam diodes have been shown to operate stably for at least  $10^5$  shots at current densities of 1 to 2 kA/cm<sup>2</sup>. Shot-to-shot stability of 3 percent implies power and impedance stability of 4 percent, which in turn implies a stability for the total efficiency of conversion of PFL energy to beam energy of the same level. Long term, the diode impedance early in time drifts upward resulting in more beam being delivered in the form of afterpulse. Depending upon the application this may or may not pose a problem. For example in this configuration an old cathode produces a rather square current pulse of decreasing voltage which could be useful for some purposes.

As to the origin of the aging, two mechanisms immediately suggest themselves. It could result from the destruction of cathode whiskers whose explosion is thought to produce the cathode plasma. This would be a process equivalent to the breaking in of DC vacuum insulators. In that case the DC voltage is raised slowly while the insulator is separated from the power source by a high impedance. Very low current discharges occur which do not damage the electrodes but do remove the major whiskers so that the hold off voltage increases with each discharge. In this way the hold off voltage is slowly brought to the desired value. In the present case the discharged current is not constrained to be small and electrode damage does occur. Nevertheless over tens of thousands of shots whisker removal may occur.

Aging could also result from the destruction or "covering over" of whiskers by anode blowback. To distinguish these two possibilities there are several options. One can look for whiskers before and after aging in an attempt to detect any net gain or loss. This may be a difficult task to perform. One may attempt to change the blowback to change the aging as for example by changing anode material or beam current density. To the extent that blowback is increased with increasing repetition rate Fig. 8 argues against its being the cause of aging because the aging process was rate independent. Finally an examination of the extent to which blowback debris covers the emitting areas of the cathode could determine whether blowback can eliminate a significant fraction of the cathode whiskers. All the above options are currently being explored.

If the aging problem results from anode blowback it could be significant to pinched beam diode operation in where blowback may be severe even with a nominal plasma anode. The present experiments are so remote from such a diode that no conclusions should be drawn. However, if the aging is a result of whisker loss, sharp edged emitters (with relatively fewer emission sites) should age faster than blunt cathodes. Thus sharp edged emitters such as the foils used in laser diodes may change their emission characteristics quite rapidly in long term service and may require either a breaking in period or periodic maintenance.

### References

1. M. T. Buttram and G. J. Rohwein, "Operation of a 300 kV, 100 Hz, 30 KW Average Power Pulsar", Proc. of the 13th Pulse Power Modulator Symposium, Buffalo, NY (1978).

# VOLTAGE DISTRIBUTION AND CURRENT IN A CYLINDRICAL RELATIVISTIC DIODE

N. W. Harris

Ion Physics Company  
Burlington, Massachusetts

## Abstract

The voltage distribution and current in a space charge limited cylindrical diode are calculated by means of a simple computer program. Relativistic formulation is used, and the results are applicable up to the limit of significant beam pinch. The accuracy is 0.1%.

## Introduction

This paper describes the calculation of current density and voltage distribution in cylindrical electron guns working in the megavolt region. The current is assumed to be space charge limited. The cathode in this example is larger than, and concentric with, the anode. The companion case, anode radius greater than cathode radius, is very similar. The current is assumed radial, and magnetic effects have been ignored. The geometry is shown in Fig. 1, the Pierce<sup>1</sup> electrodes producing the same radial electric field distribution outside the beam as the space charge produces inside the beam.

Even at low voltages, where relativistic corrections can be neglected, solution of this problem is not simple and the results are usually given in a tabular, rather than analytic form<sup>2,3</sup>. At very high voltage, the perveance is a function of voltage

and hence tabulation is not practicable for voltages in excess of 200 kV. Consequently a simple program in BASIC was written for a timeshare computer to solve cases of interest. This is appended. Fig. 2 shows a typical result, the perveance falling by 43% as the voltage is raised to 10 MV. The cathode/anode diameter ratio was 5 in this case.

## Method of Calculation

The units are MKS. Consider a unit length (1 meter), with the cathode surface at a radius  $R_1$  and the anode at a radius  $R_2$ . Let the intervening distance be divided up into a number of equal parts. If each tube or shell has a very small radial width  $D$ , we can take the space charge in it as essentially uniform.

The first step is to place a small arbitrary voltage across the first shell. The current is calculated from the plane parallel diode approximation<sup>3</sup>

$$I = \frac{4\pi \epsilon (2R_1 - D)V^{1.5}}{9D^2} \sqrt{\frac{2e}{m}}$$

This current is the same for all shells. The field on the inside surface of the first shell is  $E = 4V/3D$  as shown by Langmuir<sup>3</sup>. The average voltage in the next shell is calculated by extrapolation,

$$V' = V + ED/2$$

From this, we obtain the relativistically correct electron velocity using the two equations

$$W = (\frac{e}{m}) V' / c^2$$

$$U = c \sqrt{W^2 + 2W / (1+W)}$$

This gives us the space charge density and hence the change in field (using Gauss' theorem).

$$\frac{dE}{dR} = E_1 = \frac{D}{(R-D)} \left[ E + \frac{I}{2\pi (RU)} \right]$$

This gives the average voltage for the next shell and the calculation is repeated. The computation proceeds until the anode is reached. We then have a value for the diode voltage and its corresponding current. This process can be repeated for different values of voltage placed across the first shell, until the current/voltage characteristic is adequately described.

This method has been used for other geometries: for the plane parallel case it is more convenient than the analytic expressions that have been derived. It could also be noted that this method gives, as a byproduct, the voltage distribution in the diode. This voltage distribution is required for the design of the end electrodes.

#### Basic Program

The program listing is in BASIC and follows the method given above. Lines 10-20 read in the electrode radii, the number of shells F and the skip number S. The number of shells should be several thousand, in the listing it is 4000. The

skip number is the required number of voltage printouts. In the example given, it is 10 which means that the voltages at 9 equally spaced intermediate radii are printed out. It should be noted that F/S must be an integer.

The computer asks for a start voltage, 10 volts is convenient, and the computation proceeds as above. Lines 280-320 govern the printout of the intermediate voltages, note that K is a counter. When the iteration is completed the computer prints out the diode characteristics and asks for a fresh start voltage. The operator supplies a value such that the diode voltage is closer to the desired value. In this manner, the diode characteristics, as a function of voltage, may be mapped.

#### Accuracy

The program was checked for the low voltage case and accuracy improved with number of steps, up to a limit of 10,000. At 4000 steps the accuracy was ~0.1%. The calculations are valid up to the region of magnetic pinch. This occurs when the diode impedance is comparable to (or less than) the coaxial impedance

$$60 \ln \left( \frac{R_1}{R_2} \right)$$

#### References

- <sup>1</sup> Pierce, J. R., Theory and Design of Electron Beams, D Van Nostrand, New York 1950.
- <sup>2</sup> Spangenberg, K. R. Vacuum Tubes, McGraw-Hill, New York 1948, p. 173.
- <sup>3</sup> Langmuir, I. and Blodgett, K. B., Phys Rev, Ser 2, vol 22 pp 347-357, Oct 1923.

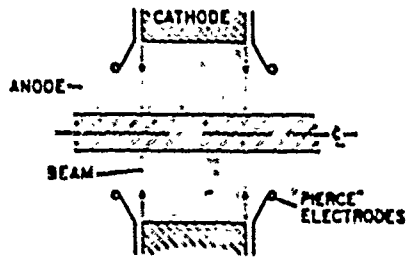


Figure 1. DIODE GEOMETRY

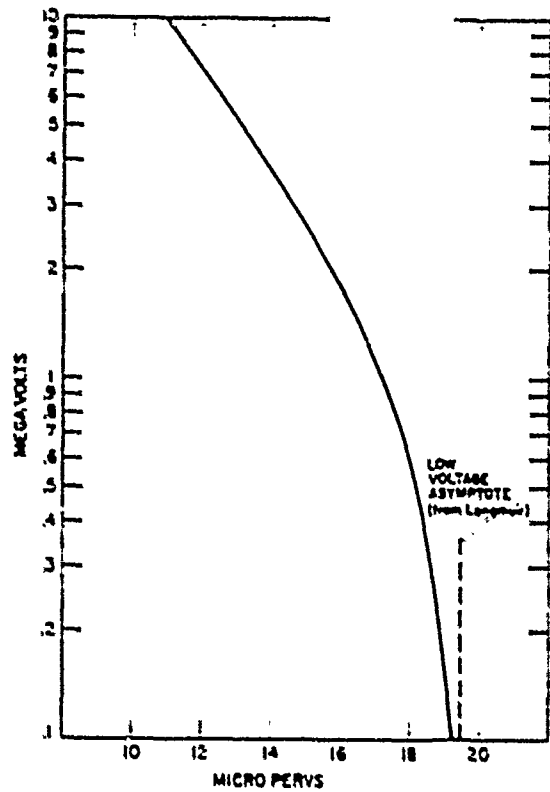


Figure 2. PERVEANCE vs VOLTAGE

```

10 READ R1,R2,F,S
20 DATA 2,1,4000,10
40 PRINT "START VOLTAGE";
50 INPUT V
60 IF V<1E-6 THEN 410
70 PRINT"CATHODE";R1;"ANODE";R2;"METERS RADIUS"
80 D=(R1-R2)/F
90 R=R1
100 I=1.4668E-5*V*1.5/D/D*(R1-D/2)
130 E=4*V/3/D
140 K=0
150 PRINT
160 PRINT"RADIUS          KV"
170 FOR N=1 TO F
180 K=K+1
190 W=1.957589E-6*(V+E/2*D)
200 U=2.99776E8*50R(W*2+2*W)/(1+W)
210 P=I/U*1.7973E10 'RHO/EPILON
220 REM E1 IS CHANGE OF ELECTRIC FIELD
230 E1=D*(P+E)/(R-D)
240 REM ON TO NEXT SHELL
250 R=R-D
260 V=V*(E+E1/2)*D
270 E=E+E1
280 IF K<F/5 THEN 330
290 V1=V/1000
300 PRINT USING 310,R,V1
310 100.000      00000.00
320 K=0
330 NEXT N
340 PRINT
350 PRINT I;"AMPS";V1;"KV"
360 Z=V/I
370 P1=1*1E6/V*1.5
380 PRINT Z;"OHMS";P1;"MICROPERVEANCE"
390 PRINT
400 GO TO 40
410 END

```

Figure 3. Program Listing

## SIMULATIONS OF INTENSE RELATIVISTIC ELECTRON BEAM GENERATION BY FOILLESS DIODES

MICHAEL E. JONES AND LESTER E. THODE

Intense Particle Beam Theory Group  
Los Alamos Scientific Laboratory  
Los Alamos, New Mexico 87545

Abstract

Foilless diodes used to produce intense annular relativistic electron beams have been simulated using the time-dependent, two-dimensional particle-in-cell code CCUBE. Current densities exceeding  $200 \text{ kA/cm}^2$  have been obtained in the simulations for a 5 MeV, 35  $\Omega$  diode. Many applications, including microwave generation, collective ion acceleration and high-density plasma heating require a laminar electron flow in the beams. The simulation results indicate that foilless diodes immersed in a strong external magnetic field can achieve such a flow. Diodes using technologically achievable magnetic field strengths ( $\sim 100 \text{ kG}$ ) and proper electrode shaping appear to be able to produce beams with an angular scatter of less than 35 mrad at the current densities and energies mentioned above. Scaling of the impedance and temperature of the beam as a function of geometry, magnetic field strength and voltage is presented.

Introduction

Foilless diodes may be used for the production of intense annular relativistic electron beams for many applications including microwave generation, collective ion acceleration and high-density plasma heating.<sup>1</sup> Conventional foil diodes have been found to suffer from an impedance collapse when plasma, generated by electrons striking the anode foil, propagate from the anode to the cathode thereby electrically shorting the diode. This problem is eliminated by using a foilless diode, thus allowing higher current densities than can be obtained with a foil diode. In addition, the electron beam generated by a foilless diode is not perturbed by passing through a foil nor is it necessary to replace a foil for repeated operation.<sup>2</sup>

Although there has been some investigation of relativistic electron beam generation by foilless diodes a firm understanding of the diode has been

lacking.<sup>2-8</sup> We have analyzed the simple diode illustrated in Fig. 1 to determine the scaling of diode impedance and beam temperature as a function of geometry, magnetic field strength and voltage. Some investigators have assumed that the foilless diode impedance is determined by the maximum current allowed by space charge in the drift tube. Our analysis indicates that the diode impedance is determined by the equilibrium that the beam obtains which is not necessarily the equilibrium which gives the space-charge limiting current.

Impedance Model

Because most applications require a beam with laminar flow it is useful to model the beam formed by the foilless diode by the cold fluid equations. In an azimuthally symmetric, axially homogeneous equilibrium, the equations describing the beam depend only on the radial coordinate,  $r$ . The equations to be solved are

$$mc^2/e \gamma \beta_0^2/r = E_r + \beta_0 B_z - \beta_z B_\theta \quad (1)$$

$$dB_z/dr = 4\pi ne\beta_0 \quad (2)$$

$$d(rB_\theta)/dr = -4\pi ner\beta_z \quad (3)$$

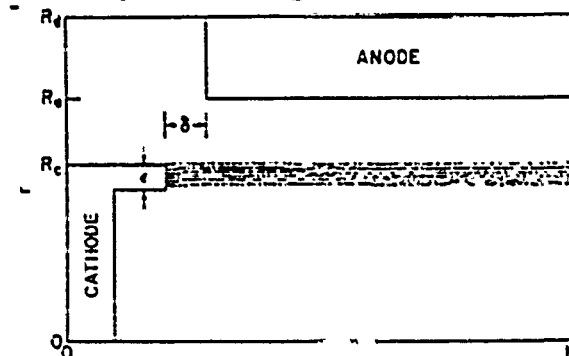


Fig. 1. Typical Foilless Diode.



$$d(rE_r)/dr = -4\pi n e r \quad (4)$$

where  $m$  and  $e$  are the mass and charge of the electron. The only nonzero fluid variables are the density  $n$  and the axial and azimuthal fluid velocities  $\beta_z$  and  $\beta_\theta$  (divided by the speed of light  $c$ ). The nonzero fluid variables are the radial electric field  $E_r$ , the azimuthal magnetic field  $B_\theta$ , and the axial magnetic field  $B_z$ . The relativistic factor is denoted by  $\gamma$ . Because the cathode is an equipotential surface, conservation of energy assumes the following form:

$$d\gamma/dr = -eE_r/mc^2 \quad (5)$$

Because there are only five equations and six unknowns another condition must be specified. A condition which leads to an analytically tractable solution of the equilibrium equations and which becomes increasingly better satisfied at larger energies, is to choose  $\beta_z$  to be independent of  $r$ .<sup>9</sup> Defining the following quantities  $\gamma_{||} = (1 - \beta_z^2)^{-1/2}$  and  $\gamma_\perp = \gamma/\gamma_{||}$  an equation for  $\gamma_\perp$  can be found whose solution is given in terms of elliptic Jacobi functions.<sup>9</sup> The total beam current  $\nu$ , measured in units of  $mc^3/e$  is given by this model as

$$\nu = [( \gamma_{||}^2 - 1)( \gamma_{\perp 0}^2 - 1)( \gamma_{\perp 0}^2 + a^2 )]^{1/2} \quad (6)$$

where  $\gamma_{\perp 0}$  is  $\gamma_\perp$  evaluated at the outside edge of the beam,  $R_0$ , and  $a$  is an arbitrary constant. Defining  $\omega_{co} = eB_0(R_0)/mc^2$  we find

$$R_0 \omega_{co}/c = (\gamma_{\perp 0}^2 - 1)^{1/2} + \gamma_{\perp 0}(\gamma_{\perp 0}^2 + a^2)^{1/2} \quad (7)$$

$$\text{and } \ln R_0/R_i = F(\phi, k)/(a^2 + 1)^{1/2} \quad (8)$$

where  $R_i$  is the inside beam radius,  $\phi = \cos^{-1}(\gamma_0^{-1})$  and  $k = a/(a^2 + 1)^{1/2}$  and  $F(\phi, k)$  is the incomplete elliptic integral of the second kind.

In addition to Eqs. (6)-(8), we require that the total energy of the electrons, kinetic and potential, be equal to the potential drop between the anode and cathode. Thus,

$$\gamma_a = \gamma_{||} \gamma_{\perp 0} + 2\nu/\beta_z \ln R_a/R_0 \quad (9)$$

where  $R_a$  is the anode radius (see Fig. 1). The relativistic factor that the electrons would have

upon reaching the anode is denoted by  $\gamma_a$ . Voronin, et al. have used these equations and additional assumptions to find the space-charge limited current as a function of magnetic field.<sup>8</sup> However, there is no a priori reason to assume that the beam produced by the diode will be launched into an equilibrium which will transmit the maximum current.

If the applied external magnetic field penetrates the cathode then conservation of canonical angular momentum takes the form:

$$(\gamma_{\perp 0}^2 - 1)^{1/2} = (R_0 \omega_{co}/c - R_c^2 \omega_c/R_0 c)/2 \quad (10)$$

where  $\omega_c = eB_0/cm^2$  and  $B_0$  is the applied magnetic field. The cathode radius is denoted by  $R_c$ . If in addition we assume that the laminar electron flow is along the self-consistent magnetic field lines, then the flux between the axis and the outer edge of the beam is equal to the applied flux between the axis and the cathode radius. On the time scale of most experiments, the magnetic field produced by the beam cannot diffuse through the anode wall. Therefore, the flux between the outer edge of the beam and the anode will be equal to the applied flux between the cathode and anode. These conditions may be written as

$$R_c^2 \omega_c/c = 2 R_0 (\gamma_{\perp 0}^2 - 1)^{1/2} + R_i (1 + a^2)^{1/2} \quad (11)$$

$$\text{and } \omega_{co}(R_a^2 - R_0^2) = \omega_c(R_a^2 - R_c^2) \quad (12)$$

Equations (6)-(12) form a complete set of equations which can be solved (numerically) to determine the impedance of the foilless diode. In order to insure laminar flow, it is necessary to apply a large external magnetic field. Therefore a useful approximation can be obtained by taking the infinite magnetic field limit. One then finds that the beam becomes infinitesimally thin with radius  $R_c$  and that the beam approaches a nonrotating equilibrium. The diode impedance in this limit becomes

$$Z = 15(\gamma_a - 1) \{ [\gamma_a/(1 + 4 \ln R_a/R_c)]^2 - 1 \}^{-1/2} \Omega \quad (13)$$

should be noted that this formula is invalid for low voltage, probably owing to our assumption of  $\beta_z$  being independent of  $r$ .

### Diode Simulations

A two-dimensional relativistic time-dependent particle-in-cell simulation code, CCUBE, has been used to test the impedance model and gain insight into the parameters affecting beam quality.<sup>10</sup> An emission algorithm in the code emits charge from the cathode surface at a sufficient rate to satisfy the space-charge limited emission boundary condition, i.e., the electric field normal at the cathode is zero. The diode simulations were run with a transverse electromagnetic (TEM) wave launched from the left in Fig. 1 onto the coaxial transmission line. By not allowing the first few cells to emit, one can control the impedance of the driver to the diode, which in all cases was taken to be 37  $\Omega$ . Typically the length of the simulation region,  $L$ , was 5 to 10 cm. Impedances and beam parameters are measured when the system consisting of the transmission line driver with the diode load had reached steady state. At this time the voltage on the diode,  $V$ , is given by

$$V = 2V_0 Z / (Z_0 + Z) \quad (14)$$

where  $Z$  is the diode impedance,  $Z_0$  is the transmission line impedance and  $V_0$  is the voltage of the TEM wave launched onto the line. Diagnostics in the code include voltage and particle current probes, Rogowski Coils as well as impedance probes located at several axial positions. At the end of the simulation region diagnostics include Faraday Cups, calorimeters and density, mean velocity, and temperature measurements as a function of radial position.

### Simulation Results

From Eq. (13) we see that for large applied magnetic fields the diode impedance depends only on the voltage and the ratio of the anode to cathode radius. Figure 2 shows the results of several simulations performed with a  $V_0 = 5.1$  MV and a cathode radius,  $R_c = 1$  cm. Because of the impedance mismatch, the voltage across the diode varied from 3.5 to 6.0 MV in accordance with Eq. (14). The open circles represent simulations performed with an applied magnetic field of 100 kG and an A-K gap,  $\delta$ , (see Fig. 1) of 0.4 cm. The triangle represents a run with the same parameters but with  $\delta = 0.2$  cm.

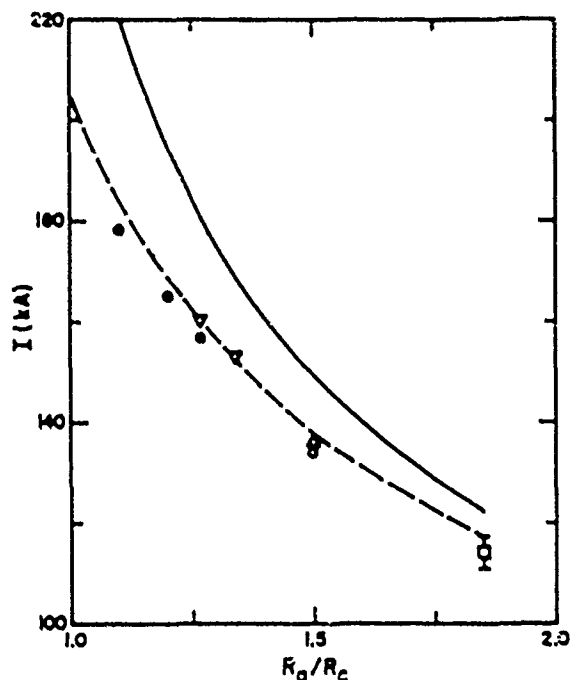


Fig. 2. Current versus ratio of anode to cathode radius for various foilless diodes. The dashed line is from Eq. (13). The solid line is the space-charge limit.

Two runs at 40 kG and  $\delta = 0.4$  cm are denoted by inverted triangles. The square designates a run at 55 kG in which the anode wall is continued straight at the original transmission line radius,  $R_d$ , of 1.85 cm so that  $\delta \approx \infty$ . The dashed line is obtained from Eq. (13). The solid line is the space limiting current for the infinitesimally thin beam in the infinite magnetic field limit.<sup>14</sup> The simulation data in all cases lies well below the space-charge limiting current and rather close to the current given by the impedance formula of Eq. (13). All the simulations were performed with a cathode tip thickness,  $\epsilon$  in Fig. 1, of 0.135 cm except the run at 55 kG which had  $\epsilon$  equal to  $R_c$ . At 100 kG the beam thickness was found to be approximately 0.03 cm, thus it is unlikely that much effect would be found for  $\epsilon$ 's larger than this value. The very thin beams can yield current densities exceeding 700 kA/cm<sup>2</sup>.

Because Eq. (13) was obtained for the infinite magnetic field limit, it is desirable to determine the effects of finite magnetic field. Figure 3 shows the results of a series of simulations performed with  $V_0 = 5.1$  MV,  $R_d = 1.27$  cm,  $\delta = 0.4$  cm,

and  $\epsilon=0.135$  cm. The dashed curve is obtained from the numerical solution of Eqs. (6)-(12). The solid curve is the space-charge limited diode theory of Voronin, et al.<sup>10</sup> The diode operates well below the space-charge limit and again agrees well with the laminar flow impedance model. The beam strikes the anode wall at 25 kG and for all values of applied field below this value the transmitted electron current gradually diminishes owing to current loss to the anode. Although the diode impedance does not vary much with magnetic field, the temperature as measured by the mean annular scatter of electrons around the beam propagation direction was found from the simulations to vary from 200 mrad at 27 kG to less than 60 mrad at 100 kG. The large magnetic field makes it more difficult for the electrons to cross field lines and create temperature by mixing.

One would expect that as  $\delta$  is increased to larger values that the beam produced by the foilless diode would come to equilibrium before it "sees" the reduced anode radius  $R_a$ . The existence of this effect is verified by the series of simulations shown in Fig. 4. The parameters of the simulations include  $B_0=100$  kG,  $V_0=5.1$  MV,  $R_c=1.5$  cm, and  $\epsilon=0.135$  cm. The upper dashed curve was calculated from Eq. (13). The lower dashed curve was also calculated from Eq. (13) but with  $R_a$  equal to outer radius of the transmission line feed  $R_0$ . As seen from the data, the diode impedance makes a sudden transition from an equilibrium with an anode radius of  $R_a$  for small  $\delta$  to an equilibrium with anode radius  $R_0$  at large  $\delta$ . The value of  $\delta$  at the transition point is roughly one-half of the cathode radius for this case. The actual transition point is probably governed by the distance the beam must

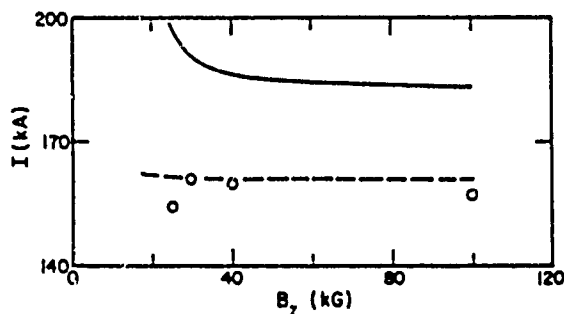


Fig. 3. The effect of finite magnetic field on diode impedance.

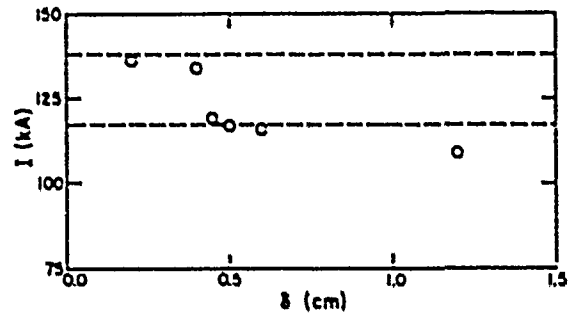


Fig. 4. Current versus A-K gap,  $\delta$ , for the foilless diode.

propagate from the cathode tip to reach equilibrium and must certainly depend upon the current density.

For large values of  $\delta$ , the beam gains kinetic energy as it approaches the region in which the anode radius is reduced to  $R_a$  making it stiffer and less likely to phase mix. Simulations have shown beam temperatures below 25 mrad for this scheme, which is near the numerical resolution of the code. Use of these ideas in diode design show promise for producing very laminar beams.

#### References

1. L. E. Thode, Los Alamos Scientific Laboratory report LA-7169-P (February 1978).
2. M. Friedman and M. Ury, Rev. Sci. Instr. **41**, 1334 (1970).
3. M. E. Read and J. A. Nation, J. Plasma Phys. **13**, 127 (1975).
4. A. A. Kolomenskii, E. G. Krastelev, and B. N. Yablokov, Pis'ma Zh. Tekh. Fiz. **2**, 271 (1976).
5. E. Ott, T. M. Antonsen and R. V. Lovelace, Phys. Fluids **20**, 1180 (1977).
6. J. Chen and R. V. Lovelace, Phys. Fluids **21**, 1623 (1978).
7. D. C. Straw and M. C. Clark, Proceeding of 1979 IEEE Particle Accelerator Conference.
8. V. S. Voronin, E. G. Krastelev, A. N. Lebedev, and B. N. Yablokov, Fiz. Plazmy **4**, 604 (1978).
9. A. V. Agafonov, V. S. Voronin, A. N. Lebedev and K. N. Pazin, Zh. Tekh. Fiz. **44**, 1909 (1974).
10. M. E. Jones and L. E. Thode, Los Alamos Sci. Lab. report LA-7600-MS (January 1979).
11. B. N. Brejzman and D. D. Ryutov, Nucl. Fusion **14**, 873 (1974).

This work was supported by the Air Force Office of Scientific Research and the US Dept. of Energy.

## ION BEAM GENERATION THROUGH A MOVING PLASMA BOUNDARY

M. Dembinski<sup>\*</sup> and P.K. JohnDept. of Physics, The University of Western Ontario  
London, Canada N6A 3K7Abstract

It is shown that ion currents extracted from a moving plasma can be increased by a factor of  $\sim v/c_s$  ( $v$ -plasma flow velocity,  $c_s$ -ion acoustic speed) as compared with a stationary plasma of the same density and temperature. A conical  $\theta$ -pinch gun is used to accelerate plasma with density  $n \sim 10^{12} \text{ cm}^{-3}$  to velocity  $v \sim 10^7 \text{ cm/s}$ . Total currents  $\sim 100 \text{ A}$  of 10-20 keV ions were obtained from an 8 cm diameter extraction system.

Introduction

Recent interest in high current ion and electron sources has been primarily due to their potential use in fusion related studies. Fast development of neutral beam injectors for plasma heating resulted in construction of high current ion sources<sup>1,2,3</sup> capable of delivering up to 100 A currents of 10-40 keV energy in quasi-steady or pulsed operation. In these sources increase of extracted ion current can be achieved by increase of plasma density or temperature. In the source described here the increase of the extracted current results from the use of a moving plasma as the source of ions. The advantage of this approach lies in the relative ease of plasma acceleration to high velocities in comparison with generation of a sufficiently dense plasma and heating it to sufficient temperature - especially in large diameter systems. Furthermore with high velocity injection of the ions into the extraction gap, the space charge limited current determined

by Child-Langmuir law increases thus allowing extraction of higher ion currents. This effect is especially significant in the case of low extraction voltages and high plasma velocities. A limitation of this type of ion source is that it is a pulsed source with pulse duration limited by plasma lifetime.

In the conventional method of ion current generation, the current per unit area collected by a negative electrode in a plasma is given by the Bohm formula<sup>4</sup> which for  $T_e \gg T_i$  gives  $J_B = 0.4ne \times (2kT_e/M_i)^{1/2}$  where  $T_e$  and  $T_i$  are the electron and ion temperatures,  $n$  is the electron density and  $M_i$  is the ion mass. The current collected is thus proportional to the ion acoustic speed  $c_s$ , the speed at which the ions enter the sheath surrounding the electrode. However if the plasma were moving at a speed  $v \gg c_s$ , in the collisionless case of  $\lambda \gg R$  (where  $\lambda$  is the collision length and  $R$  is the radius of the electrode) the current density collected by a cylindrical probe transverse to the flow direction would be given<sup>5</sup> by  $J_y = nev$ . The current for a given plasma is now limited only by the attainable flow velocity provided it is less than the space charge limited current determined by extraction system geometry and voltage. Thus it should be possible to extract ion currents much larger than the saturation ion current predicted by the Bohm theory. A pair of closely spaced transparent electrodes can be used to extract the beam from the moving plasma. If the first electrode of the extraction system is charged highly positive with respect to the plasma potential, the plasma

<sup>\*</sup>On leave from Institute of Fundamental Technological Research, Warsaw, Poland

on reaching the electrode would attain this applied potential. The electric field  $E$  in the space between the electrodes lets the gap play the role of an artificial sheath while an ion beam emerges through the second electrode. Since the ions enter the sheath at the flow velocity  $v$ , the extracted current would be given by  $J_e = nev$ , at an energy defined by the applied potential.

#### Experiment

The experimental setup is shown in figure 1. The plasma was produced in a pyrex pipe of diameter 10 cm by a conical  $\theta$ -pinch system (coil length 20 cm, angle  $15^\circ$ ). A low inductance 0.75  $\mu$ F capacitor charged up to 40 kV was discharged into the coil. The ringing period of the discharge was 2.5  $\mu$ sec. The extraction system consisted of a pair of stainless steel grid electrodes of diameter 8 cm and mesh size  $1.8 \times 1.8$  mm. The electrodes had spherical shapes of radius of curvature 9.5 cm each for beam focussing purpose and spacing between the two was variable in the range 1 to 5 mm. Variable voltages  $\pm U_g$  were supplied to the extraction gap by a 0.75  $\mu$ F capacitor. The voltage  $U_g$  was monitored by a potential divider and a low inductance shunt measured the current  $I_g$  in the gap. The extracted beam was incident on a thin stainless steel collector disc. A low inductance shunt measured the current  $I$  in the beam and a calibrated thermistor  $T$  attached to the disc was used to measure the energy in the incident beam. Hydrogen was let into the system through a fast pulse-gas valve. This reduced the probability of early breakdown in the extraction gap. Triggering of the  $\theta$ -pinch was timed such that the plasma was produced just as the pressure front reached the far end of the  $\theta$ -pinch coil. Typical operating pressure was  $\sim 1$  mTorr. Two cylindrical electrostatic probes mounted at right angles to each other were used to measure simultaneously the density, temperature and plasma flow velocity. The microwave system ( $\lambda = 3$  cm) was used to monitor plasma density.

#### Results

Measurements of the plasma parameters near the

extraction electrodes were made by the two cylindrical Langmuir probes, one parallel and the other perpendicular to the plasma flow. Temperature and density were obtained from the characteristics of the parallel probe. Current to the probe is not affected by the plasma flow since an effect<sup>6</sup> is negligible in our case. Plasma flow velocity  $v$  was determined from the ratio of ion saturation currents of the two probes. The ratio  $(i_{||}/i_{\perp}) = 0.4(\Lambda_{||}/\Lambda_{\perp})(c_s/v)$  where  $i_{||}$  and  $i_{\perp}$  refer to ion saturation currents in the parallel and perpendicular probes and  $\Lambda_{||}$  and  $\Lambda_{\perp}$  are the effective collecting areas of the probes. The plasma parameters at  $\theta$ -pinch voltages in the range 20-40 kV were:  $n = (2.5 \pm 0.9) \times 10^{11} \text{ cm}^{-3}$ ,  $T_e = 4 \pm 8 \text{ eV}$ ,  $v = (1 \pm 3) \times 10^7 \text{ cm/s}$ . Ion acoustic speed for such plasma parameters is  $\sim 3 \times 10^6 \text{ cm/s}$ .

In order to obtain the value of the extracted current  $I_e$  from the current  $I$  measured at the collector, secondary electron emission from the surface had to be taken into account. The measured current  $I = I_e(1 + \alpha)$  where  $\alpha$  is the effective secondary emission coefficient for the collector surface. Simultaneous measurements of  $I$  and  $E$ , the energy deposited on calibrated collector disc, enabled determination of  $\alpha$  which under our operating conditions was  $(1.1 \pm 0.2)$ .

Figure 2 shows a typical set of oscilloscope traces for a  $\theta$ -pinch charging voltage of 35 kV and extraction gap voltage of 16 kV. For the signal shown in figure 2b the ion beam current corrected for secondary emission gives a value  $I_e = (95 \pm 15) \text{ A}$ , the error arising from the uncertainty in the measured value of  $\alpha$ . The extracted current increases rapidly with increasing density and is terminated by electrical breakdown in the accelerating gap. The total current  $I_t \sim 100 \text{ A}$  corresponds to current density  $\sim 2 \text{ A/cm}^2$  which is larger than the space charge limited current ( $j_{sp} \sim 1.2 \text{ A/cm}^2$  for  $U_g = 15 \text{ kV}$  and gap separation  $d = 3 \text{ mm}$ ). It suggests that processes occurring in the extraction gap result in change of  $j_{sp}$ . Emission of secondary electrons from the second electrode of the extraction gap can considerably change potential distribution thus

leading to the decrease of effective gap spacing. Recently published results<sup>7</sup> show that at high ion current densities ( $> 1.1 \text{ A/cm}^2$ ) complex processes occur in the gap resulting in an increase in the effective secondary emission coefficient which causes additional neutralization of space charge. Figure 3 shows a comparison of the extracted ion beam current density  $J_i$  with the expected current  $J_{iv}$  - nav calculated from the measured values of  $n$  and  $v$  as a function of  $\delta$ -pinch voltage  $U_\delta$ . Also shown is the Bohm current  $J_b$  calculated from the measured values of  $n$  and  $T_e$ . It is seen that  $J_i$  and  $J_{iv}$  follow the same curve and show a steep increase with  $\delta$ -pinch voltage, while the Bohm current stays a relatively insensitive function of the voltage. In our range of observations the ratio ( $J_{iv}/J_b$ ) rises to  $\sim 10$  which is primarily due to the increase of  $v$  with  $\delta$ -pinch voltage.

Quality of beam focussing was tested by using variable diameter collectors which could be moved along the axis of the system. Beam size which is 5 cm at the grids was found to be less than 1 cm at the focus. Beam diameter was measured from burn marks on exposed polaroid paper. Diameter of the focal spot so measured was  $\sim 7 \text{ mm}$ . Position of the beam focus coincided with the geometric focus of the electrodes. Size of the focal spot suggests rather high value for beam emittance which we attribute mainly to the imperfections of the electrode shaping. A transverse component of velocity of the injected particles could also have contributed to the emittance.

#### Conclusion

Use of a moving plasma as a source of ions can increase extracted currents as compared to a stationary plasma with the same parameters. Ion beams with total currents  $\sim 100 \text{ A}$  corresponding to current density  $2 \text{ A/cm}^2$  were extracted over the 9 cm diameter two-electrode extraction system. Processes occurring in the extraction gap (secondary electron emission) lead to an increase of extracted current density above the limit set by the Child-Langmuir law. The system described here seems to be particularly suitable for generation

of large diameter ion beams. For  $\sim 10 \text{ cm}$  diameter extraction system it would give total ion currents in the range of 1 kA at presently observed current densities. Further increase of plasma density and velocity can theoretically increase extractable current density provided that difficult problem of suppressing voltage breakdown in the gap can be resolved by possible use of magnetic insulation. Further study of processes occurring in the gap is needed for better understanding and possible increase of extractable currents.

#### References

1. A.T. Forrester, D.M. Goebel and J.T. Crow, Appl. Phys. Lett. 33, 11 (1978).
2. K.W. Ehlers et al, J. Vac. Sci. Technol. 10, 9 (1973).
3. R. Limpacher and K.R. MacKenzie, Rev. Sci. Instrum. 44, 726 (1973).
4. D. Bohm, E.H.S. Burhop and H.S.W. Massey in "The Characteristics of Electrical Discharges in Magnetic Fields" (Ed. by A. Guthrie and R.K. Wakerling, McGraw Hill, New York 1949).
5. W.A. Clayden in Rarefied Gas Dynamics (Ed. J.A. Laurman Academic Press 1963) Vol. II, p. 435.
6. S.D. Hester, A.A. Sonin in Rarefied Gas Dynamics (Ed. L. Trilling and H. Wachman, Academic Press 1969) Vol. II, p. 1659.
7. V.M. Antonov, L.B. Gavorkian, A.G. Ponomarenko, Zh. Tech. Phys. Letters 4, 995 (1978).

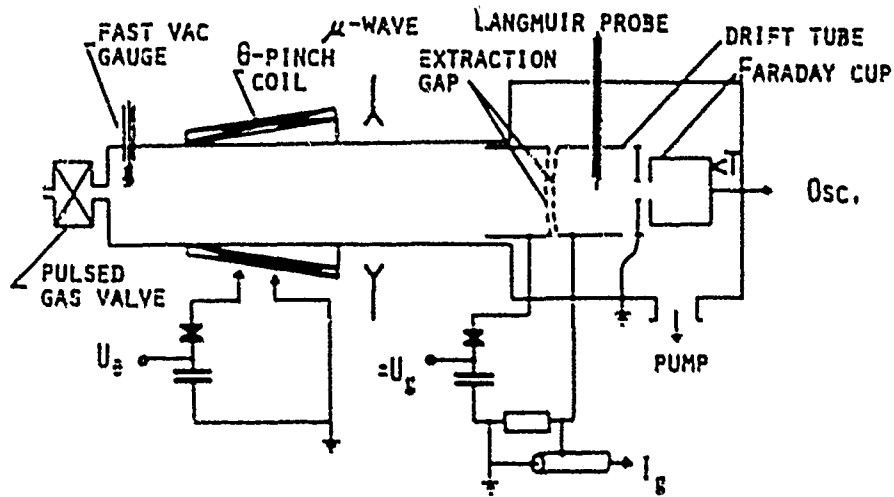
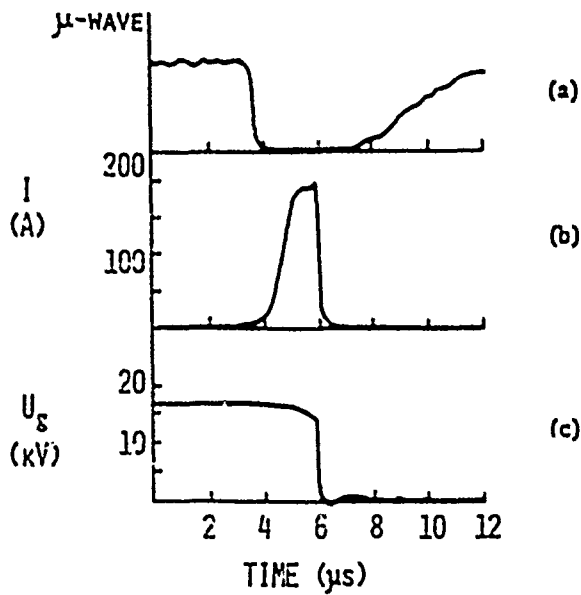
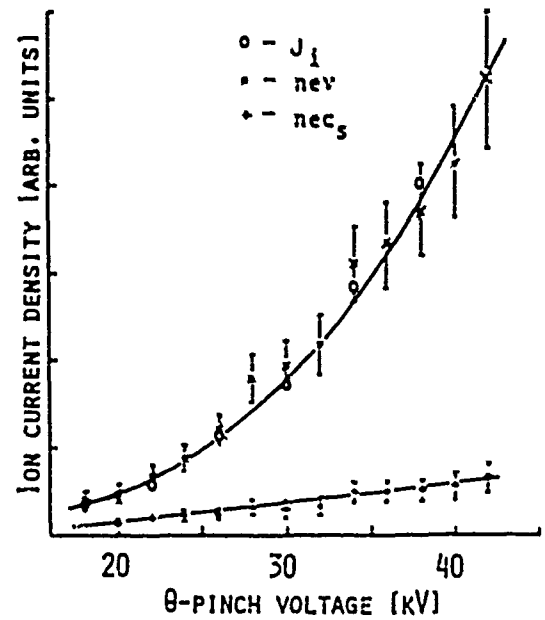


Fig. 1. The experimental setup.

Fig. 2. Time variation of: 2a - microwave signal transmitted through the plasma showing cutoff at 4  $\mu$ s. 2b - collector current, 2c - extraction gap voltage  $U_g$ .Fig. 3. Comparison of measured ion current density  $J_1$ , calculated current density  $J_v = nev$  and Bohm current density  $J_B$  as a function  $U_g$ . Solid line: least-squares curve fitted to the experimental points of  $J_1$ .

## INVITED

## FUNDAMENTAL LIMITATIONS AND DESIGN CONSIDERATIONS FOR COMPENSATED PULSED ALTERNATORS

W. F. Waldon, W. L. Bird, M. D. Briga, K. M. Tolk, H. G. Rylander, H. H. Woodson

Center for Electromechanics, The University of Texas at Austin  
Taylor Hall 167, Austin, Texas 78712

Abstract

Since the beginning of a project intended to demonstrate the feasibility of using a compensated pulsed alternator (compulsator) as a power supply for NOVA and other solid state laser systems, a great deal of interest has been generated in applying this type of machine to supply energy for other types of loads. This paper outlines the fundamental limitations imposed on the design of such a machine by the mechanical, thermal, magnetic, and electrical properties of the materials used. Using these limitations, the power and energy available from the machine are calculated as functions of machine dimensions. Several configurations for the machine and their relative merits for various applications are also discussed.

Introduction

Recently interest in pulsed power for a variety of applications including magnetic and inertial confinement fusion experiments, advanced weapons systems and industrial manufacturing processes has resulted in many developments in pulsed power supply technology. In several areas inertial energy storage has emerged as an attractive alternative to magnetic or electrostatic energy storage because of the very high energy densities available at relatively low cost. The problem of converting the stored inertial energy to electrical energy, however, has not been satisfactorily resolved in most cases. Conventional alternators are limited in power output by their own internal impedance and although pulsed homopolar generators, having low internal impedance, are capable of very high power outputs, they accomplish this at low voltages which are not always desirable.

In essence, pulse rise times are limited by inductive voltage drop ( $L \frac{di}{dt}$ ). In its simplest form an alternator consists of a single turn coil of wire spun in a magnetic field (Figure 1). Increasing the output voltage of such a machine (to produce faster  $\frac{di}{dt}$ ) requires increasing the magnetic flux density, increasing the surface speed of the rotating coil, or increasing the number of turns in the coil. Ultimately, the magnetic flux density and surface speed of the coil are limited by material properties. The alternator voltage increases linearly with the number of turns in the coil, but unfortunately the inductance, which limits pulse rise time, rises with the square of the number of turns resulting in no gain in output power.

$$(V(t))_{\max} = B l v$$

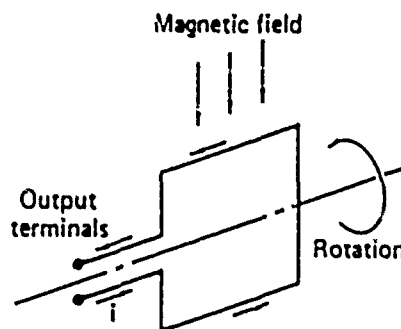


Figure 1: Simple Alternator



The compensated pulsed alternator or compulsator (Figure 2) uses a stationary coil almost identical to the rotating one and connected in series with it to increase output power by flux compression.<sup>1,2</sup> As the two coils approach one another, the magnetic field generated by the output current is trapped between them and compressed and the effective inductance is therefore reduced. When the two coil axes coincide the inductance is minimized, but the alternator voltage can be at its maximum value. This results in the generation of a very large magnitude current pulse from the machine. In addition the compulsator output voltage during the inductance change can be considerably higher than the open circuit voltage due to  $i \frac{dL}{dt}$  effects. As the rotating coil passes the stationary one the inductance again rises to its normal (higher) value, commutating the pulse off.

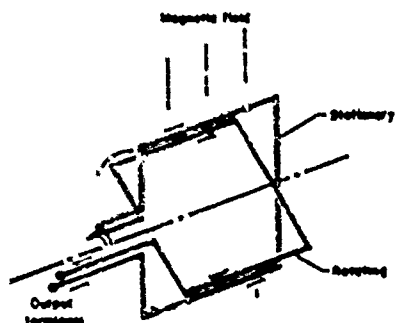


Figure 2: Compensated Pulsed Alternator

Since the compulsator is essentially a variable inductor in series with a conventional alternator, and depends upon minimizing circuit inductance to generate an output pulse, it is not well suited for driving inductive loads. It is well suited, however, to both capacitive and resistive loads.<sup>2,3</sup> The use of a pulse transformer to increase compulsator output voltage has also been investigated<sup>3</sup> and appears to reduce the net output by about 25%. This paper is intended to identify and characterize the fundamental limitations to compulsator performance and to suggest some approaches for extending these limitations. For

convenience the fundamental limitations to compulsator performance can be divided into three groups; those dealing with the effect of load characteristics, those limiting output power, and those limiting minimum pulse width.

#### Effect of Load Characteristics

A simplified (lumped parameter) circuit for a compulsator connected to a resistive load (such as a flashlamp) is shown in Figure 3.

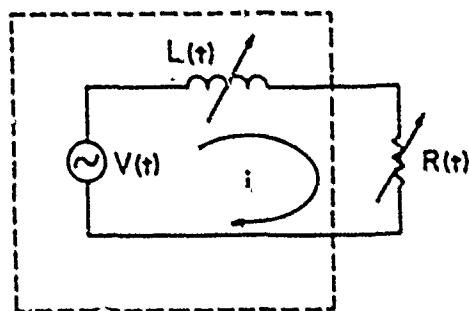


Figure 3: Simplified Circuit  
Compulsator Driving Resistive Load

The differential equation for this circuit can be written as:

$$\frac{d}{dt}(Li) + Ri = V(t) \quad (1)$$

where  $L$  and  $R$  are the total instantaneous circuit inductance and resistance,  $V(t)$  is the "alternator" voltage (open circuit voltage) due to the armature coil rotating in the applied magnetic field, and  $i$  is the instantaneous current. The solution to equation (1) is:

$$i = \frac{1}{L} \left\{ (L_0 i_0) + \int_0^t V(\tau) e^{\int_{\tau}^t \frac{R}{L} d\tau} d\tau \right\} e^{-\int_0^t \frac{R}{L} d\tau} \quad (2)$$

where  $L_0$  and  $i_0$  are initial values of inductance and current at the beginning of the pulse (when the circuit is closed). The first term within the brackets of equation (2) represents the contribution to total output current made by the flux compression aspect of the compulsator while the second term represents the current due to the volt-seconds supplied by the alternator. The

first term primarily affects the shape of the output pulse while the second term determines the energy delivered to the load. For a wide range of resistive load cases investigated the compulsator has been found to reduce the basic alternator half cycle pulse width by a factor of about 3.

For a capacitive load such as a transfer capacitor the basic circuit is shown in Figure 4 and the differential equation for the circuit is:

$$\frac{d}{dt}(Li) + Ri + \frac{1}{C} \int i dt = V(t) \quad (3)$$

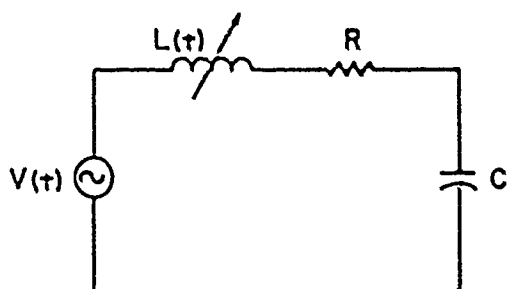


Figure 4: Simplified Circuit  
Compulsator Driving Capacitive Load

Although the analytical solution of this second order differential equation is quite cumbersome it can be solved numerically and the energy delivered to a capacitive load by a compulsator has been shown to be

$$E = \eta \frac{\left( \int_0^t V(t) dt \right)^2}{2L_{\min}} \quad (4)$$

where  $L_{\min}$  is the minimum total circuit inductance and  $\eta$  is a numerically determined constant which has been found to be around 0.5 for most cases of interest. For the capacitive load case the compulsator has been found to compress the basic alternator half cycle pulse width by a factor of about 4.

#### Limitations to Peak Output Power

It is apparent from equations (2) and (4) that the compulsator's primary advantage, in terms of high

output power, over the conventional alternator comes from flux compression, or more specifically, from the interaction of the discharge current with the inductance variation. This in turn implies that the inductance variation must be maximized and since the maximum inductance in the uncompensated position is relatively insensitive to machine variables, really requires that the minimum inductance in the compensated position be reduced as much as possible. This requirement suggests the use of radially thin air gap windings distributed uniformly over the rotor surface rather than salient pole windings or even distributed windings in slots since the slot teeth increase the winding inductance. A significant limitation to peak output power comes then from the conflict between the requirement for minimum radial air gap between the rotor and stator windings in order to minimize  $L_{\min}$  and the dielectric strength of the air gap insulation on the windings. The inductance variation is given by  $\left(\frac{\tau}{g}\right)^2$  for an iron cored machine (unsaturated) and by  $\frac{\tau}{g} \left(1 + \frac{g}{\tau}\right)$  for an air cored machine where  $\tau$  is the conductor width per pole and  $g$  is the radial air gap between conductors, so that the sensitivity of machine performance to this air gap limitation is readily apparent.

A second limitation on output power imposed by this air gap winding concerns the shear strength of the insulation system used to bond the stator and rotor windings to the stator and rotor structures. The interaction between the compulsator discharge current and the radial component of the magnetic field in the air gap due to that current causes a tangential force on the conductors which slows the rotor, converting stored inertial energy to electrical energy. This force results in a tangential shear stress on the insulation bond between the conductors and the rotor or stator. This radial magnetic field component which depends upon the time and position history of the currents as well as the permeability and eddy currents in the surrounding structure has been calculated for several cases using a transient, nonlinear, finite element magnetic field mapping code developed by

the Center for Electromechanics. For these cases an average surface current density of 10 MA/m was found to produce stresses which could be withstood by insulation systems with shear strengths of 28 MPa (4000 psi). The peak mechanical power output of the machine is simply the product of this peak allowable shear stress, the active surface area of the rotor and the rotor surface speed. For a rotor surface speed of 150 m/sec, such as is used for the Lawrence Livermore Laboratory engineering prototype compulsator (Figure 5)<sup>4,5</sup> with a laminated steel rotor, the peak output power per unit of surface area is 4.2 GW/m<sup>2</sup>. For other configurations capable of operating at much higher speeds which are described later, this limit may exceed 10 GW/m<sup>2</sup>.

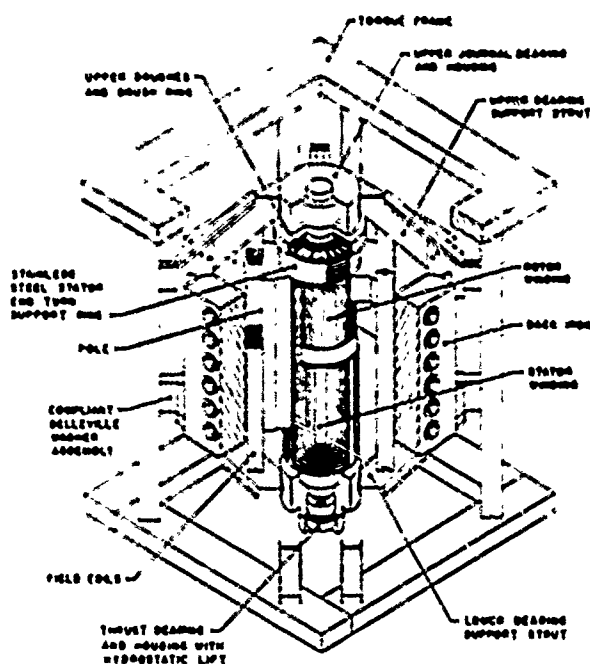


Figure 5: LLL/CEM Prototype Compulsator

Finally, the requirement that the rotor and stator conductors be radially thin in order to generate minimum inductance is in conflict with the extremely high current densities achievable in the compulsator in that thermal heating of the conductors may become a limiting factor especially in the case of repetitive pulses. This thermal limit can become even more restrictive in that

skin effects can confine the fast rising current pulses to the surfaces of the conductors resulting in even more severe heating. This skin effect can be overcome by using stranded and transposed conductors but these increase the minimum inductance somewhat as well as complicating the construction of the machine.

#### Limitations to Minimum Pulse Width

The relationship of the compulsator output pulse width to the basic (alternator) half cycle pulse width has been discussed for various loads. This, of course, suggests that as faster pulses are required the base electrical frequency of the alternator must be increased. The electrical frequency  $\omega_e$  of the alternator is given by:

$$\omega_e = \frac{P}{2} \omega_m$$

where  $P$  is the number of field poles and  $\omega_m$  is the mechanical rotor speed in radians/sec. The mechanical rotor speed is limited by the stiffness of the rotor and its dynamic behavior in the bearings and by eddy current generation due to the alternating magnetic field experienced by the rotor turning in the heteropolar excitation field. This eddy current limit can be extended by laminating the rotor, but there is a practical limit to the minimum lamination thickness which can be used; and as the rotor laminations are made thinner, rotor construction becomes more difficult and rotor mechanical stiffness suffers.

Increasing the mechanical speed of the rotor has another limitation as well. Increasing rotor speed increases centrifugal loading on the rotor air gap winding. This in turn requires additional banding material in the air gap to restrain the rotor conductors and this leads to increasing the radial air gap spacing which again increases the crucial minimum machine inductance.

This leaves only the option of increasing the number of poles to increase the alternator frequency, but here too we find a limit. As the

number of poles increases for a given machine the spacing between poles must decrease. As this pole-to-pole spacing approaches the air gap distance, the applied field leakage exceeds the useful flux cut by the rotor conductors. This point of diminishing returns makes the addition of more poles futile.

Finally, as the base frequency of the compulsator is increased, the volt-seconds per pulse supplied by the excitation field ( $\int V dt$  in equations (2) and (4)) decreases. This drastically limits the output power available from the original compulsator concept for pulse times below 100  $\mu$ sec.

#### Alternate Compulsator Configurations and How They Address Limitations

Figure 6A shows the original compulsator configuration to which the limitations discussed in this paper apply. It consists of a multipole wave winding on the rotor connected in series through slip rings with an almost identical multipole wave winding on the stator. The alternator voltage  $V(t)$  is generated by the armature winding (only) rotating in the applied magnetic field supplied by the excitation coils. As mentioned previously, the alternating magnetic field experienced by the rotor requires that the rotor be constructed of laminated steel and this results in a substantial reduction in rotor stiffness as well as additional complexity in rotor construction.

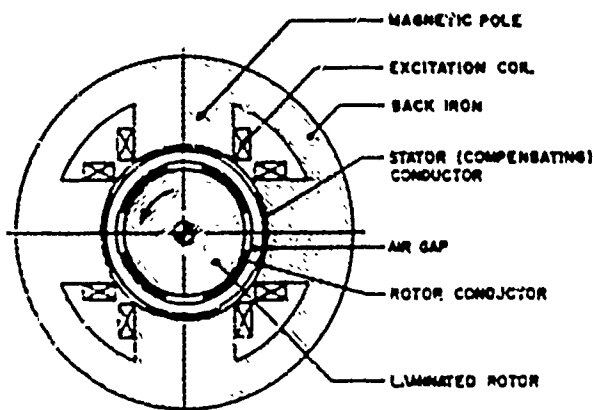


Figure 6A: Stationary Field Compulsator

The rotating field compulsator (Figure 6B) offers one solution to this problem by placing the excitation coils on the rotor, radially inboard of the armature winding. The rotor no longer experiences an alternating applied field and now may be fabricated from a solid forged steel billet. The rotor will be much stiffer and can operate at higher surface speeds. In practice the excitation coils would probably be distributed windings rather than the salient pole construction shown here for clarity. This configuration does require the stator or back iron to be laminated, but the loading of the stator is less severe and much greater design latitude exists for the stator than for the rotor. However, since the excitation coils occupy additional space in the already crowded rotor, flux path considerations dictate that this construction only be used for larger machines.

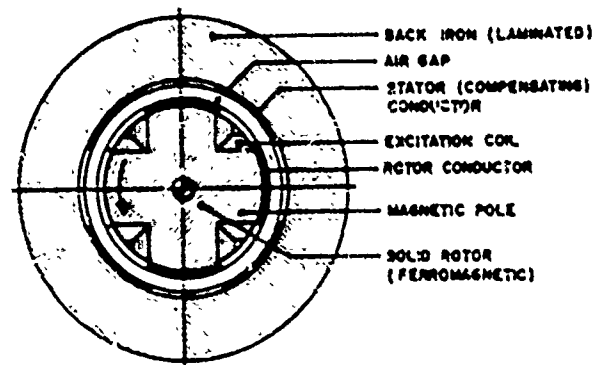


Figure 6B: Rotating Field Compulsator

Another solution to the laminated rotor problem is shown in Figure 6C. By fabricating the armature conductors into filament reinforced composite "cups" which nest together coaxially, the central iron core can remain stationary and thus be solid. Several other benefits accrue from this design as well. Since the rotor inertia is dramatically reduced, a larger portion of the inertial energy is stored in the conductors themselves. This is significant since the conductor inertial energy can be converted with  $(J \times 3)$  body forces rather than the conductor/insulator shear forces necessary to convert inertial energy stored elsewhere in the rotor structure. This alleviates the insulation shear stress limit.

tion and allows higher surface current densities and consequently higher peak output power per unit of active rotor surface area than the configurations shown in Figures 6A or 6B. In addition, the cup rotor construction allows the two halves of the armature winding to be counterrotated, doubling the open circuit voltage of the machine without increasing the circuit inductance. This innovation also doubles the base electrical frequency of the compulsator without imposing the geometric limit of the pole spacing approaching the radial air gap dimension (excessive flux leakage limitation).

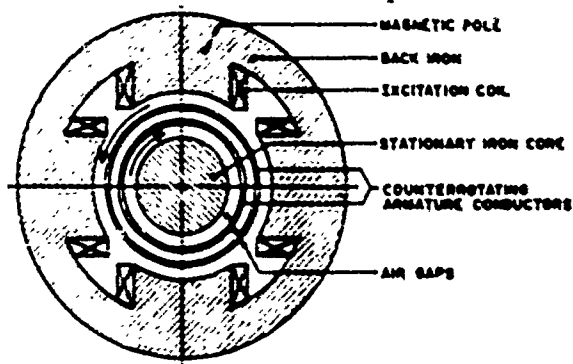


Figure 6C: Counterrotating Cup Rotor Compulsator

Finally, since for very short pulse times ( $<100$   $\mu\text{sec}$ ) the volt-second contribution of the applied magnetic field becomes a limiting factor in machine performance, configurations which supply the necessary volt-seconds from an external source (perhaps a capacitor bank or even another compulsator) have been investigated. The configuration shown in Figure 6D is an outgrowth of these investigations. The volt-seconds are supplied to the stationary winding by an external source and the applied flux is then compressed by the rotation of the fluted, conductive (probably aluminum) rotor.<sup>3</sup> The rotor is slowed by the flux compression, inertial energy in the rotor being converted to electrical energy in the stationary winding. Initial investigations have indicated that such a device is capable of producing energy gains of at least a factor of ten over the initially supplied volt-seconds, and can deliver large amounts of energy ( $>10^6$  joules) in substantially less than 100  $\mu\text{sec}$ .

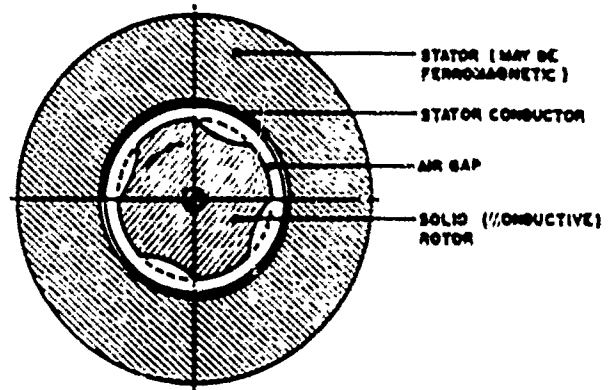


Figure 6D: Brushless Rotary Flux Compressor

### Summary and Conclusions

This paper has not only addressed the fundamental limitations to performance of the recently invented compensated pulsed alternator, but has categorized them into three groups; those dealing with the effects of load characteristics, those limiting the peak output power, and those limiting the minimum pulse width. In addition, the authors have suggested some new design approaches, which appear to extend the operating limits of the compulsator concept beyond those of the original compulsator design.

The work described in this paper was supported by Lawrence Livermore Laboratories (contract no. 3325309), Los Alamos Scientific Laboratories (contract no. EG-77-5-05-5594), the U. S. Department of Energy, the Naval Surface Weapons Center (contract no. N60921-78-C-A249), and the Texas Atomic Energy Research Foundation.

### References

1. Lawrence Livermore Laboratory's, "Compensated Pulsed Alternator," brochure concerning COMPULSATOR invented by the Center for Electromechanics, July 1975.
2. W. L. Bird, M. D. Driga, D. J. T. Mayhall, M. Brennan, W. F. Weldon, H. G. Rylander, H. H. Woodson, "Pulsed Power Supplies for Laser Flashlamps," Final Report to Lawrence Livermore Laboratory, Subcontract No. 1823209, October 1978.
3. K. M. Tolk, W. L. Bird, M. D. Driga, W. F. Weldon, H. G. Rylander, H. H. Woodson, "A Study of the Engineering Limitations to Pulse Discharge Time for a Compensated Pulsed

Alternator," Final Report to Los Alamos Scientific Laboratories, Order No. W68-0899H-1, May 1979.

4. J. H. Gully, W. L. Bird, M. D. Driga, H. G. Rylander, K. M. Toik, W. F. Weldon, H. H. Woodson, "Design of the Armature Windings of a Compensated Pulsed Alternator Engineering Prototype," 2nd IEEE International Pulsed Power Conference, Texas Tech University, Lubbock, Texas, June 12-14, 1979.
5. M. Brennan, W. L. Bird, J. H. Gully, M. L. Spann, K. M. Toik, W. F. Weldon, H. G. Rylander, H. H. Woodson, "The Mechanical Design of a Compensated Pulsed Alternator Prototype," 2nd IEEE International Pulsed Power Conference, Texas Tech University, Lubbock, Texas, June 12-14, 1979.

## USE OF TRANSFORMERS IN PRODUCING HIGH POWER OUTPUT FROM HOMOPOLAR GENERATORS

W. H. Lupton, R. D. Ford, D. Conte

H. A. Lindstrom, I. M. Vitkovitsky

Naval Research Laboratory

Washington, D. C. 20375

Abstract

Analysis is presented for systems using high current pulse transformers to exploit the high energy storage capability of homopolar generators or other limited current sources. The stepped-up secondary current can be established either by current interruption when the primary is also used for energy storage or by commutation of current into the primary from a separate storage inductor. For high-power pulse generators the primary insulation and power supply are protected by subsequent croubarring of the primary. An example is given of a design for

charging the NRL homopolar generator with 1.46 mH inductor to a 1- $\mu$ H, megavolt level inductive pulse generator.

switch<sup>4</sup>, which can carry these currents for long intervals of time, make it possible to energize the energy storage inductance directly with a current source such as a homopolar generator. One in existence at the Naval Research Laboratory<sup>5</sup> has an energy storage capability of several megajoules and typical current output of 40 kA. To significantly increase the current output from this generator would require additional current-collector brushes. This would be an expensive addition in this case since the use of fiber brushes is required by the high rotational speed. This is an exaggerated case but illustrates the fact that the current output of homopolar generators are limited by brush and contact area.

1. Introduction

Pulse power generators using inductive energy storage may have economic promise for applications requiring powers of  $10^{11}$  -  $10^{13}$  W. Studies of opening switches which must be used with inductive storage have shown that it is possible to use carefully made and operated exploding foil fuses as current interrupters<sup>1,2</sup> with high electric fields (of the order of 20 kV/cm) across the fuse. The limitations imposed by the ratio of conduction time to opening time, which is fixed by the nature of the vaporization process, has been overcome by sequentially opening several stages of switches<sup>2</sup> with power multiplication at each stage so that megavolt output pulses are typically obtained. This approach has been extended recently with the TRIDENT pulse generator<sup>3</sup> using larger fuses and requiring currents of the order of 500 kA.

The advent of the explosively driven mechanical

Any power supply with a limited current capability can nevertheless be used to deliver a large amount of energy by allowing it to energize a sufficiently large inductance. Subsequent switching which produces a change in current allows use of the transformer principle where a change in current in a multiple-turn primary winding is accompanied by a greater change in current in a secondary winding of fewer turns. This procedure was used by Walker and Early<sup>6</sup> to obtain a hundred-fold current step-up in an inductive storage system. The desire to utilize the NRL homopolar generator for the TRIDENT high-power pulser studies mentioned above provides the motivation for this analysis of transformer systems. In circuit design special attention is given to the consequences of high-voltages resulting when the system is used a part of a high-power pulse generator.

## II. Common Store and Transformer

If the energy storage inductance is a coil of many turns, a secondary winding of fewer turns can be coupled to it to become a high-current source for a pulse generator. This concept is illustrated schematically by the circuit shown in Figure 1. In the first stage of operation the homopolar generator, denoted by HPG, energizes a long time-constant coil  $L_1$  with switch  $S_1$  closed. The high current,  $i_1$ , in the secondary is established later when  $S_1$  opens to interrupt the primary current. The final, high-power stage is the opening of the switch  $S_2$  causing rapid transfer of the higher current into the load represented by the resistor  $R_L$ .

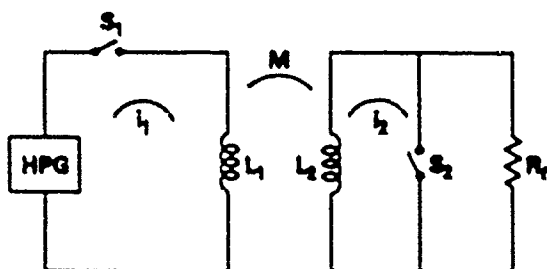


Fig. 1. Circuit for transformer and opening switches with primary energy storage.

If the primary is supplied with a peak current  $i_0$ , the stored energy is  $W_0 = (1/2) L_1 i_0^2$ . The secondary winding need not have a long time constant and secondary currents induced during energizing of the primary will quickly decay to zero. Or, if it is desirable to completely eliminate these precursor currents from the switch  $S_2$ , an additional series switch (not shown in the figure) can be incorporated into the circuit between  $L_2$  and  $S_2$ .

At the start of the second stage both  $S_1$  and  $S_2$  are closed. The primary and secondary currents have values of  $i_1 = i_0$  and  $i_2 = 0$ . During the interruption of primary current by  $S_1$  the rate of change of secondary flux is

$$M (di_1/dt) + L_2 (di_2/dt) = 0 \quad (1)$$

where  $M$  is the mutual inductance between the two parts of the transformer and  $L_2$  is the self-inductance of the secondary circuit, including the conductors composing  $S_2$ . The sign convention for current flow is chosen so that positive currents in both primary and secondary produce magnetic

flux in the same direction. The constant flux approximation of Eq. (1) is valid as long as the time constant of the secondary circuit is much greater than the interlude of current change. Integration of Eq. (1) shows that when primary current decays from  $i_0$  to 0 the secondary current increases from 0 to a value  $i_2 = (M/L_2) i_0$ , independent of the size and shape of the voltage pulse from the primary switching.

Now with  $i_1 = 0$ , the remaining stored energy is

$$W_2 = (1/2) L_2 i_2^2 = k^2 W_0 \quad (2)$$

where  $k^2 = M^2/L_1 L_2$ . If  $S_1$  remains open when  $S_2$  opens, this energy will be delivered to the load,  $R_L$ . In this case the primary voltage will be greater than the output pulse by the factor  $M/L_2$ .

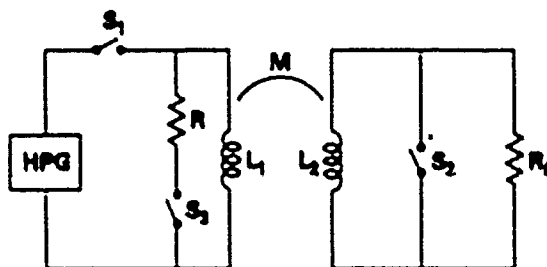


Fig. 2. Crowbar added to circuit of Fig. 1.  $S_3$  Closes before  $S_2$  Opens.

The appearance of high-voltage across the primary can be eliminated by a crowbar, shown as switch  $S_3$  in Figure 2, prior to opening  $S_2$ . If  $R=0$  upon opening of  $S_2$  primary flux does not change:

$$L_1 (di_1/dt) + M (di_2/dt) = 0 \quad (3)$$

The voltage across the load  $R_L$  and switch  $S_2$  corresponding to a decrease of secondary flux is

$$\begin{aligned} V_2 &= -M (di_1/dt) - L_2 (di_2/dt) \\ &= -(1-k^2) L_2 (di_2/dt) \end{aligned} \quad (4)$$

and the energy transferred into  $R_L$  is

$$W_2 = \int V_2 i_2 dt = (1-k^2) W_2 = (1-k^2) k^2 W_0 \quad (5)$$

The energy transfer efficiency in this latter case has a maximum of 25% when  $k^2 = .5$ .

The energy transfer efficiency has been investigated for cases intermediate between those for open-circuit and crowbarred primary by analysis of a



model for the circuit of Figure 2. The model assumes that  $S_2$  is a perfect switch opening instantaneously with no initial primary current and that  $R_2$  and  $R_1$  are constant. Primary and secondary currents were obtained by a straightforward transient calculation. From them the primary voltage

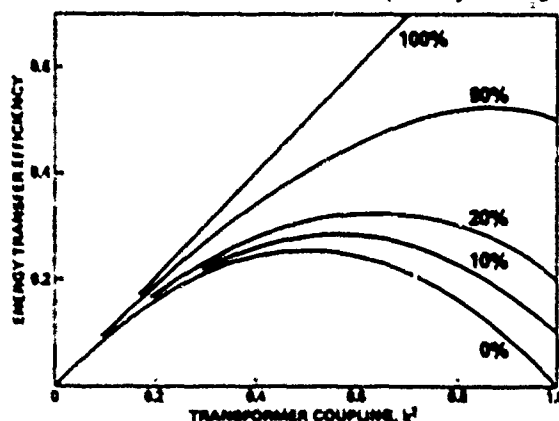


Fig. 3. Energy efficiency against  $k^2$  with resistive crowbar. Curve parameter is peak primary voltage as percent of open-circuit value.

energy dissipated in  $R_2$  were computed as functions of  $R$  and  $k^2$ . The results are shown in Figure 3 where energy transfer efficiency is shown as a function of  $k^2$  for several primary voltages. The two limiting cases are evident. With open-circuit the efficiency increases as  $k^2$  and with complete crowbar the lower curve is the efficiency predicted by Eq. (5) above.

### III. Store Separate from Transformer

Short connections are needed to the TRIDENT pulse generator with its high-voltage switch stages under water. An alternative to placing an existing massive storage coil under water is an entirely separate transformer with its primary current commutated from the storage coil. This concept is shown schematically in Figure 4. In that figure the HPG and storage coil with inductance  $L_0$  are shown to the left of the vertical dashed line. The components to the right of the line can be placed in a water tank to facilitate higher-voltage operation. The device represented by this circuit is considered to operate in three stages: slow energizing of the storage inductor, transferring current to the transformer and opening of the final

secondary switch.

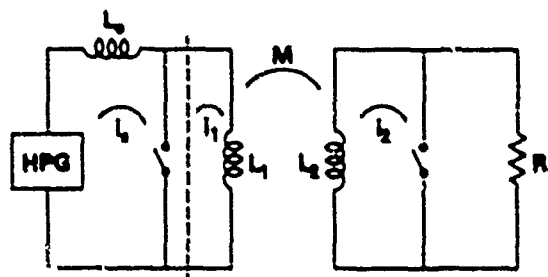


Fig. 4. Circuit for transformer and opening switches with separate energy storage.

Before the transfer stage, the storage inductor is energized by current  $i_0$  and energy  $W_0 = (1/2)L_0 i_0^2$  and both switches are closed. If the time constant of the short-circuited secondary is adequately long then Eq. (1) is applicable and secondary and primary currents are related by  $i_2 = -(M/L_2) i_1$ . The voltage appearing across the primary switch as it opens equals the rate of change of the increasing primary flux. It also equals the rate of change of the decreasing flux of the storage inductor.

$$\begin{aligned} -L_0 (di_0/dt) &= L_1 (di_1/dt) + M(di_2/dt) \\ &= (1-k^2) L_1 di_1/dt \end{aligned}$$

The current through the primary switch ultimately vanishes, after which  $i_1 = i_2$ . Integration of the above equation as primary current rises from 0 to a final value,  $i_1$ , and the storage current drops from  $i_0$  to  $i_1$  results in

$$i_1 = \frac{i_0}{1 + (1-k^2)L_1/L_0} \quad (6)$$

To avoid unduly high voltages, the primary should be crowbarred prior to opening of the secondary switch. In this case, it was determined earlier that the load voltage is given by Eq. (4). The load power is the product of this voltage and secondary current. By time integrating the power and substituting the relations determined in this section, the energy delivered to the load can be expressed as

$$W_L = \frac{k^2 (1-k^2) L_1/L_0}{(1 + (1-k^2) L_1/L_0)^2} W_0 \quad (7)$$

This relation is shown graphically in Fig. 5.

Each curve there represents the efficiency as a function of  $k^2$  for some fixed value of the parameter  $L_1/L_0$ . The upper envelope for this series of curves is the line  $k^2/4$ , corresponding to the case  $L_0 = (1-k^2)L_1$ . A maximum efficiency of 25% is approached as  $k^2$  approaches unity and  $L_1$  becomes infinite.

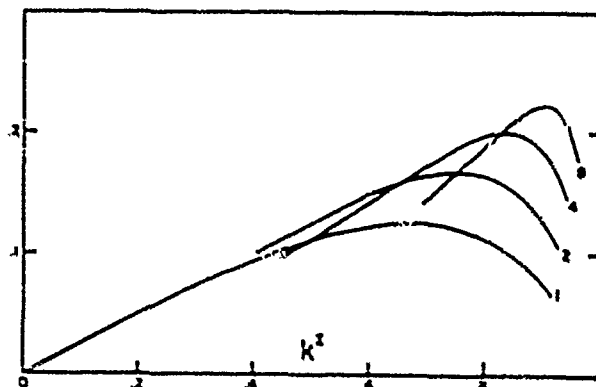


Fig. 5. Energy efficiency against  $k^2$  obtained with circuit of Fig. 4. Curve parameter is  $L_1/L_0$ .

#### IV. HPG-Transformer for TRIDENT

The NRL HPG energizes an existing air-core inductor,  $L_0 = 1.46$  mH, which will be coupled by separate transformer to the 1-mH inductance of the water-insulated TRIDENT inductive pulse generator. A double solenoid design for 20% efficiency with  $L_1/L_0 = 4$  and  $k^2 = 5/6$  is illustrated here. Since the primary time constant need not be large, the primary is wound with RG-220/U cable core (2.3 cm diameter). The impulse dielectric strength of this cable is about 450 kV so additional polyethylene must be added to allow a primary-to-secondary voltage approaching a megavolt. The need to simplify connections to the high-voltage pulse former stages dictates that the secondary coil be outside the primary. An iterative procedure of self and mutual inductance calculations determines the 2.2-m diameter and 1.6-m length resulting in  $L_1 = 5.84$  mH,  $M = 323$   $\mu$ H,  $L_2 = 10.32$   $\mu$ H and  $k^2 = .828$ . The relation  $i_2 = -(M/L_2) i_1$  implies that net radial forces on primary and secondary are equal and opposite. The primary can be wound

on a core for compressive strength. Relatively thin sheet conductors with strong insulating clamps at the output connections will withstand the strain resulting from impulse momentum given to the secondary.

#### References

1. Yu, A. Kotov et al, "Nanosecond Pulse Generator with Inductive Storage", Proc. IEEE International Pulsed Power Conference, IEEE Pub. No. 76CH1147-8 Region 3, paper IA-1, 1976.
2. Conte, D. et al, "Two Stage Opening Switch Techniques for Generation of High Inductive Voltage" Proc. 7th Symp. Engineering Problems of Fusion Research, IEEE Pub. No. 77CH1267-4-NPS, pp. 1066-70, 1977.
3. Conte, D. et al, "TRIDENT- A Megavolt Pulse Generator Using Inductive Energy Storage", Proc. of this Conference.
4. R. D. Ford and I.M. Vitkovitsky, "Explosively Actuated 100 kA Opening Switch for High Voltage Applications", NRL Memo Report 3561, Naval Research Laboratory, 1977.
5. A. E. Robson et al, "An Inductive Energy Storage System Based on a Self-Excited Monopolar Generator", Proc. 6th Symp. Engineering Problems of Fusion Research, IEEE Pub. No. 75CH1097-5-NPS, pp. 298-302, 1975.
6. R. C. Walker and M. C. Early, "Half-Megampere Magnetic-Energy-Storage Pulsar", Rev. Sci. Instr., Vol. 29, pp. 1020-1022, 1958.

Work supported by the Defense Nuclear Agency

## Design of Pulse Transformers for PFL Charging\*

G. J. Rohwein

Sandia Laboratories, Albuquerque, New Mexico 87185

Abstract

Air core pulse transformers powered by low voltage capacitor banks can be simple efficient systems for charging high-voltage (0.5 to 3 MV), pulse forming transmission lines (PFL) such as those used in electron and ion beam accelerators. In these applications pulse transformers must have the combined capability of high voltage endurance and high energy transfer efficiency, particularly in repetitive pulse systems where these features are of primary importance. The design of shielded, high-voltage, spiral, strip transformers which fulfill these requirements is described in this paper. Transformers of this type have been tested in three systems which operate with greater than 90 percent transfer efficiency and have not failed in over  $10^6$  shots.

Introduction

High voltage pulse transformer charging systems typically consist of a low voltage capacitor bank coupled to a high voltage PFL through a voltage step up transformer as illustrated in Fig. 1. These systems have the advantage of not requiring an oil tank to insulate the primary storage capacitors and are generally more compact than Marx generators. With transformer systems, however, it can be difficult to achieve both high voltage endurance and high energy transfer efficiency. The reason for this is that operation at high voltages ( $> 500$  kV) necessarily requires that voltage grading devices be placed in high electric field regions where the magnetic fields are also high. Consequently, the magnetic fields link the voltage grading structures and often induce eddy current loops with opposing magnetic fields which partially cancel the fields in the main windings. This action produces a partial internal shorting of the transformer and significantly reduces the energy transfer efficiency of the system.

To avoid this shorting effect it is necessary to design voltage grading devices such that the magnetic field can diffuse through the assembly without inducing eddy currents. A grading structure that satisfies these requirements has been developed for spiral strip transformers which

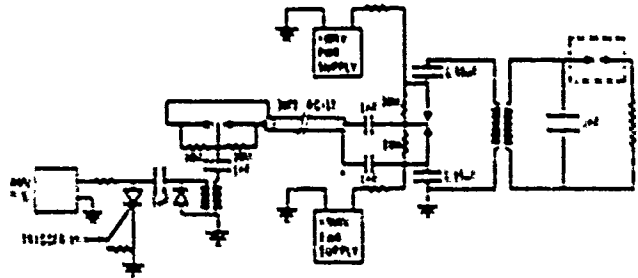


Fig. 1. Schematic of typical transformer charging circuit.

require electric field shaping across the margins of the secondary winding. It was found that a concentric ring cage, when properly assembled, was transparent to the magnetic field but maintained the proper electric field distribution in the margins. Figure 2 illustrates a typical ring cage assembly.

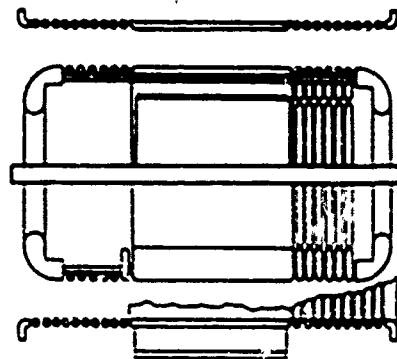


Fig. 2. Concentric ring cage assembly.

Discussion

Spiral strip transformers are in general better suited to PFL charging applications than their helical wound counterparts because they have a higher power handling capacity and because they are less vulnerable to interturn breakdown from nanosecond transients fed back into the transformer secondary by the PFL discharges. The higher endurance of spiral strip windings to transient voltage breakdown is due to a more optimum capacitance distribution through the high voltage winding.

\*This work was supported by the U.S. Department of Energy, under Contract DE-AC04-76-DPO0789.

However, a simple spiral strip transformer, illustrated in Fig. 3, has the inherent weakness of arcing from the edges of the secondary winding strip from highly enhanced electric fields along the edges. Such breakdowns usually originate at the edge of one of the final secondary turns, flash across the margin and close the arc path to the primary or one of the lower voltage turns. The ensuing discharge typically ruptures the insulation sheets and leaves a heavy carbon deposit along the path of the arc.

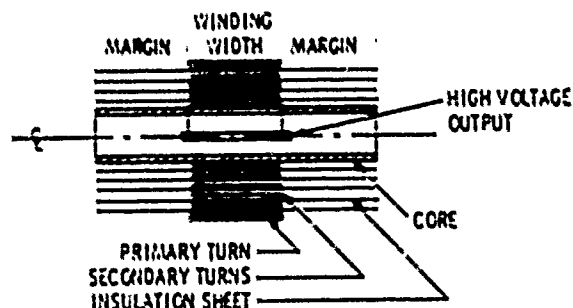


Fig. 3. Simple spiral strip transformer.

The high field enhancement along the edges of the winding is associated with the equipotential lines which emerge from between the turns and bend sharply around the edges toward the lower potential primary turn. The field enhancement in the edge regions limits the operation of a bare spiral strip to 300 to 400 kV even with the best insulating films and oils.

The edge breakdown problem can be eliminated by adding a coaxial shield across the margins of the secondary winding. The concentric shield constrains the electric field to a coaxial distribution across the margins which is nearly parallel to the uniform distribution through the thickness of the winding. Consequently, the field enhancement is greatly reduced and there is virtually no lateral field component to drive an arc across the margin.

The effectiveness of this shielding technique was demonstrated in an early transformer design shown in Fig. 4 which was tested to 1.25 MW without failure. The transformer had a single turn primary and a 1 inch thick, 30-turn, secondary winding. The shields were longitudinally slotted cylinders placed over the low voltage exterior and along the core. While this experiment clearly demonstrated that concentric shielding prevented edge breakdown, it was found that induced eddy currents in the shields as illustrated in Fig. 5 had a detrimental effect on the magnetic coupling. The open circuit gain which should have been near 30 was actually 13 and the energy transfer efficiency with a resistive load was approximately 25 percent.

#### Internal Shorting Experiments

The problem of internal transformer shorting was studied in two types of tests, inductance bridge measurements of a simulated primary turn with an

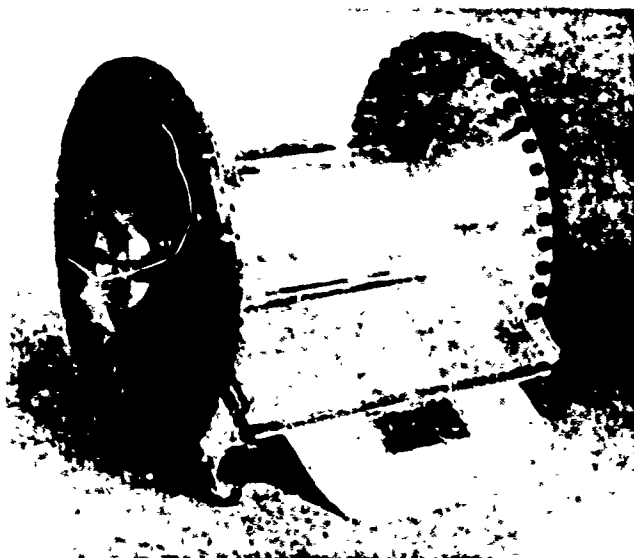


Fig. 4. Transformer with continuous concentric shields.

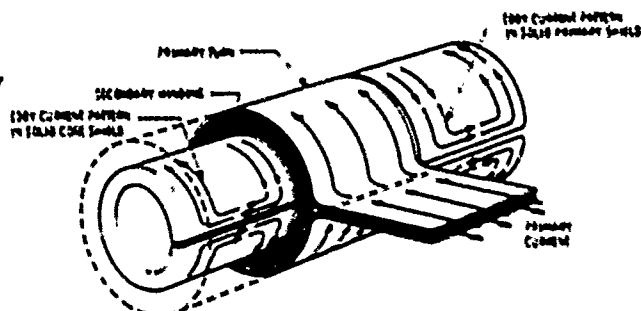


Fig. 5. Eddy currents in continuous cylindrical shields.

adjacent shield section and pulse discharge tests on a primary turn with various core configurations in the center. In both cases, shorting effects were observed as a decrease in circuit inductance from the unloaded primary turn inductance.

Figure 6 is a plot of inductance measurements on a 10 inch diameter, 6 inch wide primary turn with a 6 inch wide sleeve placed at different axial distances from one edge of the primary. The sleeve was intended to simulate a shield or structural component placed in some proximity to the magnetic field of the primary. In one case the sleeve was longitudinally slotted and in the other case it was continuous and acted as a shorted turn. The eddy current shorting effect for the slotted and shorted sleeve measurements was small but measurable as far as 4 inches away from the primary turn. With the axial spacing less than one inch, the effect was quite pronounced in both cases. With a one-half inch spacing, for example, the shorted sleeve produced a 13 percent change in the primary inductance and the open turn produced a 7.3 percent change.

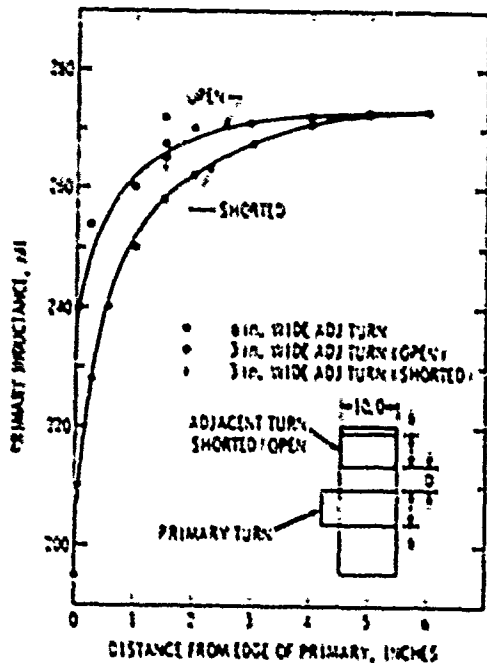


Fig. 6. Primary inductance variation with an adjacent shorted and open turn.

In the pulse discharge tests a 14.3  $\mu\text{F}$  capacitor was switched through a 4 inch diameter by 4 inch wide single turn primary coil. Circuit inductance was determined from the ringing frequency of the discharge. The unloaded inductance of the circuit (no core in the primary coil) was 98 nH. A slotted core tube of the same axial length as the primary produced no change in inductance but as the length of the slotted tube was increased to 8 inch, 12 inch and 14 inch the circuit inductance fell to 76 nH, 65 nH and 53 nH, respectively. This result indicated a shorting effect strongly dependent on shield length. Other shield configurations including screens, foils, longitudinal rods, etc. produced similar shorting effects. Only two types of shields showed virtually no shorting. One was a slotted cylinder of resistive film with a surface resistance of approximately 1000 ohms per square. The other was an array of rings interspaced approximately one eighth inch and longitudinally aligned with the axis of the primary turn. The rings were made with a gap in the hoop direction to prevent circumferential current flow and were connected together electrically along a single line opposite the line of gaps such that there were no closed loops that could conduct current in the assembly which linked the magnetic field. Pulse discharge tests on the resistive film and ring shield models showed a maximum of 3 percent inductance change with and without the shield assemblies in place.

Following these tests two prototype transformers were constructed, one with resistive film shields and one with a ring type core shield in combination with a continuous external shield which also served

as the primary turn. In testing the resistive film shielded transformer there were no measurable effects of internal shorting but the resistive film consistently broke down along the surface at voltages over 500 kV. Efforts to improve the film quality were unsuccessful. The ring core model with the continuous case was incorporated into an electrostatic beam generator (Fig. 7) and tested to 600 kV. In this application the transformer proved to have good high voltage endurance but with an energy transfer efficiency of 32 percent, it was still affected by eddy currents in the external shield. A third transformer (Fig. 8) was, therefore, constructed with ring shields on both the core and case. This transformer showed no measurable effects of internal shorting and was equal to the earlier model in high voltage endurance.

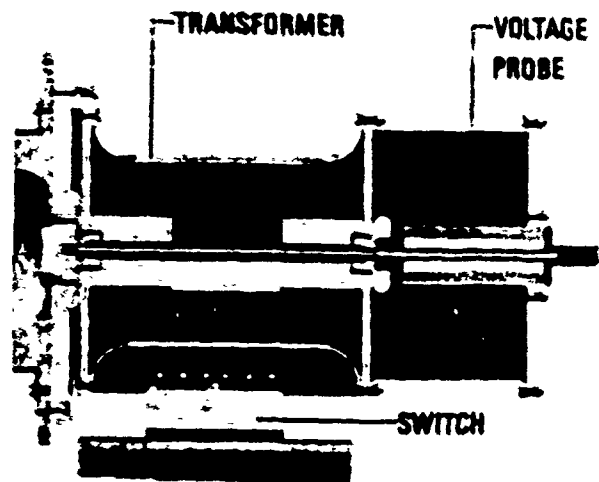


Fig. 7. Ring and cylinder shielded transformer.



Fig. 8. Concentric ring shielded transformer.

### Operational Results

After initial testing, the concentric ring shielded transformer was incorporated into a repetitive impulse test facility and used for testing dielectric solids, liquids and composites. In this application the transformer has been operated for greater than  $10^4$  shots in a voltage range between 300 kV and 1.5 MV at pulse rates from 1 to 100 pps. No winding failures or insulation flashovers have occurred throughout this service.

Two other ring shielded transformers have been built and operated in high voltage PFL charging systems. The essential features of both transformers are illustrated in Fig. 9. One is used in a 100 pps, 100 J electron beam generator for charging a 1.2 nF PFL to 700 kV. It has operated for more than  $2 \times 10^4$  shots without failure. The second is incorporated in a 10 pps, 5 kJ high voltage pulser and charges a 4 nF water capacitor to 1.5 MV (Fig. 9). Prior to the repetitive pulse application, the transformer was successfully tested in a single shot mode to 3 MV.<sup>6</sup> Since the second repetitive pulse system has only recently been placed in service long term endurance data are not yet available for this transformer.

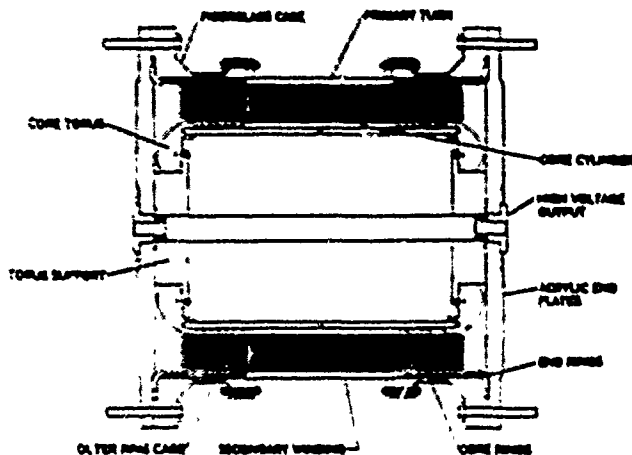


Fig. 9. PFL charging transformer.

All three ring shielded transformers have been operated in both single swing and dual resonance charging modes. With coupling coefficients ranging from 0.83 to 0.85, the energy transfer efficiency is typically around 60 percent in the single swing charge mode. In most cases, however, the transformers are operated in a dual resonance charging mode which requires matching the frequencies of the primary and secondary sections of the circuit and reducing the effective coupling coefficient to 1.0. This is accomplished with a transformer having a coupling coefficient greater than 0.6 by adding an appropriate amount of external inductance to the primary and secondary sections of the

circuit.<sup>6</sup> With the circuit properly tuned, energy transfer efficiencies are typically greater than 90 percent. It should be noted that the effects of eddy current shorting can not be compensated for by any means of external circuit tuning. The ring shielded transformers produced transfer efficiencies ranging from 91 percent for the 3 MV model to 94 percent for the 700 kV repetitive pulse model. These losses were divided in the approximate proportion of one percent in the transformer and five to eight percent in the spark gap switches and capacitors.

### Conclusions

Achieving high energy transfer efficiency in combination with high voltage endurance in an air core pulse transformers involves careful attention to the design of voltage grading devices and structural elements to avoid internal shorting. Concentric ring shielding of spiral strip type transformers has proven to be an effective technique for satisfying both requirements simultaneously. This design method has been scaled successfully from a few hundred kilovolts to 3 MV. There are no apparent reasons why even higher voltage transformers utilizing this technique could not be built. For the present, however, transformers operating up to a few megavolts have many useful applications in repetitive pulse accelerator systems where long shot life and high energy transfer efficiency are essential.

### References

1. M. Cowan, G. J. Rohwein, E. C. Crane, E. L. Meau, J. A. Mogford, W. K. Tucker and D. L. Wessenberg, Int'l. Topical Conf. on Electron Beam Res. and Tech., SAND76-5122, Vol. 1 (1976).
2. G. J. Rohwein, IEEE Trans. Nucl. Sci., NS-22, No. 3, p.1013, June 1975.
3. Electron Beam Fusion Progress Report, SAND78-0080, p. 178 (April 1978).
4. Electron Beam Fusion Progress Report, SAND77-1414, p. 151-152 (October 1977).
5. G. J. Rohwein, M. T. Suttram and K. R. Prestwich, 2nd Int'l. Topical Conf. on High Power Electron and Ion Beam Res. and Tech., Vol. 2 (1977).
6. G. J. Rohwein, IEEE Trans. Nucl. Sci., NS-26, No. 3, June 1979.

## PULSE SHARPENING IN FERRITE TRANSMISSION LINES

Maurice Weiner

Electronics Technology and Devices Laboratory  
 USA Electronics R&D Command  
 Fort Monmouth, New Jersey 07703

Abstract

Pulse sharpening effects in ferrite transmission lines may be used to obtain nV pulses with ns risetime. The exact description of the sharpening effect requires complex shock wave analysis<sup>1</sup>. In this paper an approximate but useful physical model is discussed. The ferrite is treated as a lossy but linear transmission line from which equivalent design results are obtained. In many instances the nonlinear effects present are confined to a region which is small compared to the total transmission length, which makes the linear approximation more plausible. Preliminary experimental results, based on a 130 cm long line, are in accord with the predictions of the model.

complexity and bulk, as well as lowered circuit efficiency caused by the need for bias current. Nevertheless the ferrite pulse sharpener has potential in an area where there are few technological alternatives.

In recent years the bulk of the scientific literature on ferrite pulse sharpeners has appeared in the USSR. In particular, the work by Kataev<sup>2</sup> emphasized the shock wave aspects of the wave propagating in the ferrite. Exact analysis has indicated the formation of shock waves under a variety of conditions, and such waves are important in the interpretation of pulse sharpening effects.

In this report an elementary model for the pulse sharpening effect is presented, wherein the ferrite is treated as a lossy but linear transmission line. A simplifying feature is introduced with the idea of a spin saturation front, which travels along the length of the ferrite. The shock wave nature of the problem is pointed out, but emphasis is placed on simple and useful solutions which are possible without explicitly solving the shock wave problem.

Introduction

In recent years an increasing need has arisen for nV pulsed with ns risetimes. In the area of pulsed for mm wave tubes, for example, extremely narrow pulse widths (< 5 ns) are desired for improved resolution. At the same time pulse repetition rates as high as 20 kHz, with pulse voltage and current amplitudes up to 15 kV and 1000 A, respectively, are required. These simultaneous requirements place tremendous burdens on the switch, which is the key element in the design of such a pulser. Switches now available do not simultaneously satisfy the risetime, PRR, and power requirements. For example spark gaps satisfy the risetime and peak power requirements, but are unable to satisfy the PRR requirement.

A promising solution to the switch problem is the use of a slower risetime switch in combination with a ferrite pulse sharpener. The incorporation of a ferrite pulse sharpener into the discharge circuit has the advantage of simultaneously providing fast risetime, large PRR, and large peak power levels. There are disadvantages, however, and these are added circuit

Outline of Model

We consider a ferrite transmission line which is uniformly magnetized in the direction transverse to the direction of propagation (Fig. 1). A transmission line without ferrite, with impedance  $Z_0$ , is connected to the input terminals of the ferrite. A pulse with risetime  $T_R$  is incident upon the ferrite. The polarity of the magnetic field of the pulse is opposite to that of the magnetization. As a consequence the pulse will see a large RF impedance consisting of an inductance, as well as a resistive component caused by dissipation in the ferrite. For the most part the signal will be reflected, although a substantial percentage of the incident energy will propagate into the ferrite. The region close to the start of the ferrite line will not continually appear as a large impedance, however. Eventually this portion of the ferrite will suddenly reach saturation. When this happens the large impedance will suddenly decrease to the saturated impedance,

$Z_0$ , which by design is chosen equal to  $Z_0$ , the input impedance. As shown in Fig. 1, this process continues, so that a "spin saturation front" propagates along the length of the ferrite. The velocity of this front will increase as the pulse amplitude is increased. The ferrite line is designed such that, when the front reaches the end of the ferrite line (i.e., the entire length of the ferrite is completely magnetized in the opposite direction) the pulse is near or at its plateau value. This will occur at  $t = T_0$  ignoring transit time effects, i.e., assuming the velocity in the saturated region is much larger than the velocity of the spin saturation front.

The advance of the spin saturation front must be distinguished from the region of magnetic field propagating beyond the spin saturation front. Such field penetration arises from the inherent delay which exists between the onset of the magnetic field and the time needed for the spins to change direction. The field penetration is confined to a "propagation width." Fig. 2. In this region the magnetization changes continuously between the two oppositely saturated states. At the spin saturation front the magnetization is aligned with the incident magnetic field, and the changeover to the lower saturation impedance is imminent. At the far end of the propagation width the field signal  $h_z$  has just arrived and the magnetization is still saturated and opposite to that of the field. The field is also shown as terminating abruptly at the end of the propagation width. This simplifies the model but in fact dispersion effects, which result from the presence of loss in the transmission line, will tend to cause the field to decrease more gradually.

As implied in Fig. 2 the field propagating beyond the spin reversal front will be dampened, resulting from the dissipation which accompanies the rotation of the spins. The propagation width, as well as the amount of damping, will vary, depending on the ferrite loading and numerous other parameters. In most cases the field penetration will be small, on the order of a few centimeters, compared to the total length of the ferrite line which is typically one meter long. The relatively small region to which the propagation is confined makes plausible certain simplifications in the description of pulse sharpening, without resorting to detailed shock wave analysis.

#### Analysis of Model

For concreteness we consider a coaxial transmission line in which the ferrite fills the entire space between inner and outer conductors. The analysis may be easily extended to the case where the line is partially filled with ferrite, in which we have concentric dielectric and ferrite sleeves. It is also assumed the ferrite transmission line is connected to a load  $Z_L$  while the input is connected to another line of impedance  $Z_0$  (Fig. 3).

In the saturated region of the line the ferrite has an inductance per unit length ( $L_f$ ) and a capacitance per unit length ( $C_f$ ).  $L_f$ ,  $C_f$ , and  $Z_0$  are given by standard expressions for the coaxial line.

When the ferrite magnetization is not aligned with the incident magnetic field, the ferrite will appear as a large impedance relative to the saturated impedance. When this happens most of the input energy will be reflected although a significant percentage of the energy will be transmitted into the ferrite. In order to ascertain the degree of reflection, one must calculate the electrical parameters associated with the ferrite line,  $L_f$ ,  $C_f$ ,  $R_f$  (Fig. 3).

The transmission line parameters are a function of the physical mechanisms by which the magnetization aligns itself with the magnetic field,  $h_z$ . The mechanism which appears to prevail is the Gilbert form of the Landau Lifschitz equation, from which the time dependence of the magnetization is given by (gaussian units)

$$\frac{dM_z}{dt} = \frac{\gamma M_s h_z}{S} \left[ 1 - \frac{M_z^2}{M_s^2} \right] \quad (1)$$

where  $M_z$  is the magnetization along the applied field,  $M_s$  is the saturation magnetization and  $S$  is the switching constant. Using the approximation given by Gilbert [6] the switching time  $T_0$ , for  $M_z$  to go from  $-M_s$  to  $+M_s$ , is given by

$$T_0 = \frac{S}{h_z} \quad (2)$$

Thus  $T_0$  is inversely proportional to the magnetic field. Using Eqs. (1), (2), and the circuit of Fig. 3, calculation of the network parameters  $L_f$ ,  $C_f$ , gives

$$L_f = \frac{32 \pi^2 (d-a) M_s}{L_z h_z} \times 10^{-7} \frac{h}{\Omega} \quad (3)$$

$$C_f = \frac{32 \pi^2 (d^2 - a^2) M_s}{L_z^2 S} \times 10^{-7} \frac{\Omega}{\Omega} \quad (4)$$

where  $d$  and  $a$  are the outer and inner radii of the ferrite, respectively, and  $l_m$  is the mean magnetic length. In all equations the magnetization, magnetic field, and  $S$  are given in gaussian units. All other quantities are in MKS.

In calculating  $L_f$  and  $R_f$ , using Eq. (1), we have assumed the time averaged quantity for  $M_z$ , i.e.,  $M_z = 0$ . In a sense this amounts to treating the entire propagation width as the load seen by the incident wave, since  $M_z$  varies from  $+M_s$  to  $-M_s$  in the region. Intuitively this appears to be a reasonable assumption since this length is usually small compared to the total ferrite length and is also small, or at least comparable, to the wavelengths corresponding to the frequencies present



in the incident wave.

The final network parameter needed to describe the high impedance ferrite is the capacitance per unit length  $C_p$ . No calculation is required here however since we have assumed that the magnetic properties are uncoupled from the dielectric properties. Thus  $C_p$  will be unchanged from the saturated capacitance  $C_s$ .

Once the network components  $L_p$ ,  $R_p$ , and  $C_p$  are known, one may calculate various transmission line properties such as the impedance  $Z_p$ , the reflection coefficient  $\Gamma$ , the propagation constant  $\gamma_p$ , and other quantities, using steady state transmission line expressions with frequency  $\omega$ . The phase velocity  $v_p$  is obtained from  $\omega/\beta$ , where  $\beta$  is the imaginary part of  $\gamma_p$ . Another important velocity is that of the spin saturation front,  $v_s$ , which is obtained by relating the energy delivered by the pulse to the energy needed to redirect the spins contained in the propagation width,  $L_p$ . The propagation width is defined by  $L_p = v_p T_0$ . A second important length is  $L_A = 1/\alpha$ , where  $\alpha$  is the real part of  $\gamma_p$ . When  $L_A < L_p$  substantial attenuation occurs. When  $L_A > L_p$  the loss is small. When the pulse is introduced at the start of the line the propagation width will be relatively large since the field in the ferrite is small. As the pulse increases in amplitude  $v_s$  will increase and the spin saturation front will catch up with the propagation front. The residual field penetration at the end of the line will have a time duration of  $T_0$ , given by Eq. (2), which represents the risetime limitation.

#### Model Approximations

In order to obtain mathematically tractable results several approximations have been made. The more important of these will be discussed briefly.

An important approximation is the neglect of shock waves. In the propagation region it was shown that the permeability is inversely proportional to the signal level. The lower permeability region near the spin saturation front thus supports a faster wave compared to the higher permeability near the end of the propagation region. As a result the faster waves will catch up with the slower waves, compressing the propagation region. A knowledge of such waves may be derived from the nonlinear differential equations which apply.

A second approximation is the application of the steady state solution to deal with a problem which is transient in nature, i.e., we are dealing with a pulse rather than the case of a single frequency. Further, the line is lossy and thus dispersion effects will occur. Laplacian techniques may be applied to solve such a problem, although the details are cumbersome. Although the transient calculation is not done here, one can surmise the dispersion effects at least by examining various frequencies,  $\omega$ , such that  $\omega \lesssim \omega_0$  where  $\omega_0 = 2\pi/T_0$ . Since we are interested in the fast risetime response, our interest will be centered on the higher frequencies since these

frequencies are responsible for the fast risetime. In addition one must take into account pulse broadening which results from motion of spin saturation front relative to the propagation in the saturated region.

Another approximation has to do with the time dependence of the magnetization expressed in Eq. (1). Time average values of  $L_p$  have been utilized, and their effect on the solution should be examined. Also the time change in magnetization slows down considerably near extremes  $M_z = \pm M_s$ . This will impact on the sharpness of the spin saturation front, resulting in a front which has a profile rather than one in which the change is abrupt.

Another important approximation is the neglect of magnetic field accumulation in the propagation region, arising from earlier portions of the pulse risetime. In this analysis it is assumed  $h_z$  is solely a function of the field incident on the saturation front and prior fields are ignored. Taking field accumulation into account affects the calculation of  $T_0$  as well as the network parameters  $L_p$ ,  $R_p$ .

#### Computational Results

Computation of several important quantities, based on the model, is given in Fig. 4. In order to obtain numerical results it is assumed the frequency,  $\omega$ , is given by  $2\pi/T_0$  where  $T_0$  is the delay time, i.e., the time needed for the spin saturation front to transverse the ferrite. It is assumed the pulse reaches its plateau value the moment it emerges from the ferrite. If transit time effects are ignored  $T_0 = T_r$ .

Fig. 4 shows how  $v_s$ ,  $v_p$ , and  $T_0$  change during the pulse risetime incident on the spin saturation front. It is assumed voltage incident on the front,  $V$ , has a ramp like dependence, reaching a maximum of  $6 \times 10^3$  volts at  $t = 70$  ns. As anticipated both  $v_s$  and  $v_p$  increase with signal level, although  $v_p$  levels off because of the resistive losses.  $T_0$  decreases rapidly with voltage. This is expected since the signal strength becomes large in the propagation width, and this in turn reduces  $T_0$ . The value of  $T_0$  at  $t = 70$  ns is  $\approx 2.0$  ns, which represents the residual risetime emerging from the ferrite line.  $L_p$  is approximately 5 cm as it emerges from the ferrite.

The length of the ferrite line  $L_f$  is found by integrating  $v_s$ . With the present model  $L_f$  should be approximately equal to the integral of  $v_s$ , denoted by  $L_p$ . This ignores corrections arising from the propagation width, which effectively increases  $L_p$ . In the case of Fig. 4, for example  $L_f$  is 101 cm while  $L_p$  is 90 cm.

#### Experimental Results

A 130 cm long coaxial ferrite line was constructed and tested. The magnetic material is magnesium ferrite, supplied by Trans-Tech, type TTI-3000. The saturation magnetization ( $4\pi M_s$ ) is 3000 gauss, with a remanent induction of 2000 gauss and a coercive force of 0.85 Oe. The ferrite is composed of sleeves each 1.25 cm long, with an OD of 0.5 cm and an ID of 0.25 cm.

The basic circuit for testing the pulse sharpener is shown in Fig. 5. The input switch is a thyatron, JAN 7621, which operates up to 5 kV peak. The cable PFN has a 50  $\Omega$  impedance, with the pulsewidth varying from 50 ns to 300 ns. The bias circuit provides current to "set" the ferrite. RF chokes are included to prevent pulse interaction between the bias circuit and the ferrite line. Current in a low inductance load resistor is measured with a Tektronix CT-1 transformer.

When the ferrite was biased in its "set" state very little difference was noticed in the output when the magnetic field exceeded the coercive force of 0.35 Oe. However, when the field was reduced below this value the flux reversal quickly diminished and the output changed accordingly. Pulse sharpening could be obtained with bias currents as low as 0.4 A.

Fig. 6 shows the pulse waveforms with and without bias for a 6 kV charging voltage. The effective magnetization was reduced by lowering the bias current to 0.4 A. The sharpened risetime after correction for instrumentation risetime of 2.5 ns is about 6 ns. The total delay time  $T_D$  is approximately 70 ns which includes 35 ns of transit time delay. Experimental results may be compared with the computed results in Fig. 4, assuming the parameter values listed. The model predicts a length of 101 cm and a residual risetime of 2 ns. The discrepancy in risetime is accounted for by dispersion and field accumulation effects, which have been ignored.

The net pulse sharpening can only be determined by comparison of the sharpened pulse with the incident pulse, delivered to 50  $\Omega$ , with the ferrite line disconnected. The risetime thus measured was 15 ns, indicating a net improvement of better than 2:1.

#### Conclusions

A model for the ferrite pulse sharpener based on a lossy but linear transmission line was formulated. Results derived from the model appear to be in reasonable accord with the experiments done on a 130 cm large ferrite line. Further refinements in the model and additional comparison with experimental results are planned.

#### References

1. I. G. Kataev, "Electromagnetic Shock Waves," Sovetskoye Radio Press, 1963.
2. Kikuchi, "On the Minimum of Magnetization Reversal Time," J. Appl. Phys., Vol. 27, pp. 1352-1357, November 1956.
3. Gyorgy, "Rotational Model of Flux Reversal in Square Loop Ferrites," J. Appl. Phys., Vol. 28, pp. 1011-1015, September 1957.
4. W. C. Johnson, "Transmission Lines and Networks," McGraw Hill, 1930.

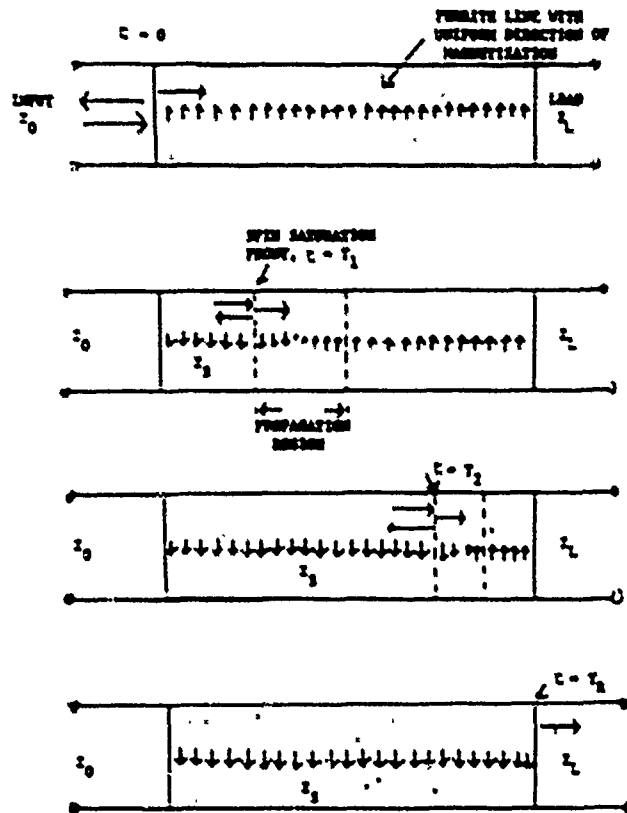


Fig. 1. Motion of Spin Saturation Front in Ferrite Transmission Line.

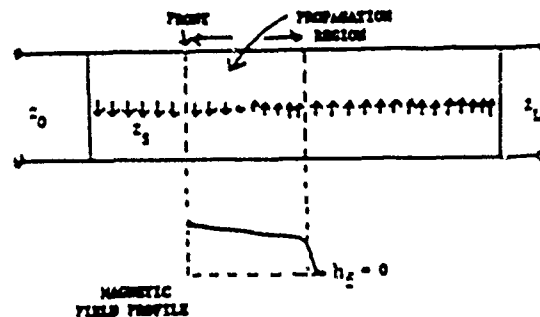


Fig. 2. Propagation Region in Ferrite Transmission Line.

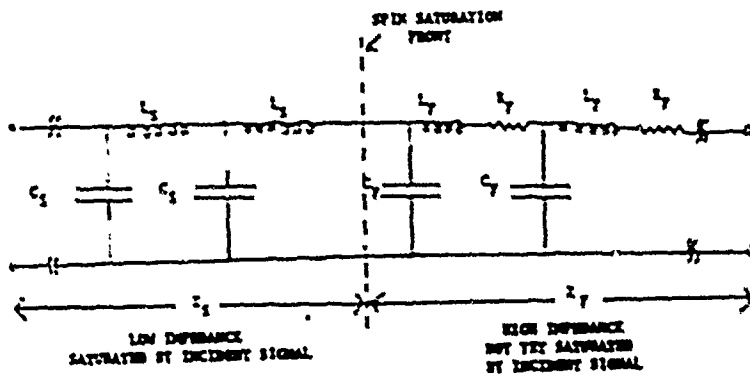


Fig. 3. Equivalent Circuit of Ferrite Transmission Line for both Saturated and Unsaturated Regions.

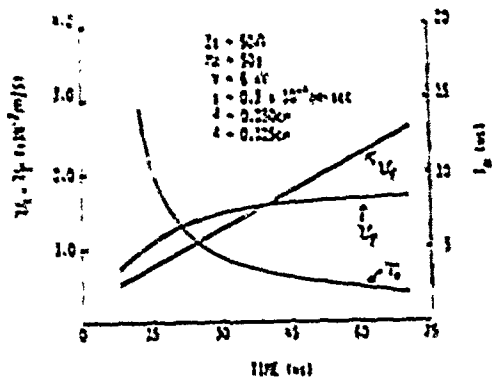


Fig. 4. Variation of Spin Saturation Front Velocity ( $v_s$ ), Phase Velocity ( $v_p$ ), and Switching Time ( $T_0$ ) as Function of Time for 70 ns Ramp Risettime.



Fig. 6. Pulse Waveforms at Output With and Without Magnetic Field Bias, Horizontal: 10 ns/cm Vertical: 1 kV/cm Voltage on 50  $\Omega$  PFN: 6 kV.

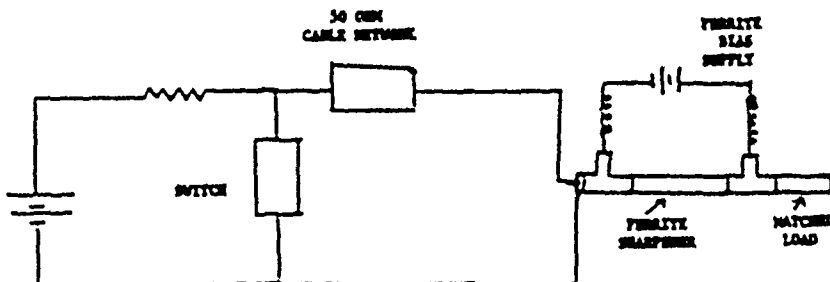


Fig. 5. Experimental Test Circuit for Ferrite Pulse Sharpener.

## HIGH POWER PULSE MODELING OF COAXIAL TRANSMISSION LINES

JAMES P. O'LOUGHLIN

AIR FORCE WEAPONS LABORATORY  
KIRTLAND AFB, NM 87117ABSTRACT

When coaxial cable is used for high voltage pulse transmission, a voltage transient appears on the outer sheath conductor. Although the magnitude of the transient is in the order of only a few per cent, this amounts to several kilovolts in many cases and must be carefully considered in terms of its effect on instrumentation, control and safety. To a first approximation, theoretically a coaxial cable should not develop any voltage on the outer sheath. A more refined analysis and model shows that the complete cancellation depends upon the self inductance of the sheath being exactly equal to the mutual inductance between the sheath and the center conductor. This condition is never exactly satisfied due to current distribution effects, even when the distribution is uniform and radially symmetric. The situation becomes worse when proximity effects are accounted for. The predicted sheath voltage agrees with experimental data within reasonable limits.

INTRODUCTION

The analysis of coaxial transmission lines is commonly based upon the incremental section model as shown in Fig 1. The self inductance of the center conductor is  $L_1$ , the outer sheath  $L_2$ , and the mutual is  $M_{12}$ . The lumped equivalent capacitance of the element is  $C$ . Also shown in Fig 1 is the equivalent model using uncoupled inductors with the corresponding relations between circuit values. Note that if  $L_2 = M_{12}$ , the effective inductance of the outer sheath is zero (short circuit) and all the loop inductance is associated with the inner conductor. In reality,  $L_2 \approx M_{12}$  to within a few percent, however, there is a multiplicative effect such that a given percentage unbalance between  $L_2$  and  $M_{12}$  leads to several times that percentage unbalance in the division of voltage between the inner conductor and sheath. This simple mechanism is the basis for explaining the existence of the voltage transient on the outer sheath. The equation relating the voltage on the sheath to the circuit values is plotted in Fig 2, and reads:

$$(1) V_2/V = K(1-a) / (1+K(1-2a))$$

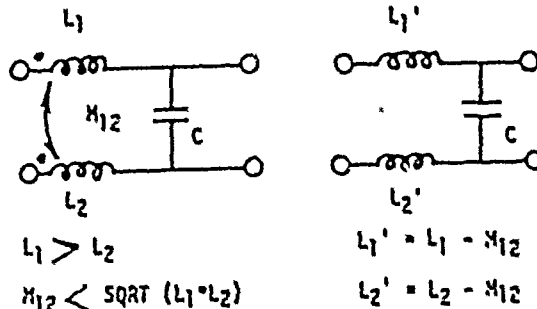
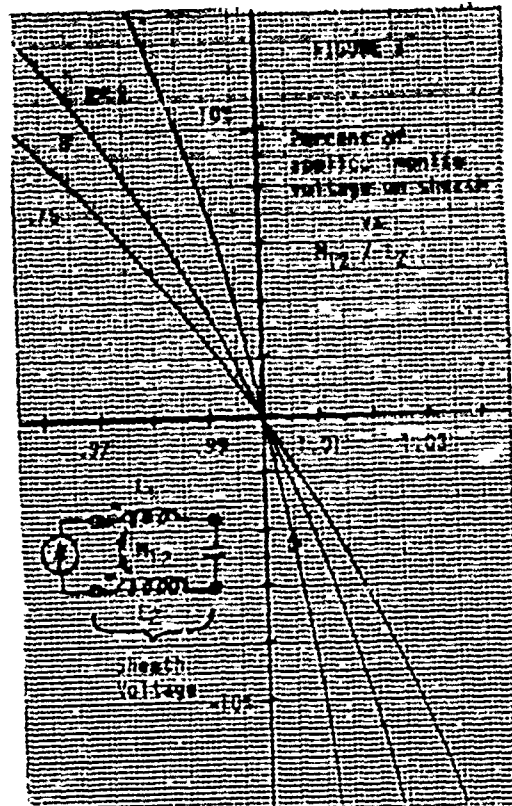


FIGURE 1  
MODEL OF INCREMENTAL SECTION  
OF TRANSMISSION LINE.



where:  $V_2$  = voltage on the sheath  
 $V_2$  = impressed voltage  
 $K = L_2/l_1$   
 $a = M_{12}^2/L_2$   
 $L_1$  = Inner conductor inductance  
 $L_2$  = Sheath inductance  
 $M_{12}$  = Mutual inductance

(Note that as  $a$  changes from  $a < 1$  to  $a > 1$ , the polarity on the sheath reverses.)

#### FACTORS AFFECTING MUTUAL INDUCTANCE

Two factors affecting mutual inductance are the distribution of flux within the finite thickness of the sheath current, and the current distribution in the cable as determined by the proximity effect of other current carrying conditions such as ground plane images, etc. Consider first the simple case illustrated in Fig 3., that of a coax cross-section with a uniform current distribution and thus a flux field which is perfectly concentric. By fundamental definition, mutual inductance is measured by the flux coupling the inner conductor due to a unit current in the outer conductor. Thus, the mutual is measured by all of the flux. Also by definition, the self inductance of the sheath is measured by the flux coupling the sheath current due to a unit sheath current. The sheath current is uniformly distributed over the thickness  $T$  and the flux varies linearly from zero at the inner surface to maximum at the outer surface; thus the flux internal to the sheath doesn't effectively couple all the sheath current, so  $L_2$  will be less than  $M_{12}$ . Modifying the inductance equation for cylindrical conductors given by Grover<sup>1</sup> to account for the uncoupled flux internal to the sheath one obtains the expression in equation (2) for the ratio  $M_{12}/L_2$ :

$$(2) M_{12}/L_2 = 1 + (1/2) \cdot \ln(1/(1-\delta)) / 2 \cdot \ln(8/R_2 - 1)$$

where:  $R_2$  = Mean radius of sheath (cm)  
 $\delta^2$  = Length (cm)  
 $T$  = Sheath thickness (cm)  
 $\delta = T/R_2$

Equation (2) is plotted in Fig 4.

Consider now the effect of a non-uniform current distribution, the radially symmetric flux of Fig 3 will no longer exist, in fact, the flux between the sheath and center conductor will no longer be zero. The simple evaluations of self and mutual inductance as above are no longer possible.

An evaluation of the proximity effect on mutual inductance for simple geometrical cases was done by computer using the model shown in Fig 5. The inner and outer conductors and their images were modeled using 100 independent current filaments, 50 for

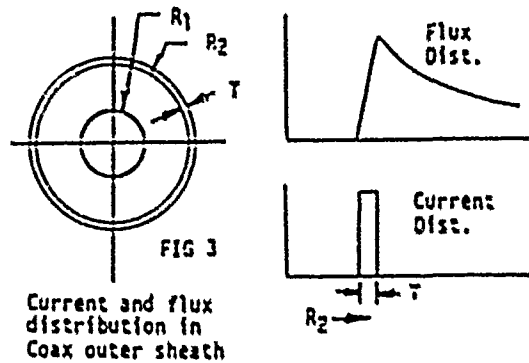


FIG 3  
Current and flux distribution in Coax outer sheath

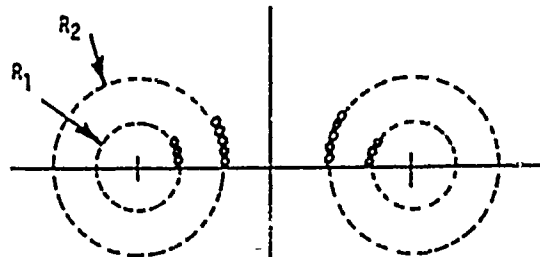
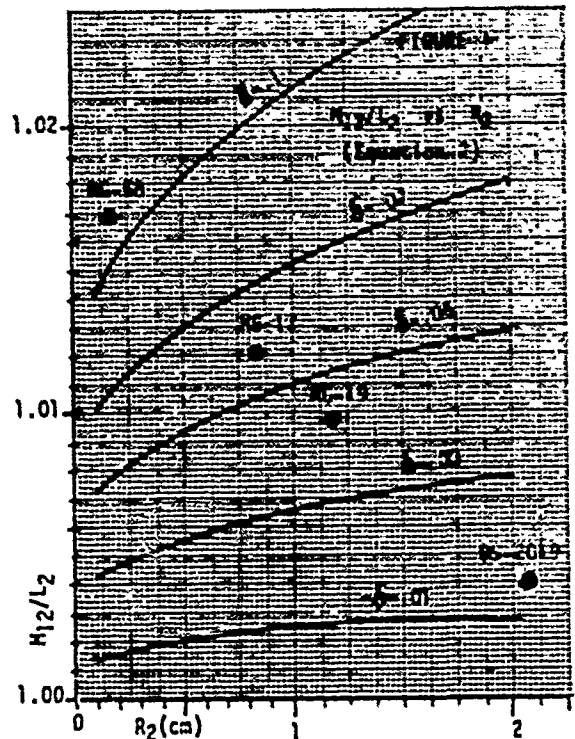


FIGURE 5  
Filamentary model of coax and ground plane image

each. By symmetry, the total number of filaments in the model is 400. Using expressions for the self and mutual inductances in terms of the geometry, a solution for the 100 independent currents was obtained using Creamers rule to solve the loop equations on a CYBER 176 computer. The ASPLIB library program DECCMP was used to evaluate the  $100 \times 100$  determinants. This model was used to evaluate only the proximity effect, thus in free space, i.e. no images. It was calibrated to give zero voltage on the sheath. This was accomplished by adjusting the diameter of the filaments to null the sheath voltage to less than one part in  $10^6$  per unit of impressed voltage. The diameter used to accomplish this was 1.07596 times the circumference of the conductor being modeled divided by 100.

The net proximity effect on  $M_{12}$  as a function of the distance of a RG-19 coax above a ground plane is shown in Fig 6. In Fig 7 are current distributions due to various proximity effects. The cases shown are for a RG-19 cable spaced 1.04 sheath radii from a ground plane. Case 1 is the distribution in the outer conductor with the coax center conductor used as a return in the normal manner. Case 2 is with the center conductor removed and an infinite ground plane carrying the return and Case 3 is with the center conductor removed and the image carrying the return (two wire open line). Notice the remarkable insensitivity to the proximity effect a coax has (1.5%) compared to the other cases. The effects of various geometrical distortions are shown in Fig 8. The initial geometry of the three cases shown is an RG-19 spaced 1.04 radii from ground. Case 1 is for the center conductor moved off center along the X axis by  $\pm .25$  sheath radii. Case 2 is

for the center conductor moved along the Y axis by  $\pm .25$  sheath radii. Case 3 is for an elliptical distortion of the sheath, elongated along the Y axis by 0 to .25 sheath radii.

Comparing the data of Figures 2, 6, and 8 it is obvious that the ratio of mutual to self inductance  $M_{12}/L_2$  is predominantly determined by the thickness of the outer sheath and the proximity and mechanical distortion effects can be neglected in most cases.

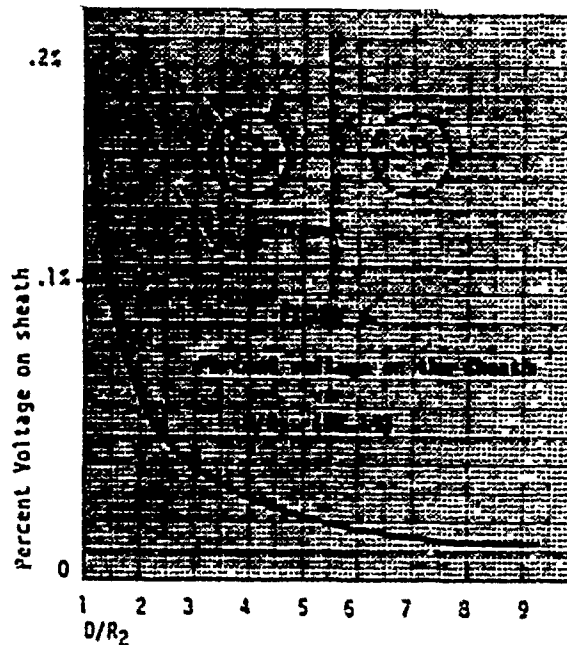


FIGURE 7

Current Distribution  
vs  
 $\theta$

CASE 1, Coax above ground plane

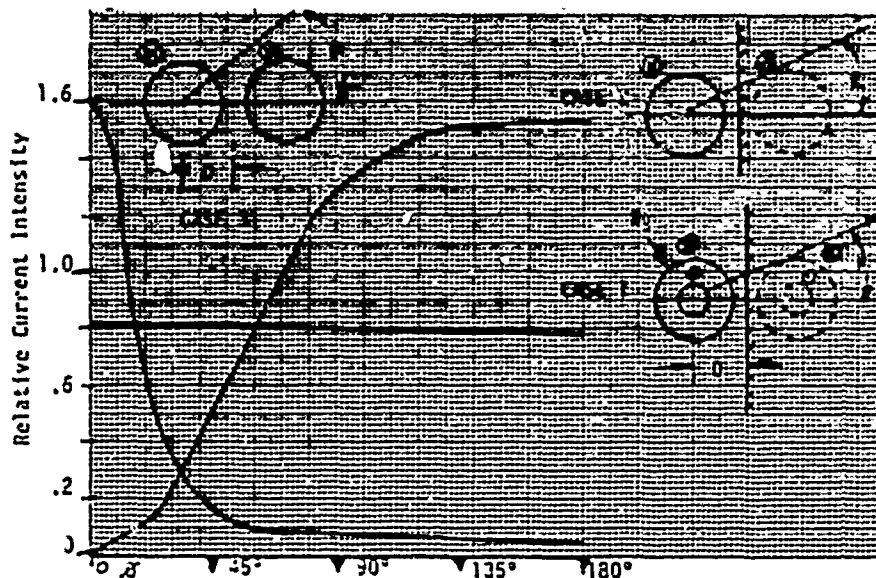
CASE 2, Round conductor above ground plane

CASE 3, Two wire pair

$$r_1 = .33 \text{ (cm)}$$

$$r_2 = 1.1933 \text{ (cm)}$$

$$D = 1.2432 \text{ (cm)}$$



### MODEL OF A REAL CIRCUIT

Shown in Fig. 9 is the circuit model of a pulse transmission coax including the ground plane. The cable is a Dielectric Sciences DS-2019, 61 meters long and modeled at an average of 15 cm above the ground plane. The distributed circuit of the cable and ground plane is modeled by 100 finite elements. The driving source is 330 KV with a one microsecond rise time and a 27.68 ohm source resistance. A FORTRAN computer code was used to solve the circuit by conventional loop current techniques. The result of the analysis giving the voltage from sheath to ground at the sending end is plotted in Fig. 10, also shown is the measured voltage. The cable was driven through a pulse transformer, CCG is the secondary to ground capacitance and RA is a 60 ohm resistor used to monitor the voltage via a current transformer.

### CONCLUSION

It is concluded that the transient voltage which develops on the sheath of a coaxial cable under pulse conditions may be explained, analyzed and reasonably well predicted based upon the difference between the mutual inductance and the sheath inductance of the cable.

### REFERENCES

1. John D. Ryder, Networks Lines and Fields, 2nd Ed, Chapt 6, Prentice Hall, 1955.
2. Frederick W. Grover, Inductance Calculations, Working Formulas and Tables, P 271, Dover, 1962.

### ACKNOWLEDGEMENTS

Appreciation is expressed for the assistance and cooperation in providing experimental data to J. J. Moriarty, P. A. Corbier, and Dr F. Donald Angelo of Raytheon Missile Systems Division.

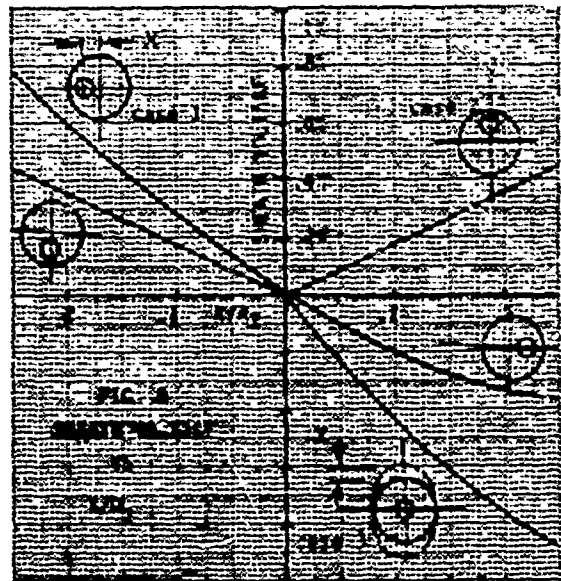
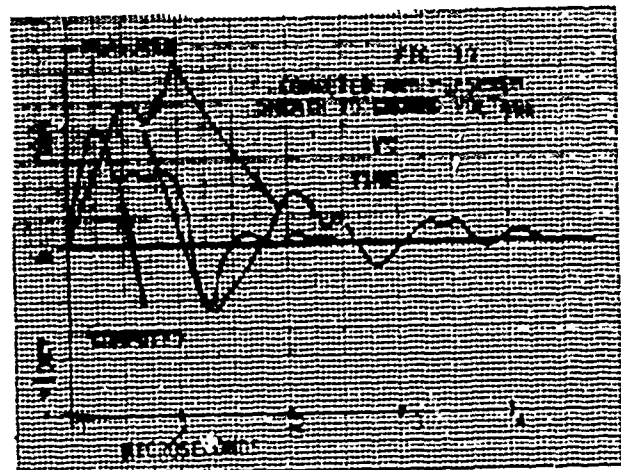


FIG. 9

MODEL OF DS 2019 CABLE 15 cm ABOVE GROUND

R 22.68	RA 60.0		
L1 1.65E-8	M12 8.03E-8	C 9.3E-11	
L2 5.77E-8	M13 3.23E-8	CG 7.98E-12	
L3 4.30E-8	M23 4.00E-8	CCG 2.0E-9	



## LIGHT ACTIVATED 10 KV LOW JITTER PULSER\*

John D. Calbraith

Los Alamos Scientific Laboratory  
Los Alamos, New Mexico 87545

**ABSTRACT**

An optically activated 10 kV pulser was designed to provide low jitter, long life, reliable triggering of ignitrons, trigatron, or midplane triggered spark gaps in high voltage electrically noisy environments. For midplane triggered spark gaps, a step-up transformer is also required. The input to a fibre optic cable is a 9.5 watt injection laser diode. The pulser detects and amplifies the fibre optic cable output to 10 kV.

**I. Introduction**

The development of this pulser is intended to bridge the gap between inexpensive, relatively slow rise time, large jitter, sometimes short lived pulsers and the expensive fast rise time, low jitter, also short lived pulsers.

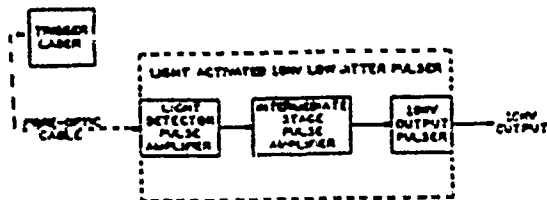
**II. Design**

The Light Activated 10 kV Low Jitter Pulser basic design consists of a Light Detector- Pulse Amplifier, an Intermediate Stage Pulse Amplifier, and a Krytron 10 kV Output Pulser. (See Fig. 1-Basic Block Diagram.)

The Light Detector-Pulse Amplifier consists of a photo diode, emitter follower and avalanche transistor.

The Intermediate Stage Pulse Amplifier is a twenty stage SCR Marx generator circuit.

The Krytron 10 kV output pulser is a two stage modified Krytron tube Marx generator circuit. The modification to this tube consists of an elongated glass envelope = 2.25" instead of the standard 0.85" for a XD-4 E. C. & C. Krytron tube. The increased glass envelope length provides for more gas thus increasing anticipated lifetime of the tube. In order to decrease the jitter of the tube, the keep alive element of the tube is pulsed with a current = 100 times the normal keep alive current for one millisecond prior to the triggering of the grid of the tube. (See Fig. 2-Modified Block Diagram.)



BASIC BLOCK DIAGRAM

FIGURE 1

\*Work performed under the auspices of the USDOE.



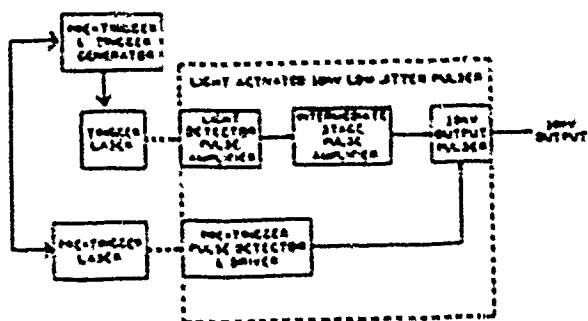


FIGURE 1  
BLOCK DIAGRAM

### III. Test

**Light Detector-Pulse Amplifier.** This circuit provides a 120 volt output pulse with < 1 nanosecond rise time, 8 nanoseconds delay time and negligible jitter for triggering the Intermediate Stage Pulse Amplifier. This pulse will be used as a reference for measuring delays of the succeeding circuits. This pulse can be used as a synchronizing pulse for triggering scopes, etc.

**Intermediate stage pulse amplifier.** This circuit provides a 1400 volt output pulse with an 6 nanosecond rise time, 15 nanoseconds delay time and negligible jitter.

**Krytron 10 kV Output Pulser.** This circuit provides a 10 kilovolt output pulse with a 5 nanosecond rise time, 35 nanoseconds delay time, and 2 nanoseconds jitter.

The complete Light Activated 10 kV Low Jitter Pulser provides a 10 kilovolt output pulse with a 5 nanosecond rise time, 50 nanoseconds delay from the reference pulse or 58 nanoseconds delay from the light pulse, and 2 nanoseconds jitter.

### IV. Future Experiments

Life testing of the present circuitry is yet to be performed. As a means of obtaining the best possible pulser with today's available technology designs of the following pulsers will also be built and tested.

1. Hydrogen Thyatron 10 kV Output Pulser (using an E. G. & G. HY-8 hydrogen thyatron)
2. SCR 10 kV Output Pulser (using A. E. I. Semiconductor XT 2105-1401 pulse thyristors)
3. RBDT 10 kV Output Pulser (using Westinghouse T40R102204 reverse bias diode thyristors)

An interest in the possible use of LASCR's has determined, through conversations with Lou Lowry at Westinghouse, that such a device is not yet available even experimentally which can be triggered with less than approximately 10 millijoules of light for a 1kV device. For a 10 kV pulser 10 LASCR's would therefore require 100 millijoules of light for triggering.

### V. Acknowledgments

Discussions with Bill Munnally and Jim Sarjeant at LASL have been most helpful in the design and testing of this pulser. Information concerning the modified Krytron tube and the method for decreasing its jitter have been provided by Spencer Merg of E. G. & G. and Jim Sarjeant at LASL.

## COMMAND CHARGE USING SATURABLE INDUCTORS

Susan Black and T. R. Burken

High Voltage/Pulse Power Laboratory  
Texas Tech University E. E. Dept.  
Lubbock, Texas 79409Abstract

Line-type pulsers operating at rep-rates greater than a few kilohertz require special circuits to insure proper operation of the switch. Specifically, thyristors and other closing switches require a "grace period" of several microseconds or more before anode voltage is reapplied; this delay allows recovery and prevents reclosure of the thyristor. One method of achieving the required delay time is by using a slightly mismatched PFN and slower-than-resonant charging. However, repetition rates of line-type modulators are limited by the characteristics of resonant charging. In order to increase rep-rates, these characteristics may be modified by using a saturable reactor as a charging inductor.

This paper describes design considerations and laboratory performance of saturable inductors used to repeatedly charge an energy storage network up to 25 kV with a delay as much as 16.5 microseconds.

Introduction

The required time delay or grace period for switch recovery may be achieved with a command charge scheme; however, the required circuitry is usually complicated and expensive. A comparatively simple and inexpensive method of achieving this charging delay is through slower than resonant charging. The major disadvantage of this method is the limitation of rep-rates to a narrow range by the characteristics of inductive charging. This rep-rate restriction may be reduced by using a saturable inductor as a charging inductor. The major disadvantage of using saturable inductors in inductive charging networks, is that their operating characteristics are voltage dependent.

A saturable inductor utilizes the non-linearity of the hysteresis curve of ferromagnetic materials. Initially, the inductor operates in the high permeability region of the B-H curve. This provides a

high inductive, low energy transfer period (delay in main charging cycle) allowing adequate recovery time for the closing switch. Upon saturation, the inductor core operates in the low permeability region of the B-H curve producing a low inductance which results in a relatively fast energy transfer. At the end of the charging cycle, the core resets to the initial conditions and the cycle repeats.

To obtain a sharp break between the saturated and unsaturated states of the saturable inductor, it is desirable to have the B-H characteristic of the core as square as possible. This provides high initial permeability for the charging delay and a low saturated permeability for fast charging (high rep-rates). In order to achieve high rep-rates, a low saturated inductance is required. Since the saturated inductance is inversely proportional to the square of the saturable flux density, a large saturated flux density results in a low saturated inductance. For efficient energy transfer, hysteresis losses should be as low as possible. To minimize this loss while maintaining a high saturation flux density, a low coercive force is desired.

A typical line-type modulator is shown in Figure 1a, with the saturable inductor used as the charging inductor. The charging time for resonant charging with a linear inductor, as seen in Figure 1b, is determined by the charging inductor and the capacitance of the pulse forming network (PFN):

$$T = \pi \sqrt{LC} \quad (1)$$

To prevent reclosure of the main discharge switch, T should be sufficiently large that a threshold vol-

voltage  $V_c$  is not exceeded within  $\tau_r$  seconds, where  $\tau_r$  is the recovery time of the switch. A slight negative mismatch of the load and PFN will increase  $T$  and affect the maximum rep-rate only slightly. The maximum rep-rate at which the switch may be operated is thus limited to approximately:

$$f = 1/T \quad (2)$$

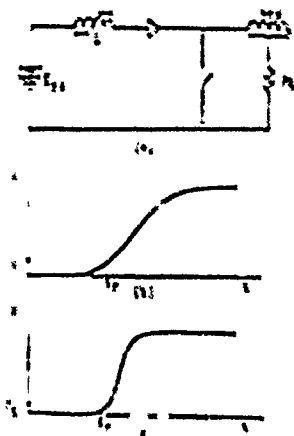


Fig. 1: (a) A line-type modulator utilizing a saturable inductor as charging inductor. The voltage charging waveform is shown using (b) a linear inductor and (c) a saturable inductor.

Use of a saturable inductor as a charging inductor will result in the waveform shown in Figure 1c. The time required to saturate the core,  $\tau_s$ , is chosen large enough to allow recovery of the switch. The charging time is now dependent upon the saturated inductance of the inductor:

$$T' = \pi \sqrt{L_{\text{sat}} C} \quad (3)$$

For reliable operation, the core should reset to approximately the same point on the B-H curve after each saturation. The time required to reset to this point is dependent upon the number of turns,  $N$ , area of the core,  $A$ , saturation flux density,  $B_s$ , and voltage applied to the core during reset,  $E_{\text{reset}}$ , such that:

$$\tau_{\text{reset}} = \frac{N A B_s}{E_{\text{reset}}} \quad (4)$$

Therefore, the maximum rep-rate is now limited to approximately:

$$f' = 1/(\tau_s + T' + \tau_{\text{reset}}) \quad (5)$$

The maximum rep-rate obtainable through using a saturable inductor for charging may be realized by

letting the saturation time of the inductor correspond to the recovery time of the thyatron and by minimizing the saturated inductance of the inductor.

#### Design Considerations

A typical hysteresis loop for ferromagnetic material suitable for use in saturable inductors is shown in Figure 2, where the coercive force,  $H_c$ , the saturated flux density,  $B_s$ , and the saturated permeability,  $\mu_s$ , are indicated. During the delay period,  $\tau_s$ , the voltage applied to the inductor is approximately constant and is equal to the power supply voltage,  $E_{ps}$ . From Faraday's law, the number of turns required for a saturable inductor with delay time of  $\tau_s$  seconds may be determined:

$$N = \frac{E_{ps} \tau_s}{S A B_s} \quad (6)$$

where  $a$  is the cross-sectional area and  $S$  is the stacking factor of the core. The saturated inductance of the inductor may be determined:

$$L = \frac{N^2 \mu_s A S}{l} \quad (7)$$

The mean magnetic path of the core is denoted by  $l$ .

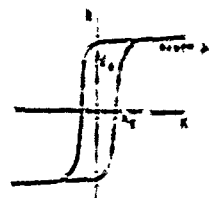


Fig. 2: Hysteresis loop of material suitable for use in saturable inductors.

Hysteresis, eddy current, and copper losses determine the rms power handling capabilities of a saturable inductor. Hysteresis loss in a cycle of operation may be determined from the volume of the core and the area enclosed by the B-H loop taken at the operating frequency. Eddy current losses are characterized by  $I^2 R$  losses in the core laminations, metallic protective cases, and etc. The total core loss is dependent upon switching speed, core material, tape thickness, and switching waveform. Hysteresis losses dominate during the delay time of the saturable inductor, while during saturation most losses are due to eddy currents. A more com-

plate description of these losses and their effects upon saturable inductors may be found in reference 1.

The volume of the core required in a saturable inductor may be determined from the desired rms power, the hysteresis loss of the core material, and the rep-rate. The window area of the core is dependent upon the rms current. The amount of current the winding is required to carry determines the winding wire size. Due to temperature considerations, copper will safely carry approximately 335 A/cm<sup>2</sup> rms current; from this value the required cross-sectional area for the wire may be determined. For wire with a circular cross section, the windings will fill approximately 75% of the available window space. The percentage of window area required for adequate insulation from turn to turn and layer to layer may be accounted for by a constant,  $A_{ins}$ , which will depend upon the desired voltage hold-off and quality of insulation. The window area may now be determined:

$$A_w = \frac{N I_{rms}}{335(.75 A_{ins})} \quad (8)$$

In order to insure reliable, cyclic operation of the saturable inductor, the core should be reset to the initial condition after each pulse. This re-orientates the iron of the core so that the next pulse will encounter the same charging delay. This operation is illustrated in Figure 3. At point 1 on the B-H curve, voltage is applied. After  $t_d$  seconds, point 2 is reached and the core saturates. The core begins to reset at point 3, but unless negative current flows through the inductor winding and negative flux is induced in the core, the core may not reset to the initial condition indicated by point 1. It is also possible to operate on a minor hysteresis loop. One such loop could be initially set at point 1a. In this instance, little negative flux would be required to achieve the initial condition. The amount of current necessary to reset the core may be determined by:

$$I_{reset} = H_c l/N \quad (9)$$

Reset may be implemented in several ways. A second winding and bias circuitry may be introduced to provide a dc bias current equal to the desired reset

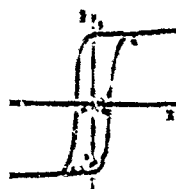


Fig. 3: Hysteresis loop showing operation of inductor core on major and minor loops.

current; however, it should be noted that the reset winding will act as a transformer to the main winding so that high voltage may be applied to the bias circuitry. (Also, additional window area would be required.) The construction of the charging diode may be such that the reverse bias leakage current is large enough to insure core reset. In this case, little or no negative flux may be induced in the core. This requires that the core operate on a minor hysteresis loop; i.e., only in the positive portion of the B-H curve. By eliminating the diode, over-resonant charging may be used which will provide the negative current needed to reset the core; however, this current may be large enough to force the core into negative saturation, reversing the charge polarity on the PFN.

#### Test Results

Based on available cores, three saturable inductors were designed for an existing modulator. The test modulator is shown in Figure 4. The type of core used was 2 mil laminated silicon steel with:

$$A = 4 \text{ cm}^2$$

$$l = 28.6 \text{ cm}$$

The rms power and current required in this application was low, so core volume and window area were not critical values. The design time delay and anode voltage are indicated in the first two columns of Table 1. From these values and manufacturer's specifications, the remaining values of Table 1 were determined.

Anode Voltage (kv)	$t_d$ (usec)	N	V/T	$L_{pac}$ (nH)
15	9.1	125	60	1.6
20	12.5	220	45	4.3
25	16.5	350	35	10.3

Table 1: Design values for saturable inductors with 2 mil silicon-steel cores.

The charging characteristics for the three inductors are shown in Figure 5. These curves indicate the charging voltage across the pulse forming line (PFL) capacitance of the test modulator, where the saturating effect of the cores can easily be seen. The voltage is held off initially due to the high inductance corresponding to the delay period. The core then saturates, producing the relatively high frequency charging waveform shown. The core then switches back to low inductance operation and resets; reset in this case was achieved with reverse-bias current from the charging diode. A change in time scale makes the saturated region more pronounced in Figures 5b and 5c.

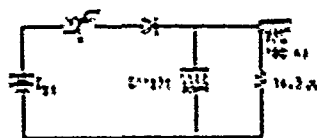


Fig. 4: Test modulator used in design and test of saturable inductors.

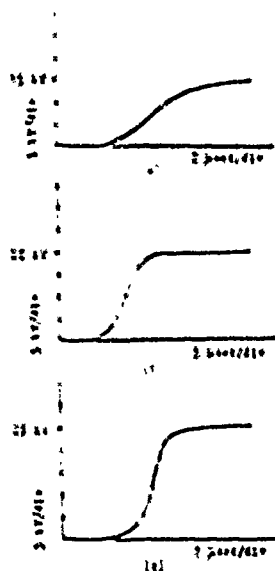


Fig. 5: Charging voltage waveform for the three saturable inductors designed.

#### Conclusion

It has been shown that the design of a saturable inductor depends upon the required rms power and rms current, the power supply voltage,  $E_{ps}$ , and the desired delay time,  $\tau_d$ . The core volume may be determined knowing the rms power, and the core window

area may be found from the rms current. From these values, the core size may be chosen. The number of turns to be wound on the core may be determined from core characteristics and size,  $E_{ps}$ , and  $\tau_d$ .

The design of the experimental inductors was based on values determined as above. In these cases, the rms power and current were low, so volume and window area were not critical. None-the-less, the use of saturable inductors in inductive charging circuits has been demonstrated. As the results have indicated, an increased "grace period" may be obtained through their use. Since the delay time of the inductor is voltage dependent, the use of saturable inductors as charge delay switches is best suited to constant voltage applications.

#### References

1. G. T. Coate and L. R. Swain, Jr., High-Power Semiconductor-Magnetic Pulse Generators, Cambridge, Mass: The M.I.T. Press, 1966.

## INVITED

## INVESTIGATIONS OF FAST INSULATOR SURFACE FLASHOVER \*

J.E. Thompson and J. Lin  
University of South Carolina  
College of Engineering  
Columbia, South Carolina

K. Mikkelsen and M. Kristiansen  
Texas Tech University  
Department of Electrical Engineering  
Lubbock, TX 79409

Abstract

Electro-optical measurements of the electric fields along insulator surfaces have been made to determine the mechanism associated with fast insulator flashover. Data will be presented that show the temporal and spatial performance of the surface fields prior to and at flashover for insulator surfaces oriented at 0° and 45° with respect to the applied field. Results show that the surface field near the cathode is enhanced and the field near the anode is reduced during the excitation. The results further show a temporal reduction in the field non-uniformity as flashover is approached. The field collapse associated with flashover occurs very rapidly for 0° surfaces. The field collapse for 45° surfaces begins at the anode and propagates at 0.33 cm/ns towards the cathode. Mechanisms consistent with these experimental measurements will be postulated.

Introduction

Conducting electrodes in high voltage devices are often separated by dielectric interfaces. The self-breakdown or flashover voltage for electrodes separated by a dielectric interface is typically less than the break-down voltage without the dielectric interface. The reduced value of breakdown voltage is generally attributed to surface charging of the dielectric interface and resulting inter-electrode field modifications which lead, eventually, to plasma formation and ionization avalanche along the dielectric interfacial surface.

The reduced flashover potential arising because of dielectric interfaces is of primary concern in the design of fast rise, high voltage accelerators. A better understanding of the basic mechanisms leading to surface flashover is required to provide technical direction for improved dielectric interface designs.

Research has therefore been conducted to determine the physical mechanisms associated with fast insulator surface flashover. Specifically, electro-optical measurements have been performed to determine the spatial and temporal behavior of fast rise time, short duration, interfacial electric fields. Voltage excitation with nanosecond rise time and duration and excitation levels of up to 100 kV/cm have been used to produce data relevant to present and future accelerator designs.

The measurement of the electric field distribution prior to and at flashover is considered particularly important since these data can determine the role of insulator surface charging for various insulator configurations and excitation levels. Insulator surface charging is postulated in most flashover models and has been measured for slower excitations.<sup>1-3</sup> However, the distribution and behavior of the surface charge and its role in surface flashover has not previously been determined for fast, nanosecond excitations.

This paper first briefly describes the surface flashover problem. This is followed by a description of the interfacial electric field measurement tech-

\* This work was supported by Sandia Laboratories

nique used and the experimental arrangement required. Results obtained are then presented, showing the temporal and spatial behavior of the surface fields for 0° and 45° insulator shapes.

#### Surface Flashover Description

A simple electrode-insulator configuration in which surface flashover occurs consists of two electrodes separated by a solid insulator. The entire arrangement is in a vacuum. This arrangement is applicable to many practical devices and is used for most of the measurements reported here. A voltage pulse is applied across the electrodes in typical applications. Voltage levels above a certain value, for a particular pulse duration, will cause an arc or flashover to occur along the insulator surface. This arc occurs at a voltage level that is much lower than the arcing potential of the electrodes without the dielectric spacer.

The physical mechanism associated with the observed flashover and the lowering of the arcing voltage has been postulated by several researchers.<sup>1-5</sup> Electrons are emitted by small "whiskers" on the electrode surface near the triple point. The emission mechanism is field emission due to the field intensification at these microscopic sharp points. Some of the field emitted electrons strike the insulator surface. Most insulators have a coefficient of secondary emission greater than one such that more secondary electrons are emitted from insulator than striking primaries. This results in a positive charging of the insulator surface. This surface charging propagates from the cathode to the anode. The process continues until a steady-state surface charge distribution is established or until flashover occurs. The steady-state charge distribution exists when the energy of returned secondaries is such that the energy dependent coefficient of secondary emission is equal to unity.<sup>2-5</sup> The charge distribution, however, does not have time to attain equilibrium for short pulse excitations. The occurrence of flashover in this case has been postulated to be due to impact ionization of gas molecules desorbed from the insulator surface.<sup>6</sup> The ionization and molecular desorption are both due to primary and secondary electrons from the

cathode and insulator surface. It is also possible that for nanosecond excitations, the flashover mechanisms operate extremely fast such that other mechanisms in addition to surface charging contribute to flashover. The field at the cathode triple junction could reach high enough values to cause a microdischarge, due to explosion of an emission site. This could release sufficient electrons and photons from the cathode and/or insulator surface to cause impact ionization of the gas molecules on the insulator surface. This in turn could lead to a plasma streamer and ultimately breakdown.

#### Measurement Technique and Experimental Arrangement

Flashover, according to postulated models, requires that the insulator surface be charged by field emitted electrons. The surface charge then enhances the electric field in the cathode region near the insulator, causing increased cathode field emission, avalanche, and ultimately breakdown. The flashover process therefore is dependent upon an inter-electrode field modification. The modifications to the interfacial electric fields along the surface of the insulator were electro-optically measured in this investigation.

Electric field measurements were made using test cell arrangements shown in Figure 1. The test cell shown in Figure 1(a) is constructed using a KDP (potassium-dihydrogen-phosphate) crystal as the insulator material while the test cell in Figure 1(b) is constructed using nylon surrounded by nitrobenzene. The surface electric fields can be determined by optically measuring the Pockels effect in

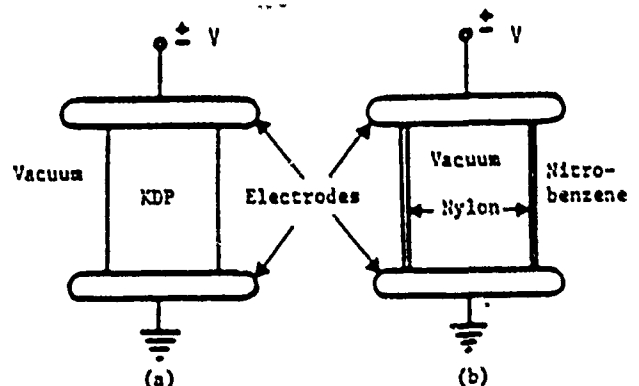


Figure 1. KDP and Nitrobenzene Test Cell.

the KDP near the vacuum flashover surface or by measuring the Kerr effect in nitrobenzene near the nylon/vacuum flashover surface. The Pockels or Kerr electro-optic effects are therefore used to infer the electric fields along the flashover surface.

The Pockels effect is characterized by the fact that linearly polarized light components polarized in directions parallel and perpendicular to the applied inter-electrode field, travel through the KDP crystal with different phase velocities. The phase velocity difference is proportional to the applied electric field such that orthogonal light components, after passing through the transparent KDP insulator, are not in phase. The magnitude of the phase introduced is given by

$$\delta = \frac{\pi r_{63} n_0^3 L E}{\lambda}$$

where  $r_{63} n_0^3$  is an electro-optic constant measured to be  $3.3 \times 10^{-11}$  (mks),  $L$  is the path length through the KDP,  $E$  is the applied field, and  $\lambda$  is the probing light wavelength.<sup>7</sup> Therefore, the phase difference between the orthogonal probing light components is indicative of the electric field in the KDP or, specifically, fields at the vacuum/KDP interface. The phase difference  $\delta$  can be measured very accurately using a polarization analyzer, to be described.

The Kerr effect can similarly be used to measure interfacial fields. Orthogonal polarization components of probing light travelling through the nitrobenzene, near the nylon surface, also experience a relative phase shift. The amount of the phase shift is given by

$$\delta = 2\pi K L E^2,$$

where  $K$  is the Kerr coefficient of the nitrobenzene ( $K = 325 \times 10^{-14}$  (mks)). Measurement of  $\delta$ , therefore, yields data regarding the electric fields at the nitrobenzene/nylon interface.

The phase shift  $\delta$  is measured using the polarization analyzer shown in Figure 2. The analyzer consists of the various beam splitters and mirrors shown, two orthogonally oriented polarizers, and a half wave plate. The analyzer produces a finite fringe interference pattern indicative of  $\delta$ .

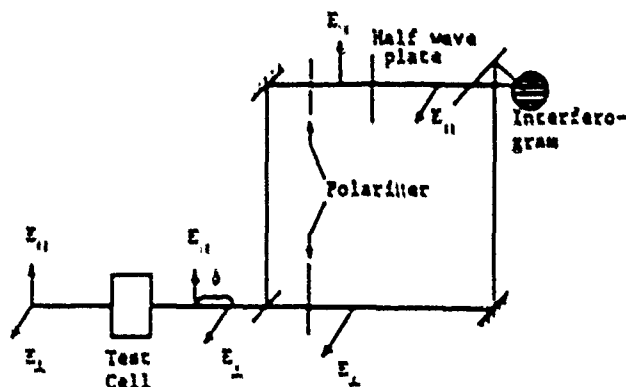


Figure 2. Polarization Analyzer.

The operation of the interferometer is described in detail in Reference 8, however, a brief description is presented in the following discussion. Linearly polarized light is passed through the test cell. Orthogonal polarization components  $E_{\parallel}$  and  $E_{\perp}$ , polarized parallel and perpendicular to the applied electric field, respectively, emerge from the test cell out of phase by an amount,  $\delta$ , as shown in Figure 2. Light entering the analyzer is divided using the beam splitter. Linear polarizers are positioned to pass only  $E_{\parallel}$  in one path, and  $E_{\perp}$  in the other path of the analyzer. A half wave plate in one path is used to change the polarization direction of  $E_{\parallel}$  so that  $E_{\parallel}$  and  $E_{\perp}$  are no longer orthogonal (orthogonal light beams will not interfere). The light beams having polarization components  $E_{\parallel}$  and  $E_{\perp}$  are then recombined using a beam splitter. The result is a finite fringe interference pattern indicative of the phase difference between the two interfering beams.

Representations of typical interferograms obtained using the analyzer are shown in Figure 3. Figures 3(a) and (b) show the interference pattern obtained using the Kerr effect test cell. The interference fringes for no applied field or for a spatially uniform field are shown in 3(a). It can be shown that a spatially non-uniform electric field will produce a fringe pattern similar to that shown in 3(b). It can further be shown that the magnitude of the fringe displacement is given by

$$\frac{\Delta y}{\Delta x} = \frac{\delta}{2\pi} = K L E^2.$$



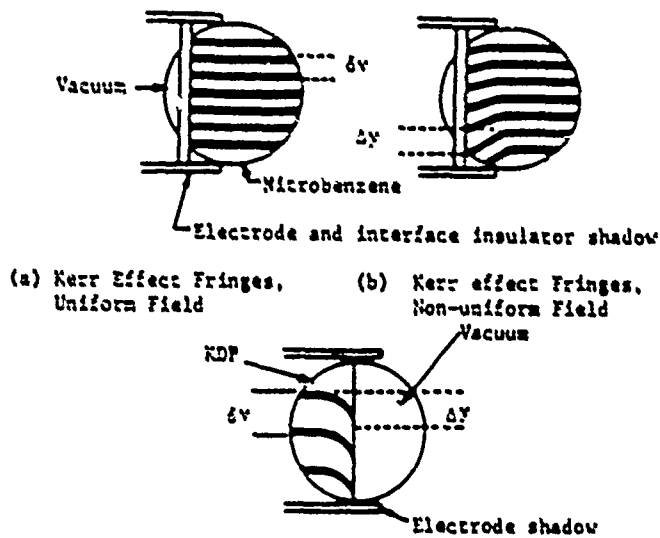


Figure 3. Representation of Typical Interferogram.

where  $\Delta y$  is the amount of fringe bending observed and  $\delta y$  is the undeviated background fringe spacing.

A similar interferogram is produced using the Pockels test cell. A representation is shown in Figure 3(c) for a non-uniform electric field near the KDP/vacuum interface. It can be shown that the fringe bending is related to the interfacial field by

$$\frac{\Delta v}{\delta y} = \frac{\lambda}{2\pi} = \frac{n_0^3 \epsilon_{63} LE}{2\lambda}$$

The position and bending of the finite fringes produced by the analyzer can, therefore, be used to determine the spatial distribution of the electric field near the vacuum interfaces. Temporal data can also be obtained by positioning a slit at the interface being examined and streaking the fringe pattern with an image converter camera. This technique is summarized in Figure 4. The specific relationships between the observed fringe bending and the spatial and temporal variation of the fields to be measured are given by

$$E(y, \tau) = \left[ \frac{\Delta v(y, \tau)}{\delta y KL} \right]^{1/2}$$

for the Kerr effect and by

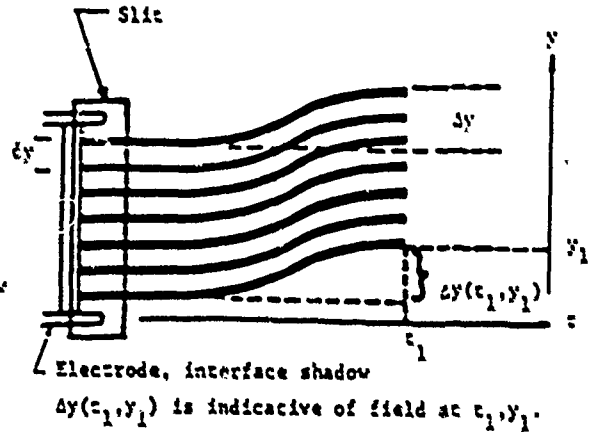


Figure 4. Slit Interferogram Streaked in Time.

$$E(y, \tau) = \frac{2\lambda}{n_0^3 \epsilon_{63} L} \frac{\Delta v(y, \tau)}{\delta y}$$

for the Pockels effect, where  $y$  is a position coordinate along the slit and  $\tau$  is time.

The components necessary for the electro-optical interfacial field measurements consist of the KDP test cell, the nitrobenzene test cell, and the polarization analyzer together with a high voltage pulse generator, probing laser, and an image converter camera.

The KDP test cell consists of a 1 cm x 1 cm x 5 cm, 45°, Z-cut KDP crystal held between two aluminum electrodes. The entrance and exit apertures of the crystal are polished to  $\lambda/4$  flatness. All other crystal sides are polished to be transparent only. The nitrobenzene test cell consists of two electrodes separated by a nylon insulator measuring 1 1/2" x 1/2" x 1 cm. The nylon insulator is hollow, having a wall thickness of 1/16". The nylon insulator ends are inserted into O-ring grooves and the interior volume evacuated.

The arrangement necessary for test cell excitation and optical diagnostics is shown in Figure 3. The arrangement consists of an FX-15 coaxial line pulse generator, a pulsed ruby laser, the test cell, the analyzer, and an image converter camera. The FX-15 power supply provides the voltage pulse to the test cell. The ruby laser is used to probe the test cell and, additionally,

to trigger the FX-15. Laser triggering of the FX-15 is necessary to reduce timing problems. The triggering technique shown uses the same ruby laser to initiate and observe the flashover. The Q switch jitter of the laser is, therefore, unimportant. The system jitter arises due to variations in the FX-15 gas gap breakdown delay. This uncertainty is presently on the order of a few nanoseconds. Both optical and electrical delay lines are utilized to synchronize the diagnostic image converter camera and fast scopes which are used for voltage and current measurements.

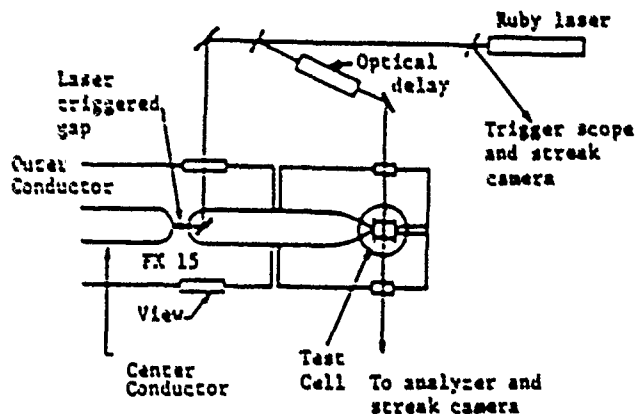


Figure 5. Test Cell Excitation and Diagnostic Arrangement.

#### Experimental Results

The electro-optical measurement technique and the experimental arrangement described have been used to measure the electric field distribution along  $90^\circ$  KDP/vacuum interfaces,  $90^\circ$  nitrobenzene/nylon/vacuum interfaces, and  $\pm 45^\circ$  nitrobenzene/nylon/vacuum interfaces. This section will present data obtained for these test cell configurations.

**90° KDP/Vacuum Results.** The KDP test cell was used to determine the temporal and spatial behavior of the intergap electric fields along a KDP solid crystal/vacuum interface. Results will be shown for excitation levels and durations where no flashover occurred and where flashover did occur.

The voltage hold-off capability of the  $90^\circ$  vacuum/solid interface was unpredictable. This is in agreement with the data obtained by Anderson.<sup>9</sup> However, data could be selected to illustrate the

interfacial field behavior for both non-flashover and flashover conditions. Figure 6 shows a line representation of an interference pattern indicative of the field distribution for no flashover. The fringe displacement is seen to increase and temporally follow the excitation field. The numbers in parenthesis indicate the total magnitude of the fringe shift at the peaks shown. The magnitude of the fringe shift (and hence the electric field) at the cathode is seen to be greater than the fringe shift at the anode. Additionally the peak fringe displacement is reached at the cathode at a later time than at the anode.

The spatial variation of the interelectrode field calculated at times  $t_1$  and  $t_2$  of Figure 6, is shown in Figure 7. Times  $t_1$  and  $t_2$  correspond to the peak fringe displacement at the anode and the cathode respectively. This figure shows that at both times the cathode field is larger than the anode field. This observed cathode field enhancement is consistent with the theory of positive charging of the interface.

Further analysis of the interferometric data of Figure 6 can be performed. Superimposed on the observed fringe pattern is another fringe pattern

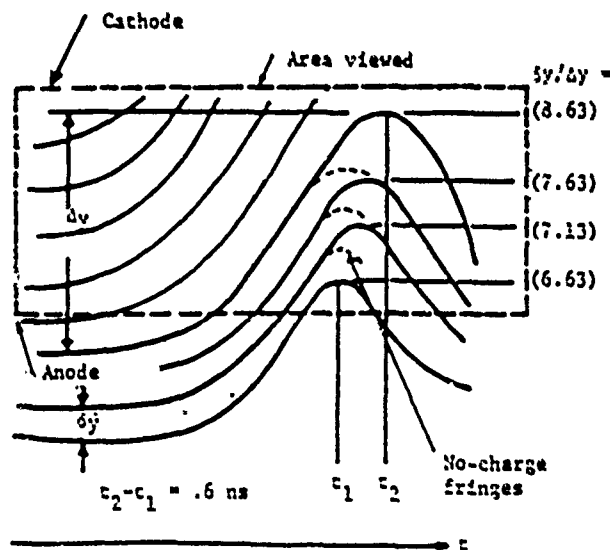


Figure 6. Representation of Streak Camera Photograph.

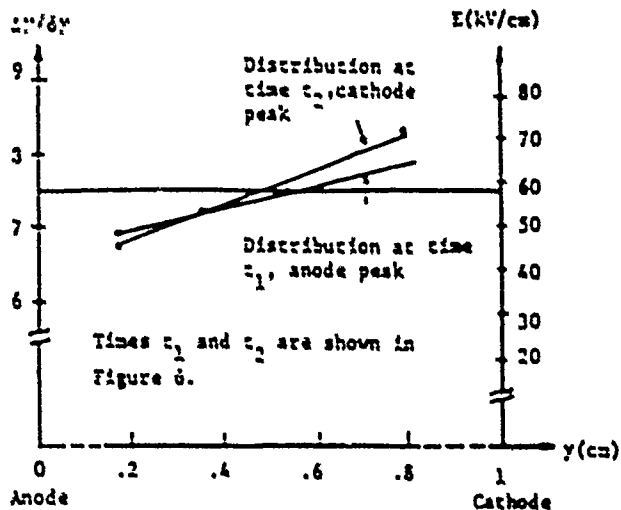


Figure 7. Surface Fields for KDP/Vacuum Interface.

shown in dotted lines. The dotted fringes correspond to no surface charging. The position of these fringes is determined by using the known temporal waveform of the excitation voltage and the known magnitude of the test cell Pockels effect. The figure shows that the observed fringes depart from the fringes for no surface charging. The separation occurs first at the cathode and later at the anode. The time difference is seen from Figure 6 to be approximately 1.14 ns. These data can be interpreted to imply that surface charging begins first at the cathode and that the surface charging propagates in 1.14 ns to the anode located 1 cm away. This corresponds to a surface charging avalanche velocity of .88 cm/ns.

Interferograms have also been obtained for excitations which resulted in flashover. The fringes again follow the excitation voltage until flashover occurs. Surface flashover is observed to begin at the anode and propagate towards the cathode. The observed time difference has been observed to be .4 ns, corresponding to a flashover propagation speed of 2.5 cm/ns. This delay is not observed consistently. It has also been observed that the flashover occurs simultaneously in the intergap region. This apparent simultaneous flashover behavior cannot be further resolved with the fastest streak unit available for this experiment, 2.5 ns/ns.

**Nitrobenzene/Nylon Results.** The nitrobenzene test cell and the optical measurement described have also been used to determine nitrobenzene/nylon interfacial fields. Data have been obtained for 90° insulator surfaces and 45° surfaces. The fields in the nitrobenzene, separated from the vacuum field by 1/16 inch, are assumed to be indicative of the vacuum fields. No attempt has been made to date to actually calculate the vacuum fields in terms of the nitrobenzene fields.

**0° Nitrobenzene/Nylon Results.** Interfacial fields have been interferometrically measured. A line representation of a typical interferogram is shown in Figure 8. The indicated behavior includes: (1) attainment of larger fringe shifts and hence higher electric fields near the cathode; (2) a

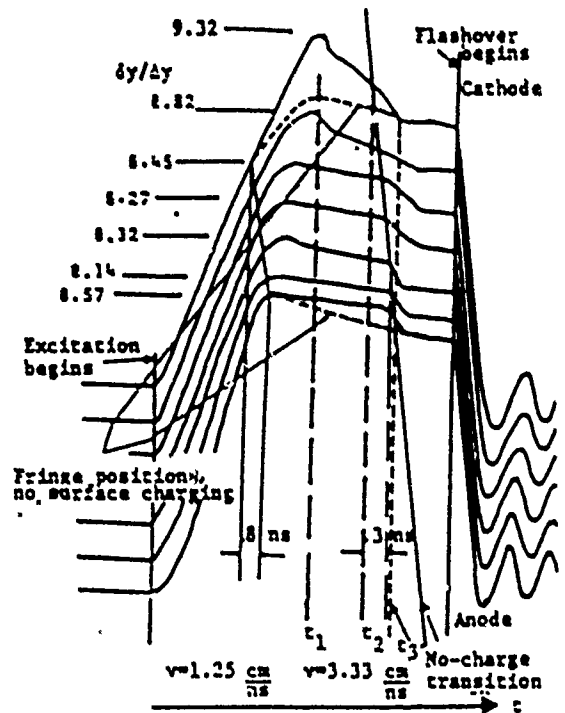


Figure 8. Representation of Streak Camera Picture for Nitrobenzene/Nylon/Vacuum Interferogram.

rapid decrease in the field enhancement near the cathode; and (3) additional decrease in the field values to another plateau value; (4) simultaneous intergap field collapse at flashover; and (5) intergap field modification beginning at the cathode and propagating to the anode.

Page 112 Missing  
and not available

DTIC-FDAC  
25 Jan 90

The flashover is observed to propagate from anode to cathode (1 cm) in 1.2 ns, corresponding to a velocity of .83 cm/ns.

#### Summary

Electro-optical measurements have been made and have determined the temporal and spatial distribution of nanosecond electric fields along vacuum/solid interfaces. The results indicate that cathode field enhancement and cathode initiated flashover are important for  $0^\circ$  insulator surfaces. The data have determined several performance features for  $0^\circ$  surfaces which have not been observed prior to this work. The features include (1) cathode field enhancement; (2) the cathode field enhancement occurs first at the cathode (a field enhancement propagation velocity has been calculated); (3) the intergap field enhancement is reduced in two steps. The first step is slower than the second. The second reduction essentially reduces the intergap fields to the uncharged insulator surface values. The velocity of propagation of this effect has been measured; (4) Flashover most often begins simultaneously between electrodes. However, anode initiated flashovers have been observed. The velocity of the anode initiated flashover field collapse has been measured.

Results obtained for  $45^\circ$  insulator surfaces are presently inconclusive and should be considered preliminary. The results do show, however: (1) Fields near the vacuum  $45^\circ$  angle are enhanced, probably because of the permittivity mismatch resulting from the electro-optic fluid; and (2) Flashover has been observed to occur first at the anode for negative  $45^\circ$  surfaces and propagate towards the cathode at a velocity of .83 cm/ns.

#### References

1. M. Boersche, et. al., "Surface Discharges Across Insulators in Vacuum," *Zeitschrift für Angewandte Physik*, **15**, pp. 510 (1963).
2. C.H. de Tourrel et. al., "Mechanism of Surface Charging of High Voltage Insulators in Vacuum," *IEEE Transactions on Electrical Insulation*, **EI-8**, 17 (1973).
3. T.S. Sudarshan and J.D. Cross, "DC Field Modifications Produced by Solid Insulators Bridging a Uniform Vacuum Gap," *IEEE Transactions on Electrical Insulation*, **EI-8**, 112, (1973).
4. J.P. Brinard and D. Jensen, "Electron Avalanche and Surface Charging on Alumina Insulators During Pulsed High Voltage Stresses," *J. Appl. Phys.*, **45**, 3260 (1976).
5. T.S. Sudarshan, et. al., "Prebreakdown Processes Associated with Surface Flashover of Solid Insulators in Vacuum," *IEEE Trans. on Electrical Insulation*, **EI-12**, 200, (1977).
6. R.A. Anderson and J.P. Brinard, "Surface Flashover Model Based on Electron-Simulated Desorption," 8th Int. Symp. on Discharges and Electrical Insulation in Vacuum, Albuquerque, September 1978.
7. I.P. Kaminov and E.H. Turner, *Applied Optics*, **5**, 1612-1617, (1966).
8. J.E. Thompson et. al., "Optical Measurement of High Electric and Magnetic Fields," *IEEE Trans. of Instrum. and Measurement*, **25**, 1 (1976).
9. R.A. Anderson, "Surface Flashover Measurements on Conical Insulators Suggesting Possible Design Improvements," Sandia Lab. Report # SAND F5066F.
10. A. Watson, *J. of Appl. Phys.*, **38**, 2019 (1967).

## BREAKDOWN IN SMALL, FLOWING GAS SPARK GAPS

W. K. Cary, Jr.  
D. D. Lindberg  
J. W. Rice

Naval Surface Weapons Center  
Dahlgren, VA. 22448

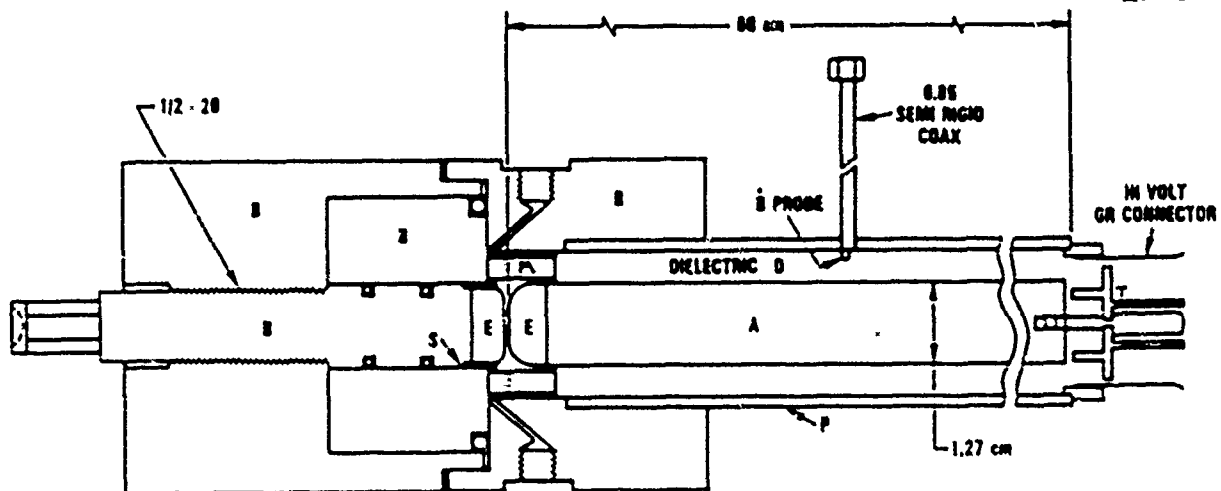
Summary

An improved method for studying electrical breakdown in small, flowing gas spark gaps is described. The apparatus and data processing yield the time to breakdown, current, resistance, power dissipation and energy loss in the spark gap during the 4 nS in which the current rises from zero to a near constant value. A specially constructed transmission line terminated in a spark gap and instrumented with a  $\delta$  probe and sampling oscilloscope is used to observe the breakdown. The initial charge on the transmission line and the current, obtained by integrating the  $\delta$  signal, provide the information needed to define the spark gap operation in a well characterized coaxial

arrangement. With a temporal resolution better than 50 pS, current components with frequencies to 10 GHz could be measured. An electronic circuit held the gap breakdown voltage and the subsequent charge in the transmission line to precise, predetermined values. A computer based data reduction system determined the current waveform from data corrected for the frequency response of the signal delay line. Results are given for argon and nitrogen, each at two overvoltages.

Introduction

This work is part of a parametric study of small gap breakdown as affected by gas species, pressure, gap length, percent overvoltage and electrode



## MATERIAL CODE:

A - SILVER PLATED BRASS  
B - BRASS  
D - STYCAST<sup>®</sup> 36 DK, EMERSON AND CUMING  
E - ELKONITE<sup>®</sup> 10W3, CM&W  
M - MACOR<sup>®</sup>, DOW CORNING CERAMIC  
T - TEFLON<sup>®</sup>  
P - COPPER PIPE, 2 cm I.D.  
S - SILVER

Figure 1. Transmission line terminated by spark gap.

material started last year and was prompted by the limited and uncorrelated data available. Small gaps ( $> 2.5$  mm) with high E fields ( $> 2 \times 10^5$  V/cm) differ significantly from larger gaps in the rate of current risel. Sorensen and Ristic<sup>2</sup> provided the starting point with their concept of a repetitively charged transmission line spark gap to study very fast transients. The waveform of the current in the gap has immediate engineering application and also provides clues to the mechanisms occurring during breakdown.

#### METODOLOGY

##### Transmission Line Spark Gap

The rapid breakdown of small gaps presents a problem in simultaneously measuring voltage and current with sufficient temporal resolution. By using the coaxial transmission line spark gap with a known  $Z_0$ , Figure 1, only the time dependent current must be measured.

The transmission line was constructed from a 60 cm long copper pipe with a 2 cm I.D. and a silver

plated brass rod 1.27 cm in diameter. The silver plating reduced line losses at microwave frequencies. Measurements of the line gave a relative dielectric constant of 4.86 and a characteristic impedance of 12.0 ohms. This low impedance allows high gap currents for resolution of low gap resistance. The dissipation factor of the dielectric is  $< 0.0008$ . A  $\frac{1}{8}$  probe placed 10 cm from the spark gap monitored the current changes in the transmission line. This probe was fashioned from SS mill semi-rigid cable by using the flattened center conductor to form a 1 mm loop. The probe self inductance with a 50 ohm system gave risetime of  $< 25$  ps.

Elkonite (10W3), an alloy of 70% W and 30% Cu, machined to an approximate Rogowski contour, was used to make the electrodes because of its excellent wear characteristics. Gas flowed across the gap at a rate of 1 liter/minute (to ATM). The gas baffle in Figure 1 surrounds the gap and forces an even distribution of gas across the gap width as

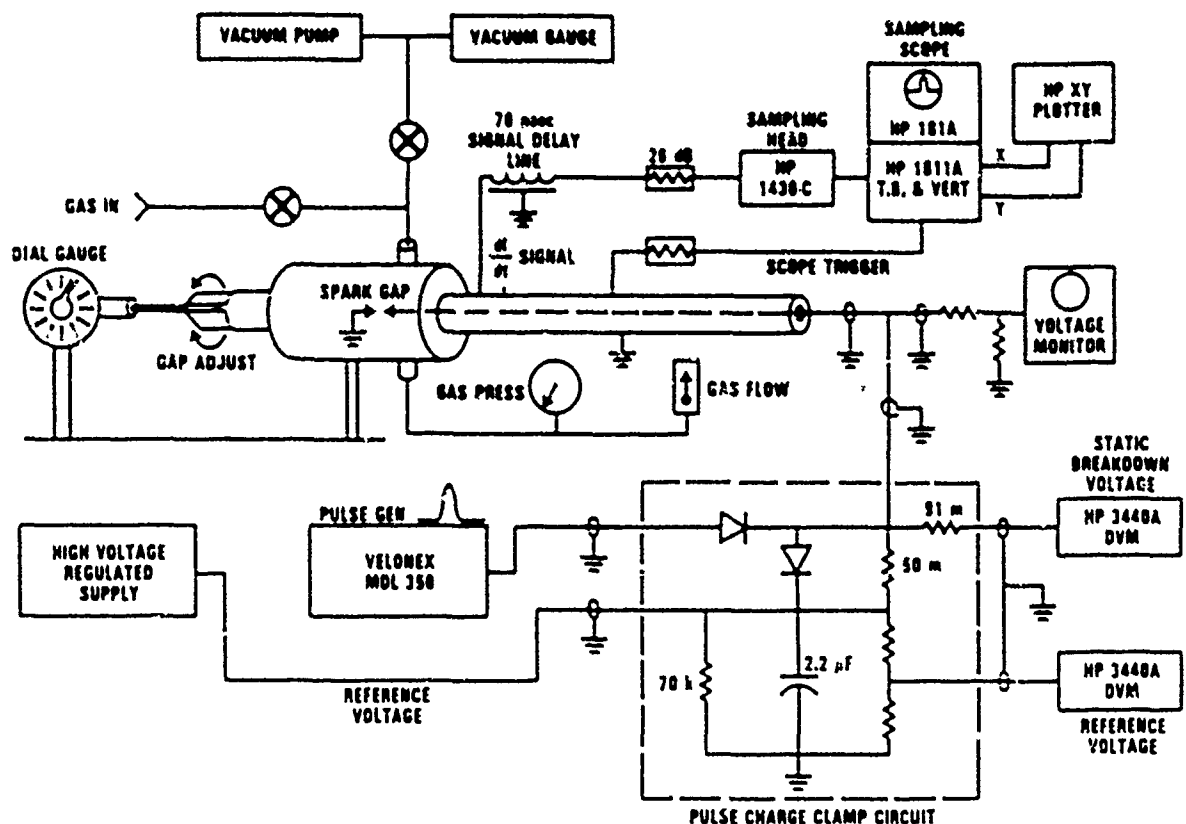


Figure 2. Experimental Set-Up.

well as preserving the line  $Z_0$  across this region. The flow rate was chosen so that at least 2 changes of gas took place between arcs. The arcs then occurred in a gas relatively free from residue and were highly repeatable. The adjustable electrode which allows gap size up to 0.5 mm is electrically shorted to the outer shell through a silver foil sliding contact placed less than 1 mm from the spark gap (Figure 1). The length of this short circuit thus is less than 1/5 of a wavelength at 10 GHz.

#### Charging Circuit

The sampling techniques to monitor the  $\dot{B}$  signal require that the line be charged to precisely the same voltage each time for minimum amplitude jitter. The high voltage pulse generator and the electronic voltage clamping circuit shown in Figure 2 held voltage variations to less than 1.5%. The risetime of the charging pulse must be fast enough to prevent the gap from breaking down before the clamp voltage is reached. Generally, risetimes of about 1 microsecond are satisfactory, but when gap overvoltages greater than 250-300% are used, faster charging pulses are needed. A digital voltmeter monitors the clamp voltage and a specially built, pulse compensated voltage probe with a oscilloscope records the charging pulse waveform. This also gives a measure of the time between application of voltage and breakdown to allow a statistical analysis of the time to breakdown.

#### Procedure

The spark gap and transmission line were characterized by determining the gap capacitance, the characteristic impedance ( $Z_0$ ) of the line and the mutual impedance of the line and  $\dot{B}$  probe. The gap capacitance is in parallel with the line and the line capacitance adds with that of the gap.

In order to determine  $Z_0$ , the velocity of propagation was measured with an Ikor pulse generator and two Tektronix sampling heads. Four points along the transmission line were accessible and were paired for three measurements. Time domain reflectometry was also used. The mean of these measurements gave a value of 45% the velocity of

light with a standard deviation of less than 6% for a  $Z_0$  of 12.0 ohms. The  $\dot{B}$  probe constant was determined from measurements with argon at 50 psia and a 50 micrometer gap while assuming a low gap resistance when the  $di/dt = 0$ .

Gas species, pressure, flow rate and gap length are selected and the static breakdown voltage measured. The clamp voltage is set based on a percent overvoltage of the static breakdown voltage. The pulse generator voltage is set approximately 50% above the clamp voltage to ensure a fast charging pulse risetime. Pulse repetition rates of 33 to 100 Hz were selected as needed to produce stable oscilloscope traces. The system is run several minutes to condition the electrodes before the charging voltage and the  $\dot{B}$  signal are recorded. When gas species is changed, the gap is disassembled, cleaned, and the electrodes polished and flushed with the new gas. The gap measurements stabilize after 2-3 minutes of operation. Significant electrode erosion or coating have not been noted during runs with argon and nitrogen.

#### Data Reduction

The sampling oscilloscope measuring the  $\dot{B}$  signal drives an X-Y plotter to record the data. These waveforms are digitized and stored in a computer. The computer smoothes the data, reconstructs the signal at the input to the delay line, solves the circuit equations for the gap resistance, power dissipated and energy lost, and plots these as a function of time. The delay line, which acts as a time invariant low pass filter, distorts the signal. The computer program finds the Fourier transform of the signal, multiplies it by the inverse Fourier transform. The current in the transmission line is simply  $I(t) = \frac{1}{k} \int v_B(t) dt$ , where  $v_B(t)$  is the  $\dot{B}$  signal and  $k$  is the mutual inductance between the  $\dot{B}$  probe and the transmission line. The time varying resistance of the gap is given<sup>2</sup> by

$$R(t) = \frac{-V_0 k + Z_0 I(t)/k}{-I(t)/k + Z_0 C_{\text{gap}}(t)}$$

where  $V_0$  is the breakdown voltage,

$C$  is the gap capacitance and it can be seen, that as  $I(t)$  gets large an accurate measure



of  $V_g$  becomes more important for accurate results. Power and energy are directly available from the current and resistance.

#### Results

The time dependence of gap resistance and instantaneous power for argon at two E/P ratios is shown in Figures 3-6. For comparison, the time functions of instantaneous gap power for nitrogen at two E/P ratios is given in Figures 7 and 8. Table 1 is a summary of some of the parameters for the four runs. The gap resistance curves fit the relationship

$$R(t) = at^{-n}$$

with  $a$  and  $n$  listed in the table.

The very high electric field in the gap makes it operate in an unusual regime. After the electrodes are conditioned, with electric fields greater than  $10^7$  V/m, cause its explosion of cathode microtips<sup>1,2</sup> and create runaway electrons from the avalanche that generate X-rays<sup>1</sup>. Thus in this regime, breakdown is very rapid and does not follow breakdown in gaps with lower fields<sup>5</sup>. An example of this can be seen in Figures 3 and 4, where at constant pd the rate of gap resistances fall increases when the charge voltage decreases.

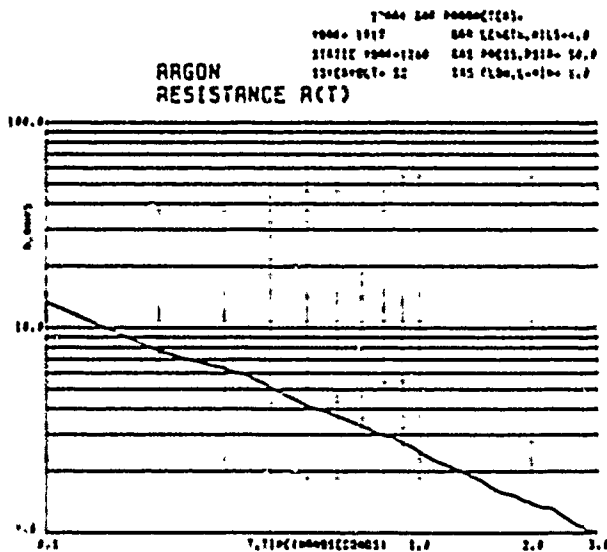


Figure 3. (Run 1)

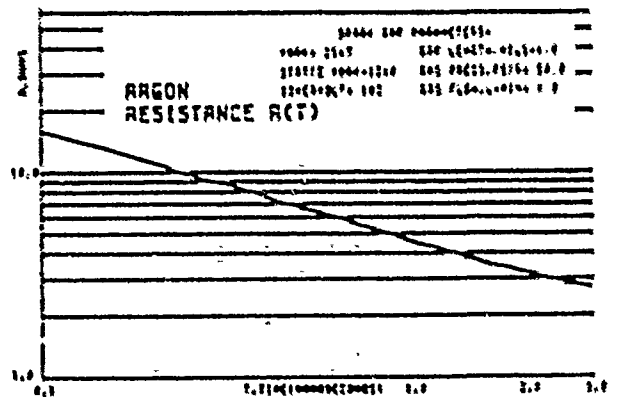


Figure 4. (Run 2)

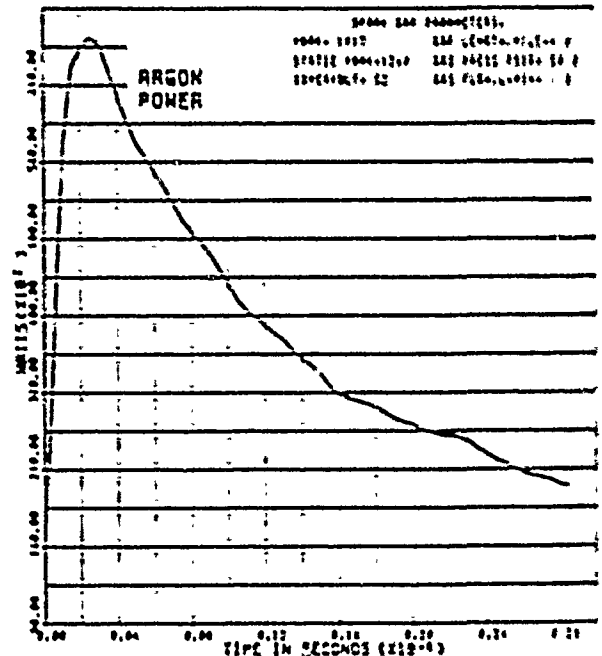


Figure 5. (Run 1)

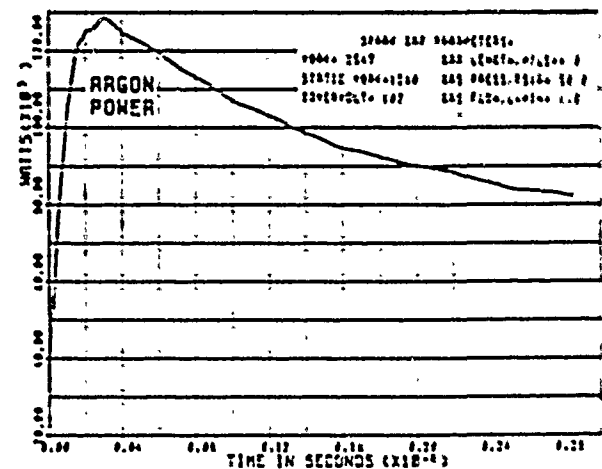


Figure 6. (Run 2)

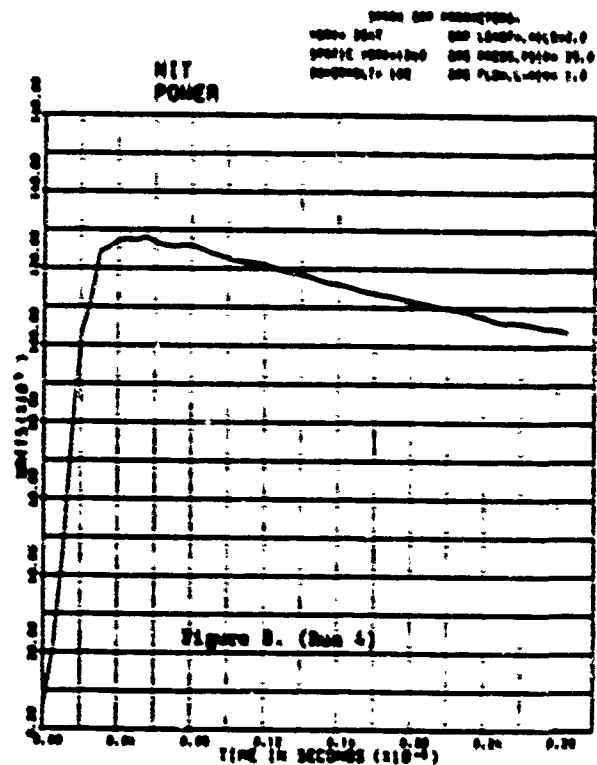
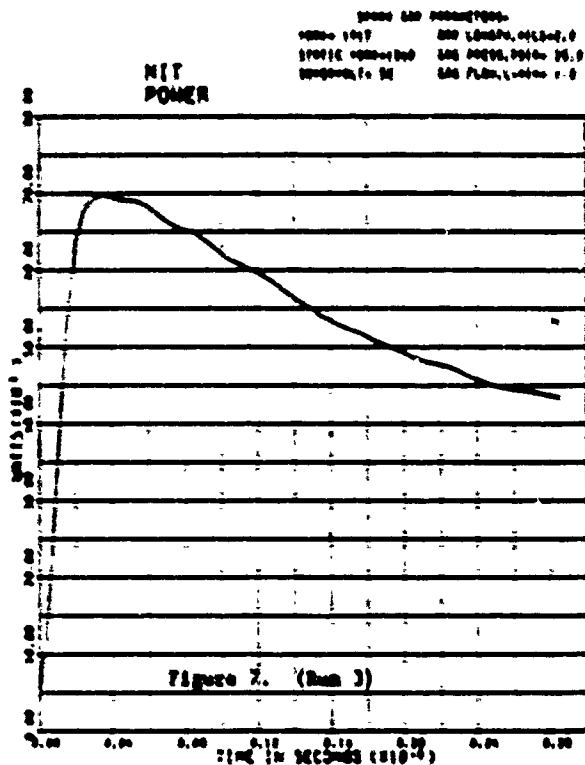


TABLE I.

Run #	Gas	$\alpha$	$\beta$	Gap Field (V/cm) $\times 10^4$	$E$ ( $\frac{V}{cm}$ ) $\times 10^6$	Max Gap Energy (mJ)	Peak Power (kW)	10-90% Current Rise Time (ps)	$p_d$ (mm-corr)
1	Argon	2.2	.766	18.9	730	.112	60	170	263
2	Argon	2.2	.547	25.1	970	.245	120	155	263
3	Nitrogen	2.7	.543	37.7	2930	.155	70	150	65.8
4	Nitrogen	6.6	.481	50.1	3070	.318	130	150	65.8

### References

1. Kassel, S.; Hendricks, C. D.; *Soviet Research and Development of High-Power Gap Discharges*, R-1333-ARPA, January 1974.
2. Sorensen, T. P.; Ristic, V. M.; *Rise Time and Time-Dependent Spark-Gap Resistance in Nitrogen and Helium*, J. Appl. Phys., Vol. 48, No. 1, January 1977.
3. Carr, W. K., Jr.; Massie, J. A.; *Time Resolved Resistance During Spark Gap Breakdown*, Proc., Second Pulsed Power Conf., May 1978.
4. Mesyats, G. A.; Bychkov, Yu. I.; Kremnev, V. V.;

*Pulsed Nanosecond Electric Discharges in Gases*, Soviet Physics - Technical Physics, Vol 16, No. 3, 1972.

5. Mesyats, G. A.; Bychkov, Yu. I.; Iskol'dskii, A. I.; *Nanosecond Formation Time of Discharges in Short Air Gaps*, Soviet Physics - Technical Physics, Vol. 13, No. 3, 1969.

## 4.3

## ELECTRON DENSITIES IN LASER-TRIGGERED SPARK GAP DISCHARGES

R. J. Crumley, P. F. Williams, M. A. Gundersen and A. Watson

Dept. Elect. Eng., Texas Tech Univ.  
Lubbock, Texas 79409Abstract

The results of experiments designed to measure electron densities from measurements of Stark broadened spectral profiles in laser-triggered discharges in hydrogen are reported. Temporally and spatially resolved data have been obtained both during and after the arc for discharges in hydrogen. Evidence of a shockwave is presented, consistent with the observations of other investigators.

Introduction

Laser-triggered spark gaps offer a number of important advantages in applications requiring switching of high voltage at high currents with low jitter in the switch closure time. In such gaps the triggering laser is focussed onto one electrode, usually entering the gap through a small hole in the opposite electrode and passing along the gap axis. Even though the gap voltage is held at a value significantly below the static breakdown value, the laser induces the gap to break down completely after only a short delay. Study of the basic processes responsible for the breakdown phenomena are of considerable interest, not only because of the direct practical value of such studies, but also because of the critical role space charge-induced fields must play in the initial breakdown.

We report the results of studies undertaken to determine the electron density in a laser-triggered hydrogen arc. Electron densities were determined from the measured full widths of the

Stark-broadened atomic linewidth using the relation<sup>1</sup>

$$\Delta\lambda = C(N_e, T) \Delta\lambda^{3/2}$$

where  $N_e$  is the electron density,  $\Delta\lambda$  is the full Stark width, and  $C(N_e, T)$  is a coefficient weakly dependent upon  $N_e$  and temperature. Time-resolved data have been obtained both during and after the arc for discharges in hydrogen, and spatially-resolved data have been obtained for times corresponding to the beginning and end of the arc.

The experimental arrangement is shown in figure 1, and consists of a spark gap enclosed in a cell which is evacuated and then backfilled to the desired pressure with hydrogen. The aluminum electrodes have a constant field profile, and a voltage less than the static breakdown voltage is impressed across them using a coaxial cable system, charged through a large resistor by a regulated power supply. The length of the cable is such that, when the load is properly matched to the transmission line, laser-triggering of the gap results in a clean current pulse of about 1  $\mu$ sec. duration. A nitrogen laser pulse,  $\approx 5$  mJ. in 10 nsec., enters the gap axially through a 2 mm. hole in one electrode and is focussed onto the other electrode, triggering the gap. The emission from the discharge exits the cell through a window transverse to the gap axis, and is spectrally-dispersed with a 0.5 m. spectrograph. An optical multichannel analyzer is used to detect

the light and a spectrum covering a range of  $200 \text{ \AA}$  is obtained in a single shot with good sensitivity. Time resolution to 50 nsec. is obtained by gating the detector. Electron densities are then determined from the Stark broadened linewidths (usually the  $H_\beta$  line).

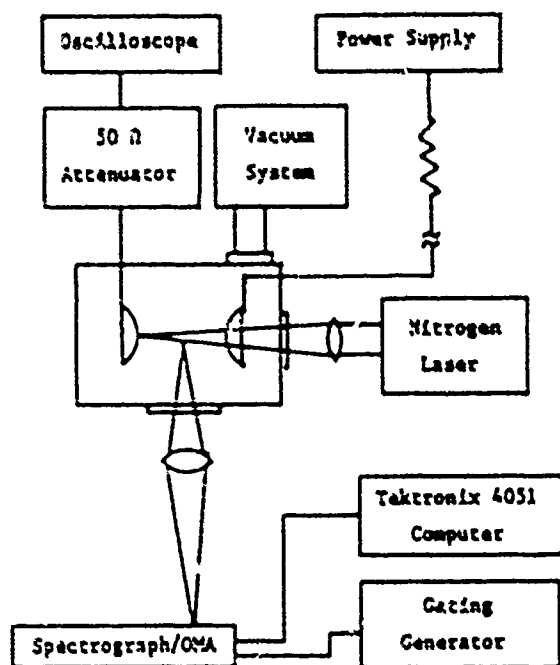


Fig. 1. Experimental Arrangement

### Results

Two sets of data are discussed here. The first set measures the electron density, averaged through the center of the arc, for times throughout the life of the arc and into the afterglow. The second set of data shows the radial variation of the electron density, at two set times.

The temporally resolved data (Fig. 2) indicates that in the arc phase a laser-triggered discharge in an under-volted gap is similar to a conventionally-induced discharge in an over-volted gap. The electron density is maximum at the time when the arc bridges the gap, causing the complete collapse of the gap voltage, and decays

fairly rapidly to a nearly constant value. After the arc is extinguished, the density decays rapidly with an apparently simple exponential time dependence having a time constant of 300 nsec.

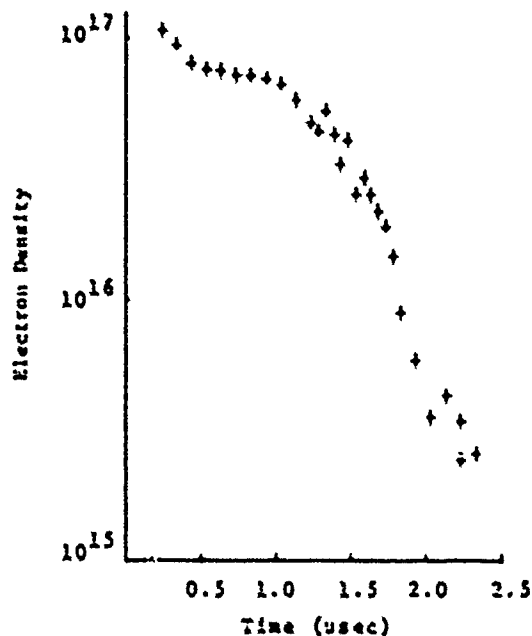


Fig. 2. Temporally-resolved electron densities observed through center of discharge.

Spatially-resolved data were obtained by taking several spectra across the diameter of the discharge and performing an Abel inversion, which extracts the radial dependence from the laterally-observed raw data. Radially-resolved data were obtained at two times corresponding to the beginning and end of the arc, and are shown in figures 3 and 4. The results of these measurements indicate that the electron density at the center of the arc corresponds to that of the temporally-resolved measurements, and falls off smoothly from those values to a point corresponding to the radius of luminosity. At the outer edges of the discharge an increase of electron density occurs. We believe this behavior to be evidence of a shockwave expanding radially from the discharge. In conventional, over-volted gaps, shockwaves have

been predicted by Braginskii,<sup>2</sup> and have been seen by Koppitz<sup>3</sup> using a Schlieren technique. The characteristics of the increase in electron density seen here are consistent with the results of Koppitz.<sup>3</sup>

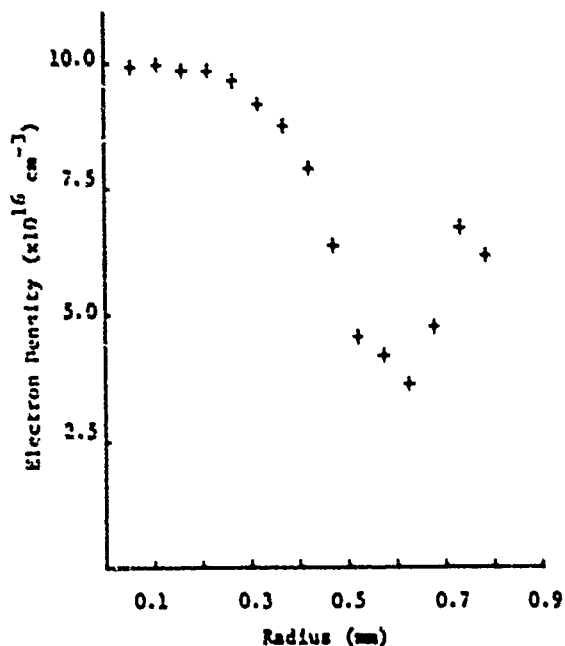


Fig. 3. Radially-resolved electron density at beginning of arc.

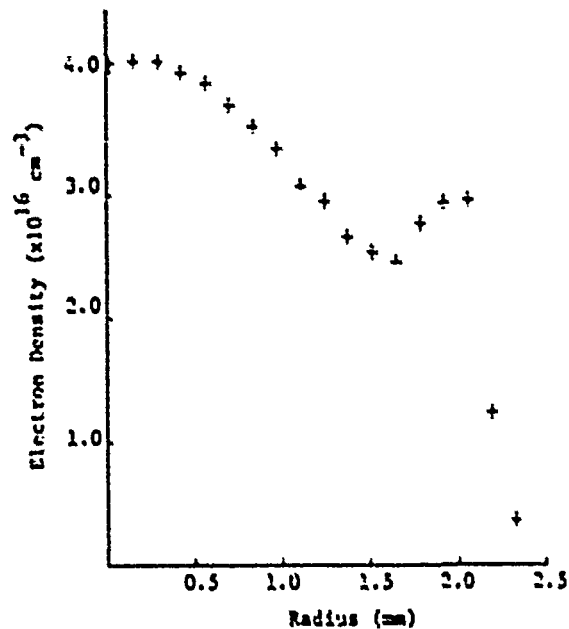


Fig. 4. Radially-resolved electron density at end of arc.

#### References

1. Griem, Hans, Plasma Spectroscopy, McGraw-Hill, 1964, p. 305.
2. Braginskii, Soviet Physics JETP, 34, p. 1548, 1958.
3. Koppitz, Jorn, Z. Naturforschg., 22a, p. 1089, 1967.

This work has been supported by the AFOSR and Research Corporation.

# ELECTRICAL BREAKDOWN IN WATER IN THE MICROSECOND REGIME

D. B. Fenneman and R. J. Gripshover

Naval Surface Weapons Center  
Dahlgren, Virginia 22448

## ABSTRACT

This paper describes the research on electrical breakdown in water currently being pursued at NSWC/DL. The experimental apparatus is described in some detail. Results of over 500 tests are presented. Breakdown events were observed predominantly in the 2-10 microsecond time domain for applied electrical fields in the range 200-500 KV/cm. The wide scatter of the breakdown time which is intrinsic to the phenomena requires a careful examination of the statistics of the data.

## Background

Water, because of its high dielectric constant, self-repairability, cheapness and ease of handling is finding increasing use as the intermediate energy store in pulse power devices. Large machines, which are high energy as well as high power devices can be expected to have the water capacitor charged in the multi-microsecond regime. The water must not suffer electrical breakdown during this charging time. These considerations have led the pulsed power group at NSWC/DL to actively pursue research on this topic. The goals of the effort are to provide empirical performance comparisons in order to establish design-trade off rationale, and provide experimental evidence to test various theories of breakdown.

In the regime to be reported on in this paper, the process of electrical breakdown has wide (apparently) statistical variation. To measure these intrinsic variations requires large numbers of tests and good control on all process variables. These consider-

ations have formed the rationale of the experimental approach.

## Apparatus

The test apparatus built at NSWC/DL explicitly for water breakdown research consists of three components (refer to Fig.(1)). A water conditioning system, an electrical system, and the test cell.

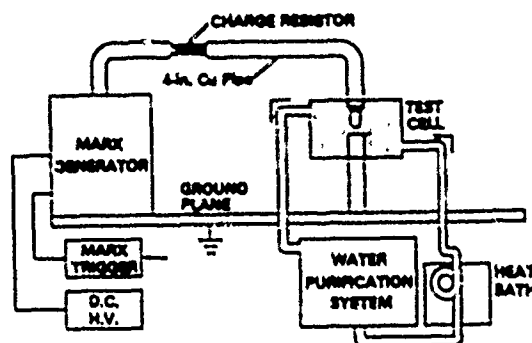


Figure 1. Water Breakdown Experimental Apparatus

The water conditioning system was designed to provide water which could be well characterized. It consists of (a) a pump of > 4 GPM capacity, (b) a mixed bed deionizer, (c) a deaeration column, (d) a heat bath to maintain temperature and (e) an ultra-violet sterilizer to suppress algae growth. This last item is used only intermittently and may not be necessary. Resistivity probes measure the resistivity of the water at the outlet of the deionizer and at the outlet of the test cell. Temperature is measured by thermistor probes located at the outlet of the heat bath, at the outlet of the test cell and in the deaeration column. The pressure in the deaeration column is maintained by

a vacuum pump, protected from water vapor fouling by a trap cooled by an alcohol-dry ice slurry, the pressure is measured by a mercury manometer. The water is conditioned for about 3 hours before testing, and continually during testing. All told, about 40 gallons of treated water are continually circulated. It takes about an hour to bring the resistivity of the water to above 18 M $\Omega$ -cm (25°C) from the 1-3 M $\Omega$ -cm value the water degrades to overnight. The resistivity obtained in the system is at or near the ultimate value for water and success in obtaining such high values is ascribed to flowing continually above 2.5 GPM and to the fact that with the exception of the test electrodes, the copper coils of the heat bath, and the small area of the stainless steel probes, the water touches no metal or glass. All pipes and valves are hard PVC, the pump has a nitrile impeller and the deaeration column is plexiglas. Deaeration takes longer than deionizing, especially if the test cell has been opened to air. At equilibrium the percent deaeration is computed as

$$p - P_{H_2O}(T)$$

$$\% \text{ Deaeration} = 100 \times \left( 1 - \frac{p - P_{H_2O}(T)}{760} \right)$$

where:  $p$  = pressure in column, torr

$P_{H_2O}(T)$  = water vapor pressure, torr

The circuit of the electrical system is shown in Figure 2. The voltage source is a 10 stage Marx generator capable of 500 KV maximum, whose erection time is a couple of hundred nsec. The Marx charges the water test cell through a 4000 $\Omega$  copper sulphate resistor. The voltage also bleeds through a Marx internal resistance of approximately 900 $\Omega$ . Circuit inductance is unimportant and the voltage across the water is closely given by

$$V(t) = .71 V_0 (e^{\omega_1 t} - e^{\omega_2 t})$$

where  $V_0$  = Erected Marx Voltage

$$-1/\omega_1 = R_M C_M = 20 \mu\text{sec}$$

$$-1/\omega_2 = R_C (C_W + C_S) = 2.0 \mu\text{sec}$$

The voltage is measured by a copper sulphate dividing resistor, the current is measured by a Rogowski coil. The observed voltage and current waveforms agree with computer modeling (which takes into account temperature and gap size effects) to the resolution of the oscilloscope traces. Break-

down time is also measured by counting a 100 MHz clock signal gated by the voltage signal. These all are recorded on a Tektronix Model 7844 Dual Beam Oscilloscope. Figure 3 shows a sample test trace.

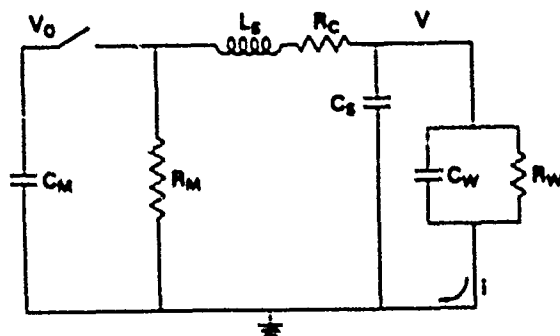


Fig. 2. Electrical Circuit

$C_M$ , Marx Capacitance	22nF
$R_M$ , Marx Internal Resistance	900 $\Omega$
$L_S$ , Stray Inductance	4 $\mu$ H
$C_S$ , Stray Capacitance	.1nF
$R_C$ , Charge Resistor	4K $\Omega$
$C_W$ , Water Capacitance	.4-.5nF
$R_W$ , Water Resistance	>300K $\Omega$

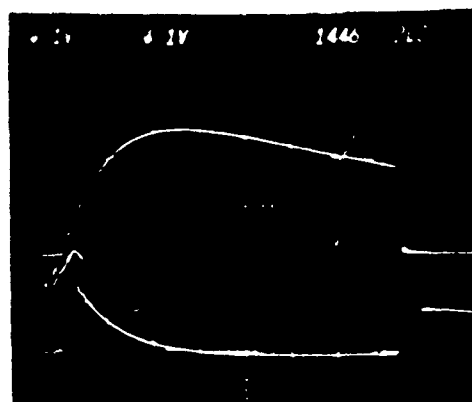


Fig. 3. Sample Data Trace

Top Curve  $V(t)$ , 1 CM = 41.7 KV

Bottom Curve  $i(t)$  1 CM = 20 A

At Breakdown  $V(t) \rightarrow 0$  and  $i(t) \rightarrow$

$V_0 \exp(-R_M C_M t) / R_C$  since capacitor is shorted. Starting glitch due to Marx gap transients.

The test cell is a plexiglas box 20"x20"x14" which holds the test electrodes. The electrodes are tough pitch electrolytic copper in a hemisphere ( $R = 1"$ )-plane configuration. The final surfacing is done by sand blasting with glass beads (Blastolite, size B1-10). This surfacing technique

is chosen, not out of any belief that it produces a superior surface, but because it produces a well-characterized, easily restored and reproducible surface. The gap spacing is measured to .001" by a cathetometer before each shot.

Process Variable	Condition
Water Temperature	19 $\pm$ 2°C
Water Flow Rate	> 2.2 GPM
Water Resistivity	> 18 MΩ-cm
Pressure in Test Cell	1.3 psig
% Deseration	> 95%
Electrode Material	Electrolytic Cu.
Surfacing	Sandblasted
Stressed Area	300 mm <sup>2</sup>
Gap Spacing	2.3-6.4 mm

Table 1. Summary of Experimental Conditions

### Results

For any real apparatus the applied field is a function of time, consequently there is a built in dependence of field at breakdown to time of breakdown for any single test. Further, any real apparatus can only span a finite region of the E-t plane. The region investigated in this work is bounded by the curves shown in Figure 4. Also displayed in this figure are the experimentally observed point pairs ( $E_{MAX}$ ,  $t_b$ ) where  $E_{MAX}$  is the maximum field experienced before breakdown and  $t_b$  is the time at which breakdown occurred, measured from onset of voltage. The touchstone of water breakdown field-time experiments is the relation due to Martin<sup>1</sup>:

$$M = E_{MAX} (t_b - t_0)^{1/3} = \text{constant}$$

Here,  $t_0$  is a time parameter usually defined as the time when the applied field exceeds some given fraction of its maximum value (e.g., 50%, 63%). A linear regression<sup>2</sup> on the relation

$$t_b = t_0 + (M/E_{MAX})^3$$

yielded from the data the values

$$M = .562 \text{ (MV/cm)} \cdot (\text{usec})^{1/3}; \quad t_0 = 0.53 \text{ usec}$$

This value of M is close to the value .6 usually quoted for uniformly stressed electrodes. The value  $t_0$  corresponds to the time  $E(t) = 0.28 E_{MAX}$ . The regression curve is also plotted in Figure 4.

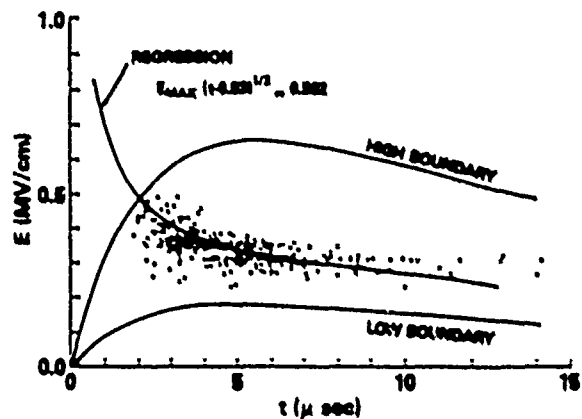


Fig. 4. Breakdown Time vs Maximum Field - Summary of Data. The dots are the experimental points ( $E_{MAX}$ ,  $t_b$ ).

To examine the properties of M as a measure of breakdown, the quantities

$$M_i = E_{MAX} i (t_{b_i} - .53)^{1/3} \quad i = 1, \dots, 294$$

were computed from the data. The result is displayed as a histogram, Figure 5. The histogram shows the mean and mode are close to the regression value of M.

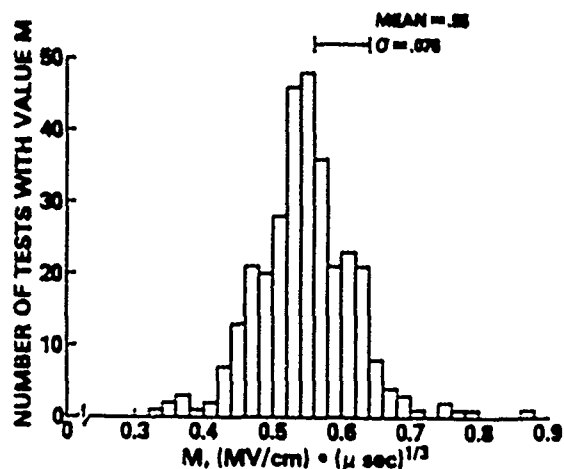


Fig 5. Histogram of Martin's Relation

A criticism of the regression analysis stems from the observation that the standard deviation of  $t_b$  is not constant over the population. This is shown in Figure 6. This graph was generated by arranging the data in order of increasing  $E_{MAX}$  and computing the means and standard deviations of  $t_b$  for all



sets of 30 ordered points. Whether this variation in the RMS deviation of  $t_b$  with  $t_b$  is intrinsic to the phenomena, or due to the particular waveform used in the experiments, or one of the process variables is a point yet to be resolved.

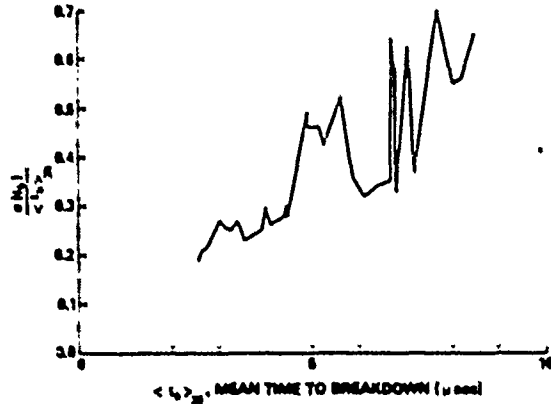


Fig. 6. Variation of Fractional Deviation of Breakdown Time with Mean Time to Breakdown, Running 30 Point Averages.

The same set of electrodes was used for all tests. These electrodes sat in deaerated water for over two months. During this time a thin, uniform patina of oxide developed on the sandblasted copper surfaces. The oxidation rate in the deaerated water was noticeably slower than when the surfaces were exposed to air. Aging (i.e., the change in breakdown character with time, or number of breakdowns suffered) due to two mechanisms could be postulated. One mechanism due to the oxide layer buildup, the other due to pitting and scarring from repeated breakdowns. Aging was studied by arranging all breakdowns in the chronological order in which they occurred and computing the running statistics of  $M$ . The results are displayed in Figure 7. There seems to be no clear trend due to aging. This is somewhat surprising for at the conclusion of the tests, the electrodes were highly scarred and pitted. The positive electrode was more severely damaged than the negative. The pits, reminiscent of Moon craters when viewed under the microscope, were of uniform diameter ( $\sim .17$  mm) and uniformly distributed over the stressed area. Breakdowns were visually observed through the cathetometer during testing and showed no tendency to occur in the same place.

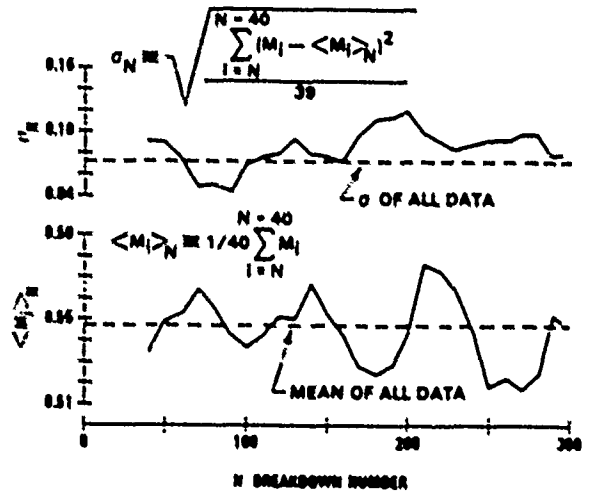


Fig. 7. Aging Study. If aging was strong, it would be expected that these curves would have a monotonic trend up or down.

An apparent threshold effect at about .275 MV/cm was observed, below this value breakdown often did not occur. Figure 8 shows the results of a series of tests used to explore this phenomenon. At these lower field values sets of at least 10 tests with identical waveforms were performed and the probability of breakdown defined as

$$\frac{\text{The no. of tests in a set breaking down}}{\text{Total no. of tests in a set}}$$

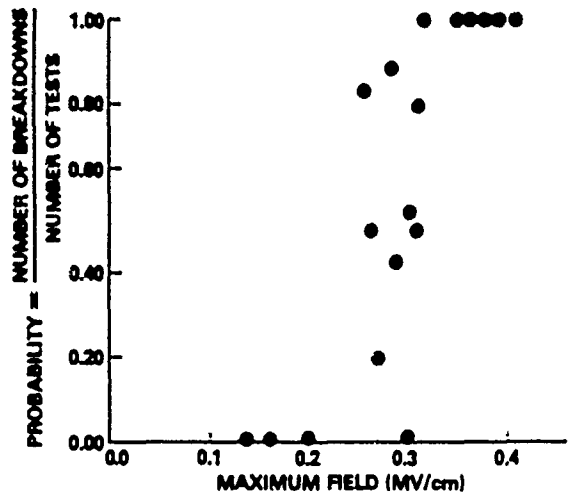


Fig. 8. Threshold Study

It should be made clear that the abscissa of Figure 8 is the maximum field the waveform would have achieved if breakdown didn't take place, which is not necessarily the same as the maximum field achieved. Also the above simple definition of breakdown probability is confounded by the experimental observation that the probability of breakdown on the nth test depends on whether the n-1st test broke down, which is to say each test is not a Bernoulli chance. This effect, which is difficult to quantify, was explored in a qualitative way. It was established that, following application of a high stress, the low stressed test would probably break down. But the application of low stress a second time would not result in break down. This effect is ascribed to transitory damage, wherein a violent breakdown produces surface conditions which weaken the hold-off strength, while a mild breakdown following repairs the damage.

#### Summary

It has been the intent of this paper to report the findings to date of the continuing research efforts on electrical breakdown in water being pursued at NSWC/DL. It has been shown that Martin's Relation is a good gross measure of breakdown in the region 2-10  $\mu$ sec, but that shot to shot variability in time of breakdown is large. Aging seems unimportant and there is evidence for a threshold. Obviously much more work must be done. The effects of temperature, resistivity, electrode material, and surfacing need to be studied. The time regime should be extended to the 20 and 50  $\mu$ second domains.

#### Acknowledgement

The authors gratefully acknowledge the skill and care of L. W. Hardesty and K. Chilton who constructed the apparatus and assisted in the testing.

#### References

1. J. C. Martin, I. Smith, and H. G. Herbert, "Dielectric Strength Notes", Staff Reports AWRE, Aldermaston, England, 1965.
2. D. H. Menzel "Fundamental Formulas of Physics", Vol 1, Dover Publications, New York 1960.

Research Program and by DARPA through the Naval Air Systems Command.

This work was supported by the NAVSWC Independent

## PULSED ELECTRON FIELD EMISSION FROM PREPARED CONDUCTORS\*

G. B. Frazier

Physics International Company  
2700 Marced Street  
San Leandro, California 94577

Abstract

The electron emission characteristics of metal cathodes subjected to pulsed electric fields in the absence of insulating magnetic fields has been investigated experimentally. Uniform electric fields in the range of 0.2-0.8 MV/cm were applied to 50 cm<sup>2</sup> surfaces under vacuum in single pulses of ~ 60 ns duration at a voltage of ~ 0.5 MV. Bare metals and metals coated with dielectric materials were studied. Results show that bare metals with freshly prepared surfaces can withstand fields of ≥ 300 kV/cm for ≥ 40 ns without significant emission. Emission-induced discharges degrade the surfaces such that full space-charge-limited current densities (100-250 A/cm<sup>2</sup> for this experiment) are obtained at fields as low as 200 kV/cm on subsequent pulses. In the case of coated surfaces, it was found that dielectrics could occasionally suppress emission completely up to ~ 300-400 kV/cm, and unlike bare metals, could partially suppress emission after having passed significant current at fields up to 0.6 MV/cm.

Introduction

Electron emission from surfaces subjected to high electric fields in a vacuum is an important consideration in a wide variety of pulsed power applications. The phenomenon has been extensively investigated for the dc case. Early work<sup>1</sup> provided valuable insight into basic emission and vacuum breakdown processes, but with the advent of high-voltage, high-current, pulsed electron accelerators, it became necessary to investigate the phenomenon on a submicrosecond time scale. Some work was done on this problem in the late sixties<sup>2</sup>

\*Work partially supported by the Lawrence Livermore Laboratory.

as part of the development program for the AURORA<sup>3</sup> generator, and more recently by Milton<sup>4</sup> using bare stainless steel cathodes. The data reported here are the result of a limited, empirical study of the phenomenon under a specific set of pulse and electrode conditions.

The experiment was conducted to investigate the feasibility of using dielectric coatings to suppress emission. Investigation of coatings under pulsed conditions was considered particularly important for advanced, high-power laser exciters because such devices typically do not produce the large, self-generated magnetic fields used to insulate structures in low impedance accelerators.<sup>5,6</sup>

Description of Experiment

The experimental apparatus (Figure 1) consisted of a 38-cm-diameter aluminum vacuum chamber containing a sample holder and current collector assembly. The samples were 23-cm-diameter by 6.35-mm-thick disks which were held in place by a radiused clamp ring. The holder was attached to the negative output electrode of a Physics International Company PULSERAD<sup>®</sup> 225-W, which produces a 12 kJ, 60 ns pulse at 5.3 Ω when configured as an REBA.

The experimental parameters are given in Table 1. The basic experimental approach was to install prepared samples, then fire the 225-W at the ~ 530 kV output level using a variety of spacings to achieve different peak electric field magnitudes. The general pattern for each sample was from low to high values of field. Most samples were initially stressed to 200-250 kV/cm (2.5-2.0 cm spacing), then subjected to gradually increased fields for successive shots. "Up-and-down" scans were often used to investigate degradation effects.



TABLE 2. TYPICAL STAINLESS STEEL RESULTS

	Shot	$E$ (kV/cm)	$J$ (A/cm <sup>2</sup> )	$J/J_{LC}$	Remarks
Sample 1	86	223	2.7	0.02	"Break" on 2nd pulse
	87	207	150	1.65	
	88	197	104	0.80	
	89	244	226	0.96	
Sample 2	91	197	3.8	0.03	"Break" as before
	93	201	129	0.96	
Sample 3	94	344	199	0.50	~ 40 ns current delay

single pulse of  $\sim 200$  kV/cm, but will emit current at the full space-charge-limited value thereafter (aluminum behaved similarly). Moreover, all samples (both metals) tested showed significant emission during the second pulse\* of the first shot, usually  $\sim 5$ -10 kA.

There is also evidence that virgin surfaces can withstand higher fields for brief times. On shot 94 a fresh sample was initially subjected to 344 kV/cm. The resultant 10 kA peak current represented approximately one-half the space-charge-limited maximum, but current onset was delayed; it occurred  $\sim 40$  ns later than on shot 93 for which a previously stressed sample was used (see Figure 3).

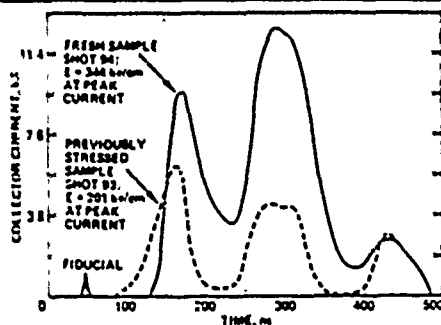


Figure 3 Current onset delay of fresh stainless steel sample.

The basic conclusions drawn from bare metal studies are that: (1) fields of between 200 and 300 kV/cm are sufficient to cause full space-charge limited electron current to be emitted from either aluminum or stainless steel surfaces which have

\*The 225-W produced a train of multiple pulses separated by  $\sim 75$  ns for this experiment because of the high impedance presented by the load.

previously been stressed; and (2) a single pulse will permanently degrade freshly prepared surfaces. Surface finish had a second order effect; the onset of first pulse current was delayed slightly when aluminum was highly polished. Highly polished stainless steel was not tested; reports from similar experiments at the Naval Research Laboratory had previously shown that little was changed by polishing.<sup>7</sup> Late-time sustaining currents, as reported by Milton,<sup>4</sup> were not observed.

#### Coated Surface Results

Several coatings were tested: aluminum anodizing, spray paints, epoxy, PRT-100 (lead-zirconate-titanate); and high vapor-pressure silicon oil. Aluminum was the only type of substrate used. Anodized samples were prepared by the Kaiser Aluminum Center for Technology, Pleasanton, California. Slow cooling was used to retard crazing, and anodizing thickness was held constant to  $\pm 0.0001$ -inch. Overall quality of anodized samples was excellent.

The electron emission characteristics of the coated surfaces differed significantly from those of bare metals. Some coatings were often able to completely suppress emission for several pulses (rather than just one) as the field was raised from the  $\sim 200$  kV/cm initial value to values as high as 300-400 kV/cm. Also, once emission did take place, some coatings continued to be partially effective because they kept emitted current levels below the space-charge-limited maximum (rather than equal to it). Degradation of coatings did occur, but its occurrence was gradual.

"Complete" emission suppression (i.e., where the emitted current level was below the detector threshold,  $J \leq 3$  A/cm<sup>2</sup>) is shown in Figure 4. Shots 63, 64, and 65 subjected the sample (which had a 0.0014-inch-thick anodized layer over a 32 finish machined surface) to 230 kV/cm, 235 kV/cm, and 310 kV/cm with minimal emission. Thereafter, current densities ranged from  $\sim 5$  A/cm<sup>2</sup> at  $\sim 250$  kV/cm ( $J/J_{LC} \sim 0.02$ ) to  $\sim 450$  A/cm<sup>2</sup> at  $\sim 500$  kV/cm ( $J/J_{LC} \sim 0.55$ ). The shaded area is called the "pre-threshold" region for this discussion.

The gradual degradation of anodized aluminum

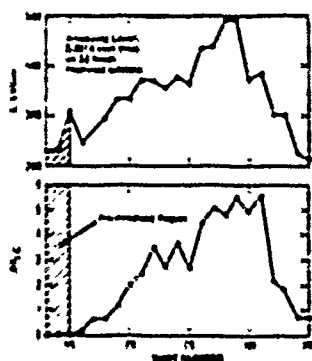


Figure 4 Shot record for anodized sample.

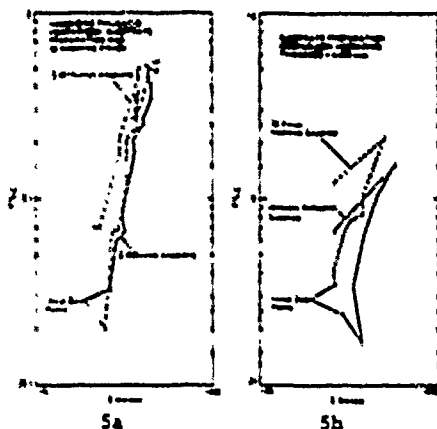


Figure 5(a, b) Comparison of anodized aluminum samples.

and the partial suppression it exhibits is shown graphically in the comparison "stress history" plots of Figure 5. "Up-and-down" scan data such as those of Figure 4 (the 0.0014 inch data of 5b are the same data as Figure 4) are plotted by connecting successive data points with lines to show the influence of the testing method. The shape of such plots depends upon both the rate at which field is increased for successive shots, and the pre-threshold stress of the sample (only post-threshold data are plotted). When pre-threshold stress includes several pulses between 200 and 250 kV/cm,  $J/J_{LC}$  tends to increase more rapidly as  $E$  is raised than if  $E \geq 250$  kV/cm is used for initial pulses. The solid curves of Figure 5 are examples of the effect. Data at the right (5b) included 5 pre-threshold shots between 200 kV/cm and 260 kV/cm; at the left (5a) initial stress was  $\geq 260$  kV/cm.

The comparison of anodizing thicknesses (Figure 5b) showed little difference between

samples. The thicker anodizing layer (0.003 inch) seems slightly more effective in suppressing emission because  $J/J_{LC}$  is  $\sim 20$  percent lower on average than the thinner sample, but the difference is too small to be considered significant. The effect of substrate finish is more striking (Figure 5a). The value of  $J/J_{LC}$  at a given value of field was  $\sim 40$  percent lower for the sample which had been prepared by using successively finer grit polishing on a J2 machine finish until optical quality specular reflection was obtained before the 0.001-inch anodizing layer was added.

The improvement made by polishing the substrate was not expected. Microprojections should be shielded by the high dielectric constant anodizing, making substrate finish less important. But the improvement was impressive; the sample withstood five pulses of between 290 kV/cm and 320 kV/cm in the pre-threshold region, then emitted a maximum of 15 percent space-charge limited current ( $J/J_{LC} = 0.15$ ) at  $E = 0.57$  MV/cm. Results, however, are not conclusive because only one such sample was tested.

Most other coated samples behaved similarly to the anodized ones; some, however, were better than others. All coated samples had some low emission pre-threshold region if initial stress was  $\sim 200$  kV/cm, and all suffered permanent degradation once significant electron current had been emitted. In the pre-threshold region, electron emission from some aluminum samples was as effectively suppressed by spray paints as by anodizing. In one example, a J2 finish machined surface covered with Xylon Flat White No. 1052 (Fed. Color Std. 595 No. 37875) did not emit above  $3 \text{ A/cm}^2$  for nine shots; the average field was  $304 \text{ kV/cm} \pm 20$  percent, and the maximum pre-threshold stress was  $401 \text{ kV/cm}$ . A simple silicon oil coating (Dow-Corning #704) was sufficient to keep  $J/J_{LC} \leq 0.16$  for fields as high as  $0.4 \text{ MV/cm}$ , if it were reapplied to a bead-blasted aluminum surface after each shot. All solid coatings were observed to suffer localized damage very similar to that described by Jedynak<sup>5</sup> in his dc experiments with epoxy.

#### Discussion of Results

It is believed<sup>9,10</sup> that large currents are

emitted from cold, bare metals by a process known as explosive emission. In this process, electrons are first field-emitted from micro-projections (whiskers) when the electric field at the tips of whiskers exceeds about  $10^7$  V/cm. The resultant field emission current then explodes these micro-projections by fast resistive heating to create local plasmas called cathode flares. Current in the vicinity of the individual flares is limited by space charge, so the total current emitted from surfaces like those used in the experiment described here would be determined by the fraction of the surface area covered by plasma from the flares. If flares expand at the postulated rate of  $\sim 10^6$  cm/s,<sup>10</sup> the 50 cm<sup>2</sup> surface area would require  $\sim 10^4$  equally spaced, simultaneous explosions to achieve  $J/J_{LC} \sim 1.0$  in  $\sim 50$  ns.

The bare metal results described here are interpreted as evidence that careful finishing tends to remove most whiskers that emit (and explode) most readily, such that when fields of several hundred kV/cm are applied, several tens of nanoseconds are required before explosions begin to occur among the remaining smaller ones. The irreversible damage caused by a single 200 kV/cm pulse is evidence that discharges have the effect of creating favorable emission sites widely over the cathode surface. This is in conflict with Milton's observations<sup>4</sup> of cathode conditioning, but tends to support the idea that microprojections are formed by the action of pondermotive forces on metal in the liquid phase near explosion sites.

The coated sample results tend to support the idea that emission can be suppressed if micro-projections are buried in a dielectric that reduces local fields and prevents free electrons from being emitted into the vacuum. However, the fact that strong emission still takes place at fields of 300-500 kV/cm, and that observable damage to coatings results, indicates that coatings fail locally as a result of bulk breakdown, leading to explosive emission from substrate metal when subsequently stressed. The bulk breakdown may be caused by imperfection in coatings, or by field increases caused by direct emission from the dielectric surface at the vacuum interface. Such emission has

been observed,<sup>11,12</sup> but further investigation is needed to quantify its influence on the results obtained here.

#### Acknowledgements

The author wishes to thank C. Stallings, who provided valuable guidance and technical input, I. Smith for many illuminating discussions, D. Pellinen for his help with diagnostics, and L. Bradley and L. Schlitt, who made the experiment possible.

#### References

1. For a review of early work see D. Alpert, D. A. Lee, E. M. Lyman, and M. F. Tomaschke, *J. Vac. Sci. Technol.*, **1**, 35 (1964); or R. Hawley, in L. L. Alston (ed.), *High Voltage Technology*, Oxford University Press, London (1968).
2. Internal Report PISR-127, Physics International Company, Vol. II, (July 1969), unpublished.
3. B. Bernstein and I. Smith, *IEEE Trans. Nucl. Sci.*, **NS-18**, 294 (1971).
4. O. Milton, *IEEE Trans. on Elect. Insul.*, **EI-9**, No. 2 (June 1974).
5. J. Creodon, *J. Appl. Phys.*, **38**, 1070 (1977).
6. I. D. Smith, P. D'A. Champney, and J. Creodon, *Proceedings 1st International IEEE Pulsed Power Conference, IICS-1* (1976).
7. D. Conze, private communication.
8. L. Jedynak, *J. Appl. Phys.*, **35**, 1727 (1964).
9. G. A. Masyats, *Proceedings VI International Symposium on Discharges and Electrical Insulation in Vacuum*, p. 21 (July 1974).
10. S. P. Bugaev, E. A. Litvinov, G. A. Masyats, and D. F. Proskurovskii, *Sov. Phys.-Usp.*, **18**, No. 1 (1975).
11. G. Frazier, unpublished.
12. R. Anderson, private communication.

## INVESTIGATION INTO TRIGGERING LIGHTNING WITH A PULSED LASER

CHARLES W. SCHUBERT, JR., CAPT. and JACK R. LIPPETT

USAF FLIGHT DYNAMICS LABORATORY, ATMOSPHERIC ELECTRICITY HAZARDS GROUP

Abstract

Theoretical and experimental considerations for the triggering of lightning with a high-power pulsed laser are discussed. The mechanisms of laser-induced clean air breakdown, aerosol breakdown, and channel heating over a long path for the purpose of initiating and possibly guiding lightning are reviewed. It is shown that long path (of the order of one kilometer) ionization through laser-induced clean air breakdown is theoretically possible. Channel heating over a long path appears possible, but requires prohibitive energies. Indications are that long path ionization can be enhanced by taking advantage of the significantly reduced power requirements for aerosol breakdown. The Mt. Baldy, New Mexico, experimental test site for 1978-1979 experiments and triggering attempts is briefly described.

Introduction

In early 1978, the Air Force Flight Dynamics Laboratory and the Air Force Weapons Laboratory initiated a joint two-year program to attempt to trigger lightning with a laser beam. In the year and a half since then, a Laser-Triggered Lightning Experiment (LTLE) test station has been assembled. Triggering attempts using this station will begin in the next few weeks.

During the course of the LTLE program, we have learned, if nothing else, that theoretical considerations for triggering lightning with a laser beam are fraught with unknowns. A review of some of those considerations is presented in this paper. The review begins with a look at the lightning process itself, and the posited criteria for triggering lightning with a laser beam. Laser effects are then summarized and compared, where possible, to the triggering criteria. A description of the test station to be used in the actual triggering attempts concludes the paper.

The Lightning Process

It is generally believed that a strike begins with

a localized breakdown, or free electron cascade, in a region of a cloud containing a high electric field. The cascade is thrust from the cloud in the form of a stepped leader which moves toward the ground in steps approximately 50 meters long, with pauses between steps of about 50 microseconds. As the leader reaches the near vicinity of the ground, it is met by a highly luminous, high-velocity return stroke, which is the component of lightning actually seen with the naked eye. The return stroke goes up the channel, progressively drawing charge deposited by the stepped leader and enters the cloud. After a pause of generally less than 100 milliseconds, a dart leader—a segment of lightning about 50 meters long—may proceed down the original path, and initiate another return stroke. The process may repeat two to twenty times to produce a single lightning flash, whose total duration may be of the order of one second. (Ref 1).

A theory explaining all aspects of this sequence of events has yet to emerge. Least understood, perhaps, is the breakdown process which begins the sequence. And specifically unknown is the set of conditions which must exist within a cloud before an initial electron cascade can begin. Many parameters are involved in establishing a suitable total environment favorable for an electron cascade, and may include any or all of the following:

- a. Electric field intensity
- b. Electric field temporal variation
- c. Electric field spatial divergence
- d. Cloud-to-ground polarity
- e. Water droplet concentration
- f. Water droplet size distribution
- g. Water droplet rate of motion
- h. Water droplet spatial distribution
- i. Free electron concentration
- j. Free electron spatial distribution
- k. Ionic concentration
- l. Ionic spatial distribution



- m. Ionic specie type
- n. Ionic rate of motion
- o. Particulate concentration
- p. Particulate spatial distribution
- q. Particulate size distribution
- r. Particulate specie type
- s. Particulate rate of motion
- t. Ice crystal concentration
- u. Ice crystal size and shape distribution
- v. Ice crystal spatial distribution
- w. Ice crystal rate of motion
- x. Temperature
- y. Relative humidity
- z. Atmospheric pressure

It is generally assumed that the electric field intensity is the predominant factor in natural lightning initiation. However, other factors could be of equal importance. Of particular significance, we feel, are parameters involving relatively rapid change over time, such as the motion of water droplets, ions, ice crystals and particulates; and temporal variations in the electric field. The single most important changing parameter is difficult to identify and may vary from discharge. Thus, in one case, a bulk motion of charge carriers may initiate a cascade by permitting the electric field intensity in some locality to build to the air breakdown threshold level. In another case, the electric field may remain constant, with threshold conditions reached because of a changing distribution of wind-blown water droplets within a local region of a cloud. Conditions which exist in active thunderstorms are not well known, and the initial phase of the lightning discharge is not well understood. Consequently, a numerical estimate of the degree, speed and spatial extent of parameter change within a cloud which is required for the initiation of natural lightning cannot be made.

#### Triggering Criteria

The triggering of lightning with a laser beam may be accomplished by at least three approaches:

(1) by generating an ionized path over the entire earth-to-ground distance, (2) by producing a rarefied column of air from the ground to a cloud, or (3) by heating and ionizing some local region near or within a cloud. In the first and second approaches, the aim is to short-circuit the cloud charge to the ground, either by providing a partially-conducting path or by lowering the earth-to-cloud dielectric constant. In the third approach, the hope is to upset the electrical balance within a cloud by altering one or more of the environmental

parameters which were listed earlier.

To establish criteria for triggering by using the earth-to-cloud ionized path method, natural lightning data can be used. Since a stepped leader is sufficiently conductive to maintain subsequent lightning components, a laser-generated ionized column with similar characteristics should be able to discharge a cloud. Electron densities within a lightning stepped leader are not known with certainty but have been estimated as being about  $10^9$  to  $10^{10}$  electrons per cubic centimeter. (Ref 1, 2). The time required for a stepped leader to go from the cloud to the ground is about  $10^{-2}$  seconds, and the time required for a return stroke to go from the ground to the cloud over the stepped leader path is approximately  $10^{-5}$  seconds. Consequently, if lightning can be triggered by generating an artificial lightning component with a laser the criteria for the triggering would be  $10^9$  to  $10^{10}$  electrons per cubic centimeter in a channel about 1 kilometer long, with a persistence time of approximately  $10^{-5}$  to  $10^{-2}$  seconds.

The results of spark gap experiments performed by Koopman and Saum can be used to estimate upper limit criteria for triggering lightning using the rarefield channel method. Koopman and Saum found in 1972 that sparks could be guided from one highly charged electrode to another by heating a path between the electrodes with a laser beam (Ref 3). According to their computations, the air density along the beam was reduced to about 64% ambient value for the triggerings.

Criteria for triggering lightning by ionizing a local region in or near a thundercloud cannot, at this point in time, be established. Too little is known about natural lightning initiation to ascertain the type and extent of disturbance which would be needed for an artificial triggering.

#### Laser Effects

To determine the likelihood of triggering lightning with a laser, it is necessary to first examine the effects of a laser beam in the atmosphere. A sufficiently intense laser beam can produce three effects of interest: (1) thermal heating, (2) clean air breakdown, and (3) aerosol (particulate) breakdown. All three effects will occur simultaneously if the laser beam is extremely intense. However, specific effects may be emphasized by a careful selection of laser beam and optical parameters.

### Thermal Heating

The effect of primary interest in thermal heating by a laser beam is the rarefaction, via thermal expansion, of air along the beam channel. The mechanical energy required to lower the density of air along a column of length  $x$  and radius  $r$  to a fraction  $F$  of ambient value is, from pressure-balance considerations

$$E = \frac{1}{2} (\pi r^2 x) n_1 k T_1 \left( \frac{1}{F} - 1 \right) \quad (1)$$

where  $T_1$  and  $n_1$  are the ambient air temperature and density, and  $k$  is the Boltzmann constant. Using a typical value for  $kT_1$  and for  $n_1$  of  $4 \times 10^{-21}$  joules and  $2.5 \times 10^{19} \text{ cm}^{-3}$ , respectively; the energy required to rarefy a column of air one kilometer long and one centimeter in radius to 64% ambient value is about 26,000 joules. Even greater laser energies would be required, since only a fraction of the energy from the laser is converted to thermal heating. Thus, the triggering of lightning with a long path of laser-rarefied air does not appear to be a viable approach.

### Clean Air Breakdown

Laser-induced clean air breakdown is a non-linear process in which laser-heated electrons undergo a cascade of ionizing collisions with atoms. Unless the laser flux intensity exceeds a certain threshold level, which for the  $\text{CO}_2$  laser is  $3 \times 10^9 \text{ W/cm}^2$ , various atomic loss processes will inhibit the cascade. When the threshold for cascade is reached, however, free electron densities rise rapidly to near full first-stage-ionization levels. A detailed theoretical analysis of long path clean air breakdown has been made in The Laser Lightning Rod System: A Feasibility Study, by an author of this paper (Ref 4). The analysis indicates that electron densities meeting or exceeding the criterion for triggering lightning can be generated over a path a kilometer or so in length through the clean air breakdown mechanism. However, the production of such a pathway would require laser flux intensities on the order of gigawatts/cm<sup>2</sup> (for  $\text{CO}_2$  radiation), over a laser aperture tens of centimeters in radius. These requirements

are beyond the capability of lasers currently available.

### Aerosol Breakdown

Aerosol breakdown occurs as the result of the heating and vaporization of particulate matter in the atmosphere. The laser flux required to initiate aerosol breakdown is dependent upon particle size, but can be as much as 100 times less than the flux required for clean air breakdown. An analytical model for aerosol breakdown over a long path has not yet been developed. However, small scale laboratory experiments performed as a part of the LTLE effort indicate that a clean air breakdown band can be lengthened by at least a factor of seven by introducing particulates into the beam path. Additional experimentation will be necessary to determine if a path of ionization can be further elongated by optimizing focusing parameters.

### Laser Effects Summary

Significant ionization or rarefaction of air over the entire earth-to-cloud distance appears unlikely with the energy-limited lasers available today. Aerosol breakdown offers some promise of ionization path elongation, but further study of the process is needed before conclusions can be drawn.

The generation of a limited disturbance in or near a thundercloud remains a viable option for triggering attempts. A laser beam can change air temperature, air pressure, free electron distribution, ion distribution, electric field intensity, water droplet concentration, particulate size distribution, and ice crystal concentration, all in times the order of microseconds. Whether lightning can be triggered by a laser beam will depend on the effect, yet unknown, of rapidly changing these parameters over a limited spatial range. Lightning has been triggered in the past by relatively small disturbances—in-flight aircraft, water plumes, and rocket-launched wires, so the outlook is not discouraging.

### LTLE Test Station Description

A diagram of the test station to be used in the actual triggering attempts is shown in Figure 1.

The lasers to be used are housed in a 35-foot expandable-side van which will be deployed to the top of Mt. Baldy, near Socorro, New Mexico. The Mt. Baldy test site was chosen primarily because of the near-daily occurrence of thunderstorms in the local area during the summer months.

The primary laser to be used in the triggering attempts is a pulsed  $\text{CO}_2$  unit with a design output of 400 joules in a one-to-two micro-second pulse. The  $\text{CO}_2$  beam will be supplemented with the output of a 15 joule Nd-Glass laser having a pulse length of about 30nanoseconds. The beams will be focused by an on-axis Cassegrain telescope comprised of a 60 centimeter diameter copper-plated aluminum primary mirror, and a 20-centimeter diameter secondary mirror, both on adjustable mounts. Deflection of the beam upward will be accomplished by a 76-centimeter diameter copper-plated honeycomb titanium turning flat. A 60-foot aluminum trestle tower adjacent to the beam path will serve as a terminus for any lightning which may be triggered. The optical system is designed for diffraction-limited operation at distances ranging from 100 to 1000 meters. Various focal ranges will be employed during the course of the experiment. Control units, data storage equipment, and personnel will be housed in a separate van adjacent to the laser van. Both vans are of sheet metal construction and are grounded, providing Faraday-cage protection for personnel. Data acquisition equipment will include a current-sensing system on the lightning strike tower, electric and magnetic field antennae, a motion picture camera and a videocassette system. Triggering attempts will be made over a month and a half period beginning in early July, 1979.

#### References

1. Uman, M.A., Lightning, New York: McGraw-Hill Book Co., 1969.
2. Klingbeil, K., and D.A. Tidman, "Theory and Computer Model of the Lightning Stepped Leader," Journal of Geophysical Research, 79:865-869, (February 20, 1974).
3. Sam, K.A. and D.W. Koopman, "Discharges Guided by Laser-Induced Rarefaction Channels," The Physics of Fluids, 15:2077-2079 (November, 1972).
4. The Laser Lightning Rod System: A Feasibility Study, AFFDL-TR-78-60, Wright Patterson Air Force Base: AFSC, June, 1978.

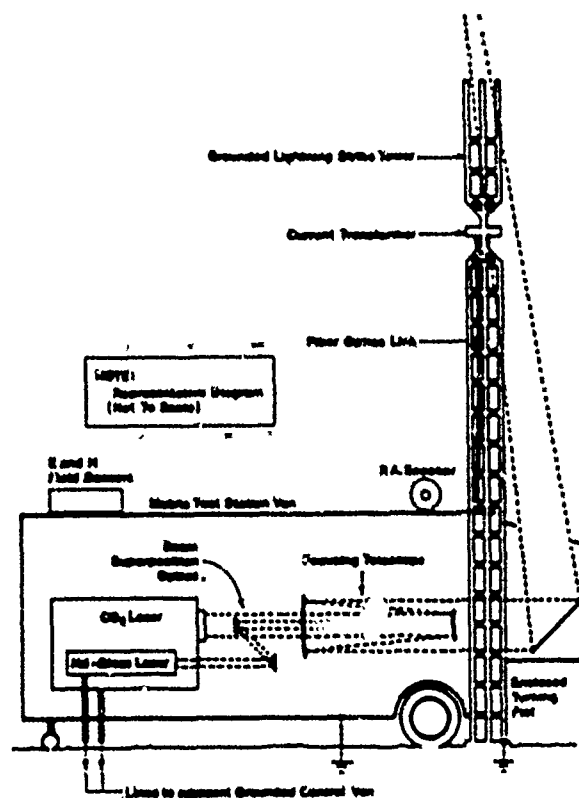


Figure 1.  
LASER TRIGGERED LIGHTNING EXPERIMENT  
REMOTE SITE SET-UP

## LONG ARC SIMULATED LIGHTNING ATTACHMENT TESTING USING A 150 KW TESLA COIL

ROBERT K. GOLKA

Project Tesla, Wendover AFB, Utah 84083  
 In conjunction with Air Force Flight Dynamics Laboratory,  
 Wright-Patterson Air Force Base

Abstract

Recent advances in direct lightning strike testing have been in lightning attachment test techniques and generator development using a very large Tesla Coil (51 feet wide). Breakthroughs in simulated lightning attachment to small scale replica aircraft models which can be adapted to full size operational aircraft have been made in the past year. New high voltage long arc generator developments have succeeded in producing voltages in excess of 15 million volts and arc lengths in excess of 40 feet. The shortest path from the discharge arc electrode to the model extremity using the long arc does not govern the attachment points to the test specimen as it does when a short arc is used to conduct simulated lightning testing. The system just described may also have application as an ultra-high mega-volt source for particle beam weaponry.

Introduction

The purpose of the program was to evaluate the Tesla Coil as a laboratory tool for lightning effects research on aircraft. The ability of a Tesla Coil to generate high voltage pulses at high rep rates results in the capability to create artificial lightning-like streamering and long electrical discharge arcs and makes it a desirable alternative to the high voltage impulse generators currently in use. Another characteristic of a Tesla Coil is that many long arcs can be generated over a very short time period. These Tesla Coil characteristics are highly desirable in lightning effects research using full scale (e.g. an actual aircraft) test specimens.

The primary objective of the program was to evaluate the Tesla Coil as a long arc source for lightning attachment studies. Secondary objectives of the program were to investigate methods for measuring the output characteristics of the Tesla Coil and the attachment characteristics of an Advanced Design Composite Aircraft (ADCA)

model.

Background

At the present time the lightning susceptibility of aircraft is investigated using high voltage impulse generators. In a typical test involving streamering, the direct effects due to arcing are determined by discharging the generator in a localized area of an aircraft in such a manner that streamering is induced without arc attachment to the aircraft. The presence of streamering is indicative of a possible ignition source for combustible vapors. The procedure is repeated until total aircraft coverage is attained. Long arc attachment tests are conducted to verify the primary zones and to identify secondary attachment zones. For these tests the probe of a high voltage impulse generator is positioned to generate a long arc that attaches to the test specimen. The test is repeated a number of times with the probe at different orientations with respect to the test specimen to eliminate the possibility of biasing the attachment point and to simulate lightning flashes approaching from various directions. This is a time consuming procedure because of the set-up time and the charging time of impulse generators.

In contrast to the existing method, a Tesla Coil streamering test requires one set-up to identify the total streamering characteristics of a test specimen. Also, the high frequency nature of the Tesla Coil can generate many long arcs, of somewhat random lengths and paths (reducing test set-up bias).

Attachment Evaluation

The Advanced Design Composite Aircraft (ADCA) model used for the attachment evaluation was designed and built by Grumman Aerospace for the Advanced Composite Structures ADP, Structural Mechanics Division, Air Force Flight Dynamics Laboratory, Wright-Patterson Air Force Base. Lightning attachment tests to the ADCA model were subcontracted to Lightning Transient Research Institute (LTRI) initially. The

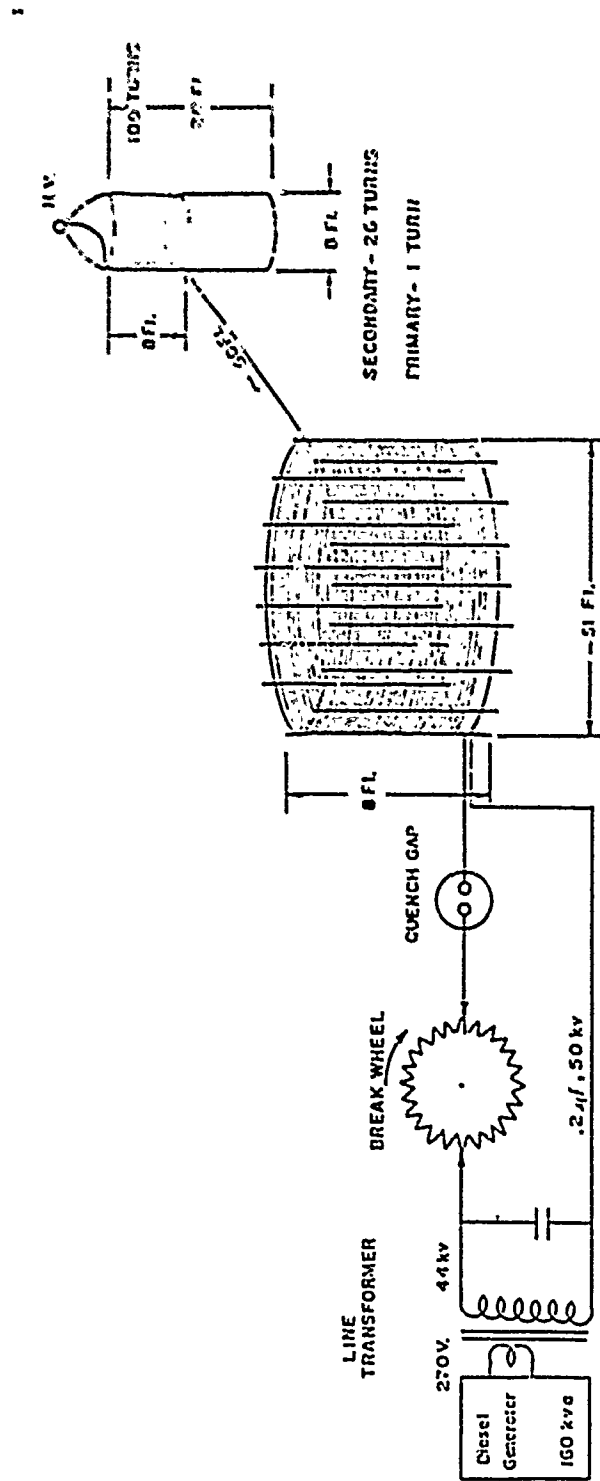


Fig 1. Schematic Diagram of Golka Apparatus at Wendover

Electromagnetic Hazards Group obtained the model after the initial attachment tests. The model was taken to Wendover, Utah to the Associates 12 million volt Tesla Facility for further attachment studies. An F-4 model was also taken and used as a preliminary test set-up model.

The Tesla Coil test was conducted to evaluate its use as a long arc source for attachment studies. Data was taken with the model in three configurations and various positions. Data was obtained for comparison to that obtained during LTRI long arc attachment tests.

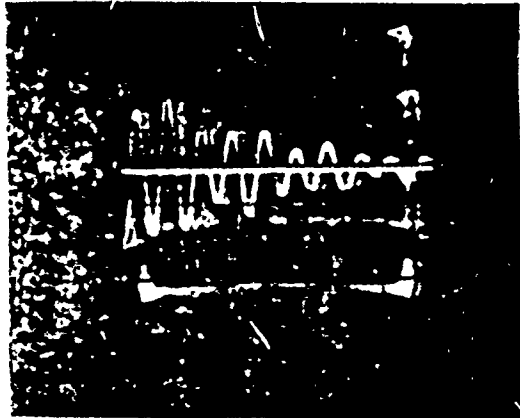


FIGURE 3: Typical Primary Circuit Current Measurement Using Pearson Current Transformer  
Vertical Scale: 1200 Amps/Div.  
Horizontal Scale: 200  $\mu$ s/Div.

#### Measurement of Tesla Coil Characteristics

Some of the physical characteristics of the Tesla Coil that were of interest were the resonant frequencies of the primary and secondary circuits, the rise and decay times, commutation rate, and input current and output current values. The Tesla Coil circuit of Golka Associates is diagrammed in Figure 1 and its equivalent circuit is presented in Figure 2.

The current in the primary circuit was measured with a Pearson, model 301 current monitoring transformer (CT). A typical current measurement is depicted in the oscillogram of Figure 3. The highest current measured was 3240 amperes.

The output voltage was determined to average about 10 megavolts. Higher voltages have been observed on different occasions, the highest being 25 megavolts. These measurements were made with capacitor divider techniques. The risetime of the output voltage was measured to be about 5 microseconds. The risetime of the output voltage is important to determine potential arc length. The risetime can affect voltage needed to break down a given air gap. 50 KC is the ringing frequency of the secondary/extra coil combination. 30 KC is the primary oscillatory frequency, the primary and secondary frequencies being pulled together somewhat due to high mutual coupling. This technique being used to prevent circulating currents between primary and secondary

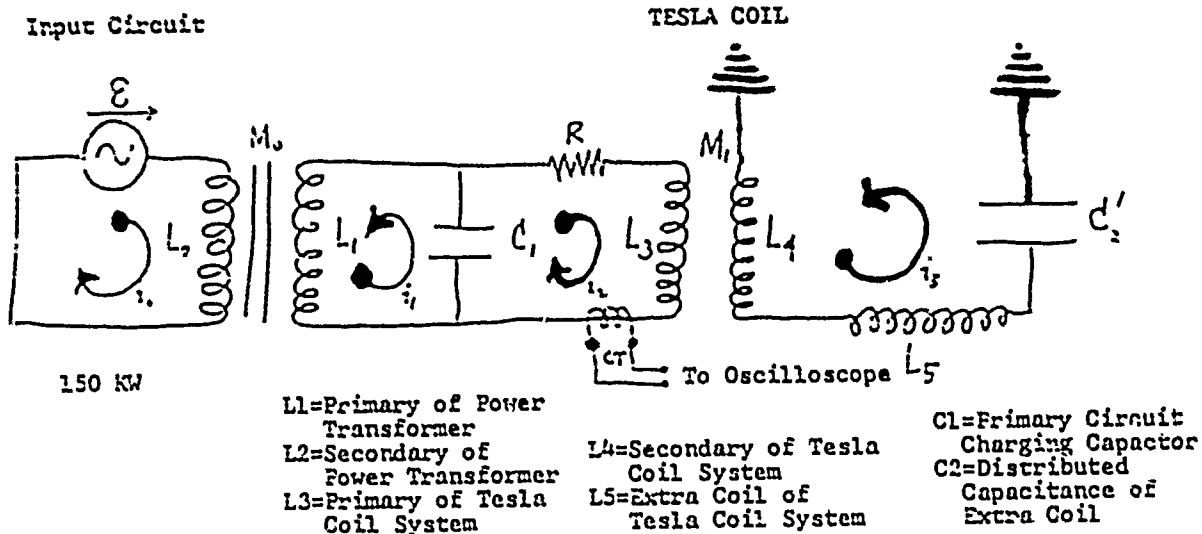
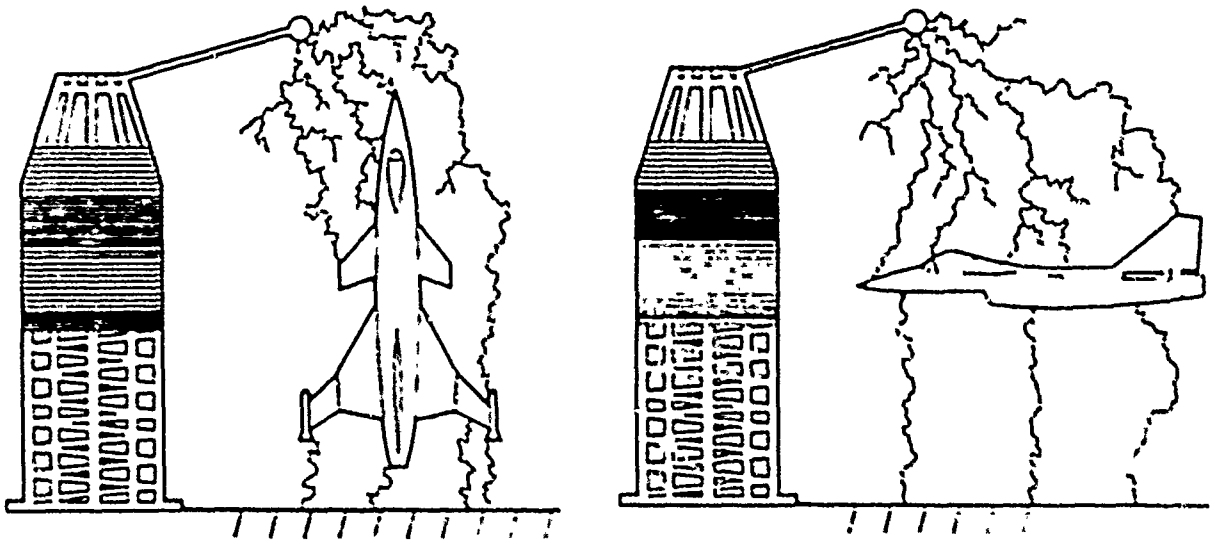
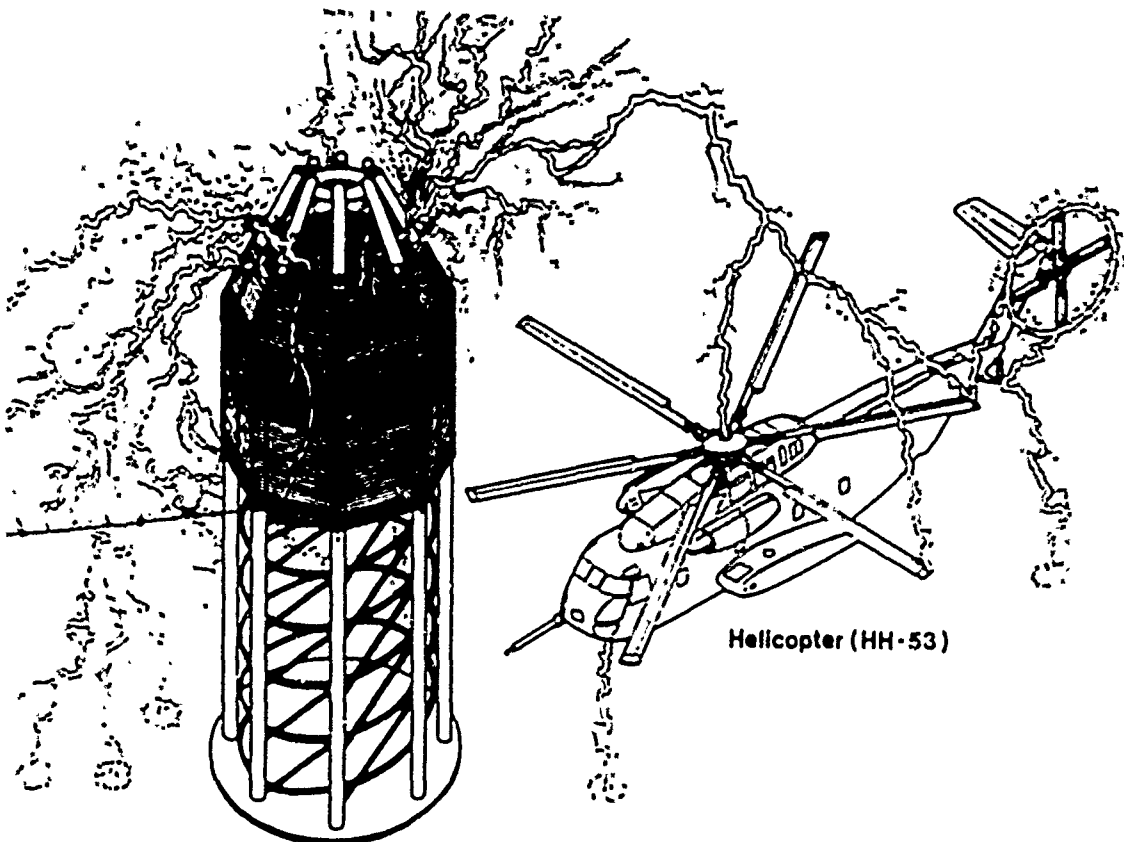


FIGURE 2: Equivalent Circuit of Golka Associates Tesla Coil



Various arrangements of models and full size aircraft along with electrode positioning and high discharge repetition rates (up to 4200 pulses per second) can now be achieved at this facility.



Golka TESLA Coil

Attachment Test  
using TESLA Coil

coils while maintaining tight coupling (.6 coupling coefficient). This prevents reignition of the quenching gap, which if reignited would generate an out of phase primary oscillation current which would beat with the secondary coil oscillating currents producing another output frequency current. This would lower the original oscillation voltage amplitude and of course broaden the spectral response. The mechanical analogy of this effect is the well known physics lab demonstration of two pendulums swinging on a common horizontal string, the driver transferring energy to the driven and the driven then transferring energy back to the driver.

During the attachment tests when the model was fairly near the discharge electrode and the Extra Coil, an arc attached to the canard and then swept up the aircraft to the nose. This phenomena can not be duplicated by Marx Generators. The reason for it appears to be due to the magnetic field sweeping the Extra Coil. The fields outside the coil near the center (half way up) loop outward, with the frequency of the output and the magnetic flux changing, the arc is being "pushed away" from the coil, thus protecting its insulation to a degree from corona and low current sparks. This may be an application for swept stroke testing and should be investigated.

Another possible application for large

scale Tesla Coil Systems is the likely possibility of using them as power supplies for ground based particle beam weaponry. The system can be made to supply hundreds of megavolts. Figure 4 is a schematic of a particle beam accelerator using a Large Scale Tesla Coil System.



Time Exposure Showing Multiple Arcs From Tesla Coil. Note the varied attachment points on the floor, accounting for varied voltage measurement on E-field sensors.

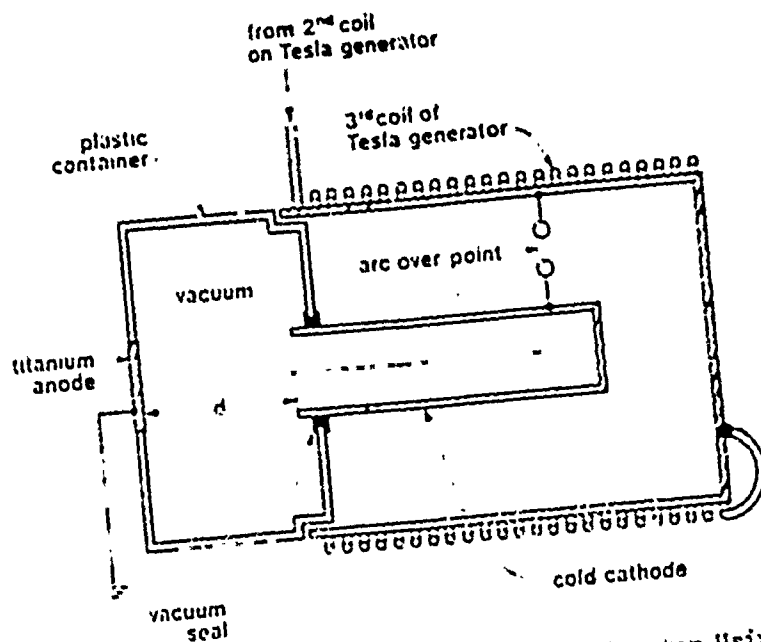


FIGURE 4: Schematic Of A Particle Beam Accelerator Using A Large Scale Tesla Coil System



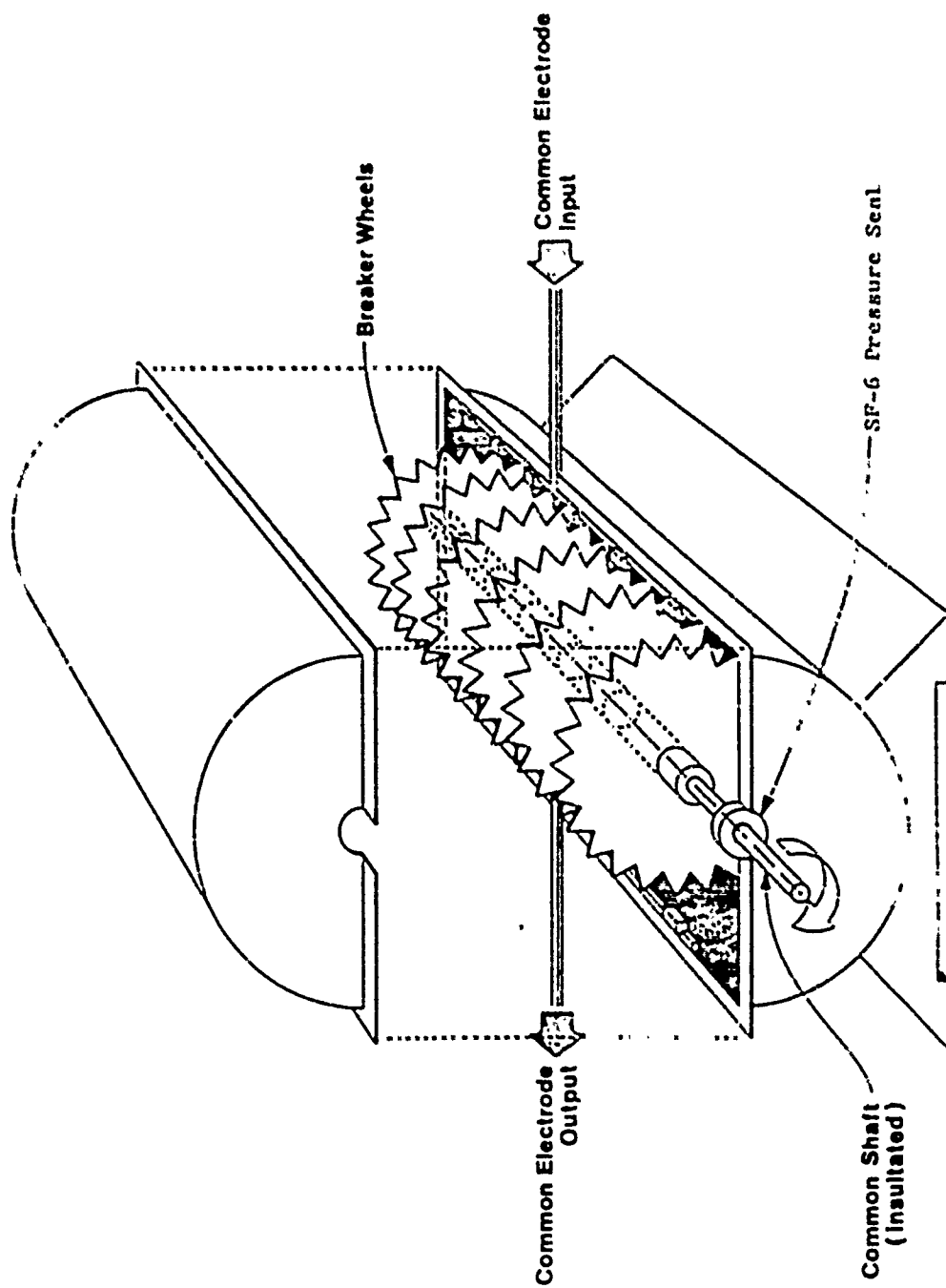


Figure 6. High Powered Ganged High Speed Switch Used with Large Scale Tesla Coil System for Powering Experimental Particle Beam Weapons

## HIGH-DENSITY Z-PINCH PULSE-POWER SUPPLY SYSTEM\*

W. C. Munnally, L. A. Jones, and S. Singer

Los Alamos Scientific Laboratory  
Los Alamos, NM 87545Abstract

The design and operation of the high-density Z-pinch experiment pulse-power supply is discussed. A 600-kV, 1-MA, 75-nH Marx bank is designed to charge a 1- $\Omega$ , 90-ns, water-insulated transmission line to  $\sim 0.6$ – $1.0$  MV. The water line is then discharged through a small laser-initiated current channel in 1–5 atm of hydrogen. The components of the Marx bank, the trigger system, the water line, and the gas load as well as the control system that uses fiber optics and air links for monitor and control are discussed.

Introduction

The high-density Z-pinch (HDZP) experiment at Los Alamos Scientific Laboratory has been constructed to investigate the plasma parameters of a laser-initiated current channel in a high-pressure gas. A 1-GW neodymium glass laser is used to initiate a conducting channel with a diameter radius on the order of 100–200  $\mu\text{m}$  between two electrodes spaced from 5 to 10 cm apart as shown in Fig. 1. The pulse-power supply ideally must produce a rapidly increasing current and thus magnetic field to prevent expansion of the ohmically heated plasma. Simple models indicate that plasmas with densities on the order of  $10^{20}$   $\text{cm}^{-3}$  can be heated to several kiloelectron volts with this system. A prototype system was constructed to develop hardware for a larger experiment. This paper discusses the main HDZP system.

Pulse-Power Supply Design

The theoretical current waveforms, determined from a very simple model, that are required for main-

\*Work performed under the auspices of the US Department of Energy.

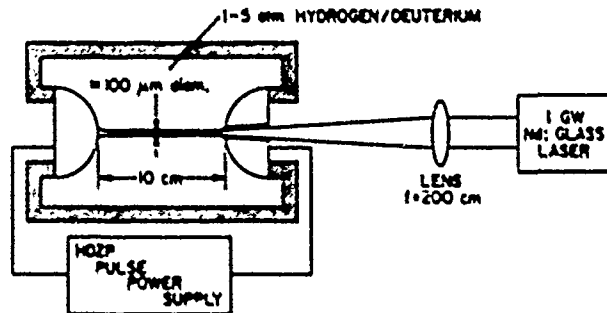


Fig. 1. Schematic of HDZP system.

taining a constant channel radius for three filling pressures are shown in Fig. 2. The gas load has an inductance on the order of 100 nH. In order to obtain the desired  $\dot{I}$  at channel initiation of  $\sim 0.5$ – $1.0 \times 10^{13}$  A/s, the initial voltage across the load must be  $\sim 0.5$ – $1.0 \times 10^6$  V. The maximum current required from the power supply is on the order of 1 MA.

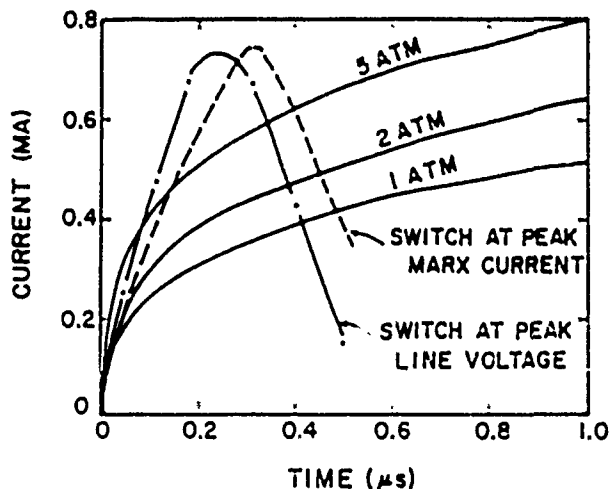


Fig. 2. HDZP current waveforms.

Several circuit configurations were evaluated and simulated using the NET 2 circuit analysis code. A system consisting of a water-insulated, intermediate storage line resonantly charged by a low-inductance Marx was chosen as the most versatile system. The basic circuit for the HDZP system is shown in Fig. 3. The system can be operated with a wide range of current risetimes and current amplitudes by laser initiating the current channel at various times during the resonant charge of the water line. The water line provides the initial high rate of current rise. The energy remaining in the Marx capacitance and the energy stored in the resonant-charging inductance provide gas load current at later times.

The HDZP water line was designed such that the impedance could be varied from 0.25 to 1.0  $\Omega$  with a transit time of 90 ns. The maximum line voltage and load current are determined by the time of current channel initiation, the Marx charge voltage, and the water line impedance. The current waveforms produced by simulation of the HDZP system are also illustrated in Fig. 2 with dashed lines.

#### Marx Bank Design

The HDZP Marx system was designed to have a minimum inductance, to operate at a nominal 500 kV output voltage and to deliver 1-MA peak current. The minimum energy store of the Marx is determined by the maximum desired inductive load energy of about 50 kJ. In order to accommodate the maximum Marx current and reduce the Marx inductance, 12, 6-stage Marx modules, each of which stores 4.3 kJ at 500 kV and provides a maximum fault current of 83.3 kA, were paralleled. The individual Marx module circuit diagram is shown in Fig. 4 and pictured in Fig. 5. Each Marx module stage consists of two parallel

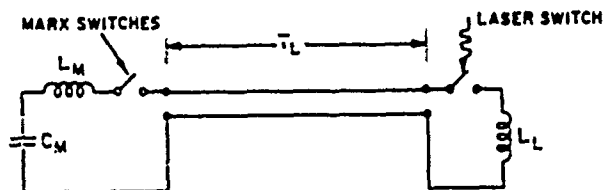


Fig. 3. HDZP circuit schematic.

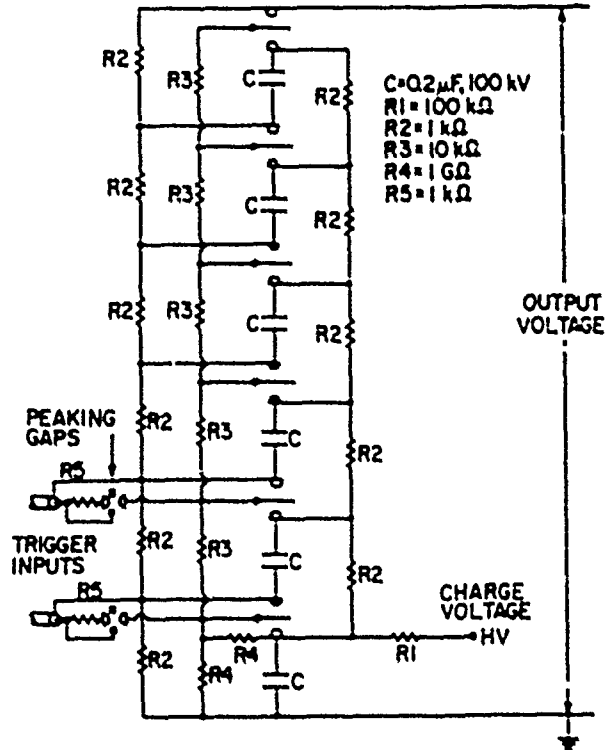


Fig. 4. HDZP Marx module schematic.

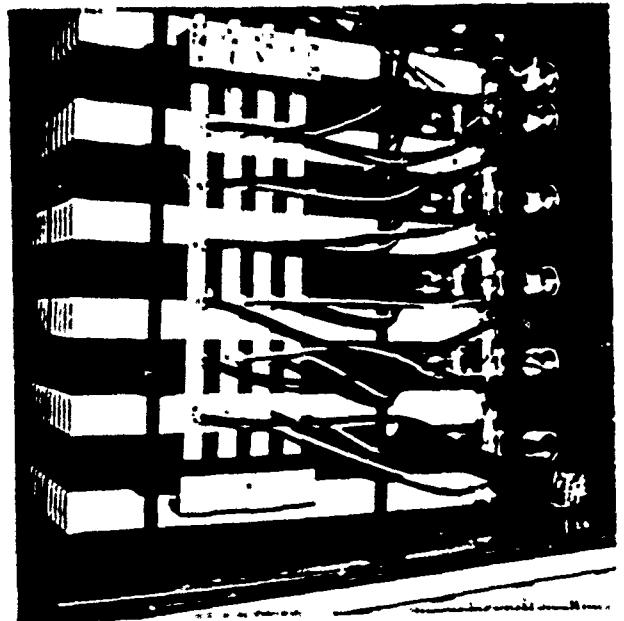


Fig. 5. Picture of Marx module.

0.1  $\mu\text{F}$ , 100-kV Maxwell series S capacitors and one Physics International T670 triggered spark gap. Each capacitor has a maximum rated current of 50 kA, and the spark gap has a maximum rated current of

100 kA. The capacitors were specified with 50% voltage reversal to accommodate a Marx output fault and resulting 75% voltage reversal at 500-kV output voltage. The Marx bank inductance at the output terminals is 75 nH. However, the transition section between the Marx bank and the water line increases the total series inductance to about 250 nH.

The Marx trigger system was designed to erect all the Marx modules in a small fraction of the minimum voltage rise on the water transmission line or within ~20 ns. The trigger circuit chosen is shown in Fig. 6. This trigger Marx arrangement is a variation of trigger circuits suggested by Fitch<sup>1</sup> and was selected because the trigger pulse of the Marx module gaps can be controlled in amplitude, risetime, and arrival time very precisely. In addition, each Marx module spark gap can be triggered with a similar trigger pulse without loading the Marx system. The simultaneous trigger pulses are generated by shorting 12 coaxial cables charged to a maximum of 100 kV with a spark gap that also serves as the trigger Marx stage gap.

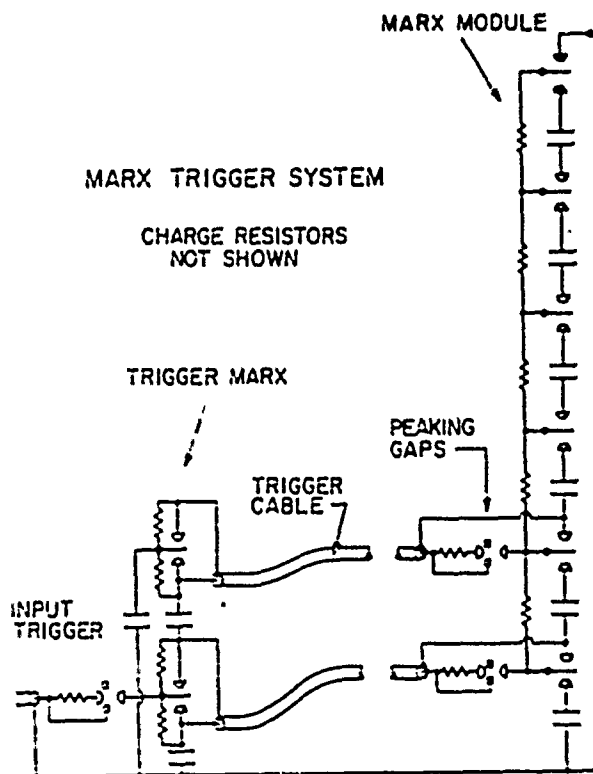


Fig. 6. HDZP trigger system schematic.

In order to minimize the jitter in erection of the main Marx modules, the trigger pulses provided by the trigger Marx must have a risetime less than the desired scatter. The 12 cables that are shorted by the trigger Marx stage gap have a characteristic impedance of about 36  $\Omega$  each or a parallel impedance,  $Z_p$ , of 3  $\Omega$ . The trigger Marx gap inductance,  $L_G$ , must be such that  $L_G/Z_p$  is on the order of 5 ns. This requires a trigger Marx gap with an inductance of about 15 to 20 nH, which operates at 85- to 100-kV dc and is easily triggered. The final design of the trigger Marx gap is shown in Fig. 7. An acrylic sheet insulator is designed to minimize tracking within the gap. The gap operates at an  $SF_6$  pressure of about 60 psig for a 100-kV charge.

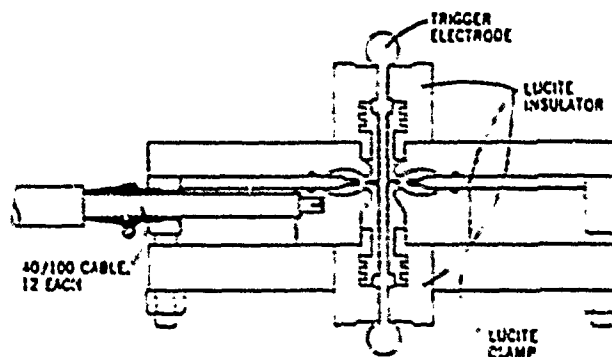


Fig. 7. Trigger Marx low-inductance spark gap.

The trigger Marx stage capacitors serve to bias the shorted cable trigger generators at a potential similar to that of the main Marx and to isolate the main Marx stage voltage from ground. A 2-stage trigger Marx that triggers only the first 2 stages of the 12 Marx modules is used because initial tests indicated additional stages are unnecessary. The coaxial trigger cable charge voltage is isolated from the main gap trigger electrodes by an "inside-out" trigatron peaking gap. The peaking gap shown in Fig. 8 also reduces the trigger pulse risetime seen by the main gap trigger electrode <7 ns with a jitter spread of <2 ns. The 2-stage trigger Marx is initiated by an 8-stage ceramic capacitor micro-Marx generating a 200-kV pulse with risetime of <20 ns and a jitter <2 ns. The micro-Marx is shown in Fig. 9.

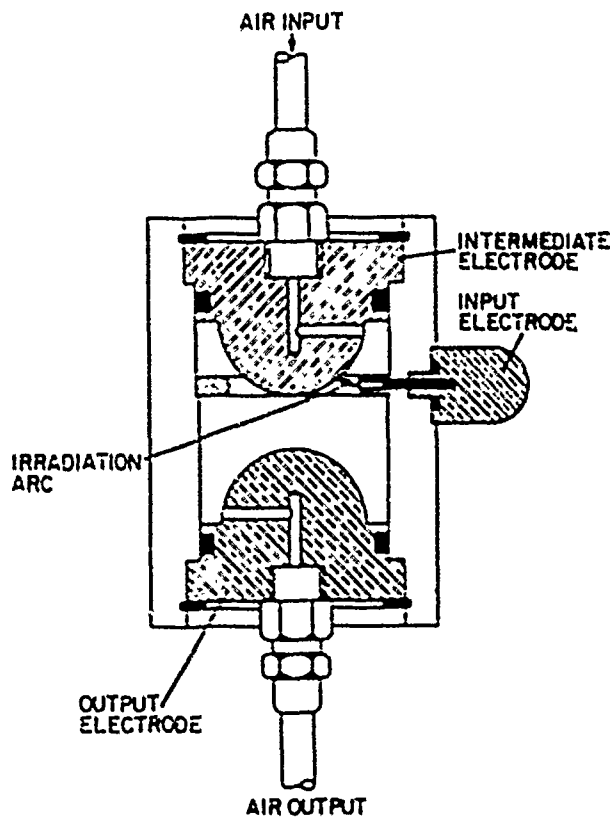


Fig. 8. Trigger system peaking gap.

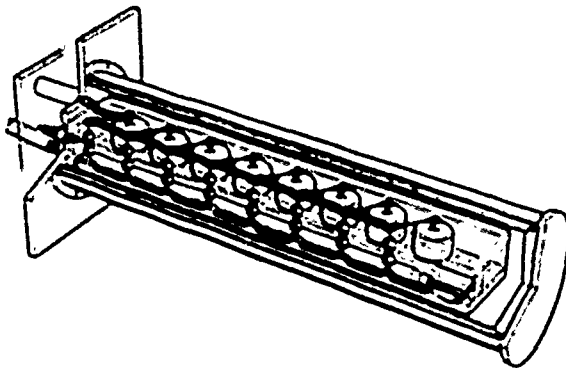


Fig. 9. Trigger micro-Marx.

#### Transmission Line Design

The water-insulated transmission line system is shown in Fig. 10. A parallel-plate transmission line was chosen over a coaxial transmission line for two reasons. First, the impedance can be easily varied by changing the number and size of the parallel plates. A large water tank was designed to hold the transmission line leaving a large amount of room for line variations. Secondly, the local-

ized nature of the laser-initiated plasma channel requires storing the pulse energy very close, physically, to the center line of the pinch channel to reduce the transition inductance. A disk transmission line with radial Marx current feed would be the optimum configuration, but building space limitations prevented using this design.

#### Gas Load

The desired characteristics of load geometry at the end of the water transmission line are a minimum inductance configuration, a uniform electric field distribution in the pinch region, and visibility and maximum access for diagnostics. The present gas load is shown in Fig. 11.

#### Control System

The control system for the MDIP experiment is completely isolated using only fiber optic links or air links for control or monitoring system operation. The major types of links are illustrated in Fig. 12. The power supply voltages, power supply currents, and capacitor bank voltages are monitored using the fiber optic link of Fig. 12a. A voltage divider or current monitor provides a voltage from 0-10 V to a voltage-to-frequency converter that modulates a LED from 10 Hz to 10 kHz. At the other end of a fiber optic cable the light pulses are detected and converted back to a voltage/current, which operates a standard trip meter. Those functions that do not require precise time operation are

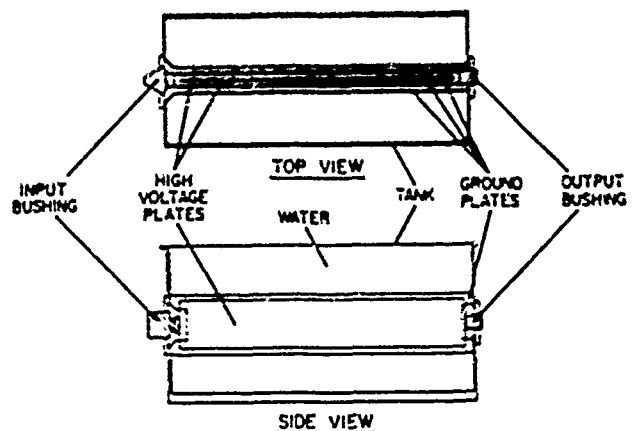


Fig. 10. Water-insulated transmission line.

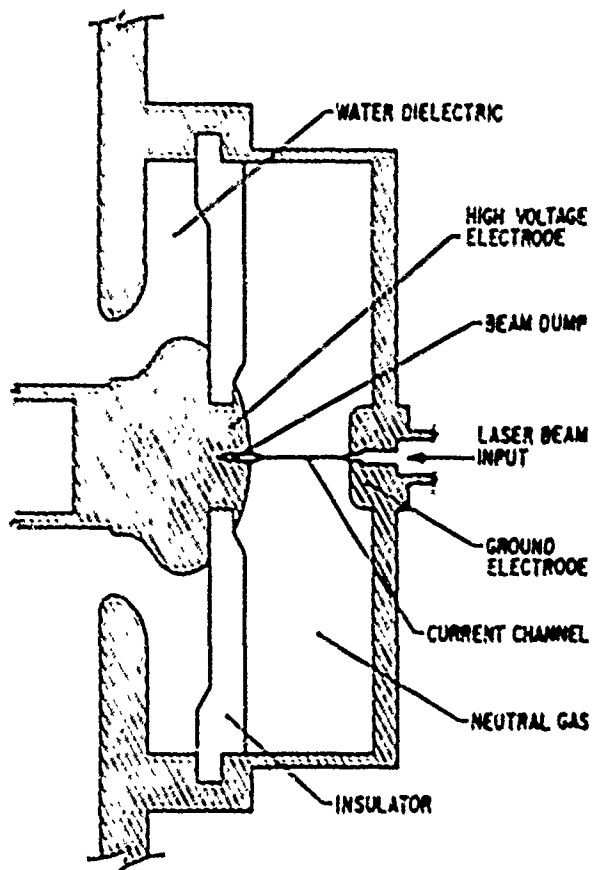


Fig. 11. HDZP gas load chamber.

implemented using compressed air, one example of which is shown in Fig. 12b. The high-voltage dump and safety switches are also actuated using air links as illustrated in Fig. 12c. The interlock systems are structured as shown in Fig. 13. Each location or function requiring an interlock was designed to provide closure of contacts, energizing a high-intensity lamp. The resulting light is conducted to the main control panel through a fiber optic cable where a phototransistor pulls in a relay if the high-intensity lamp is energized. This method is very simple and has been extremely reliable. It is fail safe in that a malfunction prevents relay closure and inhibits system operation.

The trigger system also uses fiber optic links from the time delay system in the screen room to various systems to be initiated. The trigger link system is diagrammed in Fig. 14. The basic timing system consists of a multichannel digital time delay unit that determines the timing sequence of the experiment. The time delay output signals energize injection laser pulsers, which produce 900-nm light

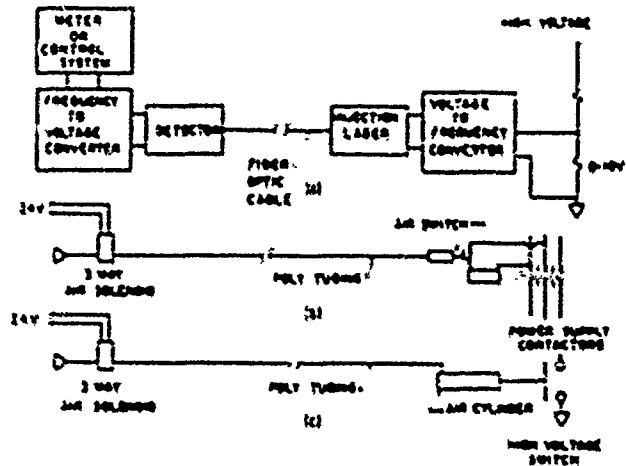


Fig. 12. HDZP control systems.

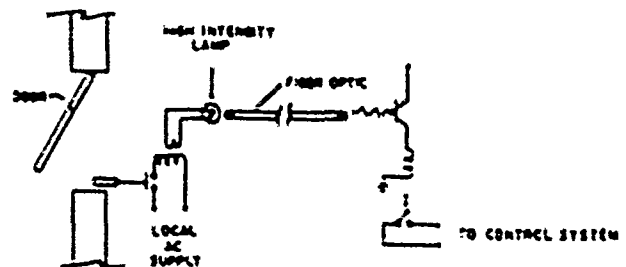


Fig. 13. HDZP interlock system.

pulses that are conducted to the various systems in the HDZP experiment through fiber optic cable. The receiver-pulse generators shown in Fig. 14 produce electrical pulses at voltages from 5 to 900 V with 10 ns risetimes and various pulse lengths and shapes. The jitter of this type of trigger link system is less than  $\pm 1$  ns. The system is extremely insensitive to the large amount of EMI present and the location of the fiber optic cable in the experiment is thus not critical.

#### System Operation

System operation is initiated by charging the Marx bank and charging the trigger Marx such that they reach the desired voltage simultaneously in about 30 s. The control system monitors bank voltages and sends a fiber optic trigger pulse into the screen room after disconnecting the power supplies. The digital time delay system then energizes the appropriate systems in the proper sequence. The main Marx is erected to pulse charge the water line in about 200-600 ns. At the desired load voltage the glass laser initiates the HDZP current channel and

at the desired time various diagnostic lasers are initiated. The jitter in erecting the Marx to charge the transmission line is  $\pm 10$  ns. The water-insulated transmission line uses self-break water switches to "crowbar" the Marx bank and reduce the Marx capacitor reversal. The system has been tested to a charge voltage of 100 kV per stage, although the Marx system was designed to operate at a charge

voltage of 85 kV per stage to allow for various fault modes. The MDZP pulse-power supply system is illustrated in Fig. 15.

#### Reference

1. R. A. Fitch, "Marx and Marx-Like High-Voltage Generators," Maxwell Labs, Inc., IEEE Trans. on Nucl. Sci. NS-18, 2 (1971).

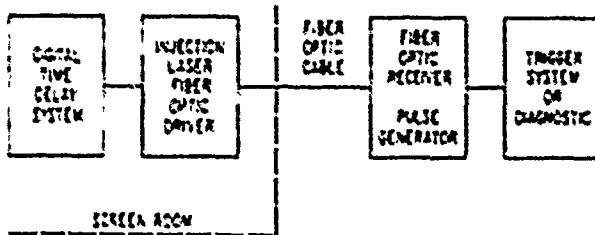


Fig. 14. MDZP timing system.

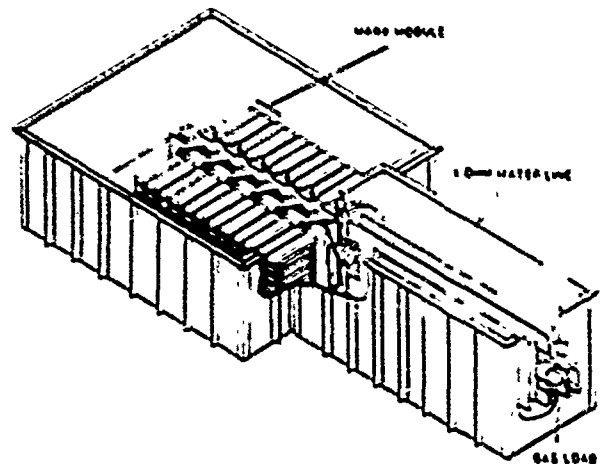


Fig. 15. Illustration of MDZP pulse-power supply system.

## THE DESIGN OF SOLENOIDS FOR GENERATING HIGH MAGNETIC FIELDS

P. Syszowski

Institute of Physics  
Polish Academy of Sciences  
Warsaw, AL. Lotnikow POLAND

Abstract

Magnetic fields of high intensity are usually generated by the pulsed discharge of capacitor banks through solenoids. In order to generate the highest fields, exploding coils or field compression techniques are used. However, for experiments it is essential that the coil withstand the electro-dynamical forces. This is achieved by employing coils in which the stress exerted by the current density and the magnetic field does not exceed the strength of the material used to build the coil.

The current density in these coils depends on the distance from the center, the external dimensions, the coil material, and the temperature. To decrease the electrical resistivity of the material the coils are cooled to liquid nitrogen temperature. The conversion rate of electrostatic energy to magnetic field energy is much smaller than in standard coils with uniform current density or in Bitter coils. To feed a coil generating a field with intensity of 600 kG requires high energy capacitor banks (in the range of 0.5 MJ). The details of stress calculations and current distribution in large solenoids are presented in the paper. Also presented are the details of experiments on the durability of solenoids in external magnetic field. The experiments and calculations are used to build a coil producing a high magnetic field.



# ANALYSIS OF A DISTRIBUTED PULSE POWER SYSTEM USING A CIRCUIT ANALYSIS CODE

LOTHAR O. MOEFT

AIR FORCE WEAPONS LABORATORY, KIRTLAND AFB, NM 87117 AND  
THE BDM CORPORATION, ALBUQUERQUE, NM 87106

## Abstract:

A sophisticated computer code (SCEPTRE), used to analyze electronic circuits, was used to evaluate the performance of a large flash X-ray machine. This device was considered to be a transmission line whose impedance varied with position. This distributed system was modeled by lumped parameter sections with time constants of 1 ns. The model was used to interpret voltage, current, and radiation measurements in terms of diode performance. The effects of tube impedance, diode model, switch behavior, and potential geometric modifications were determined. The principal conclusions were that, since radiation output depends strongly on voltage, diode impedance was much more important than the other parameters, and the charge voltage must be accurately known.

## INTRODUCTION

The prediction of overall performance of complex pulse power devices is required for achieving optimum design, identifying problems that arise during operation, and for evaluating proposed modifications. Rather simple analysis techniques may be used if the transit times of the structure are small compared to the rise time or pulse length. However, in most cases, the rise time/pulse length is comparable to the transit time of the structure and/or its discontinuities. Such systems have been treated as a series of transmission lines with capacitances added at the discontinuities<sup>1</sup>. Such techniques are tedious and lack credibility if the structure is complex. With the advent of network

analysis codes such as SCEPTRE, NET-11, etc., the pulse power system designer has a new and powerful analysis tool for predicting the performance of pulse power devices. Conceptually, the pulse power system is modelled with lumped parameter transmission line sections in which the time delay per section is small compared to the time constant of interest in the system. This concept implies that the pulse power system can be represented by a one-dimensional structure; that is, effects due to a change in direction of the electromagnetic wave are ignored. This paper presents the methodology used to construct such a model for a large DC-charged, flash x-ray machine. The use of this model to interpret measured waveforms and evaluate possible modifications is described. Finally, the principal conclusions reached by this analysis are presented.

## MODEL DEVELOPMENT

Figure 1 shows a cross-sectional view of the flash x-ray machine. The energy is stored in a 33-foot long high pressure gas insulated transmission line ( $Z_0 = 42$  ohms). This line or coaxial capacitor is charged to approximately 10 Megavolts by a van de Graaff generator. A 2-foot

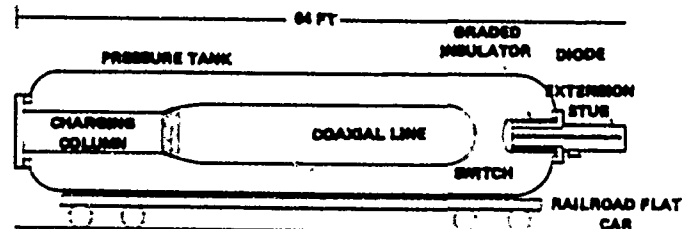


Figure 1. Cross-section of Flash X-Ray Machine

spark gap is used to switch the energy into the field emission diode via a graded insulator which separates the vacuum and high-pressure regions. The diode is located at the end of a 5-foot long vacuum transmission line. Figure 2 presents the impedance of this system as a function of distance along its axis.

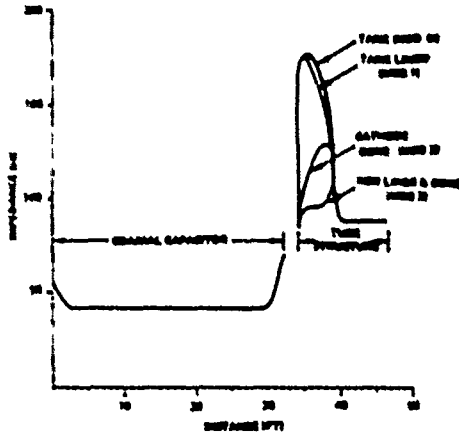


Figure 2. Impedance as a Function of Distance Along Flash X-Ray Machine

Impedance is calculated at each foot or 1-nanosecond segment using the formula  $Z = 60 \ln b/a$  where  $b$  refers to the outer, and inner radii of the line. The charging column is ignored in the analysis since it is highly resistive. The switch area is not modelled as a transmission line because it is only 2 feet long, which is small compared to the expected rise time. Each 1-nanosecond section of the system was modelled by a low-pass constant K, T-section as shown in figure 3. The switch was modelled by a series-connected inductance and resistance. At time zero the voltages on all capacitances associated with the coaxial capacitor were set to 10 megavolts and the voltages on all other capacitors were set to 0.

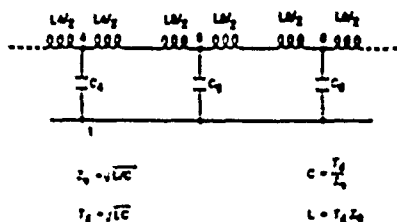


Figure 3. Lumped Parameter Representation of Transmission Line

This physical model was transformed into a network model by identifying each node with a number and specifying the location of each circuit element by pairs of node numbers. Voltages or currents are defined as occurring across a circuit element. One of the advantages of using this type of code is that diagnostic measurements can be specified at places that are normally inaccessible for physical measurements but which are important for understanding the operation of the system. For example, the voltage across the field emission diode can be specified in the code whereas the actual voltage measurement must be made some distance away because of physical limitations.

The SCEPTRE code has a feature that allows simple functions to be calculated as the network is being analyzed. In this case, the instantaneous diode power, total energy, and radiation production were calculated. Radiation production was calculated using the following equation<sup>2</sup>.

$$\text{Dose Rate} = D = 1.09 \times 10^3 V^{2.71} I \text{ (R/sec @ 1 m)}$$

$V = \text{Diode Voltage in Megavolts}$   
 $I = \text{Diode Current in Amperes}$

This dose rate was then integrated to give a number that could be compared with measurements made using thermal luminescent dosimeters (TLD's). Since most of the data on the machine was in the form of TLD measurements, this capability was extremely useful in comparing the results of the code with the machine performance.

A number of alternative models for the field emission diode were used. The simplest was a resistor that represented the tube impedance. More complex diode models included several models from the SCEPTRE code as well as a space-charged limited diode representation. In the latter case, the current is given by  $I = KV^{3/2}$  where  $K$  is the perveance.

## RESULTS

Figure 4 shows the waveforms at four different points along the cathode shank. The

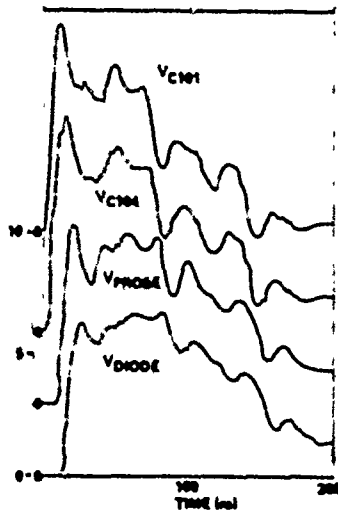


Figure 4. Voltage Waveforms Along Cathode Shank

first waveform ( $V_{C101}$ ) is at the switch electrode. The second waveform is the voltage that would be present on the cathode shank as it enters the vacuum transmission line. The third waveform is the voltage that would be measured by the capacitive probe located in the transmission line. The final waveform is the voltage across the field emission diode which is modeled in this case by a space-charge limited diode. The ringing associated with a large impedance mismatch at the switch electrode can be seen in the first waveform. This is progressively attenuated as the wave travels to the diode.

Figure 5 shows some of the other waveforms associated with the simulation. Figure 5a shows

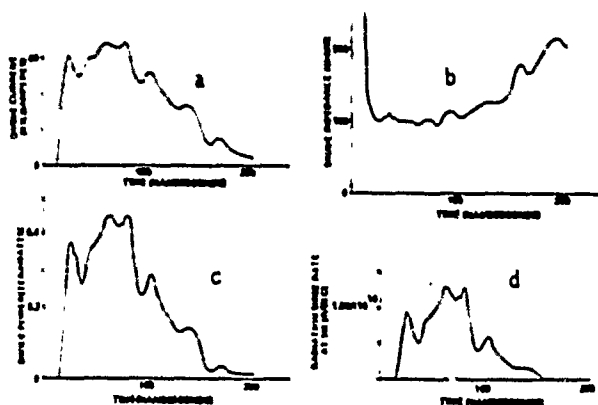


Figure 5. Waveforms Associated With Flash X-Ray Machine Simulation

the diode current which, in this case, is a nonlinear function of the voltage as described above. Figure 5b shows the instantaneous diode impedance as a function of time. Note that the impedance is relatively constant during the main portion of the pulse. Diode power and dose rate are shown in figure 5c and 5d.

The initial calculations performed using this model resulted in waveforms that were similar to those measured on the flash x-ray machine but predicted radiation doses that were three to four times higher than those measured and, in fact, were close to the design values. Therefore, a set of parametric calculations was performed to investigate the effects of varying switch parameters, tube impedance, and geometric modifications. The switch resistance was varied between 0.1 and 10 ohms and the switch inductance was varied between 500 and 1000 nano-henry's. The integrated dose did not change significantly. Consequently, poor switch performance was not considered to be the problem. Next the tube impedance was varied from 25 to 200 ohms and the impedance of the stub or vacuum transmission line was varied between 35.6 and 160.4 ohms, corresponding to cathode shank diameters between 16 and 2 inches. Figure 6 shows the effect of the tube impedance and stub transmission line impedance on the dose at one meter. The dose versus impedance curves for 4, 6, 8, and 12-inch diameter cathode shanks are evenly spaced between the curves for 2 and 16-inch shanks. Not all of the points on the curve are physically realizable. Studies at

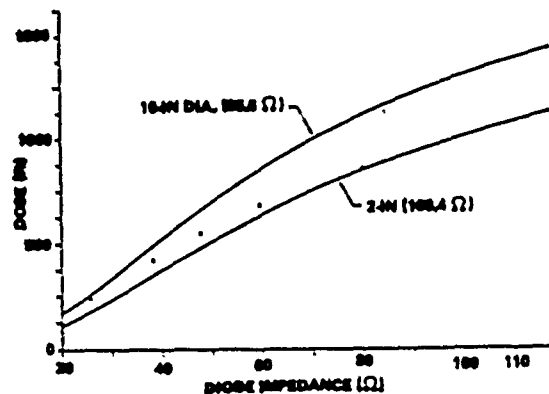


Figure 6. Effect of Diode and Stub Impedance on Dose

Sandia Laboratories<sup>3</sup> have shown that the diode impedance is approximately one-half of the stub impedance. The circles shown on figure 6 are the points where the diode impedance is half the stub impedance. In an effort to experimentally optimize performance, cathode shanks that contained sections of different diameters were tried. In fact, one of the highest measured doses used a 3.5-inch diameter shank with a 10-inch long 1-inch diameter section in the diode region. Such configurations would combine the positive advantages of the low impedance stub with those of the high impedance diode. Figure 6 demonstrates that the possible improvement in dose is much greater for variations in diode impedance than for variations in stub impedance.

The effect of stub and tube impedances was also calculated using the space-charge limited diode model. These calculations essentially confirmed the earlier ones using the constant resistance diode model but are more difficult to interpret because of a lack of intuitive understanding of the concept of perveance.

Several modifications to the geometry of the flash x-ray machine were proposed in order to avoid reflections in the region surrounding the graded insulator. The impedance changes for these modifications were shown in figure 2. As the flash x-ray machine was originally built, the impedance could be as high as 175 ohms at the base of the cathode shank. The use of a cone on the cathode shank in combination with a new tank liner could reduce the maximum impedance to about 100 ohms which is close to optimum. The effect of these modifications is shown in figure 7 where the dose is plotted versus tube impedance for the four configurations. Inspection of the waveforms indicated that these modifications reduced the ringing considerably but the total dose was not significantly changed.

The analysis described above could not identify a reason for the factor of 3 or 4 decrease in radiation output in this flash x-ray machine. One explanation for the low output is that the charge voltage is low. If the diode current is proportional to voltages, and the

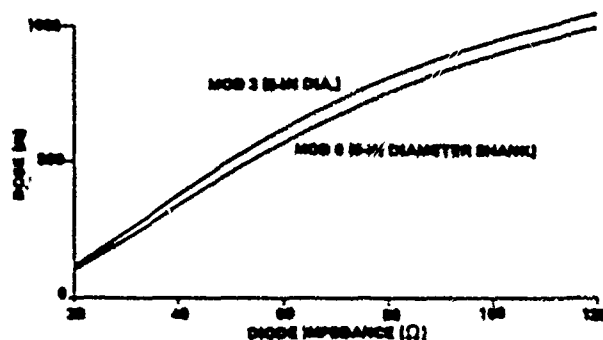


Figure 7. Effect of Geometry on the Variation of Dose With Impedance

radiation output is proportional to  $V^{2.71}$ , a 25 to 30% decrease in charge voltage reduces the radiation output by a factor of 3 or 4. Subsequent to this analysis, experimental electron beam studies confirmed that such errors probably existed.

#### CONCLUSIONS

This study has demonstrated that a network analysis code like SCEPTRE can be a very useful tool for gaining an understanding of a complex pulse power device such as a large flash x-ray machine. The effects of the stub impedance, switch behavior, and geometric modifications were of relatively minor importance compared to the diode impedance. Since the radiation output depends on the fourth power of the diode voltage, diode impedance is much more important than other parameters. The major discrepancy between the measured and predicted results could be explained by a 25 to 30% error in the charge voltage calibration.

#### REFERENCES

1. Ion Physics Corporation, "Development of an Advanced Flash X-Ray System," Report AFWL-TR-76-114, October 1976.
2. J. Creedon, C. Ford, D. Martin, S. Putnam, and D. Sloan, "Advanced X-Ray Tube Development," Report AFWL-TR-65-04, January 1966.
3. H. Martin, "Design and Performance of the Sandia Laboratories HERMES II Flash X-Ray Machine," in IEEE Trans. on Nuc. Sci., Vol NS-16, No. 3, p. 59, June 1969.

## DETERMINATION OF LINE VOLTAGE IN SELF-MAGNETICALLY INSULATED FLOWS

C. W. MENDEL, JR., J. P. VANDEVENDER, and G. W. KUSWA

Sandia Laboratories, Albuquerque, NM 87185

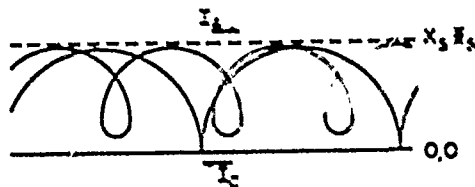
Abstract

Resistive and capacitive voltage monitors for self-magnetically insulated lines have been found to be unsatisfactory. However, it is known that the boundary current  $I_b$  and total current  $I_T$  are related to line voltage  $V^{1,2}$  and the total and boundary current can be used to infer the voltage.<sup>1,3</sup>

In this presentation we show relationships between  $V$ ,  $I_T$  and  $I_b$  which are fairly insensitive to the canonical momentum distribution of flowing electrons. Using these relations we conclude that the voltage can be calculated from  $I_T$  and  $I_b$  with moderate accuracy with no knowledge about the particular flow involved, and quite accurately if only two, experimentally determined parameters are known. The inferred voltage waveforms will be compared to experimental voltage data.

It has been found experimentally that voltage monitors placed across magnetically insulated flows lead to appreciable losses due to disruption of electron flow and to problems with surface flashover of the monitor itself. It is readily proven that the electric field at the anode is related to the anode and cathode currents (Fig. 1), and not directly to line voltage.<sup>1</sup> However, there is some relationship between anode current, cathode current and line voltage,<sup>1</sup> and we wish to show here that line voltage can be calculated from these.

Figure 1 shows a schematic of the flow and the expressions which will be used in the calculations. The subscripts A, S, and C refer to the anode, the edge of the current sheet and the cathode respectively. The current in the electron flow plus the current in the cathode  $I_C$ , add up to that in the anode,  $I_A$ . In reference 1 it is assumed that



$$E = \frac{2\phi}{\pi X_s}$$

$$X_s = \frac{2\pi I_C}{I_A} \lambda \quad I_C = \frac{2\pi m c}{4\pi e} = 0.52 \text{ kA}$$

$I_C$  = Cathode Current / Unit Width

$I_A$  = Anode Current / Unit Width

$I_b$  = Boundary Current (Total Cathode Current)

$I_T$  = Total Current (Total Anode Current)

Figure 1 Geometry, and term definition in magnetically insulated flow.

a spread in canonical momentum is introduced by the feed transition. It is found in reference 1 and in subsequent calculations that the thickness parameter is given by

$$X_s = \frac{2\pi I_C X_s}{I_A} = \lambda \sqrt{2\phi_s}$$

where  $\lambda$  is at most slowly dependent upon  $\phi_s$ . In addition it was found that

$$\frac{I_A}{I_C} - 1 = B \phi_s$$

where  $B$  is also at most slowly dependent upon  $\phi_s$ . Pressure balance (since there is no flow of particles to anode or cathode) demands that



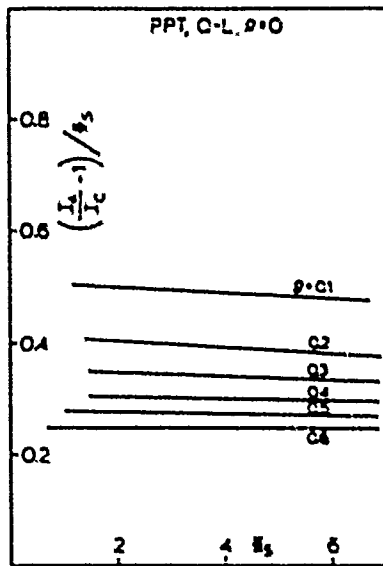


Figure 3 The parameter  $B(\phi_s) = \frac{I_A}{I_C} - 1 / \phi_s$  for the same flows as in Fig. 3.

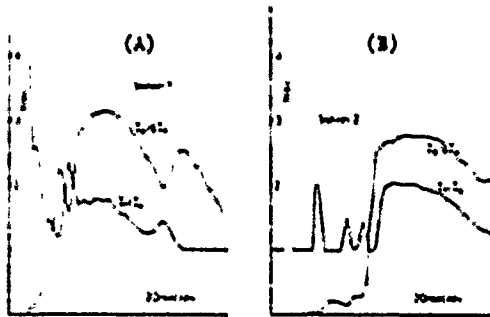


Figure 4 The data  $X_s = I_s/I_{Cs}$  and  $I_T/I_s$  versus time for the input (station 1) and output (station 2) of the uniform section of the Mite magnetically insulated line for the same experimental shot.

at the beginning of the uniform section of line, i.e., just after the feed transition. Figure 4b are the same measurements just before the load transition at the end of the uniform section. Note that there is a fair amount of difference between the two sets of data. Figures 5a and 5b show the line voltages as calculated from 4a, 4b along with the measured input voltage (time shifted). The agreement is well within expected error. The disparity in the late time 5a data is expected as the flow is mostly in the electrodes in the first part of the line, and since the voltage depends upon  $L_T - I_s$ , large errors are introduced.

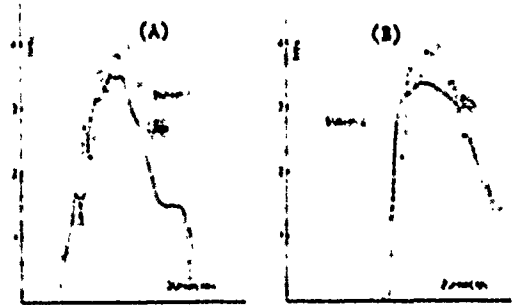


Figure 5 The voltages calculated from the data in Figure 4 compared to measured input voltage. The sharpening of the voltage front at station 2 is real and expected.

Figure 6 shows similar data for the Physics International tri-plate line experiment.<sup>7</sup> Here, however, the voltage on the load is measured close to the current monitors. The agreement is again well within expected error.

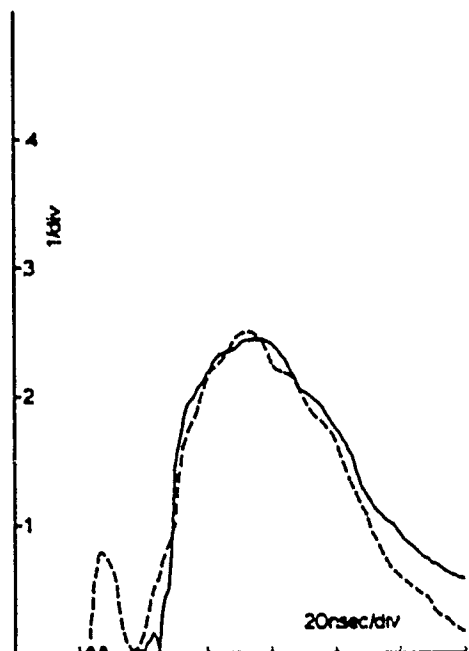


Figure 6 Calculated and measured voltage at the load in the Physics International tri-plate line experiment.

We have shown that the voltage on magnetically insulated lines can be calculated from line current data with sufficient accuracy for most applications without special knowledge of the particular flow. With experimentally determined parameters A and B,

additional accuracy may be available. This alleviates the loss problems previously seen with trans-line voltage monitors.

#### References

1. C. W. Mendel, J. Appl. Phys., July 1979.
2. J. Creedon, J. Appl. Phys., 46, 2946 (1976).
3. J. P. VanDevender, J. Appl. Phys., June 1979.
4. R. V. Lovelace and Edward Ott, Phys. of Fluids, 20, 688 (1977). A. Ron, A. A. Mondelli, and N. Rostoker, IEEE Trans. on Plasma Sci., PSI-1, 85 (1973).
5. K. L. Brower and J. P. VanDevender, 2nd Int'l. Conf. on Pulsed Power, Lubbock, TX (June 1979).
6. E. L. Neau and J. P. VanDevender, 2nd Int'l. Conf. on Pulsed Power, Lubbock, TX (June 1979).
7. M. DiCapua and D. G. Pellinen, Physics Int'l. Report PIFR-1009, Oct. 1978.

---

This work was supported by the U. S. Department of Energy, under Contract DE-AC04-76-DPO0789.



## VERSATILE HIGH ENERGY CAPACITOR DISCHARGE SYSTEM

V.N. Martin

GTE Laboratories Incorporated  
40 Sylvan Road  
Waltham, Massachusetts 02154

Abstract

The requirements for generating half sine waves of current having amplitudes over a range of 36 kA at voltages up to 1.6 kV are being met through the development of a compact, critically damped LCR discharge system containing 0.75F capacitance, which can store up to 60,000J of energy. The system comprises five cartmounted, electrically isolated capacitor banks, each containing 0.15F capacitance and chargeable to a nominal value of 400V, which is controlled by a multi-element SCR switch and can be discharged through inductors and resistors to provide one-half of a 60-cycle sinusoid at peak current values up to 36,000A. Circuit designs are presented for the isolation and status indication of each of the 500 capacitors, for inverse diodes to protect the polarized capacitors from reverse recovery voltage experiments performed after the main capacitor bank discharge, and for protection of the capacitors from overvoltage conditions.

Introduction

GTE Laboratories has recently constructed a High Energy Electrical Test Facility which includes a Primary 60 Hz Test Laboratory providing 14.5 MVA short-circuit testing capability and a Synthetic Test Facility powered by the high-energy capacitor discharge system. The Synthetic Test Facility is used as a research tool to investigate arcing phenomena, including arc interaction with electrode materials, arc quenching and current limiting techniques. This paper describes technical considerations that led to the design of this versatile pulse current generation system,

component selection and construction details.

Technical Considerations

Available floor space, floor loading, cost and delivery ruled out oil-filled paper capacitors that are found in many energy storage capacitor banks. Electrolytic capacitor manufacturers were consulted to determine off-shelf availability, capacity per unit volume for the highest voltage available, field experience with high-peak current discharge units and cost. The Mallory HES series 1500 mF/450 working volt electrolytic capacitors, having an equivalent series resistance (ESR) of 0.05Ω were selected, based upon their capability of providing 1 kA discharge currents and their proven performance at the Lawrence Livermore Laboratory, where over 50,000 units are contained in various configurations of energy storage capacitor banks. The following parameters may be derived for a system of five such racks, each containing 100 capacitors operating at 400V:

	FIVE IN SERIES	FOUR IN SERIES/ PARALLEL	FIVE IN PARALLEL
Energy	60 kJ	48 kJ	60 kJ
Capacitance	0.03F	0.15F	0.75 F
$I_{peak}$	20 kA	40 kA	100 kA
Voltage	2000V	800V	400V

Although the above values hold for the design of the capacitor bank, it must be noted that for the generation of a half-wave current sinusoid of critically damped oscillations, having a leading edge  $di/dt$  approximating 60 Hz operation, the constraints of voltage and LCR circuit parameters

limit the resulting discharge current as shown below. A set of equations was derived for the critically damped case from which the discharge current, critical inductance and damping resistance are determined for a given voltage and capacitance:

Operating Voltage (V)	Capacitance (F)	Peak Discharge Current (kA)	Critical Inductance ( $\mu$ H)	Damping Resistance ( $\Omega$ )
400	0.75	45	16.4	0.0046
400	0.6	36	20.5	0.0061
400	0.3	18	41.1	0.012
800	0.15	18	82.2	0.25
1600	0.0375	9	328	0.098

#### Circuit Design

Major circuit design considerations influencing safety to personnel and equipment are:

1. Isolation of a shorted capacitor from the network to prevent discharge of 99 or more parallel-connected capacitors through it (with possibly disastrous results).
2. Protection of series-connected banks of capacitors from overvoltage.
3. Protection of the polarized capacitor banks from the reverse polarity voltages impressed across the device under-test during recovery (reverse) voltage experiments after the discharge of the main capacitor bank.

Individual fuses or exploding wires to protect each capacitor were ruled out in favor of the 10 k $\Omega$  charging resistors shown in Figure 1, which provide isolation during the charging cycle. The superposition of 100 to 10,000 $\Omega$  resistors, each in series with a 1500 mF capacitor, provides an equivalent RC charging time constant of  $(400 + 100) \times 0.15 = 75$ s. An individual discharge diode couples each capacitor into a common external load and blocks the possible interaction from adjacent capacitors in the event of a capacitor's short-circuit.

Protection from overvoltage conditions is shown in Figure 2. Two zener diode assemblies, each rated at 180V/350W, are connected in series across the output of each capacitor rack. In the event of unbalances within the racks, the operation of the zener diodes in the operational rack(s) limits voltage to 360V to 385V and prevents over-stressing the capacitors.

Figure 3 shows a simplified schematic of the Synthetic Test Facility. It consists of a forward-current generator (the high energy capacitor bank, C1) and a low-energy recovery voltage generator that produces a reverse voltage across the device-under-test at a controllable time after the termination of current flow from the forward-current generator. Protection and awareness of inverse diode techniques are well known in pulse modulator design. To protect the polarized capacitors from reverse voltages, the following are provided: a) three parallel-connected 1N3295R diodes are connected across the output terminals of each of the five racks, b) a diode is connected from the SCR cathodes to ground, and c) a diode is connected across the discharge reactor L1 and damping resistor R2.

#### Component Selection

Three parallel-connected SCR's, type NL-602L, enable a total peak current of 18 kA to be switched. Three additional SCR's will be installed later this year to extend the current switching capacity to 36 kA. Four 82  $\mu$ H inductors made of 3/0 welding cable are pancake wound (20 in. I.D., 32 in. O.D.) and sandwiched between sheets of plywood provide the discharge inductances. The discharge isolation diodes for each capacitor are 60S8 epoxy diodes and the main inverse diodes are GE type A197P. The damping resistor, R2, is made of various lengths of 1 in  $\times$  8.9 mil thick Tophet-A resistive ribbon. A neon pilot light in parallel with the discharge diode will glow continuously if its respective capacitor shorts. If an isolating diode shorts, then its neon bulb will not glow during the charging cycle. Thus the "health" of each element in the system can be

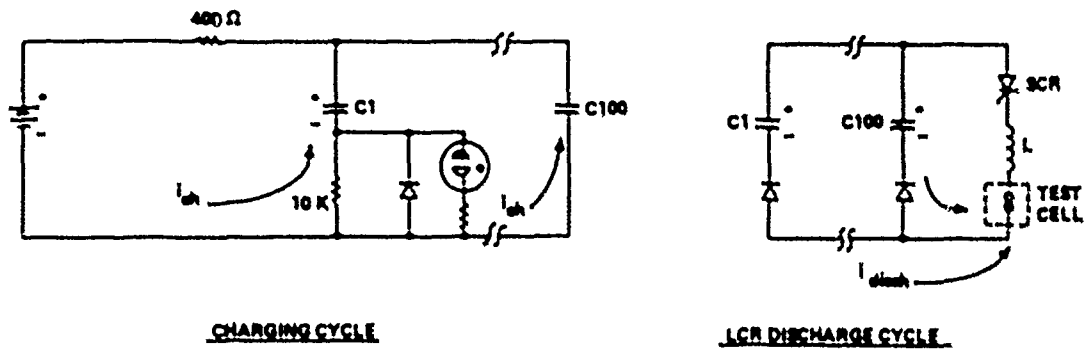


Figure 1. Energy Storage Bank Operation

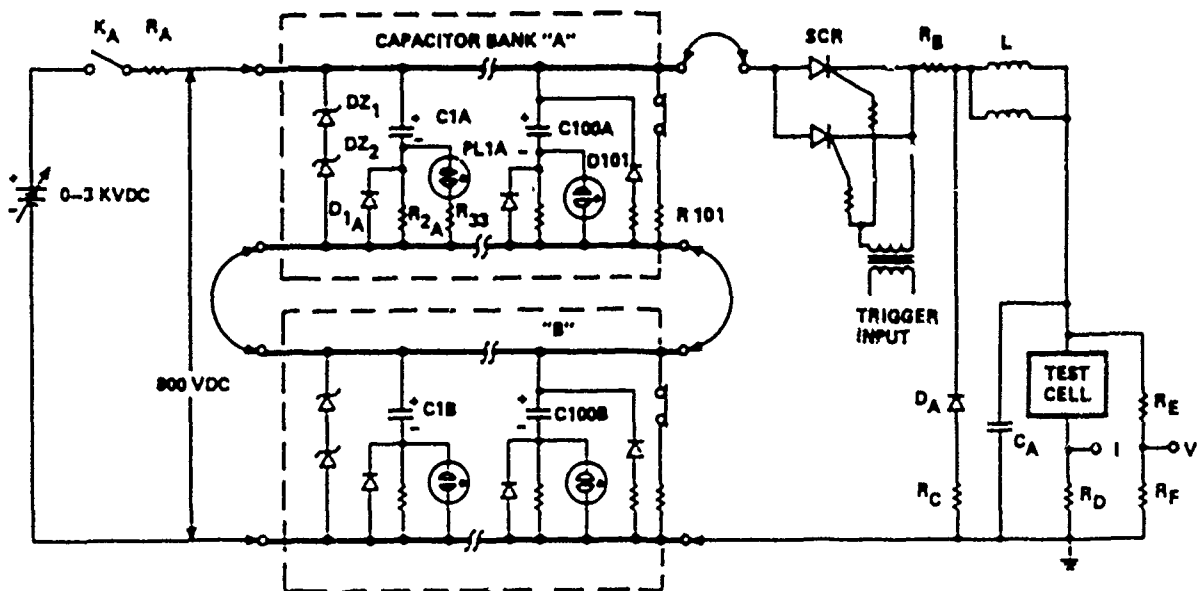


Figure 2. Synthetic Test: Simplified Schematic for Forward Voltage, High Current Discharge Circuit

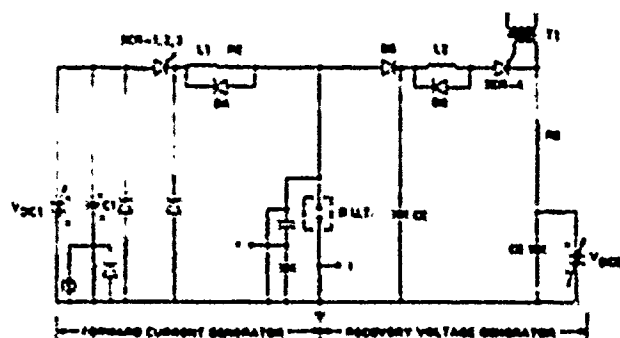


Figure 3. Simplified Schematic of Synthetic Test Facility

observed in a very simple manner during and after the charging cycle. Two large parallel-connected input and output banana plug jacks on each capacitor rack accept welding cable to connect similar connectors on the SCR's the inductors and the 4 in. x 1/4 in. copper busses feeding the test cell.

#### Construction Details

Each welded aluminum frame is 85 in. H by 20 in. W 27 in. D, is on casters, weighs approximately 300 lbs, is seven tiers high, and contains three shelves with five capacitors mounted on each shelf. The upper left shelf contains a Plexiglas housing with an exhaust fan to cool the Zener diodes, three inverse diodes, and an air-flow thermal interlock. Individual networks containing the isolation charging resistors, discharge diodes, neon bulbs and voltage dropping resistors connect between the negative terminal of each capacitor and a horizontal bus within the rack. The capacitors are mounted on aluminum shelves in the present equipment. Phenolic shelves, however, would be preferred to obviate concern for shorts between the insulated capacitor cans and ground.

Figure 4 shows the SCR's at the lower left, the inductors on the left and far walls, and the capacitor racks on the right in a room having a floor area of 8 x 10 ft. Current viewing at the test cell is provided by a T&M Research Products, Inc. noninductive current viewing shunt. Arc voltage is viewed by means of a conventional RC voltage divider.

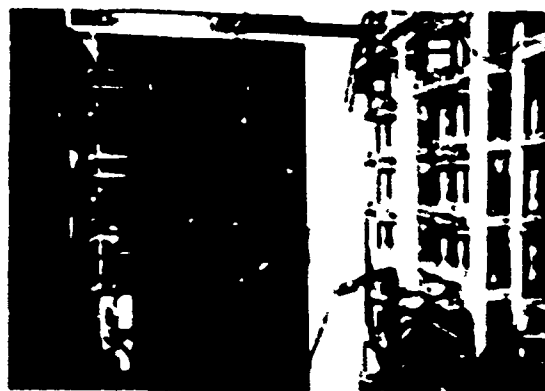


Figure 4. View of Vault Containing the Capacitor Bank, Inductors and SCR Switch Interconnections

#### Conclusion

To date, arc studies have been performed over a range of 0.2 to 14 kA discharge currents at 100V to 600V through the use of 1 to 4 racks of capacitors and various series/parallel combinations of inductors. Higher values of voltage and current are expected to be utilized later in the year.

#### Acknowledgment

The author would like to thank V.C. Oxley of GTE Laboratories and G. Pence of Lawrence Livermore Laboratory for their technical assistance.

## A 130 kV Low Impedance Multiple Output Trigger Generator

A. M. Ashnell, C. E. Dobbie, A. P. Krickhuhn

Maxwell Laboratories, Inc.  
8835 Balboa Avenue, San Diego, California 92123Abstract

A unique low impedance trigger generator has been developed which can generate 130 kV pulses having 22 ns risetime in four 50 ohm output cables. This generator uses a multichannel rail-gap switch to discharge a group of low inductance capacitors which are charged to 150 kV into the output cables. The performance of the circuit was analyzed using a computer and successfully predicted the behavior of the circuit. Time jitter between input trigger and output pulse is less than 2 ns (one standard deviation). The unit is immersed in oil in its own metal housing.

Introduction

High voltage trigger generators are used extensively to trigger various types of switching devices including spark gap switches. Typically, trigger generators for these applications range in output voltage from 10 kV to 500 kV with risetimes varying from less than 10 ns to several hundred ns.

We will start with a brief description of trigger systems and then present a detailed description of a recently developed trigger system.

Trigger generators can be divided into several classes as listed below:

- a. Charged cables
- b. Single stage charged capacitors
- c. Multiple stage charged capacitors
- d. Pulse transformer

Each of these classes will be discussed and a particular design of a single stage charged capacitor class will be discussed in detail.

Charged Cable

As shown in Figure 1, a charged cable trigger generator consists of a length of cable which is electrically charged to some potential  $V_0$  by a power supply. When switch  $S_1$  is closed, pulse travels along the cable from  $S_1$  to the output end. When the voltage pulse reaches the end of the cable the open circuit output voltage changes by  $-2V_0$ . Risetime of the output pulse is determined by switch inductance and cable impedance. Charged cable systems are probably the least complex and simplest type of trigger generator to build, but they suffer from problems of cable life as a result of the dc charge potential and 100% voltage reversal. This class of generator is often built with multiple charged cables feeding multiple loads but switched by a single switch. Also, as shown in Figure 1, a dc blocking capacitor can be used in those applications which do not permit the dc potential to be applied to the output load. Time jitter values less than 5 ns can be obtained with this class of generator.

Single-Stage Charged Capacitor

Figure 2 shows a single-stage charged capacitor trigger generator. In this case, the initial potential  $V_0$  is stored on the capacitor C and discharged into the output cable by switch  $S_1$ . The open circuit output voltage at the load end of the cable is  $2V_0$ . The charged capacitor generator offers advantages over the charged cable type since there is no dc charge potential on the cable nor is the cable subjected to voltage reversal. It is somewhat more difficult to obtain as fast a risetime from charged capacitor units as from charged cable units because of the added inductance of the capacitor and associated buswork. Time jitter values of less than 5 ns are obtained with this class of generator. Both of

these classes are capable of driving many cables and therefore are useful in systems which require many output triggers.

#### Multiple-Stage Charged Capacitors

The maximum output trigger amplitude of the single-stage charged capacitor class is typically limited by the maximum voltage rating of the switch  $S_1$ . In those applications which require output trigger potentials greater than can be obtained with a single capacitor-switch combination, Marx type trigger generators are used. A Marx generator consists of a group of capacitors charged in parallel and discharged in series; thereby multiplying the power supply by the number of capacitors. Spark gaps are normally used to switch Marx type trigger generators. Figure 3 shows a schematic diagram of a typical Marx generator. Typical Marx generators operate at potentials of 50 to 100 kV per stage and are often used to supply as much as 1 to 2 MV output potentials.

Risetime is determined by the inductance per stage and the load impedance. This class of generator tends to have somewhat higher source impedance than the two discussed above. As a consequence, Marx type trigger generators are usually used where they can be mounted in close proximity to and directly connected to the load, thus avoiding coaxial cables which would degrade risetime and limit the output potential. A properly designed Marx generator will typically have time jitter in the 10 ns region.

#### Pulse Transformer

In addition to the Marx generator approach just described, another method of obtaining large trigger potentials is to use a pulse transformer. As shown in Figure 4, the potential to which C is charged ( $V_0$ ) is stepped up by the turns-ratio of the transformer (N) so that the open-circuit output potential is  $NV_0$ .

Pulse transformer trigger generators provide a relatively high impedance trigger source at low cost. This type generator uses a switch (i.e., cold cathode switch tube, thyratron, etc.) to discharge a capacitor into the primary of a pulse transformer. Use of this type unit is limited to situations where slower

risetime and high impedance is acceptable. Because of the high source impedance, this type of generator is not used to drive coaxial cable. Therefore, the trigger generator must be placed adjacent to the unit being triggered.

#### 130 kV Low Impedance Multiple Output Trigger Generator

We have recently built a trigger generator of the single-stage charged capacitor type which can generate 130 kV pulses having 22 ns 10-90% risetime in four 50 ohm output cables. Nine of these generators will be used in a single system to provide 36 simultaneous 130 kV output triggers. A unique requirement of this application is that each output cable has a near-zero impedance short which appears at the output end of the cable early in the pulse. This system has been designed to withstand the voltage and current transients which result and still provide long trouble-free life.

A schematic diagram of one of these trigger generators is shown in Figure 5. A group of four 60 nF capacitors, in a series, parallel combination are connected to the 4 output cables by a low-inductance rail gap switch. Four capacitors are charged by an approximately constant current power supply via an isolation resistor to 150 kV. An inductor is used to reference the output size of the rail gap to ground for dc biasing. A two-resistor divider biases the trigger rail in the switch to  $V/3$ . An RC network couples the external trigger generator to the rail gap and provides dc isolation from the bias voltage. The rail gap is triggered by a Maxwell Catalog Number 40151, 100 kV trigger generator which is of the switched capacitor variety. This trigger generator provides the fast-rising pulse ( $>5$  kV/ns) required for a rail gap to operate in a multichannel mode. Nine output cables from the 50151 trigger generator are used to trigger the nine separate capacitor discharge units simultaneously.

The MLI 40151 trigger generator provides a 100 kV, fast-rising trigger pulse to the rail gap. This causes the rail gap to close in the multichannel mode. The four capacitors then discharge through the rail gap into the 12.5 ohm load of the four

50 ohm output cables. Total circuit inductance is 125 nH which provides a 10-90% risetime of 22 ns. The capacitors discharge as a decaying exponential and provide a pulse which has a full-width, half-maximum duration in excess of 300 ns, which is determined by cable impedance and trigger generator capacitance. This pulse decay continues until reflections on the cable return from the shorted output. Current waveforms were monitored by inserting a 0.5 ohm, coaxial current shunt in the braid of one of the output cables.

A cross section view of the trigger generator is shown in Figure 6. A tank provides a container for the insulating oil. The tank may rest on the floor or be suspended from the lid on mounting holes provided at each edge of the tank. All of the internal electronics are mounted on the lid to provide easy access to internal components for ease of maintenance. The rail gap is mounted between the pairs of Maxwell SS capacitors. Mylar paper insulation isolates the buswork from the rail gap.

A typical waveform of current in outer conductor of output cable is shown in Figure 7. Notice the reflection at 450 ns due to the shorted output cables used to model the actual load. A computer model of the trigger generator was developed and the results are presented in Figure 8 which shows the current in one of the cables. The computed peak current amplitude does not decay as fast as in the actual circuit because there was no loss mechanism included in the computer model. Jitter was less than 2 ns (one  $\sigma$ ). Nine of these generators have been manufactured for a system which will provide 36, 50 ohm outputs of 130 kV peak amplitude.

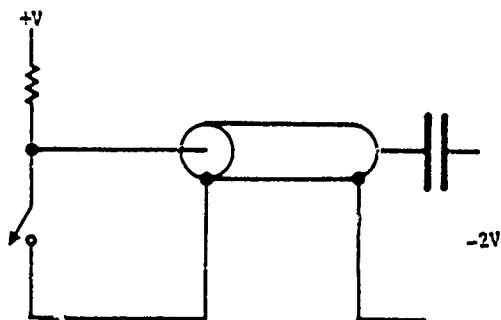


Figure 1. Charged cable trigger generator.

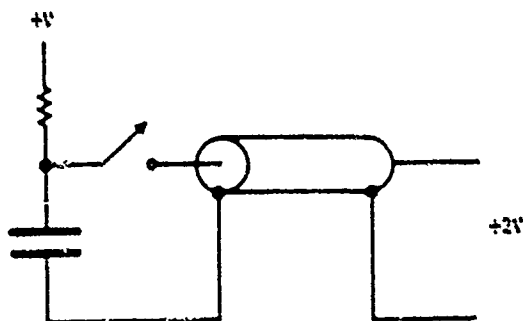


Figure 2. Charged capacitor trigger generator.

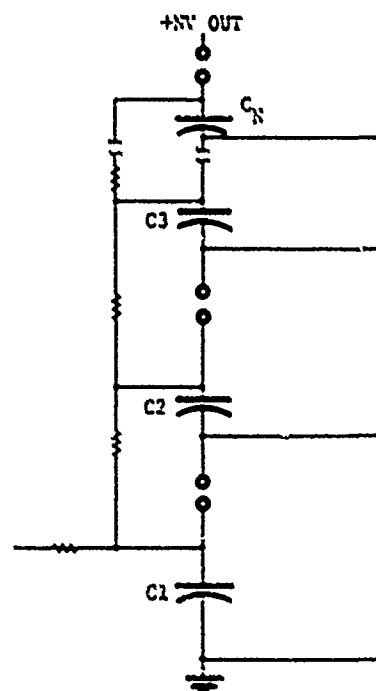


Figure 3. Marx generator/trigger generator.

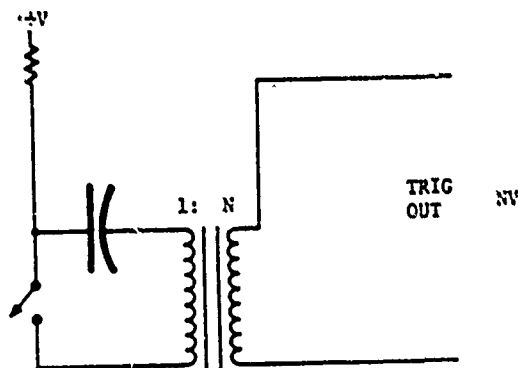


Figure 4. Pulse transformer trigger generator.

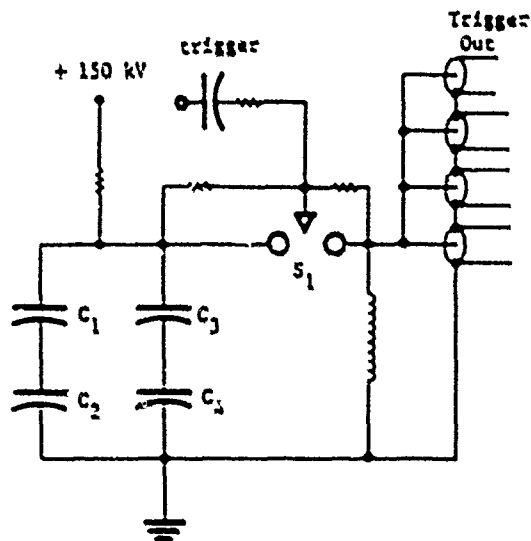


Figure 5. 130 kV trigger generator.

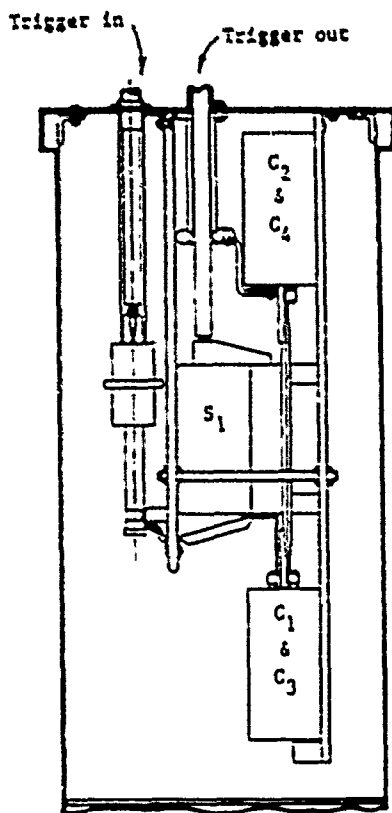
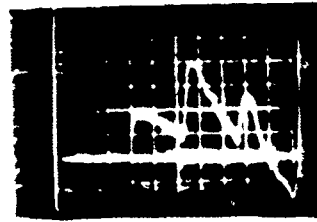


Figure 6. Cross section view of 130 kV trigger generator.



200 nsec/DIV

Figure 7. Waveform of current at output of trigger generator.

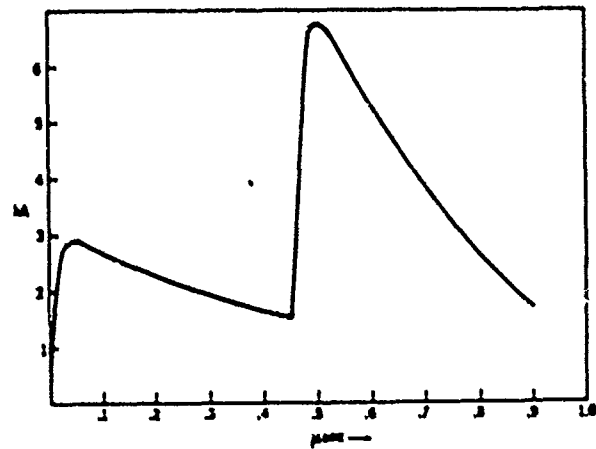


Figure 8. Plot of computer model of trigger generator.



INVITED  
LOW-IMPEDANCE, COAXIAL-TYPE MARX GENERATOR  
WITH A QUASI-RECTANGULAR OUTPUT WAVEFORM

M. UBARA, Y. SAKATO, C. H. LEE,  
T. HASHIMOTO, and T. FUJIOKA

Department of Electrical Engineering, Keio University,  
3-14-1, Niyoshi, Kohoku-ku, Yokohama-shi, 223, Japan

#### Abstract

Theoretical analysis of a low-impedance, coaxial type Marx generator, in terms of the equivalent electrical circuit, can offer the most appropriate parameters for the design of a Marx generator to produce a quasi-rectangular output waveform. The results of this theoretical analysis can be extensively applied to the design of various types of coaxial Marx generator. Based upon theoretical analysis, three Marx generators of 0.6MV, 1.0MV, and 2.6MV have been developed for the e-beam initiation of an HF chemical laser. The results of the analysis were in good agreement with the experimental results. They have a completely coaxial configuration. One advantage of these machines is that they can directly drive a low-impedance electron-beam diode, without a low-impedance PFN, for the efficient production of an intense relativistic electron beam. They are also remarkably compact.

#### 1. Introduction

Among several means for generating high voltage pulses over 100kV, the Marx generator has found widespread applications in various fields because of the ease with which it can produce high energies.<sup>1-3</sup> One such important application of the Marx generator is for relativistic electron-beam accelerators producing an intense relativistic electron beam<sup>2</sup> (IREB), which has been extensively used for collective ion acceleration<sup>3</sup>, nuclear fusion<sup>4</sup>, plasma heating, the initiation of chemical lasers<sup>5</sup>, and the excitation of gas lasers.

The requirements for these applications include a voltage pulse with a fast risetime and quasi-rectangular waveform, so that the velocities of the e-beams are identical over the entire pulse. However, conventional Marx generators have relatively high internal inductance, so that the voltage-pulse rise is slow and the pulse envelope is mainly determined by a series RLC oscillatory circuit.

The general practice has been to use a low-impedance pulse-forming network<sup>6</sup> (PFN), or Blumlein line<sup>7</sup>, charged by a conventional Marx generator, to drive a low-impedance e-beam diode. According to this scheme, no more than several tens of percent of the stored energy is available, because the stored energy of the Marx generator is inefficiently transferred to the PFN.

As the internal self-inductance of a Marx generator decreases, the voltage rise becomes

faster, and the output impedance decreases, with a corresponding improvement in the efficiency of charging the PFN.

In accordance with the above considerations, Kubota et al.<sup>8,9</sup> have succeeded in developing a low-impedance 600kV Marx generator which consists of ceramic capacitors as the individual capacitors, and which has a coaxial configuration.

We have developed low-impedance, coaxial Marx generators in order to generate intense electron beams used to initiate HF chemical lasers. We have derived an equivalent electrical circuit for this type of Marx generator. We found that an appropriate value of the stray capacitance with respect to the value of the Marx capacitor, can give a quasi-rectangular output waveform. Theoretical analysis of low-impedance, coaxial-type Marx generators would appear to establish the optimum parameters for the design of a Marx generator to produce a quasi-rectangular output waveform for any given values of pulse width, output voltage, and stored energy. The results of this analysis agreed fairly well with the experimental characteristics of 1MV 1kJ, 0.6MV 180J, and 2.6MV 2.2KJ Marx generators. In the case of the 1MV Marx generator, the output pulse contained 82% of the stored energy within the period for which the pulse height was over 90% of its peak voltage. Due both to the low impedance and to a pulse-forming effect, this pulse could drive a low-impedance e-beam diode directly without a PFN, achieving far more efficient conversion of the stored energy into e-beam output, and being more compact than the machines utilizing a PFN.

Moreover, the output voltage is 70% of the no-load voltage under the conditions for which the pulse most closely approaches a rectangular waveform, although when a PFN is used, the output voltage with a matched load is at most 50% of the charging voltage. At the expense of the output waveform, it is possible to obtain a voltage pulse higher than the voltage without load. The low-impedance, coaxial Marx generators have been developed for a REB-initiated HF chemical laser. These machines can, however, also be used in the fields of plasma physics. Therefore, we would like to report the theoretical and experimental studies on the coaxial Marx generators.

#### 2. The Structure of the Coaxial Marx Generator:

As an example, we describe the structure of a 1-MV coaxial Marx generator. A 1-MV, 1-kJ Marx generator consists of 10 Marx modules, each of

which is charged at up to  $\pm 50$  kV (plus-minus voltage charging system). The electrical circuit of this coaxial Marx generator is shown in Fig. 1.

We have adopted the following means of reducing the inductance of the Marx generator and thus its impedance (see Table I).

First, ceramic capacitors which have virtually negligible residual inductance are used as energy storage capacitors.

Second, each Marx module has a completely coaxial configuration. A gap switch is placed at the center of the Marx module, where ceramic capacitors are arranged concentrically. Marx modules are inserted in a stainless steel cylinder (560 mm in diameter and 2670 mm in overall length) which acts as the outer conductor. Each Marx module is composed of 324 SrTiO<sub>3</sub> ceramic capacitors ( $\epsilon_r = 4450$ ),<sup>9</sup> aluminum disks (460 mm in diameter and 6 mm thick), a pair of pressurized gap switches, and three charging resistors. Each ceramic capacitor is 35 mm in diameter and 24 mm in length, and has a rated nominal capacitance of 1 nF and a rated voltage of 25 kV.<sup>10</sup> To raise the working voltage of each Marx module, two capacitors are connected in series, and 81 such pairs are distributed in parallel as closely as possible. These two sets of capacitors are put between three aluminum disks. Because the ceramic capacitors are distributed so closely, one Marx module can be regarded as two 40.5 nF capacitors connected in series.

Figure 2 shows a simplified cross-sectional view of a coaxial Marx generator. Ten Marx modules are stacked in series, secured firmly by 10 plastic rods, and put at the center of the stainless steel cylinder. The Marx modules are immersed in high-voltage transformer oil. Triggering the first gap switch (pressurized with a mixture of SF<sub>6</sub> and N<sub>2</sub>) enables the Marx modules to be connected electrically in series to generate a negative high voltage. At a charging voltage of  $\pm 50$  kV, the energy stored in the Marx generator is estimated at 1.01 kJ. The loss in available energy stored in a SrTiO<sub>3</sub> capacitor in comparison with the nominal stored energy is much less than that of a BaTiO<sub>3</sub> capacitor.<sup>10</sup>

The gap switches used consist of a spherical brass (-) electrode (radius of curvature 20 mm) and a flat electrode, the gap length of which is 18 mm. The gap switches are separated by an 80 mm o. d. lucite tube and "o" ring gaskets, pressurized with an SF<sub>6</sub>/N<sub>2</sub> mixture at up to three atmospheres.<sup>11, 12</sup>

### 3. Operating Characteristics of the Coaxial Marx Generator

In order to measure the operating characteristics of the coaxial Marx generator, a copper-sulfate solution was used as a resistive load. With the structure shown in Fig. 3, this can function not only as a resistive load but also as a high-speed-response voltage divider.<sup>13</sup> The third copper disk electrode near the ground electrode enables the output voltage waveforms for a given resistance to be obtained by measuring the voltage between these two electrodes. The dividing ratio of this resistor is 1/800.

Figure 4 shows the output waveforms at a

charging voltage of  $\pm 25$  kV. As noted in this figure, the values of resistance are 12, 30, and 40  $\Omega$ .

In the case of an ordinary Marx generator connected with a given resistive load  $R$ , RLC resonant oscillation occurs, where  $L$  and  $C$  are decided mainly by the inductance of the gap switches and the capacitance of the Marx modules. In this case, the output waveforms are classified

into three types: under-damping ( $R < 2\sqrt{L/C}$ ),

critical-damping ( $R = 2\sqrt{L/C}$ ), and over-damping

( $R > 2\sqrt{L/C}$ ). From Fig. 4, the output voltage waveforms appear not to be defined by a pure RLC resonant circuit, but to be defined by some kind of pulse-forming line. This pulse-forming effect can be thought of as arising from the distributed circuit consisting of both stray capacitance between inner and outer conductors, and inductance mainly determined by gap switches. An analysis has been performed using an equivalent circuit. Discussion of this analysis follows in the next section.

### 4. Theoretical Analysis

In this 1-MV coaxial Marx generator, the capacitance of a Marx module and the inductance of the gap switch are placed in a linear sequence. There also exists a stray capacitance between the outer conductor (stainless-steel cylinder) and the circular Marx module. Here, for convenience of analysis we propose the equivalent circuit of the coaxial Marx generator shown in Fig. 5 for the analysis of the output performance. The following notation is used:

- $L_1$ : inductance of a triggered spark-gap switch,
- $L_2$ : inductance of a gap switch between individual Marx generator,
- $L_3$ : inductance of an output gap switch,
- $C_m$ : capacitance in each Marx module. A Marx module contains two  $C_m$ 's in series.
- $C_s$ : stray capacitance between the outer conductor and a cylindrical Marx module,
- $R_L$ : load resistor.

A gap switch is assumed to consist of an inductance and a switch, and to close when the applied voltage exceeds its flashover voltage. In Fig. 5, a Marx module is indicated by an area enclosed by oblique lines.

The inductance of each gap switch is thought to be composed of both a structural inductance  $L_s$ , which indicates the inductance between the gap switch and the outer conductor, and the channel inductance during discharge.<sup>14</sup> In this machine, structural inductances are estimated to be 37 nH for the triggered spark-gap switch, 65 nH for the gap switch of each Marx module, and 38 nH for the output switch. Although a discharge-channel inductance of 15 nH/cm has been reported,<sup>14</sup> a value of 28 nH/cm was, however, found to give the best fit with the experimental results in this case. From the above calculations, the total inductance

of the individual gap switches with gap spacings of 10, 15, and 15 mm, are  $L_1 = 65$  nH,  $L_2 = 115$  nH,  $L_3 = 80$  nH, respectively.

A Marx capacitance  $C_m$  was 49.5 nF. Stray capacitance  $C$  is calculated from the capacitance of a coaxial line consisting of an inner conductor (a circular Marx module is considered as one cylindrical conductor) and an outer stainless steel cylinder. In this case,  $C_s$  is estimated to be 0.10 nF.

It is assumed that each Marx capacitor  $C_m$  is initially charged at a voltage  $V_0$ , and the stray capacitor  $C_s$  is not charged initially because of the plus-minus charging scheme, before a triggered spark-gap switch is fired. Therefore, initially a voltage of  $V_0$  is applied to switches  $S_1$  and  $S_{11}$ , while a voltage of  $2V_0$  is applied to all switches  $S_2$  to  $S_{10}$ .

If in this machine only the triggered spark-gap switch  $S_1$  on the first stage is fired externally, so closing switch  $S_1$ , the voltage across gap-switch  $S_1$  starts to increase from its initial voltage of  $2V_0$ . When this voltage exceeds the breakdown voltage determined by the gap spacing and mixture pressure, the switch  $S_1$  is closed. In this way, individual switches close successively up to and including switch  $S_{11}$ , and when switch  $S_{11}$  is finally closed, the output voltage appears across the resistive load  $R_L$ . It is reasonable not to assume that all switches can close simultaneously, but to understand that according to the above discussion, gap switches will close in order with successive time-lags. In order to decrease the temporal jitter in the gap switches, the mixture pressure in each gap switch is adjusted to some 70-90% of the self-breakdown voltage for the gap switch when charging a Marx generator. It is well known that the breakdown voltage is dependent upon the time for which the voltage is applied, with higher voltages for shorter application times.<sup>13</sup> In this case, the breakdown voltage in the pulsed mode is estimated to be 1.8 times higher than in a DC mode.

Using the values cited above, the following set of circuit equations can be derived from the equivalent electrical circuit shown in Fig. 5.

If the voltages applied to the  $C_m$  and  $C_s$  on the  $n$ 'th stage are denoted  $V_N$  and  $\phi_N$ , respectively, and the current passing through the  $C_m$  is denoted as  $I_N$ ,  $I_N$  may be written as follows,

$$I_N = C_m \frac{\partial V_N}{\partial t} \quad (1)$$

Here, a variable  $K_N$  indicating the on-off switching state of the gap switch is introduced. When the switch is closed,  $K_N = 1$  and when cut off,  $K_N = 0$ . The current passing through the  $C_s$  on the  $n$ 'th stage can be written as

$$\begin{aligned} C_s \frac{\partial \phi_N}{\partial t} &= K_N I_N - K_{N+1} I_{N+1} \\ &= C_m \left( K_N \frac{\partial V_N}{\partial t} - K_{N+1} \frac{\partial V_{N+1}}{\partial t} \right) \quad (2) \end{aligned}$$

On the loop  $N = 1$ , we obtain

$$\begin{aligned} L_1 \frac{\partial I_1}{\partial t} + V_1 + \phi_1 \\ = L_1 C_m \frac{\partial^2 V_1}{\partial t^2} + V_1 + \phi_1 = 0 \quad (3) \end{aligned}$$

Similarly, on the loops  $N = 2-10$ , we obtain

$$L_2 C_m \frac{\partial^2 V_N}{\partial t^2} + 2V_N + \phi_N = \phi_{N-1} \quad (4)$$

If the voltage appearing on the resistive load  $R_L$  is written as  $V_R$ , on the loop  $N = 11$ , we obtain

$$L_1 C_m \frac{\partial^2 V_{11}}{\partial t^2} + V_{11} + V_R = \phi_{10} \quad (5)$$

$$V_R = R_L I_{11} = R_L C_m \frac{\partial V_{11}}{\partial t} \quad (6)$$

We can calculate the output voltage appearing on the resistive load, by substituting  $V_R (= V_{11} - V_{11}^0)$  as an initial value into equations (2)-(6).

Figure 4 shows the output voltage waveforms measured with the load resistors  $R_L$  of 12, 30, and 40  $\Omega$ , together with the theoretical results given by this analysis. For reference, in the case that  $R_L = 40$   $\Omega$  the voltage  $V$  appearing on the stray capacitance  $C_s$  of the  $N$ 'th Marx module, and the output voltage  $V_R$  are shown in Fig. 6. In Fig. 6, the time of firing the triggered spark-gap switch is set at  $t = 0$ , while in Fig. 4 the time when the voltage starts to appear on the resistive load is at  $t = 0$ . As is clear from Fig. 6, the voltage on the  $C_s$  of the  $n+1$ 'th stage appears later than that on the  $C_s$  of the  $n$ 'th stage. The output voltage waveform produced by this coaxial Marx generator is the result of two effects: one of which arises in an RLC resonance circuit, and the other of which arises in a distributed element circuit. In the frequency region characterized by the RLC resonance circuit, the resonance frequency of which is

$$f_{RLC} = \left( 2\pi \sqrt{(L_1 + 9L_2 + L_3) C_m / 20} \right)^{-1} = 3.3 \text{ MHz}$$

$(2\pi f_{RLC} C_m)^{-1}$  and  $2\pi f_{RLC} L_2$  are estimated to be 1.2 and 2.4  $\Omega$ , respectively. However,  $(2\pi f_{RLC} C_s)^{-1}$  is 450  $\Omega$ , which is much larger than  $C_m$  and  $L_2$ . Thus,  $C_s$  may be neglected so that the Marx generator can act as a simple oscillatory series RLC circuit.

On the other hand, in the region determined by the distributed element circuit, the resonance frequency of which is given by

$$f_{LINE} = (2\pi \sqrt{L_2 C_s})^{-1} = 47 \text{ MHz}$$

$2\pi f_{LINE} L_2$  and  $(2\pi f_{LINE} C_s)^{-1}$  are 33 and 33  $\Omega$ , respectively. However,  $(2\pi f_{LINE} C_m)^{-1}$  of  $C_m$  is  $8.7 \times 10^{-4} \Omega$ , which is much smaller than those of  $L_2$  and  $C_s$ . Therefore, in this frequency region, the Marx generator seems to function as a distributed element circuit.

Consequently, the output voltage waveforms shown in Fig. 4 can be attributed to the effect of an RLC lumped element circuit coupled with a distributed element circuit.

##### 5. Generalization of the Design of the Coaxial Marx Generator with a Quasi-Rectangular Output Waveform

In this section, we extend the analysis using the variables described below, so as to generalize

this analysis and to offer a guide for the design of a coaxial Marx generator with a quasi-rectangular output.

In this analysis,  $n$  is the number of Marx modules, and the notation for elements of the Marx module follows that of Fig. 5. If there is no stray capacitance between inner conductor and outer cylinder, the Marx generator is seen to be a simple oscillatory series RLC circuit, as indicated in Fig. 7.

The analysis reveals that variations in  $L_1$  and  $L_2$  have hardly any influence upon the overall characteristics of the device and that its output characteristics are mainly dependent upon the value of  $L_3$ . Moreover, the voltage applied to both  $L_1$  and  $L_2$  is only a half that applied to  $L_3$ , so that the gap spaces of both  $L_1$  and  $L_2$  may be reduced to decrease their inductances. Hence, for simplicity of the subsequent calculation, we assume that

$$L_1 = L_2 = L_3/2 \quad (7)$$

Using equation (7),  $L$ ,  $C$ , and  $V$  shown in Fig. 7 simplify to

$$L = L_1 + (n-1)L_2 + L_3 = nL_2 \quad (8)$$

$$C = C_m/2n \quad (9)$$

$$V = 2nV_0 \quad (10)$$

After normalization of  $V_R$  and  $t$  using these  $L$ ,  $C$ , and  $V$ , the dimensionless variables  $V_{DL}$  and  $T_{DL}$  are defined as

$$V_{DL} = V_R/V = V_R/2nV_0 \quad (11)$$

$$T_{DL} = t/2\pi\sqrt{LC} = t/2\pi\sqrt{L_2C_m/2} \quad (12)$$

where  $V_R$  is the voltage appearing across the resistive load,

$t$  is time,

$V_{DL}$  is the ratio of  $V_R$  to output voltage  $V$  with no load,

$T_{DL}$  is the ratio of  $t$  to the resonance period  $2\pi\sqrt{LC}$ .

Since the output voltage waveform of the Marx generator varies with the resistance of the resistive load, we introduce a normalized load resistance  $\lambda$  defined by

$$\lambda = \frac{R_L}{2} \sqrt{C/L} = \frac{R_L}{2} \frac{1}{n} \sqrt{C_m/2L_2} \quad (13)$$

where  $\lambda$  indicates the ratio of the load resistor  $R_L$  to  $2\sqrt{L/C}$  which is the resistance at which critical damping occurs in a simple RLC series resonance circuit. If  $\alpha$  is introduced in this manner, the conditions for damping are simply given:  $\lambda < 1$  (under-damping),  $\lambda = 1$  (critical-damping), and  $\lambda > 1$  (over-damping).

In a simple RLC series oscillatory circuit, all the output voltage waveforms can easily be characterized by such normalized parameters as  $V_{DL}$ ,  $T_{DL}$  and  $\lambda$ . However, where a pulse-forming effect exists due to stray capacitance between inner conductor and outer cylinder, a parameter indicating the degree of the pulse-forming effect is

required, because the pulse-forming effect is strongly dependent upon the stray capacitance. Therefore, we introduce a parameter  $\sigma_T$  defined by the ratio of  $\pi\sqrt{LC}$  to  $n\sqrt{L_2C_m}$ , where

$$\sigma_T = \frac{\pi\sqrt{LC}}{n\sqrt{L_2C_m}} \quad (14)$$

and where  $\pi\sqrt{LC}$  is the half period of resonance in an RLC series resonance circuit, and  $n\sqrt{L_2C_m}$  is the propagation time of an electromagnetic wave per unit length in the Marx generator.

Substituting equations (8) and (9) into (14), we have

$$\sigma_T = \frac{\pi}{n} \sqrt{C_m/2C_3} \quad (15)$$

As can easily be seen from equation (15),  $\sigma_T$  is determined by the capacitance  $C_m$  of the Marx generator.

The output-voltage waveforms calculated by this analysis using the normalized parameters are shown in Figs. 8 and 9. Figure 8 shows the theoretical waveforms as a function of  $\alpha$  with parameters  $n=20$ , and  $C_m = 3.75$ . Figure 9 shows the results obtained with such parameters as  $n = 20$ , and  $\alpha=0.3$  as a function of  $C_m$ . In Fig. 8, the unwanted deviations of the output pulse waveform are seen. For example, the pulse waveform at  $\alpha = 0.4$ , and  $C_m = 3.75$  is under-damped and is distorted into a negative tilt. In Fig. 9, the two upper pulse waveforms are negatively tilted, and two lower pulses are positively tilted. In all pulses obtained, the pulses build up sharply with time, and exhibit neither rounding (undershoot) nor glitches.

From Figs. 8 and 9, it is found that appropriate values of  $\sigma_T$  and  $\alpha$  must be chosen to obtain the most rectangular output waveform. We determined the most suitable values of  $\sigma_T$  and  $\alpha$  by the following method.

First, so as to determine the optimum  $\sigma_T$  at a fixed value of  $\alpha$  (as described below, the optimum value of  $\alpha$  is 0.8, so  $\alpha$  is fixed at 0.3) we calculate the following ratios as a function of  $\sigma_T$ :

- (a)  $T_{0.9}/T_{0.5}$ : the ratio of period for which the output voltage is at least 90% of the peak pulse voltage to the FWHM of the pulse,
- (b)  $E_R/E_C$ : the ratio of the energy dissipated in the resistive load to the energy stored in the Marx capacitors,

where these two ratios indicate the degree of pulse forming, and both values approach unity as the output pulse becomes completely rectangular.

Calculated values of  $T_{0.9}/T_{0.5}$  and  $E_R/E_C$  for  $\sigma_T = 3-4.5$  are shown in Fig. 10. Fig. 10 shows that when  $\sigma_T = 3.75$  the most rectangular waveform can be obtained. However, even over the range  $\sigma_T = 3.5-4$ , the pulse waveform is considered to be nearly rectangular, and the energy dissipated in the load is over 95% of that at  $\sigma_T = 3.75$ .

Next, so as to determine the optimum  $\alpha$  at a fixed value of  $\sigma_T = 3.75$ , we calculated the value of  $E_R/E_C$  as a function of  $\alpha$ . This result is shown in Fig. 11. In Fig. 11, it is clear that the most rectangular waveform can be obtained when  $\alpha = 0.8$ . However, even in the region of  $\alpha = 0.7-1.0$ , the pulse

waveform is nearly rectangular, and the energy dissipated in the load is calculated to be greater than 95% of that at  $C_m = 3.75$ .

Although the above theoretical analysis is only for  $n=20$ , the optimum conditions obtained by the analysis are valid for coaxial Marx generators with any number of stages, provided only that  $\alpha$  and  $C_m$  are set to the values derived above. In order to establish the validity of these results, we calculated the output voltage waveform for the case of  $n=10$ , and  $n=20$ , in both cases of which  $C_m = 3.75$  and  $\alpha = 0.8$ . The results are compared in Fig. 12.

According to the results of the theoretical analysis, it was found that parameters should meet the following requirements, in order to generate an output voltage pulse of quasi-rectangular waveform:

$$(A) \quad \sigma_T = \frac{\pi}{n} \sqrt{C_m / 2C_S} = 3.75 \quad (16)$$

Equation (16) is equivalent to the form of

$$Z_L = \frac{Z_{LINE}}{2R_{LC}} = \frac{1}{2n} \sqrt{C_m / 2C_S} = 0.60 \quad (17)$$

where  $Z_{LINE} = \sqrt{L_2 / C_S}$  is the characteristic impedance of a distributed element circuit, and

$R_{LC} = 2\sqrt{L_2 / C} = 2n\sqrt{L_2 / C_m}$  is the resistance of the load for an RLC series oscillatory circuit in which critical damping occurs.

$$(B) \quad c = \frac{R_L}{2n} \sqrt{C_m / 2L_2} = 0.80 \quad (18)$$

For a coaxial Marx generator which satisfies equations (16) and (18), the following three parameters are given:

"The impedance  $Z$ " (defined by the value of the resistive load at which the Marx generator can deliver the maximum energy over a period in which the voltage is at least 90% of the peak output voltage) is expressed as

$$Z = 0.8 \times 2n\sqrt{2L_2 / C_m} = 0.8 Z_{RLC} = 1.3 Z_{LINE} \quad (19)$$

when connected with the optimum resistive load, the maximum output voltage  $V_{R MAX}$  is given by

$$V_{R MAX} = 0.73 V = 1.5 nV_0 \quad (20)$$

when connected with the optimum resistive load, the pulsewidth of the output voltage waveform (defined as the period during which the Marx generator can produce a voltage at least 90% of the peak output value) is given by

$$T = 0.22 \times 2\pi\sqrt{LC} = 0.44\pi\sqrt{L_2 C_m / 2} \quad (21)$$

The electrical energy charging the Marx capacitors is expressed as

$$E = \frac{1}{2} CV^2 = nC_m V_0^2 \quad (22)$$

## 6. Concluding Remarks

From the theoretical analysis of the coaxial Marx generator, we derived the following conclusions:

- Fewer Marx modules and a larger  $C_m$  reduce the impedance of the Marx generator.
- Smaller values of  $L_2$  and  $C_m$  are required to shorten the pulsewidth of the output pulse.
- To obtain the most rectangular pulse, the more Marx modules there are, the smaller the ratio of  $C_S$  to  $C_m$  should be, because the

ratio of  $C / C_m$  is inversely proportional to  $n^2$  according to equation (16). This condition (c) is, fortunately, conducive to the construction of a coaxial Marx generator with a rectangular output waveform. As the output voltage increases with the increasing number of Marx modules, it becomes possible to increase the distance between the Marx module (inner conductor) and the outer conductor. This condition is advantageous for the prevention of flashover through the insulation oil that fills the Marx generator.

Using the generalized theoretical analysis of the coaxial Marx generator described in this section, we also analyzed theoretically the characteristics of the 600-kV, 180-J, 10-stage<sup>1</sup> and 2.6-MV, 2.2-kJ, 16-stage<sup>2</sup> coaxial Marx generators (Figs. 13 and 14). The specifications of these machines are shown in Table I. The output waveforms obtained theoretically were found to correspond with the experimental results.

## Acknowledgements

We would like to appreciate helpful discussion with Dr. T. Uchiyama, and to appreciate technical assistance of Mr. T. Ogura. We would also like to greatly appreciate the supports by the Ministry of Education and by the Nissan Science Foundation.

## References

- R. A. Fitch, IEEE Trans. Nucl. Sci. NS-18, 190 (1971).
- L. S. Levine, et al., IEEE Trans. Nucl. Sci. NS-20, 456 (1973).
- C. L. Olson, IEEE Trans. Nucl. Sci. NS-22, 962 (1975).
- L. S. Levine, et al., IEEE Trans. Nucl. Sci. NS-18, 255 (1971).
- R. A. Gerber, et al., Appl. Phys. Lett. 25, 281 (1974).
- T. H. Martin, IEEE Trans. Nucl. Sci. NS-20, 289 (1973).
- P. Campney, et al., IEEE Trans. Nucl. Sci. NS-22, 970 (1975).
- Y. Kubota, et al., Jpn. J. Appl. Phys. 13, 260 (1974).
- S. Kawasaki, et al., IEEE Trans. Nucl. Sci. NS-20, 280 (1973).
- Taiyo Yuden Incorporated, Technical Report, p.46 (1977).
- T. Takuma, et al., Proc. Instn. Elec. Engrs. 119, 929 (1972).
- P. R. Howard, Proc. Instn. Elect. Engrs. 104, 123 (1957).
- Y. Kubota, et al., Jpn. J. Appl. Phys. 15, 2037 (1976).
- F. B. A. Fungel, "High Speed Pulse Technology III," p.109, Academic Press, New York, (1976).
- J. D. Shipman Jr., IEEE Trans. Nucl. Sci. NS-18, 243 (1971).
- M. Obara, T. Fjioka, Y. Sakato, and T. Hashimoto unpublished.

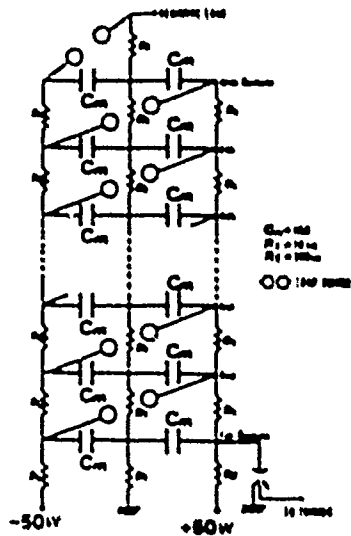


Fig. 1 Electrical circuit of the coaxial-type, 10-stage Marx generator (1MV, 1kJ).

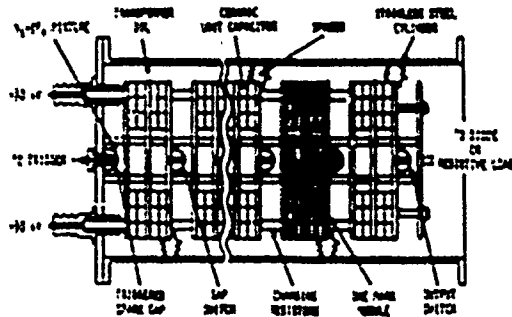


Fig. 2 Simplified cross-sectional view of a coaxial-type, 10-stage Marx generator. Not to scale.

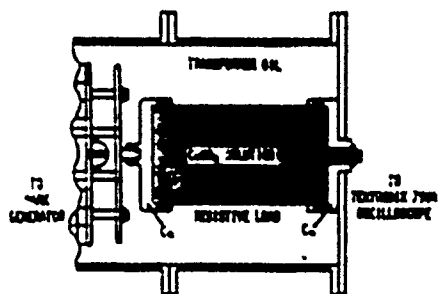


Fig. 3 Cross-sectional view of a  $\text{CuSO}_4$ -solution resistive load. (connected with a Marx generator). Not to scale.

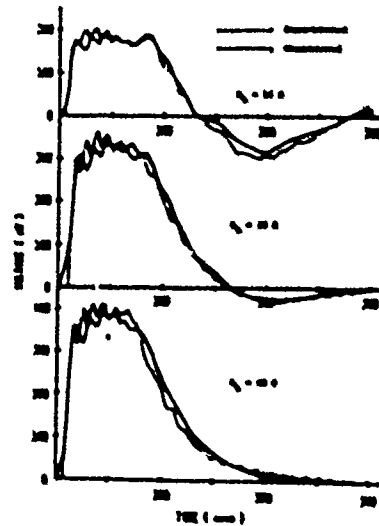


Fig. 4 Comparison of theoretical and experimental results of output voltage waveform at a charging voltage of  $\pm 25$  kV.

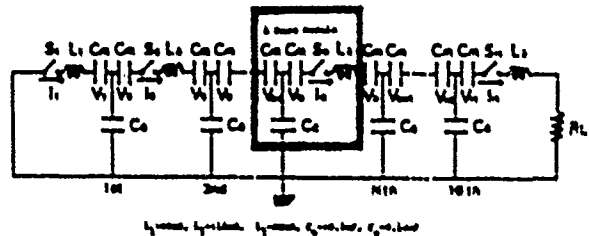


Fig. 5 Equivalent electrical circuit of a coaxial-type, 10-stage Marx generator.

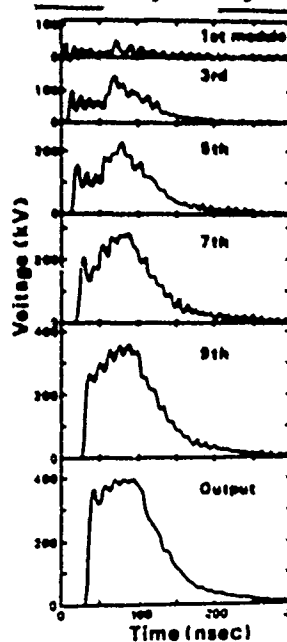


Fig. 6 Theoretical voltage waveforms appeared on  $n$ 'th Marx module with a  $40\Omega$  resistive load.

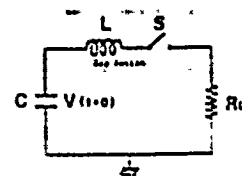


Fig. 7 Simplified electrical equivalent circuit of a Marx generator.

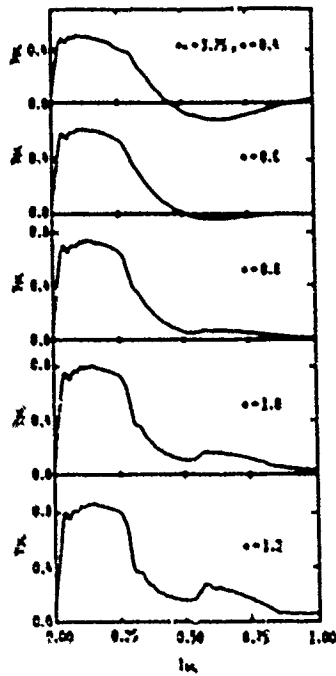


Fig. 8 Dependence of the output voltage waveforms on parameter  $\alpha$ .

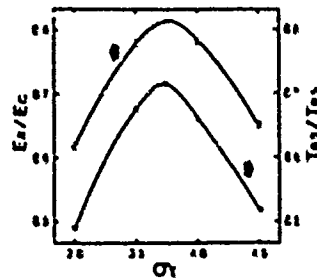


Fig. 10 Parameter  $\alpha$  vs. both  $E_R/E_C$  and  $T_{0.9}/T_{0.5}$ .

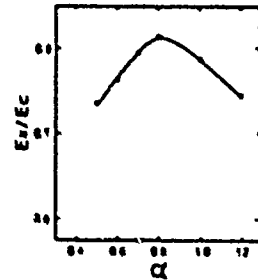


Fig. 11 Parameter  $\alpha$  vs.  $E_R/E_C$ .

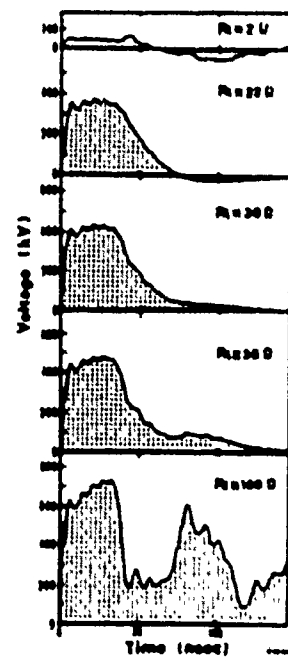


Fig. 14 Theoretical output waveform for the 0.6-MV Marx generator.

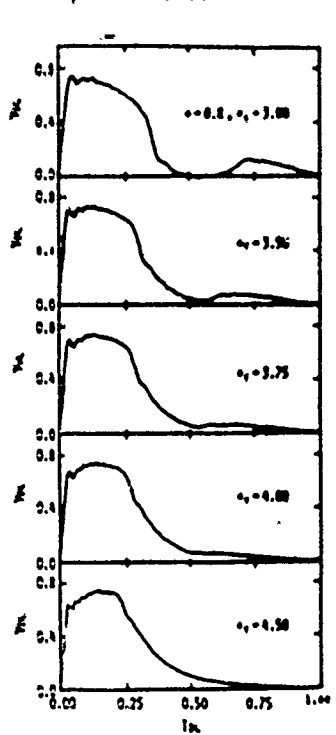


Fig. 9 Dependence of the output voltage waveforms on parameter  $\gamma_T$ .

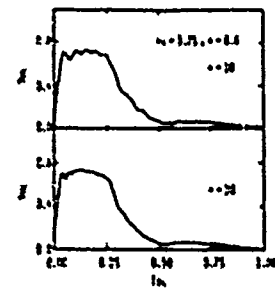


Fig. 12 Typical output voltage waveforms of coaxial Marx generator under the optimum conditions.

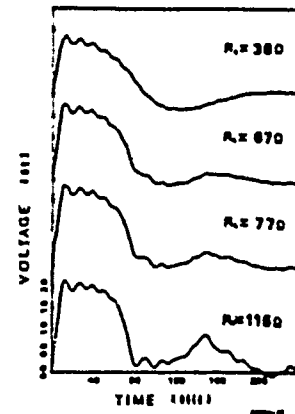


Fig. 13 Theoretical output waveform for the 2.6-MV Marx generator.

	KREDA-I	KREDA-II	KREDA-III
OUTPUT VOLTAGE	0.6MV	1.0MV	2.56MV
STORED ENERGY	0.10kJ	1.01kJ	2.21kJ
NUMBER OF STAGES	10	10	16
CHARGING VOLTAGE	-60kV	-50kV	-60kV
ELEMENT CAPACITOR	30kV 2500pF (BaTiO <sub>3</sub> )	25kV 1000pF (SrTiO <sub>3</sub> )	40kV 2700pF (BaTiO <sub>3</sub> )
NUMBER OF CAPACITORS USED	160	3200	1024
TOTAL CAPACITANCE	1000pF	2025pF	675pF
DIMENSIONS	ø267mm x1455mm	ø560mm x2670mm	ø560mm x4740mm
IMPEDANCE	30 Ohm	38 Ohm	75 Ohm
PULSEWIDTH	20nsec	66nsec	47nsec

Table 1 Specifications of the 0.6, 1.0, and 2.6MV Marx generators.

## THE DESIGN APPROACH TO A HIGH-VOLTAGE BURST GENERATOR\*

D. Cummings and M. G. Mamon, III

Physics International Company  
2700 Marced Street  
San Leandro, California 94577ABSTRACT

An increasing number of experimental programs call for a sequence of several closely spaced, high-voltage pulses. This paper presents the various design considerations for such a system. These include the kind of pulse generator, series or parallel configuration, kinds of lines, aspect ratio, choice of dielectric, switch type, triggering considerations, Marx Generator design and isolation, feed problems, pulse formation, and waveform degradation with increasing stages. The design procedure is illustrated by the M-2 pulser built for the PHERMEX Facility at the Los Alamos Scientific Laboratory. This system produces a train of up to three 40 ns pulses, variable from 600 kV to 1.4 MV with pulse separations of 100 ns to 1 ms. Results are given and waveforms presented.

1.0 INTRODUCTION

Recently there has been increasing interest in programs which require a series of several closely spaced, high-voltage pulses. These programs include studies of injection into magnetically confined fusion reactors, charged particle beam weapon propagation studies, and multiple exposure radiographic systems.

The system described in this paper is the M-2 Pulser built for the Los Alamos Scientific Laboratory. A summary of the principal performance specifications is given in Table 1. A drawing of the pulser with the dummy load is shown in Figure 1.

\*Work performed under contract from the Los Alamos Scientific Laboratory.

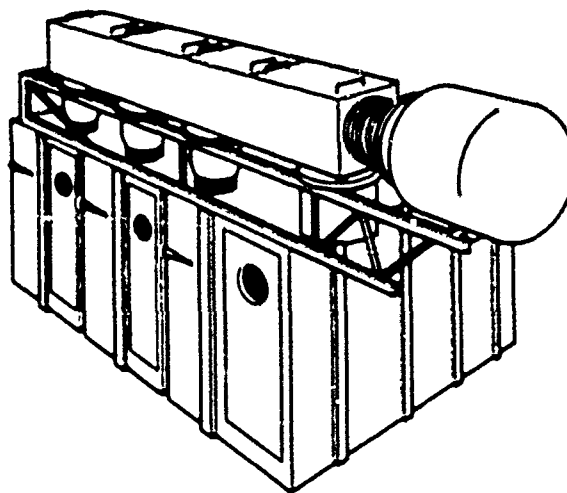


Figure 1 PHERMEX M-2 Pulser.

TABLE 1  
PHERMEX M-2 PULSER SPECIFICATIONS

1. OUTPUT	0.6 TO 1.5 MV
2. LOAD	THERMIONIC DIODE
3. LOAD IMPEDANCE	862Ω @ 1.5 MV
4. PULSE DURATION	
1 PULSE	40 ± 4 nsec
2 PULSES MERGED	80 ± 30.0 nsec
3 PULSES MERGED	120 ± 30.0 nsec
5. RISE TIME	< 25 nsec
6. FALL TIME	< 40 nsec
7. JITTER	σ < 8 nsec
8. PULSE SEPARATION	
(2nd 10% TO 1st 90%)	100 nsec min
(1st 90% TO 1st 90%)	30 μsec max
9. PULSE FLATNESS	± 10%
(15% ALLOWED FOR 25% OF DURATION)	
10. MEAN AMPLITUDE VARIATION	
(WITHIN PULSE TRAIN)	< 3%
(TRAIN TO TRAIN)	< 3%

2.0 DESIGN2.1 Kind of Generator

There are a number of important parameters to





50 ohms. Oil would also do away with the need for a diaphragm between the Marx and the line. However, the feed capacitance would tend to be relatively high. Furthermore, the M-2 pulser had to fit into an existing facility with limited length. Consequently, the choices were narrowed to water ( $\epsilon_r = 78$ ) and ethylene glycol ( $\epsilon_r = 41$ ). Water would have led to a line with an aspect ratio (length to width) of about 0.75:1. The feed diameter would be about 20% of the line length and the effects of the feed would be maximized. Lastly, with water the impedance would be low.

Consequently, ethylene glycol emerged as the final choice. The available data indicated the dielectric strength to be good. The system fit into the space available and it permitted a higher line impedance of 16.5 ohms, which is lower than optimum. However, ways were found to accommodate this level of impedances.

The self-discharge RC time for ethylene glycol can be made much longer ( $\sim 36 \mu s$ ) than the ringup half period (500 ns) with an ion exchange resin bed. The flash point is only slightly lower than oil (240° F vs. 275° F). It does absorb water from the air so desiccants are placed in air vents. The only problem from the water is a small increase in dielectric constant. The dissipation factor is higher than water (0.45 vs 0.005 at  $10^8$  Hz); however, risetime is limited by other factors. Measurements on the system using ethylene glycol show no signs of dispersion.

#### 2.4 Hybrid Line

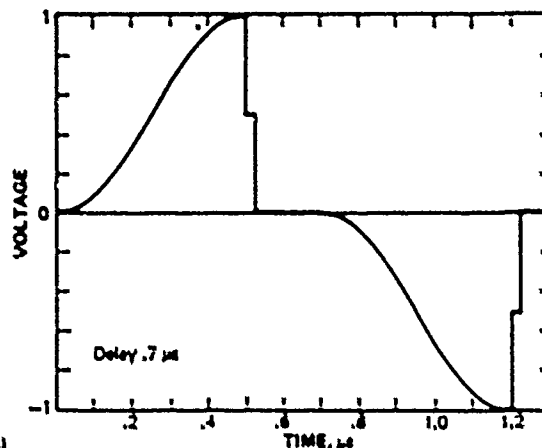
The line itself is a hybrid with a round center conductor and a square outer conductor and was chosen for two reasons: the impedance is about 5% higher than for a round line of the same size; flat sides ease the feed diaphragm design.

#### 2.5 Switch Type

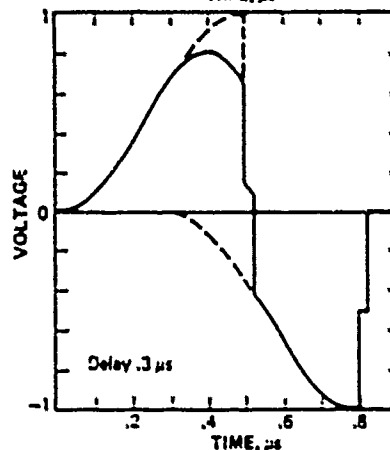
The two most important decisions in switch selection were whether to use (a) gas or liquid and (b) whether they are triggered or self-

breaking. To reduce the coupling between tandem line sections and to avoid transverse transit time effects, a gas switch was needed.

Figure 3a shows the voltage history on a switch with a delay of 700 ns between pulses. The switch first sees the charging and discharging of the line ahead. Its own line is then charged so that the polarity is reversed. The minimum delay between pulses is 180 ns, which is less than the ringup half period (500 ns). Thus, the waveform of Figure 3b can result (a delay of 300 ns is shown). With such unique and changeable waveforms, command triggering became imperative in order to meet the tight jitter requirement ( $\sigma < 8$  ns). Since both sides of the switch must each in turn be at high voltage, the switch must be symmetrical. The open switch that was designed and used is described in more detail in a companion paper entitled "A 3-MV Low Jitter Trigger Switch."



(a)



(b)

Figure 3 Voltage across line switch.

The command triggering is done with a 10-stage 250-kV trigger Marx generator located in the pulse line on the output side of the switch. The most favorable trigger mode is achieved with a negative line charge and a positive trigger on the V/A field distortion trigger electrode.

## 2.6 Marx Generator

The circuit shown in Figure 4 evolved from the following consideration. It was desirable to have the erected capacitance of the Marx generator equal to the capacitance of the pulse line and feed in order to minimize the energy left in the system at the time of firing, as the remaining energy may distort the following pulse.

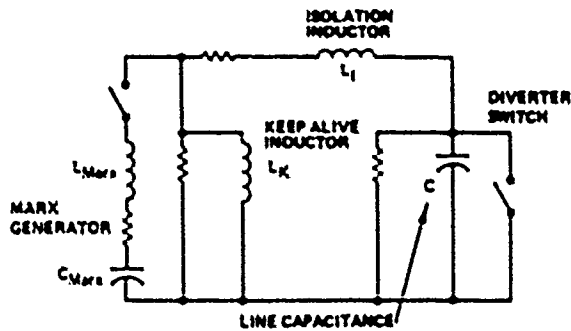


Figure 4 Pulsar ringup circuit.

If a Marx prefires, it is important to have minimum coupling to adjacent Marxes in order to avoid sympathetic triggering. Therefore, the isolation inductor was added to the feed to form an L-C filter with the output capacitance of the Marx. This inductor was made equal to the Marx generator inductance, about 14  $\mu\text{H}$ , which makes the half cycle ringup period approximately 500 ns.

Equal inductances and capacitances also make the output of the Marx generator (neglecting stray capacitance) half of the open circuit voltage throughout the ringup pulse. Thus it is possible to reduce clearances and make the Marx generator tanks small enough to fit into the available space. Separate Marx tanks made the space problem more severe, but were required for isolation, and for entry to the facility.

The "keep alive" inductor serves two

important functions. First, it provides a current tail to keep a switch conducting until the next pulse arrives. Second, it provides an isolated path to charge and fire the line switch trigger Marx, which is done by winding the inductor with coaxial cable.

One of the three Marx generators is shown in Figure 5. It is a folded design with four horizontal triggering strings. The three bottom stages are given simultaneous triggers. There are 39 stages with 0.07  $\mu\text{F}$  capacitors charged  $\pm$  50 kV, giving an erected capacitance of 1.8 nF. Since a ten-minute hold while charged is sometimes required, pains are taken to ensure dry SF<sub>6</sub> in the switches and the oil is continuously filtered. The jitter is typically 10 ns.



Figure 5 Marx generator.

## 2.7 The Feed

The feed to the pulse line is critical. It must come in the side of the line and distributed capacitance of the feed must be minimized to avoid pulse distortion. The design of the feed is shown in Figure 6. A polyurethane diaphragm separates the oil and the ethylene glycol. It is tapered to move bubbles to a low field region. The corona surfaces are designed to reduce the maximum field strength and direct it away from the dielectric surfaces.

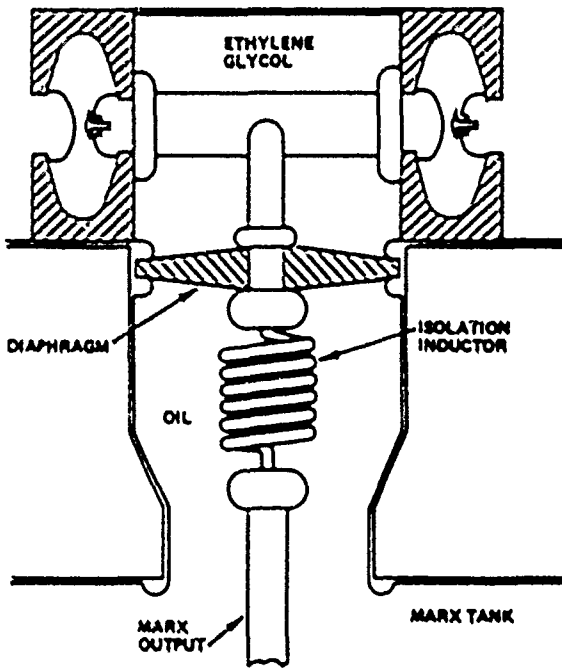


Figure 6 Vertical feed diagram.

The isolation inductor is placed in the oil just below the feed to minimize the capacitance that is seen by the line. Placing the inductor in the glycol was considered, but with the high and complicated fields near the line, breakdown was feared.

### 2.3 Pulse Line Design

Computations of circuit performance showed that the rise for the first pulse looked good but subsequent pulses were degraded. Consequently, extra capacitance before the switch was investigated as a means to improve risetime. It was thought that a tapered line on one side should give the best waveform, but computations showed that a discrete capacitance on each side performed better. Therefore, the circuit shown in Figure 7 was employed.

The value of  $C_A$  was selected for the best computed waveforms. The typical computed and measured risetimes are 13 ns for the first pulse, 16 ns for the second pulse, and 19 ns for the third pulse. The second and third pulses rise faster than would be expected from quadrature addition of time constants. The actual pulse line is shown in Figure 3.

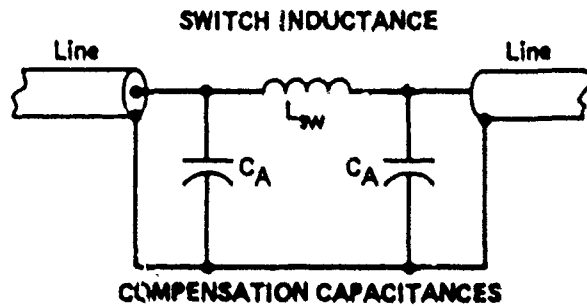


Figure 7 Switch compensation circuit.



Figure 8 Pulseline without epoxy collars.

The capacitance of the feed turned out to have a severe impact on the waveform. Therefore, epoxy collars were made to fit around the feed line inside of the ethylene glycol (see Figure 9). These collars reduced the capacitance enough to correct the waveform.



Figure 9 Pulseline with epoxy collars.

In order to minimize reflections at the end of the pulse and to connect to the load, a section of line was placed between the first switch and the termination resistance and load. To provide the trigger for switch number 1, this line also has a feed, diaphragm, and isolation inductor. The inductor is about 30  $\mu\text{H}$ , double the other isolation inductances.

### 2.9 Load Filter

Since the load itself does not provide sufficient damping, resistance in series with the load becomes important (see Figure 10). However, filament power is needed for the thermionic cathode. A filament inductor must therefore be used in parallel with the series resistance. In

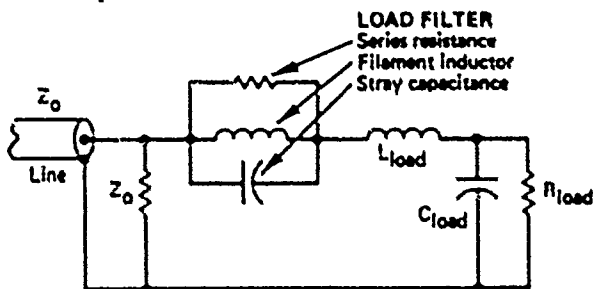


Figure 10 Load circuit with filter.

addition, the water resistor has high parallel capacitance. Thus, a parallel RC filter network is placed in series with the load. There is therefore opportunity to select the values in order to enhance the waveform. For good risetime, the filter must be underdamped. However, this makes the performance sensitive to risetime. Because the number of arc channels in a switch varies with pulse charge voltage, switch pressure and triggering, the switch inductance and thus the pulse risetime are a function of voltage. The risetime is also affected by the placement of epoxy collars on the feeds. Thus, an additional tuning mechanism is provided for waveform adjustment.

### 2.10 Pulse Generation and the Feed Problem

The effect of excess feed capacitance depends on whether the line section is generating or only

transmitting a pulse. In a generating line, the feed capacitance is charged initially and supplies too much voltage in the second half of the pulse. In a transmitting line, the feed uncharged capacitance tends to absorb energy from the first half of the pulse. The net result is a pulse with a radically different rise than that for which the filter was initially tuned. However, the reduction of capacitance in the feeds by the addition of epoxy collars and the tuning of the filter gave acceptable waveforms.

### 2.11 Merged lines

Another requirement is the ability to merge either pair of two pulses or all three. The line switch cannot be used because the two lines it connects would be charged at the same time, so there would be no voltage on the switch. The merging must therefore be done mechanically. Simply replacing a switch with a tube of the line diameter would result in a pulse which is too long. In order to overcome these problems, a bridge was designed with the same average inductance and a shorter electrical length (see Figure 11). These requirements were met with two acrylic slabs with appropriate shapes holding them.



Figure 11 Pulseline bridge.

### 3.0 FAULT MODES

Two principal fault modes have been encountered. The first is a Marx generator prefire. Usually, neither the switch ahead nor the switch behind fires, so the Marx generator and pulse line ring many times. When the voltage persists, either a switch face or a diaphragm may eventually flash over and cause damage. The same problem can occur if the line switch fails to fire.

In order to protect against these failure modes an adjustable diverter switch is placed in the line. It is spaced so that it will fire well after the peak of the first charge cycle.

### 4.0 PERFORMANCE

Figure 12, a through d, shows the performance of the system under several conditions. 12a: all three pulses are at 600 kV. The pulse separations are about 140 ns and 90 ns, respectively, which is less than the 180 ns minimum timing required. These delays were chosen in order to get all of the pulses on one trace with a fast enough sweep to show detail. Note the plateau on the fall. - 12b: pulse no. 1 is at 1.25 MV. The picture is a group of five traces overlaid. 12c: the first and second pulses merged at 850 kV. The first minimum from line no. 1 is too deep, but has since been lessened by tuning. 12d: all three pulses merged at 850 kV.

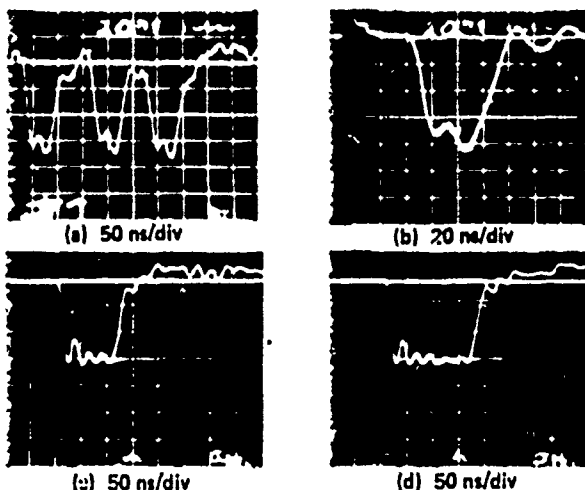


Figure 12 Pulsar waveforms.

### 5.0 CONCLUSION

The M-2 Pulsar is a unique, complicated system, built to satisfy a detailed and difficult specification. It is distinctly different from previous systems in the areas of pulse generation, switching, triggering, and load matching. A higher level of reliability has been needed than was customary in previous pulsed power equipment. However, after encountering and solving many planned and unplanned problems, the system will soon be ready for acceptance testing.

The waveform specifications are expected to be met on risetime, width, ripple, and undershoot. The fall under some conditions has a short plateau at about 25%, which makes the 90-10% time exceed 40-ns limit. However, there is good reason to believe that tuning with the collars and filter can eliminate this problem. Fortunately, the use of this kind of pulsar in other applications where impedance matching is more straight forward would make many of the waveform problems easier.

The amplitude is less than expected because the capacitance of the pulse line is greater than calculated. However, it is expected that the maximum output voltage will be about 1.4 MV.

The technology developed in this project has been hard won, but appears to be quite valuable and readily useable in a variety of other applications.

### Acknowledgements

The authors wish to thank the staff at the Los Alamos Scientific Laboratory for their contributions and cooperation, especially Jack Harwick and Fred Van Haaften. Special appreciation is also due the Project Manager Glen Rice, and to Phil Champney, Gordon Simcox, Tom Naff, Gene Mankinen, Claude Sink, and Boris Yen for their many contributions. Lastly, thanks to Steve Hogue and Charlie Wolff who make the system work.

## HIGH-PRESSURE SURFACE SPARK GAPS

W. J. Sarjeant,\* A. J. Alcock, and K. E. Leopold

Physics Division, National Research Council of Canada

Abstract

The behavior of surface discharge switches at high pressures operating into laser and resistive loads has been studied. The experiments utilized the spark gap as a transfer switch between a pulse-charged ethylene glycol transmission line, (30 ns, 1.4  $\Omega$ ) and a 17- $\Omega$  low-inductance load resistor, as well as a multiatmosphere rare-gas halide laser. The behavior of the spark gap breakdown voltage and number of channels upon charging voltage and gas pressure in the spark gap was studied in detail. The spark gap operation under laser and resistive load conditions will be compared and related to a order model of the gap breakdown. Scale-y to higher voltages will be discussed in the context of this model.

Recent experiments with high-pressure surface discharge switches have clearly illustrated their potential as transfer elements between low-impedance transmission lines and high-pressure discharge lasers.<sup>1</sup> Under pulse-charged conditions, such transfer switches demonstrate quite reproducible closure simultaneity ( $< 5$  ns) at 40 channels per meter and a switch-plus-laser hold-off of 150 kV.<sup>2</sup> It is the purpose of this note to present the characteristics of such a switch under resistive load conditions in precisely the same geometry as the laser load. In this way it will be possible to correlate the performance observed of the switch under both conditions, and we shall attempt to bring some physical understanding to the results through

an elementary model of the switch-closure phase.

The major point of interest in this device is the significant hold-off voltages that can be achieved through high-pressure operation in contrast to previous studies at atmospheric pressures.<sup>3,4,5</sup>

The switch and test geometry is shown in Figs. 1 and 2 respectively. In order to test operation with a resistive load and to eliminate the effects that the laser might have upon switch closure and hold-off, the laser head was filled with a concentrated solution of detergent in water and gave a load resistance of 17  $\Omega$ . A lower resistance was not practical as such materials as copper sulphate or acetic acid had previously been shown to have deleterious effects upon the laser components. The switch has been described in detail previously,<sup>2</sup> and the only change in this study was the reduction in the switch-electrode spacing to 1.27 cm in order to test the effects such a change might have upon laser performance. At this narrower spacing, no significant change in the laser operation was observed when the gap gas pressure was increased so that the system breakdown voltage was the same. In the tests of this switch, mounted as shown in Fig. 2, the gap was pressurized with high-purity nitrogen, and voltages on both sides were monitored. A small  $\delta$  correction ( $\sim 5\%$ ) was applied to the oscilloscope-recorded data. The performance of the spark gap with the laser was checked in this configuration, wherein the transmission line was filled with ethylene glycol, (30 ns, 1.4  $\Omega$ ). Using

\*W. J. Sarjeant was with NRC when this work was in progress. He is now a staff member at the Los Alamos Scientific Laboratory in Los Alamos, NM 87545.

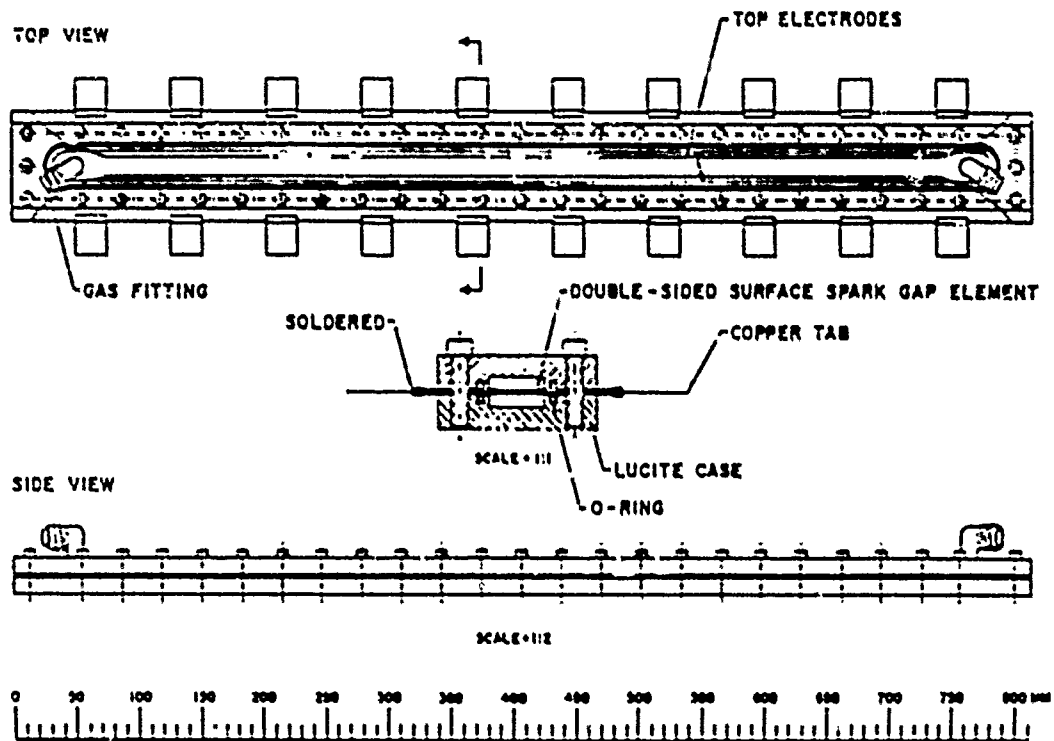


Fig. 1. Scale drawing of the high-pressure surface spark gap.

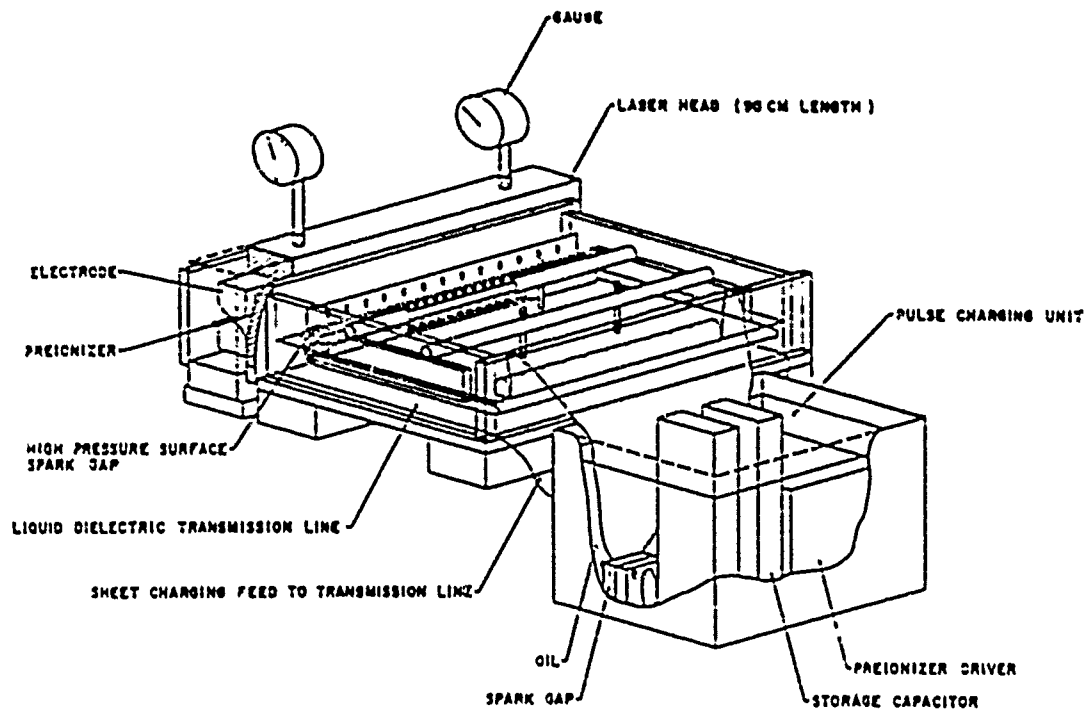


Fig. 2. Schematic view of the surface spark gap test system utilizing a 17-Ω liquid resistor in the laser discharge region as the spark gap load.



0.4  $\mu\text{F}$  as the storage capacitance gave a charging time of 90 ns at 95-kV dc. The output energy was then 0.8 J at a peak voltage of 150 kV and a gap pressure of 3 atm of nitrogen. It must be pointed out that the laser energy was a slowly varying function of everything except the laser gas composition. For this reason in particular, it was decided to study the spark gap characteristics under resistive load conditions as described below.

The breakdown field in MV/m was first studied for the two fixed dc voltages shown in Fig. 3. The field was calculated from the voltage across the spark gap at breakdown and the gap spacing. No field enhancement was incorporated into the calculated field. For both sets of data, a linear relation was expected,<sup>2</sup> but not observed for the lower voltage case. It was also observed, for the 95-kV

charging voltage (B), that the breakdown field was inversely proportional to the square of the time to breakdown. This is the same behavior as was found in the laser case at high-charging voltages,<sup>2</sup> and we will sketch a rough model for this behavior presently. At the lower voltages, the breakdown voltage per channel varied linearly with nitrogen pressure as illustrated in Fig. 4, as the charging voltage varied from 35 to 95 kV. In order to assess whether or not the absolute dc charging voltage had any effect upon the breakdown voltage, a single experiment was carried out at 1 atm of nitrogen gas pressure in the gap, and the data are shown in Fig. 5. Note that only a slight decreasing trend is evident, indicating that the breakdown electric field, increasing with dc voltage, is being scaled by some other parameter. As a result of circuit characteristics, the charging

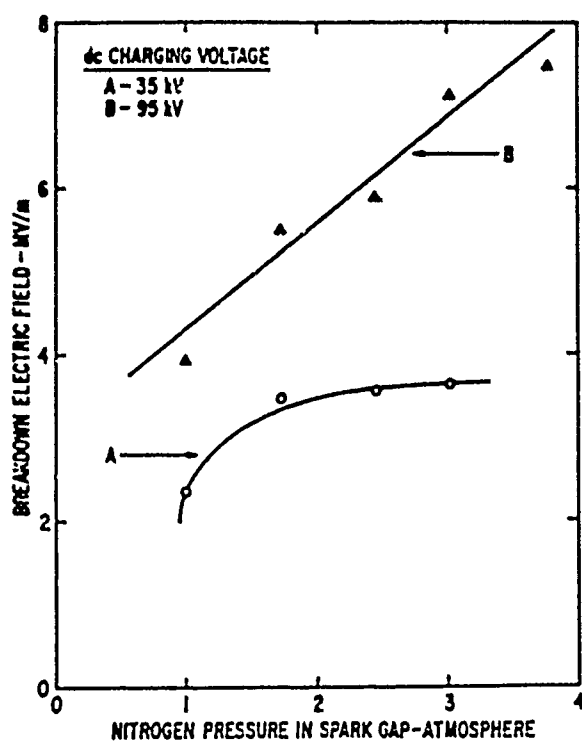


Fig. 3. Breakdown electric field,  $E$ , as a function of the nitrogen gas pressure in the surface spark gap for dc-charging voltages of (A) 35 kV and (B) 95 kV. The breakdown electric field increases linearly with gas pressure ( $E = 1.4 P_{N_2} + 3.0$ ) at the higher voltage (B).

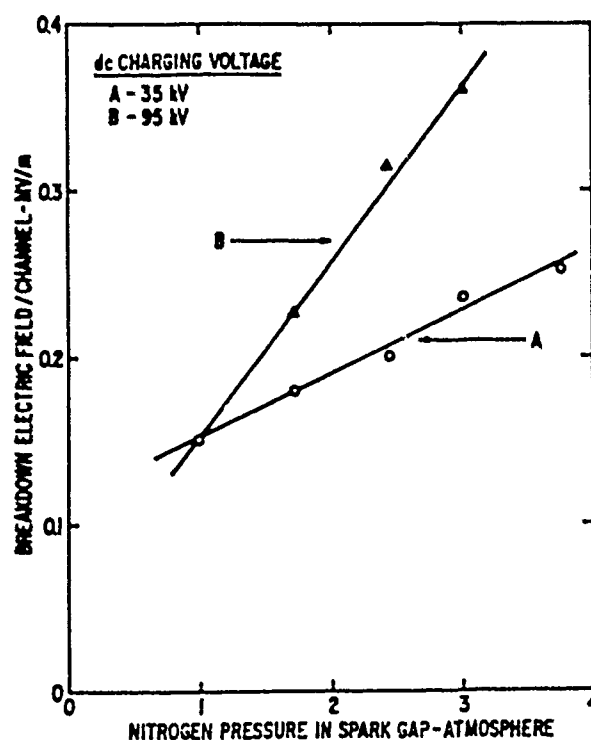


Fig. 4. Breakdown electric field per channel,  $E/n$ , for two dc-charging voltages. At a charging voltage of 35-kV dc,  $E/n = 0.04 P_{N_2} + 0.11$  and at 95 kV,  $E/n = 0.11 P_{N_2} + 0.05$ . In both cases  $E/n$  increased linearly with gap gas pressure.

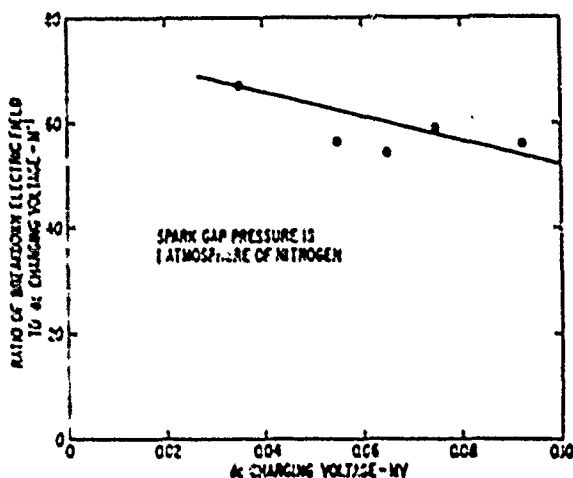


Fig. 5. Ratio of the breakdown electric field to the dc-charging voltage as a function of the latter for a fixed gap gas pressure of 1 atm of nitrogen. The data show a slow decrease as the charging voltage approaches 0.09 MV.

time is decreased as the charging voltage increases and experimentally

$$V\tau^2 = 0.6 \pm 0.1, \quad (1)$$

where  $V$  is the breakdown voltage of the spark gap in kilovolts and  $\tau$  is the time to breakdown in microseconds. This can be converted to field units (MV/m) by dividing by the gap spacing so that

$$E\tau^2 = 0.05 \pm 0.01. \quad (2)$$

Thus, the increased breakdown field,  $E$ , is obtained in this case through a faster charging time, for a fixed spark gap nitrogen gas pressure of 2.5 atm. It is interesting to speculate upon the behavior of this constant on the right of Eq. (1). For the same charging waveform risetime, gas pressure and charging voltage but a gap spacing of 2 cm, this constant was found to be 1.2 even though a water-filled transmission line was employed.<sup>2</sup> It may be then that this approximately linear variation in the constant with spacing is a fundamental parameter in surface gaps. If Eq. (1) of this note and Eq. (2) in the study with the laser load<sup>2</sup> are divided by the gap spacing, then in the field units

$$E\tau^2 d^{-1} = 4 \pm 1, \quad (3)$$

where the gap spacing,  $d$ , is in meters and the gas pressure is fixed at 2.5 atm. Since the detailed operation of this gap has not yet been measured for long charging times ( $\sim$ microseconds) and other gas pressures, the parameter limits at which Eq. (4) fails remain to be determined.

During the study of the gap hold-off for this resistive load, it was felt that a first-order model was necessary. Let us consider the gap breakdown phase for one streamer. Suppose this streamer were constrained to drifting across the gap surface at some drift velocity,  $v_d$ , and furthermore that this velocity remained sensibly constant during the time to breakdown,  $\tau$ . Then the electron current density in the streamer is roughly given by<sup>6</sup>

$$J = n_e e v_d, \quad (4)$$

where  $n_e$  is the electron density and  $e$  the electron charge. Now one can further postulate that this current density is directly related to the electric field,  $E(x,t)$ , a conductivity  $\sigma$  and a field enhancement factor,  $\alpha$ , as

$$J = E(x,t) \sigma \alpha. \quad (5)$$

In this model,  $x$  is the distance from the positive electrode in the spark gap, and its maximum value is  $J$  meters. The charging waveshape is increasing linearly with time, as determined experimentally, so that,

$$E(x,t) = E(x) t \Lambda, \quad (6)$$

where  $\Lambda$  is a constant. We are now going to assume that  $E(x)$  remains constant at  $E$  as  $x$  varies from 0 to  $d$ . Lastly we will take the mean drift velocity for the streamer as

$$v_d = \frac{d}{\tau}. \quad (7)$$

Since  $J$  is the same in Eqs. (4) and (5), a relationship between the parameters can be obtained by executing a double integration over  $x$  and  $t$ . Hence, for a fixed spark-gap nitrogen gas pressure

$$\int_0^d \int_0^{\tau} n_e v_d dt dx = \int_0^d \int_0^{\tau} c \alpha A E t dt dx, \quad (8)$$

or substituting for  $v_d$  using Eq. (7) and performing the integration yields

$$n_e e d = c \alpha A E \frac{\tau^2}{2}. \quad (9)$$

As a further simplification, it is presumed that

$$\frac{E \alpha A}{n_e e} = \text{a constant}. \quad (10)$$

Then Eq. (9) becomes

$$E \tau^2 d^{-1} = \text{a constant}. \quad (11)$$

The experimentally determined gap-breakdown field and time-to-breakdown relationship agrees then with the results of this model. The breakdown field also increases linearly with gap spacing as was observed.

Further model development will be required to explain the  $E/n$  and hold-off dependence with gas pressure. Preliminary measurements of the spark gap hold-off using  $\text{SF}_6$  as the insulating gas have shown a substantial increase in hold-off capability.

Further measurements with various gases and gas mixtures may well show that significant improvements in the device performance parameters are feasible.

#### Acknowledgments

The authors wish to acknowledge R. S. Taylor for his assistance during these experiments and G. A. Berry for mechanical fabrication of the prototype surface spark gaps.

#### References

1. W. J. Sarjeant, A. J. Alcock, and K. E. Leopold, "Parametric Study of a Constant E/N Pumped High-Power KrF Laser," IEEE J. Quantum Electron., QE-14, No. 3, pp. 177-184 (March 1978).
2. W. J. Sarjeant, R. S. Taylor, A. J. Alcock, and K. E. Leopold, "Multichannel Surface Spark Gaps," Proc. of the Thirteenth Pulse Power Modulator Symposium, June 20-22, 1978, Buffalo, New York, pp. 94-97.
3. J. C. Martin, "Pulsed Surface Tracking in Air and Various Gases," AERE SSWA/JCM/745/735, May 1974.
4. A. B. Andrezen, V. A. Burtsev, and A. B. Produvov, "Breakdown of a Solid-Dielectric Switch," Sov. Phys. Tech. Phys., 20, No. 2, pp. 187-190 (March 1975).
5. A. V. Grigor'ev, P. N. Dushuk, S. N. Markov, V. L. Shutov, and M. D. Yuryseva, "Low-Inductance Megampere-Current Commutator Based on Sliding Discharge," Instrum. Exp. Tech., (USSR), 19, No. 4, Pt. 2, pp. 1104-1106 (July-August 1976).
6. J. P. Brainard, in 1975 Annual Report of the Conference on Electrical Insulation and Dielectric Phenomena (National Academy of Sciences), Washington, DC, 1978). p. 482.

## PARALLEL COMBINATIONS of PRE-IONIZED LOW JITTER SPARK GAPS

W. A. FITZSIMMONS and L. A. ROSOCHA

National Research Group, Inc.  
P. O. Box 5321 Madison, Wisc. 53705Abstract

The properties of 10 to 30 kV four electrode field emission pre-ionized triggered spark gaps have been studied. A mid-plane off-axis trigger electrode is biased at  $+V_0/2$ , and a field emission point is located adjacent to and biased at the grounded cathode potential. Simultaneous application of a  $-V_0$  trigger pulse to both the electrodes results in the rapid sequential closing of the anode-trigger and trigger-cathode gaps. The observed jitter is about 1.5 ns. Parallel operation of these gaps (up to 10 so far) connected to a common capacitive load has been studied. A simple theory that predicts the number of gaps that may be expected to operate in parallel is discussed.

Introduction

One of the present problems in high voltage technology is the construction of low inductance high voltage switches that may be operated at high repetition rates for extended periods of time. The parallel operation of spark gaps switching a common capacitive load may be a step toward resolving one or more aspects of this problem. Spark gaps can be operated in parallel if each gap is pre-ionized thereby avoiding the statistical lag time that results in large jitter times for most triggered spark gaps.

We have studied the operation of the four electrode arrangement shown in Figure 1. A mid-plane off-axis trigger electrode is biased at  $+V_0/2$ , and a pointed field emission electrode is located adjacent to and biased at the grounded cathode potential. Simultaneous application of a  $-V_0$  trigger pulse to both the electrodes results in the following rapid sequence of events:

- a) The small jitter photo pre-ionization of the anode-trigger and perhaps the trigger-cathode gaps due to the low jitter electron emission and weak luminous excitation of the gas near the point.

- b) The subsequent closing of the anode-trigger gap, followed almost immediately by the closing of the trigger-cathode gap.

The above sequence can be observed by monitoring the trigger electrode potential during the application of the trigger pulse. As shown in Figure 2, with the closure of the anode-trigger gap the trigger potential rapidly rises to a value roughly equal to  $+V_0$ . This results in an overvoltage appearing across the trigger cathode gap that results in the closure of this gap and the return of the trigger potential, in this case, to slightly less than  $+V_0/2$ .

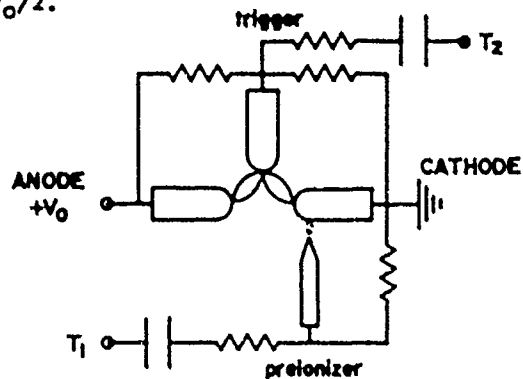


Figure 1: Electrode Arrangement in Gap

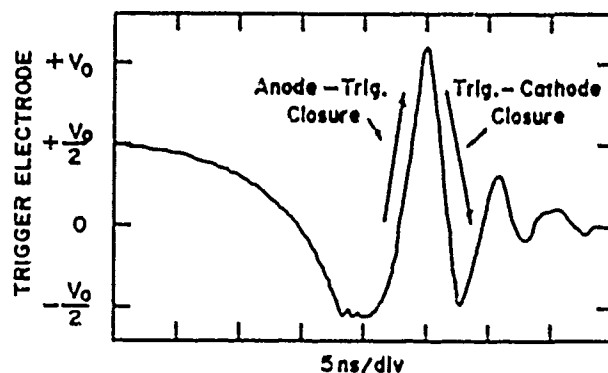


Figure 2: Trigger Electrode Voltage

A second and important characteristic of triggered spark gaps is the performance at reduced applied voltage. If  $V_0$  is defined as the max. hold-off potential (for example  $V_0$  may be 10, 20, or 30 kV etc, depending upon the pressure in the gap), then it is useful to measure the spark gap jitter time  $\tau_j$  and the firing delay time as a function of  $V/V_0$  where  $V$  is the applied DC voltage. The results of such measurements for the gaps we have been studying is shown in Figure 3. The basic conclusion that may be drawn from Figure 3 is that when  $V/V_0$  drops to about 0.75 or less, then the jitter suddenly becomes very large and the gap is no longer working properly. Observation of the trigger electrode potential during the reduced applied voltage experiments indicates that when the jitter suddenly becomes very large (near  $V/V_0 \approx 0.75$ ), the closure of the trigger-cathode gap has become very erratic.

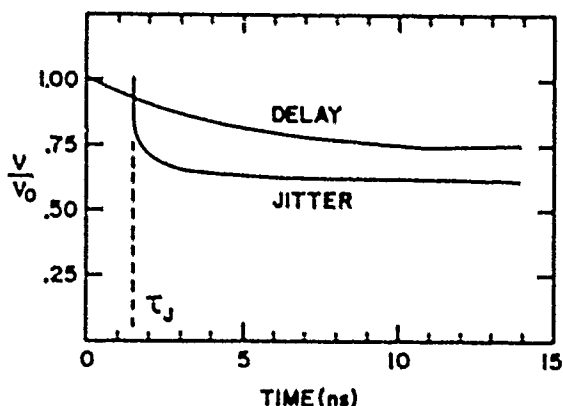


Figure 3: Firing Jitter and Delay Time vs Applied Voltage.

#### Theory

Before discussing our experimental results concerning the parallel operation of these spark gaps, it is perhaps best to describe a simple theory that predicts the number of gaps that can be made to close under given experimental conditions.

Suppose that a large number of spark gaps are connected in parallel across a common low inductance capacitive load. Assume, with an applied voltage  $V_0$  and appropriate triggering, that  $N$  switches are observed to close where  $N$  is less than the total number of available switches. Starting with the first switch that closes, the total time required to close  $N$  switches is approximately  $\tau_j(N)^{1/2}$ , where  $\tau_j$  is the jitter time for individual switches.

As the first of the switches close, the voltage across the remaining open switches begins to decrease according to:

$$V/V_0 \approx \cos \omega t = 1 - \omega^2 t^2 / 2 + \dots \quad (1)$$

Based upon our measurements of an individual switch as shown in Figure 3, if  $V_0$  is the maximum hold-off voltage, then when  $V/V_0 \approx 0.75$  the individual switches become very erratic and no more switches may be expected to close. Thus the last or  $N^{\text{th}}$  switch fires when:

$$\begin{aligned} \omega^2 t^2 / 2 &= 0.25 \\ \text{or} \quad t &= (0.5)^{1/2} / \omega = \tau_j N^{1/2} \end{aligned} \quad (2)$$

If the switches in the array are well separated so the inductance of  $N$  switches is  $L_0/N$ , where  $L_0$  is the inductance of an isolated switch, and taking  $\omega = (N/L_0 C)^{1/2}$ , where  $C$  is the total load capacitance, then the number of switches that will close is given by:

$$N = \frac{(0.5)^{1/2} (L_0 C)^{1/2}}{\tau_j} \quad (3)$$

For the switches we are studying the jitter time  $\tau_j \approx 1.5$  ns. Thus

$$N = 0.5 (L_0 C)^{1/2}, \quad (4)$$

where  $L_0$  and  $C$  are the individual switch inductance and total load capacitance in nH and nF respectively. Given below is a comparison between experiment and theory for the switches we have studied so far.

CASE	NUMBER OF SWITCHES THAT FIRED	$N = 0.5 (L_0 C)^{1/2}$
$L_0 = 30\text{nH}$ $C = 3\text{nF}$	4 to 5 out of 6	5
$L_0 = 30\text{nH}$ $C = 38\text{nF}$	9 out of 9	17
$L_0 = 30\text{nH}$ $C = 8.4\text{nF}$	7 to 8 out of 9	8
$L_0 = 30\text{nH}$ $C = 7.5\text{nF}$	7 to 8 out of 15	7.5
$L_0 = 30\text{nH}$ $C = 15\text{nF}$	9 to 10 out of 15	10.5
$L_0 = 39\text{nH}$ $C = 8.1\text{nF}$	5 out of 5	9
$L_0 = 39\text{nH}$ $C = 2.7\text{nF}$	4 to 5 out of 5	5

### Experiment

The experiments were carried out by mounting an array of four electrode spark gaps in a long square (1½" x 1½" or 2" x 2") plastic tube with a spacing of 2 inches between switches. The capacitive loads were sometimes large flat aluminum plates, or in other cases a row of barium titanate capacitors closely coupled to the anode and cathode of the switch array. The trigger and emission electrodes were each supplied with individual coupling capacitors energized from a common pulsed bus-bar. The electrode spacings were about 1.5 to 2 mm, and the operating pressures for the gaps ranged between 0 to 30 psig nitrogen for voltages between 10 and 30 kV. Easy access to the trigger electrode was found to be important as this electrode sometimes needs to be adjusted in or out in order to tune-up the array of gaps.

Figure 4 is a photograph of an early version of a 15 element array. In this case the electrodes were 1/8" dia. 1½ thoriated tungsten rods. The small diameter electrodes proved unsatisfactory for voltages above 20 kV, and the measured tungsten wear rate of  $5 \times 10^{-5}$  gm/Coul (1 atom per 40 electrons) was a bit large. It was observed that only the anode suffered significant wear, perhaps due to the additional trigger energy absorbed by this gap.

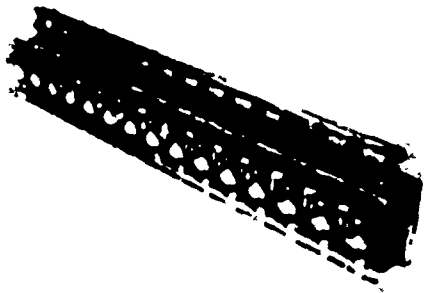


Figure 4: Early version of 15 element triggered spark gap array.



Figure 5: Later version of 6 element spark gap array having a built-in Blumlein trigger generator.

Figure 5 is a photograph of a later version of a 6 element switch for which the first element is actually switching a built-in Blumlein structure that generates the trigger pulses for the remaining 5 elements. The voltage across all elements is the applied voltage. This arrangement has the advantage that the trigger or command element can have a slightly smaller gap spacing. Thus a free-run (or not external triggered) operation of the switch will result in the triggering of all gaps, thereby preventing the accidental transfer of all the charge on the load capacitor through one of the gaps. The spark gap array shown in Figure 5 has ½" dia. 30% copper-70% tungsten electrodes, and it has been operated at voltages between 10 and 35 kV.

Most of the switches discussed in this paper have been operated at repetition rates up to 60 Hz, and in some cases for as long as 20 million pulses. Figure 6 is the open circuit output from a flat plate Blumlein charged to 20 kV and being switched by a 9 element array at 60 Hz. The capacitance being switched is 8.4 nF. The curve shown indicates an inductance and resistance of about 3.7 nH and 0.075 Ohms respectively for the 9 gap array.

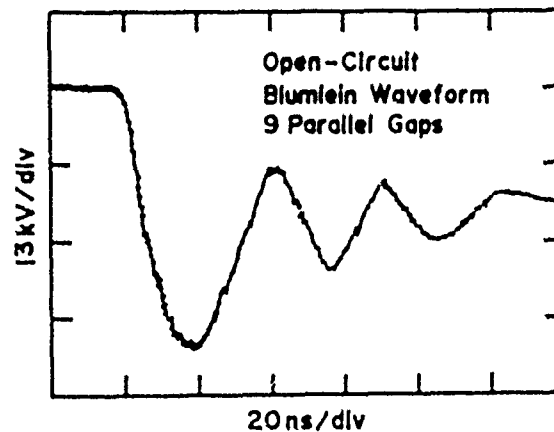


Figure 6: Open Circuit Output of Blumlein Switched by 9 Parallel Gaps.

In summary, we have studied the parallel operation of pre-ionized triggered spark gaps, and we have investigated some of the criteria that must be met for successful operation of these systems.

## A STREAMER MODEL FOR HIGH VOLTAGE WATER SWITCHES

F. J. SAZAMA and V. L. KENYON, III

Naval Surface Weapons Center  
White Oak, Silver Spring, Maryland 20910Abstract

An electrical switch model for high voltage water switches has been developed which predicts streamer-switching effects that correlate well with water-switch data from Casino over the past four years and with switch data from recent Aurora/AMP experiments. Preclosure "rounding" and postclosure resistive damping of pulseforming line voltage waveforms are explained in terms of spatially-extensive, capacitive-coupling of the conducting streamers as they propagate across the gap and in terms of time-dependent streamer resistance and inductance. The arc resistance of the Casino water switch and of a gas switch under test on Casino was determined by computer fit to be  $0.5 \pm 0.1$  ohms and  $0.3 \pm 0.06$  ohms respectively, during the time of peak current in the power pulse. Energy lost in the water switch during the first pulse is 18% of that stored in the pulseforming line while similar energy lost in the gas switch is 11%. The model is described, computer transient analyses are compared with observed water and gas switch data and the results - switch resistance, inductance and energy loss during the primary power pulse - are presented.

Introduction

The generation of terawatt power pulses in high-current relativistic electron beam machines is limited primarily by the performance of switches at the input and output to the pulseforming line. Currently water-arc switches are most commonly used in these machines and are expected to dominate high-power switch technology for some time. One of the major deficiencies of water switch technology is the lack of a suitable model which accurately describes switch performance. The experimental difficulties of accurately measuring the resistance of the water arc and the energy dissipated in the switches in an actual accelerator are considerable. This research was directed towards achieving a better understanding of water-switch electrical behavior at Casino and Aurora/AMP with the ultimate goal of aiding the development of high-power generators with improved power output and energy-transfer efficiency.

The Casino generator (Figure 1) has a single output water switch from the pulseforming line into a transformer and diode load. A review of the pulseforming line voltage measurements taken routinely during the past four years reveals that the tip of the waveform near the negative-voltage peak is occasionally rounded. This rounding was

previously thought to be due to switch closure occurring near the rounded peak in the pulseforming line's resonance-charging waveform. However, careful measurement of the Marx and pulseforming electrical parameters revealed that the switch-rounding effect was entirely independent of the rounding associated with the resonant charging peak (Figure 2). Rounding is thus a normal characteristic of water-switch closure. Closure waveforms from gas switches<sup>1</sup> being tested on Casino confirmed that switch-rounding was much more pronounced with the water switch than with the gas switch. This prompted formulation of a more complete electrical model for the switch which postulated conducting bush/streamer formation as the origin of these observed electrical effects. In this paper the switch streamer model which was developed is described and then applied to switch-voltage waveforms from Casino and Aurora/AMP.

The Switch Model

Recent observations<sup>2</sup> of prebreakdown events in transformer oil with small (2 mm) point/plane gaps reveal that multiple electrical pathways or "bushes" grow subsonically from the cathode point. After these bushes enlarge a distance which is usually about one-half the gap spacing or less, a supersonic streamer bridges the gap. The streamer apparently emanates from the bush. Additional observations<sup>3</sup> in nitrobenzene by means of Kerr fringe patterns directly confirm that (1) the cathode bush is a conducting medium and (2) there is no space-charge distortion between the leading edge of the bush and the opposite plane electrode.

When the point electrode is made positive with respect to the plane only a supersonic tree bridges the gap. Positive streamer studies in dielectric fluids for gaps between 6 and 25 mm have furthermore revealed that the positive streamers are propagated at constant velocity for at least up to 90% of the total gap. Propagation velocities were found to be proportional to the applied voltage and to decrease with increasing gap. The fact that positive streamer velocity depends upon the gap but not on its position in the gap suggests there exists a regulatory mechanism whereby the field at the streamer tip remains constant.

These research results were put into quantitative electrical terms for switches such as those on Casino or Aurora/AMP by positing that the positive tree-streamer behaves capacitively as if the anode were supersonically moving toward the cathode at

the tree-streamer growth velocity (Figure 3-top). The electrical model which was developed to represent this effect is shown in Figure 3-lower. The model describes an anode-streamer switch which transfers energy from a negatively-charged pulseforming line connected at node 1 to a transformer or diode connected at node 3.

The components  $R_u$  and  $C_u$  represent the undisturbed water resistance and capacitance of the gap and are coupled by the relationship,

$$R_u C_u = \frac{\epsilon}{\sigma}$$

where  $\epsilon$  and  $\sigma$  are the water permittivity and conductivity respectively. Similarly  $R_u$  and  $C_u$  represent the undisturbed water resistance and capacitance from the anode tree/streamer tips to the cathode at 3.  $R_s$  and  $L_s$  represent the equivalent bush/streamer resistance and inductance respectively. It is assumed that an onset time exists before which no anode tree structure exists in the gap. At instances of time before onset only components  $R_u$  and  $C_u$  are connected in the model and  $R_{us}$ ,  $C_{us}$ ,  $R_s$  and  $L_s$  are disconnected.

#### Application to Casino

The switch model was inserted into the Casino lumped parameter generator model which was derived from the existing coaxial line model for the accelerator. Computer predictions of the transient pulseline voltage preclosure "rounding" and postclosure damping effects were then compared with observed voltage waveforms for the water switch (Figure 4) and a gas switch" being tested on Casino. Preclosure rounding was well fit by invoking volume-extensive capacitive coupling between the inter-electrode anode trees and the opposite switch cathode. This volume-extensive coupling required that the entire active switch volume be eventually filled with conducting branches and pathways (bushes and trees). For the Casino water switch, propagation velocity for anode tree growth was taken to be  $3 \times 10^5$  meters per second based on estimates from Casino water switch closure-time measurements. For the gas switch a propagation velocity of  $1 \times 10^5$  meters per second was necessary to fit the observed preclosure rounding. To obtain agreement in the postclosure waveform region it was necessary for  $R_s$  and  $L_s$  to take on the time-dependent values shown in Figures 4 and 5. The times  $t_1$ ,  $t_2$ ,  $t_3$ , and  $t_4$  are respectively the time of streamer onset, streamer closure, first voltage maximum and second voltage minimum. Peak current passes through the switch between  $t_2$  and  $t_3$  hence the switch resistance and inductance during that time interval are critical to power output and energy transfer. These values imply the lack of current sharing between streamer paths in late time as a result perhaps of some paths becoming extinguished.

#### Application to Aurora/AMP

The Aurora/AMP generator differs significantly from Casino in that two switches - one at the input and one at the output of the pulseforming line - are critical. Computer predictions of the pulseline voltage waveforms using a Aurora/AMP lumped-

parameter generator model derived from the distributive coaxial line model with a modeled or "real" input switch as described here (Figure 2-lower) and an ideal, lossless, instantaneously-closing output switch are shown in Figure 6. The middle curve is the predicted voltage when a streamer resistance  $R_s$  of 2.45 ohms and a propagation velocity of  $1 \times 10^5$  meters per second are used in the input switch model. The lowest curve is the predicted voltage when both output and input switches are ideal, lossless, instantaneously-closing switches. The upper curve is the available measured data which did not extend beyond  $2.10 \times 10^{-9}$  seconds and was replaced arbitrarily by a zero baseline in this region. This surprisingly good fit to the observed waveform was achieved solely on the basis of assuming an input switch streamer resistance  $R_s$  of 2.45 ohms which was scaled from the Casino water switch results. An equally good fit to the observed pulseline voltage can be achieved by using a "real" output switch as described in this paper and positing preclosure volume-extensive capacitive coupling to the downstream transformer sections. Consequently the significant reduction (~20%) in peak pulse line voltage from that of the ideal-input, ideal-output switch prediction, can be explained equally well by two distinct mechanisms: input switch post-closure resistance or output switch preclosure capacitive coupling. When additional streamer propagation information for the switches and post-closure damped-waveform data has been obtained the relative importance of these two mechanisms will undoubtedly be established.

#### Results

An electrical streamer-switch model has been developed and successfully applied to (1) the Casino high-voltage water switch and (2) a gas switch under test in the same accelerator. Spatially-extensive capacitive coupling of supersonic tree/streamers traveling at  $5 \times 10^5$  meters per second for the water switch and traveling  $1 \times 10^5$  meters per second for the gas switch successfully explain the observed preclosure rounding effects. A time-dependent streamer-arc resistance and inductance was required to predict the observed postclosure pulseline voltage peaks and frequency. The arc resistance of the Casino water switch and of the gas switch was determined by computer sensitivity calculations to be  $0.5 \pm 0.1$  ohms and  $0.3 \pm 0.06$  ohms respectively, during the time of peak current in the power pulse. Energy dissipated in these water and gas switches, also during the first pulse, was 19.9 kJ and 12.4 kJ respectively out of 110 kJ stored in the pulseline.

An extension of these results to Aurora/AMP has succeeded in matching the observed waveforms and computer predictions suggest that two streamer-switch mechanisms, arc-streamer resistance in the input switch and spatially-extensive streamer capacitance in the output switch, are playing important roles in the pulsed-power produced by this generator. Accurate description of the Aurora/AMP pulseforming line voltage requires more accurate experimental determination of the streamer propagation velocity in both input and output switches and a determina-



tion of the postclosure damped waveforms for the system.

#### Conclusions

The role of switch streamers in accounting for the power output and energy balance in pulse power accelerators has been more clearly established by the introduction of an electrical streamer-switch model which describes the electrical effects taking place in large-area, high-voltage water switches. The streamer switch model reflects the importance of arc-streamer mechanisms in the breakdown of the water insulant. Streamer effects are of obvious importance in elucidating the mechanisms of electrical breakdown and, as illustrated by this work, are also important in establishing the electrical effects of those breakdown mechanisms in large machines where propagation velocity is a controlling factor. It is hoped that switch models as herein proposed, will become useful tools in the improvement and future design of pulsed-power accelerators.

Future effort with this model is being focused (1) on its application to Aurora, AMP and other machines, (2) its application to the development of high-power gas switches, and (3) on the development of current-dependent components that are consistent with streamer channel formation energies and hydrodynamic shock effects in water.

#### Acknowledgements

The authors would like to thank Mr. P. L. Marcin for assistance given in applying the NET-2 computer code to these problems; Mr. J. R. Shipman for the coaxial line model for Casino; Dr. G. A. Huttlin for the coaxial line model for Aurora/AMP; Dr. E. E. Nolting for closure-time analysis of the water switch data; Mr. R. A. Smith for many helpful discussions regarding the switch model; and the Casino research technicians, Mr. M. H. Ruppalt, Mr. W. R. Spicer, Mr. J. D. King and Mr. R. P. Jilinski for the archival retrieving and taking of the voltage data.

#### References

1. W. F. J. Crewson and C. H. Jones, Jr., "Engineering Improvements to the DQ Switch," Pulsar Associates Inc., Report No. PATP-78-1, February 1978; E. E. Nolting (private communication).
2. E. F. Kelley and R. E. Hebner, Jr., "Measurement of Prebreakdown Electric Fields in Liquid Insulants," Electrosystems Division, National Bureau of Standards, Washington, D.C. 20234 (in press)
3. J. C. Devins, S. J. Riaz and R. J. Schwabe, "Positive Streamer Velocities in Dielectric Fluids," Report No. 78CRD082, General Electric Corporate Research and Development, Schenectady, New York, May 1978.

This work was performed for the U. S. Defense Nuclear Agency under MIPR No. 79-501.

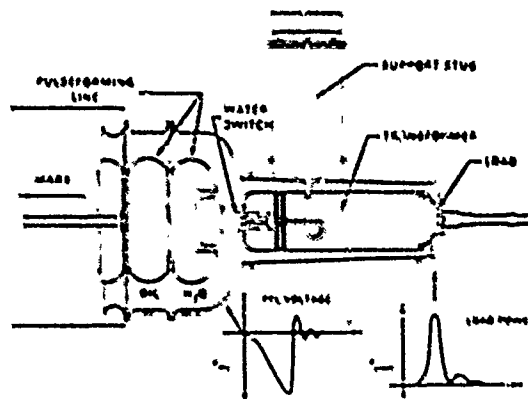


Fig. 1. Section view of the Casino generator.

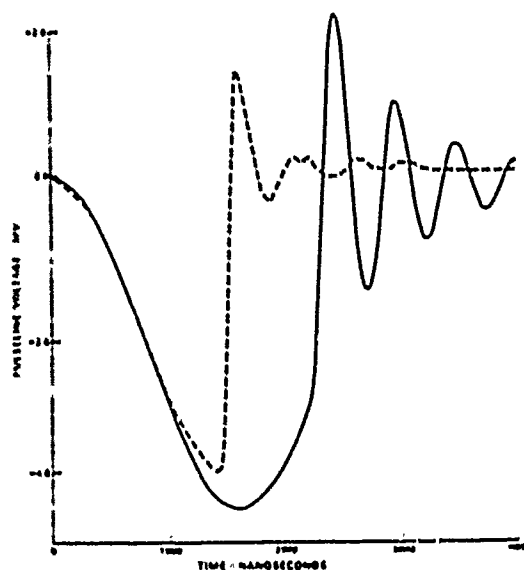


Fig. 2. Comparison of Casino pulseforming line (pfl) voltage rounding due to switch streamers (dashed) and due to resonance charging peak when switch is not closed. Same Marx charge is used in both shots.

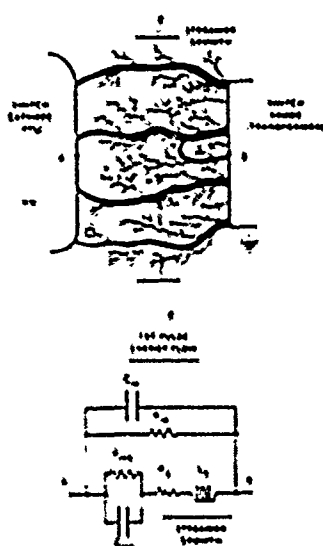


Fig. 3. Positive tree growth showing heavy streamer channels that eventually form (top) and the electrical switch model of the process (bottom).

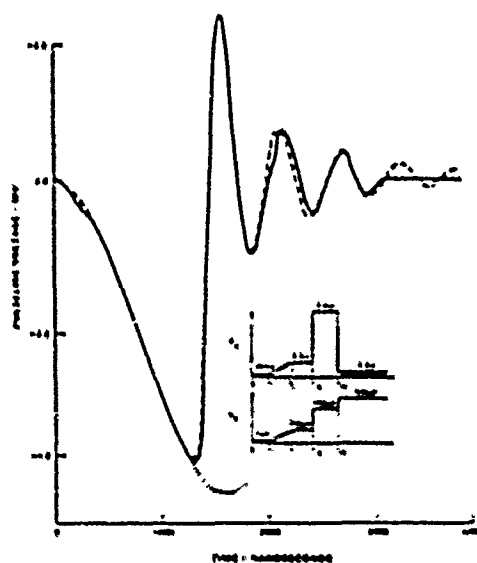


Fig. 5. Pfl voltage for a gas switch under cast on Casino comparing measured (—) and model (---) with  $1 \times 10^6$  meters per second streamer propagation velocity and a switch gap = 0.529 meters.

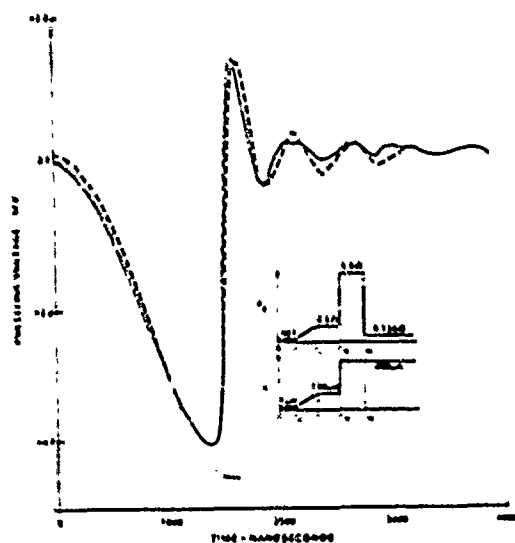


Fig. 4. Pfl voltage for the Casino water switch comparing measured (—) and model (---) with  $5 \times 10^5$  meters per second streamer propagation velocity and a switch gap = 0.219 meters.

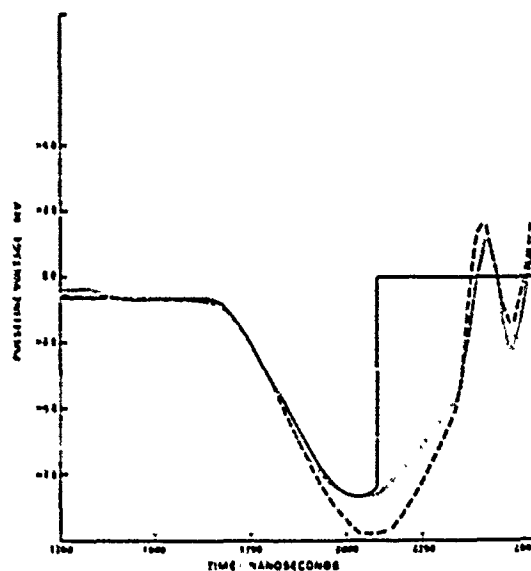


Fig. 5. Pfl voltage for Aurora/AMP water switches comparing measured (—) and model (---). The input switch streamer resistance,  $R_s$ , was taken to be 2.45 ohms while the output switch was ideal. Dashed curve is pfl voltage if both input and output switches are ideal.

## Low Prepulse, High Power Density Water Dielectric Switching\*

D. L. Johnson, J. P. VanDevender and T. H. Martin

Sandia Laboratories, Albuquerque, New Mexico 87125

Abstract

Prepulse voltage suppression has proven difficult in high power, high voltage accelerators employing self-breakdown water dielectric switches. A novel and cost effective water switch has been developed at Sandia Laboratories which reduces prepulse voltage by reducing the capacity across the switch. This prepulse suppression switch causes energy formerly stored in the switch capacity and dissipated in the arc to be useful output energy. The switching technique also allows the pulse forming lines to be stacked in parallel and electrically isolated from the load after the line has been discharged.

The switch consists of a ground plane, with several holes, inserted between the switch electrodes. The output line switch electrodes extend through the holes and face electrodes on the pulse forming line (PFL). The capacity between the PFL and the output transmission line is reduced by about 80 percent. The gap spacing between the output line electrode and the hole in the ground plane is adjusted so that breakdown occurs after the main pulse and provides a crow bar between the load and the source. Performance data from the Proto II, Mice and Ripple test facilities will be presented.

Introduction

A prepulse voltage, arising from the capacitive coupling between the pulse forming line (PFL) and the output transmission line during the PFL charge phase can cause erratic diode performance on high voltage accelerators.<sup>1</sup> Elimination of the prepulse has proven difficult. Several techniques have been employed to reduce prepulse; for example, two or more switches can be placed in series separated by sections of transmission lines, plastic barriers with gas switches can be inserted in the transmission line, and transmission lines with oil dielectric insulation and switching can be inserted in water insulated accelerators. These prepulse reducing methods involve costly additions to large accelerators. This paper describes an inexpensive and simple switching technique which reduces prepulse voltages.

\*This work was supported by the U.S. Dept. of Energy, under Contract AT(29-1)-789.

Description of Switch

Models of a flat plate pulse forming line, switch, and output transmission line are shown in Fig. 1. Figure 1a shows a conventional switching system and Fig. 1b shows a system with a ground plane between the switching electrodes. By inserting the ground plane, much of the stray capacitance between the PFL and the output line is diverted to capacitance between the PFL and ground. Energy previously stored in the capacitance between the PFL and the output line was not available for the output pulse because the switch shorted that capacitance. With the ground plane inserted, this energy is now available for the output.

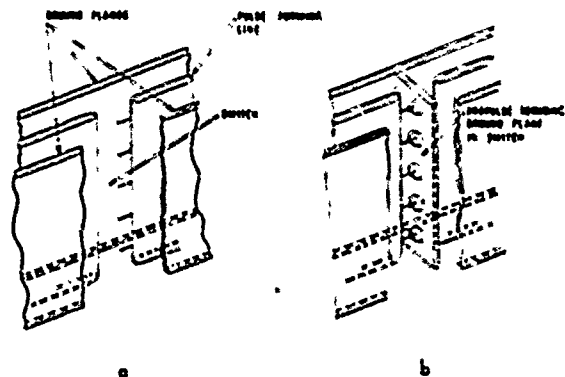


Fig. 1. a. Conventional switching system.  
b. Switching system with ground plane.

The electrode tips of the switch are field enhanced so that the breakdown streamer channels originate from the negative electrode. Electrode spacings can be determined from the following relationships derived from J. C. Martin's formula for the average streamer velocity ( $U$ ) in water.<sup>2</sup>

$$d = 4.02 \times 10^{-4} V_{BD}^{1.1} t_{eff}^{2/3} \quad (\text{MKS units}) \quad (1)$$

where  $t_{eff}$  is the time that the voltage is above 63 percent of the breakdown voltage  $V_{BD}$  and  $d$  is the gap spacing.

Since field enhancement on the edge of hole is greater than that on the rod, the diameter of the

hole in the ground plane can be determined either from Eq. 1 if the system is charged positive or from the following relationship if the system is charged negative:

$$d = .022 V_{BD}^{0.6} c_{eff}^{1/2} \quad (2)$$

where the units are the same as in Eq. 1. The hole diameter and field enhancement should be such that breakdown between the ground plane and the output line electrode originates from the ground plane and occurs after the PFL pulse had ended. After breakdown the PFL and its charging source are then isolated from the load.

The number of switching points  $N$  can be determined from the following relationship:

$$10 V_{BD} / (dV_{BD}/dt) = 0.1 \tau_{total} + 0.5 \tau_{trans} \quad (3)$$

where  $\sigma$  is the fraction standard deviation of the breakdown voltage ( $V_{BD}$ ) of the switch,  $dV_{BD}/dt$  is the rate of change on the switch at breakdown,  $\tau_{total}$  is the switch risetime and  $\tau_{trans}$  is the transit time between switch points given by  $l\sqrt{C_p}/Nc$  for a switch width  $l$  in a dielectric with constant  $C_p$  and  $c = 3 \times 10^8$  m/s. Typical values for  $\sigma$  are 0.01 to 0.03. The switch  $n$ -fold risetime is given by the following:

$$\tau_{total} = \left\{ \left( \frac{l}{Nc} \right)^2 + \left( \frac{232}{N^{1/3} \epsilon^{1/3} E^{4/3}} \right)^2 \right\}^{1/2} \quad (4)$$

where  $l$  is the inductance per switch channel,  $\epsilon$  is the sum of the PFL and output line impedances, and  $E$  is the mean electric field in the switch.

### Results and Discussion

#### Ripple and Mite

Initial testing of this switching technique was done on the Ripple test facility. A prepulse reduction of a factor of 5 was achieved with the installation of the switch ground plane. These results prompted the adaptation of the switches to the Mite facility. Mite is a testbed for developing a high power accelerator module for Sandia's electron beam fusion program. Figure 2 is a photograph of the Mite pulse forming lines and switches. There are five 12.7 mm diameter electrodes per PFL extending through 10.2 cm diameter holes in the ground plane.

Figure 3 is an oscillograph of the charging voltage in the PFL and the voltage in the output transmission line. The charging waveform is a  $(1-\cos \omega t)$  waveshape with a switch breakdown at 2.3 MV and  $\tau_{off}$  of 70 ns. Using these values in Eq. 1 an electrode separation of 80.3 mm is predicted which is very close to the actual gap spacing of 82.6 mm. The measured 10-90 percent risetime of 22 ns is also in good agreement with that calculated from Eq. 4.

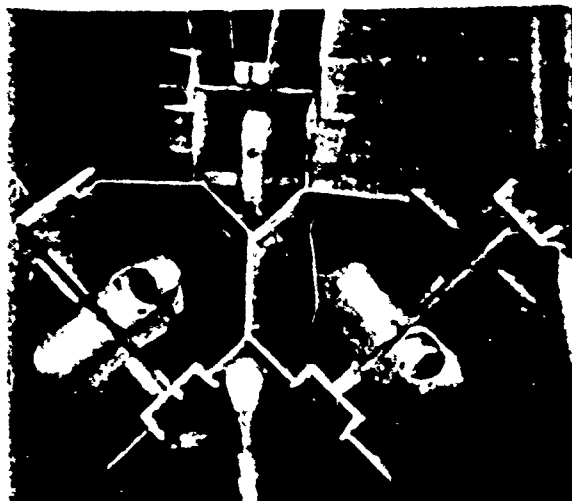


Fig. 2. Mite pulse forming lines and switches.



Fig. 3. Upper trace - PFL charge voltage.  
Lower trace - output line voltage.

Figure 4 is an open shutter photograph of the switches during breakdown. Note that all 10 switching points have closed and that most of the switches have closed to the ground plane. Since the output pulse duration was not shortened, the ground plane closures occurred after the pulse.

An advantageous feature of this switching technique is the ability to connect the pulse forming lines in parallel as shown in Fig. 2. Power densities in the output transmission lines are, therefore, increased. During low voltage testing of the lines and switches, a pulse was fed through the ground plane holes of only one PFL and the voltage on each side of the output line was monitored. The two voltages measured were within 85 percent of each other. The effect of misadjustment of the two sets of switches or abnormal switch jitter between the two sets would, therefore, be lessened by this mixing process.

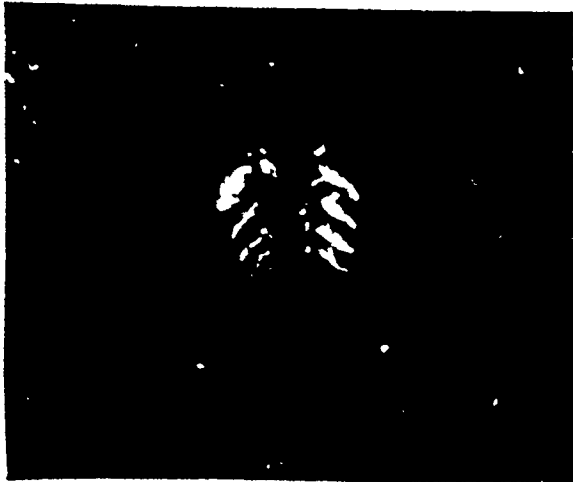


Fig. 4. Open shutter photograph of Mite switch breakdown.

Not shown in Fig. 2 is a second set of switches at the end of the output line. The switches are rod-to-plane water dielectric gaps without a ground plane shield and spaced at 6.35 mm. The measured prepulse at the diode was 6.4 kV or 0.28 percent of the 2.3 MV charge voltage on the PFL.

#### Proto II

Figure 5 shows cross sectional views of the Proto II<sup>5</sup> pulse forming lines. Sixteen of these comprise the full Proto II PFL network. The machine may be operated in two modes—a long pulse mode using line 1 as the PFL and a short pulse mode using line 2 as the PFL with line 1 as an intermediate storage capacitor. In the short pulse mode only one switching channel per PFL is used in switch 1. The prepulse on the output line consists of two parts for the short pulse mode. The voltage waveform of the first follows the line 1 charge voltage and lasts for 250 ns until switch 1 closes. During the second part, the voltage follows the line 2 charge voltage and lasts for 60 ns until switch 2 closes.

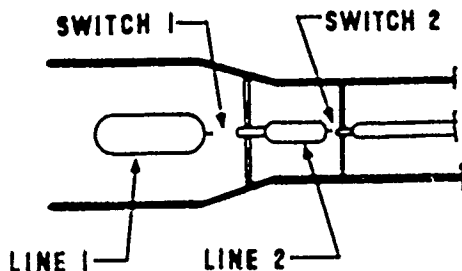


Fig. 5. Cross section of the Proto II pulse forming lines.

Table I lists the fractional prepulse on line 2 and the output line with and without ground planes, normalized to the line 1 charge voltage. The data was obtained during low voltage (50 kV) pulsing of the PFL. Case I is with switch 2 closed so the line 2 and output voltages are the same; case II is with switch 2 spaced such that it acts as only a prepulse switch; and case III is with the switches adjusted for a short pulse mode of operation.

TABLE I

Comparison of Prepulse Voltages on Proto II  
Normalized to the Line 1 Charge Voltage

		with ground plane	w/o ground plane
Case I.	V line 2	$3.7 \times 10^{-3}$	$1.6 \times 10^{-2}$
	V output	$3.7 \times 10^{-3}$	$1.6 \times 10^{-2}$
Case II.	V line 2	$1.7 \times 10^{-2}$	$7.0 \times 10^{-2}$
	V output	$1.4 \times 10^{-2}$	$3.0 \times 10^{-3}$
Case III.	V line 2	$2.8 \times 10^{-5}$	$3.1 \times 10^{-3}$
	V output	$7.1 \times 10^{-3}$	$5.7 \times 10^{-4}$

High voltage testing in the long pulse mode using switch 2 as a prepulse switch (this corresponds with case II) was done at 2 MV charge on line 1. A prepulse of 5 kV or 0.25 percent of the line 1 charge was measured. The factor of 15 higher prepulse measured is attributed to a capacitive dC/dt effect of the breakdown streamer as its leading edge approaches the output electrode. The enhanced prepulse due to this effect, however, is short compared to the line 1 charge time and appears as a foot on the leading edge of the output pulse.

#### Conclusions

This new switching technique has proven to be an effective and inexpensive method of reducing prepulse voltages on high voltage accelerators. The switches easily allow two or more pulse forming lines to be connected in parallel for increased power density.

#### References

1. B. A. Demidov, M. V. Ivkin, V. A. Petrov, E. A. Smirnova and S. D. Fanchenko, Proc. of the 2nd Int'l. Topical Conf. on High Power Electron and Ion Beam Res. and Tech., Ithaca, NY, p.771 (1977).
2. J. C. Martin, "Nanosecond Pulse Techniques", Internal Report SSWA/JCH/704/49, AWRE, Aldermaston, England (1970).
3. J. C. Martin, "Multichannel Gaps", Internal Report SSWA/JCH/703/27, AWRE, Aldermaston, England (1970).

4. J. P. VanDevender and T. H. Martin, IEEE Trans. on Nucl. Sci., NS-22 No. 3, p.979 (1975).
5. T. H. Martin, D. L. Johnson and D. M. McDaniel, Proc. of the 2nd Int'l. Topical Conf. on High Power Electron and Ion Beam Res. and Tech., Ithaca, NY, p.307 (1977).

## CONTACTS FOR PULSED HIGH CURRENT: DESIGN AND TEST

Paul Wildi

Fusion Research Center  
The University of Texas at Austin, Austin, Texas 75712

Abstract

The TEXT Tokamak required the development of a special contact for pulsed high currents for the split coils of the poloidal system at a location which is highly inaccessible. A solution was found in the form of a special plug contact. A prototype was tested to the failure point using the discharge of a homopolar machine.

Design, test setup and test results are described and the results are evaluated in view of other uses such as larger contacts and switches.

Introduction

The Texas Fusion Plasma Research Tokamak (TEXT) has in its poloidal coil system six turns inside the toroidal coil system which were dictated by magnetic field considerations [1].

Due to the geometry of the TF coils, the size of the toroidal vessel and the connection boxes these coils are inaccessible to the point where they can only be viewed through a mirror and where access with tools as would be required for a conventional bolted joint is impossible. The current in the coil has a peak value of 10 kA and a duration of approximately 300 ms followed by a 200 ms exponential decay. One shot every 120 s is anticipated and the heat effect ( $\int i^2 dt$ ) is  $4 \cdot 10^7 \text{ A}^2\text{S}$  per shot.

The Tokamak will be assembled in two halves separate from the central iron core. In this configuration there is sufficient access to mount the inner poloidal coils which are fastened to a glass epoxy coil body. In the final assembly the two

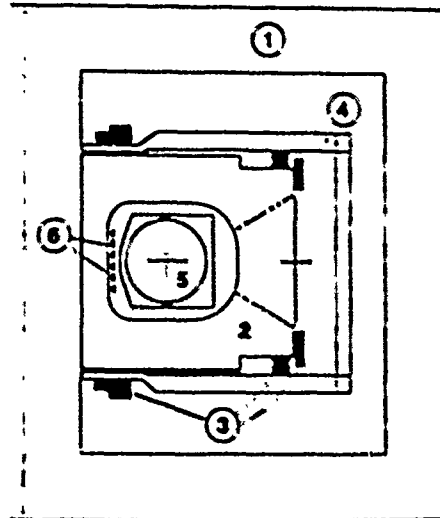


Fig. 1. Cross section of TEXT

1. Iron core
2. Toroidal coils (16)
3. Outer poloidal coils
4. Location of torque frame
5. Torus and junction boxes
6. Inner toroidal coils

sections are joined around the central core. Electrical contact plugs connecting the coil turns appeared to be the best solution. Such a plug must be able to a) carry the current with an ample factor of safety; b) have some flexibility to accommodate misalignment and inaccuracy of position; c) be capable of an axial play of approximately  $\pm 1/8$  in on account of assembly tolerances and thermal expansion and d) fit into a very limited space.

Design

Several contact configurations based on plugs with finger contacts such as they are commonly used in

switchgear were considered but had to be abandoned on account of space limitations. The plug contact finally arrived as is shown in Fig. 2. It is based on a contact strip made from beryllium copper louvers which are silver plated and thanks to their springiness, capable of accommodating a modest amount of dimensional variance. (The material in question is MULTILAM<sup>®</sup> type L11/.25.) The contact strip has 10 contact points per in of apparent contact and is rated at 350 A continuous current carrying capability per in and 17.5 kA on a 200 ms basis. Interpolations for different times of current loading have to be made with consideration of the thermal inertia of the contact points, the current carrying louvers and the adjacent base material of the contact. Since the plug shown has a total contact strip length of 5.4 in, it should be good for 2 kA continuous current and should have a 3 s rating in the order of 44 kA. The anticipated duty for our contact is considerably below these values.

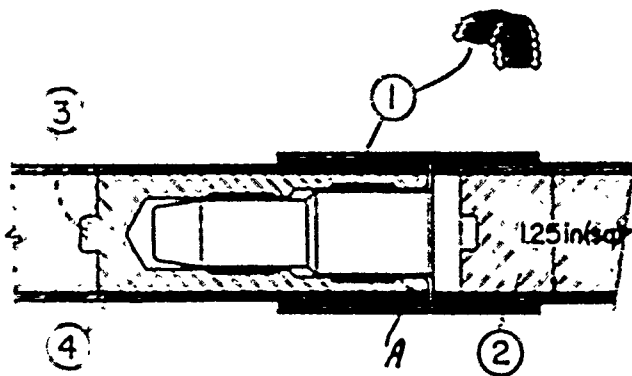


Fig. 2. Contact Plug

1. Contact spring
2. Conductor
3. Brazed joint
4. Coil insulation

#### Tests

To confirm these calculated values, tests were conducted at the Center for Electro-Mechanics of the University of Texas at Austin using the 5 MJ homopolar generator which in the chosen connection gives

a discharge in the form of an aperiodically damped pulse. In the particular experiments the excitation was switched off after .3 s which resulted in a faster than normal decay of the current. Typical oscillograms of the current are shown in Fig. 3 and 4. A total of seven tests were run. The first four tests had a current of 14 kA which represents about three times the heat input per shot of the actual duty cycle. Voltage drop over the contact was around 200 mV. Inspection of the contacts after the test showed no traces of wear. The same holds for test No. 4 at 34 kA. When the current was raised to 53 kA the oscillogram showed a voltage drop around 450 mV and some sign of contact instability. This correlates with the theoretical value of 370 mV for the melting voltage of copper(2).

TABLE 1

		Test No.			
		1 to 4	5	6	7
Peak current	kA	14.2	34.4	53.9	30.1
Heating (at location A- Figure 1)	°C	2.2	12.5	29.0	67.0
$\int i^2 dt$	$10^9 A^2 s$	0.11	0.645	1.6	3.5
Voltage drop 1	mV	120	300	450	300

Note: 1) Voltage drop = contact voltage -  $2.10^{-6} i$   
 2) After test No. 7 contact was not serviceable.

Inspection of the contact showed very slight pitting, but the material had retained its full springiness. The final test was run at 80 kA. The trace of the voltage in this test is reproduced in Fig. 5. The voltage shows heavy fluttering indicating burning on the contact spot and the median voltage drop is 800 mV. The oscillogram shows that the fluttering increases with time in spite of the decaying current



indicating clearly the distress in the contact. Inspection of the contact after the test showed superficial melting evidenced by silver droplets on the surface. The material had been completely annealed and had lost its springiness. Except for some very minor pitting, the base material was not affected. If one assumes that the second before last test represents the point of beginning distress, then the design has a safety margin of 3 with respect to current and a thermal safety margin of 25.

The tests not only confirmed the adequacy of the design but were sufficiently encouraging to use similar contacts for transfer and safety grounding switches of much larger rating [3].

#### References:

- [1] Paul Wildi, George L. Cardwell, David F. Brower, Design of the TEXT Toroidal and Poloidal Field Coils, Seventh Symposium on Engineering Problems of Fusion Research, Knoxville, Tenn., October 1977.
- [2] Ragnar Holm, Electric Contacts, Springer, New York, 1967.
- [3] Paul Wildi, Safety Grounding Switches in Large Experiments, IEEE 2nd International Pulsed Power Conference, Lubbock, Tx., June 1979.

This work was supported by the U.S. Department of Energy.

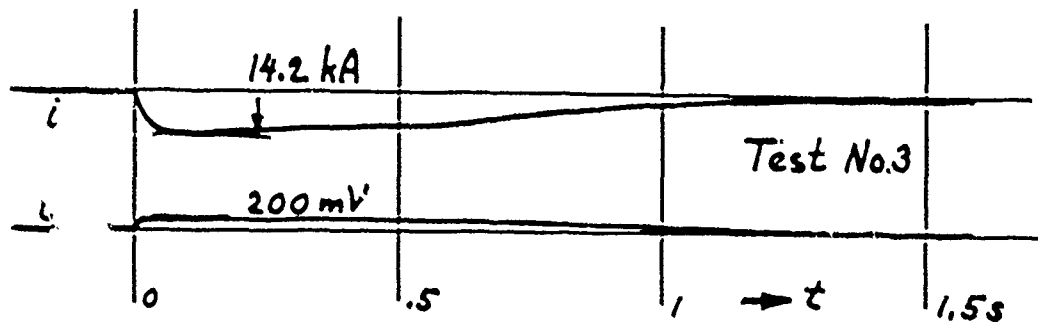


Fig. 3. Current ( $i$ ) and voltage drop ( $u$ ) over contact at 14 kA.

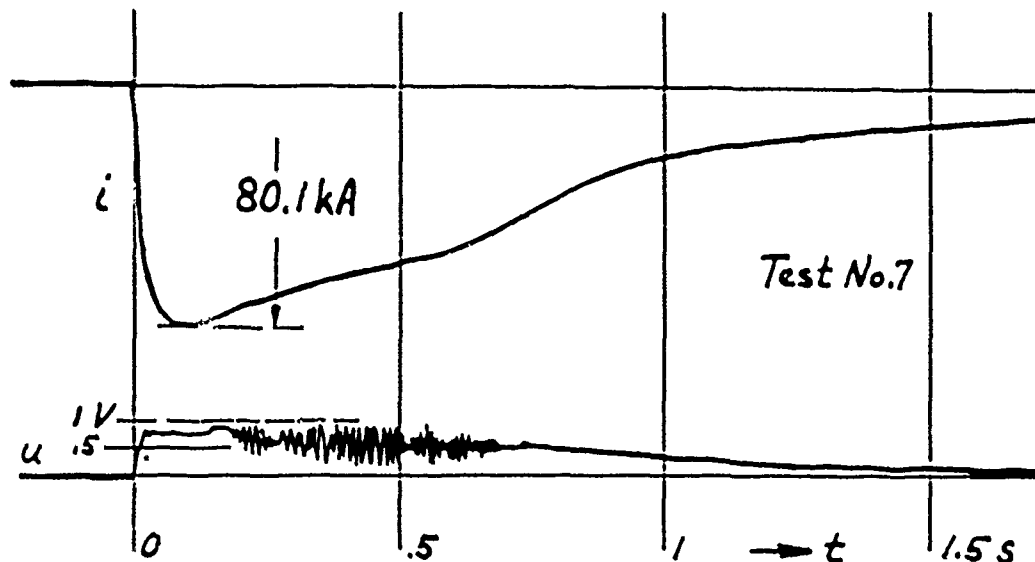


Fig. 4. Current ( $i$ ) and voltage drop ( $u$ ) over contact at 80 kA.

## THE EARLY COUNTERPULSE TECHNIQUE APPLIED TO VACUUM INTERRUPTERS\*

R. W. Warren†

Los Alamos Scientific Laboratory

ABSTRACT

Interruption of dc currents using counterpulse techniques is investigated with vacuum interrupters and a novel approach in which the counterpulse is applied before contact separation. Important increases have been achieved in this way in the maximum interruptible current and large reductions in contact erosion. The factors establishing these new limits are presented and ways are discussed to make further improvements to the maximum interruptible current.

1. INTRODUCTION

A dc current can be interrupted by a mechanical switch only if its current can be forced to zero while it is arcing. Commonly, this is accomplished either by designing the switch to generate an arc voltage greater than the source voltage or by adding an extra counterpulse circuit that injects into the switch an oppositely-directed current pulse large enough to create a transient current zero.

For several years, experiments with counterpulse circuitry have been conducted at the Los Alamos Scientific Laboratory (LASL) on interrupters to be used in fusion applications.

A conventional approach has been used following the lead of early workers such as Greenwood.<sup>1</sup> The electrodes of the switch are separated at full current and an arc occurs between them. The counterpulse is applied several milliseconds later when the electrode separation has reached approximately 1 cm. The two major limitations found with this approach are both related to the long interval of arcing at full current. The arcing heats the electrodes and generates incandescent hot spots that are prolific electron emitters. These hot spots cause reignition of the arc, providing the upper limit to the current that can be successfully interrupted.<sup>2</sup> In addition, the prolonged arc erodes the electrodes and deposits conducting films of electrode material on shields and insulating surfaces. Measurements made at LASL indicate that in spite of these problems, a vacuum interrupter can interrupt large currents and still have a long life. At 25 kA, for example, an interrupter should achieve 10,000 or more interrupting cycles before these erosion phenomena end its life.<sup>3</sup>

We have attempted to remove both of these limitations by employing a less conventional counterpulse technique. In this technique, the counterpulse is applied before the electrodes are parted so that their initial separation and subsequent arcing take place at currents much lower than the initial value. This early counterpulse (EC) technique requires a long counterpulse, a fast actuator, and a rugged interrupter. Because of its potential for lower contact erosion and a larger interruptible

---

\*Work performed under the auspices of the USDOE.

†Westinghouse Industrial staff member.

current, the EC technique has attracted other investigators. An air-blast interrupter<sup>4</sup> to be used with the tokamak JET and a special SF<sub>6</sub> switch<sup>5</sup> used with the Crossed Field Tube are examples of such developments. Vacuum interrupters have advantages relative to these other types primarily because of the lower erosion expected for the contacts and the resulting longer life.

## II. THE EARLY COUNTERPULSE TECHNIQUE

The circuit, discussed in detail elsewhere,<sup>2</sup> used in the tests is shown in Fig. 1. Energy storage capacitor C<sub>1</sub> in conjunction with switches S<sub>1</sub> and S<sub>2</sub> and inductor L<sub>1</sub> establish a slowly decaying current, I, in VI, the interrupter under test. The counterpulse is fired by closing switch S<sub>3</sub> which connects capacitor bank C<sub>2</sub> to VI. This generates the desired reverse-current pulse. L<sub>2</sub>, a saturable reactor, helps to shape the reverse-current pulse so that the switch current is close to zero for a long time. R<sub>1</sub> is used as a final dump resistor for the energy initially stored in C<sub>1</sub> and C<sub>2</sub> and is connected by S<sub>4</sub> after the interruption phenomenon is completed.

Figure 2 shows schematically, the behavior of the current flowing through VI. At time t<sub>0</sub> the counterpulse is initiated. At t<sub>1</sub> the current in the switch passes through zero for the second time and interruption may occur. At t<sub>2</sub> the capacitor C<sub>2</sub> and the saturable reactor L<sub>2</sub> have exhausted their charge and flux so that the counterpulse ends. For the EC technique to succeed, VI must open its contacts between t<sub>0</sub> and t<sub>1</sub>. With this timing an arc will start and burn at low current and interrupt as the current passes through zero at t<sub>1</sub>.

There are two obvious problems with the EC technique which must be overcome and which have become the main focus of these investigations. The first is the difficulty of opening the interrupter in the short interval between t<sub>0</sub> and t<sub>1</sub> in the face of jitter from various sources. The second is the rapid development of the

recovery voltage at a time when the arc has barely extinguished and the electrodes have barely separated. The possibility of reignition of the arc at this time is high but can be reduced by several measures.

1. A high-average velocity of separation of the electrodes.
2. A large saturable reactor and counterpulse bank.
3. A snubber circuit (an RC series combination) placed across VI.

The actuator used in these tests was made by Ross Engineering Co.<sup>6</sup> It is operated by two repulsion coils, one stationary and one connected to the moving electrode of the interrupter. The coils are energized by a 300 μF capacitor bank charged to 2 to 5 kV. The peak coil current is several tens of kilampères. The actuator was designed to maximize the acceleration of the moving electrode. Accelerations of 10<sup>6</sup> cm/sec<sup>2</sup> have been achieved. The saturable reactor is composed of 133 separate 4-mil tape-wound cores, each threaded by a 4-0 electrical cable. Each of the cores has a flux rating of 0.008 Wb for a total of about 1 Wb. Because of the gap-less tape-wound construction of these cores, their unsaturated inductance is very large.

The counterpulse bank is unusually large. We used 360 kJ of capacitance connected in different ways to provide either  $1.8 \times 10^{-3}$  F at 20 kV or  $0.45 \times 10^{-3}$  F at 40 kV.

## III. RESULTS

The first experiments were performed with a standard 7-in. interrupter,<sup>7</sup> with an actuator acceleration of  $0.3 \times 10^6$  cm/sec<sup>2</sup>, and a counterpulse bank of  $1.8 \times 10^{-3}$  F. This arrangement gives the longest possible counterpulse and potentially the largest interruptible current. The modest acceleration was chosen to avoid possible stress-induced problems with the actuator or interrupter. With conventional counterpulse techniques, such an arrangement would have given a maximum

interruptible current of 21 kA, relatively independent of recovery voltage.

The experiment proceeded by gradually raising  $I$ , the current to be interrupted, and at each current level by varying  $t_1$ , the interrupter opening time, over its full range, from  $t_0$  to  $t_1$ . The experiments were continued with currents up to 35 kA at 25 kV, the limit of the test facilities, with no failures of any kind. A striking observation concerned the visual appearance of the switch during interruption. With conventional counterpulse techniques, the ceramic envelope lights up brightly due to the enclosed arc. With EC techniques, no light could be seen. This is consistent with the reduction of the arcing current by a factor of 300 and arcing time by a factor of 10 produced by EC.

To increase the electrical stresses on the interrupter the value of  $C_2$  was reduced to  $0.45 \times 10^{-3}$  F. This change increased the recovery voltage by a factor of two and decreased the interval  $t_1 - t_0$  for opening the interrupter by a factor of two. Under these conditions reignitions were occasionally observed when  $t_1 - t_0$  was small, that is, much less than 100  $\mu$ s. The major new effects observed were a marked increase in the jitter observed in the opening time and a consistent shift of the average opening time as the current increased. These effects combined to make it difficult to time the switch's opening to occur between  $t_0$  and  $t_1$ . This effect set a maximum interruptible current of about 20 kA.

To investigate this limit, we substituted three different 4-in. interrupters for the original one keeping  $C_2 = 0.45 \times 10^{-3}$  F. With conventional techniques these switches could interrupt 6, 6, and 3 kA, respectively. With the EC technique their limits were increased by a factor of 2 to 2.5, as determined, again, by the onset of marked jitter in the opening time and its shift to later times.

Careful measurements identified two sources of the jitter and shift. One was the tendency of

the electrodes to pop apart at high currents. This shows up as a voltage jump before  $t_0$ .

The second problem was of a related kind. The "opening" of the switch occurs when the molten bridge which forms between the electrodes ruptures. The lifetime of the bridge depends upon the details of current magnitude, contact pressure, etc., in a complex way.

The effect of these phenomena is to reduce the range of counterpulse settings within which an EC interruption can be achieved. The range is reduced to zero for currents slightly above 19 kA, consistent with the findings that 20 kA is the largest current we can successfully interrupt.

#### IV. LIFE TESTS

To test the erosion reduction expected of the EC technique, a 4-in. interrupter was subjected to over 1000 interruption cycles at 10 kA. The interrupter was disassembled and the contacts examined after these wholly successful interruptions. The contacts were found to be in near-new condition, the surface markings being caused largely by contact rubbing. We estimate a reduction in erosion brought about by the EC technique of more than one hundred.

#### V. CONCLUSION

The anticipated features of the EC technique were reduced electrode erosion and increased current ratings. Substantially increased ratings have been realized in these experiments, and the reduction in erosion is very large. The components and techniques used to achieve these improvements are available, convenient to use, and relatively reliable.

The new current limit does not appear to be a basic property of the switches but is instead associated with the actuator, in particular with the force with which the electrodes are held closed. Future work will attempt to raise the current limit further by employing higher closing forces.

## VI. REFERENCES

1. Greenwood, A. H., and Lee, T. H., "Theory and Application of the Commutation Principle for HVDC Circuit Breakers," IEEE Transactions on PAS, Vol. 91, No. 4, Jul./Aug. 1972, p. 1570.
2. Warren, R. W., "Experiments with Vacuum Interrupters Used for Large DC-Current Interruption," report of Los Alamos Scientific Lab., LA-6909-MS, October 1977.
3. Warren, R., Parsons, M., Monig, M., and Lindsay, J., "Tests of Vacuum Interrupters for the Tokamak Fusion Test Reactor," report of Los Alamos Scientific Lab., LA-7759-MS, April 1979.
4. Dokopoulos, P., and Kriechbaum, K., "DC Circuit Breaker for 73 kA, 24 kV," Elektrotechnische Z, ETZ-A 5, 97, 499 (76).
5. Knauer, W., Hughes Research Lab., Malibu, Calif., private communication.
6. Ross Engr. Corp., 559 Westchester Dr., Campbell, Calif. 95008.
7. Model 4L-23231, Westinghouse Electric Corp.

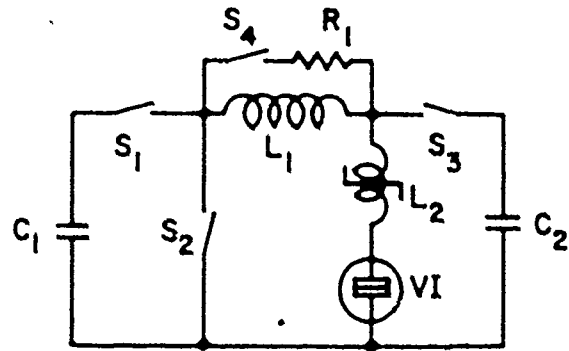


Fig. 1. Test circuit.

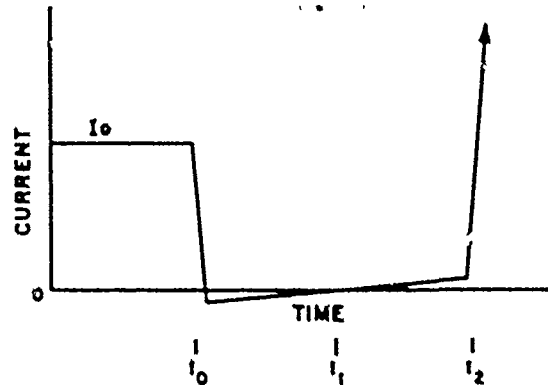


Fig. 2. Current during counterpulse.

INVITED  
DEVELOPMENT OF HIGH CURRENT ELECTRON PULSE ACCELERATORS  
AT THE INSTITUTE OF HIGH TEMPERATURES

E. A. Abramyan, G. D. Kulashov

Institute of High Temperatures, USSR Academy of Sciences  
Korovin'skaya Chaussee  
Moscow, 127412, USSR

#### Abstract

A short analysis of the problems encountered in the acceleration of long ( $10^{-4}$  sec and longer) pulsed, relativistic electron beams (REB) is given. A description of the parameters of the experimental facilities developed to study these long-pulsed beams is presented, as well.

Over the last 15 years, the power in nanosecond duration electron accelerators has increased by more than 3 orders of magnitude and the energy content of these beams has reached several MJ. It is known that in accelerators of this type the electric field gradient in the acceleration region approaches 0.5 MV/cm. The length of the applied pulse is limited by the breakdown development time. The rapid development of nanosecond accelerators has benefited from the unique characteristics of cold cathodes, i.e. the high emission density achievable in short pulses (up to  $10^4$  A/cm<sup>2</sup>) and their capability to retain good emission characteristics after arcing or vacuum rupture.

Electron beams of short duration satisfy quite a number of REB applications, particularly with respect to heating of a substance to thermonuclear temperatures in experimental installations for inertially confined fusion. However, to solve other tasks it is necessary to increase the beam lifetime and make the operation more stable. Examples of other applications are SHF generators, i.e. oscillating relativistic beams; and collective acceleration of ions [1]. The further development of several kiloampere REB's with duration of  $10^{-4}$  -  $10^{-3}$  sec, and continuous beams in the future, will make it possible to start experimental research concerning the problem of energy transfer over large distances by means of electron beams. [2].

One of the main directions of research on REB conducted at our institute is related to finding ways to create long-pulsed electron beams with currents of the order of 1 kA at an energy of 1 MeV. The program is aimed at studying new energy transfer techniques.

#### Peculiarities of the Generation of Long-Pulsed Intensive REB's

It is common knowledge that the current density in accelerating gaps is limited by the perveance of

the system and the emitting capability of the cathode. The accelerating fields in existing long-pulsed and continuous accelerators is about 0.02 - 0.05 MV/cm, considerably less than for nanosecond duration acceleration. In this case the current density of the beams to be accelerated is no greater than several amps per cm<sup>2</sup>. Some increase of perveance of the accelerating system can be achieved by the installation, between the cathode and anode, of many intermediate electrodes at appropriate potentials as well as by space charge neutralization.

One approach to the problem of intensive long-pulsed REB generation is to increase the gradient of the accelerating electric field, another the compression (focusing) of the beam to much higher densities than the initial low values. In order to make the required improvements it is necessary to combine both methods.

The capability of present, existing cathodes - e.g. lanthanum boride, iridium cerium, overheated tungsten, etc. - makes it possible to achieve current densities of the order of  $10^2$  A/cm<sup>2</sup> in pulses of  $10^{-4}$  sec and longer. The primary task is to increase the perveance of the accelerating gaps to such values as to provide higher currents.

The comparatively slow progress in improving the voltage hold-off characteristics of non-segmented high voltage vacuum gaps makes it impossible to guarantee the emission of current at high energy in systems similar to electron guns employing compression. It is more appropriate to develop accelerating devices constructed with many electrodes and

many separated parallel beams in the same diode.

In particular, a considerable improvement in electrical strength of the accelerating tube can be expected with the electrode spacing reduced to 10 - 100  $\mu\text{m}$ . It is known that micron vacuum gaps and layers of solid insulation can resist static electric fields of more than 1 MV/cm. The problem is to obtain satisfactory electric field intensities in many-layer structures containing many channels for electron acceleration. To achieve this goal it is necessary to provide for stable and uniform distribution of voltages over intermediate electrodes and, furthermore, to reduce to the utmost the number of electrons lost to the electrodes of the tube by, for instance, the application of a longitudinal magnetic field. The fabrication of such systems are of great importance as well.

Energy Recycling - One of the Key Problems in Development of Experimental Installations With Long-Pulsed REB's

The development of high voltage generators to feed long-pulsed several kA, MeV beams presents no major obstacle. For this purpose we can use inductive storage, Marx generators, or transformers. The energy content of beams that can be employed in the earlier stages of research will probably not exceed  $10^6 - 10^7 \text{ J}$ .

As far as the high voltage generators used in experimental installations, which are designed for flexible operation of the accelerating and focusing systems and for beam transfer, are concerned, their cost could be considerably reduced if one could recover the electron beam energy. In an installation of this kind the collector of the decelerating device is connected electrically to the cathode, resulting in a closed circuit with the stream of fast electrons being an integral segment of the total current flow [3]. Since a complete deceleration of the electron beam is essentially impossible, there is a small potential difference between the cathode and the collector ( $\Delta U$  is usually on the order of several percent of the anode voltage  $U$ , which is maintained by the power source).

If  $\Delta U$  is relatively small compared to the accelerating potential, then power and current losses,  $\Delta I$ , in the beam of accelerated electrons will also be small. The beam power  $IU$  can exceed many times the total of the component sources:

$$IU \gg U_{SI} + I\Delta U$$

and the effective energy content of the beam can exceed the energy accumulated in both power sources.

Experimental Facilities For Research, Generation, Transfer and Deceleration of Long-Pulsed Relativistic Beams

To study the processes of generation and recovery of long-pulsed electron beams a test facility was developed at our institute which could generate electron beams with the following parameters: electron energy 0.5 MeV, beam current 100 A, pulse length 100  $\mu\text{sec}$ . A Marx generator with the correct pulse shape [3] to obtain a constant accelerating voltage during the main part of the pulse was constructed. The accelerating device is of two types; a simple diode and a segmented one. The accelerator design makes it possible to conduct studies of other options of beam forming systems, e.g. compact multichannel acceleration tubes with small segmented sections and the combination of beams in a drift region.

In this system, the electron beam energy recovery device is mounted inside the same vacuum chamber as the accelerator. The research program using this test facility includes the studies of the optimum conditions for reverse transformation of the kinetic energy of the electron beam into electromagnetic field energy. The recovered energy is then fed to the accelerating system input. In this manner the beam power and pulse length can be increased considerably. The range of experimental research work conducted on the test facility can of course be expanded.

The test facility is a model of a more powerful installation which is under development at the present time. The design parameters of this new installation are: energy 1 MeV, current  $10^3 - 10^4 \text{ A}$ , pulse length 10  $\mu\text{sec}$ , the pulse length in the recycling mode  $\sim 100 \mu\text{sec}$ . The installation includes a 10 meter

long vacuum line which is designed for studies of methods of beam transfer with high efficiency.

Repetitively Pulsed High Voltage Generators (Pulse Duration  $\sim 10^{-4}$  sec)

In order to test various components of these long-pulse accelerators and to expand their range of applications we have designed portable high voltage sources based on shock excitation transformers. In the previously developed types of shock excitation transformers [4] the high voltage pulse duration was  $10^{-7} - 10^{-5}$  sec and hydrogen thyatrons or spark gaps were used as commutators.

Switching over to pulses with duration of about  $10^{-4}$  sec made it possible to use standard production thyristors and attach the primary winding of the transformer directly to the mains.

Rated data of the shock transformer under test now are:

Voltage: 400 kV

High voltage half pulse duration (at the base):  $3 \cdot 10^{-4}$  sec

Energy output per pulse: 30 J

Repetition Frequency: 300 Hz

Efficiency from the mains to the consumer: 60%

Operation: Continuous

References

1. Abramyan E. A., Altercop B. A., Kuleshov G. D. "Microsecond Intensive E-beams." Report on the 2nd Intern. Topical Conference on High Power Electron and Ion Beams, Ithaca, USA, Oct. 1977.
2. Symons R. S., "Electron Beam Power Transmission." Report #94 on the World Electrotechnical Congress, Moscow, June 1977.
3. Abramyan E. A., Efimov E. N., Kuleshov G. D. "Energy Recovery and Power Stabilization of Pulsed Electron Beams in Marx Generator Circuits." Report on the 2nd Intern. Topical Conference on High Power Electron and Ion Beams, Ithaca, USA, Oct. 1977.
4. Abramyan E. A., "High-Voltage Pulse Generators of the Base of the Shock Transformer". Report on the 1st Intern. IEEE Pulsed Power Conference, Lubbock, USA, Nov. 1976.

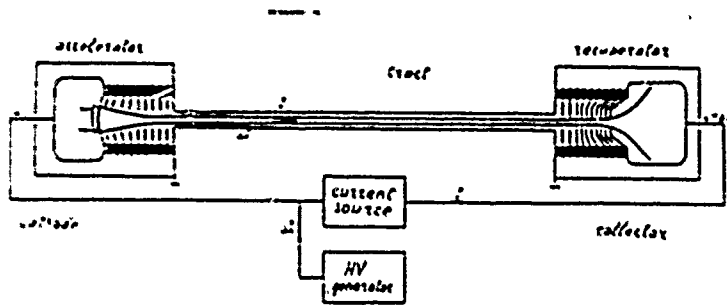


Fig. 1 Diagram of Installation with Electron Beam Energy Recycling



## STATUS OF THE UPGRADED VERSION OF THE NRL GAMBLE II PULSE POWER GENERATOR

J. R. Boller, J. K. Burton and J. D. Shipman, Jr.

Naval Research Laboratory

Washington, D. C. 20375

Abstract

The GAMBLE II water dielectric pulse power generator, in 1970, was the forerunner of the high energy ( $>50$  kJ) class of water dielectric generators. It has been redesigned internally to make maximum use of its original outer conductor shell and to optimize it for the positive polarity mode of operation for positive ion beam experimentation. The new design also initiates the use of an oil dielectric multi-channel switch at the output of the pulse forming line. This switch, because of its low capacitance, eliminates the need for an extra prepulse switch. The upgraded version has been tested up to power and energy levels which are nearly twice the original.

The GAMBLE II pulse power generator, designed and built at the U. S. Naval Research Laboratory in 1970 has been modified so that it is now delivering about  $1\frac{1}{2}$  times its former power and energy. It is hoped that as the physics experiments now using the generator need more power; the output can be gradually increased until it is up by a factor of about  $3\frac{1}{2}$ .

The original generator is shown in Figure 1. It consisted of a 215 kJ, 4 nF, Marx generator in a tank of transformer oil that charged a 7  $\Omega$ , 7 nF water dielectric, coaxial, intermediate store; which in turn charged a 6  $\Omega$ , 6 nF water dielectric coaxial pulse forming line. A single channel, but multi-branching, water output switch self closed near the peak voltage and sent a fast rising power pulse into a 6  $\Omega$ , to 1.5  $\Omega$  coaxial transformer and

delivered 65 kJ into a matched load with 63 ns FWHM. Peak power was about 1 TW.

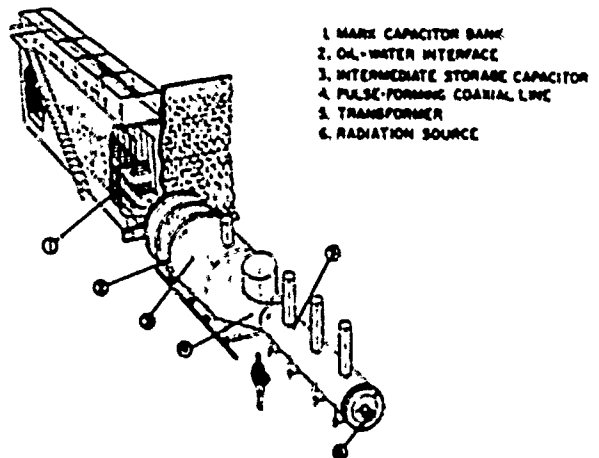


Fig. 1. GAMBLE II Pulse Power Generator in its original form

Figure 2 shows the relatively few modifications which were required to modify GAMBLE II into the upgraded IIA version. The new components of the generator are shown shaded.

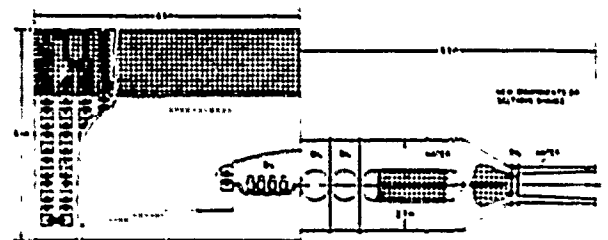


Fig. 2. GAMBLE IIA Pulse Power Generator Schematic

We found that by increasing only the height of the oil tank by 6 ft., we could enclose Marx generator components for 520 kJ stored in 13 nF. The expensive stainless steel outer conductor of the water dielectric part of GAMBLE II was left unchanged with the exception that we use only the last half of the original coaxial transformer since the pulse forming line impedance has been reduced from 6  $\Omega$  to 3  $\Omega$ . The spheres and hemispheres from the original intermediate store inner conductor with the o-ring grooves, etc., required for sealing the connections through the polyurethane diaphragms were used unchanged. The only new part in the intermediate store is the relatively inexpensive cylindrical aluminum section between the end hemispheres.

The impedance of the intermediate store is 6.7  $\Omega$ , which is the optimum impedance for storing maximum energy in either the negative or positive polarity mode. Its capacitance is 16 nF including the capacitance of its water output switch.

The pulse forming line impedance is 3.2  $\Omega$ , which is the optimum impedance for delivering maximum power to the transformer in the positive polarity mode. It is also a good choice for the negative polarity mode. Its capacitance is 10.4 nF.

The GAMBLE IIA pulse generator has a pulse forming line output switch that is unique in large water dielectric systems. It uses transformer oil instead of water as the medium in which the switch streamers propagate. Since oil has a dielectric constant about 1/36 that of water, the prepulse fed through the output switch capacitance during the charge of the pulse forming line is reduced accordingly. The polyurethane diaphragms that contain the switch oil provide support for the output end of the pulse forming line and the input end of the transformer. After each shot the oil is circulated through a filter for about 15 minutes to clear out the carbonized oil. The oil output switch used until now has been a self closing multi-channel type with 6 or 12 enhanced field, 1 inch diameter electrodes on the positive side. It

results in a 10% to 90% current rise time in a matched load of 35 to 45 ns with a prepulse of less than 1X.

The present performance of the generator is summarized in Figures 3 and 4.

	COMPUTED VALUES WITH THE INTER- MEDIATE STORE SWITCH RESISTANCE = 0 OHMS	COMPUTED VALUES WITH THE INTER- MEDIATE STORE SWITCH RESISTANCE = 2 OHMS	MEASURED VALUES ON SHOT NO. 66
PEAK POWER INTO A 2 OHM NONINDUC- TIVE LOAD	3.24 TW	1.79 TW	1.78 TW
TIME OF THE POWER INTO THE 2 OHM LOAD RESISTOR	64 ns	64 ns	71 ns
10% TO 90% RISE TIME OF THE POWER INTO THE 2 OHM LOAD RESISTOR	40 ns	40 ns	49 ns

Fig. 3. Computed and measured power into a near matched load on the GAMBLE IIA Pulse Power Generator

	COMPUTED VALUES WITH THE INTER- MEDIATE STORE SWITCH RESISTANCE = 0 OHMS	COMPUTED VALUES WITH THE INTER- MEDIATE STORE SWITCH RESISTANCE = 2 OHMS	MEASURED VALUES ON SHOT NO. 66
ENERGY IN THE MARX GENERATOR	267 kJ	267 kJ	267 kJ
ENERGY INTO THE INTERMEDIATE STORE	199 kJ	199 kJ	199 kJ
ENERGY INTO THE PULSE FORMING LINE	177 kJ	142 kJ	142 kJ
ENERGY INTO THE INPUT OF THE COAXIAL TRANSFORMER	149 kJ	120 kJ	-----
ENERGY INTO THE 2 OHM NONINDUC- TIVE LOAD	140 kJ	119 kJ	123 kJ

Fig. 4. Computed and measured energy at various stages of the GAMBLE IIA Pulse Power Generator

The right hand column of Figure 3 shows that the measured peak power into a near matched non-inductive load of 2 ohms was 1.78 TW, the FWHM of the power pulse was 71 ns, and the 10% to 90% rise time was 45 ns. The other two columns of Figure 3 show the computed results obtained by analyzing the system with the NRL codes for potential plotting, incremental capacitance calculating, and transient analysis of transmission line systems. The left column shows the values computed with no time dependent or fixed series resistance in either the water or oil switches. The center column shows the values computed when a fixed 2  $\Omega$  series resistor was included in the intermediate store output switch. It was found that this resistance has to be added to make the computed and measured values agree as indicated in Figures 3 and 4. The right hand column of Figure 4 shows the measured values of energy at various stages of the water dielectric system. As in Figure 3 the left and center columns are the computed values with zero and 2  $\Omega$  for the intermediate store switch resistance. The loss of 68 kJ between the Marx generator and the intermediate store is mainly in the 10  $\Omega$  distributed series resistance of the Marx generator circuitry. The loss of 57 kJ between the intermediate store and the pulse forming line is about half dissipated in the series resistance of the water switch and half reflected back into the intermediate store from the water switch. The loss of 19 kJ between the pulse forming line and the load is mainly energy reflected by the inductance of the oil output switch.

Figure 5 shows the measured shape of the current pulse into the 2  $\Omega$  load. The peak current was .94 MA with a FWHM of 93 ns. The 10% to 90% rise time was 45 ns. On this shot the output switch closed about 50 ns before peak charge. This results in a greater total shot energy but a somewhat longer rise time than a closure at peak charge. The power and energy delivered to the load are shown plotted below the current. The maximum power was 1.78 TW with a FWHM of 71 ns and the energy

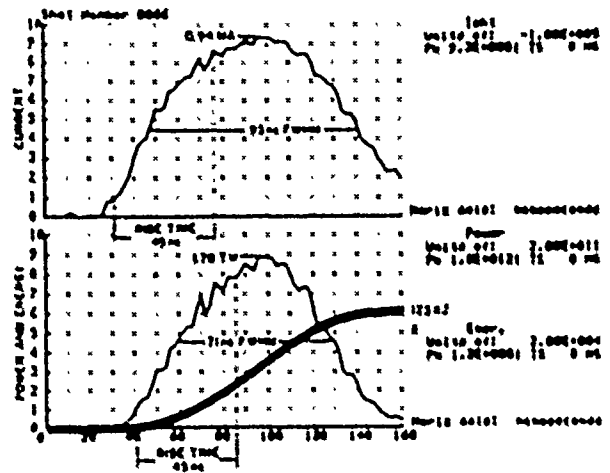


Fig. 5. Measured Current, Power and Energy into a 2  $\Omega$  noninductive load

was 123 kJ. The efficiency from the Marx to the load on this shot was 46% which is 53% higher than the 30% efficiency of the original GAMBLE II generator. The efficiency within the upgraded water system between the intermediate store and the matched load is 62%. These efficiencies are very high for such generators.

The complete system can be operated at the Marx generator level of 267 kJ for about 30 to 40 shots before some maintenance is required. At this level of operation the pulse forming line is charged to 4.4 MV in 143 ns and the polyurethane diaphragm on its output end is stressed to 271 kV/cm. If we are able to operate with the Marx generator capacitors charged to 62.5 kV, the total charge will be 520 kJ and the above diaphragm stress would be 376 kV/cm. This stress level on the oil switch diaphragm will probably be the weak link (in regard to breakdown) in the whole system. The output into a matched load at this level would be 3.5 TW and 239 kJ. These last levels will probably not be attainable in the positive polarity mode (which is the only mode of operation to this date). The maximum output in this mode will probably be limited to about 2.6 TW and 160 kJ due to calculated water breakdown in the intermediate store and the pulse forming line.

Our design goal in the upgrade was to get as much power and energy out of the water dielectric system as possible without increasing its outer dimensions and we believe we will achieve this. At least, we are certain that the GAMBLE II generator has shed its conservative label.

---

The original GAMBLE II generator was funded by the Defense Nuclear Agency. The upgrade was funded by the Office of Naval Research and the capacitors for the Marx generator were furnished by the Sandia Laboratories.

## EMITTANCE MEASUREMENTS ON FIELD EMITTER DIODES \*

Bernhard Kulke and Ronald Kihara

University of California  
Lawrence Livermore Laboratory  
P. O. Box 808, Livermore, CA. 94550

ABSTRACT

On the basis of time-integrated emittance measurements, several different types of field emitter diodes were investigated at 1-3 kA, 1 MeV. The experimental parameters were the cathode type, the anode mesh texture, the diode spacing and voltage, and the level of collimation of the emerging beam. Over a wide range, the emittance was found to be proportional to the level of collimation. With the diode spacing left fixed, the emittance was found to be essentially independent of the diode voltage and current.

The lowest emittances (30-40 mr-cm at 400 A) were obtained with a foil-type cathode in a ball-over-plane configuration.

INTRODUCTION

The flash x-ray (FXR) linear induction accelerator at Lawrence Livermore Laboratory, currently being designed, requires an injected electron beam of 2-4 kA at 1.5-2 MeV. In order to maximize the forward radiation dose produced by a beam of given diameter, it is essential to minimize the emittance. Field emitter diodes are well suited for flash x-ray applications, but measurements to date of their beam quality have largely been confined to determining the angular divergence of high current beams in the region very close to the anode<sup>1,2</sup>. Measurements on a beam that was collimated and transported over some distance have been reported by the ERA group<sup>3</sup> at Lawrence Berkeley Laboratory (LBL) who utilized a field emitter diode as the injector to a 4 MeV induction LINAC.

The proposed FXR electron source is modeled largely after the LBL injector. Thus, in order to confirm and expand on the earlier LBL results, the LBL field emitter diode gun was brought to LLL and reactivated for further emittance measurements.

APPARATUS AND EXPERIMENTAL PROCEDURE

As shown in Figure 1, the diode proper consists of a ball-over-plane or similar configuration with the planar anode formed by tungsten mesh. The electron beam traverses the anode mesh and is focused by a thin lens solenoid that in conjunction with two collimator apertures downstream from the anode, acts as a variable beam scraper. Downstream from the second collimator is mounted a pinhole mask with a square array of 1 mm dia pinholes on 5 mm centers, and this in turn is followed by a scintillator screen carrying a layer of P-11 phosphor.

The diode voltage is generated by five induction modules that are effectively connected in series by the movable cathode stem linking them. This allows convenient adjustment of the anode-cathode spacing. Each module is a ferrite-cored 1:1 pulse transformer, with the single turn primary driven from a nominal 250 kV, 56 ohm, 40 ns Blumlein, and the secondary being formed by the cathode stem. Figure 2 shows some typical pulse shapes. Note that the width of the beam current pulse is narrower after collimation.

To calculate the emittance, the scintillator image (Figure 3) typically was first scanned with a densitometer. The center of each image spot then was used to measure the

angular divergence of each beamlet from the straight-through position. A second angle, calculated from the FWHM of the image spot, represents the growth in diameter of the beamlet over the 115 mm drift distance. The corresponding phase plane representation of any one beamlet was then drawn, and finally, the emittance was calculated as  $1/\pi$  times the area of the figure circumscribing the entire phase plane plot.

Two diodes investigated here employed a number of different cathodes, with the best one (C1) consisting of a 50 mm dia., nominally spherical, polished stainless steel cup with a small, flush mounted button insert carrying a 7 mm dia. tantalum foil spiral. This was an earlier LBL design. Cathode C2 used a flat, graphite emitter button. Two other cathode geometries employed a graphite rod and a spherical-cap graphite button, respectively. Cathode C3 was a 100 mm dia., polished, stainless steel pancake carrying the 7 mm dia. emitter button of C1.

The experimental anodes consisted of tungsten mesh stretched across a 76 mm dia. circular aperture facing the cathode. They included:

- A1. Woven mesh, 0.025 mm dia., in a 0.5 x 1.8 mm array.
- A2. Etched mesh, 16 lines/cm, 0.036 mm thick x 0.061 mm wide.
- A3. Etched mesh, 24 lines/cm, 0.025 mm thick x 0.05 mm wide.

#### EXPERIMENTAL RESULTS

The lowest emittances were obtained with the C1 cathode, i.e., a simple ball-over-plane configuration, using a foil emitter. The other cathodes all tended to produce scintillator images that were poorly defined, and clearly represented beams with greater emittance. The measurements discussed in the following therefore concern only cathode C1.

The degree of collimation was controlled throughout by varying the solenoid lens field strength. For diode C1-A1, Figure 4 shows the variation of the emittance vs the collimated beam current with the A-K spacing as the para-

meter. The nearly linear relationship between the collimated beam fraction and the emittance leads one to conclude that for a beam that is already severely collimated, the remaining beam current is quite uniformly distributed in phase space. A further reduction in beam current thus corresponds linearly to a similar reduction in phase space area, or emittance.

The function of the planar anode mesh is to support a strong electrostatic field at the spherical cathode while at the same time allowing the beam electrons to pass through with minimum interception or perturbation to their trajectories. The perturbing effect of the anode mesh can be modeled by considering each open square as a miniature electrostatic lens, with the focal length given by<sup>4</sup>  $f = 4U/(E_2 - E_1)$ , where  $U$  = anode potential, referred to the cathode, and  $E_1$  and  $E_2$  represent the electric field on the cathode side and on the downstream side, respectively. For the typical case,  $E_2 = 0$ , the lens is diverging, and the divergence half angle will be proportional to the mesh spacing. Thus, one clearly does well to use the minimum mesh spacing that is consistent with good beam transmission.

In Figure 5 we have plotted the measured emittance variation with current for diode C1-A2 which used the 16 l/cm, etched tungsten mesh. It is seen that the tighter, etched anode mesh does produce somewhat lower emittance beams than the woven mesh of Figure 4. Also, there appears to be a definite minimum of emittance reached near 30 mr-cm. Further measurements<sup>5</sup> indicated that there was nothing to be gained in going from 16 to 24 lines/cm (etched) while there was visible improvement in going from 10 lines/cm (woven) to 16 lines/cm (etched).

In an attempt to gain some insight on the effect of beam voltage variations, the diode potential was changed in three steps, from 680 kV to 970 kV. The results are shown in Figure 6, and clearly, no systematic variation of the emittance with the diode potential is

evident. This is as expected, because field emitter diodes at high current levels essentially follow space-charge limited behavior. Under these conditions, the relative potential distribution within the diode, and hence, the electron trajectories and the emittance, should indeed remain unchanged. The focal length of the solenoid lens was essentially kept independent of the beam voltage by adjusting the field strength to produce identical collimation ratios.

#### SUMMARY AND CONCLUSIONS

Emittance measurements have been carried out on field-emitter diodes to investigate the separate effects of changing the cathode geometry, the anode texture, the A-K spacing, the amount of beam collimation, and the diode potential, respectively. The lowest emittances, i.e., the best quality beams, were obtained with a small-area foil cathode mounted opposite a fine-mesh anode in a ball-over-plane configuration. With beams that were initially collimated to less than one-half the original current, further collimation resulted in a proportional reduction in emittance, but there appeared to be a minimum level below which the emittance could not be reduced.

Variation of the diode potential over a 40% range and of the diode current over an 80% range produced no significant change in the emittance. Extrapolating from this result, emittances on the order of 40-60 mr-cm appear to be realizable even for a 2-4 kA, 1.5 MeV beam.

#### REFERENCES

1. J. G. Kelly, L. P. Bradley, Pinhole Diagnostics for Direct Measurements of Localized Angular Distributions in Relativistic High Current Electron Beams, SC-RR-72 0058, Sandia Laboratories, (Jan. 1972).
2. L. P. Bradley, Technique to Measure Distribution of Electron Current Density and Electron Trajectories in a High Current Relativistic Electron Beam, Rev. Sci. Instr., 48 pp. 673-676 (June 1975).

3. Glen R. Lambertson et. al., Experiments on Electron Rings at Berkeley, Particle Accel., 5 pp. 113-120, (1973).
4. A. Septier, ed., Focusing of Charged Particles, V. I, p. 296, Academic Press, New York, (1967).
5. B. Kulke and R. Kihara, Emittance Measurements on Field Emitter Diodes, UCRL-82533, Lawrence Livermore Laboratory, (April 5, 1979).

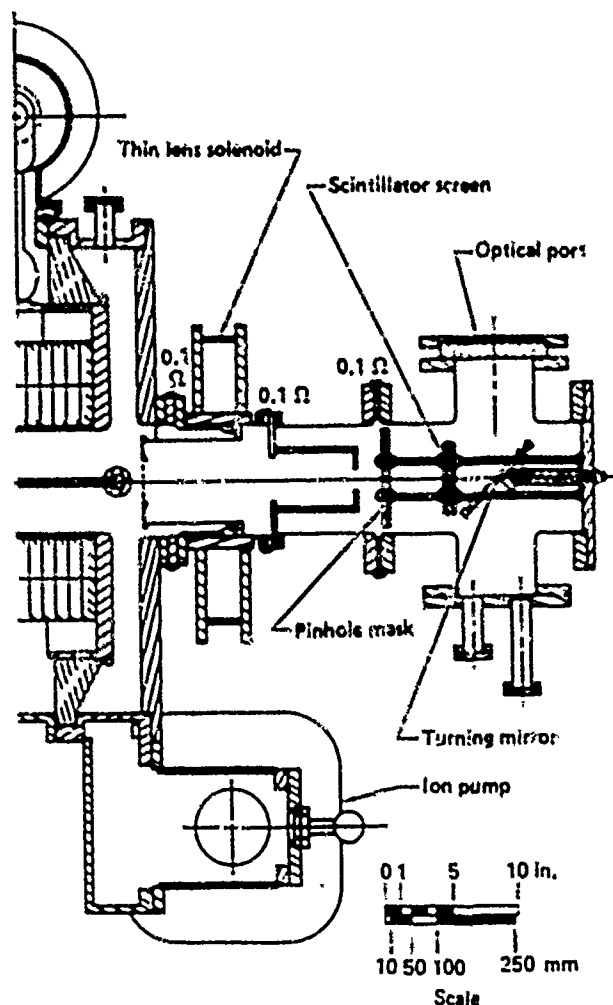


Fig. 1 Field Emitter Diode and Emittance Tester.

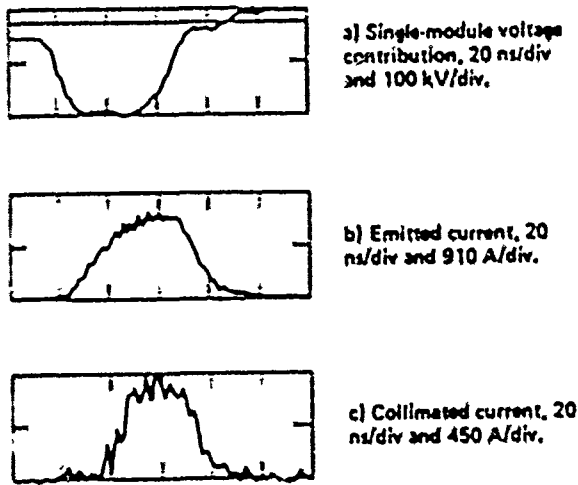


Fig. 2. Typical Voltage and Current Pulses.

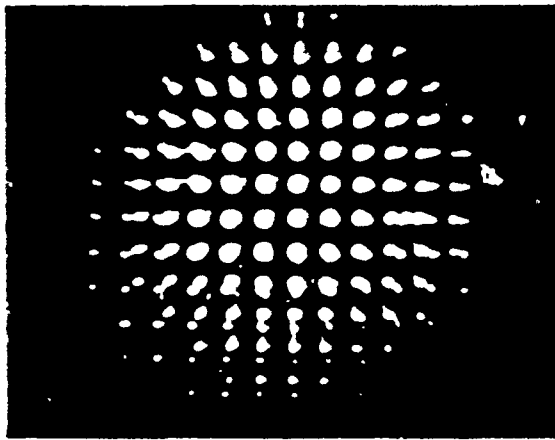


Fig. 3. Scintillator Image Corresponding to a 1460 Å Beam Collimated Down to 540 Å, at 1 MV. The emittance is 68 nr-cm.

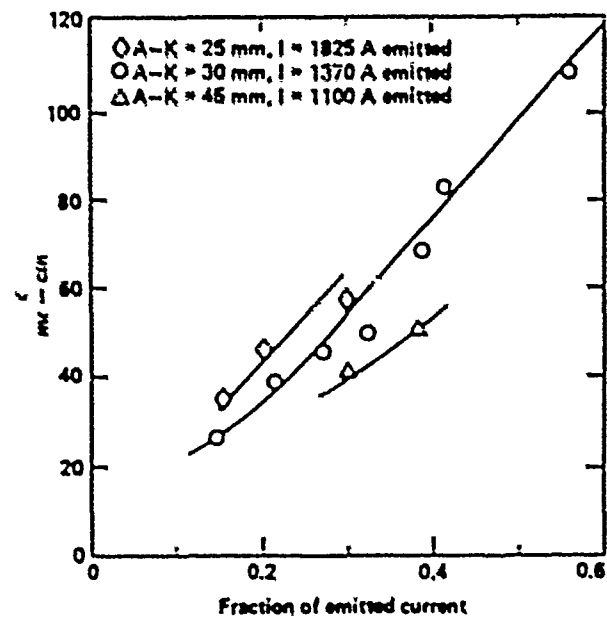


Fig. 4. Emittance vs. Collimation Ratio. Diode C1-A1 at 0.92-1.05 MV. The Parameter is the Diode Spacing.

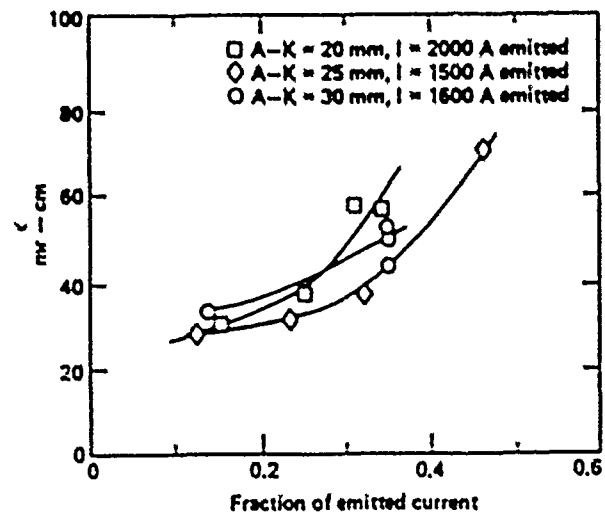


Fig. 5. Emittance vs. Collimation Ratio. Diode C1-A2 at 0.92-1.05 MV. The Parameter is the Diode Spacing.



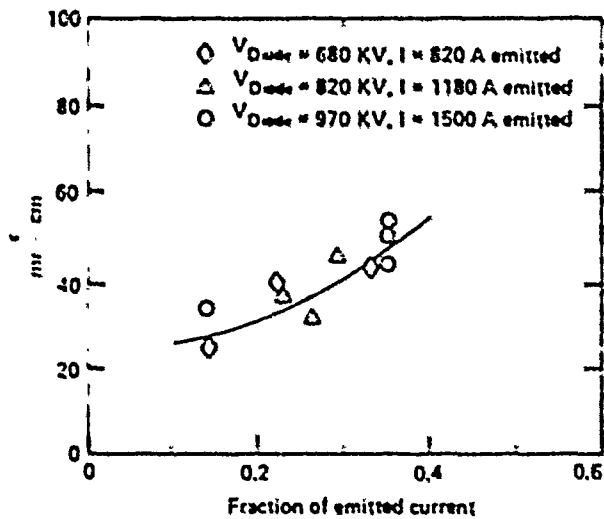


Fig. 6. Emissance vs. Collimation Ratio. Diode Cl-A3,  $\lambda - K = 30 \text{ mm}$ . The Parameter is the Diode Voltage.

\* "Work performed under the auspices of the U.S. Department of Energy by the Lawrence Livermore Laboratory under contract number W-7405-ENG-48."

#### NOTICE

"This report was prepared as an account of work sponsored by the United States Government. Neither the United States nor the United States Department of Energy, nor any of their employees, nor any of their contractors, subcontractors, or their employees, makes any warranty, express or implied, or assumes any legal liability or responsibility for the accuracy, completeness or usefulness of any information, apparatus, product or process disclosed, or represents that its use would not infringe privately-owned rights."

## ON THE DEVELOPMENT OF A REPETITIVELY PULSED ELECTRON BEAM SYSTEM

Gary A. Tripoli

Ion Physics Company  
Burlington, MassachusettsAbstract

A pulsed electron beam system -- PEBS-III -- has been developed at Ion Physics Company to generate an electron beam of 200 keV,  $4 \text{ A/cm}^2$ , 2.5 cm X 75 cm, 1.3  $\mu\text{sec}$ , at high repetition rates. That system incorporates a gas-insulated PFN Marx generator in Guillemin C network configuration to drive a cold-cathode electron gun. System performance corresponded to computer simulation of VI waveforms versus generator-parameter and impedance-collapse variations. The effort demonstrated the usability of a PFN for energization of long-pulse repetitively pulsed electron guns.

Introduction

With ever increasing power levels in electron beam technology, there is need for increased efficiency in energy transfer through the various associated pulse power subsystems. Design considerations for a repetitively pulsed electron gun are such that nominally rectangular electron beam "voltage-current pulses are therefore required. A system which generates such a pulsed electron beam - PEBS-III - shown in Figure 1 is described with regard to its theoretical design and actual operating parameters.

Theoretical Design

For purposes of generating a nominally rectangular electron beam current pulse, the PEBS-III pulse

generator was designed as a two-section Guillemin C pulse forming network (PFN). Figure 2a shows the basic network in which  $L_1$  and  $C_1$  are normalized capacitors and inductors, the actual values of which are determined by multiplying the  $L_1$  by  $Z\tau$  and the  $C_1$  by  $\tau/Z$ , where  $\tau$  is pulsewidth and  $Z$  is load impedance. Discharge of initially charged  $C_1$  through  $L_1$  into  $Z$  produces a parabolic rise and decay voltage pulse across  $Z$  as shown in Figure 2b.

By separating the  $C_1$  and  $L_1$  into a series of  $n$  capacitors and  $n$  inductors each with value  $nC_1$  and  $L_1/n$  respectively, the 2-section Guillemin C network takes the form of two parallel inductive  $n$ -stage Marx generators. Utilization of common interstage switches between the two sections assures simultaneous erection of the two Marxes. A schematic of the PFN Marx, less triggering circuitry, is shown in Figure 3.

Because actual generator capacitor and inductor values are dependent on load impedance as well as pulsewidth, a model was developed for the electron gun which constitutes the  $Z$  of the PFN.

A cold cathode electron gun with space charge limited flow is characterized by the relation:

$$j = kV^{3/2}(d-ut)^{-2},$$

where  $j$  = current density ( $\text{A/cm}^2$ ),  $V$  = gun voltage

(V),  $d = AK \text{ gap(cm)}$ ,  $u = \text{plasma propagation velocity(cm/sec)}$ ,  $t = \text{time(sec)}$  and  $k = 2.335 \times 10^{-6}$ . With consideration of required electron energy and current density, there follows the value,  $d$ , of the AK gap. An estimate of beam spread of  $1.5 d$  to  $2 d$  within the diode along with beam length requirements gives effective beam area. In such way total gun current with known gun voltage leads to gun impedance.

An initial approximation, then, for the PEBS-III gun impedance was  $Z = 56.3(1 - 2.7 \times 10^5 t)^2$ . A computer circuit analysis program, ITRAC, used to evaluate  $V$  and  $I$  waveforms for generator parameters of  $L_1 = 17 \mu\text{H}$ ,  $L_2 = 18 \mu\text{H}$ ,  $C_1 = 8.5 \text{ nF}$ ,  $C_2 = .9 \text{ nF}$ , and  $Z$  as above produced simulations shown in Figure 4.

#### Pulse Generator

The PEBS-III pulse generator comprises two parallel ten-stage inductive Marx generators in Guillemin C configuration with common triggered spark gaps as shown in Figure 1. All components including generator capacitors, generator inductors, charging inductors, spark gaps, and associated trigger circuitry are gas insulated by common location within the main pressure vessel. As shown, access to components is afforded by their positioning atop a support platform which is cantilevered from the main pressure vessel endplate.

Generator capacitors and inductors were designed so as to permit matching the PFN to the time varying electron gun impedance. Specifically, the second section capacitors were of multisection construction to allow  $\sim 20\%$  variation for risetime considerations. The generator inductors were of multiturn expandable/compressible construction to allow  $\sim 50\%$  variation for pulsewidth considerations.

Interstage charging of the PFN Marx capacitor banks is by means of charging inductors so as to

virtually eliminate the power loss associated with resistive charging. Ordinary magnet wire was wound on an acrylic cylindrical support to form each charging inductor.

Triggered mid-plane spark gaps comprising elkonite and brass electrodes were incorporated as interstage switches. Positioning of these switches within the main pressure vessel presented each switch with a large volume of gaseous dielectric, afforded UV illumination among gaps, and provided easy access for adjustment purposes. During sustained PEBS-III operation into a dummy load these ten switches each passed  $> 5 \text{ mC}$  per pulse at 55 kV, 5 kA peak, 1.3  $\mu\text{sec}$ , 20 pps.

#### Electron Gun

The PEBS-III electron beam output of  $4 \text{ A/cm}^2$  over  $2.5 \text{ cm} \times 75 \text{ cm}$  was generated by an electron gun with cathode comprising three 12  $\mu\text{m}$  thick tantalum foil blades positioned on a stainless steel focus electrode and blade support structure. A customer-supplied stainless steel water-cooled hibachi supported a 50  $\mu\text{m}$  thick aluminum anode foil.

#### System Performance and Conclusions

Overall system performance is illustrated in Figure 5 which shows a gun current pulse compared with a dummy load current pulse. Close agreement between the two actual waveforms as well as the computer generated waveform can be seen. Beam current and gun (shank) current with and without focus electrode are illustrated in Figure 6. As shown, the focus electrode increases beam current, reduces gun current, and increases gun impedance as expected.

Development of the PEBS-III has demonstrated the effectiveness of incorporating pulse forming networks for energization of repetitively pulsed electron guns. Such utilization serves to improve efficiency as required by large scale systems.

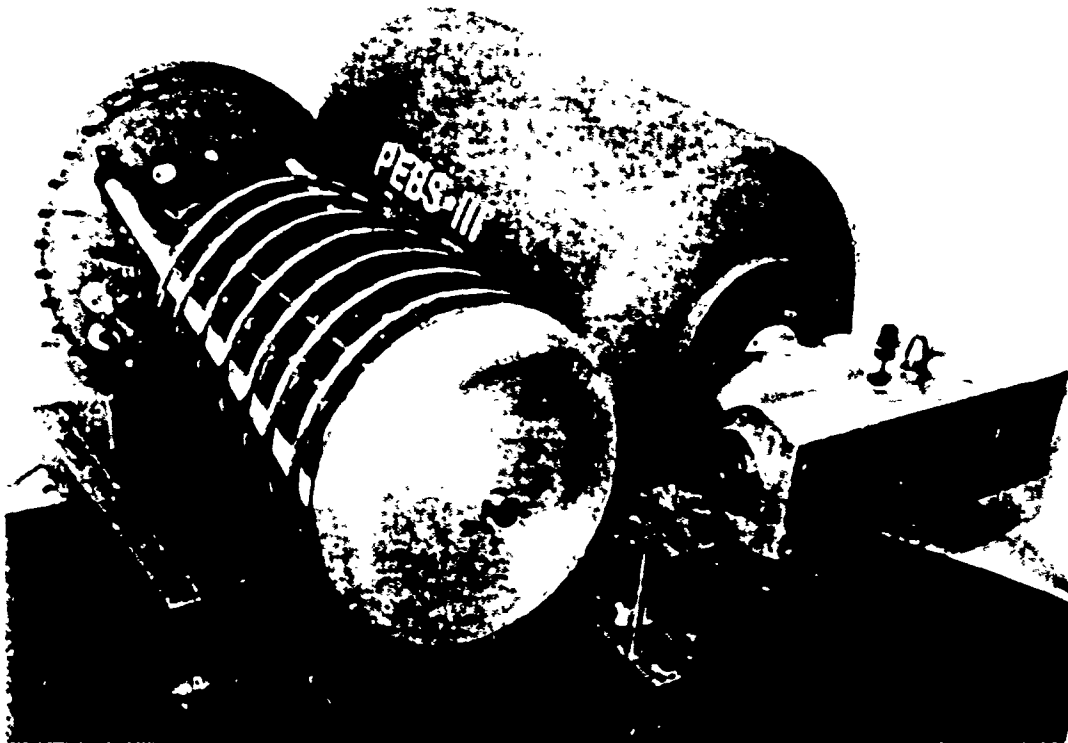


Figure 1. PEBS-III PULSED ELECTRON BEAM SYSTEM

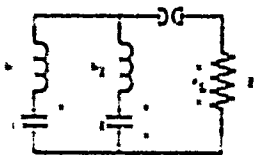


Figure 2a.  
Guillemin C Network

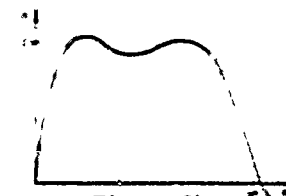


Figure 2b.  
Output Voltage Waveform

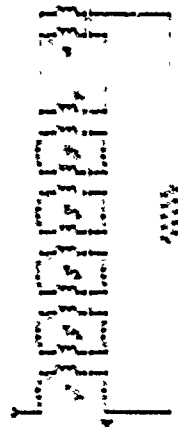


Figure 3.  
PFN Marx Network

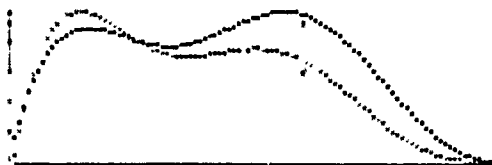
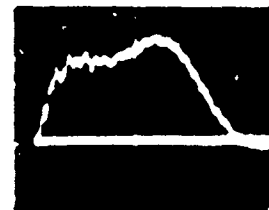


Figure 4. Computer Simulation with  
Time-Varying Load



Dummy Load



Electron Gun

Figure 5. Shank Current Traces  
5kA/div, 1μsec/div



Shank Current  
5kA/div, .5μsec/div



Beam Current  
.5kA/div, .5μsec/div



Figure 6. Effect of Focus Electrode

## DEVELOPMENT OF HIGH REPETITION-RATE PULSED POWER GENERATORS

R. J. Sojka and G. K. Simcox

Physics International Company  
2700 Merced Street  
San Leandro, California 94577

Abstract

The design and development of high repetition-rate, ( $>1$  kHz) pulsed power generators are discussed and a set of chosen design approaches presented. The ensuing technical approaches for the pulse forming network, PFN switching, and PFN charging modulators are described. Key elements of the system are the deionized-water, fast-energy store, and a flowing air spark gap switch, both capable of operation at higher than a 1 kHz repetition frequency. Based on this design and development effort, the technical issues of high repetition rate pulsed power systems are discussed, and recommendations are offered for further study and development of dielectrics, spark gap switches, and high power modulators.

Introduction

In recent years, Physics International (PI) has invested in the study and development of repetitively pulsed power systems. Some emphasis has been given to the generation of short, nanosecond regime pulses into low-impedance loads at repetition rates in excess of 1 kHz.

The water-insulated pulse forming line and spark gap were used for the critical final energy store and switch. At the outset, there were very few data to support this choice, but there were reasons to expect that the outstanding characteristics of water as a dielectric and the spark gap as a switch in single pulse systems could be retained to an adequate extent for repetitive operation.

As a result of this choice, the immediate issues to consider were:

- The special treatments for water under repetitive stresses and the assignment of suitable design stresses
- The electrical and mechanical design of a spark gap switch for maximum repetitive operation and adequate life

For the entire system, there were many issues of great significance for high repetition rate operations:

- Prime power
- Pulse forming line charge control
- Capacitor and component life
- Trigger generators
- Heat transport
- High average power dummy load
- Gas and water flows

To develop the major switch and dielectric technologies, satisfactory solutions for all these issues, and more, had to be found.

This paper gives a short description of this work and treats the important topic of spark gap switch performance in more detail.

The Experimental Arrangement

A schematic of the switch test bed is shown in Figure 1. The pulse forming line had a Blumlein configuration with an output impedance of 2.0 ohms. This line is shown as two 12.3 nF capacitors, storing a total of 31 joules at 50 kV

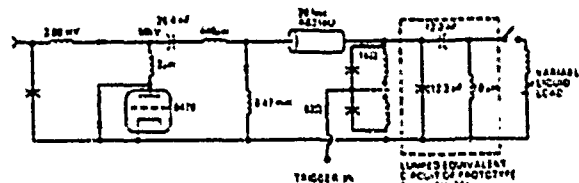


Figure 1 Electrical schematic switch and Blumlein PFL test circuit.

charge. The Blumlein was erected by the mid-plane spark gap switch under test. An output peaking spark gap switch of similar main electrode

geometry initiated the load discharge.

The pulse forming line was charged in 5-10  $\mu$ s periods by a simple modulator arrangement of a 25.4 nF capacitor and thyatron switch. This first energy store was resonantly charged from a dc power supply of about 50 kW capacity.

The test bed was equipped with diagnostic features to measure all the necessary voltages, currents, temperatures, pressures, and flows.

The computer model for this circuit and the predictions for load voltage, current, and energy as functions of time are shown in Figure 2.

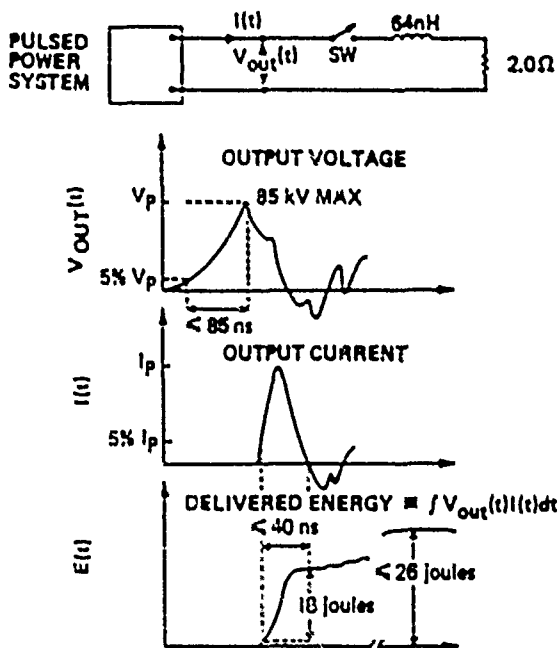


Figure 2 Circuit concept and waveforms for a 1 kHz pulsed power application.

#### General Comments on the Experiment

The test bed performed in accordance with the predictions at repetition rates up to and greater than 1 kHz for periods up to one hour. The time delay jitter of the load discharges could be stabilized at  $\pm 5$  ns, and the misfire rate during prolonged operations was insignificant.

For this successful operation, all the auxiliary functions and features of the test bed were required to operate with at least the reliability of the major PFL dielectric and switch

components. Some of the features necessary for success were: (1) the use of the thyatron's repetition and recovery characteristics in the main PFL charging circuits and the trigger generator; (2) the understanding and damping of voltage and current transients; and (3) the meticulous design and assembly of high-current-density contacts and joints.

In a system that can accumulate  $10^6$  shots in just over 15 minutes, certain key components must be rated more conservatively than usual for single-shot pulsed power designs. Figure 3 illustrates the physical differences between near-comparable capacitors for repetitive ( $10^8$ ) and single shot ( $10^4$ ) duties.

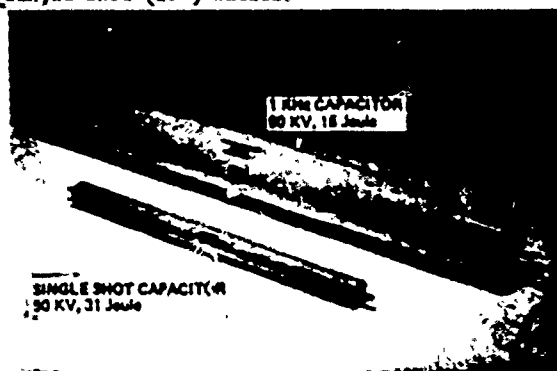


Figure 3 Repetitive and single shot capacitors.

#### Dielectric Strength of Deionized Water

Although it was not the primary aim of this work to study the breakdown strength of water as a function of frequency, some reasonable estimate was required up to 1 kHz. Therefore, as part of the charging modulator development, a water test cell was fabricated and coupled to the modulator output. For an electrode area of about 6 cm<sup>2</sup>, an effective stress time  $> 10$   $\mu$ s and with flowing water of  $\sim 10$  M $\Omega$ -cm resistivity, the breakdown strength at 1 kHz was found to be  $< 100$  kV/cm. The test cell could be operated for 5-10 minute periods without breakdown at stresses below 85 kV/cm peak.

Subsequent experience with the pulse forming line, which was designed for peak stresses of

80-85 kV/cm, confirmed this stress level to be reasonable for areas of  $10^3 \text{ cm}^2$ , provided that the water flow was symmetrical within the line structure. In addition, it was found that moderate pressure of a few atmospheres greatly enhanced the long-term reliability.

#### Performance of the Spark Gap Switch

The spark gap switch that was tested utilized vortex gas flow to provide adequate switch recovery and cooling. In this switching concept, tangentially injected air sweeps the sides of the insulators as it spirals into the spark chamber from which it exhausts through the main electrodes. The exhaust ports in the main electrodes are flared open to minimize flow impedance and aid in gas cooling. The vortex flow prevents the hot gases and spark discharge debris from coming in contact with the insulator, typically fabricated of acrylic plastic. This concept is also advantageous for switch recovery and high repetition rate operation since the debris exhausts into a field-free region (i.e., into the center ports of the main electrodes). Turbulent flow is also needed in the switch to aid in gas heat transfer during the spark discharges. For these reasons, the vortex-flow spark gap is believed to be ideally suited for high repetition rate operation.

Electrically, this switch design consists of two electrodes separated by a 1/2-inch-thick mid-plane trigger electrode. An ultraviolet illuminator is incorporated into the trigger electrode to ensure low-jitter switch operation. The electrode tips and the illuminator pin are fabricated with K-25, a copper-infiltrated tungsten alloy consisting of 75% tungsten and 25% copper by weight. The electrode tips are also contoured to avoid electric field enhancement and to promote uniform arcing and erosion over the electrode surfaces. A fabricated switch of this type is shown in Figure 4.

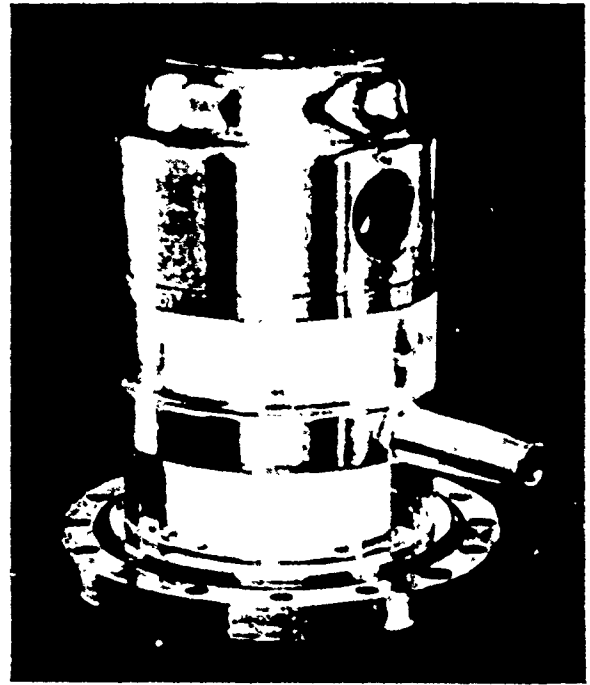


Figure 4 Fabricated spark gap switch.

This switch was tested at 1 kHz in the Blumlein PFL circuit previously mentioned. The switch performance was evaluated in terms of the PFL gain defined as

$$\text{Gain} = \frac{\text{PFL Peak Output Voltage}}{\text{PFL Charge Voltage}}$$

The current pulses in the switch were typically 22 kA peak with a half-sine duration of 100 ns. Figure 5 shows the switch performance for 50 kV

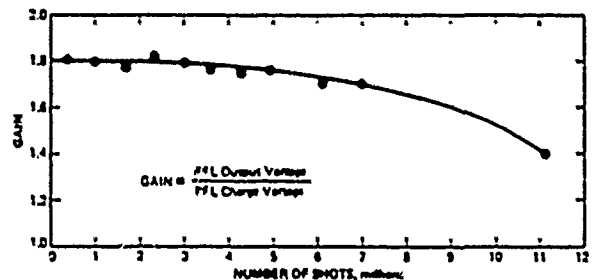


Figure 5 Switch performance.

operation at 1 kHz. Note that the PFL gain decreases rapidly after 7 million shots. This behavior is attributed both to electrode erosion and spark gap resistive phase losses. Various

empirical laws have been used to characterize the resistive phase or the time-varying impedance of spark gaps<sup>1-3</sup>. In general, these experimental investigations agree that the resistive phase losses are inversely proportional to  $E^n$ , where  $E$  is the electric field stress of the spark gap and  $n$  is an empirical constant varying between 1.0 and 2.0. As erosion occurs in the spark gap, the interelectrode spacing increases, and the operating field strength of the gap is decreased. For these conditions, the resistive phase losses will increase and reduce the PFL gain or output voltage of the generator. This behavior was also verified by the air heating in the spark gap switch. For example, at the start of testing, 7 joules per pulse were dissipated in the switch, while after 11 million shots, 10 joules per pulse were dissipated. This amount of energy represents 20-30% of the stored PFL energy for this generator. Improvement of the generator's efficiency is believed possible by optimizing the spark gap switch design. The following measures can be taken: (1) reduction of electrode gap spacings; (2) choice of proper electrode materials; and (3) better understanding of the resistive phases of various gases.

#### Overall Pulsed Power Generator Performance

The performance of the pulsed power generator was examined in terms of the energy delivered to a 63 nH, 2  $\Omega$  load consisting of a 2  $\Omega$ , water-cooled, potassium-chloride-solution resistor in series with a two-electrode, vortex-flow spark gap. The PFL output voltage and total load current waveforms were monitored with a fast-response ( $\approx 3$  ns), resistive divider and Rogowski current monitor, respectively. The waveforms were digitized on a computer, and the energy delivered to the load was determined. Within the  $\pm 5\%$  accuracy of the measurements, the following performance was achieved by the generator:

• Output voltage	60-85 kV
• Voltage Rise-time (5% to peak)	$< 83$ ns
• Fast Pulse Energy	18 joules
• Duration of Fast Energy	42 ns

• Total Pulse Energy	26 joules
• Delay Time Jitter	$< \pm 5$ ns (peak to peak)
Pulse Repetition Rate	1 kHz (continuous)

#### Conclusion

In general, the transfer of former single-shot, pulsed power technology to repetitive operation requires the inclusion of many new techniques, including those of microsecond modulator technology.

A completely new data base is required for dielectrics, enlarging upon the excellent work of AMRE, Aldermaston<sup>4</sup>. It is unlikely that the conservative stresses of the power industry can be adopted, but the literature in this area is extensive and may be used as a guide to obtaining acceptable dielectric performance in pulsed stress repetition.

The excellent potentials for the spark gap switch have been demonstrated. This switch has outstanding characteristics for fast pulse forming line applications provided that the design is specifically for this purpose. In some applications, the provision of adequate life will depend upon more elaborate mechanical design than has previously been necessary.

#### REFERENCES

1. T. P. Sorensen and V. M. Ristic, "Risetime and Time-Dependent Spark-Gap Resistance in Nitrogen and Helium," *J. Appl. Phys.*, **48**, 114-117 (1977).
2. R. C. O'Rourke, "Investigation of the Resistive Phase in High Power Gas Switching," Research and Development Report, Science Applications, Inc., La Jolla, Calif.
3. K. Cary, Jr. and J. A. Mazze, "Time-Resolved Resistance During Spark Gap Breakdown," Thirteenth Pulsed Power Modulator Symposium, *IEEE Conf. Rec.*, pp. 167-172, June 20, 1978.
4. J. C. Martin, et al., Dielectric Strength Notes, 1-16, AMRE, Aldermaston, England, November, 1965 - June, 1970.



# FROZEN-WAVE HERTZIAN GENERATORS: THEORY AND APPLICATIONS

Marie L. Forcier<sup>+</sup>, Millard F. Rose,  
Larry F. Rinehart and Ronald J. Gripshover

Naval Surface Weapons Center  
Dahlgren, Virginia 22446

## Abstract

"Frozen Wave" Hertzian generators have been built which can produce multikilowatt RF pulses in the megahertz frequency range with repetition rates of 10's of kilohertz. These generators do not have a damped sinusoidal output; they generate a discrete, controllable number of rectangular half cycles. The output waveform can be discretely changed from one half-cycle to the next. At the higher frequencies, discontinuities in the switch and dispersion in the cables round the edges of the rectangular half cycles, causing the output waveform to be nearly sinusoidal. These generators have also been used as video pulsers with variable pulse duration and interpulse spacing. Frequency, power and pulse width limitations will be discussed.

## Introduction

In recent years there has been an increased interest in Hertzian generators as a means of generating extreme RF power levels. Most of these devices (e.g. L-C oscillators) produce an RF envelope whose amplitude function is a decaying sinusoid, limited in time by internal damping as well as dissipation in an external load. They cannot generate a short RF pulse with a rectangular envelope as is frequently desired in very short-range radars and some communication requirements.

This paper describes the design and implementation of a distributed parameter "frozen wave generator" (FWG) which can be used as an RF source and as a video pulser with variable pulse duration and interpulse spacing. The first part of the paper will

consider FWG's as high repetition rate, short pulse length RF generators; the last part will describe FWG's as video pulse generators with variable pulse duration and interpulse spacing. All of the generators considered here are constructed from standard 50 ohm coaxial cable. However, any transmission line (e.g. stripline) which can be adequately matched to the switch and load could be used.

## FWG As An RF Source

To understand how the FWG operates consider an early multiple-switch version of the generator (Fig. 1a). In this device, energy from a power supply is statically stored in alternately charged sections of the transmission line. When the FWG is used as an RF source, there are an even number of cable sections, all  $\lambda/2$  in length (for the operational frequency of the device). A two cycle device is illustrated here. If the static potential on the outer conductors is plotted as a function of distance (d) along the cable, one obtains the static spatial potential distribution shown in Figure 1b. A two-cycle square wave pulse is "frozen" in the cable. The charging resistors  $R_c$  serve to isolate the power supply from the FWG, thereby protecting the power supply when the switches close. If the switches are assumed to be perfect and are closed simultaneously, a series of traveling waves is initiated in the cable sections which allows the previously frozen wave train to move through and dissipate in the load. Two traveling waves traveling in opposite directions are initiated at each switch. However, the effect of all of these waves is that two replicas of the initial frozen wave move in opposite directions toward the load.

<sup>+</sup> Work performed as part of NSWC Graduate Cooperative Program (Univ. of Virginia).

If the load is matched to the generator ( $R_L = 2 Z_0$ ),  $R_L$  effectively terminates the transmission lines and no reflections occur. Since the cables discharge into a matched impedance the potential at each side of the generator is one-half the charging potential of each cable. In this case the voltage-time waveform generated across the load is exactly analogous to the spatial waveform shown in Figure 1b. The potential on one side of the load becomes  $(+ V_0/4)$  while the other side becomes  $(- V_0/4)$ ; hence, the potential difference across the load is  $V_0/2$ . After half a period the potentials at each end of the load reverse, again developing a potential difference of  $V_0/2$  but now with the opposite polarity. The time for each half cycle (half period) is  $\lambda/2v_p$ , where  $\lambda/2$  is the length of the cable section and  $v_p$  is the propagation velocity in the cable.

If  $R_L$  does not terminate the generator transmission lines, reflections will occur at the load. These reflections will complicate the waveform across the load especially in late time. Under certain special conditions part of the load can be mismatched to obtain longer waveforms. This case will be treated in the latter half of this paper.

The multiplicity of switches needed to operate a generator in this configuration necessitates precision triggering with a switch jitter that is much less than a period of the frequencies of interest. This restriction would keep the FWG a laboratory curiosity if it were not possible to replace the multiplicity of switches with a single switch. In Figure 1a note that the ends of each cable section are at the same potential. This permits one to fold the cable sections into half loops about a single switch as shown schematically in Figure 2. The center conductor is still continuous throughout the cable sections with the load across its ends. In this configuration the static or frozen wave is stored in the cable sections just as in Figure 1a. When the switch is closed, replicas of the frozen wave again effectively travel in both directions to the load. As shown in Figure 2, the FWG is a continuous length of the cable with a discontinuity in the

outer conductor every half wavelength (i.e. the switch does not maintain the 50- $\Omega$  geometry). As more  $\lambda/2$  cable sections are added to the generator, the later cycles in the RF pulse must travel through the switch more times, causing the waveform to degrade progressively.

Attempts have been made to solve this problem by minimizing the discontinuity associated with the spark gap switch. At the present time, only about 1 cm of unshielded cable length is necessary to insert the switch.

Ideally, the addition of more cable sections to the FWG circuit should correspondingly produce more RF cycles. However, because of the discontinuity of the cable impedance at the switch, it is difficult to generate more than two or three cycles with an acceptable waveform at the hundreds-of-megahertz frequencies. Four to eight cycles are practical at tens-of-megahertz frequencies.

The repetition rate of these generators is limited chiefly by the spark-gap switch's turn-off time; the switch must open before recharging for the next pulse can begin. Dielectric gas species have been important factors in the development of the spark gap switches. A number of empirical experiments have led to a gas mixture which is 95-percent argon and 5-percent hydrogen. This mixture exhibits the fast spark-quenching characteristics of argon which are necessary for high PRF and the high-voltage standoff capability which is characteristic of hydrogen. Another advantage of this mixture is that it generates very few decomposition products in the gap.

Table 1 shows the general performance characteristics of some of the FWG's built at NAVSWC. The numbers represent levels at which the devices can perform at 10- to 20-min. intervals. Higher performance may be obtained for shorter times.

Table 1.

Device	Peak Power (kW)
2 cycle ( $\sim 130$ MHz)	60
Dual 2 cycle ( $\sim 130$ MHz)	10
2 cycle ( 40 MHz)	1400
3 cycle ( 60 MHz)	1500
2 cycle ( $\sim 800$ MHz)	20

Characteristics of FWG built by NAVSWC/DL.

### FWG As A Variable Pulse Width Video Pulse Generator

A cursory examination of the FWG schematically illustrated in Figures 1 and 2 may lead one to believe that waveforms with consecutive half cycles of different periods could be generated by merely using appropriate cable sections of unequal length. However, a closer examination indicates that this is impossible unless the frozen waveform is anti-symmetric about its center. Since the frozen wave effectively travels in both directions toward the load, any asymmetry would cause the voltage across the load to be different than that of the frozen wave since the potentials at the ends of the load would no longer invert their respective potentials at the same time (since the half periods are not equal).

To elucidate this problem further, consider a FWG with two cables of unequal lengths  $l_1$  and  $l_2$ . The static potential distribution or frozen wave of this arrangement is illustrated in Figure 3a. The temporal potential on one side of the load would be given by the waveform in Figure 3a. (Again the potential is halved because the cables are discharging into a matched load. The values for the temporal waveform are given in parenthesis.) The potential on the other side however would be the time inverse of Figure 3a given in Figure 3b. The potential across the load would therefore be the difference between the Figure 3a and 3b waveforms, i.e. Figure 3c. For the time corresponding to the half period of the short cable the output waveform is what would be expected; however, after this time gross distortions in the output wave compared to the frozen wave occur. A half period corresponding to the longer cable never occurs.

To overcome this problem the configuration of the FWG must be changed to permit an unbalanced output. Figure 4a illustrates one way to accomplish this. For simplicity a two cable generator is considered. The cables are again of unequal lengths  $l_1$  and  $l_2$ . The output of the FWG has been divided into  $R_L$  and  $R_T$ . Usually  $R_L$  is the load and  $R_T$  a terminating resistor. If  $R_L$  and  $R_T$  both equal the surge impedance ( $Z_0$ ) of the transmission lines no reflections will occur at the load. However, the wave

statically frozen in the generator is much different than in the previous configuration. Cable  $l_2$  in Figure 4a has no potential difference between its inner and outer conductors, while cable  $l_1$  has the entire potential  $V_0$  across its inner and outer conductors. If one starts at  $R_L$  and travels clockwise around the FWG cables, the static spatial potential distribution is given by Figure 4b.

The output waveform across  $R_L$ , a video pulse ( $V_0/2$ ) high and  $(l_1/v_p)$  long, is illustrated in Figure 4c. This corresponds to only half of the energy stored in the FWG; the other half is dissipated in  $R_T$ . The waveform in  $R_T$  is shown in Figure 4d. From the Figures 4c and 4d one observes that cable  $l_2$  acts merely as a delay cable for the pulse which is stored in cable  $l_1$ .

Consider now the case in which  $R_T \gg Z_0$  such that the FWG can still charge properly, but where  $R_T$  looks like an open circuit to a pulse traveling in cable  $l_2$ . Then the pulse generated in  $l_1$  and traveling through  $l_2$  will be reflected in phase at  $R_T$ . This reflected wave will then travel through  $l_2$  and  $l_1$  and be absorbed in  $R_L$ . The output waveform in  $R_L$  will then be as shown in Figure 5a. The number of pulses have doubled and theoretically all of the energy stored in the FWG is dissipated in  $R_L$ .

Consider next the case in which  $R_T \ll Z_0$ ;  $R_T$  then looks like a short circuit to a pulse traveling in cable  $l_2$ . The pulse traveling in  $l_2$  will then be inverted and reflected at  $R_T$ . The output waveform will be as shown in Figure 5b. Once again the number of pulses have doubled and theoretically all of the energy stored in the FWG is dissipated in  $R_L$ .

By using different cable lengths for cables  $l_1$  and  $l_2$  pulses of various pulse widths and pulse spacing can be obtained. By adding more cables more pulses can be obtained. The only constraint is that the later pulses must travel through the switch discontinuity more times, and they are thereby degraded.

To verify that these waveforms could be obtained, several low power ( $V_0 = 9$  volts) FWG's were constructed. A mercury wetted reed switch was used to switch these FWG's instead of spark gap switches. A generator which has the same basic configuration

as Figure 5a will now be described in more detail.

A six segment (3 cables charged and 3 delay lines) FWG was constructed. Starting at the load end ( $R_L$ ) of the generator the cable section half periods were, respectively: 50ns, 40ns, 30ns, 20ns, 10ns, and 5ns.  $R_L$  was chosen such that  $R_L \gg Z_0$ . Figure 6a is the output current waveform in  $R_L$ . As expected there is a 50-ns pulse followed respectively by a 40-ns delay, a 30-ns pulse, a 20-ns delay, a 20-ns pulse, and a 5-ns delay. The pulse then reflected by  $R_L$  follows in inverse time with the same polarity: 5-ns delay; 10-ns pulse, 20-ns delay, 30-ns pulse, 40-ns delay and 50-ns pulse. For this waveform one can also observe that the shorter pulse lengths (higher frequencies) and later pulses suffer the most degradation.

Additionally, if the terminating resistor  $R_L$  is made equal to  $Z_0$ , it will have the current waveform shown in Figure 6b. Since the 5-ns uncharged cable section is nearest  $R_L$ , the waveform will be: a 5-ns delay, 10-ns pulse, 20-ns delay, 30-ns pulse, 40-ns delay, and 50-ns pulse. This is the end of the waveform since  $R_L$  terminates the other side of the FWG; hence, there is no reflected pulse.

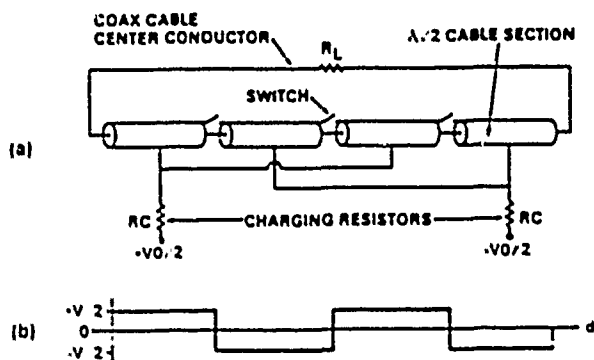


Fig. 1. Multiple Switch Frozen Wave Generator

- a) Schematically
- b) Static Spatial Potential Distribution in the Generator

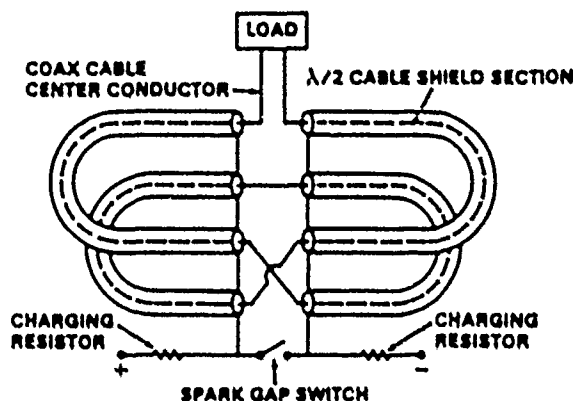


Fig. 2. Single Switch, Two Cycle FWG.

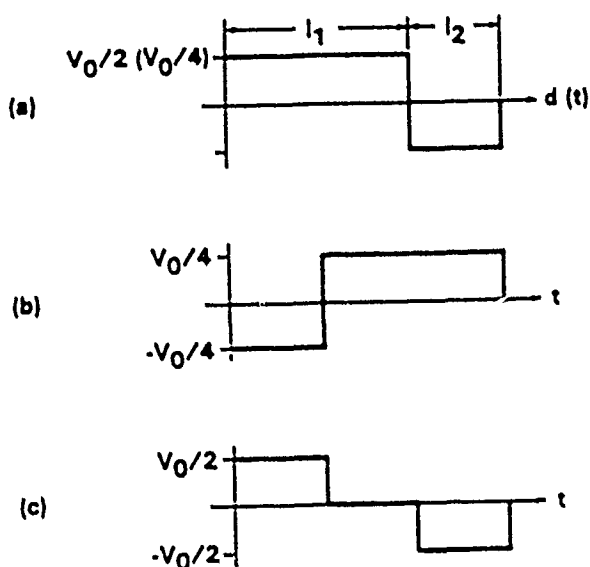


Fig. 3. (a) Static Spatial Potential Distribution for Unequal Length cables (temporal potential waveform on one side of the load is given in parenthesis)  
 (b) Time Inverse of 3a (this is the temporal potential distribution for the other side of the load)  
 (c) The Potential Difference across the Load (3b subtracted from 3a).

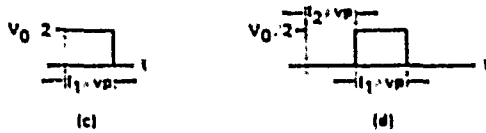
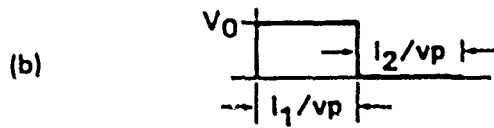
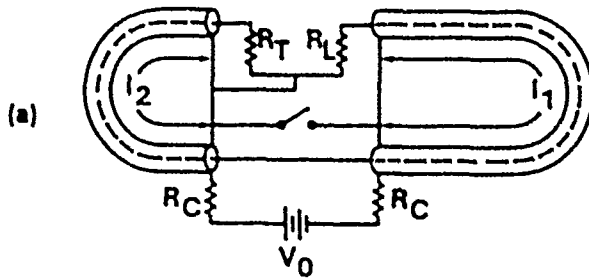


Fig. 4. Video Pulse

- (a) Schematically
- (b) Static Spatial Potential Distribution
- (c) Temporal Voltage Waveform across  $R_L$
- (d) Temporal Voltage Waveform across  $R_T$

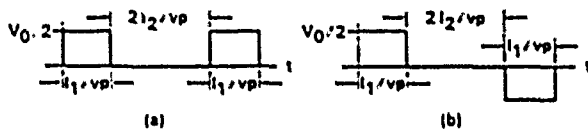


Fig. 5. (a) Voltage Waveform across  $R_L$  for  $R_T \gg Z_0$   
 (b) Voltage Waveform across  $R_L$  for  $R_T \ll Z_0$

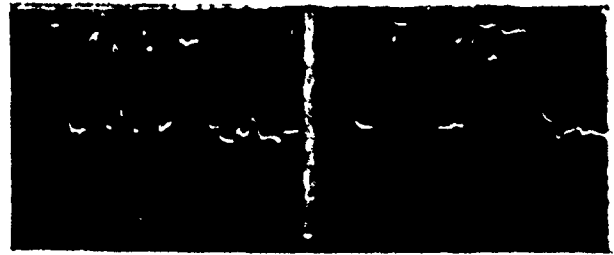


Fig. 6. Current Waveforms for a Six Element Video Pulse FWC

- (a) Current Waveform in  $R_L$  for  $R_T \gg Z_0$  (50 nS/div)
- (b) Current Waveform in  $R_T$  for  $R_L = Z_0$  (20 nS/div)

Sponsored by Advanced Research Projects Agency through the Naval Air Systems Command.

## INVITED

## A 500 kV REP-RATE MARX GENERATOR

J. SHANNON

Maxwell Laboratories, Inc.

3835 Balboa Avenue, San Diego, California 92123

Abstract

An efficient PFN/Marx generator was constructed for generating high average power electron beams. The generator consists of ten 100 kV PFN stages connected in a Marx configuration. The Marx generator employs purged gas switches. The nominal operating parameters are:

Voltage	500 kV
Current	10 kA
Pulse Duration	1 $\mu$ sec
Rep-Rate	to 100 Hz
Average Power	to 500 kW

This paper discusses the Marx charging power conditioning and the operation of the generator into resistive and electron beam loads.

Introduction

Electron beams have been used for some time in gas lasers either as a source of ionization or as the primary pumping mechanism. The extension of the gas laser technology to high average power requires the development of repetitively pulsed electron beams. In the direct pumped schemes, efficiency is of prime consideration. This limits the type of technology which can be used, especially at higher voltages and power. The work reported on in this paper is aimed at developing technology primarily for the direct pumped application.

Since a Marx generator is an inherently efficient circuit for generating high voltage, it is an attractive approach to high average power, high voltage systems. The availability of proven 100 kV rep-rate switch designs at the start of the

present program allowed the design to proceed with a minimum of switch development. By incorporating a pulse-forming network (PFN) into the Marx design, the system was made efficient with an output suitable to the electron beam load.

The goal of the program is to develop the technology for scaling to larger systems, both in the areas of the power supply and the electron beam loads. Toward this end, a 500 kV device is large enough to ensure that scaling can be demonstrated. In the present paper, the Marx generator and associated power conditioning will be primarily discussed.

Marx Generator Design Considerations

Initially, the Marx generator was used as a single-shot device in a cold cathode development program. Two circuits were considered in the design of the PFN/Marx generator; a Guillemin Type A voltage fed network (shown in Figure 1A) and a standard 5-section PFN as shown in Figure 1b. Both circuits have realistic values for components in terms of available capacitors and values of inductors.

After initial consideration, it was decided that the PFN/Marx approach was more suited to the present application. There were basically two reasons for this; first, calculations indicated that, for the present parameters, the PFN/Marx circuit would have a slightly faster risetime than a Guillemin Type A network with a single resonant circuit. The manufacture of several values of rep-rate capacitors for use in resonant circuits was considered impractical

with the then existing budget. Second, at the inception of this program, the impedance collapse in cold cathode guns was a major issue as concerns efficient energy transfer. In the PFN/Marx approach, it is more straightforward to taper the impedance profile of the transmission line to compensate for a collapsing impedance.

The output parameters of the generator were chosen to be:

Voltage	.5 MV
Current	10 kA
Pulse Length	~1 $\mu$ sec
Current Density	~10 A/cm <sup>2</sup>

These values give an impedance of 50 ohms for the generator. Because of the availability of 100 kV switches and rep-rate capacitors, a 10-stage Marx/PFN was decided upon.

A practical number of meshes in the PFNs is five. The PFN was made 10% longer in an attempt to get longer flat top on the pulse. Based on these considerations, the PFNs had the zero order design parameters of 5 ohms impedance and an electrical length of .55  $\mu$ sec.

A circuit diagram of the Marx generator is shown in Figure 2 and in outline in Figure 3. The switches and PFN stages are oil insulated and suspended by nylon straps in an oil enclosure. This design makes modifications such as changing the PFN inductors, relatively simple. After initial operation in the single-shot mode, the switches shown in Figure 3 were replaced by rep-rate switches and the gas purge lines installed.

To simplify the circuit, only the first two switches were triggered. The remaining eight gaps were two electrode switches and were closed by the erection wave in the Marx generator. To ensure reliable operation of the Marx generator, the stray capacitance to ground of the positive side of the third switch (the first two electrode gap) was enhanced by extending the ground plane between the second and third stage. This increases the over voltage of the first two electrode gap. For the Marx to erect reliably, it was necessary to install an auxiliary irradiating pin in each gap. Because

of the efficiency requirements, inductors are used to charge the PFN stages. The charging inductors must be large enough so that only a small fraction of the energy is lost during the pulse and small enough so that the Marx stages can be charged uniformly. For the 2500 nH values used here, only ~2% of the energy is lost in the inductors during the pulse and the 40 mH inductor in the intermediate store still dominates the charging.

#### Marx Charging Supply Design Considerations

It has been found that for reliable spark gap operation at rep-rate, a "grace" period is necessary before reapplying the voltage. Alternately the voltage can be reapplied so slowly that restriking will not occur. The fault mode that causes most concern is a spark gap "lock-on" where the primary supply is connected to the gap. This sometimes causes the arc to walk out of the gap and onto the insulator causing severe damage. Because of this concern, it was decided that the Marx charging should have two stages to decouple the Marx from the primary power supply.

The Marx charging circuit is shown in Figure 4. To initiate the sequence,  $S_1$  is closed and the intermediate capacitor is charged through diode  $D_1$ . After  $S_1$  has recovered,  $S_2$  is closed and the Marx is charged and fired at the peak of the charging waveform. The switches  $S_1$  and  $S_2$  are closed by superimposing a fast trigger pulse on the gap causing breakdown. It was found necessary here to have an auxiliary UV irradiator to make these gaps operate reliably.

The resistor  $R_1$  is used to control the voltage on  $C_2$ . This approach was adopted because of budgetary constraints and the desire to use proven power supply available at a somewhat higher voltage than necessary (manufactured by Electro Engineering Works). A variable voltage transformer in the primary of the supply would eliminate the need for such a large resistance. At this stage, overall efficiency is not an issue and it is more economical to throw away some power.

### Resistive Load Tests

The PFN/Marx generator was tested into a dummy load and into various types of cold cathode emitters. Typical output waveforms are shown in Figure 5 for single-shot operation into an electron beam load. For this case, the voltage risetime is  $\sim 1$   $\mu$ sec and the pulse width is  $\sim 9$   $\mu$ sec. The Marx has been tested at charge voltages from 50 kV to 100 kV and found to have an operating range a factor of approximately 2 in absolute pressure for a given voltage.

The usual operating point for the Marx is  $\sim 2/3$  of the selfbreak voltage.

A limited amount of testing under rep-rate conditions was done into a resistive load at the output of the Marx generator. The purpose of these tests was mainly to test out the various subsystems. The volume of the liquid load resistor limited the number of pulses per run to  $\sim 50$ . A typical output is shown in Figure 6 with a nominal 50 ohm load on the Marx. The Marx charging voltage and the output voltage are shown in the figure. The measured peak output voltage of 450 kV agrees well with half the open circuit voltage of 480 kV.

At the present operating parameters, the Marx generator has a one sigma jitter of  $\sim 30$  nsec. This can probably be improved by reducing the pressure, but no systematic study of this has been attempted.

### Electron Beam Tests

Experiments on various cold cathode emitters have been carried out. Typical output waveforms are shown in Figure 7. There are 50 and 100 consecutive shots in the 5 Hz and 20 Hz cases shown. The cathode in this case is a graphite felt cathode at a current density of  $\sim 10$  A/cm<sup>2</sup>. This cathode structure has been tested up to 50 Hz in short (5 sec) runs. The rep-rate is limited at present by outgassing in the diode and work is continuing in this area.

The output of the generator with an electron beam load is 500-600 kV and .10 kA. The nonlinear nature of the Child's law load tends to distort the pulse

somewhat, but the width (FWHM) of the power pulse is  $\sim 1$   $\mu$ sec which agrees with the calculated value.

For the waveforms shown in the figure, the calculated energy is 5.5 kJ per pulse compared to 5.9 kJ stored in the intermediate storage capacitor. This gives a Marx efficiency of  $>90\%$ , although the values are the same within the accuracy of the measurements. At 50 Hz operation, the average power is 275 kW into the electron beam.

### Switch Performance

There are four switch operating conditions in the system: two in the Marx charging supply and two in the Marx generator. All the switches use dry air and are fed by a gas blow-down system. Only a limited amount of work has been done to explore the operating range of the various switches and the gas flow is much more than adequate based on previous work.

The switches  $S_1$  and  $S_2$  in the Marx charging supply are identical to those described previously.<sup>1</sup> The same switch without the nested electrodes was used in the upper eight stages of the Marx generator ( $M_2$ ). Three electrode switches ( $M_1$ ) were used in the first two stages. All the switches except  $S_1$  had a grace period of  $>5$  msec before reapplication of the voltage. The recovery of  $S_1$  in Figure 4 was controlled by the diode. The operating parameters of the switches are shown in Table 1.

During the rep-rate operation consisting of  $\sim 10^4$  shots to date, no Marx prefires have been observed for the present operating conditions. A few prefires of switches  $S_1$  and  $S_2$  have occurred but were traceable to trigger generator malfunctions. The present operating values of the switches is adequate for reliable operation.

### Acknowledgement

The author would like to acknowledge the significant contributions by J. DeVoss to the design and construction of the major subsystems and by L. Houghton to the construction and operation of the facility. Acknowledgement must also be given to



R. Hunter, now of Western Research Corporation,  
under whose guidance this program was initiated.

Modulator Symposium, June 1975.

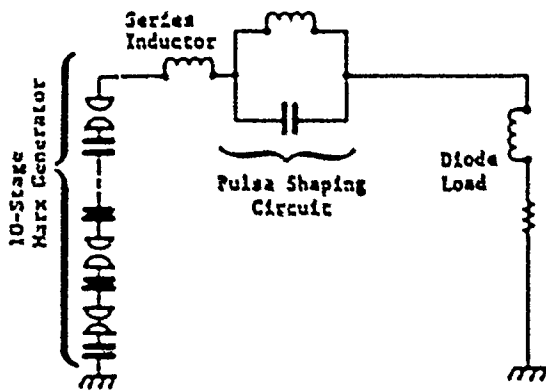
<sup>1</sup>A. Ramrus, "The Development of a 100 kV Multi-Megawatt Rep-Rate Gas Switch," 13th Pulse Power

This work was performed under Ballistic Missile  
Defense Systems Command Contract No.  
DASG 60-77-C-0058.

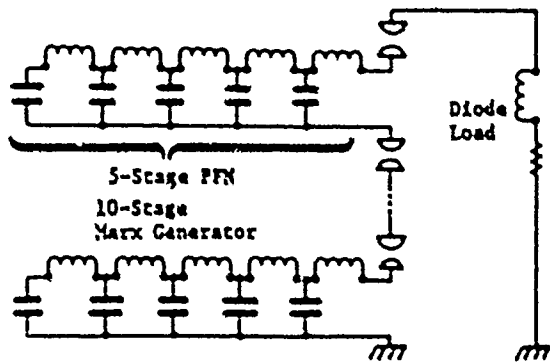
	VOLTAGE (KV)	CHARGE TRANSFER (C)	POWER AT 50 Hz (KW)	CHARGING TIME (μs)	GRACE PERIOD (μs)	PRESSURE (PSI)	FLOW SCFM
CHARGING SUPPLY S <sub>1</sub>	70	.12	300	DC	—	40	160
CHARGING SUPPLY S <sub>2</sub>	105	.12	300	4.5	> 5	65	225
MAX M <sub>1</sub> (G ELECTRODE)	~100	.011	27	.5	>10	45	110
MAX M <sub>2</sub> (Z ELECTRODE)	~100	.011	27	.5	>10	45	30

\*STANDARD CUBIC FEET PER MINUTE.

Table 1. Summary of Switch Operating Parameters.



(a) Guillemin Type A Voltage Fed Network



(b) PFN Marx Generator

Figure 1. Alternate Circuits for Electron Beam Driver.

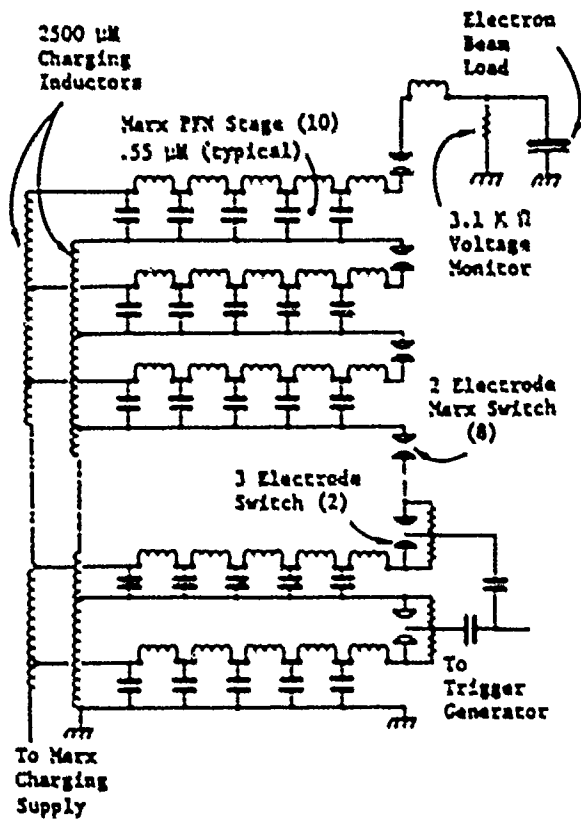


Figure 2. Equivalent Circuit of PFN/Marx Generator.

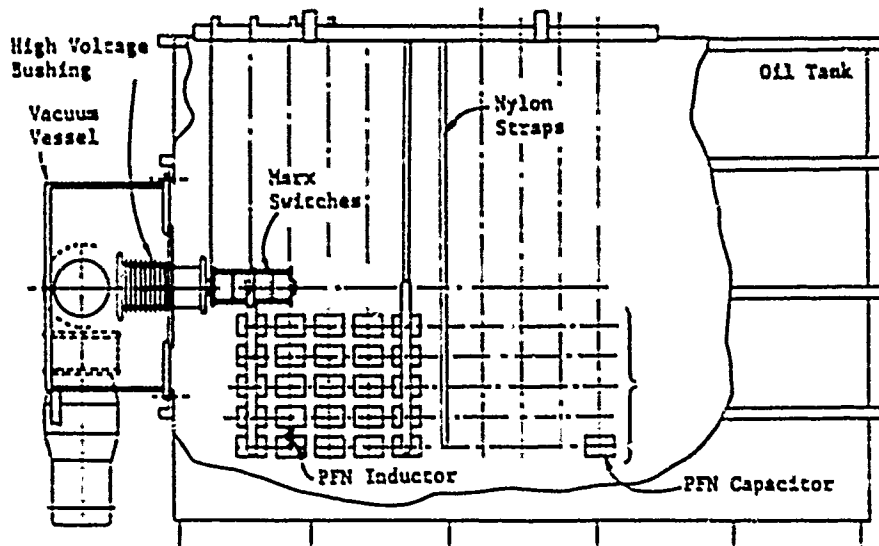


Figure 3. 500 kV Electron Beam Driver (Side View).

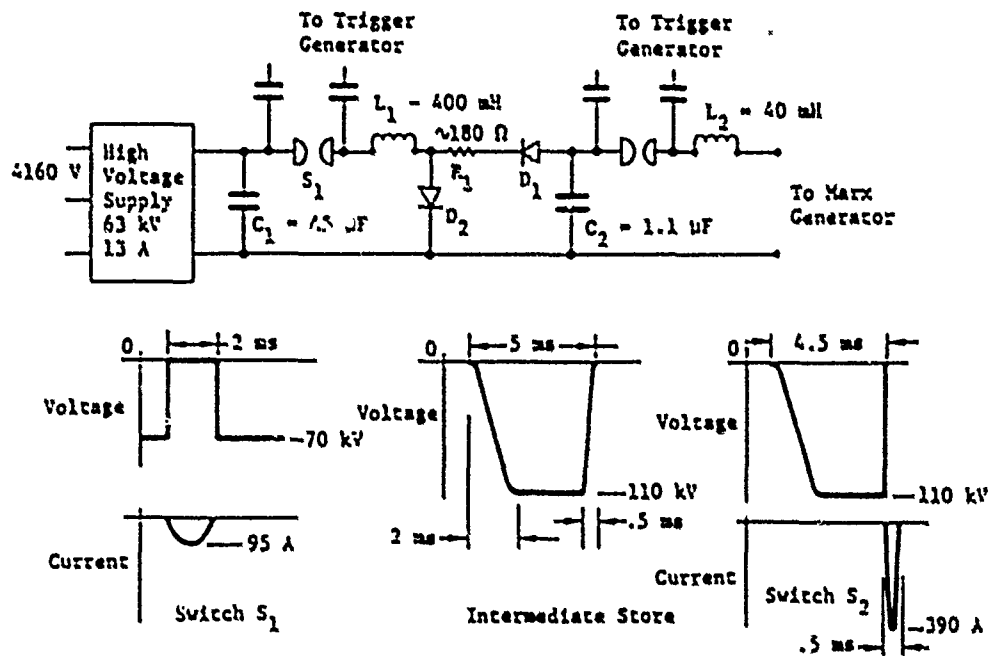


Figure 4. Marx Charging Power Supply

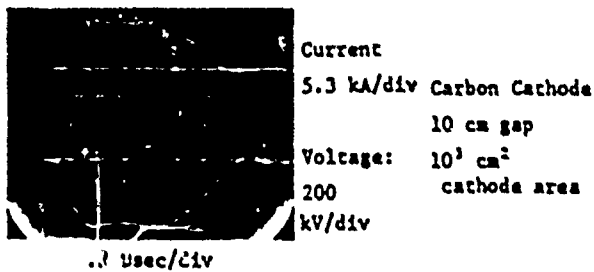
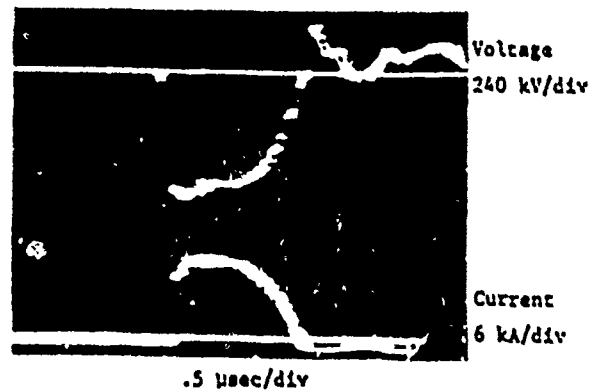


Figure 5. Typical Output Waveforms in Single-Shot Operation



(a) 5 Hz for 10 seconds

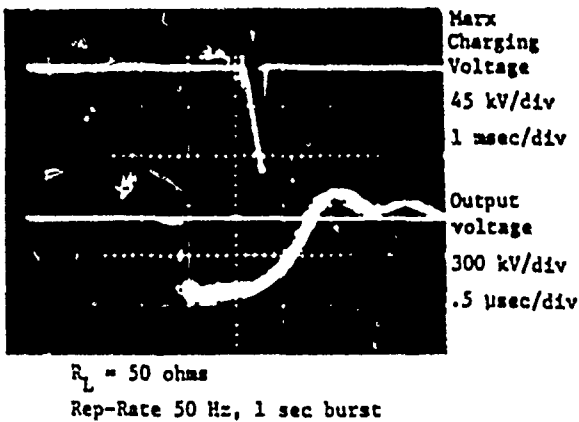
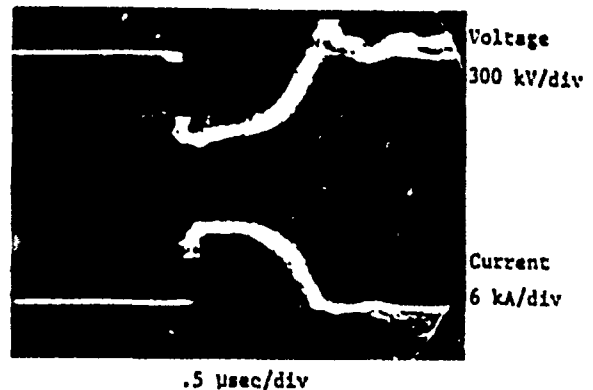


Figure 6. Rep-Rate: 50 Hz, 1 sec burst



(b) 20 Hz for 5 seconds

Figure 7. Rep-Rate Operation with an Electron Beam Load

## A HIGH CURRENT PULSER FOR EXPERIMENT #225, "NEUTRINO ELECTRON ELASTIC SCATTERING"

C. Dalton, G. Krauss, and J. Sarjeant

University of California, Los Alamos Scientific Laboratory  
Los Alamos, New Mexico 87545Abstract

With the advent of low-cost honeycomb extrusions of polypropylene sheets, flash chambers have become very attractive for large nuclear particle detector arrays. This has brought about the need for a pulse power system that will provide high peak currents and low levels of spurious radiation. Each module of 10 flash chambers will require a peak current of 20 KA with a rise time ( $\tau_r$ ) of  $< 50$  ns, giving a maximum rate of current rise  $di/dt$  of 400 KA/us. The pulser output must develop 7 KV across a load of  $0.36 \Omega$  with a pulse width of 500 ns. The repetition rate will be one per second. This paper describes the development of such a system and the impact of the physical limitations of present component technology on lifetime and pulse fidelity.

Introduction

In an article published in Nuclear Instruments and Methods, Volume 158, page 289 (1979), we discussed a system which allows rapid data collection from particle detectors known as "Flash Chambers." A flash chamber consists of a noble gas mixture confined between two conducting plates in a dielectric container. The conducting plates are pulsed to a high voltage level in coincidence with the passing of a charged particle and a plasma is then formed in the dielectric container. At this point the data may be extracted optically or in some cases electrically. Until recently, data collection from flash chambers was a slow and tedious process because a photographic method was employed. Complexity of construction and high cost have also curtailed the use of these novel detectors, but with

the advent now of low cost honeycomb extrusions of polypropylene sheets, flash chambers (Fig. 1) have become very attractive components for large particle detector arrays. The flash chamber readout system under development will output data at a rate of  $2.5 \times 10^4$  bits per interrogation. The period of one interrogation is less than 0.01 s as compared to the previous optical system outputs of several hundred bits requiring seconds or minutes to accumulate. It is clear that this new readout method will be of great value when fully developed. At this point, however, the system is dependent on substantial technology base developments in the high-voltage pulse power driver.

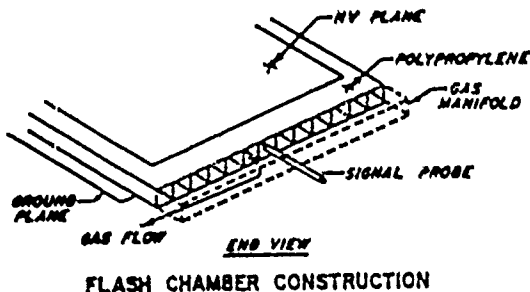


Figure 1

Figure 2 shows a simplified, overall block diagram of our instrumentation system. In this system the flash chamber readout, the high voltage pulser and the voltage monitors are the major areas of development. The high voltage pulser is of main concern at this point and is the focal point of this report. This pulser can be divided down into four separate areas: the load, energy storage, load to pulser interface, and the switch. These areas will be

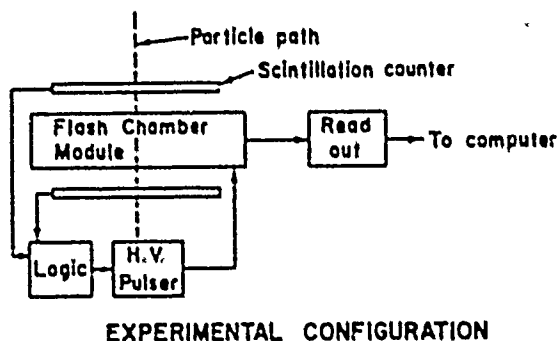


Figure 2

discussed in this order.

#### The Load

The flash chambers for this system are  $3\frac{1}{2}$  in by  $3\frac{1}{2}$  in with a thickness of 5 mm, and are clad on both sides with 0.05 mm of aluminum foil, forming a parallel plate capacitor with a capacity of 20 nF. Since these chambers have dimensions comparable to the pulse rise and fall times, they cannot be treated with conventional transmission line theory, and are being analyzed more as a lumped capacitive element than a true transmission line. However, in order to have a point of reference the impedance of a chamber was measured and found to be  $\approx 5 \Omega$ , and the transit time was measured to be 10 ns. The above parameters constitute the predominant characteristics of the flash chamber as an electrical load. In the planned experiment there will be 450 flash chambers. Each pulser will have to drive a module consisting of 10 chambers.

#### Energy Storage

For proper operation and peak efficiency the flash chambers require a rectangular pulse, with a duration of 500 ns from a source with an impedance of 5  $\Omega$ , requiring a pulse-forming network (PFN) to meet these needs. Initially a Type C PFN was used, however, difficulty with saturating toroid inductors and poor pulse fidelity on the falling edge precipitated a change to the Type B presently in use (Fig. 3). In the first stages of PFN design, computer modeling was used to arrive at a prototype design. This prototype PFN was then tested under load conditions and adjusted to compensate for distributed parameters not included in the modeling program. Since high peak currents and

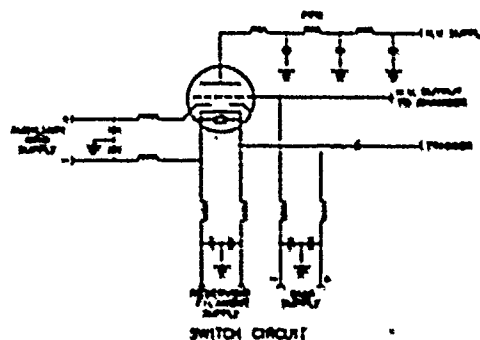


Figure 3

low inductance are required, in conjunction with a life time of  $10^7$  shots (MTBF, 90% confidence level), capacitor selection is non-trivial. At present capacitors manufactured by Axel, Sprague and Murata are under test. The mica capacitors from Axel Type MC 3AW have an equivalent series resistance (ESR) of 2.10  $\Omega$  for a 6.5 nF unit with an estimated life of  $10^{10}$  shots. The Murata DHS series capacitors have an ESR of 1.90  $\Omega$  and a guaranteed shot life of  $10^4$ . The Sprague Type 720C has an ESR of 6.4  $\Omega$  and an estimated shot life of  $10^6$ . With the above lifetime data the emphasis has been placed upon the development of PFN utilizing the Axel mica capacitors.

#### Load to Pulsar Interface

In transmitting the power from the switch and PFN assembly to the chambers, the characteristics of both strip line and coaxial transmission lines have been assessed. Coaxial lines have given the best results so far, but have not met design rise-time requirements. Coaxial lines worked well into a resistive load (Fig. 4), however, when the load of the chambers was put on to a pulser output, the shock oscillations and impedance mismatch caused a severe degradation in pulse fidelity and rise time (Fig. 5). Further development of both transmission lines is currently under way.

#### The Switch

After an extensive market study and vendor interactions, an EG&G thyatron was chosen for initial prototyping. The choice of a thyatron over a spark gap was based on the low spurious noise requirement and a  $> 10^7$  shot life. The EG&G HY-13 is now being tested and at this point test results indicate that

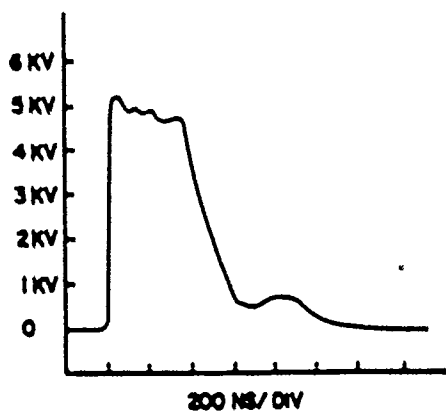
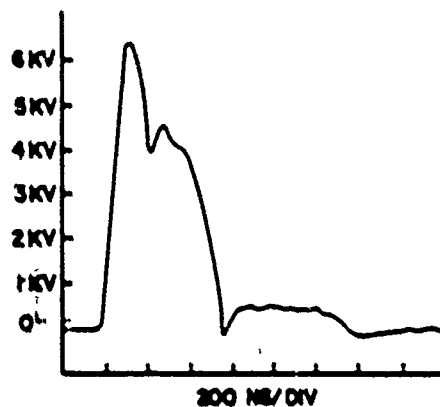
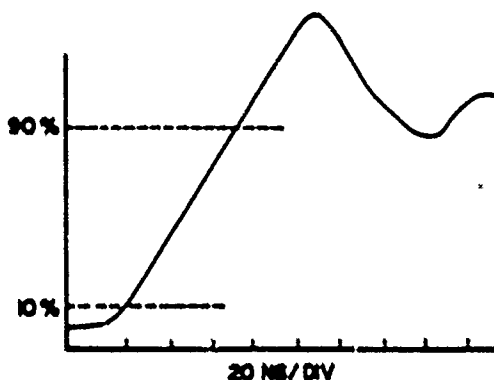
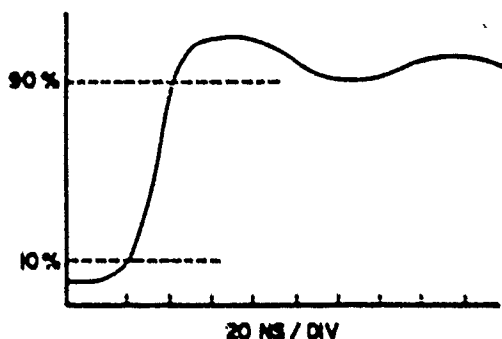
PULSE INTO 0.9  $\Omega$  LOAD

Figure 4



PULSE ON CHAMBER

Figure 5



this switch may well be just adequate to the task. In order to improve the switch performance and so reduce even further the total number of switches required, EG&G is developing a new grounded grid thyatron, the HY-1313 for our specific application and we are now preparing a test geometry for this tube. Figure 3 shows the HY-13 circuit layout. The PFN, switch loop and electrical PFN placement are the main layout changes foreseen. These changes will reduce  $\tau_r$  and improve the physical layout of the pulser. To date we have tested the HY-13 to a peak current of 5500 amperes into a 0.9  $\Omega$  load and were able to obtain a  $\tau_r$  of 10 ns. This is to be compared to the goal of 20 KA into a 1.4  $\Omega$  with a  $\tau_r$  of < 50 ns, meaning a  $di/dt$  of  $\sim 100$  KA/ns.

#### Conclusion

Considering shot life and ESR, the Axel capacitors

are being used for further testing of the PFN. The HY-13 at the present stage of testing has successfully driven 40X of the load and at this time looks acceptable. EG&G is manufacturing a new tube (HY-1313) which should improve the performance of the pulser.

In conclusion there does not appear to be a problem with the PFN or switch. The main area of concern is the interface between the switch and the load and the problem is how to transmit large currents with fast rise time into a capacitive load. This aspect of the system design is currently under detailed study.

References

1. C. Dalton and G. Krauss, Nucl. Inst. and Meth. 158, 289 (1979).
2. S. Friedman et al., "Multi-Gigawatt Hydrogen Thratrons with Nano-Second Rise Times," Modulator Symp., Buffalo, NY, 1979.
3. D. Turnquist et al., EG&G Application Note H5005A-1.
4. E. Iverson, "Electromagnetic Shock Lines," Los Alamos Scientific Laboratory, to be published.

KrF LASER-TRIGGERED SF<sub>6</sub> SPARK GAP FOR LOW-JITTER TIMING

W. R. Rapoport, J. Goldhar, J. R. Murray, and M. D'Addario

Lawrence Livermore Laboratory  
University of California  
Livermore, CA 94550Abstract

An SF<sub>6</sub> spark gap operated at field stresses of 60-180 kV/cm can be triggered with subnanosecond jitter by volume breakdown in SF<sub>6</sub> induced by as little as 10 mJ in 15 ns of KrF laser radiation.

---

Work performed under the auspices of the U. S. Department of Energy by the Lawrence Livermore Laboratory under contract number W-7405-ENG-48.



# EFFECTS OF SURROUNDING MEDIUM ON THE PERFORMANCE OF EXPLODING ALUMINUM FOIL FUSES

T. L. Berger

Naval Surface Weapons Center  
Dahlgren, Virginia 22448

## Abstract

Flat aluminum foil fuses were exploded electrically by discharging a capacitor bank into a series combination inductance ( $\sim 600$  nH) and fuse. The  $2.54 \pm 2.54 \times 0.0023$  cm foils were exploded in a sealed chamber. The time to burst and fuse voltage characteristics were investigated as a function of the fuse environment. Results are given for foils exploded in various gases and liquids.

## Introduction

Electrically exploded conductors are useful in a wide variety of pulsed power applications. Fast foil current breakers have been used to sharpen current pulses from capacitor banks<sup>1-3</sup> and from explosive magnetic flux compression generator-transformer systems<sup>4-7</sup>. In addition, fuses have been used as the high speed elements for multiple stage switching in inductive energy storage<sup>8-9</sup>. Exploding conductors have also been used to launch hypervelocity projectiles<sup>10-12</sup>.

Despite a wide variety of experimental work, there remains much that is not understood about the electrical explosion of conductors. Edge effects which lead to breakdown, for example, are not well understood. It seems reasonable that breakdown at the edges of the foil is due to corona discharge and explosions due to irregularities which are introduced when the foil is cut. There is some

evidence, however, that there may be mechanisms other than corona discharge which lead to edge breakdown<sup>13</sup>. The effect of volume changes is also not well understood. Although electrical conductivity is known to be relatively sensitive to volume changes, a constant volume approximation is generally used in order to avoid difficult hydrodynamic calculations<sup>14</sup>. Finally, we mention the effects of the surrounding medium on fuse characteristics. It is not clear, for example, what the characteristics of the surrounding medium should be in order to best inhibit electrical breakdown. On the one hand, it is suggested that the surrounding medium should confine the metal vapor in order to inhibit collisionally induced ionization and subsequent breakdown<sup>1</sup>. On the other hand, it has been suggested that heat transfer and chemical reactions with the surrounding medium can inhibit electrical breakdown<sup>15</sup>.

The purpose of this work is to attempt to gain a better understanding of the effects of the fuse environment on fuse performance. In this paper we report the results of measurements of the time to burst and peak hold off voltage for aluminum foils exploded in various gases and liquids.

## Experimental Details

Flat aluminum foils  $2.54 \times 2.54 \times 0.0023$  cm were exploded by discharging a capacitor bank into an inductance in series with the aluminum foil.

The capacitor bank is a low inductance bank with ignitron switches. The nominal charging voltage is 20 kV, the capacitance is 98  $\mu$ F, and the inductance is 80 nH. The maximum bank current is about 600 kA.

The capacitor bank is coupled into a parallel plate transmission line by 15 coaxial cables. The total inductance of the system is 620 nH.

Fuse current was measured with a low inductance current viewing resistor. Fuse voltage was measured with a resistive divider.

#### Experimental Results and Discussion

Figure 1 is a typical example of current and voltage waveforms obtained in this work. Fig. 1 shows that there are a number of well defined stages in the discharge of the capacitor bank through the foil. For approximately the first 6 microseconds of the discharge, the fuse voltage changes very little. The foil resistance also changes very little and the current is not far from what is obtained in the case of zero resistance. At  $t = 6$  microseconds, there is an abrupt change in the slope of the voltage curve. At this time, a solid to liquid phase transition is in progress. At  $t = 8$  microseconds, there is a very sharp change in the slope of the voltage curve. At this time, a liquid to vapor phase transition is in progress and fuse resistance is rapidly increasing. After about 200 nanoseconds, however, the fuse resistance begins to decrease very rapidly presumably due to ionization and breakdown of the metallic vapor.

Figure 2 is a plot of the time to burst as a function of capacitor bank voltage for foils exploded in air. Time to burst is defined as the time to peak voltage measured from the point where the current departs from its initial value of zero. The solid line in Fig. 2 was plotted according to the theory of Masionnier et al.<sup>1</sup>. According to this theory, the Joule heat power is equal to the rate of change of the internal energy of the foil. This leads to the equation

$$\frac{\sqrt{2} \omega C_1^2 V_0^2}{-S^2} \left( -\frac{1}{4} \sin 2\omega t + \frac{\omega t}{2} \right) = k_1 a. \quad (1)$$

where

$$a = \frac{\sqrt{2}}{\gamma} \gamma \int_{T_0}^{T_v} \rho^{-1} d\rho,$$

and

$C_1$  = bank capacitance

$V_0$  = initial bank voltage

$S$  = cross sectional area of the foil

$\omega$  = angular frequency of sinusoidal current

$\gamma$  = mass density of foil

$\rho$  = resistivity of foil

$a$  = internal energy per unit mass

$T_0$  = initial foil temperature

$T_v$  = foil temperature at vaporization

The quantity  $a$  can be calculated from handbook tables and has the value  $a = 2.2 \times 10^{16}$  for aluminum<sup>1</sup>. This value of  $a$  corresponds to slow adiabatic heating at atmospheric pressure. The numerical factor  $k_1$  takes into account the rapid heating encountered in exploding foils. Masionnier et al.<sup>1</sup> suggest

$$1 < k_1 < 3.$$

Using the measured value of  $\omega$  and other known values of physical parameters, Eq. (1) was solved numerically. The solid line shown in Fig. 2 was obtained with  $k_1 = 2.2$ . The fit is seen to be quite good.

Time to burst as a function of capacitor bank voltage was also measured for foils exploded in distilled water and in aluminum oxide powder. Within the limits of experimental uncertainty, the results (not given in this paper) are the same as those obtained for foils exploded in air. We have also measured the time to burst for foils exploded in various gases and liquids. The results are given in Table I. These results show that the time to burst is not sensitive to changes in the surrounding medium. Since the thermal conductivity is much greater for water than air, it seems reasonable that more energy and hence more time would be required to obtain a given resistance change of the foil in water than in air. According to Burtsev et al.<sup>16</sup>, changing the relative resistance of the foil by a factor of 20 requires 4.5 kJ/g in water and 3.2 kJ/g in air. We have not observed this effect possibly because the natural frequency of our system is smaller by about a factor of 2. Our results, however, do agree with those of Salge et al.<sup>9</sup>.

We now consider the maximum standoff electric field measurements. These measurements were made for

foils exploded in various gases at pressures ranging from 0-200 psig and in various liquids over the density range 0.9 - 3.1 g/cm<sup>3</sup>. This was done in order to test the assumption of two models: the vaporization wave model<sup>17</sup> and the heat transfer-chemical reaction model<sup>15</sup>.

According to the vaporization wave hypothesis, a vaporization wave propagates inward from the conductor surface. Ahead of the wave, the material remains in the conducting state while behind the wave, the material is in a vaporized insulating state. If the vapor cloud is free to expand, mean free path effects should eventually lead to ionization and breakdown in the vapor. This has been observed<sup>13</sup>. Breakdown should be inhibited by increasing the density of the surrounding medium.

Figure 3 is a plot of the maximum standoff electric field as a function of density for foils exploded in a 50% N<sub>2</sub> 50% O<sub>2</sub> gas mixture. This plot shows that the electric field does indeed increase with density in accordance with the vaporization wave theory. The same effect was observed for the other two gases used as shown in Table I. The peak electric field was very nearly the same in all the liquids except for transformer oil.

We now consider the heat transfer-chemical reaction model. Conte et al<sup>15</sup> have used this model to explain their results for aluminum foils exploded in water. An exothermic chemical reaction between the foil and water is thought to occur. The extra heat drives the fuse toward higher resistance and more rapid explosion. Foils exploded in H<sub>2</sub>O<sub>2</sub> exhibited higher holdoff voltage than foils exploded in H<sub>2</sub>O presumably because H<sub>2</sub>O<sub>2</sub> is more chemically active than H<sub>2</sub>O.

In this investigation, we have searched for chemical reactions in gases and liquids. According to Table I, the maximum electric field for the gases tends to decrease with increasing oxygen concentration. The peak electric field was the same for H<sub>2</sub>O as for the more chemically active H<sub>2</sub>O<sub>2</sub>. Thus, the results of this work provide no support for the chemical reaction model. We do not reject this model, however, because we have

not investigated other factors which may be important such as time to burst, foil dimensions, and rate of energy transfer.

It is interesting that at the same density, the peak electric field is greater for helium than for the other gases. This effect may be due to vapor cloud cooling since helium has a relatively high thermal conductivity.

#### Conclusions

In conclusion, this work indicates that time to burst is largely independent of the surrounding medium. We have also found no evidence that chemical reactions affect fuse performance. We have found some indication that heat transfer to the surrounding medium may inhibit breakdown. Finally, we have found that the hold off voltage increases with gas density in the pressure range 0-200 psi but there is a weak dependence on gas species.

#### References

1. C. Masionnier, J. H. Linhart, and C. Gourlan, *Rev. Sci. Instr.* **37**, 1380 (1966).
2. H. C. Early and F. J. Marcin, *Rev. Sci. Instr.* **36**, 1000 (1965).
3. J. N. Di Marco and L. C. Burkhardt, *J. Appl. Phys.* **41**, 3894 (1970).
4. Ya. I. Azarkevich et al, *Zhurnal Tekhnicheskoy Fiziki* **46**, 1957 (1976).
5. A. I. Pavlovskiy, V. A. Vasyukov, and A. S. Russkov, *Zhurnal Tekhnicheskoy Fiziki, Pis'ma v Redaktsiyu* **3**, 789 (1977).
6. C. M. Fowler, Private Communication.
7. B. Antoni, Y. Landure', and C. Nazet, in *Energy Storage, Compression, and Switching*, W. H. Bostick, V. Nardi, and O. S. F. Zucker Eds. (Plenum Press, New York, 1976), p. 481.
8. E. K. Schall, *Nature Phys. Sci.* **231**, 111 (1971).
9. J. Salge, U. Braunsberger, and U. Schwartz, in *Energy Storage, Compression, and Switching*, W. H. Bostick, V. Nardi, and O. S. F. Zucker, Eds. (Plenum Press, New York, 1976), p. 477.
10. V. E. Scherrer and P. I. Richards, *Symp. Hypervelocity Impact*, 4th, Elgin AFB, Florida (April 1960).
11. W. H. Clark et al, *Symp. Hypervelocity Impact*, 7th, Tampa, Florida (Nov. 1964).

12. A. B. Wenzel and J. W. Gehring, Jr., Symp. Hypervelocity Techniques, 4th, Tullahoma, Tennessee (Nov. 1965).
13. V. A. Burtsev, V. N. Litunovskii, and V. F. Prokopenko. Sov. Phys. Tech. Phys. **22**, 950 (1977).
14. J. D. Logan, R. S. Lee, R. C. Weingart, and K. S. Yee, J. Appl. Phys. **48**, 621 (1977).
15. D. Conte, M. Friedman, and M. Ury, Proc. First IEEE Pulsed Power Conference, Lubbock, Texas, 1976, p. II D-7.
16. V. A. Burtsev, V. N. Litunovskii, and V. F. Prokopenko, Soviet Phys. Tech. Phys. **22**, 957 (1977).
17. F. D. Bennett, in Progress in High Temperature Physics and Chemistry, Carl A. Rouse, Ed., Vol. II (Pergamon Press, Oxford, 1968).

Sponsored by NSWC Independent Research Program and the Advanced Research Projects Agency through the Naval Air Systems Command.

Table I. Experimental Summary

P = pressure  
 $\rho$  = density  
 $\bar{t}$  = average value of time to burst  
 $\bar{E}$  = average value of maximum electric field  
 MI = methylene iodide

Medium	P psig	$\rho$ mg/cm <sup>3</sup>	$\bar{t}$ usec	$\bar{E}$ kV/cm	No. Shots
50% O <sub>2</sub> 50% N <sub>2</sub>	0	1.2	8.6	3.2	6
"	25	3.4	8.7	3.6	6
"	100	9.6	8.8	4.2	6
"	200	18.1	8.9	4.6	3
AIR	0	1.2	8.7	3.2	1
	100	9.6	8.7	4.4	2
	200	18.1	8.7	5.0	6
HE	200	2.4	8.6	4.0	4
	300	3.6	8.9	4.2	1
Transformer Oil	-	0.9x10 <sup>3</sup>	8.7	4.4	2
Water	-	1.0x10 <sup>3</sup>	8.6	5.1	2
30% H <sub>2</sub> O <sub>2</sub>	-	1.1x10 <sup>3</sup>	8.7	5.0	2
CCl <sub>4</sub>	-	1.6x10 <sup>3</sup>	8.6	4.9	2
50% CCl <sub>4</sub> 50% MI	-	2.3x10 <sup>3</sup>	8.5	4.9	2
MI	-	3.1x10 <sup>3</sup>	8.4	5.0	2

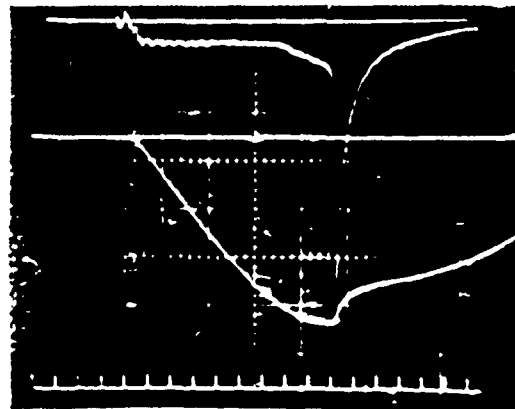


Figure 1. Current and voltage waveforms for foil exploded in 50% O<sub>2</sub>, 50% N<sub>2</sub> at 200 psig. Upper trace: Fuse voltage; 2kV per division. Middle trace: Fuse current; 20kA per division. Lower Trace: one microsecond time marks.

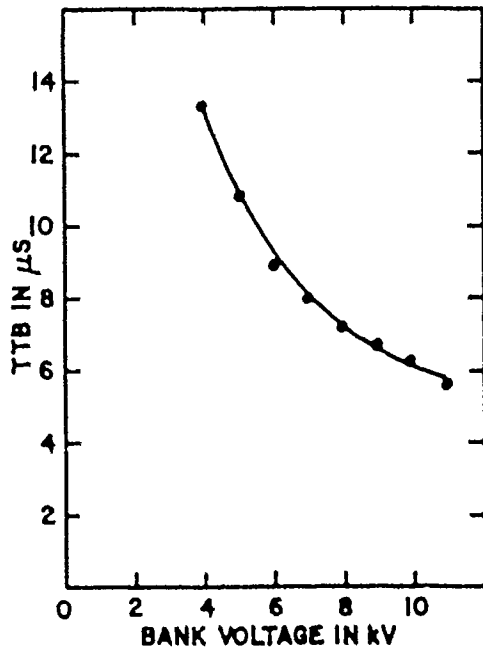


Figure 2. Time to burst (TTB) vs. bank voltage for foils exploded in air. Dots are experimental points and the curve is drawn according to the theory of Ref. 1.

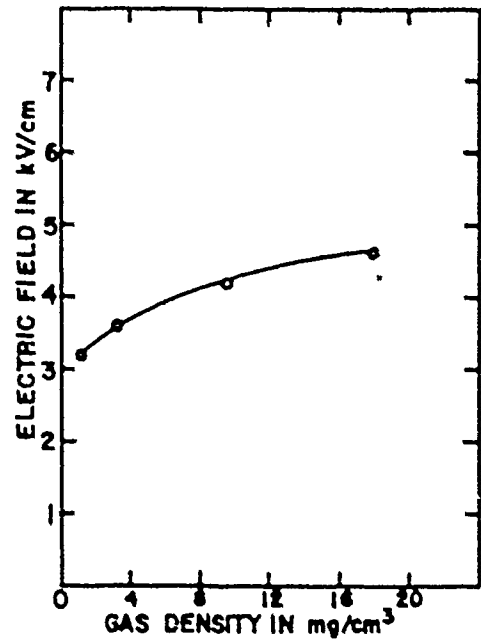


Figure 3. Peak electric field as a function of gas density for foils exploded in 50%  $\text{O}_2$ , 50%  $\text{N}_2$ .

## HIGH POWER VERY LONG PULSE TESTING OF A 200 KV. TETRODE REGULATION TUBE

Jere D. Stabley, RCA

Bob Gray, Rome Air Development Center

ABSTRACT

Tests at very long pulse lengths were conducted to evaluate the design concepts of the S94000E regulator tube at the Rome Air Development Center. Voltages as high as 200 KV have been switched for pulse lengths of 0.5 seconds and at anode dissipation levels that exceeded 2.0 million Watts. Tubes similar to the one tested will be employed as series regulators in the TOKAMAK<sup>1</sup> Fusion Test Reactor. This paper discusses the tube, test results, and operational experiences associated with those tests.

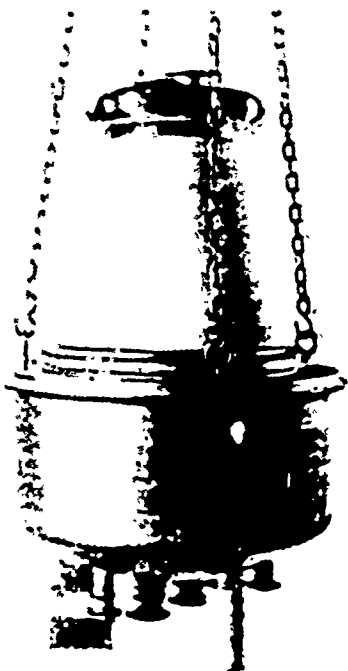


Fig. 1 - RCA S94000E Tetrode

INTRODUCTION

A high voltage beam power tetrode designated as the S94000E has been developed<sup>2</sup> by the Power Devices group of RCA and was tested at the High Power Laboratory of the Rome Air Development Center. This tube shown in Fig. 1 represents an advancement in the state of the art in terms of voltage hold-off and anode dissipation at the long pulse lengths involved.

Tubes similar to the one tested will be employed as series regulator tubes providing pulse voltages for Neutral Beam Ion sources. The use of neutral beams has proven to be a very effective way of raising plasma temperatures in previous Fusion experiments and will be used extensively in the TOKAMAK Fusion Test Reactor. This work was funded by DOE and contracted through the Plasma Physics Laboratory of Princeton University.

TUBE REQUIREMENTS FOR TSTR

Tube Type.....	Tetrode
D.C. Anode Voltage.....	200 KV
Anode Current.....	125 Amps
Anode Dissipation.....	2.0 Megawatts
Instantaneous Grid No. 1 Voltage..	Less than Zero
Screen Voltage.....	D.C.
Pulse Length.....	1 Second

GENERAL TUBE DESCRIPTION

The S94000E is a liquid-cooled ceramic to metal beam power tetrode that utilizes chlorinated tungsten filaments in a circular array of unit electron optical systems. The tube contains sixty-six individual electron guns each using a directly heated ribbon filament. The control grid and screen grid are comprised of small tungsten wires that are embedded into water-cooled copper blocks. The unique anode structure

is centrally located and is comprised of sixteen individually cooled structures that are set at an oblique angle to the electron beam axis. This angle is effective in greatly enhancing the bombarded anode area. Fig. 2 shows a simplified cross section of one electron gun.

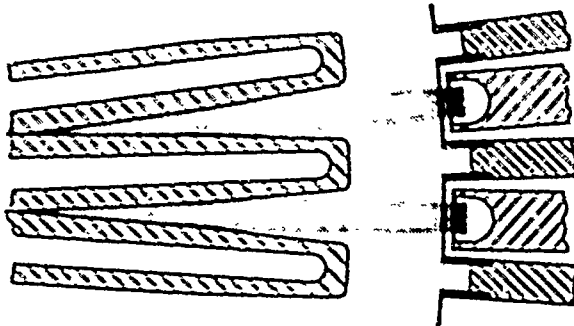


Fig. 2 - Electron Gun - Anode Crosssection

#### RADC TEST FACILITY

In order to evaluate the tube under long pulse, high voltage conditions, it was necessary to make arrangements for the use of facilities other than those available at the Lancaster, PA location. At this point in time, the facility most capable of providing 25 Megawatts of power at 200 KV is located at Griffiss Air Force Base in Rome, NY. A view of the facility is shown in Fig. 3. It is very complete and contains within one building six 65 KV 9 Amp power supplies, a high power load resistor, a complete demineralized water system, crowbar protection devices and various power supplies, both D.C. and pulse that can be incorporated for tube evaluation.



Fig. 3 - RADC Power Supply and Test Facility

For the tests on the RCA tube, the power supplies were connected in a series parallel arrangement that yielded 200 KV at 18 Amps of continuous current. RADC engineers determined after consultation with the power supply designer and the solid-state diode manufacturers that the current rating could be nearly tripled (50 Amps) if the pulse length did not exceed 0.5 seconds. Consequently, the test conditions were tailored to the RADC equipment.

The dummy load resistor that absorbs the major portion of the power during the 0.5 second pulse is located on the high side of the power supply. It is comprised of four sections of glass tubing filled with a solution of sodium chloride and water. The solution serves as a load resistor which can be changed by changing the water to solution ratio. The dummy load and its water to air heat exchanger are shown in Fig. 4. The crow-

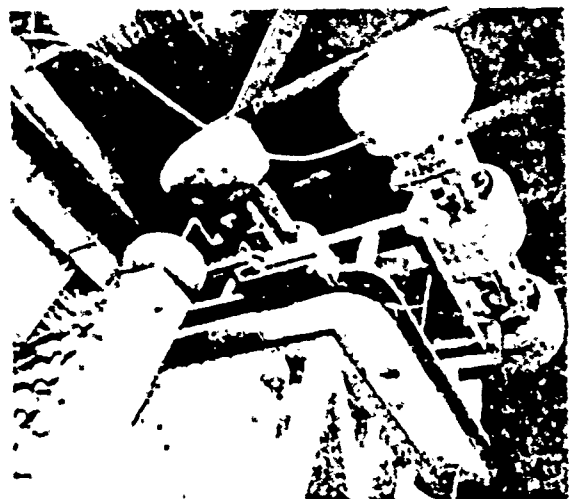


Fig. 4 - Water Load and Triggered Spark Gap

bar device<sup>3</sup> is a series of Air Gaps that are activated by applying a high pulse voltage to each Gap, which in turn breaks down and shorts the Power Supply under tube fault conditions. Detection of tube faults is accomplished by using eighty UDB5 Unitorde diodes that are immersed in oil. The diodes are back biased until the Anode Voltage drops below a pre-set reference value which represents a plate arc in the tube. A similar arrangement is used to detect screen faults. The tube

itself is contained, anode up, in a rectangular lead shielded tank that is filled with transformer oil to prevent arcing across the output ceramic. The tank is raised from the floor to allow access to the tube for connection of the leads that carry the 4000 amps of filament current and for connection of the auxiliary water hoses. The anode water which flows at a rate of 230 GPM reaches the tube through approximately 60 feet of three inch PVC pipe. The tube in its lead shielded enclosure is shown in Fig. 5. Fig. 6 shows a simplified schematic of the test circuit that was used.

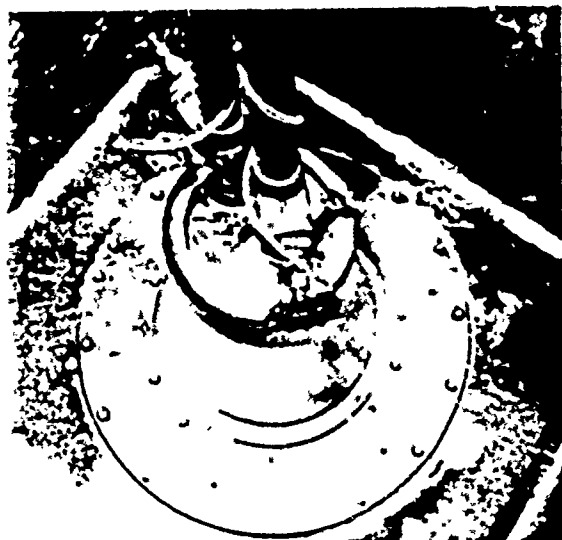
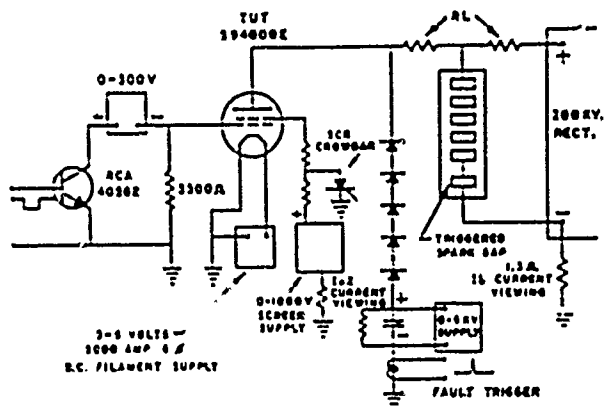


Fig. 3 - RCA 594000E in Lead Shielded Oil Container



**Fig. 6 - Simplified Schematic of Test Circuit**

## PROBLEM AREAS

Actual testing of the S94000E at Rome was scheduled to be approximately a three week exercise, however, the three weeks turned into a three month adventure. We had underestimated the problem of overstressing the RADC equipment and using it beyond its ratings. The problems associated with the equipment seemed to follow the falling domino effect that started with an exploding R/C voltage divider which caused a small fire and a considerable amount of smoke. A breaker then failed to open resulting in the power supply operating into a crowbar generated short circuit for an extended period of time. Shrapnel was a constant source of concern as sixteen high voltage capacitors either shorted or opened during the course of the tests. Last, but not least the most time consuming problem occurred when the cooling water for the dummy load leaked into the insulating plenum chamber. The noise associated with explosions that occur when 220 KV seeks a path to ground is somewhat unimaginable and after several occurrences it becomes frightening. It was apparent that the nerves of the personnel performing the tests were wearing very thin when some among us were resorting to face masks and ear plugs at the thought of applying high voltage. However, in the midst of yet another "explosion" we did inadvertently learn a very important thing about the survivability of the S94000E. It occurred during a high voltage conditioning process where the rectifier was being used with a 200 K ohm resistor and the crowbar disarmed. During this exercise, the high voltage diodes used to detect tube faults shorted which caused the series resistor to be shorted thereby applying the 200 KV rectifier to the tube with only its internal impedance. The tube faulted and hung on the line until a small 16 wire used in the set-up disintegrated. The tube had taken a serious jolt, the vacuum pressure exceeded fifty milliamperes, however, it did recover. It was processed to the 200 KV level in a matter of several hours and amazingly enough, the majority of the tests performed on the tube were made after this episode. We believe this is a highly significant event and



gives an indication of the ruggedness of the S94000E under very adverse conditions.

#### LONG PULSE TESTING

Testing a tube at very long pulse lengths, where conventional voltmeters can be used, is a much different experience to which those associated with power pulse systems have been accustomed. At RADC several other interesting things were observed. For instance, during each pulse the overhead lights dimmed slightly, the tube pressure as indicated by the vac-ion pump increased and then settled back to a lower level during the interpulse period. One gains an appreciation for what is required of the equipment and the tube's anode with regards to stresses that occur due to temperature change. Temperatures that would normally occur under continuous "on" conditions are now occurring and then changing to a totally "off" condition twelve times a minute or whatever the repetition rate of the pulse is.

Another interesting tube-circuit phenomenon occurred during the tests at Rome. As the tube pressure increased during the pulse "on" time, it was noticed that the instantaneous grid voltage was developing a tail and going more toward zero at the end of the pulse. The problem was the result of ion current being drawn through the control grid to ground external impedance. This effect was eliminated by lowering that impedance. If one did not have a vac-ion pump on the tube, developing the instantaneous grid voltage in a high resistant circuit could be used to detect gas within the tube under negative grid voltage operating conditions.

#### TEST SUMMARY AND CONCLUSIONS

The data accumulated at RADC in conjunction with the maximum tube ratings are shown in Fig. 7. It shows that 200 KV operation has been accomplished at dissipation levels that varied up to 2150 Kilowatts and at anode voltages that went as high as 62 KV. A new high water mark has been obtained with gridded tube in combining of pulse width, voltage hold-off and anode dissipation capabilities.

We are all proud of the performance of the S94000E which offers future extended capability for longer pulse length at higher anode voltages. The use of gridded tubes as series regulator for TFTR and future fusion reactors is an exciting new application.

TEST DATA SUMMARY  
Filament Current = 1300 Amps  
Pulse Length = 2.5 Seconds at 2 Pul/Minute  
200 Programmable Plate Tube  
Anode Cathode Distance = 1.11

$E_{an}$ KV	$E_g$ KV	$I_a$ Amps	$E_{g1}$ Volts	$E_{g2}$ Volts	$E_{g3}$ Volts	$P_{diss}$ KW	Anode Temp °C
115	62	27.3	525	112	+38	300/34	110
130	62	47.8	495	112	+28	1500/200	200
152	53	13.8	500	112	+24	1000/145	210
152	34	44.8	425	112	+23	1500/200	210
200	34	30.2	345	112	+18	1100/15	150

Anode Current = 10 A							
152	34	32	190	300	+14	100/12	110
202	34	43	242	300	+14	210/15	150

Tube pressure during pulse and interpulse period.

Maximum Ratings	
DC Plate Voltage .....	200 KV
Pulsed DC Plate Current .....	125 Amps
DC Grid No. 2 Voltage .....	1000 Volts
Grid No. 3 Current .....	7.5 Amps
DC Grid No. 3 Bias Voltage .....	1000 Volts
Grid No. 1 Dissipation .....	10 KW
Grid No. 2 Dissipation .....	10 KW
Anode Dissipation .....	2000 KW
DC Filament Current .....	1300 Amps

Fig. 7 - Test Data Summary and Maximum Ratings

#### REFERENCES

- 1D. Steiner, J. F. Clarke, "The TOKAMAK Model T Fusion Reactor", SCIENCE, Volume 199, 31 March 1978 pp. 1395-1403
- 2J. Eshleman, J. Mark, "Recent Development in High Power Switch Tubes for High Power Radars and Fusion Research", PROCEEDINGS INTERNATIONAL PULSED POWER CONFERENCE 1976, pp. IC5-1, IC5-5
- 3Bobby R. Gray, "High Energy Switch Device Study at RADC", CONFERENCE RECORD OF TWELFTH MODULATOR SYMPOSIUM 1976, pp. 51-57

# VERY FAST, HIGH PEAK POWER PLANAR TRIODE AMPLIFIERS FOR DRIVING OPTICAL GATES\*

M.M. Howland, S.J. Davis, W.L. Gagnon

Lawrence Livermore Laboratory  
Livermore, California 94550

## ABSTRACT

Recent extensions of the peak power capabilities of planar triodes have made possible the latter's use as very fast pulse amplifiers, to drive optical gates within high-power Nd:glass laser chains. These pulse amplifiers switch voltages in the 20 kV range with rise times of a few nanoseconds, into crystal optical gates that are essentially capacitive loads.

This paper describes a simplified procedure for designing these pulse amplifiers. It further outlines the use of bridged-T constant resistance networks to transform load capacitance into pure resistance, independent of frequency.

## Introduction

Many optical gates in the Shiva laser system at the Lawrence Livermore Laboratory are Pockels cells. An approximate electrical model of the Pockels cell is a capacitor,<sup>1</sup> whose capacitance must be charged very quickly to optimize the rise time of the cell. The planar triode is a small, rugged, microwave vacuum triode<sup>2</sup> designed for operation to 3 GHz. A cutaway drawing of a class of these centimeter-wave planar tubes is shown in

Fig. 1. The three tube types of most interest to us as Pockels cell drivers are shown in Table 1. Note that the 8941 and the X2172 both have peak power capabilities approaching the 500 kW for short (50-nsec) pulses.

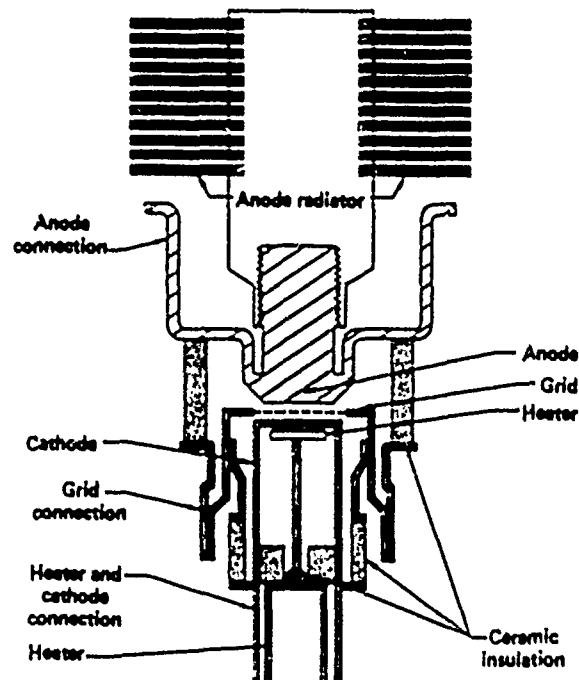


Fig. 1: Electrode arrangement of a planar triode.

\*Work performed under the auspices of the U.S. Department of Energy by Lawrence Livermore Laboratory under contract no. W-7405-Eng-48.

Reference to a company or product name does not imply approval or recommendation of a product by the University of California or the U.S. Dept. of Energy to the exclusion of others that may be suitable.

Elmac Type†	Plate Voltage	Max. Current	C Input	C Output	Mu
8940	4.5 kV	36 A	18 pf	0.11 pf	85
8941	15 kV	36 A	14 pf	0.11 pf	200
x2172	25 kV	36 A	18 pf	0.2 pf	500

Table 1. Maximum ratings of some planar triodes.

### Circuit Development

To minimize the Miller effect of the grid to cathode capacitance, the planar triode is generally used in the grounded grid configuration. This requires that the preceding stage be capable of supplying the full plate current as well as any current drawn by the grid. The common cathode connection of the tube can provide current gain, and a bridged-T network employed in the grid circuit overcomes the bandwidth limitation of the common cathode configuration. This greatly reduces the current drive requirement of the preceding stage.

Ginzton et al.<sup>3</sup> describe a negative mutual inductance circuit, termed a bridged-T connection, which is used on broad-band distributed amplifiers. This circuit can mask the input capacitance of a tube or Pockels cell. Figure 2 shows the bridged-T network and its various equivalents. Choosing the values from Fig. 2(c), we can show that the image impedance is constant, resistive, and frequency independent. This eliminates the need for terminating half sections and permits us to terminate the line with a resistor. The cutoff frequency across the midshunt capacitance in terms of  $Z_0$ ,  $L$ , and  $C$ , is shown in the appendix (Fig. 6).

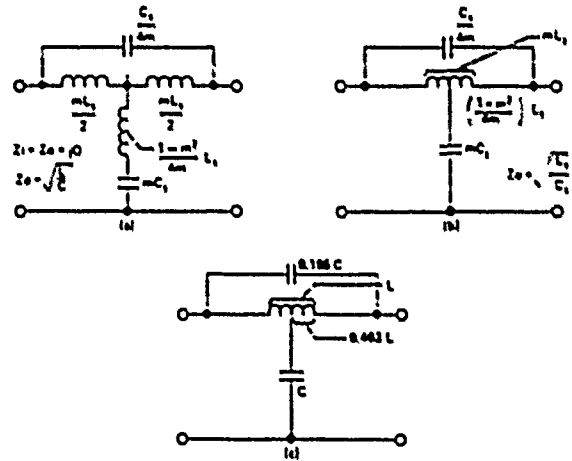


Fig. 2: (a) Constant resistance bridged-T networks  
(b) The mid-shunt inductance is obtained from the mutual inductance of this coil  
(c)  $\alpha = 1.27$  yields an optimum gain bandwidth network

### Triode Pulse Amplifier

The schematic of a pulse amplifier circuit to drive a 10-mm aperture Pockels cell is shown in Fig. 3. The Eimac 8941 planar triode is configured as a common cathode amplifier, biased just beyond cutoff. The end-to-end capacitance of the Pockels cell is 15 pF. Choosing  $Z_0$  as 130  $\Omega$ , and using the design charts in the appendix,  $L = 0.25$   $\mu$ H and the cutoff frequency across the cell is  $\sim 145$  MHz. A

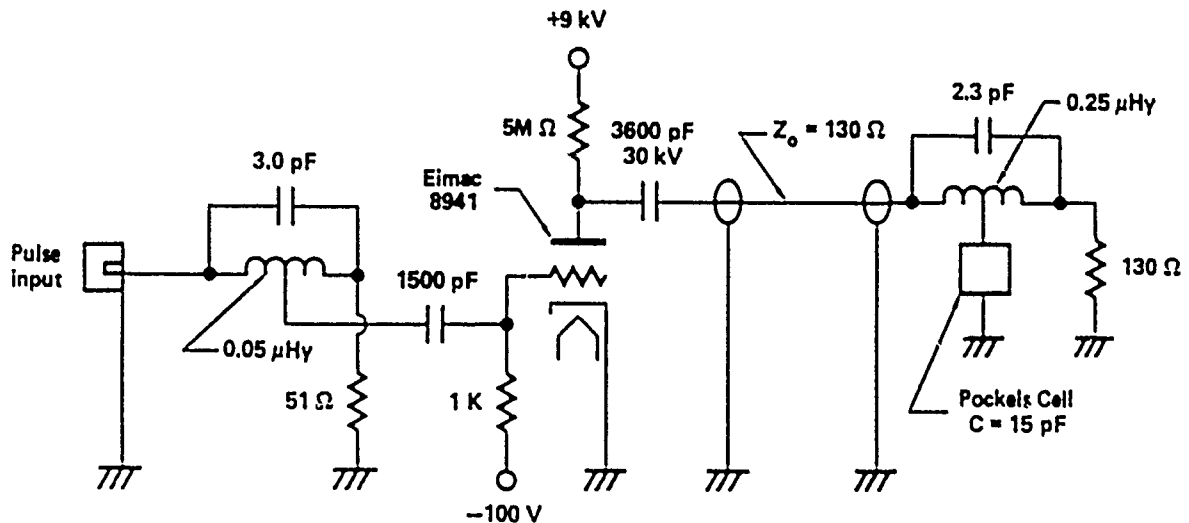


Fig. 3: Planar triode amplifier

similar network is designed for the grid circuit with  $Z_0$  equal to 50  $\Omega$ .

The load impedance for the planar triode is then 130  $\Omega$  resistive, and for a half-wave voltage at the Pockels cell of 3500 V, the peak current is 26.9 A. A load line for this case is shown on the constant current characteristics for the tube in Fig. 4. It requires that the grid be driven about 135 V positive, to achieve the necessary plate voltage swing and peak current. The voltage pulse measured at the output of this amplifier into an attenuator as shown in Fig. 5.

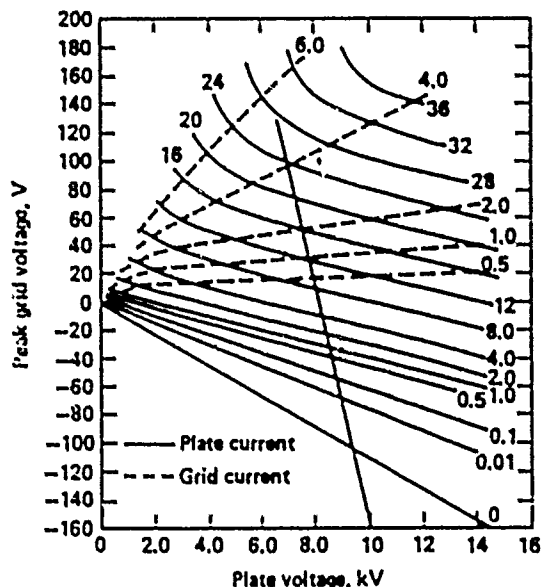
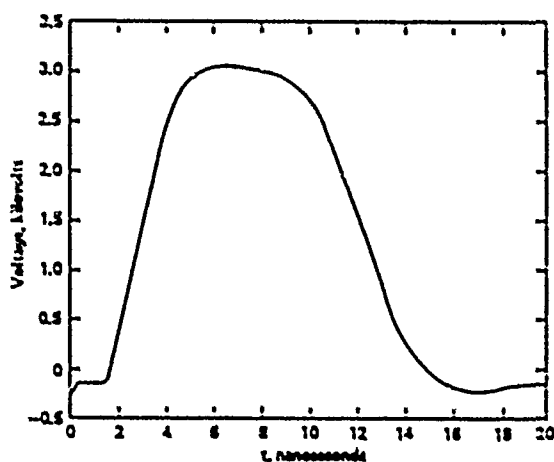


Fig. 4: The constant current characteristic of a planar triode.

From Fig. 4, the grid will draw almost 3.5 A, when it is driven positive by 135 V. The driver for the grid is an avalanche-transistor transmission line pulser that does not work into this changing load too well; so the input rise time to the triode is limited to about 2.5 nsec. This also means that when the tube grid draws current, the bridged-T network is no longer balanced; so at this time a reflection will be sent toward the driver.

The combination of high peak power and large bandwidth requires the circuit to be laid out care-



Scale - Horizontal: 5 nsec/div  
Vertical: 1000 V/div

Fig. 5: Output of the planar triode amplifier

fully. It is essential that tube lead inductances be kept low, so that the resonance associated with these electrodes will lie well above the operating band of the amplifier. Many small capacitors connected in parallel, and mounted on a low-inductance printed circuit board, serve as a bypass or coupling network. Low-value series resistors, connecting decoupling capacitors, are an effective way to isolate the nodes of the B+ supply wiring from the amplifier circuitry.

#### Discussion

Let us summarize our design of a planar triode amplifier for broad-band performance and consider the various tradeoffs involved. Normally, the load is specified first and, if it can be modeled as a capacitor it can be broad-banded in a bridged-T configuration by using the design charts in the appendix; this sets a cutoff frequency and an impedance level. The bridged-T network can be used up to  $\sim 400$  MHz. Above this figure, the small value of the components make them difficult to fabricate. The voltage necessary at the load and the impedance of the load determine the tube to be used. The cutoff frequency of the load sets the parameters of the broad-banded grid circuit. Careful component layout then assures optimum amplifier performance.

We have used the techniques presented here to design a pulse amplifier for driving a 10-mm Pockels cell. The amplifier performed as predicted. Its output characteristics are: 3600 V into 130  $\Omega$  with 2.5-nsec rise time, 3-nsec fall time, and pulse width of 5-9 nsec. The jitter is less than 100 psec.

#### Appendix<sup>4</sup>

Of the various lumped-constant lines for the anode and grid circuits studied by Ginzton et al.<sup>3</sup>, the bridged-T network provides the highest-gain bandwidth product. For a given gain, the bridged-T line provides about twice the bandwidth of the constant-K line.

We obtain the midshunt inductance from the mutual coupling between the two halves of the coil, as shown in Fig. 2(b). If we choose  $m$  to be 1.27, the inductance to the midpoint of the coil must be 40.3% of the total coil inductance.

By using the equation

$$L = \frac{r^2 n^2}{9 + 10L} \text{ uH}$$

where  $n$  is the number of turns, and  $l$  and  $r$  are the length and radius of the coil, respectively, the correct coupling results when the length of the coil is 1.35 times the coil's diameter.

The output voltage, taken across capacitor  $C$  in Fig. 2(c), has a cutoff frequency

$$F_1 = \frac{1}{\pi \sqrt{LC}}$$

and the characteristic impedance

$$Z_0 = \sqrt{\frac{L}{C}}$$

Figure 6 is a design chart for the bridged-T constant resistance network of Fig. 2(c), with the values of  $L$  and  $C$  plotted as functions of  $Z_0$  and  $F_1$ . Figure 7 is a design chart for the inductor in this network.

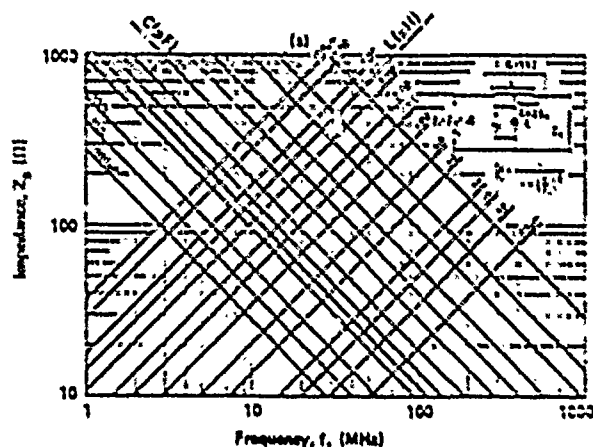


Fig. 6: Design chart for bridged-T network of Fig. 3.

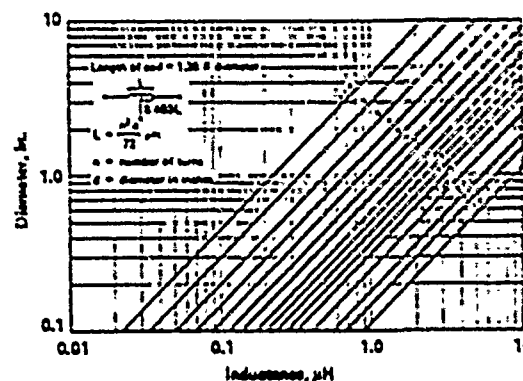


Fig. 7: Design chart of inductance for bridged-T network of Fig. 3.

#### References

1. L.L. Steinmetz, T.W. Pouliot, and B.C. Johnson, *Applied Optics* **12**, 1468 (1973).
2. *Electronics Engineers Handbook*, D.G. Fink, ed. (McGraw-Hill, 1975), pp. 9-23 to 9-28.
3. E.L. Ginzton, W.R. Hewlett, J.H. Jasberg, and J.D. Noe, "Distributed Amplification", in *Proc. IRE*, **956**, (August 1948).
4. W.L. Gagnon and B.H. Smith, "Simplified Design Techniques for Distributed Power Amplifiers", *Natl. Particle Accelerator Conf.* (Feb. 1969). Also published as UCRL 18491, Lawrence Livermore Laboratory, Livermore, California.

"This report was prepared as an account of work sponsored by the United States Government. Neither the United States nor the United States Energy Research & Development Administration, nor any of their employees, nor any of their contractors, subcontractors, or their employees, makes any warranty, express or implied, or assumes any legal liability or responsibility for the accuracy, completeness or usefulness of any information, apparatus, product or process disclosed, or represents that its use would not infringe privately-owned rights."

# VACUUM ARC SWITCHED INVERTER TESTS AT 2.5 MVA\*

RICHARD N. MILLER and A. S. GILMOUR, JR.

Department of Electrical Engineering  
Laboratory for Power and Environmental Studies  
State University of New York at Buffalo

**ABSTRACT** A mathematical analysis of the unloaded vacuum arc switch (VAS) inverter is undertaken; a key element in this analysis is the assumption of a constant voltage drop of 50 volts across each VAS while it is conducting. From this analysis a constant VAS-voltage model is developed to explain the VAS inverter operation. A comparison of data obtained from laboratory tests of the inverter is made with data obtained from this model, and agreement is found to be within 10% for up to 15 alternations.

**INTRODUCTION** High-frequency, high-power inverter circuits employing vacuum arc switches (VAS's) as the switching elements have been under development at the State University of New York at Buffalo (SUNYAB) for some time (1 - 7). The circuit used in this development is the series inverter shown in Figure 1. Several tests have been conducted on the inverter (3); using the results of these tests, a model of the inverter was developed as is described in the following paragraphs.

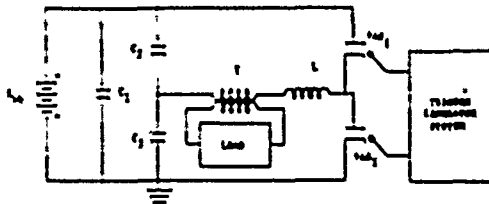


FIGURE 1. Series Vacuum Arc Switched Inverter.

\*This work was sponsored by the Air Force Aero-propulsion Laboratory, Wright-Patterson AFB, Ohio.

**INVERTER CIRCUIT ANALYSIS** The operation of the inverter circuit shown in Figure 1 has been described (6). In earlier work (1) the voltage drop across the VAS was measured and found to be nearly constant over a wide range of conducting currents. This characteristic suggests a constant  $V_{VAS}$  model for the VAS. Taking this characteristic into account, the capacitor voltages during the conduction of  $VAS_1$  can be shown to be (4)

$$v_{C_1}(t) = \frac{C_2}{C_1 + C_2} \left[ V_{VAS_1} - v_{C_2} \left( \frac{n\pi}{\omega_1} \right) \right] \left( 1 + \frac{e^{-\sigma_1 t} [-\sigma_1 \sin(\omega_1 t) - \omega_1 \cos(\omega_1 t)]}{\omega_1} \right) + v_{C_1} \left( \frac{n\pi}{\omega_1} \right), \quad (1)$$

$$v_{C_2}(t) = \left[ V_{VAS_1} - v_{C_2} \left( \frac{n\pi}{\omega_1} \right) \right] \left( \frac{e^{-\sigma_1 t} [-\sigma_1 \sin(\omega_1 t) - \omega_1 \cos(\omega_1 t)]}{\omega_1} \right) + V_{VAS_1}, \quad (2)$$

and

$$v_{C_3}(t) = \frac{C_1}{C_1 + C_3} \left[ V_{VAS_1} - v_{C_2} \left( \frac{n\pi}{\omega_1} \right) \right] \left( 1 + \frac{e^{-\sigma_1 t} [-\sigma_1 \sin(\omega_1 t) - \omega_1 \cos(\omega_1 t)]}{\omega_1} \right) + v_{C_3} \left( \frac{n\pi}{\omega_1} \right), \quad (3)$$

where 
$$c_1 = \frac{R_{CKT}}{2L},$$

$$\omega_1 = \sqrt{\frac{1}{LC_{T1}} - c_1^2},$$

and

$$C_{T1} = C_2 + \frac{C_1 C_3}{C_1 + C_3},$$

all of for which

$$\frac{n\pi}{\omega_1} \leq \tau \leq \frac{(n+1)\pi}{\omega_1}, \quad n = 0, 2, 4, \dots$$

The equations for the capacitor voltages have a similar form for the conduction of VAS<sub>2</sub> (4). Now, the initial-final conditions between alternations take the following type of form:

$$v_{C1} \left[ \frac{(n+1)\pi}{\omega_1} \right] = v_{C1} \left[ \frac{n\pi}{\omega_1} \right],$$

$$v_{C2} \left[ \frac{(n+1)\pi}{\omega_1} \right] = v_{C2} \left[ \frac{n\pi}{\omega_1} \right],$$

and

$$v_{C3} \left[ \frac{(n+1)\pi}{\omega_1} \right] = v_{C3} \left[ \frac{n\pi}{\omega_1} \right],$$

where

$$m = 2k+1,$$

$$n = 2k,$$

and k is the inverter output cycle number,

$$k = 0, 1, 2, 3, \dots$$

Equations (1) - (3), together with the initial-final conditions, comprise the Constant-V<sub>VAS</sub> Model. A comparison will now be made between data obtained from this model and data obtained in the laboratory.

**APPLYING THE MODEL** Figure 2 shows an oscillograph of  $v_{C3}(\tau)$  obtained while the inverter was operating. In this particular test, the VAS's were pulsed alternately at a 1.04 kHz rate. The L-C combination of the circuit was resonant at 9303 Hz, so the transition time between the two polarities indicated on the oscillograph was about 54 usec. This left a delay of 0.9 msec before the next VAS was fired. This 0.9 msec delay appears in the oscillograph

as the bright positive and negative peaks. This oscillograph suggests an approach to comparing data from the model with data from the test. The waveform in this oscillograph has a definite envelope; this envelope provides a good picture of the operation of the entire circuit, since, as the model equations show, an interdependence exists between all of the parameters of the circuit. Therefore, if the equations are obtained for the capacitor voltage envelopes, this form of the model will provide a basis for comparing the model with the data from the laboratory. The equations thus obtained are (4), for the positive peaks,

$$v_{C1} \left[ \frac{(n+1)\pi}{\omega_1} \right] = \frac{C_3}{C_1 + C_3} \left[ v_{VAS} - v_{C2} \left( \frac{n\pi}{\omega_1} \right) \right] \left[ 1 + \exp \left( -\frac{\sigma_1}{\omega_1} \right) \right] + v_{C1} \left( \frac{n\pi}{\omega_1} \right), \quad (4)$$

$$v_{C2} \left[ \frac{(n+1)\pi}{\omega_1} \right] = -v_{C2} \left( \frac{n\pi}{\omega_1} \right) \exp \left( -\frac{\sigma_1}{\omega_1} \right) + v_{VAS} \left[ 1 + \exp \left( -\frac{\sigma_1}{\omega_1} \right) \right], \quad (5)$$

and

$$v_{C3} \left[ \frac{(n+1)\pi}{\omega_1} \right] = \frac{C_1}{C_1 + C_3} \left[ v_{VAS} - v_{C2} \left( \frac{n\pi}{\omega_1} \right) \right] \left[ 1 + \exp \left( -\frac{\sigma_1}{\omega_1} \right) \right] + v_{C3} \left( \frac{n\pi}{\omega_1} \right), \quad (6)$$

again where

$$n = 0, 2, 4, 6, \dots$$

For the negative peaks, the equations become

$$v_{C1}(\tau) = \frac{C_2}{C_1 + C_2} \left[ v_{VAS2} - v_{C3} \left( \frac{n\pi}{\omega_2} \right) \right] \left\{ 1 + \frac{e^{-\sigma_2 \tau} [-\sigma_2 \sin(\omega_2 \tau) - \omega_2 \cos(\omega_2 \tau)]}{\omega_2} \right\} + v_{C1} \left( \frac{n\pi}{\omega_2} \right), \quad (7)$$

$$v_{C2}(\tau) = \frac{C_1}{C_1 + C_2} \left[ v_{VAS2} - v_{C3} \left( \frac{n\pi}{\omega_2} \right) \right] \left\{ 1 + \frac{e^{-\sigma_2 \tau} [-\sigma_2 \sin(\omega_2 \tau) - \omega_2 \cos(\omega_2 \tau)]}{\omega_2} \right\} + v_{C2} \left( \frac{n\pi}{\omega_2} \right), \quad (8)$$

and

$$v_{C_3}(\tau) = \left[ v_{VAS_2} - v_{C_3} \left( \frac{\pi}{\omega_2} \right) \right] \left\{ \frac{e^{-\sigma_2 \tau} [-\sigma_2 \sin(\omega_2 \tau) - \omega_2 \cos(\omega_2 \tau)]}{\omega_2} \right\} + v_{VAS_2}, \quad (9)$$

where

$$\sigma_2 = \sigma_1 = \frac{R_{CKT}}{2L},$$

$$\omega_2 = \sqrt{\frac{1}{LC_{T_2}} - \sigma_2^2},$$

and

$$C_{T_2} = C_3 + \frac{C_1 C_2}{C_1 + C_2},$$

all of for which

$$\frac{\pi}{\omega_2} \leq \tau \leq \frac{(m+1)\pi}{\omega_2}, \quad m = 1, 3, 5, \dots$$

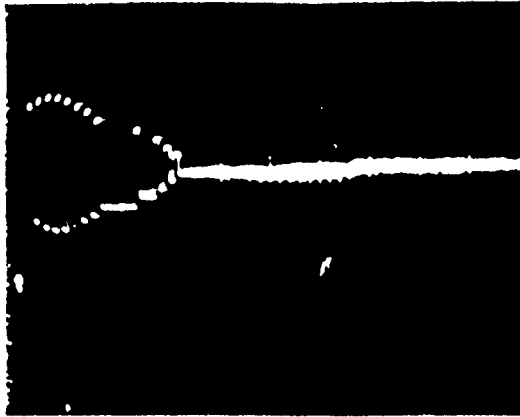


FIGURE 2. Oscillograph of  $v_{C_3}(\tau)$  during Operation of the Inverter.

Equations (4) - (9) were used to calculate the succeeding initial-final conditions on the capacitors, assuming the same pre-charged voltages used in the laboratory tests (4), and 50 volts for  $V_{VAS}$ . Table 1 shows data extracted from Figure 2 compared with data obtained from the Constant- $V_{VAS}$  Model. As can be seen, the envelope determined by the model matches quite closely the envelope obtained from the tests. Note that the envelope values determined by the model are within the estimated 10% accuracy of the test data out to the 15 alternation.

TABLE 1. Data for Comparison of Inverter Tests with the Model.

$v_{C_3}$ (mV/w) from tests (kV)	$v_{C_3}$ (mV/w) from $V_{VAS}=50V$ (kV)	Alternation No. (n)
-1.00	-1.00	0
1.25	1.26	1
-1.05	-1.14	2
1.35	1.35	3
-1.15	-1.23	4
1.40	1.39	5
-1.20	-1.26	6
1.40	1.37	7
-1.20	-1.24	8
1.30	1.29	9
-1.10	-1.17	10
1.20	1.18	11
-1.00	-1.05	12
1.10	1.02	13
-0.90	-0.90	14
0.95	0.83	15
-0.75	-0.71	16

TABLE 2. Values of Inverter Components.

Component	Value
$C_1$	960 $\mu$ F
$C_2$	4.39 $\mu$ F
$C_3$	4.89 $\mu$ F
$L$	30 $\mu$ H
$R_{CKT}$	23.2m $\Omega$

The component values used in Equations (4) - (9) in calculating the data points listed for the model in Table 1 had been obtained in earlier tests (3), and are listed in Table 2.



CONCLUSIONS For the VAS operating in a series resonant inverter, the use of a Constant- $V_{VAS}$  Model to represent the dynamic characteristics of the VAS is a valid approximation for high power (2 - 2.5 MVA) operation. Further tests are therefore warranted at other operating power levels.

#### REFERENCES

1. A. S. Gilmour, Jr., and D. L. Lockwood, "Vacuum Arc Inverter Switch Development Program", Proc. IEEE 1975 Naecon, pp281-288, June 1975
2. A. S. Gilmour, Jr., and D. C. Hopkins, "Recent Results of Vacuum Arc Switched Multi-Megawatt Inverter Tests", Proc. IEEE International Pulsed Power Conference, Texas Tech University, Lubbock, Texas, November 1976
3. D. C. Hopkins, "Construction and Energy Loss of a Vacuum Arc Switched Series Inverter", MSEE Thesis, State University of New York at Buffalo, Amherst, NY, February 1978
4. R. N. Miller, "Vacuum Arc Switched Inverters", PhD Dissertation, State University of New York at Buffalo, Amherst, NY, February 1979
5. R. N. Miller, R. E. Dollinger, and A. S. Gilmour, Jr., "High Repetition Rate, High Power Pulse Tests of Vacuum Arc Switches", Proc. IEEE Pulse Power Modulator Symposium, State University of New York at Buffalo, Amherst, NY, June 1978
6. R. N. Miller, et al, "A Multi-Megawatt, Vacuum Arc Switched Inverter for Airborne Applications", Proc. IEEE Pulse Power Modulator Symposium, State University of New York at Buffalo, Amherst, NY 1978
7. R. N. Miller, P. T. Glinski, and A. S. Gilmour, Jr., "A Facility for Testing High Power DC, AC, or Pulsed Devices", Proc. IEEE International Pulse Power Conference, Texas Tech University, Lubbock, Texas, November 1976

## 300-kJ, 200-kA MARX MODULE FOR ANTARES\*

K. B. Riepe, J. Bickford, J. Jansen, and W. Turner

University of California, Los Alamos Scientific Laboratory  
Los Alamos, NM 87545Abstract

Antares is a 100-kJ  $\text{CO}_2$  laser driver for inertial confinement fusion experiments. The power amplification stage is pumped by an electron-beam-controlled gas discharge. There are 24 annular discharge regions, each requiring energy input of 250 kJ at 550 kV, in a 2- $\mu\text{sec}$  pulse.

The energy storage module chosen for this system is a single-mesh pulse-forming network. To provide sufficient energy margin each module stores 300 kJ.

A prototype 300-kJ Marx has been built and tested at the Los Alamos Scientific Laboratory. This has been used as a test bed for components, triggering, and instrumentation.

Introduction

The Antares laser requires 24 Marx generators, each storing 300 kJ and capable of delivering more than 200 kA at 550 kV to a gas discharge load. Since reliability of this system is critical to the facility, a test and development program was implemented for critical components and a prototype Marx was built and tested. The main parameters of interest, in addition to operational reliability, were jitter and prefire rate.

Marx Design

The discharge circuit is a single-mesh pulse-forming network,<sup>1</sup> with 1.2-MV open-circuit voltage, 0.42- $\mu\text{F}$  capacitance, and <3- $\mu\text{H}$  in-

ductance. These circuit parameters are achieved using 60 kV stages with three parallel 2.8- $\mu\text{F}$  capacitors at each stage and a double-folded geometry<sup>2</sup> to give the required inductance. The double-folded geometry also results in good interstage capacitive coupling, which aids in achieving low jitter. In addition, the midplane trigger electrodes are coupled three stages down the Marx. The first three gaps are triggered externally. Charging is in the  $\pm$  mode, so the spark gaps run at 120 kV. The spark gaps are operated at a safety factor  $M = 2$  (self-breakdown voltage = 240 kV) to give a low prefire rate.

Spark Gaps

The Marx switches are high-pressure gas-filled spark gaps. These switches must handle the normal discharge conditions of 200  $\mu\text{A}$  and 1 coulomb, and occasional fault conditions of 400 kA and 5 C, while operating with very low jitter and low prefire rate. The individual switch jitter requirement is difficult to specify, because operation in a Marx generator involves many complicated transients. The switch prefire rate should be approximately  $10^{-5}$  for a system prefire probability of  $10^{-2}$  to  $10^{-3}$ , requiring that the gaps be operated with a high safety factor.

Since low Marx inductance is important the length of the spark gap should be as small as possible to keep the capacitor stacks close together.

Spark-Gap Design

The completed spark-gap design, which evolved after many modifications, is shown in Fig. 1. This switch has been tested for 2000 shots under

\*Work performed under the auspices of the U.S. Department of Energy

fault conditions with no measurable deterioration in performance. The parts are fabricated from materials as listed below:

End plates (2)  
 Electrode standoffs (2)  
 Electrode (disk) holder (1)  
 Snap ring, tapered (1)  
 Electrode hold-down bolt (2)  
 Insulating housing (2)  
 Compression thru-rods (6)  
 Compression thru-rod nuts (12)  
 Hemispherical electrodes (2)  
 Trigger disk electrode (1)

750 shots. Copper-filled tungsten more than exceeded the design criteria, lasting for 2000 shots with negligible erosion.

aluminum 6061-T6 plate or bar stock  
 aluminum bronze No. 618 bar stock  
 aluminum bronze No. 616 plate stock  
 carbon steel  
 threaded steel rod  
 cast nylon tubular bar  
 3/4-10 Permall "Superstud"  
 3/4-10 Permall ME glass  
 Plansee K25 copper-filled tungsten  
 Plansee K25 copper-filled tungsten

The overall length of the assembled switch is 25 cm, including the glass composition nuts used on the polyurethane/glass through-rods; the diameter of the switch is 25 cm. The main electrodes are hemispheres 5 cm in diameter with a gap spacing of 2.79 cm. The trigger disk electrode is 0.64-cm thick, 10.2-cm diam, with a 2.5-cm-diam center hole. The edge of the trigger disk center hole is machined with a full radius.

To keep weight and cost down, the end plates were made of aluminum. The trigger disk holder and main electrode standoffs were made from aluminum bronze, which is easily machineable and chemically more stable than aluminum or brass. The insulating housing was made from blue nylon because it had the best combination of mechanical properties, cost, and availability.

Because of the high current and charge transfer requirements, a high quality electrode material is required. It is known that the erosion of brass would be excessive at this duty. Several other electrode materials were considered. Their properties are shown in Table I.

When used in the short-circuit test (described below), molybdenum electrodes fractured in a few shots. We attribute the problem to moderate electrical (and thermal) conductivity combined with poor room temperature impact strength.

Zirconium copper survived, but eroded significantly in several hundred shots. Tungsten-filled copper eroded unacceptably after approx.

The final prototype survived 2000 consecutive operations under conditions which simulate a Marx fault. A schematic diagram of the test fixture and associated test parameters is shown in Fig. 2. A 120-kV, 27-kJ capacitor bank was switched into a low impedance circuit resulting in an oscillatory ring-down through the spark gap. This test generated a peak current of 460 kA, 9 coulombs per shot at 120 kV, a ringing frequency of 180 kHz, with a repetition rate of one shot per minute. The gap was operated with a safety factor of  $M = 2$ , requiring a pressure of 50 psig of dry air. It was purged with dry breathing air immediately after each shot. Purge duration was 10 seconds at 3.3 cfm.

After 2000 shots, the spark gap was removed from the test fixture and examined. The 5-cm diameter K25 electrode hemispheres showed insignificant wear. Black and brown surface discoloration and roughness were present indicating formations of oxides.<sup>3,4</sup> Cleaning the oxides from the surfaces revealed small amounts of surface pitting but no grain boundary erosion or cracks. The K25 trigger disk, 0.64-cm thick by 10.2-cm diam with a 2.5-cm-diam center hole exhibited some erosion. The hole had not enlarged. Preferential erosion was evident on a section of the surface oriented toward the negatively charged half of the capacitor bank. This erosion was in the form of localized pitting approximately 0.1-mm to 0.3-mm deep over an area of approxi-

TABLE I  
METALS INVESTIGATED

Metal	Property		
	Electrical Conductivity	High Temp. Strength	Room Temperature Impact Strength
Molybdenum	Fair	Excellent	Very Poor
Zirconium Copper	Excellent	Poor	Good
Tungsten-filled copper matrix	Good	Poor	Poor
Copper-filled tungsten matrix	Good	Excellent	Poor

mately  $1 \text{ cm}^2$  near the hole edge. The same oxide discoloration and roughness were present as on the hemispheres.

The interior surfaces of the nylon insulator were discolored, glazed and rough, but no cracks, burns, or electrical tracking were in evidence. It appeared as though heat had glazed the nylon, short wavelength radiation had discolored it, and hot, nonconducting metal oxides had splattered and coated the surfaces. Blue-colored powder (probably zinc oxide) had settled by gravity on the lower halves of each insulator. At the conclusion of the 2000-shot test, the dielectric strength of the nylon surface was still sufficient to hold off 120 kV for three minutes at a gas pressure of 30 psig ( $M = 1.2$ ). This test was repeated three times with several full-power shots between the three-minute holding periods.

The switch was tested for jitter at different operating voltages and pressures with a 0.25-ohm  $\text{CuSO}_4$  resistor installed to simulate actual operating conditions. A 500-ohm,  $\text{CuSO}_4$  resistor was inserted in series with the trigger electrode to simulate circuit values in the Marx generator. The test arrangement is shown in Figs. 3 and 4, and the test results are shown in Figs. 5-11. The trigger voltage amplitude and waveform (Fig. 5) was held constant for all jitter measurements. The time spread is on the order of 10 ns. The effect of trigger amplitude on jitter is shown in Figs. 11 and 12. A Hewlett-Packard 5370-A Time Interval Counter corroborated the oscilloscope data.

### Resistors

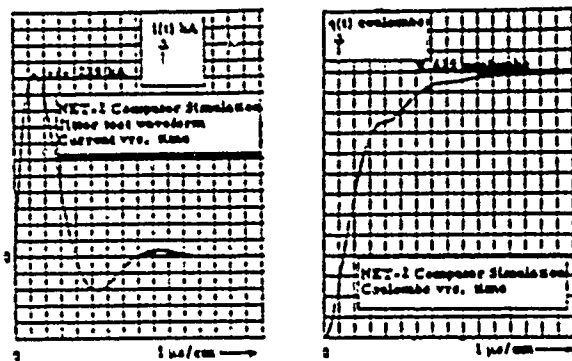
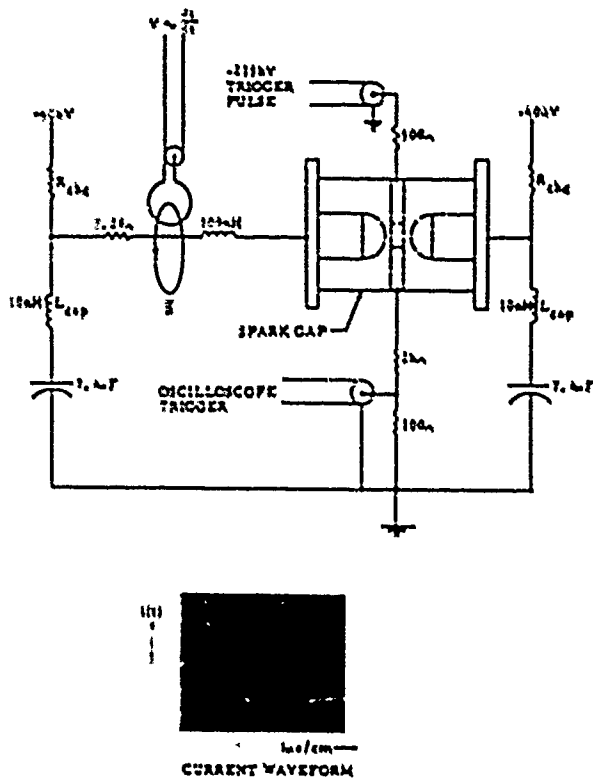
Most Marx generators have used liquid resistors for stage charging isolation and trigger coupling. We felt that liquid resistors would not provide the reliability required in this large system. Some type of solid resistor was preferred. We tested two types, wire-wound and Carborundum type AS. The test consisted of discharging a 170- $\mu\text{F}$  capacitor at voltages up to 11 kV (10 kJ) into the resistor. The resistors were first soaked in transformer oil. The wire-wound resistors were Dale 225 W, 100 ohm. They failed at 1/2 kJ, by melting of the coating. The Carborundum resistors were type 889 AS (12 in. long, 1 in. diam). They failed at 3 kJ by chipping of the material. These are rated by the manufacturer at 35 kJ when operated in air. We then tested some resistors which were coated with epoxy by the manufacturer to keep oil out of the resistor body. These were run up to 10 kJ, the limit of our test facility, without failure. This provided an adequate safety margin for use in the Marx generator.

### Marx Testing

A prototype Marx was built and tested to determine operating reliability, jitter, and pre-fire rate. Because the resistor development program was still in progress when the Marx was built, liquid resistors were used initially.

Jitter was measured using an HP-5370A time counter. The start signal was taken from the first stage of trigger amplification, a PATCO PT-70. The remainder of the trigger system con-





$I$ (peak)	• 225 kA
$V$ (solid)	• 120 kV
$q$ per shot	• 2.622 coulombs
Energy switched	• 27 kJ
$I$ ring-down	• 127 kA
Repetition rate	• 1 shot per minute

Fig. 4. Jitter test circuit parameters.

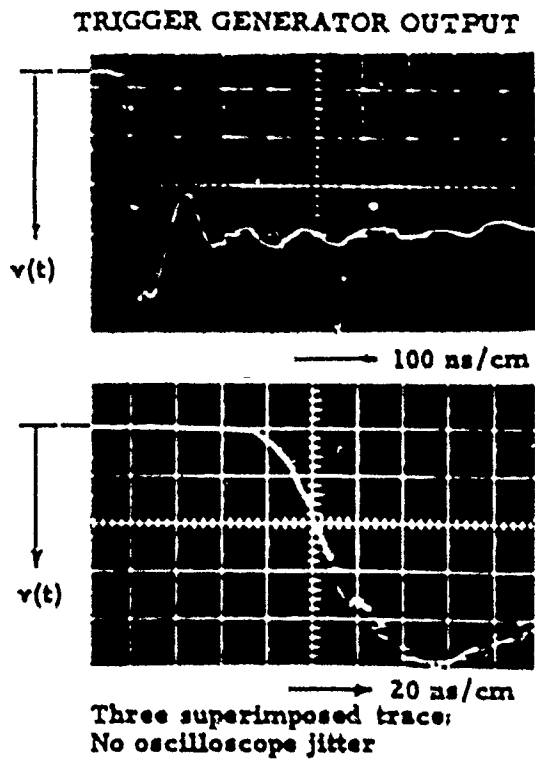


Fig. 5. Trigger generator waveform for jitter measurements.

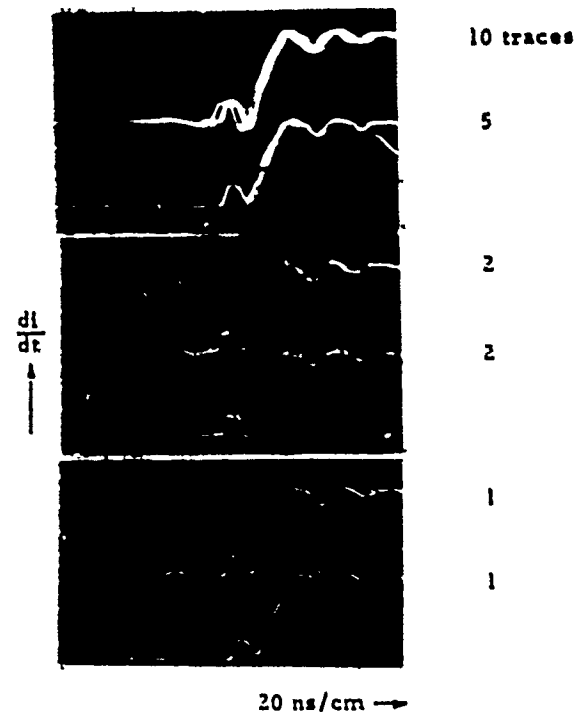
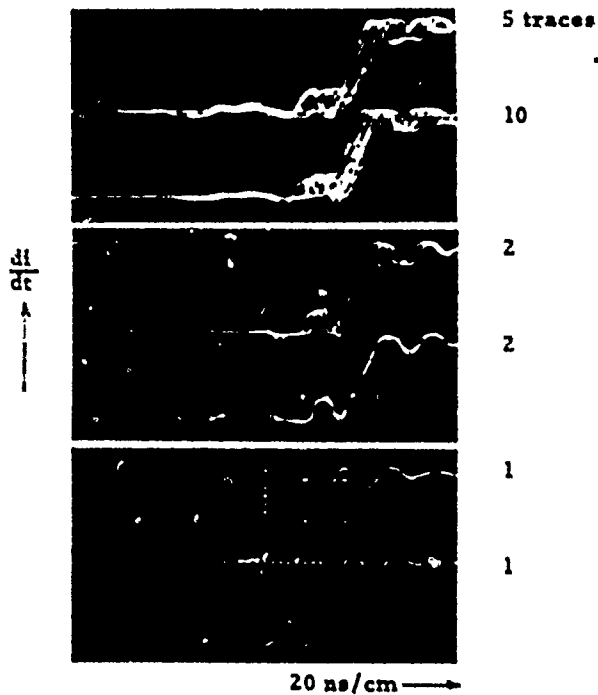
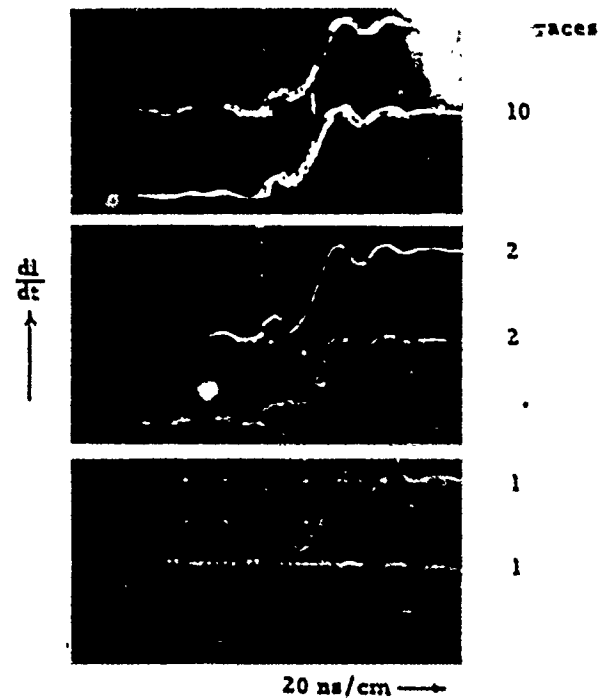


Fig. 6. Waveforms from spark-gap jitter test.



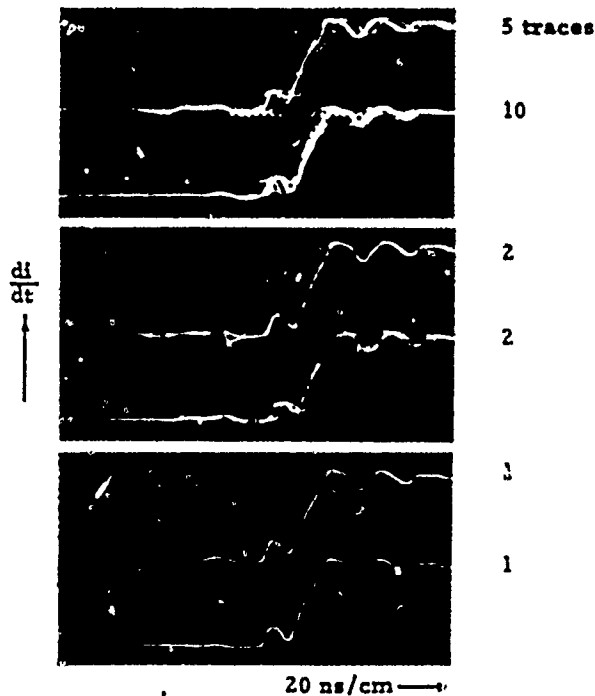
SPARK-GAP JITTER MEASUREMENT FOR  
80 kV 34 psig-air  $M_0 = 2$

Fig. 7. Waveforms from spark-gap jitter test.



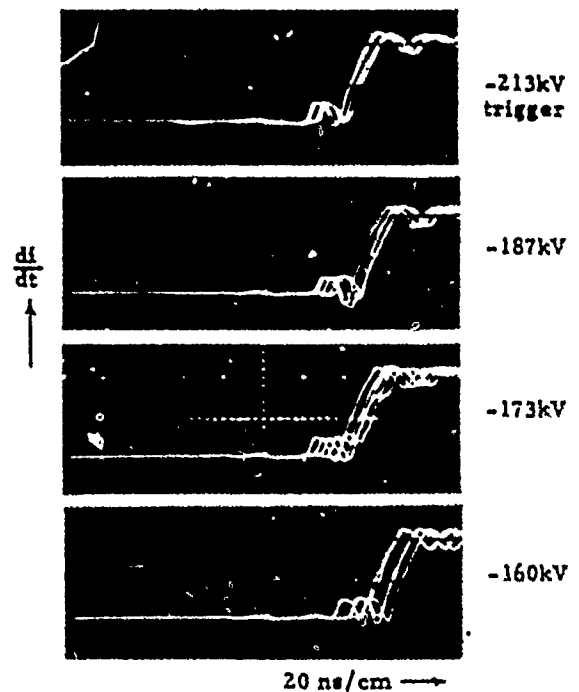
SPARK-GAP JITTER MEASUREMENT FOR  
120 kV 50 psig-air  $M_0 = 2$

Fig. 8. Waveforms from spark-gap jitter test.



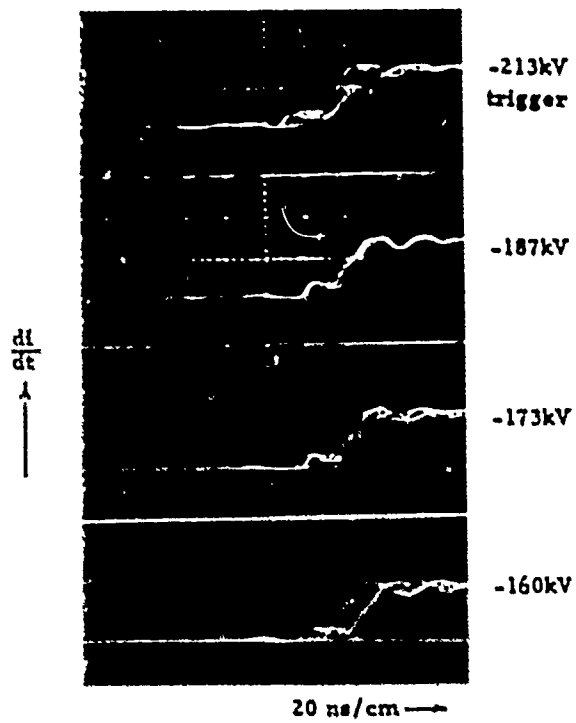
SPARK-GAP JITTER MEASUREMENT FOR  
80 kV 27.6 psig-air  $M_0 = 1.75$

Fig. 9. Waveforms from spark-gap jitter test.



JITTER vs TRIGGER VOLTAGE AMPLITUDE  
120 kV 50 psig-air  $M_0 = 2$

Fig. 10. Waveforms of jitter vs trigger amplitude.



JITTER VRS. TRIGGER VOLTAGE AMPLITUDE  
80kV 34psig-air  $M_0 = 2$

Fig. 11. Waveforms of jitter vs trigger amplitude.



## A LARGE-AREA COLD-CATHODE GRID-CONTROLLED ELECTRON GUN FOR ANTARES\*

W. R. Scarlett, K. R. Andrews, H. Jansen

University of California, Los Alamos Scientific Laboratory  
Los Alamos, NM 87545Abstract

The CO<sub>2</sub> laser amplifiers used in the Antares inertial confinement fusion project require large-area radial beams of high-energy electrons to ionize the laser medium before the main discharge pulse is applied. We have designed a grid-controlled, cold-cathode electron gun with a cylindrical anode having a window area of 9.3m<sup>2</sup>. A full diameter, 1/4 length prototype of the Antares gun has been built and tested. The design details of the Antares electron gun will be presented as well as test results from the prototype. Techniques used for the prevention and control of emission and breakdown from the grid will also be discussed.

Introduction

The Antares laser fusion system at the Los Alamos Scientific Laboratory (LASL) is designed to deliver up to 100 kJ of energy to a target in a 1-ns pulse. A low energy, short pulse of CO<sub>2</sub> laser light is split into six beams, each of which is then amplified in a laser power amplifier.

The annular pumped volume of each power amplifier is ionized by a radial beam of high-energy electrons produced in a central electron gun. Details of other aspects of the power amplifier and the Antares project are given elsewhere in these proceedings.

The electron-gun design is governed by several constraints. First, the electrons must have sufficient energy to penetrate the electron-gun window and the gas volume of laser gas between the windows and the power amplifier anode. For the range of operating pressures being considered for Antares, electrons having energy between 400 and 550 keV are required.

The second requirement is that the electron gun deliver a beam having uniform current density between 50 and 100 mA/cm<sup>2</sup> and lasting for 5 μs. This current density produces the required impedance in the gas for the main discharge.

A third constraint is that the spacing between anode and cathode must be sufficient to prevent vacuum breakdown.

Antares Electron-Gun Design

The solution to these constraints chosen for Antares is a cold-cathode, grid-controlled electron gun having a cylindrical geometry as shown in Fig.1. The cathode consists of 48 blades of 12.7-μm-thick tantalum foil, each 0.76-m long, arranged in 12 rows of 4 blades, 1 blade opposite the center of each window. An alternate design being considered is a spark cathode designed by G. Loda of Systems, Science and Software (S<sup>3</sup>) of Hayward, California.

The grid, consisting of an 80% transmitting stainless steel mesh, is self-biased by current flowing from the grid through a resistor to ground. The space charged limited current,  $I_K$ , for this geometry is given by:<sup>1</sup>

$$I_K = 14.68 \times 10^{-6} \left[ V_K - (1 - T)I_K R_g \right]^{3/2} \ell r_g^{-1} \beta^{-2} \quad (1)$$

where

$V_K$  is the cathode voltage  
 $T$  is the grid transparency  
 $R_g$  is the grid resistance  
 $L$  is the length of the cathode  
 $r_g$  is the radius of the grid

and  $\beta$  is a function of  $r_g/r_c$ , with  $r_c$  the cathode radius.

There are 48 windows in each electron gun, each 0.76 m x 0.25 m in size. Each window consists of a hitachi support structure covered by a window of 0.050-mm-thick titanium foil glued to a 0.9-mm-thick stainless steel rip-stop grid. The grid prevents damage to the interior of the electron gun in case of window failure by limiting the size of the rupture and thus the rate of rise of the internal pressure.

There are several advantages of the grid-controlled electron gun over the simpler diode geometry. First, the gun current can be controlled independently of the gun voltage and cathode-anode spacing. A diode electron gun meeting the Antares requirements would either be uneconomically large or would produce considerably more current than desired for ionizing the gas. Higher currents lead to shortened cathode and window lifetimes. The lower current of the grid-controlled gun also reduces the size of the high-voltage pulser required and reduces magnetic effects on the electron beam.

A second advantage is the current stabilization produced by the self-biased grid. This stabilizing effect certainly occurs for an ideal grid which does not show secondary emission. But it is also true that as long as the number of secondary electrons emitted from the grid surface for each primary incident is less than 1.0 the grid acts to stabilize the gun.

#### Prototype Results

In order to evaluate many aspects of the Antares design, a prototype power amplifier was constructed. Design details and initial measurements which confirmed the Antares design concept

have been reported by Leland.<sup>2</sup> After those tests were completed, it was decided to make a series of measurements to more fully characterize the electron gun.

One problem which was addressed is the control of vacuum breakdown. In the measurements reported by Leland<sup>2</sup> the cathode was shorted by a crowbar gap after 3  $\mu$ s. Even under these conditions, occasional cases of runaway cathode current were observed. During the period of these measurements, the silicon-based diffusion pump oil (Dow Corning 704) was deliberately allowed to backstream into the electron gun in order to suppress secondary emission from the grid. In this case the operation of the electron gun was in general agreement with the predictions of the space charge equation.

One of the goals of the present investigation was to eliminate the crowbar gap, thus simplifying the electron-gun pulser and improving its reliability. The electron gun must thus be capable of holding off the high voltage for a longer period of time without breakdown.

At the beginning of the present set of measurements the diffusion pump was drained, cleaned and refilled with a carbon-based pump oil (Convold 20). Once again, the pump oil was allowed to backstream into the electron gun. Two results were observed after this change. First, both the frequency and severity of breakdown increased. Upon later disassembly of the gun, several burn spots were seen on the cathode, grid, and anode. The second result was observation of anomalous grid current measurements, though the cathode current agreed with that predicted by Eq. (1).

We next disassembled the gun, carefully cleaned each part with solvent, and reassembled it, taking care to maintain cleanliness. The vacuum system was operated with a liquid  $N_2$  cold trap and a larger backing pump to prevent oil backstreaming. Other changes included the addition of corona rings to the cathode assembly to shield areas of unwanted field enhancement.

The most significant improvement made by this investigation has been the development of a grid conditioning technique consisting of first shorting

the grid to the cathode and then pulsing the grid using the electron-gun pulser. The series begins at low voltage ( $<300\text{ kV}$ ) and increases in  $50\text{-kV}$  steps until oscilloscope traces show an increase of grid emission. The voltage is then reduced until the excess emission ceases and the gun is operated for 5 to 10 shots. The gun voltage is then increased  $15\text{-}20\text{ kV}$  and the gun is operated until there is no excess emission for 5 to 10 shots. This process is repeated until a voltage is reached at which less than half of the shots show no increase of emission. In the prototype power amplifier this voltage is usually between  $-500$  and  $-600\text{ kV}$ , which is above the working voltage of the grid. The short is then removed and the gun is ready for operation.

The result of the cleaning, improved vacuum, and grid conditioning is a greatly reduced probability of breakdown. We occasionally see an increase in cathode current, but it almost always returns to normal after a few microseconds indicating that the grid is retaining control. Those pulses showing enhanced grid emission, usually do so only after approx.  $4\text{ }\mu\text{s}$  and thus, since the laser energy extraction occurs before this time, have no effect on the operation of the power amplifier.

A second result is an increase of cathode current over that predicted by Eq. (1). This effect can be, at least partially, explained by an observed increase in grid emission. This effect was not seen by Leland<sup>2</sup> and is possibly a result of the loss of inhibiting properties provided by the silicon pump oil which was used for his measurements.

Figure 2 shows the measured and calculated gun impedance as a function of time during one shot. Two calculated impedances are shown, one assuming the grid transparency is the geometrical value of  $80\%$  and the other using the measured transparency,  $T = 1 - I_{\text{grid}}/I_k$ . At present, we do not have a satisfactory explanation for the discrepancy; however, it does not have any adverse effect on the operation of the electron gun.

In order to achieve uniform pumping in the laser gas the intensity of the electron beam should be independent of position on the window. Using rectangular Faraday cups of size  $3.8\text{ cm} \times 25.4\text{ cm}$  we have measured the current density at several points on the window and found that at the edge it decreases to not less than  $80\%$  of the center value.

### Discussion

Several results have come from the prototype study which will be applied to the Antares electron gun. Since the probability of excess emission and breakdown depends on the emitter area, these problems can be expected to be worse in Antares. Thus, the grid conditioning technique and our improved understanding of the role of the grid in controlling breakdown is significant. Other prototype results give us confidence that the requirements for the Antares electron gun can be met by the present design.

### References

1. I. Langmuir and K. Blodgett, "Currents Limited by Space Charge Between Coaxial Cylinders," *Phys. Rev.*, Vol. 22, pp. 347-356, 1923.
2. W. T. Leland, et al, "Antares Prototype Power Amplifier -- Final Report," Los Alamos Scientific Laboratory Report LA-7186, 1978.

\*Work performed under the auspices of the U.S. Department of Energy

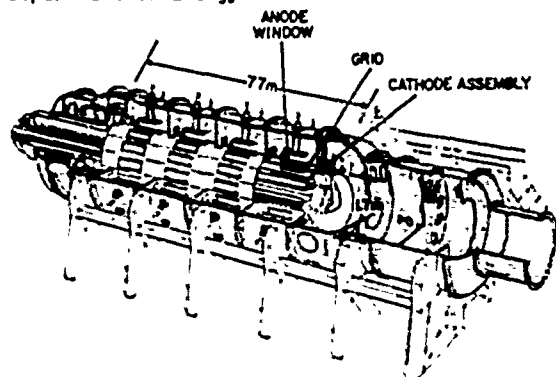


Fig. 1. Antares power amplifier schematic showing electron-gun part.

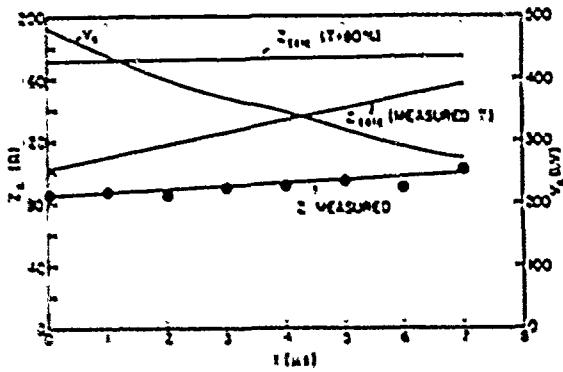


Fig. 2. Measured and calculated impedance and measured cathode voltage of the prototype electron gun with 800-ohm grid resistor as a function of time for a single shot.

## THE ANTARES LASER POWER AMPLIFIER\*

R. D. Stine, G. F. Ross, C. Silvernail

University of California, Los Alamos Scientific Laboratory  
Los Alamos, NM 87545Abstract

The overall design of the Antares laser power amplifier is discussed. The power amplifier is the last stage of amplification in the 100-kJ Antares laser. In the power amplifier a single, cylindrical, grid-controlled cold-cathode, electron gun is surrounded by 12 large-aperture CO<sub>2</sub> electron-beam sustained laser discharge sectors. Each power amplifier will deliver 18 kJ and the six modules used in Antares will produce the required 100 kJ for delivery to the target. A large-scale interaction between optical, mechanical, and electrical disciplines is required to meet the design objectives. Significant component advances required by the power amplifier design are discussed.

Introduction

The Antares laser is under construction at the Los Alamos Scientific Laboratory (LASL). This is a large (100-kJ) CO<sub>2</sub> laser for the inertial confinement fusion program. The power amplifier (Figs. 1 and 2) is the last stage of amplification in the optical chain. A cylindrical cold-cathode, grid-controlled electron gun is utilized to ionize the laser gas in the annulus surrounding the gun. Each power amplifier operates at 1800 torr of 1:4::N<sub>2</sub>:CO<sub>2</sub> laser gas and requires approximately 1 MJ of stored electrical energy at an operating voltage of 550 kV. An input light energy of less than 100 J is amplified in two passes through the power amplifier to an output energy of 18 kJ. Six power ampli-

fiers operating in parallel are required to produce the 100-kJ output for the fusion targets.

This paper discusses features of the power amplifier optical, mechanical, and electrical design, and their problem areas and solutions.

Optical Design<sup>1</sup>

A 15-cm-diameter annular input beam with an energy of less than 100 J is delivered to each power amplifier from the driver amplifier in the front end. It passes into the vacuum section through a 22-cm-diameter salt window. This input beam is divided by a central polyhedron beam splitter into 12 segments which are directed radially outward. Each of the 12 beams is reflected to a three-mirror corner cube which is used to adjust individual path lengths to obtain pulse synchronization. From the corner cube the light passes to a focus mirror then through a spatial filter. The beam enters the pressure vessel section through a 12.7-cm-diameter salt window, then through a group of four relay mirrors to the first amplifying section. The approximately 2.5-cm trapezoidal beam makes a first diverging pass through the four pumped regions to the back-reflector mirror where it is reflected for a second, near-collimated, pass through the amplifying sections. At the output of the pressure vessel the beam is transmitted through a 45-cm-diameter salt window to the two mirror periscope sections. Because of the radial geometry of the power amplifier, each amplifying sector, and therefore each beam, is a segment of an annulus. The periscope compresses the radius of the annular 12-sector beam array exiting the power amplifier to reduce the dimensions required downstream in the turning and target chambers.

---

\*Work performed under the auspices of the U.S. Department of Energy

The power amplifier design is primarily dictated by optical requirements.<sup>2</sup> The damage threshold for the transmitting windows limits the flux to about  $2 \text{ J/cm}^2$  average energy density for the nanosecond pulses. This average density provides an allowance for hot spots due to diffraction and non-uniform gain. The window damage limitation combined with state-of-the-art limits on window size means that the laser must exit through multiple output windows. For Antares this results in 12 windows per power amplifier, or 72 total output windows in the system.

An intensive development program at Harshaw Chemical Company, funded by LASL, has produced optical grade salt windows up to 45-cm diameter.<sup>3</sup> The windows are 8.9-cm thick to withstand the 3-atmosphere pressure differential. Each window is mounted between two Viton O-rings to provide a positive seal for both the 3-atmospheres pressure operating condition and the 0.1-torr vacuum when the laser gas is exchanged.

Another development program, at the Y-12 Plant of the Union Carbide Corp. in Oak Ridge, Tennessee, has produced the large mirrors used in the power amplifier (Fig. 3). Over 200 of these large mirrors are used in the power amplifiers. These mirrors utilize an aluminum substrate plated with a 1-mm-thick copper coating. The optical surface is produced by single-point diamond-turning (SPDT). Both flats and weak spherical mirrors are produced for the power amplifier. This technology provides an optical finish on odd-shaped mirrors at a reasonable cost as well as resulting in a higher damage threshold than conventionally polished mirrors.

Antiparasitic coatings such as LiF and  $\text{Fe}_3\text{O}_4$  have been developed which are highly absorptive at  $10.6 \mu\text{m}$ . These coatings will be used within the power amplifier to help eliminate harmful parasitics. Provision has been made in the power amplifier design for a saturable absorber cell to further reduce parasitics if necessary.

#### Mechanical

A number of difficult mechanical assemblies are required in the power amplifier. The pres-

sure vessel must operate at 3 atmospheres with a 1.65-m opening at one end for the electron gun and 12 openings, each 45 cm in diameter at the other end for the salt windows. Finite element analysis was utilized in the design of these complex elements to ensure adequate safety factors. The material is ASTM 516 Grade 70 pressure vessel carbon steel and was chosen because of good performance, dimensional stability, and low cost.

The electron-gun vacuum vessel is also made from ASTM 516 steel. This unit (Fig. 2) is 1.65 m in diameter and 7.7 m long. The vessel wall is penetrated by 48 openings for the electron beams. Each electron window opening is 75 cm by 25 cm with 0.8-cm wide hibachi ribs spaced on 6.3-cm centers down the length for window and shell support. The vacuum vessel is constructed from four finish machined cylinders each 1.65 m in diameter, 1.9 m long, with a 5-cm-thick wall. These cylinders are joined together using pulse-arc welding to give very low weld distortion, thus requiring no further machining after the welding.

The hibachi window openings are covered with 2-mil-thick titanium foil which allows the electron-beam to pass through and also provides the vacuum seal. The foil is attached to a punched-metal backing grid to form a rip-stop which prevents catastrophic window failure. Inserting and removing the electron gun posed a difficult mechanical problem. The solution was to develop special-shaped air bearings to fit the small space allowed, yet provide a reliable method for sliding the gun in and out of the pressure vessel with a minimum of force.

#### Electrical

The derivation of the power amplifier electrical parameters has been discussed previously.<sup>4</sup> The electrical problems in the power amplifier involve the anode, anode bushings, high-voltage cable, and the electron-gun design, including gun support bushings and electrical feed.

The high-voltage cables connect the gas pulser energy storage to the power amplifier.

These cables must withstand 550-kV pulses during operating conditions, and could see a voltage as high as 1 MV during fault conditions, e.g., when the electron-gun pulser does not operate. A fault protection gap has been designed for the power amplifier in an attempt to limit the peak voltage to <800 kV during fault conditions.

A number of utility cables were tested for this duty and only dry-cure polyethylene cables rated for at least 145-kV<sub>ac</sub> proved adequate. The outer semiconductive corona shield of the cable is used to grade the field distribution at the cable termination. These cables are about 7.5 cm in diameter. During the test program the cables were subjected to over 6000 shots at 800 kV and survived 100 shots at 1 MV.

An anode bushing was successfully tested at voltages up to 1 MV. This bushing uses shaped electrodes and silicon-rubber inserts to reduce the peak fields.

The cylindrical cold-cathode electron-gun concept was developed and tested in a full-scale prototype power amplifier.<sup>5</sup> This prototype unit is presently being used to test actual Antares hardware components under realistic operating conditions.

### Conclusion

This paper has presented the design of the Antares power amplifier and has discussed some of the key components. A number of problem areas and solutions were described.

### References

1. C. J. Silvernail and K. C. Jones, "Antares Power Amplifier Optical Design," LASL Conference on Optics '79, Los Alamos, NM, May 23, 1979.
2. T. F. Stratton and W. H. Reichelt, "Optical Design and Components for a 100-kJ CO<sub>2</sub> Laser," SPIE, Vol. 121, Optics in Adverse Environments (1977), pp. 128-130.
3. V. E. Straughan, "POLYTRAN<sup>®</sup> NaCl Windows for LASL Antares CO<sub>2</sub> Laser System," LASL Conference on Optics '79, Los Alamos, NM, May 23, 1979.
4. J. Jansen and V. L. Zeigler, "Design of the Power Amplifier for the HEGLF at LASL," Seventh Symposium on Engineering Problems of Fusion Research, Knoxville, TN, October 25-28, 1977.
5. W. T. Leland, J. T. Ganley, M. Kircher, and G. W. York, "Large-Aperture Discharge in E-Beam Sustained CO<sub>2</sub> Amplifiers," Seventh Symposium on Engineering Problems of Fusion Research, Knoxville, TN, October 25-28, 1977.

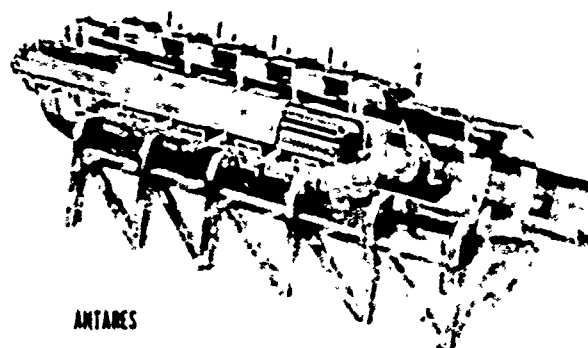


Fig. 1. The Antares Power Amplifier.

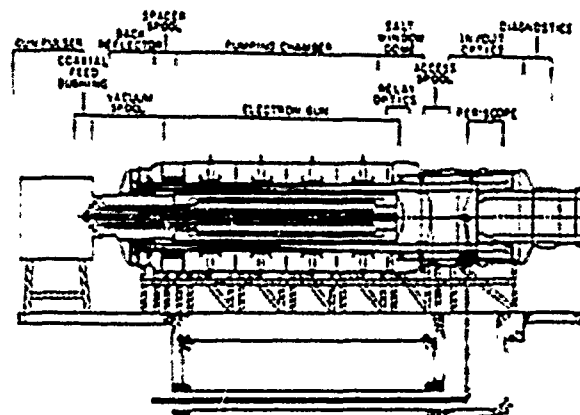


Fig. 2. Power amplifier longitudinal section.



Fig. 3. Antares power amplifier large mirror.

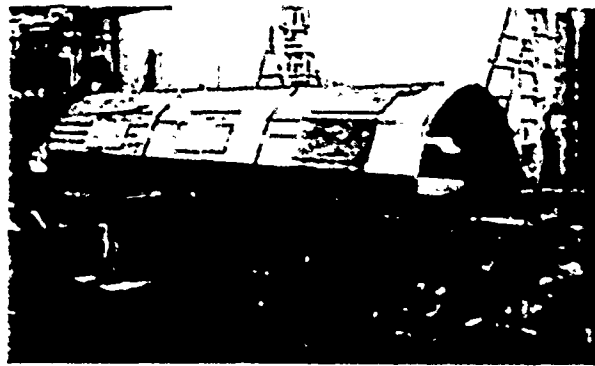


Fig. 4. Three of the four sections which make up the power amplifier electron-gun vacuum shell.



## A DOUBLE-SIDED ELECTRON BEAM GENERATOR FOR KrF LASER EXCITATION

L. SCHLITT

Univ. of Calif. Lawrence Livermore Lab,  
Livermore, California 94550

Abstract

Several laser systems excited by electron beam have been identified as candidates for pump sources for laser fusion applications. The electron beam generators required must be compact, reliable and capable of synchronization with other system components. A KrF laser, designated the A amplifier, producing a minimum output of 25 J was needed for the RAPIER (Raman Amplifier Pumped by Intensified Excimer Radiation) system. A double-sided electron beam system was designed and constructed specifically for this purpose and has produced >35 J of KrF output. Each of the two electron beam machines in the system operates with an rms jitter of 0.4 ns and together occupy  $3.5 \text{ m}^2$  of floor space.

System Design

The choice of electron energy is bounded from above by the combination of laser medium composition, maximum operating pressure, and desired output aperture, and from below by anode foil losses and the desire to keep the system impedance as large as possible. An output voltage of 300 kV was selected as a reasonable operating point. A Monte Carlo calculation of energy deposition was performed for a  $10 \times 10 \text{ cm}$  aperture by 50 cm long cell filled with 2 atm of a mixture of 96% argon and 4% krypton gases. The cell was bounded on two sides by 13  $\mu$  thick Havar foils and thick aluminum walls on the remaining sides. The calculation indicated that 30% of the energy incident on the foil is deposited in the laser medium. The spatial distribution of energy deposited as viewed in the plane transverse to the laser axis

is shown in Fig. 1 for two electron beams incident from opposite sides of the volume. Contours of equal energy deposited per unit volume are plotted for 80% and 90% of the peak value demonstrating that pumping is uniform to within  $\pm 10\%$  of the mean over nearly the entire volume. Allowing for a 20% loss to the anode foil support structure not included in the Monte Carlo calculation, the overall efficiency from the electron beam diode to energy deposited in the gas is 25%. Assuming that 5% of the deposited energy is converted to laser output, 500 J must be deposited requiring 1000 J from each electron beam which for a 60 ns pulse length implies a machine impedance of about 5  $\Omega$ . The diode current of 60 kA results in a current density of  $120 \text{ A/cm}^2$  in the diode. The required impedance and pulse length made a pulse charged water dielectric transmission line the obvious choice for forming the output pulse.

Since the A amplifier is to be used in a variety of pulse compression and stacking schemes involving synchronization with several other system components, timing jitter had to be kept to an absolute minimum. Thus a triggered output switch was chosen for the pulse forming line. The positive charged Blumlein configuration was selected for the pulse forming line because of the accessibility of the output switch for triggering and because the lower charge voltage permitted the design of a more compact four stage 400 kV Marx generator. The Blumlein itself is a cylindrically symmetric triax with an outer diameter of 36 cm. Extensive numerical calculations of electric field distributions in the output switch, pulse forming line and diode were used to minimize peak electric stress.

The output switch consists of two annular main electrodes with a disc shaped midplane trigger electrode. The interelectrode gap is 1 cm and operates at 300 kV when pressurized with 100 psig of  $\text{SF}_6$  gas. The trigger electrode is resistively biased at one-half the charge voltage and the trigger pulse is coupled to it through an oil-insulated ring capacitor. The charge current to the intermediate conductor flows along a rod which passes through this entire assembly as shown in Fig. 2.

The diode insulator is a flat lucite disc with the inner and outer line conductors shaped so that the electric field lines meet the insulator surface at  $45^\circ$ . The cathode mounting hardware is constructed of 15 cm diameter aluminum pipe housed in a chamber made from 22 cm diameter tubing in order to minimize diode inductance estimated to be  $<30$  nh. The cathode mounting hardware was polished to permit operation without spurious emission at the resulting 115 kV/cm electric fields.

#### Blumlein Tests

The Marx generator, pulse forming line, and output switch were tested and characterized prior to the completion of the diode and laser cell designs. A radial copper sulfate load resistor was constructed for the output of the line. The pulse shape obtained with the triggered output switch is shown in Fig. 3. The risetime indicates a switch inductance of 12 nh which implies that a minimum of two current carrying channels are formed when the output switch is triggered.

Obtaining low jitter operation of the output switch was crucial to the success of the A amplifier system. A trigger generator was constructed from barium titanate capacitors pulse charged from the Blumlein Marx. These capacitors were discharged by an over-volted spark gap into a 4 m long 50  $\Omega$  cable. The pulse amplitude delivered to a 50  $\Omega$  load resistor was  $\sim 150$  kV with a 10 ns risetime and an exponential decay giving 50 ns FWHM. After characterization the 50  $\Omega$  load resistor was removed and the cable connected to the

coupling capacitor of the output switch trigger electrode. A series of 20 shots were fired (one prefired) with the results shown in Fig. 4. The resulting standard deviation of the time between the arrival of the trigger pulse at the switch and the arrival of the output pulse at the load was 0.4 ns. This demonstrated the capabilities of the output switch though at present a different scheme is being used to trigger the system as described below.

#### Electron Beam Tests

Obtaining uniform emission from a cold cathode in electric fields  $<200$  kV/cm requires some gross field enhancement. A hexagonal stainless steel honeycomb material was selected for the cathode. The individual cells of the material are 3 mm across and are made of 75  $\mu$  thick foil. Electron probe images of the cathode indicate that an average of 3-4 emission sites are created at each cell resulting in acceptably uniform illumination of the anode plane.

The two nested coaxial transmission lines which make up the A amplifier Blumlein are charged in series with the innermost line charged through an inductor located near the diode insulator. During charging the voltage drop across this inductor also appears across the diode. To limit this prepulse voltage, the charging time for the line was set at 1  $\mu$ sec, the value of this inductor reduced to  $\sim 1.5$   $\mu$ h and a 100  $\Omega$  resistor placed in parallel with the inductor. This combination of parameters results in a voltage swing on the cathode from +35 kV to -20 kV during the charging of the line. These voltages are sufficiently large to cause unwanted emission from excessively field enhanced regions of the diode. To control this emission which can lead to a shorted diode by the time the output pulse arrives, the foil support structure is covered with an aluminized Kapton foil to shield it from the +35 kV portion of the prepulse electric field and the honeycomb cathode is surrounded by a stainless steel band to reduce the large field enhancement at the cathode corner. This combination shown in Fig. 5 eliminates

emission in the diode during the charging of the line.

The output pulse delivered to the diode is shown in Fig. 6. The voltage pulse which differs markedly from that obtained with a resistive load droops principally due to the low value of charging inductance required to minimize prepulse. The inductor and resistor are in parallel with the diode during the output pulse and subtract  $\sim 150$  J (12%) from the available energy. Plasma closure in the diode also contributes to the voltage droop. The shorter current pulse and slower current risetime suggest a delay in formation of the cathode plasma.

The characteristics of the electron beam after passing through the combination of anode foils and support structure were examined. The spatial profiles of the beam as measured with a film dosimeter are shown in Fig. 7. The beam energy measured with a carbon calorimeter was  $650 \pm 50$  J for each beam which is consistent with the amount of energy needed to produce 500 J deposited in the laser medium.

#### Triggering Systems

The initial laser experiments require only that the two electron beam machines fire within a few nanoseconds of each other. Rather than construct a separate trigger generator, the scheme shown in Fig. 8(a) was used. A pair of 50  $\Omega$  cables were pulse charged from each Marx. Both cables were connected to a single spark gap located midway between the two machines. This common switch operated in an over-volted mode shorting both cables and simultaneously producing trigger pulses for both machines. The rms jitter for this system has been verified as  $< 0.4$  ns.<sup>1</sup> More recently this common gap has been replaced with a trigatron gap which is triggered by a pulse formed with a laser triggered spark gap.<sup>1</sup> (Fig. 8(b)) The overall standard deviation from the arrival of the laser pulse to the arrival of the voltage pulse at the diode is 0.4 ns.

#### Summary

An electron beam system has been designed and constructed to pump a KrF laser which has produced  $> 35$  J of optical energy. The two machines which make up the system have been synchronized with each other and with another laser system with a measured rms jitter of 0.4 ns. This approach should permit the construction of larger, more complex electron beam pumped laser systems employing pulse stacking and pulse compression techniques.

#### References

1. R. Rapoport, private communication.

#### Acknowledgments

The author gratefully acknowledges contributions of T. Petach, D. Roberts, J. Swingle, D. Biggert, J. Taska and W. Smiley who assisted in design, construction, and testing of the A amplifier system. Work performed under the auspices of the U. S. Department of Energy by the Lawrence Livermore Laboratory under contract number W-7405-ENG-48.

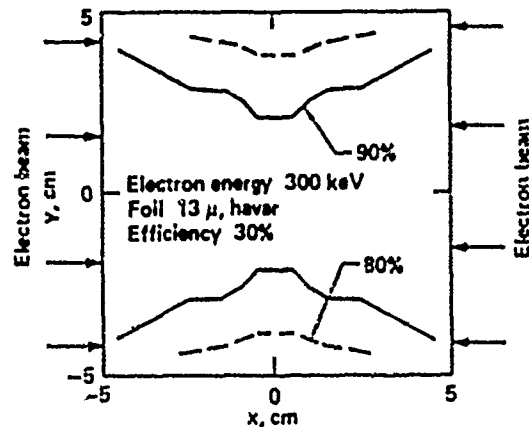


Fig. 1

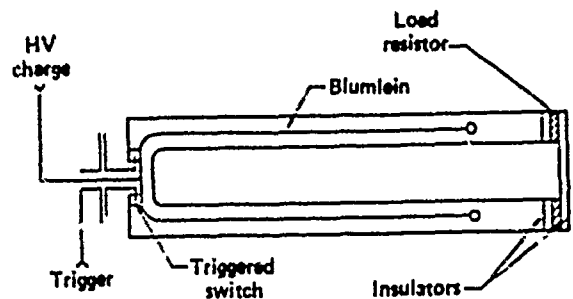


Fig. 2

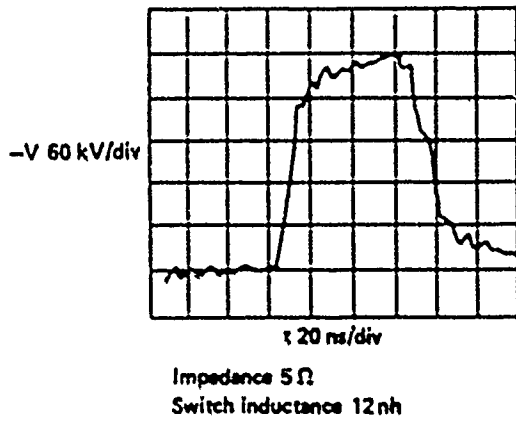


Fig. 3

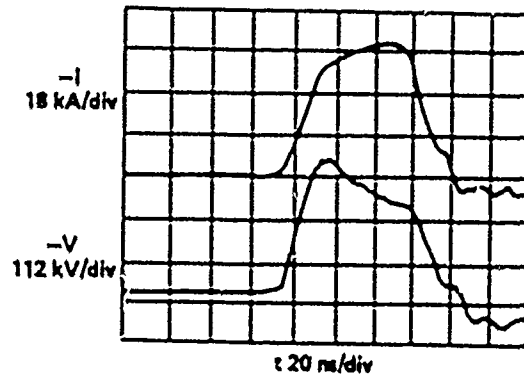


Fig. 6

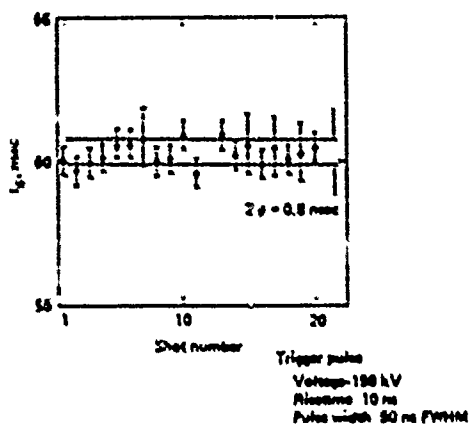


Fig. 4

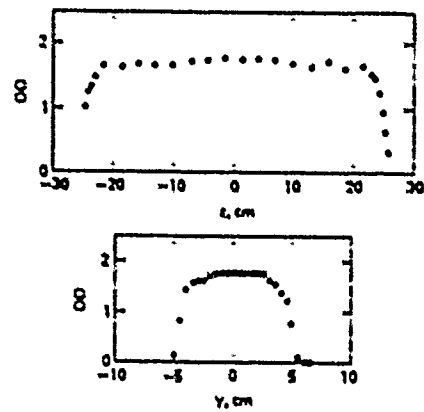


Fig. 7

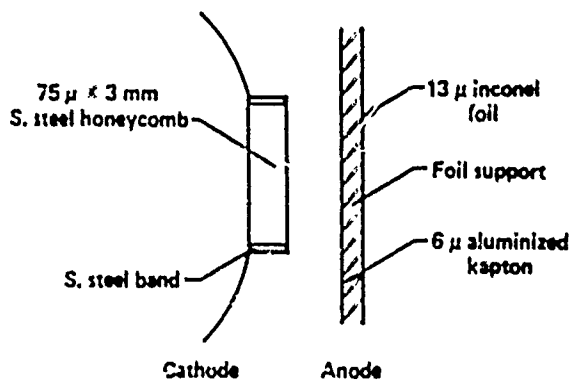


Fig. 5

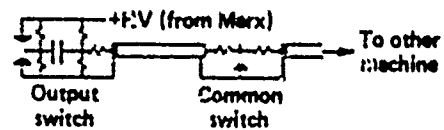
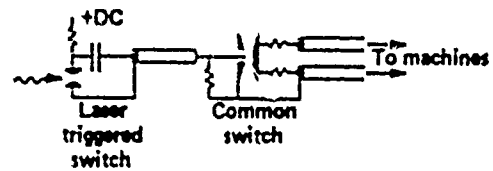
Self break trigger  $\sigma < 0.4 \text{ ns}$ Command trigger  $\sigma = 0.4 \text{ ns}$ 

Fig. 3

## ELECTRIC DISCHARGE CHARACTERISTICS OF CABLE PFN USED AS A PUMP\*

Robert R. Butcher, and Shyam H. Gurbaxani

University of California, Los Alamos Scientific Laboratory  
University of New Mexico, Los Alamos Center for Graduate StudiesAbstract

The cable pulse forming network (PFN) is an excellent pump for transverse discharge lasers. The effect of load characteristics on PFN design is discussed in detail. Experimental results are presented for a rare gas halide laser pumped by a cable PFN.

Introduction

Many pulsed laser systems require a pump capable of depositing the stored energy in a time comparable to the laser pulsewidth. For rare gas halogen (RGH) systems the pulsewidths are typically a few tens of nanoseconds. One type of pulse forming network (PFN) very well suited to this service is the co-axial cable PFN.

In order to design a PFN a few assumptions have to be made about the load. A typical transverse discharge RGH laser will have a breakdown voltage of 40 kV and an impedance of 1 ohm or less. For best laser performance the voltage on the laser should have a rate of rise ( $dV/dt$ ) of 500 V/nsec or greater. The load inductance including connections to the PFN must be kept low ( $< 10$  nH) in order to deliver the stored energy in 30 nsec.

The cable PFN shown in Fig. 1 meets these requirements quite well. The storage capacitor  $C_s$  is initially charged to a voltage  $V_0$ . On closure of the triggered spark gap switch S, the cable PFN begins charging through the interconnection inductance  $L_d$ . For charging times somewhat longer than the electrical length of the cables, the PFN can be treated as a single capacitor ( $C_c$ ) of value

$$C_c = \frac{\tau}{Z_0} \quad (1)$$

where  $\tau$  and  $Z_0$  are the one-way transit time and the characteristic impedance of the cable PFN. The voltage on the cable can be approximated by

$$V_c(t) = V_m (1 - \cos \omega t) \quad (2)$$

where the ringing frequency is calculated from

$$\omega = \frac{1}{(L_d C_{eq})^{1/2}} \quad (3)$$

where  $L_d$  is the inductance of the driver and the equivalent series capacitance is expressed by

$$C_{eq} = \frac{C_s C_c}{C_s + C_c} \quad (4)$$

where  $C_s$  is the capacitance of the storage capacitor and  $C_c$  is the cable capacitance. Since the charge divides between series capacitors, the peak voltage is expressed by the formula

$$V_m = V_0 \left( \frac{C_s}{C_s + C_c} \right) \quad (5)$$

where  $V_0$  is the initial voltage on the storage capacitor. It is worth noting that if  $C_s \gg C_c$ , the ringing frequency is determined by primarily  $C_c$  and  $L_d$ . Also, if the voltage is allowed to ring to its full peak value ( $\omega t = \pi$  radians) the voltage will nearly double. The time rate of change of voltage on the cables can be found by taking the derivative of equation (2) and is expressed as

$$\frac{dV}{dt} = V_m \omega \sin \omega t \quad (6)$$

which can be used to find the current in the switch.

$$I_s = C_c \frac{dV}{dt} \quad (7)$$

When the laser reaches breakdown the load current

will be approximately

$$I_L = [I_{PFN} + I_g] \{1 - \exp(-\frac{R_L \tau}{L_L})\} \quad (8)$$

where  $L_L$  is the load inductance,  $R_L$  is the load resistance, and the current due to the PFN is

$$I_{PFN} = \left[ \frac{V_{bd}}{R_L + Z_0} \right] \left[ U(\tau) - U(\tau - 2\tau) \right] \quad (9)$$

where  $V_{bd}$  is the breakdown voltage and the unit step functions specify a rectangular pulse of width  $2\tau$ .

#### Experimental Results

Several PFNs of this type have been used at LASL with excellent results. The following data are taken from one typical laser system. The laser discharge cross section is 12 mm x 19 mm which results in a 138 cm<sup>3</sup> volume over the 0.6 m electrode length. A gas mix of 3.05 torr F<sub>2</sub>, 55 torr Kr, and 3150 torr He was used. The PFN consisted of 48 parallel coaxial cables (Essex 40/100) of 2.44 m length. This results in an impedance ( $Z_0$ ) of 0.63 ohms and a one-way transit time ( $\tau$ ) of 15 nsec. Laser inductance was estimated at 8 nH. The electrical driver was a two-stage Marx generator having a capacitance of 150 nF per stage charged to 48 kV DC. The inductance of the driver ( $L_d$ ) was calculated at 275 nH.

The resulting voltage and current waveforms are shown in Fig. 2. The voltage rises to 42 kV breakdown in 30 nsec. At that time the current begins to flow and reaches 62 kA in 36 nsec. Figure 3 shows the resultant power and energy curves. Power is calculated from the instantaneous product of voltage and current, and energy is the time integral of the power. The ratio of voltage to current provides the time varying impedance shown in Fig. 4. The power delivered by the PFN is  $1.3 \times 10^9$  W in a 32 nsec FWHM pulse. This results in an energy deposition of 40 J during the pulse. The laser delivered an energy of 580 mJ per pulse in this configuration. The laser impedance during the pulse varies from infinite (just before breakdown) to near zero at the end of the pulse, which is probably the result of an arc.

A considerable effort has been devoted to studying the time varying resistance and its effect on PFN design, but the results are outside the scope of this paper.

#### Summary and Discussion

The cable discharge PFN has been discussed in detail, both in the charging and discharging modes of operation. Experimental results presented show this type of PFN is well suited to the generation of multi-gigawatt pulses in low impedance loads, even when the impedance varies with time. Experiments are in progress at LASL to design lower impedance higher power PFNs capable of pumping RGH lasers.

\*Work performed under the auspices of the US DOE

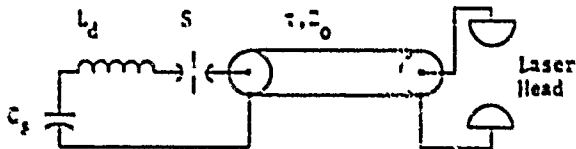


Figure 1. Schematic of Cable PFN

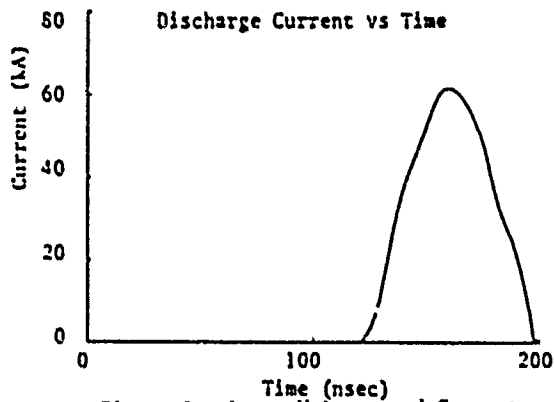
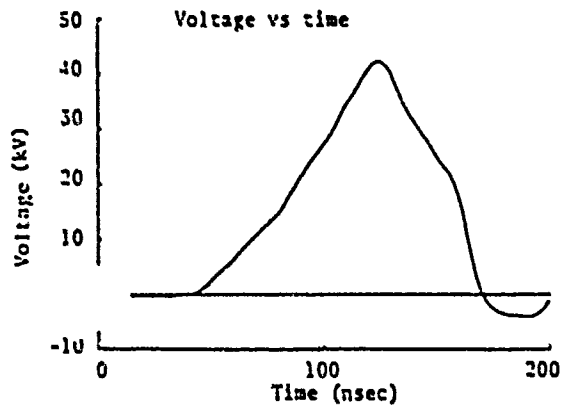


Figure 2. Laser Voltage and Current

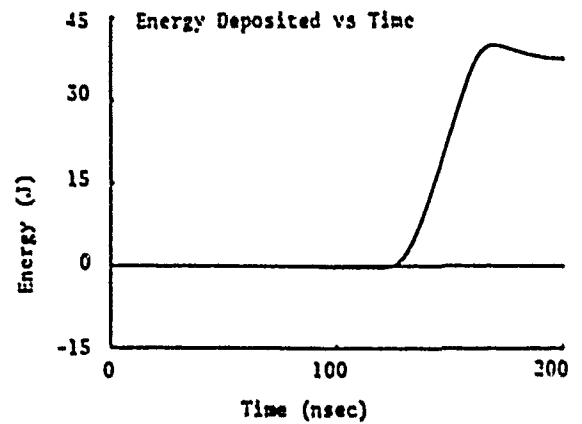
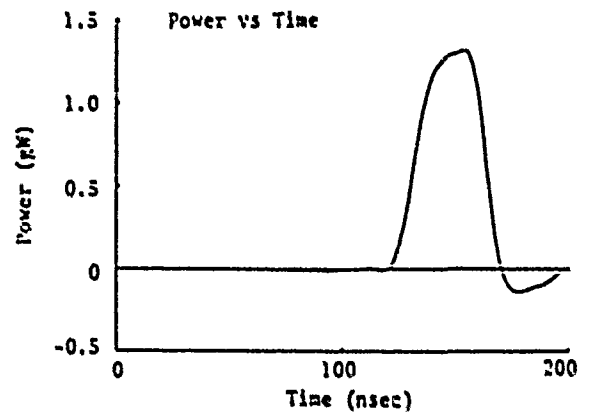


Figure 3. Instantaneous Power and Energy Deposited

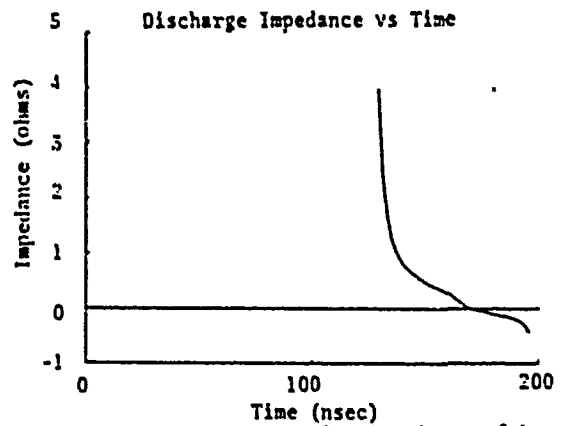


Figure 4. Time Varying Impedance of Laser

## INVITED

## TRIDENT - A MEGAVOLT PULSE GENERATOR USING INDUCTIVE ENERGY STORAGE

D. Conta, R. D. Ford, W. H. Lupton, I. M. Vitkovitsky

Naval Research Laboratory  
Washington, D.C. 20375

Abstract

A megavolt level pulse generator, TRIDENT, has been constructed utilizing an inductive store as the primary pulse forming device. The 2.5  $\mu$ H coaxial storage inductor can be energized with up to 500 kA obtained from a 500 kJ, 60 kV capacitor bank. Current interruption is accomplished using a three stage opening switch comprised of an explosively actuated switch in parallel with foil and wire fuses. The generator has been operated at the 410 kA charge level (70% energy) to produce 700 kV pulses with risetimes of 150 nsec. Energy has been deposited into a 7.5  $\Omega$  resistive load at a rate of  $5 \times 10^{10}$  W. Operation with optimized fuse dimensions and at full charge is anticipated to approach megavolt outputs at powers of  $10^{11}$  W. Future experiments include utilizing a homopolar generator as the current source.

Introduction

The development of high power pulse generators using capacitive energy storage has achieved levels of tens of terawatts at energies of a few megajoules.<sup>1,2</sup> The next generation of experiments to be performed using pulse power technology will require energies of several tens of megajoules. The combination of size, complexity, cost, and, in some cases, limitation of electrical parameters of such machines is prohibitive. In anticipation of this requirement, NRL has undertaken a program to develop compact inductive energy storage pulse generators which utilize inertial energy stores, i.e. homopolar generators,<sup>3,4</sup> as the primary energy source.

As recognized in every previous experiment applying inductive energy storage, the major component problem

is the opening switch. Our approach to this problem has been to begin with those types of switches which have exhibited the most promising characteristics (e.g. opening times, high current capabilities, rapid high hold-off recovery, low loss, etc.) with respect to the present state of technology. The results of this work indicated that an effective opening switch could be designed by paralleling explosively actuated switches with foil and wire fuses. As a demonstration of this switching scheme, the TRIDENT pulse generator was designed and fabricated. The goals of this experimental pulse generator were to demonstrate megavolt capabilities at 500 kA current levels with 100 nsec risetimes while delivering a few tens of kilojoules to a resistive load. The remainder of this paper describes the switching scheme, the design of the pulser, operation to date, and future experimental plans.

Three Stage Opening Switch

The three stage opening switch was developed especially to be compatible with the slow risetimes (seconds) typical of homopolar generators, but yet retain the fast opening potential (10's of nsecs) of wire fuses. A schematic diagram of the three stage switch circuit is shown in Fig. 1. The first stage of this switch is an explosively actuated switch. This switch has been described in detail elsewhere.<sup>5,6</sup> Briefly, it consists of a thick wall aluminum tube which acts as a current conductor. Sharp edged rings (cutters) and full radiused rings (benders) are alternately placed around the tube and spaced using polyethylene insulators. A length of primer cord is placed along the axis of the tube and



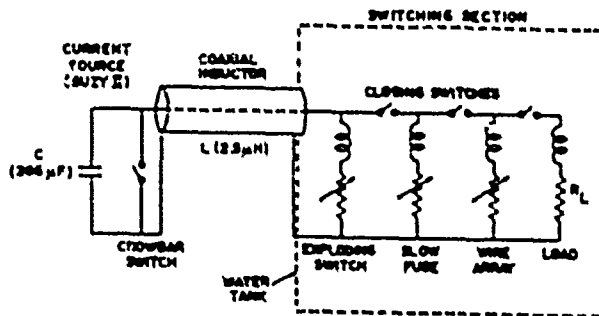


Fig. 1. Schematic diagram of the TRIDENT inductive storage pulse generator.

the tube is then filled with paraffin. Detonation of the primer cord by an exploding bridgewire detonator forces the paraffin against the tube which is then severed circumferentially by the cutting rings and folded around the bending rings. For operation in water, the region immediately adjacent to the bending rings is filled with styrofoam to exclude the water and thus provide a compressible medium into which the severed aluminum rings can be driven. Each gap generates an arc voltage of 200-700 V, depending on the current carried, with a risetime of approximately 20  $\mu\text{sec}$  (opening time). The outstanding characteristic of this switch is its low loss in the conducting state. This feature allows the storage inductor to be charged at relatively slow rates. Its slow opening time and relatively low resistance in the open state are the reasons that succeeding stages are required for high voltage, fast pulse applications. If this switch is to be operated in high voltage applications, current must be commutated away from the switch for a time period of 40-50  $\mu\text{sec}$  before any high voltage is applied. During this interval the switch has recovered to a hold-off level of 10 kV/cm.

Commutation for this interval has been accomplished with fuse elements chosen with appropriate cross sections. The majority of our work has employed water tamped aluminum foil fuses for this element. Fuses with this duration time to explosion generate maximum voltages of 6 kV per cm length of fuse. Current interruption times for these fuses range from 3 to 5  $\mu\text{sec}$ . These times are still too slow

for many applications and, in order to achieve the high voltages, the mass of the fuse material to be vaporized accounts for a significant amount of system energy.

The 100 nsec risetime, high voltage pulses can be generated by commutating the current from the foil with another fuse element with a small cross section designed to explode in the microsecond time range. These fast fuses can generate self-field stresses approaching 20 kV/cm without restrike. Most of the work at NRL has employed wire fuses for this element. Copper wires have been used over aluminum wires mainly because of the fragile nature of aluminum wires. Ideally, wires of minimum mass should be used, however, the actual cross section necessary is dependent on the recovery characteristic of the slower preceding foil fuse. A small scale experiment conducted at the 10 kA level using a two stage foil and wire fuse arrangement has produced the foil fuse recovery characteristic shown in Fig. 2. The two curves were for commutation out of the foil in the 3 and 4 kV/cm self stress range because at lower fields the fuse is not completely vaporized and at higher fields unnecessary energy dissipation occurs. The significant feature of this data is that after 2  $\mu\text{sec}$  of commutation the foil fuse can withstand electric fields of 20 to 25 kV/cm without restrike. The reason for the decrease in the recovery characteristic at times out to 10  $\mu\text{sec}$  is not understood,

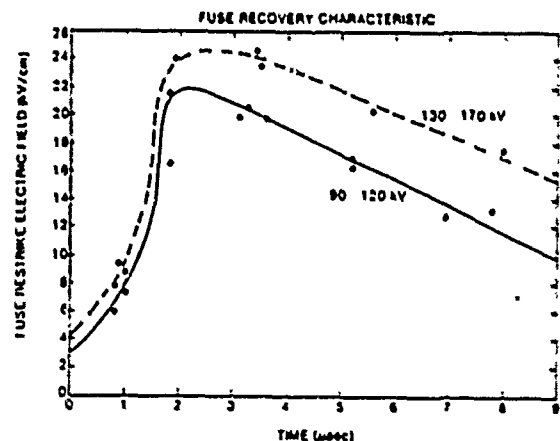


Fig. 2. Foil fuse high voltage recovery characteristic.

but has not been pursued because these longer times are presently not of interest. The factor of six gained in hold-off electric field over the self generated electric field matches, by coincidence, the factor of six in voltage multiplication typically measured from the wire fuse in our two stage switching experiments.<sup>6</sup> This rapid recovery to a high hold-off voltage minimizes the volumes of both foil and wire fuses required and hence minimizes the energy required. It also allows for a fast time to explosion to be used on the last stage and consequently the capability of attaining submicrosecond output pulses exists. Voltage waveforms from the operation of a three stage switch at the 340 kA level are shown in Fig. 7 and described in the experimental results section.

#### Design of the TRIDENT Pulse Generator

The design of the TRIDENT pulse generator was based on the requirement that voltages of 1 MV were to be produced and that currents in the sub-megampere range be employed. Additionally, the current source was to be the NRL SUZY II capacitor bank which stores 480 kJ at 60 kV (266  $\mu$ F). Calculations to predict the operation of the generator were performed at two levels. First, inasmuch as several switch component designs would be used, simple calculations based on the exploding switch arc characteristic and abrupt resistance changes for fuse elements were performed to permit construction of the inductor and tank for containing the switches. Following construction, inductances of actual switch circuits were measured and calculated. These inductances were inserted into equivalent circuits along with empirical descriptions of fuse vaporization characteristics for more precise simulations. Comparison of these calculations with actual circuit performance provides information for the design of future generators. The remainder of this section provides a description of the pulse generator which was constructed on the basis of the simple calculations. It is followed by a sample calculation in which detailed switch descriptions are used and stray inductances are included.

The early calculations indicated that a storage inductance of 2.5  $\mu$ H energized with 500 kA would pro-

duce output pulses of greater than 1 MV with rise-times of 100 nsec when discharged through the three stage opening switch. In order to eliminate mechanical problems arising from forces generated by the high currents, the storage inductor was constructed as an oil filled, 18 ft long coaxial line with an outer conductor diameter of 14 in and an inner conductor diameter of 2 in. This choice facilitated connection of the bank collector plate to the tank containing the switching arrangement as is shown in the experiment plan view of Fig. 3. The inductance of this line is 2.2  $\mu$ H. All mechanical forces acting during pulsing will tend to center the inner conductor as opposed to the coil type design in which the forces would deform the coil. The dimensions of the coaxial line were chosen so that electric breakdown would not occur for 500 nsec wide pulses until the voltage exceeded 2.2 MV. The expected pulse rise-times were long enough that transit time effects in the line would not be a major problem.

The bulk of the fuse work performed at NRL used de-ionized water as the ramping medium. To continue using this medium, the entire three stage switch system was placed in a 6 ft x 10 ft x 6 ft water tank. The switches themselves only occupy approximately 1/3 of the tank. A larger tank was fabricated to accommodate future experiments. The oil filled coaxial inductor was interfaced to the water tank through a 1 in polyurethane diaphragm to a short water insulated coaxial line. The total inductance of the circuit through a switch channel is 3.5  $\mu$ H.

To more precisely control the transfer of current between switch stages and to allow each switch to open to a desired state before the application of high voltage, closing switches are placed between elements. Because the arc voltage of the exploding switch is low and the opening times are relatively long, a solid dielectric, detonator-triggered switch is used to commutate the current to the foils. Commutation from the foils to the wires and the wires to the load is accomplished using self closing water gaps.

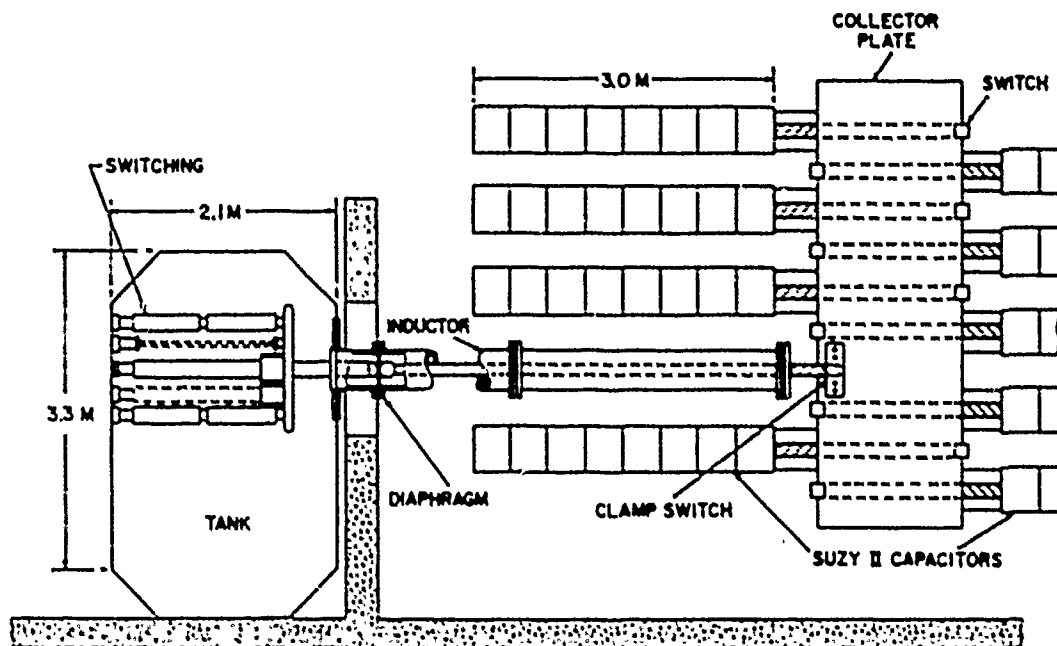


Fig. 3. TRIDENT experiment floor plan.

The quarter cycle period of the capacitor bank ringing through the inductance is approximately 50  $\mu$ sec. To provide a DC current through the inductor, the capacitor bank is crowbarred (clamped) using an explosively driven switch when the current in the inductor reaches its peak value. The e-folding decay time for the crowbarred inductor is 500  $\mu$ sec. Since the commutation time for the exploding switch is approximately 50  $\mu$ sec, the capacitor bank can be operated in the non-crowbarred mode to test the performance of the final two fuse stages independently of the explosively actuated switch.

To accommodate the switches, the inner conductor of the coaxial inductor was terminated in a "T" shape in the tank (Fig. 3). Five equally spaced 2.5 inch saddles were welded to the "T", with a similar saddle attached to the opposite wall of the tank 55 inches away. A current shunt is incorporated into the mount at the wall so that the current through each stage could be measured independently. The switching elements and a cylindrical copper sulfate resistive load could be arranged in any configuration on this "T". Typically, the switches and load were arranged to provide the most favorable for current

commutation between successive stages.

The explosively activated switches, because they employ a 2.5 in diameter tube for conduction, fit directly into the saddle shaped sockets. The fuse elements were stretched on various rack type devices. The most successful of these racks is designed around the same tube used for the exploding switches. The center section of a tube is removed and replaced with an appropriate length of insulator, usually polyethylene. Plates with clamps for foils or pegs for wires are machined so that they slide over the aluminum tube sections. They can be clamped at any location on the aluminum tube as dictated by the fuse lengths.

Measurements and calculations show that each switch stage has an inductance of approximately 1  $\mu$ H, thus forming a 3.5  $\mu$ H total loop inductance with the coaxial line. The inductance of the loops between adjacent switches is approximately .5  $\mu$ H. This is the inductance which determines the commutation time between stages. Circuit analysis has been performed using these values and allowing the fuse conductivity to vary according to an empirically determined con-

ductivity vs. energy relationship (Fig. 4). The conductivity curve was obtained from current and voltage measurements of single aluminum foil fuses operated in an open circuit (i.e. no load) condition at a peak current level of 10 kA and a time to explosion of 200  $\mu$ sec. The aluminum wires are assumed to follow the same relationship. Figure 5 shows the results of this analysis for a resistive load of 14  $\Omega$  with .5  $\mu$ H of inductance. The voltage is approximately 1 MV at the peak current of 70 kA for a peak power of  $7 \times 10^{10}$  W. For this simulation the initial inductor current was 490 kA. The explosively actuated switch arc voltage was 13 kV with a total conduction time of 30  $\mu$ sec. The aluminum foil fuses were .5 m long with a cross-section designed to explode in 40  $\mu$ sec. The aluminum wire fuses were .5m long with a cross-section designed to explode in 2.5  $\mu$ sec. The current was commutated away from the foil when the self-generated electric field was 3.2 kV/cm. These waveform shapes are characteristic of inductive energy store pulsers. The load risetimes show the opening characteristics of the final switching stage slowed by the commutating inductance.

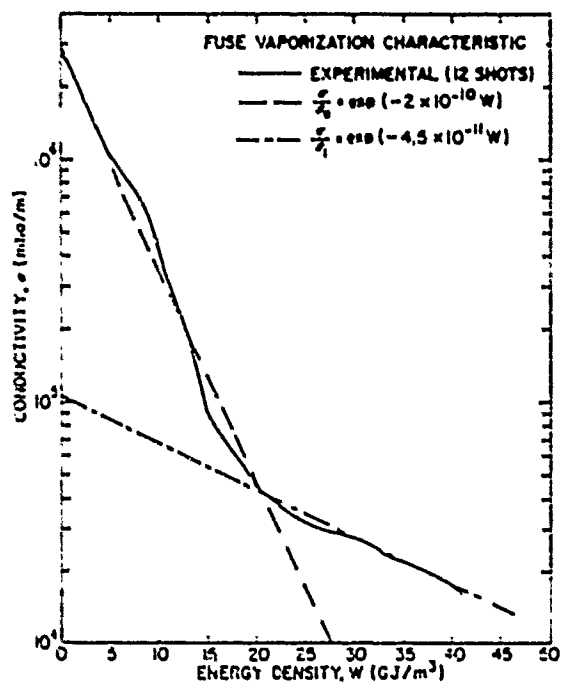


Fig. 4. Conductivity vs. internal energy relationship for aluminum foil fuse. Zero energy corresponds to the onset of vaporization.

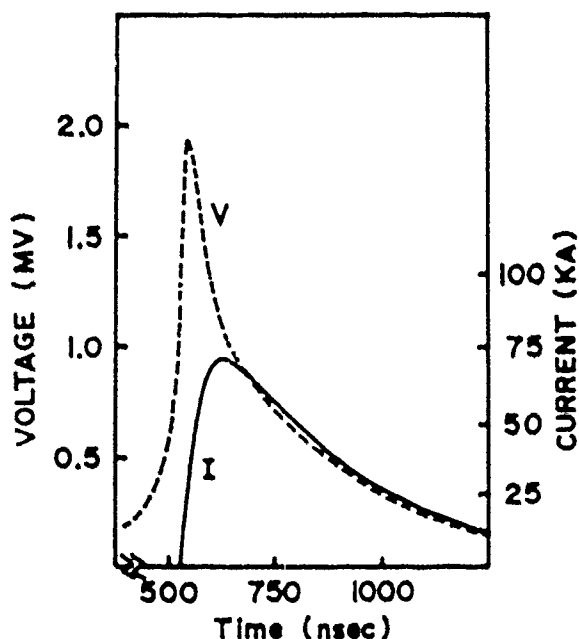


Fig. 5. Computer simulation for TRIDENT experiment driving a 14  $\Omega$  resistive load with .5  $\mu$ H of series inductance.

The fall times are the L/R decay times of the storage inductance plus load inductance through the load resistance.

#### Experimental Results

To date the TRIDENT experiment has been operated with a maximum voltage of 50 kV on the capacitor bank (388 kJ stored) which corresponds to a peak current of 410 kA in the storage inductor. This level of current has produced output pulses of 700 kV with risetimes of approximately 150 nsec. Energy has been deposited into a 7.5 resistive load at a rate of  $5 \times 10^{10}$  W. This is a power multiplication of 90 over the power level being dissipated by the resistance of the initially crowbarred inductor.

Early TRIDENT data showed that the arc resistance of the exploding switch was much lower at high currents than expected and the excessive burning in the switch degraded the recovery characteristic. For example, early prototype switches had arc resistances of approximately 300 m $\Omega$  at 50 kA, while TRIDENT shots using similar switches at 240 kA and

400 kA had arc resistances of 50 m $\Omega$  and 20 m $\Omega$ , respectively. To overcome this problem the switch was divided into two modules, a short module containing only 16 switch gaps and a long module containing 31 gaps. (Fig. 6) For circuit operation, the short module, which was placed on the ground end of the switch, was fired first. The number of sections for this module was chosen so that the voltage was sufficient for a reasonable commutation time to the foil fuse. The timing for the firing of the second module was chosen so that it would start opening just prior to complete commutation out of the exploding switch. Since this switch is opening under essentially zero current conditions, there is no burning in the switch and it presents a clean open switch to the high voltages reflected by the succeeding fuse stages.

The long module has operated at least at a recovery voltage of 10 kV/cm. The actual stress across open gaps may be higher. Due to the relatively slow propagation time of the detonation along the primer cord (7-8  $\mu$ /sec), only 60% of the gaps are probably open when the high voltage is applied. Future switches will be detonated in several locations along its length to decrease the time for complete switch opening.

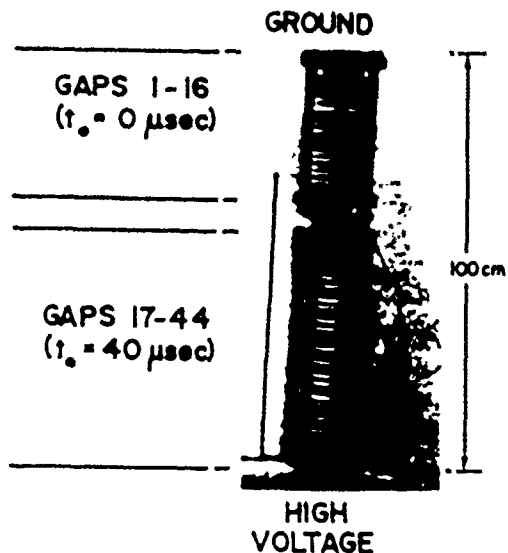


Fig. 6. Photo of double module explosively actuated switch.

Commutation of current to the foil fuse has had good success. Failure to commute has usually been caused by a failure of the closing switch in the foil path. The inductance of the commutation circuit is approximately .5  $\mu$ H and the arc voltage generated by the exploding switch is 3-7 kV, so commutation times range from 20 to 40  $\mu$ sec. A representative oscilloscope trace showing commutation from exploding switch to foil is shown in Fig. 7.

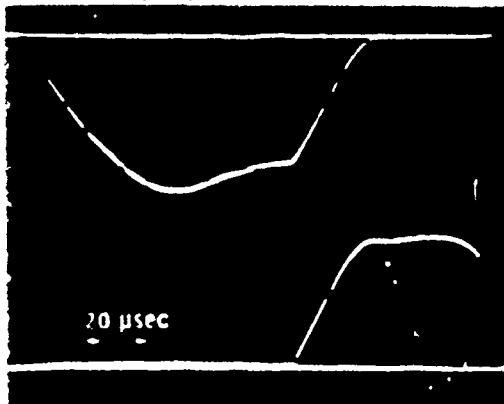
Two problems which have been associated with the operation of the large foil fuses (e.g. 50 cm (W) x 60 cm (L) x .0006 cm (T)) have been non-uniform explosion of the foils apparently caused by non-uniform current distributions in the foil and damage to the fuses inflicted when the delicate thicknesses are immersed. The first problem, evaluated using time integrated open shutter photographs and examination of the clamped ends of the foils, has been improved by mounting the foils in cylindrical and hexagonal geometries which promote symmetrical current distributions. Handling of the foils has been facilitated by sandwiching the foil between fiberglass screens which are spot welded at the foil edges to form a fuse package with strength equal to that of the fiberglass. The screen transparency allows the water to come into intimate contact with the foil and tests have shown that operation of the foil is unaltered by the screen.

Wire fuses of both aluminum and copper have been used as the final fuse stage in thicknesses ranging from 1 to 5 mils. Wire currents have ranged from 75 kA for shots with 240 kA in the exploding switch just prior to commutation to the foil fuse to 150 kA for shots with 365 kA measured in the exploding switch. The lower level shots used 28, 5 mil diameter aluminum wires, while the high current shots used 53, 3 mil diameter copper wires. The maximum self stress generated by the wires to date in the TRIDENT experiment has been 13 kV/cm, a value well below their previously demonstrated capability.

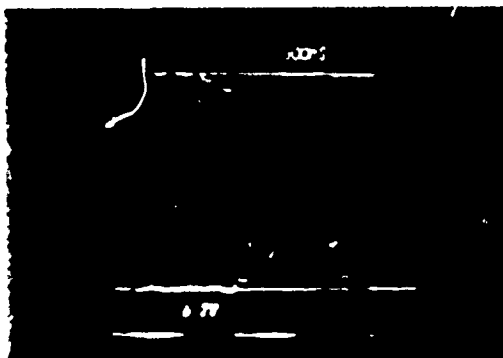
A set of typical current and voltage waveforms from a shot where the peak current through the storage

inductor was 140 kA is shown in Fig. 7. The current just prior to commutation to the foil was 270 kA. This reduction from peak is due to the combined effects of the crowbar resistance and losses in the exploding switch circuit. The commutation time to the foil was 20  $\mu$ sec. Although not shown in the photos, the arc voltage was 6.6 kV. The voltage trace shows that the self closing water switch to the wires closed when the foil voltage was 125 kV (saw-tooth ramp on extreme left of voltage trace). The wire fuse exploded 1.75  $\mu$ sec after the closure of this switch generating a peak voltage pulse of

### EXPLODING SWITCH CURRENT 340 KA PEAK



### FOIL FUSE CURRENT 195 KA PEAK OUTPUT VOLTAGE 605 KV PEAK



### WIRE FUSE CURRENT 85 KA PEAK

Fig. 7. Representative current and voltage waveforms from the TRIDENT pulse generator.

605 kV. The current commutated to the wires is shown in the bottom trace of the figure. The signal has been delayed 1.5  $\mu$ sec and therefore must be shifted three divisions to the left for time correlation with the voltage pulse.

An accurate analysis of the TRIDENT circuit was performed, as described earlier, to evaluate the experimentally observed values of current transfer to the wires against those current levels which should be expected on the basis of circuit parameters and switch properties. This analysis assumed a total exploding switch opening time of 80  $\mu$ sec, 5 kV of arc voltage, a foil fuse time to explosion of 50  $\mu$ sec, and an initiation of current commutation from the foil to the wire when the foil fuse self generated stress was 1.3 kV/cm. The results of this analysis is shown in Fig. 8 for foil fuse lengths of .5 and 1.0 meters. Fairly good agreement is shown between the analysis and TRIDENT data points. This result indicated to us that we had a good understanding of the operation of the switching elements, and, not surprisingly, the inductance associated with the switch elements and in the commutation circuits must be reduced to increase efficiency to the final stage.

#### Future Experiments

Immediate plans for the TRIDENT experiment include operating the system at full charge on the capacitor bank (60 kV). This will increase the peak current in the circuit to approximately 500 kA. This is

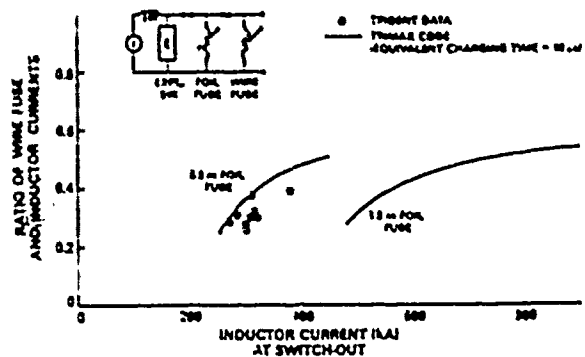


Fig. 8. Comparison of TRIDENT data to computer simulation of current transfer to wire fuse.

expected to generate output pulses of over 800 kV. In order to attain this level, a folded version of the exploding switch will be employed which will have a higher voltage hold-off capability with a very small change in the circuit inductance. Additionally, a falsework arrangement has been proposed to reduce the inductance of the switches and commutation circuits. This modification to improve energy transfer to the wires along with optimized switching between stages should produce output pulses approaching the desired goal of 1 MV.

Later in the year, the TRIDENT switching tank will be connected to the NRL homopolar generator for operation at 600 kA with an initial stored energy of 1 MJ.<sup>7</sup> This will provide the first demonstration of a complete, compact, high energy inductive storage pulser with an inertial energy store as the primary source.

Following the homopolar generator tests, a demonstration of pulse charging the capacitance of a 1 MV, moderate energy pulse forming line is planned.

#### Reference

1. T. H. Martin and K. R. Prestwich, "EBFA, A Twenty Terawatt Electron Beam Accelerator", Energy Storage, Compression, and Switching Edited by W. H. Bosnick, V. Nardi, and O. S. F. Zucker, Plenum Press, New York, 1976. pp. 57-62; G. Yonas, "Fusion Power with Particle Beams", Scientific American, Vol. 239, No. 5, Nov. 1978. pp. 50-61.
2. B. Bernstein and I. Smith, "Aurora, An Electron Beam Accelerator", IEEE Transactions on Nuclear Science, Vol. 20, 1973. p. 294.
3. H. N. Woodson, M. G. Rylander, W. F. Weldon, "Pulsed Power from Inertial Storage with Homopolar Machines for Conversion", Proceedings of First IEEE International Pulsed Power Conference, IEEE Cat. No. 76M1147-8 REC-5, Lubbock, Texas, Nov. 1976.
4. A. E. Robson, R. E. Lanham, W. M. Lupton, T. J. O'Connell, P. J. Turchi and W. L. Warnick, "An Inductive Energy Storage System Based On A Self-Excited Homopolar Generator", Proceedings of the Sixth Symposium on Engineering Problems of Fusion Research, IEEE Cat. No. 75CH 1097-5-NPS (1976). p. 298.
5. R. D. Ford and I. M. Vitkovitsky, "Explosively Actuated 100 kA Opening Switch for High Voltage Applications", NRL Memo Report 3561, July 1977.
6. D. Conte, R. D. Ford, W. M. Lupton and I. M. Vitkovitsky, "Two Stage Opening Switch Techniques for Generation of High Inductive Voltage". Proceedings of Seventh Symposium of Engineering Problems of Fusion Research, IEEE Cat. No. 77CH1267-4-NPS (1977). p. 1066.
7. W. M. Lupton, R. D. Ford, D. Conte, M. B. Lindstrom and I. M. Vitkovitsky "Use of Transformers in Producing High Power Output from Homopolar Generators", proceedings of this conference.

---

This work was sponsored by the Defense Nuclear Agency.

## INDUCTIVE STORAGE - PROSPECTS FOR HIGH POWER GENERATION

J. K. Burton, D. Conte, R. D. Ford

W. H. Lupton, V. E. Scherrer, I. M. Vickovitsky

Naval Research Laboratory

Washington, D. C. 20375

Abstract

Recent progress in the development of key elements of high power inductive storage systems makes it possible to generate high power pulses using energy storage systems (other than explosive generators) that include single-pulse inductive systems, hybrids (inductor/pulse line<sup>1</sup> and inductive devices for steepening of the capacitor output<sup>2</sup>) as well as inductive systems for generation of high power pulse trains.

Prospects for further development of opening switches and storage systems suggest potential near-term payoff. Improvements based on such developments can be expected to impact system efficiency, compactness and operational convenience.

Introduction

Magnetic storage of energy for applications, requiring large amounts of energy, is preferable to capacitive storage because of its characteristically high energy density, some  $10^2$  to  $10^3$  times higher than electrostatic energy storage. S. A. Nasar and H. H. Woodson<sup>3</sup> have surveyed the methods of energy storage for pulse power applications, concluding in 1975 that inductive storage has great potential, but that it has not been used extensively in the past. Specifically, the problem of opening switches is indicated, with the prediction that high current, high voltage opening switches will evolve from power circuit breaker technology.

This paper discusses the status of opening switches and their relation to development of large inductive storage systems designed for loads requiring high power input, and for systems with specialized output, such as pulse trains with short pulse-to-pulse separation. Prospective development of one new type of opening switch, a plasma switch, is also discussed to illustrate further possibilities for improved performance of these systems, including repetitive capabilities.

Opening Switches

The requirements imposed on the opening switches in inductive storage systems, i.e. high resistance of the opened state, high inductive electric field, high restriking voltage with the attendant rapid recovery rate and fast opening time were discussed in Ref. 4 in relation to the circuit parameters. It can be seen from the analysis of the energy transport from the inductor,  $L_0$ , to the load that the above switch characteristics strongly influence the pulser's efficiency. This is because the efficiency of transfer from one switching stage to a succeeding one (as is necessary to do in systems with large power amplification factors<sup>4</sup>) is given by

$$\frac{W}{W_0} = \left[ 1 + \frac{R}{R_0} + \frac{L}{L_0} \right]^{-1},$$

where  $W/W_0$  is the ratio of energy transferred to the next stage (characterized by resistance,  $R$ , and inductance  $L$ ) to the stored energy<sup>5</sup>. The magnitude of the effect can be estimated from  $W/W_0$  by noting that the inductance  $L$  of the next stage is always



approximately proportional to the inductive or restrike electric field. In high power systems using several opening switch stages small improvements in the value of these parameters improves the transfer efficiency substantially. In addition to the circuit efficiency, the transfer time, determined by such constraints as the recovery rate must also be short, so that non-recoverable energy losses, such as vaporization energy in the case of fuses, represents acceptably small portion of  $W_0$ .

Figure 1 maps a variety of opening switches in terms of their dependance of the restrike field (noting that it is that field rather than the inductive electric field that usually dominates the switch length) on the recovery time,  $T_R$ , needed to achieve the corresponding magnitude of the field. By normalizing  $T_R$  to the time,  $T_0$ , i.e., to the time that the switch conducts before interrupting the current,

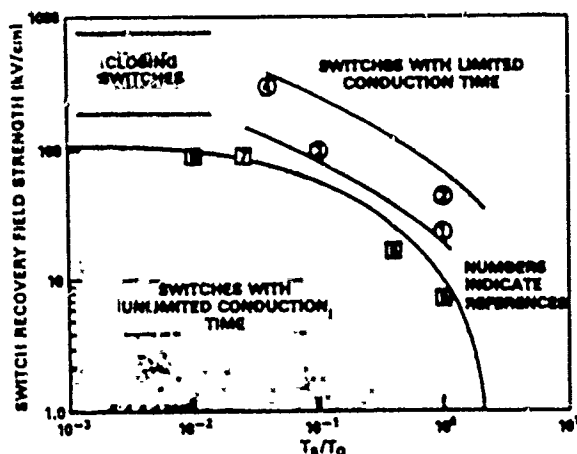


Fig. 1. Parameter space outlining the performance of opening switches. The following switches are mapped: 1-foil fuses, 2-crossed field switch<sup>6</sup>, 3-plasma switch with its prospective development described in this article, and electron-beam controlled high pressure gas switch discussed in ref.7, 4-erosion switch<sup>8</sup>, 5-magnetically operated mechanical breaker<sup>2</sup>, 6-explosively driven switch<sup>10</sup>, 7-SF<sub>6</sub> circuit breaker<sup>11</sup>, 8-vacuum breaker<sup>12</sup>.

the switches are seen to fall into two categories. Those designed to perform with (nearly) unlimited conduction time are plotted using values of  $T_0$  of the specific experiments which provide the above restrike field data.  $T_0$ , of course, cannot be shorter than the electrode separation time. In these cases, the electrodes can conduct over much longer time. The lower shaded region corresponds to switches operating with  $T_0$  longer than used in published experiments. It, thus, delineates the parameter space accessible to the inductive storage designer. The second category of switches are those with limited conduction time. Such limits arise from a constraint specific to a given type of switch. Opening switch controlled by an external electron beam is an example of the limit on the conduction time arising from the constraints on generation of the electron beams. For reference, Figure 1 also shows the hold-off voltage of closing switches, emphasizing the typically higher electric field available for the pulser design.

The ability of switches, with unlimited conduction and operating at high current levels, to open in a time about 100 times shorter than that of conventional circuit breaker<sup>9,10</sup> has recently provided a necessary technology for developing inductive storage pulsers based on rotational energy storage with typical slow rise time.

Figure 2 is a schematic of a plasma switch\* with a potential to combine fast opening and recovery times and high hold-off electric field. It is based on use of dense plasma flow (at  $10^7$  and  $10^8$  cm/s) generated by external plasma gun<sup>13</sup>. When the plasma is in the region between the electrodes, conduction of high current is possible. As the plasma exits the electrode gap, interruption of current ensues. Appropriate commutating circuit can be expected to provide very fast voltage recovery associated with that of vacuum breaker using mechanical separation of electrodes<sup>12</sup>. Promising performance of this switch, as well as that using high pressure gas

\*Concept of the switch by P. J. Turchi,  
U. S. Patent Application (1979)

with electron beam controlled conduction<sup>7</sup>, must await experimental evaluation to assess their use in efficient storage systems.

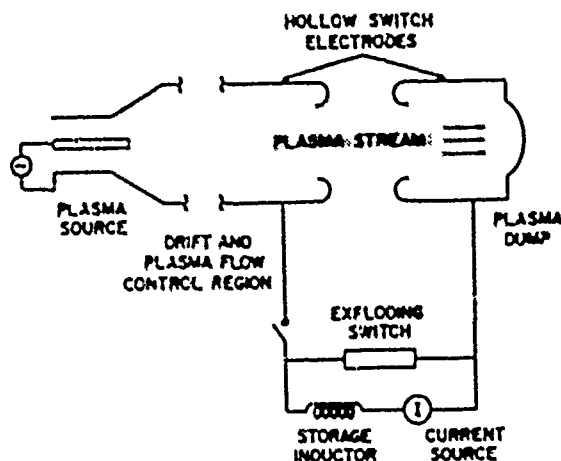


Fig. 2. Schematic configuration of plasma switch.

#### Conclusions

The development of the opening switch technology has now progressed sufficiently to a point that efficient inductive storage modules with output power exceeding  $10^{11}$  Watts can be built<sup>14</sup>. Derivatives of such systems producing pulse train output at  $10^{10}$  Watt with pulse-to-pulse separation equivalent of  $10^5$  Hz have been demonstrated<sup>15</sup>. As a result of this progress, large storage systems can be designed for use with inertial current sources that are necessary for low cost designs.

The major obstacle to wider use of the large inductive storage is the necessity to replace switches after each opening action. This suggests that the development of the opening switches that can be operated many times, in analogy to circuit-breakers used in transmission of the electric power, will be emphasized in the future. The new switches will, likely, evolve from combining desirable features of several switch types and lead to system designs superceding in all respects the capabilities of present capacitive pulsters.

#### References

1. I. M. Vitkovitsky, D. Conte, R. D. Ford, W. H. Lupton, "Inductive Storage for High Power RES Accelerators", Proc. of Second International Topical Conference on High Power Electron and Ion Beam Research Technology, Cornell University, Ithaca, NY, pp. 857-865, (1977).
2. Yu A. Kotov, N. G. Kolganov, V. S. Sadof, S. M. Kovalchuk, G. A. Mesyats, "Nanosecond Pulse Generators with Inductive Storage", Proc. of First IEEE International Pulsed Power Conference, Lubbock, Texas, Cat. No. 76CH1147-8 Reg. 5. (1976).
3. S. A. Nasar and M. H. Woodson, Proc. of Sixth Symposium on Engineering Problems of Fusion Research, San Diego, CA, IEEE Pub. No. 75-CH-1097-5-NPS (1975).
4. I. M. Vitkovitsky, Proc. of Seventh Symposium on Engineering Problems of Fusion Research, Vol. 1, p. 430 IEEE Cat. No. 77-CH-1267-4-NPS (1977).
5. I. M. Vitkovitsky, D. Conte, R. D. Ford, W. H. Lupton, Proc. of Second International Conference on High Power Electron and Ion Beam Research and Technology, Vol. II; p. 857, Laboratory of Plasma Studies, Cornell University (1977).
6. W. Knauer, Symposium Proceedings on New Concepts in Fault Current Limiters and Power Circuit Breakers, Special EPRI Report EL-276-SR, April 1977.
7. R. Fernsler, D. Conte, I. M. Vitkovitsky, "Repetitive Electron Beam Controlled Switching", published in the Proceedings of this Conference.
8. K. C. Bergeron, J. P. VanDevender, Abstracts of Conference on Plasma Science, p. 261, IEEE Cat. No. 78-CH-1357-3-NPS (1978).
9. P. D'Honnin Caupers, F. Rioux-Damidaou, to be published in the Proceedings of Second International Conference on Megagauss Magnetic Field Generation and Related Topics, Washington, D. C., June 1979.
10. D. Conte, R. D. Ford, W. H. Lupton, I. M. Vitkovitsky, p. 1066, op. cit. ref. 4.
11. J. R. Rostron, H. E. Spindle, op. cit. ref. 6.
12. G. A. Farrall, IEEE Transactions on Plasma Science, Vol. PS-6, No. 4, p. 360, (1978).
13. D. Y. Cheng, Nuclear Fusion, 305. (1970)
14. D. Conte, R. D. Ford, W. H. Lupton, I. M. Vitkovitsky, "TRIDENT- A Megavolt Pulse Generator Using Inductive Energy Storage", Pub. in the Proceedings of this Conference.
15. R. D. Ford, I. M. Vitkovitsky, Proceedings of the Thirteenth Pulse Power Modulator Symposium, Buffalo, NY, IEEE Pub. No. 78-CH-1371-4 ED (1978)

Work supported by the Defense Nuclear Agency and Office of Naval Research.

## 12.3

## INVITED

## CONSIDERATIONS FOR INDUCTIVELY DRIVEN PLASMA IMPLOSIONS

D.L. SMITH, R.P. HENDERSON, and R.E. REIMOVSKY

Air Force Weapons Laboratory  
Kirtland AFB, New MexicoAbstract

Inductive pulse forming techniques appropriate for the driving of imploding plasmas have been explored with special attention given to a suitable opening switch. Parametric investigations of circuit models indicate that imploding load performance is relatively independent of opening switch parameters. Extrapolation of existing experimental and computer simulated data leads to conceptual design criteria for a fused metal foil opening switch which will be implemented on a 1.9 MJ system. The inductive system compares favorably with the direct capacitor driven system in terms of kinetic energy with the definite advantage of shorter time scales on which the energy is delivered to the implosion.

Introduction

The Air Force Weapons Laboratory is investigating plasma implosion techniques as a desirable method for generating a very high energy density plasma suitable for use as an intense X-ray Source<sup>1</sup>. Under the SHIVA program experiments have been conducted in which a plasma formed from a thin freestanding, cylindrical metal or plastic film is driven to high velocities ( $> 20\text{cm}/\mu\text{sec}$ ) by a high current from a 1.1 MJ, 1.3  $\mu\text{s}$  capacitor bank. Proper choice of geometry and mass of the imploding plasma allow good (25-30%) coupling of electrical to kinetic energy and have efficient heating of the pinched plasma. Radiation outputs of 180 kJ (16% total efficiency) at powers in excess of 1.5 TW have been observed. Future experiments call for the delivery of much larger amounts of electrical energy (15-30 MJ), and implosion dynamics suggest that shorter implosion times (300ns) would be advantageous. To meet these requirements energy storage systems of conventional design would be exceedingly large and expensive. An attractive alternative technology

may be conceptually developed using inductive (magnetic) energy conditioning techniques<sup>2,3</sup> coupled with inertial primary energy storage<sup>4</sup>. The inertial primary store is essentially present technology. Therefore, the purpose of this work is to explore the potential applicability of inductive pulse forming techniques in the driving of imploding plasma loads. Special attention is paid to the development of a suitable opening switch. In this paper the inductively driven plasma implosion systems will be explored analytically and computationally through circuit models. The performance of currently available opening switches will be compared against the requirements developed in the analysis to assess the near term prospects for applying inductive techniques to large systems.

Simple Analysis

The circuit shown in Fig. 1 consists of a dc charged capacitor bank (C) discharging through a storage inductor ( $L_s = L_{\text{bank}} + L_{\text{ext}}$ ) and a closed switch ( $S_1$ ) that opens at peak current ( $I_0$ ) to transfer the energy through switch  $S_2$  to the load of initial inductance  $L_0$ . The load inductance increases subsequent to the initiation of current interruption thus corresponding to the implosion of the SHIVA load ( $L(t) = L_0 + \Delta L(t)$ ). The initially open switch ( $S_2$ ) isolates the load from the system until switching time ( $t_s$ ). The final load inductance is  $L = L_0 + \Delta L$  where

$$\Delta L = \frac{h u_0}{2\pi} \ln (R_0/R_f) \quad (1)$$

The parameter  $h$  is the height of the cylindrical foil, while  $R_0$  and  $R_f$  are the initial and final cylinder radii respectively. Convergence ratios ( $R_0/R_f$ ) of 12-14 are common and the shorter time scale implosion is expected to lead to a convergence

of 20. Several assumptions are employed in the simplest analysis. The final resistance of the opening switch is assumed to be large compared to the final  $L$  of the load to prevent significant sharing of current through the switch. If the imploding cylinder radius and velocity are  $r(t)$  and  $v(t)$ , one can write

$$\dot{L}(t) = \frac{v_0 h}{2\pi} \frac{v(t)}{r(t)}, \quad (2)$$

It is also assumed that the resistance rises quickly, in other words that the switching time is much less than the implosion time.

At peak current and for the short energy transfer times of interest the bank voltage and the amount by which the charge on C can change is near zero, hence for the analysis the capacitor element can be represented by a short circuit. Assuming conservation of magnetic flux, the energy stored in  $L_s$  and  $L_0$  immediately after  $t_s$  is

$$E_1 = \frac{L_s}{L_s + L_0} E_0 \quad (3)$$

where  $E_0 (= \frac{1}{2} L_0 I_0^2)$  is the energy stored in  $L_0$  prior to  $t_s$ . The energy dissipated in the rising switch resistance must be

$$E_{sw} = \frac{L_0}{L_s + L_0} E_0 \quad (4)$$

according to conservation of energy. To minimize the switch dissipation  $L_0$  must be as low as possible ( $L_0 \ll L_s$ ). After the implosion the approximate energy stored in  $L_s$ ,  $L_0$ , and  $\Delta L$  is

$$E_2 = \frac{L_s}{L_s + L_0 + \Delta L} E_0. \quad (5)$$

The kinetic energy coupled to the plasma shell during the implosion is just the difference  $E_1 - E_2$ , and a kinetic efficiency can be defined as

$$\eta_{ke} = \frac{E_{ke}}{E_0} \approx \frac{\Delta L}{L_s + \Delta L}, \quad (6)$$

if  $L_0 \ll L_s$ . If  $\Delta L \gg L_s$ , efficiency approaching unity can be realized. Thus, in general, to get most of the stored energy into kinetic energy and maximize efficiency requires  $L_0 \ll L_s \ll \Delta L$ . Unfortunately  $L_0$  is typically fixed by consideration of power flow in the load and  $\Delta L$  is fixed by the convergence

ratio and the foil height. For the SHIVA system values of  $L_0$  below 3-5 nH are unrealistic, while  $\Delta L$  can range from 6 to 24 nH, and reaching very high efficiency will be difficult. Given practical constraints upon  $L_0$  and  $\Delta L$ , the value of  $L_s$  remains as one parameter which can be adjusted. Inductively, if  $L_s$  is chosen to be very small, a large amount of energy is lost in the switching operation, if it is chosen to be large the energy transfer to the load suffers. To find the optimum choice of  $L_s$  one can take  $d\eta_{ke}/dL_s$  and set the result equal to zero. This results in a criterion on  $L_s$ , namely:

$$L_s = \sqrt{L_0^2 + L_0 \Delta L}. \quad (7)$$

Clearly for the case of the static load,  $\Delta L = 0$ , Eq. (7) gives  $L_s = L_0$ . Thus, the familiar static result is recovered, and as expected, from Eq. (3) and Eq. (4)  $E_1 = E_{sw} = 50\% E_0$ . Plotting  $\eta_{ke}$  as a function of  $L_s$  for an implosion where  $\Delta L = 12$  nH shows that the efficiency of coupling inductive to kinetic energy goes through a maximum at the predicted optimum  $L_s$  and that the optimum is broad and relatively insensitive to small variations in  $L_s$ .

For one class of opening switches, namely electrically exploded conductors, the operation of the switch is determined by the energy, (and to some extent power history) dissipated in the switch. Therefore it is useful to characterize the circuit performance in terms of the energy dissipated in the switch given by Eq. (4). Figure 2 is a plot of the minimum dissipation fraction defined as

$$\delta = \frac{E_{sw}}{E_0} = \frac{L_0}{L_s + L_0}. \quad (8)$$

When  $L_s$  is chosen by Eq. (7), Eq. (8) indicates that  $\delta$  is only a weak function of  $\Delta L$ . For small  $\Delta L$  the curve approaches 50% as expected for a static load. The significance of  $\delta$  is that it represents the minimum amount of energy that will be dissipated when the switch opens (at least 25% for practical cases), regardless of the characteristics or relative time of the operations of switches  $S_1$  and  $S_2$ . Conversely it is the minimum energy available to use to actuate a dissipation driven switch. The temptation is to develop a switch which "requires"

very little energy. Figure 3 indicates that, for example, for typical SHIVA parameters  $L_0 = 5$  nH and  $\Delta L = 12$  nH, almost 40% of the energy goes into the switch regardless of how clever the design. On the other hand, since dissipatively operated current interrupting switches may require more than the minimum energy given by 4, the fraction  $f$  of the inductively stored energy remaining after switching that is coupled to kinetic energy is also a relevant parameter. Using Eq. (3) and (5)

$$f = \frac{E_{ke}}{E_1} = 1 - \frac{L_s + L_0}{L_s + L_0 + \Delta L}. \quad (9)$$

Figure 3 is a plot of the coupling fraction  $f$ . The plot shows that for realistic values of 3 nH  $L_0 < 5$  nH and for  $\Delta L = 12$  nH approximately half of the energy remaining after switching is coupled to kinetic energy yielding for these parameters an overall  $\eta_{ke}$  of 30%. From this simple analysis, a few design criteria emerge:

- i) Minimize  $L_0$ , as much as possible,
- ii) Maximize  $\Delta L$ ,
- iii) Choose  $L_s \approx \sqrt{L_0^2 + L_0 \Delta L}$ ,
- iv) Determine the dissipated switch energy.

#### Numerical Results

In this section, the numerical solution to a circuit similar to that in Fig. 1 is discussed. Values were chosen for circuit elements which correspond to parameters of the SHIVA-I' capacitor bank system. The 267  $\mu$ F capacitor is charged to 120 kV storing 1.9 MJ. The load is modeled as a time varying resistance, having the same form as Eq. (2), in series with a time varying inductance expressed by

$$L(r) = \frac{u_0 h}{2\pi} \ln(R/r(t)). \quad (10)$$

The radii of the return conductor (chamber) and of the imploding foil are represented by  $R$  and  $r(t)$ , respectively. The initial foil radius was chosen at 5 cm and the height at 2 cm by stability arguments. The return conductor radius was chosen at 17.5 cm to give an initial value for the  $L$  of 5 nH, which corresponds to  $L_0 = 5$  nH in the analytic model. The assumption of 20:1 conversion leads to a minimum radius of 2.5 mm; a final value  $L_f$  of 17 nH; and a  $\Delta L$  of 12 nH. Thus from  $L_0$  and  $\Delta L$  a value of the

storage inductance is chosen from Eq. (7) to be 9.2 nH. The series output switch is modeled as a time varying resistor whose value is 1 megohm prior to switching time  $t_s$  and changes to 0.1 milliohm in 5 ns subsequent to  $t_s$ . The current interrupting switch is a resistance ( $R_1$ ) which is varied as a problem variable. The opening switch inductance is typically taken as less than 1 nH but will depend on the switch geometry. The fuse inductance was included in the bank side of the circuit rather than in the fuse branch because, with the coaxial SHIVA arrangement,  $L_f$  stores magnetic energy that is available to the load when switching occurs. The circuit was subjected to numerical analysis using a circuit solving code for a variety of  $R_1$  profiles and time scales and for a variety of switch times  $t_s$ .

#### Terminal Resistance

Assuming all the stored energy is transferred to the inductors, the coupled kinetic energy should be 570 kJ (30% kinetic efficiency). Choosing 33 cm/ $\mu$ s final velocity and allowing a 2.5 cm final radius the foil mass and final  $\dot{L}$  should be  $10^{-3}$  kg and 0.5  $\Omega$ . The constant flux analysis implied that the final value of  $R_1$  should be much greater than 0.5  $\Omega$  to assure that most of the current is flowing in the load. To model the situation a linear ramp resistance profile was chosen (since other shapes effected only a few percent variation in the kinetic energy), changing  $R_1$  from the initial resistance ( $R_i \approx 0$ ) at  $t_1 = 2.46$   $\mu$ s (time of peak current) to a final terminal resistance ( $R_f$ ). The switch duration ( $\Delta t$ ) was taken as 100 ns to assure that  $\Delta t \ll \tau_{imp}$ , and  $R_f$  was varied from 30 m $\Omega$  to 5  $\Omega$ . The time at which the output switch closed ( $t_s$ ), was a constant at 2.465  $\mu$ s. Figure 4 shows a plot of the kinetic energy coupled to the imploding foil and the final velocity of the foil when it had collapsed to

a radius of 2.5 mm as a function of  $R_2$ , the final switch resistance. As anticipated the kinetic energy coupled at lower values of  $R_2$  is lower than that observed at higher values. Perhaps surprising is the fact that when  $R_2 \sim \dot{L}$  peak nearly 90% of the kinetic energy predicted by the flux model is observed coupled in the numerical solution. But when  $R_2$  drops more than an order of magnitude to 30 m $\Omega$  the kinetic efficiency decreases only moderately to 62% of the efficiency predicted by the flux model. This relatively moderate impact of reducing  $R_2$  can be motivated by referring to Fig. 5 where the dissipative impedance (RLD) and  $R_2(t)$  are plotted as functions of time for the case where  $R_2 = 30$  m $\Omega$ . The plot shows that the dissipative part of the load impedance RLD rises rapidly at the very end of the implosion, and even for very modest values of  $R_2$ , RLD is less than  $R_2$  for about 90% of the implosion time. Although it is also true that most of the kinetic energy is coupled late in the implosion, it must be noted that once  $R_2$  interrupts the current and "charges" the load inductance, the time scale ( $L/R_2$ ) for current to transfer back to  $R_2$  is much longer than the 30-60 ns for which the load impedance is higher than  $R_2$ . Coupling to  $L$  is independent of  $R_2$  until late in the implosion, and most of the necessary energy has been loaded into  $L$  (which has increased to almost  $L_0 + \Delta L$  before  $\dot{L}$  overtakes  $R_2$ ). Figure 4 also exhibits a fall off of  $\eta_{ka}$  above approximately 0.5 A. This result is perhaps more surprising than the relative moderate fall off at low  $R_2$ . At larger values of  $R_2$ , excessive energy is dissipated in the fuse during opening time thus leaving less energy in the magnetic circuit to drive the implosion and thereby explaining lower overall efficiency. The conclusion is that, for implosion parameters discussed and for values of  $R_2$  that are greater than the initial  $\dot{L}$  of the load (a few milliohms) but not much greater than the final  $\dot{L}$  (one-half ohm), performance seems to be predicted by the simple model within about 20%. Thus the criteria results with  $\dot{L}_0 \ll R_2 \sim \dot{L}$  pinch.

#### Output Switch Closure Time

It was observed that earlier "closing times" ( $t_3$ )

of the series output switch  $R_2$ , resulted in improved efficiency and decreased dissipation of large values of  $R_2$ . In fact the kinetic energy approaches the 570 kJ flux model value. Presumably when  $\dot{L}$  is very large (i.e.,  $R_2$  is large and  $\Delta t$  is fixed), the time scale of current transfer is seriously affected by the  $R_2$  closing time and thus results in larger dissipation in  $R_2$ . Closing the output switch late in the interruption may be expected to result in excessive energy dissipation in the fuse and hence lower kinetic efficiency. On the other hand, closure of the output switch too early may be expected to result in lower voltages across the load and hence lower initial  $\dot{I}$ , and perhaps result in longer implosion time for a given load. Fortunately, from a practical point of view, the earliest possible closure time (after start of interruption time) appears most promising according to both the efficiency and implosion time. The 5 ns value of  $R_2$  used to generate the data in Fig. 4 is more representative of practical multi-channel switches than is the less than 1 ns value required to achieve flux model efficiency. The implication is that a "low jitter" output switch is required if large values of  $R_2$  are achieved by the fuse. Figure 6 shows a plot of kinetic energy and implosion time as functions of output switch time for a case where  $R_2$  equals 500 m $\Omega$ . The implosion mass was  $1 \times 10^{-3}$  kg, and the switch opening time ( $\Delta t$ ) was 100 ns. For reference, the fuse resistance profile is also sketched. The figure shows that both kinetic energy and implosion time are sensitive to switch closure time. As expected kinetic energy drops and implosion time increases with later closing times. The implosion time shows a tendency to flatten out for closure times near the start of the interruption (2.46  $\mu$ s).

#### Opening Time

The simple flux model presumes that the implosion is carried out in two steps. First a current interruption occurs, then an implosion phase occurs. The energy transfer is calculated on the assumption that  $L(t)$  does not change during the interruption phase (i.e., a static load). The numerical analysis shows that for time scales of about 3/4 of the implosion time the opening switch is seeing a constant  $L(t)$

to within 25% before it starts increasing rapidly. It also shows virtually no change of kinetic energy for time scales up to 100 ns which is very close to 75% of the implosion time. For opening times up to 500 ns the loss of efficiency is less than 5% and the implosion time lengthens somewhat (from 450 to 550 ns).

#### Implosion Mass/Final Velocity

One of the advantages of inductively driven implosion systems is the fact that at least in the simplest model the kinetic energy coupled is dictated only by the inductance ratios and is independent of the implosion mass. This allows relatively wide variations in final velocity to be achieved independent of kinetic energy and hence allows assessment of the effect final velocity has on the thermalization process. Figure 7 is a plot of the kinetic efficiency, final velocity, and implosion time as a function of implosion mass. The plot shows that for a full order of magnitude change of implosion mass ( $5 \times 10^{-5}$  to  $5 \times 10^{-6}$  kg) the change in velocity is given by the anticipated  $\sqrt{10}$  factor ranging from 11.9 cm/us to 37.3 cm/us. As expected the implosion time varies over a similarly wide range associated with the changing final velocity. For larger masses and for small masses, the kinetic efficiency suffers somewhat. Consideration of the circuit model shows that for the large masses the long implosion time leads to reverse charging of the bank capacitance (because a relatively large current is flowing in the "positive" direction for a long time after current peak). The energy stored in the recharging capacitor is approximately 3 times the observed loss in kinetic energy. For small values of mass the more dramatic loss results from excessive energy dissipation in the fuse resistance caused by larger values of RLD at earlier times in the implosion.

#### Conceptual Design

Finally, it is appropriate to consider the prospects for the success of a high energy inductive store/opening switch system as a driver for a practical imploding plasma load. Significant data has been published on the behavior of exploded foil fuses used as opening switches, but in general the

energy level (25 kJ) and the time scale (10 to a few hundred us) are not representative of the behavior of the fusing element in systems of interest (2 MJ, 1-3 us). The work most nearly approaching these parameters is that performed by the AFRL at the 200 kJ, 3-4 us level. Preliminary work on a 100 kJ, 100 kV, 1.2 us system has produced 150 to 200 ns fuse voltage risetimes achieving final fuse resistance values greater than  $160 \text{ m}\Omega$ . The corresponding resistivity of about 400 m $\Omega$ -cm agrees satisfactorily with previous empirical data and the models used in this paper. In this section the results of these efforts will be examined in light of the foregoing analyses and circuit calculations. Figures 8 and 9 are extracted from previous AFRL work and show current and voltage profiles for a set of copper foil fuses quenched in glass beads for a variety of physical lengths and widths which maintain a constant total fuse mass of 25 g (for 1 mil or .0254 mm thickness). For both figures the peaks occurring later in time correspond to decreasing lengths and increasing widths. Based on preceding analyses the most promising choice for a fuse might be the fuse which produces the highest storage current while still opening in times less than (but not necessarily much less than) the implosion time. It is convenient to accept the FWHM of the voltage pulse as one measure of opening time when resistance data is not readily available. From Fig. 9 it is apparent, as expected, that the shortest interrupt time is associated with the highest peak voltage (maximum  $i$ ) but not with the maximum storage current. Thus compromise will be in order. For the purpose of this analysis it was chosen to discuss the maximum voltage case. The FWHM of this case is 370 ns which is acceptable for driving a 400-450 ns implosion.

For scaling purposes we resort to Maisonnier's analysis<sup>2</sup> which suggests a cross-sectional area for a fuse based on the parameters of the driving current and on the physical properties of the fuse of interest.

$$s^2 = \frac{W^{1/2}}{V L^{1/2} \kappa_1 a} \quad (11)$$

where  $s$  = cross section of fuse ( $\text{m}^2$ ),  $W$  = stored

energy (J),  $L$  = total system inductance (H),  $V$  = charge voltage of capacitor bank (V), and  $k_1$  = set of parameters describing the material ( $\approx 1.2 \times 10^{17}$  for copper). For the data in Figs. 8 and 9,  $W = 200$  kJ,  $V = 50$  kV, and  $L = 67$  nH. Thus Eq. (22) would predict  $s = 7.6 \times 10^{-6} \text{ m}^2$ . The fuse in question was 21 cm wide and 1 mil thick so that  $s = .053 \text{ cm}^2$  or roughly 70% of that predicted by the Maisonnier model. Scaling upward for a system where  $W = 2$  MJ,  $V = 120$  kV, and  $L = 9.2$  nH, 70% of the predicted area  $s$  is  $\approx .32 \text{ cm}^2$ . A copper foil 1 mil thick would then be only 1.3 m wide. Figure 10 shows a plot of material resistivity  $\rho$  vs specific energy dissipated in the fuse. The functional relationship between  $\rho$  and specific energy is open to question but for simple approximations the empirical data of Fig. 10 will be used. Recalling that the previous analysis indicated that 670 kJ must be dissipated in the fuse, and taking approximately 6 kJ/g as the upper limit of useful specific energy from Fig. 10 indicates that 112 grams of material could be utilized. At a density of 8.94 g/cc and a cross section of  $.32 \text{ cm}^2$ , this implies a fuse length of 39.2 cm. If it reaches a maximum resistivity of 520  $\mu\Omega\text{-cm}$ , the fuse that is  $.32 \text{ cm}^2 \times 39 \text{ cm}$  has a peak resistance of 43 m $\Omega$ . From Fig. 4 a fuse with  $R_f$  of 63 m $\Omega$  would drive an implosion to better than 400 kJ of kinetic energy or 20% overall kinetic efficiency. One must note that the interpretation attached to the data in Fig. 10 is conservative because the resistivity curve appears to be clearly steepening (not yet having reached the plateau assumed in our model of  $R_f$ ). On the other hand Fig. 4 shows that while increasing resistivity (or increasing  $R_f$ ) will help somewhat the marginal gains are small.

In conclusion, it appears that simple extrapolation of already existing data leads to a conceptual design for a fused opening switch which can be implemented on a 2 MJ system. The resulting plasma implosion should be compared against that which can be obtained by directly driving the plasma from the capacitive energy storage. Using a initial SHIVA load foil geometry of 7 cm radius and 2 cm height, and requiring for stability reasons that

the direct driven implosion be complete in less than 1.4  $\mu\text{s}$ , results in the coupling of approximately 400 kJ of kinetic energy to the implosion. This performance compares very favorably with the 400+ kJ of kinetic energy implied in the previous inductive storage analysis. The advantage of the inductive system is clearly the time scale on which the energy is delivered. The inductive system promises 400 ns implosions or a factor of 3 or more faster than the direct driven implosions. At this point it appears that significant gains in thermalization and radiation are to be achieved by this modest reduction in implosion time.

#### References

1. W.L. Baker, M.C. Clark, J.H. Degan, G.F. Klutzu, C.R. McClenahan, and R.E. Reinovsky, "Electromagnetic-Implosion Generation of Pulsed High-Energy-Density Plasma," J. Appl. Phys., 49, pp. 4694-4706, September 1978.
2. Ch. Maisonnier, J.G. Linhart, and C. Courlan, "Rapid Transfer of Magnetic Energy by Means of Exploding Foils", Rev. Sci. Instrum., 37, pp. 1380-1384, October 1966.
3. J.N. DiMarzio and L.C. Burkhardt, "Characteristics of a Magnetic Energy Storage System Using Exploding Foils", J. Appl. Phys., 41, pp. 3894-3899, August 1970.
4. K.I. Thomassen, "Conceptual Engineering Design for a One-GJ Fast Discharging Homopolar Machine for the Reference Theta-Pinch Fusion Reactor", Semi-Annual Report EPRI ER-246, August 1976.
5. R.P. Henderson, D.L. Smith, and R.E. Reinovsky, "Preliminary Inductive Energy Transfer Experiments", Paper 15.1 in these proceedings.
6. C.R. McClenahan, J.H. Goforch, J.H. Degan, R.P. Henderson, W.R. Janssen, and W.E. Walton, "200 Kilojoule Copper Foil Fuses", Report AFWL-TR-78-130, Air Force Weapons Laboratory, Kirtland AFB, NM, April 1978.

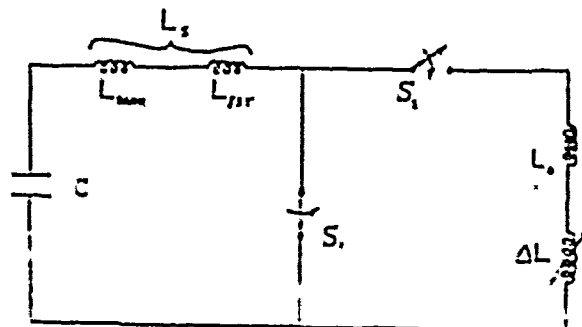


Fig. 1. Practical Circuit Representation.



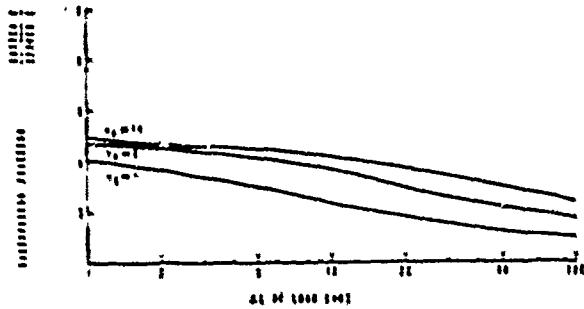


Fig. 2. Dissipation versus the Change in the Load Inductance.

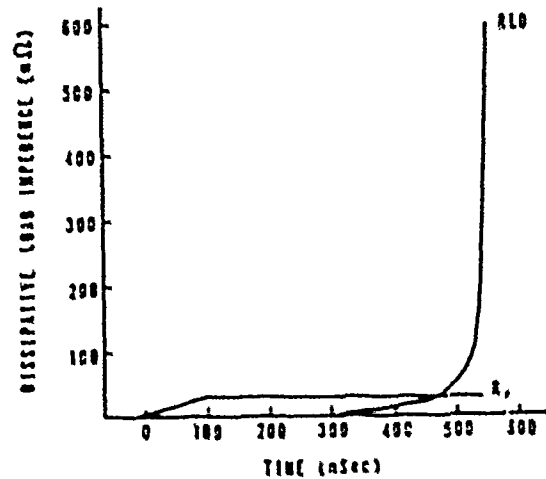


Fig. 5. Dissipative Load Impedance versus Time.

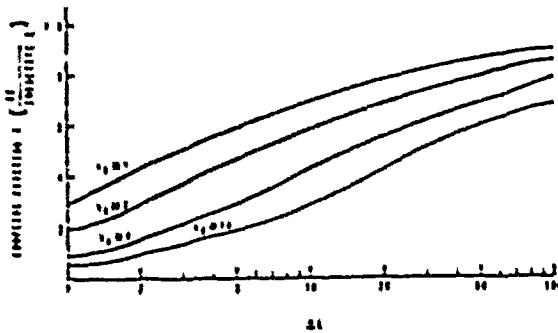


Fig. 3. Coupling Fraction versus the Change in Load Inductance.

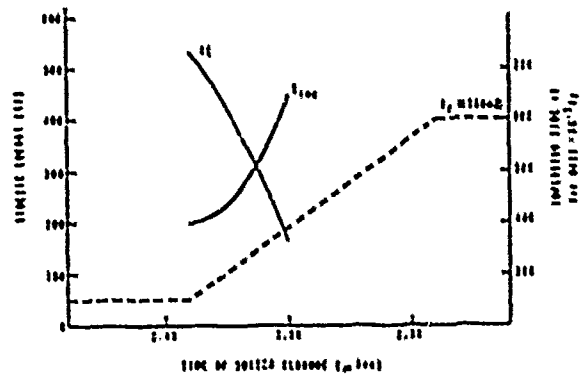


Fig. 6. Kinetic Energy and Implosion Time versus Output Switch Time.

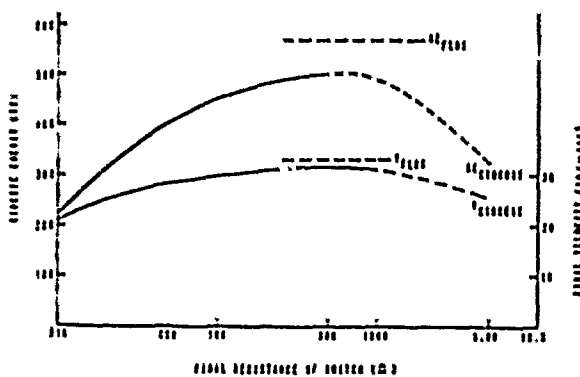


Fig. 4. Kinetic Energy and Final Velocity of the Imploding Foil versus the Final Switch Resistance.

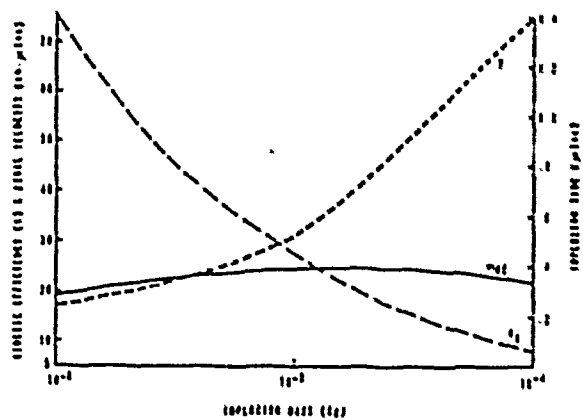


Fig. 7. Kinetic Efficiency, Final Velocity, and Implosion Time as a Function of Mass.

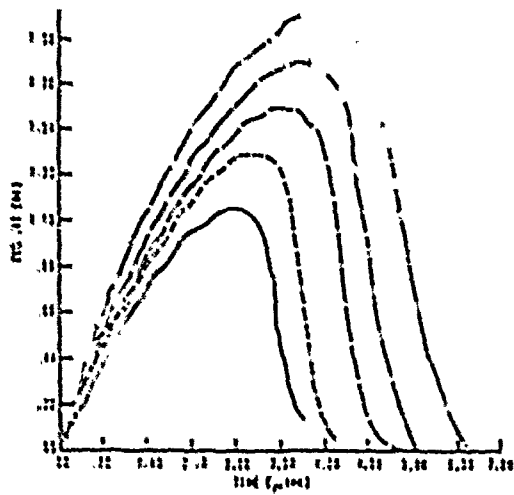


Fig. 8. Current Data for 25g Copper Foil Fuses.

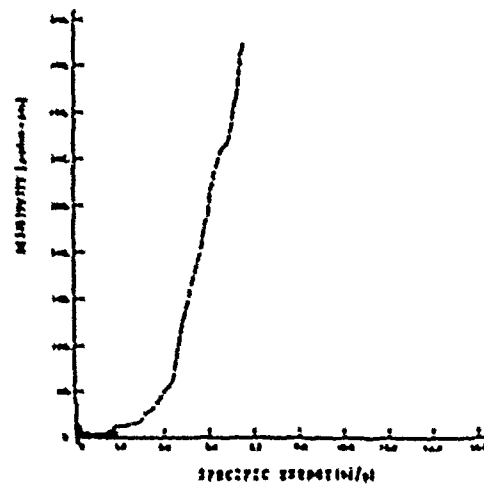


Fig. 10. Resistivity versus Specific Energy in a 25.9g Copper Fuse.

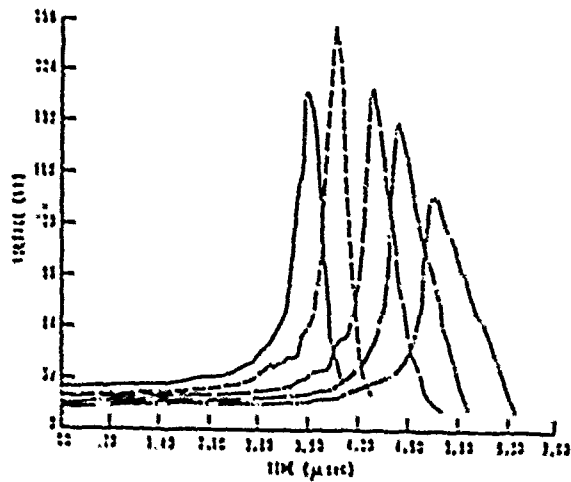


Fig. 9. Voltage Data for 25g Copper Foil Fuses.

# HIGH REPETITION RATE MINIATURE TRIGGERED SPARK SWITCH

M. F. Rose and M. T. Glancy

Naval Surface Weapons Center  
Dahlgren, Virginia 22448

## Abstract

A miniature triggered spark switch designed to operate at high repetition rates has been constructed. The device, along with associated trigger circuitry, has been incorporated into a simple L-C generator which produces an oscillatory discharge at a frequency of 150 MHz. The switch is operated in the pressure range 760 torr -  $2.6 \times 10^3$  torr using commercial dry nitrogen as the working gas. Both brass and aluminum electrodes were investigated for repetition frequencies as high as 20 kHz and for gas flow rates as high as  $8 \text{ cm}^3/\text{sec}$ . The effect of repetition rate on switch jitter and switch breakdown voltage is presented and discussed in terms of gas pressure and flow rate.

## Introduction

High repetition rate switching in the region greater than 10 kHz can be accomplished by thyatrons, and in some cases, vacuum gaps. Unfortunately, these techniques often suffer from jitter or inductance problems. A quenching spark gap, however, appears to be one of the simplest and most efficient devices for this purpose, if fast turn on and low losses are desirable. The general idea of a quenching switch is one which has a large ( $> 10$ )  $\lambda/d$  ratio and additionally, a small value of  $d$ . The quenching action is based upon the fact that small plasma volumes can maintain good electrical conductivity in the small gap spacing very soon after initiation of the switch process. After the driving potential has been removed, the small plasma volume can quickly recover. Excess thermal energy associated with the gap dissipation can be transferred to the

switch electrode surfaces or blown from the system with sufficient gas flow. It is difficult, however, to provide an adequate trigger mechanism to take advantage of the high repetition rate in applications which demand precision pulse spacing. Single stage switches of this type have gap spacings no more than a few mils which make it difficult to design and implement a "third electrode" trigger of the trigatron type. The purpose of this paper is to describe the operating characteristics of a simple, high repetition rate, quenching spark switch, under gas flow, when configured as part of a small hertzian generator of the type described by Moran<sup>1</sup> and by others in this conference<sup>2</sup>.

## Experimental

Figure 1 shows a cross-sectional view of the oscillator and the switch. The device has circular symmetry and is held together using several nylon bolts. The pressure collar is made of plexiglass and is sealed to the switch electrodes via o-rings. The electrodes are 1.02 cm in diameter, giving an  $\lambda/d$  ratio of approximately 50. In addition, the electrodes are removable for examination of wear and other electrode effects<sup>2</sup>. For our experiments, we have investigated both brass and aluminum electrodes with 6 mils gap spacing.

The electrodes are provided with a gas inlet immediately in the center of one of the switch electrodes and gas flow outlet holes located around the periphery of the other electrode. Figure 2 shows a schematic of the gas flow and pressurization scheme. While we realize that the configuration is probably not optimum from a gas dynamic point of view, it offers minimum inductance, a desirable characteristic for our application.

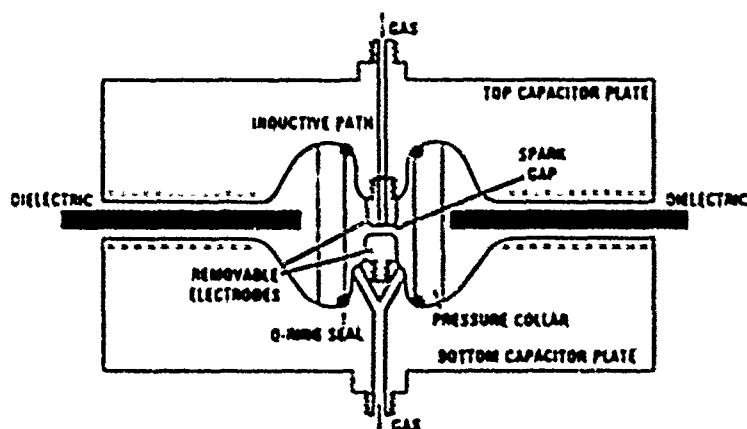


Figure 1. Cross sectional view of oscillator and switch.

The working gas used is commercial dry nitrogen. The high pressure tubing connecting the various components was constant diameter and all components were placed as close to the switch as possible. A Weiss pressure gauge was used and calibrated with an accuracy of  $\pm 1$  psig (51.7 corr). A Rate Master flow meter was used which provided the capability for accurately measuring flow rates of  $\pm 1$  cm<sup>3</sup>/sec. A bleed valve was used to flush both the oscillator and gas lines prior to operation.

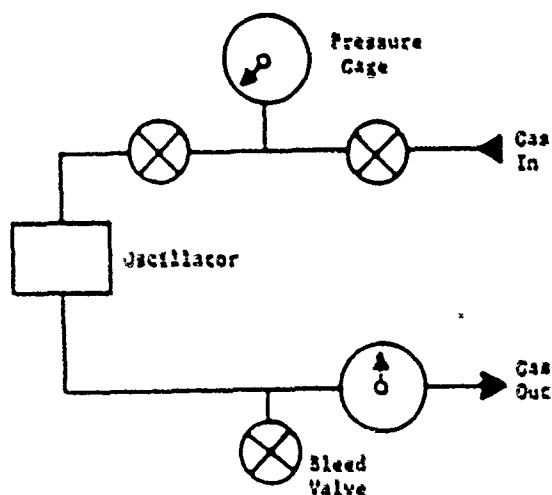


Figure 2. Schematic of the gas pressure and flow system.

Figure 1 illustrates schematically the system used to charge the oscillator and to provide a reliable trigger. The oscillator capacitance,  $C_0$ , (433 pF) is charged through a variable charging resistor  $R_c$ .

When the charging voltage on the oscillator reaches a preset value, the impulse generator (IMP) sends

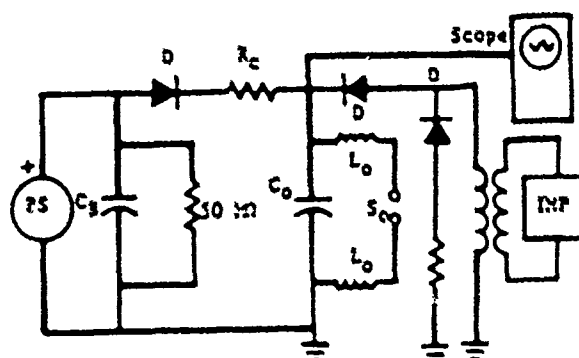


Figure 3. Schematic diagram of the oscillator charging system and trigger arrangements.

a pulse into the oscillator, rapidly overvolting the gap, and causing it to fire in a time short in comparison to the RC charge time. The diodes, D, are so arranged to prevent the oscillator from discharging through the secondary of the impulse generator transformer or alternatively through the power supply. As a result, the energy from the impulse generator is added to that of the power supply so that no energy is wasted from the trigger pulse. The energy stored in the oscillator is "latched" in and can dissipate rapidly by firing switch S or slowly leak off through the back resistances of the diodes.

The pulser itself is a Valonix model 350 with the output transformer modified to provide pulses as

high as 12 kV into a matched load. Prior to running, the surfaces were ground flat and metallurgically polished as described elsewhere<sup>2</sup>. Figure 4 summarizes the operating characteristics of the experiment. Figure 4a shows the voltage-time history as provided by the main power supply (top trace) and the output of the impulse generator (lower trace). Figure 4b illustrates the final

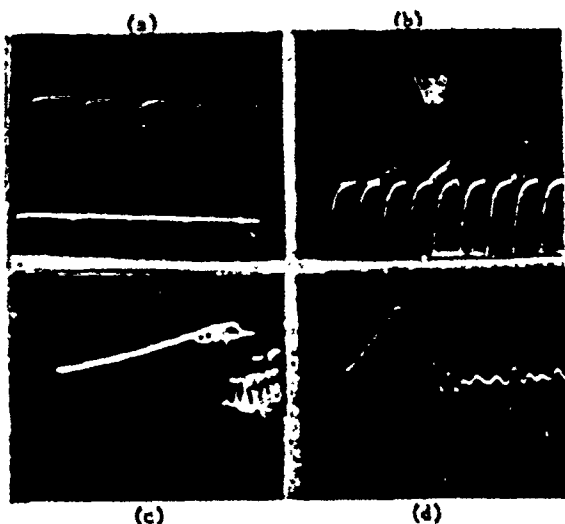


Figure 4. Voltage-time traces for the oscillator and switch.

(a) Top trace is normal RC charge for oscillator, 500 volts/cm, 2 ns/cm. Bottom trace is trigger pulse from impulse generator, 1000 volts/cm, 2 ns/cm.

(b) Bottom trace is normal RC charge for oscillator, 500 volts/cm, .2 ns/cm. Top trace shows impulse charging of oscillator and overvoltage which occurs as a result of impulse; 500 volts/cm 200 ns/cm.

(c) Superposition of 50 pulses to illustrate jitter; 500 volts/cm, 10 ns/cm.

(d) Output waveform for oscillator; 200 volts/cm 20 ns/cm.

impulse charge provided from the trigger generator. Figure 4c illustrates the repeatability of the trigger system and shows jitter. For our purposes, we define jitter as the maximum spread in switch times as integrated over several seconds or several hundred events chosen at random. For this experiment, we routinely sampled 400 separate trigger events to determine the distribution,

however, the photo shows some 50 events. Figure 4d shows the RF envelope for the oscillator output. The system impedance is about 3 ohms which ensures a large damping constant ( $Q \approx 3$ ) and maximum current in the kiloampere range.

The value of the charge resistor  $R_c$  can be chosen such that, at a given frequency, more than 90% of the energy is provided by the main power supply, thereby placing very little strain on the pulse generator. In these experiments, however, we did not always operate in this mode but held  $R_c$  constant (1.05 M $\Omega$ ) for convenience.

#### Discussion

Among the factors which could affect the breakdown voltage in a system are pulse repetition rate, gas flow rate, gas pressure, electrode material, gas species, and time rate of change of the trigger pulse. In our experiments, we varied the first four of these parameters while holding the other factors constant to a first approximation. For the range of fields investigated (up to 260 kV/cm) varying the electrode material did not appear to influence the breakdown voltage. Slight deviations were sometimes noted but these were well within the experimental error. The effect of pressure on the static breakdown voltage is well documented<sup>3</sup> and our results are consistent with Cookson<sup>4</sup>. However, under impulse charging and flowing gas conditions, the breakdown voltage (illustrated in Figure 5) increased up to a value as high as 30% greater than the static value and slowly decreases as the pulse repetition frequency is increased. At a pulse repetition frequency of 20 kHz, the firing voltage for the switch has dropped to a value about 2/3 of the static value. The effect of flow was minimal on the breakdown voltage (over the range investigated) and in general was confined to pulse frequencies less than 3 kHz. We attribute this to the multitude of other factors which could be active in determining the breakdown voltage for the gap (e.g., particulate matter of a size comparable to the gap spacing, thermal energy deposited in the electrode surface and gas, plasma in the gap due to previous discharge.)

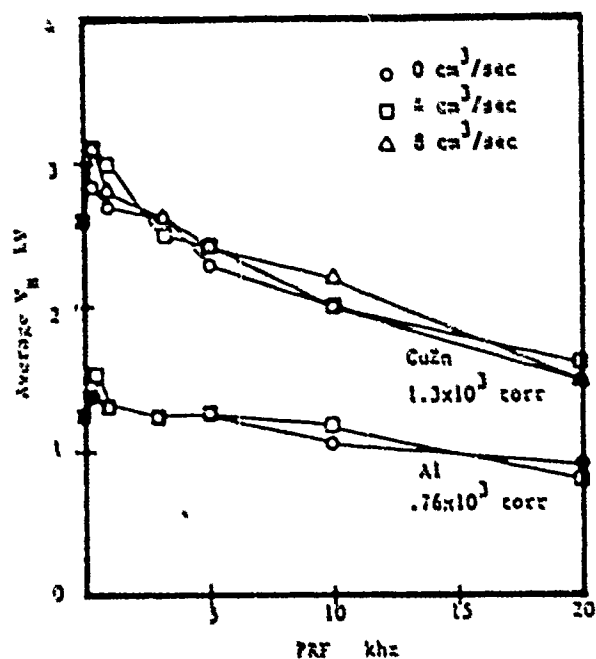


Figure 5. Effect of pulse repetition frequency and flow rate on average breakdown voltage as a function of gas flow.

At a constant gas pressure, without gas flow, strong material effects are present if the gap is to be operated in a triggered mode. For aluminum we could achieve stable triggered operation over the entire pressure range investigated with minimal jitter in the 2-3 kHz repetition range. By contrast, we could only achieve quasi-stable operation using brass electrodes. Table 1 summarizes some of the data for aluminum. The PRF at which the jitter is a minimum is not well defined but extends some 3 or 4 kHz on either side of the value quoted.

Table 1. Jitter Data for Aluminum

Pressure torr $\times 10^3$	Avg $V_b$ kV	Flow cm <sup>3</sup> /sec	Jitter min ns	Approx PRF kHz
.76	1.30	0	40	6
.76	1.25	4	10	3
1.29	2.40	0	70	4
1.29	2.20	4	70	6
1.29	2.50	3	75	3
2.38	3.20	0	20	1
2.38	3.40	4	20	1
2.38	3.60	8	20	1

The effect of flow for both aluminum and brass electrodes was to make the switch operate with less jitter over the entire range of parameters investigated. The decrease in jitter was quite dramatic in brass. Figure 6 illustrates the effect of gas flow on the switch jitter for brass electrodes at atmospheric pressure. The values given without flow showed no systematic variation with repetition frequency and are at best estimates of the maximum jitter at the time of observation.

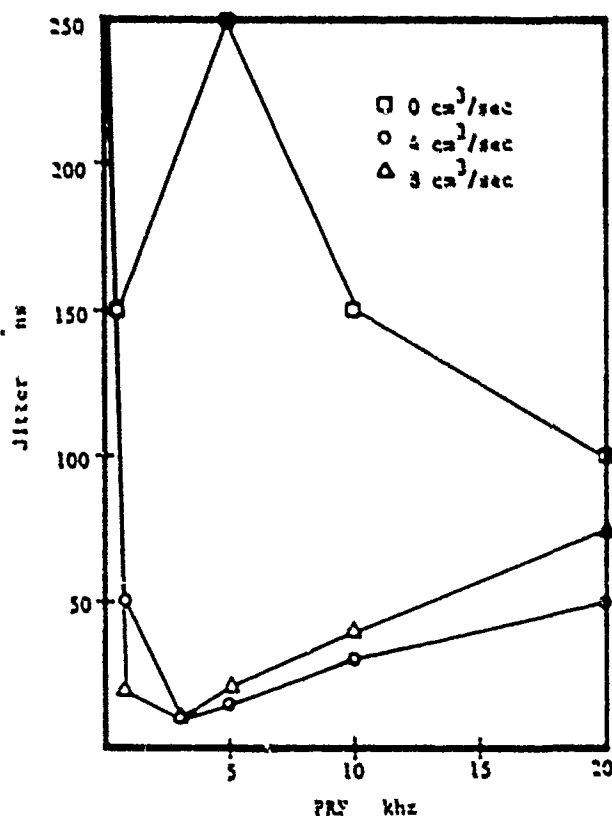


Figure 6. Effect of pulse repetition frequency on the maximum jitter for various flow rates. Electrodes are brass. Gas pressure is  $.76 \times 10^3$  torr.

When flow was initiated, the gap would run stable under any condition investigated in our experiments. At atmospheric pressure, the minimum in the jitter distribution occurred at 3 kHz similar to that observed for aluminum (Table 1) and then slowly increased up to the maximum repetition frequency investigated.

The effect of pressure is equally dramatic for constant flow rate. The trends are similar for aluminum and brass but differ considerably in absolute magnitude. Figure 7 illustrates the effect of repetition frequency on jitter using brass electrodes for several pressures. The flow rate was held constant at  $8 \text{ cm}^3/\text{sec}$ . The increase in jitter at higher repetition rates is probably associated with the increased surface damage, larger volumes of plasma still in the gap, and electrode heating effects which enhance field emission. The minimum jitter occurs at lower pulse repetition frequencies as the pressure increases. It has been shown that the diameter of the "spark discharge" increases with pressure<sup>2</sup>. If we assume that this diameter defines the amount of plasma associated with a particular event, we can readily estimate the plasma volume associated with the switch at any given gas flow rate and repetition rate. This number is approximately constant at  $3.4 \pm 1 \times 10^{-6} \text{ cm}^3$  for the data shown in Figure 7. Similar results were also obtained for aluminum.

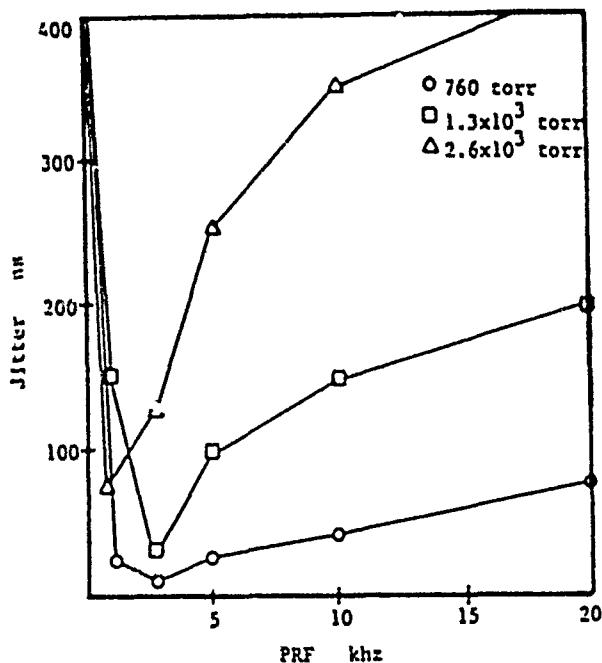


Figure 7. Effect of pulse repetition frequency on maximum switch jitter for constant flow rate ( $8 \text{ cm}^3/\text{sec}$ ) for various pressures.

Figure 8 illustrates a typical distribution of switch firings normalized with respect to the maximum in the number of switch events at a specific triggering time after the impulse was applied. These data were taken at a flow rate of  $8 \text{ cm}^3/\text{sec}$ , PRF of 5 kHz, and atmospheric pressure. The curves represent some 400 individual events, taken at random, over a period of several minutes. The distribution for brass electrodes is approximately Gaussian and the extrema agree well with the maximum jitter as observed directly from the oscilloscope. The results for aluminum were complicated, and we attribute this to local defects such as that shown in Figure 9 which eventually grow to such an extent that the gap is effectively shorted out. We did not observe similar failure in brass although running times of several hours were sometimes involved. In general, aluminum failed after some 45 minutes with a drastic increase in jitter and a decrease in breakdown voltage and in all cases a localized damage area was observed.

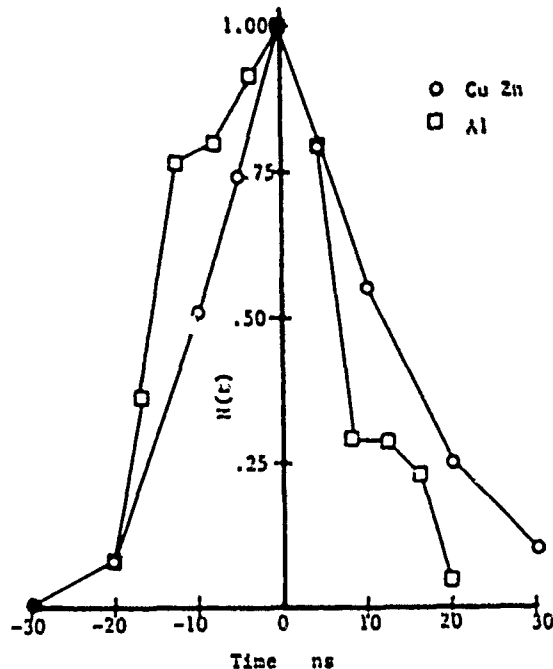


Figure 8. Jitter distribution in brass and aluminum. pressure 760 torr, flow rate  $8 \text{ cm}^3/\text{sec}$ , pulse repetition frequency 5 kHz.

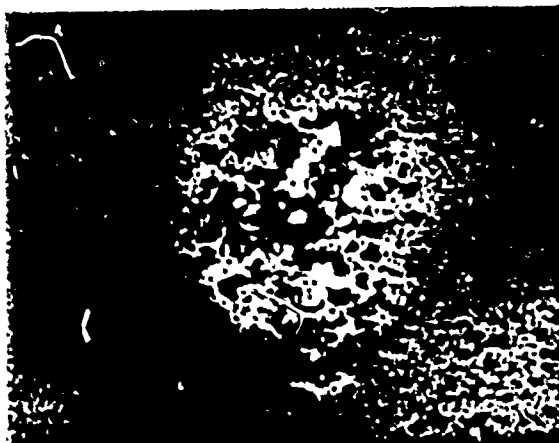


Figure 9. Failure zone on aluminum electrode surface.

#### Summary

Simple spark switches can be made to operate in a triggered mode for frequencies as high as 20 kHz with a maximum of 30% decrease in the breakdown voltage. In so far as we investigated, there is very little effect of materials on the average breakdown voltage of the switch. There are, however, large material effects associated with switch jitter which are probably due to surface chemistry and contamination of the working gas by particulate matter, blown from the surfaces. Introduction of gas flow greatly enhances stability and often results in orders of magnitude reduction in switch jitter. The effects of gas pressure are primarily to increase jitter at higher repetition frequencies and to decrease and better define the repetition frequency at which the minimum in jitter occurs.

#### Acknowledgement

This work was supported in part by the Defense Advance Projects Research Agency through the Naval Air Systems Command. We wish to thank C. E. Comford for assistance during the course of these experiments.

#### References

1. S. L. Moran, "High Repetition Rate L-C Oscillator", IEEE Conference Record of Thirteenth Pulse Power Modulator Symposium, p. 254-259, 1978.
2. M. T. Glancy and M. F. Rose, "Surface Aging in High Repetition Rate Spark Switches with Aluminum and Brass Electrodes", Proceedings of the Second IEEE International Pulsed Power Conference, 1979.
3. J. D. Cobine, Gaseous Conductors, p. 163, 1958.
4. A. H. Cookson, "Electrical Breakdown for Uniform Fields in Compressed Gases", Proc. IEEE, Vol. 117, p. 269-280, Jan. 1970.



SURFACE AGING IN HIGH REPETITION RATE  
SPARK SWITCHES WITH ALUMINUM AND BRASS ELECTRODES

M. T. Glancy and M. F. Rose

Naval Surface Weapons Center  
Dahlgren, Virginia 22448

Abstract

The surface aging of the electrodes of miniature spark switches ( $A/d \sim 50$ ) is explored using commercial dry nitrogen as the working gas. Both brass and aluminum electrodes were investigated for aging characteristics using a constant gas flow rate of  $8 \text{ cm}^3/\text{sec}$ . The gas pressure was varied from 760 torr-5200 torr. The switches were constructed as an integral part of a miniature L-C oscillator which has a ringing frequency of approximately 150 MHz. The aging process was halted at intervals ranging from one to several thousand discharges and the electrode surface examined with a scanning electron microscope.

Introduction

The problems of electrode wear are relevant to many applications involving high-speed switching such as the relay systems used in telecommunications. Previous work in this area has identified several mechanisms which govern the dynamics of the formation and subsequent growth of spark induced damage<sup>1</sup>. In addition, high repetition rate, pulsed power systems are being constructed which employ spark switches that must carry orders of magnitude greater current and energy. These systems may use different gases, electrode materials, gas pressures, and gas flow rates to minimize erosion and resistive losses while maximizing switch lifetimes and maintaining acceptable operating parameters.

Common to all of these devices are the fast transient currents which can produce discharges exhibiting glow and arc characteristics. Several investigators have explored the effect of electrode

surface coatings<sup>2,3</sup> and crystallographic orientation<sup>4</sup> on breakdowns in gases. It has been shown that even thin ( $\sim 10^{-7} \text{ cm}$ ) coatings can greatly alter the breakdown characteristics. In systems demanding high average power, surface heating can easily induce chemical reactions between the working gas and electrode material. These reactions alter the switch characteristics by forming brittle compounds which can flake off the metal surface affecting breakdown voltage and jitter.

In our laboratory, we are currently experimenting with small hertzian generators which must operate continuously for long periods of time at pulse repetition rates of 10's of kilohertz. In another paper in this conference by Rose and Glancy<sup>5</sup>, switches were described which were part of a simple oscillator with a ringing frequency of approximately 150 MHz. By employing gas flow, it is possible to operate these devices at high repetition rates (up to 30 kHz) for long periods of time. The total energy expenditure may be hundreds of kilojoules.

It is the purpose of this paper to explore the surface aging phenomenon and wear characteristics of switches of this type.

Experimental Procedure

The basic oscillator has been described by Moran<sup>6</sup>. Our only modification to this design was to provide for symmetric gas flow and removable electrodes.

In Figure 1, the basic oscillator has capacitance ( $C_0$ ) of 433 pf and inductance ( $2L_0$ ) of 4.3 nH. These values correspond to characteristic oscillator impedance of approximately 3 ohms. The oscillator is fitted with a pressure collar and flow system capable of flow rates as high as 80

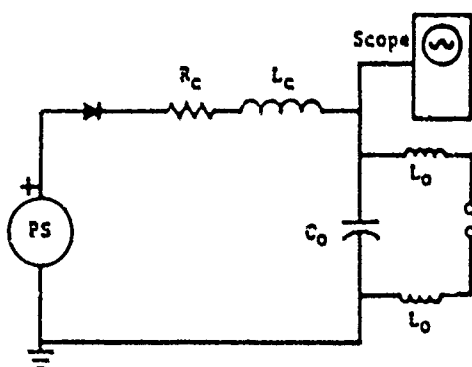


Fig. 1. Schematic of basic charging circuit. The gas flow rate was  $8 \text{ cm}^3/\text{sec}$  at pressures as high as  $11.4 \times 10^4 \text{ torr}$  with an absolute accuracy of 50 torr in pressure and flow rates of  $.4 \text{ cm}^3/\text{sec}$ . In the experiments aimed at examining single discharge spots,  $R_c$  was chosen to give a time constant on the order of .2 sec. This value was chosen to allow the gas flow to effectively cool the electrode surface and remove any effects due to gas contamination. A charging choke ( $L_c$ ) was inserted in the charging line to minimize radiation loss at 150 MHz. For these experiments, pressure was varied while maintaining a constant flow rate of  $8 \text{ cm}^3/\text{sec}$ . The oscillator was allowed to run at a low repetition rate until several hundred discharge events occurred.

The experiments to characterize long term wear and surface aging used the same experimental apparatus described by Rose and Glancy<sup>5</sup>. A pulse repetition frequency of 5 kHz and a flow rate of  $8 \text{ cm}^3/\text{sec}$  were held constant while pressure was varied.

Figure 2 shows half of the oscillator with those portions marked A and B serving as the electrode and oscillator capacitor respectively. The electrode surfaces were initially levelled on a surface plate with #500 silicon carbide paper and were then mechanically polished using .3 and .05 micron alumina powder. Each portion was given a thorough cleansing in an ultrasonic bath with a final rinse using ethyl alcohol.

Annular dielectric discs were placed between the oscillator halves to determine the system capacitance and gap spacing. A constant spacing of 6



Fig. 2. One-half of the L-C oscillator

was used throughout our experiments. Prior to the beginning of each experiment, the system was flushed for several minutes with commercial grade, water-pumped nitrogen gas, which also served as the working gas in the switch.

#### Results and Discussion

After a given experiment, the electrodes were removed and examined for surface damage using an AMR model 1000A electron microscope. The specimen was mounted in the microscope holder in such a way that the beam arrived normal to the surface within a degree or two. The error introduced by specimen tilt was therefore less than the statistical spread in spot diameter. The individual spots appeared reasonably circular with fine structure around the periphery which was pressure and energy dependent.

In each experiment, several hundred spark events were allowed to occur as shown in Figure 3 while simultaneously monitoring the voltage level at which the events occurred. In agreement with the results of Cookson<sup>3</sup> and Coates et al,<sup>7</sup> several discharges occurred before the breakdown voltage reached a relatively constant value. In our analysis, we tended to ignore small spots which we attributed to breakdowns during the initial conditioning portion of the experiment. As can be seen in Figure 3, the spark events occurred at random

on the electrode face which confirmed surface planarity and the statistical nature of the distribution of surface irregularities responsible for breakdown. Individual spots began to coalesce to form a roughened surface as the density of the spots increased.

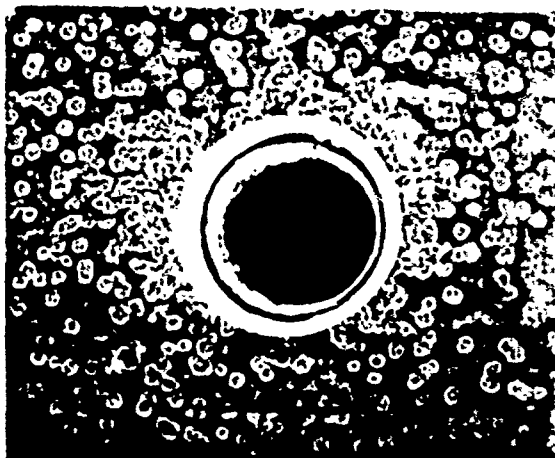


Fig. 3. Overall view of aluminum electrode after spark discharge. Gas pressure  $5.16 \times 10^3$  torr. Large center hole is inlet port for gas.

For both brass (60% Cu, 40% Zn) and aluminum (99.9%) electrodes, we observed three different regions of surface damage which could be attributed directly to a spark discharge. Each individual spot consisted of a central core containing most of the damage as evidenced by surface melting, cratering, and surface flaking. This region was surrounded by a diffuse damage area which was described by Augis et al.<sup>8</sup> as the result of a constricted glow discharge. Surrounding these areas, we observed a dark ring which was most likely a product of thermal dissipation in the surface films.

Figure 4 illustrates typical damage from individual discharges, picked from the extrema of our investigations. For both brass and aluminum, the spots shown are on the electrode initially at system ground. The damage on the side initially charged positive was similar and differed mostly in severity. It is obvious from Figure 4 that an individual discharge in aluminum produces more surface damage as indicated by melting, than it does in brass. In addition, the damaged area is larger in brass

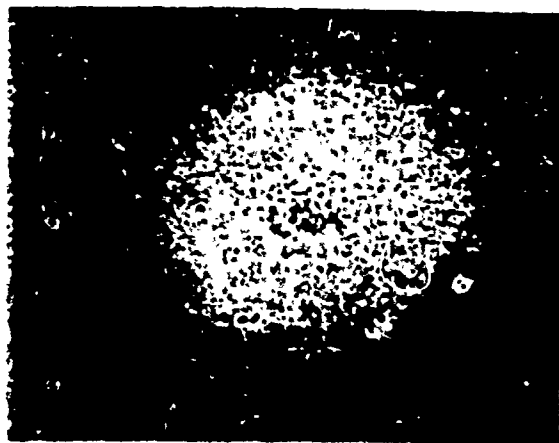
than in aluminum for the same input energy. This is consistent with a higher melting point and lower thermal conductivity for brass.

Table 1. Summary of Data for Brass and Aluminum Electrodes

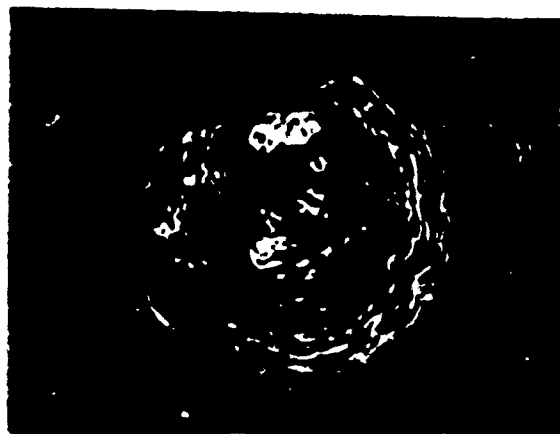
Pressure Torr x 10 <sup>3</sup>	Voltage kV	Energy mJ	Damage Area cm <sup>2</sup> x 10 <sup>-3</sup>	
			+	gnd
CuZn				
.76	1.4	.42	4.61	3.23
1.29	2.5	1.35	10.50	9.98
2.58	3.4	2.50	12.80	14.10
3.87	3.8	3.13	16.50	16.60
5.16	4.8	4.99	17.40	27.60
Al				
.76	1.4	.42	3.76	2.15
1.29	2.3	1.15	7.87	8.84
2.58	3.0	1.94	15.55	10.86
3.87	4.1	3.55	14.81	11.40
5.16	5.1	5.52	21.02	17.18

Table 1 summarizes the effects of pressure and the energy in the discharge on the damage area. This area was taken to be the area of a circle whose boundary enclosed all portions of the central core region, including filamentary traces. As the pressure in the gap was raised, the energy associated with the discharge increased with a corresponding increase in spot area.

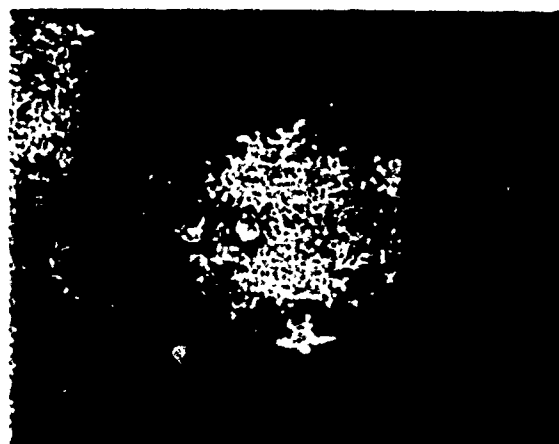
The surface of both electrode materials contained debris which spectroscopic analysis revealed to be various mixtures of the parent metal. The x-ray analyzer on the microscope was incapable of detecting elements with atomic numbers less than twelve; hence, we were unable to determine the exact composition of the debris. However, some of the particles exhibited evidence of surface charging in the electron beam which is typical of insulating materials. Because the gas composition was approximately 99.9%  $\text{N}_2$ , we infer that these particles were brittle metal nitrides which flaked off in the flowing gas stream. The formation of such particles is illustrated in Figure 5. Figure 5c shows a magnified portion of a debris field on a "fully aged" electrode surface. Both angular (insulating)



A.



B.



C.



D.

Figure 4. Typical discharge spots show the effect of pressure on spot size and damage.  
Electrode initially at system ground.

A. Aluminum  $7.6 \times 10^{-2}$  torr

C. Brass  $7.6 \times 10^{-2}$  torr

B. Aluminum  $5.16 \times 10^{-3}$  torr

D. Brass  $5.16 \times 10^{-3}$  torr

and globular (pure metal) particles can be seen.

If the device is allowed to run for thousands of shots, the individual discharge spots coalesce. To examine this phenomenon, we ran samples in the assembly described by Rose and Glancy<sup>5</sup> using the experimental parameters described previously. These parameters permitted roughly 5 discharges to occur before the gas was swept from the switch.

For short times, individual spots could be distinguished and were similar to those in Figure 3. As the number of discharges increase, spots merge to form a mottled surface, beginning first near the outer rim of the electrode surface and moving

progressively inward as the running time increases. This is consistent with the idea that hot gas and debris, flowing outward from discharges near the center, enhanced the probability of breakdown towards the periphery.

Figure 6 illustrates in both brass and aluminum the surface details of long term aging under flow. For these photographs, the pressure was one atmosphere. Similar structure was observed for higher pressures with differences only in the degree of damage.

The area to the right in Figure 6a is the area immediately beneath the flow inlet on the opposite

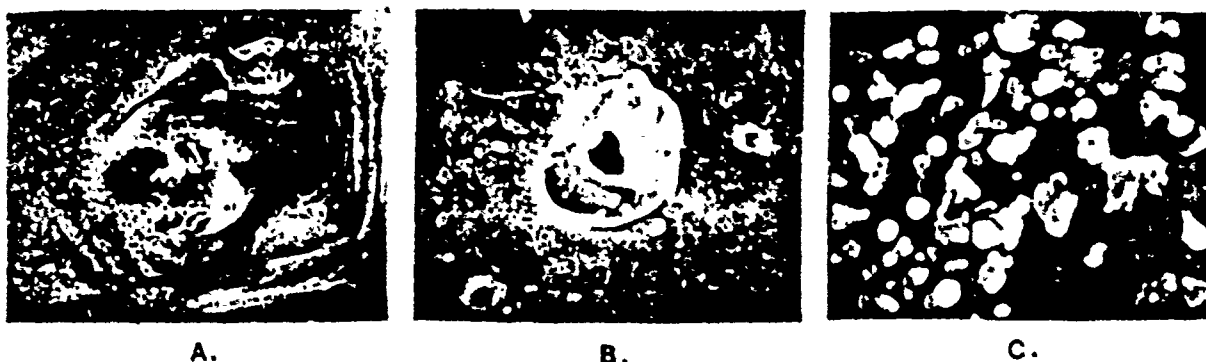


Fig. 5. Views showing flaky mechanism responsible in part for electrode wear.

- A. Interior of a discharge spot aluminum
- B. Interior of a discharge spot brass
- C. Debris field after aging brass

electrode. As one moves out along a radial, the discharge density increases until individual events are no longer discernable. Figure 6b is a higher magnification photo of the transition region between single spots and the eroded outer portion. This region is also characterized by considerable debris of the type shown in Figure 5. Figure 6c and 6d illustrate in detail the heavily worn region. Surface melting and further erosion by both metallic particles and compounds is obvious. Due to extreme temperatures evident in Figure 6, x-ray emission spectroscopy was used to determine the chemical composition in various regions along the surface. For reasons mentioned previous, the analysis is confined to elements greater than atomic number 12. In Figure 6a (brass) the intensity of the emitted x-rays, in the area beneath the flow outlet, associated with the copper and zinc, was in the ratio of 1000:500. A separate scan on a piece of the initial material confirmed this to be the intensity ratio of the brass as received. In the transition region shown in 6b, the intensity ratio changed to 1000:700 indicating a substantial increase in zinc. In the heavy wear region, the intensity ratio was 1000:350 indicating a depletion of zinc. In the region along the electrode periphery the intensity ratio returned to 1000:700 indicating zinc rich. The migration of zinc out of the system was confirmed using color photography. Free copper could be seen on the surface in the heavily damaged region. The boiling points of

copper and zinc are 2840°K and 1150°K. The melting point of brass is 1173°K. While it is impossible in our experiment to obtain a direct measurement of the temperature gradient near the electrode surface, others<sup>9</sup> have estimated the surface temperatures to be as high as 6000°K in similar experiments. It is therefore reasonable for the two constituents to separate, due to the lower boiling point of zinc, and for zinc to migrate to the cooler regions of the electrode which are obviously in the transition region and along the outer rim. Similar scans of aluminum failed to reveal anything but aluminum due to the purity of the material involved.

A surface profilometer scan is shown in Figure 7. The surfaces appeared remarkably uniform and showed surface irregularities on the order of 1 mil even though hundreds of kilojoules of energy were dissipated in the gap. The scan was measured about a line joining the center region to a point on the periphery at a similar elevation. A scan such as this presents only surface topography.

#### Summary

We have examined the surface aging characteristics of spark switches operated at an intermediate repetition rate and under gas flow. The damage produced by individual discharges was found to be a strong function of pressure and energy. As the number of discharges increased, the spots coalesced to form a mottled surface with irregularities on

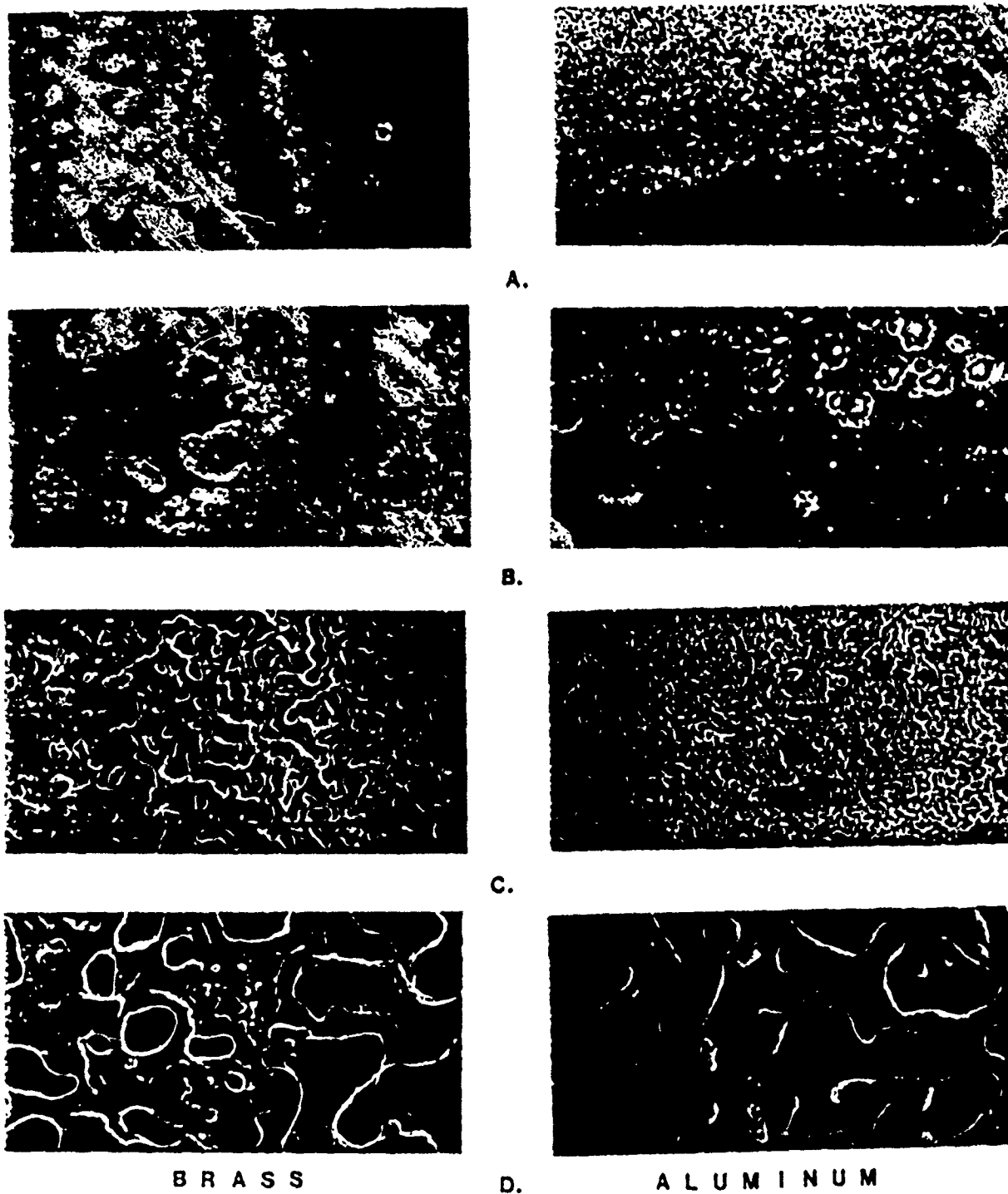


Fig. 6. Electrode surface characteristics in brass and aluminum aged for 20 min. at a pressure of  $.76 \times 10^3$  torr. A. Overall view B. Higher magnification showing transition region C. Area in which most of the discharges occurred D. High magnification photograph of the discharge area showing details of surface melting and erosion.

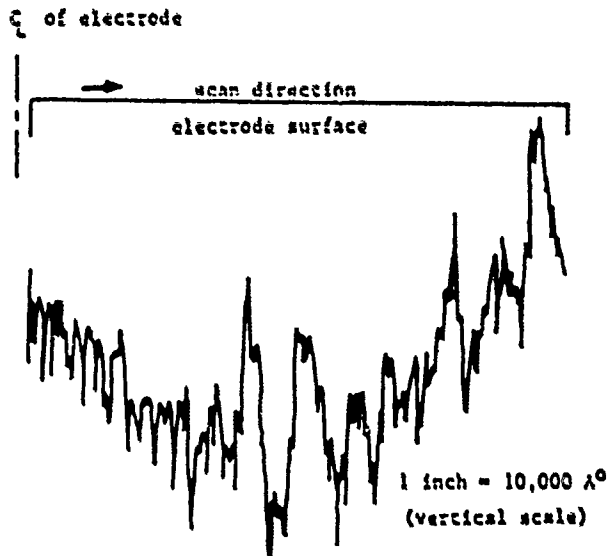


Fig. 7. Profile of brass electrode surface after aging for 30 minutes at a pressure of  $2.58 \times 10^3$  torr.

the order of 10% of the gap spacing. The primary erosion mechanisms were the formation of metal nitrides and metal particles a few microns in diameter. The erosion characteristics for brass are distinctly different than those for aluminum due to thermal induced separation of the constituents.

#### Acknowledgement

This work was sponsored in part by the Defense Advanced Research Projects Agency through the Naval Air Systems Command. In addition we wish to thank Dr. M. K. Norr and C. E. Comford for their assistance during the course of these experiments.

#### References

1. E. W. Gray, "On the Electrode Damage and Current Densities of Carbon Arcs", IEEE Transactions on Plasma Science, Vol. P5-6, pp. 384-393, Dec. 1978.
2. F. L. Jones and C. G. Moran, "Surface Films Field Emission of Electrons", Proc. Roy. Soc., A, 218, pp. 88-103, 1953.
3. A. H. Cookson, "Electrical Breakdown for Uniform Fields in Compressed Gases", Proc. IEE, Vol. 117, p. 269-280, Jan. 1970.

4. V. L. Stankevick and V. G. Kalinin, "Effect of Cathode Surface State on the Dielectric Strength of Gases and Liquids", Soviet Phys.-Technical Physics, Vol. 14, pp. 949-954, Jan. 1970.
5. M. F. Rose and M. T. Glancy, "High Repetition Rate Miniature Triggered Spark Switch", Proceedings of the Second IEEE International Pulsed Power Conference, 1979.
6. S. L. Moran, "High Repetition Rate L-C Oscillator", IEEE Conference Record of Thirteenth Pulsed Power Modulator Symposium, pp. 254-259, 1978.
7. R. Coates, J. Dutton, P. M. Harris, "Electrical Breakdown of Nitrogen at High Electric Fields", Proc. IEEE, Vol. 125, pp. 158-162, June 1978.
8. J. A. Augis, F. J. Gibson, and E. W. Gray, "Plasma and Electrode Interactions in Short Gap Discharges in Air: Electrode Effects", Int. J. Electronics, Vol. 4, pp. 315-332, 1971.
9. A. E. Guile, "Arc-Electrode Phenomena", Proc. IEE, IEE Reviews, Vol. 118, p. 1132, Sept. 1971.

## SPARK GAP EROSION RESULTS

R. Peter D. Barrett, and T. R. Surkes

Texas Tech University  
High Voltage/Pulsed Power Laboratory  
Lubbock, Texas 79409

Abstract

The erosion characteristics of a spark gap with parallel-plane electrodes are determined at atmospheric and vacuum pressures. Erosion as a loss of electrode material is measured in a range from 200 to 1000 amperes. The severity of electrode erosion is found to be related to spot formation, switching rates, melting point of the electrode, pressure, and gap length. Erosion values for a pulsed current are given for aluminum, brass, and carbon.

Introduction

The major limiting factor of spark gap lifetime is usually related, in one way or the other, to the erosion characteristics of the material used in the gap. Very little information is available on erosion of electrode material under repetitive pulse operation. The primary objective of this research is to gather data in an effort to determine the characteristics of electrode erosion under repeated, square pulse operation. The tests were conducted at both atmospheric (760 torr) and low ( $\sim 50\mu$ ) pressure and for peak currents of 200 to 1000 amperes. The rep-rates used for these tests were 10 and 30 pulses per second (pps). The materials studied were aluminum, brass, and carbon. The test gap was over-volted by a square pulse, so that anode and cathode were well defined (no ringing discharge).

It was found that spot formation, melting point of the material, rep-rate, pressure, and gap length affected electrode erosion. At low currents, the cathode undergoes a destructive process while the anode is not significantly affected. As the current is increased, a transition occurs in which the anode begins to erode. At high current, both cathode and anode erosion is measureable. Electrodes

constructed of material with low melting points perform best at low currents while high melting point materials perform best at higher currents.

Test Circuit

The spark gap is triggered by over-volting the gap. The circuit is shown in Figure 1. The output of the pulse generator consists of a well-defined rectangular pulse so that the anode and cathode are easily identified. The pulse is 20 microseconds long and has a rise and fall time of less than 1 microsecond. A Type E pulse forming network is used to shape the pulse and has a characteristic impedance of 12 ohms.<sup>1</sup>

A thyatron is used to switch the voltage across the test gap. When the gap breaks down, the major portion of the energy stored in the pulse forming network is dissipated in a copper sulfate solution resistor. When high current tests are conducted, a 2:1 transformer is inserted in the circuit as shown in Figure 2. This test circuit is capable of operation up to 500 pps and peak currents of 2.5 kilo-amps using the step down transformer.



Figure 1: Spark gap test circuit.

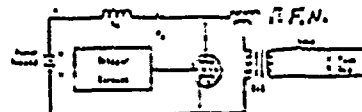


Figure 2: Spark gap test circuit with pulse transformer.



### Electrode Test Fixture

The test fixture used to hold the electrodes is shown in Figure 3. This fixture consists of a quartz glass cylinder that is held in place between two aluminum end-plates and is vacuum tight. The anode electrode is held in place by a fixed copper collet. The cathode is also held in place with a copper collet; however, it is free to move on an aluminum shank. The gap length between the sample electrodes may be varied with the use of a micrometer located on the exterior of the test chamber. Pressures as low as 20 microns may be maintained within the gap by using a mechanical roughing pump.



Figure 3: Spark gap.

### Electrode Samples

The electrodes consist of cylindrical rods arranged end-to-end in a parallel plane geometry. The ends of the electrodes are machined smooth. Before the electrodes are weighed, each is ultrasonically cleaned to remove any foreign material.

A very critical parameter related to electrode erosion is gap length. It has been shown that the anode erosion is proportional to  $\frac{I}{d}$ , where  $l$ ,  $d$ , and  $I$  are gap length, electrode diameter, and electrode current, respectively.<sup>2</sup> In order to insure that variations in gap spacing are minimized, the gap length was adjusted periodically to equal the electrode diameter. This ratio of the gap length to the electrode was maintained throughout most of the tests conducted. The electrodes were weighed on an analytical balance that allowed weight loss to be determined to an accuracy of 0.1 mg. During a typical erosion test, approximately 30 coulombs of electric charge were transferred by the gap and the gap spacing was adjusted after 15 coulombs were transferred.

### Erosion Results

The erosion results have been normalized with respect to the electric charge transferred and are presented in grams per coulomb versus peak current in Figures 4 thru 13. The electrodes were changed after each test in order to have a fresh surface imposed.

Figures 4 to 7 show the erosion curves for aluminum, brass, and carbon. The electrode diameters and gap lengths were 0.75 mm. The spark gap was operated at atmospheric pressure with a pulse rate of 10 pps. No attempt was made to flow gas through the gap. These curves show that cathode erosion is present for all materials for the lower range of pulse current ( $< 250$  A) while the anodes show no measurable wear. Aluminum and brass have anode erosion starting around the same peak current. It would seem that anode spots begin to form around 250 A. Anode and cathode erosion follow the same general trend until a plateau is reached. After the erosion curves flatten, the cathode erosion rate decreases while the anode erosion rate increases. This cathode behavior may be related to the difference in energy deposited in cathode and anode spots.<sup>3</sup> Material from the anode appears to be collecting on the cathode. One reason the cathode may accept anode material could be in the time required for the electrode spots to cool. The cathode recovers in microseconds while anode spots cannot cool in less than a millisecond, so the anode may evaporate material around a thousand times longer than the cathode.<sup>4</sup> Thus, the cathode temperature is lower than anode temperature and the anode material will condense on the cathode. Material was observed on the shank of the cathode in most of the test cases.

Another explanation for the decreases in cathode erosion may be in cathode spot division, where the number on spots have been observed to increase with current.<sup>5</sup> Spot division decreases the current density of the individual spots. Figure 14 illustrates the current density of spots as a function of current for copper.<sup>6</sup> This graph closely resembles the cathode erosion curves for aluminum and brass. The current density of spots appear to have a direct

bearing on electrode erosion.

Carbon has an interesting erosion curve in that the cathode erosion rate is constant for all values of current investigated. The anode does not show any measurable wear. Further study is required to define the conditions for anode erosion.

The melting points of the electrode materials are a factor on cathode erosion at different pulse currents. Figure 7 compares the cathode erosion curves for aluminum, brass, and carbon. Aluminum has the lowest melting point of the materials tested and performs best at currents up to 500 A. Carbon, which has the highest melting point, erodes almost twice as much as aluminum in this region. After 500 A, the brass cathode shows better erosion resistance than aluminum. The test results for carbon (Figure 6) shows no measurable anode wear and illustrates the desirability of a high melting point material for the anode electrode.

Figures 8 thru 13 compare the erosion characteristics of brass at atmospheric and vacuum pressures along with different rep rates and gap lengths. The electrode diameters and gap lengths were changed to determine the erosion dependence on gap length and electrode diameter. Comparing Figure 5 to Figure 8, it is seen that the erosion rate for brass is increased by a factor of ten when the gap length and electrode diameter are increased (from  $\approx 10^{-5}$  gm/cb at a gap length and electrode diameter of 0.75 mm to  $\approx 10^{-4}$  gm/cb at a gap spacing and electrode diameter of 2.5 mm). The gap length was adjusted to 1.0 mm with an electrode diameter of 2.5 mm and the erosion results are displayed in Figure 12. The rate of erosion is dramatically decreased (from  $\approx 10^{-4}$  gm/cb at a gap length and electrode diameter of 2.5 mm to  $\approx 10^{-6}$  gm/cb at a gap length of 1.0 mm and an electrode diameter of 2.5 mm). In order to verify these findings, a paper insert was placed in the test chamber to collect ejected electrode material. Visual observation indicated that collected material was less at a gap length of 1.0 mm than at a gap length of 2.5 mm for the same total coulombs transferred.

It is not known whether the destructive electrode processes of an arc are diminished as gap length is decreased or that the electrodes simply collect more ejected material. Gap length and electrode diameter play an important part in electrode erosion; and, by maximizing electrode diameter and minimizing gap length, the rate of erosion can be reduced.

The pulse repetition rate at which the test gap is switched has pronounced affect on cathode erosion. Referring to Figure 13, it is seen that the maximum cathode erosion point is shifted from a peak current of 500 A at 10 pps to a peak current of 300 A at 50 pps. This shift of the cathode erosion curve may be explained by the fact that more energy per unit time is deposited at the cathode at 50 pps than at 10 pps, and the average cathode temperature increases so that the condensation of anode material decreases. For constant pps, the cathode erosion of brass shows little difference between atmospheric and vacuum pressures and is assumed to be the same. The erosion rate at the anode is relatively unaffected by different pulse repetition rates.

Operation of a spark gap at vacuum or low pressure has an adverse affect on the erosion rate of the anode. The pressure in the gap was adjusted to operate below the Paschen minimum for all tests conducted at low pressure (see Reference 7). Comparing Figure 8 to Figure 10, it is seen that there is an anode erosion null for vacuum at a peak current of 700 A with a pulse repetition rate of 10 pps. The same is true for the anode at vacuum with a rep rate of 50 pps, except the anode null occurs at a peak current of 850 A (Figure 11).

Figure 9 shows a reduction of anode erosion at atmospheric pressure with a rep rate of 50 pps; however, it is not nearly as great as the anode erosion decrease at vacuum pressure. Erosion rates at low pressure require more investigation to explain the decrease of anode erosion.

### Conclusion

The results of this study clearly indicate a considerable variation of electrode erosion, both in magnitude and character, as a function of pulse current below 1000 amperes. Spot formation is an important process in that erosion rates of the respective electrodes vary with the formation of these spots. Melting points of electrode materials, gap length and electrode diameter, pulse repetition rates, and, to a degree, gap pressure affect electrode erosion. From the findings of this study, it is suggested that for spark gap construction:

1. Choose a high melting point material for the anode.
2. Minimize gap length or separation.
3. Maximize electrode diameter.
4. Optimum cathode material varies with peak current. Materials with low melting points perform best at lower peak currents, while high melting point materials perform best at higher peak currents.
5. Pulse repetition rates primarily affect the cathode erosion rate (10 to 50 pps).
6. Pressure primarily affects the anode erosion rate.

It is necessary to be able to predict erosion rates for design purposes. Although the results of this paper are for a limited range of operating parameters, these findings may be helpful in reducing the severity of electrode erosion in some applications.

### References

1. G.N. Glasoe and J.V. Lebacqz, *Pulse Generators*, New York, Dover Pub. Inc., 1948.
2. G.R. Mitchell, 'High-current vacuum arcs,' *Proc. IEEE*, vol. 117, Dec. 1970.
3. J.A. Rich and C.A. Farrall, 'Vacuum arc recovery phenomena,' *Proc. IEEE*, vol. 52, Nov. 1964.
4. W.D. Davis and H.C. Miller, 'Analysis of the electrode products emitted by dc arcs in a vacuum ambient,' *J. Appl. Phys.*, vol. 40, Apr. 1969.
5. B.E. Djakov and R. Holmes, 'Cathode spot division in vacuum arcs with solid metal cathodes,' *J. Phys. D: Appl. Phys.*, vol. 4 1971.
6. J.E. Daalder, 'Diameter and current density of single and multiple cathode discharges in vacuum,' *IEEE PES Winter Meeting*, New York, Jan. 27 - Feb. 1, 1974.
7. M.J. Schonhuber, 'Breakdown of gases below paschen minimum: basic design data of high-voltage equipment,' *IEEE. TRANS POWER APP.*, vol. 88, Feb.

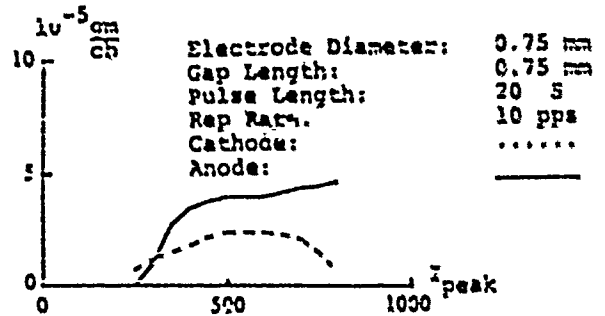


Figure 4: Erosion curve for aluminum at atmospheric pressure.

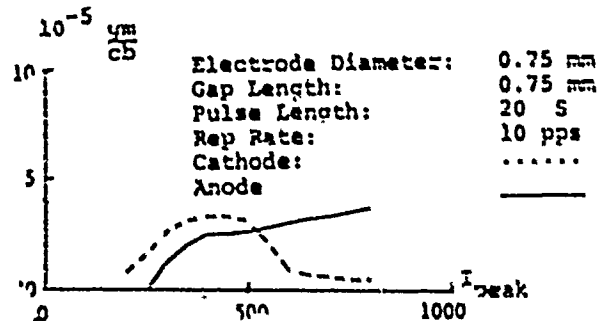


Figure 5: Erosion curve for brass at atmospheric pressure.

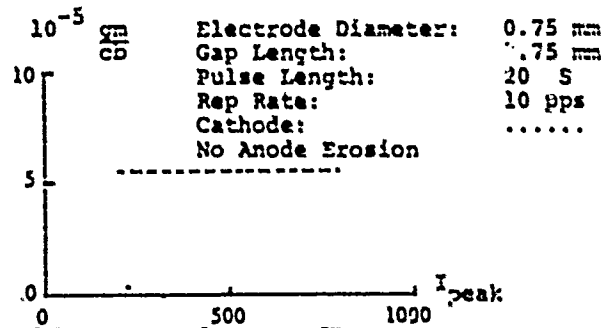


Figure 6: Erosion curve for carbon at atmospheric pressure.

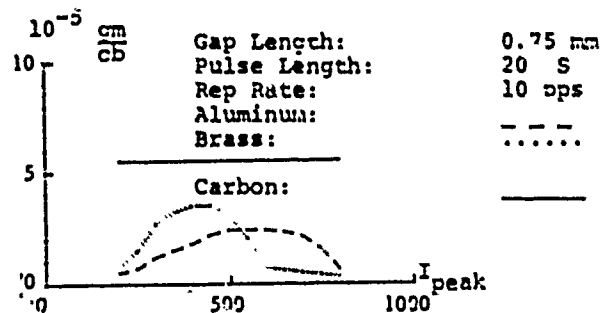


Figure 7: Erosion curve comparing cathode erosion for aluminum, brass, and carbon.

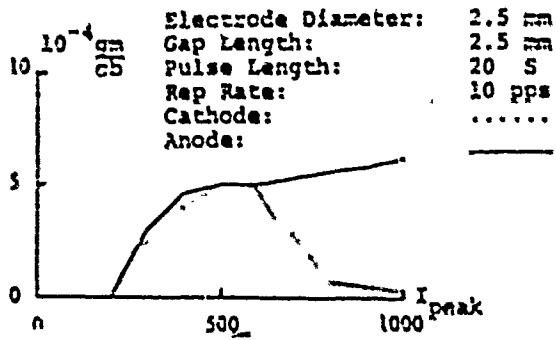


Figure 8: Erosion curve for brass at atmospheric pressure.

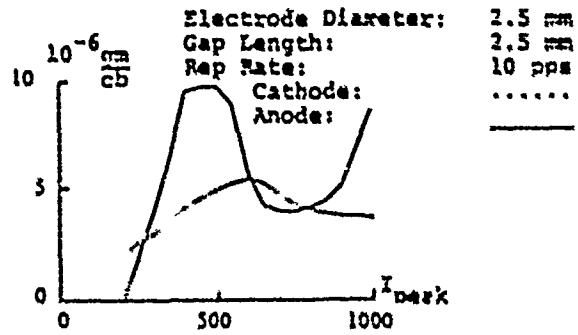


Figure 12: Erosion curve for brass with a gap length of 1.0mm at atmospheric pressure.

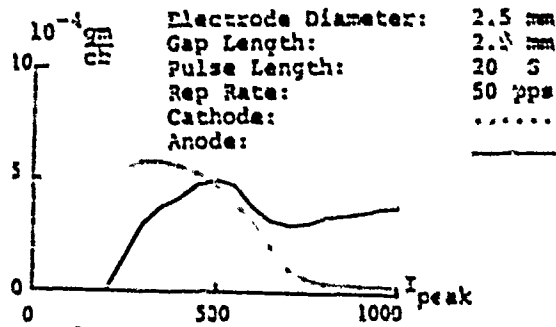


Figure 9: Erosion curve for brass at atmospheric pressure.

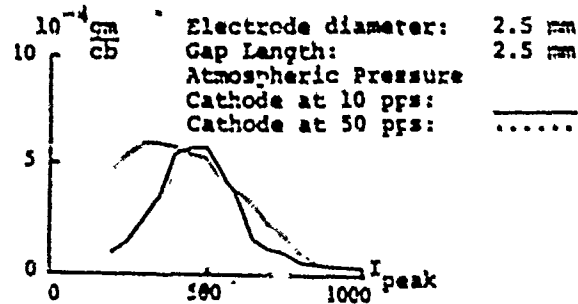


Figure 13: Comparison of brass cathode erosion rates for different switching rates.

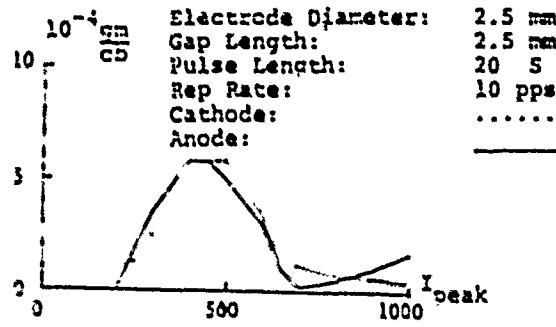


Figure 10: Erosion curve for brass at vacuum pressure.

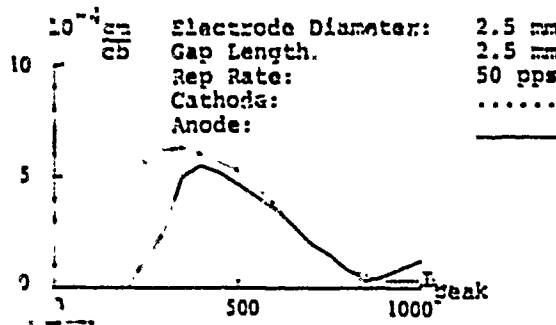


Figure 11: Erosion curve for brass at vacuum pressure.

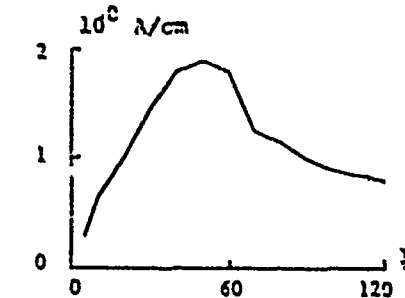


Figure 14: Spot current density versus conducted peak current.

## LONG-LIFE HIGH-REPETITION-RATE TRIGGERED SPARK GAP

HAROLD WATSON

AirResearch Manufacturing Company of California  
Torrance, California

Abstract

A forced-air-blown triggered spark gap (TSG) switch system capable of high repetition rates on a continuous basis as well as a TSG comparative study is described. The system consists of two TSG's, each discharging its own 30-ohm pulse cable into a common load. The system was operated at 30 kv, 1 kHz, for  $39 \times 10^6$  shots with erosion rates of approximately 60 ng/amp-hour. Each TSG discharged 0.423 joules in 60 nsec (FWHM) per pulse. The switching losses were about 28 percent of the stored cable energy. Calculations indicate this can reduce to 14 percent by optimizing the TSG design and surrounding air channel insulation for a more uniform E-field. Test results indicate a multielement assembly capable of switching 50 ka or more 40- to 100-nsec pulses at 1 kHz from 50 kv for  $500 \times 10^6$  shots without gap adjustment is feasible with this concept. The work was partially supported by the U.S. Energy Research and Development Administration under Contract No. EN-77-C-04-4048.

Introduction

The objective was to develop TSG's that would work in a small-scale multielement spark\* gap switch system to show the feasibility of a much larger switch system. A full-scale system is to furnish pulse power to a K<sub>F</sub> laser. The specifications are shown in Table 1.

TABLE 1

## TRIGGERED SPARK GAP SYSTEM PERFORMANCE SPECIFICATION

Voltage	50 kv	Jitter	≤10 nsec
Current	50 ka	di/dt	2x10 <sup>6</sup> amp/usec
Duration	≤100 nsec	Inductance	≤10 nh
Frequency	≥1 kHz	Closure time	≤20 nsec
		Life	≥5 x 10 <sup>8</sup> shots

\*The words sparks and arcs are used interchangeably.

Complete system studies for a switch system that will meet these requirements are described in the final report on this contract (Ref. 1). Spark gap switches have been used for many years for a variety of switching applications. Many types have been developed, each with its particular good feature, but none that would meet all the requirements of Table 1. In these contemporary systems, the power being switched is not as high as many high-powered systems; however, the requirement of switching up to 50 ka and less than 100 nsec pulses, with low jitter at 1 kHz with a switch life of  $5 \times 10^8$  pulses, is a relatively new requirement that has received little attention. The requirement of long life dictates that the closure di/dt and charge per shot per switch must be low, which means that many switches are needed for the  $500 \times 10^6$  shots, and thus it follows that they should be small so the final assembly is not unacceptably large. The system study indicated the closure time requirement of 20 nsec could be realized with small TSG's operating at 1 atm of air. A higher pressure will decrease the closure time but it will also decrease the gap spacing, which will make it more difficult to realize the  $500 \times 10^6$  shot life requirement. For example, if the gap spacing increases X percent for 5 cm, it will increase 2XX percent for 2.5 cm, all else being equal.

This paper is limited to describing the development of the TSG's in a small-scale pulser to demonstrate the feasibility of the large multielement switch system. The merits of various basic spark gap switches are described as they relate to this application. Small size, low switching losses, and low erosion rates of the electrodes and trigger were the

main factors in selecting a suitable switch. The performance data described include maximum frequency as a function of cable voltage and airflow, erosion rates after  $19 \times 10^6$  shot test run, as well as jitter as a function of cable voltage.

#### Comparison of Basic Spark Gaps

The requirements of small size, low closure losses, and 1 atm of air in the gaps tend to be mutually exclusive conditions. Small electrodes tend to have high field enhancement factors ( $f$ )\* and large gap spacing, therefore relatively high closure losses when operated at 1 atm.

A closure loss comparison is made of two parameters on four basic spark gap switches as a function of gas (air) densities. The four types are (1) two spheres forming a single arc; (2) three spheres in a row forming two series arcs; (3) three cylinders formed in the manner of rungs of a ladder, forming two series arcs; and (4) two electrodes that form a uniform field gap (UFG) and produce a single arc. When two arcs are in series, the two gap spacings are calculated independently. Then the sum of the two spacings and the average voltage across the two gaps are used to calculate the closure losses. The rationale is that closure time is a function of joules per unit distance of arc channel and time. Therefore, two series gaps would close in approximately the same manner as the single gap if all other parameters are identical. In each case the overall static breakover voltage (SBV) is kept equal to  $1.25 \times 50 \text{ kv} = 62.5 \text{ kv}$  to be rated at 50 kv, and 30 ohms was used for cable and load impedances. The electrode diameters are all kept at 1.59 cm except the uniform gap (UFG). Figures 1 and 2 show how the gap and closure losses vary as a function of gas (air) density.

Switching losses and gap spacings are estimated by equations derived from the work of J. C. Martin (Refs. 2 and 3) in conjunction with  $f$ 's from Ref. 4.

\* $f$  is the ratio of maximum electrical stress to average electrical stress just before turn-on.

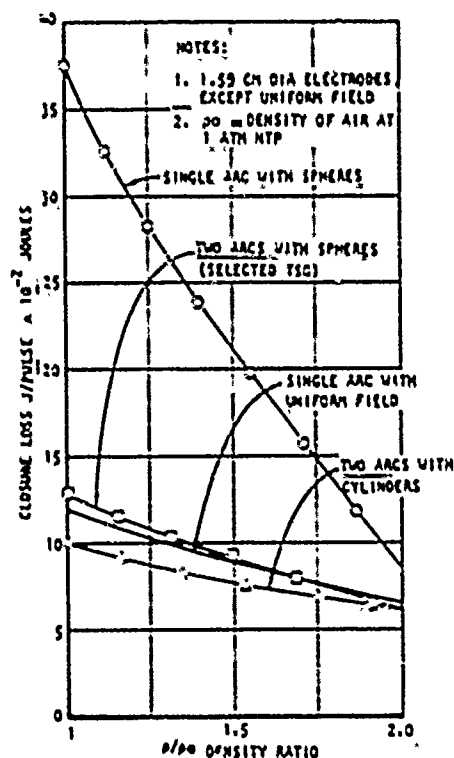


Figure 1. Closure Loss as a Function of Gas Density for Different TSG Configurations

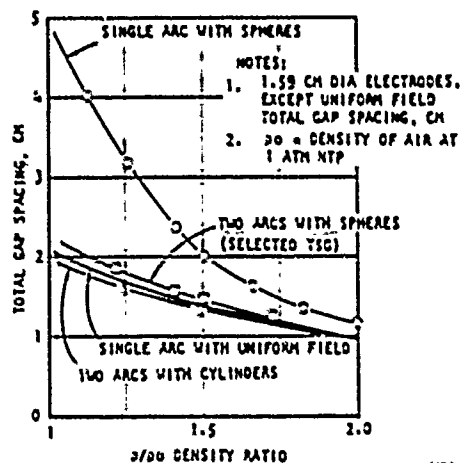


Figure 2. Gas Spacing as a Function of Gas Density for Different TSG Configurations

These equations are shown in the Appendix. Equations 1 and 14 were used to calculate these curves. The following examples show how the gap spacing and  $f$ 's compare at  $\rho/\rho_0 = 1$  for the single arc and the two series arcs:

### Single Arc

$S = 5.02$  cm from Equation 14

$f = 3.74$  from Equation 13

### Two Arcs

$S_1 + S_2 = S = 2.09$  cm (calculated for  $S_1$ , then  $S_2$ , then summed)

$f_1 = 1.72$

$f_2 = 1.16$

where

$V_2 = 50 \times 1.25 = 62.5$  single arc

$V_2 = \frac{50 \times 2}{3} \times 1.25 = 41.67$  long gap, two arcs

$V_2 = \frac{50 \times 1.25}{3} = 20.83$  short gap, two arcs

$E_{max} = 46.7$  long gaps, 42.28 short gap, from Equation 12; note  $\delta = 1$  for long gaps and  $\delta = 0.6$  for short gaps; see Figure 3 of Ref. 3.

Note the difference in  $S$ 's and  $f$ 's between the two switches.

Several conclusions can be drawn from the data presented in Figures 1 and 2:

- Most importantly, because the diameter must be small, a voltage gradient device is necessary at 1 atm to keep the total gap distance small and therefore to keep the switching losses reasonably low.
- The gap spacing in the UFG, Figure 2, is approximately equal to that of the selected TSG, and  $J_1$  is as low as is possible at 1 atm for a 1-gap UFG, as well as the selected TSG.
- It can be seen in Figure 1 that the closure losses of a single spherical arc gap at 1 atm, with a diameter of 1.59 cm are quite high and in fact the density has to be increased to 3 atm (not shown) to reduce the losses to approximately equal to the first two types.
- The two-series gap cylinder configuration has the lowest switching losses at  $p/p_0 \leq 2$ . Depending on the length of the cylinders, the life could be made very long because total effective arc surface could be quite high; however, the trigger requirements would be higher because the trigger capacitance would be greater and also the size would be larger than the spherical mid-plane TSG.

(e) These loss calculations when compared to simple on-state voltage times current during a 100-nsec pulse (or less) indicate the closure losses are so much greater than the on-state losses that the on-state losses can be neglected in favor of reducing closure losses.

Based on conclusions from the above comparison, the basic type of TSG best suited for this application utilizes the three-sphere arrangement; a practical TSG is shown in Figure 3. This results in a form of offset midplane (MP) with prespark to generate UV preionization to minimize jitter. This basic type of TSG has been in use for some time; however, generally the midplane is configured as a flat disc or bar, which would not result in the lowest  $f$  since they have dissimilar opposing surfaces. The midplane not only serves the purpose of acting as trigger and voltage gradient element but it also shields the UV prespark pin from the main arc for longer life.

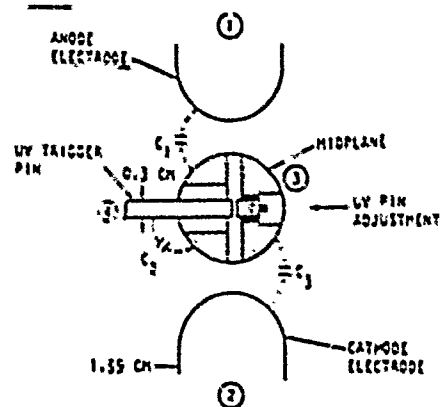


Figure 3. Cross-Section View of Selected Trigger Spark Gap

The static-breakover voltage (SBV) of the long gap was designed to be approximately 2/3 and the short gap approximately 1/3 of the overall SBV of both gaps for the lowest jitter condition.

The MP and electrodes were machined from Mallory Elkonite type 10W3. This is a relatively inexpensive contact material containing a sintered mix of 75 percent tungsten (W) and 25 percent copper (Cu) by weight, 58 percent W and 42 percent Cu by volume. As mentioned above, this basic TSG is not new and how it turns on has been described by others (see Ref. 1).

### Setup and Test Results

The pulser test bed consisted of two of the newly developed TSG's, each discharging its own 30.4-ohm pulse cable into a common load; a dc resonant charger was used to charge the cables in 67 usec; this plus an additional margin of 83 usec allowed 850 usec for the TSG's to recover at 1 kHz. Due to higher than expected core losses in the trigger pulse transformers, the overall rise time of the trigger pulse was much longer than expected. Despite this, the jitter was in the range of 3 to 4 usec peak to peak, which suggests jitter in the range of 1 nsec could be expected with adequate trigger generator redesign.

Figure 4 shows a side view of the TSG used for test in the air channel. One TSG is mounted 12 inches above the other in the same air stream. Note there is an opening for air to circulate through the MP to clear out prespark generated hot gas and dust particles.

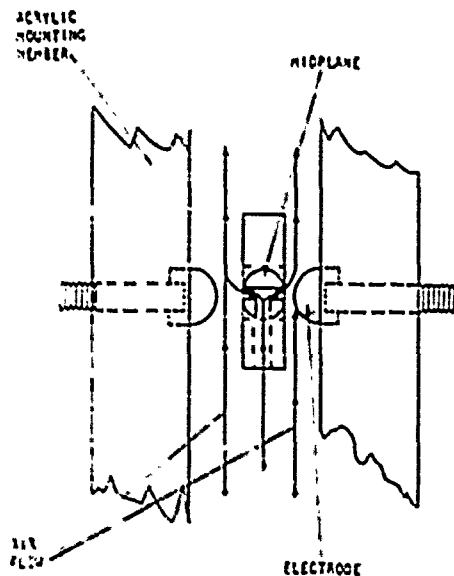


Figure 4. Side View of TSG in Test Fixture

Figure 5 shows the air velocity as measured right on top of the air channel. The fixture was originally designed for two TSG's side-by-side but because of arcover between the two TSG's, one was removed. This left a large space in which much of the air could flow. Though this decreased the air to the remaining TSG, the 1 kHz goal was reached; however, it does suggest that with the proper air flow the pulse rate could be higher. Figure 6 shows a side view picture of the TSG and load assembly. The TSG's were operating at 1 kHz when the picture was taken.

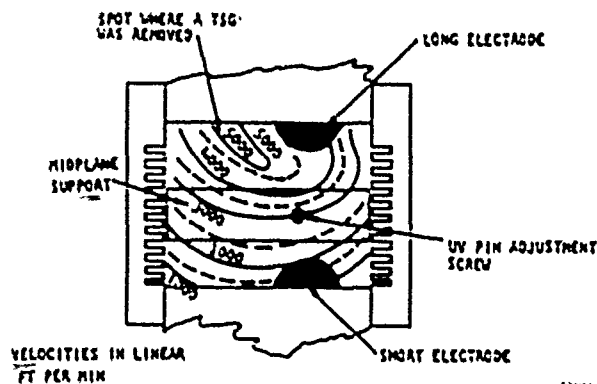


Figure 5. Airflow Pattern Over Top of Air Duct

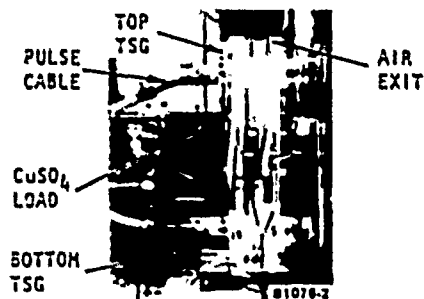


Figure 6. Switch Assembly and Load

F30229



The TSG's were rated at only 35 kv with SBV = 37.5 kv and were not holding off enough voltage in relation to their total gap spacing due to E-field distortions. Figure 7 compares measured and calculated load voltage waveforms. The actual load voltage is shown as well as what the load voltage may be if all the cable current were allowed to flow into the load. The cable current and the load current during TSG closure are not the same because a significant amount of cable current was flowing back through the UV pin. This curve was calculated by adding pin current to the load current and multiplying this times the 15-ohm load. Note how closely these two curves match. The highest SBV for this gap setting could be as high as 62.5 kv; the TSG then could be rated at 50 kv. This level (or close to it) could be brought about by redesign to make the E-field more uniform. Three additional curves are shown to indicate the output pulse if this TSG were holding off 50 kv in place of 34.1 kv. Equation 6 was used to calculate these curves.

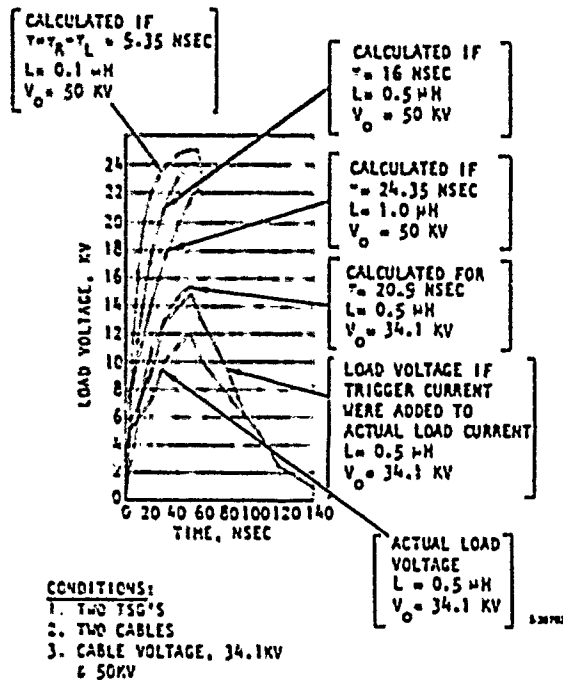


Figure 7. Actual Load Voltage, Load Voltage with Trigger Current Added, and Calculated Voltages for Different Inductance and Voltage

Using these curves as well as Equations 1, 2, and 3 for total switching losses, the following comparisons are made:

Actual pulse energy in the load\*:

$$J = 0.480 \text{ joules in load; } J_L = J_0 - J = 1.08 - 0.480 = 0.600 \text{ joules lost}$$

where

$J_0$  = energy stored in cable

Energy relationship if the trigger current were added to the measured load current\*\*:

$$J = 0.780 \text{ joules in load; } J_L = 1.8 - 0.780 = 0.300 \text{ joules lost}$$

Calculated energy relationships for the 34.1 kv curve\*\*:

$$J = 1.08 - 0.223 = 0.857 \text{ joules in load;}$$

$$J_L = 0.223 \text{ joules lost}$$

Calculated energy relationships for all 50 kv curves\*\*:

$$J = 2.33 - 0.33 = 2.0 \text{ joules in load; } J_L = 0.330 \text{ joules lost}$$

Note 0.33 joules is 14 percent of 2.33 joules.

As expected, as the cable voltage decreases, the jitter increases. Of interest is that jitter is lower at zero crossover and at the peak than at the 1/3 point of the leading edge of the load pulse. This is probably due to some of the closure current going through the UV pin to the trigger circuit. Though the 1/3 point jitter is higher than the crossover and peak jitter, it is still only about 3 nsec at 0.8 SBV and within the 10-nsec peak-to-peak from 0.75 to 0.95 SBV or 26 to 35.6 kv, respectively.

Figure 8 illustrates the maximum firing frequency as a function of peak cable voltage and air flowrate, using two TSG's and two cables. The air flowrate is taken from the highest rate in Figure 5 and is much higher than in the gaps, especially the short gap. The frequency limit was found to be about the same when one TSG discharged three cables. This result was unexpected; however, when the UV holes were blocked, the frequency dropped from a peak of 1.6 kHz to 1.1 kHz, which was expected.

\*Based on graphical analysis.

\*\*From Martin based equations, Appendix.

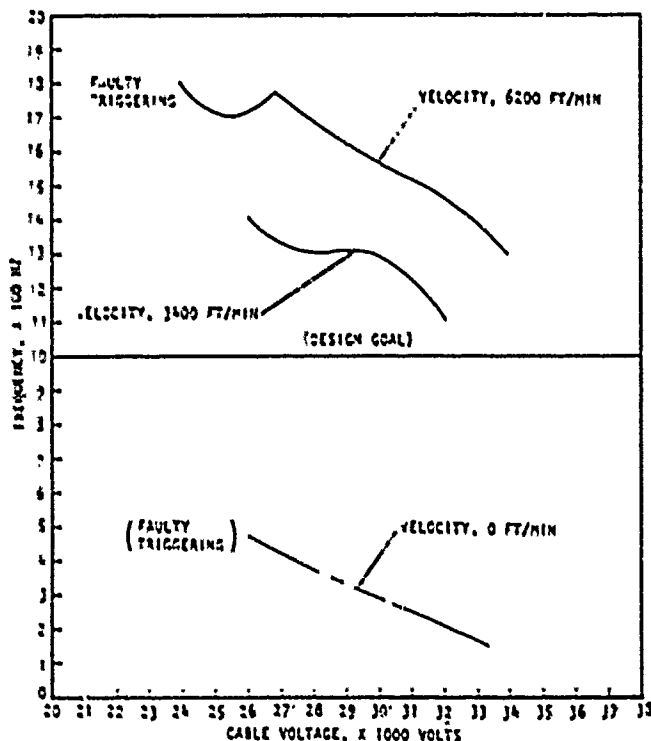


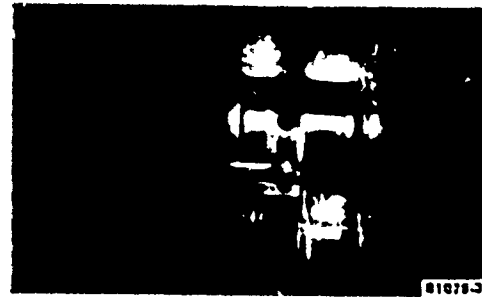
Figure 8. Maximum Firing Frequency as a Function of Cable Voltage and Blower Voltage; One Cable per TSG

There was a total of  $39 \times 10^6$  shots on the TSG's, which included about  $7 \times 10^6$  shots during the performance tests. The material loss was only about 0.03 percent of the weight of the electrodes plus stud, and with this small loss it was not possible to determine accurately material loss by before-and-after weight measurements. Blown-up profile pictures were used to calculate material loss. Only a general indication of material loss can be obtained since the erosion was not uniform over the tip. From a rough graphic study of the actual pictures, the rate of erosion appears to be about 60 mg/amp-hour. This should cause the short gap to increase only 10 percent after  $5 \times 10^8$  shots. The TSG should function well with this small increase.

An unexpected, interesting result was that the pins in the upper TSG eroded much more than the lowers. It is not known why this occurred, since the only difference was that the top airflow was slightly

hotter and less pure. The rate of erosion on the top pins appears to be about 50 mg/amp-hour, while erosion of the bottom pins is too small to determine. For a redesigned TSG the pin could be larger and the pin current would be lower.

Figure 9 shows a blown-up picture of the top TSG, No. 2, operating at 1.0 kHz. Ionized gas jets can be seen coming out of the cable side electrode.



F.30228

Figure 9. Top View of TSG No. 2 Operating at 1.0 kHz (Size Factor 1.57 x 1 in.)

#### Conclusion

The small off-set midplane described appears to be a good choice for multiclement systems where long life, high di/dt, and low jitter are needed. At 60 mg/amp-hr the short gap would increase only 10 percent after  $5 \times 10^8$  shots (139 hours of continuous operation at 1 kHz). This is based on 100 TSG's discharging 50 ka, 50 nsec pulses; with proper air flow utilization the TSG will probably operate above 1 kHz. Since the maximum frequency was about the same with one cable as with three, the charge per shot is probably not limiting the maximum frequency. The experimental voltage-to-gap ratio is too low, which in turn causes the switching losses to be higher than necessary. There are three important features that were undoubtedly causing  $f$  to be higher than needed:

- (a) The surface of the midplane was not as spherical as it could have been. Dissimilar opposing surfaces always have higher  $f$ 's than similar surfaces (Ref. 4).
- (b) The UV hole should be large enough to allow enough UV to exit but not so large as to significantly distort the E-field.

The present hole is 1/8 in., which is probably larger than needed.

(c) The dividers and nonsymmetrical surrounding structure distorts the E-field.

By proper redesign the closure losses will be reduced; however, the lowest possible figure appears to be 14 percent of the available energy. The pressure could be increased to lower the closure losses; however, this may decrease the life since the percent of increase in the now smaller gap spacing would be greater. Also, any air filter will allow some dust particles through. How much filtering is needed to keep prefire at a minimum is uncertain. The premise that two gaps could be operated in the same air stream if the air has around 10 msec between gaps to recover its dielectric strength has been shown.

#### References

1. "Multielement Spark Gap Switch System," Final Report on Contract No. EN-73-C-04-4048 for U.S. Energy Research and Development Administration.
2. Pulsed Electrical Power Circuit and Electromagnetic System Design Notes 4-1, Volume 1, Note 4, AFWL-TR-73-166.
3. Pulsed Electrical Power Dielectric Strength Notes 5-1, Note 16, AFWL-TR-73-167.
4. High-Voltage Technology, edited by L. L. Alston, Oxford University Press A68, Page 7.

#### APPENDIX

Switching losses are estimated in three steps from 0 to  $2.2\tau$ , from  $2.2\tau$  to  $\tau_0$ , and from  $\tau_0$  to  $t_0$  in the following manner:

$$1. J_1 = \int_0^{2.2\tau} V_c I_c dt = 0.4 V_0^2 \tau_R / R \quad (\text{closure losses})$$

$$2. J_2 = \int_{2.2\tau}^{\tau_0} V_c I_c dt + \int_{2.2\tau}^{\tau_0} V_c I_c dt$$

$$= \frac{V_0^2 \tau_R}{R} \left\{ \frac{e^{-2\tau_0/\tau}}{2} - e^{-\tau_0/\tau} + 0.105 \right\} +$$

$$\frac{V_c V_0}{R} \left\{ \tau_0 - 2.2\tau + (e^{-\tau_0/\tau} + 0.11) \right\}$$

$$3. J_3 = \int_{\tau_0}^{t_p} V_c I_c dt = \frac{V_c I}{2} \left\{ t_p - \tau_0 \right\}$$

$$4. V_c = V_0 - V_x - I \tau_R, \text{ drop across gap}$$

$$5. V_c = L \frac{di}{dt}$$

$$6. I_c = \frac{V_0 (1 - e^{-t/\tau})}{R}$$

$$7. R = Z + R_L \quad (\text{Ref. 2})$$

$$8. \tau = \tau_R + \tau_L, \text{ e-folding time of current pulse} \quad (\text{Ref. 2})$$

$$9. \tau_R = \frac{88}{R^{1/3} \epsilon^{4/3}} (\rho/\rho_0)^{1/2} \times 10^{-9} \text{ sec} \quad (\text{accurate within } 20\%) \quad (\text{Ref. 2.})$$

$$10. \tau_L = L/R \quad (\text{Ref. 2})$$

$$11. E = E_{\max}/f \text{ in units of } 10 \text{ kV} \quad (\text{Ref. 3})$$

$$12. E_{\max} = 24.5p + 6.7 \sqrt{p/r_{\text{eff}}} \quad (\text{Ref. 3})$$

$$13. f = K_1 S/r + K_2 \text{ (for } S \geq 0.37) \quad (\text{Ref. 4})$$

$$14. S = \frac{r V_2 K_2}{r E_{\max} - V_2 K_1} \text{ (from combining Equations 13 and 15)}$$

$$15. V_2 = SE_{\max}/f = SBV \text{ in kV} \quad (\text{Ref. 3})$$

where:

J = energy lost in joules

$V_0$  = cable voltage at  $t_0^+$ , V

L = effective series inductance, h

Z = source impedance, 30 ohms per cable

R = load resistance, 15 ohms for two TSG's and two cables

$\rho_0$  = density of air at 1 atm NTP

$\rho$  = density of air in gap

$K_1$  = 0.13 for cylinders, 0.46 for spheres (Ref. 4)

$K_2$  = 1.06 for cylinders, 0.83 for spheres (Ref. 4)

r = radius of electrodes in cm

$r_{\text{eff}} = 0.23r$  for cylinders,  $0.115r$  for spheres (Ref. 4)

E = function of S/r, slight modifier (Ref. 4)

$V_c$  = on-state voltage, 50 v assumed

$\tau_0$  = cable pulse duration, both ways, nsec

$t_p$  = duration of pulse at base, nsec

I = peak pulse current

SBV = static breakover voltage

P = pressure, atm

S = gap spacing, cm

## TESTING OF A 100 KV, 100 HZ REP-RATE GAS SWITCH

A. RAMRUS and J. SHANNON

Maxwell Laboratories, Inc.  
San Diego, California 92123Abstract

A two-electrode gas switch with a self-breakdown voltage of 100 kV was operated at a pulse-repetition rate of 100 Hz with bursts up to 10 seconds in duration. The output of a pulse transformer provided the  $(1 - \cos \omega t)$  waveform which charged the switch in about one-half millisecond. The switch discharged with a peak current of about 10 kA and a total charge transfer of about 10 mC into a damped LC circuit. A continuous purge of air through the interelectrode spacing enabled the switch to recover its breakdown voltage between discharges. Flow rates up to 35 SCFM were employed. This paper discusses the dependence of switch jitter and waveform reproducibility on air-flow rate.

1. Introduction

This switch development was performed in support of Maxwell's High Average Power Technology Development Program which is directed towards the development of a high-power electron-beam gun.<sup>1</sup> This system is now in final development; it includes a 500 kW power conditioner which charges a 1 MV hybrid Marx/pfn pulse generator to 100 kV. This pulser provides a diode with 500 kV, 1  $\mu$ sec pulse-width and a pulse-repetition rate of 100 pps. To achieve this rep-rate the pulse generator is equipped with gas switches which are continuously purged with dry air. This report presents test results on the 100 kV gas-dynamic spark gap develop 1 for this application.

2. Background

Rep-rate switching at Maxwell was studied during

two previous programs in which the objective was control of multimewatts of average power.<sup>2,3</sup> In contrast, power levels of the present program are 50 kW to satisfy requirements of a 500 kW pulser containing 10 spark gaps; there was high confidence the switching techniques previously developed were applicable but the Marx arrangement presented new problems for repetitive switching. One objective of the present test was to measure jitter vs. flow rate to determine the minimum flow rates for acceptable switch performance. A multi-switch system demands a high safety factor and should perform reliably with minimum investment in air-flow equipment.

The spark-gap design is shown in Fig. 1; it was previously shown capable of operation at 100 kV, 250 Hz, 0.24 C and 5 kA peak current. Stable operation with virtually no switch malfunctions was attained for 10-second bursts with flow rates of about 65 SCFM. Smaller flow rates should be needed for the Marx now under consideration because of the reduced power controlled by the Marx switches.

3. Specifications

A facility was constructed to provide the spark-gap duty expected during Marx operation. These requirements called for charging the spark gap to 100 kV in about 100  $\mu$ sec, and discharge of 10 mC and 10 kA (peak), as shown in Table 1.

Installed in a Marx, the switches must hold off the 100 kV Marx charging, then close with minimum jitter when the Marx erects. It was necessary, therefore, to determine optimum spark-gap pressure for minimum jitter with reliable 100 kV hold off.

#### 4. Setup

##### 4.1 Test Circuit

The test facility consisted of a primary charging circuit, a 1:12 step-up transformer, and an output circuit containing the switch under test. The power source was a 3-phase transformer which reduced power company 12 kV AC to 4160 V (rms). The 3-phase was then rectified in a 6-rectifier bridge.

Fig. 2 shows the main circuit elements. When the ignitron is triggered, the primary capacitor,  $C_1$ , resonantly charges through the 13 mH inductor to about 5 kV with a 1 msec transfer time. A thyatron (Eng. Elec. CX 1154) controls the discharge of  $C_1$  into the transformer. A diode and resistor is connected across the thyatron to allow reverse current to bypass the thyatron and to reset the transformer core while preventing damaging current reversal through the thyatron.

The transformer was a foil and mylar winding around an iron core with the primary and secondary insulated from one another and from ground permitting the primary to be charged with the secondary grounded.  $C_1$  and the thyatron had one end grounded to eliminate the need for an isolated heater supply.

The output circuit containing the switch had the required inductance and resistance to ring the current through the switch to conduct 10 mC, although  $C_2$  contained only 2.2 mC. The 3  $\Omega$  damping resistance was chosen for a circuit-Q of about three. The switch circuit inductance was about 1.5  $\mu$ H to attain the 10 kA (peak) at 100 kV.

##### 4.2 Diagnostics

###### (1) Voltage Probes

Resistive voltage dividers tapped-off the voltage on  $C_1$  and  $C_2$ . The probe on  $C_2$  capacitor indicated switch breakdown voltage. Data from these probes was stored on an Ampex tape recorder which operates at high tape speeds. The magnetic record is then played back at a slow speed and recorded on a multi-channel strip chart recorder. With this technique every pulse

in a burst can be analyzed although at the relatively low frequency bandwidth of  $\approx 20$  kHz. The  $C_2$  charge voltage was also recorded on an oscillograph.

###### (2) Current Probe

A Pearson current probe monitored switch current. The rep-rate waveforms were recorded on magnetic tape and were superimposed on an oscilloscope. Fluctuation in the amplitude of this current measured on the oscillograph indicated the jitter in breakdown voltage since this peak current is proportional to breakdown voltage. The trace width after a typical 100-shot run indicated the total spread in peak current.

###### (3) Air Pressure and Flow

Flow was determined by measurement of pressure in a pitot tube placed downstream from the switch. A Magnahelic gauge measured this pressure. The pitot tube was located in a straight section of 2-7/8" diameter PVC pipe about ten feet from the switch and three feet from the end of the pipe which exhausted into the atmosphere. Calculation of mass flow rate from measured flow velocity of 500 ft. per minute yielded 10 SCFM.

#### 5. Results

##### 5.1 Switch Hold-off Voltage vs. Pressure

An irradiation gap (Fig. 1) was provided in the aluminum flange attached to one of the switch electrodes. In this way the arc site on the nested-pair electrode was illuminated with UV from the irradiation source. In these experiments the UV source was a spark plug which fires perpendicular to the plug axis, and has an unimpeded optical path to the arc site on the nested-pair axis.

The breakdown probability vs. switch pressure is shown in Fig. 3. This data was obtained by recording the number of switch closures which occurred in a one-second, 100-shot burst, and the ratio of successful switch closures to 100 switch charges was plotted. Fig. 4 shows a typical magnetic-tape record with a missing  $C_2$  recharge which occurred when the switch

failed to fire.

The relation between breakdown probability and pressure enables the switch to be operated in a Marx by pre-setting switch pressure at the value where this probability is zero. For example, for negative polarity on the nested pair, a pressure of 40 psig (and flow rate of 500 ft/min) is suitable.

### 5.2 Switch Jitter

Jitter was estimated by computing the ratio of the total spread in the peak switch current to the average peak switch current in a given 100-shot burst. A typical set of 100 superimposed voltage and current waveforms is shown in Figure 5a in which total spread is 12% of average peak current.

Switch polarity had an influence on jitter. Best jitter was obtained when negative polarity was applied to the nested-pair electrode and when that electrode was irradiated.

For either positive or negative polarity when irradiation was absent the first switch charge had an abnormally high peak current indicating increased breakdown strength. Occasionally the first applied waveform did not breakdown the switch. After the first breakdown subsequent waveforms had lower amplitude and low jitter.

The percentage spreads in Table 2 do not include the first few anomalous charging waveforms for non-irradiation cases. If they did, those values would have substantially higher spreads.

### 5.3 Conclusions

Based on these results, when employing this switch in a rep-rated Marx, it is important to employ irradiation. Also, the switch operates more reliably and with consistently low jitter when the irradiated electrode is charged negatively. (This is not too surprising since the negative electrode provides the initiating electrons when illuminated with UV.) Regardless of polarity the non-irradiated switch has a first-pulse breakdown strength which exceeds that of the irradiated switch. This is believed caused by a stagnation region

of plasma at the arc site of the nested pair which reduces breakdown strength and provides irradiation. This volume may not purge completely preventing the switch from recovering its full breakdown strength, once the first breakdown occurs. The ratio of the first to the average breakdown voltage was variable; average 20% below that of the first value was not uncommon.

Surprisingly, anomalous first-pulse charging waveforms did not occur when the irradiated electrode was charged positively. Probably reflection of UV from the positive to the negative electrode caused the necessary initiating electrons. Also, for many tests, jitter was comparable to that of negative polarity, although not as consistent from burst to burst.

### Acknowledgements

The authors wish to extend our thanks to Mr. James DeVoss for his extensive contributions to the design, test, and data analysis throughout this program. Also, our thanks to Mr. Larry Houghton for the capable engineering and technical support he provided.

### Bibliography

1. J. Shannon, "A 500 kV Rep-rate Marx Generator", 2nd International Pulse-Power Conference, June 1979, Lubbock, Texas.
2. R. W. Clark, "A Simulation Approach to High Average Power Repetitively Pulsed Switch Testing", IEEE Transactions on Industrial Electrical and Control Ind., Vol. IEC1-23, No. 1, February 1976.
3. A. Ramrus, "Development of a 100 kV Multimewatt Rep-Rate Gas Switch", Thirteenth Pulse-Power Modulator Symposium, June 1978.

This work was performed under Ballistic Missile Defense System Command Contract No. DASG60-77-C-0058.

TABLE 1

## Spark Gap Specifications

Voltage hold-off	100 kV
Peak current	10 kA
Charge transfer	10 mC
Maximum rep-rate	100 Hz
Burst duration	10 sec.
Charging time	-0.1 msec
Flow rate	minimum

TABLE 2

Percentage spread of peak current for current amplitude variation for 100-shot bursts at 500 ft/min under various conditions of irradiation and pressure.

Shot no.	Polarity (on nested pair)	Irradiation (of nested pair)	P (PSIG)	%
175-183	-	yes	21	9
184-186	-	no	21	14 *
187-188	-	no	27	11 *
189-190	-	yes	27	10
192-194	-	yes	27	9
195-198	-	no	27	7 *
199	-	no	20	9 *

\*disregarded initial anomalously high breakdown strength.

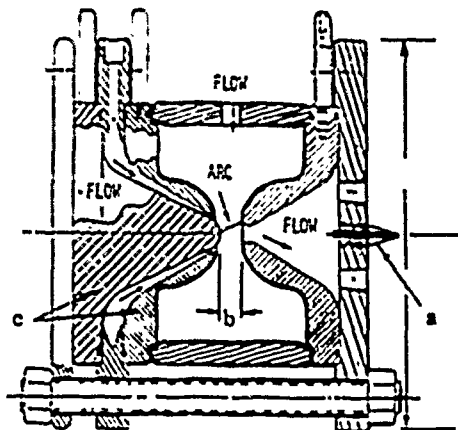


Fig. 1. Cross-section of gas-dynamic spark gap.

- a. irradiation source
- b. 1.3 cm gap
- c. nested-pair electrode

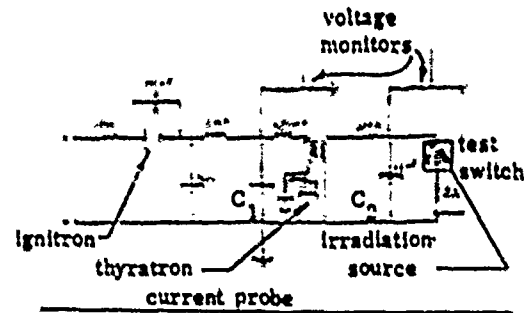


Fig. 2. Test circuit.

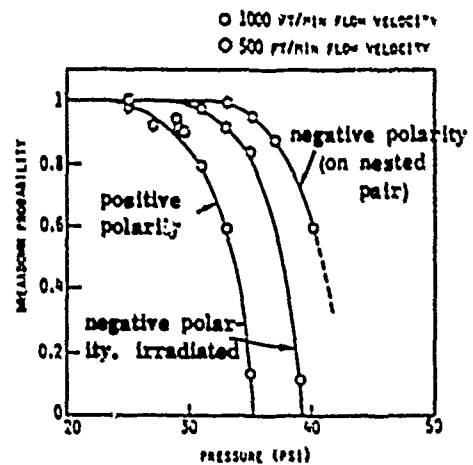


Fig. 3. Rep-rate Marx switch prefire curves.

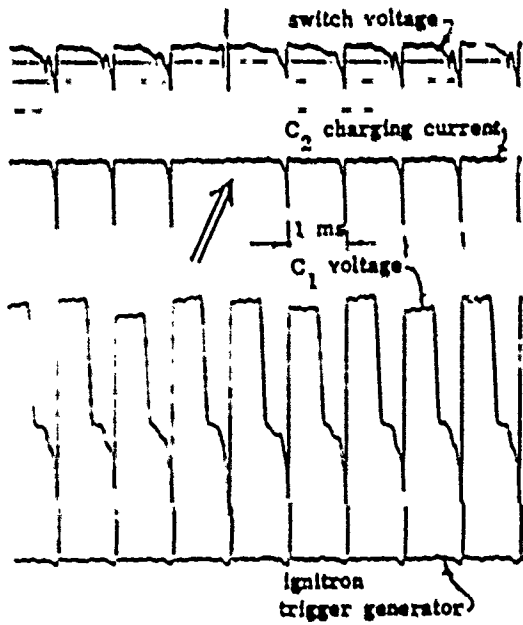


Fig. 4. Magnetic tape record. Test 153  
Arrow points to indication of  
switch no-fire.

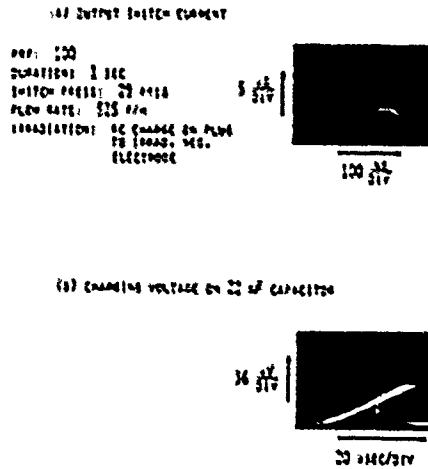


Fig. 5. Typical output switch current and  
switch charging voltage on a 100-  
shot burst (run 167). Percentage  
spread of peak current over  
average peak current is 12%.



## REBUILDING THE FIVE MEGAJOULE HOMOPOLAR MACHINE AT THE UNIVERSITY OF TEXAS

J. H. Gully, K. M. Tolk, R. C. Zovarka, M. Brennan, W. L. Bird  
W. F. Weldon, H. G. Nylander, H. H. Woodson

Center for Electromechanics, The University of Texas at Austin  
Taylor Hall 167, Austin, Texas 78712

Abstract

The role of the 5 MJ homopolar machine at the Center for Electromechanics has changed from that of a pulsed power supply experiment to that of a power supply for various experiments. Because of this change in duty, it was necessary to modify the machine to allow more efficient operation and easier connection of the machine to the load.

The experimental bearings which were on the machine were replaced with bearings of a more conventional design. These bearings exhibit a higher stiffness and lower loss than the original bearings, making the machine more reliable and reducing motoring time.

The surface of the poles were faced to make the applied field more uniform over the face of the rotor. This reduced the magnetic moment on the rotor and reduced the side forces on the rotor during discharge.

The busbars were rebuilt to lower the resistance of the output circuit and to allow quicker change of experiments. The latching mechanism of the closing switch was rebuilt for better reliability and a damper was added to lower the mechanical shock on the switch during operation.

Introduction

The 5 MJ slow discharge homopolar generator (SDHG) (Figure 1) was built in 1974 by The University of Texas Center for Electromechanics to demonstrate the feasibility of inertial energy storage using homopolar conversion. It has been discharged hundreds of times and has proven so reliable that

it is still in daily use as a pulsed power supply for other laboratory experiments. Its 730 kg steel rotor is 61 cm in diameter, 25 cm thick, and operates in a 1.6 tesla axial magnetic field. Originally designed to produce 165 kA, the machine's low internal impedance (resulting from an improved brush mechanism) permits the generator to produce up to 560 kA, stopping the rotor from half speed (2800 rpm) in 0.7 seconds.

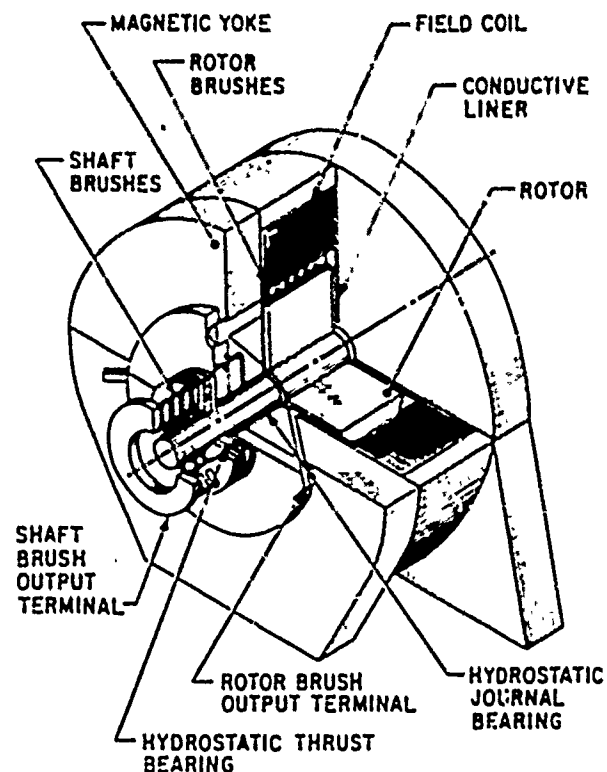


Figure 1: Schematic of 5 MJ SDHG.

After repeated discharges in the short circuit mode proved the basic reliability of the 5 MJ machine, it

was connected to various loads in order to study such machine parameters as voltage, current, pulse rise time and discharge time. Three major series of laboratory experiments have been conducted that involve operational testing of the machine as a pulsed power supply.

- 1) Discharging into the fast discharge experiment (FDX) field coil (inductive store) to obtain maximum current in the coil.<sup>1</sup>
- 2) Discharging into the FDX field coil (inductive store) while controlling the shape of the current pulse by controlling the field excitation of the 5 MJ machine.
- 3) Pulsed resistance welding of 2" mild steel pipe.<sup>2</sup>

#### Reason for Rebuild

After completing these experiments, misalignment and out-of-roundness of the experimental hydrostatic bearings installed two and one-half years before resulted in an inability of the 5 MJ homopolar machine to be motored to speed with full field. A 4" stainless steel pipe resistance welding program would soon require many high level discharges. Therefore, to address the bearing problem and observe the internal condition of the generator after some two years of operational testing, the decision was made to redesign the bearings, disassemble the machine and upgrade the overall performance. Attention was paid to making the machine as reliable as possible, reflecting the change from its previous experimental status.

#### Bearings

Homopolar machines have stringent bearing requirements. A large diameter rotor shaft is required for a disc type homopolar generator, since the shaft is used as a conductor and the larger diameter lowers the resistance. (For the 5 MJ machine, resistance of its five-inch shaft is about one-third of the total machine resistance.) Because the shaft is larger in diameter than would normally be used on a rotor of the same size and weight, the result-

ing bearing interface surface speed is much higher than in conventional rotating machines.

Desirable bearing design features include:

- 1) Very low losses (reduce motoring time).
- 2) Full stiffness at zero speeds. (Bearing loads in homopolar generators are as large at zero speed as at full speed.)
- 3) Electrical insulation (to prevent arcing during a discharge and eliminate circulating currents in the bearing).

Of the three types of bearings, rolling element (unacceptable due to high magnetic fields in the bearing location), hydrodynamic (unacceptable because of zero load capacity at zero speed) and hydrostatic, only the hydrostatic bearing can be designed to achieve all of these goals.

Two configurations of hydrostatic bearings had been tested before the rebuild. Originally, a set of stainless steel bearings, which were not insulated from the bearing housing, were used. Although they functioned satisfactorily at the original design currents, during a high-level discharge the shaft arced to the bearings, causing pitting of the shaft and bearings. Bearings made of G-9 melamine (a nonconductive, fiberglass-reinforced material) replaced the stainless steel bearings. These bearings functioned for over two years, but thermal creep ultimately resulted in bearing misalignment and loss of stiffness which necessitated that the machine be run at reduced field levels. Friction and  $I^2R$  losses would cause the shaft to expand, but the melamine bearings (which have a very low modulus) were prevented from expanding because they were confined by the stainless steel bearing housing. This resulted in reduced clearance in the bearing which increased shaft heating, further reducing bearing clearance and resulting in rubbing between the shaft and bearing. In addition, the bearing housings were misaligned and out-of-round, causing the bearings to be oval-shaped and misaligned.

The third configuration of hydrostatic bearings (Figure 2) which are currently in the machine, addressed these and other problems. A conventional bronze bearing insert with a hardened steel shaft was designed. The insert was insulated from a shrunk on steel housing with a layer of flame sprayed aluminum oxide ceramic. The bearing has six pockets and is orifice compensated. By tapering the journal bearing as shown in Figure 3 an adjustable clearance was obtained. Table 1 shows the bearing characteristics.

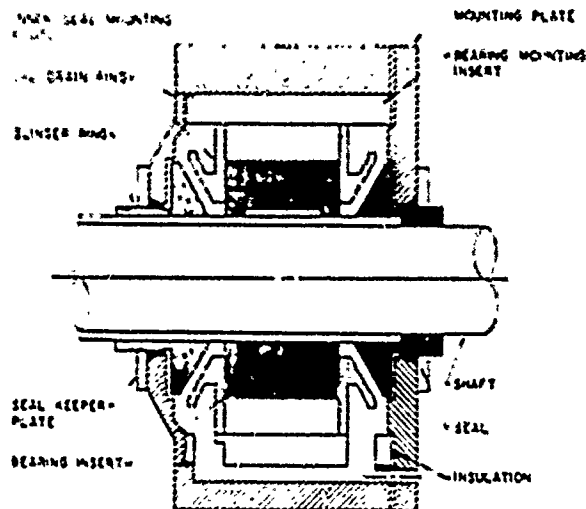


Figure 2: Hydrostatic Journal Bearing

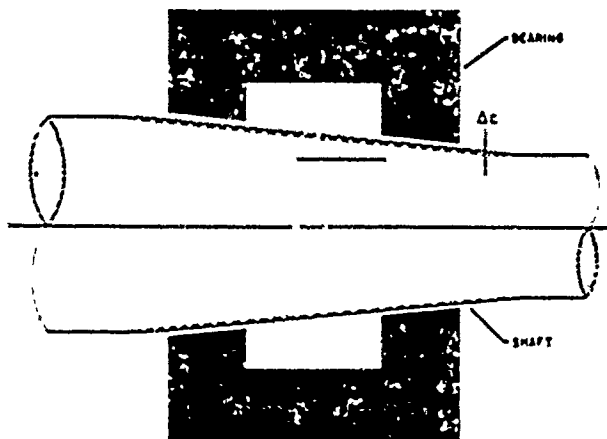


Figure 3: Tapered Shaft and Bearing

To correct the misalignment and out-of-roundness

of the bearing housings, a boring bar was built which would line bore both housings while they were installed in the S MJ yoke. In addition, a facing mechanism was attached to the boring bar, to face the poles of the machine perpendicular to the new bearing housing bore. This significantly reduced the tilt forces on the rotor caused by misalignment in the magnetic field.

One of the major problems with high-speed hydrostatic bearings involves the design of a sump system that will remove the large oil flow and prevent leakage at the high speed seal interface. The current design provides very large sumps which operate below atmospheric pressure. This allows the seals to leak air into the sump rather than leaking oil out.

#### Machine Disassembly

Careful inspection of the disassembled machine revealed that the rotor and all brushes were in good condition. As anticipated, the bearing showed signs of rubbing and some pitting had occurred on the shaft under the shaft brushes. The making switch was in good condition except for the external latching mechanism that had become loose and misaligned. Overall, the disassembly resulted in no surprises and the machine was sound.

#### Making Switch

Upgrading of the machine included disassembly and rework of the generator making switch (Figure 4). All electrical contacts and conductors were in good condition and were reassembled without rework. Rework of the switch included:

- 1) Pins at the pivot points on the latch mechanism showed excessive wear and damage from impact loading, resulting in a lack of reliability of the hold-open latch. The pins were increased in size to reduce unit loading, assembly tolerances were tightened, a new damper was added to reduce the impact of the pneumatic cylinder, and the latch was reground and repositioned.

Table 1  
Hydrostatic Bearing Characteristics

Oil Viscosity cp (Reyn)	Radial Clearance mm (in.)	Load* N(lb)	Stiffness N/m (lb/in.)	Flow Liter/min (gpm)	Total Loss kW (hp)
62.1 ( $9 \times 10^{-6}$ )	0.102 (0.004)	$3.47 \times 10^4$ (7800)	$1.70 \times 10^8$ ( $0.972 \times 10^6$ )	15.7 (4.16)	20.4 (27.4)
13.8 ( $2 \times 10^{-6}$ )	0.038 (0.0015)	$1.24 \times 10^4$ (2781)	$5.91 \times 10^8$ ( $5.09 \times 10^6$ )	8.25 (2.18)	9.10 (12.2)

\*Load: Given for a minimum film thickness of 0.025 mm (0.001 in.).

- 2) The original electromagnetic solenoid, which initiates switch actuation, was a surplus unit and was replaced with a commercial unit.
- 3) Redesign of the latch adjusting mechanism now allows adjustment to be made with the solenoid in place.

#### Busbars

Before the rebuild, the output busbars and making switch had to be removed before the generator could be disassembled (Figure 5). The new design rotated the 2.86 cm by 30.5 cm aluminum discharge busbars 90° so that they face the FDX generator. Lifting eyes were attached to the top of the yoke providing quick access to the machines interior for inspection and repair.

By rotating the FDX field coil 90° toward the 5 MJ SDHC it was possible to attach the coil directly into the switch output. This made the low impedance copper busbars used previously to connect FDX to the 5 MJ generator free for quick installation of other experiments. The new busbar arrangement lowered both the resistance and inductance of the output circuit.

#### Conclusion

Many high current discharges have been accomplished

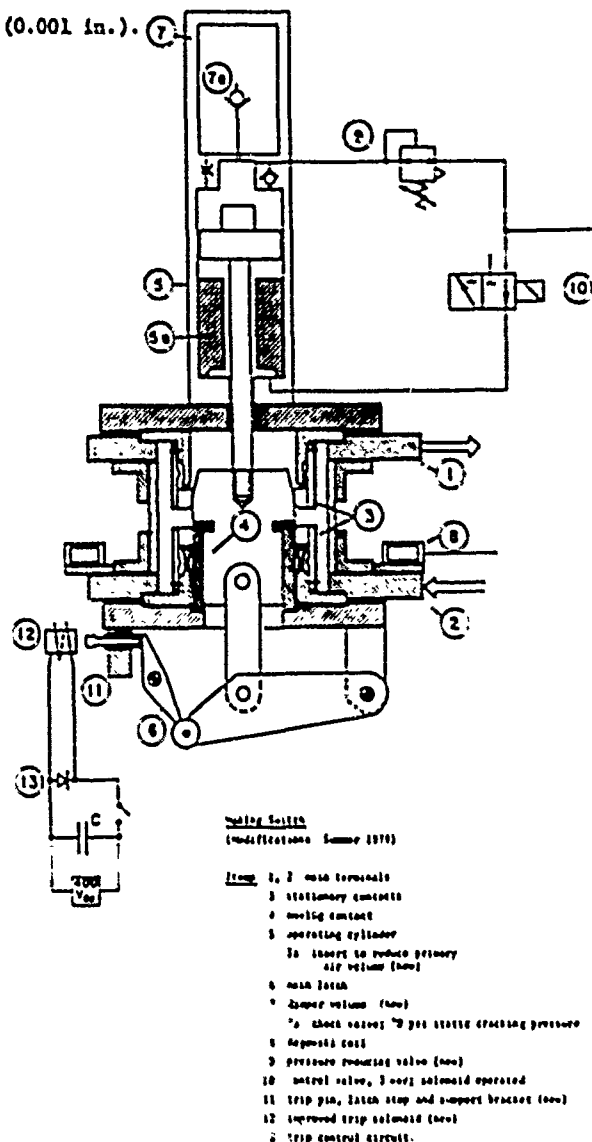


Figure 4: Making Switch

since the rebuild (Table 2). The machine has proven to be reliable and maintenance free. In the near future, welding and heating experiments will continue. Other possible experiments include FDX, pulse compression and some rail gun experiments. The 5 MJ SDHG is no longer an experiment; it is now a reliable pulsed power supply for high energy experiments.

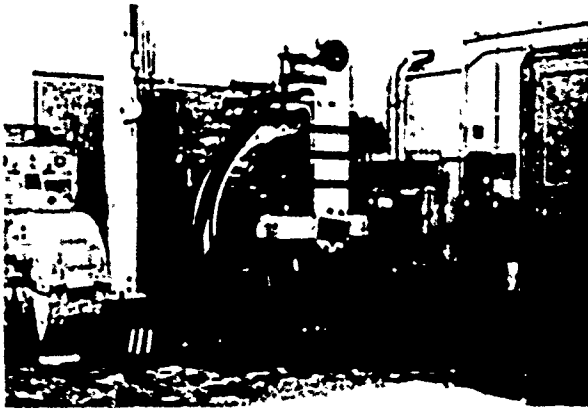


Figure 5: Old Busbar

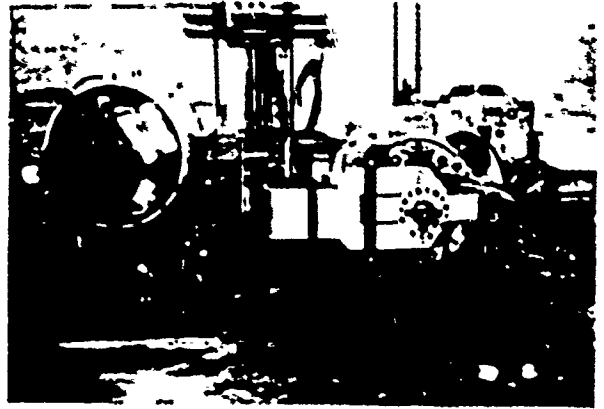


Figure 5: New Busbar

#### References

1. W. F. Weldon, M. D. Driga, H. H. Woodson, H. G. Rylander, "The Design, Fabrication, and Testing of a Five Megajoule Homopolar Motor-Generator," *Proceedings: International Conference on Energy Storage, Compression, and Switching*, Torino, Italy, November 5-7, 1974.
2. G. B. Grant, W. M. Featherston, R. E. Keith, W. F. Weldon, H. G. Rylander, H. H. Woodson, "Homopolar Pulse Resistance Welding, A New Welding Process - based on the unique electrical characteristics of pulsed homopolar generators," *American Welding Society, 60th Annual Meeting*, Detroit, Michigan, April 2-6, 1979.

#### Acknowledgments

This work was performed under contracts with the U.S. Department of Defense and the Texas Atomic Energy Research Foundation.

Table 2: 5 MJ SDHG Discharge Levels

	0-50 kA	50-100 kA	100-150 kA	150-200 kA	200-250 kA	250-300 kA	300-350 kA	560 kA
Before Rebuild	54	98	20	20		2	1	1
After Rebuild	1	26	7	2	0	17	28	

COMPUTER BASED ELECTRICAL ANALYSIS OF HOMOPOLAR GENERATOR  
DRIVEN, BITTER PLATE STORAGE INDUCTORS WITH  
RADIAL CURRENT DIFFUSION

D.J.T. Mayhall<sup>+</sup>, H.G. Rylander, W.F. Weldon,  
and H.N. Woodson

Center for Electromechanics  
The University of Texas at Austin  
Austin, Texas 78712

### Abstract

Maxwell's equations are solved for the operational admittance in the magnetic quasi-static approximation for nonmagnetic cylindrical coils with azimuthal currents and axial magnetic fields. An infinite series, Bessel function solution is obtained and solved for copper coils with given radial dimensions. Coil turns numbers and lengths are design parameters. A multiple branch, shunt network coil model with series resistances and inductances is derived. The UT CEM 5 MJ homopolar generator is modeled with a torque-speed equation including brush and seal drag torques. The brush contact voltage drop is modeled versus surface speed and brush current. Transmission system resistances and inductances are included. Effective depths of current penetration, effective coil resistances and inductances, and peak temperatures are calculated versus time. Coil currents and voltages are obtained, as are system energy storages and dissipations. Peak current times and system discharge times are determined. Slightly underdamped configurations are found.

### Admittance Solutions for Model Cylindrical Coils

Square Bitter plate coils with eccentric bores are approximated with a cylindrical, axisymmetric model. The operational admittance approach of Moxanu [1] accounts for radial current diffusion. The coil model is shown in Figure 1. The coil length is  $l_c$ ; its thickness is  $b-a$ . The  $\vec{H}$  field is purely axial; the  $\vec{E}$  field purely azimuthal. Displacement current effects are neglected.

The boundary conditions for the Laplace transform fields are  $\vec{H}_z(r) = \text{constant}$ ,  $0 \leq r \leq a$ , and  $\oint_c \vec{H}(r) \cdot d\vec{\ell} = \vec{I}(p)$ , where the contour  $c$  is shown in Figure 1,  $\vec{I}(p)$  is the transform current, and  $p$  is the transform variable. For nonmagnetic coil material, Maxwell's equations give

$$\frac{1}{r} \frac{d}{dr} \left( r \frac{d\vec{H}_z}{dr} \right) = q^2 \vec{H}_z, \quad q^2 = \mu_0 \gamma p \quad (1)$$

where  $\mu_0 = 4\pi \times 10^{-7}$  H/m and  $\gamma$  is the coil conductivity. A solution to eq. (1) is

$$\vec{H}_z = A J_0(jqr) + B Y_0(jqr) \quad (2)$$

where  $J$  and  $Y$  are Bessel functions of the first and second kind,  $j = \sqrt{-1}$ , and  $A$  and  $B$  are constants. The  $\vec{E}$  field is

$$\vec{E}_\theta = \frac{j\omega}{\sigma} [A J_1(jqr) + B Y_1(jqr)] \quad (3)$$

The transform voltage across the coil terminals is taken as

$$V(p) = \vec{E}_\theta(b) 2\pi b \quad (4)$$

The operational admittance is  $Y(p) = I(p)/V(p)$ .

Application of the boundary conditions and use of the residue theorem [2] gives the temporal admittance as

$$y(c) = \sum_{i=1}^{\infty} \lambda_i e^{-\beta_i t} \quad (5)$$

$$\lambda_i = \frac{\frac{l_c}{2\pi b \mu_0} \left\{ \alpha_{si}^2 \left[ J_0(\alpha_{si}a) Y_0(\alpha_{si}b) - Y_0(\alpha_{si}a) J_0(\alpha_{si}b) \right] - 2\alpha_{si} \left[ Y_1(\alpha_{si}a) J_0(\alpha_{si}b) - J_1(\alpha_{si}a) Y_0(\alpha_{si}b) \right] - \frac{4}{\pi a} \right\}}{\alpha_{si}^2} \quad (6)$$

$$\alpha_{si} \left\{ \frac{a^2 \alpha_{si}^2}{2} \left[ Y_0(\alpha_{si}a) J_1(\alpha_{si}b) - J_0(\alpha_{si}a) Y_1(\alpha_{si}b) \right] + a b \alpha_{si} \left[ Y_0(\alpha_{si}a) J_0(\alpha_{si}b) - J_0(\alpha_{si}a) Y_0(\alpha_{si}b) \right] + 2b \left[ J_1(\alpha_{si}a) Y_0(\alpha_{si}b) - Y_1(\alpha_{si}a) J_0(\alpha_{si}b) \right] \right\} \\ \beta_i = \alpha_{si}^2 / \mu_0 \sigma \quad (7)$$

The  $\alpha_{si}$  are the roots of the equation

$$\alpha_{si} \left[ Y_0(\alpha_{si}a) J_1(\alpha_{si}b) - J_0(\alpha_{si}a) Y_1(\alpha_{si}b) \right] - 2 \left[ Y_1(\alpha_{si}a) J_1(\alpha_{si}b) - J_1(\alpha_{si}a) Y_1(\alpha_{si}b) \right] = 0 \quad (8)$$

### Solutions for Particular Coil Dimensions

The roots of eq. (8) are solved for  $a = 0.3048$  m (12 in) and  $b = 0.508$  m (20 in) with routines

<sup>+</sup>Presently at Lawrence Livermore Laboratory, Livermore, CA 94550

MCBSJ3, MCBSJ1, MCBSYN, ZREAL1, and ZREAL2 of the International Mathematical and Statistical Library (IMSL). The first 4 roots are  $\alpha_{s1} = 3.127309270 \text{ a}^{-1}$ ,  $\alpha_{s2} = 7.401705666 \text{ a}^{-1}$ ,  $\alpha_{s3} = 11.96715946 \text{ a}^{-1}$ ,  $\alpha_{s4} = 16.64197700 \text{ a}^{-1}$ .  $\lambda_1$  and  $\beta_1$  are calculated for  $i_c = i_{co} = 0.9144 \text{ m}$  and  $r = 5.800 \times 10^7 (\Omega \cdot \text{m})^{-1}$ . The first 4 values of  $\lambda$  are  $6.466691304 \times 10^6$ ,  $9.924480604 \times 10^6$ ,  $2.509179152 \times 10^6$ ,  $1.441670278 \times 10^6$ . Those of  $\beta$  are  $1.444322999$ ,  $8.090703477$ ,  $21.22045119$ ,  $40.90086543$ .

#### Shunt Equivalent Circuit for the Coil

When eq. (5) is transformed and variable coil lengths  $i_c$  and multiple coil turns of number  $N_T$  are allowed, the operational admittance may be written

$$Y(p) = \sum_{i=1}^n \frac{1}{R_i + L_i p} = \sum_{i=1}^n \left[ \frac{\beta_i}{\lambda_i} \frac{i_{co}}{i_c} N_T^2 + \frac{1}{\lambda_i} \frac{i_{co}}{i_c} N_T^2 p \right]^{-1} \quad (9)$$

The coil may be thus represented by the infinite branch, shunt network shown at the right side of Figure 2. Each branch consists of a resistance  $R_i$  and an inductance  $L_i$  in series. The proper number of branches  $n$  is determined by trial.

#### Model for the UT-CEM SMJ Homopolar Generator

The UT-CEM SMJ homopolar generator is shown on the left side of Figure 2. Its voltage  $V_H = \omega \phi / 2\pi$ , where  $\omega$  is the generator angular frequency and  $\phi$  is the magnetic flux. The generator internal resistance  $R_H$  is taken as  $13.1 \text{ m}\Omega$  and the internal inductance  $L_H$  as  $0.5 \mu\text{H}$ . The torque equation for the generator coast down mode is

$$I \frac{d\omega}{dt} = -\phi i_T / 2\pi - T_{br} - T_s \quad (10)$$

where  $I$  is the rotor rotational inertia,  $i_T$  is the series current,  $T_{br}$  is the brush drag torque, and  $T_s$  is the seal drag torque. Bearing losses are ignored.  $T_{br}$  is taken as  $446 \text{ m}\cdot\text{nt}$ ;  $T_s$  as  $13.6 \text{ m}\cdot\text{nt}$ .

The brush voltage drop resistance  $R_{br}$ , which varies with brush current and generator speed, is approximated by

$$R_{br} = \left[ v_{s0} \left( 1 - e^{-1.753 \times 10^{-5} |i_T|} \right) + v_{r0} \left( 1 - e^{-1.006 \times 10^{-5} |i_T|} \right) \right] |i_T|^{-1} \quad (11)$$

with the rotor brush voltage coefficient given by

$$v_{r0} = \begin{cases} 0.74, & \omega < 88.6 \text{ rad/sec} \\ 0.676 + 7.27 \times 10^{-4} \omega, & \omega > 88.6 \text{ rad/sec} \end{cases} \quad (12)$$

and the shaft brush voltage coefficient given by

$$v_{s0} = \begin{cases} 0.74, & \omega < 425 \text{ rad/sec} \\ 0.676 + 1.51 \times 10^{-4} \omega, & \omega > 425 \text{ rad/sec} \end{cases} \quad (13)$$

The estimated resistance of the bus system is  $29.9 \mu\Omega$ ; the estimated inductance is  $0.3 \mu\text{H}$ .

#### Effective Parameters for the Coil

An effective coil resistance is defined as

$$R_{eff} = \frac{i_T^{-2}}{i_1} \sum_{i=1}^n R_i i_i^2, \text{ where } i_i \text{ is the current}$$

in the  $i$ th branch. An effective coil inductance

$$\text{is defined as } L_{eff} = \frac{i_T^{-2}}{i_1} \sum_{i=1}^n L_i i_i^2. \text{ The current}$$

density is approximated by  $j(r, t) = i_T N_T (r / i_c) \ln$

$$\left( 1 + \frac{d_{eff}}{a} \right)^{-1}, \text{ where } d_{eff} \text{ is the effective depth}$$

of current penetration. The temperature rise at  $r = a$  for ETP copper is taken as

$$\Delta \theta_{max} = 5.47 \times 10^{-14} \int_0^t i_T^2 N_T^2 i_c^{-2} \left[ \ln \left( 1 + \frac{d_{eff}}{a} \right) \right]^{-2} dt, \text{ } ^\circ\text{C}.$$

#### Solution of Circuit Equations for an Example Coil

The circuit equations for Figure 2 are integrated in time on a CDC 6600 computer. Example results are given for a 12 turn, 72 plate coil (6 plates/turn) of length  $0.1524 \text{ m}$ , plate thickness  $5.13 \times 10^{-3} \text{ m}$ , and zero thickness insulation. Resistance increase with temperature is neglected. The generator has an initial speed of  $584 \text{ rad/sec}$  and an initial voltage of  $42 \text{ V}$ . Fourteen branches are used for the coil network.

Generator speed and current are shown in Figure 3, along with the coil voltage and the temperature rise at the inner radius of the  $0.1524 \text{ m}$  thick neck of the real coil. The rotor kinetic energy, coil inductive energy, system resistive dissipated energy, and drag friction dissipated energy are shown in Figure 4. The effective coil resistance, inductance and depth of current penetration are shown in Figure 5. The series current is slightly underdamped. The peak current of  $120.6 \text{ kA}$  occurs at  $0.855 \text{ sec}$ ; the peak coil energy of  $0.814 \text{ MJ}$  occurs at  $0.908 \text{ sec}$ . The generator reverses direction at  $3.64 \text{ sec}$ ; the current reverses at  $4.57 \text{ sec}$ .

#### Acknowledgements

Thanks are due to W. L. Bird, M. Brennan, G. Cardwell, M. D. Driga, K. M. Tolk, P. Wildi, and R. Zaworka for their most kind help.

This work was supported by the U. S. Department of Energy and the Texas Atomic Energy Research Foundation.

#### References

- [1] G.I. Mocanu, "The Equivalent Schemes of Cylindrical Conductors At Transient Skin Effect," 71 TP 667-PWR, IEEE Summer Meeting and Int. Symp. on High Power Testing, pp. 884-852, July 18-23, 1971.

[2] J. C. Jaeger, "III. Magnetic Screening by Hollow Circular Cylinders," *Phil. Mag.* 29, pp. 18-31, 1940.

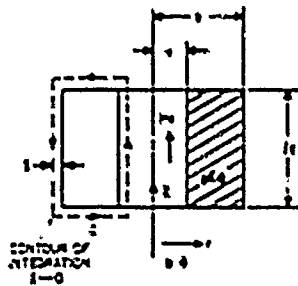


FIG. 1 - CYLINDRICAL COIL MODEL

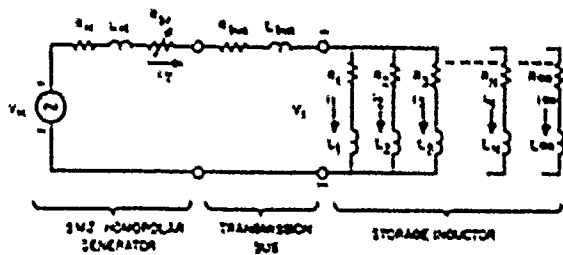


FIG. 2 EQUIV CIRCUIT FOR 3MJ HOMOPOLAR GENERATOR AND STORAGE INDUCTOR w/ RADIAL CURRENT DIFFUSION.

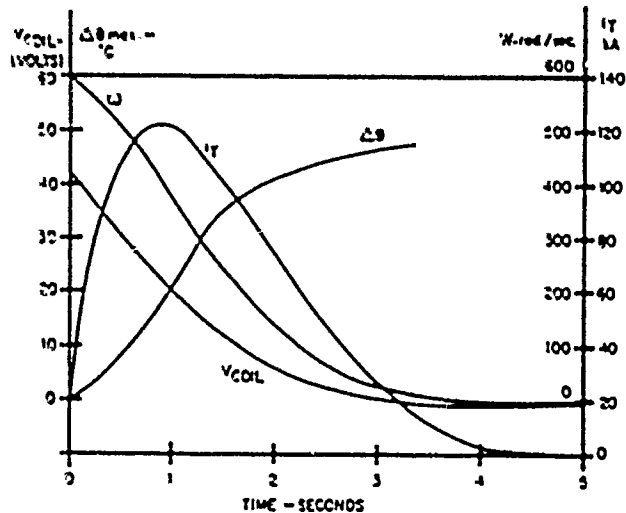


FIG. 3 - MACHINE SPEED, CURRENT, COIL VOLTAGE AND PEAK COIL TEMP RISE Vs TIME

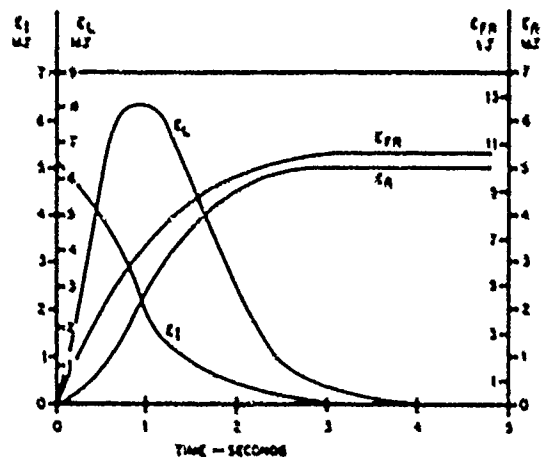


FIG. 4 - SYSTEM ENERGY STORAGE AND DISSIPATION Vs TIME

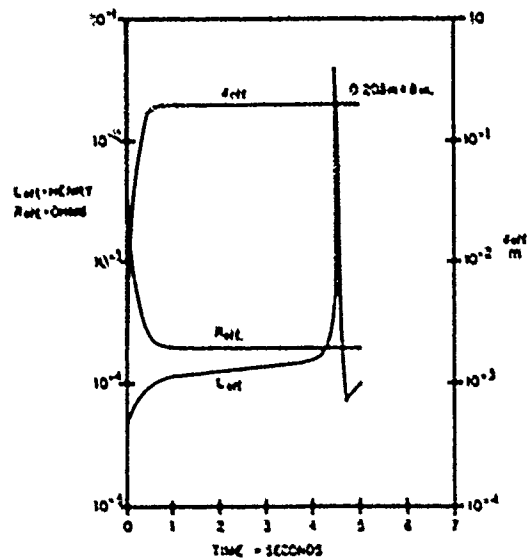


FIG. 5 - VARIATION OF EFFECTIVE COIL PARAMETERS WITH TIME.



## INVITED

## TESTING AND ANALYSIS OF A FAST DISCHARGE HOMOPOLAR MACHINE (FDX)

T. M. Bullion, R. Zovarka, M. D. Driga, J. H. Gully, H. G. Rylander,  
K. M. Tolk, W. F. Weldon, and H. H. Woodson

Center for Electromechanics, The University of Texas at Austin  
Taylor Hall 167, Austin, Texas 78712

Abstract

The Fast Discharge Experiment (FDX) is a 0.36 MJ, 200 V homopolar machine designed to discharge in one millisecond. This experiment is intended to establish the fundamental limitations involved in extracting energy in the shortest time from a flywheel using homopolar conversion. FDX features a room temperature  $1.6 \times 10^6$  A-t copper coil pulsed by a 5 MJ slow discharge homopolar machine, two 30.5 cm diameter counterrotating aluminum rotors with flame sprayed copper slip rings, low inductance return conductors, coaxial transmission line, four fast closing (30 usec) 1/2 MA making switches, hydrostatic journal bearings, squeeze film thrust bearings and dual brush activation systems.

After initial testing of FDX was completed and data was analyzed, problems limiting performance were identified. Various components of the machine were redesigned and modified to correct these problems. A second set of tests, including short circuit discharges from various speeds, has recently been conducted. Results and analysis of these tests will be presented. New problems encountered as well as recommendations for additional work will also be given.

Introduction

A homopolar machine which uses a simple rotor without windings as both flywheel and generator armature is a very simple, inexpensive and efficient pulsed power supply. This type of machine uses its flywheel to inertially store large amounts of energy over a relatively long time and electrically extracts this energy in a very short time.

The Center for Electromechanics (CEM) at The University of Texas at Austin has been engaged for some time in experiments involving homopolar machines and has built and tested several such machines. The first homopolar to be designed, fabricated and tested by the CEM was a 0.5 MJ machine in 1972. This machine exceeded its design goals by discharging from 6000 rpm in 7 seconds with a peak current of over 14,000 A. After this successful testing, a second homopolar machine with a storage capacity of 5 MJ was designed and built. This was not merely a scaled-up version, but a new machine implementing new ideas learned from the earlier machine. Due to improved internal impedance, this machine discharged into a short circuit from 2800 rpm, half its rated speed, in a much shorter time (0.7 sec) and at a much higher current level (550,000 A). The success of these two projects led to the question of the fundamental limitations to discharge time of homopolar machines.

In 1973 and 1974, a study was undertaken by the CEM to answer this question. For discussion, consider a machine with a rotor which carries a radial current  $i$  in the presence of an axial magnetic field  $B$ . The electrical connections to the rotor are made through sliding contacts from cylindrically symmetrical conductors which carry equal currents. If the rotor is turning at some speed about its axis, several phenomena limit the rapidity with which electromagnetic forces resulting from interactions of current and magnetic field can decelerate the rotor and extract the stored inertial energy electrically.

Deceleration is accomplished by the interaction of current and magnetic field. Either current or

magnetic field can be present without deceleration and deceleration can be accomplished by establishing the other. If there is no magnetic coupling between the field coil and the rotor circuit, the problems of establishing current and magnetic field rapidly are independent.

First, consider the problem of establishing magnetic field. A voltage must be applied to the field coil to produce a current which builds up at a rate determined by  $V = L \frac{di}{dt}$ . The rate of buildup of current in the field coil is limited by its internal insulation which in turn limits the voltage that can be applied to it. Even if the coil current builds up quite rapidly, the establishment of magnetic field inside the rotor is limited by the decay time of eddy currents in the rotor.

Next, consider the problem of establishing rotor current rapidly. The current must first diffuse into the rotor and return conductors. This is a transient eddy current problem that is affected by material properties and geometry. Even if current diffuses rapidly into the rotors and return conductors, the rotor current must be established by the voltage generated in the rotor applied to the inductance of the armature circuits.

If the magnetic field and rotor current can be established rapidly enough, the discharge time is limited by how rapidly the  $J \times B$  forces can decelerate the rotor compared to the electrical loss rate in the rotor, brushes and return conductors. This requires high magnetic fields, good electrical conductors and low resistance sliding contacts.

There are also some mechanical problems which may arise during discharge. If the  $J \times B$  force distribution does not match the deceleration force density, then shear stresses must be transmitted by the rotor material and they may be substantial for fast discharge. Diffusion of current into the rotor may produce nonuniform force densities and high shear stresses. Nonuniform current densities, caused by the existence of eddy currents, can cause nonuniform

heating leading to thermal stresses that degrade the mechanical stress capability of the rotor material.

The Fast Discharge Experiment (FDX) (Figure 1) was designed, not as a fast pulsed power supply, but to investigate homopolar discharge limitations. Therefore, several parameters, such as mechanical stresses, brush current densities, and interface speeds are at their predicted performance limits.

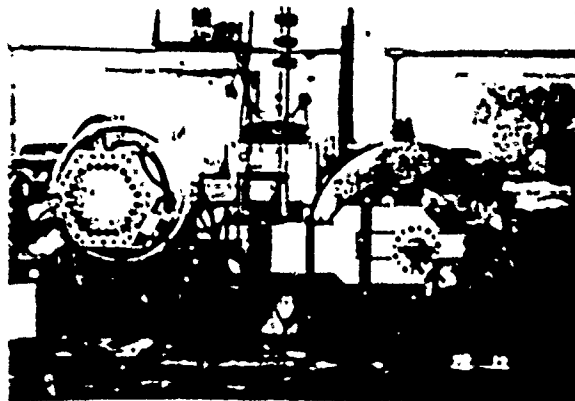


Figure 1: Fast Discharge Experiment

FDX was designed and fabricated during a period from 1975 to 1977. Initial testing, such as pulsing the field coil, coast down tests, voltage generation and low speed, short circuit discharges began in the fall of 1977. After this initial testing of FDX was completed and data was analyzed, various problems limiting performance were identified. Several components of the machine were then redesigned and modified to correct these problems.

A second set of tests on FDX, including short circuit discharges over a range of speeds has recently been completed and the results of this testing are presented here.

#### Original FDX Design

Several possible configurations were considered for FDX with the fastest possible discharge time for minimum cost as the limiting objective. After extensive analysis into the topology of fast discharge machines,<sup>1</sup> it was concluded that the multiple disk or "spool" configuration has a smaller effective

capacitance due to a smaller moment of inertia than an equivalent drum configuration for a given flux linkage (Figure 2). As a result, the "spool" machine has an inherently shorter discharge time. The spool configuration also allows the rotor to link a larger percentage of the flux generated by the field coil than does the drum configuration.

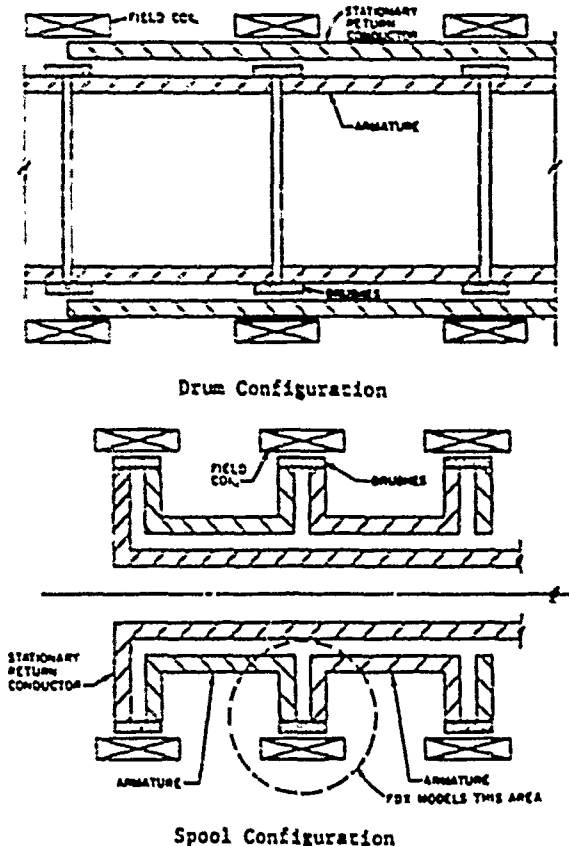


Figure 2: Homopolar Generator Configurations

Considerations of performance, time, funds and desired experimental results were involved in the design of FDX. As a result, FDX models one coil and the corresponding halves of two adjacent counter-rotating rotors of a "spool" machine (Figure 2). Also because of cost and time considerations, the high magnetic field required for FDX is supplied by a room temperature copper coil powered by the existing CEM 5.0 MJ slow discharge homopolar generator.

FDX (Figure 3) is a fully compensated, pulsed field homopolar generator.<sup>2</sup> Using two counterrotating

rotors shaped for minimum inertia, the machine stores 0.36 MJ of energy at an angular velocity of 3000 rad/sec (28,650 rpm). From half speed, 1500 rad/sec, the rotors are predicted to stop in approximately one millisecond when discharged into a short circuit with an output current of 1.9 MA. (Figure 4). Because of high current densities in the brushes, the machine cannot discharge into a short circuit from full speed. The pulsed magnetic field in the rotors averages 4.0 T, resulting in a machine voltage of 208 V at full speed.

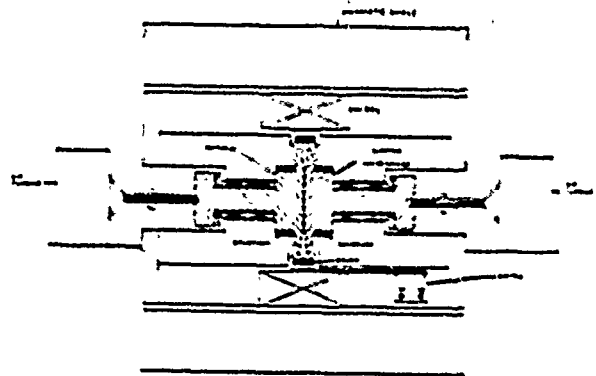


Figure 3: FDX Homopolar Machine

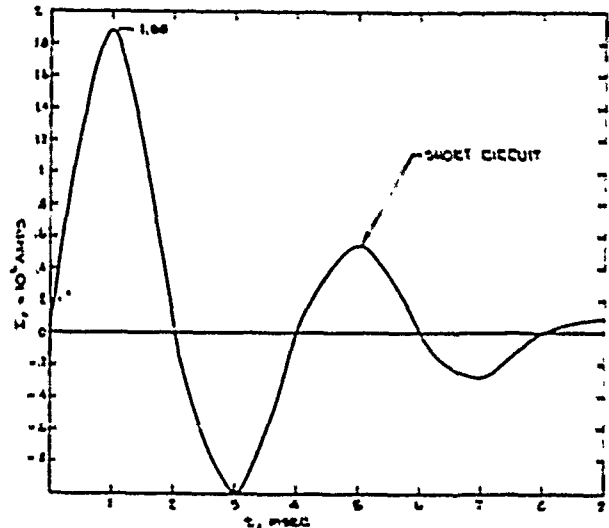


Figure 4: Predicted FDX Output Current

The FDX machine exceeds the state of the art in some parameters. The current collection system has to operate in very high magnetic fields (up to 6.0 T), withstand large current densities (up to 8000 A/cm<sup>2</sup>) and make contact with a rotor moving at 450 m/sec.

FDX utilizes two 30.5 cm diameter, 2.5 cm thick counterrotating rotors made from a 7050 aluminum alloy. Slip ring surfaces are flame sprayed with a layer of copper to provide a suitable surface for copper-graphite brushes. The rotor shaft and thrust bearing runner are hard anodized to provide electrical insulation and a wear resistant bearing surface. The rotors are supported in a cantilevered fashion by oil-lubricated hydrostatic journal bearings inside the FDX field coil. These bearings provide extremely high stiffness and introduce damping into the rotor-bearing system. One hydrostatic thrust bearing is used to axially position each rotor. Upon discharge each bearing changes to a squeeze film regime to counteract the large force ( $4.5 \times 10^5$  N) trying to bring the rotors together. Due to the pulsed magnetic field, the rotors are unable to self motor and are driven through shear links by turbines which operate on compressed air. Upon discharge, the rotors rapidly decelerate, causing the links to shear and decoupling the turbine from the rotor.

The FDX field coil is a  $1.6 \times 10^6$  A-c room temperature copper coil pulsed by the CEM 5 MJ machine. It has a total inductance of 8.5  $\mu$ H and a resistance which rises from 62  $\mu$  $\Omega$  to 74  $\mu$  $\Omega$  during the pulse due to the temperature rise of the coil.

The FDX discharge circuit consists of dual current collection systems, an aluminum coaxial transmission line and four fast closing 1/2 MA making switches. Two brush mechanisms and current transfer designs were required; one to collect current from the rotor's shoulders and transfer it to the stationary compensating turns, and the other to transfer current from the outer periphery of one rotor to the other (Figure 5). Both brush mechanisms use sintered copper graphite brushes, previously tested and used on the CEM 5 MJ machine.<sup>3</sup> The brush packing factors of both mechanisms exceeded 90% due to the large current densities involved.

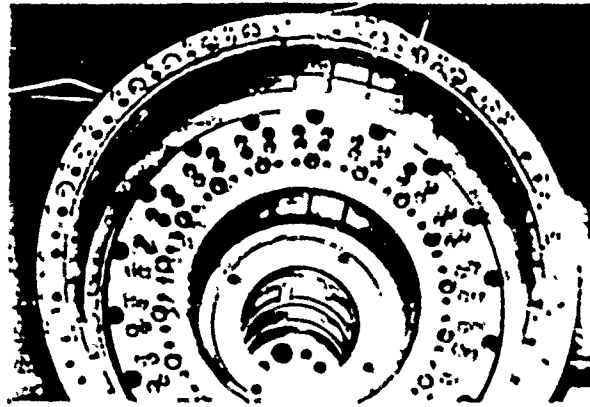


Figure 5: FDX Dual Brush Mechanisms

Due to eddy current and field penetration problems, the coaxial transmission line is made of aluminum instead of copper. The lower conductivity of aluminum avoids exaggerated values of eddy currents and accelerates field penetration. Because of the extremely fast rise time (2900 A/usec) anticipated for the large discharge current ( $1.9 \times 10^6$  A), a one shot mechanical switch based on the magnetic repulsion principle was employed.<sup>4</sup> This very low impedance switch initiates the FDX discharge current by rapidly (30 usec) expanding an annealed aluminum ring which bridges two stationary contacts. In order to maintain uniform current distribution in FDX, four such switches (each 1/2 MA) are located symmetrically around the outside of the coaxial transmission line.

#### Initial Test Results and Problems Encountered

During the fall of 1977, initial testing of FDX began. Preliminary testing of several components of the machine was necessary before a short circuit discharge could be attempted. The FDX field coil was tested first by pulsing it for various current levels with the CEM 5 MJ machine. This was done with and without the rotors and compensating conductors in place to enable the rotors to be centered in the magnetic field as well as to evaluate the difference in magnetic flux distribution with and without the eddy currents generated in the rotors and compensating conductors. The 5 MJ machine was discharged from various speeds and current in the

coil and magnetic field was recorded. This measured field very closely matched the field calculated previously.

The two brush mechanisms were tested individually and together by activating the brush mechanisms in various combinations. The objective of these tests was to wear in the brushes, determine how long each mechanism took to activate and verify predicted brush losses. From 7000 rpm, the rotors stopped from brush losses approximately 0.4 sec after both brush mechanisms were seated. This rapid deceleration was expected from predicted brush losses. Voltage generation tests were performed on FDX by exciting the field coil and activating both brush mechanisms with the rotors spinning. Machine voltage and movement of the rotors as a result of the magnetic field were monitored.

After these tests were complete, four short circuit discharge tests were performed. On one of these tests, the 5 MJ machine generated 140,000 A into the FDX field coil, producing an average magnetic field of 2.4 T inside the bore of the coil. From 2500 rpm, the rotors stopped in 20 milliseconds and the machine generated approximately 60,000 A. The FDX machine voltage was 19 V. While this was the fastest discharge of a homopolar machine to date, the time was still an order of magnitude greater than the predicted results. Also, on other tests, it became apparent that current could not be maintained at speeds over 2500 rpm. This was due largely to brush bounce, either electromagnetic or dynamic in nature. Because of a very fast current rise before breaking up, a one millisecond discharge still seemed feasible if brush contact could be maintained. Therefore, an extensive rework of FDX began late in 1977.

The internal resistance of FDX was higher than expected because of a high resistance bolted joint in the return conductor. If FDX was to discharge in one millisecond this resistance would have to be decreased.

Another problem with FDX which affected predicted performance was insufficient air supply to the turbines which motor the machine. If the specified 15,000 rpm was to be reached, larger air lines and more air inlets to each turbine would have to be used.

Upon dismantling the machine, several other problems were noted. The surfaces of the outer rotor slip rings as well as the rotor brushes showed signs of arcing but the rotor was not seriously pitted. This indicated that the suspected brush bounce was occurring in the rotor brush mechanism. Also, there was considerable oil in the rotor cavity, indicating that the inside bearing seals were not functioning properly. Further examination and testing using displacement transducers showed that the rotors ran out approximately 0.015 cm. This could be one cause of brush bounce.

In general, all components of FDX except those noted above were in good shape. Therefore, to make FDX perform as predicted, a complete redesign and rebuild of these components was needed. Coinciding with the FDX rebuild, was a rebuild of the CEM 5 MJ machine to increase its performance.

#### FDX Rebuild

FDX has an 8.3 cm diameter shaft which rotates at speeds up to 15,000 rpm. This gives a very high interface speed for a hydrostatic bearing. Because of this high shaft surface speed and the roughness of the hard anodized shaft on which they rubbed, the original lip seals used in FDX wore out rapidly. Also, the oil sump in the inner bearing scavenge system was slightly pressurized due to line restrictions and dynamic effects of oil flowing out of the bearing pocket. These two problems combined to allow oil leakage into the rotor cavity. The oil sump and lip seal were redesigned to prevent this. For an oil scavenge system to work correctly, a vacuum must be maintained to assure that air will flow by the seal into the sump. Flow should be laminar at the sump inlet and large return lines and manifolds should be used to assure that return flow is not

restricted. The FDX scavenge system was rebuilt to increase the cross sectional area of the scavenge by adding two larger (1.9 cm) return passages. Also a dam and small reservoir were added to the sump. The dam serves to force oil away from the rotating shaft and into the reservoir to keep oil off the shaft, reducing turbulence. To avoid excessive horsepower losses, low loss seals had been used on FDX. After a search for a suitable lip seal, only one was found which could perform at the necessary high speeds with low losses. This was a Mather lip seal. Due to the roughness of the hard anodized shaft, it was necessary to shrink fit a 4340 steel sleeve on the rotor seal shoulder (Figure 6). Because this ring was hardened and ground, it provided a suitable surface for the seal to run on.

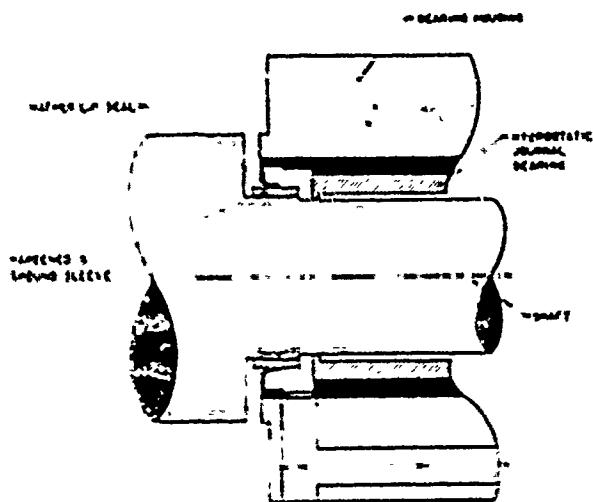


Figure 6: Mather Lip Seal and Rebuilt Sump

Current collection systems have always been difficult in monopolar machines because of high magnetic fields, large current densities and high surface velocities. While most brush mechanisms transfer current from a rotor to a stationary conductor, the FDX rotor brush mechanism transfers current from one rotor to another spinning in the opposite direction. No brush in use before FDX had been run at comparable speeds or current densities. Therefore a somewhat unique brush mechanism was required. The original FDX rotor brush mechanism didn't work properly for several reasons. Because the rotors were each about 0.025 cm out of round, a single

brush could not follow both surfaces. Because the brushes were not supported close enough to the rotor surface, a substantial moment was applied to the brushes causing them to bind in their holders. The polymer diaphragm used to actuate the brushes was not sufficiently stiff to prevent brush bounce and it leaked due to tears in mounting holes and reaction with the oil which had leaked into the rotor cavity.

The rotor brush mechanism was redesigned to solve these problems as well as to implement some new ideas. The rotor slip ring surfaces were machined to very close tolerances to assure that they were round and the same diameter. They were then balanced in the bearings so the total runout was less than 0.003 cm. This small runout makes it easier for a brush to follow the rotor. The rebuilt brush mechanism consists of 120, 0.64 cm wide sintered copper graphite brushes supported on each end by slotted fiberglass reinforced epoxy rings (Figure 7). The brushes are activated by an air pulse behind a cast polyurethane diaphragm and retracted by two compression springs per brush (Figure 8).

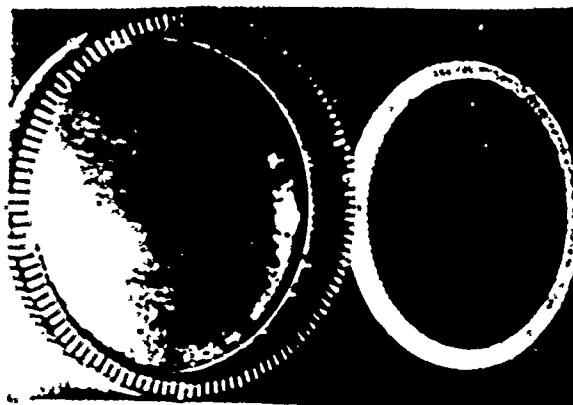


Figure 7: FDX Rotor Brushes and Support Rings

More brushes are used on the rebuilt mechanism than on the original mechanism (120 vs 36) because of the theory on the current carrying ability of brushes, that discrete points of contact rather than total surface area of contact is important.<sup>3</sup> According to this theory, number of points of contact is independent of amount of surface area. Because the brushes are supported over their entire height in

a slot, applied moment and tendency to bind are reduced. The new diaphragm is much stiffer and tougher than the old one, making higher accuation pressure and greater downforce possible.

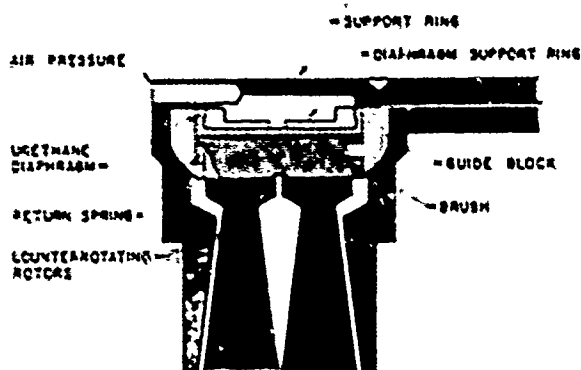


Figure 8: FDX Rotor Brush Mechanism

The high resistance bolted joint in the return conductors of FDX was eliminated on the rebuild. This was accomplished by welding the compensating turn to the outer coaxial transmission line (Figures 9 and 10). This served to decrease the internal resistance of FDX, allowing a faster discharge.

#### Second FDX Discharge Tests

After the rebuild of FDX was completed, a second set of tests was performed beginning in fall 1978. Before attempting a short circuit discharge, it was necessary to test the rebuilt components as well as verify that all other components were still functioning properly. The rotor brush mechanism was activated with both rotors spinning, to wear in the brushes and to determine the time required for the brushes to seat. Since the rotor brush mechanism required longer to seat than the shoulder brush mechanism, the two solenoids controlling them were put on different electrical circuits to allow the two brush mechanisms to activate simultaneously. The Mather lip seal and rebuilt sump and return lines were also tested with the rotor spinning at high speed. No leaks were evident and higher rotor speeds were possible due to the lower losses of the new seal. After the performance of the other components was verified, several short circuit discharges were performed with varying rotor speed and field.

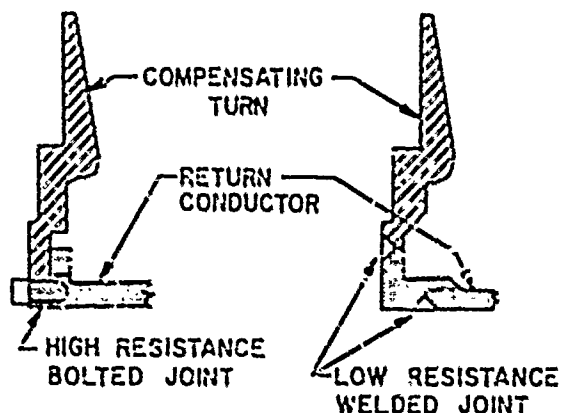


Figure 9: Current Transmission Line Bolted vs Welded Joint

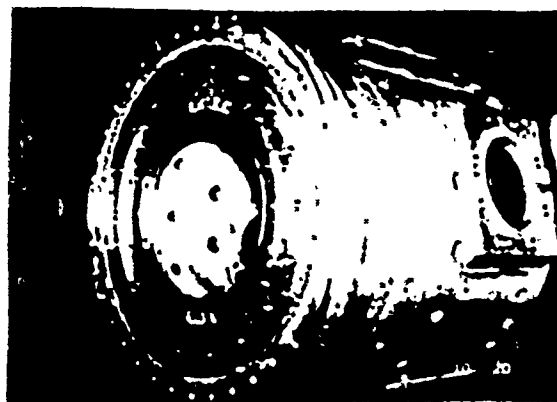


Figure 10: Welded Joint

The testing program called for a high speed, high field first discharge after careful evaluation and testing of the rebuilt components. It was desired to produce a one millisecond discharge from a respectable energy store. Initial discharges produced a choppy 240,000 A discharge and stopped the rotors in 20 msec. The energy store was then lowered in an attempt to attain the fastest known discharge of a homopolar machine. This was achieved on December 21, 1978 when oscillograms showed a continuous short circuit current output of 90,000 A that stopped the rotors in 5 msec. Results of that test allowed calculation of bulk circuit parameters as well as in depth analysis of machine performance and identification of problem areas.

Two important pieces of instrumentation were added in the FDX rebuild: a high resistance shoulder brush and a split and insulated rotor brush (Figure 11). This separated the terminal voltage into useful components and allowed analysis of the machine's internal operation. Up until the ninth run, discharge current had not been continuous during the complete discharge cycle. Calculated bulk circuit parameters from erratic data were unreliable. The shoulder brush drop 2-1 was continuous in early runs but the brush drop from 3-1 was choppy and followed the current nonuniformity. A discharge from lower speed with high volume accumulators plumbed to the rotor brushes produced the first continuous current waveform.

#### Machine Parameters

(The rotors as referred to as Rotor 1 and Rotor 2).

##### Rotor Speeds

$$\omega_1 = 188.5 \frac{\text{r}}{\text{sec}} (1800 \text{ rpm})$$

$$\omega_2 = 167.5 \frac{\text{r}}{\text{sec}} (1600 \text{ rpm})$$

##### Energy Stored

$$\frac{1}{2} L \omega^2 = \frac{1}{2} (.0446) (188.5)^2 + \frac{1}{2} (.0446) (167.5)^2 \\ = 1.418 \text{ kJ}$$

##### Voltage

$$V_{12}(\tau_2) = 5.3 \text{ V experimental}$$

$$\bar{E} = \frac{2\pi V}{\omega} = .177 \text{ V-sec}$$

$$B = \frac{\bar{E}}{\omega} = \frac{.177}{188.5} = 9.38 \times 10^{-4} \text{ T}$$

Produced by 223,000 A discharge of 5 MJ  
homopolar into FDX AIR CORE FIELD COIL

$$V_2 = \frac{\omega B}{2\pi} = 4.72 \text{ V}$$

##### Current

$$I_{\text{peak}} = 90,700 \text{ experimental}$$

##### Capacitance

$$C_1 = \frac{4\pi^2 I}{\omega^2} = 56.2 \text{ F}$$

$$C_2 = 28.1 \text{ F}$$

#### Resistance

##### Rotor

There is very little rotor speed variation between  $\tau=0$  and  $\tau_{\text{peak}}$

$$R = \frac{V_{12}(\tau=0) - V_{12}(\tau_{\text{peak}})}{I_{\text{peak}}} = \frac{5.3 - .626}{90,700} \\ = 14.3 \times 10^{-6} \Omega$$

##### Shoulder brushes

$$R = \frac{V_{12}}{I_{\text{peak}}} = \frac{.9}{90,700} = 9.9 \times 10^{-6} \Omega$$

##### Switches

Voltage drop across 4 switches in parallel at  $\tau_{\text{peak}} = .626 \text{ V}$ .

The currents in the switches are measured with hall probes that sense the  $\theta_0$  component of flux in the coaxial switch.

$$R_{\text{sw}1} = \frac{.626}{24300} = 25 \times 10^{-6} \Omega$$

$$R_{\text{sw}2} = \frac{.626}{17100} = 36 \times 10^{-6} \Omega$$

$$R_{\text{sw}3} = \frac{.626}{30500} = 20.5 \times 10^{-6} \Omega$$

$$R_{\text{sw}4} = \frac{.626}{18300} = 34.2 \times 10^{-6} \Omega$$

$$R = 6.85 \times 10^{-6} \Omega$$

##### Coax Output Bus

$$R = \frac{V_{11} - V_{\text{sw}}}{I_{\text{peak}}} \text{ at } \tau_{\text{peak}} = \frac{5.33 - .626}{90700} \\ = 51.8 \times 10^{-6} \Omega$$

#### Inductance

Slope of current rise

$$2.66 \times 10^8 \frac{\text{A}}{\text{sec}} \text{ experimental}$$

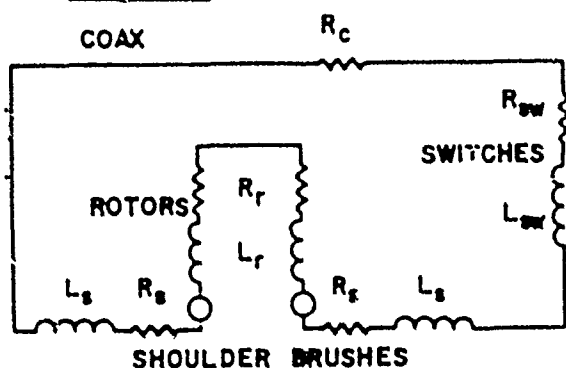
$$L_{23} = \frac{V_{23}(\tau=0) - V_{23}(\tau=0^+)}{\text{slope}} = \frac{2.3}{2.66 \times 10^8} \\ = 8.6 \times 10^{-9} \text{ H}$$

$$L_{12} = \frac{V_{12}(\tau=0) - V_{12}(\tau=0^+)}{\text{slope}} = \frac{2.3}{2.66 \times 10^8} \\ = 8.6 \times 10^{-9} \text{ H}$$

$$L_{\text{switch}} = 5 \times 10^{-9} \text{ H (Reference 4)}$$



### Bulk Circuit



$$R_F = 51.8 \times 10^{-6} \Omega$$

$$R_{\text{eq}} = 6.85 \times 10^{-6} \Omega$$

$$L_{\text{W}} = 5 \times 10^{-9} \text{ H}$$

$$R_f = 143 \times 10^{-6} \Omega$$

$$L_f = 8.6 \times 10^{-9} \text{ H}$$

$$R_s = 9.9 \times 10^{-6} \Omega$$

$$L_g = 8.6 \times 10^{-9} \text{ H}$$

C = 28.1 F

$$R_T = 107 \times 10^{-6} \Omega$$

$$L_T = 39.4 \times 10^{-9} \text{ H}$$

$$\text{Damping Coefficient} = \frac{R}{2Z_0} = \frac{107 \times 10^{-6}}{2 \sqrt{\frac{39.4 \times 10^{-9}}{28.1}}} = 1.43$$

$$\tau_{\text{peak}} = \frac{\ln \frac{R^2 c}{L}}{\frac{R}{r} - \frac{1}{RC}} = \frac{2.09}{2716 - 332} = .00086$$

Even in the continuous current discharge the rotor instrumentation brush unseated at 0.8 msec into the discharge and resealed at 3.2 msec. Total discharge current never went to zero. This indicates that the current repulsion between flow in the brush and output coax is aiding the down force on the rotor brushes. The decay of the current waveform shortly after current peak did not follow the R-C decay predicted from bulk parameters. The resistance change occurred because full brush seating was not maintained. Also it can be concluded that the force causing brush bounce is either mechanical or eddy

current related because the rotor instrumentation brush which does not carry current also bounces. Therefore current constriction and brush melting can be eliminated as causes of bounce. The engineering solution will probably be the separation of the rotor brushes into two independent rotor tracking mechanisms. Also if expanded flux plots in the rotor brush area show an eddy current force, brush lamination may also be considered. The present mechanism functioned well enough to provide the 5 msec discharge from low energy store which explored the fundamental limitation. New mechanisms will make fast discharge homopolars viable pulsed power supplies.

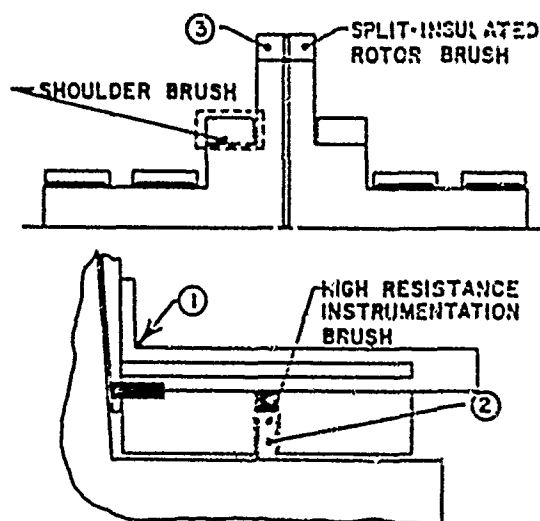


**Figure 11: FDX Instrumentation**

## Conclusions

Even though a one millisecond discharge of FDX was not achieved, further testing is warranted due to the very fast current rise times seen in the second set of tests. Since the main problem with FDX is current breakup due to the bouncing of rotor brushes, the configuration of this mechanism must be changed to allow it to continuously transfer current between the two counterrotating rotors. Experience from both FDX rotor brush mechanisms has shown that this cannot be done successfully by using a single brush bridging both rotors. A separate brush mechanism should therefore be used on each rotor with a flexible, current-carrying strap joining the two. Also, because controlling the speeds of the two rotors by

manually controlling air flow is difficult, a circuit should be designed to synchronize the rotor speeds.

The 5 millisecond discharge achieved by FDX is the fastest discharge ever for a homopolar machine. Still, the fast current rise times demonstrate that a shorter discharge time is possible. A second generation fast discharge machine would be very similar to FDX with two significant changes. Two separate rotor brush mechanisms, as explained above, would be used to transfer current between the two rotors. A steady state superconducting field coil would replace the present pulsed field coil to provide the necessary high field. This superconducting coil would allow higher fields if necessary, enable the uniformity of the field to be controlled and allow the rotors to self motor. Also because the field would be steady state, the return conductors could be made of copper rather than aluminum, thus decreasing the resistance of the machine and increasing the output current.

#### Acknowledgements

This work was performed under contracts to the U.S. Department of Energy (DOE), the Electric Power Research Institute (EPRI) and the Texas Atomic Energy Research Foundation (TAERF).

#### References

1. M. D. Driga, S. A. Nasar, H. G. Rylander, W. F. Weldon and H. H. Woodson, "Fundamental Limitations and Topological Considerations for Fast Discharge Homopolar Machines," IEEE Transactions of Plasma Science, Vol. PS 3, No. 4, December 1975, pp 209-215.
2. J. H. Gully, M. D. Driga, B. Grant, H. G. Rylander, K. M. Tolks, W. F. Weldon, and H. H. Woodson, "One Millisecond Discharge Time Homopolar Machine (FDX)", presented at the IEEE International Pulsed Power Conference, Lubbock, Texas, November 9-11, 1976.
3. M. Brennan, Z. Eliezer, W. F. Weldon, H. G. Rylander, and H. H. Woodson, "The Testing of Sliding Electrical Contacts for Homopolar Generators," IEEE Transactions on Components Hybrids and Manufacturing Technology, Vol. CHMT-2, No. 1, March 1979.
4. P. Wildi, "A Fast Metallic Contact Closing Switch for the FDX Experiment," Seminar on Energy Storage, Compression and Switching at the Australian National University, Canberra Australia and the University of Sydney, Sydney, Australia, November 15-21, 1977.

## PULSAR: AN INDUCTIVE PULSE POWER SOURCE\*

E. C. CHARE, W. P. BROOKS, and M. COWAN

Sandia Laboratories  
Albuquerque, NM 87185Abstract

The PULSAR concept of inductive pulsed power source uses a flux-compressing metallic or plasma armature rather than a fast opening switch to transfer magnetic flux to a load. The inductive store may be a relatively unsophisticated DC superconducting magnet since no magnetic energy is taken from it, and no large current transients are induced in it. Initial experimental efforts employed either expendable or reusable metallic armatures with a 200 kJ, 450 mm diameter superconducting magnet. Attention is now being focused on the development of much faster plasma armatures for use in larger systems of one and two metres diameter. Techniques used to generate the required high magnetic Reynolds number flow will be described and initial experimental results will be presented.

Introduction

PULSAR is a system which produces pulsed power by magnetic flux compression with metallic or plasma armatures. A superconducting magnet supplies the flux and chemical energy produces high magnetic Reynolds number armatures for the compression. Various forms of PULSAR<sup>1,2</sup> have been proposed for use in coal-fired and inertial fusion power plants as topping stages which have the potential of increasing plant efficiency to greater than 50%. As a prime pulse power source PULSAR becomes more economically attractive the larger the required pulse energy. It becomes competitive at about 10 MJ when its dimensions are the order of a few metres.

The first experimental model of PULSAR generator employed a 0.45 m diameter magnet. When tested  
\*This work was supported by the U.S. Department of Energy.

with metallic armatures the pulse rise time ranged from 80  $\mu$ s in the radial mode to 600  $\mu$ s in the axial mode. Comparison between predictions and experiments showed that PULSAR performance with metallic armatures could be accurately anticipated. However, for some applications there is greater interest in the much faster rise times which can be achieved with plasma armatures. Unfortunately, with plasma armatures it is much more difficult to match theory and experiment. Therefore, to establish dependable scaling laws for plasma armatures an experimental program is being carried out, to extend generator size into the "full scale" region. This will be done with low energy magnets to keep costs down. The program calls for construction of two additional experimental generators, one utilizing a 1 m diameter, 200 kJ magnet and another with a 2 m diameter, 2 MJ magnet. Figure 1 shows the original 0.45 m magnet and the



Fig. 1. One m and 0.45 m Superconducting Magnets for PULSAR

new 1 m magnet which will be involved in generator experiments during the later part of 1970.

This paper will describe a new technique for generating the required high magnetic Reynolds number

plasma armatures which will be used for the larger systems. Results obtained with the new technique in the 0.45 m system will be presented and compared both to those obtained in previous experiments and to predictions of a numerical model.

#### Plasma Armatures

Previous plasma armature systems<sup>3</sup> consisted of a centrally located, axially initiated explosive charge that was used to radially expand a weakly preionized deuterium gas. The best performance of such a plasma armature produced only about 1/50th the current of a radially expanded metallic armature. In contrast, results of a computer model<sup>4</sup> of the plasma armature predicted about the same peak current as that from a metallic armature due to ohmic heating of the plasma front which "bootstrapped" the conductivity to high values. The suspected reason for the disagreement is that the code does not allow particle exchange between zones so mixing and cooling at the explosive-gas interface is neglected. Because the flow was subsonic, these processes were probably very important, but accounting for them would have required major code changes. This was not warranted since plasma armatures produced by this experimental system were clearly inadequate. Instead, a new experimental approach was developed which more nearly approached the conditions of the optimistic code. A supersonic plasma-producing armature system was developed. Supersonic flow produces a shock with clean "test gas" between the shock front and the explosive-gas contact surface.

The magnetic Reynolds number of the plasma flow is given by

$$R_m = \mu_0 \sigma v l$$

where  $\mu_0$  is the magnetic permeability,  $\sigma$  is the plasma conductivity,  $v$  is the plasma velocity and  $l$  is the plasma flow distance. Since the conductivity is proportional to  $T^{3/2}$  and the temperature behind a strong shock is proportional to  $v^2$ , the magnetic Reynolds number is proportional to  $v^4$ .

The technique we have pursued to obtain higher velocity flow is illustrated in Figure 2. The PUL-SAR magnet and generator coil are nested at the

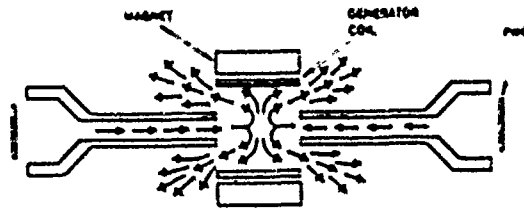


Fig. 2. Schematic for Producing High Speed Plasma Flow  
center of the assembly and two electrically detonated explosive plane wave generators<sup>5</sup> located behind blast shields drive high speed flows which stagnate and expand in the generator coil as shown in the figure. The shields were designed to accommodate straight gas flows through the connecting channels or flows converged from larger diameter explosives into the channels for still higher velocities.<sup>6</sup> In addition, the channels were obtained in 0.60, 0.90, and 1.50 m lengths to determine the effect of channel length on plasma armature quality.

#### Experimental Results

The experimental setup to test the plasma armature system depicted schematically in Figure 2 is shown in Figure 3. At the time of the test, the LHe devar is removed from the test area and the super-

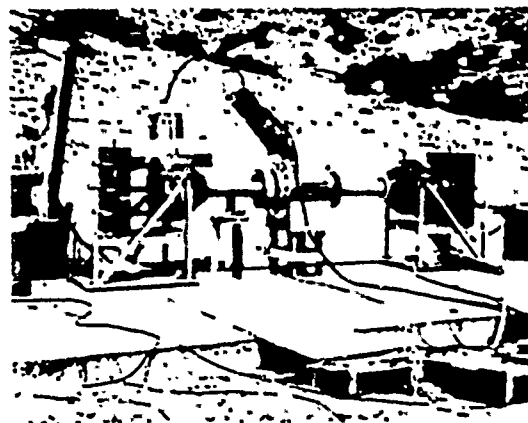


Fig. 3. PULSAR Test Setup for High Speed Plasma Armatures

conducting magnet is operated on its own life reservoir. The 10-cm diameter plane wave generators were mounted about even with the open end of the conical blast shields and the low pressure gas channels extend from the explosive to the central expansion chamber. Gas flow velocities in this system were about 20 km/s axial in the channels and 10 to 15 km/s radial in the central chamber. Output current pulses measured in the standard 0.55  $\mu\text{H}$  load for the three channel lengths are graphed in Figure 4 and have been aligned to a common zero time. The magnet current for this test series was 2/3 of maximum so the output can be scaled up by 3/2 for comparisons to previously reported results. The dependence on channel

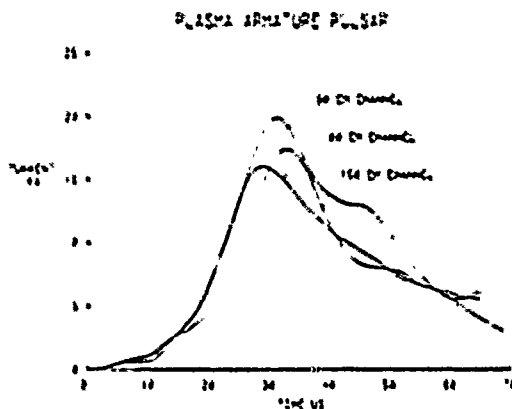


Fig. 4. Plasma Armature PULSAR Output Current Histories

length is seen to be weak with the best of the three tests producing about 8 times more current than the best subsonic plasma armatures and about 1/5th of the code-predicted output.

In a test for which the terminals of the generator were shorted, the output current increased about 23%. Assuming similar flux efficiency for the shorted test and tests with the 0.55  $\mu\text{H}$  load, the minimum leakage inductance of the generator was determined to be 2.4  $\mu\text{H}$ . This inductance implies a plasma skin depth of about 3 cm which is consistent with a plasma temperature of a few eV. This is much higher than the temperature expected from shock heating, indicating that some bootstrapping of the plasma conductivity occurred. The energy

in the leakage and load inductances exceeded 1200 J but 80% of this was in the leakage inductance. For full-scale PULSAR systems, the ratio of load to leakage inductance energy will greatly favor the load.

#### Conclusions

A new supersonic plasma armature system produces an order of magnitude better flux compression than the old subsonic one. Experimental results indicate that some bootstrapping of the conductivity by ohmic heating did occur but not as much as a numerical model has predicted. Skin depth in the plasma armature was about 3 cm which for a small system precludes the delivery of a large fraction of the generated electrical energy to an external load. This will not be a problem for full-scale plasma armatures even if plasma properties do not improve.

#### Acknowledgments

The authors would like to acknowledge the participation of B. W. Duggin in this study for developing the mesh-initiated plane wave generators and for designing the blast shields. The assistance of E. R. Ratcliff, R. R. Callegos, and L. Yellowhorse in fielding the experiments and gathering the data is also greatly appreciated.

#### References

1. M. Cowan, et al., "Pulsed Energy Conversion with a DC Superconducting Magnet," *Cryogenics*, December 1976, 699.
2. M. Cowan, et al., "PULSAR - A Flux Compression Topping Stage for Coal-Fired Power Plants," *Proc. ICEC 6* (1976) 135.
3. E. C. Cnare, et al., "Pulsed Power Conversion with Inductive Storage," *Proc. 7th Sym. Eng. Prob. of Fusion Res.* (1977) 1049.
4. T. P. Wright, et al., "Magnetic Flux Compression by Expanding Plasma Armatures," 2nd Int. Conf. on Megagauss Magnetic Field Generation and Related Topics (1979) to be published.
5. R. I. Butler, et al., "Mesh-Initiated Large Area Detonators," *Rev. Sci. Instr.* V. 47, No. 10 (1979) 1261.

6. M. Covan and D. A. Freivald, "Strongly Ionizing High Explosive Shocks," Proc. 7th Int. Shock Tube Symposium (1969) 432.

## PRELIMINARY INDUCTIVE ENERGY TRANSFER EXPERIMENTS

R.P. HENDERSON, D.L. SMITH, and R.E. REINOVSKY

Air Force Weapons Laboratory  
Kirtland AFB, New MexicoAbstract

The use of inductive storage systems has been studied as an attractive alternative to the more conventional capacitive energy storage systems to drive a cylindrical imploding plasma and produce X-rays for nuclear simulation. Preliminary experiments have been conducted using a 200 kJ, 4 $\mu$ s capacitor bank and a 100 kJ, 1 $\mu$ s capacitor bank to explore the basic performance of electrically exploded foil opening switches. Peak voltage and opening time have been characterized as a function of quench media and capacitor bank risetime. Risetime and energetic efficiency of current transfer to inductive dummy loads have also been measured. These experimental results are contributing to conceptual designs for a 1.9 MJ capacitor driven inductive pulse shortening system.

Introduction

In anticipation of applying an inductive pulse shortening circuit to the SHIVA system<sup>1</sup>, investigations using metal foil fuses as fast opening switches are being conducted on two intermediate energy systems. This experimental effort is aimed at verifying the operation of electrically exploded foil switches at high currents and fast risetimes to permit scaling of these switch designs to higher energy (2 MJ) systems than those which have been previously explored<sup>2</sup>. A general schematic diagram of an inductive pulse forming circuit is shown in Fig. 1. For the near future the primary energy storage device consists of a dc charged capacitor bank which discharges through some storage inductance and an initially closed switch that opens at peak current. A load in series with an initially open isolation switch is placed across the opening switch as shown. The performance of such a circuit

is characterized by how quickly the opening switch can interrupt the primary current and transfer energy to the load without dissipating an unacceptably large fraction of the stored energy. The peak current and voltage across the switch are also a measure of its performance. For a matched inductive load a maximum of 25% of the initial energy in the storage inductor can be transferred to the load<sup>3</sup>; however, a significantly higher fraction can be transferred if the load is dissipative as in the case of a SHIVA implosion<sup>1</sup>.

Experimental Arrangement

Two capacitor bank systems were used for these experiments. Both banks are discharged by multiple pressurized gas, field distortion rail gap switches connected in parallel. The operational characteristics of the two facilities are as follows:

Total Energy (kJ)	200	110
Charging Voltage (kV)	50	100
Bank Capacitance ( $\mu$ F)	158	22
Primary Inductance (nH)	36	26
Quarter Period ( $\mu$ s)	3.7	1.2

Currents and voltages are monitored on oscilloscopes and transient digitizers to facilitate the interpretation of the data. Currents are measured with Rogowski belts which can be integrated both passively and actively as desired. Voltages are measured with resistive divider high voltage probes. Figure 2 shows a cross-sectional edge view of a typical single folded fuse package. Rectangular metal foils are folded around an insulator and clamped to transmission lines at opposite ends. The medium which must rapidly quench the expanding vapor/liquid from the exploded foil is packed on all sides of the fuse. The criteria originally reported by Maisonnier<sup>3</sup> placing conditions on the

fuse cross section in terms of the system capacitance and inductance, initial bank voltage, and the fuse material properties is used as a guide for these fuse designs.

#### Simple Fuse Results

Analytic and computational models of the switching requirements imposed by future imploding plasma experiments imply that the two relevant parameters are the switch opening time and the switch final impedance. From the models opening times of 150 ns or less are required, and final impedances of the same order as the  $\frac{1}{2}$   $\Omega$  final impedance of the imploding SHIVA load are necessary. Experiments have been conducted on the two test facilities employing both copper and aluminum fuses quenched in glass beads of diameter 62 to 105  $\mu$ m ("Blast-O-Lite" BI-12). Figure 3 shows current and voltage data from a 1 mil (.0254 mm) copper fuse interrupting 1.5 MA and generating a voltage of 220 kV (4.4 multiplication) on the 200 kJ facility with a current risetime of about 3  $\mu$ s. Taking the FWHM of the voltage pulse as an approximate measure of the risetime of the impedance, the temporal compression (time of peak voltage/FWHM) is just over 10. Data from an experiment on the faster 100 kJ experiment which was designed to interrupt the same peak current (1.5 MA) using a 1 mil aluminum fuse is shown in Fig. 4. The fuse generates a 270 kV pulse (3.3 multiplication) of 120 ns width for a 12.5 temporal compression.

From the data in Fig. 4, the resistance of the fuse can be calculated after suitable inductive calculations are applied. And hence a resistivity for the 40 cm x 20 cm x 1 mil thick fuse can be found. This resistivity, which is plotted in Fig. 5, shows a peak resistivity of 2.5 m $\Omega$ -cm, with the last 90% of the rise occurring in 100 ns. The peak resistivity occurs at the time of peak voltage and when the current has fallen to less than 20% of its peak value. As the current falls to zero, the resistivity found from  $V_{corrected}/I$  takes on widely varying values which are suppressed in Fig. 5. At peak resistance the fuse has dissipated 70 kJ of energy for a specific energy of 13 kJ/g. Scaling this data to the large (2 MJ) experiment results

in a fuse 0.37 cm<sup>2</sup> in cross section and 21.4 cm long. This fuse would produce a resistance of 60 m $\Omega$  at similar energy densities. Such a switch is very attractive based on the concepts of projected load performance<sup>4</sup>.

#### Quench Media

The final fuse resistance values and the corresponding resistivities seem to be influenced by the choice of quenching media in the switch packages. Electrical and mechanical considerations in the design of a full scale system suggest that a large number of small packages<sup>2</sup> may not be acceptable and that the use of thin (preferably solid) media may be preferred. Thus a limited survey of quenching material was conducted, and the results in Table I rank the different media (for one aluminum foil geometry) with respect to the maximum fuse voltages ( $V_p$ ), the minimum full-width-half-maximum (FWHM<sub>v</sub>) of the voltage spike, and the highest peak fuse current ( $I_p$ ). The combination of material refers to the media used outside/inside the hairpin folded fuse.

Table I

<u>4.0 <math>\mu</math>s Bank</u>	$V_p$	FWHM <sub>v</sub>	$I_p$
Beads/Beads	1.00	1.00	1.00
Beads/Mylar	.97	.99	.98
BI/BI	.95	.71	.92
AFB/AFB	.86	.71	.99
FC/PVC	.79	.73	-
PVC/PVC	.59	.56	.92
LN <sub>2</sub> /LN <sub>2</sub>	.45	.91	.99
Mylar/Mylar	.28	.45	1.00

#### 1.0 $\mu$ s Bank

Beads/Beads	1.00	1.00	1.00
Beads/Mylar	.55	.86	.90
BI/BI	.35	.67	.90

Similar studies with similar results for near-Maisonniere copper fuses (no load) have been performed at the Los Alamos Scientific Labs<sup>5</sup>. For the above results BI, AFB, FC, PVC, and LN<sub>2</sub> refer to R19 fiberglass building insulation, acoustical fiberglass batting, fine fiberglass cloth, polyvinyl chloride sheets, and liquid nitrogen respectively. The conclusions from this survey are that foil switch



packages with glass beads on both sides or on one side with mylar backing are preferable for optimum fuse performance, absorbing acoustical shocks, tracking, and restrike holdoff. Coarser sand or beads appear to result in significantly longer turn-off times<sup>6</sup>. Foil vapor can be expected to expand at speeds of a fraction to a few m/us. Thus material within one millimeter of the fuse foil may be expected to be involved in the quenching action. Following a fuse shot, a brittle "potato chip" section of the quenched fuse material may be recovered when the glass beads are used. An edge view of one of these 1 mm thick sections is shown in the top of Fig. 6 with a 100X magnification using a scanning electron microscope (SEM). The fuse foil was originally to the left of the loosely packed beads, and the heat from the switching action apparently melted and joined the beads nearest the foil. The beads farther from the foil are connected by "cold solder" joints of the recondensed aluminum. The top right photograph shows the aluminum to be uniformly deposited throughout the depth of the chip instead of predominantly near the foil location as expected. The 1000X magnification of one bead in the lower photographs of Fig. 6 demonstrates how the aluminum droplets have settled on the surface of the beads with practically no conductive paths between the droplets.

#### Load Experiments

Hardware has been constructed to allow fuse behavior to be evaluated when a parallel load is employed. Since the SHIVA load is initially lower in inductance than the storage inductor, the load circuit (Fig. 7) was designed to consist of a 2.2 nH transmission line and output switch and a 6.0 nH load for operation on the 200 kJ bank for a ratio of storage inductance to load inductance of about 4. Initial experiments employed a self breaking solid dielectric output switch. Currents of 1.4 MA were interrupted and currents of 600 kA transferred to the load with a risetime of approximately 100 ns. Simplest considerations suggest that the current risetime into a load of inductance  $L_L$  from a store of inductance  $L_s$  with a switch

$$\text{resistance } R \text{ should be}$$

$$\tau = \frac{L_L}{R} \left[ \frac{L_s}{L_s + L_L} \right]$$

For the experiment the fuse resistance reached approximately 40 m which implies a risetime of 160 ns which is slightly longer than the measured risetime. Analysis has shown that the time of the output switch closure is fairly critical, and although current risetime was good, current transfer was less efficient than expected presumably because output switch closure prevented proper operation of the fuse.

#### Conclusion

By designing fuse geometries to somewhat less (70%) than the Maisonnier criteria the prospects for efficient high energy transfers to a load appear to be good, especially when a low-jitter output switch is incorporated into the circuit. Fuse experiments on a facility slower than the SHIVA system and on one that is faster indicate that 200 - 300 ns pulses can be delivered to the SHIVA load. The observed fuse resistivities are promising according to the SHIVA parameters, and the glass beads will be the primary quenching material for upcoming inductive storage applications.

#### References

1. W.L. Baker, M.C. Clark, J.H. Degnan, G.F. Kiuttu, C.R. McClenahan, and R.E. Reinovsky, "Electromagnetic-Implosion Generation of Pulsed High-Energy-Density-Plasma," J. Appl. Phys., 49, pp. 4694-4706, September 1978.
2. J.N. DiMarco and L.C. Burkhardt, "Characteristics of a Magnetic Energy Storage System Using Exploding Foils", J. Appl. Phys., 41, pp. 3894-3899, August 1970.
3. Ch. Maisonnier, J.G. Linhart, and C. Goullan, "Rapid Transfer of Magnetic Energy by Means of Exploding Foils", Rev. Sci. Instrum., 37, pp. 1380-1384, October 1966.
4. D.L. Smith, R.P. Henderson, and R.E. Reinovsky, "Considerations for Inductively Driven Plasma Implosions," Paper 12.3 in these proceedings.
5. R.A. Haarman, R.S. Dike, and M.J. Hollen, "Exploding Foil Development for Inductive Energy Circuit", in proceedings of Fifth Symposium on Engineering Problems of Fusion Research, and Report LA-UR-73-1610, Los Alamos Scientific Laboratory, Los Alamos, NM, 1973.
6. C.R. McClenahan, J.H. Goforth, J.H. Degnan, B.M. Henderson, W.R. Janssen, and W.E. Walton, "200 Kilojoule Copper Foil Fuses", Report AFWL-IR-78-130, Air Force Weapons Laboratory, Kirtland AFB, NM, April 1978.

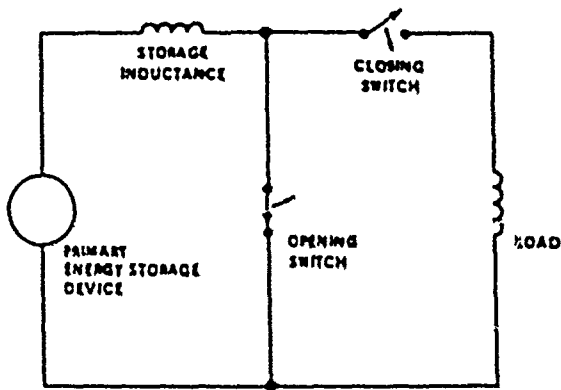


Fig. 1. Inductive Energy Storage Circuit.

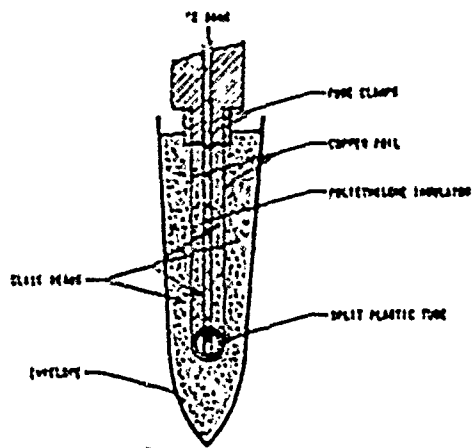


Fig. 2. Cross Sectional View of Fuse Package.

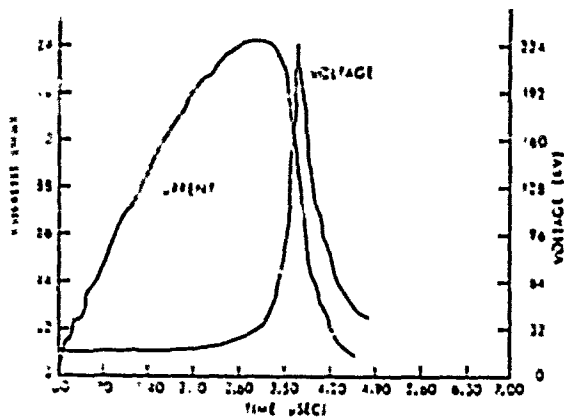


Fig. 3. Copper Foil V and I Waveforms.

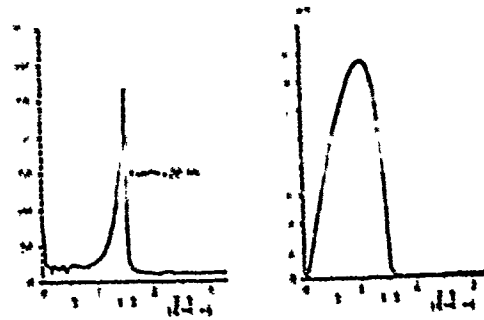


Fig. 4. Aluminum Foil V and I Waveforms.

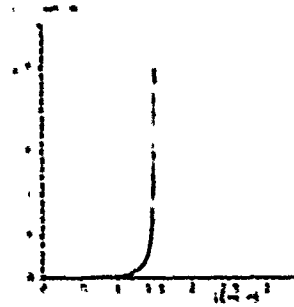


Fig. 5. Aluminum Foil Resistivity Versus Time.

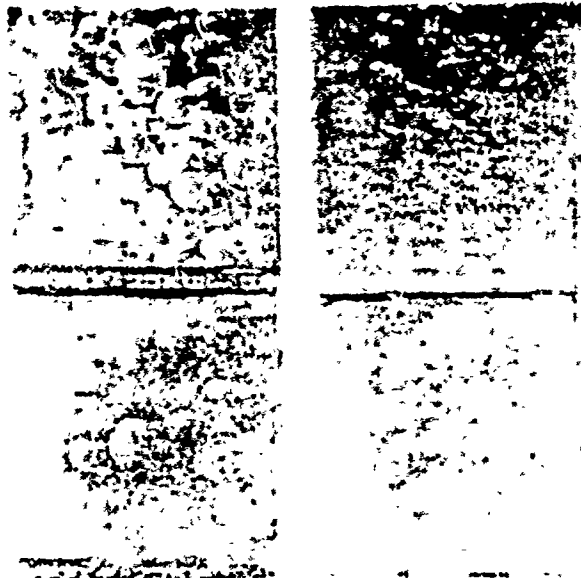


Fig. 6. SEM Pictures of Beads After Fusing.

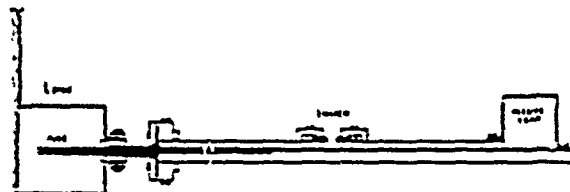


Fig. 7. Parallel Load Experiment.

## APPLICATION OF PFN CAPACITORS IN HIGH POWER SYSTEMS

ROBERT D. PARKER

Hughes Aircraft Company, Culver City, California

Abstract

The application of lightweight reliable capacitors in a mobile energy store is discussed. The relationship of system design parameters to capacitor size and life is displayed. Electric fields and weights of a 21 J/lb and a 77 J/lb pulse discharge capacitor design are given. Estimates of future near-term development are made.

INTRODUCTION

In the vast majority of aerospace applications, the capacitor may be successfully treated by circuit and system engineers as a black box containing an essentially ideal passive circuit element. Capacitors are normally applied well within their ratings, and are designed extremely conservatively, even for high voltage applications. Recently, however, a new class of mobile pulsed-power systems has emerged. In these systems, a capacitive energy store may comprise a substantial fraction of the weight and volume of the entire system. Because of the "black box" design approach, system parameters are often selected without a clear understanding of their combined effect on the weight, life, and reliability of the energy storage capacitors. Since a major design goal in a mobile system is to reduce system size and weight, designs are sometimes produced for which no appropriate capacitors are available, or in which non-ideal capacitors must be used in a make-do situation, resulting in generally unsatisfactory component performance.

The designer is hampered by the total lack of all but rudimentary data on the application of the component, often because no testing has been done by manufacturers or published in the literature. The manufacturing processes themselves are poorly controlled, resulting in high part-to-part non-uniformity as well as lot-to-lot non-uniformity. Finally, except for measurements of capacitance and dissipation factor, no industry or military specifications or standards exist for the measurement of various parameters important to pulse discharge application.

This paper discusses the application of large capacitors in high power pulse forming networks. The impact of system parameters such as pulse width, pulse rise time and repetition rate upon the weight, life, and reliability of the energy

store is discussed. The problem of application in hostile environments is examined. Present experimental results are reviewed, and projections of achievable weight and volume for mobile energy store are made.

APPLICATION

Many system level parameters affect the application of pulse-discharge capacitors in a reliable mobile energy store. These are:

- Pulse width and shape
- Load impedance
- Pulse repetition rate
- Charge voltage and waveshape
- Burst duty cycle
- Load match
- Thermal impedance of mount
- Available cooling
- Operational temperature range
- Air pressure/altitude
- Air quality-contaminants

Each of these impacts electrical and thermal failure mechanisms. In the sections below, each parameter is discussed and its effects displayed. The motive here is to show how to make the operating environment less severe; a less severe environment allows smaller, lighter, more reliable capacitors.

PULSE WIDTH AND SHAPE

These two parameters determine the frequency spectrum and relative magnitude of the discharge currents for each PFN capacitor. For a system where all other parameters remain the same, a shorter output pulse results in a larger amount of power dissipated, and therefore a higher operating temperature and shorter life. Similarly, a given pulse width with faster rise time requires more PFN sections, and this has the same effect as a shorter pulse.

It is easy to show, for a given energy storage, that the power dissipation is linear in  $1/\tau$ , where  $\tau$  is the output pulse width. This ignores the fact that dissipation factor is not constant with frequency,

but normally this is not as large an effect, and must be worked out for each insulating system. The pulse rise time will be approximately  $2\pi/(2N+1)$ , where  $N$  is the number of PFN sections. As the number of sections increases for a given energy, the frequency dependence of dissipation factor (or ESR) will generally cause the power dissipation to increase.

#### LOAD IMPEDANCE

Low impedance loads are more difficult to drive because they require high currents. Real problems arise only if capacitor currents above about 20 kA are necessary, because of the extreme mechanical forces.

#### PULSE REPETITION RATE

The pulse width and shape determine the power dissipated in the capacitor for each pulse. The pulse repetition rate determines the power dissipated per unit time during the pulse burst:

$$\bar{P}_{\text{burst}} = P_{\text{pulse}} \times \text{PRR}$$

This, in turn, is linearly related to the internal temperature and thus to capacitor life.

#### CHARGE VOLTAGE AND WAVESHAPES

Very high charging voltages cause an increase in weight, because additional interconnections and insulation between case and capacitor element are required. Various curves have been presented. One rule of thumb is 5 percent weight increase 20 to 30 kV, 10 to 15 percent increase in the 30 to 40 kV range, and at least 20 percent increase above 40 kV. Because very high voltage capacitors require additional series sections and therefore additional interconnections, overall reliability is lower.

Charge waveshape affects the capacitor dissipation during the charging cycle. Surprisingly, systems have been designed for which the dissipation during charge was as large as the dissipation during discharge, and since designers normally neglect charge dissipation, such systems normally burn up. Some dielectric systems used in energy storage capacitors have very high dissipation factors at normal charge frequencies. It is wise to utilize as much of the interpulse spacing as possible to charge the store, since power dissipation increases as the peak current increases.

#### BURST DUTY CYCLE

A capacitor of average dimensions (5 x 5 x 7 in.) or larger has a long thermal time constant, because even with heavy foil, the capacitor element has an extremely poor thermal diffusivity. Time constants are in the range of several hours. Therefore, the burst duty cycle determines the highest service temperature seen during a given mission. Since the time constant is so large, variation of burst length and spacing on a scale much smaller than the time constant has little effect on the temperature, provided the energy transferred remains the same.

#### LOAD MATCH

It is normally possible to match the energy store to the load within a few percent, even for loads which exhibit complex time-dependent transfer characteristics. Failure to match the load results in a large voltage reversal. This drastically shortens component life. The system level result is shorter-lived, extremely heavy components, with weights being between 2 and 5 times as large as what would have been possible with a matched load.

#### PASSIVE THERMAL CONSIDERATIONS

The thermal impedance of the mounting and the available cooling determine the temperature rise during a series of bursts over a time longer than an hour. It is important to provide cooling to limit this rise to prolong capacitor life. The absolute temperature reached depends on the operating ambient. Systems which operate in high ambient or with poor cooling will be several times larger than the ideal.

#### ALTITUDE

Two important problems obtain from the operation of an energy store at high or variable altitude. One problem is that it is difficult to provide a highly reliable termination for this service; the second problem is the variation of atmospheric pressure may cause pressure variation within the oil-filled components in the energy store.

The termination and interconnection problem in this type of system in a variable pressure environment is severe. Prototype systems usually employ make-shift non-demountable high current connectors. Normally available high altitude high voltage connectors cannot handle the high peak currents and the large RMS currents during the burst. Probably the best solution is to fabricate custom connectors for each installation.

If the cases of the oil-filled components are flexible, as are most light-weight cases, the reduction in pressure at high altitude causes a reduction in the pressure of the oil below atmospheric. This is well known to cause immediate and significant degradation of corona inception voltage, and will cause short life and premature failure. Flexible cases must be supported or other methods must be used to maintain oil pressure under any operating condition.

#### AIR QUALITY

Some mobile installations operate in high humidity environments or other situations where prototype connections and terminations will cause substantial system malfunction. Interconnections of the type used in high altitude operation are usually sufficient to protect against these types of malfunction. However, the added weight of these extra precautions needs to be considered.

### RECENT EXPERIMENTAL RESULTS

As has been discussed previously, the unavoidable failure mechanism in a well-constructed capacitor is uniform corona damage at the foil edges. In this section, several dielectric systems presently in use are described, and electric fields for satisfactory operation with  $10^5$  to  $10^6$  shot life are given. Several complete capacitors are described, and their energy density displayed.

#### CAPACITOR STRUCTURE

The capacitor structure tested is a flat-wound foil capacitor employing liquid impregnated five layer dielectrics. All capacitors to be described employed EIB kraft paper and polysulfone as the dielectric, and either mineral oil or dioctylphthalate as the fluid. Capacitor sections were made in the range 1.1 to 3.3  $\mu\text{F}$ , with anticipated operating voltages in the range 5 to 7.5 kV. Complete capacitors valued 2.2  $\mu\text{F}$  15 kV were assembled from these components.

It was determined by a series of indirect measurements that the thickness of the oil layers in these components was 1.0  $\mu\text{m}$  for each pair of surfaces. Thus, a component with 5 solid dielectric layers also contained about 6.0  $\mu\text{m}$  of fluid. This is approximately 32 percent less fluid than is normally found in an oil-filled capacitor. The extreme thinness and uniformity of the fluid layers is thought to be partially responsible for the high layer operating fields and uniform degradation found experimentally.

#### ELECTRICAL SERVICE CONDITION

Tests on all components and sections were run with a minimum duty profile of 300 pps for 1 minute, with 2 hours between bursts. Components were tested in an apparatus which duplicates frequency distribution and current magnitudes of PFN operation. Discharge pulse width was 20  $\mu\text{s}$ , and voltage reversal was 25 percent. Expected life was  $10^5$  pulses minimum, or 5.5 full bursts.

#### LIMITING ELECTRICAL FIELDS

The maximum fields found for two different impregnants at reliable life greater than  $10^5$  pulses are shown in the following table for otherwise identical structures.

##### a) Mineral Oil Impregnant - Average Field 3750 V/mil

Material	Field V/mil
Paper	2424
Plastic	3714
Fluid	5235

##### b) Dioctylphthalate Impregnant - Average Field 4460 V/mil

Material	Field V/mil
Paper	3430
Plastic	5266
Fluid	2761

The higher average field possible for the higher dielectric constant impregnant is due to better field balance in the dioctylphthalate part. The design goal is to have operating electric fields in the same ratio as known break-down voltages. Limiting fields occurred in the fluid with mineral oil, and in both paper and plastic with dioctylphthalate. Some improvement may be possible in this design, but no more than 10 percent.

#### COMPLETE CAPACITORS

Two different complete capacitors have been assembled, both with 2.2  $\mu\text{F}$  15 kV rating. One design employed mineral oil, and was designed at moderate stress and with sturdy construction. The operating fields were:

Material	Field V/mil
Paper	1904
Plastic	2916
Fluid	4113

This component was very reliable, and had life in excess of  $10^6$  shots on a routine basis. The second component used dioctylphthalate, and was designed for absolute minimum weight. The operating fields are listed in the previous section. A breakdown of the weight of each component is shown below.

Item	Design 1 Weight	Design 2 Weight
Sections (wet)	3.126 kg	1.126 kg
Case	892 g	96 g
Terminal	57 g	57 g
Case Insulation	546 g	102 g
Extra Oil	599 g	101 g
Totals	5.22 kg	1.482 kg
Specific Weight	20.86 g/J	5.93 g/J
True Energy Density	0.087 J/cm <sup>3</sup>	0.265 J/cm <sup>3</sup>
"Energy Density"	21.7 J/lb	76.5 J/lb

## DISCUSSION

The AC electric fields being reached over a large area of the polymer film in design 2 are about 70 percent of the short-term small area "intrinsic" breakdown test value for the film. The failure analyses indicate that, with the present designs, the limit for the paper is also quite close. It is therefore estimated that, at best, a 10 percent improvement in field is possible without foil edge modification. This translates to a 21 percent improvement in "energy density".

## ESTIMATES

For the aid of systems engineers, herewith is a short discussion of near term improvement possibilities and real values for real systems.

### ULTIMATE ENERGY DENSITY

Using presently available materials and techniques, the absolute best attainable energy density for an individual capacitor in a metallic case will be in the range of 80 to 110 J/lb for the type of service discussed above. For DC service with low ripple, short-lived but reliable components may be designed in the range 200 - 400 J/lb. Components intended for customary military usage will be a factor of 2 heavier, because of sturdy construction and the necessity of wide temperature operation.

### IMPROVEMENT

Two avenues are open for the improvement of these figures. First, foil edge treatment has shown promise in raising corona inception voltages of small sections of foil edges, the improvement being about 15 percent. Second, improved solid sheet dielectrics could be made, either by improving the mechanical perfection of the films or by modifying them to provide improved electrical properties.

## ACKNOWLEDGEMENT

The continued support and encouragement of Richard J. Verga, Michael P. Dougherty, and Dr. Phillip Stover of the Air Force Aero Propulsion Laboratory have been vital to this work and are greatly appreciated. Technical comments by James P. O'Loughlin of the Air Force Weapons Laboratory have been very helpful, particularly in the area of foil edge conditioning and case optimization.

This work was supported by the Air Force Aero Propulsion Laboratory under Contract F33615-75-C-2021.

## SAFETY GROUNDING SWITCHES IN LARGE EXPERIMENTS; GENERAL CONSIDERATIONS AND THE TEXT APPLICATION

Paul Wildi

Fusion Research Center  
The University of Texas at Austin, Austin, Texas 78712

### Abstract

The electrical installations of a large fusion experiment present many potential dangers such as residual charges on capacitor banks and cables, power rectifiers and other related power supplies, etc. The commonly used voltages of 1 to 20 kV are lethal and the available power is sufficient to cause severe arc damage.

Many experiments require frequent safe access with a minimum of time loss by both operating personnel and experimenters. Safety must be automatic since the people involved are likely to be preoccupied with the experiments.

The paper reviews some commonly employed practices and discusses the adequacy and safety of various grounding devices. The safety grounding scheme for the TEXT Tokamak is described. Specially designed switches, their contact and operating mechanism, are shown and the integration of the switches in the overall control and safety system is discussed.

### Introduction

Large fusion experiments have many high voltage carrying circuits which can be dangerous to the experimenters. Generally, the experimental area is cleared of personnel immediately before a shot, but the nature of the work requires frequent access by people primarily concerned with their experiments, often being under pressure of time and not paying much attention to safety. It is mandatory to institute safety procedures which cannot be bypassed and to secure all conductors which are

connected to electrical power sources through grounding and/or short circuiting switches. Such switches are necessary even, if in the normal procedure, the circuits are deenergized since there is always the possibility of malfunction. Typical hazards are, for example: residual charges on capacitor banks and cables, remanence voltages of rotating machines, residual voltages of phased out rectifiers, etc. The voltages involved in typical power supplies of fusion experiments are high enough to be lethal, and the sources have a low impedance and very high current capability. Therefore, a flashover can lead to heavy arc damage, both to personnel and equipment.

### Some Commonly Employed Practices

In utility systems rather elaborate clearance procedures are used before any personnel are allowed to work on high voltage carrying equipment. These procedures normally include disconnection, grounding at several locations and redundant checking at several levels of supervision. The procedure is very reliable but time consuming and not suitable for a laboratory operation.

Manual grounding with grounding sticks is very popular in a laboratory experiment. It is adequate when used as a redundant grounding in deenergized circuits, but rather dangerous when accidentally practiced on a hot circuit such as, for example, a charged capacitor bank where the discharge flash is liable to cause ear and eye injuries. Since the method depends upon the discipline of the people

using it, accidents may occur due to negligence or forgetfulness of the personnel involved.

Grounding switches of modest current carrying capability of the high voltage contact type are commonly used on capacitors, very often with current limiting resistors in series. These are normally solenoid operated and closed by gravity or spring action. For high power sources their current carrying ability is generally too small.

Some grounding safety switches have been built using the old grounding chain as a contact system. They consist of some hand operated mechanism lowering grounding chains over exposed busbars. The presumption is that an accidentally energized circuit will initiate an arc before any personnel gets in contact with the hot circuits.

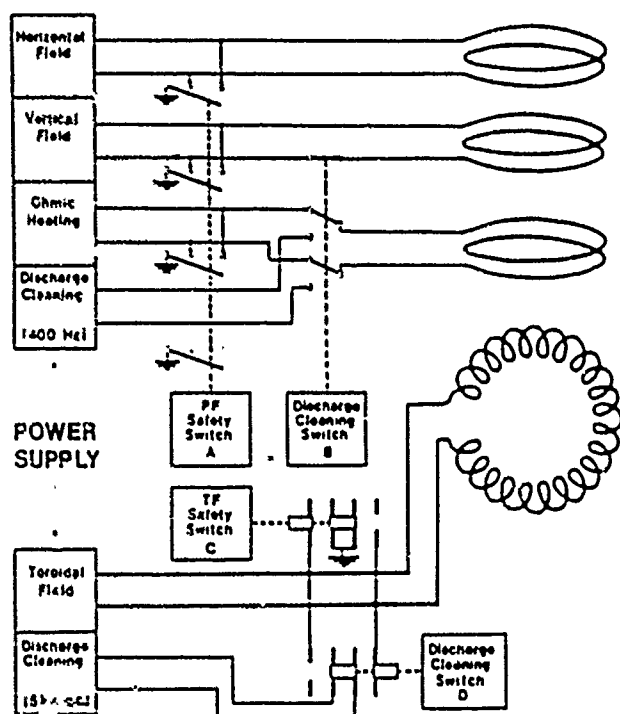


Fig. 1. TEXT; Diagram of Safety Switches and Transfer Switches for Discharge Cleaning

#### Grounding System for the TEXT Tokamak

The Texas Fusion Plasma Research Tokamak<sup>[1]</sup> is planned as a user facility for the purpose of

running a multitude of smaller experiments. As a consequence there will be many experimenters and some will be unfamiliar with the device. There will also be the need for frequent access to the test area without undue time loss. Under these circumstances the best solution appears to be an automatic interlocked system as schematically indicated in Fig. 1. Interlocking is such that the safety switches are permitted to close only after the power supplies are deenergized. In turn, the access doors are unlocked only after the safety switches have transferred to the grounded position. The interlock scheme further provides for Switch A to be closed and the main switch to the toroidal field power supply to be opened before the discharge cleaning switches can be transferred. In this operating condition, personnel access to the Tokamak is permissible. Additional surveillance by the experimenter will still be required (for example, closed circuit television), and all personnel will be asked to observe warning lights.

#### Rating of the Switches

Except for the contingency of a control malfunction, the switches will always make and break deenergized circuits. However, they are laid out for the highest possible short circuit current, both dynamically and thermally. This is in order to insure safety should, for some reason, a circuit be energized during the personnel access period. Since switches of the same type are used to connect the discharge cleaning power supplies; the contact systems are also designed for a continuous duty. Transfer time is of little importance as long as it does not delay the personnel access and is arbitrarily set at 10 s or less. Insulation level is 10 kV, which is 5 times the highest service voltage. The nominal ratings are tabulated in Table 1.

An attempt made to procure commercial switches for this duty was abandoned for economical and availability reasons.



Table 1

		Switch	
		A	B
Peak current	kA	40	400
3 sec current	kA	20	160
Continuous current	kA	1.2	6
$\int i^2 dt$	$10^9 A^2 s$	1.2	75
Test voltage (dc) (open gap and to ground)	kV	10	10
Mode of operation		pneumatic	el. motor

#### Design Features

Switch A, the protective switch for the poloidal coil system is shown in Fig. 2. It is a four pole knife switch with grounded blades. In the closed position the switch short circuits and grounds the outputs of all three poloidal field supplies and the coil system. The fourth pole of the switch is a spare for possible future use. The switch is driven by a pneumatic cylinder controlled through a solenoid four way valve and is mechanically latched in either end position against accidental motion. The contact system consists of dual copper blades straddling the stationary contacts. The blades are spring loaded and so designed that the electro-magnetic forces of the current increase the contact pressure. The key data of the switch are tabulated in Table 1.

A switch of similar design (B), but laid out as a double throw switch, is used to connect the poloidal coil system to the discharge cleaning power supply. Switches A and B are pneumatically interlocked so that the discharge cleaning can only be activated if switch A is in the safety position.

Switch C, the protective switch for the toroidal field system is designed for a peak current of 400 kA, and since a switch of identical design is to be used to connect the toroidal field coils to a continuous dc supply during discharge cleaning, it had to be laid out for a 5 kA continuous current. The design chosen for this duty is pictured in

Fig. 3 which shows the switch in the closed position. It is a sliding contact design with a cylindrical moving contact of 4" diameter and 3/8" copper wall. The stationary contacts are rings fitted with contact spring bands ("MULTILAM" ®) guaranteeing an adequate springy connection between the stationary and the moveable contact. Rating of the switch is based both on manufacturer's data and experiments performed with the same material on a plug-in contact<sup>[2]</sup> and suitably derated to guarantee an adequate safety margin.

The two moveable contacts are cemented on a glass epoxy tubular support which at its end carries a nut engaging in the drive screw. This screw is driven by a gear motor, the direction of which can be reversed to produce motion in either direction. Auxiliary switches operated directly by the moveable contact assembly assure stopping of the drive motor in either end position and serve as remote indicators for the position of the switch and for the purpose of interlock control. Since the screw drive-gear motor combination is self-locking, mechanical end locks were not necessary in this design.

An identical switch (D) will be used to connect an auxiliary power supply to the TF coil which will feed 5,000 A into this coil system during discharge cleaning of the vacuum torus.

#### References:

- [1] P. Wildi, G.L. Cardwell and D.F. Brower, "Design of the TEXT Toroidal and Poloidal Field Coils," Seventh Symposium on Engineering Problems of Fusion Research, Knoxville, Tenn., October 1977.
- [2] Paul Wildi, "Contacts for Pulsed High Current; Design and Text," IEEE 2nd International Pulsed Power Conference, Lubbock, Tx., June 1979.

This work was supported by the U.S. Department of Energy.

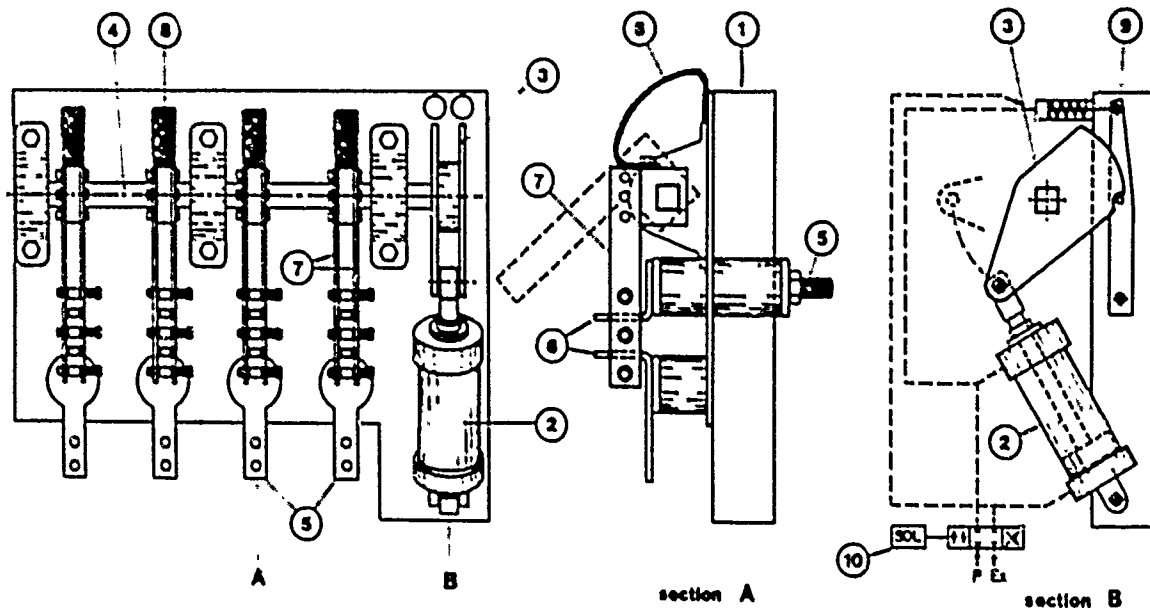


Fig. 2. Grounding Switch for PF Coil System

- |                       |                        |
|-----------------------|------------------------|
| 1) Main frame         | 6) Stationary contacts |
| 2) Operating cylinder | 7) Moving contacts     |
| 3) Drive lever        | 8) Ground strap        |
| 4) Shaft              | 9) Locking mechanism   |
| 5) Terminals          | 10) Control valve      |

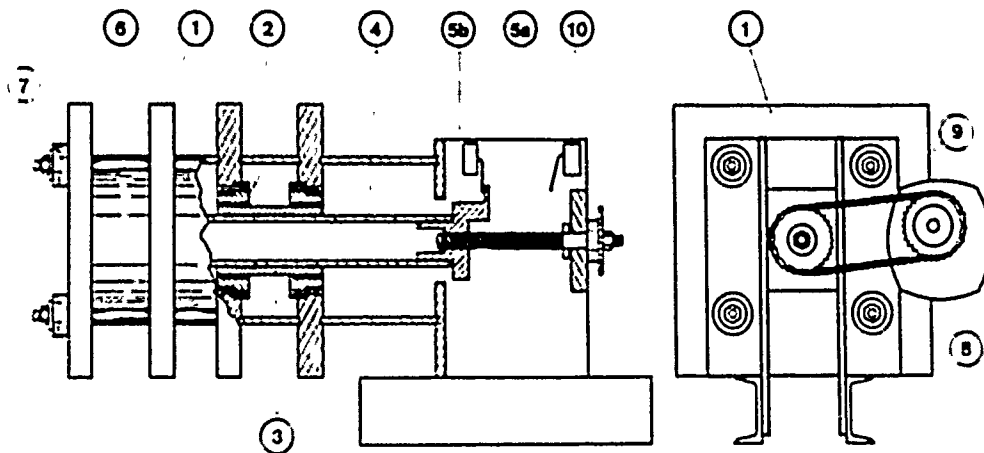


Fig. 3. Grounding Switch for TF System

- |                                       |                        |
|---------------------------------------|------------------------|
| 1) Terminal plates                    | 6) Insulating support  |
| 2) Stationary contact                 | 7) Tie-rod             |
| 3) Moving contact                     | 8) Drive motor         |
| 4) Insulating operating rod           | 9) Chain drive         |
| 5) Operating screw (a) and<br>nut (b) | 10) Auxiliary switches |

# INDUCTANCE AND RESISTANCE CHARACTERISTICS OF SINGLE-SITE UNTRIGGERED WATER SWITCHES IN WATER TRANSFER CAPACITOR CIRCUITS

P. W. Spence, Y. G. Chen, G. Frazier, and H. Calvin

Physics International Company  
San Leandro, California 94577

## Abstract

Inductance and resistance characteristics of single-site untriggered water switch arc-channels have been investigated by measurement of their effects on frequency and voltage gain in a water capacitor transfer circuit. Data are presented for two distinct switch configurations covering a voltage range from 3 to 6 MV, gaps from 7 to 35 cm, and mean switching fields from 150 to 350 kV/cm. A simple lumped circuit model is postulated with switch  $L$  and  $R$  varying linearly with gap spacing under low voltage conditions. Extrapolation of this zero-order model to higher voltage conditions compares favorably with measured circuit characteristics. Energy loss in the water switch is observed to be approximately a factor of two in excess of maximum losses predicted from previous estimates.<sup>1,2</sup>

## Introduction

Water transfer capacitor circuits are often applied in the design of high-power, low-impedance, short-pulse generators. In practice the circuit provides an intermediate power amplification stage in which energy from a Marx generator is input (over a few microsecond timescale) to a capacitor and then transferred (over a few hundred nanosecond timescale) via a switch to a second capacitor. The principal benefits afforded by such circuits are: (1) the ability to operate the second capacitor at higher stress levels than possible through direct charging by the Marx; and (2) the relaxation of switching requirements on the second capacitor stage. Both benefits result from a reduction in

the second stage charge time. Within certain limitations, single-site untriggered water switches can be used to accomplish the transfer of energy between the two capacitors in the circuit. Two of these limitations, inductance and effective resistance of the switch arc-channel, are the subject of this paper.

Conclusions from pioneer work by J. C. Martin and his associates at AWEI,<sup>1</sup> summarized in a set of semi-empirical formulae meant to roughly estimate energy loss, inductance, and the duration of the resistive phase of such arc-channels, have remained basically unaltered over the last decade and have provided valuable tools in the design of switches over a wide parameter range. As recently as 1977, VanDevender<sup>2</sup> reported current risetime and energy loss in a  $< 1.8$  MV water switch to be adequately described by J. C. Martin's semi-empirical relations; he additionally observed no evidence of a later time plateau resistance phase which had been observed in previous lower-energy and lower-voltage switch experiments.<sup>3</sup>

Accurate direct measurement of the inductance and time-varying resistance of water sparks under high voltage and high energy density conditions is a formidable task. Indirect inference of inductance and resistance from transfer circuit frequency and voltage gain presents a more tractable measurement problem but introduces considerable uncertainty accumulated from a combination monitor calibration accuracy, wave transmission effects, and accuracy of estimating the various fixed  $L$ 's and  $C$ 's for realistic capacitor and electrode geometries. In contrast to past studies, the unique features of

\*Work supported by the Defense Nuclear Agency.

the present work lie in: (1) the improved accuracy of inferred resistance and inductance made possible by comparison of two different switch configurations under virtually identical conditions for all other experimental parameters (i.e., voltage, C's, fixed L's, and monitors); and (2) the extension of experimental conditions over a factor of 5 range in arc-channel lengths for the same basic circuit.

### Apparatus

The physical and electrical configuration of the transfer circuit is shown schematically in Figure 1. The lumped circuit approximation assumes that the transfer circuit response is completely decoupled from the Marx charging of capacitor 1; although this assumption is not strictly correct, transfer circuit response data were analyzed only for a narrow range of transfer switch closure times (350 to 450 ns prior to peak of the resonance charge on capacitor 1) such that small differences in gain on capacitor 2 due to different transfer switch closure times were minimized.

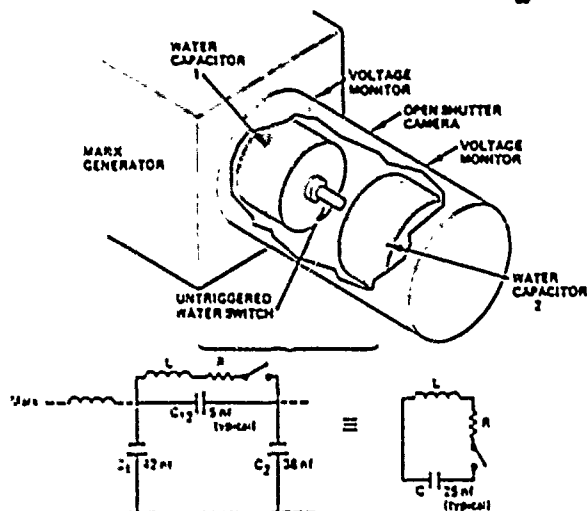


Figure 1 Transfer circuit physical and electrical (lumped circuit approximation) configuration.

Figure 2 shows the geometry of the water switch region in more detail with estimates of the fixed electrode inductances for the initial low-voltage tests. Two distinct ball/plane geometry switch configurations were tested, corresponding to hemispherical ball diameters of 5 cm and 15 cm. The initial voltage polarity on capacitor 1 was

negative, giving negatively enhanced switch operation throughout the 19 to 35 cm and 7 to 24 cm ranges of gap spacings.

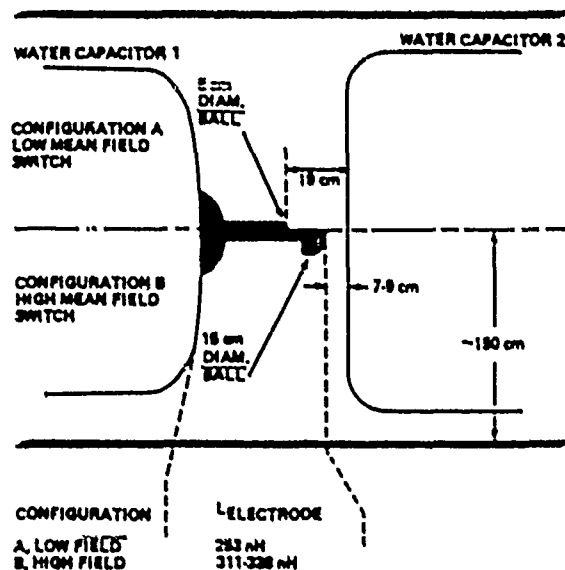


Figure 2 Switch geometry and electrode inductance estimates for low voltage tests.

### Experimental Results and Analysis

The post-switching voltage on capacitor 2 was found to be closely approximated by a  $(1 - \cos \omega t)$  waveform. Figure 3 exhibits an overlay of a typical measured voltage waveform and a  $(1 - \cos \omega t)$  waveform added to the measured prepulse voltage level. The waveforms typically matched well up to the time when capacitor 2 was switched to a sub-

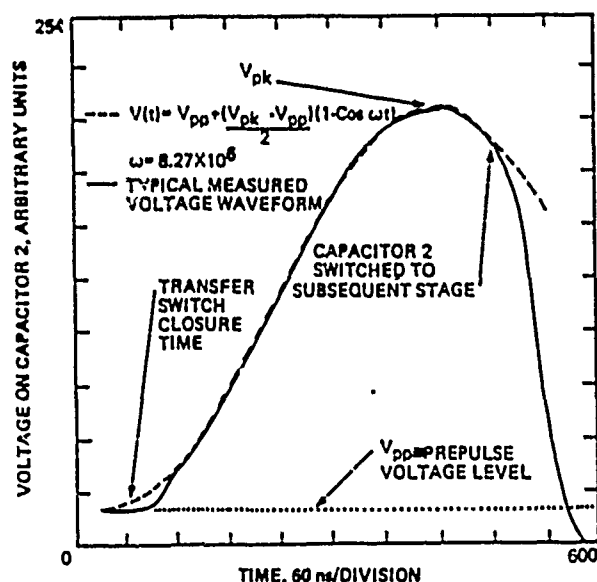


Figure 3 Comparison of transfer circuit waveform to  $1 - \cos \omega t$ .

sequent stage, with the exception of a steepening of the very early-time voltage waveform ( $\sim 50$  ns into the transfer period) and a few percent overshoot from  $(1 - \cos \omega t)$  about 100 ns prior to the transfer voltage peak. These minor discrepancies are consistent with an early-time, rapidly varying resistive phase of the switch arc and transmission line effects which have been modeled elsewhere in a more complete transmission line code (NET-2) analysis of the circuit.

Figure 4 compares the circuit waveforms for the two switch configurations under virtually identical conditions for all other experimental parameters; relative voltage gain and circuit frequency are measurably higher for the shorter arc-channel configuration. Allowing for measurement error and uncertainties in choosing a best fit to the  $(1 - \cos \omega t)$  waveforms, we obtain  $(\omega_B/\omega_A)^2 = 1.19 \pm 0.04$  and  $(G_B/G_A) = 1.05 \pm 0.02$  for the two configurations, where  $\omega$  = frequency and  $G = V_{PK} - V_{PP}$ . Following the lumped circuit approximation, the frequency and voltage gain are related to the circuit parameters as  $\omega^2 = 1/LC$  (for these data  $R^2C/4L \sim 10^{-2}$ ) and  $G = [1 + \exp(-\pi \omega RC/2)]$ .

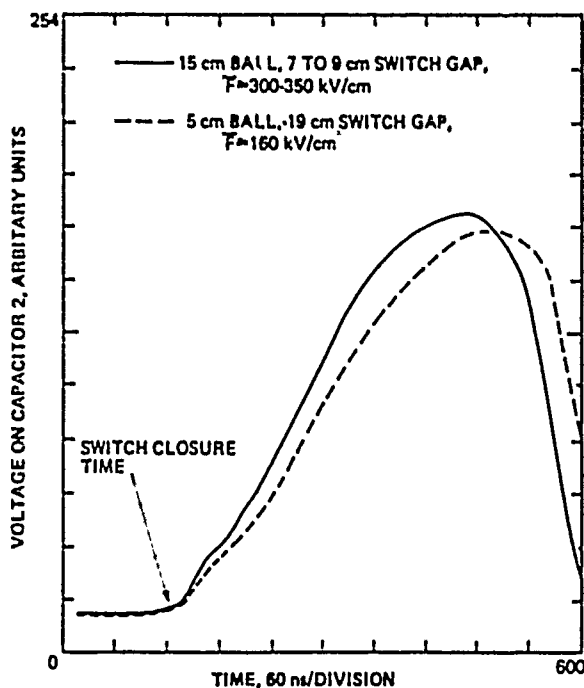


Figure 4 Low voltage ( $\sim 3.4$  MV) transfer circuit waveforms.

To interpret the observed circuit performance in terms of arc-channel characteristics we assumed, in the spirit of a zero-order analysis, that the circuit inductance and resistance were described by assigning a constant inductance and resistance per unit switch gap length ( $\lambda$  and  $\rho$ ):

$$Z = L_{\text{electrode}} + \lambda d, \quad R = \rho d$$

where  $d$  = switch gap spacing. From the measured frequency and gain ratio data, these assumptions imply  $\lambda = 13.4 \pm 1.5$  nH/cm (an effective arc-channel diameter of 3.7 mm ( $-2, +4$  mm)) and  $\rho = 35 \pm 14$   $\mu\Omega$ /cm.

The applicability of this zero-order model was explored by its extrapolation to higher voltage (i.e., larger switch gap spacing) conditions in the transfer circuit using the values of  $\rho$  and  $\lambda$  determined from the low-voltage tests. Figure 5 exhibits such an extrapolation for the 5-cm-diameter switch at 35 cm spacing. Similar general agreement was obtained for a large number of high voltage tests, within the trends that a 35  $\mu\Omega$ /cm arc resistance adequately described the measured gain and a somewhat lower arc inductance (11 to 13.4 nH/cm) was necessary to match the measured frequencies.

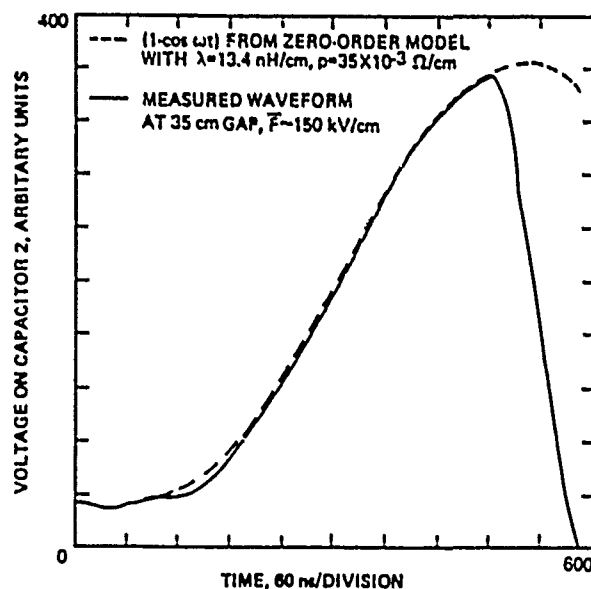


Figure 5 Comparison of high voltage ( $\sim 6$  MV) data with model-5 cm diameter electrode.

### Discussion and Conclusions

It is not surprising that a constant inductance per unit gap length model appears to fit the data. The values deduced for inductance appear consistent with observed damage patterns (pits) on the electrodes and previous channel expansion velocity estimates.<sup>1</sup> The observed trend toward slight reduction in inductance per unit length at larger gap spacings may be due to the development of arc-channel branches near the anode side of the switch.

The somewhat surprising applicability of a constant resistance per unit gap length model has significant implications in extrapolation to even higher-voltage water capacitor transfer circuits. In the context of the zero-order model, this resistance represents a time-averaged, "effective," resistance insofar as it affects circuit gain during the first half-period. This resistance appears to be distinct from the classic early-time resistive phase<sup>1</sup> ( $\tau_R$  is in the few tens of nanoseconds range and  $\ll \tau_L$  for all configurations tested) and represents a longer timescale "plateau" resistance phase. Resolution of the time dependence of this plateau phase is beyond the scope of this discussion; however, the observed voltage waveform fit to  $(1-\cos\omega t)$  does hint that any time dependence is probably weak for the first half-period.

The most important implication of the results is the increased energy loss ( $I^2R$ ) in long water spark channels due to the plateau resistance. Measured losses ranged from 8% to 26% for the extrema in switch spacings compared with 4% to 14% expected from J. C. Martin's<sup>1</sup> relations for the maximum energy loss condition  $\tau_L \ll \tau_R$ :

$$E_{\text{LOSS}} \approx \frac{V^2}{42} \tau_R, \quad \tau_R \approx \frac{5}{\omega^{1/3} (F)^{4/3}},$$

in units of ns, ohms, MV/cm.

### COMPARISON OF SWITCH LOSSES ( $I^2R$ ) WITH J. C. MARTIN'S SEMI-EMPIRICAL FORMULAE

Switch Dimensions	$\tau_{\text{Loss}}/\tau_L (\tau_L \ll \tau_R)$ (J. C. Martin's semi-empirical)	$\tau_{\text{Loss}}/\tau_L (\tau_L \gg \tau_R)$ (J. C. Martin's semi-empirical)
3 cm Electrode at 75 cm	17%	11%
3 cm Electrode at 75 cm	16%	11%
15 cm Electrode at 8 cm	6%	4%
15 cm Electrode at 21 cm	17%	6%

For cases where  $\tau_L \gg \tau_R$  (more characteristic of the present tests), even lower switch losses are estimated from the semi-empirical formulae.

In conclusion, we have analyzed the behavior of a single-site, high-voltage, high-power, water transfer switch in a specific transfer circuit in terms of a zero-order model with constant inductance and "plateau" resistance per unit gap length and found: (1) inductance values consistent with arc-channel diameters of a few millimeters; (2) average resistance values of  $35 \pm 14 \text{ m}\Omega/\text{cm}$ ; and (3) switch energy losses in excess of previously established estimates. Further experiments at higher voltage and with larger gaps would be desirable in establishing the relevance of this model to a wider parameter range.

### Acknowledgements

The authors would like to acknowledge the particularly important contributions of the following individuals: M. Di Capua and T. Sullivan, for their help in digitizing the experimental data; W. Furrow, for timely and quality hardware construction; D. Strachan and others, for experimental assistance and facility operations; and K. Childers, for imaginative contributions to nomenclature.

### References

1. J. C. Martin, Duration of the Resistive Phase and Inductance of Spark Channels, SSWA/JCM/1065125, Dec. 1965 (unpublished).
2. J. Pace VanDevender, "The Resistive Phase of a High Voltage Water Spark," J. Appl. Phys. **49**, 5 (1978).
3. V. M. Kuleshov, S. L. Medoseev, V. P. Sainov, and A. M. Spektor, Sov. Phys.-Tech. Phys. **19**, 1 (1974).

## HOLLOW-ANODE MULTIGAP THYRATRONS

H. Menown and C. V. Neale

English Electric Valve Company Limited  
Chelmsford, CM1 2QU  
United Kingdom

Abstract

Subsequent to the introduction of single-gap, hollow-anode tubes in 1978, a new range of multigap hollow-anode tubes is being introduced. There are many applications where high rates of rise of inverse voltage cause premature failure of conventional multigap thyratrons due to arc-back. One solution has been to use double-cathode tubes, which are capable of reverse conduction without deterioration of performance. The hollow-anode tubes offer the similar advantage of tolerating reverse conduction without requiring extra high-voltage-isolated supplies. The operation of these tubes in low-inductance circuits is compared with conventional solid-anode tubes.

## HIGH FREQUENCY THYRATRON EVALUATION

Gregory A. Hill

The BDM Corporation

and

T. R. Burkes

Texas Tech University

Abstract

The high frequency characteristics of a triple grid thyatron are investigated. The pentode thyatron has three closely spaced grids and operates much like a conventional tetrode thyatron. The first grid has a dual function. It functions as a priming grid, preionizing the grid cathode space, as well as a shield grid, isolating the control grid from the cathode plasma during the recovery phase. The second grid is the control grid, with negative control characteristics. The third grid is a shield grid, designed to enhance the control grid aperture deionization. This thyatron is tested in a line-type pulser to determine its high frequency limitations. It proves capable of operating at pulse repetition frequencies of up to 180 kHz.

Introduction

It has become clear that advances in switching technology are vital to the growth and development of pulsed power technology. A need exists for fast rise-time, high repetition rate switches that will switch high voltages and currents. One promising type of switch is the hydrogen thyatron. A new type of thyatron, the triple-grid thyatron, has recently been developed. This switch is rated by its manufacturer to operate at repetition rates of up to 100 kHz. This paper describes a test and evaluation of the triple-grid thyatron's high frequency operational characteristics, with the goal of gaining insight into the direction of future thyatron development.

The Pentode Thyatron

The triple grid, or pentode, thyatron is shown schematically in Figure 1. Its operation is like that of a tetrode thyatron. The first grid is the primer, or auxiliary, electrode. The second grid is the control grid, with negative control characteristics. The third grid is a shield grid. This grid, along with Grid #1, completely shields the control grid from the rest of the tube.

This shielding has two positive effects on recovery. Since the grids are closely spaced, the volume of the grid aperture regions is small. Thus this space has a small characteristic dimension,  $\lambda$ , resulting in very fast deionization. Therefore, the shielding reduces the recovery time.

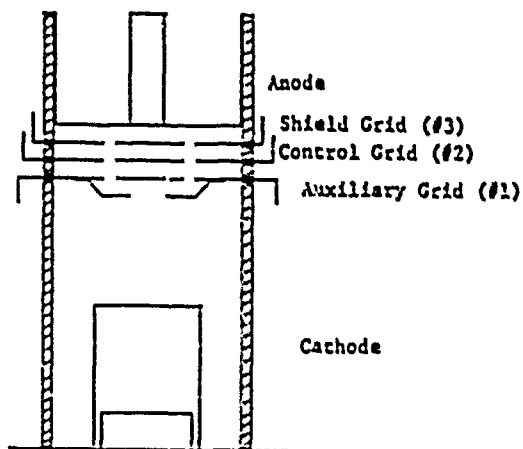


Figure 1. Triple Grid Thyatron



The second effect is due primarily to the shielding of the control grid by the auxiliary grid. Since the control grid is effectively isolated from the slowly decaying cathode plasma, the density of this plasma will not appreciably affect the control grid current during recovery. Thus a higher-impedance bias supply may be used to achieve recovery with a pentode thyatron than is necessary with a single grid thyatron.

The English Electric Valve Company is now producing a triple-grid thyatron, designated Type CX 1535. This thyatron is designed to switch high-power pulses at high repetition rates. It features massive grids with large external cooling fins, and is designed to be operated totally immersed in coolant. Thus any heat generated in the tube should be quickly removed. The published maximum ratings for the CX1535 are given in Table 1. That the ratings are nonsimultaneous is readily apparent upon close examination. Although the tube is rated to switch 12.5 MW, this may only be achieved at pulse repetition frequencies up to 20 kHz without exceeding the anode heating factor. At the rated frequency of 100 kHz, the maximum output is limited to 2.5 MW. The relationship between peak output power and repetition frequency is shown in Figure 2.

The reliable operation of this thyatron within its published ratings has been established [1]. However, the true limits of its capabilities have not previously been explored. Therefore, this test was designed to provide an evaluation of the triple-grid thyatron's capabilities beyond its published limitations.

#### Test Design

The triple-grid thyatron was tested in a standard line-type pulser. The pulse-forming line (PFL) was designed to deliver a 100 nanosecond pulse to the 17.5 ohm load. A 0.2 microhenry inductor was used to limit the current rise-time to 30 nanoseconds. The shield (#3) grid was grounded to the cathode. The auxiliary (#1) grid was biased with a 100 milliamperere current source. The control grid

Anode Voltage	25,000	V
Peak Anode Current	1,000	A
Rate of Anode Current Rise	5,000	A/ $\mu$ s
Anode Heating Factor	$500 \times 10^9$	V.A.p.p.s.
Peak Output Power	12.5	MW
Pulse Repetition Frequency	100	KHz
Envelope Temperature	150	$^{\circ}$ C
Average Anode Current	1.25	A

Table 1. Maximum ratings of the CX1535 thyatron.

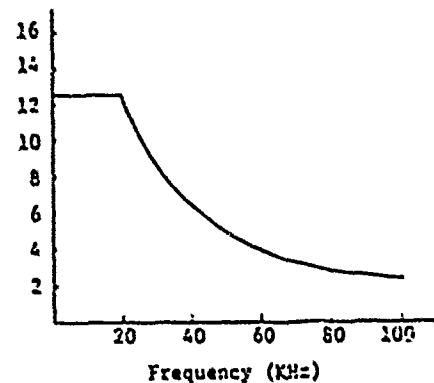


Figure 2. Rated Anode Heating Limitations

was biased to a negative 200 volts. Regulated 6.3 volt direct current supplies were used to power the cathode and reservoir heaters. Probes were included, to monitor all electrode voltages and currents. The anode temperature was monitored with thermocouple temperature probes. The assembly was immersed in oil, and was provided with the capability of force-cooling the anode. Inductive charging of the PFL was employed, with a charging rectifier being used in some portions of the test.

The test proceeded in three phases. Initially a set of low frequency characterization tests were performed. This involved measuring all of the electrode voltages and currents while operating the pulser at a low repetition frequency (3 kHz).

The second phase was a thermal limitations test.

The anode temperature rise was measured while the pulser was operated with different combinations of anode voltage and repetition frequencies. This test was repeated with different gas pressures (controlled by the reservoir voltage) in the thyatron.

Finally, the high-frequency recovery limited characteristics were investigated. At different repetition frequencies, the pulser was operated in either resonant or 20% slower than resonant charging modes. The anode voltage was increased slowly until the thyatron failed to recover.

### Results

The grid waveform measurements provided some useful information about the deionization and recovery of the thyatron. The control grid deionization current had a decay time constant of  $0.7\mu\text{s}$ , indicating that the control grid region deionize very rapidly and that the tube will recover within a few microseconds. The cathode space, however, takes much longer to deionize, as evidenced by the auxiliary grid voltage. Before anode conduction the auxiliary grid voltage was 18 V. with 100 mA of current flowing. At the initiation of anode conduction, the voltage dropped to 2 V. and remained at that level until the cathode space deionized. The cathode-space deionization time ranged from  $50\mu\text{s}$  for 200 A. of anode current to  $70\mu\text{s}$  for a 1000 A. anode current pulse. These results do show that the control grid is effectively shielded from the cathode plasma and that the shielding does aid recovery of the thyatron.

The high frequency recovery characteristics of the pentode thyatron are plotted in Figure 3, which clearly shows that the thyatron will operate at frequencies up to 180 kHz. Use of 20% slower than resonant charging increased the maximum voltage by 15% at 100 kHz; however, the improvement over resonant charging was insignificant at frequencies above 140 kHz. A thermal penalty was associated with the use of slower than resonant charging. The anode dissipation was increased by

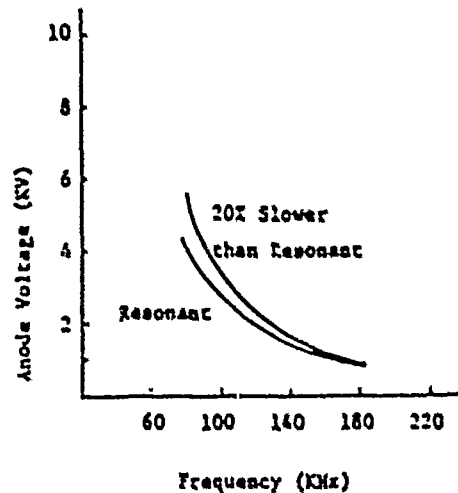


Figure 3. High-Frequency Maximum Anode Voltage

10% when slower than resonant charging was employed. This increase is attributed to inverse anode dissipation due to the inverse anode voltage immediately following conduction.

Figure 4 shows some constant-temperature curves as functions of peak pulse power and repetition frequency. The maximum permissible temperature rise is  $100^{\circ}\text{C}$  based on the maximum rated envelope temperature of  $150^{\circ}\text{C}$  and ambient temperatures ranging to  $50^{\circ}\text{C}$ . The effective anode heating factor based on a  $100^{\circ}\text{C}$  temperature rise may be found from Figure 4 to be  $185 \times 10^9$  VAPPS. It is not surprising that this is much smaller than the rated anode heating factor, since the rise time of the switched current is 40 ns - a factor of five less than the 200 ns minimum rise time calculated from the rated peak anode current (1000 A) and the maximum rate of rise of anode current ( $5000 \text{ A}/\mu\text{s}$ ). With such a short risetime the maximum anode heating factor should be derated by a factor of 5 to  $100 \times 10^9$  VAPPS [2]. Therefore the thermal limitations are well beyond those expected from the manufacturer's ratings.

Two techniques were used to further increase the thermal limitations. Force-cooling the anode with an oil stream having a velocity of 1.5 m/s reduced the temperature rise by more than 25%. Increasing

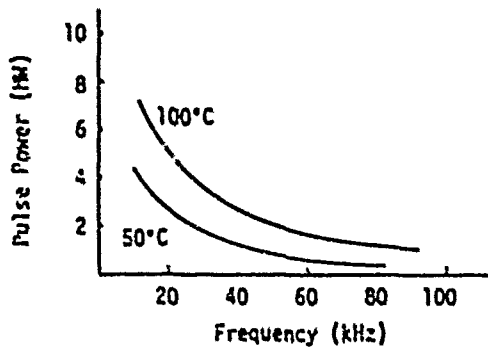


Figure 4. Constant Anode Temperature Rise Curves

the reservoir voltage from 6.3 V. to 10.0 V. decreased anode dissipation by 40%. This decrease was due to the faster switching times achieved with the increased tube pressure.

#### Conclusion

A composite curve showing the thyatron's limitations in the test circuit is shown in Figure 6. At frequencies above 80 KHz, the thyatron is recovery limited and capable of operating at frequencies up to 180 KHz - well above the manufacturer's specification. At lower frequencies the thyatron is thermally limited, but capable of operating beyond its ratings for the switching conditions experienced during the test. These capabilities may be extended by such techniques as improved cooling processes and varying the gas pressure within the tube.

Although the triplegrid thyatron is a significant advance of the state of the art, much development has yet to be done. This development may require more research into the fundamentals of gas discharges. Complete understanding of the processes will lead to new designs and techniques to further advance high speed switching.

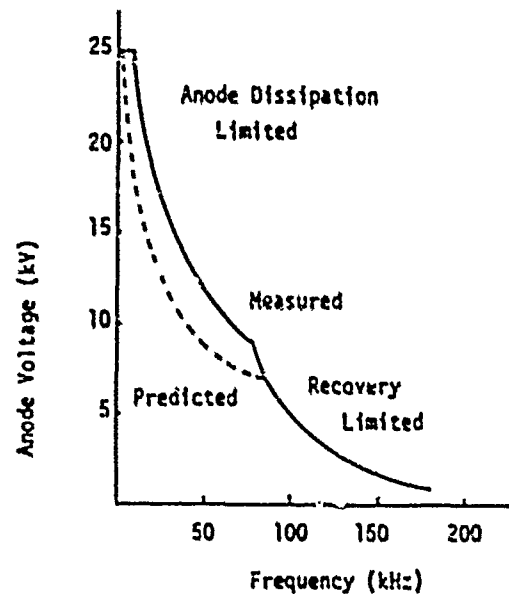


Figure 5. Composite of Measured Limitations

#### References

1. L. J. Kettle and R. J. Wheldon, "A Triple Grid Thyatron," Conf. Record of 12th Modulator Symposium, February, 1976.
2. S. Goldberg, et. al., "Research Study on Hydrogen Thyatrons" Final Report to U.S. Army Signal Corps., Edgerton, Germeshausen, & Grier, Inc., Boston, Mass., 1956.

## REPETITIVE ELECTRON BEAM CONTROLLED SWITCHING

R. F. FERNSLER,\* D. CONTE, I. M. VITKOVITSKY

Naval Research Laboratory  
Washington, D.C. 20375Abstract

Previous investigators have demonstrated the feasibility of using an ionizing electron beam to control the conductivity of a gaseous, volume-discharge switch. We have considered the possibility of using such switches repetitively at high power levels (up to  $10^{10}$  W), with switch opening and closing times as short as several nanoseconds. An analysis of the relevant gas chemistry has indicated that these requirements can best be met by using a non-electronegative base gas diluted with a small percentage of an electronegative gas. Detailed chemistry simulations, using the non-electronegative gas  $N_2$  and the electronegative gas  $O_2$ , have been performed and will be presented to support this analysis. Also discussed will be the limitations imposed by switch heating and gas breakdown.

Introduction

Hunter<sup>1</sup>, O'Loughlin<sup>2</sup>, and Kovalchuk and Mesyats<sup>3</sup> have described and demonstrated a switch concept which appears to be well suited to fast, high-power, repetitive switching. This concept consists (see Fig. 1) of a pair of planar electrodes separated by a high pressure gas. The switch is made to conduct by passing an ionizing electron beam through the gas, such that a volume discharge can be maintained between the switch electrodes. Such volume discharges have the property that once the electron beam is removed, the discharge rapidly extinguishes and the gas can again hold off the high voltage.

The use of high gas pressure allows for small electrode separation, thereby minimizing switch induc-

tance. As a result, switch opening and closing are determined primarily by the electron beam and gas chemistry characteristics. The use of large electrode surfaces, on the other hand, allows large switch currents to be conducted before switch heating destroys proper switch behavior. The present paper seeks to assess the overall capabilities of these electron-beam controlled switches.

Gas Chemistry

The switch resistance is controlled by the electron density  $n_e$  of the gas medium. For a volume discharge whose dominant ionization source is an electron beam of current density  $J_b$ ,  $n_e$  varies according to

$$\frac{d}{dt} n_e = J_b \frac{\sigma_i N}{e} - \alpha n_e - \beta n_e^2 - \gamma n_e^3 \quad (1)$$

where  $\sigma_i$  is the cross-section for ionization by the electron beam,  $N$  is the gas density,  $\alpha$  is the attachment rate,  $\beta$  is the two-body recombination coefficient, and  $\gamma$  is the three-body recombination coefficient. Eq. (1) must be supplemented by the circuit equation and by the switch current density equation

$$J_s = e n_e v_d (E/N) \quad (2)$$

where  $v_d$  is the electron drift velocity due to the electric field  $E$  appearing across the switch.

Eq. (1) and (2) dictate that the minimum switch closing time is given by

$$\tau_c (\text{min}) = \frac{J_s}{J_b} = \frac{1}{\sigma_i N v_d} \quad (3)$$

where the bar denotes the steady-state value in the

closed (conducting) circuit state. Eqs. (1) and (2) similarly determine the minimum switch opening time, which is defined as the time for  $n_e$  to decay from  $\bar{n}_e$  to  $0.1 \bar{n}_e$ . For a switch dominated by electron attachment, the minimum opening time is

$$\tau_a = 2.3 \tau_c \quad (4a)$$

for a switch dominated by two-body recombination, it is

$$\tau_2 = 10 \tau_c \quad (4b)$$

and for a switch dominated by three-body recombination, it is

$$\tau_3 = 50 \tau_c \quad (4c)$$

These latter three equations demonstrate that attachment-dominated switches minimize the switch opening time, without seriously compromising the switch closing time. (A second advantage is flexibility, in that the attachment rate  $\alpha$  can be readily varied by using a non-attaching base gas diluted with controlled percentages of an attaching gas.)

To insure that the gas is everywhere ionized, the beam electrons must have sufficient energy to traverse the entire discharge. Simple analysis shows that this energy constraint leads to

$$\tau_c \text{ (min)} > Q \frac{C_1}{e E_0 \bar{v}_d} \quad (5)$$

where the switch efficiency  $Q$  is the ratio of the power dissipated in the load to that consumed by the electron beam generator, where  $C_1$  is the average energy required per beam ionization in the gas, and where  $E_0$  is the open-circuit field strength originally appearing across the switch. This equation demonstrates that a trade-off exists between high efficiency  $Q$ , and short opening and closing times  $\tau_c$ .

Switching characteristics of 10 atm of  $N_2$  with small admixtures of  $O_2$  have been calculated using a detailed air chemistry code.<sup>4</sup> These sample calculations were designed to assess the performance of a

switch soon to be constructed and tested at the Naval Research Laboratory. The switch nominally imposes 200 kV across a 20  $\Omega$  load. The switch electrodes are 1000  $cm^2$  in area and are separated by 2 cm. Nominal switch efficiency is  $Q \sim 10$ . The calculations assume that the electron beam current rises instantaneously to full value (1 kA) at time zero, and instantaneously decays to zero at 100 nsec. The predicted behavior, shown in Fig. 2, demonstrates that the  $O_2$  concentration significantly affects the switch opening time, without significantly affecting the switch closing time.

#### Multipulse Operation and Other Considerations

Volumetric switches minimize the volumetric heating rate such that the gas temperature and physical state of the gas are largely unaltered by a short, single switching pulse. This factor accounts for the rapid recovery and short opening times of volume discharges, as compared with the behavior of filamentary arc discharges.<sup>5</sup>

Conversely, volumetric switches cannot be cooled rapidly, and hence gas heating may eventually pose problems for switches that are repetitively pulsed. These problems take three forms.

The first relates to cumulative changes in the chemical and electrical properties of the gas. Studies of discharges in  $N_2$  suggest that such alterations are unimportant until sufficient energy has been deposited to raise the gas temperature to above 2000° K.<sup>5</sup>

The second problem is a structural one related to excessive pressures generated by the heated gas. This problem is severely compounded by the use of a thin foil window (see Fig. 1) required to pass the electron beam into the discharge volume.

The third problem concerns reductions in the gas density  $N$  produced by the elevated gas pressure. The main problem here stems from the constraints imposed on the ratio  $E_0/N$ , where  $E_0$  is the open-circuit field strength. To justify ignoring cascade

ionization of the gas by the gas conduction electrons,  $E_0/N$  must typically satisfy<sup>6</sup>

$$E_0/N \leq 10^{-16} \text{ volts} \cdot \text{cm}^2. \quad (6)$$

At the same time, Eq. (5) demonstrates that  $E_0$  must be maximized to obtain high efficiency  $Q$  and short closing times  $\tau_c$  (min). Hence, reductions in  $N$ , due to elevated gas pressures, reduce the allowed field strength  $E_0$ , thereby degrading  $Q$  and/or  $\tau_c$  (min).

The preceding discussions suggest that a conservatively operated switch is one for which the total energy deposited within the switch from a given pulse train is less than, say, the total kinetic energy originally contained in the gas. This prescription insures that alterations in the gas temperature, pressure, and density will be less than a factor of 2.

The total energy deposited in the switch, from the electron beam and from Joule dissipation, can be related to the total energy absorbed by the load via a net efficiency factor  $Q'$ , where  $Q' \leq Q$ . For a pulse train consisting of  $m$  pulses, each of conduction time  $\tau_p$ , we thus require that

$$(m \tau_p \bar{J}_s E_0) / Q' < \frac{3}{2} N k T_0 \quad (7)$$

where  $k$  is Boltzmann's constant and  $T_0$  is the initial gas temperature. The breakdown constraint (6) thus suggests that, for  $T_0 = 300^\circ \text{K}$ , gas heating effects can generally be ignored provided

$$m \tau_p \bar{J}_s \leq 10^{-5} Q' \text{ A} \cdot \text{sec/cm}^2 \quad (8)$$

Several other limitations apply to electron beam controlled switches. An important one is the inherent switch inductance, which is minimally given in nH by the electrode separation distance in cm. Using constraint (6), this inductance can be shown to limit the switch opening and closing times to

$$\tau(\text{sec}) \geq 10^7 \frac{\bar{I}_s (\text{A})}{N(\text{cm}^{-3})} \quad (9)$$

where  $\bar{I}_s$  is the desired switch current. This result reiterates that optimum performance is attained by maximizing the gas density  $N$ . It is interesting to

note that constraint (9), coupled to Eq. (3), limits the maximum practical electron beam current to a value typically given by

$$I_b \leq 10^4 \text{ A}; \quad (10)$$

i.e., raising  $I_b$  above this inductive limit only degrades switch performance by reducing efficiency  $Q$  without reducing opening or closing times  $\tau$ .

### Summary

The preceding sections have outlined the general features of electron beam controlled switches. These devices may be viewed as current amplifiers in which a small beam current regulates a large discharge current. They may be operated either in a fast, high-power mode or in a slow, high-energy transfer mode. In the former case, the present analysis indicates that, at 10 atm gas pressure, current switching rates can approach  $10^{13} \text{ A/sec}$ ; these rates correspond to switch closing times of several nsec and switch opening times of tens of nsec, for switch efficiencies  $Q, Q' \sim 10$ . Total energy transfer would be roughly limited, however, to 10 Joules per cubic centimeter of discharge volume. Higher energy transfer can be obtained by degrading switch response time, or by raising the gas pressure.

### References

1. R. O. Hunter, "Electron Beam Controlled Switch", Proceedings of the 1st International Pulsed Power Conference, IEEE Cat. No. 76CH1147-8 REG 5, Lubbock, Texas (1976).
2. J. P. O'Loughlin, "PFN Design Interface with E-Beam Sustained Gas Discharge", op. cit.
3. B. M. Kovalchuk and G. A. Mesyats, Sov. Tech. Phys. Lett. 2, 252 (1976).
4. R. Fernsler, A. W. Ali, J. R. Greig, and I. M. Vitkovitsky, "An Air Chemistry Code", Bull. Am. Phys. Soc. 23, 775 (1978).
5. T. H. Lee, Physics and Engineering of High Power Devices, MIT Press, Cambridge, Mass. (1975).
6. S. C. Brown, Basic Data of Plasma Physics, Technology Press, Cambridge, Mass. (1959).

Work sponsored by the Office of Naval Research.

\*JAYCOR, Inc.

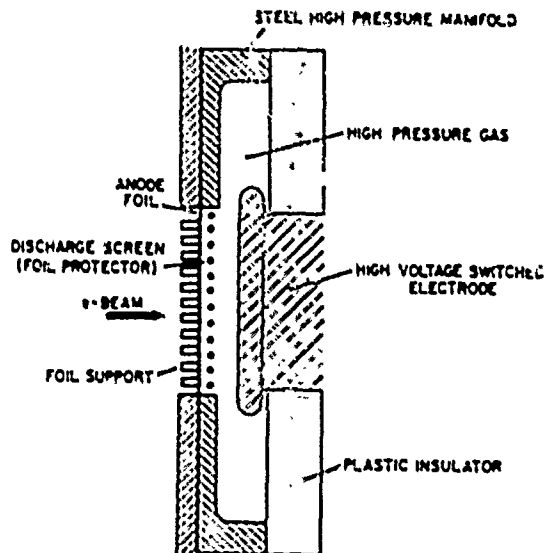


Fig. 1. Cross-sectional schematic of an electron beam controlled switch.

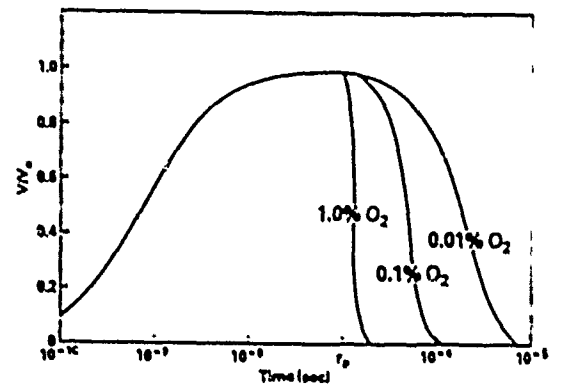


Fig. 2. Typical characteristics of an electron beam controlled switch operating in 10 atm  $N_2$  with different  $O_2$  admixtures.  $V$  is the voltage across a 20  $\Omega$  resistive load, while  $V_0$  (200 kV) is the source voltage. A 150 keV, 1 kA electron beam is passed through the discharge volume of 2 cm by 1000  $cm^2$  for a time  $\tau_p = 100$  nsec.

ORIENTATION INDEPENDENT IGNITRON<sup>\*</sup>

ROBIN J. HARVEY and JOHN R. BAYLESS

Hughes Research Laboratories  
Malibu, CA 90265Abstract

An orientation independent ignition (OII) has been operated at 30 kV, 15 kA with 10  $\mu$ sec wide pulses at frequencies up to 100 Hz. The cathode of the OII is a thin mercury film which is held in place by surface tension on a cooled molybdenum substrate. This device has been shown to have a basic voltage withstand of over 60 kV, trigger characteristics comparable to conventional ignitrons, a current rate of rise in excess of 10 kA/ $\mu$ s at 30 kV, and a mean stable run time at 8 A average current of 22 s in the burst mode. reformation of the film occurs during and following the pulse burst with a recycle time on the order of 10 min.

Introduction

The orientation independent ignitron (OII) is a new ignitron-type closing switch suitable for mobile applications. It displays the electrical properties characteristic of ignitrons, but with the added advantage of a mechanically stable cathode. This is accomplished by replacing the conventional liquid mercury pool by a cooled solid cathode covered by a mercury film. This design provides better mechanical and thermal control of the mercury, thereby leading to reduced recovery times when operating at high current levels. The film is held in place by surface tension forces, making the device orientation and vibration insensitive. The mercury volume of the film, which is sufficient for a charge transfer of several hundred coulombs, is introduced into the vacuum envelope prior to sealing off the OII. The film is

continuously replenished by evaporation and condensation processes. The vacuum envelope and anode operate at room temperature or above, while the cathode is cooled slightly relative to them in order to facilitate mercury reflux. The anode of the OII is cooled by natural convection to the external environment during off-periods. For the 30 kV device, interelectrode spacings are maintained at 1 to 2 cm to avoid Paschen breakdown.

Figure 1 shows a schematic diagram of the switch. The cathode is constructed using molybdenum. It is supported by a thermally insulating section of thin-walled, stainless steel tubing attached to the switch body. Cooling is provided via a copper heat pipe screwed into the cathode from below. The anode and sidewalls of the OII are made of stainless steel. A boron carbide igniter, which is adjusted by means of a bellows assembly, makes contact with the cathode as shown in Fig. 2. The completed OII is shown in Fig. 3. It includes additional diagnostic and vacuum appendages and a high voltage bushing. All of these, plus the main flange and most of the igniter assembly are incidental to the intrinsic device, and are included to facilitate the acquisition of design data.

Low Average Power Test Results

The prototype OII was first tested in dc and single pulse modes at Hughes Research Laboratories. Hg fills of about 0.1 and 0.25 ml used. With the larger fill, the tube was high-potted to 60 kV and a 7.5 A dc current could be conducted for over 90 s before the current extinguished due to Hg



evaporation from the cathode. In the single pulse mode, the anode fall time was observed to vary with the anode voltage, changing from 1  $\mu$ s at 250 V to 0.15  $\mu$ s at 30 kV. However, the Hg film on the cathode was thick enough to show signs of droplet formation.

The smaller Hg fill was chosen to eliminate any potential problem with droplet formation. The associated dc conduction time was limited to about 60 s at 7.5 A. During a 60 s dc run, the mercury vapor pressure varied from 0.6 to 6 mTorr depending on the cathode temperature as expected from vapor pressure data. An increase in the jitter and increasingly erratic anode fall behavior are also more evident with the lower Hg fill.

#### High Average Power Test Results

The OII was tested at the ERADCOM High Power Test Facility at Ft. Monmouth starting with the circuit shown in Fig. 4. The circuit was calibrated using a MAPS 40 Thyratron. A comparison of the pulse current waveforms for these two devices show little difference at the same voltage except for the larger jitter of the OII. A typical current waveform generated at 30 kV is shown in Fig. 5. Figure 6 shows a typical overlay of all pulses occurring during a 20 second run of the OII at 50 Hz. The variation in timing is found to average about  $\pm 1$   $\mu$ s. The charging inductor was reduced to 1.5 H to achieve a 120 Hz effective recharge rate and the device ran at up to 100 Hz without noticeable difficulty in voltage recovery; refer to Fig. 7.

The cathode was cooled using ice water during these runs at high power. The energy dissipated at the cathode was measured thermally to be about 1 to 2 J/pulse or an equivalent voltage drop of 5 to 10 V at the cathode. The anode dissipation was probably somewhat higher.

The anode temperature excursions were typically 30°C for a run of 1000 pulses. A high anode temperature did not affect the tube behavior, but

a high cathode temperature ( $\sim 60^\circ\text{C}$ ) led to Paschen breakdown. The introduction of impurity gases had no noticeable effect on the tube behavior below the Paschen limit.

The run time before tube instabilities become excessive is shown in Fig. 8. The total charge transfer is proportional to the product of the frequency and the run time. Evidently, Hg vapor reflux makes up a significant contribution to the Hg film volume during a time on the order of 0.03 s since the charge transfer at 30 Hz is nearly double that at 100 Hz.

During the course of these experiments, the tube was physically rotated by 180° with no detectable change in operation. Also, the end of line clipper was removed without noticeable change in the tube reliability.

#### Summary

Table I outlines the developmental goals and the test results actually achieved. Obviously, most of the goals have been reached with this first prototype model of an orientation independent ignitron, thereby making an ignitron-type switch available for airborne or mobile applications for the first time.

#### Acknowledgements

The authors are indebted to Mr. John Creedon who facilitated the high power tests at ERADCOM, to Mr. James O'Loughlin (AFWL) and Dr. Wilfried O. Eckhardt (HRL) for technical discussions, and to Mr. Robert W. Holly (HRL) for engineering support.

\* This work supported by U.S. Air Force Weapons Laboratory, Kirtland, AFB, Contract No. N60921-76-C-0138 through the Naval Surface Weapons Center, Dahlgren, Virginia.

TABLE I

PARAMETER	GOAL LEVELS	TEST LEVELS
Peak Current, kA	15	15
Pulse Width, $\mu$ s	10	10 (90% Points)
Current Rate of Rise, kA/ $\mu$ s	10	10
Pulse Repetition Frequency, Hz	50	100
Average Current, A	7.5	15
Peak Operating Forward Voltage, kV	30	30
Orientation	Any	Normal and Inverted
Operating Duty Cycle (@ 50 Hz)	90 s On 2 Hrs. Off	22 sec On 10 min Off
Life	100 On Periods (450,000 Pulses)	> 15,000 Pulses
Weight, kg	3	Essential Components < 3
Warm-Up Time	0	0
Standby Power	0	0
Trigger Energy, J	< 3	1.5
Jitter	—	$\pm 1 \mu$ s

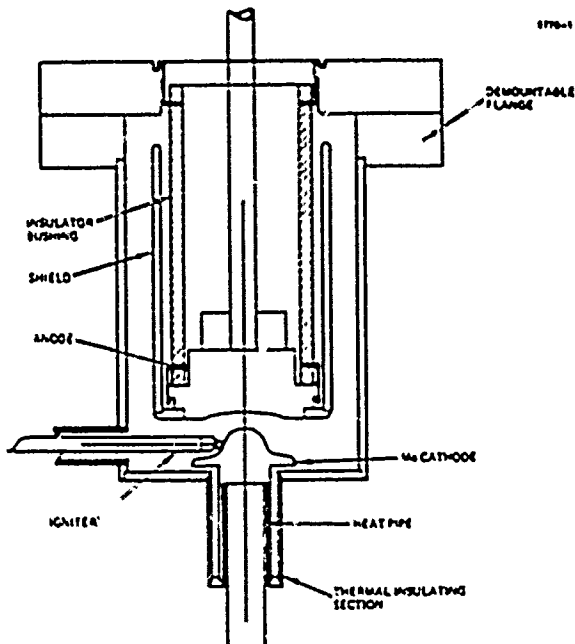


Fig. 1. Schematic diagram of OII.

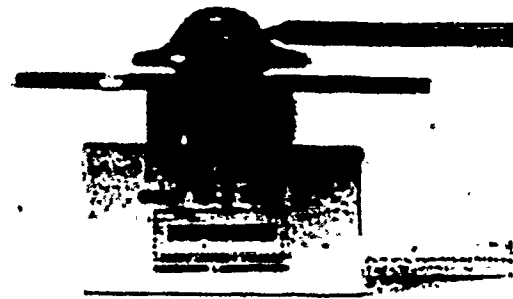


Fig. 2. Cathode and Igniter assembly.

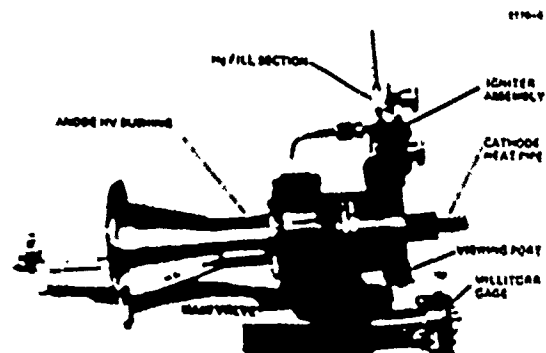


Fig. 3. Completed OII.

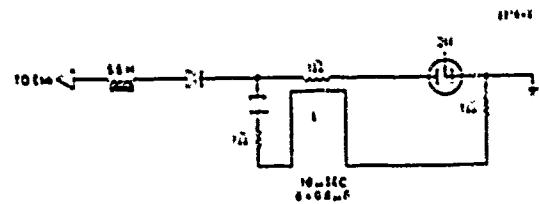


Fig. 4. Test Circuit.

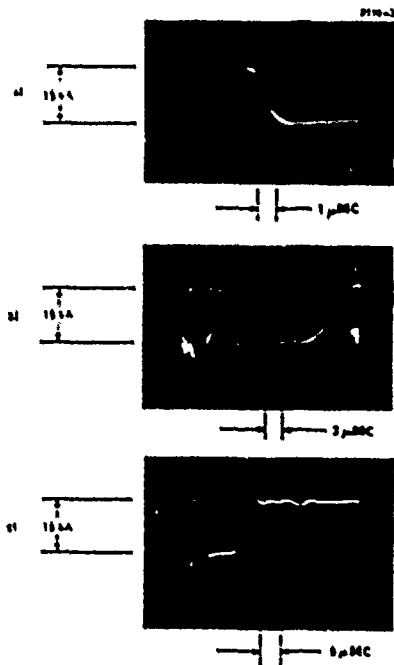


Fig. 5. OII switched current waveform at 30 kV, with three different oscilloscope sweep speeds.

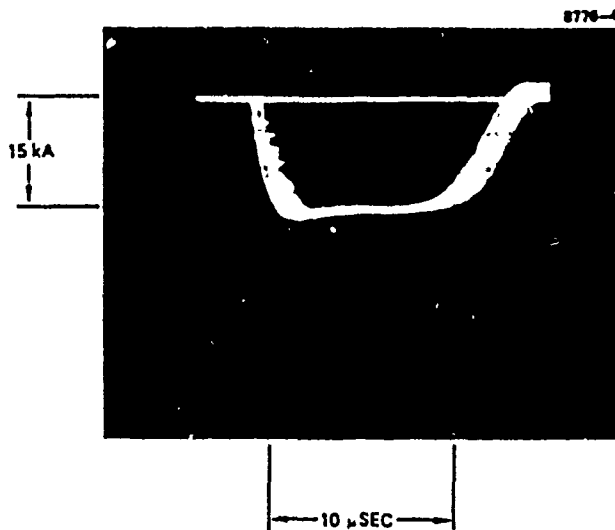


Fig. 6. Overlay of 1000 current pulses.

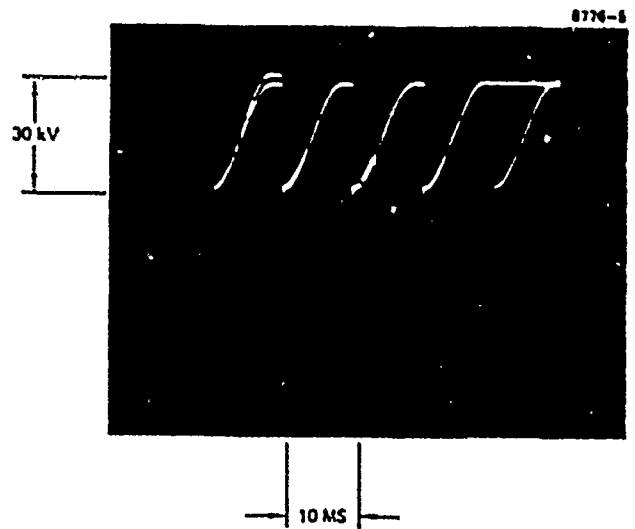


Fig. 7. Voltage waveforms at 100 Hz. (Overlay of 400 pulses total, then first and last pulses are visible).

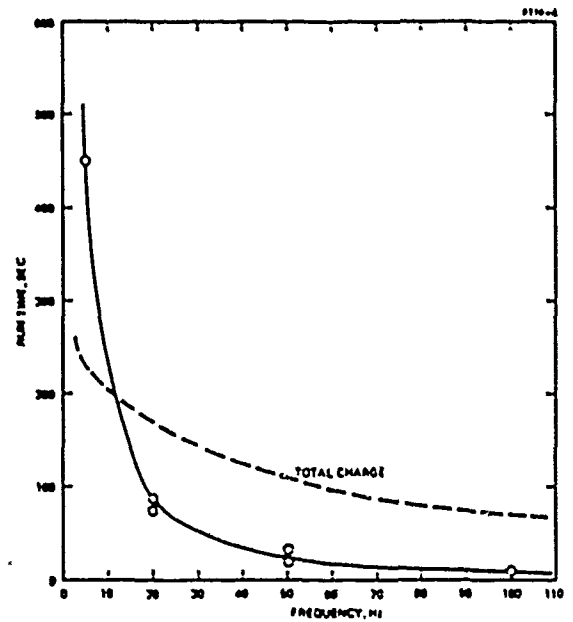


Fig. 8. Stable run time as a function of frequency at 30 kV, 15 kA.

## STABILIZATION OF METAL-OXIDE BULK SWITCHING DEVICES WITH DIFFUSED BI CONTACTS

1

B. LALEVIC, M. SNOGA and M. GVISHI\*\*  
Dept. Elect. Eng., Rutgers Univ.  
Piscataway, NJ 08854

S. LEVY  
Elec. Tech. and Devices Lab.  
U.S. Army ENADCOM, Ft. Monmouth, NJ 07703

Abstract

Threshold switching from the high to low resistance state has been investigated in the polycrystalline and single crystal  $\text{NbO}_x$  (where  $x = 2$ ) metal-oxide devices. Stable and reproducible switching performance is observed in a configuration Bi- $\text{NbO}_2$ -Bi where Bi electrodes were covered with Au films. Improvement in the device performance is attributed to the Bi diffusion into  $\text{NbO}_x$  which has been confirmed by the Auger electron spectroscopy. Typical off state resistance of these devices is  $\sim 100 \text{ k}\Omega$  and threshold switching voltage in the range from 100 to 2500 V. The delay time  $\tau_d$  is exponentially dependent on the applied voltage  $V_{\text{appl}}$  and at larger  $V_{\text{appl}}$ , the delay time is less than a nanosecond. Recovery time of a device is  $\sim 0.5 \text{ }\mu\text{s}$  as determined by the method of decreasing time interval between two successive pulses. Holding voltage is  $\sim 40 \text{ V}$ . The pulsed switch devices can withstand pulse durations between 0.1-3  $\mu\text{s}$ , repetition rate of 100 C/s and current intensities of 10-15 A, or 25 A peak with the applied pulse duration of 20  $\mu\text{s}$ , single shot.

Introduction

Reversible threshold switching has been observed and investigated in a polycrystalline and single crystals  $\text{NbO}_2$  devices with their potential application as transient suppressors<sup>1,2,3,4</sup>. These devices have shown a capability of shunting transient current pulses of higher intensity. Fast response ( $< 1 \text{ nsec}$ ), high resistance in the off state and low capacitance ( $< 10 \text{ pF}$ ) satisfy the requirement for a protection of RF receiver inputs and other applications. The devices have shown, how-

ever, variations in the values of switching parameters after several switching events and sparking has often inhibited proper device operation.

Considerable improvements in the reproducibility in values of characteristic switching parameters of  $\text{NbO}_2$  achieved in this work by deposition of Bi electrodes on  $\text{NbO}_2$ . As a result we have observed reproducible switching behavior at applied pulses as high as 10 A, with repetition rate of  $10^3 \text{ C/s}$  and with a variation in switching parameters of not more than 10%. The improved behavior of these devices is attributed to the diffusion of Bi into  $\text{NbO}_2$  with a subsequent stabilization of current filament during a switching event. Diffusion of Bi into polycrystalline and single crystals of  $\text{NbO}_2$  was confirmed by the Auger electron spectroscopy (AES) analysis and by observed changes in transport and dielectric properties.

Sample Preparation

Thin polycrystalline niobium oxide disks were prepared by oxidation of freshly cleaned surfaces of NbO. Single crystals of metallic NbO were fabricated by the Czochralsky-Kyropoulos technique in a triarc furnace<sup>3</sup>. Devices were made from a 0.6 mm thick, approximately 3 mm diameter NbO single crystal, oriented in the {100} direction with a polycrystalline  $\text{NbO}_2$  layer 10 to 15  $\mu\text{m}$  thick on one face of the wafer. Single crystals of  $\text{NbO}_2$  were also produced in a triarc furnace in an argon atmosphere by Dr. Joseph Millstein of the Naval Research Laboratory.

They were subsequently sliced and polished to a thickness between 40 and 50  $\mu\text{m}$  which should result in a threshold switching value of 1000 to 1250 V

assuming 25 V per micron thickness<sup>6</sup> for the switching at nanosecond pulse widths. The wafers were chemically cleaned and then Bi electrodes of about 1000 Å thick were deposited in a vacuum better than  $10^{-5}$  Torr. Top electrode areas were either 0.87 mm<sup>2</sup> or 2 mm<sup>2</sup>. Lower electrode covered most of the wafer area. Thin gold films, about 500 Å in thickness were evaporated over the Bi electrodes for better electrical contacts. Most of the data presented in this paper was collected with the device mounted onto a brass block and a mechanical microprobe positioned under a microscope so the tungsten tip of the microprobe wire just touching the Au-Bi contact. This was checked by measuring the off-state resistance with a Dana 3800 A digital multimeter. Typical off-state resistance values were from 60 to 250KΩ. Recently, the wafers were etched with NH<sub>4</sub>F-HF solution at 100°C. These results were remarkably different and will be discussed later in this report.

### Results

Threshold switching in the Bi-NbO<sub>2</sub>-Bi devices was first tested using a Tektronix curve tracer. The curve tracer scans the I-V characteristic with a repetition rate of 120 sweeps per second. A typical switch is shown in Figure 1. From this figure one can directly determine a threshold voltage  $V_{th}$ , holding voltage  $V_h$  and holding current  $I_h$ . The horizontal axis in Figure 1 is voltage at 10 V per division and the vertical axis is current at 10 milliamperes per division. (For this device the threshold value is 70 V, holding voltage is 20 V and holding current is 20 milliamperes.) It must be mentioned that the threshold voltage is a function of the rate of voltage applied and a device with a curve tracer value of 100 V could have a fast pulse value of 1000 V.

The following characteristic switching parameters were investigated: delay time  $\tau_d$  as a function of applied voltage; recovery time  $\tau_r$ ; current pulse rise time; holding voltage  $V_h$  and holding current  $I_h$  as a function of applied voltage; and reproducibility of off-state resistance after a large number of switching events.

### Delay Time

Delay time was measured using a Cober 650 F pulser with a 60 nanosecond rise time with the voltage monitored with a Tektronix 100 to 1 probe and the current with a CT-1 current transformer. The information was stored on a Tektronix 7834 storage scope. Delay time,  $\tau_d$ , as a function of applied pulse voltage was measured by increasing the pulser output and storing the single shot switching events in the oscilloscope. Typical decrease in  $\tau_d$  with increasing voltage is shown in Fig. 3. This last figure, shows

a superposition of increasing pulse voltages and the resulting delayed currents. Quantitative dependence of  $\tau_d$  on  $V_{appl}$  is shown in Fig. 4 where  $\log \tau_d$  is plotted vs  $V_{appl}$ . As shown  $\tau_d$  varies exponentially with  $V_{appl}$  and the relationship can be represented as:

$$\tau_d = \tau_{d, \text{threshold}} \exp \left[ K \frac{V_{appl}}{V_{th}} \right] \text{ where } K = 1.4 \quad (1)$$

Above the value of  $V_{appl}/V_{th} = 1.9$ ,  $\tau_d$  becomes less than 1 nanosecond which is the limit of our present measurements. This relationship is true for both single crystal and polycrystalline devices.

### Recovery Time and Current Rise Time

Recovery time  $\tau_r$  was measured by using the method of two successive voltage pulses. Recovery time is defined as a minimum time interval between two applied pulses where the device has recovered after the first pulse and switches again on the second pulse. Recovery time determined by this method is about 0.5 usec with a slight dependence on the applied voltage.

The current rise time measurement was made with the device mounted in a MODPAK containing a 50 Ω stripline with the device in series with the upper lead. The NbO wafer is attached to the stripline via a thin gold wire ball bonded onto the gold-bismuth contact. A SFL model 25 transmission line pulser supplied an 800 V pulse into the MODPAK. The current via a CT-1 current transformer was viewed on the 7834 oscilloscope. The pulser delivers a pulse with a half nanosecond risetime. With the device exhibiting a 300 V threshold the

current risetime was less than 0.8 nanoseconds for a current of 25 A.

#### Holding Voltage and Current

Holding voltage  $V_h$  and holding current  $I_h$  were read out directly from the switching pulse trace. It was found that  $V_h$  exhibits a slow dependence on  $V_{appl}$  in the range from  $V_{th}$  to 2000 V. Typically  $V_h$  varied from 10 to 40 V and holding current  $I_h$  between 1 and 5 A (for the same range of applied voltage pulses).

#### Off-State Resistance

Figure 2 shows the voltage waveform (top trace) and current (bottom trace) for a single crystal device at the beginning of test. It displayed an initial threshold voltage of 1400 V and an off-state resistance prior to switching of 227 k $\Omega$ . The voltage sensitivity in this photo was 100 V per small division and the current was 1 A per small division. Pulse width was 0.8  $\mu$ sec. The device was switched into a matched load. After the first 2 K switching events the threshold dropped to 900 V with 121 k $\Omega$  off-state resistance. It was then pulsed at 10 KHz. After 24 K pulses with the applied pulse voltage varying from threshold to 2200 V there was no discernible change in off-state resistance. Some sparking was observed underneath the tungsten tip of the microprobe after a few thousand pulses. Sparking was erratic and at the end of 10,000 pulses the off-state resistance had dropped below 100,000  $\Omega$ . The test was terminated after 40,000 pulses at which time Fig. 6 was recorded. Here the voltage is 50 V per small division and the current 1 A per small division. The off-state resistance was 37 k $\Omega$ . Lifting the tungsten tip uncovered a deep eroded pit caused by poor contact between tip and device.

#### Transport and Dielectric Properties

The next figure, Fig. 5a, shows a Schottky plot of  $\log I/T^2$  vs  $V^{1/2}/T$ . Prior to switching the Bi-NbO<sub>2</sub>-Bi device shows a Schottky barrier to exist. After switching Fig. 5b shows the barrier is gone and the  $\log I$  vs  $\log V$  plot shows the device whether single crystal or polycrystalline, to be space-charge limited. The next figure, Fig. 6a, shows the C-f dependence which again exhibited the

characteristic capacitance associated with a Schottky barrier being eliminated by switching. Last in this series is Fig. 6b which shows the increase in the dc component contribution to ac conductivity upon switching.

#### Discussion

Stability and reproducibility of the characteristic switching parameters of Bi-NbO<sub>2</sub>-Bi devices as compared to Au (or Al)-NbO<sub>2</sub>-Au (or Al) devices are attributed to the Bi diffusion into polycrystalline and single crystal NbO<sub>2</sub>. The diffusion of Bi in NbO<sub>2</sub> has been confirmed by the Auger electron spectroscopy measurements and shown in Fig. 5a. Bi diffusion 300 Å deep in single crystal of NbO<sub>2</sub> was measured.

Further Bi diffusion is enhanced by the application of voltage pulses as shown in Fig. 5b. Diffusion of Bi under the influence of applied field is responsible for the observed lowering of  $R_{off}$  resistance after the repeated switching applications. Comparison of devices with Bi or Au electrodes shows the following differences in the transport and dielectric properties caused by the Bi diffusion: change from Schottky barrier to space charge conduction mechanism, decrease in thermal activation energy, increase in dc component contribution to ac conductivity and change in C-f and C-V dependences.

The relative insensitivity of  $R_{on}$  on the electrode area would tend to indicate a formation of a stable high current density path along the region doped with Bi.

Based on the above observation one can assume Lucic's<sup>5</sup> switching model of filling the recombination centers and subsequent collapse of the high resistance state. The critical current density for switching to low resistance state is given in that model by:

$$J_{cr} = 2LqN_D/\tau_d \quad (2)$$

where  $\tau_d$  is the time required to fill recombination centers,  $N_D$  is the density of recombination centers and  $L$  is to be of the thickness of NbO<sub>2</sub>, i.e.  $\sim 10$   $\mu$ m, one obtains for  $J_{cr}$  the value of  $7.7 \times 10^5$  amp/cm<sup>2</sup>, while the measured value is  $J_{cr} = 1.8 \times 10^6$  amp/cm<sup>2</sup> which represents a fair agreement.

### Etched Sample

The etched device shows another improvement over the unetched sample. Figure 8 shows the I-V taken from the Tektronix curve tracer. (The voltage is now 20 V per division and current still 10 milliamperes per division.)

Notice the disappearance of the holding current. The switched device returns to the origin now. This information is new and has not been analyzed as yet. A device consisting of a single crystal sample etched, ball-bonded and mounted in the MOD-PAK was pulsed 15 A with no change in any of its characteristics for over 400 pulses. At 26 A the device showed a slight reduction in off-state resistance. On the second or third shot the gold bond lifted off the samples. However there was no evidence of damage to the  $\text{NbO}_2$  wafer.

In conclusion,  $\text{Bi-NbO}_2\text{-Bi}$  etched devices have shown a satisfactory performance as suppressors of high transient currents needed to protect RF inputs.

In conclusion,  $\text{Bi-NbO}_2\text{-Bi}$  devices have shown a satisfactory performance as suppressors of the high intensity current transients.

### References

1. G. K. Gaule, P. LaPlante, S. Levy and S. Schneider, "Pulse Sharpening with Metal-Oxide Bulk Switching Devices," Proc. of the Int. Pulse Power Conf., 78CH1147-of Rep. 5, PIC-6, Nov. 1976.
2. G. K. Gaule and P. LaPlante, "Metal Oxide Sub-nanosecond Suppressors," 25th El. Comp. Conf. (IEEE) Washington, DC, pp. 390-394, May 1975.
3. S. M. Shin, T. Halpern and P. Raccach, "High Speed, High-Current Field Switching  $\text{NbO}_2$ ," J. Appl. Phys., Vol. 48, pp. 3150-3153, July 1977.
4. G. K. Gaule, P. LaPlante, S. Levy and S. Schneider, "Metal-Oxide Devices for Rapid Current Switching," Int. Elec. Device Mtg., Washington, DC, pp. 279-281, Dec. 1976.
5. I. Lucas, "Switching Mechanism in Amorphous Semiconductors," J. Non-Crystalline Solids, Vol. 8, p. 293, 1972.

5. L. M. Levinson, M. R. Philipp, G. A. Slack, "Protective Coaxial Switching Devices," GE Research and Development Center Final Report Contract ECOM: 76-1331-F, Oct. 1977, p. 85.

\*Research supported by the Army Research Office  
\*\*On leave of absence from the Israeli Ministry of Defense

\*\*\*Here we have assumed  $\tau_d$  to be equal to the observed delay time

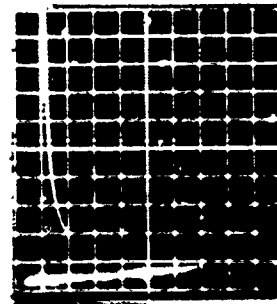


Fig. 1. Switching in  $\text{Bi-NbO}_2\text{-Bi}$  devices taken by Tektronix curve tracer, horizontal scale 10 V/Div. vertical scale 10 mA/Div.



Fig. 2. Initial pulse switching and switching characteristics after  $4 \times 10^4$  pulses. a) Initial voltage pulse, b) Initial current pulse, c) Voltage and current pulse after the application of  $4 \times 10^4$  pulses at the repetition rate of 10 Hz. Time scale 200 ns/Div.



Fig. 3. Delay time as a function of increasing applied voltage. Accumulated switching events with increasing applied voltage. Time scale 2  $\mu$ s/Div.



Fig. 4. The log of  $\tau_d$  (delay time) as a function of applied voltage for the Bi-NbO<sub>2</sub>-Bi devices

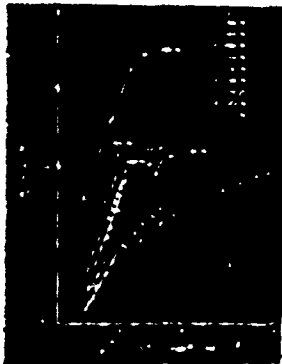


Fig. 5a. Shows a Schottky plot before switching



Fig. 5b. Log I vs Log V plot shows the elimination of Schottky barrier after switching

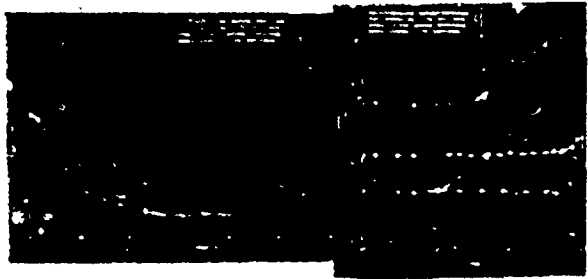
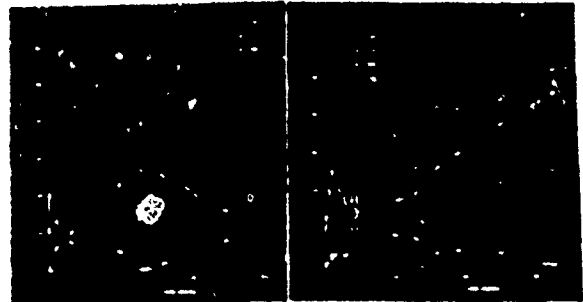


Fig. 6a & b. C-f, G-f plot before and after switching



7a



7b

7c

Fig. 7a. Auger electron spectroscopy analysis of the Au-Bi-NbO<sub>2</sub>-Bi-Au single crystal shows diffusion of Bi into NbO<sub>2</sub> in the depth of 300 Å before switching

Fig. 7b. Shows diffusion of Bi into NbO<sub>2</sub> polycrystalline after switching

Fig. 7c. Shows an increased diffusion of Bi in NbO<sub>2</sub> polycrystalline after switching

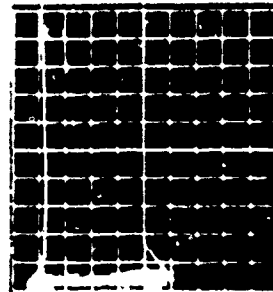


Fig. 8. I-V plot taken from Tektronix curve tracer



## MAGNET OPTIMIZATION FOR PULSED ENERGY CONVERSION\*

W. K. TUCKER, E. C. CHARE, and W. P. BROOKS  
Sandia Laboratories, Albuquerque, New Mexico 87185

R. E. WILCOX and W. D. MARKIEWICZ  
Intermagetics General, Guilderland, New York

Abstract

A flux compression generator called PULSAR is being developed to meet power requirements for future fusion reactors. Key components of the generator are superconducting magnet, generator coil of normal conductor, and an armature, either a metallic conductor or plasma. Chemical energy is used to increase the mutual inductance between the armature and nested generator coil and superconducting magnet. Flux compression occurs and electrical energy is transferred to a load inductance. This paper will present the results of a study that was conducted to design a suitable superconducting magnet for the PULSAR device.

Introduction

A pulsed energy generator, PULSAR,<sup>1-5</sup> is being developed to meet energy requirements of future fusion research. The primary components of the generator, illustrated in Figure 1, are a superconducting magnet, a generator coil of normal

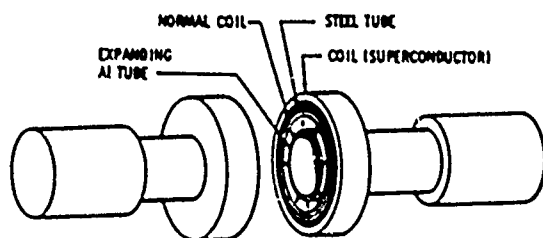


Fig. 1. PULSAR Generator

conductor, and an aluminum armature. The superconducting magnet supplies the initial flux to the bore of the nested generator coil. The load, connected in series with the generator coil, is not

inductively coupled to the remainder of the system. The armature is nested inside the generator coil bore and is initially loosely coupled to the generator coil. Additional components are required for structural support of the generator coil and shielding of the superconducting magnet.

Chemical energy is used to impart an initial velocity to the armature causing the armature to expand in the bore of the generator. Mutual inductance of the generator coil and armature increases, converting kinetic energy of the armature to electrical energy in the load. During the energy pulse, currents are generated in the various components resulting in forces on these elements. The superconducting magnet unless properly designed may quench when subjected to these conditions. The results of a study conducted to optimize the magnet for a fixed load energy output from a PULSAR generator operated with a metallic armature are presented in this paper.

System Analysis

Figure 2 shows a simplified circuit diagram for PULSAR. Additional circuits are required to model

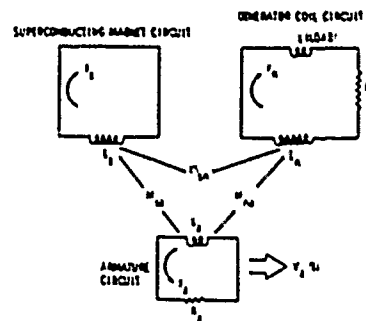


Fig. 2. Circuits Used to Model PULSAR

\*This work was supported by the U.S. Department of Energy, under Contract AT(29-1)-789.

structural and shielding components. The superconducting magnet and generator coil may be modeled as a single circuit since each is wound to control current distribution. All other components are modeled by dividing each component into radial and axial pieces to account for radial diffusion and axial drift of current. Each piece has self-inductance, resistance, and mutual inductances to all other circuits. Since the armature is expanding, its self-inductance, resistance, and all mutual inductances to the armature are functions of armature position. The forces acting on the armature are calculated, summed, and the resulting motion determined. Initial conditions for the system are the superconducting magnet current, the mass, initial position and velocity of the armature, and the electrical properties of all components.

Two computer codes, PULSRAD and CYLSEG, have been written to solve the equations which describe PULSAR performance. Although similar, each has distinct advantages in certain areas, and both have been used for this work.

The PULSRAD code will solve 10 sets of circuits of unequal length each with uniform axial current density. PULSRAD is not capable of using divided components. The CYLSEG code will solve 4 sets of circuits of unequal length, two with uniform axial current density and two capable of being divided both axially and radially. Additionally, PULSRAD has two modes of solution; flux equations and voltage equations. The flux solution uses conservation of flux and gives results that are lossless upper limits of a PULSAR device. The voltage mode of PULSRAD uses summation of voltage equations and gives results that are in close agreement with experiment.<sup>5</sup> CYLSEG operates in exactly the same manner as PULSRAD voltage mode.

#### Parameter Study

A small scale PULSAR device (~10 kJ output) has been in operation for several years.<sup>6</sup> To determine magnet characteristics for larger PULSAR systems a 10 MJ output was selected as standard. The flux mode of PULSRAD code was used to size various

systems to produce the standard output. Two principal constraints are readily apparent: (1) it is desirable to use well-known superconducting materials; therefore, the magnetic field density of the magnet should be limited to 5T or less; (2) structures become increasingly hard to build if pulsed fields of 20T are repeatedly applied, therefore, the axial field at the generator wall should be limited to 20T or less.

Four Pulsar systems, listed in Table I, were designed to meet the 10 MJ output requirement. A preliminary evaluation of System 1 established that excessively high fields and energies would be produced and a detailed design was not completed. Systems 2, 3, and 4 are comparable in terms of energy and field. System 4, will of course, have a larger cryostat, which will be more expensive. Savings will be evident in the amount of superconductor required in System 4.

#### Magnet Design

The magnets of Systems 2, 3, and 4 were design by Intermagnetics General Corp, Guilderland, NY. Key factors considered were shielding against the transient field, conductor design, winding design, cryostat design, and cost.

A number of different shielding position alternatives are available. Referring to Figure 3, shields of copper or aluminum could be used with placement either inside the warm bore, in the vacuum space or on the actual winding form. Analysis of the various materials and possible locations resulted in

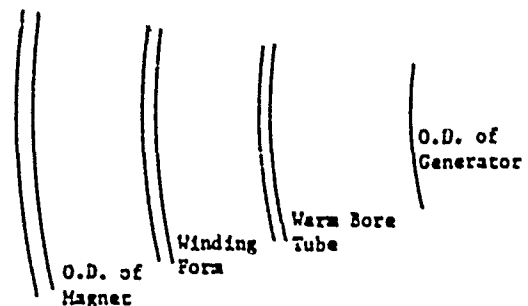


Fig. 3. Possible Shield Locations placing the shield between the magnet winding form and warm bore. This location has several advantages: (1) the shield serves as a heat shield, (2) heat in-

duced into the shield is not directly coupled to the liquid helium and (3) there is significant material saving by operating at reduced temperature. Calculations show the shield will reduce the transient field to 1% or less of its original value for pulses as long as 100 ms.

The design of the superconductive cable is based on conservative cryostable winding design practices and a normal state heat flux of  $0.2 \text{ watts/cm}^2$ .

Figure 4 illustrates the PULSAR cable. The design

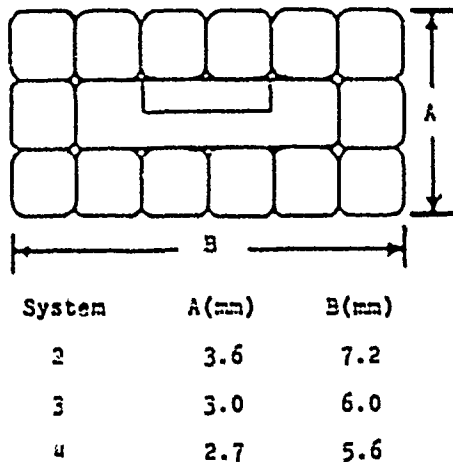


Fig. 4. PULSAR Conductor

of the coil is intentionally conservative and eliminates the possibility of the magnet compromising the pulsed energy output. Two areas that may lend themselves to reductions in size and thus savings are the conductor design and the shield design. The conductor normal state heat flux and the shield thickness has been based on PULSRAD and CYLSEC computer runs and equations approximating the performance of the copper shield. A larger than normal design margin was used in these areas to reflect the uncertainty of the input data. A smaller margin could perhaps be established depending upon a performance evaluation of this system and a computer code combining the PULSRAD and CYLSEC codes. For all three systems, even with the magnetic shield in place there is a dB/dt at the winding. Therefore, it is advantageous to move the NbTi superconductor to the interior of the conductor. The additional copper surrounding the superconductor acts as a final shield.

The winding design of the three coils is relatively simple and straightforward. The parameter study yielded the magnet's energy, field, size, and ampere-turns. From this information and the conductor design, the number of turns, turns per layer, number of layers, and length of conductor is determined. These data are given in Table II. The design of the PULSAR coils relies upon a fully constrained conductor. This conservative approach is taken because of the possibility of mechanical shock during the pulse generation.

#### Cost Estimates

Cost estimates for the three main systems are summarized in Table III. The costs, in 1976 dollars, include labor and material costs for the conductor, winding, cryostat, electronics (power supply, protection circuits, and controls) and engineering. Of immediate interest is the cost decreases as magnet energy increases. However, if one assumes a constant magnet field level of 1.96 T for Systems 3 and 4, the energy each would store is 45 MJ and 70 MJ, respectively. It is apparent that Systems 3 and 4 are under-utilized and that the decreased cost of wire will not offset the increased cost of materials due to larger size. System 1, dropped from consideration because of high field levels, was not designed and only a preliminary cost estimate was conducted. This estimate indicated a cost higher than System 2. Therefore, a valley in the cost curve does exist, and System 2 is the most cost effective of the four systems studied.

Large PULSAR systems, capable of producing energy pulses of several 100 MJ, are under study at the present time. Magnet cost per joule will decrease for these systems. Additionally, present work on plasma armatures<sup>6</sup> will lower cost of 10 MJ and larger systems because of reduced shielding requirements due to faster pulse risetimes. Flux losses in the center of the PULSAR device are reduced with plasma armatures yielding additional saving on total system cost.

#### Summary

The PULSAR system provides a unique application of a superconducting magnet. Three different size de-

signs have been developed, allowing flexibility in the armature-generator configuration. The basic differences in the designs are of geometry and field. System 2, despite its smaller diameter, has the highest energy due to its much higher field. The dimensionally largest system is System 4, however, due to its low field it has the lowest stored energy of the three. System 2 has the most cost effective magnet.

TABLE I  
System Specifications

PULSAR System	1	2	3	4
Outside Radius of Armature Expanded (m)	0.6	0.9	1.15	1.4
Mean Radius of Generator (m)	0.61	0.91	1.16	1.41
Warm Bore Radius (m)	0.76	0.97	1.23	1.47
Winding Inside Radius of Superconductive Coil (m)	0.99	1.24	1.51	1.72
Coil Length (m)	1.2	1.8	2.3	2.8
Initial Axial Magnetic Field (T)	4.9	1.9	1.14	0.77
Axial Field at Wall of Generator (T)	25.4	15.8	12.4	10.0
Superconducting Magnet Energy (MJ)	85.0	27.0	16.7	12.3

TABLE II  
Turns Specification

System	Turns/Layer	Layers	Wire Length (km)
2	247	20	40.3
3	377	12	43.7
4	509	8	45.8

TABLE III  
Cost Estimates for PULSAR Magnets (K\$)

System	Magnet	Cryostat	Other	Total
2	357	490	248	1095
3	304	632	248	1184
4	275	824	248	1347

#### References

1. M. Cowan, et al., "Multimegajoule Pulsed Power Generation from a Reusable Compressed Magnetic Field Device," Proc. Int. Conf. on Energy Storage, Compression, and Switching, Torino, Italy, 1974.
2. M. Cowan, et al., "Electron Beam Power from Inductive Storage," Proc. Int. Top. Conf. on Electron Beam Research & Technology, p. 490, 1975.
3. M. Cowan, et al., "PULSAR - A Field Compression Generator for Pulsed Power," Proc. 6th Symp. on Engineering Problems of Fusion Research, p. 308, 1975.
4. E. C. Cnara, et al., "PULSAR - The Experimental Program," Proc. 6th Symp. on Engineering Problems of Fusion Research, p. 312, 1975.
5. M. Cowan, et al., "Pulsed Energy Conversion with a DC Superconducting Magnet," *Cryogenics*, December 1976, p. 699.
6. E. C. Cnara, W. P. Brooks, and M. Cowan, "PULSAR: An Inductive Pulse Power Source," this proceeding.

# DESIGN OF THE ARMATURE WINDINGS OF A COMPENSATED PULSED ALTERNATOR ENGINEERING PROTOTYPE

J. H. Gully, W. L. Bird, T. M. Bullion, M. G. Rylander, W. F. Weldon, H. H. Woodson

Center for Electromechanics, The University of Texas at Austin  
Taylor Mall 167, Austin, Texas 78712

## Abstract

The design of the armature windings of a 6 kV, 70 kA compensated pulsed alternator engineering prototype now under construction at The University of Texas at Austin is presented. Electromagnetic forces acting on the windings and the resulting mechanical and electrical stresses placed on the armature insulation are given. Test results of a program to select the ground plane insulation system are described. Finally, fabrication methods, tooling, and problems encountered during construction are discussed.

## Introduction

The compensated pulsed alternator (compulsator) is presently being developed by the Center for Electromechanics (CEM) at The University of Texas at Austin.<sup>1,2</sup> An engineering prototype compulsator rated at 6 kV, 70 kA peak has been designed to deliver approximately 200 kJ to a xenon flashlamp load and is now under construction.<sup>3</sup> A cutaway drawing of the machine is shown in Figure 1.

Basically, the generator is a single phase alternator with stationary field and a rotating armature. The armature winding and an identical stationary winding are connected in series, so that at one point per cycle the inductance of the armature circuit is minimized. The variable armature inductance leads to flux compression action, which, coupled with alternator action delivers high current pulses to the flashlamp load. Typical performance parameters are listed in Table 1.

## Winding Configuration

Both the armature winding and the compensating

winding are located in the magnetic air gap between the rotor periphery and the stator bore. The conductors are not imbedded in slots, but are held in place by the adhesive bond formed by the ground plane insulation (glass filled epoxy) and the steel rotor or stator. The air gap configuration has been proposed for large synchronous generators<sup>4,5</sup> and has been used for the armature winding of superconducting alternators.<sup>6</sup> The configuration is used in the compulsator to reduce the minimum armature inductance and increase flux compression action to improve machine performance.

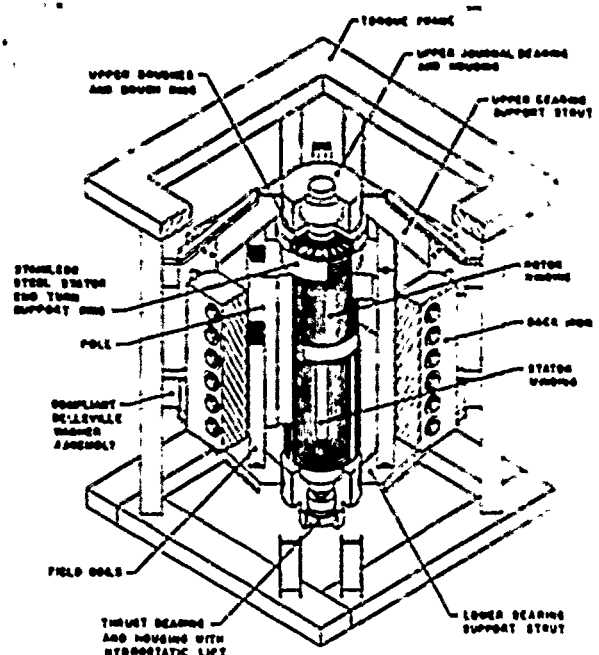


Figure 1: Schematic of Compulsator

To minimize inductance the conductors are radially thin and the radial separation between the rotor

winding and stator winding is as small as electrical and mechanical constraints permit. Since the conductors are fully exposed to the applied magnetic field, the mechanical forces on the conductors and insulation are larger than in conventional machinery where the primary forces are exerted on the rotor teeth. Therefore, multi-layer windings and windings with crossovers, such as the lap and spiral windings shown in Figure 2, are avoided. A single layer, multi-turn wave winding is used. The wave winding is modified to eliminate the crossover by removing one conductor under one pole and using the closely coupled compensating winding as the current return.

See Figure 3. Notice that both windings have one missing conductor and that slip rings are located at both ends of the rotor.

Table 1: Engineering Prototype Parameters

Number of poles	4
Rotor Speed (rpm)	5400
Rotor Angular Velocity ( $\text{sec}^{-1}$ )	565
Open Circuit Frequency (Hz)	180
Peak Open Circuit Voltage (kV)	5.7
Minimum Armature Inductance ( $\mu\text{H}$ )	27
Armature Resistance at 20°C ( $\text{m}\Omega$ )	45
Compensating Winding Axis (rad)	0.147
Peak Load Current (kA)	72
Peak Load Voltage (kV)	6
Peak Power to Load (MW)	430
Pulse Half Width ( $\mu\text{sec}$ )	560
Delivered energy (kJ)	200
Peak Mechanical Power (Average) (MW) (at $\omega_m = 543 \text{ sec}^{-1}$ )	500
Armature Temperature Rise (°C)	8.9
Peak Fault Current (kA)	150
Peak Mechanical Power (Average) (MW) (at $\omega_m = 534 \text{ sec}^{-1}$ )	1450
Armature Temperature Rise Under Fault 40 (°C)	

#### Missing Conductor Force

Since one conductor of both rotor and stator windings are removed, the magnetic pressure in the gap under

one pole will be reduced at the moment of peak current. The resulting magnetic force toward the weak pole will approach  $3.2 \times 10^5 \text{ N}$  (185,000 lbf) under fault conditions if damping forces are neglected. This force is removed by shifting the center lines of the conductor belts adjacent to the weak pole approximately 0.042 radians (2.4 degrees). This displacement does introduce an additional mass imbalance which must be removed during rotor balancing.

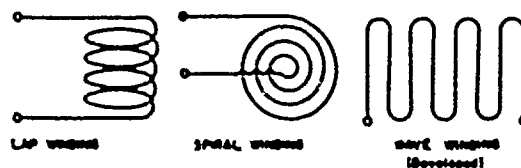


Figure 2: Conventional Armature Windings

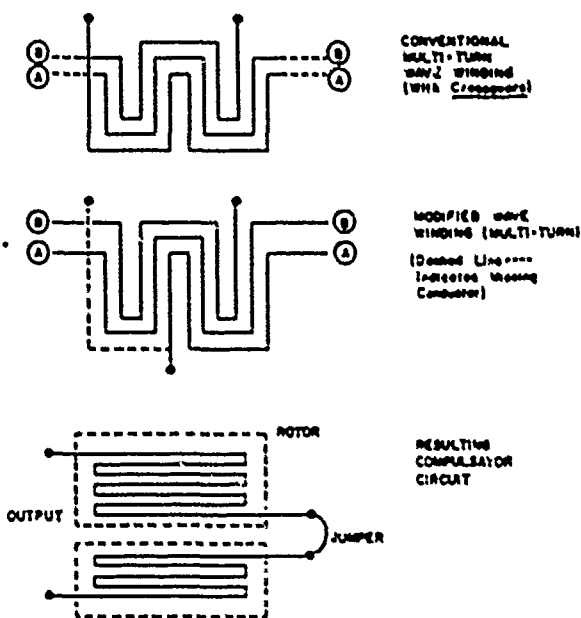


Figure 3: Modified Wave Winding

#### Conductor Design

The rotor conductors are stranded and transposed to hold eddy current losses to an acceptable level. Each rotor conductor consists of ten 0.165 cm x 0.508 cm type 3 Litz wires (wound ten-in-hand) supplied by New England Electric Wire Company.

Each Litz wire consists of 12 bundles of seven #30 AWG AF Bondex (Phelps-Dodge) bondable magnet wires which are stranded six around one. Each of the ten Litz wires is wrapped with Hexcel F159/120 pre-preg glass filled epoxy tape in a linear wrap rather than a spiral wrap because of the minimum slitting width of pre-preg tape. A cross-sectional end view of the insulation system is shown in Figure 4.

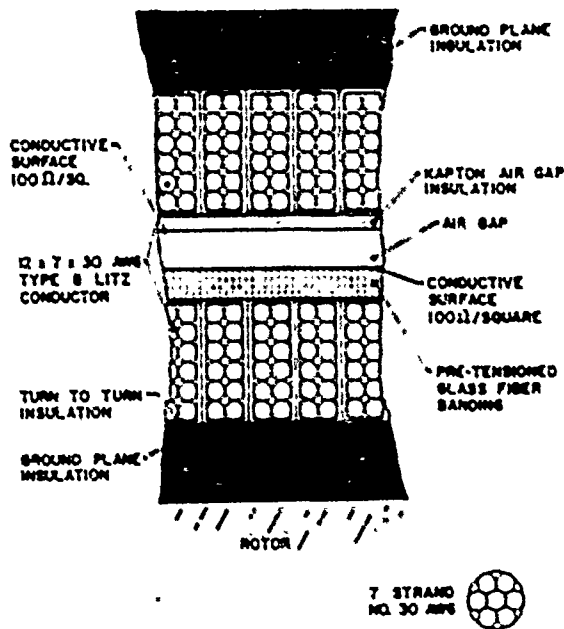


Figure 4: Insulation System

There are 12 conductors per pole for three poles and 11 conductors on one pole due to the missing conductors for a total of 47 conductors. Therefore, there are nominally 120 Litz wires per pole.

It is not necessary to transpose the 10 Litz wires in a conductor bundle since the modified wave winding provides a natural transposition. A wire occupying the inside position under south poles occupies the outside position under north poles.

#### Rotor Ground Plane Insulation

The ground plane insulation must withstand the armature voltage to ground, nominally 6 kV peak, but most importantly, must transmit the torque required to decelerate the inertia of the rotor laminations and shaft. The maximum average shear stress placed on the adhesive bond is 7.1 MPa (1030 psi) under

normal conditions and 17.3 MPa (2500 psi) under fault. The estimated stress concentration factor due to non-uniform flux distribution is 1.5. Therefore, the insulation system is subject to a cyclic load of 10.6 MPa (1540 psi) and 26 MPa (3780 psi) under short circuit. The insulation is loaded in compression at the time of peak shear stress by the magnetic pressure in the air gap. The maximum compressive loading occurs 100  $\mu$ sec after the peak shear stress and is a maximum of 33 MPa (4000 psi) under short circuit.

Hexcel F159/1581 has been selected for this application based on static rotary shear strength tests performed by the Center for Electromechanics. Similar tests for copper/epoxy bonds performed by Grumman Aerospace also show Hexcel to be a good selection.<sup>7</sup> The tape is supplied in 5 cm width by 0.24 mm thick and is applied in seven half lap wraps for a total build of 0.335 cm. Nominal dielectric stress is 18 kV/cm (45 VPM). The peak dielectric stress anticipated is 30 kV/cm (76 VPM), which can be impressed on the insulation in the event that the lamps fail to trigger.

#### Stator Ground Plane Insulation

The stator ground plane insulation must transmit the reaction torque to ground through the adhesive bond between the insulation and the stator bore. It is similar in construction to the rotor ground plane insulation.

#### Rotor Banding

The centrifugal forces on the rotor conductors are taken by a pre-tensioned glass banding tape which is wound on the outer diameter of the rotor. General Electric Banding Tape No. 76843 (60 end tape 1.9 cm wide) is applied in two half lap wraps under 2200 N (500 lbf) tension. The banding tape also serves as electrical insulation between windings and is normally stressed at 20 kV/cm (51 VPM). The maximum expected dielectric stress is 33 kV/cm (85 VPM).

#### Stator Gap Insulation

The stator conductors are wound on a thin 0.64 mm

layer of Kapton insulating film. The insulation is formed by 9 layers of an Araldite adhesive coated Kapton tape R7021 (0.076 mm x 2.54 cm wide) manufactured by the Rogers Corporation, Chandler, Arizona. The tape is normally stressed at 54 kV/cm (13/ VPM) with the maximum of 90 kV/cm (230 VPM). The stator gap insulation is not required to transmit large mechanical forces as are the other insulation systems.

#### Mechanical Clearance (Electrical Air Gap)

The minimum armature inductance is directly proportional to the effective separation of the rotor winding and compensating winding. The inductance variation or flux compression ratio, varies as the inverse square of the effective separation. Therefore, the mechanical air gap must be minimized to obtain peak performance. The mechanical clearance of the 0.38 m diameter rotor in the stator bore is 1.6 mm (63 mils) on a radius. This clearance is dictated by the dynamic mechanical response of the rotor and the voltage stress across the gap.

#### Corona Suppression

If steps were not taken to shunt the air gap capacitance with a low resistance, the air in the gap would be stressed beyond its dielectric strength. To avoid this situation, both the outer diameter of the rotor and the stator bore are coated with thin layers of conductive paint and are joined at each end through miniature brushes on copper slip rings. The surface resistivity of the conductive paint is 100 ohms per square (Technit Acrylic -100 #73-40052). The peak stress on the air gap is reduced to less than 6.3 kV/cm at the maximum anticipated voltage (10 kV) and frequency (10 kHz).

#### Armature Brush Mechanism

Using the winding configuration shown in Figure 3, current is collected at both ends of the rotor. Each brush mechanism consists of 30 copper graphite brushes (Morganite CMS) which ride on a 25.4 cm diameter copper slip ring. Each brush has an apparent contact area of 17 cm<sup>2</sup> and the maximum velocity is 70 m/sec. Air cylinders, clevis mounted in G-10 rings, actuate the brushes which are

attached to the copper output conductors by means of cantilevered 1.6 cm thick copper straps. These straps are attached to provide a trailing arm brush configuration. The output conductor rings, fabricated from ET copper, are grooved to provide uniform current distribution around the slip ring.

#### Rotary Shear Tests

A variety of static shear tests were made using the double shear test fixture shown in Figure 5. The test jig is made of mild steel and is cleaned prior to each test as follows:

1. Sand surfaces with 180 grit emery paper.
2. Degrease with soap and water.
3. Dip in solvent (methanol).
4. Soak jig 10-12 minutes in American Cyanamide Prebond 700 @ 35°C.
5. Rinse in distilled water.
6. Rinse in methanol.
7. Oven dry at 150°C.

The tape under test is supplied or cut to 2.5 cm widths and is wrapped on the mandrels with a total build greater than the housing bore. The tape is compressed approximately 15 percent when the mandrel housing is clamped tight.

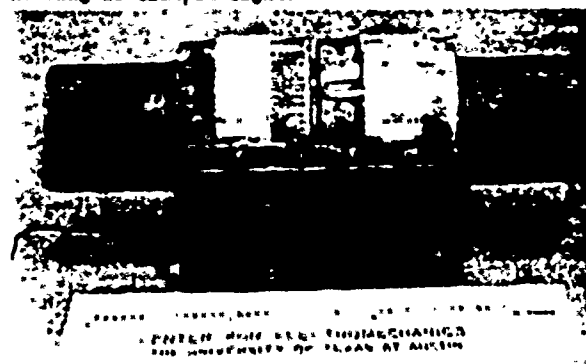


Figure 5: Photo-Shear Test Jig

Test results for a variety of insulation candidates are given in Table 2.

The final test of the Hexcel was performed to test the bond strength between two Hexcel surfaces, one previously cured and machined. The average shear



strength was reduced thirty percent.

Table 2: Torsional Shear Test Results

Material	Shear Stress		Failure Mode
	MPa(psi)		
G.E. Mica Mat 77937	2.06(300)		Adhesive
G.E. Mica Mat 77918	4.82(700)		Interlaminar
Dow DER 332 Mat Layup	13.8(2000)		Adhesive
Scotchply 1003	27.6(4000)		Interlaminar
Hexcel F159/7781	29.6(4300)		Interlaminar
Hexcel F159/7781	27.1(3919)*		Interlaminar
Hexcel F159/7781	15.7(2270)*		Machined Interface

\*Tests performed at end of material shelf life  
(2 months at 40°F)

#### Tooling and Fabrication

A variety of tooling is required for fabricating the rotor winding and compensating winding. This tooling includes the following:

1. Collapsible stator winding mandrel.
2. Turn-to-turn insulation wrapping machine.
3. Litz wire feeding mechanism for winding ten-in-hand.
4. Rotor/stator mandrel support fixture.
3. Tape tension device/banding machine.

The collapsible stator winding mandrel is shown in Figure 6.

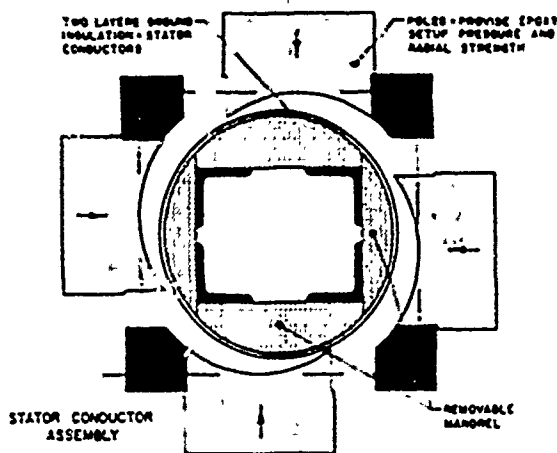


Figure 6: Stator Conductor Assembly

The litz wire turn-to-turn insulation is applied linearly as shown in Figure 7.

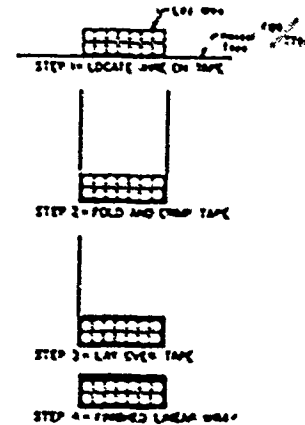


Figure 7: Turn-to-Turn Tape Folding

A completed wire sample is shown in Figure 8.

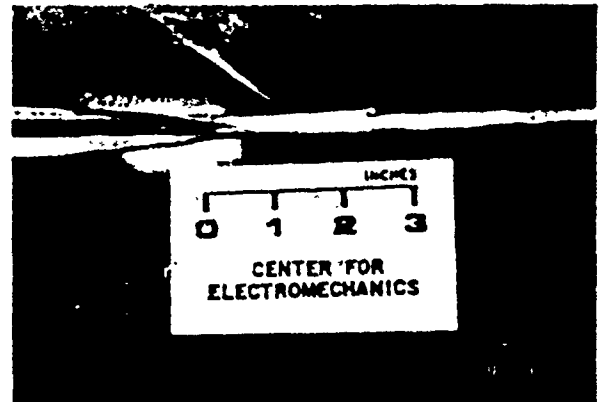


Figure 8: Photo-Sample Litz Wire

The following table presents each step of the winding sequence and solutions to the miscellaneous problems encountered during fabrication are listed.

#### References

1. W. L. Bird, D. J. T. Mayhall, W. F. Weldon, H. G. Rylander, H. H. Woodson, "Applying a Compensated Pulsed Alternator to a Flashlamp Load for NOVA-Part II," 2nd IEEE International Pulsed Power Conference, Texas Tech University, Lubbock, Texas, June 12-14, 1979.
2. W. F. Weldon, W. L. Bird, M. D. Drigs, K. M. Tolk, H. G. Rylander, H. H. Woodson, "Fundamental Limitations and Design Considerations for Compensated Pulsed Alternators," 2nd IEEE

Table 1: Fabrication of Compensating Winding,  
Problems and Solutions

<u>Procedure</u>	<u>Problems</u>	<u>Solution</u>
Fabricate air gap winding spacers	Insulating material, compound angle at end turns prevents conventional machining	Laminated structure out of 0.3 mm G-10 sheets using EPOXY 828 epoxy. Grind shape by hand.
Wrap Mexcel F159/720 turn-to-turn insulation	Epoxy flows at room temperature causing tape to stretch and epoxy to coat jig rollers.	Move process to refrigerated room at 10°C
Wrap Kapton stator air gap insulation on winding mandrel. Bond G-10 spacers in position	Kapton shifts during cure cycle. Laminated G-10 spacers warp	Cure in two steps. Use disposable heat shrink tape to control Kapton diameter. Bond G-10 spacers with Mexcel resin. Hold spacers in place with both hose clamps and shrink film.
Wind Litz wire ten in hand	Wires must move independently. Must hold in place as rotate horizontally	Made jigs to locate each bundle of 10 wires with respect to spacers. Use inner tubes to hold wires in place.
Wrap Mexcel F159/1581 ground plane insulation	Voids must be filled to prevent air bubbles	Paint on epoxy before wrapping
Clamp poles around mandrel	Voids or wrinkles in tape after 10% compression causes stress concentration	Built jigs to locate 4 pole pieces. Each piece rotated into place rather than sliding at interface.
Curing of insulation system	Large structure/no available oven	Bonded nichrome element resistors to heat plates with thermion heat transfer cement. Strapped resistors to poles and bore of stator mandrel.

International Pulsed Power Conference, Texas Tech University, Lubbock, Texas, June 12-14, 1979.

3. B. Carder, "Applying a Compensated Pulsed Alternator to a Flashlamp Load for NOVA-Part 2," 2nd IEEE International Pulsed Power Conference, Texas Tech University, Lubbock, Texas.
4. E. Spooner, "Fully Slotless Turbogenerators," Proceedings, IEE Vol. 120, No. 12, December 1973, pp. 1507-1518.
5. E. J. Davies, "Airgap Windings for large Turbogenerators," Proceedings, IEE Vol. 118, No. 3/4, March/April 1971, pp. 529-535.
6. J. Kirtley, Jr., "Design and Construction of an Armature for an Alternator With a Superconduction Field Winding," Doctoral Dissertation, Massachusetts Institute of Technology, Boston, Mass., August, 1971.
7. C. Burke, "Coil Integrity Insulation Mechanical Screening Interim Test Report," ADAC 11.3.4-2, Report No. EP-D-016 to Princeton Plasma Physics Laboratory, Grumman Aerospace Corp., December 13, 1977.

#### Acknowledgments

This work was performed under Lawrence Livermore Laboratory Purchase Order No. 3325309 with support of the U. S. Department of Energy and the Texas Atomic Energy Research Foundation.

# THE MECHANICAL DESIGN OF A COMPENSATED PULSED ALTERNATOR PROTOTYPE

M. Brennan, W. L. Bird, J. M. Gully, M. L. Spann, K. M. Tolik, W. F. Weldon,  
M. C. Rylander, M. H. Woodson

Center for Electromechanics, The University of Texas at Austin  
Taylor Hall 167, Austin, Texas 78712

## Abstract

A prototype of a compensated pulsed alternator (compulsator) is presently under construction at the Center for Electromechanics (CEM) of The University of Texas at Austin. The unique machine configuration and peak output current (150 kA) generate large forces not typically seen by conventional rotating machines. The rotor is made of 2913 laminations shrink fitted on a vertical shaft. Since the rotor has an L/D of 3.2 and a maximum speed of 5400 rpm, these insulated laminations are clamped on the ends with large Belleville washers to increase the effective stiffness. The stator is mounted on a torque frame which allows it to rotate during discharge to reduce the forces transmitted to ground. The mechanical considerations and design of this machine are presented.

## Introduction

The compulsator is a rotating energy storage device which provides high-voltage, high-current pulses by utilizing the principles of magnetic induction and flux compression. Although initially invented to power the flashlamps used in the Shiva Nova laser fusion facility at the Lawrence Livermore Laboratory, the compulsator is also presently under study as a power supply for other applications requiring compact, high-energy, high-power repetitive or single pulses. The engineering prototype compulsator under construction is a one-half scale model of one of the machines to be used in the Shiva Nova laser facility.

This paper presents the mechanical design. For details of the principal of operation, electrical design, and armature winding design, see references 1, 2, and 3 respectively.

## Design

Figure 1 shows a cut-away isometric drawing of the compulsator without external connections such as oil lines and pumps for the bearings, motor-drive system, field coil connections and power supply, and output connectors to the flashlamp load. The three major mechanical components discussed are: 1) rotor, 2) back iron and 3) torque frame.

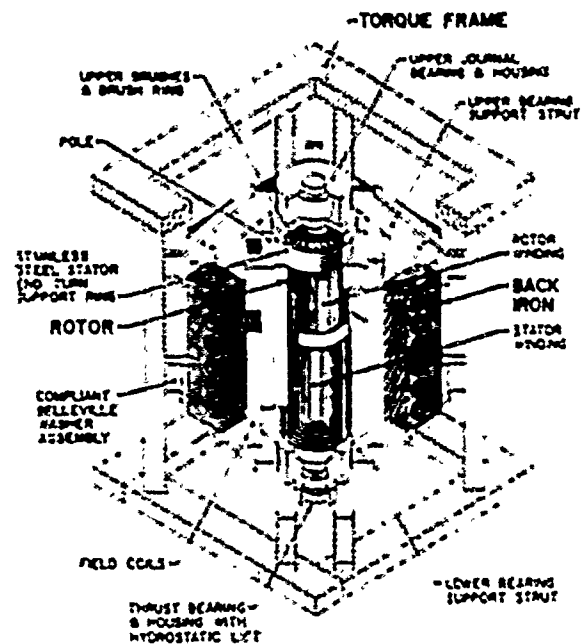


Figure 1. Cutaway Isometric of Compulsator

### 1. Rotor

In order to reduce eddy current losses, the rotor is made of 2913 steel (M-19) laminations, 0.036 cm (0.014 in) thick, 38.1 cm (15 in) in diameter and

shrink fitted on to an AISI 4340 steel shaft heat treated to  $R_c 34$ . Because the nominal shaft diameter of 9.65 cm (3.8 in) is insufficient to keep the first rotor critical above the maximum operating speed of 5400 rpm, it is necessary to compress the laminations in order to increase the effective flexural modulus of the rotor, hence the rotor stiffness. The rotor cannot be allowed to pass through a critical because hysteretic losses from sliding of the lamination interfaces would result in a rotor instability<sup>4</sup>. The lamination preload is applied with two (one per end) large, titanium Belleville washers, 6.03 cm (2.375 in) thick and 38.1 cm (15 in) in diameter. Because of the Belleville washer configuration, the preload of  $2.67 \times 10^6$  N (600,000 lb) preferentially loads the outside diameter of the laminations although the washer will be flattened to partially load the inner diameter also.

The required preload was not arbitrarily selected, but resulted from a series of tests performed on sample stacks of laminations. The two guiding design criteria were the interlaminar resistance and effective modulus versus load. With increasing load, the effective flexural modulus of the stack of laminations increases as the interlaminar resistance decreases.

The desired lamination core plating, C-5, could not be obtained on the schedule required for construction of the prototype. The plating received, C-0, was unacceptable and required that an interlaminar insulation be applied that could take the high loads. The first type of insulation tested was Sterling U-87/PS, an air dry varnish.

Figure 2 shows the measured overall resistance versus load of two separate stacks of laminations. The bottom curve is the test results of a stack of 1000 varnished laminations. Even as the load was held steady, the resistance continued to drop and at  $1.33 \times 10^6$  N (300,000 lb), measured 182 ohms. This was unacceptable since a value of 782 ohms was desired in order to keep the eddy current losses at an acceptable level.

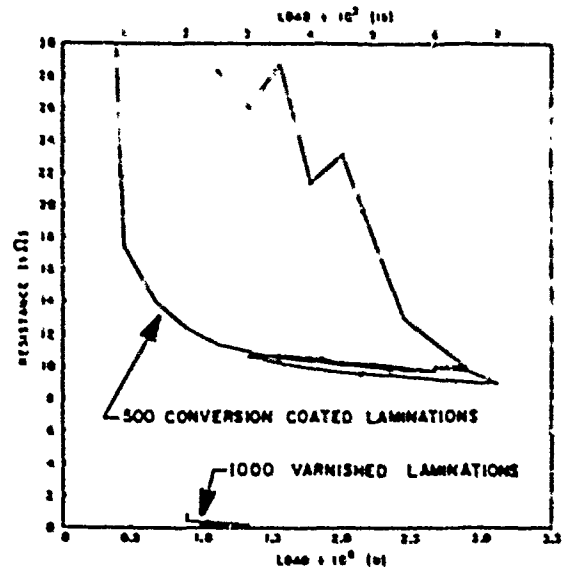


Figure 2. Resistance vs Load

The next insulation tested and finally used was a military refinish concentrate made by Atlanta Cutlery. It is a chemical conversion coating which phosphatizes the surface. The varnish previously applied was baked off the laminations before the chemical conversion coating was applied. The resistance versus load of a stack of 500 coated laminations is also shown in Figure 2 and at  $3.11 \times 10^6$  N (700,000 lb) measured 9,040 ohms, over an order of magnitude above the design goal of 391 ohms. Note that even as the load was fluctuated, the resistance remained relatively stable and repeatable. The resistance did register lower after c. a load was decreased than when the load was initially applied. This is probably due to an increasing number of small asperities breaking through the insulation as the load is increased and then remaining in contact with the adjacent lamination as the load is decreased.

During the same test with the chemical conversion coated laminations, the amount of axial compression versus load was measured and is shown in Figure 3a. When the stack is initially compressed, the total deflection is significant. This is a result of the air being squeezed out from between each lamination,

small asperities being flattened, and any warpage in the lamination being flattened. When the same stack is then compressed a second time, even after sitting unloaded for one day, the total deflection is considerably less. The interesting fact is that the slope of the curve as the load is decreased is the same, indicating that after the stack is loaded, its mechanical characteristics are repeatable.

Figure 3b is an enlarged section of the first loading curve and shows some other interesting facts.

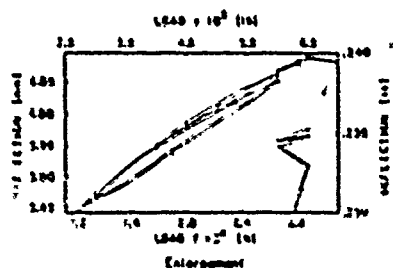


Figure 3b

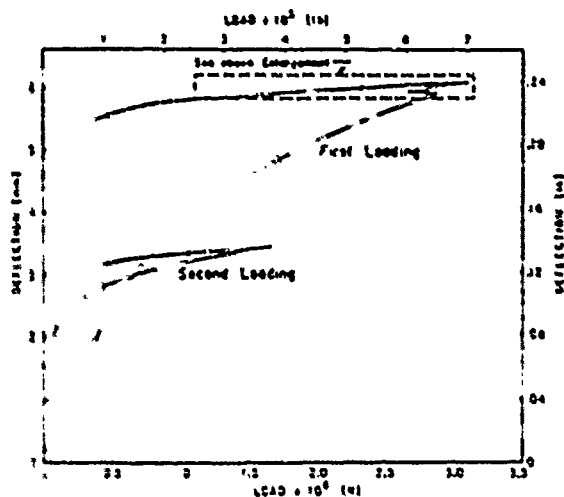


Figure 3a

#### Deflection vs Load

First note that as the stack is brought to full load, at two points the load is reduced and the stack still shows an increase in deflection. This was noticed in other tests not presented here and is due to the amount of time the stack is allowed to sit at load before the deflection measurement is made. If the load is held steady, the stack will continue to compress for many minutes. It is

suspected this time element is a result of the air being squeezed out from between the laminations. Another important fact is that after the stack stops creeping and the load is fluctuated, the stack does not load and unload along the same curve, indicating some hysteresis in the stack.

Since the resistance remained high for all the loads tested, the level of load to be used is determined by mechanical limitations. The Belleville washers, which apply the preload, are held in place with two large nuts which also serve as the bearing journals. These nuts will be tightened using a stud tensioner loaned to CEM by the DuPont chemical processing plant in Victoria, Texas. The device works by stretching the stud (in our case, the shaft) and then "hand tightening" the nut down against the Belleville washer. The device has a  $3.56 \times 10^6$  N (800,000 lb) pulling capacity which produces the maximum stresses the modified 60° stub-tooth Acme threads and shaft can take. Due to relaxation in the threads as the load is transferred from the stud tensioner to the nut, the resulting preload will be less although the minimum desired is  $2.67 \times 10^6$  N (600,000 lb).

Clamped up sections of laminations 22.9 cm (9 in) long were bored with a taper of  $6.86 \times 10^{-3}$  cm (0.0027 in) on the diameter and the shaft then ground to match. After the application of the lamination insulation, the inner bore of the laminations were aligned for the shrink fit by pulling one lamination at a time up against two small ground shafts glued together and inserted down the bore. The entire stack was then clamped as tightly as possible without affecting the bore alignment. The alignment was checked by lowering the shaft in at room temperature until the tapers matched. The final shrink fit was done by chilling the shaft in liquid nitrogen and then dropping it into the laminations. Figure 4 is a picture of the rotor with the Belleville washers and nuts in place and the back iron in the background.



Figure 4. Rotor and Back Iron

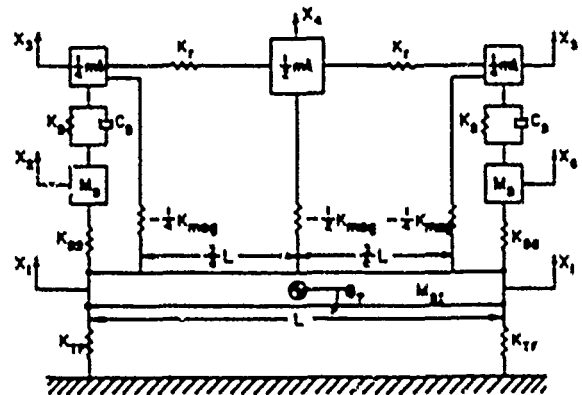
The inverse of the slope of the curve in Figure 3 can be considered an effective Young's Modulus,  $E_{eff}$ , of the stack of laminations in compression. Using the data obtained on the final unloading in Figure 3b,  $E_{eff} = 1.88 \times 10^{10}$  MPa ( $2.72 \times 10^6$  psi). Although what is actually desired is the flexural modulus, it could not be measured and the above  $E_{eff}$  should be sufficient for the dynamic calculations.

A discrete, lumped mass model of the rotor-bearing-support system (see Figure 5) was performed using a CDC 6600 computer to solve for the complex eigenvectors and complex eigenvalues. The torque frame, bearing supports, bearings (including damping), and rotor are included in the model. The first rotor critical is calculated to be 621 rad/sec, 10% above maximum operating speed.

The radial bearings for the machine are tilting pad, oil lubricated, hydrodynamic bearings made by Kingsbury, Inc. A special design feature incorporated into the bearing is spherical buttons on the back of the pads which allow for axial misalignment or cocking of the shaft. Each bearing is instrumented with a resistance temperature detector (RTD) embedded in the babbit to monitor pad temperatures.

The thrust bearing is a two sided, self aligning, tilting pad, hydrodynamic bearing made by Kingsbury, Inc. Each side is instrumented with a RTD and the loaded side has two load cells to measure steady state and dynamic loads.

Since this is an experimental machine and will be started and stopped many times, a high pressure oil inlet at the end of the shaft is used to lift the machine off the thrust bearing pads at zero speed to avoid excessive wear of the pads. This will only be used during start up.



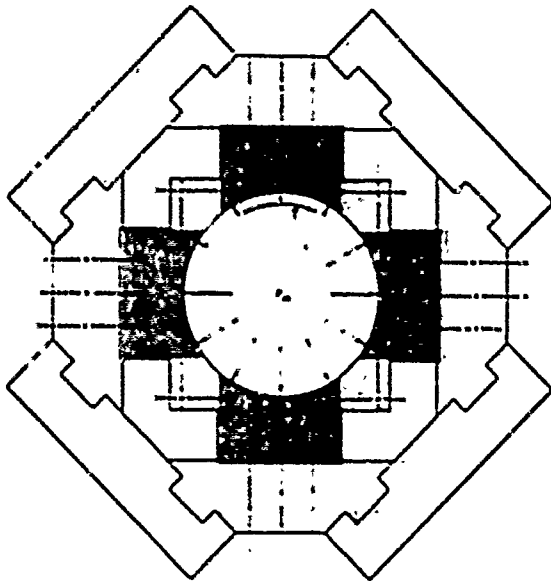
- $K_{TF}$  = TORQUE FRAME STIFFNESS =  $5.04 \times 10^7$  N/m
- $K_{BS}$  = BEARING SUPPORT STIFFNESS =  $1.29 \times 10^3$  N/m
- $K_B$  = BEARING STIFFNESS = VARIED
- $C_B$  = BEARING DAMPING = VARIED
- $E_{eff}$  = EFFECTIVE YOUNG'S MODULUS OF ROTOR = VARIED
- $K_R$  = ROTOR STIFFNESS; INCLUDES SHEAR DEFLECTION;  
DEPENDENT UPON  $E_{eff}$  = VARIED
- $K_{MS}$  = MAGNETIC SPRING STIFFNESS =  $3.97 \times 10^7$  N/m
- $M_R$  = MASS OF ROTOR =  $1.08 \times 10^3$  kg
- $M_{BI}$  = MASS OF BACK IRON =  $9.07 \times 10^3$  kg
- $M_B$  = MASS OF BEARING HOUSING = 230 kg

Figure 5. Lumped Mass Dynamic Model

## 2. Back Iron

During a discharge, the back iron must withstand two forces generated from J X B forces and flux compression. These forces appear as a torque and an internal pressure applied at the inner diameter of the back iron where the stator conductors are located (see Figure 6). The back iron is designed to withstand these forces under steady state conditions for a peak fault current of 150 kA although

this peak current only exists instantaneously during the pulse.



DISCHARGE FORCES: (FAULT MODE, 3400 RPM, 150 kA)  
 $T = \text{PEAK DISCHARGE TORQUE} = 2.7 \times 10^6 \text{ N-m}$   
 $P_m = \text{PEAK MAGNETIC PRESSURE} = 20.7 \text{ MPa (3000 psi)}$

Figure 6. Back Iron

The reaction torque of  $2.70 \times 10^6 \text{ N-m}$  ( $1.99 \times 10^6 \text{ ft-lb}$ ) and internal pressure of 20.7 MPa (3000 psi) must be sustained with no relative movement of the pieces. The stator conductor is epoxied to the inner diameter<sup>3</sup> of the back iron and any slippage of a back iron member could initiate a crack in the epoxy. The ideal geometry for these forces would be a cylindrical vessel, but a casting could not be obtained in time. An irregular octagonal structure made of 16.5 cm (6.5 in) plate as seen in Figure 6 evolved with the sides interlocked with closely toleranced keys and slots. This allowed for most of the load to be taken by the keys in shear.

Another significant design feature of the back iron and poles is that they do not extend the length of the rotor. If this had been done, the axial forces on the end turns at each end of the rotor from the applied field and the current in the conductors would be very large and any asymmetry in the field would pull the rotor to one end and overload the thrust bearing. Therefore, the back iron only

extends the active length of the conductors and the stator end turns are supported by stainless steel rings bolted to the end of the poles. Figure 7 shows the back iron supported in the torque frame.

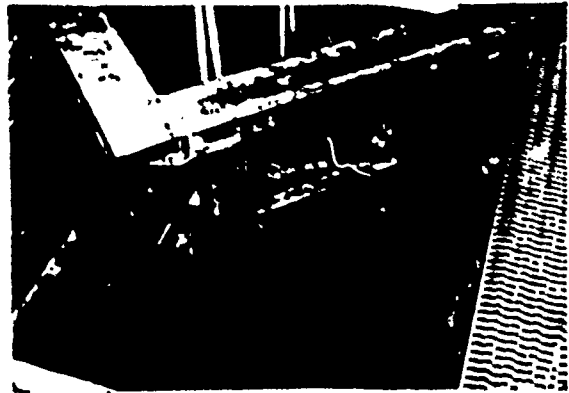


Figure 7. Back Iron In Torque Frame

### 3. Torque Frame

The torque frame is a structure designed to support the compulsator and allow a slight rotation of the back iron during a discharge (see Figures 1, 5 and 7). By allowing the back iron to rotate, the total peak load transferred to the torque frame as a result of the discharge torque is reduced from  $6.82 \times 10^6 \text{ N}$  ( $1.53 \times 10^6 \text{ lb}$ ) to  $1.15 \times 10^5 \text{ N}$  ( $2.56 \times 10^4 \text{ lb}$ ). As the back iron rotates, it compresses Belleville washers against I beams which form the structure of the torque frame. The springs are essentially serving as force attenuators. There are two sets of Belleville washers being compressed at each of the four corners of the torque frame located at a radius of 79.4 cm (31.3 in) from the center of the compulsator. The back iron is allowed to rotate 0.00733 radians, compressing the Belleville springs 0.582 cm (0.23 in). The torque frame is constructed of eight I beams (6112.5), two per corner, which are connected at the top and bottom by a square formed from rectangular tubing. In addition to resisting the discharge torque, the frame must support the mass of the compulsator, approximately  $9.07 \times 10^3 \text{ kg}$ .

### Acknowledgements

This work is supported by the U.S. Department of Energy, Lawrence Livermore Laboratories (Purchase Order 3325309), and the Texas Atomic Energy Research Foundation.



# References

1. W. F. Weldon, W. L. Bird, M. D. Driga, K. M. Tolks, H. G. Rylander, and H. H. Woodson, "Fundamental Limitations and Design Considerations for Compensated Pulsed Alternators," 2nd International IEEE Pulsed Power Conference, June 12-14, 1979, Texas Tech University, Lubbock, Texas.
2. W. L. Bird, D. J. T. Mayhall, W. F. Weldon, H. G. Rylander, and H. H. Woodson, "Applying a Compensated Pulsed Alternator to a Flashlamp Load for NOVA-Part II," 2nd International IEEE Pulsed Power Conference, June 12-14, 1979, Texas Tech University, Lubbock, Texas.
3. J. H. Gully, W. L. Bird, M. D. Driga, H. G. Rylander, K. M. Tolks, W. F. Weldon, and H. H. Woodson, "Design of the Armature Windings of a Compensated Pulsed Alternator Engineering Prototype," 2nd International IEEE Pulsed Power Conference, June 12-14, 1979, Texas Tech University, Lubbock, Texas.
4. R. C. Loewy and V. J. Piarulli, Dynamics of Rotating Shafts, Washington, D.C.: Navy Publication and Printing Service Office, 1969, pp. 31-34.

# THE DESIGN, ASSEMBLY, AND TESTING OF A DESK MODEL COMPENSATED PULSED ALTERNATOR

M. A. Pichot, W. L. Bird, M. Brennan, M. D. Driga, J. H. Gully  
H. G. Rylander, K. M. Tolik, W. F. Waldon, H. H. Woodson

Center for Electromechanics, The University of Texas at Austin  
Taylor Hall 167, Austin, Texas 78712

## Abstract

The Center for Electromechanics (CEM) at The University of Texas is currently involved in the design, fabrication, and testing of a prototype compensated pulsed alternator (compulsator). This machine, a new concept in pulsed power technology, utilizes the principles of magnetic induction and flux compression to convert rotational energy directly into electrical energy.<sup>1</sup>

The subject of this paper is a one-fifth scale version of the CEM prototype. This desk model compulsator is a portable demonstration machine designed to operate in the same fashion as the full scale model.

## Introduction

The compulsator was invented to reduce the large volume and high costs associated with large pulsed power sources. Because of the machine's unique characteristics, it is able to produce the high-voltage, high-current pulses of capacitors in a more compact and economical form.

Although the compulsator offers volume and cost savings at high power levels, the advantages become less prominent as the size of the power source is reduced. Because of this, the desk model compulsator is not intended to compete with other power sources in its output range, but rather to demonstrate the operation of larger compulsators.

## Principle of Operation

The design feature that makes the compulsator unique is a stationary coil almost identical to the rotating winding. When the two coils are in their closest proximity, the stationary coil counteracts the

inductance of the rotating coil, reducing it to a small fraction of its normal value. At this instant, a very intense pulse is generated; after the pulse, the inductance again rises to its original value.<sup>2</sup>

## Design Philosophy

The desk model compulsator, intended as a portable demonstration device, is designed to operate from a 120 Vac wall outlet. The motoring system and magnetic circuit of the machine are sized accordingly.

## Rotor

The rotor consists of 6.99 cm outer diameter ring-type laminations shrunk fit onto a 2.54 cm diameter stainless steel shaft. In addition to the shrink fit, the laminations are compressed axially by stainless steel nuts on each end of the shaft. Attached to the O.D. of the laminations, the rotating coil is wound in a serpentine like shape (Figure 1). The coil conductors are stranded and transposed (Litz) wire used to reduce the losses associated with skin and proximity effects. The shaft is supported both radially and axially by ball-bearing units press fitted onto each of its ends.

The limiting speed of the machine is determined by the rotor's first critical frequency. For a worst case assumption, the shaft alone is assumed to provide the rotor's stiffness (additional stiffness is expected from the compressed laminations). The resulting rotor stiffness is  $3.713 \times 10^6$  Nt/m. The ball bearings are supported by an aluminum structure bolted to the compulsator's outer housing (back iron); the bearing support stiffness in its weakest

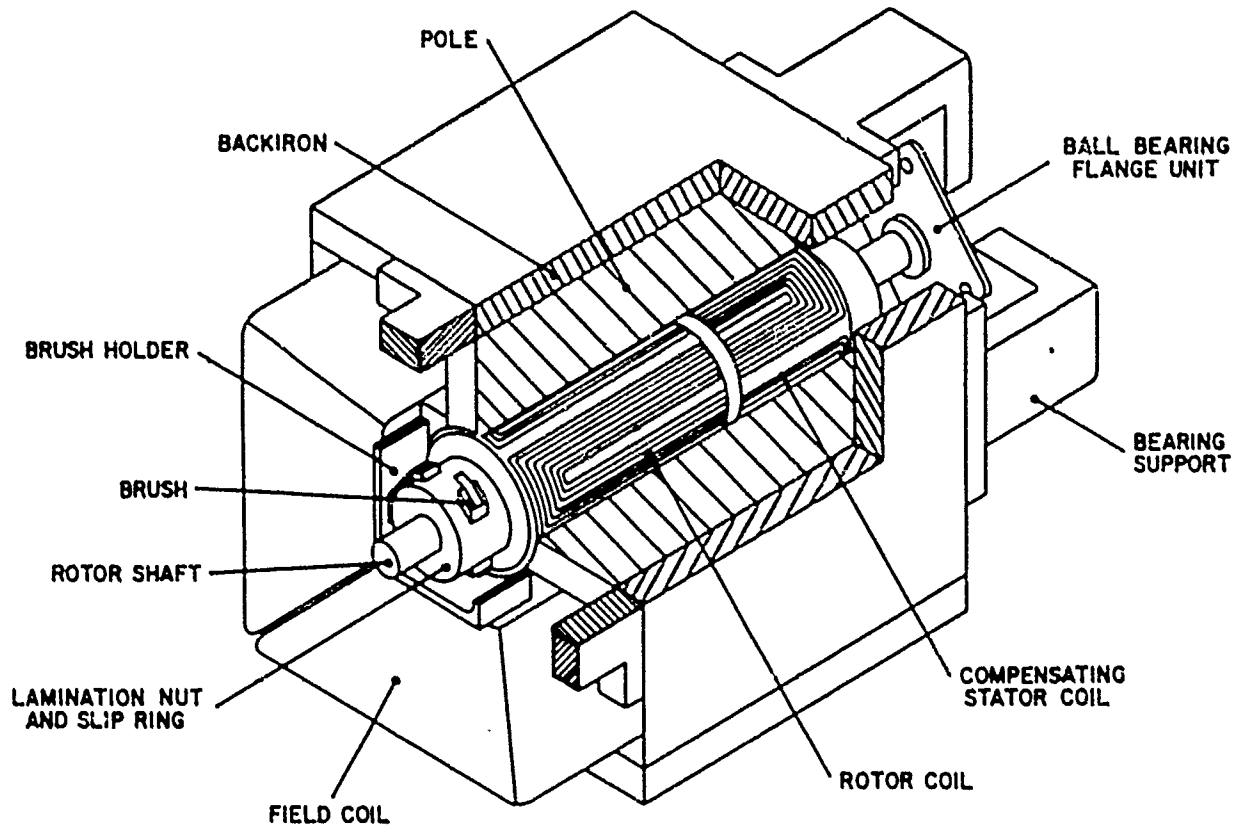


Figure 1: Desk Model Compulsator

mode is  $9.19 \times 10 \text{ Nt/m}$ . The effective spring constant is:

$$K_{\text{eff}} = \frac{K_B K_R}{K_B + K_R} = 3.569 \times 10^6 \text{ Nt/m} \quad (1)$$

( $2.038 \times 10^6 \text{ lb/in.}$ )

where  $K_B$  is the bearing support stiffness and  $K_R$  is the rotor stiffness. The first critical frequency is then:

$$\omega_1 = \left( \frac{K_{\text{eff}}}{M_T} \right)^{1/2} = 738 \text{ rad/sec} \quad (2)$$

where  $M_T$  is the combined shaft and rotor mass.

#### Magnetic Circuit

The magnetic circuit of the desk model compulsator is designed to operate at a flux density of 1.5 T. Because the machine is to operate from a 120 Vac wall outlet and be portable, this is the highest

field attainable. The magnetic air gap between the rotor laminations and each of the four poles is 0.511 cm. The number of ampere-turns required to give the desired flux density in the gap is (assuming no losses in the back iron):

$$N_{fc} = \frac{B_g}{\mu_0} = 6.096 \times 10^3 \text{ Ampere-turns}$$

where  $B$  is the magnetic flux density,  $g$  is the magnetic air gap, and  $\mu_0$  is the magnetic permeability of air.

The field coils are wound from No. 13 copper magnet wire in a conical shape around the poles (Figure 1). For a single field coil of 462 turns, the current required is 13.19 Amps. The corresponding length of the coil is 302.3 m. The coil resistance is given by:

$$R_{fc} = \frac{\rho L_{fc}}{A} = 2.03 \text{ ohms} \quad (3)$$

where  $\rho$  is the electrical resistivity of copper,  $L_{fc}$  is the length of the wire in the coil, and  $A$  is the cross-sectional area of the wire. The four field coils' voltage and power requirements are:

$$V_{fc} = 4(i_{fc})R_{fc} = 107.1 \text{ Volts} \quad (4)$$

$$P_{fc} = 4(i_{fc})^2 R_{fc} = 1413 \text{ Watts} \quad (5)$$

where  $i_{fc}$  is the field coil current. Note that the voltage is such that it can be conveniently provided by a full-bridge rectifier using a 120 Vac outlet.

The temperature rise is obtained by assuming that all the power input results in heating of the coil wire. For 60 second operation, the temperature rise is:

$$\Delta T = \frac{P_{fc} \Delta t}{M_{fc} C_p} = 7.8^\circ\text{C} \quad (6)$$

where  $M_{fc}$  is the mass of the coil,  $C_p$  is the specific heat of copper, and  $\Delta t$  is the period of operation.

This is a conservative coil design in terms of temperature rise, since the desk model will be used only for intermittent duty.

#### Motoring

The desk model is driven by a 0.75 kW (1 hp) universal motor. The motor is directly coupled to the compulsator's shaft by a high-speed flexible coupling. Speed variation is accomplished by an electronic speed control, permitting a wide range of operating speeds and the flexibility to adjust to differing loads.

#### Brushes

This machine uses solid brushes made of copper-graphite, chosen because of low voltage drop, as well as friction, heating, and wear considerations. The contact area of the brushes is such that the resulting current densities present no difficulties.

The brush arrangement consists of four 1.27 cm

square brushes at each end of the rotor (Figure 1). The brushes ride on slip rings which are mounted on top of the nuts used for compressing the laminations. The brushes are spring loaded onto the slip rings, the spring force provided by a cantilevered strap that also serves to carry the discharge current out from the machine.

#### Electrical Performance

The desk model compulsator has the following electrical characteristics at an intermediate operating speed of 565 rad/sec:

Inertial Energy Stored	= 600 joules
Peak Terminal Voltage	= 200 volts
Peak Current	= 500 amps
Armature Resistance	= 320 mΩ
Minimum Armature Inductance	= 8.6 μH
Inductance Variation	= 1.45:1

Predicted performance into a three circuit flashlamp load as well as short circuit current characteristics are shown in Figure 2. The plots

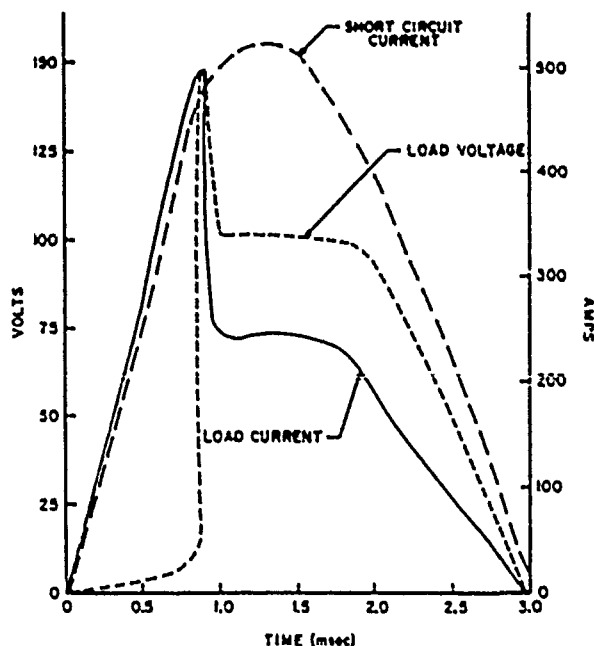


Figure 2: Desk Model Predicted Performance

shown are for simplified flashlamp circuits using ideal switches at a machine speed of 565 rad/sec. Trigger and start-up are accomplished by methods

discussed in reference 3.

The curves indicate little flux compression effect in the desk model. This is a consequence of scaling down from the larger diameter machine; that is, flux compression improves with the increase in machine diameter.

Additional information concerning fundamental limitations and load applications of compulsators can be found in references 3, 4, and 5.

#### Fabrication and Assembly

Fabrication and assembly of the desk model are now underway at The University of Texas.

The shaft was machined from type 304 stainless steel bar stock. Ring laminations were purchased from Arnold Engineering Co.; the inside diameter of the laminations was bored to the 2.54 cm shaft diameter, and the laminations were shrunk onto the shaft.

The back iron and pole assembly was manufactured from cold-rolled steel plates. The 1.905 cm thick back iron plates were assembled to form a 21.59 cm square structure 20.96 cm long. Four 3.81 cm pole plates were then fastened to the inside of the back iron structure.

The field coils will be wound from No. 13 magnet wire around each of the four poles. Epoxy is to be applied to the coils after each layer of wire is wound, so that the field coils form spool-type units. In addition, the coils can be removed from the poles should repairs become necessary.

Additional preparations for the desk model will include winding both the rotor and compensating stator coils, fabricating the brush set-up, and manufacturing the bearing supports.

#### Testing

After assembly has been completed, the desk model compulsator will be thoroughly tested. Some of the testing program's objectives will include:

- a) experimentally verifying the basic machine constants,
- b) comparison of actual machine performance to predicted values,
- c) attempting to minimize the various sources of mechanical and electrical losses, and
- d) determining machine efficiency in various modes of operation.

The desk model compulsator research project is funded by Lawrence Livermore Laboratory, the U. S. Department of Energy, and the Texas Atomic Energy Research Foundation.

#### References

1. Lawrence Livermore Laboratory's, "Compensated Pulsed Alternator," brochure concerning the compulsator invented by the Center for Electromechanics, July 1978.
2. W. F. Weldon, H. G. Rylander, H. H. Woodson, "Invention from Research," DISCOVERY: Research and Scholarship at The University of Texas at Austin, Volume III, Number 2, December 1975.
3. B. M. Carder, "Applying a Compensated Pulsed Alternator to a Flashlamp Load for NOVA-Part I," 2nd IEEE International Pulsed Power Conference, Texas Tech University, Lubbock, Texas, June 12-14, 1979.
4. W. F. Weldon, W. L. Bird, M. D. Driga, K. M. Tolk, H. G. Rylander, H. H. Woodson, "Fundamental Limitations and Design Considerations for Compensated Pulsed Alternators," 2nd IEEE International Pulsed Power Conference, Texas Tech University, Lubbock, Texas, June 12-14, 1979.
5. W. L. Bird, D. J. T. Mayhall, W. F. Weldon, H. G. Rylander, H. H. Woodson, "Applying a Compensated Pulsed Alternator to a Flashlamp Load for NOVA-Part II," 2nd IEEE International Pulsed Power Conference, Texas Tech University, Lubbock, Texas, June 12-14, 1979.

## A COMPRESSED MAGNETIC FIELD GENERATOR SYSTEMS MODEL

James E. Cover

Sandia Laboratories  
Albuquerque, New Mexico 87185ABSTRACT

A model relating the volume of a compressed magnetic field generator pulsed power system to its electrical energy output is developed. This systems model includes energy density and power density models of the electronic components and a CMF generator model which has been confirmed experimentally for system output energies up to 5000 joules. For a given output energy there exists an optimum selection of the pulsed power components to give an overall minimum system volume. Under optimum conditions the volume of the CMF generator is equal to one-half of the overall system volume and the overall system volume increases with the one-half power of the systems output energy. In an all electronic system there is a linear relationship between system volume and output energy.

Description of CMF System

A CMF generator may be employed as an electrical energy amplifier. Energy stored in the explosive of an armature is converted into electrical energy through a magnetic field compression process. This results in an output electrical energy several times greater than the initial electrical "injection" energy supplied to the generator. The physics of operation of CMF generators are well understood in a qualitative sense and significant progress has been made in recent years toward developing improved quantitative models<sup>1</sup>.

The overall CMF generator pulsed power system considered for these studies is shown in schematic-block diagram form in Fig. 1. The battery supplies a low voltage (tens of volts) input that is converted to the kilovolt range by the dc-dc converters. The output from the converters is used to charge a

capacitor. When the capacitor is charged, the switch is triggered and the capacitor discharges into the coil of the CMF generator. When the current in the CMF generator coil reaches a maximum value the explosive in the CMF armature is detonated and the electrical energy amplification process is initiated.

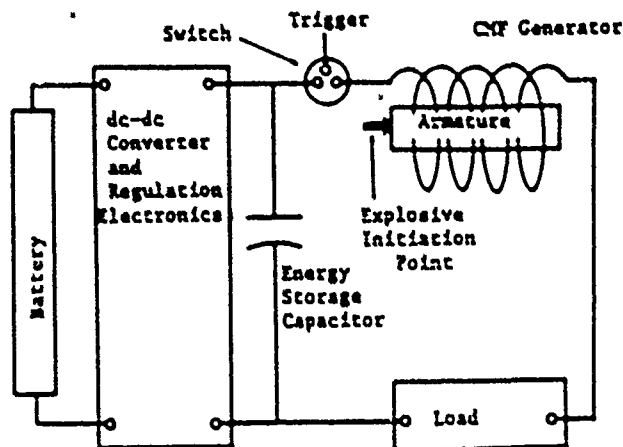


Fig. 1: CMF Generator Pulsed Power System That Is Utilized For System Optimization Studies.

Component Volume Scaling

## A. Battery

The volume of a battery operating in the tens to several hundred watts range of output power scales roughly with the output energy of the battery<sup>2</sup>. Thus,

$$V_b = k_b E_b$$

where  $V_b$  is the battery volume,  $E_b$  is the electrical output energy of the battery and  $k_b$ , the scaling coefficient, is roughly  $10^{-3} \text{ cm}^3/\text{joule}$ .

## B. Converter and Regulation Electronics

Experience by dc-dc converter developers has shown

that dc-dc converter volume scales linearly with output power, or

$$V_c = \frac{k_e E_e}{\tau},$$

where  $V_c$  is the volume of the dc-dc converter and regulation electronics,  $E_e$  is the output electrical energy of the converters,  $\tau$  is the time required to charge the energy storage capacitor and  $k_e$  is the scaling coefficient<sup>3</sup>. A significant range of values of  $k_e$  may be obtained depending upon regulation and reliability requirements, technology choices and operating life. For these studies the range

$$5 \frac{\text{cm}^3}{\text{watt}} \leq k_e \leq 20 \frac{\text{cm}^3}{\text{watt}}$$

is selected.

The efficiency of dc-dc converters may range from 20% to 90% depending upon the type of converter design. An efficiency factor,  $\epsilon_e$ , is defined such that

$$E_e = \epsilon_e E_b.$$

#### C. Energy Storage Capacitor

Once one chooses the dielectric material of a capacitor, an upper limit is obtained for the maximum electric field at which the capacitor may be operated, i.e., the breakdown field of the dielectric. The permittivity is also fixed. Thus an upper limit is obtained for the energy density of a capacitor. In practice, capacitors are operated at electric field values much less than the breakdown strength of the dielectric. One accepted practice is to determine the average breakdown voltage and the standard deviation of the breakdown voltage of a large number of capacitors and limit the operation of the capacitor to voltages that are four standard deviations below the average breakdown voltage. This operational practice results in capacitors that are extremely reliable; however, their energy density is much less than that suggested by the breakdown field of the dielectric.

We model the capacitor volume as

$$V_c = k_c E_e$$

where  $V_c$  is the capacitor volume and  $k_c$  is the scaling coefficient. Employing the high reliability design approach as outlined above, designing the

capacitor to maintain this reliability over a broad temperature range and maintaining a high pulse life results in values for  $k_c^{-1}$  of 0.06 joules/cm<sup>3</sup> for dry mylar and mica paper capacitors. It has been demonstrated that the energy density of mylar energy storage capacitors may increase to values as high as 0.3 joule/cm<sup>3</sup> by flooding the mylar with Fluorinert. Refinement of this design method could result in energy storage capacitors whose energy density is as high as 1 joule/cm<sup>3</sup> without diminishing reliability, temperature range or pulse life capabilities<sup>4</sup>. Hence,

$$16 \text{ cm}^3/\text{joule} \geq k_c \geq 3 \text{ cm}^3/\text{joule}$$

with potential for obtaining  $k_c = 1 \text{ cm}^3/\text{joule}$ .

#### D. Switch and CMF Coil Resistance Losses

When the switch is triggered and the energy storage capacitor is discharged into the CMF generator coil, energy is lost to joule heating in the switch and coil. Hence,

$$E_{ig} = \epsilon_g E_e$$

where  $E_{ig}$  is the initial magnetic field energy in the generator and  $\epsilon_g$  is the electric field to magnetic field conversion efficiency. For most cases of practical interest

$$0.9 \geq \epsilon_g \geq 0.7.$$

#### E. CMF Generator

We have found by empirical methods that helical CMF generators have an energy gain per unit volume that is independent of their volume<sup>5</sup>. That is

$$\frac{E_{og}}{E_{ig}} = k_g \frac{V_g}{E_e}$$

where  $E_{og}$  is the output electrical energy of the generator,  $V_g$  is the generator volume and  $k_g$  is the generator scaling constant. This model was arrived at by observing data obtained from several generator designs whose output energy ranged from 50 joules to 5000 joules. Validity of the model above 5000 joules output energy cannot be claimed because of lack of experimental data. Furthermore, it is clear that at values of output energy in the megajoule region this scaling is not valid because the electrical output of the generator would exceed the energy stored in the armature's explosive.

Our experiments demonstrate that  $k_g$  has a range of values

$$0.04/\text{cm}^3 \leq k_g \leq 0.08/\text{cm}^3$$

over a broad range of load inductance values and injection currents or injection energy.

#### Systems Model

The total volume,  $V_{gs}$ , of the pulsed power system is the sum of the volumes of the components or

$$V_{gs} = V_b + V_a + V_c + V_g$$

where we have ignored: (1) the circuit that detonates the explosive armature, (2) the trigger circuit for the switch, and (3) the switch. Packaging factors of individual components are not included.

From the scaling definitions it is easy to show that

$$V_{gs} = \frac{1}{\epsilon_s k_g} \left( \frac{E_{og}}{E_a} \right) + E_a \left( k_c + \frac{k_a}{\tau} + \frac{k_b}{\epsilon_a} \right).$$

Investigation of this equation for the range of scaling coefficients shows that

$$\frac{k_b}{\epsilon_a} \ll k_c + \frac{k_a}{\tau}$$

or the battery volume and the efficiency of the dc-dc converters do not impact the overall system volume; therefore, this term is ignored in further calculations.

One may note that the volume of an all electronic system,  $V_{es}$ , or the system with the CMF generator eliminated is

$$V_{es} = E_a \left( k_c + \frac{k_a}{\tau} \right),$$

or a linear relationship exists between output energy and system volume.

The value of  $E_a$  that results in minimum CMF system volume for a given system output energy may be obtained by taking the partial derivative of the volume equation with respect to  $E_a$  and setting the result equal to zero. This gives

$$V_{gs}^* = 2 \left[ (\epsilon_s k_g)^{-1} \left( k_c + \frac{k_a}{\tau} \right) \right]^{1/2} E_{og}^{*1/2}$$

where the asterisks denote minimum volume conditions. Under these conditions the volume of the CMF generator is exactly equal to one-half the

overall system volume. This general relationship for CMF generator pulsed power sources has been observed by others<sup>6</sup>.

The sensitivities of the volumes of the CMF generator and the overall CMF system to optimum selection of components are illustrated in Fig. 2 for an output energy of 5000 joules. These data are based upon:  $k_a = 10 \text{ cm}^3/\text{watt}$ ,  $k_g = 0.04/\text{cm}^3$ ,  $k_c = 16 \text{ cm}^3/\text{joule}$ ,  $\epsilon_s = 0.8$  and  $\tau = 1$  second.

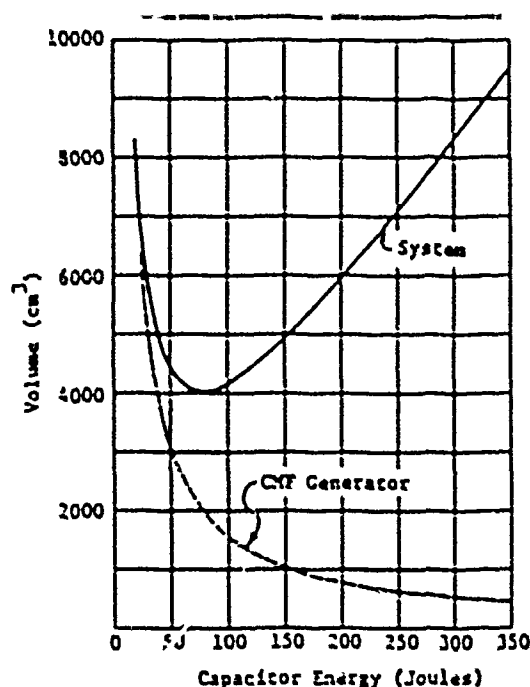


Fig. 2: Sensitivity of CMF Generator System Volume and CMF Generator Volume to Optimum Choice of Components for a 5000 Joule System Output.

Note that the volume of the system is not significantly affected by a range of capacitor energy between 60 joules and 100 joules. However in this energy range there is a dramatic variation in CMF generator volume.

The volumes of each of the components are shown as a function of output energy in Fig. 3. The scaling coefficients are identical to those used for Fig. 2. The volume of an all electronic system over this energy range is also included for comparison purposes. The scaling coefficients of the electronics are identical to those used for the CMF



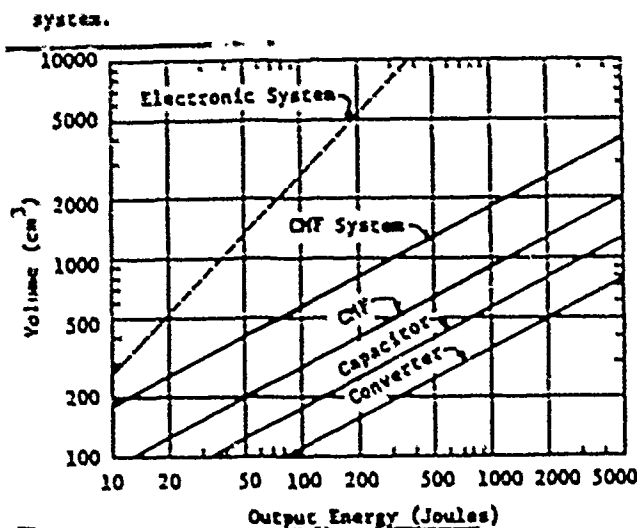


Fig. 3: Volumes of Electronic and Optimally Designed CMF Generator Pulsed Power Systems as a Function of Output Energy. The Energy Dependence of the CMF System Components are Compared. The Charge Time of the Capacitor is Taken as 1 Second.

The comparison between the CMF system and the electronics system shown in Fig. 3 represents one extreme that is most favorable to the CMF system. The other extreme that makes the electronics system more favorable is shown in Fig. 4.

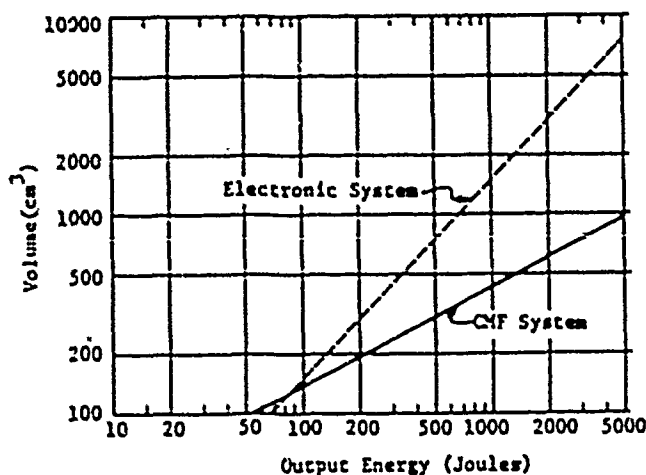


Fig. 4: Comparison of Volumes of CMF and Electronic Pulsed Power Systems as a Function of Output Energy. The Capacitor charge time is 10 Seconds and Optimistic Scaling Coefficients were Selected for the Electronics.

In this case the scaling coefficients are taken as:  $k_e = 3 \text{ cm}^3/\text{watt}$ ,  $k_g = 0.04/\text{cm}^3$ ,  $k_c = 1 \text{ cm}^3/\text{joule}$ ,  $\epsilon_g = 0.5$  and  $\tau = 10$  seconds, or the systems employ the most advanced power electronics technology and a conservative CMF generator design.

Other calculations illustrate that the volume of the CMF system is insensitive to capacitor charging times greater than 5 seconds.

#### References

1. "Proceedings of Second International Conference on Megagauss Magnetic Field Generation and Related Topics", 29 May - 1 June, 1979.
2. Personal Communication, B. H. Van Doremel, SLA, Albuquerque, New Mexico.
3. Personal Communication, J. M. Strichman, SLA, Albuquerque, New Mexico.
4. Personal Communication, G. M. Maudlin, SLA, Albuquerque, New Mexico.
5. Personal Communication, A. E. Minder, J. E. Leeman and O. M. Stuetzler, SLA, Albuquerque, New Mexico.
6. Personal Communication, Malcolm Jones, Atomic Weapons Research Establishment, Reading, UK.

## APPLICATION OF SUBSYSTEM SUMMARY ALGORITHMS FOR HIGH POWER SYSTEM STUDIES

FREDERICK C. BROCKMURST

Air Force Aero Propulsion Laboratory  
Wright-Patterson Air Force Base, Ohio 45433Abstract

This paper describes the application of subsystem summary algorithms for self-contained power system configuration trade-off studies, and presents the results of a recently completed study. The development of summary weight algorithms for rocket turbines and rotating electrical generators is described. These new algorithms are combined with previously developed power conditioning subsystem algorithms in a computer program to automatically study various system configurations. A flow chart of the computer program is included in the paper. The computer program was used to find a minimum weight self-contained power system. Results of the study are presented in this paper.

Introduction

Computer aided design has long been recognized as a most effective technique for determining optimum designs of components and subsystems. The Air Force Aero Propulsion Laboratory is committed to developing computer aided design techniques for the optimized design of complete self contained power systems. A three step concept has been adopted: determination of system feasibility, detailed component design, and dynamic system simulation.

System feasibility is determined by the use of summary algorithms representing each component of the system. These algorithms relate each component's weight and volume to the operating parameters that most affect each. The operating parameters are iterated through rather broad ranges until a combination of components meeting the desired system requirements is found. After a

combination has been found, the operating parameters of that combination are converted to component design specifications.

The component design specifications are automatically fed to detailed component design computer programs. These programs generate enough detail to completely specify the design of components such as generators, transformers, turbines, and rectifiers. The cooling requirements of each component are specified, but the total cooling system is designed as part of a dynamic simulation package. The final step in the component design process is calculation of the matrix coefficients required for the dynamic simulation.

The matrix coefficients are automatically fed to dynamic simulation programs which fully simulate the electrical and thermal performance of the interconnected components. A main emphasis of the electrical simulation is voltage and current transients. There is also a capability to adjust control philosophies in an attempt to minimize transients. Data from the thermal simulation is retained as an operating profile from which the cooling system is designed.

This paper discusses the summary algorithms used to determine system feasibility. Algorithm development is described. A computer program that combines the algorithms and calculates system weight is discussed, and the results of a sample system study are presented.

Algorithm Development

A summary algorithm describes the weight or volume of a component as a function of those operating, or design, parameters that affect the weight or

volume. Examples of parameters that affect weight and volume are power level, voltage, and frequency. Each algorithm is normally valid for only a narrow range of parameter values, otherwise accuracy is sacrificed.

Data used to develop the summary algorithms is generated from the detailed design computer programs. The design programs are used to produce numerous designs within the parameter ranges of interest. The data from these designs is organized such that standard curve fitting techniques can be used to form the algorithm. Algorithms developed to date use simple logarithmic curves; however, techniques for using higher order polynomial curve fitting are being implemented.

Two examples of summary algorithms are listed here for completeness. The first was derived from 65 detailed turbine system designs using a mixture of liquid oxygen and liquid hydrogen as the fuel. This algorithm includes tankage, gas generator, pumps, gearboxes, and the turbine.

$$\begin{aligned} \text{TURBINE SYS WEIGHT} &= 6991 \left\{ .262 + .738 \left( \frac{\text{HP}}{5000} \right) \right\} \\ &\times \left\{ 1.5 - .5 \left( \frac{\text{RPM}}{12000} \right)^{.556} \right\} \times \left\{ .265 + .735 \left( \frac{T}{1000} \right) \right\} \\ &\times \left\{ .9824 + .0176 \left( \frac{\text{NS}}{10} \right) \right\} \text{ LBS.} \end{aligned}$$

Where: HP = turbine shaft horsepower

RPM = turbine shaft speed

T = total run time (Sec.)

NS = number of starts during T

The second algorithm is for the specific weight of conventional round rotor alternators. This algorithm was derived from 77 detailed designs.

$$\begin{aligned} \text{LBS/KW} &= .157 \left\{ 1.28 - .26 \left( \frac{P}{5} \right)^{.449} \right\} \times \\ &\left\{ -.06 + 1.06 \left( \frac{\text{RPM}}{14000} \right)^{-.6205} \right\} \times \\ &\left\{ .8567 + .1433 \left( \frac{V}{3} \right) \right\} \end{aligned}$$

Where: P = power output (KW)

RPM = rotor speed

V = terminal voltage (KV<sub>L-L</sub>)

#### Development of Computer Program

A computer program that automatically arranges the summary algorithms into possible system configurations was developed for the study reported in this paper. Of particular importance in a study such

as this is the propagation of inefficiencies through the system. The program must recognize that the input power demanded by a component is that component's output power plus the power lost to inefficiencies within the component. Figure 1 is a flow chart of the computer program as it presently exists.

#### Results of System Study

A study was made to find the lightest system configuration that satisfies the following conditions:

Main Power - 5 MW electrical  
Aux. Power - .5 MW electrical  
Voltage - 100 KVDC - 100 KVDC  
Run Time - 500 sec. - 1400 sec.

The three power sources considered were fuel cells, turbine with conventional alternator, and turbine with permanent magnet alternator. Power conditioning components considered included transformers, rectifiers, and inverters. Figures 2 and 3 depict the possible systems configurations that meet the requirements. There are nine possible combinations of components, as listed in Table 1.

The object of the study was to find the lightest weight system from those of Table 1. Since the computer must use efficiencies, the following efficiencies were assumed:

Filters - 99.9%  
Rectifiers - 95%  
Transformers - 97%  
Inverters - 85%  
Alternators - 95%

The power levels and voltage ranges are fixed; therefore, the variables include turbine alternator speeds and inverter frequencies. Figures 4 thru 7 show results of the study. The minimum weight system, from Figure 5, is a turbine driven permanent magnet alternator with transformer/rectifier power conditioners in both power channels. The alternator frequency is 2.2 KHZ. Figure 6 indicates that a 100% variation of the inverter frequency causes less than 100 pounds difference in the weights of systems 7, 8, and 9. Figure 7 indicates negligible impact on system weight for

60Kv change in the output voltage.

TABLE 1  
SYSTEM CONFIGURATIONS

SYSTEM	SOURCE	MAIN CHANNEL	AUX. CHANNEL
1	Gen. Alt.	Trans.-Rect.	Trans.-Rect.
2	FM Alt.	Trans.-Rect.	Trans.-Rect.
3	Conv Alt.	Trans.-Rect.	Inverter
4	FM Alt.	Trans.-Rect.	Inverter
5	Conv Alt.	Inverter	Trans.-Rect.
6	FM Alt.	Inverter	Trans.-Rect.
7	Conv Alt.	Inverter	Inverter
8	FM Alt.	Inverter	Inverter
9	Fuel Cell	Inverter	Inverter

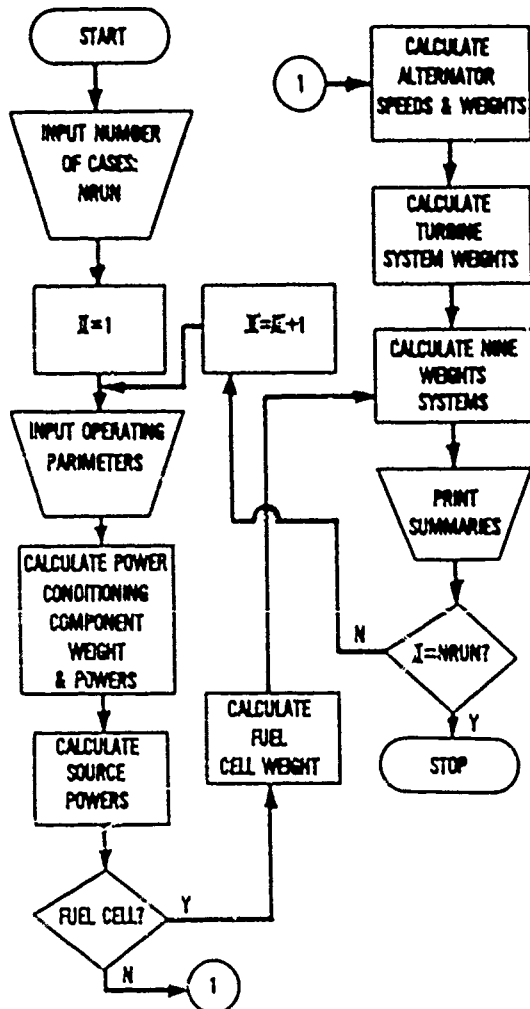


Fig. 1 Flow Chart of Prog. to Cal. Sys. Weights

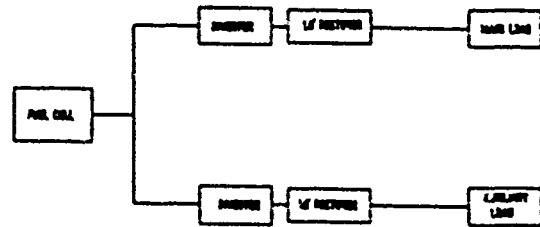


Fig. 2 System Using Fuel Cell Source

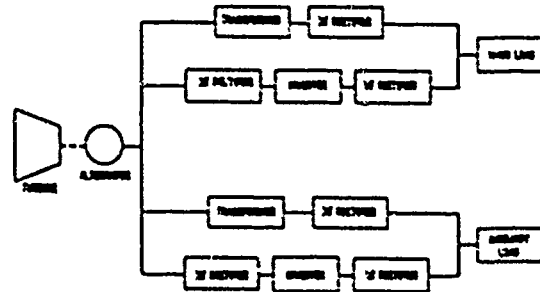


Fig. 3 Systems Using Turbine/Alternator Sources

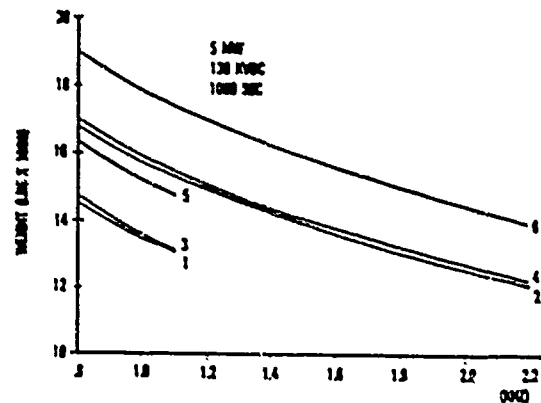


Fig. 4 System Weights as a Function of Alternator Frequency

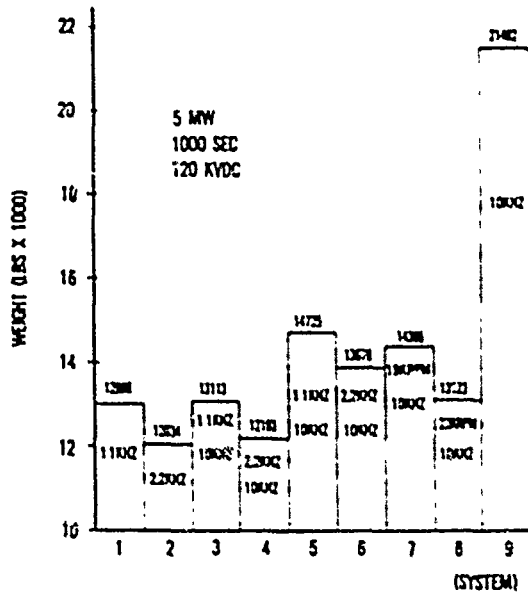


Fig. 6 Minimum Weight Systems

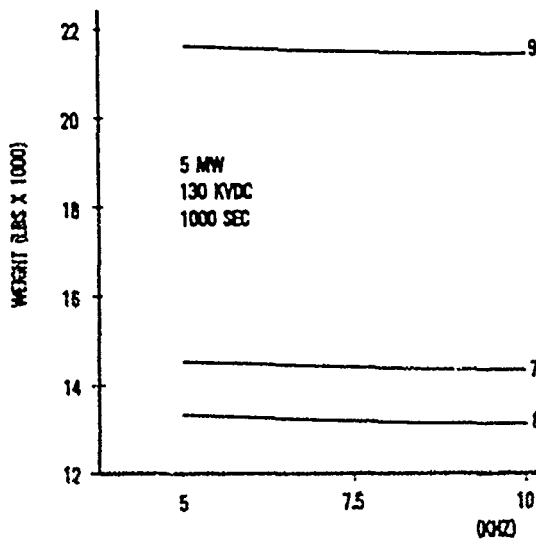


Fig. 7 System Weights as a Function of Inverter Frequency

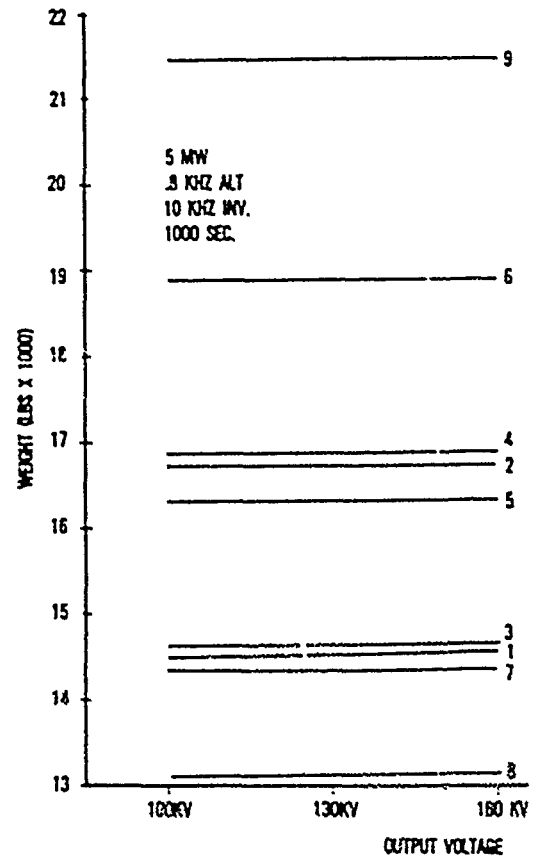


Fig. 8 System Weight as a Function of Output Voltage

## A COMPUTERIZED MEASURING SYSTEM FOR NANOSECOND RISETIME PULSED ACCELERATORS\*

D. Pellinen, S. Ashby, P. Gillis, K. Nielson and P. Spence

Physics International Company  
2700 Merced Street  
San Leandro, California 94577

Abstract

We have developed a new computerized diagnostic system for high voltage, high current pulsed. This diagnostic system uses electronic circuits connected to nanosecond response transducers to measure machine performance at critical points. The voltage outputs of these circuits are converted to digital form and directly read by a computer. The major advantages of this system are cost effectiveness and greater accuracy than commonly used oscilloscope or transient analyzer systems in applications where it is not necessary to record full analog diagnostic waveforms. Operation is fully computerized and requires a minimum number of personnel; the system is scalable to very large multi-module generators.

Historically, pulsed accelerators have been diagnosed by placing a sensor in an accelerator, connecting the sensor to a cathode ray oscilloscope by a coaxial cable, and photographing the resulting waveform. The data were reduced by measuring key amplitudes or times, or by manually digitizing the photograph. Although computerized digitizers and waveform analyzers were an improvement, they basically were still the same as oscilloscopes, but read out digitally. These methods were adequate when pulsed consisted of only a few modules with single switches. The current trend is toward very large pulsed with multiple switches or toward machines with many modules.<sup>1,2,3</sup> On these newer machines the requirements for synchronous operation are considerably more severe, and the number of channels for diagnostics must be far greater than

previously used. The use of oscilloscopes or transient analyzers would be very costly on these large systems and would provide an unmanageable mountain of data to analyze.

For these reasons, we have developed a new computerized diagnostic system for the pulsed modules on one such large system, the modular bremsstrahlung source (MBS). This diagnostic system uses electronic circuits to measure machine performance at critical points. The voltage outputs of these circuits are converted to digital form and directly read by a computer. The major advantages of this system are:

1. A single data channel can be completely implemented for about \$100 compared with ~ \$20 K for a transient analyzer.
2. The system is more accurate than an oscilloscope or transient analyzer.
3. Operation is fully computerized and requires a minimum number of personnel to operate.
4. The system is scalable to very large multi-module generators.

The approach used was to locate areas where problems could occur in the MBS modules and place appropriate nanosecond response transducers, such as voltage and current sensors, at these locations. These sensors are connected to circuits that will record and hold the parameter we are measuring, such as time, a peak amplitude, or an integral of a voltage. The data are converted to digital form, read, and processed by a digital computer.

We assembled a prototype system of this sort

---

\*Work supported by Defense Nuclear Agency.

using commercial CAMAC<sup>4</sup> equipment and tested it on the MBS module under development. Additional diagnostic system data were collected for approximately two months while the diagnostic system ran automatically under computer control. We found that by using good grounding and shielding techniques, we could use conventional inexpensive hardwired connections to transmit fast signals without causing spurious responses or damage to the circuitry or computer.

The two circuits used were a time-to-digital converter and a gated charge integrating module with an analog-to-digital converter. Specifications for the instruments are shown in Table 1. The assembled system is shown in Figure 1.

We will illustrate the operation of the system with data from seven consecutive pulses on MBS (Figure 2). These seven shots were selected since they show two distinct diode impedance conditions, and three of the shots show diode insulator flashes. Also, photos overlaying

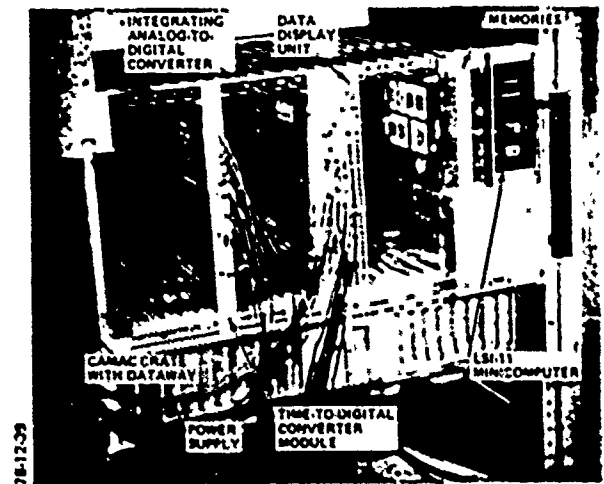


Figure 1 Prototype CAMAC data acquisition system.

Table 1

CONVERTER RESPONSE

Device	Resolution	Linearity
Time-to-Digital Converter	11 bits (1/2048) 50 PS, 100 PS or 250 PS switchable	$\pm 2$ counts ( $\pm 0.1\%$ )
Analog-to-Digital Converter	10 bits (1/1024) (0.256 picocoulomb)	$9.25\% \pm 2$ counts

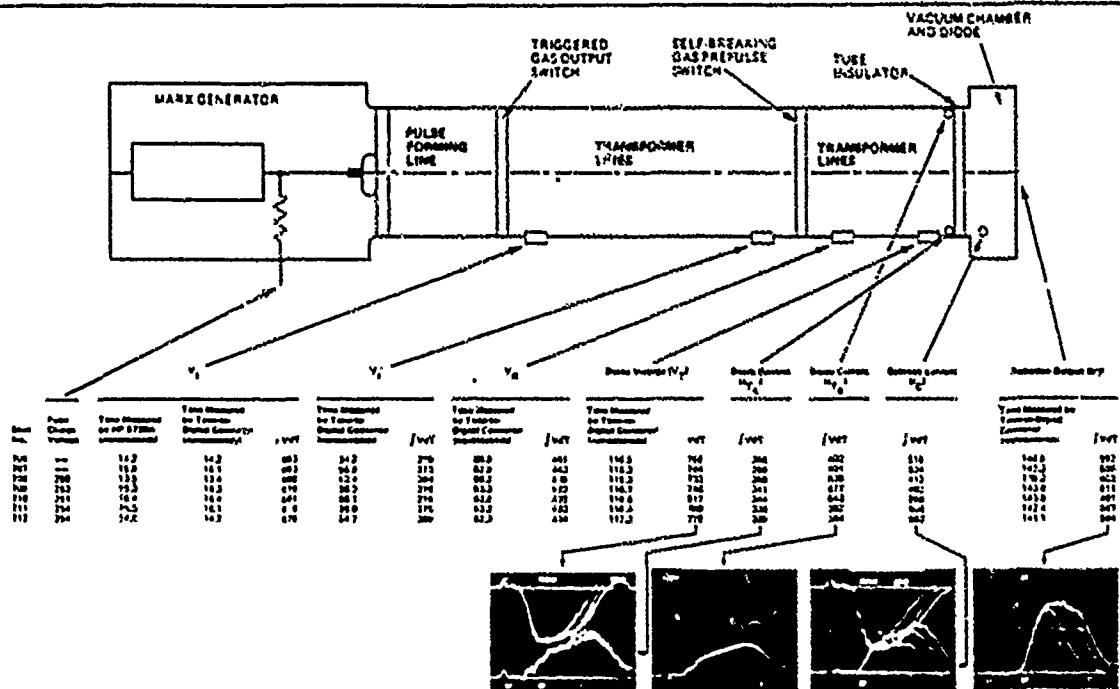


Figure 2 Summary of data from MBS pulses 706 to 712.

oscilloscope traces were taken, illustrating the insulator flashes.

The table in Figure 2 shows the output of the electronic sensors—the time in nanoseconds after the trigger and the integral of the pulse for every trace except the pulse charge. The integrals are in arbitrary units, since we did not fold in calibration factors on the sensors. Shots 706 and 707 are normal shots with a time spread of 1.5 to 2.0 ns between the pulses. The diode was opened at this point and readjusted. Shots 708, 709, and 710 show an insulator flash in the vicinity of current monitor 8. Shots 711 and 712 are normal shots obtained at a slightly higher diode impedance.

Below the tabulated data are overlays of oscilloscope traces from pulses 709 through 712. There is little difference between the tabulated integrals for  $V_{PC}$ ,  $V_1$ , and  $V_2$ . At first glance, the oscilloscope traces appear to be from one pulse, and the deviation on the integrals about 1/2 percent. The oscilloscope photo for  $V_2$  shows three distinct traces having the same peak amplitude, but beginning to drop to the baseline at different times. The wider trace appears brighter and is probably an overlay of traces 711 and 712. The integrals of  $V_2$  on shots 709 and 710 are indeed lower than those on shots 711 and 712.  $I_m$ , the current on one-half the diode shows little change both on the oscilloscope waveforms and digital outputs; however,  $I_m$  shows a much enlarged digital output on shots 709 and 710. The oscilloscope traces show one heavy normal trace which is an overlay of pulses 711 and 712 and two lighter traces diverging to higher amplitudes about 25 and 35 nanoseconds into the pulse.  $I_C$ , the current monitor on the diode past the diode insulator, shows a drop in the integral of the current on pulses 709 and 710 from readings on pulses 711 and 712, indicating a loss prior to the anode-cathode gap. The  $I_C$  waveform shows a bright, high-amplitude trace representing normal

shots 711 and 712 and two distinct shorter lower-amplitude pulses.

The radiation diagnostics show correspondingly low outputs on pulses 709 and 710. There are no oscilloscope traces shown for shots 706 and 707, but they were normal shots with slightly lower voltage amplitudes as are the digital outputs. This condition implies a lower mean voltage, which probably caused the radiation outputs to be 13 percent lower than on shots 711 and 712.

Timing and synchronization of modules is important for a pulser such as MBS. We use a "time-to-digital" converter to measure the time between the trigger pulse and the output pulse flowing in the line or radiation appearing at the target. The first two columns of Table 2 show a

Table 2  
NORMALIZED DATA FROM SHOTS 706 TO 712

	Delay, Trigger to $V_2$ (nanoseconds)		Radiation Output (nanoseconds)
	HP 3730A	Time-to-Digital Converter	
Mean Time Delay	15.33	15.31	141.7
Standard Deviation	1.23	1.21	1.35
Variance	1.56	1.56	1.57

comparison of results for the time interval between the trigger and output voltage pulse in the line. The deviation between the measurements on the two detectors is a few tenths of nanoseconds. The timing data on voltage and radiation outputs follow. A further check on our timing methods is to measure the difference in time between monitors fixed in the line with no intervening switches. The standard deviation ( $\sigma$ ) between pulse arrival time at  $V_2$  and  $V_2'$  on these seven pulses was 3.122 ns. Our quantizing error was  $\pm 0.1$  ns. These checks are stringent tests, since signals actually come from detectors on the pulser and are passed through the entire signal handling system.



## REFERENCES

1. T. H. Martin, D. L. Johnson, and D. H. McDaniel, Proceedings of the 2nd International Topical Conference on High Power Electron and Ion Beam Research and Technology, Laboratory of Plasma Studies, Cornell University, Ithaca, N.Y., 807-15 (1977).
2. G. Yonas, Scientific American, 239, 50 (1978).
3. T. H. Martin, et al., Proceedings of the 2nd IEEE International Pulsed Power Conference, Lubbock, Texas, June 1979.
4. The Standards for CAMAC are defined by the following Standards, IEEE Standards Office, New York.
  - IEEE Standard 583-1975
  - IEEE Standard 595-1976
  - IEEE Standard 596-1976
  - IEEE Standard 682-1976

## A 33-GVA INTERRUPTER TEST FACILITY\*

W. M. Parsons, E. M. Honig, and R. W. Warren<sup>†</sup>

Los Alamos Scientific Laboratory

ABSTRACT

The use of commercial ac circuit breakers for dc switching operations requires that they be evaluated to determine their dc limitations. Two 2.4-GVA facilities have been constructed and used for this purpose at LASL during the last several years. In response to the increased demands on switching technology, a 33-GVA facility has been constructed. Novel features incorporated into this facility include (1) separate capacitive and cryogenic inductive energy storage systems, (2) fiber-optic controls and optically-coupled data links, and (3) digital data acquisition systems. Facility details and planned tests on an experimental rod-array vacuum interrupter are presented.

INTRODUCTION

Since 1975 the Los Alamos Scientific Laboratory (LASL) has been conducting experiments with commercial ac circuit breakers to determine their direct-current ratings for potential application in various fusion devices.<sup>1,2</sup> Particular attention has been paid to the vacuum interrupter due to its low cost, mechanical simplicity, and its ruggedness. Because of these advantages, fusion experiments such as Alcator, TFTR, and Doublet III utilize vacuum interrupters in their switching systems. Interrupters used in both TFTR and Doublet III require current interruption in the 25 kA to 30 kA range with as-

sociated recovery voltages of 20 kV to 25 kV. Preliminary designs for larger devices such as ETF indicate that a trend towards higher currents may be economical if low-cost switching systems exist that can satisfy the interruption requirements. For this reason a facility has been constructed at LASL which is capable of evaluating circuit breakers for application in the next generation of fusion experiments.

PRESENT TEST FACILITIES

In addition to the facility discussed in this paper, two smaller facilities are presently used for interrupter testing.<sup>3</sup> These facilities are essentially identical and are rated at 2.4 GVA each. They can be connected in parallel for high-current tests, or operated independently for tests up to 40 kA. The new 33-GVA facility will be capable of tests as high as 280 kA. A summary of the facilities ratings is given in Table I.

TABLE I.  
SUMMARY OF FACILITIES RATINGS

	<u>FACILITY</u>		
	<u>A</u>	<u>B</u>	<u>C</u>
Peak power	2.4	2.4	33.6
Stored energy (kJ)	450	450	2250
Rated current (kA)	40	40	280
Max. recovery voltage (kV)	60	60	120
Completion date	1975	1977	1979

\*Industrial Staff Member for Westinghouse Research Laboratory

<sup>†</sup>Work performed under the auspices of the U.S. Department of Energy

## FACILITY DETAILS

**Energy Storage Systems.** The facility is unique in that it has two independent primary energy storage systems. The first is a capacitive system, the second is a cryogenic inductor system.

The capacitive system consists of seven modules, each containing 270 kJ of 20 kV capacitors, a four-segment 60-kA inductor, two independent shorting systems, fuses, and associated hardware. A schematic and photograph of a storage module are shown in Figs. 1 and 2.

Current is initiated in inductor L, and the load by discharging capacitor C through ignitron  $I_{g1}$ . At peak current, self-firing ignitrons  $I_{g2}$  and  $I_{g3}$  crowbar the capacitor thereby preventing oscillation. The current trapped in the inductor now serves as the load current for the switch under test.

Figure 3 is a schematic showing a typical test circuit which uses these storage modules. The load current supplied by inductors L circulates through the test breaker,  $B_T$ , and its saturable reactor,  $L_{SR}$ . The breaker is then opened. A counterpulse from capacitors  $C_2$  brings the current in the breaker to zero where it interrupts. The residual energy in L is transferred to  $C_2$ , generating a recovery voltage across the test breaker. Figure 4 is a photograph of the seven storage modules during construction.

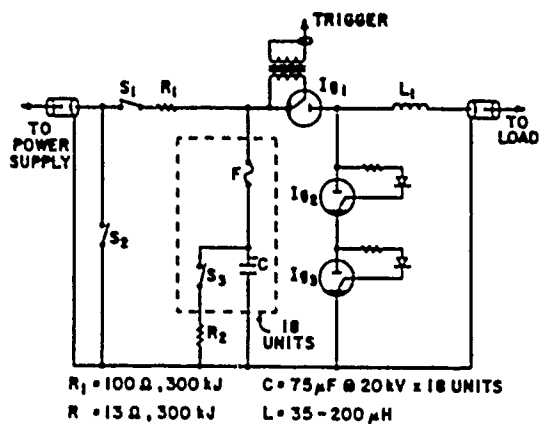


Fig. 1. Capacitive storage module schematic.



Fig. 2. Capacitive storage module photograph.

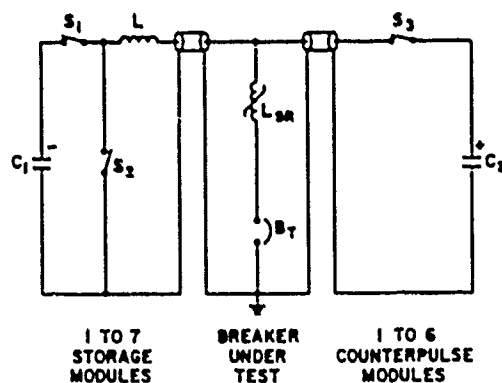


Fig. 3. Typical test circuit which uses storage modules.

The second energy storage system consists of six cryogenic inductors, which operate in a liquid  $N_2$  bath at 80 K. These are charged externally by a 40-kA 12-V power supply. A test circuit which uses this scheme is shown in Fig. 5.

This test circuit is specifically designed to simulate the higher  $I^2t$  duty seen by an interrupter in the poloidal field coil system of a fusion device. In this circuit, current in cryo-inductor L and test breaker  $B_T$  is ramped up



Fig. 4. Capacitive storage modules during construction.

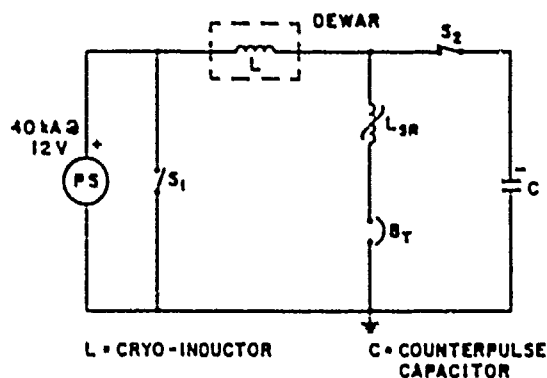


Fig. 5. Test circuit with cryogenic inductors.

by the dc power supply. At full current the power supply is turned off and switch  $S_1$  closed. The test breaker opens, current is commutated, and the residual energy in  $L$  is transferred to  $C$  as in the previous scheme using capacitive storage. The total energy in this system is small compared to the capacitive system and will only be used for specialized tests.

**Counterpulse System.** The counterpulse system used with either storage system consists of six modules, each containing 300  $\mu\text{F}$  of 20-kV capacitors. Each module has an independent shorting system and start ignitron. A schematic and photograph are shown in Figs. 6 and 7.

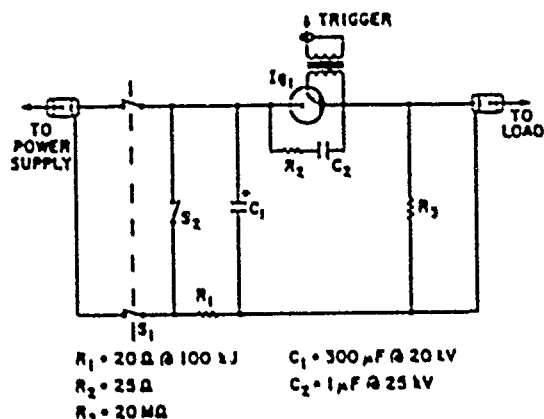


Fig. 6. Counterpulse module, schematic.

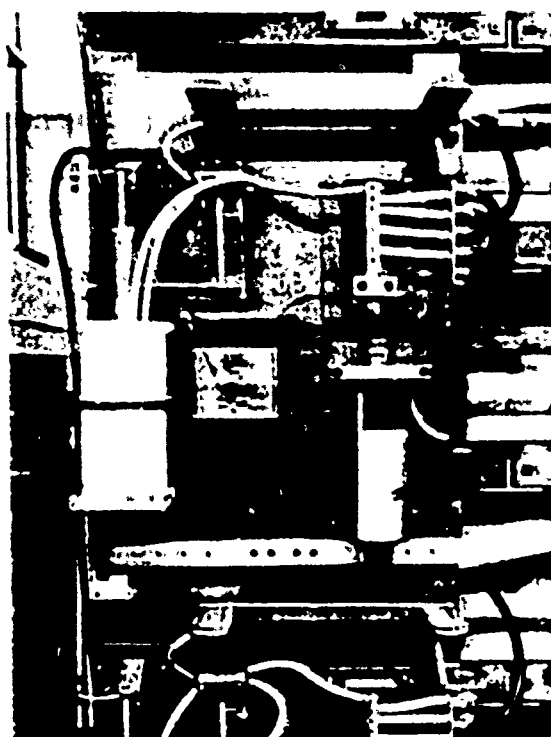


Fig. 7. Counterpulse module photograph.

These six modules can be connected in a series, a series-parallel, or a parallel arrangement depending on the capacitance and recovery voltage requirements for a particular set of tests.  $S_1$  represents a DPST charging switch with 150-kV isolation between all contacts. This switch allows the counterpulse bank to be operated as a Marx generator where the modules are charged in parallel with a 20-kV power supply

and then discharged in series at voltages up to 120 kV. Also, provisions have been made on each counterpulse modules for the connection of up to 300  $\mu$ F of additional capacitance. This will be necessary in certain experiments, such as early counterpulsing, which require an unusually large counterpulse bank. The six counterpulse modules are pictured in Fig. 8.

Control System. The control system for the 33-GVA facility is a hybrid electrical-optical-pneumatic system with emphasis on the optical segment. Slow commands, such as shorting switches, isolation switches, and power supply signals, are transmitted electrically from the main control station to a midstation located just inside the facility doors. Here they are converted to optical signals which branch out to the various modules. At the modules these optical signals then operate electrical and pneumatic devices.

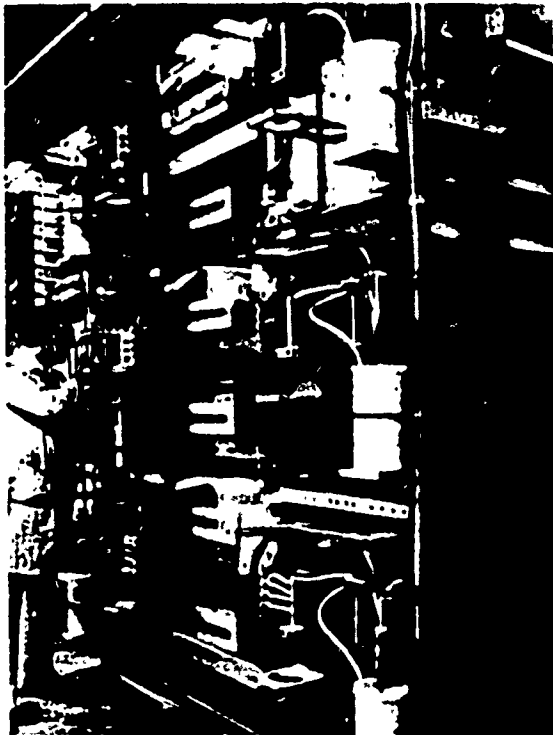


Fig. 8. Counterpulse modules under construction.

All fast commands for triggering ignitrons and breaker actuators originate at the control main station from a fifteen-channel digital delay generator. These triggers are immediately converted to optical pulses and transmitted via fiber-optic cables to high-voltage pulsers or actuator drivers located within the test facility. Power supply charging voltages and currents are converted to FM signals in the test facility and then transmitted optically to the main control station. Here they are demodulated and used to operate meters. This intense use of optical signals in high emf areas is of great benefit in the avoidance of ground loops and in the protection of personnel and sensitive control equipment.

Data Acquisition. Voltage and current waveforms are measured by voltage dividers and noninductive shunts in the test facility and converted to analog light signals. The analog light signals are transmitted on fiber-optic cables to the main control area where they are converted back to analog electrical signals. These signals are fed into digital oscilloscopes where they can be viewed. A small computer is also connected to the oscilloscopes and is capable of performing routine data analysis as well as storing waveforms on magnetic tape.

#### UPCOMING TESTS ON AN EXPERIMENTAL ROD-ARRAY VACUUM INTERRUPTER

The first breaker testing in the 33-GVA facility is planned for September, 1979. The interrupter to be tested is an experimental interrupter made by the General Electric Company. The device is referred to as a rod-array vacuum interrupter due to a novel internal geometry and shown promise of interrupting unusually large currents because of its ability to maintain a diffuse arc.<sup>4</sup>

Figure 9 is a general schematic of the circuit to be used in testing this interrupter. This circuit differs from the standard circuit of Fig. 3 in that each module now contains a saturable reactor and a vacuum interrupter in its primary discharge leg. After the test breaker,

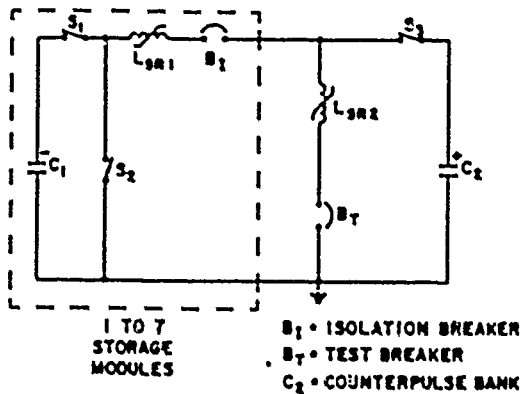


Fig. 9. Test circuit for experimental G.E. interrupter.

$B_1$  has interrupted the load current, the energy in the load coil and saturable reactor,  $LSR_1$ , is transferred to the counterpulse capacitor,  $C_2$ . At the instant of complete transfer, which is a current zero for  $B_1$  and  $LSR_1$ ,  $B_1$  interrupts. This prevents further oscillation of  $LSR_1$  and  $C_2$ , thereby holding the recovery voltage on  $C_2$  and  $B_1$ . A waveform for this type of test is shown in Fig. 10.

The recovery voltage will be maintain on the test breaker for 50 to 100 ms. This simulates intended use in tokamak systems and insures that the interrupter has fully recovered its dielectric strength.

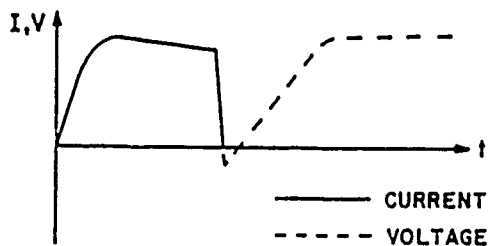


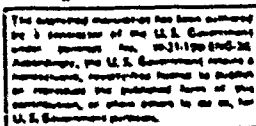
Fig. 10. Waveforms for experimental G.E. interrupter test.

## CONCLUSIONS

A 33-GVA interrupter test facility has been constructed which is capable of testing interrupters for the next generation of experimental fusion devices. The facility is capable of producing currents of 280 kA with associated recovery voltages of 120 kV. Tests are planned on an experimental G.E. interrupter.

## REFERENCES

1. C. E. Swannack, R. A. Haarman, J. D. G. Lindsay, and D. M. Weldon, "HVDC Interrupter Experiments for Large Magnetic Energy Transfer and Storage (NETS) Systems," Proc. 6th Symp. Eng. Problems of Fusion Res., San Diego, CA, Nov. 18-21, 1975; IEEE Pub. No. 75CH 1097-5 NPS, 662, (1976).
2. R. Warren, M. Parsons, E. Honig, and J. Lindsay, "Tests of Vacuum Interrupters for the Tokamak Fusion Test Reactor," Informal report LA-7759-MS, April 1979.
3. E. M. Honig, "Dual 30-kA, HVDC Interrupter Test Facility", Proc. 7th Symp. Eng. Problems of Fusion Res., Knoxville, TN., 35-28 October 1977; IEEE Pub. No. 77CH 1267-4-NPS.
4. J. A. Rich and C. P. Goudy, "Diffuse Vacuum Arcs," Conf. Records of IEEE 1977 International Conf. on Plasma Science, Troy, NY, May 23-25, 1977; IEEE Pub. No. 77CH 1205-4-NPS.



## ANALYSIS OF THE MULTIPHASE INDUCTOR-CONVERTER BRIDGE\*

Mehrdad Ehsani,<sup>†</sup> Robert L. Kustom, and Raymond E. FujaArgonne National Laboratory  
Argonne, Illinois 60439Abstract

Analytical derivations are presented for inductor-converter bridge (ICB) circuits in which energy is transferred from a storage inductor to a load inductor with solid state bridges. These derivations provide complete analytical circuit solution in contrast to previously available numerical (non-analytical) procedures. The analysis is based on two parallel methods: (1) Fourier expansion of the inverter waveforms and (2) a novel method based on the inherent waveforms of the ICB, labeled square functions. Our analytical values of power flow, inductor currents, and voltages compare favorably with the results of a three-phase ICB experiment at Argonne National Laboratory.

Introduction

The inductor-converter bridge (ICB) is a solid state dc-ac-dc converter system for reversible energy transfer between two inductors. This system is especially suitable for pulsed power supply applications greater than several hundred megawatts and durations from a fraction of a second to many seconds. Two such applications are the superconductive equilibrium field coils of the projected tokamak fusion power reactors and superconductive magnets to be used in future particle accelerators.

The ICB system is inherently efficient, controllable in real time and allows isolation of large

pulsed reactive loads from the power grid. Thus, only the average system losses are drawn from the grid.

Operation of the ICB Circuit

Detailed operation of the ICB may be found in references 1 and 2. Figure 1 shows a three-phase ICB where the storage and the load coil is represented by  $L_S$  and  $L_L$ , respectively. At a typical instant during the energy transfer, dc currents  $i_S$  and  $i_L$  will be flowing in the storage and load coils, respectively. The SCR's of the left hand side (storage side) are fired in the normal Graetz bridge sequence:  $S_{L1} S_{L5}$ ,  $S_{L1} S_{L6}$ ,  $S_{L2} S_{L6}$ ,  $S_{L2} S_{L4}$ ,  $S_{L3} S_{L4}$ ,  $S_{L3} S_{L5}$ ,  $S_{L1} S_{L5}$ , .... The SCR's of the right-hand side (load side) follow the same sequence but may be out of step with respect to the storage side. The direction and the level of power flow is determined by the relative timing between the source and the load bridge switching sequences such that a load bridge lead will cause power flow into the load and vice versa. The Y-connected capacitors in the middle serve as the intermediate energy store between the storage and load coils and they provide the reverse voltages to commutate the inductor circuits from one SCR to the next. Thus, no external counterpulse circuit is needed.

Only a very small fraction of each coil energy is extracted in each bridge cycle. Therefore, by varying the relative timing between the source and load switching sequences and/or the frequency of operation, very fine control over the rate of energy transfer can be achieved. The functional dependence of the power on the relative timing

\*Work supported by the U.S. Department of Energy.

<sup>†</sup>Also at the University of Wisconsin.

(relative phase difference) and the frequency will be illustrated in the following sections.

#### Circuit Analysis Based on Fourier Components

Figure 2 shows an  $m$ -phase ICB. For this analysis, the SCR's have been replaced by ideal switches. This idealization implies a lossless system and operation within the successful commutation bounds. Since each bridge cycle changes the coil energies by a very small amount, the inductor currents are nearly constant in one cycle. Viewing such inductor-converter half from the  $m$ -phase ac lines, one will see an  $m$ -phase square wave current source system, each phase being  $\frac{2\pi}{m}$  radians displaced from the next and the wave amplitude being equal to the instantaneous coil current, Fig. 3. Since the average power is divided equally between the phases, it may be calculated from a one-phase diagram, Fig. 4.

The calculated instantaneous average power from the left-hand source (storage) to the right-hand source (load) is

$$\langle p_{Sa}(t) \rangle = \sum_n \frac{1}{2n\omega C} (a_{nSa} b_{nLa} - b_{nSa} a_{nLa})$$

where the  $a$ 's and  $b$ 's are the Fourier coefficients of the storage and load source waveforms as indicated by the subscripts. For illustration, the Fourier coefficients of the symmetrical waveform of Fig. 5 which is for when  $m$  is odd will be used.

$$\begin{cases} i_{Sa}(t) = \sum_n \frac{2I_S}{\pi n} \left[ 1 - (-1)^n \right] \sin \frac{n\pi}{m} \cos n\omega t \\ i_{La}(t) = \sum_n \frac{2I_L}{\pi n} \left[ 1 - (-1)^n \right] \sin \frac{n\pi}{m} \cos n(\omega t + \alpha) \end{cases}$$

where  $\alpha$  is the angle by which the load bridge leads the storage bridge. After substitution, the average power per phase will simplify to

$$\langle p_{Sa}(t) \rangle = \sum_n \frac{2I_S I_L}{\pi^2 n^2 \omega C} \left[ 1 - (-1)^n \right]^2 \left( \sin \frac{n\pi}{m} \right)^2 \sin n\alpha$$

The total instantaneous average power delivered from the storage coil is  $m$  times the above, or

$$\langle p_S(t) \rangle = \sum_n \frac{2m I_S I_L}{\pi^2 n^2 \omega C} \left[ 1 - (-1)^n \right]^2 \left( \sin \frac{n\pi}{m} \right)^2 \sin n\alpha$$

The effect of the relative phase,  $\alpha$ , and the bridge switching frequency,  $\omega$ , on the power flow is evident in the above relationship. Note also that the contribution of higher harmonics is attenuated by the  $\frac{1}{n^2}$  term. Figure 6 represents the plot of the instantaneous average power as a function of  $\alpha$  with the number of phases,  $m$ , as the parameter. For  $m = 3$ , over 99.5% of the net power is delivered by the fundamental frequency, making the  $m = 3$  curve in Fig. 6 almost purely sinusoidal.

The time functions of average coil currents, power, and voltages may now be calculated. For simplicity, let

$$k = \sum_n \frac{2m}{\pi^2 n^2 \omega C} \left[ 1 - (-1)^n \right]^2 \left( \sin \frac{n\pi}{m} \right)^2 \sin n\alpha$$

Then from

$$\langle p_S(t) \rangle = -\frac{d}{dt} \frac{E_S(t)}{C} = \frac{d}{dt} \frac{E_L(t)}{C}$$

$$\begin{cases} k \langle i_S \rangle \langle i_L \rangle = -\frac{d}{dt} \left( \frac{1}{2} L_S \langle i_S \rangle^2 \right) \\ k \langle i_S \rangle \langle i_L \rangle = \frac{d}{dt} \left( \frac{1}{2} L_L \langle i_L \rangle^2 \right) \end{cases}$$

Solving these equations with the initial conditions

$$\begin{cases} i_S|_{t=0} = I_0 = \text{initial storage current} \\ i_L|_{t=0} = 0 \end{cases}$$

we obtain



$$\begin{cases} \langle i_S \rangle (\tau) = I_0 \cos \frac{K}{\sqrt{L_S L_L}} \tau \\ \langle i_L \rangle (\tau) = I_0 \sqrt{\frac{L_S}{L_L}} \sin \frac{K}{\sqrt{L_S L_L}} \tau. \end{cases}$$

The average power will become

$$\langle p_S \rangle (\tau) = 1/2 K I_0^2 \sqrt{\frac{L_S}{L_L}} \sin \frac{2K}{\sqrt{L_S L_L}} \tau$$

and the average coil voltages from

$$\begin{cases} \langle v_S \rangle (\tau) = K I_0 \sqrt{\frac{L_S}{L_L}} \sin \frac{k}{\sqrt{L_S L_L}} \tau \\ \langle v_L \rangle (\tau) = K I_0 \cos \frac{k}{\sqrt{L_S L_L}} \tau \end{cases}$$

#### Circuit Analysis Based on Square Function

##### Calculations

The preceding Fourier method shows the influence of harmonics in the system. However, for real time control, solving the equations of the form

$$\langle p \rangle = \sum_n i_n(\alpha)$$

for  $\alpha$  is time consuming and possibly inaccurate. The following technique will provide closed form equations that are efficiently solved by a microcomputer in real time control.

The calculations are based on specially tailored functions symbolized by Sq (X) and Tr (X), Fig. 7. These waveforms are inherent in the operation of the ICB circuits. The Sq function is a good mathematical representation of the ac phase currents of the system. The Tr function is the integral form of Sq and is a good representation of the capacitor voltages due to the phase currents. A brief mathematical development of the Sq and Tr functions is presented in the Appendix.

Figure 8 shows how a phase current of the equivalent three-phase circuit may be decomposed into two Sq functions. Thus, the currents  $i_{Sa}$  and  $i_{La}$  of Fig. 4 may be written as

$$\begin{cases} i_{Sa}(\tau) = \frac{I_S}{2} \left[ \text{Sq} \left( \tau + \frac{T}{6} - \tau_0 \right) + \text{Sq} \left( \tau - \tau_0 \right) \right] \\ i_{La}(\tau) = \frac{I_L}{2} \left[ \text{Sq} \left( \tau + \frac{T}{6} \right) + \text{Sq}(\tau) \right], \end{cases}$$

$$0 \leq \tau \leq T, 0 \leq \tau \leq T, 0 \leq \tau \leq 1/2$$

where  $\tau_0$  is the relative lag time of the storage bridge.

These current representations for one period are adequate for instantaneous average power calculations. The net power out of storage per phase, results from the interaction of  $i_{Sa}$  and  $v_{La}$ , the capacitor voltage due to the load phase current:

$$v_{La}(\tau) = \frac{1}{C} \int_0^\tau i_{La} d\tau = \frac{I_L}{2C} \left[ \text{Tr} \left( \tau + \frac{T}{6} \right) + \text{Tr}(\tau) \right].$$

This power is

$$\begin{aligned} p_{Sa}(\tau) = i_{Sa} v_{La} = \frac{I_S I_L}{4C} & \left[ \text{Sq} \left( \tau + \frac{T}{6} - \tau_0 \right) \cdot \text{Tr} \left( \tau + \frac{T}{6} \right) \right. \\ & + \text{Sq} \left( \tau + \frac{T}{6} - \tau_0 \right) \cdot \text{Tr}(\tau) + \text{Sq}(\tau - \tau_0) \\ & \left. \cdot \text{Tr} \left( \tau + \frac{T}{6} \right) + \text{Sq}(\tau - \tau_0) \cdot \text{Tr}(\tau) \right]. \end{aligned}$$

The instantaneous average power per phase is

$$\begin{aligned} \langle p_{Sa} \rangle = \frac{1}{T} \int_0^T i_{Sa} v_{La} dt = \frac{I_S I_L}{4TC} & \int_0^T \left[ \text{Sq} \left( \tau + \frac{T}{6} - \tau_0 \right) \right. \\ & \cdot \text{Tr} \left( \tau + \frac{T}{6} \right) + \text{Sq} \left( \tau + \frac{T}{6} - \tau_0 \right) \cdot \text{Tr}(\tau) + \\ & \text{Sq}(\tau - \tau_0) \cdot \text{Tr} \left( \tau + \frac{T}{6} \right) + \text{Sq}(\tau - \tau_0) \\ & \left. \cdot \text{Tr}(\tau) \right] d\tau. \end{aligned}$$

The four terms in the integrand are first transformed to the normalized variable functions shown in the Appendix, then each term is evaluated by using the proper integral identity in the Appendix. The result is then multiplied by three for the total three-phase power

$$\langle p_{sa} \rangle = \begin{cases} \frac{T I_S I_L}{C} (2 \gamma_0 - 3 \gamma_0^2), & 0 \leq \gamma \leq \frac{1}{6} \\ \frac{T I_S I_L}{C} (3 \gamma_0 - 6 \gamma_0^2 - \frac{1}{12}), & \frac{1}{6} \leq \gamma \leq \frac{1}{3} \\ \frac{T I_S I_L}{C} (\gamma_0 - 3 \gamma_0^2 + \frac{1}{4}), & \frac{1}{3} \leq \gamma \leq \frac{1}{2} \end{cases}$$

where  $\gamma_0 = \frac{\tau_0}{T} = \frac{\alpha}{360}$  is the normalized lag time of the storage bridge relative to the load bridge and the frequency is represented by the period  $T$ . This is the closed form of the  $\langle p \rangle$  vs  $\alpha$  curve for  $n = 3$  in Fig. 6. The time functions of the average coil currents, power and voltages may be calculated as before. The only difference being that  $K(\gamma_0)$  is in closed form.

Expressing the actual circuit waveforms analytically, allows other useful calculations such as the actual capacitor voltages throughout the transfer cycle, the study of commutation throughout the cycle, and the actual coil voltages and instantaneous currents, without resorting to numerical procedures.

#### Comparison with Test Results

A model three-phase ICB has been built and tested at Argonne National Laboratory. This system uses two identical superconducting coils capable of storing 125 kJ at 250 A, as the storage and load inductors. Other system parameters are:

$$L_S = L_L = 4 \text{ H}, I_0 = 100 \text{ A}$$

$$C = 10^{-6} \text{ F}, \quad \alpha = 90^\circ$$

$$\omega = 4084 \text{ rad/s}$$

The system equations are derived from substitution of these parameters and  $n = 3$  into the time functions shown in the Fourier analysis section:

$$\langle i_S \rangle(t) = 100 \cos 0.5609 t \quad \text{A}$$

$$\langle i_L \rangle(t) = 100 \sin 0.5609 t \quad \text{A}$$

$$\langle v_S \rangle(t) = 224.4 \sin 0.5609 t \quad \text{V}$$

$$\langle v_L \rangle(t) = 224.4 \cos 0.5609 t \quad \text{V}$$

$$\langle p_S \rangle(t) = 11218 \sin 1.1218 t \quad \text{W}$$

A plot of these equations appears in Fig. 9.

Figure 10 shows the average coil voltages and currents obtained experimentally. Good agreement exists between the analytical and the experimental results. Note, however, that the experimental initial storage current is somewhat higher than the final load current. This is due to the losses in the system which is neglected in this analysis, but may be incorporated in the differential equations leading to the average time functions.

#### Conclusions

The behavior of the multiphase inductor-converter bridges have been studied by two analytical techniques. The conventional Fourier technique produces the average circuit power, currents, and voltages as a function of time. It also shows the effect of the existing harmonics in the circuit behavior. The square function technique is particularly designed for the ICB and other SCR circuits in which rectangular waveforms appear. The identities defined on the special functions  $Sq(X)$  and  $Tr(X)$  operate directly on the circuit waveforms. Thus, much more information about instantaneous behavior of the circuit is available for analysis, system design, and the development of real time control algorithms. Preliminary tests with open loop microcomputer control have been conducted with satisfactory results. The development of an optimal closed loop control algorithm is currently in progress.

#### Appendix

The  $Sq$  function is defined as the sum of unit step functions as follows,

$$Sq(\gamma + \gamma_0) \triangleq u(\gamma) - 2u(\gamma - \frac{1}{2} + \gamma_0) + 2$$

$$u(\gamma - 1 + \gamma_0) - u(\gamma_0 - 1),$$

$$0 \leq \gamma_0 \leq \frac{1}{2}, \quad 0 < \gamma \leq 1.$$

The Tr function is defined as the integral value of the Sq functions,

$$\text{Tr}(\gamma + \gamma_0) \triangleq \int_0^\gamma \text{Sq}(\xi + \gamma_0) d\xi$$

$$u(\gamma + \gamma_0) = 2(\gamma - \frac{1}{2} + \gamma_0)$$

$$u(\gamma - \frac{1}{2} + \gamma_0) = 2(\gamma - 1 + \gamma_0)$$

$$u(\gamma - 1 + \gamma_0) = (\gamma - 1) u(\gamma - 1)$$

The following integral is extensively used in calculating the average power flow in the circuits of interest. Therefore, it will be stated as an identity which may be directly verified,

$$\int_0^1 [\text{Sq}(\gamma + \gamma_1) \cdot \begin{cases} -2\gamma_1^2 - \gamma_1 + 4\gamma_1\gamma_2 + \gamma_2 \\ -2\gamma_2^2, \gamma_1 \leq \gamma_2 \\ 2\gamma_2^2 - \gamma_1 - 4\gamma_1\gamma_2 + \gamma_2 \\ + 2\gamma_1^2, \gamma_1 \geq \gamma_2 \end{cases} \text{Tr}(\gamma + \gamma_2)] d\gamma$$

$$0 \leq \gamma \leq \frac{1}{2}, 0 \leq \gamma_2 \leq \frac{1}{2}.$$

The following identities will also be of considerable value

$$\text{Sq}(\gamma - \gamma_0) = -\text{Sq}[\gamma + (1/2 - \gamma_0)],$$

$$\text{Tr}(\gamma - \gamma_0) = -\text{Tr}[\gamma + (1/2 - \gamma_0)], \quad 0 \leq \gamma_0 \leq \frac{1}{2}$$

which may be verified by direct substitution.

Note that by using these identities, we can easily evaluate the above integral for any combination of leading and lagging functions.

The above Sq and Tr functions have been defined for a period equal to 1. For periods other than 1, the argument should be multiplied by the appropriate constant:

$$\text{Sq}(t + t_0) = \text{Sq}(\gamma + \gamma_0), \quad \begin{cases} 0 \leq t \leq T, 0 \leq t_0 \leq \frac{T}{2} \\ 0 \leq \gamma \leq 1, 0 \leq \gamma_0 \leq \frac{1}{2} \end{cases}$$

$$\text{Tr}(t + t_0) = \int_0^t \text{Sq}(\sigma + t_0) d\sigma, \quad \begin{cases} 0 \leq t \leq T \\ 0 \leq t_0 \leq \frac{T}{2} \end{cases}$$

where  $\gamma = \frac{t}{T}$  and  $\gamma_0 = \frac{t_0}{T}$ .

Substitution of  $\gamma$  and  $\gamma_0$  in the above integral will give

$$\begin{aligned} \text{Tr}(t + t_0) &= T \int_0^\gamma \text{Sq}(\xi + \gamma_0) d\xi \\ &= T [\text{Tr}(\gamma + \gamma_0)] = t u(t) - 2 \\ &\quad (t - \frac{T}{2} + t_0) u(t - \frac{T}{2} + t_0) \\ &\quad + 2(t - T + t_0) u(t - T + t_0) \\ &\quad - (t - T) u(t - T). \end{aligned}$$

For time base calculations, these functions may be used.

#### References

1. R. L. Kustom et al., "The Use of Multiphase Inductor-Converter Bridges as Actively Controlled Power Supplies for Tokamak Coils," Argonne National Laboratory Report ANL/FPP/TH-78 (April 11, 1977).
2. H. A. Peterson et al., "Superconductive Inductor-Converter Units for Pulsed Power Loads," Proceedings of International Conference on Energy Storage, Compression and Switching, Asti-Torino, Italy (November 1974).
3. M. Ehsani, R. L. Kustom, "Analysis of the Multiphase Inductor Converter Bridge," Argonne National Laboratory Report ANL/FPP/TH-114 (August 1978).
4. M. Ehsani, R. L. Kustom, "Square Function Analysis of the Inductor-Converter Bridge," Argonne National Laboratory Report ANL/FPP/TH-118 (March 1979).
5. N. Mohan, H. A. Peterson, "Superconductive Inductor Storage and Converters for Pulsed Power Loads," Proceedings of the International Pulsed Power Conference, Lubbock, TX (November 1976).

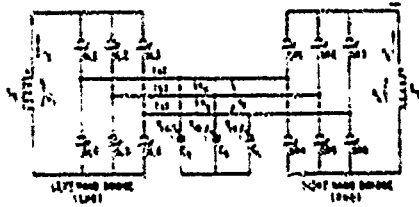


Fig. 1. Circuit Diagram for the 3-Capacitor Model IC Bridge.



Fig. 2. Circuit Diagram for an m-phase ICB.

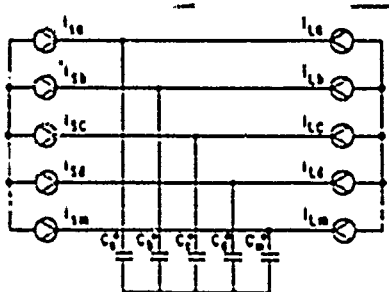


Fig. 3. Equivalent Diagram of an m-phase ICB.

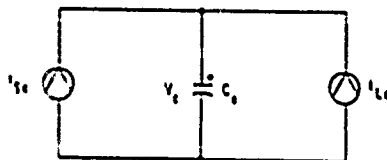


Fig. 4. One Phase Equivalent Circuit of an m-phase ICB.

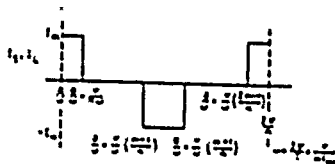


Fig. 5. Single Phase Current Source Waveform for an m-phase ICB Circuit.

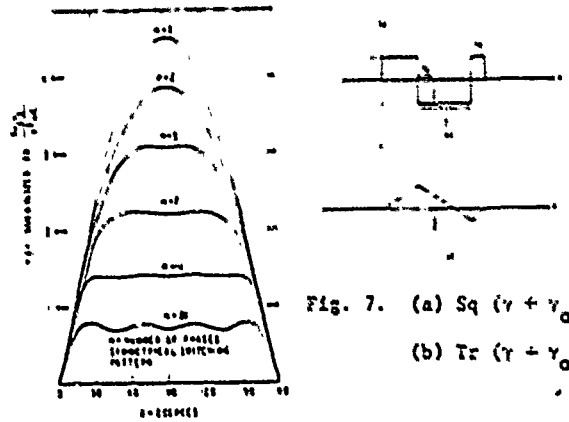


Fig. 6. Plot of  $\langle p \rangle$  vs  $\alpha$ .

Fig. 7. (a)  $S_q(\gamma + \gamma_0)$ ,  
(b)  $Tr(\gamma + \gamma_0)$ .

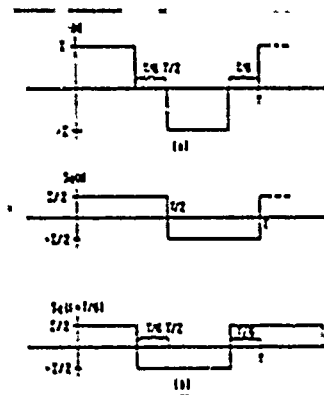


Fig. 8.

(a) Phase Current in a Three-Phase ICB  
(b) Decomposition of the Phase Current into Two  $S_q$  Functions.

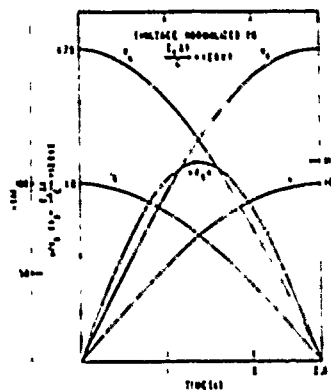


Fig. 9.

Average Coil Currents, Voltages, and Power vs Time.

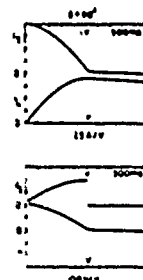


Fig. 10.

Experimental Average Coil Voltage and Current Traces.

## DISTRIBUTED PARAMETER MODEL OF THE TRESTLE PULSER\*

T. H. LEMMAN, R. L. HUTCHINS, R. FISHER<sup>†</sup>

BDM Corporation, Albuquerque

Abstract

A distributed parameter circuit analog model was developed to evaluate design improvements for the TRESTLE pulser. The approach for specifying the model network and estimating model parameters is given. Model results are shown to compare favorably to available measurements. The model's flexibility and economy allowed ready evaluation of potential modifications.

Introduction

A desired output of EMP simulators is to produce working volume fields that approximate the waveform given by

$$E = 5.25 \times 10^4 (e^{-4 \times 10^6 t} - e^{-4.76 \times 10^6 t}) \text{ V/m}$$

Applying this criteria to the TRESTLE simulator implies that the output voltage of the TRESTLE pulsers should be on the order of 5MV with a risetime of approximately 10 nsec. The configuration is shown in Figure 1. This arrangement of Marx generators and peaking circuits has a smooth transition into the TRESTLE antenna system and was required to support TEM fields up to 100 MHz. This bandwidth requirement introduced uncertainty into the pulser design since the pulser is electrically large at 100 MHz.

\*This work supported by the Air Force Weapons Laboratory under subcontract to McDonnell-Douglas Astronautics Company, Contract F29601-73-C-0090

<sup>†</sup>Mr. Fisher is currently with ElectroMagnetics Applications, Inc.

Simple lumped parameter models were developed to determine the design parameters for the pulsers. However, after the first pulser module was built and tested, test results indicated that improved pulser response was desired (Figure 2). The most obvious difference is the increase in measured risetime over the predicted (25 nsec vs. 8 nsec). Additional anomalies included the measured notch at 225 nsec. and a prepulse of approximately 30 percent of charge voltage.

Before any major modifications were made to the pulser in order to improve its performance, a more detailed model of the pulser was developed. In particular, this model was required to have the capability to account for both the extended geometry of the pulser, and the stray capacitance and inductance of the peakers and Marx generators.

Approach

The model was restricted to account for TEM mode propagation only. With this restriction, a distributed network analog model was attractive for many reasons. First, the solutions could be obtained in the time domain alleviating the problem associated with the non-linear behavior of the switches. Second, distributed network analog models are compatible with measured parameter estimation. The most serious deficiency associated with these models is that it is difficult to account for the effects of radiation resistance and diffraction.

The peaker arms and Marx generators were modeled by dividing the length of the pulser into 16 segments. The segment unit cell is

illustrated in Figure 3. Note that both the effects of internal and external phenomena are modeled.

The output switch and the load of the pulser were modeled separately. A model of a coaxial switch is shown in Figure 4. This model includes the effects of the transit time along the switch, the stray capacitance of the switch corona ring, the stray capacitance of the switch gap, the internal inductance of the switch and a back impedance. The back impedance included the effects of the output switch probe and the radiation resistance of the pulser.

The integrated pulser model was formed by combining the prescribed number of unit cells and attaching both the switch model and load element. This is illustrated in Figure 5 for the case of an idealized switch and a lumped load impedance.

#### Model Parameter Estimation

Since the network analog model of the pulser is not based on a self-consistent solution of Maxwell's equation, the model parameters were estimated from experimental results, numerical analyses and simple analytical formulas. The methods for estimating all of the model parameters are summarized in Table 1. In particular the values of the components representing internal parameters were obtained from the results of experiments and were supplied by the pulser manufacturer (reference 1). The values of the components representing the external parameters (stray and mutual capacitance and inductance) of the peaker-Marx configuration were calculated using a 3-dimensional static method of moments code. The details of these calculations are contained in reference 2. Reference 3 provides criteria for modeling radiation resistance.

#### Results

The response of the network analog of the TRESTLE pulser was calculated using the NET-2 network analysis code. About 400 elements were needed. The calculations were performed in the

time domain and the predicted output waveform was compared to the measured output (Figure 6 and Figure 7). It is evident that the responses obtained from the model calculations are in good agreement with the measured responses except near the peak value of the waveform. The flattening of the measured response waveform in this region was attributed to diffraction effects which are not included in the network analog model.

Next the sensitivity of the model was investigated by varying the component parameters over their range of uncertainty. Since the output was not sensitive to small parameter variations, we concluded precise parameter estimates were not required (reference 2).

Finally various pulser modifications were evaluated (reference 2) with the aid of the model. It was found feasible to eliminate the waveform notch by increasing peaker capacitance. For other features, it was found that the pulser design was near optimum given high voltage and geometry constraints.

#### Conclusions

The modeling approach used for TRESTLE appears to be useful for other electrically large high voltage systems. A combination of simple experiments and analyses can yield adequate data for distributed parameter equivalent circuits. With existing circuit analysis codes such as SEPTRE or NET-2, model changes are simple and computer run times are modest (1-3 minutes per run on a CDC 6600 for the TRESTLE study).

#### References

1. "TRESTLE Pulser Subsystem Design Analysis Final Report," Report No. MRL-228, Maxwell Laboratories, Inc., January 1973.
2. "TRESTLE Pulser Analysis Final Report," Report No. BDM/A-27-75-TR, BDM Corp., March 1975.
3. "Matching a Particular Pulser to a Parallel Plate Simulator," Tetra Tech Inc., Final Report for Contract F29601-74-C-00115 for the Air Force, August 1974.

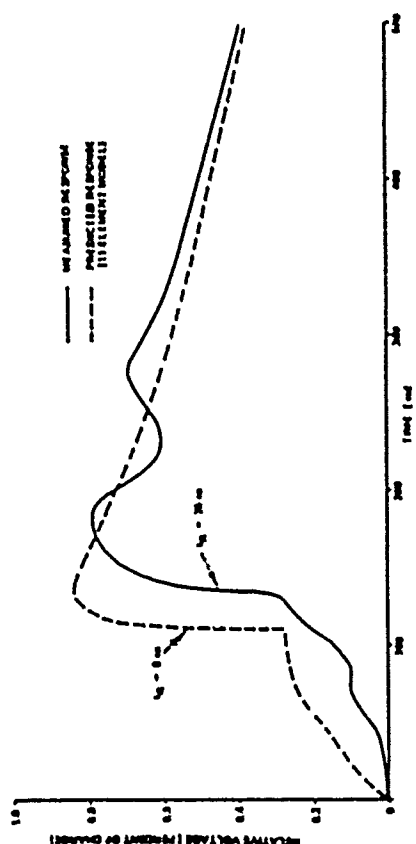


Figure 2. Comparison of Measured and Predicted Response (IV Element Model)

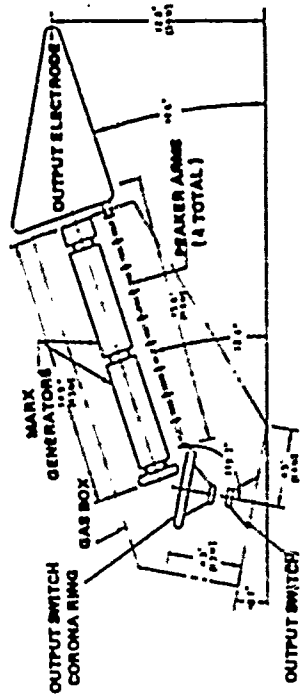


Figure 1. Pulsar Module Geometry (Bicone Switch)

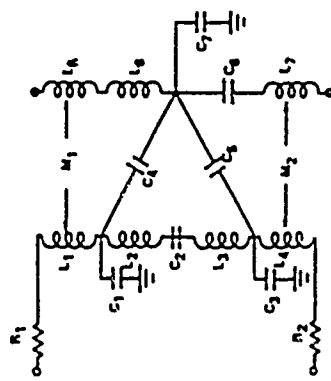
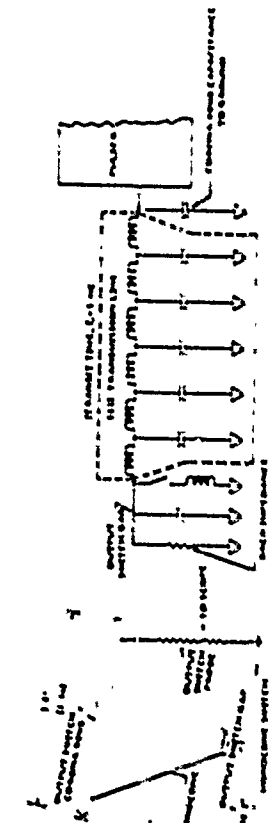


Figure 3. Pulsar Model Unit Cell



(a) Monopole Switch Model (b) Monopole Switch Model

Figure 4. Monopole Switch Geometry and Model

TABLE 1. SUMMARY OF MODEL PARAMETER ESTIMATION METHODS

PARAMETER	ESTIMATION METHOD	SUMMARY
• Main Internal Capacitance	• Measured (Reference 1)	• Main Internal Inductance includes Main switch inductance
• Main Charging Resistance		• Peak Internal Inductance includes loop inductance of parallel peak wire
• Peak Internal Capacitance		• Stray Inductance = $\{(\text{Speed of Light})^2 \times \text{Stray Capacitance}\}^{1/2}$
• Peak Internal Inductance		• Includes resistance of output switch pulse and radiation resistance
• Main Stray Capacitance	• Calculated (3-D Static Method of Moments, Reference 2)	• Inductance includes spark channel inductance and electrode inductance
• Peak Stray Capacitance	• Calculated (Reference 2)	• Switches are closed sequentially at equally spaced intervals
• Peak Stray Inductance		• Switch is closed on the rise of peak output waveform
• Peak/Stray Mutual Capacitance		• Load impedance is assumed to be equal to transmission line characteristic impedance
• Peak/Stray Mutual Inductance		
• Back Impedance		
• Output switch Inductance and Stray Capacitance	• Calculated (Stray Capacitance) Measured (Reference 1)	
• Main Switch Closure Time	• Calculated (assume all switches close within a prescribed time)	
• Output Switch Closure Time	• Calculated (Reference 1)	
• Load Impedance	• Calculated (2-D Static Method of Moments)	

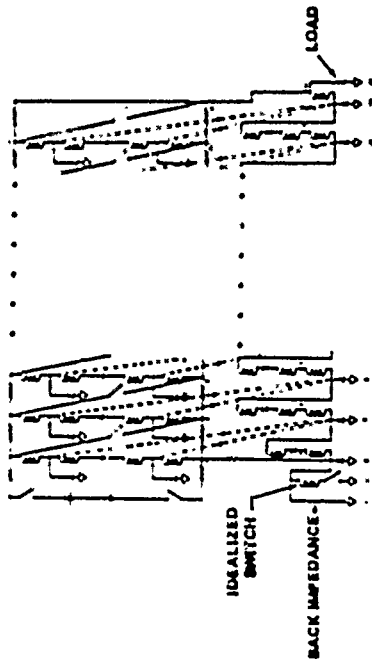


Figure 5. Integrated Pulsar Model

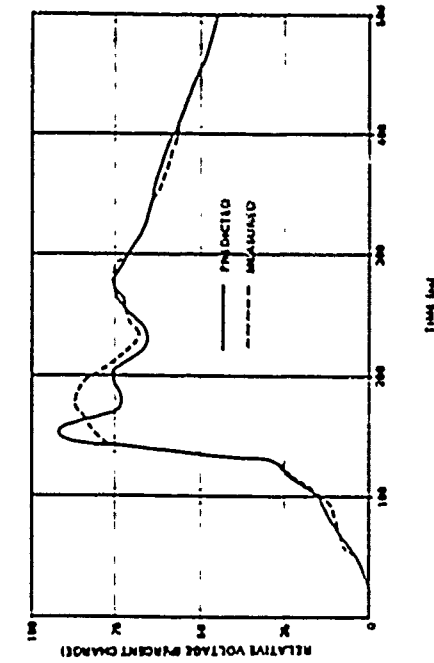


Figure 6. Comparison of Model and Measured Response (Monococone Switch)

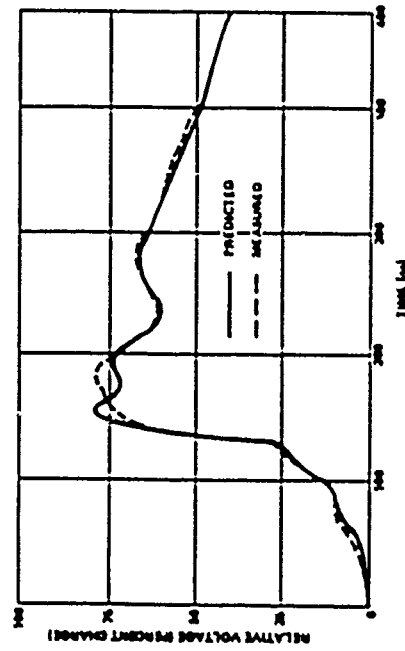


Figure 7. Comparison of Model and Measured Response (Bicocone Switch)



# COMPTON SCATTERING OF PHOTONS FROM ELECTRONS IN MAGNETICALLY INSULATED TRANSMISSION LINES\*

K. L. Brower and J. P. VanDevender

Sandia Laboratories, Albuquerque, New Mexico 87185

## Abstract

Self-magnetically insulated transmission lines are used for power transport between the vacuum insulator and the diode in high current particle accelerators. Since the efficiency of the power transport depends on the details of the initial line geometry, i.e., the injector, the dependence of the electron canonical momentum distribution on the injector geometry should reveal the loss mechanism. We propose to study that dependence experimentally through a Compton scattering diagnostic. The spectrum of scattered light reveals the electron velocity distribution perpendicular to the direction of flow. The design of the diagnostic is in progress. Our preliminary analysis is based on the conservation of energy and canonical momentum for a single electron in the  $\vec{E}$  and  $\vec{B}$  fields determined from 2-D calculations. For the Mite<sup>1</sup> accelerator with power flow along Z, the normalized canonical momentum,  $\mu$ , is in the range  $-0.7 < \mu < 0$ . For  $\vec{k}_i \parallel \hat{y}$ , and  $\vec{k}_s \parallel \hat{x}$ , our analysis indicates that the scattered photons have  $1.1 \text{ eV} < h\nu_s < 5.6 \text{ eV}$  for ruby laser scattering and can be detected with PM tubes.

## Introduction

Self-magnetically insulated transmission lines are being developed for power transport in the particle beam fusion accelerator EBFA at Sandia. The efficiency of power and energy transport is sensitive to variations in line geometry which occur at the input and output convolutes. In this paper we consider how the dynamics of electron flow might be probed by Compton scattering. The evaluation has several steps. First, the distributions of the electric and magnetic fields in the EBFA self magnetically insulated line<sup>1</sup> are inferred from simulations<sup>2</sup> and 1-D theory.<sup>3</sup> Then the relationship between the energy of a photon scattered from an electron with an axial canonical momentum  $P_z$  is calculated at various positions in the electron flow, for the  $\vec{E}$  and  $\vec{B}$  fields from the 2-D simulations and for those from the 1-D theory. A comparison of the two relationships illustrates the sensitivity of the diagnostic to the model for  $\vec{E}$  and  $\vec{B}$ . The particle trajectories for an assumed distribution of canonical momentum  $P_z$  in the axial direction are then calculated at a given position in the vacuum gap. Finally, the spectrum of scattered photons

for two different assumed canonical momentum distributions are calculated to illustrate the diagnostic. Each step will be examined in turn.

## Electromagnetic Field Calculations

The triplate transmission line which is being incorporated into EBFA is represented by an equivalent coaxial transmission line with  $r_c = 0.07 \text{ m}$  and  $r_a = 0.08 \text{ m}$ . This coax and the basic features in the Compton scattering experiment are shown in Fig. 1. From simulations<sup>2</sup> of this coaxial line,<sup>1</sup> the power flow is represented by a boundary current,  $I_B$ , of 243 kA and a total current,  $I_T$ , of 450 kA at  $V_0 = 2.4 \text{ MV}$ . The current  $I_E = I_T - I_B = 207 \text{ kA}$  is carried by electrons in the vacuum gap between conductors. The  $\vec{E}$  and  $\vec{B}$  fields for this particular case have been calculated previously by Bergeron and Poukey with a 2-D electromagnetic particle simulation code.<sup>2</sup> The agreement between the experiment and the code results for  $V$ ,  $I_T$ , and  $I_B$  are excellent. We have also calculated the  $\vec{E}$  and  $\vec{B}$  fields for these initial conditions from parapotential theory.<sup>3</sup> We noticed that under these conditions of power flow the value of  $C_1$  as calculated by Eqs. (29) and (36) in Creedon's paper<sup>3</sup> were inconsistent. This theory requires self-consistency which we achieved by optimizing  $N_0$  so that  $V_0 = \omega_0 c^2 (7_0 - 1)/e$  is 2.4505 MV instead of 2.4 MV. This

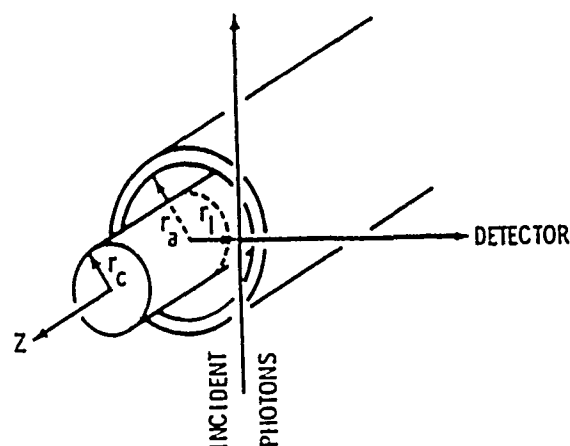


Fig. 1. Coax with basic features of Compton scattering experiment. Directions of electron power flow (+Z), incident photons, and detector are all mutually perpendicular.

\*This work was supported by the U.S. Dept. of Energy, under Contract DE-AC04-76-DP00789.

value of  $V_0$  gives a self-consistent set of parameters  $V_0$ ,  $L_T$ ,  $I_0$ , and  $Z_0$  for parapotential theory and is well within experimental error in the measurements and the numerical fluctuations in the computational results. The  $\vec{E}$  and  $\vec{B}$  fields from 2-D calculations and the self-consistent (SC) parapotential theory are shown in Fig. 2.

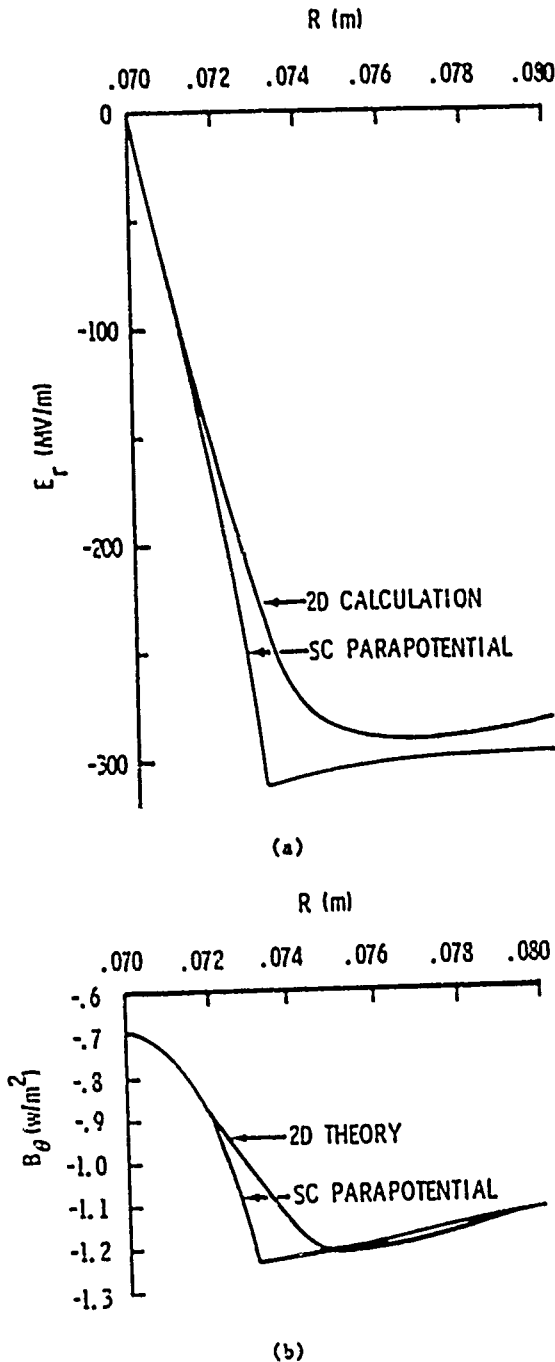


Fig. 2. Plot of  $\vec{E}$  and  $\vec{B}$  fields extrapolated from data points of Bergeron and Piquet and according to SC parapotential theory.

#### The Photon Energy as a Function of Electron Canonical Momentum

In order to calculate the frequency of a Compton scattered photon, the velocity vector of the scattering electron needs to be known. From the conservation of energy and momentum for a single electron, Mendel<sup>4</sup> has shown that

$$\gamma^2 \frac{v_r^2}{c^2} = [1 + \phi(r)]^2 - 1 - [\alpha(r) + \mu]^2 \quad (1)$$

where

- $v_r$   $\equiv$  radial velocity component,
- $\phi(r)$   $\equiv$  normalized scalar potential ( $= e\phi/mc^2$  with  $\vec{E} = -\nabla\phi$ ),
- $\alpha(r)$   $\equiv$  Z-component of normalized vector potential ( $= eA_z(r)/mc$  with  $\vec{B} = \nabla A$ ),
- $\mu$   $\equiv$  Z-component of normalized canonical momentum ( $= eP_z/mc$  with  $P_z = \gamma m v_z + qA_z$ ), and
- $\gamma \equiv (1 - v^2/c^2)^{-1/2} = 1 + \phi(r)$  (by energy conservation).

In Eq. (1) a new parameter,  $\mu$ , is introduced which is the normalized canonical momentum.<sup>5</sup> For steady-state electron flow in a transmission line in which  $\partial/\partial z \neq 0$ ,  $\mu$  is a constant of the electron motion. If the electron originates from the cathode where  $\phi = V_2 = -\alpha = 0$ , then  $\mu = 0$ . Consequently, it is often assumed that  $\mu = 0$  for all electrons in the flow. However, self-magnetically insulated transmission lines have a transition section between the weakly, electrically stressed vacuum insulator and the highly stressed line. In the transition section,  $\partial/\partial z \neq 0$  and  $\mu$  is not a constant of motion. Consequently, electrons with  $\mu \neq 0$  can be injected into the uniform line, and produce a distribution  $F(\mu)$  with a finite width  $\Delta\mu$ , for the electron flow. It is thought that the detail structure in  $F(\mu)$  determines the power transport in long, self-magnetically insulated lines,<sup>6,7</sup> and the stability of the electron flow may be understood by studying  $F(\mu)$  under various conditions. Stable orbits corresponding to solutions of Eq. (1) for which  $v_r \geq 0$  in the gap can be found for various values of  $\mu$ . In Fig. 3 we have plotted the radial position of the lower and upper turning points for stable orbits as a function of  $\mu$ . These results show that the orbits are very similar for scalar and vector potentials based on parapotential and 2-D calculations. We also see that for  $\mu = 0$ , the orbits are contained within the sheath and return to the cathode surface. Orbits with  $\mu < 0$  have upper turning points beyond the sheath and tend to remain isolated from the cathode surface. The minimum  $\mu$  corresponds to those orbits whose upper turning point just grazes the anode.

According to Compton scattering theory for the geometry shown in Fig. 1, the energy of the scattered photons,  $h\nu_s$ , is related to  $V(r_1, \mu)$  by the expression

$$h\nu_s = \frac{h\nu_i}{1 - V(r_1, \mu)/c} \quad (2)$$

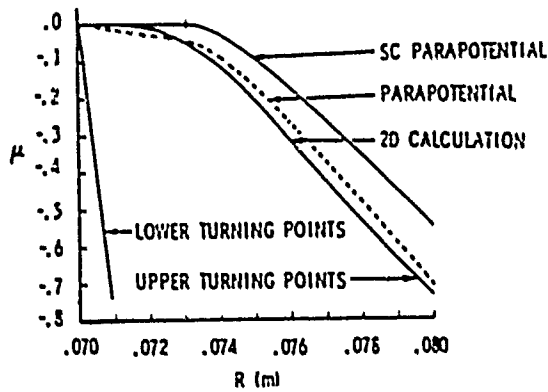


Fig. 3. Plot of  $\mu$  vs. the position of lower and upper turning points. The dotted line was calculated by parapotential theory using same  $I_0$ ,  $I_r$ , and  $V_0$  as was used for 2-D calculation.

where  $r_i$  is the radial position of the incident laser beam in the gap. Scattered photon energies as a function of  $\mu$  are plotted in Fig. 4 for various values of  $r_i$  with  $h\nu_i = 1.786$  eV from a ruby laser. The values of  $V_-(r_i, \mu)$  needed in Eq. (2) were determined from Eq. (1) using potentials from 2-D calculations with  $\mu_{\text{lower}} \leq \mu \leq \mu_{\text{upper}}$ . These results indicate that for this geometry, optical detection is required.

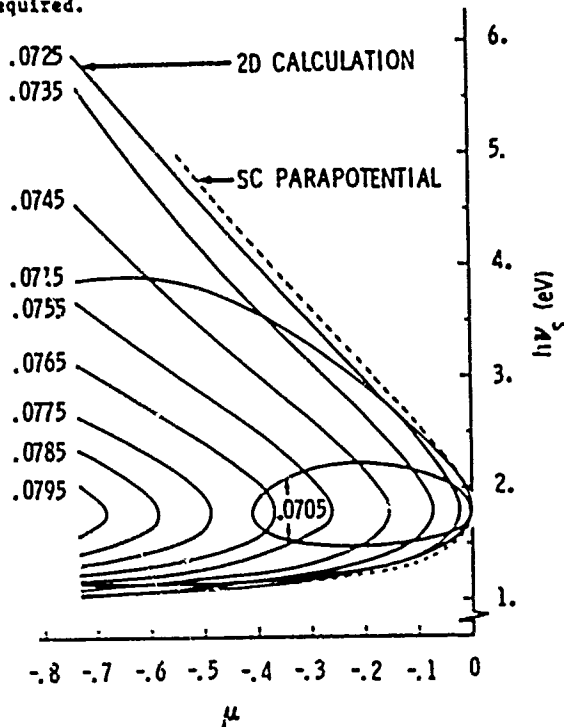


Fig. 4. Plot of scattered photon energies vs.  $\mu$  for various positions for the fields from the 2-D computations and, of the laser probe beam. The dotted line has  $h\nu_s(\mu)$  from the fields from the self-consistent parapotential calculation at  $r_i = 0.0725$  m for comparison.

#### Calculated Spectra for an Assumed $F(\mu)$ .

The number of scattered photons with energy between  $E$ ,  $E + dE$  is given by the expression

$$\frac{dN}{dE} = \frac{UL}{h\nu_i} D(r_i) F(\mu) \left| \frac{dG}{dE} \right|^{-1} \int_0^{\Omega} \frac{d\sigma}{d\Omega} d\Omega \quad (3)$$

where

- $U$  = energy of incident laser pulse,
- $L$  = interaction length of beam and electron plasma visible to the detector.
- $D(r_i)$  = number of electrons/ $\text{m}^3$  at  $r_i$  from Ref. 2.
- $F(\mu)$  = fraction of electrons with normalized canonical momentum  $\mu$ ,
- $G(r_i, E)$  = normalized canonical momentum at some position in the gap,  $r_i$ , as a function of scattered photon energies (see Fig. 4), and
- $\frac{d\sigma}{d\Omega}$  = Compton differential scattering cross section.

In using Eq. (3) to calculate the scattered spectra, we assume the laser energy is 1 joule, the collector system subtends one steradian of solid angle, and the electron number density is  $10^{18} \text{ m}^{-3}$ . For a uniform canonical momentum distribution,  $dN/dE$  versus  $E$  ( $=h\nu_s$ ) is plotted in Fig. 5 for several positions of the probing laser beam. The total number of scattered photons is also noted as  $N_p$  in these plots. We also assumed a Gaussian distribution,  $\exp(-0.5(\mu - \mu_0)/\delta\mu)^2)$ , with  $\mu_0 = 0$  and  $\delta\mu = 0.1$ ; the results of the calculation using this distribution is plotted in Fig. 6.

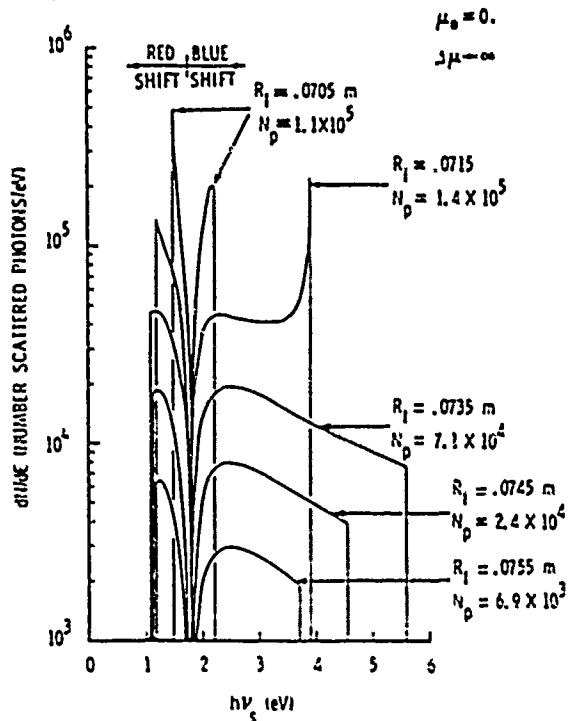


Fig. 5. Plot of  $dN/dE$  vs.  $h\nu_s$  for uniform distribution in  $\mu$ .

$$\mu_0 = 0.$$

$$\Delta\mu = 0.1$$

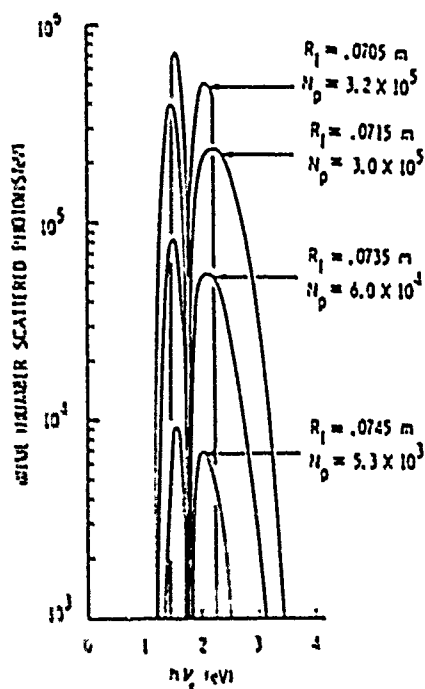


Fig. 6. Plot of  $dN/dE$  vs.  $h\nu$  for Gaussian distribution in  $\mu$  centered about  $\mu_0 = 0$  with  $\Delta\mu = 0.1$ .

#### Discussion

In the proposed experiment to measure  $F(\mu)$  in an EBFA-1 self-magnetically insulated transmission line, the total number of collected photons will be  $N_p \approx 10^5$ . The photons will be in the visible region of the spectrum and they will be spectrally resolved with a grating and recorded with a photomultiplier and oscilloscope combination for each data channel. Assume that the spectrometer has a transmission efficiency  $\epsilon_s = 0.2$ , the photomultiplier has a quantum efficiency  $\epsilon_{pm} = 0.03$  and a gain  $G = 10^6$ . If the data is recorded in a  $\Delta t = 10$  ns pulse into  $N_s = 5$  data channels, then the average signal into a 50 ohm oscilloscope will be

$$V = 50 \frac{N_p \epsilon_s \epsilon_{pm} G}{N_s \Delta t} = 0.6 \text{ volts}$$

which is easily recordable.

The functional relationship between  $h\nu$  and  $\mu$  features a reasonably strong correspondence of  $F(h\nu)$  to  $F(\mu)$  for the proposed experiment and the interpretation of the data is reasonably insensitive to the assumed model for the electromagnetic field distribution in the electron flow.

The electrons produce a bremsstrahlung x-ray pulse that will produce a signal on the detector. The scattered light can be optically delayed until the detector recovers from the x-ray pulse so the x-ray background can be tolerated.

The limiting factor to the Compton scattering diagnostic to measure  $F(\mu)$  appears to be the background light from the plasma on the cathode. A significant amount of light can be expected, but no measurements have been made of its intensity or spectral distribution. The ratio of scattered light to plasma light improves as the bandwidth  $\Delta\nu$  of the scattered light decreases. If the width  $\Delta\mu$  of  $F(\mu)$  is  $\approx 10^{-6}$ , as recent calculations<sup>7</sup> have indicated, the scattered light has a wavelength spread of only  $3 \text{ \AA}$ , which would give a very favorable ratio of scattered light to plasma light.

#### Conclusion

The Compton scattering diagnostic is capable in principle of resolving the canonical momentum distribution  $F(\mu)$  in self-magnetically insulated electron flow. The limiting factor is the ratio of background plasma light from the cathode plasma and the scattered light, which is strongly dependent on the width of  $F(\mu)$  itself.

#### References

1. J. P. VanDevender, J. Appl. Phys. **50**, No. 6 (1979).
2. K. D. Bergeron and J. W. Poukey, Appl. Phys. Lett. **32**, 8 (1978).
3. J. M. Creedon, J. Appl. Phys. **46**, 2946 (1975).
4. C. W. Mendel, J. Appl. Phys. **50**, No. 7 (1979).
5. J. D. Jackson, *Classical Electrodynamics* (Wiley, NY, 1975), p.574.
6. J. P. VanDevender, Proc. 2nd Int'l. Conf. on Pulsed Power, Lubbock, TX (1979).
7. E. L. Neau and J. P. VanDevender, same as Ref. 6.
8. G. Ward and R. E. Pechacek, Phys. Fluids **15**, 2202 (1972).

SIMULATION OF INDUCTIVE AND ELECTROMAGNETIC EFFECTS  
ASSOCIATED WITH SINGLE AND MULTICHANNEL  
TRIGGERED SPARK GAPS

S. Levinson, E.E. Kunhardt, M. Kristiansen  
A.H. Guenther

Dept. of Electrical Engineering  
Texas Tech University  
Lubbock, TX 79409

Abstract

When breakdown of a pressurized spark gap is initiated by a high power laser, a narrow spark channel is quickly established. In this case, the risetime of the current in the external circuit due to the breakdown of the gap is determined in a large measure by the properties of this spark channel. To study the inductive and electromagnetic effects associated with the channel dimensions and the resulting physical discontinuities, experiments have been conducted using spark gaps where the discharge channel is simulated by a very thin wire. Current risetime measurements for various wire sizes (i.e., spark channel radius), wire position (i.e., on or off axis), and number of wires (i.e., multichanneling) have been carried out. The risetime values thus obtained agree quite well with the laser-triggered, single and multichannel, spark gap results. These results can be qualitatively explained using simple inductive circuits which dramatically underline the inductive character of the breakdown. The significance of these results in revealing the mechanism of spark gap breakdown will be discussed.

As current risetimes in sparkgap switches approach nanoseconds, it becomes increasingly important to understand the electromagnetic effects that are associated with the geometry of the spark-gap and arc channel. This is particularly important in the case of high impedance, triggered systems where the effects of the resistive phase of breakdown are not important. For example, Guenther and Bettis<sup>1</sup> conducted experiments using a 50 ohm, laser triggered system where the risetime was determined almost exclusively by the inductive phase. In this case, those electromagnetic effects, associated with the dimensions of the electrode and the arc channel, can be investigated by simulating the channel with thin wires.

The experimental arrangement, shown in Fig. 1,

was used to simulate a high impedance system for the investigation of these aforementioned electromagnetic effects. The gap region was formed by an interruption in the center conductor of a constant impedance (50 ohm) coaxial line which is terminated in a matched load. Thin wires are placed across the gap to simulate the conduction paths.

The simulation arrangement may be thought of as a set of three cascaded transmission lines (shown in center of Fig. 2) with the gap section, in this case, having a very high characteristic impedance. Because of this, and for the purpose of calculating risetimes, the system may be modeled by the inductive circuit shown at the bottom of Fig. 2. In this circuit, the inductance is given by<sup>2</sup>:

$$L = \frac{60l}{c} \ln(b/a) \quad (1)$$

where  $a$  and  $b$  are the diameters of the wire and outer conductor of the transmission line respectively;  $c$  is the speed of light in meters per second, and  $l$  is the gap distance in meters. Since transmission line techniques do not account for the three dimensionality of the problem, this circuit model is useful for determining the current risetime only to a first approximation. Because of boundary conditions, the transverse electric field must be zero at the discontinuities occurring at the electrode-channel junctions. Higher order modes are created here to satisfy these boundary conditions, while still allowing for the propagation of the current pulse through the gap<sup>3</sup>. If these modes are evanescent and non-interactive, it is possible to modify the transmission line and circuit models by placing capacitors at each discontinuity<sup>3</sup> and at each end of the inductor, respectively. Some of these higher order modes do

propagate, however, and in general will, making this modified model unacceptable for the accurate determination of current or voltage risetime.

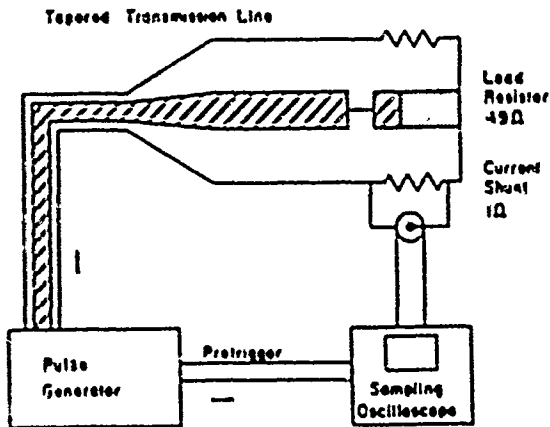


Fig. 1 Experimental Arrangement

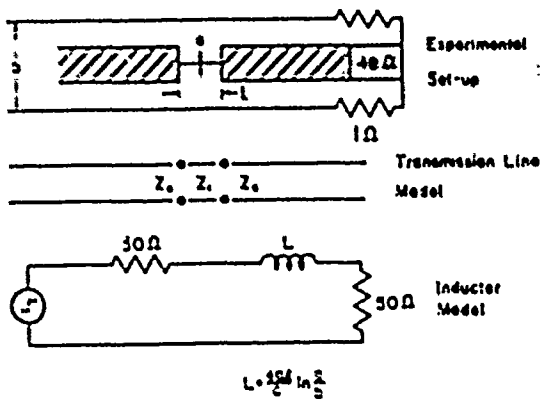


Fig. 2

Using sampling techniques and the setup in Fig. 1, we have experimentally determined the geometrical effects associated with gap spacing, number of channels, channel position, and channel diameter on the risetime of an incident voltage pulse (Fig. 3). The experimental risetimes were determined using the relation:

$$\tau_a^2 = \tau_o^2 - \tau_i^2 \quad (2)$$

where  $\tau_o$  = observed risetime

$\tau_i$  = risetime of incident pulse

We have compared these results with risetimes calculated from the circuit model at the bottom of Fig. 2 with the risetime given by:

$$\tau_R = 2.2 \frac{L}{\Delta Z_o} \quad (3)$$

A graph of the risetime (after being corrected for the finite bandwidth of the current shunt and in-

cident pulse) versus gap distance is shown in Fig. 4. The risetime of the transmitted pulse decreases as gap distance decreases in both the experimental case and the case when the risetime is determined from equation 3. This is explained by the fact the inductance of the channel and, therefore, the associated time constant decrease with decreasing gap distance. One should also note that while the relative difference between the calculated and experimental risetime remains fairly constant, the percentage difference actually increases as the gap distance is decreased from 3.3 cm. This may be explained by the fact that the high order modes, created at each discontinuity, interact more with each other as the spacing decreases, and this interaction tends to have an increasing effect on risetime. Note, however, that as gap distance is reduced further still, from 1 cm, the capacitance of the gap plays a greater but opposite role, causing the percentage difference between the calculated and experimentally determined risetimes to decrease (see Fig. 4).

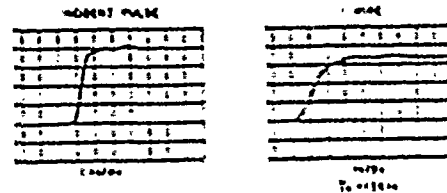


Fig. 3

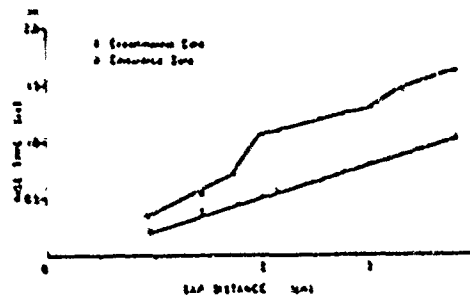


Fig. 4

The geometrical effects associated with multichannel discharges were simulated by placing various number of wires at different positions in the gap. Since the characteristic inductance of the gap section decreases with increasing numbers of wires, it is expected that the risetime should

decrease also. This decrease is particularly acute between rise times associated with one and two wire channels (see Figs. 5 and 7).

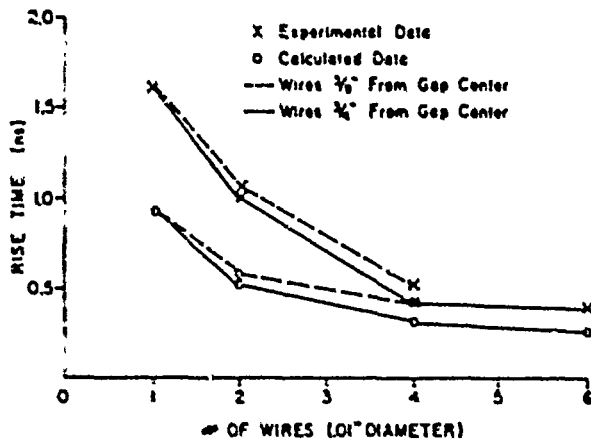


Fig. 5

As the number of wires increases, the electromagnetic field distribution more accurately approximates that of a larger diameter wire. It then follows that large numbers of wires placed at the edge of the gap have an associated risetime that is smaller than the case when the same number of wires are placed closer to the axis of the gap since the associated inductance of the "effective" large diameter channel is smaller. Similarly it follows that the experimental risetime should more closely match the rise time calculated from equation 3 since the "effective" large diameter wire produces less of a discontinuity to the transverse electromagnetic fields of the incident pulse, than the smaller "effective" diameter wire. This is verified by the graph in Fig. 5.

Finally the effects of channel thickness on risetime were determined by varying the diameter of the wires used to simulate the channel. Again, since the characteristic inductance of the gap section associated with the thicker wires is less than that associated with thinner wires, it is expected that risetimes should also be less. This is shown in the plot of risetime versus channel diameter in Fig. 6. Note that the difference between calculated and experimentally determined risetimes tends to become smaller as the thickness

of the channel is increased. This decrease is due to two reasons. First, less high order modes are generated in the gap section when thicker wires are used, hence shorter risetimes for the experimental case. Secondly, as wire thickness begins to approach the diameter of the center conductor of the main line, we no longer have the necessary condition that the impedance of the gap be much greater than the impedance of the main line rendering the risetimes calculated from the inductor model too large for the very large diameter wires that we tested.

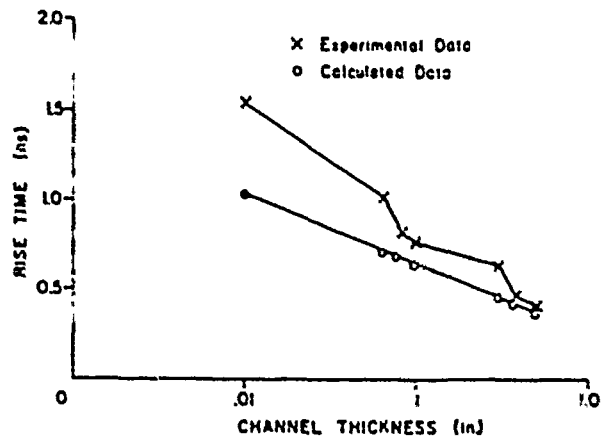


Fig. 6

The importance of these effects in high impedance triggered systems, may be further ascertained by comparing the results obtained in our simulation with the data obtained by Guenther and Bettis<sup>1</sup> using the laser trigger system mentioned previously. They studied the risetime of single and dual channel sparkgaps triggered by one or two laser beams focused on the cathode. A risetime of 2 ns for a single channel and 1.12 ns for dual channels were obtained in their experiment. This is a 44% difference between the two cases. Figure 7 shows a comparison between photographs of oscilloscope traces when one and two .01 inch diameter wires are used to simulate the arc channels. We have a 34% difference between the risetimes of the single and dual wire cases. Considering that the discontinuities in their experiment are more abrupt, (i.e. the cutoff frequency for the higher order modes in their experiment was 200 MHz, whereas in ours it was 600 A ), the results compared

favorable. Moreover, note that the increase in the risetime for the single channel case is consistent with our explanation.

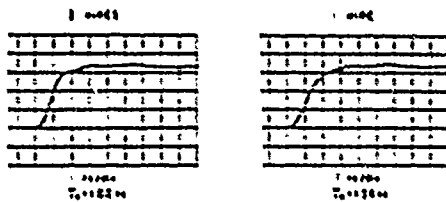


Fig. 7

It is apparent from these results that in nanosecond regimes, current risetime is strongly dependent on the geometry of the spark gap and arc channel system. If minimization of current risetime is to be achieved, reduction in the electromagnetic discontinuities must be considered. One way to accomplish this is by multi-channelling. From our results, the most desirable condition, for this case, is the simultaneous creation of either two or four channels at the outer edges of the spark gap. Considering the problems of simultaneously producing four channels, it seems that the percentage reduction using two channels may render this case to be the most practical.

Work supported by AFOSR under Grant #AFOSR-76-3124.

1. Guenther, A.H. and Bettis, J.R., J. Phys. D: Appl. Phys. 1, 1577-1613, 1978
2. Metzger, George and Jean-Paul Vabre, Transmission Lines with Pulse Excitation, 131-138, Academic Press, 1969.
3. Whinnery, J.R. and Jamieson, H.W., Proc. I.R.E., 32, pp. 98-114, 1944.



## AN ELECTRON-BEAM-TRIGGERED SPARK GAP

K. McDonald, M. Newton, E. E. Kunhardt, and M. Kristiansen  
Dept. of Electrical Engineering, Texas Tech University  
Lubbock, Texas 79409

A. H. Guenther  
Air Force Weapons Laboratory  
Kirtland AFB, NM 87117

Abstract

Studies on the triggering of a high-voltage, gas-insulated spark gap by an electron beam have been conducted. Risetimes of approximately 2.5 ns and subnanosecond jitter have been obtained for 3 cm gaps with gap voltages as low as 50% of the self-breakdown voltage (variable to 1 MV). The switch delay (including the diode) was 50 ns. The working media were  $N_2$ , and mixtures of  $N_2$  and Ar, and of  $N_2$  and  $SF_6$  at pressures of 1-3 atm. Open shutter photographs show that the discharge is broad in cross-section.

Voltage, current, and jitter measurements have been made for a wide range of gap conditions and electron-beam parameters. Variations in the character of the discharge have been inferred using streak and open shutter photography. Correlation between electron beam width, beam energy, discharge channel width, current risetime, delay, and jitter are discussed.

Introduction

Several current high priority research efforts such as fusion, the production of high energy-particle beams, and the simulation of environments associated with nuclear weapons detonations, require the generation of very high voltage, high peak power pulses. One of the principle prerequisites to achieving this objective is the

development of switches that will allow fast transfer of energy from an energy storage system to the load or transducer. We are currently engaged in a research program designed to improve the physical understanding of switching processes for the subsequent development of an advanced, low inductance, fast rise time, command fired spark gap switch, capable of operating at very high voltages (MV). Encouraging results toward this goal have been achieved by laser triggered switching<sup>1</sup> (LTS), and by e-beam triggered switching<sup>2,3</sup> (EBTS). This paper discusses an investigation into e-beam initiated breakdown which leads to the formation of a volume discharge (proportional to the cross-sectional area of the injected beam), which helps reduce electrode erosion and switch inductance.

The Experimental Arrangement

The experiment consists of an energy storage element, a gas insulated, pressurized spark gap, and a source of energetic electrons. (Fig. 1). The energy storage element and the spark gap are both contained within the high pressure vessel of the Ion Physics Corporation FX-15 (Fig 2). The energy storage element is a Van de Graaff charged co-axial line. It is capable of producing a 1 MV rectangular pulse of approximately 10 ns FWHM duration. The spark gap is formed by an interruption in the center conductor of the line. The stainless steel electrodes have a Bruce profile and are 21.5 cm in diameter. The high pressure in-

Work supported by AFOSR under Grant No.

AFOSR-76-3124

insulating gas also serves as the dielectric for the co-axial line. The electron beam is generated by a cold cathode, field emission vacuum diode, which is located behind the grounded electrode. It is actually placed inside the inner conductor of the output co-axial line, so as to introduce the e-beam axially through a 1" diameter aperture in the center of the electrode. In order to maintain a uniform field distribution in the gap and to protect the foil from the discharge, the aperture was covered with a stainless steel mesh (0.050"). The diode<sup>4</sup> (Fig. 3), designed and built at Texas Tech University, utilizes a spiral grooved graphite cathode, and a thin foil anode. Graphite was chosen because of its fast "turn on" properties<sup>5</sup>. The diode was designed to have an impedance of 70  $\Omega$  to match that of the driving generator. This generator is a 25 stage modified Marx pulse forming network (Heds pulser)<sup>6</sup>. It combines the voltage multiplicative feature of the standard Marx circuit with the pulse shaping characteristics of a lumped parameter network. The sequence of events in the experiment is as follows: The Marx erects to give an output waveform characterized by a 250 kV trapezoidal pulse of 50 ns FWHM duration with a 4 ns risetime. This pulse propagates down a 70  $\Omega$ , oil-filled, co-axial transmission line and appears across the anode-cathode gap of the diode. The diode emits, through a 1 mil. titanium foil, a 1.5 kA, 200 keV burst of electrons with a 0-50% risetime of 1.5 ns and a duration of 15 ns. This pulsed beam of electrons travels through 1.5 cm of the high pressure gas before it enters the spark gap. The insulating gas is ionized by electron impact, resulting in the subsequent formation of an ionized conduction path and the collapse of the voltage across the gap. The charged co-axial line of the FX-15 discharges, and the resulting wave propagates down a 50  $\Omega$ , oil-filled output transmission line, which is terminated in a matching  $\text{AlCl}_3$  water resistor. The outer conductor of the Marx Generator to diode transmission line also serves as the inner conductor for the FX-15 output transmission line.

#### Experimental Approach

The characteristics of the spark gap breakdown

investigated were: (1) the risetime of the transmitted voltage pulse, (2) the switch delay and jitter, and (3) the spatial character of the breakdown. The diagnostics used were open shutter and streak photography to record the character of the discharge, and a capacitive divider probe ( $C_1$ ), located in the FX-15 output transmission line, to monitor the voltage pulse generated at breakdown.

The parameters that we varied during the course of our investigation include: (1) The gap polarity (depending on how the Van de Graaff was charged, the target electrode was either positive or negative. When charged positive the injected e-beam was accelerated by the initial electric field in the gap, and for the target electrode negative the beam was decelerated), (2) the gap voltage  $V_g$  ( $V_g$  was varied between 50% and 98% of the self-breakdown voltage which ranged from 75 kV to 400kV), (3) gas pressure (1-3 atm), (4) the type of gas ( $\text{N}_2$ , mixtures of  $\text{N}_2$  and Ar, and mixtures of  $\text{N}_2$  and  $\text{SF}_6$ ), (5) the e-beam diameter (1.25 cm and 2.50 cm), and (6) the e-beam energy (150 keV to 250 keV).

#### Results

The pulse risetime was observed to vary with the beam energy and ranged from 2.5 to 3 ns. The larger value was obtained for a beam energy of 150 keV and  $V_g = 100$  kV or, 50%  $V_{SB}$ . The jitter was found to be virtually identical throughout the range of our investigation. Fig. 4a is representative of all jitter measurements. There are 15 separate, superimposed traces of the voltage pulse as monitored by the capacitive probe ( $C_1$ ), and displayed on a Tektronix 519 oscilloscope. The scope was triggered with the signal from the  $\beta$  probe ( $\beta_1$ ) located on the diode transmission line. The sweep speed was 2 ns/div, thus, the resolution is approximately 0.2 ns and the jitter can be seen to be no greater than this amount. These traces correspond to breakdown of a 3.2 cm gap in  $\text{N}_2$  at 3 atm. The gap voltage was  $V_g = 235$  kV or 94%  $V_{SB}$ . The self-breakdown voltage was 250 kV. The traces in Fig. 4b are further examples of the excellent jitter characteristics. With all other parameters identical to those given above, the beam was

injected when  $V_g = 130$  kV or  $52\% V_{SB}$ . Again, the jitter was below the capabilities of our resolution. These two experiments were conducted for positive and negative polarities, yielding identical results. The delay was obtained from figure 5 (a-a), where the  $\dot{B}$  signal from the diode transmission line is delayed to appear after the FX-15 voltage pulse. The delay time was measured to be 52 ns in pure  $N_2$ , which is consistent with previous studies<sup>3</sup>. The figure also demonstrates that (for these low voltages and pressures) the delay was invariant to both the pressure and the gap voltage (as a function of the self-breakdown voltage). We should also note that these results were obtained with a DC charged gap; one would expect the performance to be better for a pulse charged gap.

The character of the gas discharge for e-beam initiated breakdown was determined from open shutter photographs. This is shown in Fig. 6a when the target electrode was charged positive and in Fig 6b for a negative charged electrode. These two photographs are representative of the spatial character of the discharges observed throughout the range of our investigation. For the same polarity, the light intensity varied as we changed experimental characteristics. For different polarities, the character of the light emission are different, indicating that there is probably a difference in the breakdown processes. Note that for both cases, the breakdown takes the form of a volume discharge. No localized spark channels were seen.

Fig. 7 demonstrates the variation of the discharge as a function of the e-beam diameter. Note that the volume of the discharge is proportional to the cross-sectional area of the injected beam.

Fig. 8 depicts the variation in the dimensions of the discharge cross-section as a function of the energy of the injected beam. The light intensity is seen to be significantly increased when a more energetic beam is introduced into the gap. To investigate the significance of this observation, voltage pulses for varying e-beam energy were recorded (Fig. 9). The amplitude of the pulse is

also observed to be a function of the beam energy. These results indicate that the degree of ionization in the discharge plasma, hence the resistivity varies with the beam energy. The voltage drop across the gap is, therefore, a function of the e-beam energy.

Streak photographs of the discharge are shown in Fig. 10. Again, we can observe a difference between the cases of positive and negative target electrodes in the gap. Preliminary analysis indicate that the early emission of light corresponds to the actual breakdown (the time duration is the same as the voltage pulse), and the second emission is the result of the recombination process. Further analysis of these observations are presently being made.

#### Conclusions

The results obtained in this series of experiments on e-beam triggered switching are summarized as follows: (1) fast risetime (2.5 ns), (2) low jitter (less than 0.2 ns for  $V_g \geq 50\% V_{SB}$ ), and (3) volume discharge. The characteristics make e-beam triggered switches highly desirable for many applications.

The risetimes of the self-breakdown and the triggered voltage pulses were virtually identical, as demonstrated by the superimposed traces shown in figure 11. This is due to the fact that the pulse risetimes were generator limited rather than spark gap limited.

The demonstrated low jitter (particularly when operated at voltages well below the self-breakdown voltage), is one of the most significant contributions of this work. Small jitter is crucial to the successful operation of any pulse power system, however, it becomes extremely critical in any scheme that utilizes the simultaneous discharge of parallel pulse forming lines into a common load. Prefires can be virtually eliminated, due to the ability of the switch to function reliably at low voltage levels. The diode and, therefore, the switch has a very good single shot reliability, which eliminates most misfires.

The EDTS breakdown was observed to take the form of a volume discharge (proportional to the size of

the injected beam). This large area breakdown offers several advantages over the narrow channel breakdown found with most switches (e.g. LTS). These are: (1) The EBTS can be scaled up to very large area electrodes and transmission lines while maintaining a low switch inductance (a particularly attractive concept is an annular geometry), whereas other switches cannot duplicate this, unless multiple, current-sharing channels are formed. This, however, is not easily accomplished. In LTS, for example, multiple channels can be triggered by geometrical beam splitting<sup>1</sup>, but this method has optical alignment and maintenance problems particularly on large systems. This problem however, can probably be circumvented by the use of fiber optics<sup>7</sup>. (2) The volume discharge should result in a substantial lowering of the switch inductance<sup>4</sup>, hence, faster risetimes. (3) The volume discharge minimizes electrode erosion, thereby enhancing the switch lifetime and thus promoting the possibility of developing a reliable rep-rated EBTS. The recovery time should also be reduced as contrasted to the narrow channel discharge case because of the lower degree of ionization per unit volume.

#### References

1. A. H. Guenther and J. R. Bettis; "The Laser Triggering of High Voltage Switches". J. Phys. D.: Appl. Phys., Vol. 11, 1577, (1978).
2. E. A. Abramyan, V. V. Borob'ev, A. A. Egorov, V. A. Elkin, and A. G. Ponomarenko; "Initiation of a Discharge in a Megavolt Gas Spark Gap". Nuclear Physics Institute, Siberian Branch, Academy of Sciences of the USSR, Novosibirsk, January 1971.
3. A. S. El'chaninov, V. G. Emel'yanov, B. M. Koval'chuk, G. A. Mesyats, and Yu F. Potapitsyn; "Nanosecond-range Triggering of Megavolt Switches". Sov. Phys. Tech. Phys., Vol 20, No. 1, 51, (1975).
4. M. Newton, K. McDonald, E. E. Kunhardt, M. Kristiansen, and A. H. Guenther; "Applications of Electron Beams for Precise Switching of High Voltages". 3rd International Topical Conf. on High Power Electron and Ion Beam Research and Technology, Institute of Nuclear Physics, Novosibirsk, USSR, July, 1979.
5. R. K. Parker; "Explosive Electron Emission and the Characteristics of High-Current Electron Flow". Technical Report No. AFWL-TR-73-92, Jan., 1973.
6. J. K. Trolan, F. M. Charbonnier, F. M. Collins, and A. H. Guenther; "A Versatile Ultrafast Pulse Power System". Exploding Wires III, pp. 361-389, Plenum Press, 1964.
7. L. L. Macfield, H. C. Harjes, M. Kristiansen, A. H. Guenther, and K. H. Schönbach; "Low Jitter Laser Triggered Spark Gap Using Fiber Optics". 2nd IEEE Int. Pulsed Power Conf., Lubbock, Texas, June, 1979.

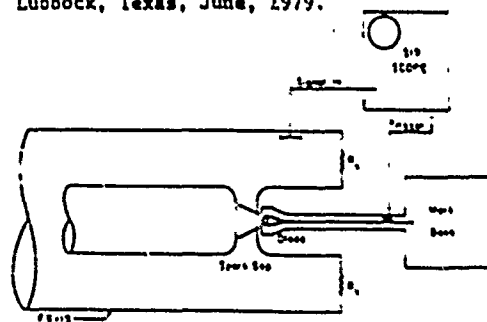


Figure 1: Basic Arrangement

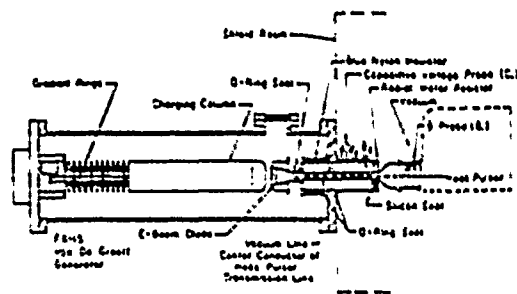


Figure 2: Experimental Arrangement

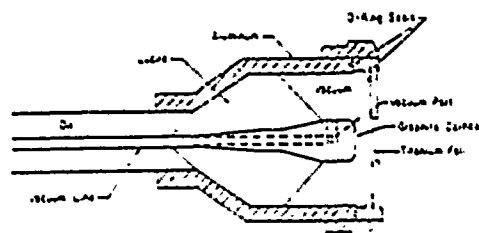


Figure 3: The Diode

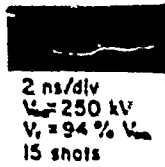


Figure 4a

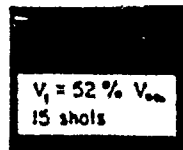


Figure 4b

Fig. 4 Jitter

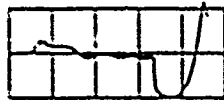


Figure 5: Delay

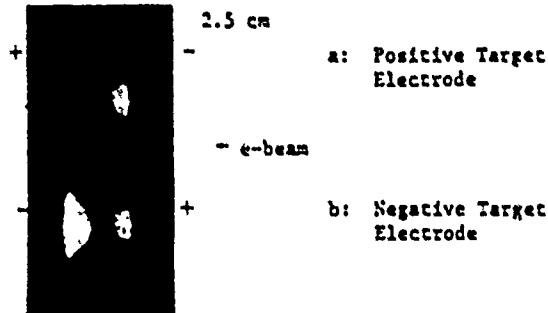


Figure 6:  
 Variation in the open shutter photographs of the discharge as a function of the polarity of the target electrode

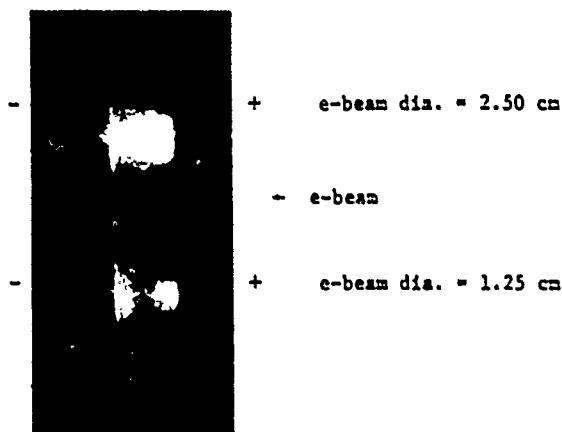


Figure 7:

Variation in the open shutter photographs of the discharge as a function of the e-beam cross-sectional area

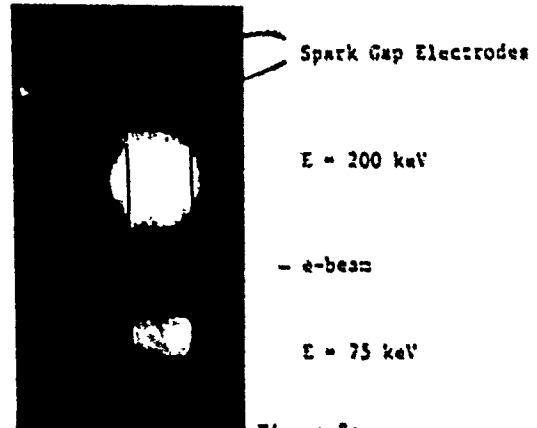


Figure 8:

Variation in the open shutter photographs of the discharge as a function of the e-beam energy

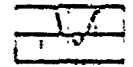
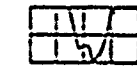


Figure 9:  
 Pulse Amplitude as a Function of the E-Beam Energy

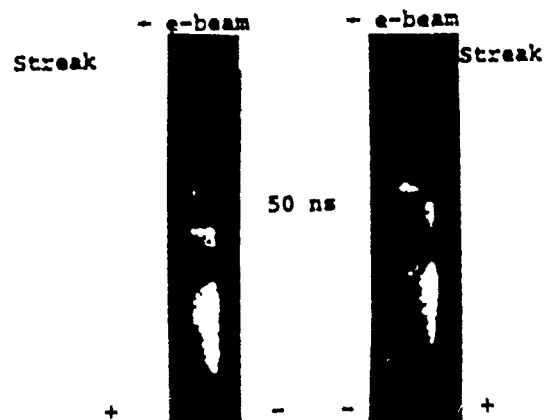


Figure 10a Positive Case  
 Figure 10b Negative Case  
 Fig. 10 Streak Photographs of E-Beam Initiated Breakdown

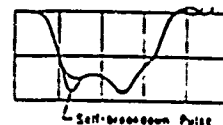


Figure 11:

Superimposed self-breakdown and e-beam initiated breakdown voltage pulses

# LOW JITTER LASER TRIGGERED SPARK GAP USING FIBER OPTIC

L.L. Hatfield, Dept. of Physics, H.C. Harjes,  
M. Kristiansen, and A.H. Guenther, Dept. of Elect. Engr.  
and K.M. Schönbach \*

Texas Tech University  
Lubbock, Texas 79409

## Abstract

Laser triggering of a pulse charged gas switch is described. The laser triggering results in low jitter switching relative to the timing of the laser pulse. A novel feature is the use of a single element, 1mm, quartz, optical fiber to transmit the laser beam. The switch parameters, such as gas pressure, gas composition, and laser beam focal point location have been optimized to produce nanosecond delay and jitter with as little laser power as possible. The laser optical system has been optimized for best overall efficiency in a configuration suitable for illumination of many fibers by a single laser. Typical operating parameters for the switch are: 2 cm gap, 2500 Torr pressure, 50% Ar - 50% N<sub>2</sub> gas mixture, and a charging voltage of 200 kV. Laser power in the gap is typically a few megawatts with an overall efficiency greater than 50% for the optical system.

## Introduction

Laser triggering is one of the most reliable ways to trigger a spark gap, however; in order to use this technique the laser light must have an optical path into the gap. If the laser and gap are separated by appreciable distances, this path could become awkward and present problems in align-

ment and exposure of the optics to the environment. By using an optical fiber to transmit the laser light from the laser to the gap, all alignment and environmental problems can be confined to the ends of the fiber.

Figure 1 shows the experimental arrangement that was used to investigate the application of fiber optics in this way. The spark gap is a switch on a water dielectric, coaxial Blumlein. The intermediate conductor of the Blumlein is charged by a three stage Marx bank. The Marx bank has:  $C = 60$  nf,  $V_{\text{max}} = 300$  kV,  $W_{\text{max}} = 2700$  J, and an erection time of 250 ns, when fired into the Blumlein generator. The Blumlein has:  $C = 6$  nf,  $V_{\text{max}} = 250$  kV,  $W_{\text{max}} = 210$  J, and on one shot at 250 kV 1.4 nC are switched from the Blumlein through the gap. The voltage on the intermediate conductor was monitored by a capacitive probe located near the gap (Fig. 1) and the current in the load was monitored by a resistive probe in the load resistor. A  $\beta$  probe located behind the gap

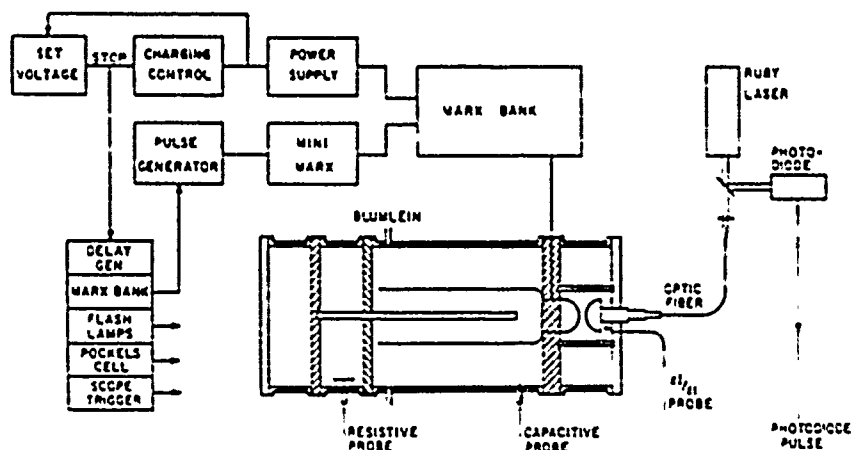


Fig. 1 Experimental Arrangement

was used to monitor the gap breakdown, while a photodiode was used to determine both the laser pulse shape and the time of laser firing. By using these two signals, the delay between the laser entry into the gap and the gap breakdown was measured. The laser light entered the gap through a hole in the cathode and was focused onto the anode. Figure 2 shows the optics that were used between the laser and the gap. The fiber was a step index, single strand of quartz with a numerical aperture of .22 and a diameter of one millimeter. On the output end of the fiber light exists with a divergence full angle of  $18^\circ$  at the  $e^{-1}$  points. Since the light diverges from the fiber, an uncoated quartz lens was positioned to collimate this light while another uncoated quartz lens focused the light onto the anode as shown in Figure 2. The light was coupled into the fiber

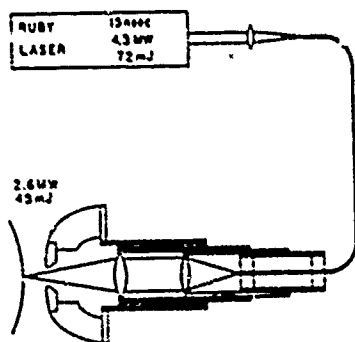


Fig. 2 Optics

using an uncoated quartz lens to reduce the beam diameter. The light was allowed to pass through the focus and diverge before entering the fiber. This was done so that the light would not come to a focus inside the fiber. At laser power levels which do not produce surface damage on the fiber, there was no air breakdown. Flat surfaces on the fiber ends were obtained by stripping the cladding back, scratching the quartz circumferentially, and then breaking the fiber. When ends prepared by this method were examined under a microscope the surfaces appeared to be flat and smooth over 2% of the area with a flaw always appearing on the edge where the break finished. After breaking the fiber, it was necessary to reclad the ends,

otherwise the output divergence angle would increase significantly.

A typical laser pulse had a half width of 15 ns, an energy of 72 mJ, peak power of 4.3 MW. After passing through the optical system and into the gap, the laser energy was 45 mJ and the peak power was 2.6 MW. The optical system had a transmission efficiency of 61% despite the fact that three uncoated lenses, each representing an 8% loss were used. If these lenses were coated the efficiency would increase to 78%.

The timing which took place in the experiment is shown in Fig. 3. After the Marx bank was charged, the flashlamps on the laser were flashed and then the Marx bank was fired. Approximately 150 ns later the laser pulse entered the gap and after a certain delay the gap broke down.

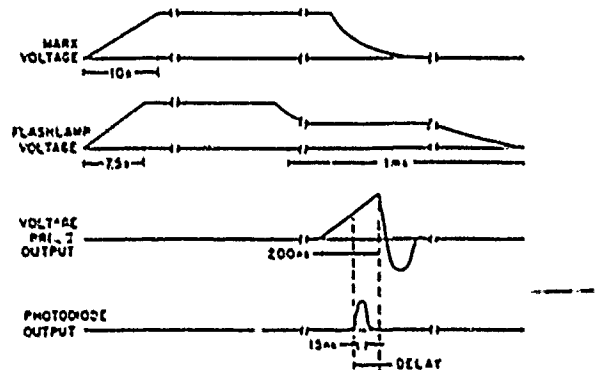


Fig. 3 Timing

Figures 4-6 show results obtained with a 2 cm gap pressurized to 2700 Torr with different mixtures of Argon and Nitrogen. The graphs show the dependence of delay upon the percentage of self-breakdown voltage which appears across the gap when the laser enters the gap. The self-breakdown voltage was determined by firing the Marx into the Blumlein and allowing the voltage across the gap to rise steadily until breakdown occurred (Fig. 7a). Figure 4 shows two curves which correspond to different ways of charging the Blumlein. Curve A corresponds to data obtained when the voltage across the gap rose steadily until triggering occurred. Curve B of Figure 4 and Figures 5-6 corresponds to data obtained when the voltage across the gap leveled off

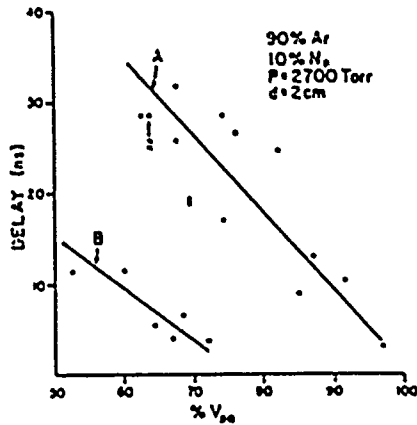


Fig. 4

Delay versus percentage of  $V_{SB}$  for a gas mixture of a gas mixture of 90% Ar and 10% N<sub>2</sub>. "A" shows data obtained when the Blumlein was charged as in Fig. 7a. "B" shows data obtained when the Blumlein was charged as in Fig. 7b.

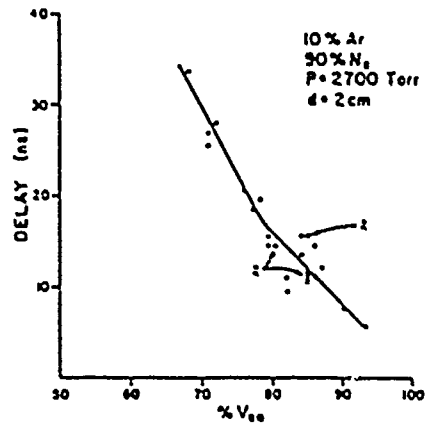


Fig. 6

Delay versus percentage of  $V_{SB}$  for a gas mixture of 10% Ar and 90% N<sub>2</sub>.

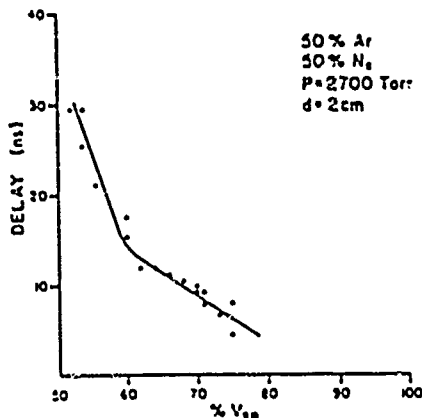


Fig. 5

Delay versus percentage of  $V_{SB}$  for a gas mixture of 50% Ar and 50% N<sub>2</sub>.

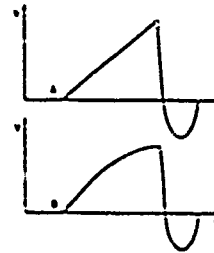


Fig. 7

The time dependence of the voltage across the gap for different charging conditions. (A) The voltage rises steadily to breakdown. (B) The voltage levels off before breakdown.

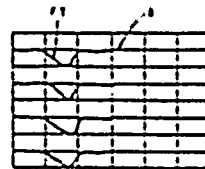


Fig. 3

Four consecutive Tektronix 519 oscilloscope traces with a horizontal scale of 10 ns/div. F.T. is a fast trigger pulse derived from the laser pulse and the trace disappears because the  $\delta$  signal is so fast. These shots show nanosecond jitter.



before triggering (Fig. 7b). Figure 4b shows that in a gas mixture of 90% Argon and 10% Nitrogen the delay ranged from 3 to 11 ns as the percentage of  $V_{SB}$  ranged from 70 to 50. In 50% Argon and 50% Nitrogen, the delay ranged from 5 to 29 ns while the percentage of  $V_{SB}$  ranged from 75 to 55 (Fig. 5). In 10% Argon and 90% Nitrogen, the delay ranged from 5 to 33 ns while the percentage of  $V_{SB}$  ranged from 93 to 68. These graphs also show that under the same charging conditions the delay at a certain percentage of  $V_{SB}$  decreases as the concentration of Argon goes up. Figures 5 and 6 also show breakpoints at approximately 15 ns which is the laser pulse width. Once the laser turns off, the delay increases at a faster rate as the percentage of  $V_{SB}$  decreases. Figure 8 shows four shots in 10% Argon and 90% Nitrogen at 85%  $V_{SB}$  which demonstrate nanosecond jitter.

In the curves shown, all the data were obtained with the laser focused on the anode; however, when the focus was moved to the center of the gap, no significant change in results was observed. This observation can be explained by noting that an image of the fiber appeared at the anode because the fiber was not a point source of light. Under such conditions the spot size on either side of the focal plane changes slowly. Therefore the power density on the surface of the anode did not decrease enough to make a significant difference in triggering when the focus was moved to the center of the gap.

#### Conclusion

The results in Figures 4-6 demonstrate the same characteristics of laser triggering as presented by Guenther and Bettis<sup>1</sup>, thus proving that it is possible to laser trigger a spark gap through an optical fiber and obtain low delay and jitter. The fact that the location of the focal spot is not critical (not true in the work of Guenther and Bettis) is probably due to the beam divergence introduced by the fiber.

\* On leave from Technische Hochschule Darmstadt, FRG.

#### References

1. Guenther, A.H. and Bettis, J.R., 1978, J. Phys. D: Appl. Phys. 11, 1577-1613.

## A 3-MV LOW-JITTER TRIGGERED GAS SWITCH\*

D.B. CUNNINGHAM and H.G. HAMMON, III

Physics International Company  
2700 Merced Street  
San Leandro, California 94577

Abstract

Physics International Company has designed, built, and tested a 3 MV, low jitter, triggered gas switch. The switch operates in a 16.5  $\Omega$  coaxial pulse line. The system design requires that the pulse line switches perform the difficult task of first holding off a reverse pulse charge, then of holding off the forward pulse charge, then, finally, of triggering on command. The trigger for the switch is generated by a trigger Marx placed within the output pulse line. The remainder of the triggering circuit includes a trigger isolation gap. A V/N-type trigger electrode is situated within the main gap. To date, the switch has been shown to hold voltage and trigger reliably for pulse charges from 0.9 MV to 2.5 MV. The rms jitter of the switch firing time is less than 6 ns. At an operating voltage of 2.5 MV, the switch transfers a charge of up to 0.1 coulomb per shot, with a peak current of 30 kA.

Introduction

Physics International has designed, built and tested a 3 MV, low-jitter, triggered gas switch. Figure 1 shows the major components of the switch and how they are assembled. In tests, including more than 5000 shots in the M-2 pulser built for the PHERMEX facility at Los Alamos Scientific Laboratory, the switch has met all design expectations. In operation, the switch sees a  $(1 - \cos \omega t)$  pulse charge, with the voltage rising from zero to peak in 450 ns. We have operated the switch with pulse charges from slightly under 1 MV to approximately 2.5 MV. Over the entire triggering range, the total system jitter, including that

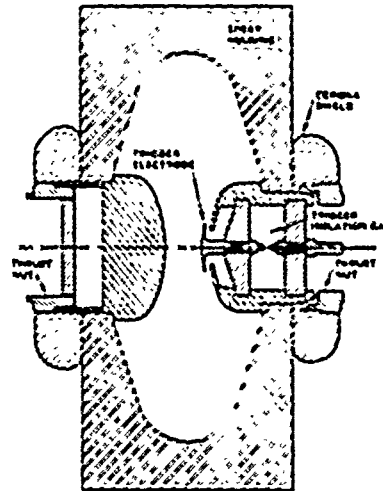


Figure 1 Line switch schematic.

of the triggering circuit, is less than 5 ns. Assuming the jitter of the switch adds in quadrature to that of its triggering system, the switch jitter alone is less than 6 ns. The self-break curve of the switch (Figure 2) shows that the

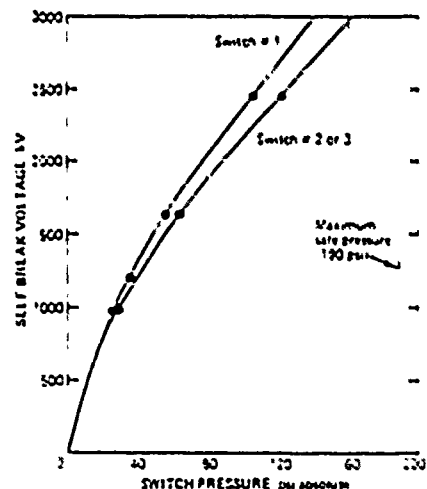


Figure 2 Self-break voltage versus pressure.

\* Work performed under contract from Los Alamos Scientific Laboratory.

switch can be expected to operate well to its design level of about 3 MV. The M-2 pulser as a whole is limited to about 2.8 MV, preventing our testing the switch to its design limit.

The basic switch design requirements were imposed by the customer's specifications for the M-2 pulser in which the switch was to operate. The pulser specifications of interest are listed in Table 1, and the overall configuration of the pulser designed to meet the specifications is shown schematically in Figure 3. Each of the

TABLE 1

## System Requirements for the M-2 Pulser

1. Output	0.6 to 1.5 MV
2. Pulse Duration	
1 pulse	$40 \pm 4$ ns
2 pulses merged	$80 \begin{smallmatrix} +20 \\ -0 \end{smallmatrix}$ ns
3 pulses merged	$120 \begin{smallmatrix} +30 \\ -0 \end{smallmatrix}$ ns
3. Risetime	$< 25$ ns
4. Jitter	$< 8$ ns
5. Pulse Separation	180 ns minimum 30 $\mu$ s maximum
6. Reliability	$> 90\%$ of shots good in all respects
7. Maintenance	Not more frequent than every 1000 shots

system specifications has its effect on the final choice of a switch design. For example, the output voltage specification defines the voltage range over which the switch must operate. The operating range impacts the choice of the switch electrode gap, the gas pressure range for the switch, the type of gas to be used, the shape of the switch housing, etc. The risetime specification defines the minimum switch inductance and thus puts restrictions on switch length and geometry as well as on the switch gap and triggering scheme. (A pulse sharpening switch close to the load would be no mean feat, since we have three pulses in series, each of which must meet the risetime specification.)

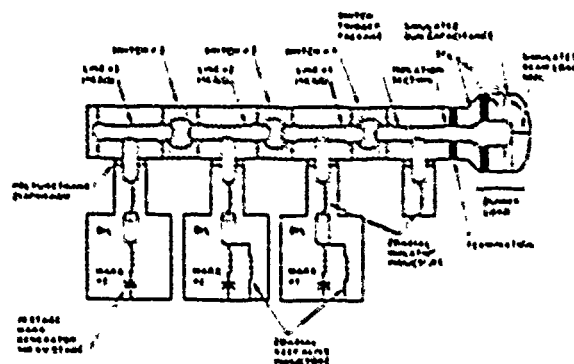


Figure 3 PHERMEX M-2 Pulser--schematic diagram.

## Design Particulars

The design criteria for the primary elements of a high voltage switch are deeply interrelated, making it totally impossible to complete the design of any one switch component without first knowing how the rest of the switch is to be constructed. Switch design is, therefore, a fundamentally iterative process. For clarity in presentation, however, the design of individual switch elements will be discussed, as much as possible, as independent activities.

The obvious place to begin is the criterion which forced the choice of a gas rather than a liquid switch. Stringent specifications on pulse shape, prepulse, and jitter require that each pulse line be electrically isolated from the adjacent pulse lines. This requirement means that the switch capacitance must be small compared to the pulse line capacitance. This can best be accomplished by assuring that the dielectric constant of the switch volume is well below that of the pulse line insulator. For our ethylene glycol insulated pulse line, we chose to make gas switches with housings machined from individual epoxy castings. The capacitance with which the switch couples the pulse lines is roughly  $5 \times 10^{-11}$  fd, small compared to the pulse line capacitance of  $2 \times 10^{-9}$  fd.

The configuration of the system, with the line switches separating adjacent pulse lines, imposes another important restriction on switch design (Figure 3). The complexities associated with

holding off first a reverse pulse charge, then firing, with low jitter, at the peak of the forward pulse charge, require that the switches have nearly symmetric electrodes and a low-jitter trigger system (Figure 1).<sup>1</sup>

The remaining features of the electrode geometry are defined primarily by three criteria: maximum voltage holdoff, triggering range, and switch inductance. Data, largely empirical, are available on the self-break voltage of uniform-field switches, as a function of gas type and pressure.<sup>2</sup> The maximum anticipated pulse charge thus specifies a minimum electrode gap. The triggering range (the switch must be able to fire at voltages as low as 40 percent of the maximum) combines with the maximum allowable inductance (to meet risetime requirements) in specifying the maximum allowable gap. One only hopes that, since the maximum and minimum gaps are defined by different criteria, the maximum allowable gap is not smaller than the minimum gap. In fact, if the electrode diameter chosen is too small, extracting a high inductance penalty per unit length, this can actually happen. The choice of electrode diameter, therefore, is made along with the choice of the switch gap, based primarily on inductance and holdoff requirements. To meet the 25 ns risetime specification, the switch inductance must be  $\leq 200$  nH. The switch inductance as designed is  $\sim 130$  nH (2 arc channels).

Other details of the shapes of the individual electrodes are also defined by considerations based on the maximum voltage holdoff. For example, in addition to holding off voltage across the gap, the switch must be resistant to tracking along its surfaces. The JASON computer code is used to calculate the electric fields near the electrodes. The final electrode shape is chosen to produce a field which: (1) is as small as possible at the junction of the electrode with the epoxy; (2) has its maximum between the two switch electrodes; and (3) is nearly uniform within the gap (Figure 4).

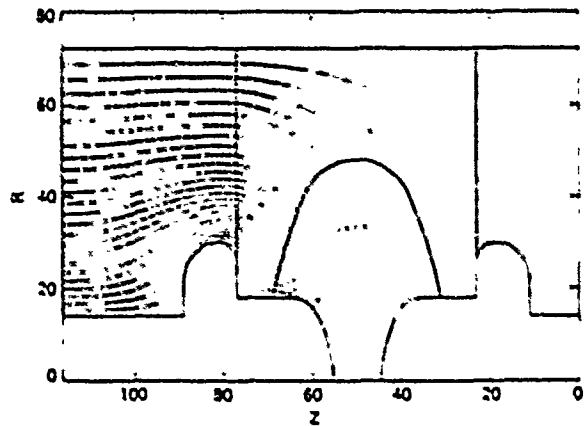


Figure 4 PHERMEX switch equipotential plot.

The JASON code is also used to develop a housing shape that will be resistant to tracking along its gas-plastic interface. Operating at its design level of 1 MV pulse charge, the component of the electrode field parallel to the gas-epoxy interface reaches a maximum of 130 kV/cm. Furthermore, the peak field is located well away from bottom-dead-center, where debris might collect and promote tracking. The mechanical strength of the housing is checked using MARC, a finite element code available from Computer Data Corporation, to ensure that the housing will be able to hold pressures well above those required for normal operation.

To meet the requirements on jitter and triggering ranges, the switch must be triggered, rather than relying on self-breaking. The primary components of the triggering system are the trigger electrode and the trigger isolation gap (TIG) (Figure 1). Both the TIG and the trigger electrode stick-out can be adjusted to optimize switch triggering and holdoff. The TIG serves the purpose of decoupling the trigger electrode from the trigger Marx, which supplies the actual trigger signal. The potential of the trigger electrode is thus allowed to float, as the switch is pulse charged, to a level which minimizes its disturbance of the overall gap field. When the trigger signal arrives, the TIG breaks down and the trigger electrode is pulled off its "no disturbance" potential. At this voltage, the trigger electrode has a very large enhancement, streamers are launched from the trigger electrode,

and the switch gap breaks down. The interval required for this switch to trigger is reproducible to within less than 6 ns for a given pulse charge.

Several primarily mechanical features of the switch are of interest. The switch contains two isolated pressure volumes, one for the main gap and trigger electrode, the other for the TIG. This feature is necessary as the TIG and the main gap are switches of different enhancements and see different voltage histories. The switches thus cannot be expected to track each other. Customer specifications require that a two-person crew can remove a switch and replace it with a spare in not more than 4 hours. The threaded stainless steel thrust nuts, indicated in Figure 1, seal the switch and make the electrical connections to the adjacent pulse lines. The simplicity of this attachment scheme allows rapid switch replacement without jeopardizing the voltage holding characteristics of the switch or of the pulse lines, both of which are highly stressed at full voltage.

#### Conclusions

The 3 MV switch, designed for use in the M-2 pulser, has performed well for more than 5000 system shots. Though the switches carry peak currents as high as 80 kA and transfer as much as 0.1 coulomb per shot, we have seen negligible electrode wear to date. The jitter, holdoff, triggering range, and inductance of the switch are well within the design limits. It may be possible to use the switch without significant design changes in other high voltage systems. Furthermore, the success of this switch design provides information that will be of assistance in the design of other high voltage switches. Switch operating characteristics are summarized in Table 2.

TABLE 2

#### Switch Parameters and Characteristics

Operating Range:	~ 900 kV to ~ 3 MV
Trigger Voltage:	~ 250 kV pulse
Pressure Range:	to 175 psig (SF <sub>6</sub> )
Main Electrode Gap:	7 cm
External Dimensions:	36 inch diameter 20 inches thick
Peak Field (gas-epoxy interface):	130 kV/cm at 3.0 MV
Switch Inductance:	~ 130 nH

#### Acknowledgements

The authors wish to thank the staff at Los Alamos Scientific Laboratory for their contributions and cooperation, especially Jack Harwick and Fred Van Haaften. Special appreciation is also due the project manager, Glen Rice, and to Phil Chaopney, Gordon Simcox, Tom Naff, and Steve Hogue for their many contributions.

#### References

1. For a more complete discussion of this problem and of the system as a whole, see: D.E. Cummings and H.G. Hammon, III, "The Design Approach to a High-Voltage Burst Generator," Proceedings of the 2nd IEEE International Pulsed Power Conference, Lubbock, Texas, June 1979.
2. See for example, D. Legg, "Insulation Applied to Circuit Breakers," Power Circuit Breakers Theory and Design, C.H. Flurscheim, ed., (Peter Peregrinus, Ltd., Hertsfordshire, England) International Scholarly Book Services, Inc., Forest Grove, Oregon, 1975.

## CHARACTERIZATION OF HIGH POWER GAS SWITCH FAILURE MECHANISMS

E. E. NOLTING

Naval Surface Weapons Center  
White Oak, Silver Spring, Maryland 20910

Abstract

A multistage, 4 MV, low jitter, command triggered gas switch is being developed for use on large pulse power devices. Experiments to date have shown that the performance and operational life of the switch are severely limited by mechanical and electrical failure of the insulating housing. Estimates of the internal overpressure produced during switch closure have been made which indicate the severity of the blast containment problem; this information has led to the development of a mechanically stronger switch design. Surface analyses performed on both switch electrode and insulator surfaces were used to investigate observed electrical failure of the insulators. A layer of closely spaced metal particles were found imbedded in the insulator walls.

Introduction

During the past year and a half the Naval Surface Weapons Center, White Oak Laboratory (NSWC/WOL), and Pulsar Associates, Inc. (PAI)\*, have cooperated on the development of a 4 MV, low jitter, command triggered, gas switch. The fully developed switch is intended for use on high power, single pulse devices and testing has been performed on the Defense Nuclear Agency's Casino nuclear weapons effects simulator. At present the Casino simulator has four three-electrode water switches which each transfer a nominal 100 kJ from four 2.5 n pulse-forming lines into matched loads. The gas switches, when fully operational, will be used to replace the water switches.

There are several reasons why operable gas switches would be preferable to the existing water switches. First, recent computer studies of switch parameters indicate that water switches are inherently more resistive and suffer from time dependent capacitive coupling effects.<sup>1</sup> Therefore, water switches have a substantially greater loss in delivered power and energy than those with a gas dielectric. Second, gas switches can be operated with less jitter, an important consideration when synchronization is required. Third, the mechanical shock associated with switch closure is considerably less with a gas dielectric switch. Reduction of mechanical shock lengthens both switch and machine lifetimes. Fourth, current distribution

in gas switches is more controllable than in water switches; therefore, switch inductance and resistance exhibit less shot-to-shot variation.

The design goals for the gas switch development are: (1) a maximum hold off voltage of 4 MV with a pulseline charge time of 1.5  $\mu$ sec, (2) a transfer of .05 coulomb and 100 kJ in a single pulse, and (3) a command trigger with a maximum jitter of less than 10 ns. Presently there are no switches which meet all of these requirements.<sup>2,3</sup>

Description of Switch

Figure 1 illustrates the design of a single section of the multistage switch tested at Casino. Switch voltage is equally divided across each stage (within five percent), an arrangement that gives the maximum voltage hold off for the multistage switch configuration for a fixed gas pressure. Several gas dielectrics have been tried. An equal part mixture of sulfur hexafluoride and argon has been found to give most satisfactory results in terms of dielectric strength and cleanliness.

Various triggering schemes have been employed to command fire the gas switches; however, all the methods have used the same fundamental design. A high voltage signal is input at the positive end of the switch producing ultraviolet illumination of the negative electrode. The illuminated electrode emits electrons which initiate rapid closure of the triggered stage. An annular electrode configuration allows the ultraviolet radiation produced by the closure of the triggered gap to radiate the second stage. Each succeeding stage is illuminated by the preceding gap in the same manner until the entire switch is closed.

The entire switch column assembly was rigidly connected at the positive output end of the switch. At the opposite end, the switch columns were attached to a plate which was electrically connected by several short, braided straps. This cantilevered switch assembly allowed shifting of the pulseline and transformer, when transmission line fluids were transferred, without creating stresses in the switch components. Figure 2 shows location and mounting of the switch assembly.

Illuminated, multistage switches of similar design have demonstrated low jitter operation.<sup>3</sup> The maximum voltage the switch is able to sustain is determined by switch length. i.e., the number

\*Pulsar Associates, Inc.  
11491 Sorrento Valley Road  
San Diego, California 92121

of stages employed.

#### Discussion of Mechanical Failure in Gas Switch

The first gas switch tested at Casino had 2.5 cm diameter brass electrodes and an acrylic insulator 2.4 cm in length and 5 cm in diameter. The entire switch assembly consisted of six parallel columns, each with 18 stages, evenly spaced on a 25 cm diameter bolt circle. This configuration provided about 5 ns isolation between adjacent columns which was intended to force all of them to share currents equally. Unfortunately, simultaneous closure of the columns did not consistently occur. The one column that transferred all the energy catastrophically failed even at modest voltages (2.5 MV).

The primary failure mode was fracturing of the tie rods caused by the axial expansion of the switch column produced by the large gas pressures generated by the arc. Axial expansion of the switch column occurred because of deformation of the assembly end plate located at the pulseline end of the switch. Insulators, usually the ones located at both ends of the column, were also destroyed as the unbroken tie rods would rapidly restore the column to its original length.

Although an occasional failure would be produced by a water arc occurring outside the switch column, most were caused by internal pressures generated in the gas by the passage of large switching currents. The amount of energy deposited in the switch is difficult to measure, but calculations indicate that energies of 30 kJ (peak current of 500 kA) are deposited in the switch in about .5  $\mu$ sec. These calculations, together with an estimate of an equation of state for the gas, lead to a prediction of  $9.5 \times 10^6$  Pa (1400psi) for peak switch pressures. Containment of dynamic pressures of this magnitude required a redesign of the original switch hardware. Two different approaches were used to prevent the mechanical failures.

NSWC/WOL tested several plastics to determine which materials were most compatible for switch insulator and tie rod use. Four types of plastics (high molecular weight polyethylene, polypropylene, acrylic, and polycarbonate) were studied for insulator use. Each of the plastics were pressure tested under static and dynamic loading. Both the polyethylene and polypropylene were found to distort sufficiently under pressure to cause o-ring seals to be broken. Furthermore, the polyethylene eroded badly due to surface tracking during electrical tests performed on Casino. The polycarbonate insulators were found to survive static and dynamic pressure tests of up to  $7.4 \times 10^6$  Pa (1100psi), while the acrylic plastic failed at static pressures as low as  $3.4 \times 10^6$  Pa (500psi) after cycling.

A glass-reinforced polycarbonate (30% random-oriented glass fiber, 70% polycarbonate resin) was tested, both for strength and electrical properties, as a possible tie rod material. It was found that the glass-filled polycarbonate tie rods exhibited much less elongation and failed at about the same tensile stresses as the pure polycarbonate samples. Pulse testing on Casino revealed no

electrical failure when where impressed across a built a three column switch the glass-filled polycarb. 5 cm ID, lexan insulators. up to 4.2 MV rods. NSWC/WOL which used 4x and 1/4 column assembly was clamped between two 1.3 (3") steel plates that were held by three 5 cm (2") diameter polycarbonate tie bolts to prevent the switches from axially expanding. With this arrangement the switch has been operated at voltages up to 4.2 MV with all energy transferred through one switch column without mechanical failure. During these higher voltage test switch current was sufficient to melt electrode solder joints and electrodes had to be welded to the electric grading fin for support.

PAI built a single column, 10-stage switch that increased the acrylic insulator length, inside diameter, and wall thickness by a factor of two. By increasing the switch column by a factor of eight the pressures at the insulator wall were greatly reduced. The pure polycarbonate tie rods were also doubled in diameter. This single switch exhibited no mechanical failures during testing of voltage up to 4 MV.

Both designs worked satisfactorily in stopping the failure of the column insulators and tie rods due to the overpressure. The single-column design is more inductive than the six-column switch, but because the insulating surface was moved further from the arc path it is likely to exhibit longer switch life. A single column switch has been used in all subsequent testing.

#### Discussion of Insulator Electrical Failure

After the switch assembly was designed so that it no longer exhibited mechanical failures, it was discovered that the maximum hold off voltage of the switch degraded with switch use. For a given gas pressure setting the voltage at which the switch would close without command trigger decrease as much as 1.5 MV over a ten-shot firing sequence. Since low jitter, command trigger operation requires the voltage across the switch at the time of trigger arrival to be within about 10% of the self-breakdown voltage, it was not possible to make jitter measurements.

Inspection of the insulator walls showed that faint tracks bridged the length of some of the insulators. Figure 1 indicates location of wall tracks. It was evident that little energy was actually transferred along the insulator wall because of the lack of damage found on either the insulator or the adjacent grading fin. Apparently current passing along the inside wall acts as trigger mechanism for the associated electrodes. Initiation of the main gap closure may occur because of imbalance of the electric field at electrodes due to the surface tracks causing asymmetric field distortion. Another possible mechanism is the generation of ultraviolet radiation at the insulator wall that illuminates the electrode.

Attempts to stop the sliding sparks by convoluting the inside insulator wall did not have any measurable effect. The surface contours required that the

sliding sparks, starting at grading fin-insulator-gas triple point, would have to reverse direction against the potential gradient. Furthermore, the convolutions were designed so that blast and ultraviolet radiation from the main gap closure were not directly incident at the triple point. Experiments on Casino showed that the tracking still occurred with tracks passing directly across the convolutions.

Tests of a single stage of a switch at comparable voltages, but much less transferred energy than at Casino, were conducted at PAI. No decrease in the insulator's maximum voltage hold off were observed. These results indicated that insulator breakdown phenomena is energy dependent.

It was hypothesized that the source of the insulator electrical failure was due to one or more of the following: contamination from by-products formed by the electrical breakdown of the sulfur hexafluoride used as the insulating gas<sup>6</sup>; ultraviolet radiation charged<sup>7</sup>, causing insulator surface to become charged; micro-fractures of the insulator formed by the dynamic overpressure of the arced insulating gas; insulator surface erosion by hot gases creating a microscopic surface structure that is electrically weaker; or electrode material being plated on the insulator surface. To test these, hypothesis samples of the insulators were sent for surface analyses.\* The insulators analyzed included unused plastic, heavily and lightly cracked insulators, and used insulator with no observable insulator tracks.

Scanning Electron Microscopy (SEM) was used to show insulator inner wall topography. Figure 3 shows a comparison of the surface of an unused insulator and one exposed to several switch closures. There is an obvious difference in the contamination level between the two insulators.

Transmission Electron Microscopy (TEM) was used to provide high magnification (up to 50,000x) of the insulators internal structure. A thin section (~1000A thick) TEM micrograph is shown in Figure 4. The micrograph shows copper and zinc deposits (black dots) imbedded in the insulator surface. The size of these particles range from about 250A to 1000A in diameter. No stress cracks were observed in the body of the insulator indicating a lack of obvious structural damage due to blast.

The inside surface of the insulators were analyzed by Energy Dispersive Electron Probe Microanalysis (EDX) to determine the main elemental components several microns into the surface. These tests results showed the presence of copper and zinc on all used insulators, with the cracked insulators exhibiting the largest amounts. The quantity of copper and zinc were found to be approximately equal; a finding that is consistent with the lower energy requirement for the vaporization of zinc and the approximate 2.5 to one concentration superiority of copper in the brass electrodes.

Electron Scan for Chemical Analysis (ESCA) was used to measure the insulator surface properties

\*Structure Probe, Inc.  
230 Forrest Street, Metuchen, NJ 08840

to a depth of about 20A. The advantage of ESCA is that it not only detects the elements present but also indicates the types of chemical compounds formed. While considerable fluorine was found on the used insulator surfaces, the analysis showed that the oxidation states of the copper and zinc were not due to that element. Also, very little free sulfur was found on the surface of the insulator. These results imply that the breakdown of SF<sub>6</sub> was not likely the cause of the insulator failures.

The brass electrodes were analyzed by Scanning Auger Microscopy (SAM). These tests gave the somewhat surprising result that on the used electrode surface the ratio of copper to zinc was approximately one to one rather than 2.5:1 deeper (~100A) into the metal. The higher zinc concentration is caused by the preferential oxidation of the zinc at the surface. The oxidation of the zinc causes a diffusion gradient which leads to an enhancement of zinc at the surface.

All the surface analyses results point toward deposition of metal electrode particles on the insulators. It cannot be directly proved that the metal particulate is the cause of electrical failure of the insulators. However, the extensive metalization found by the surface analyses will limit switch life and should be suppressed.

#### Conclusions

Design considerations of gas switches to be used in high voltage, large power systems must take into account the sizable energy that is dissipated in the switch. To reduce the likelihood of mechanical failure the best approach appears to be to increase the volume of the gas which lessens peak pressures to be withstood by the switch components. Consideration of the energy scored in the pressurized gas should be made so that a break of the switch housing does not result in major damage to surrounding equipment.

Surface analyses comparison of used and unused insulators indicate a substantial plating of electrode material on the insulator. Two approaches are suggested for preventing the metal plating on the insulator: first, a change in the electrode material from brass to a tungsten-copper composite may substantially reduce this effect, second, the use of mechanical shields which do not allow a direct line of sight from the arc gap to the insulator. Designs incorporating both of these features are being readied for testing.

#### References

1. F. J. Szazama and V. L. Kenyon (Proceedings this Conference)
2. M. Kristiansen and M. O. Hagler, "Critical Analysis and Assessment of High Power Switches" T. R. Burke, P.I., Texas Tech University, Lubbock, Tx. Aug 1, 1978.
3. S. Kassel, "Pulsed-Power Research and Development in the USSR," RAND/R-2212-ARPA, RAND, Santa Monica, CA. 90406, May 1978.



4. D. Conte, Naval Research Laboratory (Private Communication).
5. "Test Report, DQ Switch Tests at Gamble II," PAR 75-1, Pulsar Associates, Inc. Sep 19, 1975.
6. A. A. Hudson, "Degradation of SF<sub>6</sub> in Electrical Equipment: Toxic and Corrosive Effects - A Resume' of Published Information," ERA REP(G.b.) 5815 1967.

7. W. Crewson, Pulsar Associates, Inc. (Private Communication)
8. J. S. Duerr, Structure Probe, Inc. (Private Communication)

This work has been supported by the Defense Nuclear Agency under Contract No. 001-76-C-0315-P00404 and MIPR No. 79-501.

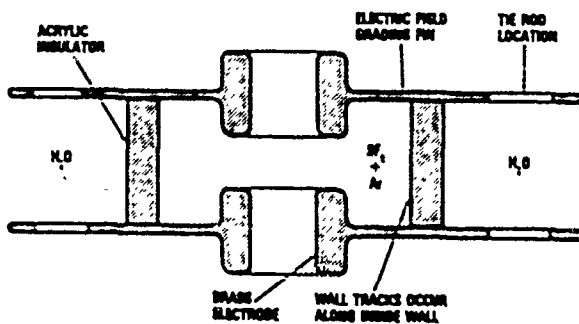


Fig. 1. Cross-sectional view of single section of multistage gas switch.

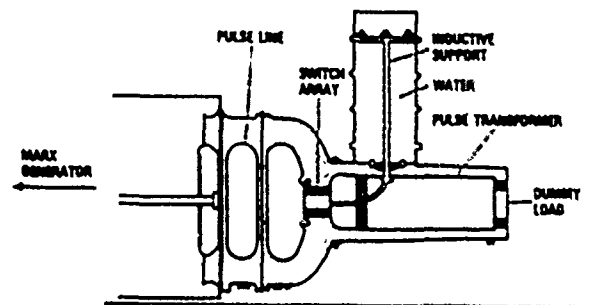


Fig. 2. Experimental arrangement used for testing gas switches on the Casino simulator.

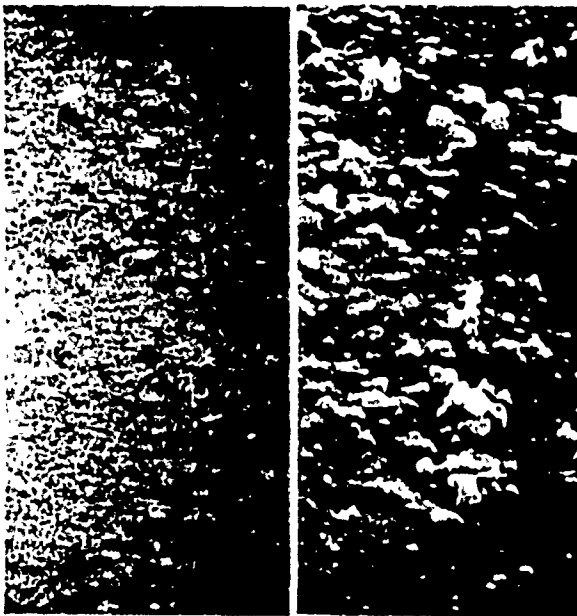


Fig. 3. SEM micrographs (10,000X) comparing surface contamination of unused plastic (left photo) with insulator exposed to ten switch closures.



Fig. 4. TEM micrograph (50,000X) cross-sectional view of insulator exposed to ten switch closures. Black dots along the insulator surface are copper and zinc particles which originate from the brass electrodes. Insulator structure lies to right of metal particles.

## BALANCED, PARALLEL OPERATION OF FLASHLAMPS\*

B.M. Carder, B.T. Merritt

Lawrence Livermore Laboratory  
Livermore, California 94550ABSTRACT

A new energy store, the Compensated Pulsed Alternator (CPA), promises to be a cost effective substitute for capacitors to drive flashlamps that pump large Nd:glass lasers. Because the CPA is large and discrete, it will be necessary that it drive many parallel flashlamp circuits, presenting a problem in equal current distribution. Current division to  $\pm 20\%$  between parallel flashlamps has been achieved, but this is marginal for laser pumping. A method is presented here that provides equal current sharing to about  $1\%$ , and it includes fused protection against short circuit faults. The method was tested with eight parallel circuits, including both open-circuit and short-circuit fault tests.

Introduction

The new Nova solid state laser will require an energy storage system of at least 100 MJ size to drive the 5 to 10 thousand flashlamps that will pump the glass. This type of distributed load is normally driven with an equally distributed energy store - namely a capacitor bank of many modules. Alternative stores to capacitors, such as the compensated pulsed alternator, are only practical in large single sizes, however, so the requirement exists to learn how to drive many parallel flashlamps.

Flashlamps are nonlinear resistive loads with a resistance that decreases as the current through them increases. Equal current sharing will therefore not necessarily be achieved when the lamps are operated in parallel. Inall<sup>1</sup> has demonstrated parallel operation of 16 flashlamp circuits with

equal current sharing to within 20%, provided all lamps are properly preionized. In this paper, we report upon a simple method using inductors with reacting mutuals in each lamp circuit, that provides parallel current sharing within about one percent. The method requires no special pre-ionization circuitry: lamp triggering is accomplished with the LC ringup between the inductor and the lamp cable capacitance.

Summary of Results

An experimental system was constructed in which eight parallel flashlamp circuits, were driven by a single 200 kJ, 20 kV capacitor bank. Each circuit comprised two series 44-inch long, 15-mm bore, xenon filled flashlamps, a fuse, and an inductor. With an inductance of 112  $\mu\text{H}$  in each circuit, equal current division to about 4% was achieved. When inductors were stacked together so that the mutuals subtracted, they became balancing reactors. With this arrangement, current division within measurement error ( $\sim 1\%$ ) was achieved and the effective series inductance in each circuit dropped to about 15  $\mu\text{H}$ .

Open circuit tests were also made. When one of the flashlamps was disconnected, the remaining seven circuits shared the full bank energy, and balancing was achieved as before.

The worst-case unbalance occurs when a flashlamp breaks and the circuit becomes shorted. This case was simulated with a deliberate short in place of the lamp. With a 112  $\mu\text{H}$  inductor in each circuit, the currents in the seven normal circuits balanced well, but the current in the shorted circuit rose at three times the nominal value until the fuse



inductors were paralleled for each circuit. The resulting series inductance in each circuit was 15  $\mu\text{H}$ . Normal operation and one circuit open tests were run. A short circuit test was not possible due to current limitations on the balancing reactors.

#### Test Results

Selected current waveforms from tests that used series inductors for current balancing are given in Fig. 2. Short circuit test waveforms are given in Fig. 3, and waveforms of tests using balancing reactors are given in Fig. 4.

#### Current Balancing via Series Inductors

Tests with 450  $\mu\text{H}$ , 225  $\mu\text{H}$ , and 112  $\mu\text{H}$  series inductors in each of the eight flashlamp circuits demonstrated a maximum current imbalance of about 4%. The case with the greatest imbalance (112  $\mu\text{H}$ ) is presented in Fig. 2. Figures 2a and b each show four traces with two circuits per trace, and normal operation (no opens or shorts). In Fig. 2a the capacitors are charged to 16 kV, giving 120 kJ for the 8 circuits. Figure 2b is with 22 kV charge and 225 kJ total.

Figure 2c is 16 kV (120 kJ) and one circuit open. Three of the traces have two live circuits each, showing good balancing. The single trace with only one live circuit shows just half the current of the others. Thus the current divides properly in all seven active circuits. Analysis shows that the average energy dissipated by each circuit is just 3/7 of that dissipated by the normal case when all eight circuits are active (Fig. 2a).

#### Short Circuit Tests

Figures 3a and b are short circuit tests at 16 kV charge and with 112  $\mu\text{H}$  balancing inductors. In each picture, three circuits are strung through each of two of the Pearson probes. A single normal circuit is strung through the third probe and the shorted circuit through the fourth. In each case, analysis shows that all seven normal circuits balance well (within a few %). The shorted circuit, however, draws about three times

the current of the other circuits until the fuse blows. The 7000 A/1.5 msec fuse (Fig. 3a) blows at 22 kA, and the 3000 A/1.5 msec fuse (Fig. 3b) blows at 15 kA.

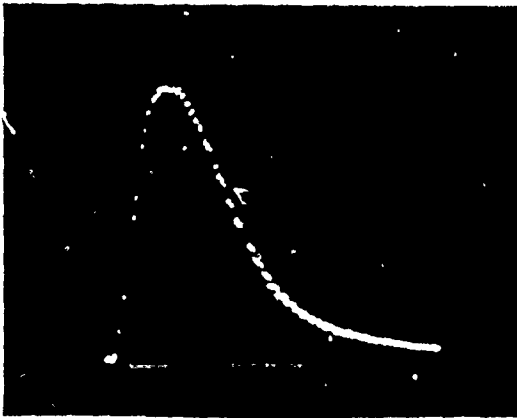
In the first case, the energy dissipated by the shorted circuit was about 40 kJ instead of the normal 15 kJ. In the second case, with the smaller fuse, about 29 kJ instead of 15 kJ were dissipated by the short. A third short circuit test (not illustrated) was made with the smaller fuse, and with the bank charged to 20 kV (190 kJ). In this case, the fuse blew at 17 kA and the shorted circuit dissipated 34 kJ, instead of the normal 24 kJ.

Note that the energy dissipated by a shorted circuit would be a very small fraction of the energy in a large parallel lamp system. Since the fuse limits the energy dissipated by the short, regardless of system size, no significant degradation of laser system performance is anticipated because of a shorted circuit.

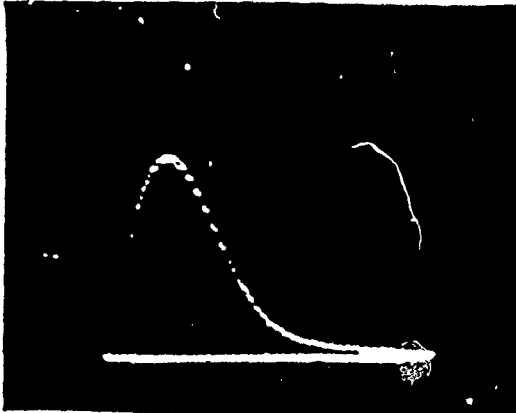
#### Current Balancing via Balancing Reactors

The results for current sharing tests using balancing reactors is given in Fig. 4a. Four traces are shown (two circuits per trace), and the bank is charged to 16 kV. Since the traces lie one on top of the other, with no separation, we surmise that current balancing is achieved within measurement error ( $\sim 1\%$ ).

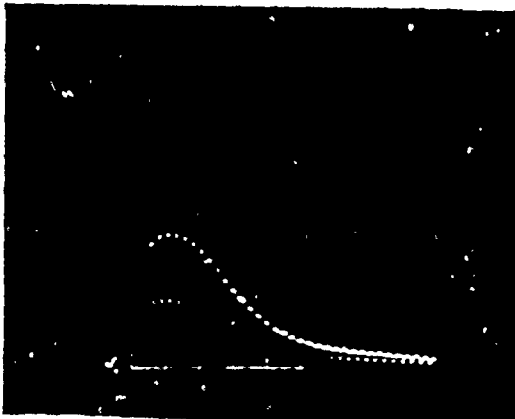
An open circuit test is presented in Fig. 4b. Here, the seven normal circuits balance within measurement error, and they share equally all of the circuit energy.



a. 15 kV charge, 1000 A/div, 100  $\mu$ sec/div



b. 22 kV charge, 2500 A/div, 100  $\mu$ sec/div

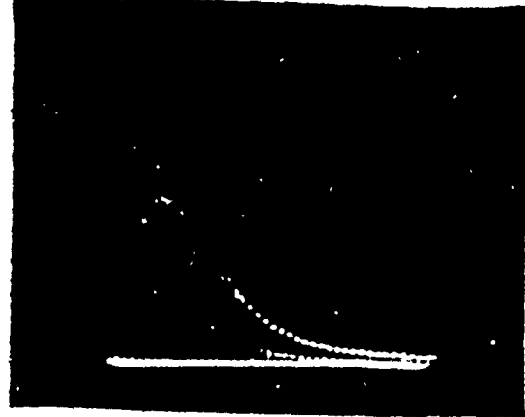


c. 16 kV charge, 2500 A/div, 100  $\mu$ sec/div  
one circuit open

Fig. 2: (a,b,c) Eight-circuit parallel flashlamp test using 112  $\mu$ H inductors in each circuit

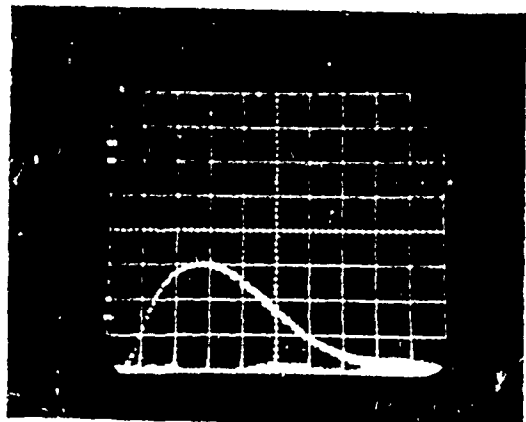


a. 7000 A fuse in shorted leg

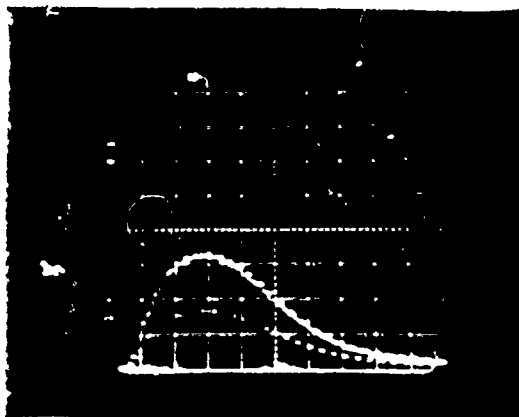


b. 5000 A fuse in shorted leg  
2500 A/div, 100  $\mu$ sec/div

Fig. 3: (a,b) Short circuit test. 112  $\mu$ H inductors in each of 8 parallel flashlamp circuits, with two fuse sizes in shorted circuit.



a. Eight normal circuits



- b. One circuit open  
16 kV charge, 2500 A/div, 100  $\mu$ sec/div

Fig. 4: (a,b) Eight-circuit parallel flashlamp tests using current balancing reactors with effective 15  $\mu$ H inductance in each circuit.

#### Reference

1. E.K. Inall "Powering Laser Flashlamps from a Storage Inductor", High Power High Energy Pulse Production and Application, ANU Press, Canberra, Australia, 1978.

"Work performed under the auspices of the U.S. Department of Energy by the Lawrence Livermore Laboratory under contract number W-7405-ENG-48."

Reference to a company or product name does not imply approval or recommendation of the product by the University of California or the U.S. Department of Energy to the exclusion of others that may be suitable.

#### NOTICE

"This report was prepared as an account of work sponsored by the United States Government. Neither the United States nor the United States Energy Research & Development Administration, nor any of their employees, nor any of their contractors, subcontractors, or their employees, makes any warranty, express or implied, or assumes any legal liability or responsibility for the accuracy, completeness or usefulness of any information, apparatus, product or process disclosed, or represents that its use would not infringe privately-owned rights."

# APPLYING A COMPENSATED PULSED ALTERNATOR TO A FLASHLAMP LOAD FOR NOVA\*

B.M. Carder, B.T. Merritt

Lawrence Livermore Laboratory  
Livermore, California 94550

## ABSTRACT

The Compensated Pulsed Alternator (CPA) is a large rotating machine that will convert mechanical, rotationally stored energy into a single electrical impulse of very high power. It is being optimized for driving flashlamps in the very large Nova Nd:glass laser system. The machine is a rotary flux compression device, and for maximum performance, it requires start-up current. We report upon a circuit that will provide this current and that will also assist in triggering the flashlamps. This circuit has been tested with a 200 kJ capacitor bank and it is now being tested with a small 200 kJ CPA. Large Nova-size machines will require output energies in excess of 5 MJ. We also present empirically tested formulae that will assist in matching the Nova flashlamp load to any given size CPA machine.

## Introduction

The Compensated Pulsed Alternator (Compulsator) is a very large rotary energy store that is a candidate source for driving the 5 to 10 thousand flashlamps that will pump the Nova laser. It is presently under development by the University of Texas at Austin (UT) and the Lawrence Livermore Laboratory (LLL). In the final (Nova) version, the machine will deliver a pulsed output energy of 5 to 20 MJ in about a half millisecond time with a peak voltage of about 13 kV. The order of a 100 MJ total energy will be needed for the Nova flashlamps.

\*Work performed under the auspices of the U.S. Dept. of Energy by the Lawrence Livermore Laboratory under contract no. W-7405-Eng-48.

At present, a small 200 kJ Compulsator is starting through a comprehensive test program at UT. The magnetics, mechanics and electrical characteristics of the machine are to be determined, and the machine will be used for driving 16 parallel flashlamps in an LLL laser amplifier head. The test data for the small machine will be used in the design of the large Nova-size machines.

In this paper, we report upon the circuit that will couple the 200 kJ Compulsator to its 16-flashlamp load. A similar circuit will be used for each Nova Compulsator, where hundreds of lamps will be driven by a single machine. These circuits provide start-up current for the Compulsator as well as providing triggering to all of the parallel flashlamp circuits.

Matching the Compulsator to the flashlamp load is another important task in this program. Empirical data have been collected for the large Nova flashlamps that enable us to characterize this type of load over a broad range of operating conditions. Briefly, we find that the energy  $W$  delivered to a flashlamp is given by,  $W = fK i_p^{3/2} \Delta t$  (Eq. 1), where  $i_p$  is the peak current through the lamp and  $\Delta t$  is the time for full-width at half-maximum (FWHM) of the current pulse. The factor  $f$  is a unitless current waveshape form factor that has a range of values from 0.8 to 1.02. For the Compulsator waveshape,  $f$  is very nearly unity ( $\approx 22$ ). The parameter  $K$  has been found to be constant within two percent over a broad range of energies and pulse durations. It is defined by  $K = V/\sqrt{I}$ , where  $V$  is the voltage across the flashlamp and  $I$  is the current through it. Thus the flashlamp resistance is

$$R = V/I = K/\sqrt{I}. \quad (2)$$

Derivations of these formulae and examples of their use are presented in the paper.

### Test Circuit

The simplified circuit for testing the 200 kJ Compulsator and load is given in Fig. 1. The start-up capacitor will store 2.5 to 10 kJ of energy. It will be initially charged to a negative voltage to facilitate immediate current flow when the ignitron switch is fired. At the same time, the flashlamp reflector is bumped by the pulse transformer, breaking down the flashlamps. A small reverse current flows through the lamps into the start-up capacitor, helping them to turn on.

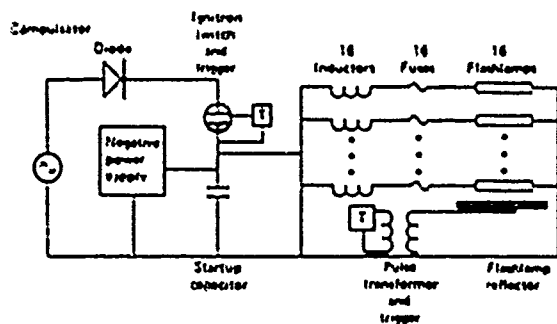


Fig. 1: Simplified Compulsator test circuit.

As current flows through the Compulsator, it becomes compressed and amplified. This causes the start-up capacitor to be positively charged. Current then flows through the lamps in the positive direction, and they are driven in the normal manner by the machine's impulse.

After the positive current impulse, the machine provides a soft zero crossing, and the ignitron switch and flashlamps go out. This extinction is facilitated by the diode, because it allows a small reverse voltage to appear across the switch that helps to clean up hot ions. The second positive pulse will appear about 3 ms after the switch extinguishes. This should be ample time for the ignitron to recover, but if it does not, a backup vacuum interrupter is being provided (not shown in Fig. 1) that will insure that repeated

pulses do not occur.

### Summary of Testing to Date

The Compulsator load circuit was tested at LLL with a 0.01-F capacitor bank in place of the Compulsator, and a start-up capacitor comprised of one 175  $\mu$ F can. Initial testing of the flashlamp circuit demonstrated that the flashlamps hold off 12 kV before they self-fire. Testing of the flashlamp/start-up-capacitor circuit alone demonstrated that all 16 lamps would fire when the flashlamp reflector circuit was bumped and the start-up capacitor was charged to minus 4 kV. Verification of flashlamp firing was provided by 16 current bugs that drive two 3-channel scopes.

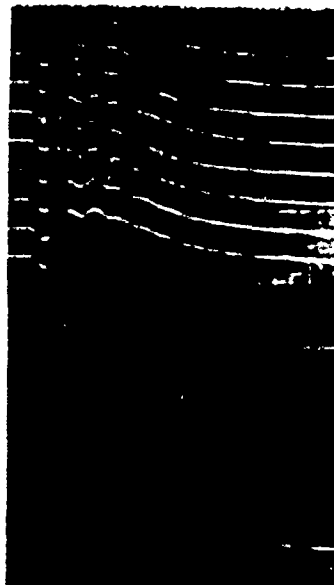
The system was next tested without diodes, but with the 0.01-F capacitor bank (200 kJ at 6.3 kV) substituted for the Compulsator in Fig. 1. The flashlamp reflector was pulsed 150  $\mu$ sec before the ignitron was fired to assure that all flashlamps would be conducting before the low impedance 0.01-F capacitor bank shunted the start-up capacitor. (With the Compulsator, this time delay will probably not be necessary). The circuit performed normally, and the flashlamp current was first negative because of the negative voltage from the start-up capacitor. This negative current reversed direction as the positively-charged bank capacitor rung into the start-up capacitor and discharged through the flashlamps, Fig. 2.

These tests demonstrate that the circuit provides the triggering to the flashlamps as anticipated, and that all 16 parallel flashlamp circuits balance well by virtue of a 125  $\mu$ H series inductor in each circuit leg. The circuit and flashlamps are presently being shipped to Austin, Texas where testing of the 200 kJ Compulsator will begin shortly.

### Characterizing the Flashlamp

In 1965, Goncz<sup>1</sup> characterized a flashlamp by the equation  $\rho^2 j = k_1 = \text{constant}$ , where  $\rho$  is the plasma resistivity and  $j$  is the flashlamp current density. Goncz was dealing with small tubes with bores completely filled with plasma. This relationship





(a)

(b)  
200 usec/div.

Fig. 2: Current waveforms from sixteen parallel flashlamps. Sixteen parallel flashlamps are driven first negatively with a 175- $\mu$ F, -5 kV start-up capacitor, followed 150 usec later with a 0.01-F, +6.4 kV capacitor bank. a). Sixteen circuits displayed individually from a single shot. b). Eight circuits per trace, showing that parallel flashlamp circuits balance well on each shot.

leads directly to Eq. (2), i.e.  $R = K/i$ , where the "flashlamp constant",  $K = \frac{L}{d} \frac{k_1}{\pi}$  (Eq. 4). Later, in 1974, Dillington, et al.<sup>2</sup> introduced an empirical relationship for the effective plasma diameter  $d$  in Eq. (4) to account for the early growth of the plasma streamer before the bore is filled: i.e.

(in mks units),  $d \approx 9.5 \times 10^{-4} (W/l)^{0.6}$  (Eq. 5) where  $W/l$  is the deposited energy per unit length in the gas. They also noted the existence of a transition region between  $d = d(\text{free space})$  and  $d = d(\text{bore})$ , where the final arc growth slows down due to the influence of the flashlamp wall. Finally, Noble and Kretschmer<sup>3</sup> and others have noted a fill pressure and gas type relationship for the flashlamp constant. For xenon, this relationship is  $K_1 = 1.27(P/450)^{0.2}(l/d)$ , (Eq. 6), where  $P$  is the fill pressure in Torr.

The present Nova standard flashlamp has an arc length  $l = 1.12\text{-m}$ , a bore diameter  $d = 0.015\text{-m}$ , and a fill pressure of 300 Torr xenon. By use of Eq. (6), we have  $K = 1.27(300/450)^{0.2}(1.12/0.015) = 87.3$ , assuming the bore to be completely plasma filled (neglecting Eq. (5)).

Note that since  $R = K/\sqrt{i}$ , we have  $R_{\min} = K/\sqrt{i_p}$  at peak current and  $V_p = i_p R_{\min} = K\sqrt{i_p}$ . We can therefore define  $K$  as,  $K = V_p/\sqrt{i_p}$  (Eq. 7). Using this definition,  $K$  was calculated for the Nova lamps by measuring the peak voltages and currents, recorded simultaneously from many discharges. The range of energies varied from 5 to 27 kJ, the peak currents varied from 2.8 to 6 kA and the current FWHM times varied from 480 to 800 usec. Over this range,  $K$  remained constant at  $86.5 \pm 2$ . This value agrees with the  $K = 87.3$  number obtained from the Noble/Kretschmer relationship. Because of the long pulse duration of 0.5 msec or more desired for Nova, we are assuming (for now) that the bore becomes filled early and that Eq. (2) is valid with  $K = 87 \text{ ohms}\sqrt{\text{amp}}$ .

Using Eq. (2) for the resistance, the instantaneous power dissipated by the flashlamp will be  $i^2 R = K i^{3/2}$ . The energy dissipated by the flashlamp will therefore be,

$$W = K \int_{t_1}^{t_2} i^{3/2} dt \quad (8)$$

The value under this integral will depend upon the waveshape of the current pulse. For a square pulse (constant current),  $t_2 - t_1 = \Delta t$  (i.e., the total pulsewidth and the FWHM are the same), and

$W_{sq.} = K i_p^{3/2} \Delta t$  (Eq. 9). Combining (8) and (9),

we can define a waveshape form factor as,

$$f = \frac{W}{W_{sq.}} = \frac{\int_{t_1}^{t_2} i^{3/2} dt}{i_p^{3/2} \Delta t} = \int_{x_1}^{x_2} y^{3/2} dx \quad (10)$$

where the normalizations of  $x = t/\Delta t$  and  $y = i/i_p$  are made. Form factors for a number of waveshapes have been calculated,<sup>4</sup> and they vary from a minimum of 0.5 (for a triangular wave) to slightly more than 1. For the anticipated Compulsator waveform,  $f$  is very nearly unity ( $\approx 1.2$ ). Rearranging (10) and substituting (9) we obtain Eq. (1), namely,

$$W = f W_{sq.} = f K i_p^{3/2} \Delta t \quad (1)$$

and this is the equation that enables us to match the flashlamp load to the Compulsator. For the Nova flashlamp, with the Compulsator waveform,  $W \approx 37 i_p^{3/2} \Delta t$ . (11)

#### Matching Flashlamps and Compulsators

Equation (11) applies for a single Nova-size flashlamp. As a rule, two of these lamps will be driven in series, and many in parallel by a single Compulsator. For a flashlamp system of  $n_s$  series by  $n_p$  parallel lamps, the required Compulsator energy (assuming  $f = 1$ ),

$W_c = n_s n_p W = K n_s n_p i_p^{3/2} \Delta t$  (Eq. 12), and the required Compulsator peak current,  $i_c = n_p i_p$  (Eq. 13). The

peak Compulsator voltage will be,  $V_c = n_s V = n_s K i_p^{1/2} \Delta t$  (Eq. 14), and so the peak Compulsator power is  $P_c = V_c i_c = K n_s n_p i_p^{3/2} \Delta t = W_c / \Delta t$  (Eq. 15). Two

examples are given in Table 1, assuming  $K = 37$ . With the small prototype Compulsator, we desire to provide 200 kJ into 16 parallel Nova flashlamps with a half-millisecond pulse. A typical 5 MJ Nova Compulsator would provide a half-millisecond pulse into 200 parallel by 2 series flashlamps (400 total). The actual terminal output voltage of the machine will need to be somewhat higher than that given in the table to make up for losses in the system. Note that losses will also increase the peak power and the energy output requirement, but these should be small ( $\sim 10\%$ ) in a typical system.

200 kJ  
Prototype

5 MJ  
Nova

#### Flashlamps

$n_s$	1	2
$n_p$	16	200
Total lamps	16	400
$W$ (kJ)	12.5	12.5
$i_p$ (kA)	4.4	4.4
$\Delta t$ (msec)	0.5	0.5

#### Compulsator

$W_c$ (kJ)	200	5000
$i_p$ (kA)	70	370
$\Delta t$ (msec)	0.5	0.5
$V_c$ (kV)	5.7	11.5
$P_c$ (GW)	0.4	10

Table 1

#### References

1. J.H. Conner, "Resistivity of Xenon Plasma", *J. Appl. Physics*, Vol. 16, No. 3, March 1975, pp. 36-42.
2. R.H. Disington, W.R. Hook, and R.P. Hilberg, "Flashlamp Discharge and Laser Efficiency", *Appl. Optics*, Vol. 13, No. 10, Oct. 1974, pp. 2300-2312.
3. L. Noble and C.B. Kretschmer, "Optical Pumps for Lasers", Tri Annual Report No. 1, ECOM-0239-1, Contract DAA807-71-C0239, March 1972.
4. B. Carder and B. Merritt, "Compulsator Optimization" (Appendix 1), LLL Engineering Note EE#78-192 (LEN 64), 11/29/78.

Reference to a company or product name does not imply approval or recommendation of the product by the University of California or the U. S. Department of Energy to the exclusion of others that may be suitable.

#### NOTICE

"This report was prepared as an account of work sponsored by the United States Government. Neither the United States nor the United States Energy Research & Development Administration nor any of their employees, nor any of their contractors, subcontractors, or their employees, makes any warranty, express or implied, or assumes any legal liability or responsibility for the accuracy, completeness or usefulness of any information, apparatus, product or process disclosed, or represents that its use would not infringe privately-owned rights."

# APPLYING A COMPENSATED PULSED ALTERNATOR TO A FLASHLAMP LOAD FOR NOVA-PART II

W. L. Bird, D. J. T. Mayhall, W. F. Weldon, H. G. Rylander and H. N. Woodson

Center for Electromechanics, The University of Texas at Austin  
Taylor Hall 167, Austin, Texas 78712

## Abstract

The compensated pulsed alternator (compulsator) has been proposed as a possible alternative to capacitor banks for driving xenon flashlamps for pumping neodymium glass laser amplifiers for NOVA. An algorithm for sizing rotor diameter and angular velocity as a function of flashlamp impedance, peak current, and delivered energy is described. It is shown that the armature inductance variation is a major consideration when matching the pulsed alternator to the load. Finally, conceptual design parameters of a four pole, laminated rotor compulsator are presented.

## Introduction

The Center for Electromechanics (CEM) of The University of Texas at Austin has proposed the compensated pulsed alternator as an alternative power supply for driving xenon flashlamps for the NOVA Laser Program at Lawrence Livermore Laboratory. The compulsator is a single phase alternator with a laminated rotor (armature) and solid steel stator with copper field windings wound on salient poles. The subtransient reactance of the machine is minimized by connecting a compensating (damper) winding on the quadrature axis of the stator in series with the rotor armature winding. A sectional end view of a simple compulsator is shown in Figure 1.

The compulsator differs from a conventional short circuit generator in several ways. The armature winding is located on the rotor, and is connected in series with the compensating winding via slip rings. Therefore, the compensating or damper winding is not closed on itself, but carries full armature current. Secondly, the compensating winding has the same number of turns as the rotor

winding and is of the same geometry, rather than being constructed in squirrel cage fashion. Finally, both windings are located in the air gap, rather than being imbedded in slots. The operation of the machine is described in detail in other papers presented at this conference.<sup>1,2,3</sup>

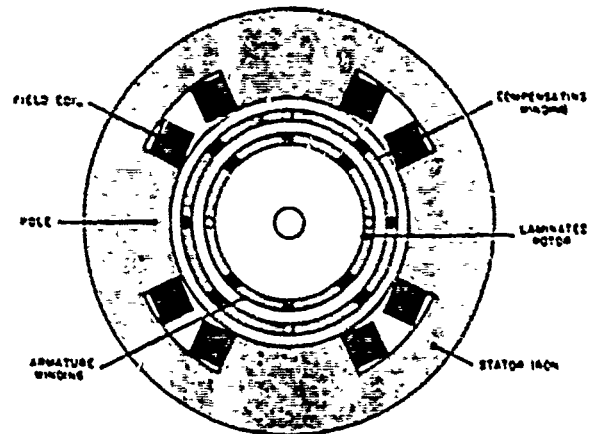


Figure 1: Cross Section of Compensated Pulsed Alternator

## Output Current Waveshape

The varying coupling between the armature winding and compensating winding results in rotary compression of the armature flux which increases the amplitude and decreases the half width of the output current pulse. Therefore, a compulsator with an open circuit sinusoidal frequency of 120 to 180 Hz can deliver 0.5 - 1.0 msec pulses to a low impedance load such as a xenon flashtube. A typical single current pulse waveform is shown in Figure 2.

## Flashlamp Load

The compulsator is a low impedance device with the

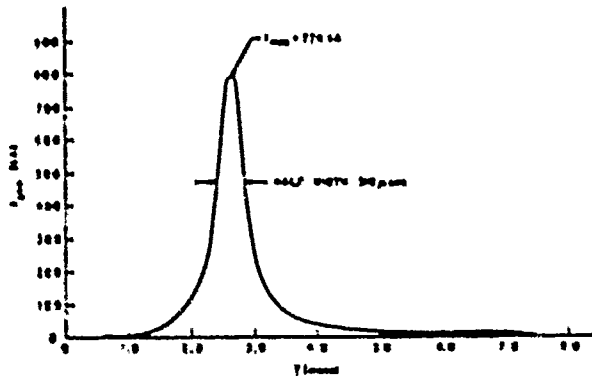


Figure 2: Typical Current Pulse Into Flashlamp Load

capacity to deliver current pulses of several hundred kilamps. It is therefore necessary to connect multiple flashlamp circuits in parallel to maximize energy delivery per pulse. One lamp configuration now being considered for NOVA consists of two 15 mm x 20 mm x 112 cm long xenon flashlamps connected in series. One hundred or more of these series circuits are connected in parallel with inductors placed in each leg to insure proper current division. The equivalent impedance of the flashlamp load is modeled as a nonlinear resistance given by

$$R_{load} = n_s K_p (n_p i_{load})^{-1/2} \text{ ohms} \quad (1)$$

where  $K_p$  is the lamp impedance constant (one lamp),  $n_s$  is the number of lamps in series per circuit (2),  $n_p$  is the number of parallel lamp circuits, and  $i_{load}$  is the total load current. It is shown in a companion paper that the energy delivered per pulse to each flashlamp is given by<sup>4</sup>

$$W_{lamp} = f K_p i_p^{3/2} \Delta t \text{ joules} \quad (2)$$

where  $\Delta t$  is the half width of the pulse,  $f$  is a waveshape factor,  $i_p$  is the peak current per lamp, and  $K_p$  is the impedance constant of the lamp (87.5 ohm-amp<sup>1/2</sup> per lamp, 175 ohm-amp<sup>1/2</sup> for series pair).

If the energy delivered per pulse, peak lamp current, and lamp impedance constant are specified, then the compensator must be designed to provide the proper current waveshape.

$$(\Delta t)_{compensator} = \left( \frac{W_{lamp}}{K_p} \right) i_p^{-3/2} \text{ (sec)} \quad (3)$$

#### Rotor Diameter and Speed

One algorithm that has been used to determine the angular velocity of the rotor is based on the observation that for typical circuits the effective armature flux linkage is constant during the main portion of the output current pulse. That is the product of the effective transient armature inductance and current is a constant. Therefore, the output current  $i_{load}$  may be described by

$$i_{load}(\theta_m) = L_0 i_0 / L(\theta_m) \text{ amps} \quad (4)$$

where  $\theta_m$  is the angular displacement between the axes of the rotor and compensating windings, and  $L_0$  and  $i_0$  are initial values of inductance and current at  $\theta_m = \theta_{m0}$  established during the startup phase of the discharge. The effective armature inductance versus angular position is given by

$$L(\theta_m) = L_{min} + \Delta L [1 - \cos(N_p \theta_m / 2)] \text{ H} \quad (5)$$

Using Equations 4 and 5 the pulse half width  $\Delta t$  is given by

$$\Delta t = (2 / N_p \omega_m) \cos^{-1} (1 - a / \lambda_k) \quad (6)$$

where  $N_p$  is the number of poles,  $\omega_m$  is the angular velocity of the rotor and the terms  $a$  and  $\lambda_k$  are

$$a = 1 - \cos(N_p \theta_{m0} / 2) \quad (7)$$

$$\lambda_k = L_0 / L_{min} - 1 \quad (8)$$

$\lambda_k$  is defined as the flux compression factor. Again, using Equations 4 and 5 and integrating the resistive power dissipated in the flashlamps, the LHS of Equation 3 is given by

$$(f \Delta t) = 2 S \omega_m / S \quad (9)$$

where  $S$  is a constant of integration which depends on  $N_p$ ,  $\theta_{m0}$ , and  $\lambda_k$ . A typical value of  $S$  is 0.255 for a four pole machine with  $\theta_{m0} = -0.294$  and a flux compression factor  $\lambda_k$  equal to 14. The angular

velocity of the rotor  $\omega_m$  can then be plotted as a function of diameter to provide the proper pulse width if the flux compression factor  $A_k$  is known as a function of machine diameter and number of poles. A typical curve is plotted in Figure 3.

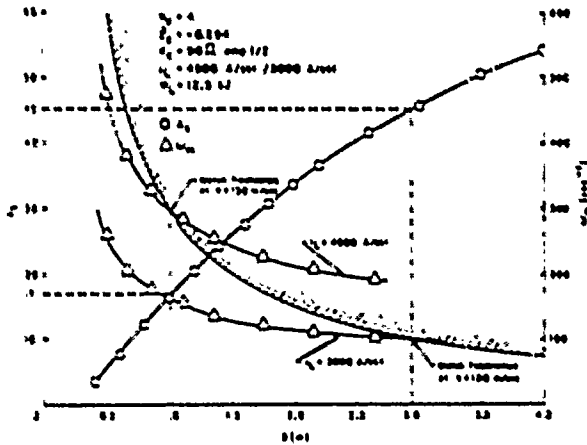


Figure 3: Flux Compression Factor and Angular Velocity versus Rotor Diameter for Flashlamp Load

Assuming that the maximum allowable tip speed for the rotor is 150 m/sec based on centrifugal forces acting on the air gap rotor winding, the diameter of the rotor is found by the intersection of the angular velocity curve and the constant tip speed curve. It can be seen from Figure 3 that a 1.02 m diameter four pole compulsator will drive the flashlamps at a peak current of approximately 4500 amps per circuit and a pulse width of 500 usec.

#### Flux Compression Factor $A_k$

The factor  $A_k$  scales as  $(\tau/g)^2$  where  $g$  is the effective air gap between the windings and  $\tau$  is the polar pitch ( $\pi D/N_p$ ).<sup>5</sup> Therefore,

$$A_k \propto \left(\frac{D}{gN_p}\right)^2 \quad (10)$$

Since the ratio of effective air gap to diameter does not scale linearly, the compression factor  $A_k$  generally increases with diameter.  $A_k$  decreases with the square of the number of poles. Other factors which influence  $A_k$  include system voltage (insulation thickness), radial build of air gap conductors, mechanical gap clearance, and pole construction (laminated versus solid). To

maximize delivered energy, the minimum inductance  $L_{min}$  must be reduced as far as possible. The factor  $A_k$  is chosen to match the desired pulse width and peak current and is selected based on tradeoffs including mechanical stress in the alternator, external switching requirements, and amplifier gain.

#### Conceptual Design

Assuming a rotor diameter of 1.02 m and a rotational speed of 2800 rpm from Figure 3, a conceptual design of a compensated pulsed alternator was developed. It should be noted that the final alternator design and flashlamp configuration have yet to be frozen. However, this one design does indicate the type of machine used to drive multiple flashlamp circuits that are anticipated. The basic generator performance parameters are listed in Table 1. A sectional view is shown in Figure 4.

Table 1: Compulsator Parameters

Number of poles	4
Rotor diameter (m)	1.02
Rotor tip speed (m/sec)	150
Angular velocity ( $\text{sec}^{-1}$ )	294
Flux compression factor $A_k$	17.6
Open circuit voltage (kV)	10.3
No. of rotor conductors	23
Armature resistance (m $\Omega$ )	8.5
Minimum inductance ( $\mu\text{H}$ )	5.6
Effective air gap (mm)	4.05
Magnetic air gap-main field (cm)	4.3
Field MMF/pole (kA-c)	105
No. turns/pole	28
Field current-pulsed (kA)	3.76
Field power/pole (kW)	114
Outer diameter of back iron (m)	2.51
Shaft diameter (m)	0.32
Shaft length (m)	4.8
Total mass (metric ton)	87.6
Inertial Energy Store (MJ)	105

System performance parameters are listed in Table 2. The tabulated case includes realistic models for

the ignitron switches, includes the growth of the plasma diameter from startup to full bore, and utilizes capacitive assist startup as described in the companion paper.<sup>4</sup>

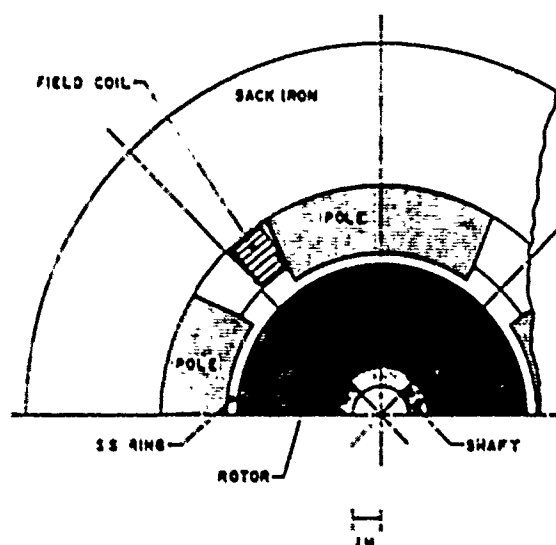


Figure 1: Cross Section of Conceptual Compensated Pulsed Alternator Power Supply for NOVA

Table 2: System Performance Parameters

Peak lamp voltage (kV)	10.9 (12.5)*
Peak current (kA)	774 (933)
No. lamp circuits	198
Energy delivered (MJ)	4.52 (6.2)
Pulse half width (μsec)	510 (510)

\*Numbers in parentheses for  $\pm 3\pi/64$  radian phase shift of compensating winding past quadrature axis.

Note that the delivered energy is increased if the axis of the compensating winding is shifted so that the point of minimum inductance lags the point of maximum open circuit voltage. The increased delivered energy must be weighted against increased localized shear stress on the adhesive bond between the air gap winding and the surface of the rotor. However, the  $3\pi/64$  phase shift should be satisfactory mechanically.

#### Summary

The conceptual design of a compensated pulsed

alternator matched to a specific flashlamp load typical of the lamp characteristics anticipated for NOVA has been presented. Final selection of the flashlamp load and alternator parameters are yet to be made, however, pending results of an engineering prototype test program.

#### Acknowledgements

The authors wish to thank Mr. Bernard Merritt, Lawrence Livermore Laboratory, for his invaluable assistance in performing the computer circuit analysis for the complete discharge circuit.

This work was performed under Lawrence Livermore Laboratory Subcontract No. 1823209 with support of the U. S. Department of Energy and the Texas Atomic Energy Research Foundation.

#### References

1. W. F. Weldon, W. L. Bird, M. D. Driga, K. M. Tolk, M. G. Rylander, H. H. Woodson, "Fundamental Limitations and Design Considerations for Compensated Pulsed Alternators," 2nd IEEE International Pulsed Power Conference, Texas Tech University, Lubbock, Texas, June 12-14, 1979.
2. J. H. Gully, W. L. Bird, M. D. Driga, H. G. Rylander, K. M. Tolk, W. F. Weldon, H. H. Woodson, "Design of the Armature Windings of a Compensated Pulsed Alternator Engineering Prototype," 2nd IEEE International Pulsed Power Conference, Texas Tech University, Lubbock, Texas, June 12-14, 1979.
3. M. Brennan, W. L. Bird, J. H. Gully, M. L. Spann, K. M. Tolk, W. F. Weldon, H. G. Rylander, H. H. Woodson, "The Mechanical Design of a Compensated Pulsed Alternator Prototype," 2nd IEEE International Pulsed Power Conference, Texas Tech University, Lubbock, Texas, June 12-14, 1979.
4. B. Carder, "Applying a Compensated Pulsed Alternator to a Flashlamp Load for NOVA-Part I," 2nd IEEE International Pulsed Power Conference, Texas Tech University, Lubbock, Texas, June 12-14, 1979.
5. W. L. Bird, M. D. Driga, D. J. T. Mayhall, M. Brennan, W. F. Weldon, H. G. Rylander, H. H. Woodson, "Pulsed Power Supplies for Laser Flashlamps," Final Report for Lawrence Livermore Laboratory, Subcontract No. 1823209, October 1978.

# A COMPACT $5 \times 10^{12}$ AMP/SEC RAIL-GUN PULSER FOR A LASER PLASMA SHUTTER\*

L.P. Braginsky, E.L. Orham, and I.F. Stowers

Lawrence Livermore Laboratory  
Livermore, California 94550

## ABSTRACT

We have developed a rail-gun plasma source to produce a plasma of  $10^{21} \text{ cm}^{-3}$  particle density and project it with a velocity of 3.9 cm/us. This device will be used in an output spatial filter of Nova to project a critical density plasma across an optical beam path and block laser retro-reflected light. The object of this paper is to describe the design of a pulser appropriate to the Shiva laser fusion facility, and to describe the preliminary design of a higher current prototype pulser for Nova the laser fusion research facility under construction at Lawrence Livermore Laboratory.

## Experimental Configuration for the Shiva Gun

The experiment is contained in a multiport vacuum chamber configured as a 20 cm aperture spatial filter with  $f/10$  optics, as shown in Fig. 1. The wire which foras the plasma is located near the focal point of the optics, as shown in more detail in Fig. 2. The 3 mm long, 127  $\mu\text{m}$  diameter aluminum wire is located between two electrodes in a 1 mm deep, 150  $\mu\text{m}$  wide slot in a dielectric material. The slot constitutes a nozzle to confine the plasma during heating and to direct it across the optical beam path into a dump tank. Such a geometry increases the on axis density and reduces the leakage toward the optics.

The electrodes are connected via a low inductance parallel plate transmission line to the pulser. The pulser, containing 6 parallel Maxwell Type

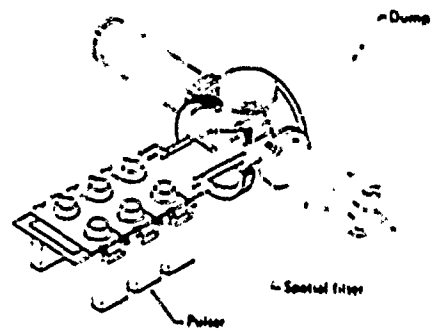


Fig. 1 Plasma shutter experimental configuration

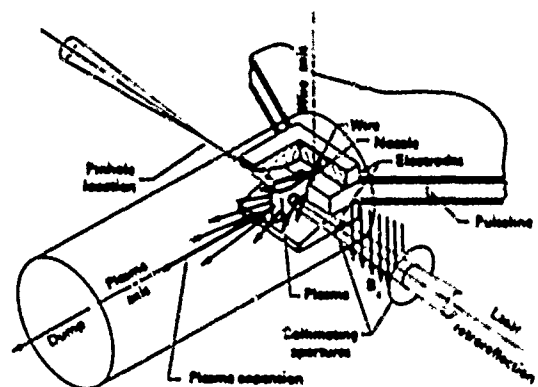


Fig. 2 Plasma gun geometry

S, 0.22  $\mu\text{F}$  capacitors is connected to the transmission line by 6 independent switches as shown in Fig. 1, and more detail in Fig. 3. The switches are midplane triggered, uv illuminated spark gaps<sup>1</sup> retrofitted into Tachisto 501 switch bodies. This trigger configuration is similar to that used in the Pulsar SW50K gap, but provides lower net inductance. The trigger is fed through the trigger pin and first arcs across to the illuminator which is connected to ground via a current limiting resistor. The small gap preilluminates the main gap

\*Work performed under the auspices of the U.S. Dept. of Energy by the Lawrence Livermore Laboratory under contract no. W-7405-Eng-48.

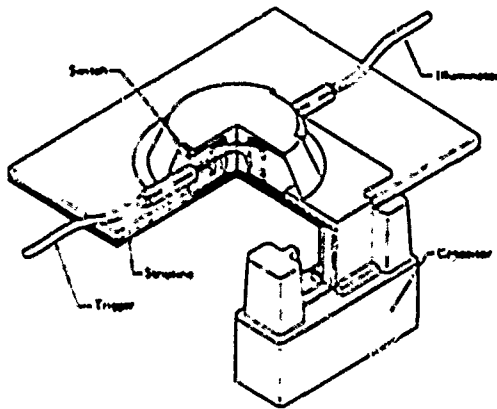


Fig. 3 1 ns jitter, low inductance switch geometry and sharpens the trigger rise time. This provides nanosecond jitter with a rounded trigger pin and is not sensitive to erosion. An equivalent circuit (common also to the Nova pulser) is shown in Fig. 4.

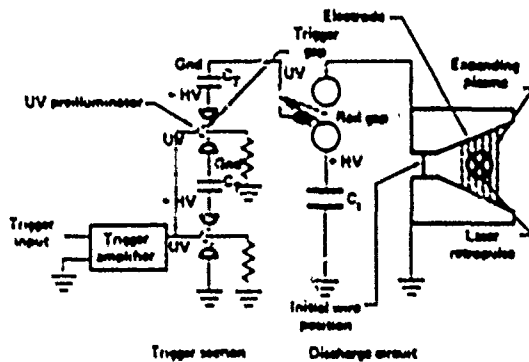


Fig. 4 Equivalent circuit of plasma gun and trigger

The pulser when charged to 50 kV provides a current rise time of  $5 \times 10^{12}$  A/sec. These main spark gaps, when triggered with a fast rising trigger pulse, provided nanosecond jitter and hence excellent current sharing of the parallel gaps and synchronization with the laser and diagnostics. When connected to the wire, including the large feed-through inductance, the current has a quarter period of 300 ns.

#### Affect of Nonlinear Load

Initially while the wire is inertially confined, heating is resistive and follows a linear temperature variation. After burst, the resistance is characterized by a Spitzer resistivity. We

conceptually distinguish two phases that dominate the plasma acceleration. A heating phase occurs near burst when the resistivity is high. Thereafter a  $J \times B$  force increases the plasma directed velocity. By tailoring the current pulse history, we can to some degree separately control the plasma temperature and net plasma velocity, and thereby select both the divergence and closure time.

#### Experimental Results

The plasma velocity was determined by using streak camera photographs and a Faraday cup located 39 cm from the wire and axially centered on the plasma axis. Experimental results and a code<sup>2</sup> prediction for 20 kV charge voltage are summarized in Fig. 5. Such correlations of data and prediction reflect the present level of design.

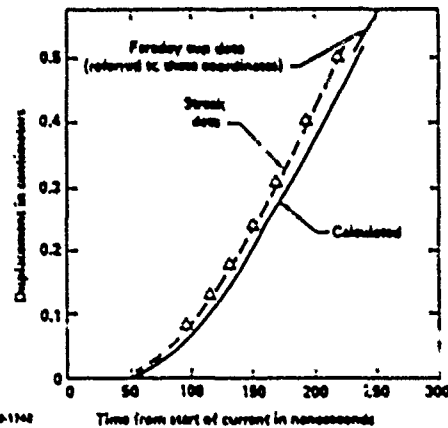


Fig. 5 Measured and calculated plasma velocity

#### Nova Pulser Design

We require a critical density plasma to obscure a 6 mm diameter region with a closing velocity appropriate to a shutter to target distance of 40 m. We conducted a parametric survey with the code to establish the prototype characteristics. We constrained the design such that all capacitors and switches must be standard elements within the state of the art and were thus able to concentrate on improving these elements to ensure reliability.

The prototype design contains 8 parallel 0.66  $\mu$ F, 20 nH 50 kV capacitors connected through 4 parallel 10 nH rail gaps via a coaxial 3 nH vacuum feed-



through to the load. The total pulser inductance is 10 nH. This design is shown isometrically in Fig. 6 and in cross section in Fig. 7. The equivalent circuit is shown in Fig. 4. A logic signal is amplified by a Pulsepak 10A and transformer. A coaxial two stage Marx using the switch shown in Fig. 3 provides an output of 100 kV rising in 8 ns to trigger the rail gaps.

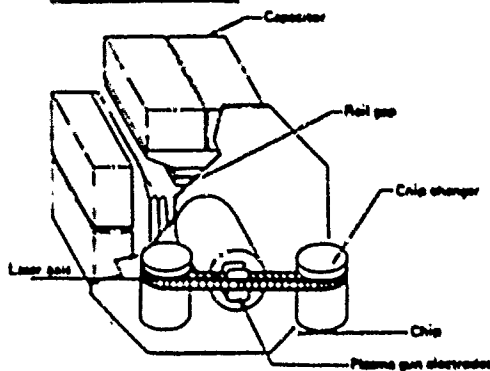


Fig. 6 Nova plasma shutter geometry



Fig. 7 Plasma shutter pulser cross section

The rail gap shown in Fig. 8 has semi-rogowski electrodes and a long graded trigger blade. The trigger pulse is fed through a peaking gap on the end with its spark located on axis with the rails, thereby preilluminating them. The switching gas is 20%  $\text{SF}_6$  and 80% Ar. The function of the uv produced primarily in the argon is to provide free electrons and metastable states in the main gap region. These electrons help in initiating avalanches and streamers, and also cause precise closing<sup>3</sup> of the streamer. A segment of the Nova pulser has been extensively tested and characterized, and provides nanosecond jitter. With the dc

charge voltage, it provides multichannel operation, a feature which is somewhat insensitive to rail edge sharpness, thus tending to maintain reliability with age. We are presently testing electrode materials including low lead brass, Schwarzkopf K25 tungsten and Poco AXF5QC and ACF10Q graphite to reduce erosion and most importantly to minimize prefire.

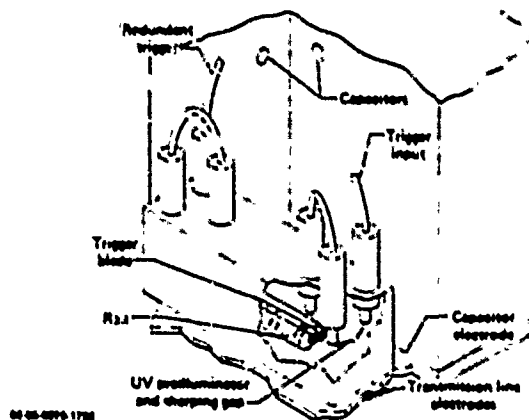


Fig. 8 UV preilluminated rail gap

The 0.66  $\mu\text{F}$ , 20 kV capacitors developed by Maxwell for this application are similar to the Garching type, and have a plastic case with a parallel rail-header. The internal construction is similar to the proven Sylac capacitor. Internal inductance is 20 nH and the expected life is  $10^6$  shots.

The dielectric is a semiconductor coated polyurethane elastomer being cast in the shape required for the coaxial feedthrough. The effect of surface corona is minimized by employing a semiconductor coating; the uncoated polyurethane minimizes tracking under switches and capacitors. Its elastic behavior will restore its shape and in particular its contact with the conductors after magnetically induced deformations. The coaxial design minimizes the number of high voltage edges.

The pulser is housed in an electromagnetic shield and filled with atmospheric pressure  $\text{SF}_6$ . Two trigger generators located in the shield provide via separate peaking gaps a redundant trigger pulse to each blade.

### Conclusions

We have developed and are continuing to develop reliable, low inductance, high current pulsers having nanosecond jitter. All spark gaps use uv preillumination to pulse sharpen the trigger, to minimize jitter, and to minimize the effect of electrode erosion with age. The systems are coaxial to minimize inductance and edge effects. A semiconductor coated elastomer dielectric minimizes surface corona and tracking. These pulsers are utilized with a rail-gun to propel a high density plasma to a high velocity.

### Acknowledgements

We thank R. Duffus, J. Braucht, H. Rien, C. McFann and M. Thorne for their contributions.

### References

1. H. Bacchi and J.C. Pauwek, Proc. of the 9th Int. Conf. on High Speed Photography, p. 489, Denver, Aug. 2-7, 1970.
2. Peter Koert, UCRL 81363, 1978 (to be published).  
  
L.P. Bradley and Peter Koert, "Plasma Shutter for High Power Glass Lasers", 8th Int. Symp. on Discharges and Electrical Insulation in Vacuum, Albuquerque, Sept. 5-7, 1979.
3. L.P. Bradley, "Preionization Control of Streamer Propagation", J. Appl. Phys. 43, 586, 1972.  
  
L.P. Bradley and T.J. Davies, "Laser Controlled Switching", IEEE J. Quantum Electronics 7, 464, 1971.

Reference to a company or product name does not imply approval or recommendation of the product by the University of California or the U.S. Department of Energy to the exclusion of others that may be suitable.

### NOTICE

"This report was prepared as an account of work sponsored by the United States Government. Neither the United States nor the United States Department of Energy, nor any of their employees, nor any of their contractors, subcontractors, or their employees, makes any warranty, express or implied, or assumes any legal liability or responsibility for the accuracy, completeness or usefulness of any information, apparatus, product or process disclosed, or represents that its use would not infringe privately-owned rights."

## FAST RISING TRANSIENT HEAVY CURRENT SPARK DAMAGE TO ELECTRODES

ALAN WATSON

Dept. Elect. Eng., Texas Tech Univ.  
Lubbock, Texas 79409

Dept. Elect. Eng., Univ. of Windsor  
Windsor, Ontario, Canada

Abstract

Crests of displaced metal have been observed in rings beyond the crater produced on electrodes by short duration (10-100 ns) heavy current sparks in a variety of dielectric media. Metal is presumed to have melted and flowed radially, the hydromagnetic forces supporting a standing canal wave which is identified with the crest. Analysis shows this situation to be invariant under steady melting and the ring diameter is proportional to the square root of spark current, as measurement verifies. Erosion is proposed to occur by the breaking of this crest or by its removal under the action of electrostatic forces, in accord with reported experimental data.

Introduction

In the course of experience with high power flash X-ray machines\* it has been observed that electrode damage from heavy current switching sparks appear to have some features in common. In a current range up to about 250 kA lasting for 20 to 70 ns in high pressure gas each electrode displays a crest of frozen metal in a ring around the site which was struck by the spark (Figure 1). There is a small crater at this spot which corresponds in diameter with that to be expected for a heavy current spark channel expanding for the known duration of the discharge. This is surrounded by a flat undulating expanse of metal which had obviously been molten and which extends beyond the crest already mentioned. The radius of the ring has been measured in three cases for which the current was calculable. It appears that the

radius increases as the square root of the current, independently of the pulse duration. Significantly, there is extremely little visible depression of the metal level within the damage ring.

Investigations of spark damage in vacuum have revealed that in certain cases damage of a similar nature takes place (Figure 2). In addition, a region outside the damage ring was found to be covered with molten droplets adhering to the surface. Further data from pulsed discharges in water and oil show the same characteristic damage ring for various metals.

One feature in common with all of these discharges is probably that the current pulse was fast rising. In vacuum this is not always the case and the incidence of such damage is less frequent. Replicas were made and microphotographs prepared of damage sites on flash X-ray machines for a wide range of calculated currents and pulse durations. In Fig. 4 the crest radius on stainless steel appears to vary as the square root of the spark current so that  $I/r^2 = 1.5 \times 10^{10} \text{ Am}^{-2}$ .

A mechanism sufficient to explain these phenomena must, therefore, be independent of the type of discharge and more reliant upon the electrodynamics of the current growth within the electrodes. The purpose of the present work is to describe such a mechanism and to throw some light upon the electrode erosion process.

\*Ion Physics Corporation models FX-15, FX-45 and FX-100.

## THEORY OF THE MECHANISM

Hydromagnetic Flow

No initial account will be taken here of spark channel expansion and it will be formalized simply as a fixed conducting cylinder produced instantaneously between two high voltage electrodes. Current, however, cannot be established until magnetic flux has penetrated into the conductors. The channel conductivity is much less than that of the electrode metal and diffusion into it is therefore rapid enough to be considered instantaneous by comparison.

Progressive flux penetration into the electrode surface will cause melting because of the accompanying resistive power dissipation. Electromagnetic forces also act normally into the electrode surface, but decrease in strength radially. Since the liquid surface layer tends to 'freeze in' the magnetic flux with a radial electromagnetic pressure variation, a steady fluid flow will develop in such a manner as to neutralize this.

The problem can now be formulated as that of determining the hydromagnetic flow pattern of a fluid with a free surface flowing radially outwards across an azimuthal magnetic field, as shown in Figure 3. Hydromagnetic flow will be considered radially across an azimuthal magnetic field distribution for a disc of conducting fluid of non-uniform depth  $h$ , but with a free surface. There is no indication from the conditions of the problem that melting occurs to a uniform depth. Azimuthal symmetry will be assumed so as to reduce the problem to two dimensions.

Flux transport into the mobile pool is determined by equating  $\partial \vec{B} / \partial t$  with the rotation of the overall electric field strength given by  $\text{curl}(\vec{C}^{-1} \vec{J} + \vec{u} \times \vec{B})$ . Beneath the melting floor there is no Lorentz field and flux is transported by diffusion. At this interface there must be continuity in  $\partial \vec{B} / \partial t$  and this will be achieved if the Lorentz field is irrotational.

A flow solution relating  $u$  and  $H$  must satisfy this condition, and the following relationships will be shown to be adequate for the purpose of describing the flow over an anode surface as in Figure 3.

$$\sqrt{C} \vec{u} = - \sqrt{u} h \text{curl } \vec{H} = - \sqrt{\mu} h \vec{J} \quad (1)$$

$$\sqrt{u} \vec{H} = \sqrt{\rho} h \text{curl } \vec{u} = \sqrt{\rho} h \vec{\omega} \quad (2)$$

where  $h$  is the pool depth.

Hence the vorticity vector lies parallel to the magnetic field lines while the fluid velocity is parallel to the current density. It follows moreover that the electromagnetic body force  $\vec{J} \times \vec{B}$  is equal to the inertial force  $-\rho \vec{u} \times \vec{u}$  which exists by virtue of the vorticity everywhere in the flow and the momentum equation reduces to the hydromagnetic form of Bernoulli's equation. It is necessary now, however, to explain the origin of vorticity in the flowing pool of metal.

There will be a discontinuity in the fluid entropy in crossing the liquid-solid interface due to the change in state. This interface is the limiting streamline for the flow and so according to Crocco's theorem of fluid mechanics (2) there will necessarily be a corresponding jump in vorticity from zero in the solid to a finite value within the flow. Neglecting viscosity, Kelvin's theorem indicates that the vorticity will be invariant within the pool. Kelvin's theorem of conservation of vorticity can thus be applied to the pool flow. The vorticity  $\omega$  is given by  $-du/dx$  and since this is fixed everywhere it can also be written as  $u/h$ . By equating these terms it is seen that the velocity will decline exponentially from its value  $u$  at the free surface to zero at the liquid-solid metal interface.

Power is dissipated at a fixed volume rate which is absorbed in maintaining melting. The Lorentz field given by  $h\vec{B}$  is equal to  $\vec{J}/\sigma$  and  $\vec{J}$  can be represented by  $I/2\pi rh$ .  $= H/h$ . Thus it follows that  $H$  declines exponentially with depth and  $hH = 1/\mu\sigma = \eta$  and the floor must therefore recede according to the expression

$$h^2 = 2 \eta t \dots \dots \dots (3)$$

The exponential variation of  $u$  and  $H$  within the flow follows immediately from the simultaneous solution of (1) and (2) which are in turn unified to one single expression if

$$\mu \rho u^2 = \mu H^2 \dots \dots \dots (4)$$

At any annulus of the pool the current density  $J_p$  flowing through it is given instantaneously by

$I_p/2\pi r h$ . (Where the subscript 'p' refers to the pool). A radius  $r$  may be selected for which  $I_p = (r/h) I$  which clearly permits  $J_p$  to be represented by  $I/2\pi r^2$ .

The pool current  $I_p$  must be employed in calculating the Ohmic power dissipation in a cylindrical annulus of the flow. This is equated with the power absorbed in melting at the rate  $\dot{h}$  which in turn is eliminated using the equation of the streamline,  $\dot{h}/h = u/r$ . Hence

$$[I(h/r)]^2 = (4\pi^2 \rho \Lambda \sigma h^2 u) r \dots (5)$$

in which  $ur$  must be constant to ensure incompressible flow of the fluid. Thus, since  $u = dr/dc$  the flow obeys the rule that  $r^2$  is proportional to  $c$  just like  $h^2$  and their ratio  $(h/r)$  is hence invariant in time. Equation (5) readily reduces to  $dr^2/dc = 2\eta(uh^2/\rho\Lambda)$  and by comparison with (3) then

$$(h/r)^2 = (uh^2/\rho\Lambda) \dots (6)$$

From (1), (2), & (4) the vorticity and current density are related, the latter being further given by (5) so that

$$u = (u/\rho)^{1/2} J = (\Lambda/\eta) (uh^2/\rho\Lambda) = (\Lambda^{1/2}/\eta) u \dots (7)$$

and since  $u = u/h$  then

$$h = \eta/\Lambda^{1/2} \dots (8)$$

Within the molten pool heat is transferred by conduction according to

$$K \nabla^2 T - \rho \sigma \partial T / \partial t = J^2 / \sigma = h^2 / h^2 \sigma \dots (9)$$

At the molten interface the temperature is fixed at the melting point  $T_m$ . When the floor recedes at a rate  $\dot{h}$  (4) acquires an additional driving term  $\nabla \times (\dot{h} \times \vec{B})$  on the right hand side and the expression reduces to

$$\eta \nabla^2 \vec{H} - \partial \vec{H} / \partial t = H \dot{h} / h = \eta H / h^2 \dots (10)$$

In the mobile reference frame of the floor the Lorentz and Ohmic fields neutralize each other as stated, and  $\text{curl } \vec{E} = 0$  so by Faraday's law  $H$  is constant and the last equation shows that it decays exponentially. At the interface the constant value of  $H = H_m$  is given by comparing (9) and (10) above which are equivalent if  $H_m^2 = \sigma K T_m \dots (11)$

#### The Magnetofluid Tidal Wave

The square of the velocity of propagation,  $c$ , of a tidal wave is given by the product of the depth  $h$

of the fluid and the gravitational acceleration. By analogy here the force acting down into the pool per unit mass is  $\vec{J} \times \vec{B} / \rho$  and this has been shown to be equal to the inertial acceleration  $-\vec{\omega} \times \vec{u}$ . Fluid velocity vectors radiate from the arc root and terminate upon free vortex rings on the molten interface. As melting proceeds, these rings are stretched and give rise to the accelerating force which replaces gravity in this analogue of tidal wave motion. Thus

$$c^2 = h |\vec{J} \times \vec{B}| / \rho = (u/h) h (I_p / 2\pi r^2) (r/h) h \dots (12)$$

Since  $u = u/h$  it follows that  $c = \pm u$  and a tidal disturbance propagated inwards towards the arc root along the surface of the outwardly flowing fluid will give rise to a standing crest. It remains to derive a relationship between the location of this crest and the current flowing in the arc. This is accomplished by evaluating (12), making substitutions for each of its terms using

$$(6), (8) \text{ \& (11). Thus } I_p / r^2 = 2\pi u^{3/2} \sigma^2 K T_m / \rho^{1/2} \dots (13)$$

The ring defined by the wave crest divides the flow into two regimes. Outside of it the pool conditions referred to in the analysis so far will pertain. Only in that region can there exist a flow together with a propagating wave because  $ur$  is constant and a radius exists within which  $u$  exceeds  $c$ . Fluid flows out from the inner region and accumulates in the crest so that an upward velocity component is acquired in that particular annulus. The Lorentz field due to this will drive a current density through the annulus in opposition to the supplementary current mentioned above and in passing through the wave the current is restored to the measured value  $I$ . Thus the pool current  $I_p$  should be replaced by  $I$  in (13) in order to calculate the crest radius.

A calculation has been made from (13) for stainless steel electrodes using values of resistivity  $\rho$ , and thermal conductivity  $K$  for stainless steel at  $1000^\circ\text{C}$  since these figures were the best available although the melting point is  $1800^\circ\text{K}$ . The result gave  $I/r^2 = 2.90 \times 10^{10} \text{ Am}^{-2}$  which is in reasonable agreement with the measured value.

#### Conclusions

The electrode damage mechanism is thus feasibly

demonstrated but it further suggests the way in which erosion occurs. Continuing growth of the crest would inevitably lead to breakup of the wave and splashing of the droplets on to the opposing electrode as shown in Fig. 2. Incipient droplet formation seems to appear in Fig. 1. which shows cusps of metal on the crest which are distributed around it as though a flute instability had developed.

#### References

1. Ferraro, and Plumpton, "An Introduction to Magneto-Fluid Mechanics" Oxford U.P. (1961).
2. Milne-Thomson, L. M. "Theoretical Hydrodynamics" (4th Edition) MacMillan (1962).

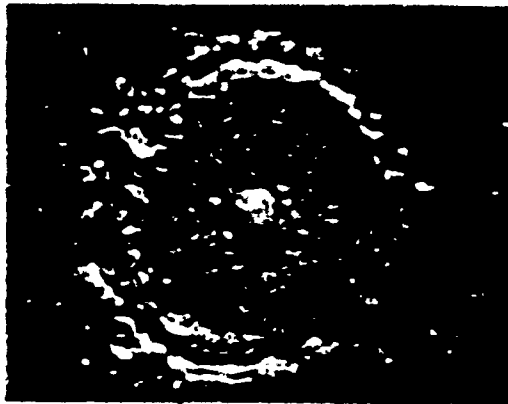


Figure 1. Damage From a 5.5 kV Spark

Output Impedance = 57  $\Omega$   
 Estimated Current = 100 ka  
 Discharge Duration = 25 nsec

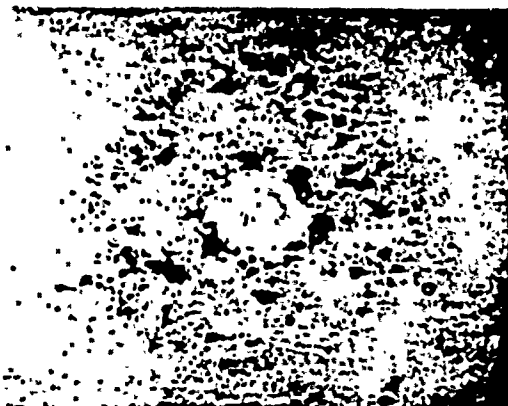


Figure 2. Vacuum Spark Damage Showing Metal Globules Around Molten Area

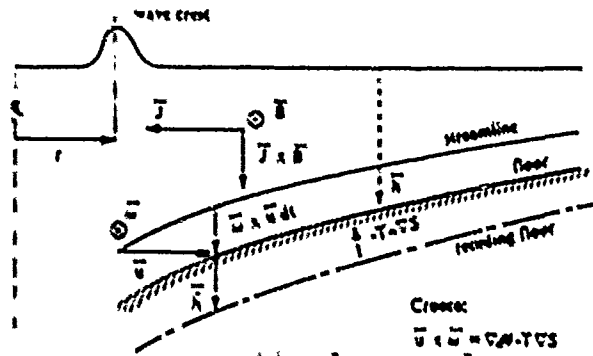


Figure 3. Schematic diagram of the molten pool showing current flow towards the arc axis on the center line and the hydromagnetic body force. A specific vorticity appears according to Crocco's Theorem at the molten floor as it recedes, and the inertial and hydromagnetic body forces are equal. This body force drives a tidal wave along the free surface against the flow, producing a standing crest.

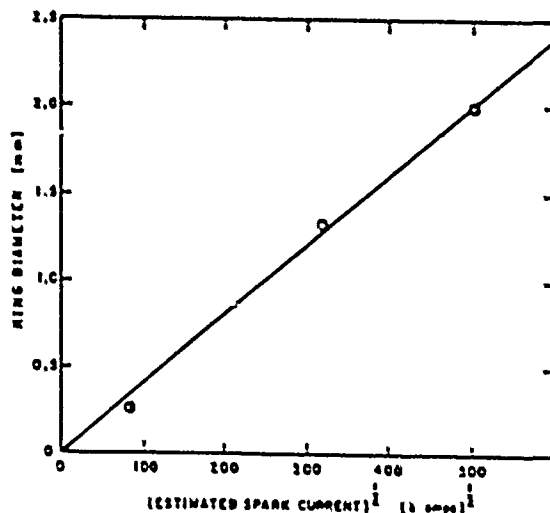


Figure 4. Scale of Damage as a Function of Current

# INFLUENCE OF NONUNIFORM EXTERNAL MAGNETIC FIELDS AND ANODE-CATHODE SHAPING ON MAGNETIC INSULATION IN COAXIAL TRANSMISSION LINES

MICHAEL A. MOSTROM

Intense Particle Beam Theory Group  
Los Alamos Scientific Laboratory  
Los Alamos, New Mexico 87545

## Abstract

Coaxial transmission lines, used to transfer the high voltage pulse into the diode region of a relativistic electron beam generator, have been studied using the two-dimensional time-dependent fully relativistic and electromagnetic particle simulation code CCUBE. A simple theory of magnetic insulation that agrees well with simulation results for a straight cylindrical coax in a uniform external magnetic field is used to interpret the effects of anode-cathode shaping and nonuniform external magnetic fields. Loss of magnetic insulation appears to be minimized by satisfying two conditions: (1) the cathode surface should follow a flux surface of the external magnetic field; (2) the anode should then be shaped to insure that the magnetic insulation impedance, including transients, is always greater than the effective load impedance wherever there is an electron flow in the anode-cathode gap.

## Introduction

Elsewhere in these proceedings, Mike Jones has described both theory and simulation of foilless diodes. The achievement of high voltage ( $> 5$  MeV), high current density ( $> 500$  ka/cm<sup>2</sup>), laminar electron beams by such diodes appears at present to require external magnetic fields on the order of 100 kg. The fringing fields from the external magnetic field coils will flare out to low values back in the coaxial transmission line feeding the diode. Also, in this same fringe field region the transmission line anode and cathode radii may taper dramatically in order to provide the proper transition in impedance and size between the diode and the insulator stack. However, previous theory<sup>1-4</sup> and simulation<sup>5</sup> of transmission lines has dealt only with straight coaxial transmission lines and no external magnetic field or with parallel plate transmission lines

with a uniform external magnetic field. We are, therefore, in the process of addressing the following three questions: (1) What is the impedance of a straight coaxial transmission line with a uniform external magnetic field; (2) in a tapered coaxial transmission line with a nonuniform external magnetic field, what is the proper cathode shape relative to the external magnetic field lines; (3) What constraints on the impedance profile along the transmission line minimize the loss of magnetic insulation? These questions are being studied using the two-dimensional time-dependent fully relativistic and electromagnetic particle simulation code CCUBE<sup>6</sup> and simple theories. Preliminary results are given below.

## Straight Coaxial Transmission Line, Uniform $B_0$

An analytic theory of magnetic insulation in a straight coaxial transmission line with a uniform external axial magnetic field  $B_0 = B_0 \hat{z}$  appears to require some further simplifying assumption or approximation (e.g., ignoring the axial self-magnetic field or imposing some relation between radius and one or more velocity components). The choice of such a simplifying approximation can perhaps be guided by simulations, but at the time of writing this paper, only the simplest possible theory has been completed and compared with simulations.

This theory first involves generalizing the critical current calculation by Creedon<sup>4</sup> to include the uniform external field  $B_0$ . The result is

$$I_c = \frac{I_a}{2\ln(b/a)} \left[ \gamma_0^2 - 1 - \left( \frac{\omega_c}{c} \frac{b^2 - a^2}{2b} \right)^2 \right]^{\frac{1}{2}} \quad (1)$$

where  $I_a = 2\pi m_e c / \mu_0 e \approx 8500$  A,  $\gamma_0 = 1 + eV_0/m_e c^2$  with  $V_0$  the anode-cathode potential,  $\omega_c = eB_0/m_e c$ , and  $a$  and  $b$  are respectively the cathode and anode radii. Our simple theory involves assuming a relation between  $I_c$  and the actual total current  $I_H$  flowing in the transmission line.

Our motivation for this assumption stems from existing magnetic insulation theory<sup>4</sup> for straight coaxial transmission lines with  $B_0 = 0$ . In all of these theories a free parameter exists. One possibility is a continuum of magnetic insulation states corresponding to different conditions on the electrons in regions where there is a  $x$ -variation along the transmission line. Another possibility is a previously overlooked general principle which would allow the electrons to pick a unique insulation state. We believe that the latter is more likely in a transmission line and that the general principle involved is maximization of the entropy production rate. This translates into maximizing the power flow since in a transmission line the terminating load impedance is equivalent to a resistor.\* If the impedance at the input to the transmission line is  $Z_I$  and the incoming (or right going) voltage there is  $V_I$ , then the voltage  $V_L$  across the line is

$$V_L = 2 V_I Z_L / (Z_I + Z_L) \quad (2)$$

where  $Z_L = V_L/I_L$  is the line impedance and  $I_L$  is the total line current. The transmitted power  $P = V_L I_L = I_L (2V_I - Z_I I_L)$  has a maximum at  $I_L = V_I/Z_I$  and decreases for higher currents. If one includes the effect of insulation loss at an impedance rise, the total or effective  $Z_I$  (as viewed from the line) always satisfies  $Z_I \geq Z_L$  which implies  $I_L \geq V_I/Z_I$ .

\*Note that this power flow argument cannot in general be applied to the operating characteristics of a diode because a highly ordered electron beam is not equivalent to a resistor.

Thus, maximum power flow requires an electron current distribution that minimizes the total line current  $I_L$ . Furthermore, the existing theories<sup>4</sup> with  $B_0 = 0$  all have very close to the same value for the minimum  $I_L$ . Finally, this value agrees well with simulation results<sup>5,7</sup> for the steady-state magnetic insulation current over a wide voltage range (1-20 MeV), and this value is always approximately 1/0.82 larger than the critical current  $I_c$  (with  $B_0 = 0$ ).

Thus, we take the steady-state magnetic insulation current to be  $I_H = I_c/\alpha$  even when  $B_0 \neq 0$ . The corresponding steady state magnetic insulation impedance  $Z_H = V_0/I_H$  is then

$$\frac{Z_H}{Z_0} = \alpha \left( \frac{\gamma_0 - 1}{\gamma_0 + 1} \right)^{\frac{1}{2}} \left/ \left[ 1 - \frac{1}{\gamma_0^2 - 1} \left( \frac{\omega_c}{c} \frac{b^2 - a^2}{2b} \right)^2 \right] \right|^{\frac{1}{2}} \quad (3)$$

where  $Z_0 \approx 60 \Omega \ln(b/a)$  is the vacuum coaxial transmission line impedance,  $V_0$  is the anode-cathode potential, and  $\alpha = 0.82 \pm 0.01$  is determined from a fit to simulation results. As  $B_0$  increases, however,  $I_c \rightarrow 0$  while we know  $Z_H/Z_0 \leq 1$ . Hence, Eq. (3) can be correct only for sufficiently small  $B_0$  or large  $V_0$ . This is demonstrated in Fig. 1 where Eq. (2) is used to find  $V_0 = V_L$  with  $Z_L = Z_H$  obtained from Eq. (3).  $V_I$  is fixed at either 1.5 MeV or 6.14 MeV,  $Z_I = Z_0 = 37 \Omega$ ,  $a = 1$  cm, and  $b = 1.853$  cm. The agreement between simulation and this simple theory, especially at high voltage, is sufficient to help design and interpret the results of the more complex simulations described next.

#### Field Line Orientation

The next simplest configuration one might try is a straight coaxial transmission line with a nonuniform external magnetic field  $B_0$ . The results are indicated in Fig. 2. Here  $B_0$  increases from 0.5 kg to 100 kg in a length of 60 cm with  $a = 1$  cm,  $b = 1.853$  cm, and  $V_I = 6.14$  MeV. The magnetic insulation initially proceeds about the same as with  $B_0 = 0$  until the position is reached where  $B_0 \approx 20$  kg.



Electrons emitted in the weaker field region cannot pass this position but rather go to the anode. Electrons emitted in the higher  $B_0$  region acquire a negative  $z$ -velocity and also go to the anode (for a total current loss of 40%) thereby reducing the actual operating impedance by an additional factor of 1/2 over Eq. (3) with  $B_0 = 0$ . The negative  $v_z$  of the electrons in the high  $B_0$  region is due to the strong  $v_\theta \times B_r$  force overtaking the  $-v_r \times B_\theta$  force as the  $B_0$  field lines converge toward the axis. Clearly, one should avoid having a component  $B_1 \hat{x} B_0 v_1/v_\theta$  of  $B_0$  perpendicular to the cathode.

Thus, the next configurations tried have cathodes that follow a flux surface of  $B_0$ . In Fig. 3, the cathode is shaped in this fashion until the straight section is reached where  $B_0$  continues to increase from 18 kg to 80 kg. Also, the anode radius drops linearly from 12.85 cm to 1.85 cm while the cathode drops linearly from 4.4 cm to 1 cm, and  $V_T = 8.35$  MeV. There is very little loss of insulation in the tapered section, but approximately 30% of the total current is lost to the anode in the straight section. In Fig. 4, the cathode is shaped to follow  $B_0$  over the entire length of 33 cm where  $B_0$  goes from 2 kg to 80 kg. The anode tapers roughly linearly from 23.6 cm to 2 cm while the cathode tapers as shown from 8.4 cm to 1.2 cm, and  $V_T = 8.35$  MeV. Once again the electrons emitted in the low  $B_0$  region cannot pass a critical  $B_0$  position (here when  $B_0 \approx 3.5$  kg). However, the current loss to the anode is only about 7%, and it is spread over about 1.5 cm (along  $z$ ) for a current density of less than  $0.1 \text{ kA/cm}^2$  at the anode surface. In the next section we offer a possible explanation for this loss.

#### Impedance Revisited

In the shaped transmission lines described above (Figs. 3 and 4), the vacuum impedance  $Z_0(z)$  monotonically decreased by about a factor of two with increasing axial position  $z$ . In simulations with  $B_0 = 0$ , this impedance drop

insured that only a slight transient insulation loss occurred. The discrepancy between this case and the  $B_0 \neq 0$  case (Figs. 3 and 4) might be interpreted by saying that complete magnetic insulation requires  $Z_H(z) \geq Z_T$  wherever  $Z_H(z) < Z_0(z)$  due to the electron flow, where  $Z_T$  is the terminating or load impedance. Otherwise, there will be some steady loss of insulation in the region around the absolute minimum of the impedance.

This would explain the insulation loss in Fig. 3 because Eq. (3) gives  $Z_H(z) > Z_T$  only up to near the straight section where  $Z_0 = Z_T$ . Near the start of the straight section (where  $B_0$  is still small)  $Z_H < Z_0 = Z_T$ , and as we move into the high  $B_0$  region the electrons are clamped to the cathode and  $Z_H$  rises up to  $Z_0 = Z_T$ .

The explanation of the small insulation loss in Fig. 4 is more subtle because the effective load impedance  $Z_E(z, t)$  differs from  $Z_T$  due to the rise time of the high voltage pulse. Using the telegrapher's equations, with the subscript "T" denoting measurement at the terminating position  $z_T$ , and assuming a small time derivative  $\dot{V}_T$ , gives

$$\frac{Z_E(z, t)}{Z_T} = 1 + \frac{\dot{V}_T}{V_T c} \int_z^{z_T} \left[ \frac{Z_0(z)}{Z_T} - \frac{Z_T}{Z_0(z)} \right] dz \quad (4)$$

For our case where  $Z_0(z) \geq Z_T = Z_0(z_T)$  and  $\dot{V}_T \geq 0$ ,  $Z_E(z, t) \geq Z_T$ . In spite of this, for the case shown in Fig. 4, Eq. (3) gives  $Z_H(z) \geq Z_E(z, t)$  and yet there is still some small loss of insulation. The problem is that in magnetic insulation there are transients where the impedance  $Z_H(z, t)$  drops (by as much as 30%) below the final steady state value  $Z_H(z)$  given by Eq. (3). Indeed, in the loss region shown in Fig. 4, measurements indicate  $Z_H(z, t) < Z_E(z, t)$  by about 7%. Furthermore, once this loss region forms (due to a transient where  $Z_H < Z_E$ ) and propagates to the high  $B_0$  region (where  $Z_H$  rises to  $Z_0$ ) it appears to be difficult to get rid of. Thus, complete magnetic insulation seems to require the stricter condition  $Z_H(z, t) \geq Z_E(z, t)$  wherever  $Z_H(z) < Z_0(z)$ .

### Tentative Conclusions

Minimization of magnetic insulation loss appears to require two conditions: (1) the cathode surface should coincide with a flux surface of the external magnetic field  $B_0$  at least until  $B_0 \ll B_0 v_r/v_0$ ; (2) the vacuum impedance  $Z_0(z)$  should drop sufficiently and the rise time  $V_T/\dot{V}_T$  should be sufficiently long that  $Z_H(z,t) \approx Z_E(z,t)$ , including all transients, wherever  $Z_H(z) < Z_C(z)$ .

### References

1. R. V. Lovelace and E. Ott, Phys. Fluids **17**, 1263 (1974).
2. A. Ron, A. A. Mondelli, and N. Rostoker, IEEE Trans. Plas. Sci. **PS-1**, 85 (1973).
3. V. S. Voronin and A. N. Lebedev, Sov. Phys. Tech. Phys. **18**, 1627 (1974).
4. J. H. Crendon, J. Appl. Phys. **46**, 2946 (1975); J. Appl. Phys. **48**, 1070 (1977).
5. J. W. Poukey and K. D. Bergeron, Appl. Phys. Lett. **22**, 8 (1978).
6. L. E. Thode, B. B. Godfrey, and W. R. Shanahan, Phys. Fluids **22**, 747 (1979).
7. Our own simulation results (unpublished) are in agreement with those of Ref. 5.

This work was supported by the Air Force Office of Scientific Research and the U.S. Department of Energy.

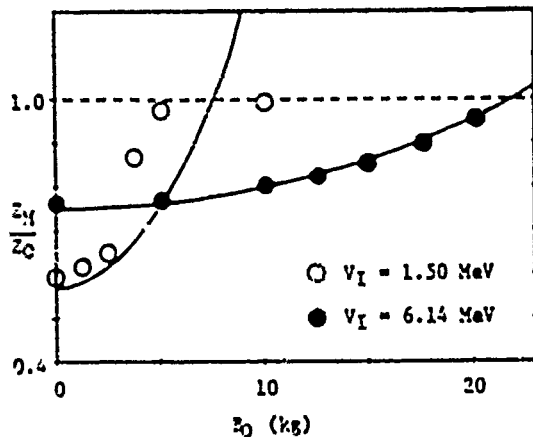


Fig. 1. Impedance of straight coax vs. uniform  $B_0$ . Solid lines are theory, Eq. (3), with  $\alpha = 0.82$ . Open and closed circles are from simulations.

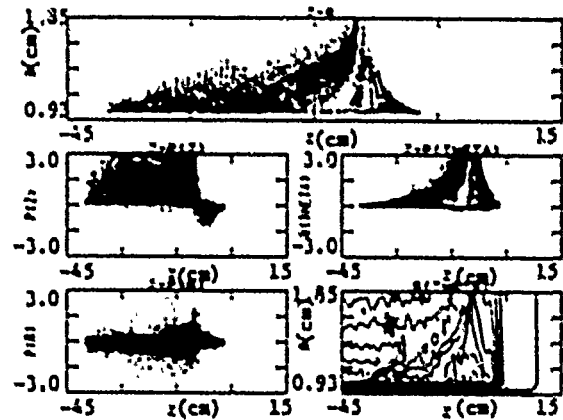


Fig. 2. Straight coaxial transmission line, non-uniform  $B_0$ . Time = 1.72 nsec.

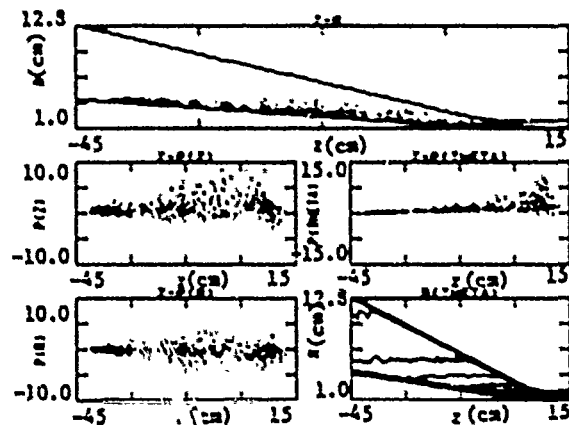


Fig. 3. Shaped coaxial transmission line, non-uniform  $B_0$ . Time = 5.98 nsec.

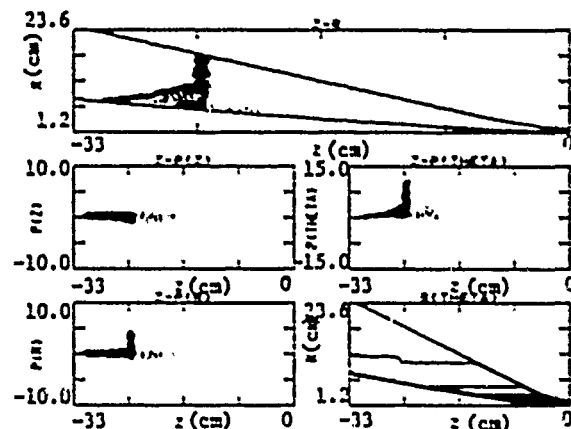


Fig. 4. Shaped coaxial transmission line, non-uniform  $B_0$ . Time = 19.5 nsec.

# MITL - A 2-D Code to Investigate Electron Flow Through Non-Uniform Field Region of Magnetically Insulated Transmission Lines\*

E. L. Neu and J. P. VanDevender

Sandia Laboratories, Albuquerque, New Mexico 87185

## Abstract

Self-magnetically insulated, high voltage transmission lines are used in inertial confinement fusion particle accelerators<sup>1</sup> to transmit power from the vacuum insulator to the diode. Injection and output convoluted sections pose special problems in establishing the desired electron flow pattern needed to maintain high overall efficiency. A time independent, 2-D numerical code for planar or triplate geometries calculates the motion of a test electron through the tapered input or output convolutes. The 1-D parapotential model is assumed to be appropriate at each position and the magnetic field and potential distribution are calculated in the vicinity of the particle. The electric field is then calculated from Gauss's Law, and the electron motion is calculated relativistically. The results show that the electron canonical momentum in the direction of flow changes as the electron passes through a convoluted geometry. As shown by Mendel,<sup>2</sup> these electrons flow between the conductors after the convolute without re-intersecting the cathode. We hypothesize that these electrons lead to the losses observed in long self-magnetically insulated lines. Results of calculations are correlated with results of the Mite power flow experiment.<sup>3</sup>

## Introduction

Transition sections into the magnetically insulated transmission lines can excite an apparent instability in the electron flow within the transport section<sup>3,4</sup> and cause severe energy losses. A numerical, time independent 2-D code, MITL, has been written to investigate the effects of these transition sections on the flow pattern within the transport section. The code is used to examine the input transition in the Mite experiment.<sup>3,4</sup>

The results suggest that the input transitions produce electron flow in which the axial canonical momentum  $P_z$  is approximately  $10^{-7}$  kg-m/s or  $10^{-6}$  of that allowed in the line. The transitions that produce broad canonical momentum distributions  $F(P_z)$  are correlated with efficient power transport in the experiments. Those that produce narrow distributions are correlated with lossy transport experimentally.

\*This work was supported by the U.S. Dept. of Energy, under contract DE-AC04-76-DP00789.

## Description of the Problem and the Approach

The rectangular geometry used in MITL is appropriate to triplate type transition sections and is shown in Fig. 1. The effective width  $w$  of the lines perpendicular to  $\vec{E}$  and  $\vec{E} \times \vec{B}$ , and the conductor separation  $d$  are variables that specify the geometry of either the input or the output transition section. Time independence is assumed in MITL since the transit time through the transition sections are typically a few nanoseconds and are much shorter than the pulse duration. Electromagnetic fields within the magnetically insulated lines are calculated on the assumption that the 1-D parapotential equations derived by Creedon<sup>5</sup> are appropriate for each position in the 2-D convolute. The justification for using the 1-D parapotential model is two fold: First, the scale length for the geometry variation is long compared to the separation between conductors so the flow is approximately one dimensional at each position. Secondly, the parapotential theory adequately describes the relationship between the total current  $I_T$ , the boundary current  $I_B$  inside the negative conductor, and the voltage  $V_0$  for a given line with a vacuum wave impedance  $Z_0$ . The agreement with 2-D electromagnetic PIC simulations<sup>6</sup> and experiments<sup>3,6</sup> is within the numerical and experimental uncertainties respectively. The electromagnetic fields from the 2-D calculation<sup>6</sup> for a Mite like line at 2.4 MV with  $I_T = 450$  kA and  $I_B = 243$  kA in a coaxial geometry with  $Z_0 = 8\Omega$ , have been compared in Refs. 6 and 7, and the agreement justifies the use of parapotential theory in these calculations.

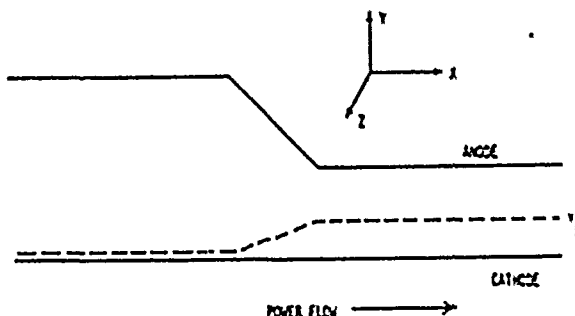


Fig. 1. Transition section geometry in MITL. The line width is specified in the Z direction.

The test electron is then injected into the convolute and its motion followed through the convolute and into the uniform self-magnetically insulated transmission line. Once inside the uniform line, the canonical momentum

$$P_x = \gamma_m u_x - eA_x \quad (1)$$

is a constant of its motion, where  $m$  is the electron rest mass,  $e$  is the electron charge,  $u_x$  is its axial velocity,  $A_x$  is the axial component of the magnetic vector potential and

$$\gamma_m \equiv 1/(1 - u^2/c^2)^{1/2} \quad (2)$$

for an electron of speed  $u$  and  $c = 3 \times 10^8$  m/s. The sum of its kinetic and potential energy is also a constant of its motion. Since the problem is assumed to be electrostatic, the energy is not changed by the convolute. However, since  $dL/dx \neq 0$  in the convolute, then  $P_x$  is changed by  $\Delta P_x$  according to Lagrange's equation as the electron moves through the convolute. Consequently, the problem is reduced to calculating  $\Delta P_x$  accurately. Generally, the limitations of finite cell size and a finite number of particles in 2-D self-consistent simulations severely limit the accuracy with which  $\Delta P_x$  can be computed. The numerical noise is avoided, at the expense of self-consistency, by using analytic equations for  $\bar{E}$  and  $\bar{B}$ . Without self-consistency the calculations are not, however, quantitatively exact. The value of these calculations is the insight they provide into the effect of convolutes on the electron flow.

#### Description of the Program

The program involves the choice of the initial conditions for the electron as it leaves the cathode plasma in the convolute, the calculation of the electric  $\bar{E}$  and magnetic  $\bar{B}$  fields in the vicinity of the test electron, and the integration of the relativistic equation of motion as the particle progresses through the convolute and the uniform transmission line. Each feature will be discussed and then the results of the Mite calculations will be presented.

The test particles are assumed to originate in a cathode plasma at a  $y$  coordinate  $y_0 = 10^{-3}$  m, where the voltage is  $< 0.3$  eV and the magnetic vector potential is  $A_0$ , which is calculated from the parapotential theory.<sup>3</sup> The initial energy of the electron is chosen between 1 and 10 eV to simulate the effect of electron emission from a few eV plasma. The initial particle energy determines the absolute value of the electrons initial velocity  $u_0$ . The initial canonical momentum  $\bar{P} = \gamma_m \bar{u} \times$  is assumed to be zero, so initially,

$$\begin{aligned} u_x &= \frac{eA_0}{\gamma_m} \\ u_y &= \sqrt{u_0^2 - u_x^2} \end{aligned} \quad (3)$$

The initial value of  $X = X_0$  is chosen for each calculation.

The total current flowing through a magnetically insulated line is given by

$$I_T = I_{a0} \gamma_m \{ \ln[\gamma_m + (\gamma_m^2 - 1)^{1/2}] + \frac{\gamma_0 - \gamma_m}{(\gamma_m^2 - 1)^{1/2}} \} \quad (4)$$

$$\gamma = \frac{eV}{m_0 c^2} + 1 \quad (5)$$

where  $\gamma_m$  is the value of  $\gamma$  at  $Y_m$  the edge of the flow pattern, and  $\gamma_0$  is given by the applied line voltage. The local line geometry determines the value of

$$E = \frac{60}{r} = \frac{u(x)}{r d(x)} \quad (6)$$

The input parameters are the line profile  $u(x)$  and  $d(x)$  for each axial position  $x$ , the voltage  $V_0$  at the anode for  $V = 0$  at the cathode, and the total current  $I_T$  through the structure. For a given position  $(x, y)$ , the value of  $\gamma_m(x)$  is calculated from Eq. 4. The voltage  $V(x, y)$  is given by

$$V = \frac{mc^2}{e} (\cosh \frac{Y}{C_1} - 1) \quad 0 \leq Y \leq Y_m \quad (7a)$$

or

$$V = \frac{mc^2}{e} \left( \frac{\gamma_0(Y - Y_m) - \gamma_m(Y_T - d)}{d - Y_m} \right) \quad Y_m < Y \leq Y_0 \quad (7b)$$

where

$$C_1 = d I_{a0} \gamma_m / I_0 \quad (8)$$

and

$$Y_m = C_1 \ln [\gamma_m + (\gamma_m^2 - 1)^{1/2}] \quad (9)$$

where  $Y_m$  is the position of the sheath,  $Y_0$  is the position of the anode and the cathode is at  $Y = 0$ . The values of  $V$  at four positions equally spaced about  $(x, y)$  are calculated and the electric field is calculated from

$$\bar{E} = -\nabla V \quad (10)$$

The local magnetic field  $\bar{B} = B_z \hat{z}$  is given by

$$B_z = -\frac{mc^2}{e} (\gamma - 1) \quad 0 \leq Y \leq Y_m \quad (11a)$$

$$B_z = -\frac{\mu_0 I_T}{2\pi r} \quad \text{if } Y_m < Y \leq Y_0 \quad (11b)$$

The relativistic equation of motion for the electrons is

$$\frac{d}{dt} (\gamma_m \bar{u}) = -e (\bar{E} + \bar{u} \times \bar{B}) \quad (12)$$

and is combined with the local electric and magnetic fields. It is then solved using the integration routine STFOBE<sup>6</sup> to find the new particle position and velocity components, within a given error criteria, after a time increment. The particle is progressively accelerated through the transition and transport sections of line for successive time steps.

#### Results

The Mite experiment<sup>3,4</sup> used two transition geometries to change the gap spacing from 0.02 to

0.01 m in a triplate vacuum transmission line with an effective width  $w = 0.50$  m. In the first geometry, the transition was made over an axial length of 0.04 m and 40 percent of the power was lost between 0.30 and 1.4 m from the beginning of the uniform line. The second transition was made over an axial length of 0.14 m and the power transport was about 100 percent efficient. These two geometries were simulated with typical Mite parameters of  $V_0 = 2.0$  MV,  $I_0 = 0.4$  MA.

The effect of having space charge in the vacuum gap is illustrated in Fig. 2. The equipotentials for a 1 cm taper are shown for the Mite parameters of  $V_0$  and  $I_0$ . The position of the edge of the electron sheath is  $Y_m$  and is shown. The effect of the space charge is to produce a positive  $E_x$  near the cathode and to distort the distribution of  $E_y$  and  $B_z$ .

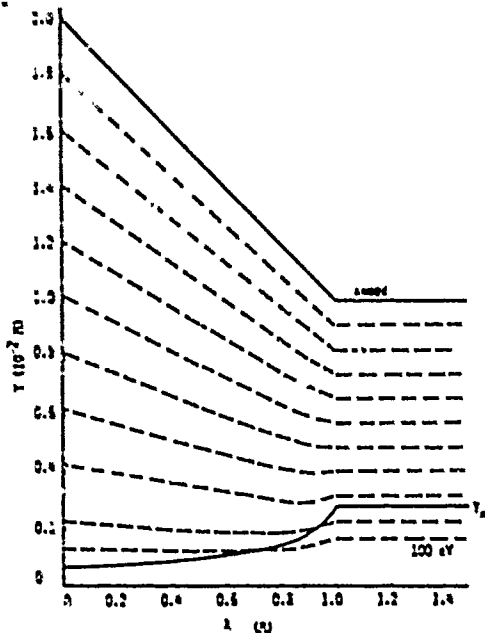


Fig. 2. Effect of space charge in vacuum gap of 1 cm long transition is shown. The dotted lines are equipotential at 200 kV intervals and  $Y_m$  is the electron sheath position.

For the severe 0.01 m long transition the distortion is not very large. The maximum value of  $E_x/(V_0/d)$  is only 0.005 for the 1 cm taper and is much less for the 0.04 m and 0.14 m tapers. Consequently, the effect of the convolute on the electron motion is small and must be calculated with a very small relative and absolute errors of  $\delta = 10^{-6}$ .

The current  $I_0$  carried by the electron flow increases steadily as the spacing between conductors is reduced in the transition section, as shown in Fig. 3 for the 0.14 m taper. The final canonical momentum that the electron achieves as it is accelerated through the convolute is shown as a function of its initial position  $X_0$  in Fig. 4 and 5 for the 0.04 m and 0.14 m convolutes respectively.

The emission current as a function of  $X_0$  is also shown. Since the differential electron current  $J_s(x) = \Delta I_s/\Delta X$  is supplied from the cathode, the approximate shape of the canonical momentum distribution  $F(P_x)$  can be approximated by

$$F(P_x) \approx \frac{1}{\sqrt{v_{ec}}} \frac{J_s(x(P_x))}{dP_x/dx}$$

which is shown in Fig. 6 for both tapers under the assumption that the initial energy  $U_0$  of the electrons is 10 eV at the cathode surface.

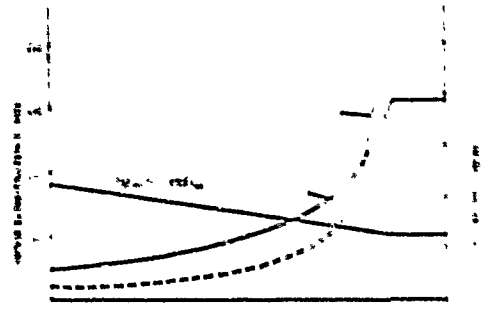


Fig. 3. The electron current  $I_s$  and the calculated emission current per unit length for the 0.14 m long transition is shown.

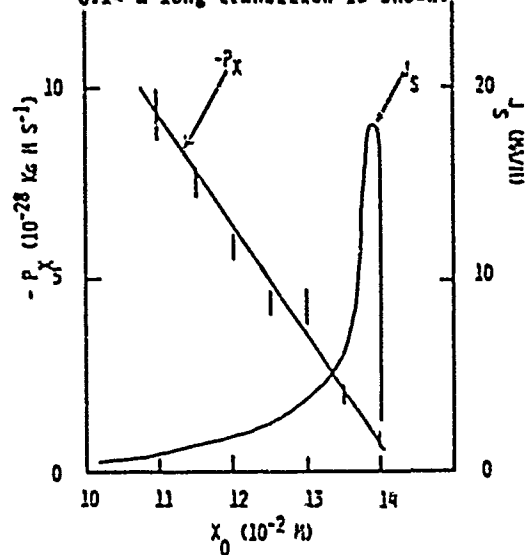


Fig. 4. The final canonical momentum  $P_x$  and the electron emission current  $J_s$  vs. the initial electron position  $X_0$  for the 0.04 m taper.

#### Discussion and Conclusions

In both cases, the canonical momentum is negative and  $F(P_x)$  has a very small width. The spread in  $P_x$  is  $\approx 10^{-6}$  of that allowed in the uniform line. The small values of  $P_x$  obtained with space charge are much less than the values estimated from the vacuum fields alone.

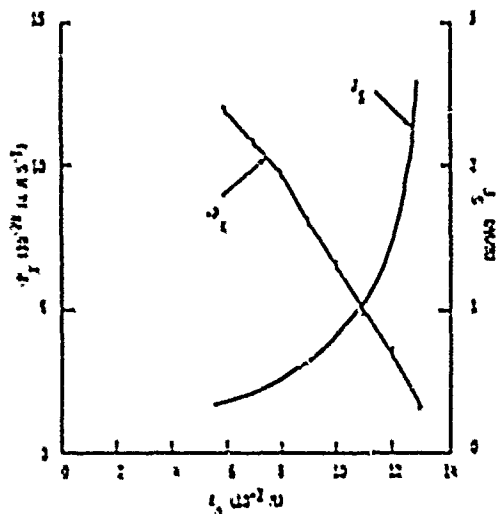


Fig. 5. Plot of  $P_x$  and  $J_x$  vs.  $X_0$  for the 0.14 m taper.

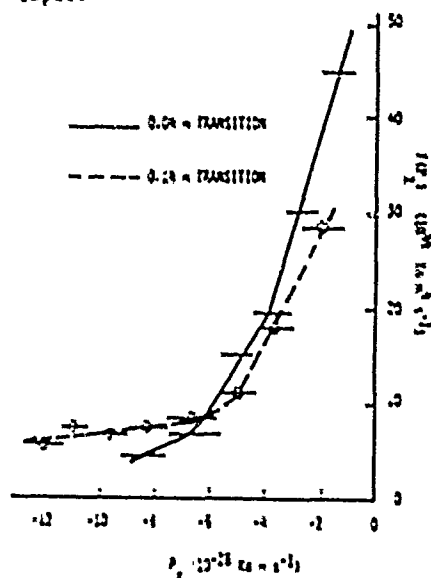


Fig. 6. The calculated distributions  $F(P_x)$  for the Mite transition sections.

The fact that  $P_x < 0$  for the injected electrons means that they will flow for many Larmor radii. Electron with  $W_0 = 10$  eV travel through the line past the 0.50 m position at which the losses occur and could be susceptible to an instability with a spatial growth length much less than 0.50 m, as hypothesized to explain the Mite results.

Since the electron current is a very strong function of the separation between plates, the bulk of the electrons in the flow have small values of  $P_x$ . Even though the gradients in the fields are larger near the end of the transition, the electrons are accelerated through the transition section before they acquire a large negative canonical momentum.

The electrons with more negative values of  $P_x$  originate further from the output of the transition section. The effect of using a more gradually tapered transition section is to broaden the canonical momentum distribution. Since the more gradual taper has efficient power propagation, the results indicate that a broader  $F(P_x)$  provide more reliable transport in long lines. An injector designed such that  $J_x$  approximately equals a constant through a long transition section should be the optimum arrangement. Such a transition section will be designed and tested on the Mite experiment.

In conclusion, the simulations indicate that the difference between the distributions  $F(P_x)$  for the lossy and the efficient transitions is small but significant. The results suggest a way to improve the transition and define experiment and theory development required to explore the implications further. The results indicate that an experiment to measure  $F(P_x)$  for the Mite transition sections should be capable of resolving the distributions in Fig. 6. Finally, the stability of electron flow with  $F(P_x)$  similar to those presented in Fig. 6 should be examined under the conditions of the large  $E_y$  and  $B_z$  present in self magnetically insulated transmission lines.

#### References

1. T. H. Martin, D. L. Johnson and D. H. McDaniel, Proc. of 2nd Topical Conf. on High Power Electron and Ion Beam Res. and Tech., Cornell Univ., Ithaca, NY, 807 (1977).
2. C. W. Mendel, J. Appl. Phys. **50**, No. 7 (1979).
3. J. P. VanDevender, J. Appl. Phys. **50**, No. 6, (1979).
4. J. P. VanDevender, Proc. of 2nd Int'l. Pulsed Power Conf., Lubbock, TX, June 12-14, 1979.
5. J. M. Creedon, J. Appl. Phys. **46**, 2946 (1975).
6. K. D. Bergeron, J. W. Poukey, M. S. DiCapua and D. G. Pallinan, accepted for publication in J. Appl. Phys. (1979).
7. K. L. Brover and J. P. VanDevender, same as Ref. 4.
8. B. L. Hulme and S. L. Daniel, "Using STODE/COLODE to Solve Stiff Ordinary Differential Equations" SAND74-0380 (Dec. 1974).
9. C. W. Mendel, same as Ref. 4.

## MAGNETIC INSULATION IN SHORT COAXIAL VACUUM STRUCTURES\*

Marco S. Di Capua and Timothy S. Sullivan

Physics International Company  
2700 Merced Street  
San Leandro, California 94577

Abstract

Magnetically insulated vacuum structures (MIVS) can be used to overcome the limitation on power flow in liquid dielectrics and dielectric vacuum interfaces in pulsed high power accelerators. A short (1 m), low-impedance ( $Z_0 = 50$ ) coaxial MIVS with a gap of 5 mm was studied experimentally. Power flows of  $1.5 \times 10^{10}$  W cm<sup>-2</sup> were observed. The current pulse showed some erosion before the onset of magnetic insulation. The transverse electron current arising from this erosion was observed with Faraday cups imbedded in the wall. Magnetic insulation was lost about 60-70 ns into the pulse. This loss was also observed in the Faraday cups and radiation diagnostics. This loss of magnetic insulation is associated with closure of the gap by cathode plasma.

Introduction

Magnetically insulated vacuum structures (MIVS) may be used to overcome limitations on power flow in liquid dielectrics and dielectric vacuum interfaces in pulsed high power accelerators. However, there are limitations in the energy transport efficiency in MIVS arising from:

1. Transverse electron flow in the gap as magnetic insulation is established. This electron current erodes the front of the pulse.
2. Current loss to the anode due to instabilities in the longitudinal space charge flow once insulation is established.
3. Loss of insulation due to closure of the gap before the end of the power pulse. This

closure is due to motion of the cathode plasma across the gap.

4. Ion flow across the gap once a plasma has been established at the anode by electron leakage current.

An experiment has been designed and diagnostics have been developed to investigate how magnetic insulation is established and lost in a coaxial MIVS, therefore providing some insight on the limitations above.

The measurements revealed that the width of the front which establishes magnetic insulation is much shorter than the length of the MIVS under investigation. Therefore, even though the MIVS is short by the conventional definition<sup>1</sup> ( $l \ll ct$  where  $l$  is the length of the structure and  $t$  is the risetime of the pulse), it exhibits the properties which have been attributed in the literature to a long structure ( $l \gg ct$ ).

It is suggested, therefore, that the distinction between a "short" and "long" structure should be based upon a comparison of the length of the structure and the width of the propagating front which establishes magnetic insulation.

Measurements also revealed that the apparent velocity of the front is substantially lower than that predicted by theory<sup>2,3</sup> for the voltages measured in the experiments.

While bounds have been established on the magnitude of the leakage current which may be due to instabilities in the electron flow, plasma closure has been identified as the cause of loss of magnetic insulation. The current flow across the gap, once magnetic insulation is lost, has been determined to be due to electrons. Calculations show that there is not enough energy

\*Work sponsored by the Defense Nuclear Agency.

deposited in the anode to produce a plasma which could be a source of ions.

#### Experimental Apparatus and Diagnostics

A schematic of the coaxial MIVS, drawn to scale, appears in Figure 1. The figure shows the coax ( $l = 1.0$  m) terminated with a focusing diode

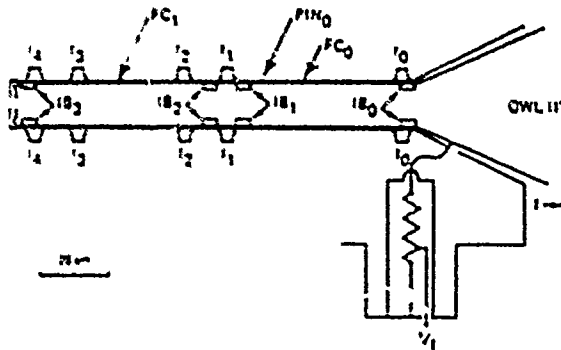


Figure 1 Vacuum coax apparatus.

load. The inner radius  $r$  of the coax is 6.2 cm, the radial gap  $d$  is 2 mm, and the geometrical factor<sup>4</sup>  $g$  equals 12.6 ( $g = 600/r_0$ ). To minimize the disturbances to the space charge flow,  $g_{\text{bicone}} = g_{\text{coax}} = g_{\text{diode}}$  were chosen.

The coaxial MIVS was attached to the output of the OWL II' accelerator through a biconic adapter. This ~ 1 TW accelerator with a water dielectric coaxial output circuit has an effective source impedance of 1.20. Prepulse was reduced to less than 4.1 kV peak.

The diagnostics used in the experiments were:

1. A vacuum voltage monitor at the input of the transmission line<sup>5</sup>.
2. Self-integrating Rogowski coils<sup>6</sup> placed in grooves in the cathode and anode of the structure; their locations are shown in Figure 1.
3. A high-current graphite shunt<sup>7</sup> was placed at the  $I_4$  location where electron bombardment caused the epoxy potted coils to fail.
4. Faraday cups consisting of a 0.32-cm-o.d. collector, nested in a 0.46-cm-diameter hole in the anode, shunted to ground via a ~ 10 resistor.

#### Experimental Results

The solid waveform in Figure 2 is the input

voltage to the coax ( $V_1$ ) with a  $g = 12.6$  diode load. The dashed and dotted waveforms are the

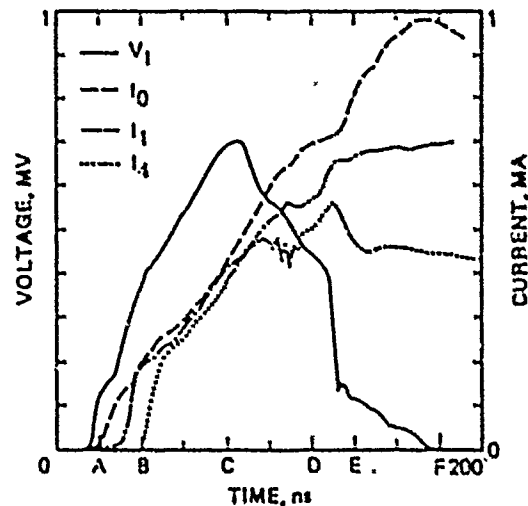


Figure 2 Voltage and current waveforms.

currents  $I_0$  and  $I_4$  at the input and output of the coax, respectively. The most significant features of the waveforms are the following:

- a) There are about 120 kV on the line before current ( $I_0$ ), which is in excess of the displacement current, begins to flow (A in Figure 2). This voltage corresponds to a mean field of  $240 \text{ kV cm}^{-1}$ . A field of this magnitude is required to achieve field emission from exploding whiskers on the cathode<sup>8</sup>.
- b) The current at the output ( $I_4$ ) rises 20 ns after the current at the input  $I_0$  (A-B in Figure 2). It is also 40 kA less than the current at the input until shortly after peak voltage (B-C in Figure 2), when impedance collapse takes place in the structure. It takes place in two phases described below.
- c) In the first phase, the current shows an upward inflection as the voltage peaks and then drops (C in Figure 2). As the voltage continues to drop,  $I_4$  diverges from  $I_0$  and some high frequency structure appears on the  $I_4$  waveform (C-D in Figure 2).
- d) In the second phase, the input voltage ( $V_1$ ) drops 100 kV in a few nanoseconds (D-E in Figure 2). The current at the input ( $I_0$ ) displays an abrupt rise



while  $I_4$  at the output rises slightly, at first, then drops and finally clamps.

The signal from the Faraday cups, which yield a local measurement of current density at the anode, explains the difference between the input and output current waveforms displayed in Figure 1. The Faraday cup waveforms appear in Figure 3. The axial locations of  $FC_0$  (dashed waveform) and  $FC_1$  (dotted waveform) are 31 and 85 cm from the cone to coax transition, respectively. The solid line in the same figure shows the difference,  $I_{loss}$ , between the input ( $I_0$ ) and output ( $I_4$ ) currents.

Both Faraday cups peak at the beginning of the pulse (A-B in Figure 3). These peaks, which fit temporally under the broader peak of  $I_{loss}$ , arise from transverse electron current, that is, current flowing across the gap. The signal from  $FC_0$  arises before the signal from  $FC_1$ . This transverse electron flow (pulse front) is required to establish magnetic insulation.

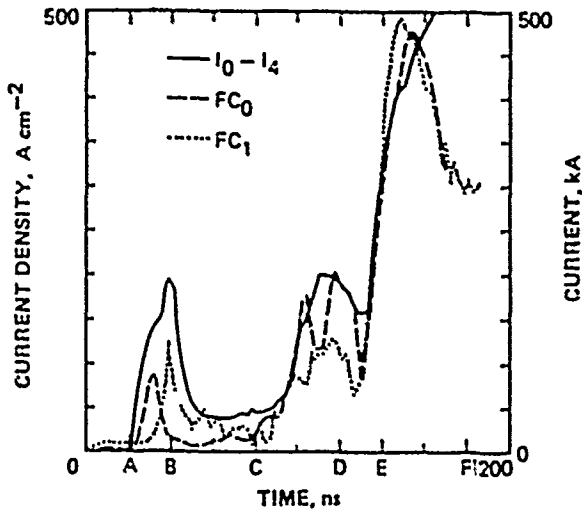


Figure 3 Faraday cup and current loss waveforms.

Another feature of the Faraday cup and current loss waveforms is the rise that occurs simultaneously and has roughly the same duration as the drop in voltage (C-D in Figures 2 and 3). This loss reaches a plateau before there is a rapid rise in the current loss and Faraday cup signals, which is simultaneous with the rapid drop in  $V_1$  (D-E in Figures 2 and 3).

The time between the two peaks of the Faraday

cup allows a calculation of the apparent velocity of the pulse front, since the distance between the cups is fixed. For the waveforms of Figure 3, the velocity is  $6.4 \times 10^7 \text{ m s}^{-1}$  while the velocity for seven experiments performed under similar conditions is  $5.2 \pm 1.2 \times 10^7 \text{ m s}^{-1}$  corresponding to  $\beta = 0.17 \pm 0.4$ . The spreads in the results are standard deviations about the mean of the experimental data for seven experiments performed under identical conditions. Since the voltage behind the front is approximately 340 kV, the velocity is substantially below the velocity

$$\beta = \sqrt{1 - 1/\gamma_0^2} = 0.5$$

predicted by present theories.<sup>2,3</sup>

The spatial extent of the front may be calculated under the assumption of constant apparent front velocity using a straightforward  $t = x/v$  transformation. The mean FWHM of the  $FC_0$  and  $FC_1$  fronts for the same seven experiments are  $6.9 \pm 2.7 \text{ ns}$  and  $7.4 \pm 1.6 \text{ ns}$ , respectively. These values yield a front width of  $37 \pm 14.3 \text{ cm}$  at both locations. This analysis indicates that although the MIVS is short compared to the characteristic time scales of the experiment, it is long compared to the spatial extent of the front, which establishes magnetic insulation.

The difference between  $I_0$  and  $I_4$  ( $I_{loss}$ ) shows a low level of transverse electron flow in the interval B-C of Figures 2-3 after insulation has been established and before the voltage begins to drop. For the seven experiments, this loss averages  $55 \pm 20 \text{ kA}$ , which is equivalent to  $12 \pm 4 \text{ A cm}^{-2}$ . This loss could arise from instabilities in the electron flow.

Experiments were performed with filters, covering the Faraday cups, to discriminate ion emission current, which could produce a signal distinguishable from electron impact current. The measurements revealed that the signals were indeed due to electron impact.

Cap closure has not been measured in these experiments. Indirect evidence of gap closure, however, was obtained from the current and voltage waveforms. It was observed that the current in the structure agreed very closely with that corresponding to saturated parapotential flow during

the time interval B-C of Figure 2. The current became substantially larger thereafter, suggesting that closure of the gap could be responsible for the increase.

The gap in the coax is obtained as a function of time by dividing the current corresponding to saturated flow<sup>2</sup>  $I_p/q = I_2 \gamma \ln(\gamma + (\gamma^2 - 1)^{1/2})$  by the measured input current ( $I_0$ ) and multiplying the quotient by  $R$ . Since  $q = R/d$ , the result of the calculation is  $d(t)$ . In the calculation  $\gamma = eV_2/m_0c^2 = 1$  and  $I_2 = 8500$  A. Figure 4 displays the result of the calculation with the waveforms of Figure 2. The plot shows that  $d$  remains equal to 5 mm for 40 ns after magnetic insulation has been established in the coax. Then gap closure begins shortly before peak voltage as

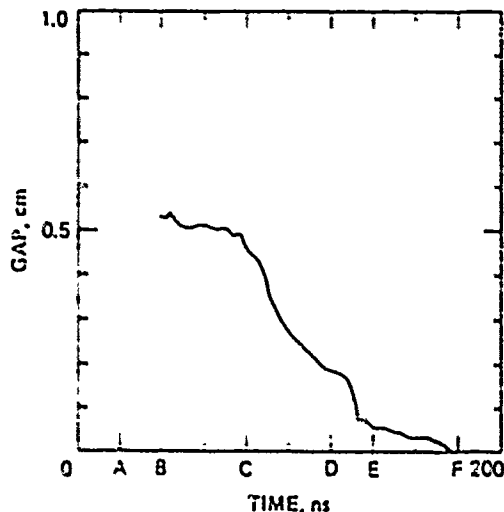


Figure 4 Coax gap as a function of time.

the Faraday cup signals start to rise. The gap in the coax has been calculated by this method for the seven experiments for which the Faraday cup data have been discussed. Before closure begins, the calculated average gap is  $5.3 \pm 0.2$  mm, which compares well to the 5 mm gap in the coax. The average closure velocity for  $5 \text{ mm} > d > 2 \text{ mm}$  is  $4.6 \pm 3.8 \text{ cm } \mu\text{s}^{-1}$ .

#### Acknowledgements

The authors deeply appreciate the cooperation of Walter Backmann, Jimmy Figures, Gloria Lawler, Lila Lowell, Al McConnell, and Don Pellinen in this effort. Special thanks are due to Kari Hashimoto and Marlan Gitting, who were instrumental in the preparation and fielding of the experiment. John Creedon's generous contributions to the interpretation of the data is also gratefully acknowledged.

#### REFERENCES

1. E. I. Baranchikov, et al., Proc. of the 6th Int. Conf. on Plasma Physics and Controlled Thermonuclear Research, Berchtesgaden, IAEA-CN-35/P7A, 185, STI/PUB/439, Vienna (1977).
2. E. I. Baranchikov, A. V. Gordeev, V. D. Korolev, V. P. Smirnov, Proc. of the 2nd Symposium on Collective Methods of Acceleration, 271, Dubna (1977).
3. M. Di Capua and D. G. Pellinen, J. Appl. Phys., 1979; PIR-1009, Physics International Company, San Leandro, California.
4. J. Creedon, J. Appl. Phys., 48, 1070 (1977).
5. D. G. Pellinen and M. S. DiCapua (unpublished).
6. D. G. Pellinen and P. W. Spence, Rev. Sci. Instr., 42, 1699 (1971).
7. D. G. Pellinen, M. S. DiCapua and W. Backmann (unpublished).
8. R. X. Parker, R. E. Anderson, and C. V. Duncan, J. Appl. Phys., 45, 2463 (1974).

## A LOW-INDUCTANCE 2-MV TUBE

Y. C. Chen, K. Mashima, and J. Benford

Physics International Company, 2700 Merced Street, San Leandro, California 94577

Abstract

A new multi-stage low-inductance tube for the coaxial water generator OWL II has been designed. Low inductance is achieved by means of a plastic lens in the water, which produces a field distribution with improved uniformity.

The OWL II coaxial water dielectric generator has an output transformer impedance of 1.8 ohms, an operating voltage on the tube of 1.5 MV, and an FWHM pulse duration of 80 ns. The tube originally employed a radial insulator configuration at the turn between the coaxial water line and the radial vacuum feed.<sup>1</sup> The tube had a Brewster angle interface, which caused the electromagnetic wave in the water dielectric to strike the plastic insulator at an angle to its surface. In propagating around the corner in the plastic, the wave emerged into the vacuum with an electric field distribution that was nonuniform along the insulator surface. The electric field was lowest at the triple point where the vacuum, plastic, and cathode surfaces meet and increased by a factor of 2.8 near the anode end of the insulator surface. This design was used to reduce the electric field at the triple point where electron emission could cause flashover along the entire insulator surface. The average field along this insulator surface was 43 kV/cm.

Because of recent advances in the design of multi-staged stacked insulator tubes as well as the age of the original radial tube, a new tube was designed and tested. The objective of the new design was to improve the breakdown characteristics so that the probability of breakdown would be less than 1% at 2 MV and less than 50% at 2.5 MV. The inductance was

to be reduced below 25 nH compared to the 30 nH of the vacuum region in the old tube.

The new tube employs stacked insulators and a dielectric lens to achieve high uniformity of field grading along with minimum inductance. Figure 1 shows a JASON electrostatic field code calculation of the field in the region of the turn from the coaxial to the radial line. Naturally the field is nonuniform in



Figure 1 Electrostatic equipotentials for OWL II water coax, multi-stage tube, and radial vacuum line.

the coaxial region, and would become uniform in the radial section if the radial water line were to extend far enough inward; however, for compatibility with the present experimental apparatus, the tube insulator had to be located very near the turn. Figure 1 shows a 9-stage tube separating the water from the vacuum side. Clearly the field grading is quite nonuniform, and a simple multistage tube design would be dominated by the high electric fields near the cathode surface.

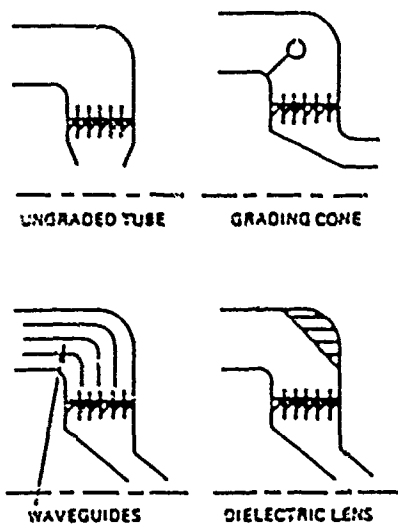


Figure 2 Methods of improving field uniformity along multi-stage insulators.

Several methods have been employed to grade multistage tubes (Figure 2). In high-impedance, oil-insulated machines, a grading cone is placed at the corner, and the cathode stalk is shaped.<sup>2</sup> This method has the effect of moving field lines toward the anode plane, thereby improving the uniformity. In low-impedance water machines, a number of wave guides or flux excluders are used to guide flux tubes into a uniform grading of the tube. The term flux excluder applies if these wave guides have considerable cross-section to reduce impedance mismatches in the water region. Flux excluders, however, have the drawbacks of being mounted directly to the insulators and of having delicate construction for use in water machines where considerable water shock occurs from the switches.

The new tube discussed here employs a dielectric lens in the region of the turn in the water line near the anode plane. The lower dielectric constant of the plastic draws equipotential lines into that region. After leaving the plastic they enter the tube insulator with a more uniform distribution. This design was suggested by Ian Smith.

Figure 3 shows our initial electrostatic field calculation of a dielectric lens for the CML II tube. The lens action is clearly shown, and field grading on the insulator is quite uniform in

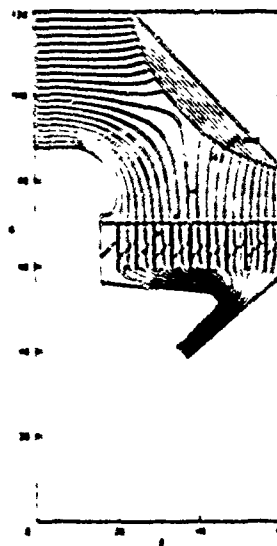


Figure 3 Equipotential plot for CML II tube with dielectric lens in water.

comparison to the no-lens case. We varied the thickness of the lens in the calculation and found that the grading along the insulator is relatively insensitive to the thickness of the lens. For ease of fabrication we shaped the lens with flat sides (Figure 4). The grading remained uniform along the stack. Figure 5 shows the distribution of electric field along the tie rod located just outside the insulator stack. The field at the knuckle in Figure 3 is 136 kV/cm, and in the plastic it is 280 kV/cm. Therefore, the water line has a safety factor of

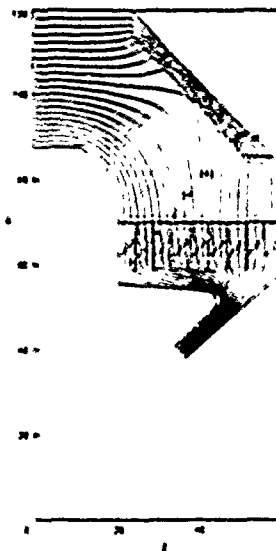


Figure 4 Final design of CML II dielectric lens.

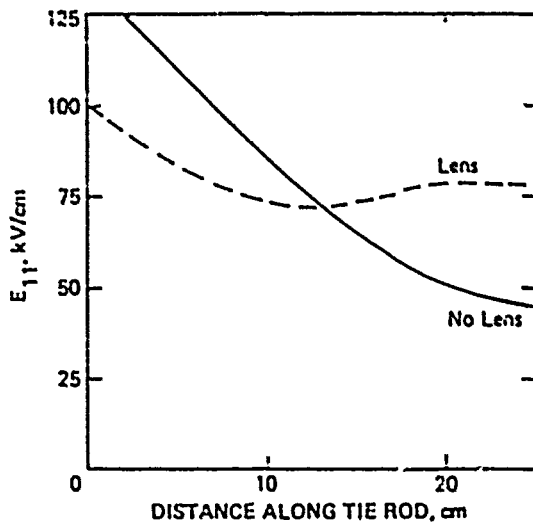


Figure 5 Effect of dielectric on field grading along 9-stage insulator. Distance is measured from cathode to anode planes.

1.8. The plastic is considerably below the breakdown point. On the insulator the time-dependent breakdown field is 120 kV/cm, and the average field on the stack is about 80 kV/cm giving a safety factor of 1.5.

The physical configuration of the new tube is shown in Figure 6. The cast polyurethane dielectric lens is 23 cm long and 3.5 cm thick. The insulators, made of acrylic, are 2.5 cm thick with an angle on the surface of 45 degrees. The insulator area is

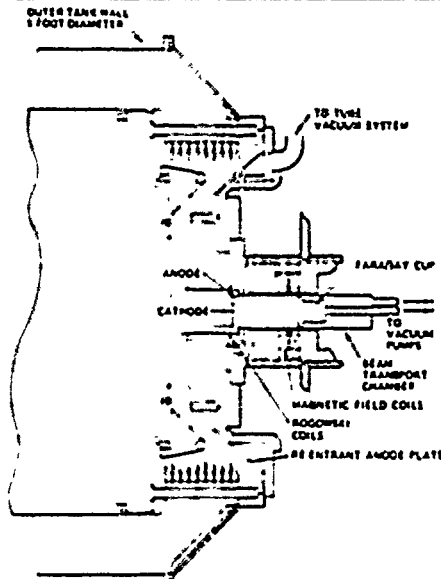


Figure 6 Layout of new OWL II tube and diode load.

$10^4 \text{ cm}^2$ . Radially interior to the insulators, there is a constant-impedance, 5 ohm vacuum feed, which then becomes a constant-gap vacuum line feeding the cathode shank and diode. The calculated inductance of the insulator stack plus vacuum feed up to the constant gap section is 19 nH. A photograph of the tube is shown as Figure 7.



Figure 7 Photograph of the new tube.

The grading along the insulator rings was measured by injecting a pulse from the diode and observing the grading of the wave, which reflects from the prepulse slab at the far end of the output transformer. The measured grading is shown in Figure 8; clearly the measured effect of the dielectric lens is quite close to the calculated values.

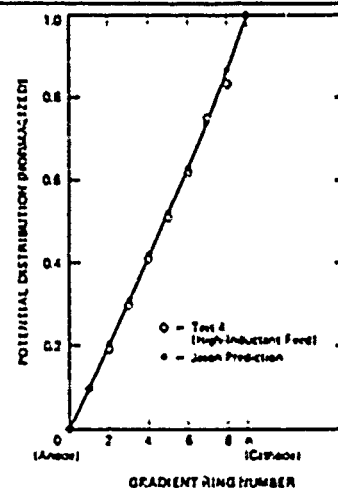


Figure 8 Comparison of calculated and measured potential distribution along insulator stack.

The tube installed on CWL II is shown in Figure 9.

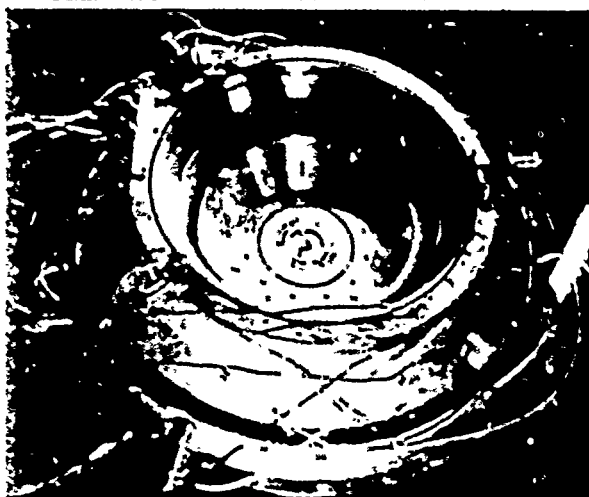


Figure 9 Vacuum region of new CWL II tube with re-entrant cathode in place.

#### Acknowledgements

We wish to thank G. Frazier for helpful discussions and L. Connelly, G. Rice, and S. Sampayan for technical assistance in fabrication and calibration.

#### References

1. G. Frazier, J. Vac. Sci. Technol. 12, 1183 (1975).
2. B. Bernstein and I. Smith, IEEE Trans. Nucl. Sci. NS-18, 294 (1971).

## INDEX TO AUTHORS

- Abramyan, E., 202  
 Alcock, A. J., 179  
 Andrews, K. R., 261  
 Ashby, S., 410  
 Barrett, D., 308  
 Basenkov, S. V., 25  
 Bayless, J. R., 372  
 Benford, J., 487  
 Berger, T. L., 237  
 Bickford, J., 254  
 Bird, W. L., 76, 325, 385, 392, 398, 463  
 Black, S., 102  
 Boller, J. R., 205  
 Bradley, L. P., 467  
 Brennan, M., 325, 392, 398  
 Brockhurst, F. C., 406  
 Brooks, W. P., 343, 381  
 Brower, K. L., 429  
 Bullion, T. M., 333, 385  
 Burkes, T. R., 102, 308, 364  
 Burton, J. K., 205, 284  
 Bushnell, A. H., 161  
 Butcher, R. R., 273  
 Buttram, M. T., 61  
 Byszewski, P., 148  
 Calvin, H., 359  
 Canavan, G., 1  
 Carder, B. M., 454, 459  
 Caristi, R., 17  
 Cary, W. K., Jr., 114  
 Chen, Y. G., 359, 487  
 Chetvertkov, V. I., 25  
 Cnare, E. C., 343, 381  
 Conte, L., 83, 276, 284, 368  
 Cowan, M., 343  
 Crumley, R. J., 119  
 Cummings, D. B., 172, 446  
 D'Addario, M., 236  
 Davis, S. J., 246  
 Dalton, C., 232  
 Dembinski, M., 72  
 DiCapua, M., 483  
 Dobbie, C. B., 161  
 Driga, M. D., 76, 333, 398  
 Ehsani, M., 419  
 Fenneman, D., 122  
 Fernsler, R. F., 368  
 Fine, K., 42  
 Fisher, R., 425  
 Fitch, R., 49  
 Fitzsimmons, W. A., 184  
 Forcier, M. L., 221  
 Ford, R. D., 83, 276, 284  
 Frazier, G. B., 127, 359  
 Freytag, E. K., 49  
 Friedman, S., 17  
 Fuja, R. E., 419  
 Fujioka, T., 165  
 Gagnon, W. L., 49, 246  
 Galbraith, J. D., 100  
 Gillis, P., 410  
 Gilmour, A. S., Jr., 250  
 Glancy, M. T., 295, 301  
 Goldhar, J., 236  
 Golka, R., 136  
 Gover, J. E., 402  
 Gray, B. R., 242  
 Gripshover, R., 122, 221

- Guenther, A. H., 433, 437, 442  
 Gully, J. H., 325, 333, 385, 392, 398  
 Gundersen, M., 119  
 Gurbaxani, S. H., 273  
 Gusev, O. A., 25  
 Gvishi, M., 376  
 Hammon, H. G., III, 172, 446  
 Harjes, H. C., 442  
 Harris, N. W., 65  
 Harvey, R. J., 372  
 Hashimoto, T., 165  
 Hatfield, L. L., 442  
 Henderson, R. P., 287, 347  
 Hill, G., 364  
 Koeft, L. O., 149  
 Honig, E. M., 414  
 Howland, M. M., 246  
 Hutchins, R. L., 425  
 Istomin, J. A., 25  
 Jampol'skii, I. R., 25  
 Jansen, H., 261  
 Jansen, J., 31, 254  
 John, P. K., 72  
 Johnson, D. J., 191  
 Jones, L. A., 142  
 Jones, M. E., 68  
 Kenyon, V. L., III, 187  
 Kihara, R., 209  
 Koba, J. V., 25  
 Kolm, H., 42  
 Krausse, G., 232  
 Krickhuhn, A. P., 161  
 Kristiansen, M., 106, 433, 437, 442  
 Kulshov, G. D., 202  
 Kulke, B., 209  
 Kunhardt, E. E., 433, 437  
 Kustom, R. L., 419  
 Kuswa, G. W., 153  
 Lalevic, B., 376  
 Latmanizova, G. M., 25  
 Lee, C. H., 165  
 Lehman, T. H., 425  
 Leopold, K. E., 179  
 Levinson, S., 433  
 Levy, S., 376  
 Lin, J., 106  
 Lindberg, D. D., 114  
 Lindstrom, H. B., 83  
 Lippert, J. R., 132  
 Lupton, W. H., 83, 276, 284  
 Markiewicz, W. D., 381  
 Martin, T. H., 2, 191  
 Martin, V. N., 157  
 Mashima, K., 487  
 Mayhall, D. J. T., 330, 463  
 McDonald, K., 437  
 Mendel, C. W., Jr., 153  
 Menown, H., 363  
 Merritt, B. T., 454, 459  
 Merz, S., 17  
 Mesyats, G. A., 9  
 Mikkelsen, K., 106  
 Miller, R. N., 250  
 Mongeau, P., 42  
 Mostrom, M. A., 475  
 Murray, J. R., 236  
 Neale, C. V., 363  
 Neau, E. L., 479  
 Newton, M., 437



- Nielsen, K., 410  
 Nolting, E. E., 450  
 Nunnally, W. C., 142  
 Obara, M., 165  
 O'Loughlin, J. P., 96  
 Orham, E. L., 467  
 Parker, R. D., 351  
 Parsons, W. M., 414  
 Pasechnikov, A. M., 25  
 Pecherskii, O. P., 25  
 Pellinen, D., 410  
 Perlin, A. S., 25  
 Petr, R., 308  
 Pevchev, B. P., 25  
 Pichot, M., 398  
 Plante, R., 17  
 Ramrus, A., 320  
 Rapaport, W. R., 236  
 Reinhardt, N., 17  
 Reinovsky, R. E., 287, 347  
 Rice, J. W., 114  
 Riepe, K. B., 254  
 Rinehart, L. F., 221  
 Rohwein, G. J., 87  
 Rose, M. F., 221, 295, 301  
 Rosocha, L., 184  
 Ross, G. F., 265  
 Rudakov, L. I., 25  
 Rylander, H. G., 76, 325, 330,  
 333, 385, 392, 398, 463  
 Sakato, Y., 165  
 Sarjeant, W. J., 179, 232  
 Sazama, F. J., 187  
 Scarlett, W. R., 261  
 Scherrer, V. E., 284  
 Schlitt, L., 269  
 Schönbach, K. H., 442  
 Schubert, C. W., Jr., 132  
 Shannon, J., 226, 320  
 Shipman, J. D., Jr., 205  
 Shoga, M., 376  
 Silvernail, C., 265  
 Simcox, G. K., 217  
 Singer, S., 142  
 Smirnov, V. P., 25  
 Smith, D. L., 287, 347  
 Sojka, R. J., 217  
 Spann, M. L., 392  
 Spence, P. W., 359, 410  
 Stabley, J., 242  
 Stine, R. D., 265  
 Stowers, I. F., 467  
 Sullivan, T. S., 483  
 Thode, L. E., 68  
 Thompson, J. E., 106  
 Tolk, K. M., 76, 325, 333,  
 392, 398  
 Tripoli, G. A., 214  
 Tucker, W. K., 381  
 Turner, W. C., 254  
 Turnquist, D., 17  
 VanDevender, J. P., 55, 153, 191,  
 429, 479  
 Vitkovitsky, I. M., 83, 276, 284, 368  
 Warren, R. W., 198, 414  
 Watson, A., 119, 471  
 Watson, H., 313  
 Weiner, M., 91  
 Weldon, W. F., 76, 325, 330, 333,  
 385, 392, 398, 463  
 Wilcox, R. E., 381  
 Wildi, P., 195, 355  
 Williams, P. F., 42, 119

Woodson, H. H., 76, 325, 330,  
333, 385, 392, 398, 463

Zowarka, R. C., 325, 333

## 2nd IEEE International Pulsed Power Conference - Attendance List

Ya. A. Abramyan  
Institute of High Temperatures  
Korovinskoe Road  
Moscow 127412 USSR

Michael Alley  
Dept. of Electrical Engineering  
Texas Tech University  
Lubbock, TX 79409

Alex Auyeung  
Dept. of Electrical Engineering  
Texas Tech University  
Lubbock, TX 79409

William L. Baker  
Air Force Weapons Lab/DYP  
Kirtland AFB  
New Mexico 87117

Don G. Ball  
Lawrence Livermore Labs  
P.O. Box 808  
Livermore, CA 94550

G. W. Barr  
Sandia Labs  
Pulsed Power Project Div. 4251  
Albuquerque, NM 87185

David Barrett  
Dept. of Electrical Engineering  
Texas Tech University  
Lubbock, TX 79409

Jon E. Barth  
IEEE  
1300 Wyoming St.  
Boulder City, NV 89005

Steve Beckerich  
Dept. of Electrical Engineering  
Texas Tech University  
Lubbock, TX 79409

William C. Beggs  
AMERIEL  
4110 Shawnee Lane NE  
Atlanta, GA 30319

James Benford  
Physics International  
2700 Merced St.  
San Leandro, CA 94577

T. L. Berger  
Naval Surface Weapons Center  
Code F-12  
Dahlgren, VA 22448

Ernest E. Bergmann  
Group L-9 MS 535  
Los Alamos Scientific Labs  
Los Alamos, NM 87544

Bernard H. Bernstein  
Physics International  
2700 Merced St.  
San Leandro, CA 94577

J. Bickford  
Los Alamos Scientific Labs  
Los Alamos, NM 87545

William L. Bird, Jr.  
Center for Electromagnetics  
University of Texas/Austin  
Taylor Hall 167  
Austin, TX 78712

Susan Black  
Dept. of Electrical Engineering  
Texas Tech University  
Lubbock, TX 79409

Boyd Blackwell  
Dept. of Electrical Engineering  
Texas Tech University  
Lubbock, TX 79409

Gus A. Blume  
NWSC-Crane  
Code 7071 G  
Crane, Ind. 47522

John R. Boller  
Naval Research Laboratory  
Code 6773  
Washington, DC

R. J. Bostek  
Harry Daimond Labs  
4103 Necostin Way  
Annandale, VA 22003

Laird Bradley  
Lawrence Livermore Labs  
P.O. Box 808  
Livermore, CA 94550

Lt. Michael R. Brasher  
Air Force Rocket Propulsion Lab  
AFRPL/LKDH (Stop 24)  
Edwards AFB, CA 92523

L. W. Braverman  
GTE Sylvania  
Box 188  
Mountain View, CA 94047

Mike Brennan  
University of Texas/Austin  
Taylor Hall 167  
Austin, TX 78712

Jerome B. Brewster  
Westinghouse Electric  
1310 Beulah Rd.  
Pittsburgh, PA

Frederick C. Brockhurst  
Air Force Aero Propulsion Lab  
AFAPL/POD-1  
Wright-Patterson AFB  
Ohio 45433

David F. Brower  
Fusion Research Center  
R. L. Moore Hall Rm. 202  
University of Texas  
Austin, TX 78712

Jacques Buchet  
Commissariat A L'Energie Atomique  
Etablissement T  
Boite Postale No. 7  
93270 SEVRAN  
France

Bob Burch  
Dept. of Physics  
Texas Tech University  
Lubbock, TX 79409

T. R. Burkes  
Dept. of Electrical Engineering  
Texas Tech University  
Lubbock, TX 79409

Joseph K. Burton  
Naval Research Laboratory  
Code 6770  
Washington, DC 20375

Andrew Bushnell  
Maxwell Laboratories  
8835 Balboa Avenue  
San Diego, CA 92123

Bob Butcher  
Los Alamos Scientific Labs  
Los Alamos, NM 87545

Malcolm Buttram  
Sandia Labs  
Div. 4253  
Albuquerque, NM 87185

W. Byszewski  
Dept. of Electrical Engineering  
Texas Tech University  
Lubbock, TX 79409

Paul A. Caldwell  
Harry Diamond Labs  
Adelphi, MD 20783

Bruce M. Carder  
Lawrence Livermore Labs  
P.O. Box 5508  
Livermore, CA 94550

George Cardwell  
RLM Hall 11.312  
University of Texas  
Austin, TX 78712

R. Caristi  
E G & G  
35 Congress St.  
Salem, Mass 01970

Bill Cary  
Naval Surface Weapons Center  
F-12  
Dahlgren, VA 22448

Matija Cenanovic  
Ontario Hydro Research Lab  
800 Kipling Ave.  
Toronto, Canada M8Z5S4

Y. G. Chen  
Physics International  
2700 Merced St.  
San Leandro, CA 94577

Edmond Y. Chu  
Maxwell Labs  
9244 Balboa Ave.  
San Diego, CA 92123

Hans-Jurgen Cirkel  
Kraftwerk Union Aktiengesellschaft  
Hammerbacher Strabe 12 + 14  
D 8520 Erlangen, West Germany

G. Clark  
E G & G  
35 Congress St.  
Salem, Mass 01970

Wayne Clark  
Maxwell Labs  
8835 Balboa Ave.  
San Diego, CA 92123

Eugene C. Cnare  
Sandia Labs  
P.O. Box 5800  
Albuquerque, NM 87185

Dale Coleman  
Dept. of Electrical Engineering  
Texas Tech University  
Lubbock, TX 79409

Dominick Conte  
Naval Research Lab  
Code 6777  
Washington, DC 20375

Edward G. Cook  
Lawrence Livermore Labs  
P.O. Box 808 L-321  
Livermore, CA 94550

Paul Corbiere  
Raytheon  
Hartford Road  
Bedford, MA 01730

Jacques Cortella  
Commissariat A L'Energie Atomique  
BP n 14  
21120-IS-SUR-TILLE  
France

Gerald W. Coutts  
Lawrence Livermore Labs  
P.O. Box 808  
Livermore, CA 94550

M. Cowan, Jr.  
Sandia Labs  
P.O. Box 5800  
Albuquerque, NM 87185

James L. Cox, Jr.  
Old Dominion University  
600 Downing Crescent  
Virginia Beach, VA

Randy Crumley  
Dept. of Electrical Engineering  
Texas Tech University  
Lubbock, TX 79409

D. Cummings  
Physics International  
2700 Merced St.  
San Leandro, CA 94577

Charlie Dalton  
Los Alamos Scientific Labs  
P.O. Box 1663  
Los Alamos, NM

K. DasGupta  
Dept. of Physics  
Texas Tech University  
Lubbock, TX 79409

Stephen J. Davis  
Lawrence Livermore Labs  
P.O. Box 808  
Livermore, CA 94550

Michael Dembinski  
Univ. of Western Ontario  
Dept. of Physics  
London, Ontario  
NGA 3K7 Canada

A. Stuart Denholm  
Energy Sciences, Inc.  
8 Gill St.  
Woburn, Mass 01801

Frank DeLurgio  
Emerson Elect. Co.  
5100 W. Florissant Ave.  
St. Louis, MO 63136

Col. Robert A. Detweiler  
USAF  
AFGR/NK  
Boiling AFB  
Washington, DC 20532

Dr. Peter J. DiBona  
Naval Surface Weapons Center  
Explosives Div. Code R-13  
Bldg. 315  
Silver Spring, MD 20910

M. DiCapua  
Physics International  
2700 Merced St.  
San Leandro, CA 94577

Bob Druce  
Dept. of Electrical Engineering  
Texas Tech University  
Lubbock, TX 79409

Joe Dutkowski  
NWSC-Crane  
Code 70715  
Crane, Ind. 47522

John W. Dzimianski  
Westinghouse Elect. Corp.  
MS 3714  
P.O. Box 1521  
Baltimore, MD 21203

Mehrdad Ehsani  
Argonne National Laboratory  
210 S. Whitney Way  
Madison, WI 53705

Jan E. Eninger  
Avco Everett Res. Lab  
2385 Revere Beach Parkway  
Everett, MA 02149

George F. Erickson  
Los Alamos Scientific Lab  
P.O. Box 1663 MS 566  
Los Alamos, NM 87545

M. Etzion  
Soreq NRC  
Yavne, Israel

Jon Farber  
Defense Nuclear Agency  
Washington, DC 20305

Dr. David B. Fenneman  
Naval Surface Weapons Center  
Code F-12  
Dahlgren, VA 22448

Richard Fernsler  
JAYCOR  
5902 Euclid St.  
Cheverly, MD 20785

Karl Fertl  
MIT-Natl. Magnet Lab  
150 Albany St. NW 14 2126  
Cambridge, MA

Richard Fitch  
Precipco, Inc.  
c/o Maxwell Laboratories  
9244 Balboa Avenue  
San Diego, CA 92123

William A. Fitzsimmons  
National Research Group, Inc.  
P.O. Box 5321  
Madison, WI 53705

D. Fleischer  
E G & G  
35 Congress St.  
Salem, MA 01970

Robert E. Fontana  
Air Force Institute of Technology  
AFIT/ENG  
Wright-Patterson AFB  
Ohio 45433

Richard Ford  
Naval Research Lab  
4555 Overlook Ave.  
Washington, DC 20375

Col. Paul E. Fortin  
USAF  
HQ AFSC/DLW  
Andrews AFB, MD 20334

G. M. Fowler  
Los Alamos Scientific Labs  
Los Alamos, NM 87545

Bill Fox  
Maxwell Labs  
8835 Balboa Ave.  
San Diego, CA 92123

George Frazier  
Physics International  
2700 Merced St.  
San Leandro, CA 94707

E. Karl Freytag  
Lawrence Livermore Labs  
P.O. Box 808 L-469  
Livermore, CA 94550

S. Friedman  
E G & G  
35 Congress St.  
Salem, MA 01970

Otto M. Freidrich, Jr.  
University of Texas/Austin  
1125 Shady Lane  
Austin, TX 78721

William Gagnon  
Lawrence Livermore Labs  
P.O. Box 808  
Livermore, CA 94550

J. D. Galbraith  
Los Alamos Scientific Labs  
P.O. Box 1663  
Los Alamos, NM 87545

Dr. Scott Gilmour  
State University of New York  
4232 Ridge Lea Road  
Amherst, NY 14226

Ms. Mary T. Glancy  
Naval Surface Weapons Center  
Dahlgren Laboratory, Code F 12  
Dahlgren, VA 22448

Terry F. Godlove  
Dept. of Energy  
MS C 404  
Germantown, MD 20545

Jerry Goldlust  
Dielectric Sciences  
48 Cummings Pk  
Woburn, MA 01801

Robert K. Golka  
Wendover ABF  
Box 537  
Wendover, UT 84083

Robert A. Goodman  
Lawrence Livermore Laboratory  
Mirror Fusion Test Facility  
P.O. Box 808/L-542  
Livermore, CA 94550

James E. Gover  
Sandia Labs  
Division 2165  
Albuquerque, NM 87185

Bobby R. Gray  
RADC/OCTP  
Griffiss AFB, NY 13441

Edward E. Grazda  
Van Nosttrand Reinhold Co.  
261 Green Moore Place  
Thousand Oaks, CA 91360

Ronald J. Gripshover  
Naval Surface Weapons Center  
Code F 12  
Dahlgren, VA 22448

Henry C. Grunwald  
ITT Electron Tube Division  
P.O. Box 100  
Easton, PA 18042

J. H. Gully  
Center for Electromagnetics  
Taylor Hall 167  
University of Texas/Austin  
Austin, TX 78712

Arthur H. Guenther  
Air Force Weapons Laboratory/CA  
Kirtland AFB  
Albuquerque, NM 87117

Peter Haas  
9232 East Parkhill Dr.  
Bethesda, MD 20014

M. O. Hagler  
Dept. of Electrical Engineering  
Texas Tech University  
Lubbock, TX 79409

J. R. Hall  
Rockwell Int.-Rocketdyne  
6633 Canoga Avenue  
Canoga Park, CA 91304

J. Hammond  
Physics International  
2700 Merced St.  
San Leandro, CA 94577

George Hanna  
Continental Electronics  
P.O. Box 270879  
Dallas, TX 75227

Chuck Harjes  
Dept. of Electrical Engineering  
Texas Tech University  
Lubbock, TX 79409

Fred Harmon  
Southwestern Engineering & Equipment  
6260 E. Mockingbird Lane  
Dallas, TX 75214

N. W. Harris  
Ion Physics Co.  
South Bedford Rd.  
Burlington, MA 01803

John Harrison  
Maxwell Laboratories  
8835 Balboa Ave.  
San Diego, CA 92123

Robin Harvey  
Hughes Research Lab  
3011 Malibu Cyn Rd.  
Malibu, CA 90265

Lynn Hatfield  
Dept. of Physics  
Texas Tech University  
Lubbock, TX 79409

R. E. Hebner  
National Bureau of Standards  
Bldg. 220, R344  
Washington, DC 20234

Bill Heidbrink  
Maxwell Laboratories  
8835 Balboa Ave.  
San Diego, CA 92123

Richard P. Henderson  
3225 34th St. Apt. E  
Kirtland AFB  
Albuquerque, NM 87116

Henrik Henriksen  
Nea-Lindberg  
Industriparken 39-43  
2750 Pallerup  
Denmark

Prof. Fritz Herlach  
Katholieke Universiteit Leuven  
Celestijnenlaan 200 D  
B3030 Leuven  
Belgium

Stuart J. Hesselton  
EEV, Inc.  
7 Westchester Plaza  
Elmsford, NY 10523

Gregory A. Hill  
BDM Corp.  
2600 Yale Blvd. S.E.  
Albuquerque, NM 87106

J. A. Hirsch  
Carborundum  
Graphite Products Div.  
Globas Plant  
P.O. Box 339  
Niagara Falls, NY 14302



Lothar E. Hoeft  
BDM Corp  
2600 Yale Blvd. S.E.  
Albuquerque, NM 87106

Gunter Hofmann  
Maxwell Laboratories  
8835 Balboa Ave.  
San Diego, CA 92123

Ronald W. Holloway  
Lawrence Livermore Laboratory  
P.O. Box 5508  
Livermore, CA 94550

E. M. Honig  
CTR-9, MS 464  
Los Alamos Scientific Labs  
Los Alamos, NM 87545

Michael M. Howland  
Lawrence Livermore Laboratory  
P.O. Box 5508  
Livermore, CA 94550

Robert L. Hutchins  
BDM Corp.  
2600 Yale Blvd. S.E.  
Albuquerque, NM 87106

Igor A. Ivanov  
Kurchatov Institute  
D-98  
Moscow, USSR

Jorg Jansen  
Los Alamos Scientific Labs  
Group L-10 MS 532  
Los Alamos, NM 87544

J. S. Jasper  
Exxon Nuclear Co.  
P.O. Box 130  
Richland, WA 99352

David L. Johnson  
701 Guadalupe Ct. N.W.  
Albuquerque, NM 87114

Michael Jones  
Los Alamos Scientific Laboratory  
Group T-15 MS-608  
Los Alamos, NM 87545

J. C. Jouys  
Commissariat a l'Energie Atomique  
Centre d'Etudes de Limeil  
Boite Postale 27  
94190 Villeneuve St. Georges  
France

E. L. Kemp  
Los Alamos Scientific Labs  
P.O. Box 1663  
Los Alamos, NM 87545

Kenneth L. Kennerud  
The Boeing Co.  
915 S. 251  
Kent, WA 98031

Dean O. Kippenhan  
Lawrence Livermore Laboratory  
P.O. Box 808-L-539  
Livermore, CA 94550

Hank Kohnexi  
Transrex  
1160 El Watson Center Rd.  
Carson, CA 90745

Alan Kolb  
Maxwell Laboratories  
8835 Balboa Ave.  
San Diego, CA 92123

Dr. Henry H. Kolm  
Massachusetts Institute of Technology  
Weir Meadow  
Wayland, MA 01778

M. Kolpin  
Physics International  
2700 Merced St.  
San Leandro, CA 94577

Peter Korn  
Maxwell Laboratories  
8835 Balboa Ave.  
San Diego, CA 92123

Irv Kovalik  
ILC Technology  
399 Java Drive  
Sunnyvale, CA 94086

George Krausse  
Los Alamos Scientific Labs  
MS-846 MP-4  
Los Alamos, NM 87545

Dr. M. Kristiansen  
Dept. of Electrical Engineering  
Texas Tech University  
Lubbock, TX 79409

Robert Kuenning  
Lawrence Livermore Laboratory  
P.O. Box 5504 L-153  
Livermore, CA 94550

Bernhard Kulke  
Lawrence Livermore Laboratory  
P.O. Box 5504  
Livermore, CA 94550

E. E. Kunhardt  
Dept. of Electrical Engineering  
Texas Tech University  
Lubbock, TX 79409

Boris Larionov  
F. Efremov Scientific Institute  
188631 Leningrad  
USSR

Robert LeBrun  
LeCroy Research Systems  
1806 Embarcadero Road  
Palo Alto, CA 94303

Jacques Lefebure  
Commissariat a L'Energie Atomique  
Etablissement T  
Boite Postale n 7  
93270 Sevran  
France

Gerald Levy  
IEEE  
Fairchild Republic Co.  
Plasma Lab  
Farmingdale, NY 11743

Stephen Levy  
U. S. Army Electronics Technology  
and Devices Lab  
Ft. Monmouth, NJ 07703

Scott Levinson  
Dept. of Electrical Engineering  
Texas Tech University  
Lubbock, TX 79409

Jack Lippert  
USAF Flight Dynamics Lab  
AFFDL/FES  
Wright-Patterson AFB, OH 45433

Lawrence H. Luessen  
Naval Surface Weapons Center  
Code F 12  
Dahlgren, VA 22448

William H. Lupton  
Naval Research Lab  
Washington, DC 20375

Charles W. McCulley, Jr.  
Maxwell Laboratories  
8835 Balboa Ave.  
San Diego, CA 92123

Ken McDonald  
Dept. of Electrical Engineering  
Texas Tech University  
Lubbock, TX 79409

Glen McDuff  
Dept. of Electrical Engineering  
Texas Tech University  
Lubbock, TX 79409

Sterling McNees  
EIMAC Div. of Varian  
301 Industrial Way  
San Carlos, CA 94070

Ronald H. McKnight  
National Bureau of Standards  
Bldg. 220, Rm. B344  
Washington, DC 20234

Phil Mace  
Los Alamos Scientific Labs  
MS 566  
Los Alamos, NM 87544

Armen E. Mardigian  
USAF European Office of Aerospace  
Research and Development  
Box 14  
FPO NY 09510

Richard A. Marshall  
Center for Electromagnetics  
Taylor Hall 167  
University of Texas/Austin  
Austin, TX 78712

T. H. Martin  
Dept. 4250  
Sandia Laboratories  
Albuquerque, NM 87113

V. Nicholas Martin  
GTE Laboratories  
40 Sylvan Rd.  
Waltham, MA 01701

Levi Martinez  
Los Alamos Scientific Labs  
P.O. Box 1663  
Los Alamos, NM 87544

David J. T. Mayhall  
Lawrence Livermore Laboratory  
Mirror Fusion Test Facility  
P.O. Box 808/L 542  
Livermore, CA 94550

Clifford W. Mendel  
Sandia Laboratories  
Albuquerque, NM 87113

Hugh Menown  
English Electric Valve Co., Ltd.  
Waterhouse Lane  
Chelmsford, Essex  
CMI-2QU  
England

Bernard T. Merritt  
Lawrence Livermore Laboratory  
P.O. Box 5508  
Livermore, CA 94550

G. A. Mesyats  
Institute of Atmospheric Optics  
Siberian Branch of AN SSSR  
Tomsk, USSR

Richard N. Miller  
SCEEE  
7300 Lake Ellenor Drive  
Orlando, Fla 32809

Marshall Molen  
Old Dominion University  
Dept. of Electrical Engineering  
Norfolk, VA 23508

Peter Mongeau  
National Magnet Lab  
Massachusetts Institute of Technology  
Cambridge, MA 02139

J. Moriarty  
Raytheon Co.  
Hartwall Rd.  
Bedford, MA 01730

Michael A. Mostrom  
Los Alamos Scientific Laboratory  
Group T-k5, MS-608  
P.O. Box 1663  
Los Alamos, NM 87545

Eugene Neau  
Sandia Labs  
Div. 4252  
P.O. Box 5800  
Albuquerque, NM 87185

W. Nevins  
The Machlett Laboratories, Inc.  
1063 Hope St.  
Stamford, Conn 06807

Mark Newton  
Dept. of Electrical Engineering  
Texas Tech University  
Lubbock, TX 79409

Torben Glar Nielsen  
Nea-Lindberg  
Industreparken 39-43  
2750 Ballerup  
Denmark

Eugene E. Nolting  
Naval Surface Weapons Center  
White Oak Lab  
Silver Spring, MD 20910

W. C. Nunnally  
Los Alamos Scientific Labs  
MS 429 Div. E4  
Los Alamos, NM 87545

Minoru Obara  
Dept. of Electrical Engineering  
Keio University  
3-14-1  
Hiyoshi, Kohuku-ku  
Yokohama-shi  
044-63-1141  
Japan

Henry B. Odom  
Naval Surface Weapons Center  
Code F-12  
Dahlgren, VA 22448

James O'Loughlin  
Air Force Weapons Lab/PGS  
Kirtland AFB  
Albuquerque, NM 87117

Edward L. Orham  
Lawrence Livermore Labs  
P.O. Box 5508  
Livermore, CA 94550

Thomas J. Pacala  
J.P.L.  
4800 Oakgrove Drive  
MS 183-601  
Pasadena, CA 91103

Robert Parker  
Hughes Aircraft Co.  
Culver City, CA 90230

W. M. Parsons  
Los Alamos Scientific Labs  
P.O. Box 1663 MS 464  
Los Alamos, NM 87544

Albert Passethnikov  
Kurchotov Institute of Atomic Energy  
D-98  
Moscow, USSR

Todd A. Pelley  
Lawrence Livermore Labs  
P.O. Box 5508  
Livermore, CA 94550

D. Pellinen  
Physics International  
2700 Merced St.  
San Leandro, CA 94577

Gerald J. Peters  
Naval Surface Weapons Center  
White Oak Lab R41  
Silver Spring, MD 20910

Rod Petr  
Dept. of Electrical Engineering  
Texas Tech University  
Lubbock, TX 79409

Babuel Peyrissac  
Commissariat a l' Energie Atomique  
Centre d'Etudes de Limeil  
Boite Postale 27  
94190 Villeneuve St. Georges  
France

M. A. Pichot  
Center for Electromagnetics  
Taylor Hall 167  
University of Texas/Austin  
Austin, TX 78712

R. Plante  
E G & G  
35 Congress St.  
Salem, MA 01970

John Power  
Dept. of Electrical Engineering  
Texas Tech University  
Lubbock, TX 79409

Kenneth R. Prestwich  
Sandia Labs  
Div. 4253  
P.O. Box 5800  
Albuquerque, NM 87185

S. Putnam  
Physics International  
2700 Merced St.  
San Leandro, CA 94577

Bill H. Quon  
TRW System Groups  
1 Space Park, RI-1070  
Redondo Beach, CA 90250

Al Ramrus  
Maxwell Laboratories  
8835 Balboa Ave.  
San Diego, CA 92123

William Rapoport  
Lawrence Livermore Labs  
1-470  
Livermore, CA 94550

N. Reinhardt  
E G & G  
35 Congress St.  
Salem, MA 01970

Thomas Reinhardt  
Tufts University  
10 Eliot Road  
Lexington, MA 02173

Robert E. Reinovsky  
Air Force Weapons Lab  
Kirtland  
Albuquerque, NM 87117

B. ...  
Electron Tube Division  
1000 Balboa Blvd.  
Northridge, CA 91325

K. Riepe  
Los Alamos Scientific Labs  
P.O. Box 1663  
Los Alamos, NM 87545

Douglas M. Risch  
Mirror Fusion Test Facility  
Lawrence Livermore Lab  
P.O. Box 808/L542  
Livermore, CA 94550

Kenneth I. Robinson  
Carborundum-Graphite Prod. Div.  
1999 S. Bascom Ave. Suite 935  
Camphill, CA 95008

Doyle Rogers  
Lawrence Livermore Labs  
P.O. Box 808  
Livermore, CA 94550

Gerald J. Rohwein  
Sandia Labs  
P.O. Box 5800  
Albuquerque, NM 87115

M. F. Rose  
Naval Surface Weapons Center  
Code F-404  
Dahlgren, VA 22448

Randall I. Ross  
Lawrence Livermore Labs  
MS 1-540  
P.O. Box 808  
Livermore, CA 94550

W. J. Sarjeant  
Los Alamos Scientific Labs  
MS 429  
P.O. Box 1663  
Los Alamos, NM 87545

Franklin J. Sazama  
Naval Surface Weapons Center  
White Oak Lab  
Silver Spring, MD 20910

R. Scarlett  
Los Alamos Scientific Labs  
P.O. Box 1663  
Los Alamos, NM 87545

Raymond Scarpetti  
Lawrence Livermore Labs  
L-153  
P.O. Box 5504  
Livermore, CA 94550

Lt. Col. J. F. Schaefer  
Air Force Weapons Lab/CA  
Kirtland AFB  
Albuquerque, NM 87117

Victor E. Scherrer  
Naval Research Lab  
Overlook Ave.  
Washington, DC 20375

Leland Schlitt  
Lawrence Livermore Lab  
P.O. Box 808  
Livermore, CA 94550

Karl Schönbach  
Dept. of Electrical Engineering  
Texas Tech University  
Lubbock, TX 79409

Sol Schneider  
U. S. Army Electronics Technology  
and Devices Lab  
Ft. Monmouth, NJ 07703

Charles W. Schubert, Jr.  
7062 Bascomb Dr.  
Dayton, OH 45424

Peter Seibt  
Dept. of Physics  
Texas Tech University  
Lubbock, TX 79409

John Shannon  
Maxwell Laboratories  
8835 Balboa Ave.  
San Diego, CA 92123

G. Simcox  
Raytheon Corp.  
South Bedford St.  
Burlington, MA 01803

David L. Smith  
2095-B Falcon Place  
Albuquerque, NM 87118

F. H. Smith  
ARO, Inc. AEDC Div.  
Arnold Air Force Station  
Tennessee 37389

Franklin R. Smith  
U.S. Army Engineers  
HND ED-FD  
Huntsville, AL 35802

Ian D. Smith  
3115 Gibbons Dr.  
Alameda, CA 94501

Richard A. Smith  
Naval Surface Weapons Center  
White Oak Lab  
Silver Spring, MD 20910

R. L. Snelling  
English Electric Valve Co. Ltd.  
Waterhouse Lane  
Chelmsford Essex CMI-2QU  
England

P. Spence  
Physics International  
2700 Merced St.  
San Leandro, CA 94577

Thomas E. Springer  
Los Alamos Scientific Laboratory  
MS-429, E-4  
P.O. Box 1663  
Los Alamos, NM 87545

Jere D. Stabley  
RCA  
New Holland Pike  
Lancaster, PA 17601

Charles H. Stallings  
Physics International  
2700 Merced St.  
San Leandro, CA 94577

Alex G. Stewart  
Harry Diamond Labs  
2800 Powder Mill Rd.  
Adelphi, MD 20783

Robert Stine  
Los Alamos Scientific Labs  
P.O. Box 1663  
Los Alamos, NM 87545

Regan W. Stinnett  
Sandia Laboratories  
Div. 4252  
P.O. Box 5800  
Albuquerque, NM 87115

T. H. Storr  
AWRE Aldermaston  
BLDG. H36  
Berks, RG 7 4 PR  
Tadley 4111  
England

J. V. Stover  
Hughes Aircraft Company  
Bldg. 600 MS F145  
P. O. Box 3310  
Fullerton, CA 92634

Gordon F. Thomas  
Naval Surface Weapons Center  
Code DR-54  
Dahlgren, VA 22448

Don Thomas  
R & D Associates  
4667 Admiralty Way  
Marina Del Rey, CA 92017

Jim Thompson  
College of Engineering  
University of South Carolina  
Columbia, SC 29208

Gary A Tripoli  
Ion Physics  
South Bedford St.  
Burlington, MA 01809

William K. Tucker  
Sandia Labs  
Div. 4253  
Albuquerque, NM 87115

David Turnquist  
E G & G  
35 Congress St.  
Salem, MA 01970

Peter J. Turchi  
Naval Research Lab  
Code 6770  
Washington, DC 20375

V. D. Valencia  
Exxon Nuclear Co.  
P. O. Box 130  
Richland, VA 99352

Fred Van Haaften  
Los Alamos Scientific Laboratory  
P. O. Box 1663  
Los Alamos, NM 87544

Richard Verga  
Air Force Aero Propulsion Lab  
POD  
Wright-Patterson AFB, OH 45433

I. M. Vitkovitsky  
Naval Research Lab  
Code 6770  
Washington, DC 20375

G. Wakalopoulos  
High Energy Device Dev. Section  
Hughes Aircraft Co.  
Aerospace Groups 6/C129  
Culver City, CA 90230

Roger Warren  
Rt. 3 Box 36  
Santa Fe, NM 87501

Alan Watson  
Dept. of Electrical Engineering  
Texas Tech University  
Lubbock, TX 79409

Harold Watson  
AiResearch Mfg. Co.  
MS T-42  
2525 W. 190th  
Torrance, CA 90509

Richard J. Wasneski  
Naval Air Systems Command  
350-F  
Washington, DC 20361

Maurice Weiner  
U. S. Army Elect. Technology  
and Device Lab  
Ft. Monmouth, NJ 07703

William F. Weldon  
167 Taylor Hall  
University of Texas/Austin  
Austin, TX 78712

Frazer Williams  
Dept. of Electrical Engineering  
Texas Tech University  
Lubbock, TX 79409

Charles B. Wharton  
Occidental Research Lab/Phillips Hall  
Cornell University  
Ithaca, NY 14853

Forest E. White  
BDM Corp.  
2600 Yale Blvd. SE  
Albuquerque, NM 87106

R. A. White  
Sandia Labs  
Pulsed Power Project Div. 4251  
Albuquerque, NM 87185

Roger White  
Maxwell Laboratories  
8835 Balboa Avenue  
San Diego, CA 92123

Kenneth Whitham  
Lawrence Livermore Labs  
P. O. Box 808 L-464  
Livermore, CA 94550

Paul Wildi  
Fusion Research Center RLM 12.3  
University of Texas/Austin  
Austin, TX 78712

James W. Willis  
Naval Air Systems Command  
AIR 310B  
Washington, DC 20361

Walter L. Willis  
Los Alamos Scientific Labs  
MS 566  
P. O. Box 1663  
Los Alamos, NM 87545